Challa S. S. R. Kumar *Editor*

Surface Science Tools for Nanomaterials Characterization

INCLUDED IN SPRINGERMATERIALS.COM

Springer

Surface Science Tools for Nanomaterials Characterization

Challa S. S. R. Kumar
Editor

Surface Science Tools for Nanomaterials Characterization

With 293 Figures and 10 Tables

Springer

Editor
Challa S. S. R. Kumar
Center for Advanced Microstructures and Devices
Baton Rouge, LA, USA

ISBN 978-3-662-44550-1 ISBN 978-3-662-44551-8 (eBook)
DOI 10.1007/978-3-662-44551-8
Springer Heidelberg New York Dordrecht London

Library of Congress Control Number: 2015930198

© Springer-Verlag Berlin Heidelberg 2015
This work is subject to copyright. All rights are reserved by the Publisher, whether the whole or part of the material is concerned, specifically the rights of translation, reprinting, reuse of illustrations, recitation, broadcasting, reproduction on microfilms or in any other physical way, and transmission or information storage and retrieval, electronic adaptation, computer software, or by similar or dissimilar methodology now known or hereafter developed. Exempted from this legal reservation are brief excerpts in connection with reviews or scholarly analysis or material supplied specifically for the purpose of being entered and executed on a computer system, for exclusive use by the purchaser of the work. Duplication of this publication or parts thereof is permitted only under the provisions of the Copyright Law of the Publisher's location, in its current version, and permission for use must always be obtained from Springer. Permissions for use may be obtained through RightsLink at the Copyright Clearance Center. Violations are liable to prosecution under the respective Copyright Law.
The use of general descriptive names, registered names, trademarks, service marks, etc. in this publication does not imply, even in the absence of a specific statement, that such names are exempt from the relevant protective laws and regulations and therefore free for general use.
While the advice and information in this book are believed to be true and accurate at the date of publication, neither the authors nor the editors nor the publisher can accept any legal responsibility for any errors or omissions that may be made. The publisher makes no warranty, express or implied, with respect to the material contained herein.

Printed on acid-free paper

Springer is part of Springer Science+Business Media (www.springer.com)

Contents

1 Scanning Electrochemical Potential Microscopy (SECPM) and Electrochemical STM (EC-STM) 1
Max Herpich, Jochen Friedl, and Ulrich Stimming

2 Recovering Time-Resolved Imaging Forces in Solution by Scanning Probe Acceleration Microscopy: Theory and Application 69
Maxmore Chaibva, Nicole Shamitko-Klingensmith, and Justin Legleiter

3 Scanning Probe Microscopy for Nanolithography 91
C. B. Samantaray

4 Kelvin Probe Force Microscopy in Nanoscience and Nanotechnology 117
Da Luo, Hao Sun, and Yan Li

5 Field Ion Microscopy for the Characterization of Scanning Probes 159
William Paul and Peter Grütter

6 Scanning Conductive Torsion Mode Microscopy 199
Ling Sun and Elmar Bonaccurso

7 Field Ion and Field Desorption Microscopy: Principles and Applications 227
Yuri Suchorski

8 Noncontact Atomic Force Microscopy for Atomic-Scale Characterization of Material Surfaces 273
Mehmet Z. Baykara

9 Applications of Synchrotron-Based X-Ray Photoelectron Spectroscopy in the Characterization of Nanomaterials 317
W. H. Doh, V. Papaefthimiou, and S. Zafeiratos

10 Exploration into the Valence Band Structures of Organic Semiconductors by Angle-Resolved Photoelectron Spectroscopy 367
Yasuo Nakayama and Hisao Ishii

11 Band Bending at Metal-Semiconductor Interfaces, Ferroelectric Surfaces and Metal-Ferroelectric Interfaces Investigated by Photoelectron Spectroscopy 405
Nicoleta Georgiana Apostol and Cristian-Mihail Teodorescu

12 Higher Resolution Scanning Probe Methods for Magnetic Imaging 463
S. N. Piramanayagam and Binni Varghese

13 Imaging and Characterization of Magnetic Micro- and Nanostructures Using Force Microscopy 489
Stephan Block

14 Combining Micromanipulation, Kerr Magnetometry and Magnetic Force Microscopy for Characterization of Three-Dimensional Magnetic Nanostructures 531
Amalio Fernández-Pacheco, Russell P. Cowburn, Luis E. Serrano-Ramón, M. Ricardo Ibarra, and José M. De Teresa

15 High Resolution STM Imaging 561
Alexander N. Chaika

16 Numerical and Finite Element Simulations of Nanotips for FIM/FEM 621
Moh'd Rezeq, Ahmed E. Ali, and Dirar Homouz

Index 645

Contributors

Ahmed E. Ali Department of Electrical and Computer Engineering, Khalifa University of Science, Technology and Research (KUSTAR), Abu Dhabi, UAE

Nicoleta Georgiana Apostol National Institute of Materials Physics, Magurele-Ilfov, Romania

Mehmet Z. Baykara Department of Mechanical Engineering and UNAM – Institute of Materials Science and Nanotechnology, Bilkent University, Ankara, Turkey

Stephan Block Department of Physics, Ernst–Moritz–Arndt University of Greifswald, Greifswald, Germany

Applied Physics, Chalmers University of Technology, Gothenburg, Sweden

Elmar Bonaccurso Center of Smart Interfaces, Technische Universität Darmstadt, Darmstadt, Germany

Airbus Group Innovations, Metallic Technologies and Surface Engineering – TX2, Munich, Germany

Maxmore Chaibva The C. Eugene Bennett Department of Chemistry, West Virginia University, Morgantown, WV, USA

WV NanoSAFE, West Virginia University, Morgantown, WV, USA

Alexander N. Chaika Institute of Solid State Physics, Russian Academy of Sciences, Chernogolovka, Moscow District, Russia

Centre for Research on Adaptive Nanostructures and Nanodevices (CRANN), School of Physics, Trinity College Dublin, Dublin, Ireland

Russell P. Cowburn Cavendish Laboratory, University of Cambridge, Cambridge, UK

José M. De Teresa Instituto de Ciencia de Materiales de Aragón (ICMA), Departamento de Física de la Materia Condensada, Universidad de Zaragoza–CSIC, Zaragoza, Spain

Laboratorio de Microscopias Avanzadas (LMA), Instituto de Nanociencia de Aragón (INA), Universidad de Zaragoza, Zaragoza, Spain

W. H. Doh Institut de chimie et procédés pour l'énergie, l'environnement et la santé (ICPEES), UMR 7515 du CNRS-Université de Strasbourg, ECPM, Strasbourg, France

Amalio Fernández-Pacheco Cavendish Laboratory, University of Cambridge, Cambridge, UK

Jochen Friedl TUM CREATE, 1 CREATE Way, CREATE Tower, Singapore, Singapore

Department of Physics E19, Technische Universität München, Garching, Germany

Peter Grütter Physics Department, McGill University, Montréal, QC, Canada

Max Herpich TUM CREATE, 1 CREATE Way, CREATE Tower, Singapore, Singapore

Department of Physics E19, Technische Universität München, Garching, Germany

Dirar Homouz Department of Applied Mathematics and Sciences, Khalifa University of Science, Technology and Research (KUSTAR), Abu Dhabi, UAE

M. Ricardo Ibarra Departamento de Física de la Materia Condensada, Universidad de Zaragoza, Zaragoza, Spain

Laboratorio de Microscopias Avanzadas (LMA), Instituto de Nanociencia de Aragón (INA), Universidad de Zaragoza, Zaragoza, Spain

Hisao Ishii Graduate School of Advanced Integration Science, Chiba University, Chiba, Japan

Center for Frontier Science, Chiba University, Chiba, Japan

Justin Legleiter The C. Eugene Bennett Department of Chemistry, West Virginia University, Morgantown, WV, USA

WV NanoSAFE, West Virginia University, Morgantown, WV, USA

The Center for Neurosciences, West Virginia University, Morgantown, WV, USA

Yan Li Beijing National Laboratory for Molecular Sciences, Key Laboratory for the Physics and Chemistry of Nanodevices, College of Chemistry and Molecular Engineering, Peking University, Beijing, China

Da Luo Beijing National Laboratory for Molecular Sciences, Key Laboratory for the Physics and Chemistry of Nanodevices, College of Chemistry and Molecular Engineering, Peking University, Beijing, China

Yasuo Nakayama Graduate School of Advanced Integration Science, Chiba University, Chiba, Japan

V. Papaefthimiou Institut de chimie et procédés pour l'énergie, l'environnement et la santé (ICPEES), UMR 7515 du CNRS-Université de Strasbourg, ECPM, Strasbourg, France

William Paul IBM Research Division, Almaden Research Center, San Jose, CA, USA

S. N. Piramanayagam Data Storage Institute, A*STAR (Agency for Science, Technology and Research), Singapore, Singapore

Moh'd Rezeq Department of Applied Mathematics and Sciences and Department of Electrical and Computer Engineering, Khalifa University of Science, Technology and Research (KUSTAR), Abu Dhabi, UAE

C. B. Samantaray College of Engineering & Technology, Virginia State University, Petersburg, VA, USA

Luis E. Serrano-Ramón Instituto de Ciencia de Materiales de Aragón (ICMA), Departamento de Física de la Materia Condensada, Universidad de Zaragoza-CSIC, Zaragoza, Spain

Nicole Shamitko-Klingensmith The C. Eugene Bennett Department of Chemistry, West Virginia University, Morgantown, WV, USA

WV NanoSAFE, West Virginia University, Morgantown, WV, USA

Ulrich Stimming School of Chemistry, Bedson Building, Newcastle University, Newcastle upon Tyne, UK

Fakultaet fuer Informatik, Technische Universität München, Garching, Germany

Yuri Suchorski Institute of Materials Chemistry, Vienna University of Technology, Vienna, Austria

Hao Sun Nano Surfaces Division, Bruker (Beijing) Scientific Technology Co., Ltd, Beijing, China

Ling Sun Department of Micro- and Nanotechnology, Technical University of Denmark, Kgs. Lyngby, Denmark

Cristian-Mihail Teodorescu National Institute of Materials Physics, Magurele-Ilfov, Romania

Binni Varghese Data Storage Institute, A*STAR (Agency for Science, Technology and Research), Singapore, Singapore

S. Zafeiratos Institut de chimie et procédés pour l'énergie, l'environnement et la santé (ICPEES), UMR 7515 du CNRS-Université de Strasbourg, ECPM, Strasbourg, France

Scanning Electrochemical Potential Microscopy (SECPM) and Electrochemical STM (EC-STM)

1

Max Herpich, Jochen Friedl, and Ulrich Stimming

Contents

1 Definition of the Topic 2
2 Overview 2
3 Introduction 3
4 Experimental and Instrumental Methodology 4
  4.1 STM 4
  4.2 EC-STM 6
  4.3 SECPM 7
  4.4 Local Activity Measurements 8
  4.5 Deconvolution of Images 9
5 Key Research Findings: Electrocatalysis on Metal Single-Crystal Surfaces 14
  5.1 Sample Preparation 16
  5.2 Platinum Substrates 18
  5.3 Gold Substrates 27
  5.4 SPM on Single-Crystal Surfaces 33
6 Key Research Findings: Biomolecules 37
  6.1 Introduction 37
  6.2 Unraveling the Electron Transfer Mode Through Adsorbed Biomolecules in EC-STM 43

M. Herpich • J. Friedl
TUM CREATE, 1 CREATE Way, CREATE Tower, Singapore, Singapore

Department of Physics E19, Technische Universität München, Garching, Germany

U. Stimming (✉)
School of Chemistry, Bedson Building, Newcastle University, Newcastle upon Tyne, UK

Fakultaet fuer Informatik, Technische Universität München, Garching, Germany
e-mail: Ulrich.Stimming@newcastle.ac.uk

© Springer-Verlag Berlin Heidelberg 2015

C.S.S.R. Kumar (ed.), *Surface Science Tools for Nanomaterials Characterization*,
DOI 10.1007/978-3-662-44551-8_1

6.3 Shape and Size of Biomolecules 48
6.4 Applications, Designing Devices 58
7 Conclusions and Future Perspective 60
References 61

Keywords

Scanning probe microscopy • Scanning electrochemical potential microscopy • Electrochemical scanning tunneling microscopy • Electrocatalysis

Dedicated to Maria-Elisabeth Michel-Beyerle and Rudolph A. Marcus; their seminal work provided an important basis for the review given here.

1 Definition of the Topic

Scanning electrochemical potential microscopy (SECPM) and electrochemical scanning tunnelling microscopy (EC-STM) allow for imaging the solid-liquid interface under in situ electrochemical conditions. In this chapter we take a look at two important aspects of SECPM and EC-STM studies: First, investigations on model electrode systems relevant for electrocatalysis are presented. Second, studies on the behavior of biomolecules immobilized on electrodes are shown. In both cases the use of EC-STM or SECPM allows for insights into the electrochemistry at a molecular level which cannot be achieved by other, rather integrating, methods.

2 Overview

EC-STM and SECPM are able to show samples immersed in electrolyte at very high resolutions, for EC-STM atomic resolution was realized. The imaging principles for both techniques, however, are intricate. Therefore, we will describe the origin of images in detail. Then we will review recent publications for both EC-STM and SECPM, concentrating on studies on metal single crystals for catalysis and redox-active biomolecules.

Electrochemical interfaces are of a fundamental interest and at the core of electrical energy storage and energy conversion applications such as batteries, fuel cells, and supercapacitors. At the same time, nanostructured surfaces and interfaces are of ever-increasing importance in other fields. On the one hand, nanostructured surfaces typically show enhanced transport properties and an increased electrochemical active surface area. On the other hand, new functionalities emerge for nanoparticles or sub-monolayers of catalysts on supports.

Typical electrochemical investigation techniques, however, are not sensitive to the local structure of one single nano-sized spot on the electrode; they monitor the average activity of the whole surface, which might consist of an ensemble of

nanoparticles and support. This is where the high local resolution enabled by the tip of EC-STM or SECPM steps in. Both methods are in situ techniques; they can monitor the interface at a specific point under full current or potential control. The point of interest can be a single nanoparticle, a grain boundary, a step edge, a single biomolecule, etc.

3 Introduction

As Enrico Fermi (1901–1954) put it: "God made the solid phase and left the surface to the devil" [1]. This statement stresses the intricacy of surface studies, wherever two or more phases meet. As such, the devil must have greatly resented Binnig's and Rohrer's development of the scanning tunnelling microscope (STM) in 1982 [2]. For the first time it was possible to investigate surfaces on a sub-nanometer scale. In 1986 Sonnenfeld and Hansma showed that it is possible to transfer the STM setup into liquid environments and the EC-STM was created [3]. Since then EC-STM has become a powerful tool for observing electrochemical processes at the solid-electrolyte interface with the capability to monitor single molecules or even atoms. In 2006 SECPM was introduced by Bard et al. adding the possibility of surface potential mapping to the field of electrochemical scanning probe microscopy (SPM) [4]. One of the most important advantages of SECPM over EC-STM is that the former does not require (semi)conducting samples, as not a current but a local potential distribution is measured and used to generate images.

Section 4 of this chapter will deal with the introduction of EC-STM and SECPM. Theoretical background, experimental setups, and operating principles will be explained. While EC-STM and SECPM are very powerful techniques, their imaging principle is less intuitive than it is for other microscopes, and especially the electrolyte can complicate things considerably. Therefore, we will also critically look into the interpretation of data obtained from these two in situ SPMs.

The ultimate goal of catalyst research is to design and tune the activity of catalysts by carefully controlling of their structural and compositional properties, down to the level of single atoms [5, 6]. This atomistic engineering of surfaces requires potent imaging techniques. Historically, ultrahigh vacuum (UHV) methods such as low-energy electron diffraction (LEED) or STM were extremely important for the study of surfaces [7]. However, these ex situ methods could not reproduce the real electrochemical environment, even though it was possible to immerse electrodes with intact electrochemical double layer [8]. Therefore, EC-STM and SECPM are the ideal tools to investigate electrodes directly in an electrolyte. For model catalyst studies, it is important to investigate the composition and structure of catalysts before and during electrochemical reactions and to measure the local activity at certain sites. In Sect. 5 we will present SPM microscopy studies on model catalysts.

The study of redox-active enzymes and proteins is somewhat related to the former topic of model catalysts. Enzymes are the most accomplished expression of molecular catalysis and perform very specific tasks. They are the building blocks of life and prime actors of cell metabolism. Therefore, the study of single

biomolecules via EC-STM and SECPM can be very rewarding. In Sect. 6 we will show how horseradish peroxidase can be visualized with SECPM to reveal stunning details on the location of the active site. Furthermore, we will present how interplay of theoretical and experimental studies led to the elucidation of the electron transfer mechanism from tip to sample via redox-active molecule or vice versa. We will also introduce efforts to create bioelectronics such as storage devices and transistors from proteins immobilized on electrodes.

After the presentation of the key research findings, Sects. 5, 6, and 7 will give a conclusion and a further outlook for the application of SECPM and EC-STM as characterization tools for nanoscience and nanotechnology.

4 Experimental and Instrumental Methodology

4.1 STM

The scanning tunnelling microscope utilizes the quantum mechanical tunnelling of electrons between a sharp metal tip and a conductive sample to create an "image" of a flat surface. When a bias voltage U_{bias} is applied between tip and sample and the tip is brought close to the surface, electrons will tunnel through the gap. They will either move from the tip into unoccupied states of the sample surface or from occupied surface states into the tip where the direction of electron flow depends on the polarity of the bias voltage. This means the tunnelling current is proportional to the overlap integral of the density of states in the sample at the position of the tip [9]. Atoms of different materials or in different electronic states can show different apparent heights on the STM image while actually resting at exactly the same height. The high distance resolution in STM stems from the fact that the tunnelling current I_t falls exponentially with the gap distance z:

$$I_t \propto U_{\text{bias}} \exp\left[-A\sqrt{\Phi_{\text{eff}}}\, z\right] \tag{1.1}$$

Here Φ_{eff} is the effective barrier height and a vacuum value $A = 10.12\ \text{eV}^{-1/2}\,\text{nm}^{-1}$. For most samples this leads to a current drop of about one order of magnitude per Å increase in z.

A surface profile can be obtained by scanning the tip across the sample while measuring the current through an amplifier. In each line scan the tunnelling current is measured hundreds of times, and hundreds of these line scans are combined to form a two-dimensional image of the surface. During the measurement, a piezoelectric scanner controls the movement of either tip or sample in sub-nanometer steps while the other is held in position.

There are two modes of operation for the STM. In constant current mode (Fig. 1.1), the tunnelling current is held at a constant, pre-adjusted set point value, usually in the pico- or nano-Ampère region. Through a feedback loop, the tip height is adjusted to match the set point current with each scanning step, keeping

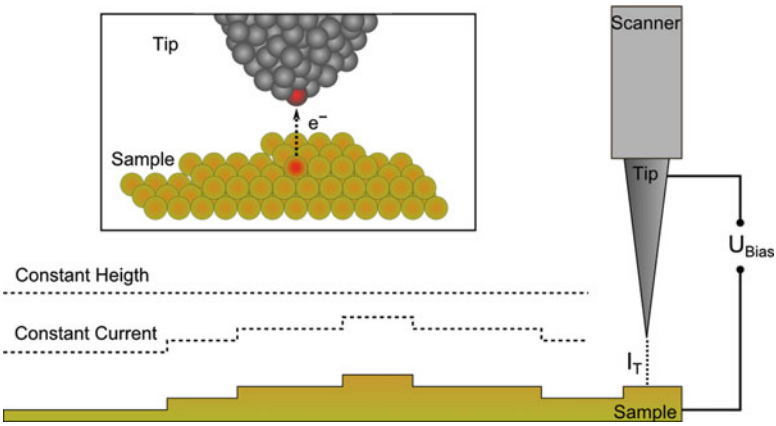


Fig. 1.1 Schematic of STM functionality. The scanner moves the tip across the sample in close proximity while a bias voltage U_{bias} is applied that causes electrons to tunnel through the gap between the two. The *dashed lines* symbolize the path of the tip in the different modes of operation. The *inset* shows an illustration of the ideal tunnelling measurement where only one atom on the end of the tip causes most of the tunnelling current

the distance between tip and sample more or less fixed. The voltage necessary to move the scanner piezo in z-direction is recorded and converted into a height profile of the sample. The best image quality can be achieved on flat surfaces where the feedback loop does not have to adjust much change. Also, the maximum scan height is usually limited by the range of the scanner piezo to a few micrometers.

In constant height mode (Fig. 1.1), the tip is scanned across the sample at a fixed distance while the tunnelling current is measured and directly converted into an image. This mode allows much faster scan speeds because it is not limited by the speed of the feedback loop. Due to the fixed height, however, on rougher samples, the tip can come into direct contact with the sample which can cause damage to both tip and sample, so the use of this mode is only advisable for very flat samples and small scan areas. All STM images shown in this chapter were acquired in constant current mode unless stated otherwise.

STM tips are generally made of metal wire and there is a wide range of materials that can be used. Most wires are electrochemically etched until a sharp end with a curvature radius of ideally only a few nanometers is produced. A common material for STM measurements in air or vacuum is tungsten because of its high stiffness which makes the tips more durable; however, it will slowly oxidize in air. Another way to prepare sharp tips is by cutting. This works best on Pt/Ir wires and is a much faster way of preparation. A typical cut tip has not one sharp apex like an etched one but several small protrusions, the longest of which is responsible for the tunnelling. On rougher samples this may lead to bad image quality because different protrusions can cause a tunnelling current at different positions over the sample. In electrolyte, the measured current will be the sum of the tunnelling current and unavoidable faradaic charge transfer currents. Since it is not possible to distinguish between those currents, it is

necessary to reduce the electrochemical currents to a value below the tunnelling current. This can be achieved by coating the tip with an insulating and inert material, leaving only a small part at the apex uncoated. The small exposed area reduces the faradaic currents, while the tunnelling current is not affected because only the last few atoms of the apex contribute to it. Typical coating materials include Apiezon wax, hot-melt glue (polyethylene), glass, electrophoretic paint, and nail polish.

The material for the STM tips has to be chosen to be inert under experimental conditions. Electrochemical reactions at the tip can lead to deposition of material on the tip, broadening the apex and decreasing the resolution. Currents from those reactions will be measured in addition to the tunnelling current, making image acquisition impossible. Also reactions may cause changes of electrochemical conditions around the tip such as ion concentration in the electrolyte and shifting of the potential which can alter the reactions at the sample in the scanned region. The most common materials are tips etched from gold and platinum/iridium wires because they have a wide potential window in which they can be operated.

Another critical factor for STM operation is the isolation of the system from external vibration, especially building vibrations. Because of the small length scales in the measurement, even the smallest vibrations can cause distorted images or even damage to the tip if it comes into contact with the sample. Suspending the microscope on springs or an active vibration reduction system will cancel out most vibrations. Also it is advisable to protect the setup from acoustic noise and air flow which can also deteriorate image quality.

4.2 EC-STM

EC-STM is used to investigate processes in the solid-electrolyte interface region. Since electrolytes are not electronically conductive, they can function as a dielectric like vacuum or air. Thus the basic principle of operation is the same as previously explained for STM, but a few modifications to the setup have to be made to allow full electrochemical control and successful measurement of the tunnelling current.

For electrochemical tunnelling experiments, the potentials of tip (U_{tip}) and sample (U_{sample}) have to be controlled separately, instead of only controlling $U_{\text{bias}} = U_{\text{tip}} - U_{\text{sample}}$. Therefore a bipotentiostat is often introduced into the STM setup. Both potentials are measured versus a reference electrode (RE) which in most cases consists of a metal that acts as a pseudo reference electrode while another wire functions as counter electrode (CE). An example for an electrochemical cell for EC-STM with this four-electrode setup is depicted in Fig. 1.2. The sample functions as working electrode, and a cell made of inert material is placed on top of it, held in place by screws or clips in a way that the sample surface makes up the bottom of the cell. The electrolyte is filled in from the top, and CE, RE, and the coated tip are inserted from the top. Special caution has to be taken here that the contact area between cell and sample is sealed tight that no electrolyte can leak through. Sometimes this is accomplished by using an O-ring between cell and sample.

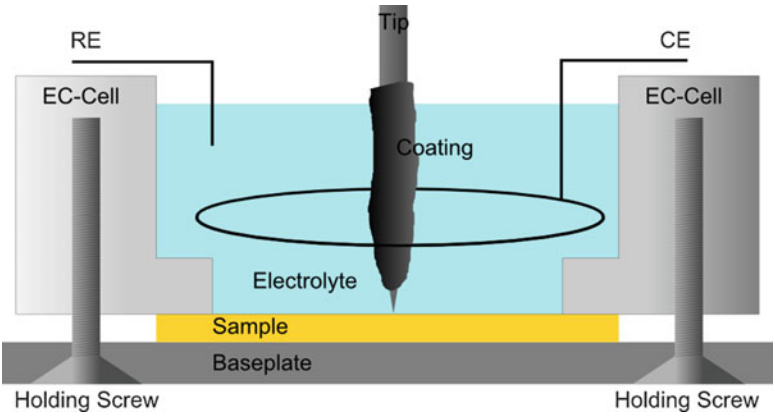


Fig. 1.2 Example for an EC-STM cell setup. The sample sits on a conductive baseplate for electrical contact while the cell is pressed tight on the sample with screws. The cell is filled with electrolyte and the coated tip, counter electrode (CE), and reference electrode (RE) are immersed in the liquid

4.3 SECPM

In 2004 Woo et al. [10] showed a way to probe the electrochemical double layer (ECDL) of the solid-electrolyte interface in sub-nanometer spatial resolution on a Au(111) surface in $NaBF_4$ solution of various concentrations. A probe similar to an EC-STM tip was designed. In a four-electrode setup, the probe was left at open circuit while different potentials were applied to the Au working electrode. Far from the surface, the potential measured at the tip showed the bulk potential of the solution. By slowly approaching the surface, the tip entered the ECDL region, and the measured potential gradually changed until the applied electrode potential was reached when probe and surface came into contact. To make sure the exact value at the tip position is read, the exposed part of the tip cannot protrude far from the coating because that would lead to different areas of the tip being in contact with different regions of the double layer with different potentials, leading to lower spatial resolution. In order to reach this requirement, the tip apex was etched until a disk-shaped area remained. It also has to be taken into consideration that the measured potential is a result of the overlapping ECDLs of probe and sample.

This method was further developed into scanning electrochemical potential microscopy by Bard et al. [4] in 2006. While the cell setup for SECPM remains the same as for EC-STM, instead of the tunnelling current, the potential difference between the tip and the potential gradient in the sample's ECDL is used to map the surface. The current preamplifier of STM measurements has to be replaced by a high-impedance potential difference amplifier. Most systems capable of SECPM have both amplifiers installed, allowing the user to switch between the two modes through the control software without making physical changes to the setup. This enables scans of the same region of the sample surface with both techniques for a

direct comparison of surface topography and potential map [11, 12]. The scanning procedure for SECPM is comparable to that for STM, and equivalent to constant current and constant height mode there are the two modes of constant potential and constant height in SECPM.

4.4 Local Activity Measurements

Beyond imaging the surface and nanoscopic objects thereon, the STM setup is also suitable to investigate electrochemical activity with a nano-resolution [13–15]. As an example, electrochemically active nanoparticles on a rather inert surface can be studied, e.g., with respect to hydrogen evolution. In this case a potential is applied to the electrode where hydrogen is evolved predominantly from the active particle but less from the substrate. The STM tip – being out of tunnelling mode – acts as a sensor electrode (the potential is set to a value where hydrogen is oxidized) which records a current that is proportional to hydrogen evolution. For small particles $<1/10$ of the tip diameter, the collection efficiency is unity.

The idea behind this technique is that the reaction products of an active species on the working electrode are reversibly converted into faradaic current at the tip. For example, the hydrogen evolution reaction (HER)

$$2H^+ + 2e^- \rightarrow H_2 \tag{1.2}$$

under investigation at a nanoparticle leads to the reverse hydrogen oxidation reaction (HOR) at the STM tip

$$H_2 \rightarrow 2H^+ + 2e^- \tag{1.3}$$

which can then be detected. A sequence of steps has to be performed for the local reactivity measurement. First, the tip is placed over the position where the reactivity will be measured and then retracted $\approx$10 nm, far enough that no more tunnelling current adds to the measured value. Next, a potential pulse is applied to the sample, so HER takes place at the particle and the HOR current can be recorded at the tip (Fig. 1.3 left). The tip stays retracted for several seconds to record the HOR current (Fig. 1.3 right). Last, the tip is retracted to tunnelling distance again in order to record an image to make sure the position and morphology of the investigated object did not change. The measured current (corrected by subtracting the background current) is then integrated to gain the total charge and divided by pulse time to get the average current. Knowing the morphology of the particle, the current density j and the exchange current density j_0 can be calculated.

The use of current-potential curves for analysis of reaction mechanisms averages over the whole surface of the sample. However, heterogeneous reactions show nonuniform reaction rates depending on the position on the surface. Zhang et al. demonstrated that EC-STM can be used to measure local reaction rates on the nm scale [16] under potential control. Thus STM measurements can be used to evaluate electrochemical kinetics on a nanoscopic scale.

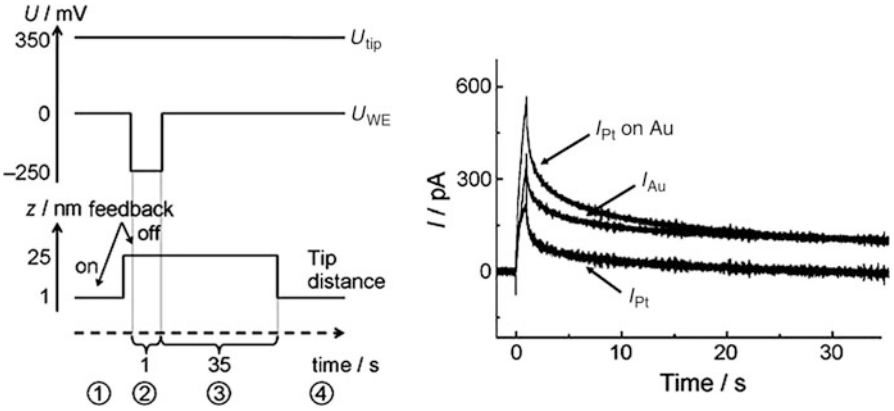


Fig. 1.3 *Left*: potential distribution at the tip and working electrode together with tip distance in nm during reactivity measurements. *Right*: typical current transient of local reactivity measurements, showing reactivity of bare gold (I_{Au}), after creation of a Pt cluster ($I_{Pt\ on\ Au}$) and the corrected current evolved by the Pt particle (I_{Pt}) (Reprinted from Ref. [15]. Copyright 2010. Reprinted by permission of Wiley-VCH Verlag GmbH & Co)

4.5 Deconvolution of Images

Microscopes rely on absorption, transmission, diffraction, or interaction of beams of light or electrons and usually directly monitor topology or composition of a sample. STM, EC-STM, and SECPM use a less intuitive mechanism. Therefore, it is worthwhile to take a look at what is actually monitored by the interplay of the tip and sample.

The fact that one sample might look completely different at two different potentials adds to the complexity. However, this intricacy allows for detailed mapping of the electronic structure of samples. In addition, the presence of the electrolyte in the case of EC-STM and SECPM leads to some additional signals that have to be considered and taken into account in searching for a "topography" of the surface.

4.5.1 EC-STM: Influence of Electrolyte and Electron Transfer Modes Through Adsorbed Molecules

In their seminal work about the theory of STM, Tersoff and Hamann found the tunnelling current to be proportional to the local density of states (LDOS) of the sample at the position of the tip [9]. It was stated in the previous sections that the tunnelling current shows an exponential dependency on the distance between the tip and sample Eq. 1.1. However, this exponential character of the curve has so far not been observed for EC-STM during investigations of the solid-liquid interface [17]. Three exemplary graphs for the approach of an STM tip towards a highly oriented pyrolytic graphite (HOPG) surface are shown in Fig. 1.4. While the curve in air matches the theoretical curve quite well, the curve in water exhibits almost linear distance behavior [18]. This effect was attributed to the presence of a layer of water molecules at the solid-liquid interface; they were too mobile to be imaged though.

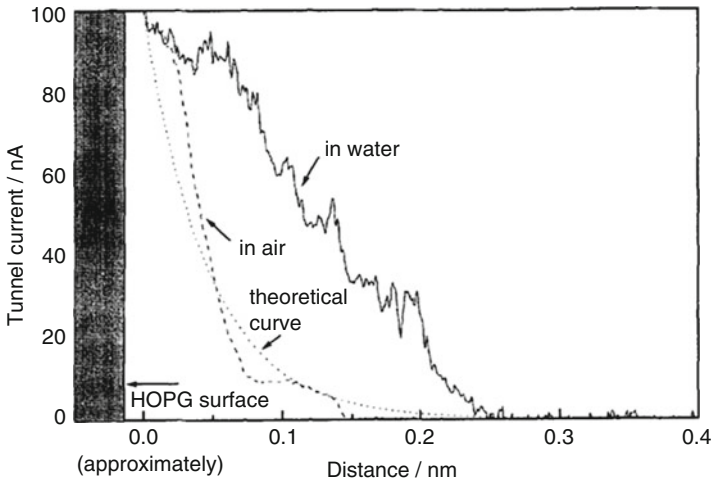


Fig. 1.4 Tunnelling current over the distance for the approach of a tungsten tip to a HOPG surface. The theoretical curve was calculated using an equation similar to Eq. 1.1 (Reprinted from Ref. [18]. Copyright 1996. Reprinted by permission of Elsevier)

Hugelmann and Schindler found oscillations in the tunnelling probability with a period of 0.35 nm when they probed the tunnelling current at a water-Au(111) interface [17]. As this periodicity corresponds well with the theoretical spacing of interfacial water layers, the authors suggested that the tunnelling process at the solid-liquid interface depends strongly on the electrolyte in the tunnelling gap. Recalculating this modulation to a varying Φ_{eff}, Hugelmann et al. found values ranging from below 1 eV to around 2.3 eV [19]. It was reported as early as 1995 that dipole resonances of ordered water molecules form intermediate states both at the tip/electrolyte and electrolyte/sample interface and that they can lead to a lowered tunnelling barrier for EC-STM [20].

Even earlier, in 1993, noise induced by movement of adsorbed atoms was theoretically studied [21, 22]. Particles diffusively moving within the tunnelling gap scatter electrons and therefore lead to a low-frequency current noise.

Therefore, it is safe to say that images obtained with EC-STM are not only a convolution of the LDOS of sample and tip, but that the properties of the electrolyte within the tunnelling gap will merge into the picture. Theoretical studies were performed to determine the contribution of the solvent in greater detail [21–24].

Another interesting property of EC-STM is enabled by the bipotentiostatic setup. U_{tip} and U_{sample} can be adjusted separately. Single molecules are characterized by a large separation between energy levels even at room temperature; this discrete nature of energy is caused by their small size. In contrast metallic tip and sample show a continuum of energy states which are filled with electrons until the Fermi level (E_F). When redox-active molecules are attached to the substrate, several modes of electron transfer (ET) from tip to substrate (or vice versa) via redox states of the molecule are conceivable [25, 26]. Schematic representations of these modes are shown in Fig. 1.5.

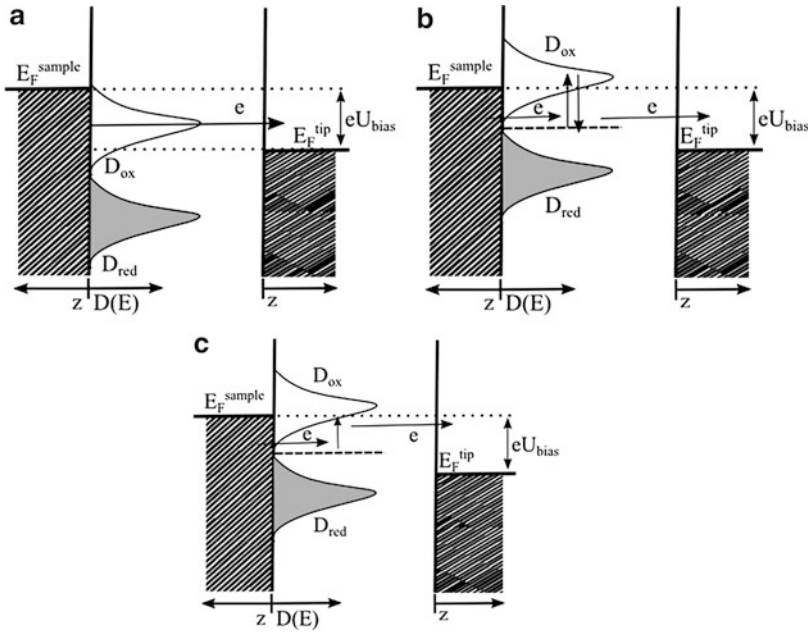


Fig. 1.5 Modes of electron transfer conceivable for tunnelling of an electron from the EC-STM sample to the tip via an adsorbed redox-active molecule. (**a**) Resonant tunnelling D_{ox} and Fermi levels E_F are aligned. (**b**) Sequential two-step ET. In the shown example, the sample is oxidized by the molecule in a first step and then the tip is reduced by the molecule. (**c**) Vibrationally coherent model. During the process of relaxation from the activated state to the unoccupied state of the molecule, the molecule is oxidized by the tip

One possible mode is resonant tunnelling (Fig. 1.5a). U_{sample} can be adjusted in a way that E_F of tip and sample is aligned with D_{ox}, the density of oxidized states of the adsorbed molecule [27]. D_{ox} and D_{red}, the density of reduced states, are not sharp energy levels but broadened to parabolic shape. This is caused by the interaction of the redox molecules with the solvent, according to Gerischer's theory [28, 29].

This alignment of E_F and D_{ox} leads to resonant tunnelling which in turn leads to a multifold increase in I_t, as observed by Tao experimentally [30]. The theory of resonant tunnelling was revisited and combined with stochastic dynamics later [31]. While in the initial theoretical approach, electrons could never be trapped in D_{ox}, in the stochastic adiabatic model of Schmickler and Kuznetsov, energy fluctuations of the redox level lead to short times when tunnelling is not permitted. This is represented in Fig. 1.5a by D_{ox} extending below the dashed line given by the Fermi Energy of the tip E_F^{tip}. Interaction with the solvent molecules can lead to configurations of the redox molecule with a free energy lower than E_F^{tip}, the electron cannot tunnel to the tip in that case, and it is trapped.

Another mode is sequential two-step ET (Fig. 1.5b). This mechanism is valid for the limiting case that the electron transfer is much slower than redox energy

fluctuations. Initial ET occurs between the negatively biased substrate and a transition state (activated complex) of the redox molecule [32]. From the activated complex, the electron relaxes to D_{ox}. In a second step, the electron is excited back into the transition state and then hops from the molecule onto the positively biased tip. Both processes are enabled by thermal activation and have no memory of each other [33].

A third possible mode is the vibrationally coherent two-step ET mode (Fig. 1.5c), which can be defined as intermediate between the two former cases [26, 34]. Similarly to sequential two-step ET, first ET takes place between the negatively biased substrate and the molecule. However, in this case the vibrational coherence between the first and second ET is not lost as the second step happens before the system is fully relaxed.

Sequential and coherent ET is physically different. The former can be formulated by electrochemical single-ET theory because only the tunnel factor of the rate-determining step appears in the rate equation; the more facile ET is in equilibrium. The latter contains the tunnelling factor of both transitions [35]. Which of these three modes actually takes place was investigated by a multitude of theoretical and experimental studies. These will be presented in Sect. 6.2 when we discuss the electron transfer mode through adsorbed biomolecules.

Zhang et al. published an extensive review on single-molecule electron transfer in electrochemical systems in 2008 [36]. A more recent review, dealing with interfacial electrochemistry of metalloproteins, was published in 2011 [37]. For an in-depth treatment of the theory of interfacial ET on macroscopic and molecular scale, the reader is referred to these publications.

4.5.2 SECPM: Theory of Electrochemical Double Layer and Convolution

In contrast to EC-STM, which maps the electron density, SECPM monitors the surface potential [12]. The observable is the potential difference $\Delta U = U_{\text{sample}} - U_{\text{tip}}$ in dependence of either tip position or distance z. When scanning the tip across the surface, a topographical image of the surface potential is created [12, 38]. We refer to this mode as potential mapping. Another possibility is to generate approach curves, measuring ΔU at fixed position. The results are curves similar to Fig. 1.4 but with ΔU as ordinate instead of I_t. Often the potential is normalized with respect to the tip potential at infinite distance from the sample $U_{\text{tip}}{}^{\text{inf}}$ [4]. This mode aims for directly recording the potential distribution in the ECDL. This potential distribution is predicted by the Gouy-Chapman-Stern (GCS) model which is an expansion to earlier models. Further refinement by Grahame includes specific adsorption and recognizes three distinct regions [39, 40]. They are, with increasing distance from the electrode:

- Inner Helmholtz plane (IHP). Formed by specific adsorption of anions onto the electrode
- Outer Helmholtz plane (OHP). Caused by electrostatic interaction of ions and the electrode
- Diffuse layer which shows an exponential decay of the potential

Both Helmholtz planes are rigid, independent of the electrode potential, and water molecules contribute greatly to them (compare Sect. 4.5.1). The extension of the diffuse layer depends on the properties of the supporting electrolyte such as the ion concentration.

In order to experimentally visualize this dependence of the diffuse layer on surface potential and electrolyte concentration, Hurth et al. approached a Pt/Ir tip to a Pt foil, with constant U_{sample}, in KCl [4]. Their key findings were:

- Potentiometric approach curves (normalized ΔU vs. z) in 10^{-5} and 10^{-4} M KCl were in good agreement with GCS theory. The potential had decayed after approximately 60 and 30 nm respectively.
- An approach curve in 10^{-3} M KCl, however, did not decay faster than the one in 10^{-4} M KCl. This result did not reproduce GCS theory correctly.
- Approach curves recorded in 10^{-5} M KCl at varying U_{sample} overlapped. This result also failed to reproduce GCS theory.

Calculated Debye lengths for 10^{-5}, 10^{-4}, and 10^{-3} M are 96, 30, and 9.6 nm [40]. Therefore, Hurth et al. concluded that SECPM cannot monitor the ECDL correctly when the size of the exposed tip exceeds the Debye length.

A similar experiment repeated for a polycrystalline Au sample in 10^{-6}, 10^{-4}, and 10^{-3} M KF gave a trend of decreasing potential decay that was in good agreement with GCS theory [41].

While the experimental result on polycrystalline Au is promising, the Debye length sets a fundamental limit to the extension of the tip and its ability to resolve potential drops. Furthermore the problem does not only consist in limited resolution, but it is also difficult to generate a tip with a vertical extension smaller than the thickness of the ECDL of the sample. An additional problem is that every potential probe non-infinitely small will form its own ECDL that can interact and overlap with the ECDL under investigation; so, a procedure for deconvolution of the overlapping double layers is necessary.

Computational modeling may alleviate the experimental limitation by calculating and eliminating the contribution of the tip. The problem statement is as follows:

> What is the influence of a metallic tip at open circuit potential (OCV) during its approach towards a sample at fixed potential.

OCV imposes an electroneutral boundary condition onto the tip; its charge must always cancel out the total charge in the nanogap between the tip and sample [4]. A first take on resolving this issue was performed by Woo et al. based on linear superposition approximation (LSA) [10]. In two reports Hamou et al. investigated the effect of the protrusion shape of the metallic probe [42, 43], overlap of ECDLs [42], and Debye screening [43]. They used the finite element method and their results were:

- A flattened metallic protrusion has significant advantages over sharpened tips for determining potential values. Sharp tips, as commonly used for STM measurements, lead to a nonuniform distribution of surface charge density.

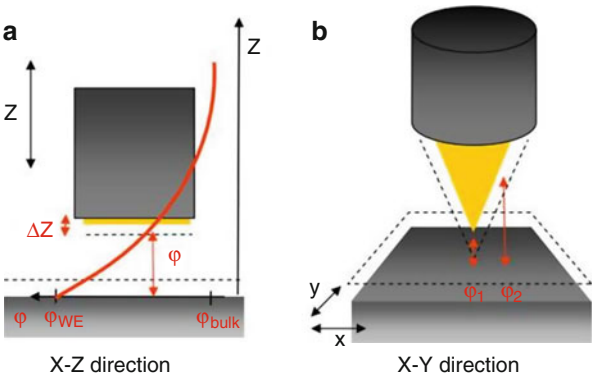


Fig. 1.6 Scheme how the shape of the tip influences the SECPM measurement. (**a**) For potential-approach curves, a flat tip is advantageous so that only a single spot in the electrochemical double layer is probed. (**b**) For potential mapping a sharp tip is required to obtain high resolution (Reprinted from Ref. [12]. Copyright 2009. Reprinted by permission of John Wiley & Sons, Inc)

- A theory for the overlap of ECDLs and their screening effects was developed which is able to explain experimental findings of Hurth et al. [4, 41].
- Surface potential mapping is less affected by ECDL distortion and screening effects, and therefore this mode is more reliable, as suggested by our group earlier [12].

The second and the third of above findings hold the prospect of a golden future for experimental application of SECPM.

The second statement indicates that a deconvolution of the overlapping ECDLs can be done by computational methods. This makes potential-approach curves a viable experimental method. However, in order for computational methods to be effectively applied to experimental data, novel techniques for reproducible tip etching and tip coating need to be developed.

The third statement expresses that the potential-mapping mode is more reliable than approach curves and provides valid results without the need for computational posttreatment. The reason is that in potential mapping, the tip is measuring potential contrast between adjacent sites in the x-y plane; exact values of potential are less important. The lateral resolution of this potential contrast depends on the tips. They should be as sharp as possible, a demand which is diametrical to the request for flattened tips for good vertical potential resolution (Fig. 1.6). Apparent size of monitored structures depends on the concentration of ions in the electrolyte. It increases with decreasing electrolyte concentration.

5 Key Research Findings: Electrocatalysis on Metal Single-Crystal Surfaces

To achieve the goal of catalyst research, "design and tune the activity of catalysts by careful control of their compositional and structural properties, down to the level of atoms" [6], a basic understanding of the relation between catalytic activity and surface structure on an atomic scale is essential. EC-STM and SECPM are perfect tools for this field of research since they can reach the required resolution and are able to be performed in situ. This enables the researcher to directly compare

electrochemical data and surface structure and study electrochemical processes on the nanometer scale. Another important factor is that if not measured in situ, the transfer of the sample to vacuum or gas atmosphere may cause changes in the surface structure, e.g., oxide formation or changes in the atomic structure [44].

A catalyst is defined as "a substance that increases the rate of a reaction without modifying the overall standard Gibbs energy change in the reaction" and while not being consumed by it [45]. In order to do so, the material has to fulfill the following functions of a catalyst [6]:

- Adsorb the target molecule and cleave its bonds.
- Keep the reactants near the boundary surface.
- Facilitate the target reaction or open up new reaction paths for it.
- Release the reaction products to reactivate the reaction site.

A way to describe how strongly a catalyst influences a given reaction is by its activity, which can be measured through the exchange current density j_0. It has been shown by Conway and Bockris [46] that j_0 is correlated to the electronic work function, the binding energy of electrons close to the Fermi level in the material. In a theoretical study of the relation between the exchange current density and the adsorption of atomic hydrogen on the electrode through the free adsorption energy ΔG_H, it was shown by Parsons [47] that $\log j_0$ reaches a maximum at $\Delta G_H \approx 0$ eV. This agrees with the Sabatier principle which states that the catalytic activity of a material is best if its interaction with the surface is neither too strong nor too weak. Much effort has been put into finding the most efficient catalyst materials for the HOR/HER which play a major role in many applications, e.g., fuel cells and electrolysis. Figure 1.7 shows a comparison between theoretical calculations and experimental data of the exchange current density vs. the free adsorption energy for the HOR/HER on different metal surfaces [48]. This plot, due to its shape called volcano plot, shows a maximum at $\Delta G_H \approx 0$ and shows platinum as the most active catalyst.

In reality, for many reactions the catalytic activity is higher for systems composed of two or more materials and for nanostructured surfaces, which makes real catalysts much more complex than the materials examined in Fig. 1.7. When one noble metal is deposited onto another, the size, structure, and dispersion of the deposited particles/islands influence the activity as well as interactions between surface and deposited material and the surface structure of the substrate. For multilayer depositions the structure and thickness of the adlayer and also the underlying atomic structure of the substrate play a role. Another possibility for combining different metals is the use of metal alloy single crystals. In order to understand the reasons for the increased activity in these systems, it is of great importance to use well-defined model surfaces to minimize the influence from uncontrollable parameters. In some systems, however, there are segregation effects of one component rendering the single-crystal surface with a different composition than the substrate. Metal single-crystal surfaces can be used as simple model systems. Another advantage is that due to their highly ordered structure and large terraces, it is possible to perform SPM with atomic resolution.

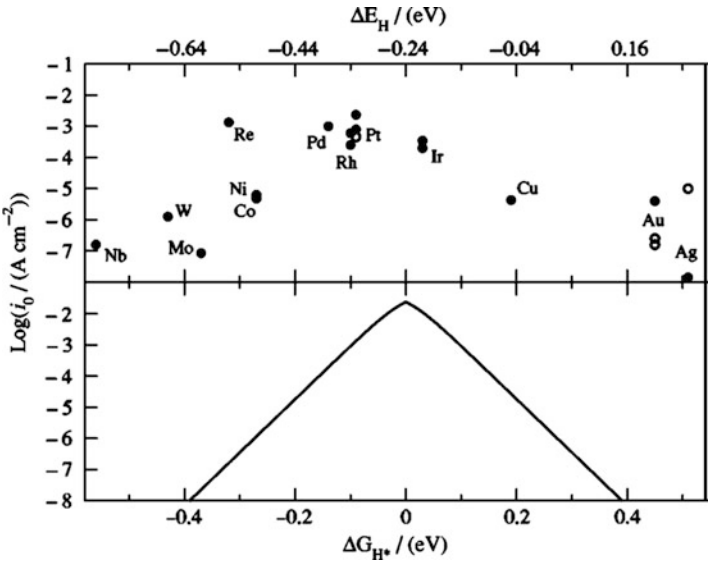


Fig. 1.7 *Top*: experimental data of the exchange current density for HER/HOR versus the calculated hydrogen chemisorption energy per atom ΔE_H over different metal surfaces. *Open circles* indicate single crystals, *filled circles* polycrystalline materials. *Bottom*: simple kinetic model plotted as a function of the free hydrogen adsorption energy $\Delta G_{H^*} = \Delta E_H + 0.24$ eV (Reprinted from Ref. [48]. Copyright 2005. Reprinted by permission of The Electrochemical Society)

5.1 Sample Preparation

The development of techniques for reliable production of stable and well-defined noble metal single-crystal surfaces in 1980 [44, 49] opened the door for detailed studies of electrocatalytic reactions. Single-crystal surfaces can be prepared by several methods. The most common are polishing and annealing of surfaces of bulk single crystal, careful melting of the end of a wire to form a bead with single-crystal surface facets, and the annealing of thin films deposited on a substrate plate, e.g., mica or glass. As mentioned before, the activity of the system can be greatly influenced by depositing another metal on the surface.

5.1.1 Epitaxial Layer Growth

Epitaxial growth of metal on metal can follow one of three thermodynamic growth modes, depending on the surface energies of substrate and deposited material as well as energy in the interface between the two such as lattice strain and chemical processes [50]. In *Frank-van der Merwe* (FM) growth, the material is deposited layer by layer, a new layer only starts growing once the previous one is completed, forming an atomically flat surface [51]. The *Volmer-Weber* (VW) growth describes the opposite case, the following layer and further ones nucleate before a full monolayer (ML) is formed, leading to the formation of three-dimensional structures

and a rough surface [52]. Finally, the *Stranski-Krastanov* (SK) mode has features of both previous modes. After the completion of a first full monolayer, as in FM growth, the following layers nucleate before the previous ones are completed as in VW growth, again resulting in a rough surface with three-dimensional structures [53].

The electrochemical deposition of one metal onto another can be divided into two different regimes: the underpotential deposition range (UPD) and the overpotential or bulk deposition range (OPD). In either case, before deposition the substrate is kept at potentials much more positive than the deposition potential and then scanned or stepped in negative direction to the desired value. UPD takes place at potentials positive from the Nernst equilibrium potential of the three-dimensional bulk metal phase and occurs when the interaction between the deposited metal adatoms (M) and the substrate (S) is stronger than the M-M interaction in a bulk crystal. For this reason UPD is generally limited to the growth of one monolayer because for further deposition M would have to be deposited on M which falls into the bulk deposition regime. OPD, on the other hand, takes place at values negative from the Nernst potential where the adlayer growth will follow one of the three models introduced above.

As mentioned in Sect. 4.1, a well-defined and flat surface such as a UPD grown two-dimensional adlayer may be preferable to three-dimensional bulk structures for SPM study of catalysts. However, many of the materials relevant for catalysis cannot be underpotentially deposited on each other. One way to work around this problem is the surface-limited redox replacement (SLRR), first described by Brankovic and Adzic [54]. In this two-step method, first a UPD monolayer of a metal is formed on the substrate. Then this adlayer is replaced by a more noble metal P in an electroless deposition. During the replacement step, the UPD adlayer is oxidatively dissolved by P in an irreversible and spontaneous process while at the same time P is reduced and deposited on the surface. This process only functions if P is less noble than the surface because otherwise the surface will be oxidized. The replacement reaction can be described by

$$M^0_{\mathrm{UPD}} + (m/z)P^{z+} \rightarrow M^{m+} + (m/z)P^0 \tag{1.4}$$

where M^0_{UPD} is a UPD adatom on the surface and P^{z+} is a noble metal cation. M^{m+} is the dissolved metal cation after replacement and P^0 a deposited noble metal atom. The replacement reaction is driven by a positive difference of the equilibrium potentials of P and M. An iterative multilayer growth can be accomplished if M can form a UPD layer on the deposited layer of P [55].

5.1.2 Nanoparticle Deposition

The influence of size and atomic structure of nanoparticles is also of interest in catalysis studies. For SPM analysis these particles have to be deposited on a suitable flat surface. If the electrochemical activity is to be investigated, an inert substrate should be chosen. Au single-crystal surfaces are often used since they fulfill both requirements. Nanoparticles can easily be deposited by OPD. For this method a

short OPD pulse is applied where the particle size and distribution can be influenced by the variation of pulse length and potential [15, 56, 57]. Another, though less controllable, method for nanoparticle growth is the spontaneous deposition where the sample is simply immersed into a solution containing the metal which is to be deposited [58, 59]. The deposited amount can be roughly controlled by the immersion time.

It is also possible to deposit a single nanoparticle on a sample surface, using the STM tip as a deposition tool [60–62]. One advantage of this method is that the particle can be deposited at a controlled location on the substrate surface and easily be located after deposition since the same tip is used for imaging the surface and for local activity measurements, as explained in Sect. 4.4. In a first step metal ions from a solution are electrochemically deposited on the STM tip. The tip is then transferred into the EC-STM cell to scan the sample in order to find a suitable position on the surface for the particle deposition. Once the tip is positioned over the right location, the scanning is stopped and the tip brought closer to the sample until a *jump-to-contact* occurs. This means the metal deposited on the tip forms a thin connection between the tip and sample. Now the tip is retracted again, leaving a small cluster of the metal on the surface. The size of the particle can be varied by varying the height of the voltage pulse on the z-piezo. This nanoparticle can be imaged immediately with the same tip.

5.2 Platinum Substrates

Platinum as the most active one-component catalyst material is a substrate often used in experiments aimed at improving catalytic activity, starting with a Pt single-crystal surface on which other metals are grown. It is a commonly used electrocatalyst in fuel cells; however, it is prone to adsorb carbon monoxide (CO), poisoning the electrode and reducing the fuel cells' performance.

5.2.1 Palladium on Platinum

Hoyer et al. studied the initial stages of palladium deposition on Pt(111) surfaces [62] and examined the CO oxidation activity, comparing the results to bulk Pd single crystals. Pd was deposited from sulfate- and chloride-containing solutions on the (111) facets of a Pt bead produced by the wire-melting method. In chloride-containing solution, deposition started in the UPD range, while without chloride Pd deposition is hindered and requires to apply an overpotential. EC-STM imaging during the deposition showed that in either solution, first a complete pseudomorphic monolayer is formed. However, after completion of that first layer, in the chloride-free solution, an SK growth is observed, forming 3D clusters, while in the presence of Cl^-, a layer-by-layer growth behavior is observed. These findings were verified by cyclic voltammetry where the peaks for hydrogen and sulfate adsorption/desorption differ for mono- and multilayer Pd deposits. The ML peak disappeared faster for the layer-by-layer growth sample showing a more even coverage of the surface.

To compare the activity of deposited Pd films of various coverages with bare Pt(111) and Pd(111), the oxidative stripping of an adsorbed CO layer was used. The CO oxidation peak on bare Pt(111) at about 0.45 V shifted to more positive potentials between 0.52 and 0.60 V in the presence of Pd. On bare Pd(111) the oxidation potential is situated at 0.8 V but after increasing the defect density by electrochemical roughening of the surface the value is shifted to 0.6 V. For coverages of 5 Pd ML and more, the potentials for both surfaces match, showing no more influence of the Pt substrate.

5.2.2 Copper on Platinum

Varela et al. have investigated the reduction of CO_2 on Cu overlayers on Pt(111) and Pt(211) surfaces in 0.1 M $KHCO_3$ solution [63]. Cu is the only metal known to produce larger amounts of hydrocarbons during CO_2 reduction, but due to high overpotentials and a wide variety of products such as CO, formic acid, methane, and ethylene and H_2 formation, the efficiency is rather low. Since the activity and selectivity depend on the surface structure, flat Pt(111) and stepped Pt(211) surfaces were used as substrates. CO is known to induce structural changes in bimetallic surfaces which can be observed with EC-STM.

Cu UPD on Pt single-crystal surfaces showed that the activity of the Cu-coated surfaces for CO_2 reduction lies between those of pure Pt and Cu. While the total current density is higher than on bulk Cu, the main product of the reaction is hydrogen instead of hydrocarbons. The high activity towards HER was measured in the presence of CO, although CO is known to be a catalyst poison. EC-STM measurements were able to resolve this puzzling behavior. They showed that the CO destabilizes the Cu overlayer which changes from a smooth pseudomorphic to a granular structure and exposes parts of the underlying Pt surface (Fig. 1.8), because of its higher binding energy on Pt than on Cu. Since Pt is highly active towards the HER, these surface changes lead to an increased hydrogen production.

The finding of the sensitivity of the Cu adlayer structure to the reaction conditions shows how suitable EC-STM can be for understanding such behavior. An in situ imaging tool was required to observe the roughened Cu overlayer and to therefore acquire information not accessible by integral electrochemical techniques.

5.2.3 Ruthenium on Platinum

The addition of ruthenium to a platinum surface increases the CO tolerance of the electrode by enhancing oxidation of CO and small organic molecules such as methanol. In the past various explanations for this effect have been given. In the ligand effect approximation, addition of Ru increases the CO tolerance via electronic interactions, for example, by increasing the Pt-CO bond strength [64–66]. Also, a bifunctional mechanism has been proposed where Ru provides an oxygenated surface species from water dissociation at a lower potential than Pt sites do [67, 68]. This increases the CO_2 formation and decreases CO poisoning.

Maillard et al. [69] presented a detailed study and review on the topic for a better understanding of details behind the increase in CO tolerance. Further studies

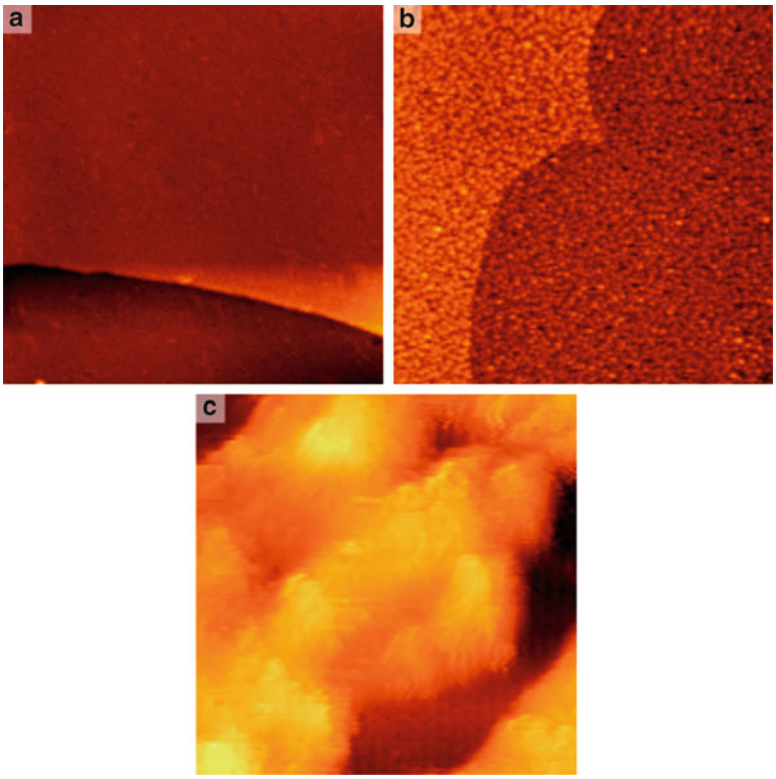


Fig. 1.8 EC-STM images of (**a**) atomically flat Cu overlayer on Pt(111) in C-free electrolyte (499 nm)^2. (**b**) Granular morphology after exposure to a CO-saturated electrolyte (499 nm)^2. (**c**) Disordered Cu overlayer with (2 × 2)-Co structure (Reprinted from Ref. [63]. Copyright 2005. Reprinted by permission of ACP Publications)

demonstrated that mainly the bifunctional mechanism is responsible for the enhanced CO tolerance, while the modified CO-binding energy only plays a small role. In CO stripping voltammetry, a splitting of the CO oxidation peak was found in contrast to a single peak on Pt/Ru alloys. The split peak is linked to the presence of two different CO populations on the surface, CO linearly adsorbed on Pt sites and CO linearly adsorbed on Ru sites. The latter can be consecutively electrooxidized. The peak split exposes slow oxidation kinetics at the Ru islands and is removed with increasing Ru coverage. It was also shown that CO can move from the Ru to the Pt sites at a certain rate and the Pt/Ru edge was found to provide active sites for water dissociation which generates the OH species that react with CO to form CO_2. During CO oxidation the Pt sites surrounding the island edges are quickly covered by hydroxy groups coexisting with adsorbed CO. On these sites CO is oxidized producing CO_2 and solution protons. CO adsorbed on the bare Pt surface is assumed to diffuse to the Ru islands with a local CO diffusion limitation at the Pt/Ru edge being responsible for the peak splitting. Alternatively the split and

the slow CO oxidation kinetics at the edge can be explained by a slow change in the Ru oxidation state which induces a slow delivery of OH for the reaction. A final distinction about the role of those two mechanisms could not be made.

Strbac et al. studied the spontaneous deposition of Ru nanoislands on Pt(111) [70] to gain more insight in the structure of the deposited Ru particles. After one deposition step of three minutes, the surface was covered with hexagonal Ru nanoislands with a diameter of 1–3 nm with mostly monoatomic height. During a second deposition step with the same parameters, deposition on top of already existing islands is favored.

EC-STM measurements showed that the island size is strongly influenced by the electrode potential. The oxidation state of Ru might be the determining factor. By increasing the potential from 0.31 to 0.56 V[1], the island size increased, which is possibly induced by a transformation of metallic Ru to Ru oxides which takes place in this potential range. After decreasing the potential back to 0.31 V, however, the surface morphology changed into a state that resembles that after a single deposition with a higher number of small islands. This becomes even more apparent when applying higher potentials of 0.71 and 0.91 V.

In chronoamperometric measurements for methanol oxidation on pure Pt(111), the current decreases to a very low value because active Pt sites are blocked by adsorbed CO. The Ru present after one deposition step increases the methanol oxidation current. This effect becomes even stronger after the second Ru deposition. However, after the oxidation and reduction step, the current decreases again to a value between those of one and two deposition steps. This is attributed to a decrease in available Pt sites because of the higher surface coverage. Therefore, EC-STM was able to show that Ruthenium coverage is potential dependent and that existing Ruthenium islands from a first deposition step are preferred sites for deposition during a second step.

CO stripping measurements were also carried out by Strbac in the same publication [70] on Ru/Pt(111) surfaces and compared to results on Os/Pt(111) and Ru/Au(111) surfaces. Voltammetry shows the known CO oxidation peak splitting. This is attributed to the existence of two different types of Ru sites, in the island centers and on the island edges. The oxidation onset for Os/Pt(111) is about 70 mV more positive than for Ru. This is explained by the difference in oxophilicity of Os and Ru which influences the ability to provide oxygen-containing species (like –OH groups) for the CO oxidation. At 0.48 V and higher potentials, the Os system is more active for methanol oxidation than the Ru/Pt(111) system. Comparing the oxidation peaks on Ru/Pt(111) and Ru/Au(111), it was found that the substrate material has a strong influence on the reaction. On Au(111) the peak shifts to a more positive potential compared to the known value for Ru(0001) while on Pt(111) it shifts in negative direction. The former can be explained by strain on the Ru lattice caused by the Au(111) surface, changing the electronic properties which leads to a

[1]Potentials in this publication were measured vs. a Ag/AgCl, KCl (3 M) RE and are here converted to vs. NHE.

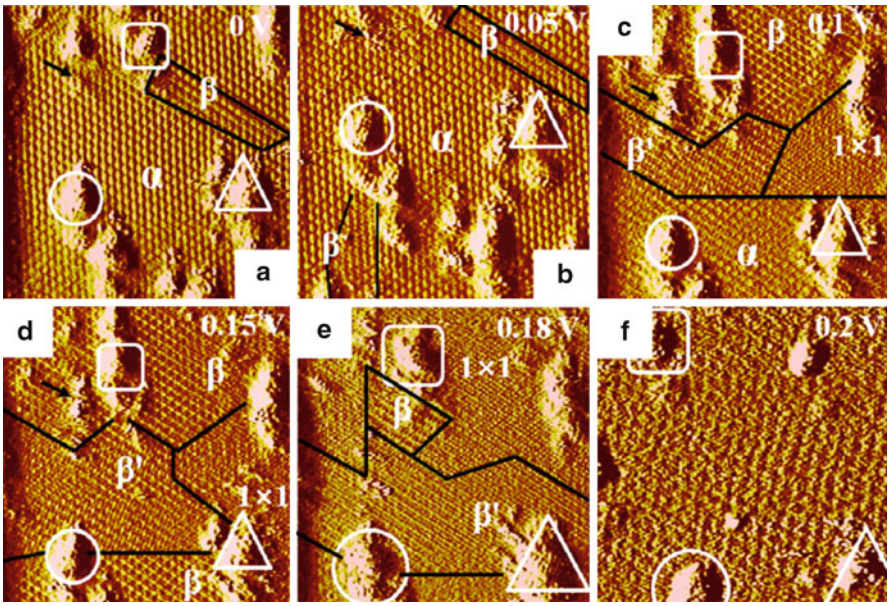


Fig. 1.9 Sequential STM images observed during CO preoxidation at (**a**) 0.21 V, (**b**) 0.26 V, (**c**) 0.31 V, (**d**) 0.36 V, (**e**) 0.39 V, and (**f**) 0.41 V, all potentials versus NHE (the potentials given in the images were measured vs. a Ag/AgCl reference electrode and converted to vs. NHE). Ru islands are marked by triangles, circles, and squares. Arrows indicate unstable protrusions. Image size for all scans is 20 × 20 nm (Reprinted from Ref. [58]. Copyright 2010. Reprinted by permission of Elsevier)

stronger Ru-CO bond. The opposite effect for Ru/Pt(111) is explained by a weakening of Ru-OH_{ads} bond strength due to reduction in Ru-Ru neighbors vs. bulk Ru or by a more loosely packed CO adlattice structure that allows more OH_{ads} nucleation next to the CO-occupied sites.

To understand the role of ruthenium in CO oxidation, Jung et al. studied the structural evolution of adsorbed CO during the preoxidation peak (at potentials lower than the main oxidation peak) of CO oxidation on a Ru/Pt(111) surface [58]. Ru was spontaneously deposited, resulting in a surface similar to the one reported above, as shown with EC-STM (Fig. 1.9). In CO stripping measurements, the typical oxidation peak shift and splitting were observed as well. Figure 1.9 shows EC-STM images of the same area at different potentials, acquired during the CO preoxidation on the Ru/Pt(111) surface after one Ru deposition step with a Ru coverage of 27 %.

The circles, triangles, and squares in the images mark Ru islands with a ($\sqrt{3} \times \sqrt{2}$)R30° structure. The other protrusions (marked by arrows) which appear less stable could not be clearly identified. From image (a) to (f), the potential was increased stepwise from 0 to 0.2 V, showing gradual changes in the CO surface structure from (2 × 2)-α to (2 × 2)-β over (1 × 1) (β′ in image (d) is a hybrid of the (2 × 2)-β and (1 × 1) phases) into a ($\sqrt{19} \times \sqrt{19}$) domain which indicates the

completion of CO preoxidation. Comparison of CO preoxidation on samples with different Ru coverage shows similar behavior with all separate phases appearing before formation of the ($\sqrt{19} \times \sqrt{19}$) domain. However, with increasing Ru coverage the transitions take place at lower potentials, which may be caused by increased mobility of the adsorbed CO [71]. A comparison of the peak shift for preoxidation showed that for small Ru coverages up to 10 % the main oxidation peak shifted from 0.66 to 0.51 V but remained constant at higher coverage. This indicates that the two oxidation processes are affected by the presence of Ru in different ways. In this study EC-STM was employed to get a microscopic picture of the structural evolution of CO during preoxidation.

Alloys of platinum and ruthenium also show increased catalytic activity for oxidation of small organic molecules other than CO. El-Aziz et al. examined the electrochemical behavior of a Pt/Ru alloy single crystal [72] consisting of equal parts of platinum and ruthenium. During initial measurements it was found that depending on the cooling conditions after an annealing process for surface preparation, the surface had electrochemical properties similar to either Pt(111) or Ru(0001). After cooling down the sample in inert nitrogen cooling gas or in reducing atmosphere (addition of H_2 or CO to the cooling gas), a cyclic voltammogram (CV) closely resembles that of a Pt(111) surface in the same solution. Small peak shifts in hydrogen adsorption and surface oxidation to higher overpotentials compared to a pure Pt(111) single crystal are attributed to alteration of the electronic behavior of the surface by the underlying alloy crystal. However, when oxygen is added to the cooling gas, the recorded CV shows the characteristic peaks for a Ru(0001) surface, with a shift for hydrogen adsorption and surface oxidation to lower overpotentials. EC-STM measurements were performed to obtain more information about the surface structure.

After cooling in Ar + H_2 atomic resolution was achieved (Fig. 1.10b) and the STM image showed strong apparent height variations (compare Sect. 4.1) between different atoms of up to 0.1 nm. There are only a few brighter spots in the image that can be attributed to Ru atoms, which are distributed randomly. Therefore, EC-STM revealed that the Pt/Ru alloy single crystal exhibiting Pt-like electrochemical characteristics featured a surface almost entirely devoid of Ru. After cooling in O_2 + Ar, the terraces appear covered by a smooth layer with small holes (Fig. 1.10d) which covers the whole surface except the area immediately on top of step edges between terraces. Here the surface consists mostly of Ru atoms that show a high affinity for oxygen, and the surface is expected to be covered with an oxide layer. Atomic resolution could not be achieved on this surface. Nevertheless, EC-STM indicated that the Pt/Ru alloy single crystal exhibiting Ru-like electrochemical characteristics showed a surface dominated by Ru. It should be noted here that Pt is known to segregate to the surface of the alloy single crystal during heating, which might have influenced the results in this study.

As a final examination, Cu was underpotentially deposited from a H_2SO_4 solution on both surfaces (Pt rich and Ru rich), and CVs of the resulting surfaces resembled closely either Cu/Pt(111) or Cu/Ru(0001). For the Pt-rich surface, the total determined charge density for Cu deposition points towards the formation of a

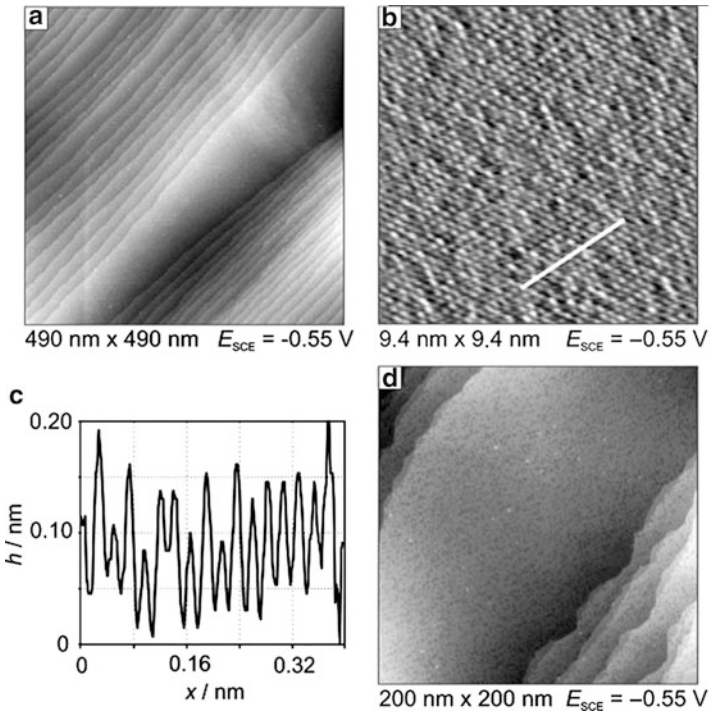


Fig. 1.10 EC-STM images of Pt/Ru(111) in 0.01 M NaF after heating and cooling in (**a**) CO + Ar, (**b**) H_2 + Ar, and (**d**) O_2 + Ar. (**c**) shows the height profile along the line in (**b**). The potential given in the images equals a potential of −0.79 V versus NHE (Reprinted from Ref. [72]. Copyright 2010. Reprinted by permission of WILEY-VCH Verlag)

full Cu monolayer as known on Pt(111). For the Ru-rich surface, a strong oxide formation peak as on Ru(0001) could not be found under the experimental conditions, but Cu deposition seems kinetically hindered and overlaps with bulk deposition. Minor differences in peak shape and position are attributed to the different electronic configuration of the surface atoms.

Through the surface segregation during the cooling step, a "fine-tuning" of the adsorption properties for hydrogen is possible by variation of the bulk composition of the two materials. EC-STM was able to show that the different electrochemical signals stem from a transformation of the Pt/Ru alloy single-crystal surface from a 50/50 Pt/Ru ratio into an almost pure single component structure.

5.2.4 Step Edges on Platinum Surfaces

Studies on the oxidation of adsorbed CO monolayers on platinum surfaces have shown that the reaction occurs between 0.7 and 1.0 V, while the equilibrium potential lies at −0.104 V. This can be explained by a protective CO surface layer blocking water molecules from accessing the surface Pt atoms. In some cases a preoxidation peak can be found in the range of 0.3–0.5 V, depending on the surface structure and

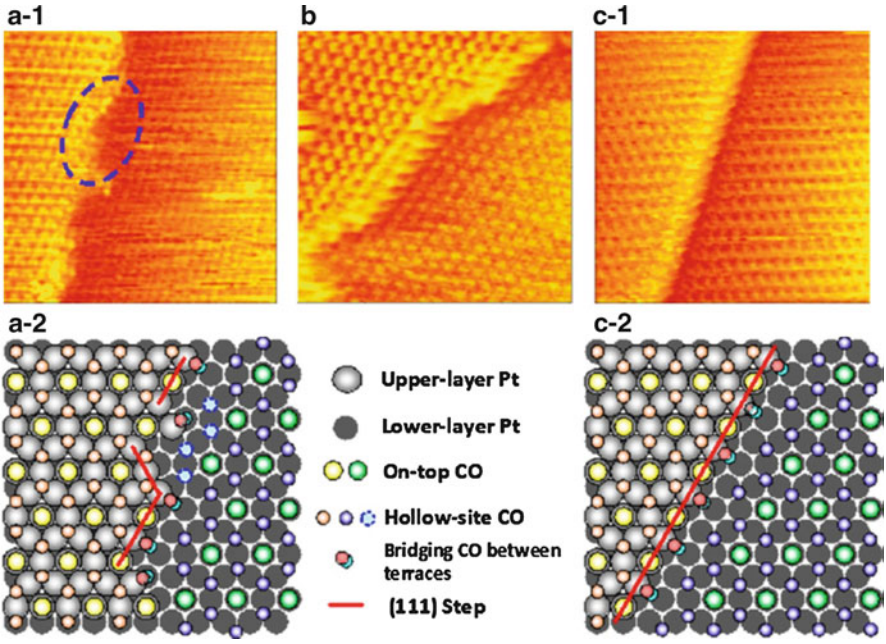


Fig. 1.11 All STM images are 10 × 10 nm in CO-saturated $HClO_4$ at 0.55 V. (**a-1**) before cycling, (**a-2**) structure model for marked area in (**a-1**), (**b**) after 5 potential cycles, (**c-1**) after 30 cycles, (**c-2**) structural model for (**c-1**) (Reprinted from Ref. [73]. Copyright 2010. Reprinted by permission of ACS Publications)

the CO adsorption potential. This peak disappears if the sample is cycled over a large potential range such as 0.1–1.0 V in the presence of dissolved CO. The origins of this peak have been linked to the existence of step edges and defects. To gain a better understanding of the effects behind the preoxidation, Inukai et al. have examined the Pt(111) surface with an EC-STM during CO oxidation [73]. Repeated potential cycling of a Pt(111) single-crystal surface from 0.07 to 0.6 V showed an onset of the CO oxidation peak at 0.4 V which remained stable for 30 cycles. When cycled up to 0.95 V, the prepeak decreased rapidly with each cycle and disappeared almost completely after 30 cycles. To understand the effect of potential cycling in the presence of CO on the surface, the pristine sample and one previously treated in CO-saturated solution were cycled in the absence of any CO. Spikes at 0.8 V increased slightly, indicating a small increase of terrace flatness for the cycled sample. A slight change in small peaks from hydrogen adsorption/desorption at (111) steps indicates changes in the step structure.

To visualize these changes in detail, EC-STM was carried out. The microscope can clearly resolve the (2 × 2) – 3CO structure; however, STM scans can only resolve CO in atop position on Pt(111). As can be seen in Fig. 1.11a-1, recorded before potential cycling, the step edge is not straight but consists of many small kinks and adatoms. The periodic structure on the terraces is the adsorbed CO, which was found to be adsorbed more distinctly on the upper terrace and much less on the

lower terrace near the step edge. The red lines in Fig. 1.11a-2 indicate the existence of local (111) steps. Figure 1.11b shows the same area after 5 cycles to 0.95 V. After 30 cycles (Fig. 1.11c-1), where the preoxidation peak has disappeared, the (111) step became completely straight.

These results indicate a strong preference to form steps following (111) direction during cycling to higher potentials in the presence of dissolved CO. The decreased CO oxidation activity can be associated with the step transformation from disordered to straight. The first image was taken at 0.55 V where CO preoxidation already occurs. Since no changes in the CO structure were detected during the measurement, CO oxidation is proposed to take place on the rising face of the step edge and in close proximity on the lower terrace where no CO can be seen on the image.

For comparison, those experiments were also performed on a Pt(10 10 9) surface which has an increased number of (111) terraces. The current density for CO preoxidation was in a similar range as for the Pt(111) surface. It is therefore not proportional to the number of step edges. As on Pt(111), the prepeak vanished after 30 cycles. EC-STM imaging showed a straightening of the steps while their number and distribution remained unchanged. Density functional theory (DFT) calculations agree with the experimental results, showing that in the absence of CO (100), steps are energetically slightly favored over (111), but when CO is added, (111) steps are significantly more favored. The reason is a different geometry of the Pt atoms at the different steps.

Furthermore, Inukai et al. investigated a Pt(20 19 19) surface, which has (111) oriented terraces with (100) steps. CV measurements were carried out the same way as for the previous samples. The onset for the prepeak only started at 0.5 V and the current density was smaller, indicating a lower CO oxidation activity. Also the intensity of the peak decreased faster with cycling. EC-STM imaging showed very straight step edges before cycling with few defects. Here, after cycling, the edges became rougher with more defects, forming a zigzag shape. A closer look revealed that upon cycling more and more local (111) step regions form in the previous (100) steps, which causes the roughening.

Since the CO oxidation behavior of the sample only changes if at potentials above 0.8 V, where the CO adsorbed on terraces is oxidized, it appears to be a prerequisite for step oxidation to remove adsorbed CO. If the potential is cycled to 0.95 V, it is assumed that either of the following reactions takes place [73]:

$$\mathrm{Pt(OH)_2} \rightarrow \mathrm{PtO_2} + 2\mathrm{H^+} + 2\mathrm{e^-} \tag{1.5}$$

$$\mathrm{PtO} + \mathrm{H_2O} \rightarrow \mathrm{PtO_2} + 2\mathrm{H^+} + 2\mathrm{e^-} \tag{1.6}$$

When the potential is cycled to 0.8 V, either $Pt(OH)_2$ or PtO can be dissolved to produce $Pt(H_2O)_4^{2+}$ and if the potential is cycled to 0.95 V, PtO_2 can be reduced to form the same complex:

$$\mathrm{PtO_2} + 2\mathrm{H_2O} + 4\mathrm{H^+} + 2\mathrm{e^-} \rightarrow \mathrm{Pt(H_2O)_4^{2+}} \tag{1.7}$$

The $Pt(H_2O)_4^{2+}$ can then react with CO to produce $Pt(CO)_4^{2+}$. Alternatively a Pt adatom can be deposited on the terrace as $Pt(CO)_2$ which has been shown to be stable by DFT calculations. Because of strong binding to the two CO molecules, the bond to the surface is weakened, making it more mobile. The single atomic Pt species can then redeposit at a nearby step in an energetically favorable configuration. DFT calculations show that the Pt atom would retain both CO if deposited at a (100) step but release one at a (111) step or at a corner between (100) and (111) steps. In summary, CO oxidation activities at the different step types decreased in this order: (111) step with defect > straight (100) step > (100) step with (111) local steps ≈ (111) straight step. From the measured and calculated data, it was found that for perfect (111) step edges, CO molecules adsorb with a highly regular surface arrangement from upper to lower terraces across the step edge, blocking the underlying Pt from reacting. This is the proposed reason for the low reactivity of the CO-covered (111) steps and the restructured (100) steps. The CO layer is disturbed by single adatoms at the step edges, increasing the activity again.

EC-STM provides a clear conclusion regarding the reaction site, showing relationship between atomic-level structures at the steps on the Pt(111) surface and the activity towards CO oxidation.

5.3 Gold Substrates

For hydrogen catalysis, gold is rather inert compared to platinum, making it a suitable support material for the studies of nanoparticles or thin layers since measured currents can be completely attributed to the particles or adlayer. As will be seen, however, the gold substrate may induce some structural changes in the surface with consequences to its reactivity.

5.3.1 Silver and Lead Composite on Gold

To examine the effects of thickness and composition of Ag-Pb UPD composites on Au(111) on nitrate electroreduction, Hwang et al. [74] combined cyclic voltammetry with in situ STM studies. Ag and Pb were electrochemically deposited on an annealed gold surface subsequently from two separate solutions. Before Pb deposition (at 0.23 V), STM scans show small Ag particles of monoatomic height. A potential decrease to 0.03 V leads to the formation of a full Pb monolayer, followed by second layer island formation and a third layer growing on top of the islands at −0.02 V which was previously unknown for Pb grown directly on Au (111)[2]. The island growth is thought to be caused by Pb depositing on larger Ag islands that form because of the high Ag mobility during Pb UPD. The third layer on top of the islands then is caused by Pb deposition on Ag atoms on the lower island layer that moved to the surface through site exchange with Pb atoms.

[2]Potentials in this publication were measured vs. a mercury/mercurous sulfate RE and converted to vs. NHE.

Investigations on the catalytic effects on nitrate reduction showed that the reduction current increases linearly with the concentration of nitrate in the solution, demonstrating that the current can be attributed to catalytic effects. This was confirmed by nitrate reduction measurements on Pb/Au(111), Ag/Au(111), and Pb/Ag(111) systems which all show only very weak reduction currents. For further confirmation colorimetric detection of nitrite, a product of nitrate reduction was used. The Griess reaction changes the color of the electrolyte in the presence of nitrite, and a strong change in color was only found for the Ag-Pb/Au(111) composite system. These results show that the trimetallic composition is important for nitrate reduction. Furthermore, it was found that increasing the amount of Ag deposited in the first deposition step increases the catalytic current at low nitrate concentrations.

While the exact nature of the increased activity and the detailed structure of the composite still require a more detailed examination, EC-STM measurements showed the growth behavior and surface structure of the Ag-Pb alloy on the Au(111) surface.

5.3.2 Ruthenium on Gold

In their previously mentioned publication about Ru deposition on Pt(111), Strbac et al. also investigated Ru deposited on Au(111) surfaces [70]. Ru was spontaneously deposited on Au(111), and in situ EC-STM was used to characterize the surface after different deposition times. The images show that most Ru deposits on the Au step edges. High-resolution EC-STM images indicate a hexagonal shape for the Ru islands. CO was adsorbed to examine the effects of Ru deposition on CO stripping. The peak positions of the two stripping peaks are more positive than both the single CO oxidation peak of bulk Ru and of Ru(0001). Stripping was completed in a single sweep. The shift to more positive potentials reflects the stronger bond between CO and Ru due to the Ru lattice expansion as mentioned in Sect. 5.2.3. The existence of two peaks is again attributed to the two types of Ru sites (island centers and island edges).

5.3.3 Palladium on Gold

Wolfschmidt et al. [57] examined Pd deposited on Au(111) in sub-ML coverage to study the influence of particle size and dispersion and of the substrate material on important electrocatalytic reactions such as HOR, HER, and the oxygen reduction reaction (ORR). Pd was deposited by potential pulse method [75–77], and the deposited amount was determined by integrating the current during deposition and confirmed by STM and hydrogen adsorption measurements. To investigate the reactivity for HOR of Pd MLs and sub-MLs, measurements were carried out in H_2-saturated $HClO_4$ using potentiostatic pulses at different overpotentials. By normalizing the current density to the active area of Pd, it was found that the specific activity of Pd increases by two orders of magnitude when coverage is decreased from 0.74 ML to 0.1 ML. This increase in activity can be explained by the lattice mismatch between Pd and Au of 4.8 %, where the Pd adlayers are strained, changing the electronic properties. This effect becomes weaker with increasing island height. Another influence is a spillover effect, described by

Eikerling et al. [14], where adsorbed atomic hydrogen from the Pd nanoparticles with high hydrogen coverage spills over to the Au surface which is almost hydrogen-free. There the recombination of adsorbed atomic hydrogen to adsorbed molecular hydrogen can take place. As this process frees active sites on the active Pd particle, it accelerates the release of generated hydrogen.

A combined theoretical and experimental study on the influence of foreign support on catalytically active materials was done by Quaino et al. [56], using Pd nanostructured Au(111) surfaces. DFT calculations on the adsorption energy of hydrogen on different surface sites show that adsorption is much more favorable on Pd than on Au and that the most favored Pd site is a cluster of four atoms. Palladium monolayers and clusters of three palladium atoms show an intermediate reactivity. EC-STM shows Pd nanoparticles on the monoatomically flat Au surface with equal size distribution (approx. 4–5 nm diameter). The ratio of particle area/particle diameter was determined for different surface coverages in the sub-monolayer domain. There is a strong increase in this ratio for increasing coverages in the range below 0.1 ML and again above 0.5 ML where smaller islands grow together to form larger ones. DFT calculations on the electronic density of states (DOS) show for a pure Au(111) surface that the d-band ends about 1.5 eV below the Fermi level while for Pd(111) surfaces the band reaches the Fermi level, making Pd a much more effective catalyst. In mixed systems strain effects and chemical interactions influence the DOS and depend on the distribution of Pd atoms on the Au surface. Under the assumption that the gold support material is inactive, the effect of Pd composition on the HER and HOR was evaluated using potentiostatic pulses at various overpotentials. For HOR the specific current with respect to the Pd area was found to increase with decreasing coverage (more than one order of magnitude from 0.74 ML to 0.1 ML), indicating a strong increase in specific reactivity. The results for the HER showed a similar increase. Both agree with the theoretical calculations for the exchange current density.

Multilayer palladium on Au(111) was examined by Sheridan et al. [78] in terms of SLRR (introduced in Sect. 5.1.1) growth characteristics (compare Sect. 5.1.1) as well as hydrogen adsorption, absorption, and desorption. EC-STM scans after the first three deposition cycles show the growth of evenly dispersed monoatomically high islands (Fig. 1.12a–c), indicating an FM growth mechanism. After the Pd deposition, iodine, which is known to increase the surface mobility of Pd and other metals, was adsorbed on the surface to increase Pd terrace size and surface order (Fig. 1.12d–f).

Hydrogen adsorption was investigated for samples with Pd depositions between 1 and 30 cycles where still no 3D growth was observed. CVs between 0.41 and −0.04 V of samples with one and two deposition cycles show two hydrogen adsorption/desorption peaks that could be identified because they did not appear on bare Au(111).[3] For higher Pd coverages, the peaks shift in the negative direction,

[3]Potentials in this publication were measured vs. a Ag/AgCl, KCl (3 M) RE and converted to vs. NHE.

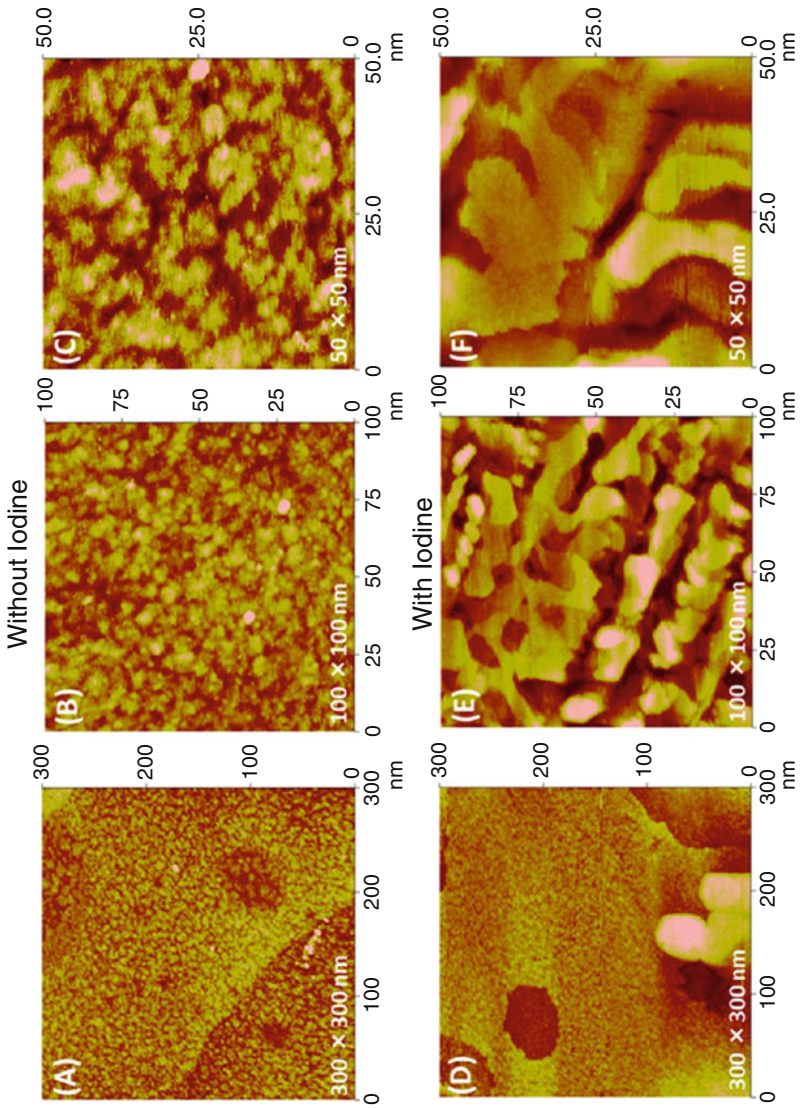


Fig. 1.12 EC-STM images of three cycles of Pd SLRR on Au(111). (**a**–**c**) As-deposited Pd. (**d**–**f**) After iodine adsorption (Reprinted from Ref. [78]. Copyright 2013. Reprinted by permission of ACS Publications)

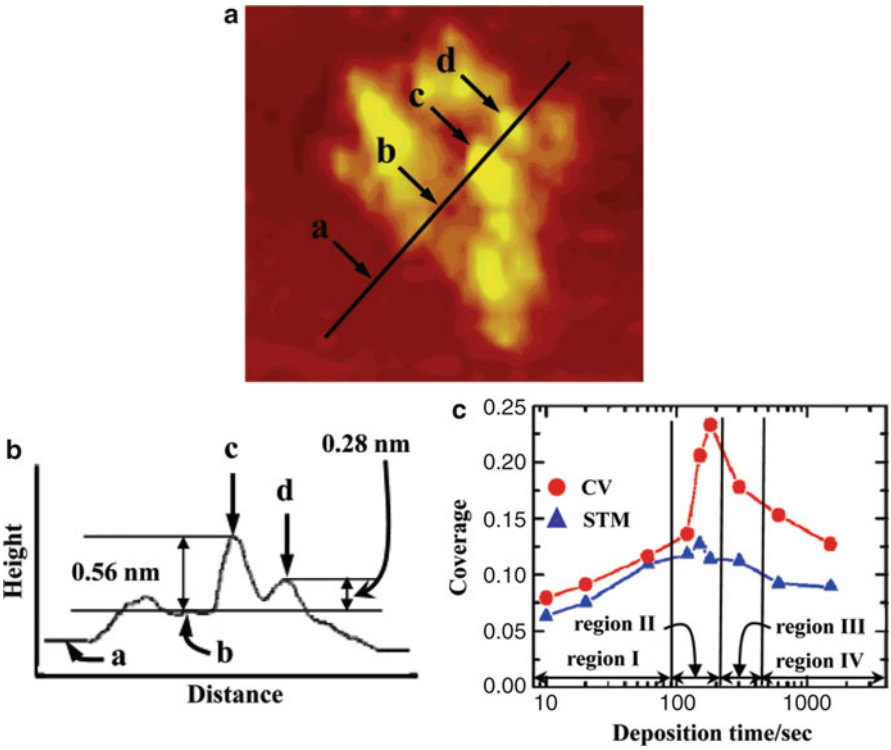


Fig. 1.13 (**a**) Au(111) island with Pt deposits (150 s), 25 × 25 nm, (**b**) line profile for a, (**c**) two-layer thick Pt deposits are colored *red*, 40 × 40 nm (Reprinted from Ref. [59]. Copyright 2007. Reprinted by permission of ACS Publications)

and for more than five cycles, they display more reversibility and overlap. Also they resemble closely the CVs for bulk Pd(111). Highest adsorption was found for the three-cycle films. If cycled to lower voltages (starting just below 0.11 V), hydrogen absorption becomes evident. Hydrogen to Pd molar ratios (H/Pd) were obtained by saturating the Pd film with hydrogen at −0.04 V and subsequent oxidative coulometry at 0.36 V. Afterwards the amount of Pd was determined by stripping in HCl. An average H/Pd ratio of 0.6 was found for 3-, 5-, 10-, and 30-cycle films. Furthermore it was found that repeated cycling in the sorption range causes change in the peak shape and positions which is attributed to a surface restructuring similar to the previously presented iodine annealing process.

5.3.4 Platinum on Gold

Kim et al. investigated the oxidation of formic acid and methanol on spontaneously deposited Pt on Au(111) [59]. For 10 s deposition time, particles are smaller (2–5 nm width) and deposit preferably on step edges, and with increasing deposition time, smaller particles cluster together to form large structures (10–20 nm width). Figure 1.13a shows a Au(111) island after a 150 s Pt deposition,

position *a* is on a large Au terrace, and *b* on the surface of a monoatomic Au island. Positions *c* and *d* show Pt deposits of different heights. The line profile in Fig. 1.13b is measured along the line shown in Fig. 1.13a where *c* is two Pt layers thick and *d* only one. More detailed EC-STM scans (not shown here) reveal that the monoatomic Pt deposits show a $(\sqrt{3} \times \sqrt{3})$R30°-Pt structure, while the two-layer thick deposit has (1×1)-Pt structure. Pt coverage was determined in two ways: From STM images the area of Au surface covered with Pt (geometric coverage) was measured, while hydrogen adsorption/desorption voltammograms were used to calculate the ratio of electrochemically active Pt atoms to that of Au surface atoms (coulometric coverage). Figure 1.13c shows that for deposition times below 100 s, both values are identical within experimental uncertainty, since most Pt deposits are of monoatomic height. Between 100 and 150 s, the geometric coverage remains stable, while the coulometric coverage increases rapidly because of the second layer growth with a different atomic structure, increasing the number of active Pt atoms available. Higher deposition times let the deposits grow vertically decreasing the coulometric coverage, and after several 100 s of seconds, even the geometric coverage decreases.

Oxidation of formic acid can be attributed to the Pt clusters because Au shows no activity towards the formic acid oxidation. Comparison with oxidation on pure Pt(111) shows a ten times higher oxidation current for the 150 s Pt/Au(111) sample and a peak shift in from 0.55 to 0.41 V.[4] Also the anodic and cathodic scans give similar currents, indicating less catalytic poison forms on Pt-decorated Au during the adsorption of formic acid than on pure Pt(111). Methanol oxidation experiments show almost no oxidation current for samples with less than 60 s deposition time and clearly distinguishable current only for more than 600 s, however much less than on Pt(111). The turnover frequency during oxidation, defined as the number of oxidized organic molecules per Pt atom within 1 s, is equivalent to the normalized catalytic activity. For formic acid it increases slowly for deposition times between 10 and 100 s, shows a sudden increase between 120 and 150 s where the second Pt layer forms, and then slowly declines for higher deposition times. At the maximum at 150 s, the turnover frequency changes from 17 s^{-1} for Pt(111) to 327 s^{-1} for the Pt deposits, an enhancement of almost 20 times. In this study EC-STM was used to show the growth behavior of Pt spontaneous deposition and to determine the geometric Pt coverage.

In the previously mentioned publication by Wolfschmidt et al. [57], also platinum deposits on Au(111) were studied in respect to HER, HOR, and ORR. Platinum was deposited in the sub-monolayer range, resulting in particles of monoatomic height. The Pt surface coverage was measured by hydrogen adsorption and CO stripping and by deposition charge. For coverage below 0.1 ML also STM images were used to determine the coverage. A Au(111) surface with less than 1 % of a ML, Pt shows a largely increased activity per area Pt, up to three orders of magnitude compared to an extended Pt(111) surface. For HOR a similar but less

[4]Potentials in this publication were measured vs. a Ag/AgCl RE and converted to vs. NHE.

strong trend was observed, approximately two orders of magnitude higher activity than on Pt(111). Also these results are significantly higher than for the Pd/Au(111) system. Again, the increased activity can be explained by a combination of the previously mentioned altered electronic properties from lattice strain and the spillover effect. The lattice mismatch of 4 % causes lattice strain which in turn leads to a shift in the Pt d-band which has a beneficial effect on the activity/free adsorption energy. For the ORR lower Pt coverages give lower current densities; the activity decreases with Pt coverage while the specific current density remains stable. This indicates that the Au surface is not involved in the catalytic process and also that the strain and spillover effects are not beneficial for the ORR. A similar effect, that the substrate is not involved in catalysis, was seen for Pt nanoparticles on HOPG and boron-doped diamond by Brülle et al. [75, 79].

The activity of deposits on Au(111) for hydrogen reactions was further investigated by Wolfschmidt et al. [15] by depositing flat islands electrochemically and single nanoparticles using the STM tip *jump-to-contact* method explained in Sect. 5.1.2. The exchange current density was then measured for the different Pt coverages by means of potential steps and micropolarization curves in the range of $\pm$ 10 mV around the equilibrium potential (Fig. 1.14 left). Both methods give the same results. For reference a Pt(111) single crystal was also investigated and shows behavior in line with the results (Fig. 1.14 left). Even at the highest coverage of 7.8 ML, the activity was larger than on Pt(111) and slightly increases with decreasing coverage to 0.1 ML. For lower coverages the Pt-specific exchange current density increases much more rapidly.

Figure 1.15 shows a *jump-to-contact* deposited single Pt particle. Here the exchange current density was measured locally with the STM tip (compare Sect. 4.4). The dependence of activity on the particle height, ranging from one to five atomic layers, was investigated and was found to increase exponentially with decreasing height (Fig. 1.14 right). The absolute value for j_0 for single particles can reach more than 40 A cm^{-2}. Possible reasons for this dramatically increased activity are the already mentioned strain from lattice mismatch as well as the hydrogen spillover effect. Also, a high number of reactive step and defect sites may play a role. Lastly an enhanced mass transport for small particles due to hemispherical diffusion as compared to planar diffusion for extended surfaces may lead to higher current densities for very low coverages. In this case the measured values for j_0 on extended surfaces may not represent the true reaction kinetics so adjustments would have to be made to the volcano plot presented in Sect. 5.

5.4 SPM on Single-Crystal Surfaces

To investigate the properties of various metal single-crystalline surface films and compare SECPM, EC-STM, and AFM imaging, Wolfschmidt et al. compared images of atomic force microscopy (AFM), EC-STM, and SECPM and also performed electrochemical characterization [11]. Metal films of Ru(0001), Rh(111), Ir(111),

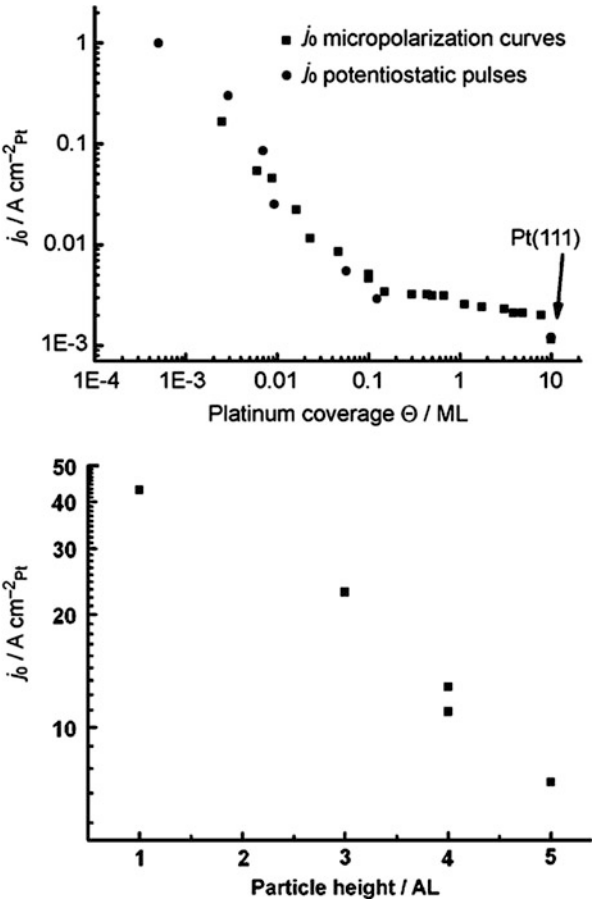


Fig. 1.14 *Left*: exchange current density for hydrogen reactions versus Pt coverage on Au(111). Values were obtained from potentiostatic pulses (*circles*) and micropolarization curves (*squares*). *Right*: j_0 versus particle height of single Pt particles (Reprinted from Ref. [15]. Copyright 2010. Reprinted by permission of Wiley-VCH Verlag GmbH & Co)

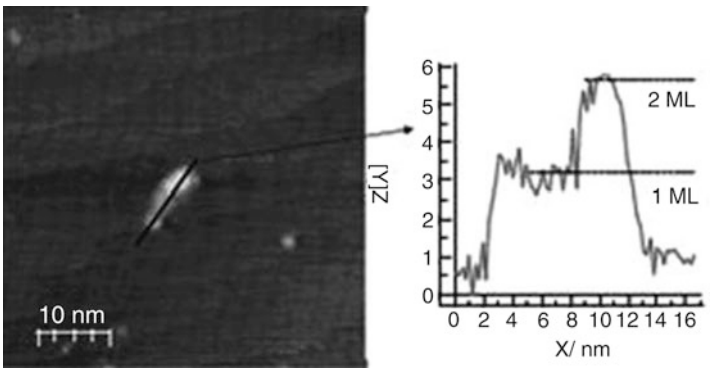


Fig. 1.15 EC-STM image of a Pt particle deposited from the STM tip, the height profile shows the difference between the 2 ML (Reprinted from Ref. [15]. Copyright 2010. Reprinted by permission of Wiley-VCH Verlag GmbH & Co)

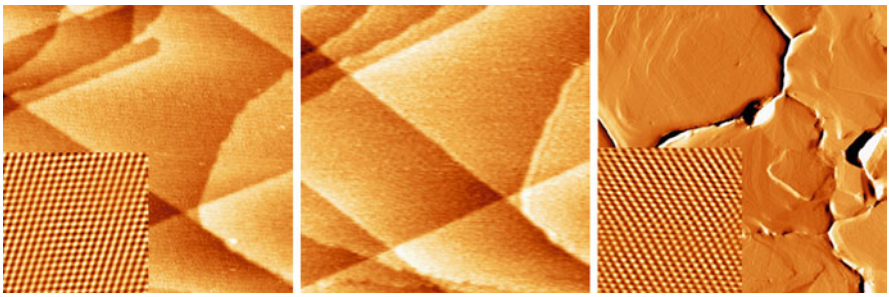


Fig. 1.16 Images of the Au(111) surface. *Left*: EC-STM scan (150 × 150 nm) of a Au(111) single crystal in 0.1 M $HClO_4$ at 0.5 V. *Center*: SECPM scan of the same area and under the same conditions as *left* image. *Right*: AFM scan (2 × 2 μm) of a fiber-textured Au film. *Left* and *right* images show atomic resolution scans of the same surface as the larger one (Reprinted from Ref. [11]. Copyright 2010. Reprinted by permission of MDPI)

and Ir(100) were deposited via e-beam evaporation onto a 40 nm thick yttria-stabilized zirconia (YSZ)-coated Si(111) or Si(100) substrate. Typical film thicknesses were about 150 nm.

5.4.1 Au(111)

Figure 1.16 shows a typical Au(111) single-crystal surface measured with EC-STM (left), SECPM (center), and contact mode AFM (right). The EC-STM and SECPM images (150 × 150 nm) were recorded in 0.1 M $HClO_4$ at 0.5 V where no chemical reaction takes place. The images show atomically flat terraces (the inlay in the EC-STM image shows an atomic resolution scan) and are recorded at the same position. The analysis of the step height and angle between the two edges in the center of the image gives no significant differences, showing that the SECPM technique gives equally good results as EC-STM. The AFM scan is of a larger area of 2 × 2 μm of a (111) fiber-textured gold film instead of the massive single crystal used for the previous images and was recorded in air. Comparing atomic spacing measured with both EC-STM (0.286 nm) and AFM (0.276 nm) with the literature value of 0.289 nm shows good agreement given the accuracy of the technique. For SECPM atomic resolution was not achieved.

5.4.2 Ru(0001)

When imaging Ru(0001) surfaces, all three SPM methods give similar quality images of the surface which is characterized by atomically flat terraces with average width of up to 100 nm. The sharp step edges in the EC-STM scan (Fig. 1.17 left) appear fringed in SECPM (center), indicating that the different electronic properties measured, such as conductivity for STM and potential distribution for SECPM, lead to different resulting images. This shows that more information can be obtained by using both microscopy methods. The AFM image (right) performed in air shows similar results as EC-STM. Atomic resolution was achieved (inset) and the measured atomic distance of 0.27 nm agrees well with the literature lattice constant of 0.271 nm. Since the AFM image was recorded in air,

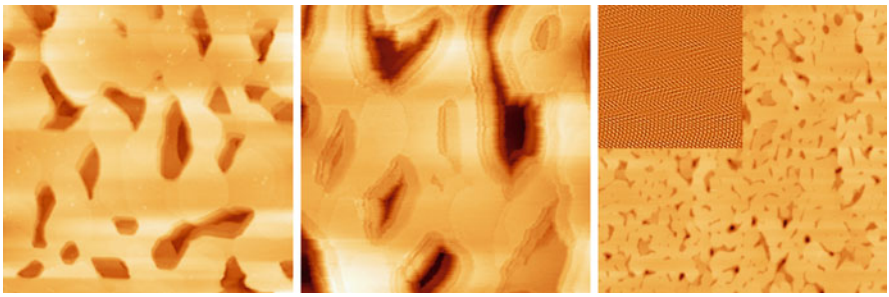


Fig. 1.17 Images of the Ru(0001) surface. *Left*: EC-STM image (500 × 500 nm) in 0.1 M $HClO_4$ at 0.5 V. Center: SECPM image (500 × 500 nm) under the same conditions. *Right*: AFM image (5 × 5 μm) with atomic resolution inset (Reprinted from Ref. [11]. Copyright 2010. Reprinted by permission of MDPI)

an oxygen adlayer forms on the surface and the atomic resolution image might show this oxygen layer instead of the Ru atoms. However the adlayer forms a (1 × 1) periodicity for higher coverages and thus the measured lattice constant will be the same as for the underlying Ru surface.

Electrochemical characterization was done in sulfuric and perchloric acid in different concentrations. The CVs all agree well with the literature results for Ru single-crystal surfaces, showing the high quality of the surface.

5.4.3 Rh(111), Ir(111), and Ir(100)

For the rhodium sample, the same measurements as for Ru(0001) were performed. Measured step heights of the triangular surface structures of 0.210 nm for EC-STM and 0.222 nm for SECPM agree well with the calculated values of 0.221 and 0.219 nm calculated from theoretical and experimental lattice constant. Differences in the angles between step edges for the SECPM scan from both literature and EC-STM values are attributed to the slow scan rate of SECPM which makes it more sensitive to thermal drift effects. Electrochemical measurements in sulfuric and perchloric acid again show good agreement with literature for massive single crystals, however, with slightly reduced peak sharpness.

Iridium, as a neighbor of platinum in the periodic table, has similar physical and chemical properties. For Ir(111) the angles between steps of the triangular surface structures could only be correctly resolved with AFM; thermal drift effects caused a slight distortion of the image. The measured step height, 0.24–0.25 nm for SECPM and 0.23 nm for STM, agrees well with literature (0.221 nm). A few large holes were found on the surface, which are attributed to defect sites from the growth process. For Ir(100) a totally different surface structure than on Ir(111) was found, not showing any triangular terraces but many 90° angle edge intersections. Also the defect density was much lower than for Ir(111). The electrochemical characterization in sulfuric and perchloric acid again showed the same features as literature CV for the massive crystal surface with wider, less pronounced peaks.

All surfaces show the specific characteristics of massive single-crystal surfaces with slightly lower peak sharpness which is caused by defects and smaller terrace size. However the electrochemical measurements are very sensitive to structural properties and still show the good quality of these samples which can be used as a cheaper alternative for massive single crystals as support materials for catalysis research. Also it was shown that SECPM can produce image quality comparable to EC-STM and AFM.

6 Key Research Findings: Biomolecules

6.1 Introduction

Proteins are biological macromolecules and form the main functional operators in biological systems. Metalloproteins, proteins containing metal atoms, make up about 30 % of the known proteins. The subgroup of redox metalloproteins plays an important role in biological electron transfer and is essential for respiration, photosynthesis, and catalytic reactions [26, 35]. Ions of metals such as vanadium, manganese, iron, copper, tungsten, and zinc form the active site of metalloproteins, and their reversible electron transfer properties add the redox functionality to the proteins. In addition to metal ions, organic redox molecules such as flavin adenine dinucleotide (FAD) can be employed as redox shuttle. FAD undergoes two proton-coupled electron transfers to form the reduced $FADH_2$. It is an active part of glucose oxidase (GOx).

As for coordination complexes, the electron transfer reactions of metalloproteins can be described with Marcus theory [28, 80, 81]. Metalloproteins whose primary function is electron transport usually undergo only minimal structural changes during electron transfer. This feature keeps the inner reorganization energy λ_{in} at a minimum. Electrostatic shielding of the redox center from the dipoles of the solvent by the amino acids of the protein shell limits the outer shell reorganization energy λ_{os}. The heme group of cytochrome c, for example, is located within the hydrophobic interior of the molecule, which minimizes its exposure to bulk water [82]. A study based on X-ray structures of cytochrome estimated that λ_{os} is five times smaller when the heme group is placed within the protein as compared to being dissolved in water ($\lambda_{os} = 0.28$ and 1.39 eV, respectively) [83]. According to the fundamental Marcus theory, the electron transfer rate depends exponentially on the sum ($\lambda_{in} + \lambda_{os}$), and therefore metalloproteins usually exhibit fast and facile electron transfer. The introduction of an EC-STM tip as electron acceptor or donor, i.e., the change from homogeneous Eq. 1.8 to heterogeneous Eq. 1.9 electron transfer, introduces a number of changes to λ_{os} as it depends on the environmental details. Corni calculated this difference for Azurin (Az) [84]:

$$[\mathrm{Az(I)} - \mathrm{Az(II)}]_{enc} \rightarrow [\mathrm{Az(II)} - \mathrm{Az(I)}]_{enc} \tag{1.8}$$

$$\mathrm{Az(II)} + \mathrm{electrode}[\mathrm{n\,e^-}] \rightarrow \mathrm{Az(I)} + \mathrm{electrode}[(\mathrm{n}-1)\,\mathrm{e^-}] \tag{1.9}$$

With the term $[Az(I) - Az(II)]_{enc}$, the author represents the encounter complex formed by one oxidized and one reduced molecule. Oxidation states stem from the Cu ion contained in Azurin. On the one hand, the metallic tip displaces water molecules and therefore λ_{os} is reduced. On the other hand, the distance between the molecule and tip will generally be larger in an EC-STM experiment (∼5 Å) than the intermolecular distance for the encounter complex. As proximity of active sites diminishes λ_{os} too, it cannot universally be stated which case, homogeneous or heterogeneous, entails the smaller λ_{os}.

The group of M. E. Michel-Beyerle theoretically investigated intramolecular ET to compare experimental rates with rates calculated from reorganization energies and studied the influence of donor-acceptor distance [85], dielectric relaxation [86], and solvent polarity [87, 88].

Another general feature of the electron transfer of metalloproteins is that it often is coupled to simultaneous proton transfer. Proton-coupled electron transfer (PCET) avoids high-energy intermediates which enhances stability of the oxidized molecule [89].

Table 1.1 lists EC-STM and SECPM studies performed on redox-active biomolecules. Published in 1996, the report by Tao on Fe-protoporphyrin [30] precedes all the other studies by far. Only the study by Baier and Stimming [12] employs SECPM for their biomolecular studies. The following chapter will give an overview about the listed reports, ranging from fundamental investigations focusing on the electron transfer to efforts using the molecules as building blocks for molecular electronics.

Before getting immersed in results and conclusions of the presented studies, we start with two introductory sections. As the reader might be unfamiliar with biological terms, we dedicate a few lines to introducing the biomolecules which were investigated with EC-STM or SECPM. We give their mass in kilodalton (kDa) so that the reader can get an idea of the size of the molecules.

Subsequently we dedicate one paragraph on how to anchor the molecules on a chosen substrate.

The immobilization requires a well-considered trade-off between good control and working under physiological conditions.

6.1.1 Introducing the Investigated Biomolecules

For the later discussion important cofactors are the active site of proteins that add functionality to the bigger molecules. One distinguishes between tightly bound cofactors, so-called prosthetic groups, and coenzymes that are only loosely bound [102].

Protoporphyrin IX (∼0.6 kDa) investigated by Tao is an organic ring that can contain an Fe ion [30]. This carrier molecule for iron, Fe-protoporphyrin, constitutes the heme cofactor (prosthetic group) of heme proteins such as hemoglobin. Hemoglobin is essential for oxygen transport in red blood cells.

Another heme protein containing Fe-protoporphyrin is cytochrome (∼12 kDa). In studies [92, 93] the whole protein was investigated, not only the cofactor as by Tao [30]. Cytochrome is responsible for the generation of adenosine triphosphate

Table 1.1 Published studies on in situ electrochemical investigation of biomolecules with either EC-STM or SECPM. The abbreviation org. denotes that the active site in the case of glucose oxidase is an organic group, the quinone/hydroquinone redox couple

Molecule (redox site)	Method	Tip	Coating	Substrate	Anchorage	Comments	References
Fe-protoporphyrin (Fe)	EC-STM	W, $Pt_{0.8}Ir_{0.2}$	Apiezon	HOPG	Adsorbed	Resonant tunnelling through redox state	[30]
Ferritin (Fe), apoferritin, horseradish peroxidase (Fe)	EC-STM, SECPM	Au	Apiezon	Oxidized HOPG	Adsorbed	Currentless, high-resolution measurement with SECPM	[12]
Glucose oxidase (org.)	EC-STM	Au	Apiezon	Oxidized HOPG	Adsorbed	Theoretical calculations in parallel	[25]
Glucose oxidase (org.)	EC-STM	Au, Pt/Ir	Apiezon, phoretic paint	Oxidized HOPG	Adsorbed		[90]
Copper nitrite reductase (Cu)	EC-STM	$Pt_{0.8}Ir_{0.2}$	Apiezon	Au(111)	Chemisorbed	Perspective for NO_2^- monitoring	[91]
Cytochrome (Fe)	EC-STM	Pt/Ir		Au	Chemisorbed to tip and substrate	Single-molecule conductance measurement	[92]
Cytochrome (Fe), Azurin (Zn)	EC-STM	Au	Apiezon	Au	Chemisorbed	Also CP-AFM measurements	[93]
Azurin (Cu & Zn)	EC-STM	$Pt_{0.8}Ir_{0.2}$	Apiezon	Au(111)	Chemisorbed	Cu shows tunnelling, Zn does not	[94]
Azurin (Cu & Zn)	EC-STM	Au-stylus	Apiezon	Au	Chemisorbed to tip	Single-molecule transistor	[95]
Azurin (Cu)	EC-STM	W, $Pt_{0.8}Ir_{0.2}$	Apiezon	Au(111)	Alkanethiols	SAM of varying length	[96]
Azurin (Cu)	EC-STM	Pt/Ir	Nail polish	Au	Chemisorbed	Single-molecule memory device	[97]
Azurin (Cu)	EC-STM	$Pt_{0.8}Ir_{0.2}$	Apiezon	Au(111)	Chemisorbed	Switching of molecule "on-off"	[98]

(*continued*)

Table 1.1 (continued)

Molecule (redox site)	Method	Tip	Coating	Substrate	Anchorage	Comments	References
Diheme cytochrome c_4 (Fe)	EC-STM	$Pt_{0.8}Ir_{0.2}$	Apiezon	Au(111)	Chemisorbed	Focus on intramolecular electron transfer	[99]
Insulin	EC-STM	W, $Pt_{0.8}Ir_{0.2}$	Apiezon	Au(111), Au (100), Au(110)	Chemisorbed	Comparison of single-crystal surfaces	[100]
Laccases, bilirubin oxidase (Cu)	EC-STM	W	Apiezon	Au(111)	Adsorbed, chemisorbed	Various SAMs, electrocatalysis	[101]

SAM stands for self-assembled monolayer

via electron transport, and due to its central role in living organisms, it is one of the most extensively studied proteins [103].

In comparison to the other proteins, a giant ferritin (∼450 kDa) contains about 4,500 Fe^{III} ions. This iron-storage protein and apoferritin, the hollow protein shell without iron, were investigated by our group using EC-STM and SECPM [12, 104]. In the same study horseradish peroxidase (HPR) was investigated. Being much smaller (∼44 kDa), HPR contains only one Fe ion as part of the heme group.

GOx (160 kDa) is an enzyme that helps to break down glucose. It obtains its redox activity from an organic group, the two electron quinone/hydroquinone redox couple on its FAD cofactor. FAD is not covalently bound and can be released from GOx. As mentioned earlier, FAD is an example for an organic active site [25, 90].

Half of the studies listed in Table 1.1 were performed on Azurin (14.6 kDa), containing either a Cu or Zn ion. Containing a Cu ion, Azurin belongs to the family of the so-called blue copper proteins, and its reversible redox reaction Cu^{1+}/Cu^{2+} enables it to shuttle electrons between molecular partners [26]. The equilibrium potential of the cuprous/cupric redox couple is significantly higher within Azurin than it is for the copper ion in water (0.360 V vs. NHE compared to 0.155 V vs. NHE) [98]. This shift is caused by the binding of the ion to the molecules via five amino acids (cysteine, two histidines, methionine, and main chain carbonyl oxygen). The Cu ion in an Azurin protein can be replaced by a Zn ion [105].

Insulin (5.8 kDa) is a hormone important for the regulation of the uptake of glucose within cells [100, 106]. The active form is the insulin monomer; dimers are formed by hydrophobic monomer/monomer interactions at concentrations higher than 1 ng mL^{-1} [107]. Insufficient insulin production (in pancreatic β-cells) and cellular resistances (i.e., diabetes) lead to a shortage of glucose supply to the cells.

Biological ET is typically dominated by large proteins containing several metal ions. Therefore, intramolecular ET is important, albeit complicated to the study [37]. The next two presented proteins contain two Fe or four Cu ions and can therefore be regarded as model systems for larger metalloproteins for the investigation of intramolecular ET. Especially the group of Jens Ulstrup contributed to the investigations of these multi-ion proteins.

The diheme protein cytochrome c_4 consists of two very similar globular domains. Each domain contains one heme group, and the two parts are connected by a 12-residue peptide chain [99, 108]. The distance between the two Fe ions is 19 Å. Since one of the heme groups is N-terminal and the other one is C-terminal, they have slightly different macroscopic equilibrium potentials, $U_{eq} \approx 0.240$ V vs. NHE and $U_{eq} \approx 0.330$ V vs. NHE, respectively [108].

In reference [101] voltammetry and electrocatalysis of the four blue multicopper oxidases are investigated. These enzymes are bilirubin oxidase and laccases from three fungal model organisms (*M. thermophila*, *C. cinereus*, and *S. coelicolor*). The laccases contain four Cu ions within a three-domain single enzyme unit [109]. During operation one of the Cu ions (type I) accepts an electron homogenously or heterogeneously; the remaining three Cu ions form the second site (type II) which induces O_2 reduction [101]. Oxidation of four equivalents of substrate at the single Cu ion is followed by sequential four-electron transfer to

reduce O_2 to H_2O [110]. Therefore, multicopper oxidases as electrocatalysts for O_2 reduction were extensively investigated [101]. Bilirubin oxidase is similar to the laccases.

6.1.2 Anchoring Biomolecules on a Substrate

Immobilization of biomolecules on electrode surfaces can be beneficial for a number of challenges imposed when electrochemically investigating metalloproteins in solution: small diffusion coefficients, redox centers which are located deep within the organic shell, and protein denaturation due to adsorption on the electrode [89]. All these issues are avoided by immobilization, and increased electron transfer rates between redox center and electrode are achieved. For microscopy studies reliable immobilization is a prerequisite.

When anchoring the biomolecules on a substrate, researchers need to find a reasonable compromise between rigid anchorage and loose electrostatic interaction. Della Pia et al. covalently bound a single cytochrome molecule to the tip and sample simultaneously [92]. By introducing cysteine residues that allow for metal-thiol interactions, they were even able to control the orientation of the protein. This approach is certainly on the rigid/controlled side of the anchoring spectrum. This is suitable when the aim of the study is not to investigate the molecule under native, physiological conditions but, for example, to identify molecules with fast electron transfer suitable for bimolecular devices.

The other extreme, which one can describe as self-assembly or bottom-up approach, was performed by Tao when he exposed a graphite substrate to a solution containing Fe-protoporphyrin and protoporphyrin without Fe ion [30]. The organic rings condensed into monolayer films on the substrate and autonomously formed a two-dimensional lattice within some minutes [111].

Basal planes of HOPG are sp^2 hybridized, exhibit a small electrochemical double-layer capacitance (2 μF cm^{-2}), and do not offer many binding sites [112]. Therefore, a viable strategy for providing anchorage for biomolecules, a bit more sophisticated than total self-assembly, is to oxidize the graphite which produces edge planes (60 μF cm^{-2}). These are sp^3 hybridized and are generally much better binding sites. Reproducible oxidation can be achieved electrochemically by applying potential sweeps in diluted acids or buffer solutions. This procedure generates surface functional groups like hydroxyl and carbonyl which improve adhesion of the biomolecules [113]. Zhang et al. reported that using a freshly cleaved, non-oxidized HOPG as substrate for HRP led to the formation of irregular islands of HPR [114]. On electrochemically oxidized HOPG, however, HRP molecules are dispersed uniformly on graphite. This benign behavior is caused by amine groups of the protein that react with carboxylic groups [12].

Looking at Table 1.1 it is apparent that Azurin was exclusively investigated by scanning probe microscopy methods on gold substrates. The reason is that Azurin has by default an anchor for the surface of metals such as Au, Pt, or Ag: the exposed amino acids Cys3 and Cys26 readily form a disulfide bridge between the protein and the gold surface [94]. Subsequent reduction transforms those bridges into gold thiolates which immobilize Azurin on gold. This method

leads to an orientation of the Azurin with the copper center facing away from the substrate, with a distance Cu ion to electrode of 26 Å [96]. Retained redox activity of immobilized Azurin, as the first redox protein, tethered to gold in that fashion was proven by Chi et al. in 1999 [115]. The density of proteins on the surface can be tuned by parameters such as incubation time, temperature, or protein concentration [98].

Cytochrome can be similarly chemisorbed on Au substrates; however, in contrast to Azurin it does not self-assemble, but a disulfide-reducing agent needs to be added [93].

Welinder et al. compared the adsorption of insulin on three low-index gold surface: Au(111), Au(100), and Au(110) [100]. This was the first study of its kind for protein-surface studies. In addition, insulin monomers or dimers in solution are structurally more flexible than other (metallo)proteins which leads to diverse adsorption patterns. Interaction of insulin with the gold surface forces the protein to unfold; exposed sulfur residues then form strong bonds with the gold surfaces. In situ STM studies revealed that adsorption of molecules was the most facile with highest coverages on Au(110) surfaces. Extensive deformation or unfolding of insulin took place on Au(110) electrodes. On Au(111) and Au(100) electrode surfaces, coverages were lower than for Au(110) and more intact insulin molecules were observed [100].

In reference [101] multicopper oxidases were either directly immobilized on Au (111) surfaces or anchored on thiol-based SAMs. Interestingly, the terminating group of the SAM had an influence on the enzyme activity towards O_2 reduction. This dependence on the terminating groups was different for the four individual oxidases under investigation. Bilirubin oxidase showed activity when adsorbed on bare gold, on a cysteine-modified SAM, and on a carboxylate-modified SAM. On alkyl- or amino-terminated SAMs, the enzyme showed no clear activity. The laccase from *M. thermophila* exhibited no activity towards O_2 reduction on any SAM. The authors explained this dependence of activity on the properties of the SAM by the surface characteristics around the type I Cu ion site. The electrochemically inactive *M. thermophila*, for example, exhibits a negative surface potential around the type I site. The authors hypothesized that this feature might prevent ET via the SAM. The successive steps of laccase immobilization on SAMs were monitored in another study [116].

6.2 Unraveling the Electron Transfer Mode Through Adsorbed Biomolecules in EC-STM

The bipotentiostatic setup of scanning probe experiments offers full control of occurring reactions by tuning the electrochemical potential, i.e., Fermi levels of the two working electrodes. Tao was the first who took full advantage of that feature for the investigation of biomolecules [30]. With the help of potential control, he was able to distinguish between Fe-protoporphyrin IX (FePP) and protoporphyrin IX (PP), although they are morphologically very similar. Both molecules are presented in

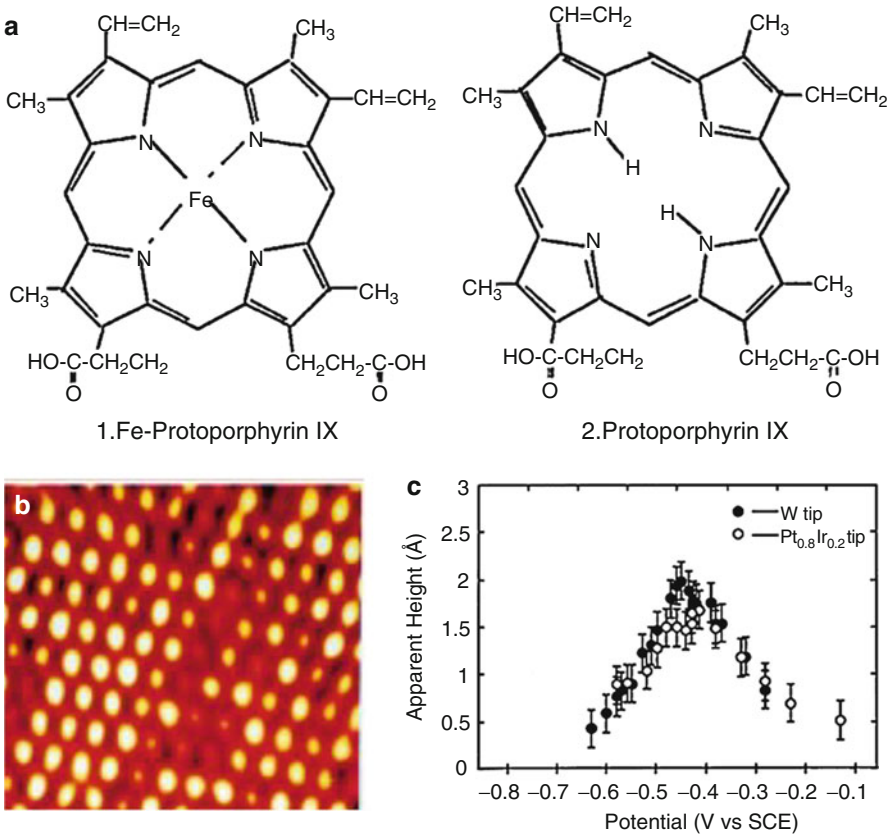


Fig. 1.18 (**a**) Comparison of FePP and PP without Fe-redox center. (**b**) EC-STM micrograph at $U_{sample} = -0.166$ V versus NHE and therefore 70 mV lower than the equilibrium potential of FePP. Four times more FePP than PP was deposited on the graphite and FePP is imaged as bright spots. The image section is approximately 20×15 nm^2 and height is not given in the reference, but values are stated in the graph on the right. (**c**) Apparent height of FePP over U_{sample} for a W and a $Pt_{0.8}Ir_{0.2}$ tip (Adapted from Ref. [30]. Copyright 1996. Reprinted by permission of the American Physical Society)

Fig. 1.18a for direct comparison. As (quasi)reference electrode he employed a silver wire which was calibrated against a saturated calomel electrode (SCE; +0.244 V vs. NHE). STM tips were electrochemically etched from $Pt_{0.8}Ir_{0.2}$ and W wires and coated with Apiezon wax. Tao stated that "the tips were not the sharpest, but they had very small leakage current (<1 pA) over a broad potential range."

The experiment was conducted as follows: FePP and PP were coadsorbed on HOPG and they self-assembled into a two-dimensional lattice [111]. The redox-active FePP undergoes electron transfer at $U_{eq} = -0.236$ V vs. NHE due to the $Fe^{II/III}$ redox couple stored within the cofactor. Using the bipotentiostatic setup U_{sample} and U_{tip} were controlled independently. Changing U_{sample} shifted the free energy of D_{ox}

and D_{red} of FePP by $e\,U_{sample}$. If U_{sample} was chosen in a way that D_{ox} aligns with the substrate Fermi level ($U_{sample} = -0.186$ V vs. NHE), the redox-active FePP "lit up" in the micrograph, while PP remained dark. This is shown in Fig. 1.18b which displays a monolayer of biomolecules on graphite with four times more FePP than PP.

A plot of the apparent height of FePP over U_{sample} shows a clear peak which is quite symmetrical and has a maximum at $U_{sample} = -0.186$ V vs. NHE (Fig. 1.18c). Tao attributes this increase in apparent height, which is equivalent to an increase in current at fixed tip-sample distance, to resonant tunnelling at an adequate U_{sample}.

In addition he stated that the full width at half maximum (FWHM) for the distribution in Fig. 1.18c should be given by $4(\lambda\, k_B\, T \ln 2)^{1/2}$, a formula that contains the reorganization energy λ. This broadening should reproduce the broadening due to fluctuations of polar solvent molecules that interact with the redox center (Gerischer's theory [28, 29]).

The observed FWHM is considerably smaller than the value of the lowest unoccupied molecular orbital Tao expected, ~0.3 and ~0.5 eV, respectively [30]. Why the maximum transition of electrons is centered at $U_{sample} = -0.186$ V vs. NHE and not at a potential closer to U_{eq} is not discussed. Nevertheless, it was the first report that electron tunnelling through cofactors adsorbed on HOPG can be tuned in and out of resonance by adjusting U_{sample}.

A similar observation was reported by Facci et al. some years later, in 2001 [98]. Their study of Azurin containing a Cu ion was the first evidence of potential-dependent tunnelling in proteins, since Tao was only looking at the cofactor FePP. Within a potential window of approx. 300 mV around U_{eq}, the authors were able to see the Azurin as bright spots on the Au substrate. The authors stated that due to "experimental uncertainties," they are not able to conclude whether resonant tunnelling or two-step electron transfer is the observed mechanism. However, they mentioned the striking similarity of the size of the potential window leading to increased apparent height when comparing it to Tao's result.

In 2003 Alessandrini et al. were able to clearly show that indeed the Cu ion is the active site within Azurin and responsible for mediating the electron transfer [94]. They compared Azurin containing a Cu ion and Azurin with Zn as metal ion. While structurally very similar, the apparent height of Cu-Azurin was much larger than the one of Zn-Azurin at appropriate potentials close to U_{eq} of the protein. Also, a gold surface covered exclusively in Zn-Azurin did not show any potential dependence.

In Sect. 4.5.1 we introduced three conceivable modes of electron transfer between substrate and sample assisted by the redox state of adsorbed molecules. The authors tested if their experimental results from Cu-Azurin fulfilled theoretical predictions of either resonant tunnelling according to Schmickler's model [117, 118] or two-step ET, either sequential or vibrationally coherent, as described by Kuznetsov et al. [34, 119].

For a single-step ET, resonant tunnelling, the potential of the substrate U_{sample} at which maximum current tunnelling is measured U_{sample}^{max} is given by [27]

Table 1.2 Extracted parameters to calculate the total reorganization energy in resonant tunnelling mode (λ_{res}) and in two-step electron transfer mode (λ_{two})

	U^{max}_{sample}/V	U_0 /V	U_{bias}/V	λ_{res}/eV	λ_{two}/eV	References
FePP	−0.43	−0.48	−0.1	0.00	0.10	[30]
Azurin (Cu)	−0.22	0.12	0.4	0.13	0.53	[94]
Cytochrome	0.31	0.32	−0.3	0.16	−0.14	[93]

$$U^{max}_{sample} = U_{eq} - \lambda - \frac{U_{bias}}{2} \tag{1.10}$$

Two-step ET manifests itself in a slightly different relation between U^{max}_{sample} and U_{bias} [34]:

$$U^{max}_{sample} = U_{eq} - \lambda + \alpha\, U_{bias} \tag{1.11}$$

The symmetry factor α ($0 < \alpha < 1$) gives the part of U_{bias} that drops at the redox site. A typical value for α is 0.5 [94]. Both equations state that there is an offset between U_{eq} and U^{max}_{sample} that is given by the total reorganization energy λ for small U_{bias}. An offset that was also seen by Tao but was not commented on [30]. The problem of discerning between the two different ET modes should therefore boil down to obtaining legitimate estimations for λ and comparing it to the experimental results. For comparison with literature values, one has to take the influence of the tip into account, as discussed in Sect. 6.1. In Table 1.2 we summarize values for the parameters of Eqs. 1.10 and 1.11 for some studies [30, 93, 94] and calculated the resulting reorganization energy in the resonant (λ_{res}) and two-step (λ_{two}) mode. The value for α was assumed to be 0.5 and the values for U^{max}_{sample} are extracted from graphs [30], [94].

Tao himself assumed a reorganization energy of FePP of $\lambda = 1$ eV. Obviously the values obtained for λ from Eqs. 1.10 and 1.11 are smaller than this estimated value (0.00 and 0.10 eV, respectively). Alessandrini et al. compared their values of the reorganization energy of Azurin to $\lambda_{lit} = 0.8$ eV [94]. Even if the perturbing influence of the tip as possible source of error is kept in mind, the deviations of $\lambda_{lit} - \lambda_{res} = 0.67$ eV and $\lambda_{lit} - \lambda_{two} = 0.27$ eV are too large to reliably distinguish between the two mechanisms, as conceded by the authors.

To eradicate the uncertainty introduced by the metallic tip, Corni investigated the outer-sphere reorganization energy λ_{os} both in the homogeneous and heterogeneous case, as already stated in Sect. 6.1 [84]. While Corni took the inner contribution $\lambda_{in} = 0.146$ eV for Azurin from the literature [120], λ_{os} was calculated with a quantum mechanical treatment. In the case of heterogeneous electron transfer Eq. 1.9, λ_{os} was calculated to be 0.29 eV, yielding a total reorganization energy of $\lambda = 0.43$ eV. This value is certainly much closer to λ_{two} than it is to λ_{res} for Cu-Azurin (compare Table 1.2) which indicates that indeed a two-step ET with relaxation might take place.

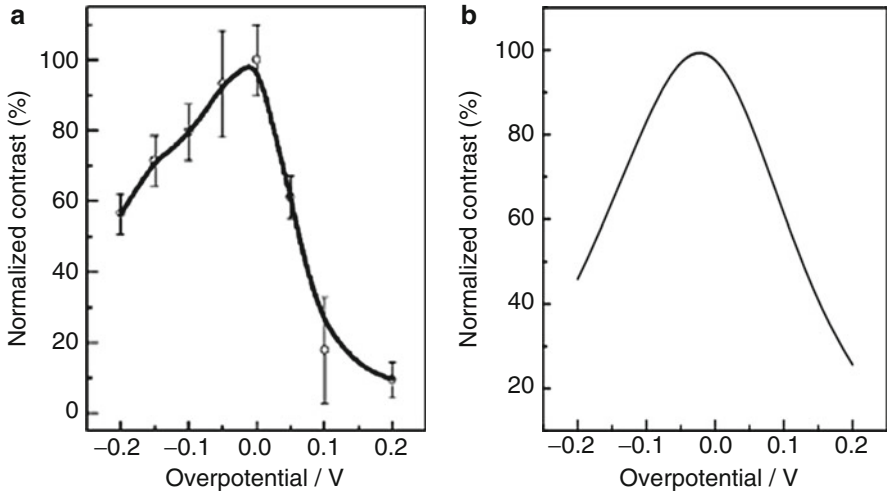


Fig. 1.19 (**a**) Experimental and (**b**) theoretical correlation between normalized contrast and overpotential of the GOx molecule. Data was derived from multiple EC-STM micrographs recorded at bias voltage: 100 mV (*tip positive*). Set point: 0.5 nA (Adapted from Refs. [25, 90]. Copyright 2008. (**a**) Reprinted by permission of ACS Publications. (**b**) Reprinted by permission of Wiley-VCH Verlag GmbH & Co)

In contrast to the combined effort of ref. [84, 94], a study that investigated cytochrome c with an EC-STM was much less optimistic about discerning between the modes of ET [93]. Davis et al. did not find an appreciable offset between U_{eq} and U_{sample}^{max}, as shown in Table 1.2. They stated that the combination of low reorganization energy of biomolecules and the masking effect of U_{bias} makes the distinction difficult.

Studies on glucose oxidase, with its cofactor FAD, performed by our group also yielded a potential-dependent behavior [25, 90]. The image of the molecules became clearly visible when the potential applied to the surface was tuned to U_{eq} of the redox center. Comparison of the apparent height vs. potential FWHM with expected broadening due to redox center-polar solvent interaction, as performed by Tao for FePP [30], led to good agreement. A new feature was that the curve exhibited a nonsymmetrical dependence on the applied overpotential. The experimental normalized current versus the overpotential is depicted in Fig. 1.19a. The normalized contrast decayed more rapidly on the positive overpotential side at small bias potentials ($U_{bias} = 50$ mV). This asymmetrical shape is in good agreement with model systems comprising Fermi levels of substrate and tip and the energy levels or ET molecules [96]. Comparison of the experimental curve (Fig. 1.19a) with one obtained assuming two-step electron transfer model gave excellent agreement. The modeled curve is depicted in Fig. 1.19b [25, 90]. The computations provided good understanding of the ET mechanisms and several conclusions were drawn:

- U_{sample} has an obvious influence on apparent height of the redox molecule.
- The rate-limiting step is the ET between the tip and GOx. In the calculations the reaction rate of the ET from the molecule to the sample turned out to be 450 times faster than the rate between the tip and redox molecule.
- The reorganization energy was estimated at $\lambda = 0.36–0.40$ eV, which is in good agreement with the value determined from the FWHM (Fig. 1.19a).
- The distribution of the bias voltage in the tunnelling gap is asymmetric.

Summarizing, two studies that combined experimental and theoretical efforts [25, 26, 90, 94] concluded that ET between the tip and substrate through the redox states proceeds via a two-step ET mechanism.

ET reactions responsible for the catalytic activity towards oxygen reduction of electrode-immobilized multicopper oxidase are more complicated and involve interfacial and intramolecular ET steps [91, 101, 121]. Interfacial ET takes place between the electrode and the type I Cu ion as well as between the O_2/H_2O couple and the three type II Cu ions; intramolecular ET occurs between the type I and type II sites. In different potential regions, the electron transfer constants k for interfacial and intramolecular ET are different, and therefore the rate-determining step may vary for different potentials.

The image pattern of the enzymes immobilized on the electrode is dependent both on the applied potential and the presence of oxygen. In pure argon atmosphere, no enzyme-related structures can be observed with EC-STM [101]. Only in the presence of oxygen single-molecule features appear in potential ranges related to catalytic activity. EC-STM can only image the molecule in its catalytically active (reduced) state. Switching between the "on" and "off" states is possible by potential control. This study adds the novel "catalysis aspect," the prerequisite of a chemical species (O_2) for transformation, to the studies previously described.

Chi et al. were able to determine the interfacial and intramolecular ET rate for the diheme protein cytochrome c_4 in great detail [99]. For that purpose the metalloprotein was immobilized in sub-monolayers on negatively or positively charge SAMs. The upright standing orientation of the protein was confirmed with EC-STM. The high resolution of the determined ET rates was possible because the cytochrome was immobilized on flat, single-crystal electrode and therefore not prone to diffusion. It was found that the intramolecular ET rate is very fast, on the order of $k \approx 10^4\ s^{-1}$. On the other hand, the interfacial ET rate was determined to be a function of the distance between redox center and substrate. The value was adjusted by the length of the SAM linker chain (ω-mercapto-alkanoic acid) which anchored the metalloprotein on the Au(111) substrate. For all length the interfacial ET rate was at least two orders of magnitudes smaller than the intramolecular ET rate.

6.3 Shape and Size of Biomolecules

In the previous chapter, the fundamental question "how electron tunnels form sample to the tip via the redox state of a biomolecule or vice versa" has been

elucidated for EC-STM. Now we turn our attention to the morphological information that can be obtained by EC-STM or SECPM.

6.3.1 Influences on the Shape of Biomolecules when Measured with EC-STM

As we have seen in the previous chapter, EC-STM images are dependent on the applied potentials; biomolecules are only visible when they participate in the electron transfer, and they do so only when the substrate potential is tuned to a proper region around U_{eq}. This feature differentiates EC-STM from other methods such as scanning force microscopy (SFM) which was employed in one study in parallel to EC-STM to image Cu-Azurin [98]. However, while SFM is less intricate in terms of electronic structure, it comes with its own penalty [122]. Tip-adsorbate convolution is a common effect for force microscopy and in above study it led to a magnification of the lateral size of Cu-Azurin. In addition, the measured molecule height is smaller than crystallographic data suggests; a fact which was attributed to pressure applied by the tip.

Apparent height changes of molecules in an EC-STM micrograph can be attributed to an actual change in physical height, its conductance (related to U_{sample}), or both [25, 123].

With a clear model of how the electron transfer takes place, as stated in the previous subsection, the task is to obtain the true shape and size of biomolecules from the potential-dependent apparent height and shape. In our group three possible perturbing influences were identified, and their impact on the shape and size of the molecules was analyzed. These possible sources of disturbances are:

- Convolution of electronic properties of the tip/molecule/substrate [25, 90]
- The ECDL of the molecule-decorated substrate [25]
- Faradaic currents at the tip [90]

Their influence on the apparent shape and height will be discussed in the following.

Using a two-step ET model, Wang et al. visualized the impact of changes of the redox molecule's work function W on the imaging of small objects [25]. W contains the Fermi Energy as well as the applied potential:

$$W = -eU - E_F \tag{1.12}$$

The tunnelling current in EC-STM measurements depends on the distance between tip d and sample, U_{bias}, and is also related to the work function W according to Eq. 1.1. In constant current mode, d is initially kept constant, while there is a change in barrier (W), when the tip is scanned from bare substrate to the substrate decorated with biomolecules. Thus, the tunnelling current is affected by the electronic structure.

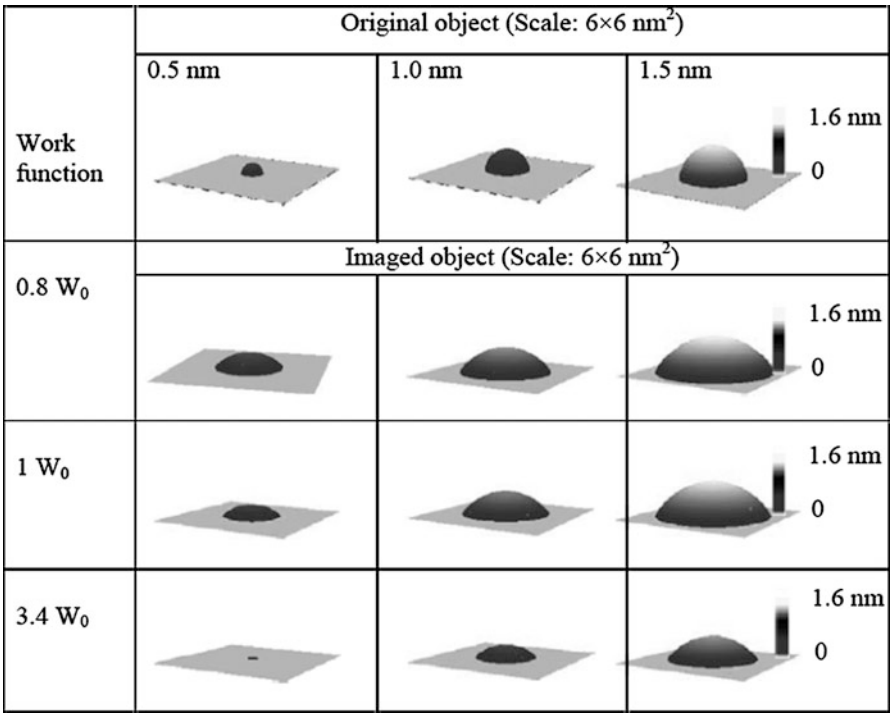


Fig. 1.20 Calculated effect of tip-sample convolution for small particles. Imaged objects for original objects with sizes 0.5, 1.0, and 1.5 nm were drawn in dependence on the molecule's work function given as a product with substrate work function W_0 (Reprinted from Ref. [90]. Copyright 2008. Reprinted by permission of ACS Publications)

The results for theoretical small objects with dimensions 0.5, 1.0, and 1.5 nm are reproduced in Fig. 1.20. W_0 is the work function of a graphite sample with a value of 5.2 eV and the initial tip-sample distance was 1.4 nm.

The simulation shows that there are minor distortions when the work function of the object is smaller than W_0; the lateral dimensions of the image are larger than the original object. When the sample's radius increases, the distortion becomes larger. Very interesting is the case of high work function (3.4 W_0) for a particle which dimension is much smaller than the tip-sample distance ($0.5 < 1.4$ nm). The imaged object has an apparent height which is virtually zero [25]. When the work function is too large, the particle cannot participate in the ET process; it loses its conductivity.

This potential-dependent switching of the molecule conductivity, from insulating barrier to intermediate redox state, was observed for GOx by Wang et al., supporting the above theoretical study [90]. A series of EC-STM micrographs is shown in Fig. 1.21. At overpotentials of +200 and +100 mV (Fig. 1.21a, b), GOx is hardly visible on the HOPG substrate; the contrast enhances with decreasing overpotentials showing the highest apparent height at 0 and −50 mV. The authors

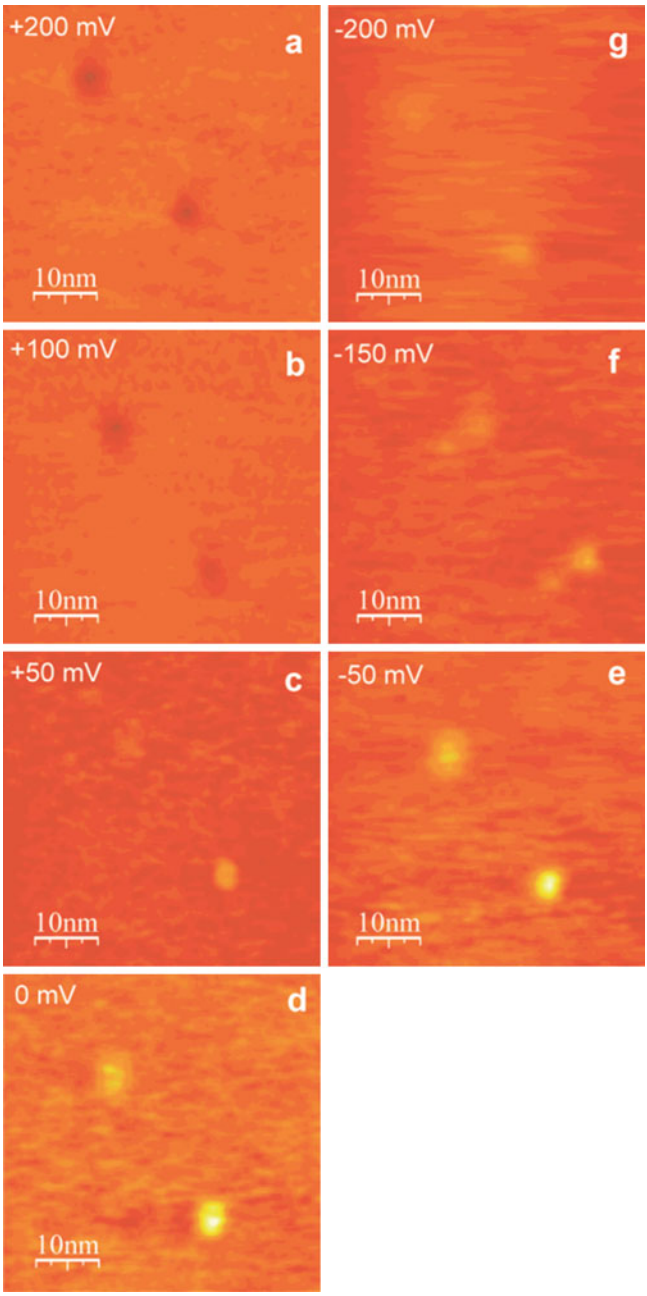


Fig. 1.21 Series of EC-STM micrographs of adsorbed GOx on HOPG in phosphate-buffered solution. The overpotentials are given in the upper left corner of the individual subfigures. The vertical range was 8 Å. Bias voltage: 100 mV (tip positive). Set point: 0.5 nA. Scan rate: 2 Hz (Reprinted from Ref. [90]. Copyright 2008. Reprinted by permission of ACS Publications)

extracted the apparent height and plotted them at the corresponding overpotential; we showed that graph earlier (Fig. 1.19a).

Figure 1.21 was recorded in constant current mode and the set point was 0.5 nA. When scanning the HOPG surface, the distance of the tip will adjust itself to the correct z-value so that I_t matches the set point in dependence of the effective barrier height ϕ_{eff} (see Eq. 1.1).

In the case of Fig. 1.21a, U_{sample} is set to an overpotential at which the GOx is "switched-off," not redox active. The tunnelling barrier ϕ_{eff} is then higher than in the case of bare HOPG and the feedback loop will decrease z so that I_t matches the set point. Therefore, the molecule is seen as a darker indent on the substrate.

In Fig. 1.21e the diametrical scenario is shown. The applied overpotential of −50 mV shifts the energy states of GOx so that it is now "switched on." It can now participate in the ET between the sample and tip, most likely via a two-step mechanism [25]. This participation reduces ϕ_{eff} and z is increased so that I_t is not larger than the set point. Therefore, the molecule is seen as a bright spot on the HOPG substrate. The other images of Fig. 1.21 are intermediate cases.

Besides tip-sample convolution, another perturbing factor is that the tip might be moving within the ECDL of the substrate [25]. To get quantitative values for the ECDL induced by U_{sample} current-potential curves can be measured with an interrupted feedback method [13, 60]. The method was originally developed to measure the activity of single supported nanoparticles, but it is also suitable to investigate the influence of an ECDL on the EC-STM imaging process. Wang et al. found that the double-layer thickness in their experiment was at least six times larger than the tunnelling gap. Therefore, the tunnelling current could be compensated or increased by effects such as screening of charges by countercharges of the ECDL. The effect is aggravated by the fact that the ion concentration in the supporting electrolyte should be low (∼10 mM) in order to obtain good STM images. At higher concentrations, however, the ECDL would not extend as far (compare Sect. 4.5.2). Employing electrochemical impedance spectroscopy (EIS), it was established that the capacitance of a GOx-modified HOPG electrode changes with applied U_{sample}. A minimum double-layer capacitance was observed around U_{eq} of the molecule [90].

The measured current at the tip during an EC-STM experiment is the sum of faradaic and tunnelling current. The biomolecules undergo redox reactions and transfer single electrons (FePP, cytochrome, Cu-Azurin) or two electrons (GOx). In constant current mode the total current is set to a set point value I^0. The feedback loop adjusts the total current to match I^0. An illustration of this behavior is shown in Fig. 1.22. A positive faradaic contribution I_F to the total current I will lead to an increased apparent molecule height, as the tip-sample distance is increased to reduce the tunnelling current I_t. Similarly, the apparent height is lower than that of the original object ($H < H^0$) when there is a negative I_F, when the molecule is reduced by the current from the tip [90]. Typically, it is assumed that present oxygen molecules contribute to the faradaic currents, for example, by a transfer of negative charge from the FAD cofactor to form O_2^- [124, 125].

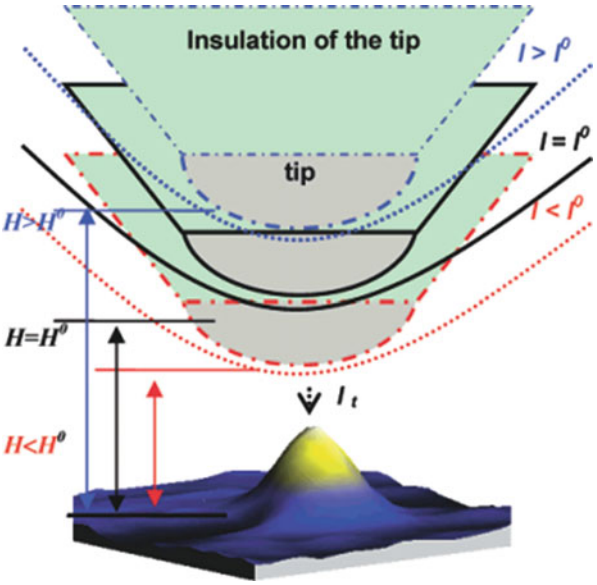


Fig. 1.22 Effect of current on the apparent height of biomolecules in EC-STM measurements. The original height of the molecule was set at H^0 when the tunnelling current is at set point I^0. Faradaic contributions to the current vary lead to an apparent height different from H^0 (Reprinted from Ref. [90]. Copyright 2008. Reprinted by permission of ACS Publications)

Wang et al. estimated that due to the slow turnover rates of GOx, the effect on the measured tip current should not exceed 10 %.

While the contribution of faradaic currents can be seen as an impediment to EC-STM measurements of redox-active molecules, it can also be understood as a powerful, future scientific tool, if wielded correctly. Jens Ulstrup and co-workers developed the theoretical framework for single-molecule electron transfer in electrochemical systems [36, 37]. Due to its small size, an EC-STM tip hovering over a redox molecule should be able to record only the faradaic current from one single molecule. Investigations of ET reactions of a single molecule would be feasible, and fundamental electron transfer constants k_0 could be determined. Of course there are experimental problems, like subtracting all the current signals which are non-faradaic and minimizing the drift of the tip, but the insights that can be gained are unprecedented in studying interfacial charge transfer reactions.

6.3.2 Resolving Single Biomolecules with EC-STM and SECPM

Despite above intricacies, Wang et al. were able to distinguish between the butterfly and the spherical shape of GOx. The former corresponds with a lying configuration while the latter shows a standing molecule [90, 126]. Average lateral sizes of these two shapes corresponded well with crystallographic data. Their measured height (4–10 Å), however, is always smaller than values reported by X-ray crystallographic studies [90]. This reduction in height was attributed to the interactions reported above.

In the following we will directly compare EC-STM and SECPM measurements on biomolecules. First, we will juxtapose images taken of bare HOPG substrate by

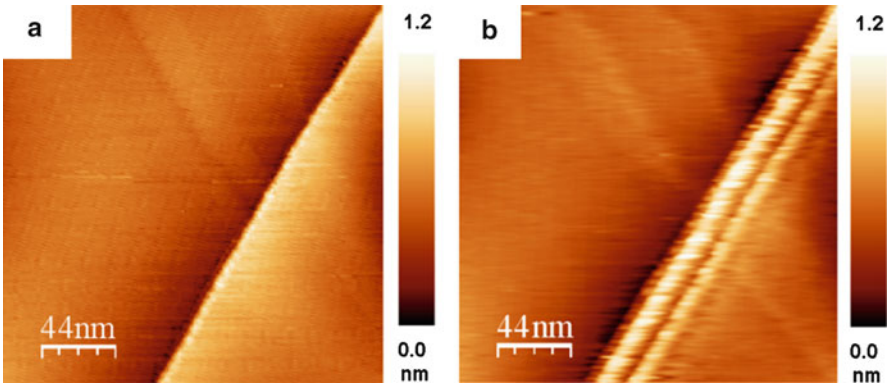


Fig. 1.23 Micrographs of basal plane HOPG surface with one clearly visible step edge obtained in 0.1 M $HClO_4$ at $U_{sample} = 300$ mV versus NHE. (**a**) EC-STM, bias voltage, 100 mV; set point, 1.0 nA. (**b**) SECPM: $\Delta U = 5$ mV (The picture is taken from Ref. [40])

the two techniques and comment on the differences and similarities. Second, we will do the same for HOPG decorated with single iron-storage proteins ferritin. Third, images of HPR by SECPM and EC-STM will be compared.

SECPM in potential-mapping mode was employed to image ferritin, apoferritin, and HPR to compare it to the images obtained by EC-STM [12]. While the challenges of SECPM were illustrated in the subsection 4.5.2, we also stated that the potential-mapping mode does not suffer from fundamental problems, such as the overlap of ECDLs, as much as potential-approach curves.

Figure 1.23 shows micrographs of bare HOPG substrate. It is in ideal starting point for comparative studies as it is often used as a calibration tool, atomic resolution is easily obtainable, and because it is the substrate for many adsorbed molecules (compare Table 1.1). While the left image was recorded with EC-STM, the right one was obtained by SECPM [40]. The micrographs show the same image section with the characteristic atomically flat basal planes and one step edge crossing diagonally. Both techniques depict the basal planes as smooth, flat surfaces. The step edge of HOPG, however, appears much broader and shows a higher contrast in SECPM than it does in EC-STM. Macroscopic techniques such as differential capacitance measurements or EIS only yield spatially averaged information for the surface of HOPG, whereas SECPM is able to resolve its anisotropy. In the literature it is well established that step edges and defects are sites of increased [127] or decreased [128] activity for electron transfer reactions. At a graphite step the specific capacitance suddenly jumps from 2 μF cm^{-2} of the basal plane to 60 μF cm^{-2} of the edge plane, an effect attributed to the low DOS of basal plane HOPG [112]. This change is visible in SECPM; the sudden alteration in the ECDL might cause the tip to oscillate slightly, as seen in Fig. 1.25b. More experiments, e.g., employing variable scan speeds, should be performed to elucidate the origin of these oscillations. Figure 1.23 suggests that anisotropies in the graphite surface can be better resolved by SECPM than by EC-STM.

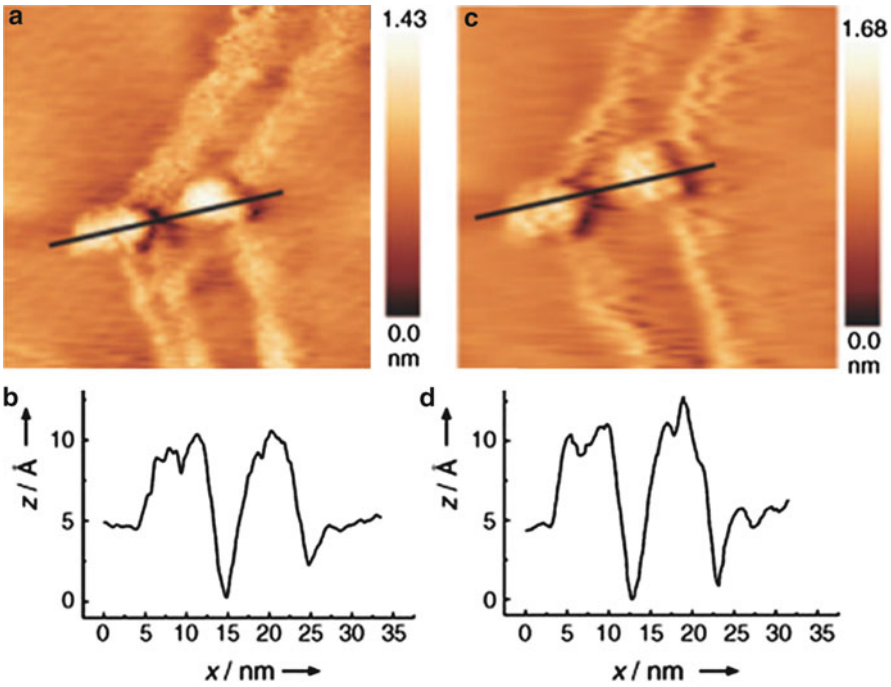


Fig. 1.24 Micrographs of two ferritin proteins on 40 × 40 nm electrochemically oxidized HOPG and their corresponding line scan in 10 mM phosphate-buffered solution. (**a**, **b**) EC-STM: bias voltage, 100 mV (*tip positive*). Set point: 0.5 nA. (**c**, **d**) SECPM: set potential difference, 0.5 mV (Reprinted from Ref. [12]. Copyright 2009. Reprinted by permission of John Wiley & Sons, Inc)

Two single iron-storage proteins ferritin and their respective line scans are shown in Fig. 1.24. They are adsorbed on line defects of electrochemically oxidized HOPG [12]. While the left image was obtained by EC-STM, the right one was taken by SECPM. The two images resemble each other; however, Baier et al. stated that the SECPM mode was not prone to disturbances due to tip-electrode interactions in contrast to the EC-STM mode which picked up some perturbations, and some artifacts were recorded [12].

The diameter of the imaged molecules was determined to be 7.5 nm (left enzyme) and 6.9 nm (right enzyme) with an apparent height of 0.5 nm. Comparison with structural data of ferritin indicates that mostly the iron-containing core was imaged, as its size of 8 nm corresponds well with the experimentally found diameter. The whole structure of the molecule, iron core plus protein shell, is significantly larger (12 nm) [129].

This notion, that the iron ions inside the protein dominate the imaging process, was affirmed by fruitless efforts to image the ironless apoferritin with EC-STM [12]. This might be due to the low conductivity of the protein polypeptide.

In contrast to the EC-STM study which could not resolve apoferritin, examination with SECPM yielded images of single molecules with a diameter of

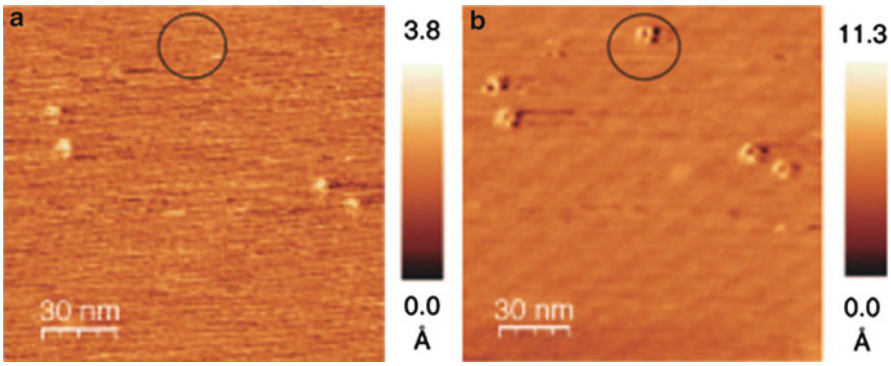


Fig. 1.25 Horseradish peroxidase proteins on oxidized HOPG in 10 mM phosphate-buffered solution. (**a**) EC-STM: bias voltage, 100 mV (*tip positive*). Set point: 0.5 nA. (**b**) SECPM: set potential difference: 0.5 mV (Reprinted from Ref. [12]. Copyright 2009. Reprinted by permission of John Wiley & Sons, Inc)

approximately 12 nm. That the hollow apoferritin was found to be bigger than the iron-filled ferritin (~7 nm) was assigned to the rather even potential distribution of the former and the predominance of the signal of the iron ions inside of the cavity of the latter [12]. This domination might mask the signal of the protein shell, but SECPM is certainly able to resolve this low-conductivity part of ferritin.

In the same study as ferritin, HPR was investigated on HOPG substrate by EC-STM and SECPM [12]. The one heme group containing enzyme can be seen in Fig. 1.24.

EC-STM is able to image four single molecules, albeit with a low resolution. The determined size ($43 \times 34 \times 2.4$ Å^3) does not match earlier reports ($68 \times 44 \times 40$ Å^3) [114]. Baier et al. assumed that poor contact between the substrate and the enzyme impaired the image quality. During measurement a set point current of 0.5 nA equals an electron transfer rate of approximately 10^9 s^{-1} through one single molecule. The authors hypothesize that this current might have a detrimental effect on the protein structure. Recorded CVs of HPR-modified HOPG showed a redox reaction centered around $U_{eq} = 0.200$ V vs. NHE, confirming the electron transfer between graphite and enzyme [40].

Imaging HPR with SECPM and comparing that image section (Fig. 1.24b) to the same one visualized by EC-STM (Fig. 1.24a), the first striking difference is that SECPM resolves one more molecule than EC-STM (highlighted by black circles). This might be due to a poor electrical contact which prohibits electron transfer for EC-STM, but since SECPM only maps the charge distribution, it is unaffected by low conductivity [12]. SECPM shows slightly bigger molecules ($54 \times 52 \times 3.2$ Å^3) than EC-STM and the resolution is better; the open-loop-shaped structure is clearly visible for all the enzymes in Fig. 1.24b.

In a 3D representation (Fig. 1.26a) and a contour plot (Fig. 1.26b) of two of the HPR, the open loop shape is clearly visible. X-ray crystallographic data (Fig. 1.26c)

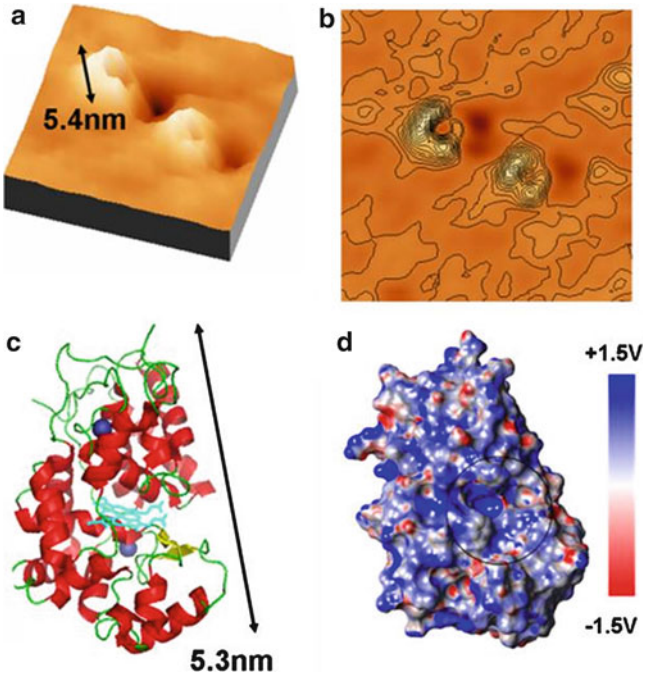


Fig. 1.26 (**a**) 3D representation of SECPM image of two horseradish peroxidase proteins (HPR) on HOPG. It is detailed in Fig. 1.25a. (**b**) Corresponding contour plot. (**c**) 3D plot of the X-ray crystal structure of HPR. The heme group is shown in *turquoise*, calcium ions in *blue*, α-helices in *red*, and β-sheets in *yellow*. (**d**) Surface potential of HPR in 10 mM phosphate-buffered solution (pH 7) (Reprinted from Ref. [12]. Copyright 2009. Reprinted by permission of John Wiley & Sons, Inc)

suggests that heme group resides in the semi-cavity and that this shape corresponds to the open loop seen with SECPM. Transformation from pure crystallographic data to an image of charge distribution (Fig. 1.26d) can be performed by simulation with YASARA [130]. This allows for a qualitative comparison with SECPM images.

In conclusion, to avoid two inherent problems of EC-STM, namely, need for good contact between substrate and biomolecule and the possible current damage to the sample under investigation, our group was the first to employ SECPM for monitoring biomolecules under in situ conditions [12].

The presented results show that SECPM can be a superior technique for imaging biomolecules at the solid-liquid interface as compared to EC-STM. Higher resolution can be achieved; samples with low conductivity such as protein polypeptides or hardly anchored proteins can be imaged [40]. Furthermore the biomolecules cannot be detrimentally influenced by the electron current which makes SECPM a noninvasive tool suitable for soft biomolecules. Further studies, such as measuring the local activity or potential-dependent imaging, should reveal if new insights into fundamental properties of biomolecules and electrocatalytic properties of redox molecules can be found by potentiometric techniques. However, as of now, ref. [12]

is the only publication reporting the application of SECPM for biomolecules. New studies have to show if other systems behave equally benign as the ferritin/apoferritin and HPR molecules on HOPG. Another important milestone would be the achievement of atomic resolution with SECPM.

6.4 Applications, Designing Devices

In the previous chapters we have seen that the conductivity of biomolecules on a substrate can be switched on and off, as a function of substrate potential. GOx, for example, possesses this property [25, 90]. This tunable switching behavior makes biomolecules a promising candidate for biomolecular electronics and nanosensing purposes [131, 132].

The work group of Paolo Facci expanded on their fundamental work with Cu-Azurin [94, 98] and investigated the same metalloprotein between two electrically biased gold electrodes [95]. The aim of the study was to realize an electrochemically gated single-molecule transistor in aqueous environment. Again, they exploited the fact that Azurin readily chemisorbs on gold via the naturally occurring disulfide bridges. After incubation of the insulated gold tip in 10^{-4} M Azurin they were able to determine the number of chemisorbed biomolecules to approximately 10^6 by integrating the current peak of a CV. A schematic of the experimental setup with the Azurin-modified gold tip can be seen in Fig. 1.27a. A TEM image of the $\sim 10^6$ proteins chemisorbed on the gold tip is shown in Fig. 1.27b. Despite the large number of present molecules, Alessandrini et al. hypothesize that only few Azurin molecules participate in the ET. They argue that the tunnelling probability drops exponentially with substrate-molecule distance, and since the proteins are relatively large (3–4 nm), Azurin molecules positioned away from the apex are inactive.

The idea of the setup is that the electrochemical control of the electron transfer reactions is used in an analogous way to the gate voltage in devices such as a single-molecule and/or single electron transistor [95, 133, 134]. Therefore, I_{tip} was measured in dependence of the tip potential U_{tip} and U_{bias}. U_{tip} determines whether the proteins are conducting or nonconducting (or "in resonance" or "off resonance" as named by Alessandrini et al.) analogous to U_{sample} in the earlier sections. Figure 1.27c shows linear potential sweeps in which U_{tip} was increased by 2.4 V/s in a waterfall plot. The lowest curve was obtained at $U_{bias} = 0.05$ V. This value was incremented by 0.05 V to obtain the other curves and the final curve was measured at $U_{bias} = 0.35$ V. From the graph it is immediately clear that appreciable current is only flowing at potentials -0.1 V vs. SCE $< U_{tip} < 0.1$ V vs. SCE (0.14 V vs. SCE $< U_{tip} < 0.34$ V vs. NHE). In the inset the current values over the steps in U_{bias} are shown. "Off resonance" is always the I_{tip} value at $U_{tip} = -0.2$ V vs. SCE (0.04 V vs. NHE), and "in resonance" is I_{tip} at the current peak. The slopes can be converted to resistances of (3.28 ± 0.25) GΩ and (660 ± 30) MΩ, respectively. Alessandrini et al. stated that this result, as a single metalloprotein-based transistor, is a crucial step towards future biomolecular electronics devices [95].

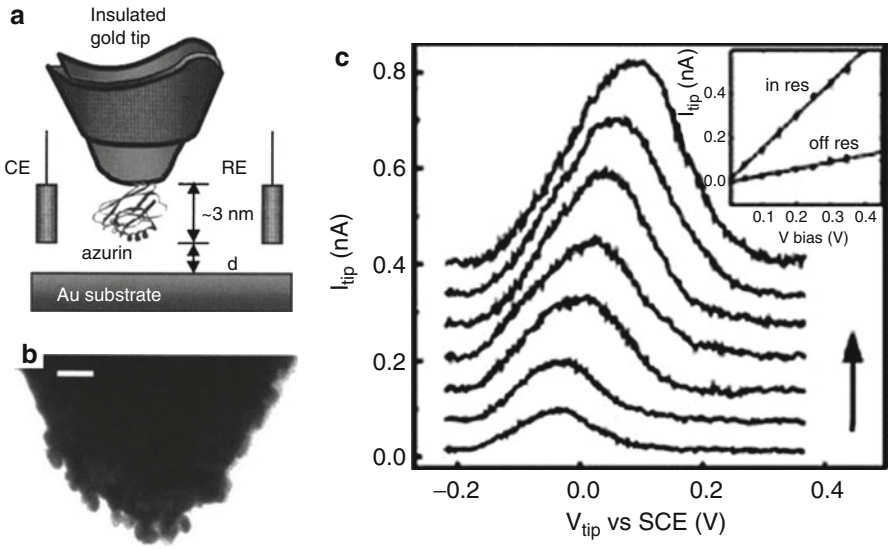


Fig. 1.27 (**a**) Schematic representation of the experimental setup for a protein transistor. (**b**) Transmission electron microscopy image of the Azurin-coated gold tip. The *white* bar has a length of 10 nm for reference. (**c**) Curves obtained at different U_{bias} using a scan rate of 2.4 V s^{-1}. Inset shows I_{tip} versus U_{bias} for the off resonance (at $U_{tip} = -0.2$ V vs. SCE) and in resonance (maximum I_{tip}, variable U_{tip}) case (Reprinted from Ref. [95]. Copyright 2005. Reprinted by permission of the American Physical Society)

Commenting on this we wonder why they call it a *single* metalloprotein-based transistor as certainly more than one Azurin protein takes part in the ET. Figure 1.27b clearly shows that many molecules are close to the apex of the tip.

Also studying Cu-Azurin, Chi et al. introduced variable-length alkanethiols to anchor the protein on a gold electrode [96]. These alkanethiols served both as tunnelling barrier and as anchorage for Azurin. The long-range interfacial ET properties and mapping of redox-gated tunnelling processes were of special interest. As in previous studies, the redox molecule showed a potential-dependent I_{tip} centered around U_{eq}. The current decayed asymmetrically with higher or lower potentials. The system of Azurin/alkanethiol/gold proved to be fairly stable, and approximately 80 % of the redox activity was retained after 5,000 successive cycles. The rate of the electron transfer was investigated in dependence of the linker length, and a sharp drop in the activity was detected at lengths larger than 16 Å.

Another possible area of application for Azurin is memory devices [97, 135–137]. Underlying concept of such devices is that the redox protein Azurin has two distinct states, Cu^{II} and Cu^{I}. By oxidation or reduction, the states can be transformed. A device consisting of Azurin immobilized on gold electrodes exhibited an information retention time of more than 2 weeks and showed no performance degradation for more than 10,000 switching operations [137]. By applying open circuit potential, the two states can be read. One study by Kim et al. employed EC-STM to monitor the

Azurin molecules on the gold electrode [97]. They confirmed once more the potential-dependent behavior of Azurin; however, no genuinely new information was added in terms of scanning probe microscopy.

7 Conclusions and Future Perspective

In Sect. 4.5 we described how the micrographs obtained from EC-STM and SECPM can be interpreted. For in situ STM measurements, the influence of the electrolyte has to be taken into account. On the one hand, molecules of a water layer can act as intermediate states at the interface; on the other hand, diffusion of adsorbed particles can add noise due to electron scattering. We briefly discussed the conceivable modes of electron transfer from EC-STM tip to sample (or vice versa) via a redox molecule within the tunnelling gap.

For SECPM we concluded that one has to distinguish between potential-approach curves and a potential-mapping mode. While experimental potential-approach curves still fail to reproduce theoretical predictions, the latter can yield valuable results. This notion is supported by SECPM micrographs of biomolecules ((apo)ferritin, HPR) on HOPG. In a direct comparison the SECPM images especially of biomolecules exceed the quality of EC-STM images [12]. One reason is that SECPM is able to monitor nonconductive sample, a feature EC-STM does not possess. Another cause is that for SECPM, no current has to flow from molecule to substrate and therefore the linkage between the two does not have to be as good as it is required for EC-STM. A third advantage of SECPM is that "current damage" to the sensitive biomolecules is avoided; during EC-STM with a typical current set point, 10^9 electrons are transported through the molecule per second. We hope that the above study and named advantages inspire an increased future use of SECPM for imaging of biomolecules. Table 1.1 listed 15 SPM studies of biomolecules, only a single one employed SECPM, all the others were performed with EC-STM.

In Sect. 5 we reviewed recent studies on electrocatalysis on metal surfaces using EC-STM and SECPM. It can be concluded that there is a wide range of possibilities for improvement in electrode activity. The combination of two or more active metals through adsorption or alloying and the variation of particle size and distribution have proven to be effective measures to increase the catalytic activity for certain important reactions such as HER, HOR, ORR, and CO oxidation. In order to effectively improve catalyst materials, it is crucial to understand the effects causing changes in the activity. Electrochemical STM is a very useful instrument in which combination with other electrochemical techniques such as cyclic voltammetry can directly link catalytic behavior to surface structure and processes on the nanoscale. SECPM can further enhance the insights gained from these experiments and can also be easily combined with EC-STM, to the point of measuring the exact same region of the surface with both methods for direct comparison. Also, as shown in the SECPM measurements on the step edges of Ru(0001) [11], it is sensitive to different properties of the material under examination.

In Sect. 6 we reviewed key research findings of SPM studies on redox-active biomolecules. In an introductory part we laid the foundation for the discussion of microscopy studies on biological systems. Some properties of metalloproteins were discussed; single proteins and cofactors were introduced. Also the importance of immobilization and means to do so were pointed out.

In Sect. 6.2 the interplay of theoretical and experimental work which led to the successful unraveling of the electron transfer mechanism from the tip to sample via a metalloprotein was described. For a metalloprotein with a single redox site, it was established that the interfacial electron transfer takes place via a two-step vibrationally coherent mechanism. This was the conclusion of two independent work groups, both combining theoretical efforts with experimental studies [25, 26, 90, 94]. Proteins containing more redox sites are more complicated and first investigations were performed in recent years. One of the key insights gained was that for the diheme protein cytochrome c_4 intramolecular ET is much faster than interfacial ET [99].

Section 6.3 deals with correlating the imaged and the real shape of biomolecules. Three major influences were identified, namely, the convolution of electronic properties of the tip, molecule, and substrate, the ECDL of the molecule-decorated substrate, and faradaic currents at the tip [25, 90]. It was especially pointed out that while faradaic currents might make it difficult to discern the true tunnelling current, they hold the promise of investigating single-molecule electron transfer rates.

As stated earlier, SECPM can be superior to EC-STM when monitoring biomolecules, as it avoids the intrinsic problems of the latter. More studies should be performed with SECPM to see if other biological systems behave as benign ferritin/apoferritin and horseradish peroxidase. In addition to EC-STM SECPM might provide new insights into the protein structure paving the way for future structure-function studies. Achieving atomic resolution with an SECPM would also be an important milestone [40].

In the last Sect. 6.4, some efforts at designing biomolecular electronics were described. Due to their potential-dependent conductivity, redox proteins seem to be good candidates for the development of single-molecule transistors [96]. The study, albeit a spirited effort, did reveal significant problems that need to be solved in order to make future applications feasible. Stability of the protein/SAM/electrode assembly was one of these challenges. EC-STM and SECPM are valuable tools that will play an important role for the development of such biomimetic devices.

References

1. Biener J, Wittstock A, Baumann TF, Weissmüller J, Bäumer M, Hamza AV (2009) Surface chemistry in nanoscale materials. Materials (Basel) 2(4):2404–2428
2. Binnig G, Rohrer H (1982) Scanning tunneling microscopy. Surf Sci 126:236–244
3. Sonnenfeld R, Hansma PK (1986) Atomic-resolution microscopy in water. Science 232(4747):211–213

4. Hurth C, Li C, Bard AJ (2007) Direct probing of electrical double layers by scanning electrochemical potential microscopy. J Phys Chem C 111(12):4620–4627
5. Hammer B, Nørskov JK (1995) Electronic factors determining the reactivity of metal surfaces. Surf Sci 343:211–220
6. Friedl J, Stimming U (2013) Model catalyst studies on hydrogen and ethanol oxidation for fuel cells. Electrochim Acta 101:41–58
7. Kolb DM (2001) Electrochemical surface science. Angew Chemie 40(7):1162–1181
8. Hansen W, Wang C, Humphryes T (1978) Electrode emersion and the double layer. J Electroanal Chem Interfacial Electrochem 90:137–141
9. Tersoff J, Hamann D (1985) Theory of the scanning tunneling microscope. Phys Rev B 31(2):805–813
10. Woo D, Yoo J, Park S, Jeon IC, Kang H (2004) Direct probing into the electrochemical interface using a novel potential probe: Au(111) electrode / NaBF4 solution interface. Bull Korean Chem Soc 25(4):577–580
11. Wolfschmidt H, Baier C, Gsell S, Fischer M, Schreck M, Stimming U (2010) STM, SECPM, AFM and electrochemistry on single crystalline surfaces. Materials (Basel) 3(8):4196–4213
12. Baier C, Stimming U (2009) Imaging single enzyme molecules under in situ conditions. Angew Chem Int Ed Engl 48(30):5542–5544
13. Meier J, Friedrich KA, Stimming U (2002) Novel method for the investigation of single nanoparticle reactivity. Faraday Discuss 121:365–372
14. Eikerling M, Meier J, Stimming U (2003) Hydrogen evolution at a single supported nanoparticle: a kinetic model. Zeitschrift für Phys Chemie 217(4–2003):395–414
15. Wolfschmidt H, Weingarth D, Stimming U (2010) Enhanced reactivity for hydrogen reactions at Pt nanoislands on Au(111). Chemphyschem 11(7):1533–1541
16. Zhang MG, Stimming U (1990) The use of time-resolved scanning tunneling microscopy for the determination of microscopic reaction rates. J Electroanal Chem 291:273–279
17. Hugelmann M, Schindler W (2003) Tunnel barrier height oscillations at the solid/liquid interface. Surf Sci 541(1–3):L643–L648
18. Nagy G (1996) Water structure at the graphite (0001) surface by STM measurements. J Electroanal Chem 409:19–23
19. Hugelmann M, Hugelmann P, Lorenz WJ, Schindler W (2005) Nanoelectrochemistry and nanophysics at electrochemical interfaces. Surf Sci 597(1–3):156–172
20. Halbritter J, Repphun G, Vinzelberg S (1995) Tunneling mechanisms in electrochemical STM—distance and voltage tunneling spectroscopy. Electrochim Acta 40(10):1385–1394
21. Sumetskii M, Kornyshev A (1993) Noise in STM due to atoms moving in the tunneling space. Phys Rev B 48(23):493–506
22. Sumetskii M, Kornyshev A, Stimming U (1994) Adatom diffusion characteristics from STM noise: theory. Surf Sci 307–209:23–27
23. Kornyshev AA, Kuznetsov AM (2006) Potential distribution in an in situ nano-gap. Electrochem Commun 8(5):679–682
24. Kornyshev AA, Kuznetsov AM (2006) A new type of in situ single-molecule rectifier. ChemPhysChem 7(5):1036–1040
25. Wang M, Bugarski S, Stimming U (2008) Probing single flavoprotein molecules on graphite in aqueous solution with scanning tunneling microscopy. Small 4(8):1110–1114
26. Alessandrini A, Corni S, Facci P (2006) Unravelling single metalloprotein electron transfer by scanning probe techniques. Phys Chem Chem Phys 8(38):4383–4397
27. Schmickler W, Tao N (1997) Measuring the inverted region of an electron transfer reaction with a scanning tunneling microscope. Electrochim Acta 42(18):2809–2815
28. Schmickler W (1986) A theory of adiabatic electron-transfer reactions. J Electroanal Chem Interfacial Electrochem 204(1–2):31–43
29. Gerischer H (1960) Über den Ablauf von Redoxreaktionen an Metallen und an Halbleitern. Zeitschrift für Phys Chemie 26:223–247

30. Tao N (1996) Probing potential-tuned resonant tunneling through redox molecules with scanning tunneling microscopy. Phys Rev Lett 76(21):4066–4069
31. Kuznetsov AN, Schmickler W (2002) Mediated electron exchange between an electrode and the tip of a scanning tunneling microscope – a stochastic approach. Chem Phys 282(3):371–377
32. Weaver MJ (1987) Redox reactions at metal–solution interfaces. In: Compton RG (ed) Electrode kinetics: reactions, vol 27. Elsevier, Amsterdam, pp 1–60
33. Zhang J, Chi Q, Kuznetsov AM, Hansen AG, Wackerbarth H, Christensen HEM, Andersen JET, Ulstrup J (2002) Electronic properties of functional biomolecules at metal/aqueous solution interfaces. J Phys Chem B 106(6):1131–1152
34. Friis E, Kharkats Y, Kuznetsov A, Ulstrup J (1998) In situ scanning tunneling microscopy of a redox molecule as a vibrationally coherent electronic three-level process. J Phys Chem A 5639(98):7851–7859
35. Friis EP, Andersen JE, Kharkats YI, Kuznetsov AM, Nichols RJ, Zhang JD, Ulstrup J (1999) An approach to long-range electron transfer mechanisms in metalloproteins: in situ scanning tunneling microscopy with submolecular resolution. Proc Natl Acad Sci U S A 96(4):1379–1384
36. Zhang J, Kuznetsov AM, Medvedev IG, Chi Q, Albrecht T, Jensen PS, Ulstrup J (2008) Single-molecule electron transfer in electrochemical environments. Chem Rev 108(7):2737–2791
37. Zhang J, Chi Q, Hansen AG, Jensen PS, Salvatore P, Ulstrup J (2012) Interfacial electrochemical electron transfer in biology – towards the level of the single molecule. FEBS Lett 586(5):526–535
38. Corbella C, Pascual E, Oncins G, Canal C, Andújar JL, Bertran E (2005) Composition and morphology of metal-containing diamond-like carbon films obtained by reactive magnetron sputtering. Thin Solid Films 482(1–2):293–298
39. Grahame DC (1947) The electrical double layer and the theory of electrocapillarity. Chem Rev 41(3):441–501
40. Baier C (2010) Electron transfer phenomena in interfacial bioelectrochemistry. Dissertation, Technische Universität München
41. Hurth CM (2005) Scanning probe microscopy studies of active enzymes at solid surfaces. Dissertation, The University of Texas at Austin
42. Hamou RF, Biedermann PU, Erbe A, Rohwerder M (2010) Numerical simulation of probing the electric double layer by scanning electrochemical potential microscopy. Electrochim Acta 55(18):5210–5222
43. Hamou RF, Biedermann PU, Erbe A, Rohwerder M (2010) Numerical analysis of debye screening effect in electrode surface potential mapping by scanning electrochemical potential microscopy. Electrochem Commun 12(10):1391–1394
44. Hubbard AT (1980) Electrochemistry of well-defined surfaces. Acc Chem Res 13:177–184
45. Laidler KJ (1996) Commission on chemical kinetics * a glossary of terms used in chemical kinetics, including reaction dynamics. Pure Appl Chem 68(1):149–192
46. Conway BE, Bockris JO (1957) Electrolytic hydrogen evolution kinetics and its relation to the electronic and adsorptive properties of the metal. J Chem Phys 26(3):532
47. Parsons R (1958) The rate of electrolytic hydrogen evolution and the heat of adsorption of hydrogen. Trans Faraday Soc 54:1053–1063
48. Nørskov JK, Bligaard T, Logadottir A, Kitchin JR, Chen JG, Pandelov S, Stimming U (2005) Trends in the exchange current for hydrogen evolution. J Electrochem Soc 152(3):J23
49. Clavilier J, Faure R, Guinet G, Durand R (1980) Preparation of monocrystalline Pt microelectrodes and electrochemical study of the plane surfaces cut in the direction of the {111} and {110} planes. J Electroanal Chem 107:205–209
50. Bauer E (1958) Phaenomenologische Theorie der Kristallabscheidung an Oberflaechen I. Zeitschrift für Krist 110:372–394

51. Frank FC, van der Merwe JH (1949) One-dimensional dislocations. Proc R Soc Lond A Math Phys Sci 198(1053):205–216
52. Volmer M, Weber A (1926) Keimbildung in übersättigten Gebilden. Z Phys Chem 119:277
53. Stranski JN, Krastanov L (1938) Zur Theorie der orientierten Ausscheidung von Ionenkristallen aufeinander. Sitz Ber Akad Wiss Wien, Mat Nat 146:797–810
54. Brankovic SR, Wang JX, Adzic RR (2001) Metal monolayer deposition by replacement of metal adlayers on electrode surfaces. Surf Sci 474:L173–L179
55. Vasilic R, Viyannalage L, Dimitrov N (2006) Epitaxial growth of Ag on Au(111) by galvanic displacement of Pb and Tl monolayers. J Electrochem Soc 153:648–655
56. Quaino P, Santos E, Wolfschmidt H, Montero M, Stimming U (2011) Theory meets experiment: electrocatalysis of hydrogen oxidation/evolution at Pd–Au nanostructures. Catal Today 177(1):55–63
57. Wolfschmidt H, Bussar R, Stimming U (2008) Charge transfer reactions at nanostructured Au(111) surfaces: influence of the substrate material on electrocatalytic activity. J Phys Condens Matter 20(37):374127
58. Jung C, Kim J, Kyun C (2010) CO preoxidation on Ru-modified Pt(111). Electrochem Commun 12:1363–1366
59. Kim J, Jung C, Rhee CK, Lim T (2007) Electrocatalytic oxidation of formic acid and methanol on Pt deposits on Au(111). Langmuir 23(21):10831–10836
60. Meier J, Schiøtz J, Liu P, Nørskov JK, Stimming U (2004) Nano-scale effects in electrochemistry. Chem Phys Lett 390(4–6):440–444
61. Kolb DM, Simeone FC (2005) Electrochemical nanostructuring with an STM: a status report. Electrochim Acta 50(15):2989–2996
62. Hoyer R, Kibler L, Kolb D (2003) The initial stages of palladium deposition onto Pt(111). Electrochim Acta 49:63–72
63. Varela AS, Schlaup C, Jovanov ZP, Malacrida P, Horch S, Stephens IEL, Chorkendorff I (2013) CO 2 Electroreduction on well-defined bimetallic surfaces: Cu overlayers on Pt(111) and Pt(211). J Phys Chem C 117(111):20500–20508
64. Krausa M, Vielstich W (1994) Study of the electrocatalytic influence of Pt/Ru and Ru on the oxidation of residues of small organic molecules. J Electroanal Chem 379(1–2):307–314
65. Frelink T, Visscher W, van Veen JAR (1995) On the role of Ru and Sn as promotors of methanol electro-oxidation over Pt. Surf Sci 335:353–360
66. Tong Y, Kim HS, Babu PK, Waszczuk P, Wieckowski A, Oldfield E (2002) An NMR investigation of CO tolerance in a Pt/Ru fuel cell catalyst. J Am Chem Soc 124:468–473
67. Watanabe M, Motoo S (1975) Electrocatalysis by ad-atoms: part II. Enhancement of the oxidation of methanol on platinum by ruthenium ad-atoms. J Electroanal Chem Interfacial Electrochem 60:267–273
68. Yajima T, Wakabayashi N, Uchida H, Watanabe M (2003) Adsorbed water for the electro-oxidation of methanol at Pt-Ru alloy. Chem Commun (Camb) 7:828–829
69. Maillard F, Lu G-Q, Wieckowski A, Stimming U (2005) Ru-decorated Pt surfaces as model fuel cell electrocatalysts for CO electrooxidation. J Phys Chem B 109(34):16230–16243
70. Strbac S, Johnston CM, Lu GQ, Crown A, Wieckowski A (2004) In situ STM study of nanosized Ru and Os islands spontaneously deposited on Pt(111) and Au(111) electrodes. Surf Sci 573:80–99
71. Friedrich KA, Geyzers KP, Dickinson AJ, Stimming U (2002) Fundamental aspects in electrocatalysis: from the reactivity of single-crystals to fuel cell electrocatalysts. J Electroanal Chem 524–525:261–272
72. El-Aziz AM, Hoyer R, Kibler LA (2010) Preparation and electrochemical behavior of PtRu(111) alloy single-crystal surfaces. Chem Phys Chem 11(13):2906–2911
73. Inukai J, Tryk DA, Abe T, Wakisaka M, Uchida H, Watanabe M (2013) Direct STM elucidation of the Effects of atomic-level structure on Pt(111) electrodes for dissolved CO oxidation. J Am Chem Soc 135(111):1476–1490

74. Hwang S, Lee J, Kwak J (2005) Nitrate reduction catalyzed by nanocomposite layer of Ag and Pb on Au(111). J Electroanal Chem 579:143–152
75. Brülle T, Stimming U (2009) Platinum nanostructured HOPG – Preparation, characterization and reactivity. J Electroanal Chem 636(1–2):10–17
76. Ustarroz J, Ke X, Hubin A, Bals S, Terryn H (2012) New insights into the early stages of nanoparticle electrodeposition. J Phys Chem C 116(3):2322–2329
77. Hyde ME, Compton RG (2003) A review of the analysis of multiple nucleation with diffusion controlled growth. J Electroanal Chem 549:1–12
78. Sheridan L, Kim Y (2013) Palladium nanofilms formed on Au (111) by electrochemical atomic layer deposition (E-ALD): studies using voltammetry and in situ scanning tunneling microscopy. J Phys Chem C 117(111):15728–15740
79. Brülle T, Denisenko A, Sternschulte H, Stimming U (2011) Catalytic activity of platinum nanoparticles on highly boron-doped and 100-oriented epitaxial diamond towards HER and HOR. Phys Chem Chem Phys 13(28):12883–12891
80. Zwolinski BJ, Marcus RJ, Eyring H (1955) Inorganic oxidation-reduction reactions in solution. Chem Rev 55(1):157–180
81. Marcus RA (1960) Exchange reactions and electron transfer reactions including isotopic exchange. Theory of oxidation-reduction reactions involving electron transfer. Part 4.-A statistical-mechanical basis for treating contributions from solvent, ligands, and inert salt. Discuss Faraday Soc 29:21–31
82. Fedurco M (2000) Redox reactions of heme-containing metalloproteins: dynamic effects of self-assembled monolayers on thermodynamics and kinetics of cytochrome c electron-transfer reactions. Coord Chem Rev 209(1):263–331
83. Churg A, Weiss R (1983) On the action of cytochrome c: correlating geometry changes upon oxidation with activation energies of electron transfer. J Phys Chem 87:1683–1694
84. Corni S (2005) The reorganization energy of azurin in bulk solution and in the electrochemical scanning tunneling microscopy setup. J Phys Chem B 109(8):3423–3430
85. Heitele H, Michel-Beyerle M (1985) Electron transfer through aromatic spacers in bridged electron-donor-acceptor molecules. J Am Chem Soc 107:8286–8288
86. Heitele H, Michel-Beyerle ME, Finckh P (1987) The influence of dielectric relaxation on intramolecular electron transfer. Chem Phys Lett 138(2):237–243
87. Heitele H, Pöllinger F, Weeren S, Michel-Beyerle M (1990) Influence of solvent polarity on intramolecular electron transfer. A consistency test of free energies of reaction and solvent reorganization with experimental rates. Chem Phys 143:325–332
88. Heitele H, Pöllinger F, Weeren A, Michel-Beyerle ME (1990) Solvent polarity effects on intramolecular electron transfer: an estimate of activation entropies. Chem Phys Lett 168(6):598–604
89. Weinberg DR, Gagliardi CJ, Hull JF, Murphy CF, Kent CA, Westlake BC, Paul A, Ess DH, McCafferty DG, Meyer TJ (2012) Proton-coupled electron transfer. Chem Rev 112(7):4016–4093
90. Wang M, Bugarski S, Stimming U (2008) Topological and electron-transfer properties of glucose oxidase adsorbed on highly oriented pyrolytic graphite electrodes. J Phys Chem C 112(13):5165–5173
91. Zhang J, Welinder AC, Hansen AG, Christensen HEM, Ulstrup J (2003) Catalytic monolayer voltammetry and in situ scanning tunneling microscopy of copper nitrite reductase on cysteamine-modified Au(111) electrodes. J Phys Chem B 107(45):12480–12484
92. Della Pia EA, Chi Q, Macdonald JE, Ulstrup J, Jones DD, Elliott M (2012) Fast electron transfer through a single molecule natively structured redox protein. Nanoscale 4(22):7106–7113
93. Davis JJ, Peters B, Xi W (2008) Force modulation and electrochemical gating of conductance in a cytochrome. J Phys Condens Matter 20(37):374123
94. Alessandrini A, Gerunda M, Canters GW, Verbeet MP, Facci P (2003) Electron tunnelling through azurin is mediated by the active site Cu ion. Chem Phys Lett 376(5–6):625–630

95. Alessandrini A, Salerno M, Frabboni S, Facci P (2005) Single-metalloprotein wet biotransistor. Appl Phys Lett 86(13):133902
96. Chi Q, Farver O, Ulstrup J (2005) Long-range protein electron transfer observed at the single-molecule level: in situ mapping of redox-gated tunneling resonance. Proc Natl Acad Sci U S A 102(45):16203–16208
97. Kim S-U, Yagati AK, Min J, Choi J-W (2010) Nanoscale protein-based memory device composed of recombinant azurin. Biomaterials 31(6):1293–1298
98. Facci P, Alliata D, Cannistraro S (2001) Potential-induced resonant tunneling through a redox metalloprotein investigated by electrochemical scanning probe microscopy. Ultramicroscopy 89(4):291–298
99. Chi Q, Zhang J, Arslan T, Borg L, Pedersen GW, Christensen HEM, Nazmudtinov RR, Ulstrup J (2010) Approach to interfacial and intramolecular electron transfer of the diheme protein cytochrome c4 assembled on Au(111) surfaces. J Phys Chem B 114(16):5617–5624
100. Welinder AC, Zhang J, Steensgaard DB, Ulstrup J (2010) Adsorption of human insulin on single-crystal gold surfaces investigated by in situ scanning tunnelling microscopy and electrochemistry. Phys Chem Chem Phys 12(34):9999–10011
101. Climent V, Zhang J, Friis EP, Østergaard LH, Ulstrup J (2012) Voltammetry and single-molecule in situ scanning tunneling microscopy of laccases and bilirubin oxidase in electrocatalytic dioxygen reduction on Au(111) single-crystal electrodes. J Phys Chem C 116(1):1232–1243
102. Walsh C (1980) Flavin coenzymes: at the crossroads of biological redox chemistry. Acc Chem Res 13:148–155
103. Marcus R, Sutin N (1985) Electron transfers in chemistry and biology. Biochim Biophys Acta 811:265–322
104. Macara IG, Hoy TG, Harrison PM (1972) The formation of ferritin from apoferritin. Biochem J 126:151–162
105. Nar H, Huber R, Messerschmidt A, Filippou AC, Barth M, Jaquinod M, van de Kamp M, Canters GW (1992) Characterization and crystal structure of zinc azurin, a by-product of heterologous expression in escherichia coli of pseudomonas aeruginosa copper azurin. Eur J Biochem 205(3):1123–1129
106. Saltiel A, Kahn C (2001) Insulin signalling and the regulation of glucose and lipid metabolism. Nature 414:799–806
107. Pekar A, Frank B (1972) Conformation of proinsulin. Comparison of insulin and proinsulin self-association at neutral pH. Biochemistry 11(22):4013–4016
108. Raffalt AC, Schmidt L, Christensen HEM, Chi Q, Ulstrup J (2009) Electron transfer patterns of the di-heme protein cytochrome c(4) from Pseudomonas stutzeri. J Inorg Biochem 103(5):717–722
109. Solomon EI, Sundaram UM, Machonkin TE (1996) Multicopper oxidases and oxygenases. Chem Rev 96(7):2563–2606
110. Farver O, Tepper AWJW, Wherland S, Canters GW, Pecht I (2009) Site-site interactions enhances intramolecular electron transfer in streptomyces coelicolor laccase. J Am Chem Soc 131(51):18226–18227
111. Tao N, Cardenas G, Cunha F, Shi Z (1995) In situ STM and AFM study of protoporphyrin and iron (III) and zinc (II) protoporphyrins adsorbed on graphite in aqueous solutions. Langmuir 11:4445–4448
112. McCreery RL (2008) Advanced carbon electrode materials for molecular electrochemistry. Chem Rev 108(7):2646–2687
113. Choo H-S, Kinumoto T, Jeong S-K, Iriyama Y, Abe T, Ogumi Z (2007) Mechanism for electrochemical oxidation of highly oriented pyrolytic graphite in sulfuric acid solution. J Electrochem Soc 154(10):B1017
114. Zhang J, Chi Q, Dong S, Wang E (1996) In situ electrochemical scanning tunnelling microscopy investigation of structure for horseradish peroxidase and its electricatalytic property. Bioelectrochem Bioenerg 39:267–274

115. Chi Q, Zhang J, Friis EP, Andersen JET, Ulstrup J (1999) Electrochemistry of self-assembled monolayers of the blue copper protein pseudomonas aeruginosa azurin on Au(111). Electrochem Commun 1(3–4):91–96
116. Vaz-Dominguez C, Pita M, de Lacey AL, Shleev S, Cuesta A (2012) Combined ATR-SEIRAS and EC-STM study of the immobilization of laccase on chemically modified au electrodes. J Phys Chem C 116:16532–16540
117. Schmickler W, Widrig C (1992) The investigation of redox reactions with a scanning tunneling microscope: experimental and theoretical aspects. J Electroanal Chem 336:213–221
118. Schmickler W (1993) Investigation of electrochemical electron transfer reactions with a scanning tunneling microscope: a theoretical study. Surf Sci 295(1–2):43–56
119. Kuznetsov A, Sommer-Larsen P, Ulstrup J (1992) Resonance and environmental fluctuation effects in STM currents through large adsorbed molecules. Surf Sci 275:52–64
120. Ryde U, Olsson M (2001) Structure, strain, and reorganization energy of blue copper models in the protein. Int J Quantum Chem 81(2001):335–347
121. Dos Santos L, Climent V, Blanford CF, Armstrong FA (2010) Mechanistic studies of the 'blue'Cu enzyme, bilirubin oxidase, as a highly efficient electrocatalyst for the oxygen reduction reaction. Phys Chem Chem Phys 12:13962–13974
122. Vesenka J, Miller R, Henderson E (1994) Three-dimensional probe reconstruction for atomic force microscopy. Rev Sci Instrum 65(7):2249
123. Li Z, Han B, Meszaros G, Pobelov I, Wandlowski T, Błaszczyk A, Mayor M (2006) Two-dimensional assembly and local redox-activity of molecular hybrid structures in an electrochemical environment. Faraday Discuss 131:121
124. Zhang J, Ulstrup J (2007) Oxygen-free in situ scanning tunnelling microscopy. J Electroanal Chem 599(2):213–220
125. Roth JP, Klinman JP (2003) Catalysis of electron transfer during activation of O2 by the flavoprotein glucose oxidase. Proc Natl Acad Sci U S A 100(1):62–67
126. Losic D, Shapter J, Gooding J (2002) Scanning tunneling microscopy studies of glucose oxidase on gold surfaces. Langmuir 18(14):5422–5428
127. Rice RJ, McCreery RL (1989) Quantitative relationship between electron transfer rate and surface microstructure of laser-modified graphite electrodes. Anal Chem 61(15):1637–1641
128. Friedl J, Bauer C, Rinaldi A, Stimming U (2013) Electron transfer kinetics of the VO2+/VO2+ – reaction on multi-walled carbon nanotubes. Carbon NY 63:228–239
129. Crichton RR (1973) Structure and function of ferritin. Angew Chem Int Ed Engl 12(1):57–65
130. Krieger E, Darden T, Nabuurs SB, Finkelstein A, Vriend G (2004) Making optimal use of empirical energy functions: force-field parameterization in crystal space. Proteins 57(4):678–683
131. Joachim C, Gimzewski JK, Aviram A (2000) Electronics using hybrid-molecular and mono-molecular devices. Nature 408(6812):541–548
132. Maruccio G, Biasco A, Visconti P, Bramanti A, Pompa PP, Calabi F, Cingolani R, Rinaldi R, Corni S, Di Felice R, Molinari E, Verbeet MP, Canters GW (2005) Towards protein field-effect transistors: report and model of a prototype. Adv Mater 17(7):816–822
133. Tans S, Verschueren A, Dekker C (1998) Room-temperature transistor based on a single carbon nanotube. Nature 672(1989):669–672
134. Kubatkin S, Danilov A, Hjort M, Cornil J (2003) Single-electron transistor of a single organic molecule with access to several redox states. Nature 425(6959):698–701
135. Choi J-W, Oh B-K, Kim YJ, Min J (2007) Protein-based biomemory device consisting of the cysteine-modified azurin. Appl Phys Lett 91(26):263902
136. Lee T, Kim S-U, Min J, Choi J-W (2010) Multilevel biomemory device consisting of recombinant azurin/cytochrome C. Adv Mater 22(4):510–514
137. Yagati AK, Kim S-U, Min J, Choi J-W (2009) Multi-bit biomemory consisting of recombinant protein variants, azurin. Biosens Bioelectron 24(5):1503–1507

2 Recovering Time-Resolved Imaging Forces in Solution by Scanning Probe Acceleration Microscopy: Theory and Application

Maxmore Chaibva, Nicole Shamitko-Klingensmith, and Justin Legleiter

Contents

1 Definition of Topic 70
2 Overview 70
3 Introduction 70
4 Experimental Methodology 73
4.1 Numerical Model of the Entire Imaging Process of TMAFM in Solution 73
4.2 Basic Principles Underlying SPAM 77
5 Key Research Findings 78
5.1 Features of the Time-Resolved Tip/Sample Force are Independent of Surface Topography 78
5.2 Features of the Time-Resolved Tip/Sample Force Provide Insight into Surface Mechanical Properties 79
5.3 The Impact of Imaging Parameters on Time-Resolved Tip/Sample Force 82
5.4 Applications of SPAM to Real Systems 85
6 Conclusions and Future Perspective 87
References 88

M. Chaibva • N. Shamitko-Klingensmith
The C. Eugene Bennett Department of Chemistry, West Virginia University, Morgantown, WV, USA

WV NanoSAFE, West Virginia University, Morgantown, WV, USA

J. Legleiter (✉)
The C. Eugene Bennett Department of Chemistry, West Virginia University, Morgantown, WV, USA

WV NanoSAFE, West Virginia University, Morgantown, WV, USA

The Center for Neurosciences, West Virginia University, Morgantown, WV, USA
e-mail: justin.legleiter@mail.wvu.edu

© Springer-Verlag Berlin Heidelberg 2015

C.S.S.R. Kumar (ed.), *Surface Science Tools for Nanomaterials Characterization*,
DOI 10.1007/978-3-662-44551-8_2

Keywords
Imaging forces • Dynamic mode atomic force microcopy • Tapping mode atomic force microcopy • AFM force reconstruction

1 Definition of Topic

Scanning probe acceleration microscopy (SPAM) is a technique that reconstructs the time-resolved tip/sample forces during standard tapping-mode atomic force microscopy (TMAFM) imaging in solution, allowing for the simultaneous mapping of topography and mechanical properties of surfaces. Here, we describe the relationship between tapping forces and sample mechanical properties, the theoretical basis for the SPAM technique, and its application to a variety of systems.

2 Overview

For many applications, the ability to simultaneously map the topography and mechanical properties of surfaces with high spatial resolution is desirable. In regard to topography, tapping-mode atomic force microscopy (TMAFM) has proven to be a widely used technique for imaging surfaces; however, recent advances in reconstructing the time-resolved tip/sample force during the acquisition of a tapping-mode image have provided further access to information relating to the mechanical properties of these surfaces. An advantage of such force reconstruction approaches is that they allow for the direct correlation of topographic features with relative changes in mechanical properties. One of the traditional advantages of TMAFM is its ability to image surfaces in solution, and scanning probe acceleration microscopy (SPAM) is a method for reconstructing the time-resolved tip/sample forces associated with TMAFM operated in solution. In SPAM, the cantilever acceleration, which is directly related to the tip/sample force, is obtained by taking the second derivative of the cantilever deflection signal, and as a result, this technique does not require specially designed cantilevers. In this chapter, the theory behind the use of time-resolved tip/sample forces to obtain insight into the mechanical properties of surfaces with a particular focus on the application of SPAM in fluid TMAFM experiments is described. This is accomplished by a combination of numerical simulations and actual AFM experiments.

3 Introduction

Tapping-mode atomic force microscopy (TMAFM) [1], a widely used dynamic scanning probe technique, obtains topography images of surfaces by monitoring the oscillation amplitude of a cantilever integrated with an ultrasharp probe tip. In this imaging mode, the cantilever is commonly driven near its resonance

frequency, ω_o, by a piezoelectric bimorph element mounted near the cantilever root. The probe tip is placed in close proximity to the sample surface and allowed to intermittently contact the sample leading to a decrease of the cantilever oscillation amplitude from the "free" amplitude, A_o, to a tapping amplitude, A [2, 3]. For rigid surfaces, the cantilever oscillation amplitude decreases linearly as the distance between the tip and the sample, D_o, becomes smaller. As a result, surface topography is mapped by raster scanning the probe across the surface while using a feedback loop to continuously adjust the vertical (in the z direction) extension of a piezoelectric scanner to maintain a constant tapping amplitude or set-point ratio, $s = A/A_o$.

There is significant interest in using TMAFM to simultaneously map topography and mechanical properties of surfaces, and a variety of methods have been developed toward achieving this goal. While monitoring the phase of the cantilever in tapping mode is a common method to acquire some insight into the mechanical properties of surfaces [4, 5], such images can be difficult to interpret due to various causes of energy dissipation including capillary forces [6], viscoelasticity of the sample [7], cross talk with topography [8], and frictional forces associated with the tilt of the cantilever and/or surface [9]. Furthermore, the phase behavior of the cantilever becomes increasingly complicated when imaging in solution. For example, it has been demonstrated that the phase contrast associated with soft cantilevers imaging in solution can arise from either (i) energy propagation during the tapping event that excites higher eigenmodes of the cantilever mediated by conservative short-range interactions, or (ii) tip/sample energy dissipation [10].

A more straightforward way to gain insight into sample mechanics is by obtaining the time-resolved force interaction between the surface and the tip during standard TMAFM operation. While controlling the force between the tip and sample during TMAFM experiments is important for imaging soft materials and optimizing resolution, understanding the time-resolved tapping forces can provide insight into mechanical properties, such as adhesion and Young's modulus, of a sample. The first successful reconstruction of time-resolved tip/sample forces in a TMAFM experiment was accomplished by taking the inverse Fourier transform of the Fourier-transformed cantilever trajectory divided by its transfer function [11]. Since then, a variety of other methods have been developed that are capable of obtaining time-resolved tip/sample forces and constructing images based on these forces [12–19].

There are several experimental advantages to using tapping forces as a method to map mechanical properties of surfaces. Due to their basis in the tapping mode, such methods offer high spatial resolution and are relatively nondestructive. Other traditional AFM techniques used to measure and/or map mechanical properties of surfaces (i.e., force volume imaging and nanoindentation) often require large deformation of soft samples leading to decreased spatial resolution and possibly irreversible sample damage, whereas tapping-mode forces are adaptive to changes in surfaces properties. As scan rates used for simple tapping-mode AFM imaging are typically much faster than other methods, the mapping of surface properties can be accomplished in a more timely manner. This, perhaps,

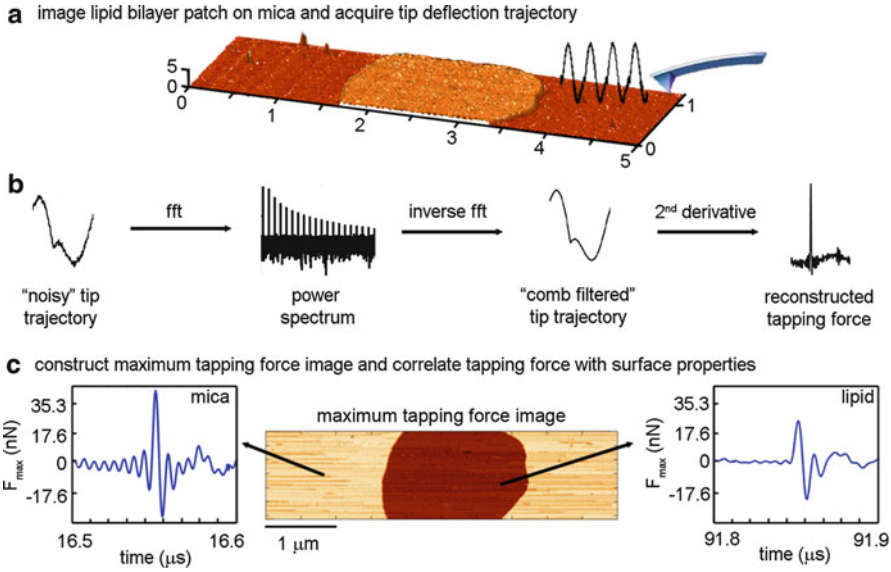


Fig. 2.1 Scanning probe acceleration microscopy is a method for reconstructing the time-resolved tip/sample force associated with TMAFM imaging in solution. In this example, (**a**) a mica substrate with small supported lipid bilayer patche is imaged to acquire the surface topography while acquiring the entire cantilever deflection signal. (**b**) The trajectory of the cantilever is filtered using a "comb-filter" based on Fourier transforms, and the second derivative of the deflection trajectory is used to reconstruct the tip/sample force. (**c**) Images can be constructed based on specific features of the tip/sample force such as the maximum tapping force, which can be related to surface mechanical properties

could provide the ability to probe dynamic changes in a surface's mechanical properties in response to some external stimulus or environmental change.

A method to recover the time-resolved tip/sample force in TMAFM while operated in aqueous solution is scanning probe acceleration microscopy (SPAM), which was developed in the laboratory of Dr. Tomasz Kowalewski at Carnegie Mellon University (Fig. 2.1) [14]. The underlying principle behind SPAM is that the cantilever in TMAFM acts as an accelerometer, which can be used to extract tip-sample forces during standard tapping-mode operation by calculating the second derivative of the cantilever deflection signal. Real deflection signals from TMAFM experiments contain noise that is amplified by this analysis. As the signal-to-noise ratio in most commercially available AFMs would overcome the ability to reconstruct the tapping force by this simple method, a means to filter these signals is crucial if SPAM is to be useful experimentally. This problem is solved by taking advantage of the fact that most of the information about the deflection trajectory and the tapping event is contained in higher harmonic frequencies associated with the drive [11, 20, 21], making it possible to filter the signal by "comb" filtering, i.e., by taking its Fourier transform and inverting it while selectively retaining only the intensities at integer harmonic frequencies of the drive.

Such a comb filtering method works particularly well in fluid TMAFM because of the highly distorted character of the deflection signal [22–24]. The SPAM approach has been validated via numerical simulations and in situ tapping-mode AFM experiments on a variety of systems [14, 25–27].

Here, we review the fundamentals behind SPAM to recover time-resolved tip/sample forces, present numerical simulations that demonstrate how imaging forces depend on experimental parameters and surface properties, and conclude with examples of applying SPAM to a variety of systems. As experimental application of SPAM has been limited to imaging in solution, this chapter focuses on the underlying physics of operating TMAFM in solution. While this chapter focuses on SPAM as a method of force reconstruction, many of the relationships between imaging parameters, surface mechanical properties, and specific features of time-resolved tapping forces are applicable to a broad range of techniques that recover or measure these forces while imaging in the tapping mode.

4 Experimental Methodology

4.1 Numerical Model of the Entire Imaging Process of TMAFM in Solution

To more fully understand the tip/sample interaction associated with TMAFM, numeric simulations are often performed that describe the dynamics of the cantilever as a single-degree-of-freedom, driven, damped harmonic oscillator [28]:

$$m_{\text{eff}}\ddot{z} + b\dot{z} + k[z - D_o + a_o \sin(\omega t)] = F_{\text{ext}} \tag{2.1}$$

where m_{eff} is the effective mass of a cantilever, b is the damping coefficient, k is the cantilever spring constant, z is the position of the cantilever with respect to the surface, D_{o} is the resting position of the cantilever base, a_{o} is the drive oscillation amplitude, ω is the drive frequency, t is the time, and F_{ext} is the tip/sample force. Although cantilever position, z, is often monitored in AFM simulations, in real experiments, most microscopes monitor the amplitude of the cantilever deflection, y, which is simply related to the position by

$$y = z - D_o + a_o \sin(\omega t). \tag{2.2}$$

The major contrast between TMAFM in air and in fluids is in the quality factor (Q) of the cantilever [23, 29], which can be practically described by the following relationship:

$$Q = \frac{A_o}{a_o} \tag{2.3}$$

where A_o is the free cantilever oscillation amplitude. Q is typically in the range of ~200–400, whereas in fluids it is only ~1–5. This lower Q is primarily due to the

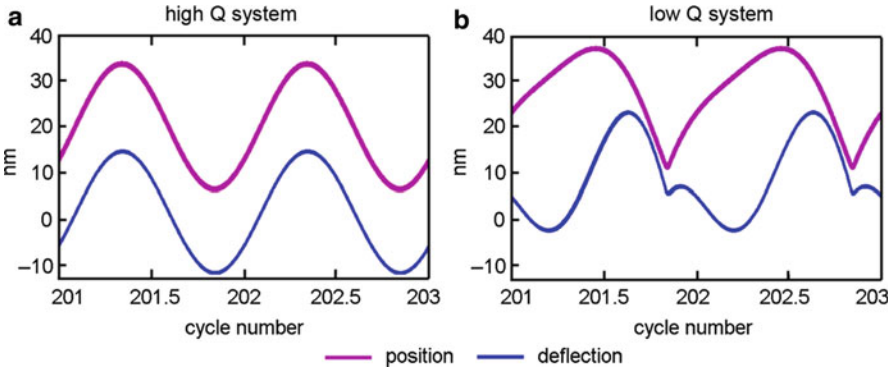


Fig. 2.2 Comparison of simulated cantilever position and deflection trajectories in high Q and low Q systems. Simulations with high Q systems are applicable to TMAFM in air; there is minimal difference between the position and deflection trajectories. In low Q systems, which are associated with TMAFM imaging in solution, there are distinct differences between the position and deflection trajectories

large hydrodynamic damping associated with oscillating the cantilever in fluids. In high Q systems, the free cantilever oscillation amplitude is significantly larger than the drive oscillation amplitude. Subsequently, the cantilever position and deflection trajectories are nearly identical during tapping events except for an offset due to the differing frames of reference (Fig. 2.2a). When operating TMAFM in a low Q system, i.e. in liquid, the cantilever deflection and position trajectories differ significantly during tapping events as the drive amplitude is comparable to the free amplitude. As a result, a characteristic anharmonic distortion is produced in the deflection trajectory as the cantilever tip contacts the sample surface (Fig. 2.2b). Thus, to model TMAFM in solution which is associated with a low Q cantilever, it is necessary to rewrite the cantilever motion in terms of deflection as

$$m_{\text{eff}}\left[\ddot{y} - a_o\omega^2 \sin(\omega t)\right] + b[y + a_o\omega\cos(\omega t)] + ky = F_{\text{ext}}. \tag{2.4}$$

It should be noted that the second mode of the cantilever deflection, which is not incorporated into this model, can play a significant role in cantilever motion near surfaces in fluids [30]; however, such contributions from the second mode are often negligible when imaging soft biological samples in solution [31]. Still higher eigenmodes of the cantilever can complicate analysis of higher harmonic signals. One should also be aware that there are several sources of distortion in cantilever deflection signals in experimental systems, including nonlinearities of the detector and electronics of the AFM that may need to be accounted for when comparing numerical simulations to experimental results.

In TMAFM, the cantilever oscillation continuously changes the separation distance between the probe tip and the surface, allowing the tip to intermittently

contact the sample during each oscillation cycle. Thus, there are two tip/sample interaction regimes required for modeling the time-resolved imaging force: (a) when the cantilever tip and sample surface are not in contact and (b) when the tip and surface make contact during the tapping event. For scenario (a), the separation distance between the cantilever tip and the sample surface, z, is greater than the interatomic distance, a_{DMT}, and during the contact portion (b), z is equal to or smaller than a_{DMT}. For scenario (a) the force can be described by the Derjaguin-Landau-Verway-Overbeek (DLVO) theory [32]; however, because most biological experiments are performed under near physiological conditions in a saline buffer, the force associated with the electric double layer effect is negligible, resulting in a short Debye length [31]. Thus for simplicity, the non-contact force can be approximated using the van der Waals interaction between a sphere (the cantilever tip) and a flat surface [32]:

$$F_{\mathrm{ext}} = -\frac{HR_{\mathrm{tip}}}{6z^2} \quad \text{for} \quad z > a_{\mathrm{DMT}} \tag{2.5}$$

where H is the Hamaker constant and R_{tip} is the tip radius [33]. For scenario (b), the tip/sample force interaction can be described using a Derjaguin-Muller-Toporov (DMT) potential:

$$F_{\mathrm{ext}} = \frac{4}{3\kappa_{\mathrm{eff}}}\sqrt{R_{\mathrm{tip}}}(a_{\mathrm{DMT}} - z)^{\frac{3}{2}} - \frac{HR_{\mathrm{tip}}}{6a_{\mathrm{DMT}}^2} \quad \text{for } z \leq a_{\mathrm{DMT}} \tag{2.6}$$

where

$$\kappa_{\mathrm{eff}} = \frac{1 - v_{\mathrm{tip}}^2}{\pi E_{\mathrm{tip}}} + \frac{1 - v_{\mathrm{sample}}^2}{\pi E_{\mathrm{sample}}} \tag{2.7}$$

where E is the Young's modulus and v is the Poisson coefficient of the tip or sample.

In addition, a feedback loop equipped with an integral gain can be incorporated into this numerical model to simulate the entire TMAFM imaging process. Implementation of a feedback loop can be accomplished by systematically determining the cantilever amplitude for each oscillation cycle, directly comparing this amplitude to a predetermined set-point amplitude, and adjusting the tip/surface separation distance to maintain the set-point amplitude. In this way, a simulated trace of the surface, which is simply the required correction in tip/surface separation distance, can be obtained for different model surface topographies. Combined with the ability to change the values of the Hamaker constant and/or surface Young's modulus, simulations of imaging a wide array of surfaces with TMAFM can be performed to fully understand how the time-resolved tip/sample force responds to surface properties.

To demonstrate the validity of this numerical model, simulations of TMAFM in a low-Q system can be compared to AFM experiments performed in

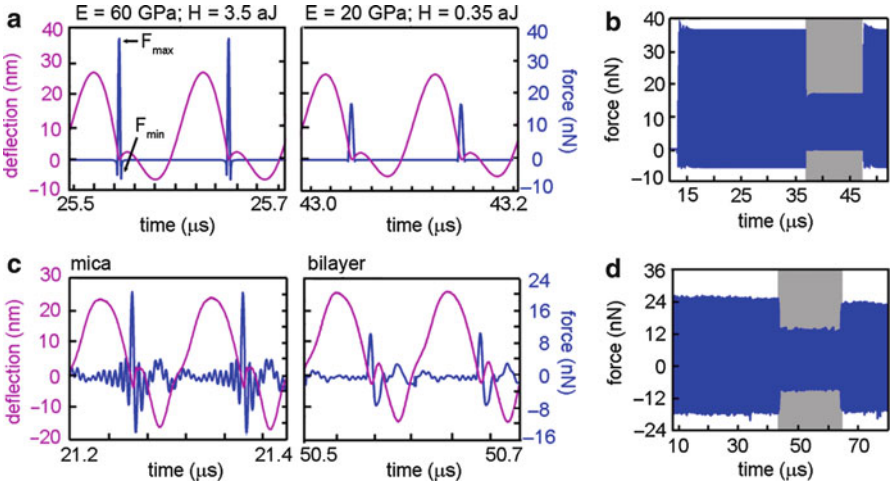


Fig. 2.3 Comparison of cantilever deflection and force trajectories for simulations (**a**, **b**) and experiment (**c**, **d**). (**a**) Simulations of the cantilever deflection trajectory (*purple*) and the force trajectory (*blue*) on a hard ($E = 60$ GPa, $H = 3.5$ aJ) or soft ($E = 20$ GPa, $H = 0.35$ aJ) surfaces, respectively. (**b**) Simulated force trajectory of the entire model surface, which included a 5 nm soft step, the location of which is indicated by gray shading. (**c**) Experimental deflection and force trajectories of a mica surface and a supported lipid bilayer patch, respectively. (**d**) An experimental force trajectory for an entire scan line on a mica surface with a supported lipid bilayer patch in the center, which is indicated by *gray shading*

solution (Fig. 2.3). For the presented numerical simulations, the model surface contained a hard region (with a Young's modulus, E, of 60 GPa and Hamaker constant, H, of 3.5 aJ) that surrounded a 5 nm tall softer region (with E of 20 GPa and H of 0.35 aJ). These simulation parameters were chosen to model a TMAFM experiment of a supported lipid bilayer patch (the typical uncompressed height of a lipid membrane is ~5 nm) on a mica surface so that comparisons could be made between simulation and experiment. The time-resolved tip/sample force from experiments were obtained using SPAM. The simulated deflection trajectories capture the characteristic anharmonic deflection trajectory that is a hallmark of TMAFM experiments performed in solution [23]. There are two features of the tapping force that are of interest here: (1) the maximum tapping force, F_{max}, defined as the most positive force experienced between the cantilever tip and the sample surface during each cantilever oscillation cycle, and (2) the minimum tapping force, F_{min}, defined as the most negative force experienced between the cantilever tip and the sample surface. The magnitude of both F_{max} and F_{min} associated with imaging the model step in simulation or the supported lipid bilayer in experiment respond in an analogous way, confirming that the numerical model is able to capture qualitative features in both cantilever deflection and tip/sample force associated with TMAFM. The actual relationship between F_{max}, F_{min}, E, and H will be explored in greater detail later.

4.2 Basic Principles Underlying SPAM

By simple rearrangement of Eq. 2.4, it can be shown that the acceleration of the cantilever is directly related to the tip/sample force scaled by the effective mass of the cantilever:

$$\ddot{y} = \frac{1}{m_{\text{eff}}}\left[F_{\text{ext}} - b\dot{y} - ky + m_{\text{eff}}\omega^2 a_o \sin(\omega t) - ba_o\omega\cos(\omega t)\right]. \tag{2.8}$$

This suggests that by taking the second derivative of the measured deflection signal, the time-resolved tip/sample force can be recovered. In its simplest form, this process amounts to treating the cantilever as a local accelerometer that can be raster scanned across a surface. In this way, topographic and tip/sample force information can be obtained in one experiment simultaneously. This is the basis for SPAM. The last four terms of Eq. 2.8 are all related to the action of driving the cantilever, and as a result, oscillate at the drive frequency. This allows these extraneous terms to be easily distinguished from the tip/sample force, or even filtered out.

As previously mentioned, real cantilever deflection trajectories contain noise. The deflection trajectory of the cantilever can be filtered using a Fourier transform-based harmonic comb filter. In this process, a sliding window Fourier transform is performed on the cantilever deflection signal, only intensities in the resulting power spectrum corresponding to integer harmonic frequencies of the drive are kept, and these are used to reconstruct a deflection signal, $y_{\text{rec}}(t)$, by an inverse Fourier transform based on the equation

$$y_{\text{rec}}(t) = \hat{f}^{-1}\left[y(\omega)\sum\nolimits_{k=1}^{N}\delta\left(\omega - kw_{\text{oper}}\right)\right] \tag{2.9}$$

where δ is Dirac's delta function, ω_{oper} is the operating frequency, and N is the highest harmonic distinguishable about the noise level. The effectiveness of the use of the comb filter to accurately reconstruct the deflection trajectory requires a sufficient number of harmonics, typically more than 18, to be above the noise level in the power spectrum. As previously mentioned, TMAFM in fluids is characterized by a distinct distortion in the cantilever deflection trajectory associated with the tapping event [23, 24, 29], and this distortion inherent in fluid TMAFM results in an adequate number of higher harmonics above the noise to facilitate comb filtering and reconstruction of the tip/sample tapping force from the second derivative (or acceleration) of the cantilever deflection signal. The sliding window of this filter typically contains 5–10 oscillation cycles, and the window is advanced one oscillation cycle at a time to maintain local information about the tip/sample interaction. Nonetheless, with this ability to filter cantilever deflection trajectories, spatially resolved force maps

can be constructed based on the second derivative. The extraneous terms in Eq. 2.8 can be suppressed from the reconstructed force by excluding the fundamental frequency, i.e., drive frequency, from the inverse Fourier transform; however, excluding this frequency diminishes the accuracy of the recovered force by reducing its magnitude. The reconstructed trajectory obtained from the comb filter also loses information contained in harmonics below the noise level. Furthermore, it should be noted that the harmonic comb filter should only be applied to periodic motion of the kind commonly observed in TMAFM and is not applicable to motion exhibiting period doubling or aperiodic/chaotic character.

5 Key Research Findings

5.1 Features of the Time-Resolved Tip/Sample Force are Independent of Surface Topography

TMAFM can be used to image a wide variety of sample surfaces with a range of topographic features. In TMAFM experiments, surface features may vary in height from sub-nanometer to several micrometers. If tapping-mode imaging forces are to be applicable to mapping mechanical properties of surfaces, the features of the time-resolved tip/sample tapping force must be independent of the surface topography. To determine the role of surface topography on tip/sample tapping forces, simulations of complete TMAFM experiments can be performed to understand the impact of a variety of model surfaces with distinct morphologies on imaging forces (Fig. 2.4a). Here, we present three model surfaces: (1) a region with increased RMS roughness, (2) a flat step, and (3) a round feature. These model surfaces represent a large number of the potential topographies that may be encountered in real AFM experiments. The size of these features can be systematically increased to determine changes in F_{max} and F_{min} associated with imaging these model surfaces. All other surface characteristics (such as Young's modulus, Hamaker constant, etc.) and imaging parameters (set-point ratio, free amplitude, cantilever spring constant, etc.) were held constant in these simulations. Importantly, the average F_{max} and F_{min} associated with imaging all three of these surfaces do not change as a function of the size of the feature in the model, as long as the feedback loop is able to maintain proper tracking of the surface. F_{max} for the various topographies were averaged over the altered surface feature (the rough patch, the step, or the round feature) and had an approximate value of 25 nN for each type of surface and each height variation (Fig. 2.4d–f). The F_{min} for each surface variation was approximately -2 nN, which was exactly the same as the flat region of the surface. This indicates that as long as the feedback loop is optimized, changes in the time-resolved tapping forces are independent of topographic features.

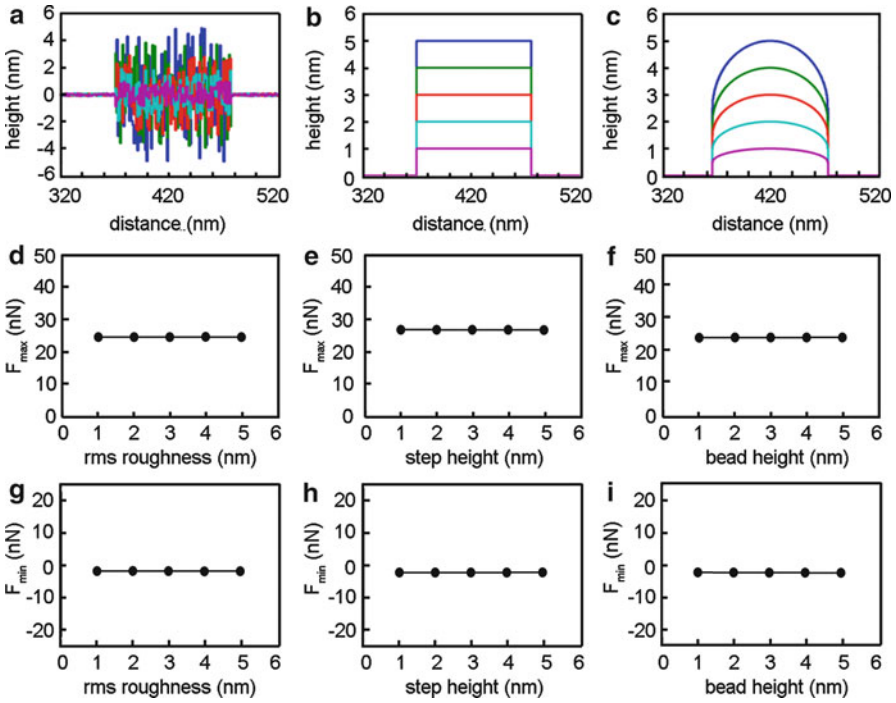


Fig. 2.4 Simulating the effect of surface topography on tip/sample imaging forces. Surface topography was modeled as (**a**) a rough surface, (**b**) a flat step, and (**c**) a round feature where roughness or height was varied from 1 to 5 nm. The maximum and minimum tapping forces, (**d**–**f**) and (**g**–**i**) respectively, were averaged over the altered surface topography and found to be independent of variations in surface topography

5.2 Features of the Time-Resolved Tip/Sample Force Provide Insight into Surface Mechanical Properties

While $F_{\max}$ and $F_{\min}$ are both independent of surface topography, the relationship between these features of the tapping force and surface mechanical properties needs to be understood to effectively map changes in such properties across a sample. To gain insight into how the relative changes in the rigidity of the surface or surface adhesion to the AFM probe are reflected in the tip/sample force, further simulations can be performed. Simulating changes in the rigidity of the sample can be accomplished by altering the Young's modulus of the sample (E_{sample}) in Eq. 2.7. To model changes in adhesion, the Hamaker constant can be altered in Eqs. 2.5 and 2.6 as the surface free energy, γ, (and thus adhesive force) between the tip and sample is related to the Hamaker constant by [32]:

$$\gamma = \frac{H}{24\pi a_{\text{DMT}}} \approx \frac{H}{2.1 \times 10^{-21}}. \tag{2.10}$$

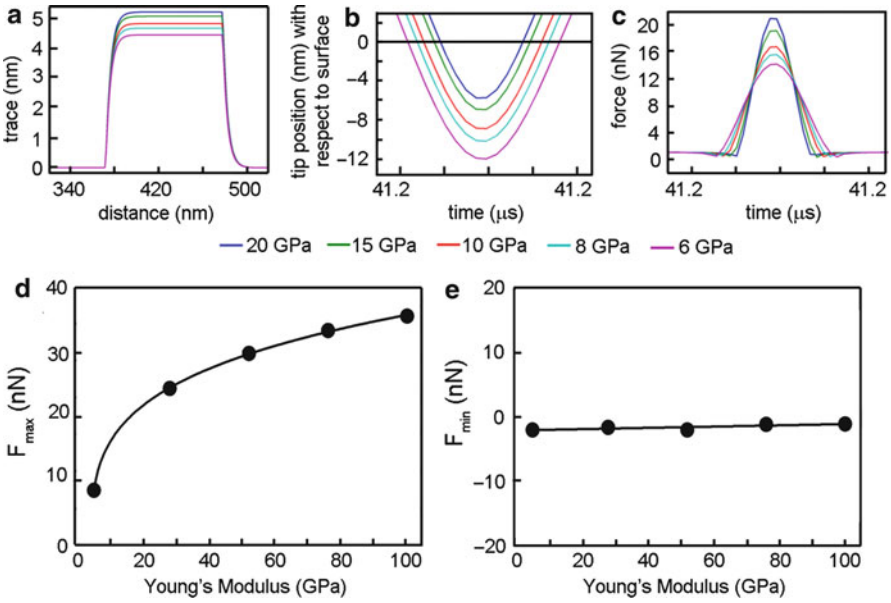


Fig. 2.5 Simulations demonstrating the impact of altering surface Young's modulus on tip/sample imaging forces. The model surface topography includes a step, with changing values of E, surrounded by a hard surface. (**a**) The measured topography of the step as a function of E associated with the surface. (**b**) The position of the cantilever with respect to the sample surface corresponding to the tapping event. (**c**) The tip/sample force corresponding to the tapping event. (**d**) The average value of the maximum tapping force, F_{max}, plotted as a function of surface Young's modulus. (**e**) The average value of the minimum tapping force, F_{min}, plotted as a function of surface Young's modulus

Here, we present illustrative simulations in which the Young's modulus and the Hamaker constant were systematically altered on a predetermined area of a model surface to determine the impact of surface rigidity and adhesion on tapping forces. Changes in surface properties were applied to a 5 nm tall soft step region on a hard surface. The step was included in the model to determine how changes in mechanical properties resulted in compression of the feature due to imaging forces. The Young's modulus and Hamaker constant of the surface regions surrounding this step were held constant at $E = 60$ GPa and $H = 3.0$ aJ for all simulations. Simulation parameters included an amplitude set point of 0.7, a free cantilever oscillation amplitude of 15 nm (and thereby a tapping amplitude of 10.5 nm), a drive frequency of 9.5 kHz, and a spring constant of 0.5 N/m. The simulations were set up to be the equivalent of obtaining a 2 μm scan line at a scan rate of 2 Hz. These simulation parameters were chosen because they correspond to TMAFM imaging parameters commonly used during experimentation.

First, Young's modulus on the step region of the model surface was systematically altered from 6 to 100 GPa. As the modulus decreases, the model step becomes more compliant to compression due to the externally applied force applied by the AFM probe, and the simulated measured height becomes smaller (Fig. 2.5a).

As a result of the increased compliance of the model step, the AFM probe pushes deeper into the sample, causing this decreased height measurement, and is in contact with the surface for a longer time during each oscillation cycle (Fig. 2.5b). As TMAFM images surfaces by maintaining the set-point amplitude, and thus the total force per cantilever oscillation cycle, the way this force is distributed changed in response to increased compliance associated with smaller values of surface Young's modulus (Fig. 2.5c). Specifically, the force is spread out over the longer contact time on more compliant surfaces, resulting in a reduced F_{max} associated with softer samples. As a result, only the magnitude of the F_{max} is altered with larger values of Young's modulus while F_{min} is unresponsive to these changes (Fig. 2.5d). Furthermore, the relationship between F_{max} and Young's modulus can be described by a power law. These simulations suggest that F_{max} can act as an indicator of the relative rigidity of surfaces; however, as we will see, this notion is complicated by changes in adhesion between the tip and surface.

The impact of changing the surface free energy (and thus adhesion) between the tip and surface on the time-resolved tip/sample force was explored by simulations with the Hamaker constant (based on Eq. 2.10), ranging from 0.5 to 2 aJ on the step region of a model surface with a constant Young's modulus of 5 GPa and all other parameters held constant (Fig. 2.6). As the Hamaker constant increased, the simulated measured height of the step decreased (Fig. 2.6a), as a result of a larger magnitude (more negative) tip/sample attractive force between the tip and surface. This increased attractive force between the tip and surface caused the tip to be pulled deeper into the compliant model surface (Fig. 2.6b). On more rigid surfaces, this effect is minimized. While the tip is pulled deeper into a compliant surface with larger values of the Hamaker constant, the contact time between the tip and surface does not appreciably change (Fig. 2.6b). Increasing the Hamaker constant results in larger magnitude, i.e. more negative, attractive forces between the tip and surface (Fig. 2.6c); however, the total force per oscillation cycle must be maintained by the feedback loop, which is a prerequisite to successful tracking of the surface topography. As a result, the F_{max}, to compensate for the increased attractive force associated with each tapping event, also increases in magnitude with larger values of the Hamaker constant (Fig. 2.6c). The increased magnitude of F_{max} due to this increased Hamaker constant can be directly associated with the deeper penetration of the probe into the surface, which enlarged the force associated with the Hertzian term in Eq. 2.6. Due to this, the magnitude of both F_{max} and F_{min} responds linearly with changes in the Hamaker constant (Fig. 2.6d, e).

Collectively, simulations of imaging model surfaces with altered Young's modulus or Hamaker constant demonstrate that specific features of the time-resolved tip/sample tapping force can be used to determine and map relative changes in the mechanical properties of sample surfaces. Specifically, F_{min} changes linearly in response to increased adhesive force between the tip and surface as simulated by changing the Hamaker constant and changes in F_{min} are independent of the Young's modulus. As a result, F_{min} images provide direct measurement of the adhesion between an AFM tip and surface. Deducing the

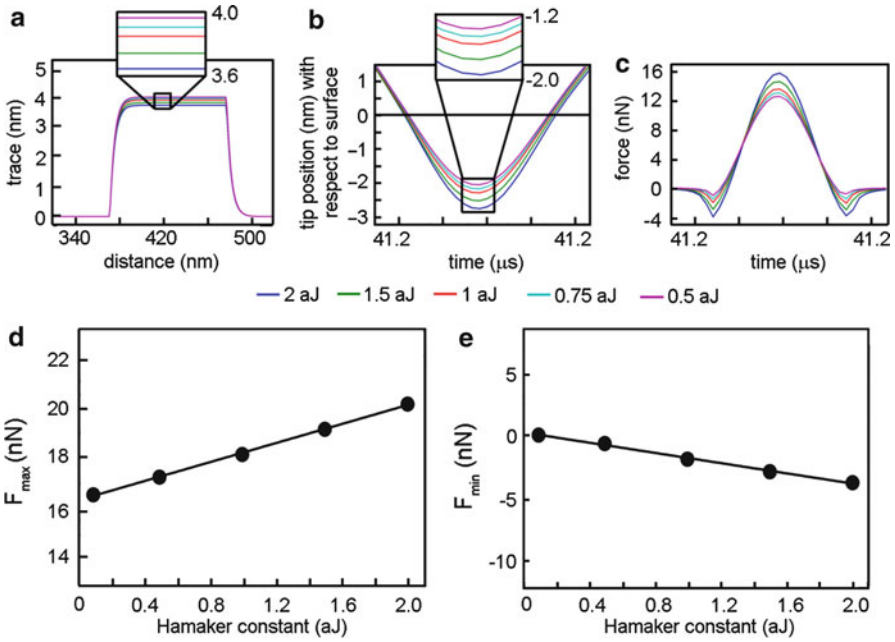


Fig. 2.6 Simulations demonstrating the impact of altering the Hamaker constant on tip/sample imaging forces. The model surface topography includes a step, with changing values of H. (**a**) The measured topography of the step as a function of H associated with the surface. (**b**) The position of the cantilever with respect to the sample surface corresponding to the tapping event. (**c**) The tip/sample force corresponding to the tapping event. (**d**) The average value of the maximum tapping force, F_{max}, plotted as a function of Hamaker constant. (**e**) The average value of the minimum tapping force, F_{min}, plotted as a function of Hamaker constant

relative changes in Young's modulus is complicated by the fact that F_{max} is dependent on both the Hamaker constant (linearly) and Young's modulus (power law). However, the contribution to F_{max} due to changes in the Hamaker constant can be estimated from F_{min}, which can be used to determine if observed changes in F_{max} are at least partially derived from variations in the Young's modulus of the surface.

5.3 The Impact of Imaging Parameters on Time-Resolved Tip/Sample Force

While previous simulations and studies indicate that F_{max} and F_{min} change predictably to reflect the mechanical properties of surfaces, it is necessary to understand how specific imaging parameters (such as spring constant, free amplitude, and set-point ratio) impact time-resolved tip/sample forces to facilitate

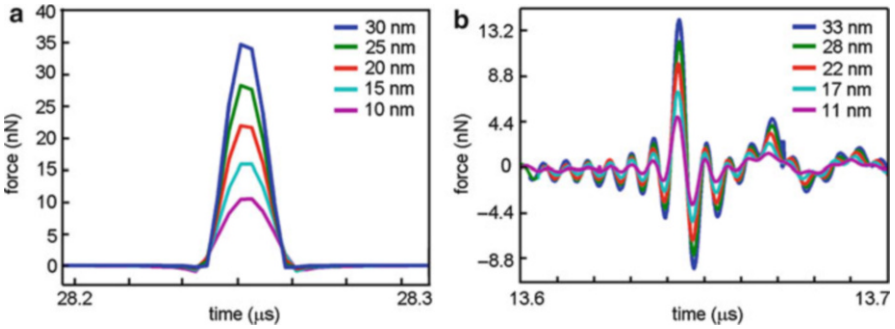


Fig. 2.7 Simulations (**a**) and experiments (**b**) of the TMAFM process in liquid demonstrate the effect of cantilever free amplitude on the average tapping force per oscillation cycle. Experiments were performed on a mica surface in saline buffer. Cantilever free oscillation amplitude was systematically decreased for both simulations and experiments by altering the drive amplitude, and the set-point ratio was maintained for fair comparisons

accurate comparisons between samples. These imaging parameters can be related to the total tip/sample force per oscillation cycle [34]:

$$F_{\text{total}} \approx 0.5ka_o\frac{\Delta A}{A_o}. \tag{2.11}$$

where ΔA is the difference between the free amplitude (or the oscillation amplitude when no tapping event is occurring) and the tapping amplitude, $A_o - A$. Several studies have explored, both numerically and experimentally, the relationship between such imaging parameters and the resulting tapping forces [25, 27, 35].

Based on Eq. 2.11, it is expected that as the drive amplitude, and thus the free amplitude, is increased for any given cantilever, the total imaging force per oscillation cycle increases systematically if the set-point ratio is maintained. This is confirmed via simulation and experiment (Fig. 2.7). For both simulations and experiments, the drive amplitude was increased, resulting in a larger free amplitude, and the set-point ratio was maintained. All other imaging parameters were held constant in both simulation and experiment. Under such conditions, the contact time between the tip and surface is independent of free amplitude; therefore, the observed increase in F_{max} is caused by a larger total force per oscillation cycle associated with increasing free amplitude.

For any given free amplitude, decreasing the set-point ratio results in an increase in the total force per oscillation cycle. Simulations and experiments have also been performed to demonstrate the effect of A_{sp} on tapping forces [26, 36]. If only the value of A_{sp} is modified while all other imaging parameters are maintained, the total tapping force per oscillation cycle and F_{max} increase with a power law dependence as A_{sp} is reduced for both simulation and experiment (Fig. 2.8). Consistent with previous simulations described in Sect. 5.2, the tip/sample forces were dependent on the Young's modulus of the surface.

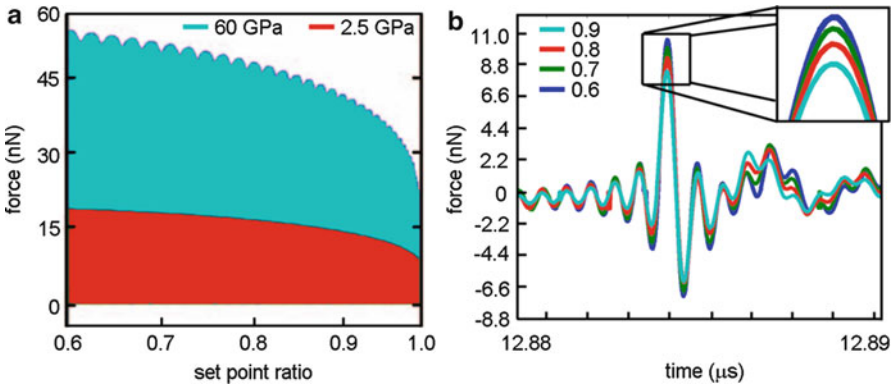


Fig. 2.8 Simulations (**a**) and experiments (**b**) of the TMAFM process in liquid demonstrate the effect of amplitude set-point, A_{sp}, on the average tapping force per oscillation cycle, with a constant cantilever free amplitude. Two model surfaces used for simulation: $E = 60$ GPa (*blue*) and $E = 2.5$ GPa (*red*). Experiments were performed on a mica surface in saline buffer. A_{sp} was systematically decreased from 0.9 to 0.6 for experiments

These results demonstrate that the actual force applied to the sample can be controlled by adjusting imaging parameters; however, the relative relationships between mechanical surface properties and specific features of the time-resolved tip/sample force are still valid, provided that imaging parameters are maintained throughout the analysis.

Numerical simulations can also be performed to determine the impact of changing the spring constant of the cantilever on imaging forces, specifically F_{max} and F_{min}. To facilitate comparisons between the different spring constants, other imaging parameters were maintained between simulations including the set-point ratio, the drive amplitude, the free amplitude, the resonance frequency and the drive frequency. For the first set of simulations, the value of Young's modulus was modified as the Hamaker constant of the surface was held constant. Increasing the spring constant from 0.1 to 1.0 N/m resulted in a shift in the magnitude of F_{max} for any given surface Young's modulus, but the power law dependence of F_{max} on Young's modulus was maintained for any given cantilever spring constant (Fig. 2.9a). F_{min}, however, was unaffected by modification of the spring constant (Fig. 2.9b). When simulations were performed to determine how increasing the cantilever spring constant altered imaging forces related to changes in the Hamaker constant, a similar trend is observed: as the spring constant increases, F_{max} increased for any given Hamaker constant, with no change in F_{min} (Fig. 2.9c). However, as the Hamaker constant is systematically increased from 0.1 to 1.0 aJ, the linear relationships between both F_{max} and F_{min} with the Hamaker constant are maintained for any given spring constant. These results suggest that as long as a single cantilever is used, features of tapping forces can be directly compared to determine relative changes in surface mechanical properties.

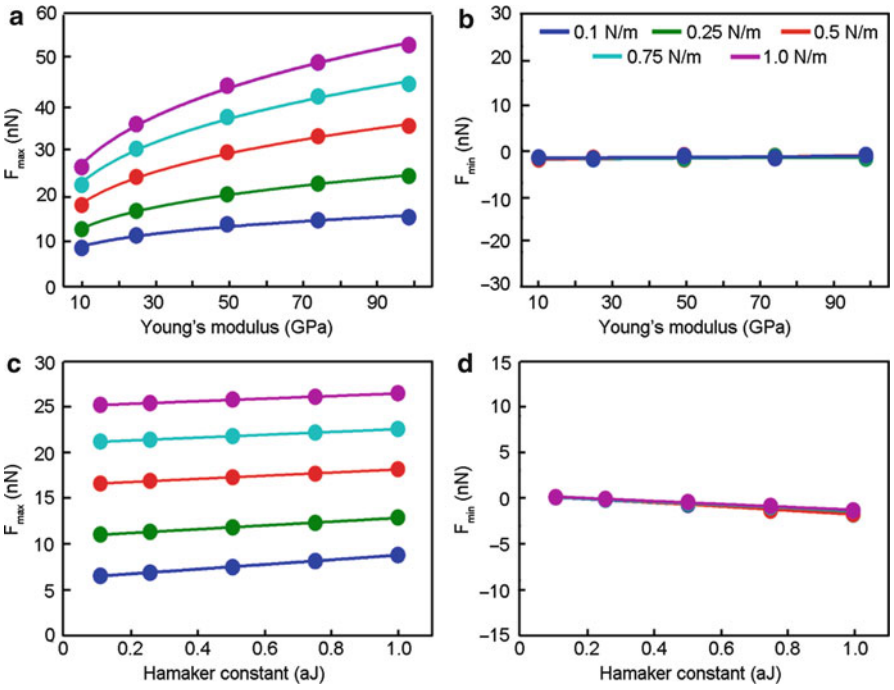


Fig. 2.9 Simulations to determine the effect of cantilever spring constant on tip/sample imaging forces. (**a**) Maximum tapping forces, F_{max}, as a function of Young's modulus with various values of spring constant (legend in (**b**) applies to all subplots). (**b**) Minimum tapping forces, F_{min}, as a function of Young's modulus. (**c**) Maximum tapping forces, F_{max}, as a function of the Hamaker constant with various values of spring constant. (**d**) Minimum tapping forces, F_{min}, as a function of the Hamaker constant

5.4 Applications of SPAM to Real Systems

Supported lipid bilayer patches on mica represented the first successful application of the SPAM technique on an experimental system (Fig. 2.10). Supported bilayers have a considerably lower elastic modulus compared to mica, so this system provides a surface with a soft region (supported bilayer) and hard region (exposed mica). Histograms of F_{max} and F_{min} associated with imaging this system are distinctly bimodal, with each mode corresponding to either the mica or bilayer portions of surface and providing excellent contrast in the reconstructed force images (Fig. 2.10b, c). Consistent with the simulation results, the values of F_{max} corresponding to the bilayer were lower in comparison with those corresponding to mica. The magnitude of F_{min} associated with imaging mica was larger than that for the bilayer patch, indicating that the tip adhered more strongly to the mica surface. Interestingly, there were small regions on the supported bilayer patch, ~30–150 nm wide, that appeared to be a second bilayer stacked on top of the first

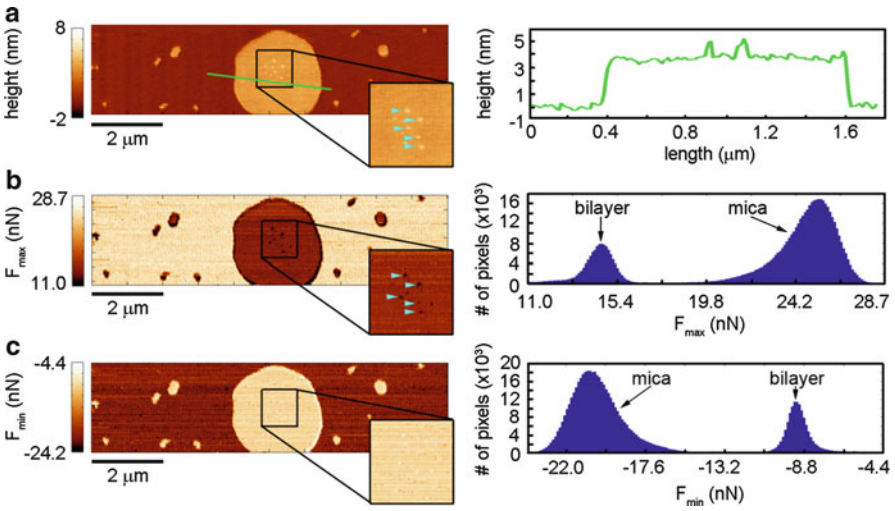


Fig. 2.10 SPAM imaging of a supported lipid bilayer patch on mica. (**a**) Topography image with the *green line* corresponding the height profile to the *left*. (**b**) F_{max} and (**c**) F_{min} images are presented with histograms of these respective forces for every tapping event presented to the *left* of the images. The *insets* zoom in on small areas containing small, stacked bilayer on the patch (*blue arrows*)

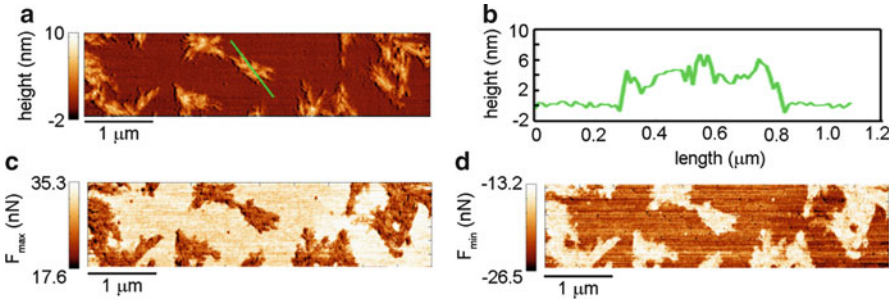


Fig. 2.11 SPAM imaging of aggregates of a polyglutamine peptide deposited on a mica substrate. (**a**) Topography image with the *green line* corresponding the (**b**) height profile. Both the (**c**) F_{max} and (**d**) F_{min} images display excellent contrast between the proteinaceous material and the mica substrate

(Fig. 2.10, blue arrows). The appearance of these regions was associated with a decrease in F_{max}, with no discernible change in F_{min}, suggesting that stacked bilayers have a reduced Young's modulus without a corresponding increase in adhesion. Several studies have measured mechanical changes in supported lipid membranes using SPAM. For example, SPAM has been used to determine the effect of cholesterol on the modulus of lipid bilayers [27], how exposure to

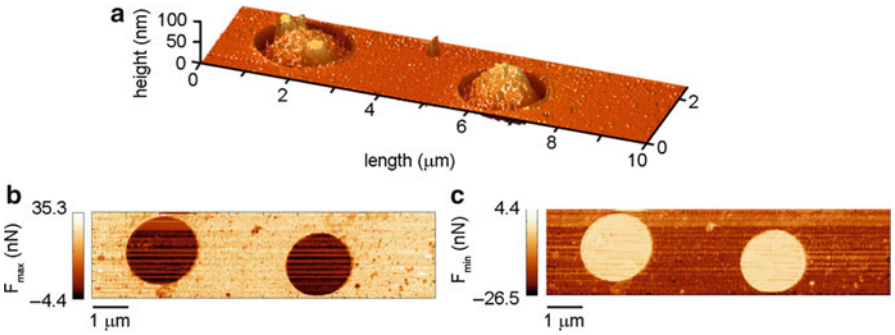


Fig. 2.12 SPAM imaging of a film consisting of a blend of Polystyrene (PS, elastic modulus of ~2 GPa) and Polyolefin Elastomer (LDPE, elastic modulus of ~0.1 GPa) supported on a silicon substrate. (**a**) Topography, (**b**) F_{max}, and (**c**) F_{min} images display excellent contrast between the two domains of the film

lipoprotein particles alter membrane mechanics [37], and how membrane disruption caused by a variety amyloid-forming proteins alter local mechanical properties of lipid bilayers [25, 38–40].

While most studies utilizing SPAM have focused on supported lipid membranes, it can be applied to a variety of systems. For example, SPAM has been used to verify the magnitude of tapping forces associated with imaging fragile viral capsids [31]. Contrast associated with imaging forces is achievable between protein aggregates and an underlying mica substrate (Fig. 2.11). Contrast in F_{max} and F_{min} can also be achieved using SPAM on a variety of materials imaged in solution such as a film consisting of a blend of Polystyrene (PS, elastic modulus of ~2 GPa) and Polyolefin Elastomer (LDPE, elastic modulus of ~0.1 GPa) supported on a silicon substrate (Fig. 2.12).

6 Conclusions and Future Perspective

Simultaneous mapping of topography and mechanical properties of surfaces is an attractive feature of proximal probe-based microscopies, and accomplishing this functionality has long been a focus within the field. While recent advances have made this a reality (with SPAM representing just one such technique), there is still considerable effort required to refine these techniques. We have highlighted the applicability of the SPAM technique for simultaneously imaging and mapping the mechanical properties of surfaces through a combination of simulations and experiments on a variety of samples. The insights provided by simulations into the relationship between tapping forces, surface mechanical properties, and imaging parameters are applicable to other force reconstruction techniques based on TMAFM. Importantly, spatially resolved maps of specific features of the time-resolved tip/sample force are directly correlated to material properties of the surface such as modulus and adhesion. As the SPAM technique is especially useful in fluid TMAFM, it has significant potential in biological applications.

References

1. Zhong Q, Inniss D, Kjoller K, Elings VB (1993) Fractured polymer/silica fiber surface studied by tapping mode atomic force microscopy. Surf Sci 290(1–2):L688–L692
2. Burnham NA, Behrend OP, Oulevey F, Gremaud G et al (1997) How does a tip tap? Nanotechnology 8(2):67–75
3. Nony L, Boisgard R, Aime JP (1999) Nonlinear dynamical properties of an oscillating tip-cantilever system in the tapping mode. J Chem Phys 111(4):1615–1627
4. Cleveland JP, Anczykowski B, Schmid AE, Elings VB (1998) Energy dissipation in tapping-mode atomic force microscopy. Appl Phys Lett 72(20):2613–2615
5. Tamayo J, Garcia R (1998) Relationship between phase shift and energy dissipation in tapping-mode scanning force microscopy. Appl Phys Lett 73(20):2926–2928
6. Zitzler L, Herminghaus S, Mugele F (2002) Capillary forces in tapping mode atomic force microscopy. Phys Rev B 66(15):155436
7. Garcia R, Tamayo J, San Paulo A (1999) Phase contrast and surface energy hysteresis in tapping mode scanning force microsopy. Surf Interface Anal 27(5–6):312–316
8. Stark M, Möller C, Müller DJ, Guckenberger R (2001) From images to interactions: high-resolution phase imaging in tapping-mode atomic force microscopy. Biophys J 80(6):3009–3018
9. Marcus MS, Carpick RW, Sasaki DY, Eriksson MA (2002) Material anisotropy revealed by phase contrast in intermittent contact atomic force microscopy. Phys Rev Lett 88(22):226103
10. Melcher J, Carrasco C, Xu X, Carrascosa JL et al (2009) Origins of phase contrast in the atomic force microscope in liquids. Proc Natl Acad Sci U S A 106(33):13655–13660
11. Stark M, Stark RW, Heckl WM, Guckenberger R (2002) Inverting dynamic force microscopy: from signals to time-resolved interaction forces. Proc Natl Acad Sci U S A 99(13):8473–8478
12. Balantekin M, Onaran AG, Degertekin FL (2008) Quantitative mechanical characterization of materials at the nanoscale through direct measurement of time-resolved tip-sample interaction forces. Nanotechnology 19(8):085704
13. Garcia R, Herruzo ET (2012) The emergence of multifrequency force microscopy. Nat Nanotechnol 7(4):217–226
14. Legleiter J, Park M, Cusick B, Kowalewski T (2006) Scanning probe acceleration microscopy (SPAM) in fluids: mapping mechanical properties of surfaces at the nanoscale. Proc Natl Acad Sci U S A 103:4813–4818
15. Sahin O, Magonov S, Su C, Quate CF et al (2007) An atomic force microscope tip designed to measure time-varying nanomechanical forces. Nat Nanotechnol 2(8):507–514
16. Sahin O, Quate CF, Solgaard O, Atalar A (2004) Resonant harmonic response in tapping-mode atomic force microscopy. Phys Rev B 69(16):165416
17. Sahin O, Yaralioglu G, Grow R, Zappe SF et al (2004) High-resolution imaging of elastic properties using harmonic cantilevers. Sensor Actuat A-Phys 114(2–3):183–190
18. Sarioglu AF, Magonov S, Solgaard O (2012) Tapping-mode force spectroscopy using cantilevers with interferometric high-bandwidth force sensors. Appl Phys Lett 100(5):053109
19. Sarioglu AF, Solgaard O (2011) Modeling, design, and analysis of interferometric cantilevers for time-resolved force measurements in tapping-mode atomic force microscopy. J Appl Phys 109(6):064316
20. Hillenbrand R, Stark M, Guckenberger R (2000) Higher-harmonics generation in tapping-mode atomic-force microscopy: insights into the tip-sample interaction. Appl Phys Lett 76(23):3478–3480
21. Stark RW, Hecki WM (2003) Higher harmonics imaging in tapping-mode atomic-force microscopy. Rev Sci Instrum 74(12):5111
22. Chen GY, Warmack RJ, Oden PI, Thundat T (1996) Transient response of tapping scanning force microscopy in liquids. J Vac Sci Technol B 14(2):1313–1317
23. Legleiter J, Kowalewski T (2005) Insights into fluid tapping-mode atomic force microscopy provided by numerical simulations. Appl Phys Lett 87:163120/1–163120/3

24. Putman CAJ, Vanderwerf KO, Degrooth BG, Vanhulst NF et al (1994) Tapping mode atomic-force microscopy in liquid. Appl Phys Lett 64(18):2454–2456
25. Burke KA, Yates EA, Legleiter J (2013) Amyloid-forming proteins alter the local mechanical properties of lipid membranes. Biochemistry 52(5):808–817
26. Kumar B, Pifer PM, Giovengo A, Legleiter J (2010) The effect of set point ratio and surface Young's modulus on maximum tapping forces in fluid tapping mode atomic force microscopy. J Appl Phys 107
27. Shamitko-Klingensmith N, Molchanoff KM, Burke KA, Magnone GJ et al (2012) Mapping the mechanical properties of cholesterol-containing supported lipid bilayers with nanoscale spatial resolution. Langmuir 28:13411–13422
28. Garcia R, Perez R (2002) Dynamic atomic force microscopy methods. Surf Sci Rep 47(6–8):197–301
29. Tamayo J (1999) Energy dissipation in tapping-mode scanning force microscopy with low quality factors. Appl Phys Lett 75(22):3569–3571
30. Basak S, Raman A (2007) Dynamics of tapping mode atomic force microscopy in liquids: theory and experiments. Appl Phys Lett 91(6):064107-3
31. Xu X, Carrasco C, Jose de Pablo P, Gomez-Herrero J et al (2008) Unmasking imaging forces on soft biological samples in liquids when using dynamic atomic force microscopy: a case study on viral capsids. Biophys J 95(5):2520–2528
32. Israelachvili J (1992) Intermolecular & surface forces. Academic, London
33. Derjaguin BV, Muller VM, Toporov YP (1975) Effect of contact deformations on the adhesion of particles. J Colloid Interf Sci 53(2):314–326
34. Kowalewski T, Legleiter J (2006) Imaging stability and average tip-sample force in tapping mode atomic force microscopy. J Appl Phys 99:064903/1–064903/5
35. Guzman HV, Perrino AP, Garcia R (2013) Peak forces in high-resolution imaging of soft matter in liquid. ACS Nano 7(4):3198–3204
36. Legleiter J (2009) The effect of drive frequency and set point amplitude on tapping forces in atomic force microscopy: simulation and experiment. Nanotechnology 20:245703/1–245703/10
37. Legleiter J, Fryer JD, Holtzman DM, Kowalewski T (2011) The modulating effect of mechanical changes in lipid bilayers caused by apoE-containing lipoproteins on Aβ induced membrane disruption. ACS Chem Neurosci 2:588–599
38. Yates EA, Owens SL, Lynch MF, Cucco EM et al (2013) Specific domains of abeta facilitate aggregation on and association with lipid bilayers. J Mol Biol 425(11):1915–1933
39. Burke KA, Kauffman KJ, Umbaugh CS, Frey SL et al (2013) The interaction of polyglutamine peptides with lipid membranes is regulated by flanking sequences associated with huntingtin. J Biol Chem 288(21):14993–15005
40. Burke KA, Hensal KM, Umbaugh CS, Chaibva M et al (2013) Huntingtin disrupts lipid bilayers in a polyQ-length dependent manner. BBA Biomembr 1828(8):1953–1961

Scanning Probe Microscopy for Nanolithography

3

C. B. Samantaray

Contents

1 Definition of the Topic 91
2 Overview 92
3 Introduction 92
4 Experimental and Instrumental Methodology 94
5 Key Research Findings 96
5.1 Scanning Probe Lithography-I 96
5.2 Scanning Probe Lithography-II 99
5.3 Scanning Probe Lithography (SPL)-III 101
5.4 Equivalent Direct-Write Approaches 104
6 Conclusions and Future Perspective 107
References 109

1 Definition of the Topic

Scanning probe microscopy (SPM) has been used for both fabrication and characterization techniques of nanomaterials, nanostructures, or nanopatterning. There are two fundamental approaches such as scanning tunneling microscopy (STM) and atomic force microscopy (AFM) that are being used for the scanning probe lithography (SPL) process. In this chapter, we will discuss a recent development of nanolithography based upon new ideas and innovations of scanning probe microscopy and direct-write approach.

C.B. Samantaray (✉)
College of Engineering & Technology, Virginia State University, Petersburg, VA, USA
e-mail: csamantaray@vsu.edu

© Springer-Verlag Berlin Heidelberg 2015

C.S.S.R. Kumar (ed.), *Surface Science Tools for Nanomaterials Characterization*,
DOI 10.1007/978-3-662-44551-8_3

2 Overview

Nanofabrication and their corresponding lithography techniques that have attracted much attention in making low-dimensional nanostructures are being used in all sectors of electronics, energy, and medicine applications. As of Moore's law of rapid miniaturizations of transistor and IC circuits, it is urgent to make at least sub-10 nm features to maintain the current trends in device engineering. Therefore, it is timely to develop the key concepts of modern lithography with the combination of both top-bottom and bottom-top approaches working from a single platform and novel search for the high-resolution nanopatterns or nanostructures ever.

There are a dozen of contact mode microcopies as well as lithography tools that have been used since decades. SPL techniques are basically tip-based nanofabrication tools utilized for a detailed study of molecular phenomenon and devices. Further, SPL is the most versatile tool to fabricate and even restructure a biochemical or bioenergetic surface by molecule-to-molecule approach and analyze the image as well as the reaction mechanism at sub-nm length scale. Compared to other lithography systems, SPL is relatively cost-effective, easy to operate on a wide variety of inorganic, organic, as well as biological substrates, in a broader range of reproducibility.

3 Introduction

The origins and functionality of Scanning probe microscopy as well as lithography are possible due to the early invention of both the scanning tunneling microscope and the atomic force microscopy [1–3]. The simultaneous development of both scanning tunneling and atomic force probes revolutionized our understanding of surface chemistry, physics, and engineering by providing real-space information at nanoscale resolution too.

However, from the industrial application point of view and especially in semiconductor device manufacturing units, a further miniaturization to sub-10-nm scale is urgent in an effort to improve the circuit integration modules and support affordable cost. Among several conventional nanolithography tools so far available, scanning probe microscopy-based techniques have a lot of advantages and accessibility for molecular or nano-bio-device fabrications and their characterizations [4–18]. Tseng et al. reviewed scanning probe lithography considering the advantages of ultrahigh-resolution capability, inexpensive instrumentation, and relatively easy operation that lead to next-generation nanoscale manufacturing and productivity [19]. Saavedra et al. reported hybrid lithography, possibly a new fabrication technique to visualize high performance and technologically feasible devices at nanoscale regime (1–20 nm) [20, 21]. The review is about the nanoscale precision and atomic resolution of scanning probe lithography that enables for the fabrication and in-situ characterization of localized and site-specific functional structures.

Compared to other nanolithography tools, scanning probe lithography exploits the physical or biochemical interactions between the substrate and the probe in a microscopy system [22–32]. The scanning probes or tips used in the SPL techniques

are to be electrically conductive, wear resistant, and able to control the hydrophobicity; thereby exhibits nano-scale patterning as well as greater understanding of molecular dynamics. A variety of probe-based lithography approaches such as dip-pen nanolithography, nanoshaving, nanografting, scanning near-field lithography, etc. have been developed for successful nanofabrications and nano-characterizations a decade ago [4–7, 33–43]. Recent study on nanoscale imaging of physical and biochemical phenomena using scanning local-probe techniques represents the advances in probing functionality and tip-substrate interactions to be useful for a variety of current topics of superconductivity, electron spin, plasmon field focusing, surface diffusion, bond vibration, molecular interface contact, and phase transformations [44, 45]. The major classes of local probes are discussed for electron correlations, surface chemistry, optical interactions, and electromagnetic and electromechanical coupling. In order to fabricate 2D and 3D asymmetric features of polymers, metals, and ceramics, a technological review investigates the geometry, materials, and surface properties along with their analytical and empirical relationships [46].

STM- and AFM-based techniques that have been used for nanolithography or nanopatterning are not still overcoming the sub-diffraction limit below ~1 nm [47, 48]. In contrast to a specific direct-write approach, focused electron beam-induced deposition (FEBID) technique is in the recent discussions of making high-resolution patterns as close as to ~1 nm feature [49–52]. Additionally, electron beam lithography (EBL) with an aberration corrected scanning transmission electron microscope (STEM) has obtained close to ~2 nm isolated feature and ~5 nm half-pitch in hydrogen silsesquioxane resist [53]. Therefore, both SPL and FEBID are being considered as modern nanofabrication tools irrespective of their source, functionality, and limitation to the slow pattern speed in first or chemical purity issues in the second case of studies. Further, a new approach of using liquid precursors in place of the conventional gas phase in focused electron beam-induced deposition (called liquid-phase EBID: LPEBID) resolved the issues of material purity through reaction kinetics of both solvated as well as secondary electrons and becomes able to fabricate bimetallic nanostructures or nanoalloy successively [54–64]. LPEBID is a resist-free lithography technique based upon scanning electron beam lithography (EBL) system fixed the chemical purity issue, still suffers from the pattern placement error and line-edge roughness limitations.

Therefore, here we report the current lithography technique using scanning probe microscopy and comparative approaches using focused electron- or laser beam-based direct-write approaches not only to fabricate low-dimensional nanostructures but also to achieve a better understanding of nanoscale phenomenon that may be useful for chemical, biomedical, and microelectronics industrial applications. Certainly, a discussion of trivial issues and effects in next-generation SPM-based nanolithography and equivalent techniques is worth taking and will have tremendous impact in modern-day nanotechnology.

Here we subdivide the current research and methods in the scanning probe microscopy for nanolithography into four sections. SPL-I deals with conventional

studies on dip-pen and related tip-based lithography, SPL-II for local-oxidation and ferroelectric lithography, SPL-III for optical force-based techniques, and finally equivalent approaches for focused electron- or laser beam-induced deposition.

4 Experimental and Instrumental Methodology

Scanning probe lithography usually makes nanoscale patterns using most versatile techniques of AFM and STM. However, most of the SPM methods are of tip-based technique that has been investigated through the molecular phenomenon in between surface and the probe. Here we discuss few of the experimental methods used for the current SPL and equivalent direct-write lithography technology.

Using the conventional dip-pen nanolithography (DPN), a new approach has being investigated such as scanning probe block copolymer lithography (SPBCL) that uses block copolymer ink coated onto AFM tip for nanopatterning especially on semiconductors (such as Si or SiN) at room temperature [65]. While, polymer-pen lithography (PPL) that adds a pattern process through enzyme stamping method and compared to others controlled by capillary-force and soft-lithography approaches [66, 67]. Furthermore, scanning thermal lithography and scanning thermal twisted microscopy (STTM)-based lithography use either a heatable AFM probe or plasma polyacrylonitrile films coated onto the probe, respectively [68, 69]. Scanning electrochemical microscopy (SECM) method uses a bias-activated tip that is already dip-coated into the desired ionic solution [70]. Scanning ion conductance microscopy (SICM) uses both contact and noncontact probe-assisted nanopatterning tool [71].

Oxidation scanning probe lithography (OSPL) is a hybrid approach that uses both top-down nanolithography such as SPL and the electron beam lithography (EBL) [72]. Tip-induced local anodic oxidation (LAO) method uses applied voltage on the AFM tip during writing and even controls all the pattern parameters including relative humidity in the nano-oxidation process [73]. Ferroelectric lithography (FL) enables to write domain wall structures on $LiNbO_3$ single crystals by using a HeCd laser beam at ~325 nm focused through liquid electrodes [74]. Kelvin probe force microscopy (KPFM) uses the conductive SPM tip coated with Pt layer and scanned over the sample at a small tip-surface separation even in a liquid environment [75]. The KPFM method has been applied for direct measurements of change in work function of an Au substrate coated with self-assembly monolayer (SAM) from different solvents and for different substrates too. Indentation lithography (IndL) enables 3D nanostructures using a diamond tip on hard oxide and metal surfaces over large area [76].

Similarly, optical force stamping lithography (OFSL) follows a multi-beam splitting technique of a primary laser beam using a spatial light modulator that is focused onto a substrate through a colloidal solution of the nanoparticles and eventually produces optical patterns [77]. OFSL, a *far-field* optical technique that can obtain patterns made of Au nanoparticles (NPs), shows a spatial deviation from the desired positions of $\leq$45 nm, less than $\lambda/10$ of the laser wavelength of 532 nm! Femtosecond pump-probe microscope (FPM) could be used as next-generation

lithography tool for probing with a spatiotemporal high-resolution patterning through diffraction-limited pump-probe beams [78]. Furthermore, an intrinsically 3D direct-write approach of multiphoton lithography (MPL) has been established to patterns Pd and Pt type of metallic nanostructures [79]. Scanning near-field photolithography (SNPL) exhibits higher resolution pattering supported by the near-field probe consists of a tapered optical fiber attached to a tuning fork, operating in shear-force mode across an ODPA/TiO_2 monolayer [80]. However, in case of photocatalytic lithography, a Ti-coated scanning near-field optical microscopy probe could be useful for the patterning of self-assembled monolayer (SAMs) based on the localized photocatalytic degradation of adsorbates [81].

The established gas-phase electron beam-induced deposition (EBID) is usually performed in an electron microscopy system with a focused, high-energy electron beam typically between 5 and 200 keV in a low-vacuum (10^{-5}–10^{-3} Torr) environment. A suitable gas injection system uses the volatile organometallic species to be directed toward the substrate, and the growth of deposits or nanomaterials occurs only when transiently adsorbed precursor molecules decompose at the point of intersection between the incident electron beam and the substrate. Additionally, electron beam-induced reactions of organometallics adsorbed onto solid substrates under high vacuum use different metal carbonyl precursors such as Ni $(CO)_4$, Fe $(CO)_5$, and $W(CO)_6$. For example, van Dorp et al. used W $(CO)_6$ as the precursor used for deposition on the substrates of amorphous carbon or Si_3N_4 membranes at ambient pressures in the region of 10^{-3} Torr at a substrate temperature of 150 °C to reduce the effect of contamination that usually happens during this process [49, 50, 82].

Water-soluble precursors are used in case of LPEBID is a novel method to achieve the highest % purity in the deposited materials even though they are fabricated on polyimide substrates. Danov et al. fabricated the platinum (Pt) from chloroplatinic acid (H_2PtCl_6) in deionized (18 MΩ) water carried out together in QuantomiX QX-102 WETSEM capsules that separate the liquid from the vacuum chamber using a thin (∼150 nm) polyimide membrane [54]. Different high-resolution patterns are exposed including single-pixel dots at doses ranging from 2 to 27 pC using beam energy of 20 keV and beam current of 200 pA in a Raithe_LiNE electron beam lithography system. Pt was successfully deposited on the membrane due to the electron-metallic ion interactions through the liquid precursors. A similar procedure has also been adopted for the preparations of bimetallic nanoalloy of AuPt and AuAg on polyimide membranes in deionized water from H_2PtCl_6, $HAuCl_4$, and $AgNO_3$ using beam energy of 20 keV at a beam current of 1.3 nA using the EBL system [62]. AuPt dots were patterned in arrays with doses ranging from100 to 1,100 pC per dot with periods of 350 nm and AuAg dots with doses ranging from 50 to 150 pC per dot with periods of 2 mm. Elemental analysis was conducted with energy-dispersive X-ray spectroscopy (EDS) using a 20 keV primary beam, and further the bimetallic deposits or nanoalloy confirmed in transmission electron microscopy (TEM). Monte Carlo simulation based analysis using NIST DTSA-II software package was used to quantify the deposit % of composition. Recently, interest has been growing in using bulk-liquid reactants for focused electron beam-induced processing (FEBIP) in both closed liquid cells

and in environmental SEMs [63, 64]. Liquid reactants potentially offer a wider range of accessible materials, faster processing, and higher-purity deposition. There are two recent advances in FEPIB using aqueous solutions: specifically, the controlled etching of silicon nitride (SiN_x) using potassium hydroxide (KOH) and the high-purity deposition of palladium from sodium tetrachloropalladate (Na_2PdCl_4) have been reported. Roberts et al. discussed laser-assisted electron beam-induced deposition (LAEBID) process, a similar direct-write approach which integrates an electron beam to a synchronized pulsed laser step to induce thermal desorption of reaction by-products and successive Pt deposition with high resolution and purity [83].

5 Key Research Findings

5.1 Scanning Probe Lithography-I

Here we focus current trends in scanning probe microscopy-based nanolithography using various methods and their developments.

5.1.1 Dip-Pen Nanolithography (DPN)

The mechanism of dip-pen nanolithography (DPN) is the flow of organic molecules from tip to substrate surface due to the capillary action and favors functionalization for nanosensor-type devices. Piner et al. reported direct-write dip-pen (DPN) nanolithography through an AFM tip to write alkanethiols with ~30 nm lines on Au thin film [4]. Similarly, Wu et al. investigated the role of a tip-cleaning procedure and transport mechanism that influences the tip lifetime in DPN processes [84]. Further, specialized SPL probes are being used for nanopatterning as well as studying nanoscale phenomenon owing to their thermal, electrical, or photonic applications at large scale. Shim et al. reported graphene-coated hard-tip soft-spring lithography (HSL) tip arrays that are cantilever-free and successfully applied to electrochemical desorption and thermal dip-pen technique (t-DPN) [85]. In contrast to electron/ion beam-based fabrication, DPN patterns are preferred for ligand mobility, such as controlling ligand spatial organization in synthetic membranes and cells that allow lipid molecules to move across the nanostructures [86].

5.1.2 Scanning Probe Block Copolymer Lithography (SPBCL)

Scanning probe block copolymer lithography (SPBCL) technique has the capability of using both SPL with bottom-up nanosynthesis approach which remains the most useful fabrication technique for metallic nanostructures of sub ~50 nm feature in a specific orientation as well as in selective dimensions on a solid substrate [65]. The writing process has the positional control offered by molecular printing techniques such as DPN in order to deliver an attoliter volume of metal-coordinated block copolymers to the desired surface. The method has the capability of preparing metallic, semiconducting, and compound nanostructures too. Further discussion is carried out for an improved design of sparse topographic templates to direct the

assembly of block copolymer patterns with a controlled *inplane* orientation for sub-10 nm features [87–89]. The current progress of advanced nanolithography using epitaxial self-assembly and graphoepitaxy have been synergistically integrated with conventional photolithography, yield a tremendous industrial impact [90].

5.1.3 Polymer-Pen Lithography (PPL)

In a unique way, restraining from using the conventional probe technique, polymer-pen lithography (PPL) uses a polymer tip to "write" any arbitrary nanopattern over a large substrate surface. Additionally, the technique has been utilized for a faster speed and control over different optimization parameters during the pattern process [66]. In case of protein engineering, PPL is being considered as a potential nanofabrication process, as it can control incubation temperature, crystalline morphology, and even enzyme concentrations that eventually enhance the writing speed. The technique and pattern could be compared to another approach called metal-mesh lithography which can create binary patterns on periodic arrays of ink-free regions through backfilling [67].

5.1.4 Scanning Thermal Lithography (SThL)

There is a special type of energy-limited lithography tool called scanning thermal lithography (SThL) that fabricates nanopatterns on polymer substrates strictly based on *joule-heat exchange method*. The idea is of using heat-sensitive probe materials to prevent energy dissipation during the pattern process. Further care has been taken to preserve energy loss using heat-resistant polyimide films as substrate materials especially due to its lower thermal conductivity. The technique follows thermochemical process at nanoscale and is therefore called as localized thermal analysis (LTA) or microthermal analysis (μTA). Huang et al. studied SThL process using poly-methyl-methacrylate (PMMA) thin films preloaded with benzoyl peroxide (BPO) and silver nitrate ($AgNO_3$) [91]. It has been clearly established that in-situ release of energy obtained from peroxide decomposition during the thermochemical process just compensates the joule shortage and rapid cooling in the polymer film. Furthermore, SThL process has the uniqueness of controlling over reactive surface, interfaces, or any selective topography during pattern process as well.

Additionally, the greatest advantage of SThL-type technique is free from any kind of proximity effect that appears due to the back-scattered electrons that usually matter in case of electron beam lithography (EBL) systems [92]. Further, in comparison to spatial-phase-locking EBL system, thermal-SPL also enables a closed-loop lithography providing direct feedback on the patterning process and alignment. During patterning process thermal probes or tips are in contact with polyphthalaldehyde (PPA)-type resist that triggers the self-amplified depolymerization of the resist into the gaseous phase. The sub-nm sensitivity to the surface topographic features allows direct field stitching and overlay without having to resort to special purpose alignment markers with nm-scale precision.

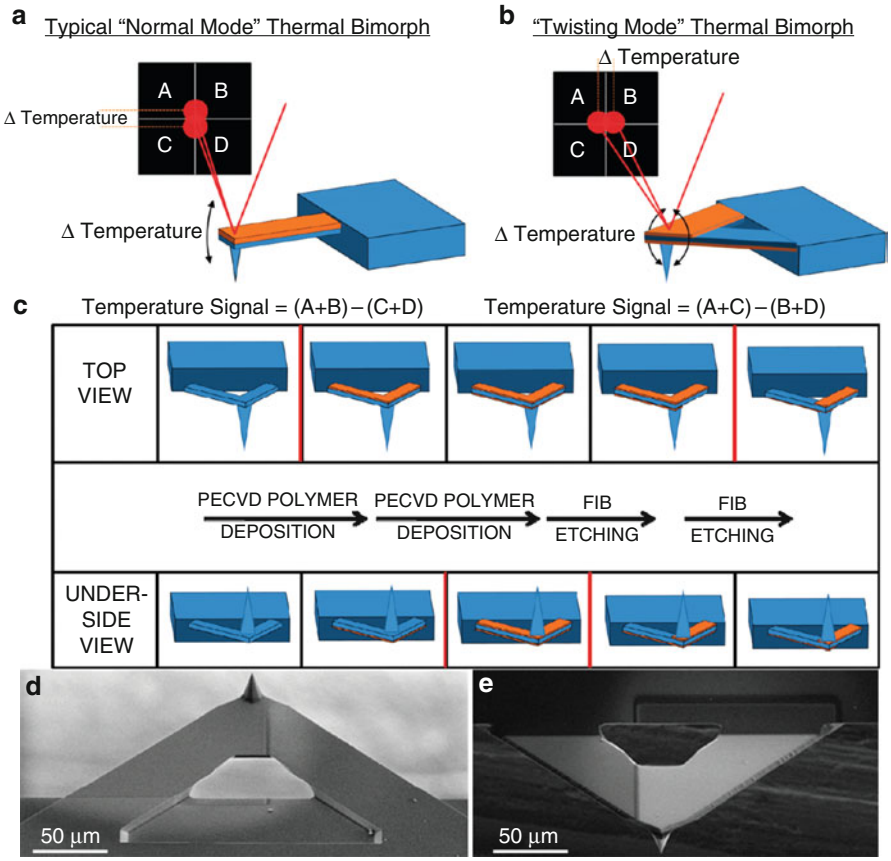


Fig. 3.1 (**a**) A schematic of the bending motion of a typical thermal bimorph. (**b**) A schematic of the twisting motion of a thermal twisting bimorph. (**c**) A schematic indicating the fabrication process used for making V-shaped thermal twisting probes. (**d**) Tip side-oriented and (**e**) backside-oriented scanning electron micrographs of an STTM probe (Reprinted with permission from Ref. [69], copyright 2012, American Chemical Society)

5.1.5 Scanning Thermal Twisted Microscopy (STTM)

As scanning thermal microscopy (SThM) has been used for investigating different thermal sensing and imaging systems, it can be further extended for nanoscale lithography/fabrications based upon thermal bimorph bending mechanism [68]. Due to the further limitation of scanning probe technique, a *twisted version* has been proposed that is well fitted to obtain high-spatial as well as thermal imaging resolution, called scanning thermal twisted microscopy (STTM) [69].

Figure 3.1a shows the normal deflection mode of the laser spot in the quadrant photodiode, while Fig. 3.1b addresses a bifunctional operation of using the lateral deflection signal for thermal imaging, and maintaining the normal deflection signal for concurrent topographical imaging, just by twisting the microfabricated

cantilever. Furthermore, the fabrication method of twisting probes is performed by plasma-polymerized film deposition on both sides of V-shaped tapping cantilever, followed by top and bottom side coating removal as shown in Fig. 3.1c. Figure 3.1d, e depict the scanning electron microscopy images of a twisting bimorph cantilever.

5.1.6 Scanning Electrochemical Microscopy (SECM)

Scanning electrochemical microscopy (SECM) is an SPM-based technique capable to understand electrochemical reactions during the process. The method can be extended for electrochemical nanolithography by using conventional way of tip immersion into ionic liquids or solutions and applying proper bias [70]. A lot of endeavors were carried out for different metals such as Ag, and Cu, through surface tip interaction or reactions on selective substrates [91, 92]. It has been established that scanning tunneling microscopy is also suitable for the chemical reaction process of the above materials; especially for the Cu clusters on Au electrodes, other bimetallic alloy or nanomaterials synthesis [93–95]. Additionally, other vital chemical reaction mechanisms including oxidation and reduction process could be achieved through the nano-mechanics effect successfully [33, 96–98].

5.1.7 Scanning Ion Conductance Microscopy (SICM)

Lipson et al. reported a timely article on conductive scanning probe microscopy (c-SPM) for imaging and nanopatterning using both contact and noncontact probe-based techniques [71]. In a better comparison, scanning ion conductance microscopy (SICM) enables noncontact imaging in electrolyte solutions, while scanning electrochemical microscopy (SECM) uses microelectrode integrated into the tip to spatially map eventful changes in electrochemistry.

5.2 Scanning Probe Lithography-II

5.2.1 Local-Oxidation Lithography

As semiconductor industry is approaching toward the development of nanoelectronics at the molecular scale, conventional oxidation methods of device fabrications could be modified by using a special scanning probe technique such as local-oxidation lithography in addition to the clean room technology. Generally, local-oxidation lithography process is performed using atomic force or scanning tunneling microcopy systems. However, the former technique is much convenient to achieve large-scale patterns with sub-10 nm diffraction limit. Furthermore, amplitude modulation in AFM technique makes the nano-oxidation process more effective as it controls the water meniscus in between tip and surface precisely [99–104]. Recently, channels of nanowire-based transistors were fabricated using two top-down nanolithography approaches such as oxidation scanning probe lithography (OSPL) and electron beam lithography (EBL). Although transistor property remains unaltered due to either of the fabrication processes, still SPL provides smaller channel widths than the EBL [72].

5.2.2 Tip-Induced Local Anodic Oxidation (LAO)

AFM nanolithography technique has been widely used for the fabricating nanostructures or nanoarrays owing to their multi-operational principles of force-, bias-, and thermal-assisted phenomenon and characterizations. Dehzangi et al. reported one of the bias-assisted AFM nanolithography method called tip-induced local anodic oxidation (LAO) and discussed various issues of applied voltage-on-tip, writing speed or tip materials, and even the relative humidity in order to attain the sub-nm structures [73].

5.2.3 Ferroelectric Lithography (FL)

The advantage of ferroelectric lithography (FL) is its applicability over a large surface area from mm to cm and further control over surface assembly processes with a nanoscale precision. Haussmann et al. reported assembly of metallic nanowires for next-generation nanoelectronic functionality using ferroelectric lithography (FL) technique [74]. During litho-process, ferroelectric domains act as the templates for the assembly of different functional nanostructures. Further, successful imaging of the domain distribution is operated by using piezoresponse force microscopy (PFM).

5.2.4 Kelvin Probe Lithography (KPL)

Kelvin probe lithography (KPL) is a well-established patterning technique based upon two of the main workhorses of scanning Kelvin probe microscopy (SKPM) and electrostatic force microscopy (EFM) used for the local probing, lithography, and imaging. However, there is a difference of using probe mechanism in the conventional AFM technique and those used in EFM and SKPM. The probes used in AFM topography are via a short range Lennard-Jones-type (LJ) type potential, while in case of EFM and SKPM, the potential is considered through the Coulomb interaction. As an application view, dynamic scanning force microscopy (DSFM) in combination with Kelvin probe force microscopy can achieve the local topographic and potentiostatic properties of ferroelectric nanowires too.

Domanskiy et al. reported great details of Kelvin probe force microscopy (KPFM) performed on a standard liquid environment [75]. In a novel approach, KPFM is able to calculate the contact potential difference (CPD) between a sample surface and the SPM tip, typically coated with Pt layer and also can measure the work function shift. Figure 3.2 shows the scanning probe images of triangular Au areas close to ~20 nm thickness in the center on a SiO_x reference substrate, and the obtained work function differences are in excellent agreement with other measurements.

5.2.5 Indentation Lithography (IndL)

Indentation lithography (IndL) is a new fabrication process with many conceptual similarities to the scanning probe lithography (SPL). Although, IndL can produce patterns on hard oxide and metal surfaces, still lacks resolution and accuracy in positioning, compared to SPL techniques. Although IndL can produce patterns on hard oxide and metal surfaces, it still lacks resolution and accuracy in positioning, compared to SPL [76]. Similarly, molecular pattern of high-conductance

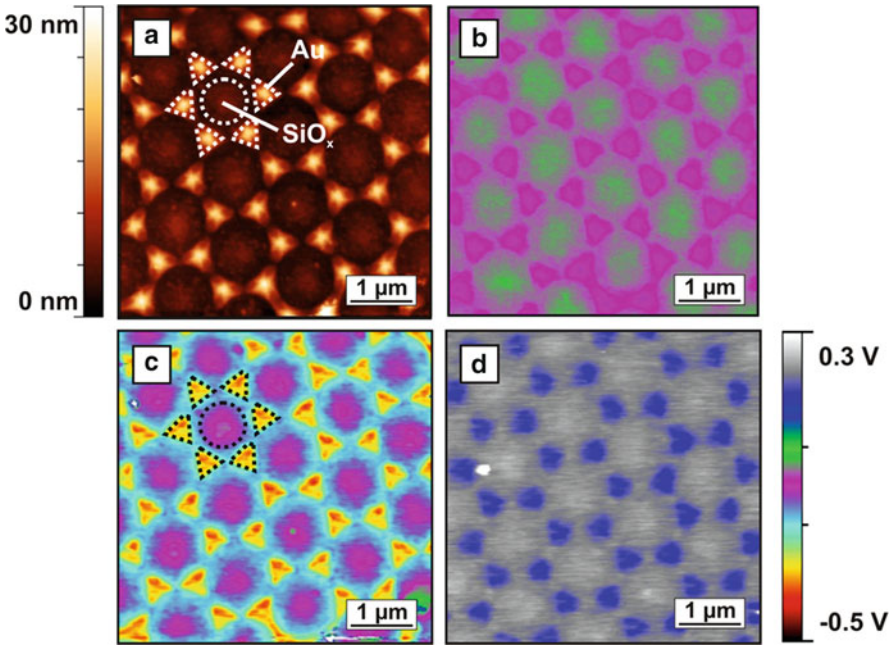


Fig. 3.2 SPM images of Au structures prepared by nanosphere lithography. (**a**) Topography measured in decane: At the position of the former contact area of the polystyrene (PS) colloids, there exists an approximately 4 nm thick layer which consists most probably of residual PS of the colloids that could not entirely be removed by chloroform and Ar plasma treatment. (**b**) Contact potential difference (CPD) measured in ambient air. (**c**) Contact potential difference measured in decane. (**d**) Contact potential difference measured in decane after exposing Au structures to hexadecanethiol solution for 90 min (Reprinted with permission from Ref. [75], copyright 2012, American Chemical Society)

oligomer/polymer are formed on Si substrates using conductive AFM has been investigated recently [105]. The process is made through the oligomerization or polymerization in a precursor, which is covalently grafted onto the surface through electrical stimulation via local probes. Similarly, silicon nitride (Si_3N_4)-based probe tip is used to produce nanogrooves in contrast to three-sided pyramidal diamond tip especially for surface plasmon characterizations [106].

5.3 Scanning Probe Lithography (SPL)-III

5.3.1 Optical Force Stamping Lithography (OFSL)

Optical force stamping lithography (OFSL) is one of the novel tools to make nanopatterns by employing *optical force* on individual particles and rearranging them to a site-specific position by focused laser beam [77]. Interestingly, it is worthy to say here that during this process, the optical force may not be directly responsible to trap nanoparticles; instead the repulsive force exerted by the laser

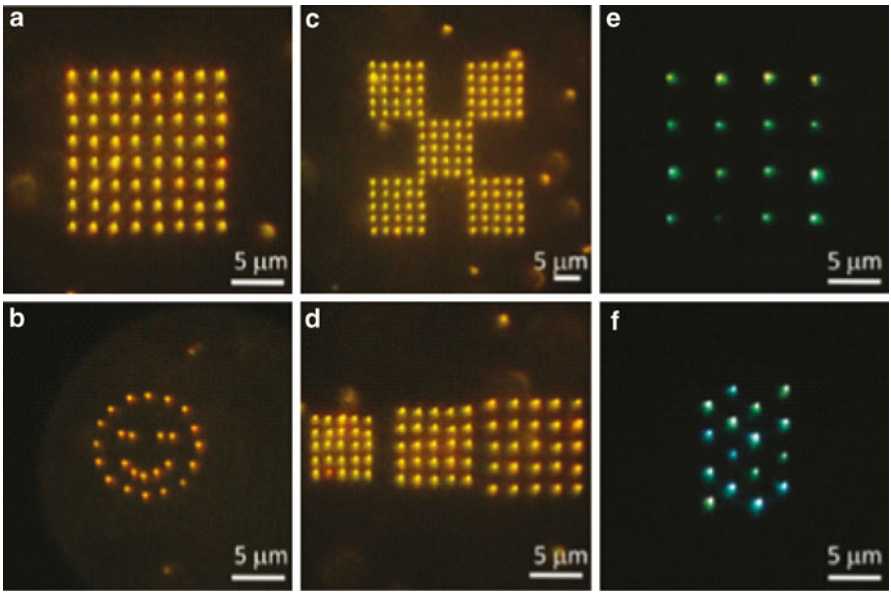


Fig. 3.3 Versatility of optical force stamping lithography. Dark-field images of patterns stamped on a glass substrate: (**a**) A square 8 × 8 and (**b**) an arbitrary "smiley" pattern both composed of single 80 nm gold nanoparticles. (**c**) Five square 5 × 5 patterns stamped sequentially in a chessboard-like manner by shifting the Fourier image displayed at the spatial light modulator (SLM). (**d**) Three sequentially stamped square 5 × 5 patterns with different pitch size. Both the pitch size and the position of the pattern are controlled by the SLM. (**e**) A square and (**f**) a hexagonal pattern comprised of 80 nm silver nanoparticles. A continuous wave laser operating at 532 nm is used to stamp these patterns. A real-time video showing the stamping process of an 8 × 8 pattern is available in the supporting information (Reprinted with permission from Ref. [77], copyright 2011, American Chemical Society)

beam accelerates them along the directions of the light energy flux and sets them at desired positions on a substrate surface (Fig. 3.3).

5.3.2 Femtosecond Pump-Probe Microscope (FPM)

Gabriel et al. developed a femtosecond pump-probe microscopy (FPM) technique by photoexciting single nanostructure in one location and probing at other, using a high- spatial and temporal resolution method [78]. The experimental setup attached with diffraction-limited pump-probe beams (PPB) is able to image the carrier population over time and thus evaluate rapid free carriers and the rate of migration of trapped carriers as well. Figure 3.4 shows the image of charge cloud produced by photoexcitation of a localized spot and spreading of this cloud along the Si nanowire axis.

5.3.3 Multiphoton Lithography (MPL)

Zarzar et al. described a novel approach of multiphoton lithography (MPL), an intrinsically 3D direct-write technique to pattern Pd and Pt nanostructures [79].

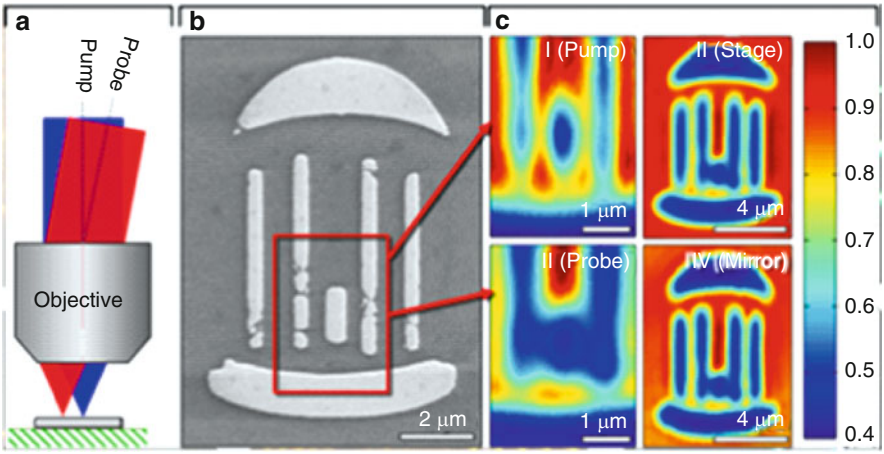


Fig. 3.4 (**a**) Schematic illustration of spatially separated scanning. (**b**) Image of the UNC logo defined in Au by electron beam lithography; scale bar, 2 μm. (**c**) *Left*, optical transmission images obtained with the pump (I) and probe (II) beams scanned over a lower-center portion of the Au structure, as denoted by the *inset box* in panel (**b**), that contains an ~400 nm gap; scale bars, 1 μm. *Red* indicates maximum transmission and *blue* minimum transmission. *Right*, comparison of transmission images acquired by raster-scanning the probe beam over the entire Au structure shown in panel (**b**) using either the x − y stage (III) or the mirror assembly (IV); scale bars, 4 μm (Reprinted with permission from Ref. [78], copyright 2013, American Chemical Society)

As verified, nanomaterials show excellent electrochemical and catalytic properties and can be integrated to 3D fluidic device architectures. Alternative patterning technique has been developed through laser photoreduction of silver from a liquid which is controlled by a scanning AFM tip. The result represents a major step toward a direct, negative-tone, tip-based patterning of functional materials [107]. In another method, patterning of metallic nanoparticles on substrate surface has been studied through laser-induced melting and evaporation process [108]. The pattern process has the capability to control nanoassembly of particles by combining their unique optical and thermophysical properties.

5.3.4 Scanning Near-Field Optical Lithography (SNOL)

SNOL is derived from the basic principle of scanning near-field optical microscopy (SNOM). The technique has been considered as a nondestructive direct-write method suitable for nanofabrication of polymers and biomolecules, especially making protein or DNA array on solid surfaces. Credgington et al. have used SNOL to pattern conjugate polymers of high-resolution (~50 nm) nanostructures and periodic 2D arrays [80]. SNOL is also feasible for fluid or bimolecular solution that creates a novel approach of sample-probe interaction within a near-field zone, thus obtaining high-resolution patterns as reported for alkylthiolates and siloxane films in Fig. 3.5 [109, 110]. Dostert et al. reported sub-10 nm near-field nanoassembly and nanopattern through chemical reaction method that is strongly affected due to molecular interaction of metallic nanoparticles located in close

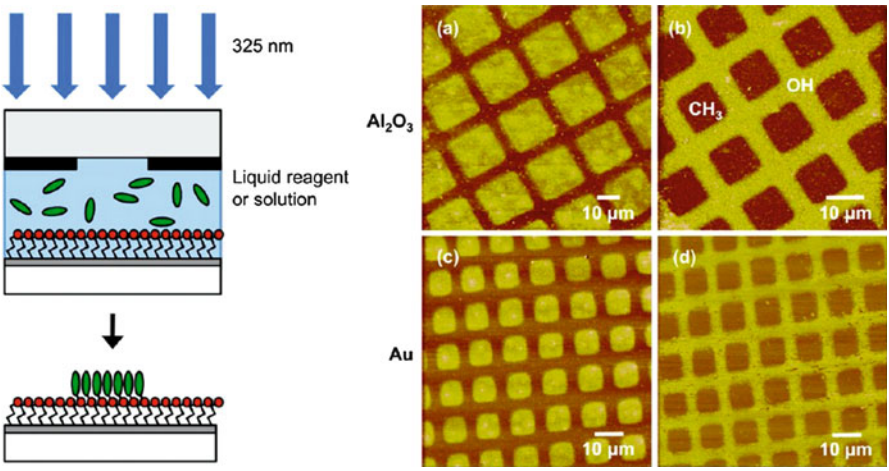


Fig. 3.5 Schematic diagram showing the process used to fabricate two-component micrometer-scale patterns and (**a**–**d**) friction force microscopy images of aryl azide-terminated SAMs on (**a** and **b**) aluminum oxide and (**c** and **d**) gold following initial mask-based exposure under (**a** and **c**) ethanolamine or (**b** and **d**) octadecylamine followed by maskless exposure under either (**a** and **c**) octadecylamine or (**b** and **d**) ethanolamine (Reprinted with permission from Ref. [109], copyright 2013, American Chemical Society)

proximity [111]. Recently, there is a fusion of the "millipede" that deploys a massive parallelism with scanning near-field photolithography to yield a "Snomipede," is capable of large-scale parallel chemical transformations over 1 mm range [42].

5.3.5 Photocatalytic Lithography

Additionally, Ti-coated SNOM probe could be useful for the patterning of self-assembled monolayer (SAMs) based on the localized photocatalytic degradation of adsorbates, called the photocatalytic lithography. [81]. Lin et al. presented periodic Au and Cu nanostructures that are fabricated sequentially using particle lithography, and the overlapped regions serve as Moiré patterns at nm scale [112]. The Moiré effect in these regions can be directly visualized from NSOM images, from which periodicity and structural details are accurately determined. Similarly high-resolution pattern and signal-to-noise (SNR) development have been carried out for different SAMs activated on metallic or oxide substrates using electron beam lithography technique [113–117].

5.4 Equivalent Direct-Write Approaches

This section describes SPL equivalent direct-write techniques that are being adopted for high-resolution pattern formations using focused electron and laser beam-induced techniques.

5.4.1 Gas-Phase Electron Beam-Induced Deposition (GEBID)

Gas-phase EBID has been well established over decades for successful nanostructure fabrications and characterizations. The process needs focused electron beam reaction to organometallics that adsorbed onto solid substrates under high-vacuum ambient. Different nanostructures have been fabricated using metal carbonyl precursors such as Ni $(CO)_4$, Fe $(CO)_5$, and W $(CO)_6$. For example, van Dorp et al. used W $(CO)_6$ as the precursor materials to be deposited on amorphous carbon and Si_3N_4 membranes at the substrate temperature of 150 °C and pressure of 10^{-3} Torr for a highly resolved nanostructure with an average diameter of 0.72 nm with reduced contamination [49, 50]. Surprisingly, that has the current record for the smallest feature written by either an electron or conventional optical lithography tool ever. Attempts have been already performed through molecule-by-molecule writing using organometallic precursor on graphene with FEBID technique [82]. The key behind ultrahigh-resolution nanopatterns is definitely through electron beam reaction on the adsorbed carbonyls and further control over rate of reaction or kinetics [118, 119]. Additionally, gas-phase FEBID is a direct-write nanolithography tool of unprecedented resolution capability in the growth of magnetic nanostructures too [120]. A recent study of ~30 nm cobalt nanostructures grown by focused electron beam has been reported. Recent study shows EBID of a ~3 nm half-pitch patterns on bulk Si using a scanning electron beam lithography system and followed major technical steps to complete diffusion of reactants into the exposed area; minimize the effect of noise during exposure; and finally, avoid proximity effects [121].

5.4.2 Liquid-Phase Electron Beam-Induced Deposition (LPEBID)

Generally, gas-phase EBID produce high-resolution patterns that are not free from the material purity issues; while liquid-phase precursors are able to fabricate high-purity metallic Pt nanostructures on polyimide substrates (Fig. 3.6) [54–56]. Based upon above liquid precursor principles, Au and Ag metallic nanostructures are also being developed in successive attempts [58, 60]. It has been established that the % of material deposits was varied to the electron beam energy from 2, 5, and 20 keV and verified optimal energies exist for maximum growth rate and for minimum feature sizes. Liu et al. fabricated Si nanostructures and provide fundamental insights into the mechanism for liquid-phase electron beam-induced deposition, keeping eye upon tremendous impact in semiconductor and nanoelectronic device applications [61].

Si nanodots were prepared from $SiCl_4$ liquid precursor in a transmission electron microscope-based electron beam-induced reaction with major contribution from the secondary electrons (SE) generated at the substrate surface [61]. Further, Donev et al. fabricated 3D metallic nanostructures on SiN membrane using similar procedure of LPEBID [57]. This is the first observation of performing LPEBID on bare and metal-coated SiN membranes, and a result has been compared to the Pt deposits to that obtained on polyimide membranes in a close proximity of nucleation, morphology, and size dependence on electron dose and purity.

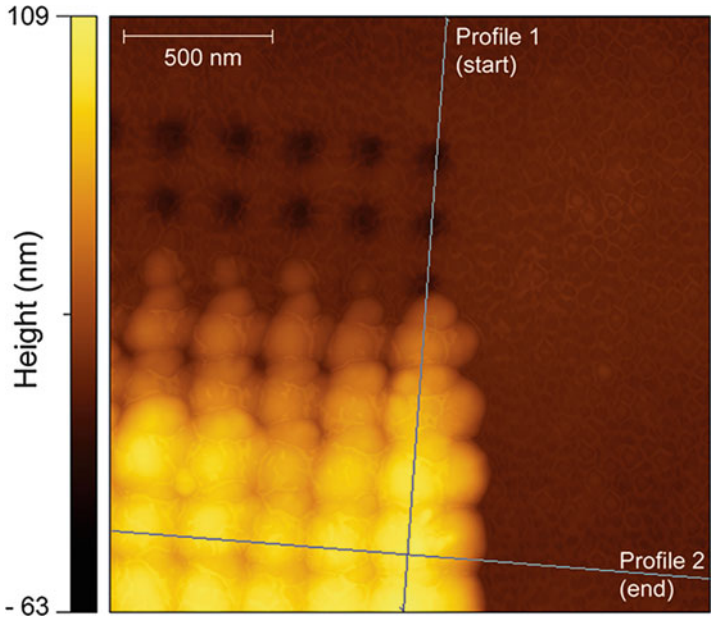


Fig. 3.6 Topographic AFM image of nanostructures deposited by liquid-phase EBID on polyimide membrane, showing accumulation of Pt as the lithographic e-beam scan progresses (*right* to *left* and *bottom* to *top* on the image). Finally, only "dimples" (*dark spots*) develop, possibly indicative of a nucleation threshold for e-beam-induced Pt growth (Reprinted with permission from Ref. [54], copyright 2009, American Chemical Society)

The LPEBID approach has been extended further toward nano-biotechnology and biomedical areas of applications too. Electron beam-induced deposition and nanopatterning on a live cell membrane have been demonstrated as a nano-stimulation for individual mechanochemical receptor on the cell membrane. Especially, EBID is carried out using liquid precursor of 3, 4-ethylenedioxythiophene with the following steps of electron beam (2.5–10 keV) irradiation and exposure through a 100 nm thick SiN nanomembrane for pattern and ablation on a living cell membrane in the cell culturing chamber [59, 122]. LPEBID can also induce chemical solution deposition or polymerization using secondary electrons through the nanomembrane window of a wet cell chamber. Furthermore, liquid-phase EBID offers a new route to fabricate not only 3D metallic nanostructures but also bimetallic nanoalloys without complex multistep processing. Recently, bimetallic AuPt and AuAg nanoalloys have been prepared on polyimide membranes and the process kinetics explained on the basis of effective role of solvated electrons along with secondary electrons, like pulsed radiolysis [62].

5.4.3 Focused Electron Beam-Induced Processing (FEBIP)

FEBIP is widely employed for nanoscale site-specific etching too. The technique has been proven useful for device prototyping, interconnection with chemically

synthesized nanostructures, and integrated circuit mask repair. Recently, interest has also been growing in using bulk-liquid reactants for FEBIP in both closed liquid cells and in environmental SEMs [63, 64]. Liquid reactants potentially offer a wider range of accessible materials, faster processing, and higher-purity deposition. The advances in FEPIB using aqueous solutions, specifically in the controlled etching of silicon nitride (SiN_x) using potassium hydroxide (KOH), and the high-purity deposition of palladium from sodium tetrachloropalladate (Na_2PdCl_4) have been investigated [63]. However, in due course, EBID has been performing direct-write patterning of metallic as well as bimetallic nanostructures and suffers material purity issues and thus low throughput. These limitations are mitigated by combining EBID process with atomic layer deposition (ALD) technique [123]. The process makes patterns of a thin seed layer by EBID followed by selective ALD growth with a comparatively lower dose and throughput to the electron beam lithography (EBL).

5.4.4 Laser-Assisted Electron Beam-Induced Deposition (LAEBID)

Roberts et al. discussed laser-assisted electron beam-induced deposition process, a similar direct-write approach which integrates an electron beam to a synchronized pulsed laser step to induce thermal desorption of reaction by-products and successive Pt deposition with high resolution and purity [83]. As FEBID has the limitation to the purity %, the above experiments show that purification of Pt deposits could be enhanced by reduction of carbon content by ~50 % with the addition of synchronized laser pulses. Furthermore, metallic behavior of LAEBID platinum is verified with resistivity measurement up to 4×10^3 μΩ cm, which is lower than the lowest reported EBID platinum resistivity value of 1.4×10^4 μΩ cm. Interestingly, it has also been noted that water ice can act as resist for high-resolution nanopatterns (sub-10 nm) in focused electron beam, called ice lithography. This has been reported about the special properties of liquid resist that allow direct patterning of high-purity metal and even fabrication of high-quality carbon nanotube-based field-effect transistors (FETs) [124].

6 Conclusions and Future Perspective

Here we discuss how scanning probes as well as focused beams are being used as direct-write lithography and image analysis using different instrumental techniques. In most cases of the SPL, tip-based interaction to the substrate surface and chemical reaction mechanism takes important role of fabricating nanoscale structures and understanding related phenomenon. Additionally, a variety of SPM-equivalent focused electron- or laser-induced processing methods that are capable of making high-resolution pattern are also discussed. According to the current trend in the Moore's law, the ultimate goal is to fabricate as well as characterize nano- or molecular-level transistor-related devices with no reliability issues. Therefore, both SPM and SPM-like nanolithography techniques are most usable even if their limitations to writing speed or material purity in the deposition process are being discussed in the scientific community.

Let us put remark on future applications of scanning probe imaging or nanopatterning methods in the emerging area of computing, energy, or photonic applications. In spite of various conventional memory devices such as ferroelectric random access memory (FeRAM), phase change memory (PCM), magnetoresistive random access memory (MRAM) are being used in semiconductor industries; resistance switching memory (ReRAM) has also a significant role of obtaining nonvolatile memory effect and thus considered as an alternative memory devices in the future. However, ReRAM is not free from technical limitations due to the presence of the localized filamentary conducting paths in a close vicinity of the electrode/film interface. Therefore, SPM have been used to view the filament path in a high spatial resolution at nanoscale along both lateral and vertical directions [125]. Further investigation of atomic structure of conducting nano-filaments in TiO_2-based resistive switching memory has been reported too [126]. In addition to the high-resolution imaging, SPM could be further extended for patterning of the above materials to make nanoscale-resistive memory device applications. Similarly, scanning probe techniques are of intense use in energy materials and devices especially for photovoltaics, thermoelectrics, catalysts, batteries, and energy harvesting. The nanoscale SPM characterization is urgent due to the paradigm shift that occurred from structure-process correlations in bulk/thin films to structure-function correlations in patterns. There are multiple parameters involved during the nanoscale metrology or measurement of optical/dielectric, ion/electron mobility, photochemical/catalytic reactions, and surface roughness/work function [127–132]. Additionally, Lipson et al. report the conductive SPM for the characterization and nanopatterning of electronic and energy materials. The discussion begins by describing the methodologies used to characterize organic photovoltaics, transparent conducting oxides, Li-ion batteries, and other electrochemical systems [71]. Nanostructures that are prepared from block copolymer (BCP) self-assembly and nanotemplates are being suitable to nanolithography that is compatible to the CMOS process and memory technology. The study shows that a dramatic reduction of switching power of phase change memory (PCM) devices by investigating BCP self-assembly process is of near-commercialized nonvolatile memory devices so far discussed using the self-assembly technology [133].

Another potential application and study is of making SPM probes and their functioning with high accuracy and sensitivity. Recently, polymeric AFM probes covered by graphene monolayer that already prepatterned on Cu-coated substrates are being discussed. The study shows how graphene improves the functionality of the probes by making them conductive and more resistant to wear [134]. Therefore, graphene-coated AFM probes will be most useful for analyzing thermomechanical and surface engineering phenomenon at nanoscale [85]. Different important variables such as friction, adhesion, and conductivity could be accurately hypothesized using such nanoprobes. Furthermore, AFM-based lithography techniques are used for fabrication of very short constrictions ($L \sim 15$ nm) between the graphene quantum dots and electrodes for study of transport spectroscopic events. However, comparison to the conventional resist-based lithography, AFM-based SPL never make the graphene sheet clean or defect-free for the nanoscale measurements [135].

Lastly, the use of SPL, FEBID, and LABID technique is to be explored more for successful nanoscale patterning and understanding reaction mechanism at molecular or atomic scale.

References

1. Binnig G, Rohrer H, Gerber C, Weibel E (1982) Tunneling through a controllable vacuum gap. Appl Phys Lett 40:178–180
2. Binning G, Rohrer H, Gerber C, Weibel E (1982) Surface studies by scanning tunneling techniques. Phys Rev Lett 49:57–61
3. Binnig G, Quate CF, Gerber C (1986) Atomic force microscope. Phys Rev Lett 56:930–933
4. Piner RD, Zhu J, Xu F, Hong S, Mirkin CA (1999) "Dip-Pen" nanolithography. Science 283:661–663
5. Amro NA, Xu S, Liu G-Y (2000) Patterning surfaces using tip-directed displacement and self-assembly. Langmuir 16:3006–3009
6. Maoz R, Frydman E, Cohen SR, Sagiv J (2000) Constructive nanolithography: site-defined silver self-assembly on nanoelectrochemically patterned monolayer surfaces. Adv Mater 12:424–429
7. Maoz R, Frydman E, Cohen SR, Sagiv J (2000) Constructive nanolithography: inert monolayers as patternable templates for in-situ nanofabrication of metal–semiconductor- organic surface structures; a generic approach. Adv Mater 12:725–731
8. Demers L, Ginger DS, Park S-J, Li Z, Chung S-W, Mirkin CA (2002) Direct patterning of modified oligonucleotides on metals and Li, insulators by dip-pen nanolithography. Science 296:1836–1838
9. Lee K-B, Park S-J, Mirkin CA, Smith JC, Mrksich M (2002) Protein nanoarrays generated by dip-pen nanolithography. Science 295:1702–1705
10. Hyun J, Ahn SJ, Lee WK, Chilkoti A, Zauscher S (2002) Molecular recognition-mediated fabrication of protein nanostructures by dip-pen lithography. Nano Lett 2:1203–1207
11. Lee K-B, Lim J-H, Mirkin CA (2003) Protein nanostructures formed via direct-write dip-pen nanolithography. J Am Chem Soc 125:5588–5589
12. Chow DC, Lee W-K, Zauscher S, Chilkoti A (2005) Enzymatic fabrication of DNA nanostructures: extension of a self-assembled oligonucleotide monolayer on gold arrays. J Am Chem Soc 127:14122–14123
13. LaFratta CN, Walt DR (2008) Very high density sensing array. Chem Rev 108:614–637
14. Jonkheijm P, Weinrich D, Schröder H, Niemeyer CM, Waldmann H (2008) Chemical strategies for generating protein biochips. Angew Chem Int Ed 47:9618–9647
15. Braunschweig AB, Huo F, Mirkin CA (2009) Molecular printing. Nat Chem 1:353–358
16. Paxton WF, Spruell JM, Stoddart JF (2009) Heterogeneous catalysis of a copper-coated atomic force microscopy tip for direct-write click chemistry. J Am Chem Soc 131:6692–6694
17. Unruh DA, Mauldin C, Pastine SJ, Rolandi M, Fréchet JMJ (2010) Bifunctional patterning of mixed monolayer surfaces using scanning probe lithography for multiplexed directed assembly. J Am Chem Soc 132:6890–6891
18. Lei Y, Yang S, Wu M, Wilde G (2011) Surface patterning using templates: concept, properties and device applications. Chem Soc Rev 40:1247–1258
19. Tseng AA, Notargiacomo A, Chen TP (2005) Nanofabrication by scanning probe microscope lithography: a review. J Vac Sci Technol B 23(3):877–894
20. Saavedra HM, Mullen TJ, Zhang P, Dewey DC, Claridge SA, Weiss PS (2010) Hybrid strategies in nanolithography. Rep Prog Phys 73:036501
21. Moreno-Flores S, Toca-Herrera JL (2013) Hybridizing surface probe microcopies: towards a full description of the meso- and nanoworlds. CRC Press/Taylor & Francis Group, New York

22. Abraham DW, Mamin HJ, Ganz E, Clarke J (1986) Surface modification with the scanning tunneling microscope. IBM J Res Dev 30:492–499
23. McCord MA, Pease RFW (1986) Lithography with the scanning tunneling microscope. J Vac Sci Technol B 4:86–88
24. McCord MA, Pease RFW (1987) Exposure of calcium-fluoride resist with the scanning tunneling microscope. J Vac Sci Technol B 5:430–433
25. McCord MA, Kern DP, Chang THP (1988) Direct deposition of 10-nm metallic features with the scanning tunneling microscope. J Vac Sci Technol B 6:1877–1880
26. Dagata JA, Schneir J, Harary HH, Evans CJ, Postek MT, Bennett J (1990) Modification of hydrogen-passivated silicon by a scanning tunneling microscope operating in air. Appl Phys Lett 56:2001–2003
27. Snow ES, Campbell PM (1994) Fabrication of Si nanostructures with an atomic-force microscope. Appl Phys Lett 64:1932–1934
28. Sheats JR, Smith BW (eds) (1998) Microlithography: science and technology. Dekker, New York
29. Cappella B, Sturm H (2002) Comparison between dynamic plowing lithography and nanoindentation methods. J Appl Phys 91:506–512
30. Iwasaki H, Yoshinobu T, Sudoh K (2003) Nanolithography on SiO_2/Si with a scanning tunnelling microscope. Nanotechnology 14:R55–R62
31. Sugimoto Y, Abe M, Hirayama S, Oyabu N, Custance O, Morita S (2005) Atom inlays performed at room temperature using atomic force microscopy. Nat Mater 4:156–159
32. Sykes ECH, Fernandez-Torres LC, Nanayakkara SU, Mantooth BA, Nevin RM, Weiss PS (2005) Observation and manipulation of subsurface hydride in Pd{111} and its effect on surface chemical, physical, and electronic properties. Proc Natl Acad Sci USA 102:17907–17911
33. Li Y, Maynor BW, Liu J (2001) Electrochemical AFM 'dip-pen' nanolithography. J Am Chem Soc 123:2105–2106
34. Ginger DS, Zhang H, Mirkin CA (2004) The evolution of dip-pen nanolithography. Angew Chem Int Ed 43:30–45
35. Salaita K, Wang Y, Fragala J, Vega RA, Liu C, Mirkin CA (2006) Massively parallel dip-pen nanolithography with 55000-Pen two-dimensional arrays. Angew Chem Int Ed 45:7220–7223
36. Huo F, Zheng Z, Zheng G, Giam LR, Zhang H, Mirkin CA (2008) Polymer pen lithography. Science 321:1658–1660
37. Wadu-Mesthrige K, Amro NA, Garno JC, Xu S, Liu G-Y (2001) Fabrication of nanometer-sized protein patterns using atomic force microscopy and selective immobilization. Biophys J 80:1891–1899
38. Shi J, Chen J, Cremer PS (2008) Sub-100 nm of supported bilayers by nanoshaving lithography. J Am Chem Soc 130:2718–2719
39. Sun S, Chong KSL, Leggett GJ (2002) Nanoscale molecular patterns fabricated by using scanning near-field optical lithography. J Am Chem Soc 124:2414–2415
40. Sun S, Leggett GJ (2002) Generation of nanostructures by scanning near-field photolithography of self-assembled monolayers and wet chemical etching. Nano Lett 2:1223–1227
41. Sun S, Leggett GJ (2004) Matching the resolution of electron beam lithography by scanning near-field photolithography. Nano Lett 4:1381–1384
42. Ul-Haq E, Liu Z, Zhang Y, Ahmad SAA, Wong L-S, Armes SP, Hobbs JK, Leggett G, Micklefield J, Roberts CJ, Weaver JMR (2010) Parallel scanning near-field photolithography: the snomipede. Nano Lett 10:4375–4380
43. Leggett GJ (2012) Light-directed nanosynthesis: near-field optical approaches to integration of the top-down and bottom-up fabrication paradigms. Nanoscale 4:1840–1855
44. Bonnell DA, Basov DN, Bode M, Diebold U, Kalinin SV, Madhavan V, Novotny L, Salmeron M, Schwarz UD, Weiss PS (2012) Imaging physical phenomena with local probes: from electrons to photons. Rev Mod Phys 84:1343–1381

45. Bonnell DA, Kalinin SV (2013) Scanning probe microscopy for energy research. World Scientific, Singapore
46. Tawfick S, Volder MD, Copic D, Park SJ, Oliver CR, Polsen ES, Roberts MJ, Hart AJ (2012) Engineering of micro- and nano structured surfaces with anisotropic geometries and properties. Adv Mater 24:1628–1674
47. Scappucci G, Capellini G, Johnston B, Klesse WM, Miwa JA, Simmons MY (2011) A complete fabrication route for atomic-scale donor-based devices in single-crystal Germanium. Nano Lett 11:2272–2279
48. Scappucci G, Capellini G, Lee WCT, Simmons MY (2009) Atomic-scale patterning of hydrogen terminated Ge(001) by scanning tunneling microscopy. Nanotechnology 20:495302 (6 pp)
49. van Dorp WF, van Someren B, Hagen CW, Kruit P, Crozier PA (2005) Approaching the resolution limit of nanometer-scale electron beam-induced deposition. Nano Lett 5:1303–1307
50. van Dorp WF, Hagen CW, Crozier PA, Kruit P (2008) Growth behavior near the ultimate resolution of nanometer-scale focused electron beam-induced deposition. Nanotechnology 19:225305 (9 pp)
51. Fuechsle M, Miwa JA, Mahapatra S, Ryu H, Lee S, Warschkow O, Hollenberg LCL, Klimeck G, Simmons MY (2012) A single-atom transistor. Nat Nanotechnol 7:242
52. Utke I, Moshkalev S, Russel P (eds) (2012) Nanofabrication using focused ion and electron beams: principles and applications. Oxford University Press, New York
53. Manfrinato VR, Zhang L, Su D, Duan H, Hobbs RG, Stach EA, Berggren KK (2013) Resolution limits of electron-beam lithography toward the atomic scale. Nano Lett 13:1555–1558
54. Donev EU, Hastings JT (2009) Electron-beam-induced deposition of platinum from a liquid precursor. Nano Lett 9:2715–2718
55. Donev EU, Hastings JT (2009) Liquid-precursor electron-beam-induced deposition of Pt nanostructures: dose, proximity, resolution. Nanotechnology 20:505302 (7 pp)
56. Donev EU, Nehru N, Schardein G, Wright J, Chamberlain A, Samantaray CB, Hastings JT (2011) Recent advances in liquid-phase electron-beam induced deposition: characterizing growth processes and optical properties. Microsc Microanal 17:438
57. Donev EU, Schardein G, Wright JC, Hastings JT (2011) Substrate effects on the electron-beam-induced deposition of platinum from a liquid precursor. Nanoscale 3:2709–2717
58. Schardein G, Donev EU, Hastings JT (2011) Electron-beam-induced deposition of gold from aqueous solutions. Nanotechnology 22:015301
59. Hoshino T, Morishima K (2011) Electron-beam direct processing on living cell membrane. Appl Phys Lett 99:174102–1
60. Ocola LE, Joshi-Imre A, Kessel C, Chen B, Park J, Gosztola D, Divan R (2012) Growth characterization of electron-beam-induced silver deposition from liquid precursor. J Vac Sci Technol B 30:06FF08-07
61. Liu Y, Chen X, Noh KW, Dillon SJ (2012) Electron beam induced deposition of silicon nanostructures from a liquid phase precursor. Nanotechnology 23:385302
62. Bresin M, Chamberlain A, Donev EU, Samantaray CB, Schardein GS, Hastings JT (2013) Electron-beam induced deposition of bimetallic nanostructures from bulk liquids. Angew Chem Int Ed 52:1–5
63. Donev EU, Samantaray CB, Bresin M, Hastings JT (2013) Recent advances in liquid phase electron beam induced processing, silicon nitride etching and palladium deposition. In: Proceedings of the 39th international conference on micro and nano engineering (MNE), 16–19 Sept London, UK, 2013
64. Bresin M, Nehru N, Hastings JT (2013) Focused electron-beam induced deposition of plasmonic nanostructures from aqueous solutions. Proc SPIE 8613:861306
65. Giam LR, He S, Horwitz NE, Eichelsdoerfer DJ, Chai J, Zheng Z, Kim D, Shim W, Mirkin CA (2012) Positionally defined, binary semiconductor nanoparticles synthesized by scanning probe block copolymer lithography. Nano Lett 12:1022–1025

66. Ganesh M, Nachman J, Mao Z, Lyons A, Rafailovich M, Gross R (2013) Patterned enzymatic degradation of poly (ε-caprolactone) by high-affinity microcontact printing and polymer pen lithography. Biomacromolecules 14:2470–2476
67. Tang Z, Wei Q, Wei A (2011) Metal-mesh lithography. ACS Appl Mater Interfaces 3:4812–4818
68. Duvigneau J, Schönherr H, Vancso GJ (2011) Scanning thermal lithography of tailored tert-Butyl ester protected carboxylic acid functionalized (Meth) acrylate polymer platforms. ACS Appl Mater Interfaces 3:3855–3865
69. McConney ME, Kulkarni DD, Jiang H, Bunning TJ, Tsukruk VV (2012) A new twist on scanning thermal microscopy. Nano Lett 12:1218–1223
70. Fan F-RF, Bard A (1995) STM on wet insulators: electrochemistry or tunneling. Science 270:1849–1851
71. Lipson AL, Hersam MC (2013) Conductive scanning probe characterization and nanopatterning of electronic and energy materials. J Phys Chem C 117:7953–7963
72. Ryu YK, Chiesa M, Garcia R (2013) Electrical characteristics of silicon nanowire transistors fabricated by scanning probe and electron beam lithographies. Nanotechnology 24:315205 (7 pp)
73. Dehzangi A, Larki F, Hutagalung SD, Naseri MG, Majlis BY, Navasery M, Hamid NA, Noor MM (2013) Impact of parameter variation in fabrication of nanostructure by atomic force microscopy nanolithography. PLOSONE 8:e65409
74. Haussmann A, Milde P, Erler C, Eng LM (2009) Ferroelectric lithography: bottom-up assembly and electrical performance of a single metallic nanowire. Nano Lett 9:763–768
75. Domanski L, Sengupta E, Bley K, Untch MB, Weber SAL, Landfester K, Weiss CK, Butt H-J, Berger R (2012) Kelvin probe force microscopy in nonpolar liquids. Langmuir 28:13892–13899
76. Gong J, Lipomi DJ, Deng J, Nie Z, Chen X, Randall NX, Nair R, Whitesides GM (2010) Micro- and nanopatterning of inorganic and polymeric substrates by indentation lithography. Nano Lett 10:2702–2708
77. Nedev S, Urban AS, Lutich AA, Feldmann J (2011) Optical force stamping lithography. Nano Lett 11:5066–5070
78. Gabriel MM, Kirschbrown JR, Christesen JD, Pinion CW, Zigler DF, Grumstrup EM, Mehl BP, Cating EEM, Cahoon JF, Papanikolas JM (2013) Direct imaging of free carrier and trap carrier motion in silicon nanowires by spatially-separated femto second pump − probe microscopy. Nano Lett 13:1336–1340
79. Zarzar LD, Swartzentruber BS, Harper JC, Dunphy DR, Brinker CJ, Aizenberg J, Kaehr B (2012) Multiphoton lithography of nanocrystalline platinum and palladium for site-specific catalysis in 3D microenvironments. J Am Chem Soc 134:4007–4010
80. Credgington D, Fenwick O, Charas A, Morgado J, Suhling K, Cacialli F (2010) High-resolution scanning near-field optical lithography of conjugated polymers. Adv Funct Mater 20:2842–2847
81. Ul-Haq E, Patole S, Moxey M, Amstad E, Vasilev C, Hunter CN, Leggett GJ, Spencer ND, Williams NH (2013) Photocatalytic nanolithography of self-assembled monolayers and proteins. ACS Nano 7(9):7610–7618
82. van Dorp WF, Zhang X, Feringa BL, Hansen TW, Wagner JB, Hosson JTMD (2012) Molecule-by-molecule writing using a focused electron beam. ACS Nano 6:10076–10081
83. Roberts NA, Fowlkes JD, Magel GA, Rack PD (2013) Enhanced material purity and resolution via synchronized laser assisted electron beam induced deposition of platinum. Nanoscale 5:408–415
84. Wu T-H, Lu H-H, Lin C-W (2012) Dependence of transport rate on area of lithography and pretreatment of tip in dip-pen nanolithography. Langmuir 28:14509–14513
85. Shim W, Brown KA, Zhou X, Rasin B, Liao X, Mirkin CA (2012) Multifunctional cantilever-free scanning probe arrays coated with multilayer graphene. Proc Natl Acad Sci U S A 109:18312–18317

86. Narui Y, Salaita KS (2012) Dip-pen nanolithography of optically transparent cationic polymers to manipulate spatial organization of proteolipid membranes. Chem Sci 3:794–799
87. Chang JB, Son JG, Hannon AF, Alexander-Katz A, Ross CA, Berggren KK (2012) Aligned sub-10-nm block copolymer patterns templated by post arrays. ACS Nano 6:2071–2077
88. Mickiewicz RA, Yang JKW, Hannon AF, Jung YS, Alexander-Katz A, Berggren KK, Ross CA (2010) Enhancing the potential of block copolymer lithography with polymer self-consistent field theory simulations. Macromolecules 43:8290–8295
89. Son JG, Chang JB, Berggren KK, Ross CA (2011) Assembly of sub-10-nm block copolymer patterns with mixed morphology and period using electron irradiation and solvent annealing. Nano Lett 11:5079–5084
90. Jeong S–J, Kim JY, Kim BH, Moon H–S, Kim SO (2013) Directed self-assembly of block copolymers for next generation nanolithography. Mater Today 16:468–473
91. Huang C-M, Yeh C-H, Chen L, Huang D–A, Kuo C (2013) Energetic-assisted scanning thermal lithography for patterning silver nanoparticles in polymer films. ACS Appl Mater Interfaces 5:120–127
92. Cheong LL, Paul P, Holzner F, Despont M, Coady DJ, Hedrick JL, Allen R, Knoll AW, Duerig U (2013) Thermal probe maskless lithography for 27.5 nm half-pitch Si technology. Nano Lett 13:4485–4491
93. Craston DH, Lin CW, Bard AJ (1988) High resolution deposition of silver in Nafion films with the scanning tunneling microscope. J Electrochem Soc 135(3):785–786
94. Kolb DM, Ullmann R, Will T (1997) Nanofabrication of small copper clusters on gold (111) electrodes by a scanning tunneling microscope. Science 275:1097–1099
95. Ullmann R, Will T, Kolb DM (1993) Nanoscale decoration of Au (111) electrodes with Cu clusters by an STM. Chem Phys Lett 209:238–242
96. Maynor BW, Li Y, Liu J (2001) Au "Ink" for AFM "Dip-Pen" nanolithography. Langmuir 17:2575–2578
97. Kwon G, Chu H, Yoo J, Kim H, Han C, Chung C, Lee J, Lee H (2012) Fabrication of uniform and high resolution copper nanowire using intermediate self-assembled monolayers through direct AFM lithography. Nanotechnology 23:185307
98. Li W, Virtanen JA, Penner RM (1992) Nanometer-scale electrochemical deposition of silver on graphite using a scanning tunneling microscope. Appl Phys Lett 60:1181
99. Losilla NS, Oxtoby NS, Martinez J, Garcia F, Garcia R, Torrent MM, Veciana J, Rovira C (2008) Sub-50 nm positioning of organic compounds onto silicon oxide patterns fabricated by local oxidation nanolithography. Nanotechnology 19:455308 (6 pp)
100. Chiesa M, Garcia R (2010) Nanoscale space charge generation in local oxidation nanolithography. Appl Phys Lett 96:263112
101. Garcia R, Martinez RV, Martínez J (2006) Nano-chemistry and scanning probe nanolithographies. Chem Soc Rev 35:29–38
102. Martínez RV, Martínez J, Garcia R (2010) Silicon nanowire circuits fabricated by AFM oxidation nanolithography. Nanotechnology 21:245301 (5 pp)
103. Martinez J, Losilla NS, Biscarini F, Schmidt G, Borzenko T, Molenkamp LW, Garcia R (2006) Development of a parallel local oxidation nanolithography instrument. Rev Sci Instrum 77:086106-1-3
104. Martínez RV, García F, García R, Coronado E, Aliaga AF, Romero FM, Tatay S (2007) Nanoscale deposition of single-molecule magnets onto SiO_2 patterns. Adv Mater 19:291–295
105. Lee JS, Chi YS, Choi IS, Kim J (2012) Local scanning probe polymerization of an organic monolayer covalently grafted on silicon. Langmuir 28:14496–14501
106. König T, Papke T, Kopyshev A, Santer S (2013) Atomic force microscopy nanolithography: fabrication of metallic nano-slits using silicon nitride tips. J Mater Sci 48:3863–3869
107. Jarro CA, Donev EU, Menguç MP, Hastings JT (2012) Silver patterning using an atomic force microscope tip and laser-induced chemical deposition from liquids. J Vac Sci Tech B 30:06FD02-6

108. Hawes EA, Hastings JT, Crofcheck C, Mengüç MP (2008) Spatially selective melting and evaporation of nanosized gold particles. Opt Lett 33:1383–1385
109. Zubir OE, Barlow I, Haq EU, Tajuddin HA, Williams NH, Leggett GJ (2013) Generic methods for micrometer- and nanometer-sale surface derivatization based on photochemical coupling of primary amines to monolayers of aryl azides on gold and aluminum oxide surfaces. Langmuir 29:1083–1092
110. Tizazu G, Adawi AM, Leggett GJ, Lidzey DG (2009) Photopatterning, etching, and derivatization of self-assembled monolayers of phosphonic acids on the native oxide of titanium. Langmuir 25(18):10746–10753
111. Dostert KH, Álvarez M, Koynov K, del Campo A, Butt HJ, Kreiter M (2012) Near field guided chemical nanopatterning. Langmuir 28:3699–3703
112. Lin WF, Li JR, Liu GY (2012) Near-field scanning optical microscopy enables direct observation of Moiré effects at the nanometer scale. ACS Nano 6:9141–9149
113. Samantaray CB, Hastings JT (2009) Amino-propyl-triethoxy-silane (APTES) on aluminum fiducial grids for spatial-phase-locked electron-beam lithography. J Vac Sci Technol B 27:2558
114. Samantaray CB, Todd Hastings J (2008) Self-assembled monolayer fiducial grids for spatial-phase-locked electron-beam lithography. J Vac Sci Technol B 26:2351
115. Samantaray CB, Hastings JT (2011) Deep UV patterning of 3-amino-propyl-triethoxy-silane self-assembled molecular layers on alumina. J Vac Sci Technol B 29:041603
116. Cheong LL, Lobez JM, Moon EE, Hastings JT, Smith HI (2011) Secondary-electron signal level measurements of self-assembled monolayers for spatial-phase-locked electron-beam lithography. J Vac Sci Technol B 29:06F308
117. Jung YS, Chang JB, Verploegen E, Berggren KK, Ross CA (2010) A path to ultranarrow patterns using self-assembled lithography. Nano Lett 10:1000–1005
118. Rosenberg SG, Barclay M, Fairbrother DH (2013) Electron induced reactions of surface adsorbed tungsten hexacarbonyl W $(CO)_6$. Phys Chem Chem Phys 15:4002–4015
119. Böhler E, Warneke J, Swiderek P (2013) Control of chemical reactions and synthesis by low-energy electrons. Chem Soc Rev 42:9219–9231
120. Ramon LS, Cordoba R, Rodríguez LA, Magén C, Snoeck E, Gatel C, Serrano I, Ibarra MR, Teresa JMD (2011) Ultrasmall functional ferromagnetic nanostructures grown by focused electron-beam-induced deposition. ACS Nano 5:7781–7787
121. van Oven JC, Berwald F, Berggren KK, Kruit P, Hagen CW (2011) Electron-beam-induced deposition of 3-nm-half-pitch patterns on bulk Si. J Vac Sci Technol B 29:06F305
122. Hoshino T, Morishima K (2010) Electron beam induced in situ spatiotemporal nanofabrication towards intracellular nanorobotics. In: Proceedings of the 214th international conference on miniaturized systems for chemistry and life sciences, 3–7 Oct 2010, Groningen, p 1637
123. Mackus AJM, Thissen NFW, Mulders JJL, Trompenaars PHF, Verheijen MA, Bol AA, Kessels WMM (2013) Direct-write atomic layer deposition of high-quality Pt nanostructures: selective growth conditions and seed layer requirements. J Phys Chem C 117:10788–10798
124. Han A, Vlassarev D, Wang J, Golovchenko JA, Branton D (2010) Ice lithography for nanodevice. Nano Lett 10:5056–5059
125. Lee MH, Hwang CS (2011) Resistive switching memory: observations with scanning probe microscopy. Nanoscale 3:490–502
126. Kwon DH, Kim KM, Jang JH, Jeon JM, Lee MH, Kim GH, Li XS, Park GS, Lee B, Han S, Kim M, Hwang CS (2010) Atomic structure of conducting nanofilaments in TiO_2 resistive switching memory. Nat Nanotechnol 5:148–153
127. Balke N, Bonnell D, Ginger DS, Kemerink M (2012) Scanning probes for new energy materials: probing local structure and function. MRS Bull 37:633–641
128. O'Dea R, Brown LM, Hoepker N, Marohn JA, Sadewasser S (2012) Scanning probe microscopy of solar cells: from inorganic thin films to organic photovoltaics. MRS Bull 37:642–650
129. Jesse S, Kumar A, Arruda TM, Kim Y, Kalinin SV, Ciucci F (2012) Electrochemical strain microscopy: probing ionic and electrochemical phenomena in solids at the nanometer level. MRS Bull 37:651–658

130. Lee W, Prinz FB, Chen X, Nonnenmann S, Bonnell DA, O'Hayre RP (2012) Nanoscale impedance and complex properties in energy-related systems. MRS Bull 37:659–667
131. Lai SCS, Macpherson JV, Unwin PR (2012) In situ scanning electrochemical probe microscopy for energy applications. MRS Bull 37:668–676
132. Besenbacher F, Thostrup P, Salmero M (2012) The structure and reactivity of surfaces revealed by scanning tunneling microscopy. MRS Bull 37:677–681
133. Park WI, You BK, Mun BH, Seo HK, Lee JY, Hosaka S, Yin Y, Ross CA, Lee KJ, Jung YS (2013) Self-assembled incorporation of modulated block copolymer nanostructures in phase-change memory for switching power reduction. ACS Nano 7:2651–2658
134. Olmos CM, Rasool HI, Weiller BH, Gimzewski JK (2013) Graphene MEMS: AFM probe performance improvement. ACS Nano 7(5):4164–4170
135. Puddy RK, Chua CJ, Buitelaar MR (2013) Transport spectroscopy of a graphene quantum dot fabricated by atomic force microscope nanolithography. Appl Phys Lett 103:183117

Kelvin Probe Force Microscopy in Nanoscience and Nanotechnology

4

Da Luo, Hao Sun, and Yan Li

Contents

1 Definition of the Topic 118
2 Overview 118
3 Introduction 118
4 Physical Background and Theory for Kelvin Probe Method 119
4.1 Fundamentals 119
4.2 Electric Force and Electric Force Gradient 121
4.3 AM-KPFM 122
4.4 FM-KPFM 124
4.5 KPFM Without Potential Feedback 126
5 KPFM Measurement 127
5.1 Lock-In Settings for KPFM Measurement 127
5.2 KPFM Resolution 131
5.3 KPFM Sensitivity 133
5.4 KPFM Repeatability 134
6 Applications of KPFM in Nanoscale Characterization 134
6.1 Surface Charge 134
6.2 Work Function and Doping Level 137
6.3 Charge Transfer 144
6.4 Field Effect Transistors 148
6.5 Atomic Resolution KPFM 151
References 154

D. Luo (✉) • Y. Li (✉)
Beijing National Laboratory for Molecular Sciences, Key Laboratory for the Physics and Chemistry of Nanodevices, College of Chemistry and Molecular Engineering, Peking University, Beijing, China
e-mail: yanli@pku.edu.cn

H. Sun
Nano Surfaces Division, Bruker (Beijing) Scientific Technology Co., Ltd, Beijing, China

© Springer-Verlag Berlin Heidelberg 2015

C.S.S.R. Kumar (ed.), *Surface Science Tools for Nanomaterials Characterization*,
DOI 10.1007/978-3-662-44551-8_4

1 Definition of the Topic

Kelvin probe force microscopy (KPFM) is applicable to measure surface potential and work function in a localized nanoscale surface area. In this chapter, we describe the theory and measurement of KPFM and its applications in the characterization of inorganic nanostructure and nanomaterials.

2 Overview

We will focus on fundamentals of KPFM and its applications in inorganic nanostructures and nanomaterials, such as carbon nanotubes (CNTs), graphene, nanocrystals, Si-based nano-devices, and so on. We will review the physical background of Kelvin probe method for electrical measurement and then focus on the two kinds of KPFM methods: one is called amplitude modulation KPFM (AM-KPFM) and the other is called frequency modulation KPFM (FM-KPFM). We will also discuss a special method, KPFM without feedback, which is used to detect high voltage. Then, we will analyze how to realize above KPFM methods by instruments and the influencing factors which can affect KPFM resolution, accuracy, sensitivity, and repeatability. Finally, we will discuss the applications of KPFM in characterization of inorganic nanostructure and nanomaterials. We will mainly focus on five KPFM applications: surface charge detection, work function and doping level study, charge transfer study, field effect transistors, and atomic resolution KPFM.

3 Introduction

Kelvin probe method, first introduced by Lord Kelvin in 1898 [1], is used to measure the contact potential difference (CPD) between metals. In this method, an external voltage is applied to null the electrical field generated by CPD between two metal materials. However, the electrical field is not directly perceived through the senses and cannot be measured very easily. In 1932, Zisman introduced a vibrating reference surface to improve Kelvin probe method into an alternating current (AC) way [2]. The vibrating reference surface leads to capacitance change between two metal plates, which induce a small AC current that can be detected very easily. Although it is an easy way to use Kelvin method and can achieve $\sim$1 mV resolution, the major disadvantage for this method is that only average surface potential of the whole metal plate can be obtained, that means one cannot get any local surface potential information at all. This method is only applicable to macroscopic measurement.

After the invention of scanning probe microscope (SPM), it is the first time Kelvin method can be down to nanoscale world and measuring local surface potential was possible. Kelvin probe force microscopy (KPFM) [3, 4], also called scanning Kelvin probe microscopy (SKPM) or scanning potential microscopy (SPoM),

was developed by Wickramasinghe et al. in 1991 [5] and maps local electrostatic potential at sample surfaces to provide information about material work function [6], electronic structure [7], doping level variations [8], and trapped charges [9], in applications ranging from organic photovoltaic research [10] to field effect transistor (FET) characterization [11]. KPFM has obvious advantages in electrical measurement. First of all, the scanning probe technique takes KPFM method into nanoscale, and the high-resolution local potential imaging becomes possible. Second, it is a quantitate method which can tell us the potential value.

In this chapter, we will discuss about KPFM principles and its applications in inorganic nanostructures and nanomaterials.

4 Physical Background and Theory for Kelvin Probe Method

4.1 Fundamentals

When two metals contact with each other, their Fermi energy levels will be brought to the same level, because the energy of the highest occupied energy levels is different. The Fermi level of a metal is a concept in quantum mechanics usually referring to the energy level of the highest occupied quantum state in a system of fermions at absolute zero temperature, where all states below are occupied and all above are empty. In this case, the fermions are electrons. We define the difference of energy between electrons in vacuum state and that at Fermi energy level as "work function." So the metal which the Fermi energy level is higher has a lower work function; meanwhile, the one which the Fermi energy level is lower has a higher work function. In other words, higher work function means stronger electron binding. When two metal plates are connected to each other, the electrons will flow from the material which has lower work function to the material which has higher work function. The opposite charges are produced on these two metal plates, leading to CPD generation. An electric field can be detected if the potentials on the two metal plates are different. If we carefully adjust an external bias V_{CPD}, a compensatory potential, to nullify the electric field, at equilibrium, when the electric field is nulled, the applied bias is equal to the CPD and all surface charges are disappear. At this point, if the work function of one metal plate is known, suppose it is $Ø_1$ here, one can easily get the work function of the other metal plate, that is, $Ø_2 = Ø_1 - eV_{CPD}$, where e is quantity of electric charge of one electron. All Kelvin probe methods are based on this concept and the only difference is the way to detect this charge-free state.

Figure 4.1 illustrates the basic concept of Kelvin probe method. Before two metals contact with each other, they have different Fermi energy levels (E_{F1} for metal 1 and E_{F2} for metal 2). Suppose E_V is the vacuum level, the energy difference between E_F and E_V is the "work function." For $E_{F1} < E_{F2}$, we can get $Ø_1 > Ø_2$. If we connect the two metals, electrons in metal 2, which have higher energy, will flow to metal 1 and finally result in a state of equilibrium. In this state, metal 1 will be negative charged because it obtains more electrons, and metal 2 will be positive

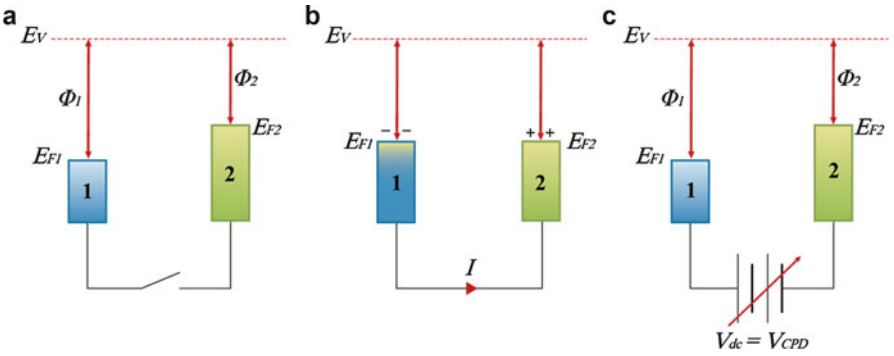


Fig. 4.1 Basic concepts of Kelvin probe method

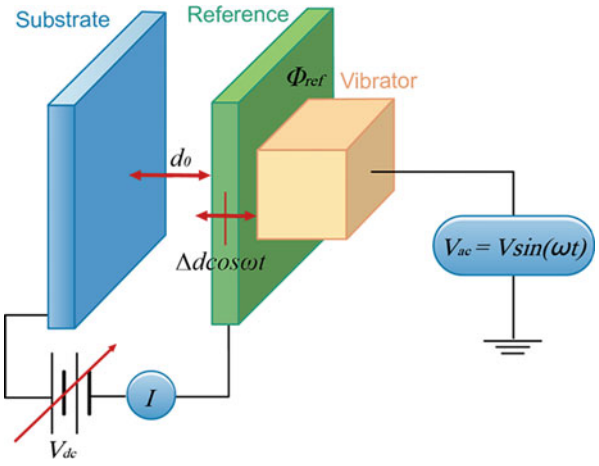


Fig. 4.2 AC Kelvin probe method experiment setup (Zisman)

charged because it loses some electrons. Kelvin probe method uses an adjustable external voltage source to null the surface charge on both metals. When all surface charges disappear, the external bias equals to the contact potential difference.

Zisman used a vibrating reference to improve the Kelvin probe method to an AC way [2]. In this setting, the way to detect charge-free state is to find the compensatory potential that can make the AC current between two metal plates zero. The experiment setup of Zisman is shown in Fig. 4.2. In this experiment setup, a metal plate is fixed (substrate in Fig. 4.2) and the other metal plate (Reference in Fig. 4.2, which has known work function) is vibrating at frequency ω. The mechanical oscillation induces the change of system capacitance, and thus an AC current will be detected if the potential difference between the two metal plates is not zero.

If the distance between the two metal plates is d_0, when the reference plate is vibrating at frequency ω with amplitude Δd, the distance between the two metal plates can be given by

$$d = d_0 + \Delta d \cos \omega t \tag{4.1}$$

The modulated system capacitance C is given by

$$C(t) = \epsilon_0 \frac{A}{d_0 + \Delta d \cos \omega t} \tag{4.2}$$

where A is the area of metal plate and $\in_0$ is the dielectric constant of the free space. For $\Delta d \ll d_0$, Eq. 4.2 can be rewritten by

$$C(t) = \in_0 \frac{A}{d_0} \left(1 - \frac{\Delta d}{d_0} \cos \omega t\right) \tag{4.3}$$

If we note the CPD between the two plates as ΔV, and apply a DC compensatory voltage V_{CPD} to nullify the CPD, the surface charge Q on the metal plates is given by

$$Q(t) = C(t)(\Delta V - V_{CPD}) \tag{4.4}$$

Thus, the current *i(t)* between the two metal plates is

$$i(t) = \frac{\partial Q(t)}{\partial t} = -\in_0 \frac{A}{d_0^2} \omega (\Delta V - V_{CPD}) \Delta d \sin \omega t \tag{4.5}$$

When $V_{CPD} = \Delta V$, *i(t)* goes to zero.

4.2 Electric Force and Electric Force Gradient

Let us start from a simple model: a capacitor composed by two metal plates.

If charge + Q is on a metal plate, whose area is A, according to Gauss's law, the electric field E_+ can be given by

$$E_+ = \frac{\sigma}{2\epsilon_0} \tag{4.6}$$

where σ is areal density of the electrical charge, equals to Q divided by area A.

In similar fashion, if charge –Q is on a metal plate, the electric field E_ also can be got easily

$$E_- = \frac{\sigma}{2\epsilon_0} \tag{4.7}$$

When we put the two metal plates together to make a capacitor, the electric field outside the capacitor becomes zero and that between the two plates becomes

$$E = E_+ + E_- = \frac{\sigma}{\epsilon_0} = \frac{Q}{A\epsilon_0} \tag{4.8}$$

If the potential difference between the two metal plates is ΔV, it can be written as

$$\Delta V = Ed = \frac{Qd}{\in_0 A} \tag{4.9}$$

where d is the distance of the two metal plates. Thus, the system capacitance C is

$$C = \frac{Q}{\Delta V} = \frac{\in_0 A}{d} \tag{4.10}$$

The derivative of capacitance is given by

$$\left[\frac{\partial C}{\partial z}\right]_{z=d} = -\frac{\in_0 A}{d^2} \tag{4.11}$$

Consequently, the electric force (attractive) between the two metal plates is

$$F = -\frac{1}{2}QE = \frac{1}{2}\left(\frac{\in_0 A}{d^2}\right)(\Delta V)^2 \tag{4.12}$$

According to Eq. 4.11, Eq. 4.12 can be rewritten as

$$F = -\frac{1}{2}\frac{\partial C}{\partial z}(\Delta V)^2 \tag{4.13}$$

So the electric force gradient between the two metal plates is

$$\frac{\partial F}{\partial z} = -\frac{1}{2}\frac{\partial^2 C}{\partial z^2}(\Delta V)^2 \tag{4.14}$$

Equations 4.13 and 4.14 are the key results for parallel-plate condenser model.

In KPFM, a conductive probe and a conductive sample form the two plates of the plate condenser model. The electric force and electric force gradient can be expressed as exactly the same equation as Eqs. 4.13 and 4.14.

4.3 AM-KPFM

In AM-KPFM, an AC bias with frequency ω_m and amplitude V_{ac}, superimposed on a DC bias V_{dc}, is applied between tip and sample. An oscillating electric force, according to Eq. 4.13, is generated between tip and sample, which can be written as

$$F_e = -\frac{1}{2}\frac{\partial C}{\partial z}\left[V_{dc} - \Delta V + V_{ac}\sin(\omega_m t)\right]^2 \tag{4.15}$$

where ΔV is the CPD between tip and sample.

The above equation yields the following three components of the electric force, one at DC, that is,

$$F_{dc} = -\frac{1}{2}\frac{\partial C}{\partial z}\left[(V_{dc} - \Delta V)^2 + \frac{1}{2}V_{ac}^2\right] \tag{4.16}$$

the second one at ω_m

$$F_\omega = -\frac{\partial C}{\partial z}(V_{dc} - \Delta V)V_{ac}\sin(\omega_m t) \tag{4.17}$$

and the third one at $2\omega_m$

$$F_{2\omega} = \frac{1}{4}\frac{\partial C}{\partial z}V_{ac}^2\cos(2\omega_m t) \tag{4.18}$$

The above equations indicate that the applied AC bias at frequency ω_m is causing the electric force to be modulated at both ω_m and $2\omega_m$. In Eq. 4.17, we notice that when V_{dc} is adjusted to exactly the same as ΔV, F_ω drops to zero; due to the damping, the amplitude of cantilever at frequency ω_m also goes to zero. It is the core idea that "nulling" electric force to measure the local surface potential in AM-KPFM.

In AM-KPFM, the frequency of AC bias is usually, but not necessary, a selected cantilever resonance frequency ω_0, e.g., $\omega_m = \omega_0$, for enhanced sensitivity afforded by cantilever's quality factor Q. A potential feedback loop uses amplitude at ω_0 as input and adjusts the feedback signal V_{dc} until the amplitude at ω_0 drops to zero. At this point, V_{dc} equals to CPD between tip and sample; consequently, the 2D local potential mapping is obtained by moving the tip over the sample. In this case, AM-KPFM is done via a dual pass process. The first pass is usually a standard tapping mode or PeakForce tapping (PFT) mode, which measures surface topography. The second pass is KPFM measurement; cantilever is forced to oscillate by an AC bias at cantilever resonance frequency ω_0. AM-KPFM also can be done via a single pass procedure, which is called "dual-frequency mode." In dual-frequency mode, an AC bias at frequency ω_m is applied to the tip or sample to null the potential difference between sample and tip, and at the same time, the tapping drive signal at cantilever resonance frequency ω_0 is applied continuously as the tip scans the surface for topographic information. In this case, two different frequencies are involved during imaging process. Usually, the tapping drive frequency is much higher than the surface potential drive frequency, to avoid cross talk of two signals at different frequencies. Dual-frequency mode is more efficient than the dual pass procedure, which saves time and is particularly

suitable for large (>1 V) variations in potential, but the requirement of working far away from cantilever resonance frequency limits the sensitivity of the potential detection. For very small potential variations (<100 mV), the dual pass method is often preferred.

4.4 FM-KPFM

The same as AM-KPFM, in FM-KPFM, an AC bias with frequency ω_m and amplitude V_{ac}, superimposed on a DC bias V_{dc}, is applied between tip and sample [12, 13]. However, the core idea of FM-KPFM is "nulling" the electric force gradient to measure the local surface potential, instead of "nulling" electric force in AM-KPFM. An oscillating electric force gradient, according to Eq. 4.14, is generated between tip and sample, which can be given by

$$\frac{\partial F_e}{\partial z} = -\frac{1}{2}\frac{\partial^2 C}{\partial z^2}\left[V_{dc} - \Delta V + V_{ac}\sin(\omega_m t)\right]^2 \tag{4.19}$$

In the same way, the above equation yields the following three components of the electric force gradient: one at DC

$$\frac{\partial F_{dc}}{\partial z} = -\frac{1}{2}\frac{\partial^2 C}{\partial z^2}\left[(V_{dc} - \Delta V)^2 + \frac{1}{2}V_{ac}^2\right] \tag{4.20}$$

the second one at ω_m

$$\frac{\partial F_{\omega}}{\partial z} = -\frac{\partial^2 C}{\partial z^2}(V_{dc} - \Delta V)V_{ac}\sin(\omega_m t) \tag{4.21}$$

and the third one at $2\omega_m$

$$\frac{\partial F_{2\omega}}{\partial z} = \frac{1}{4}\frac{\partial^2 C}{\partial z^2}V_{ac}^2\cos(2\omega_m t). \tag{4.22}$$

We can find in Eq. 4.21 that when V_{dc} is adjusted to exactly the same as ΔV, $\frac{\partial F_{\omega}}{\partial z}$ drops to zero. However, the detection of electric force gradient is not straightforward like amplitude detection. Cantilever resonance frequency shift is usually used to measure electric force gradient.

The fundamental resonance frequency of cantilever ω_0 can be expressed as

$$\omega_0 = \sqrt{\frac{k}{m^*}} \tag{4.23}$$

where k is the spring constant of the cantilever and m^* is the effective mass of the cantilever.

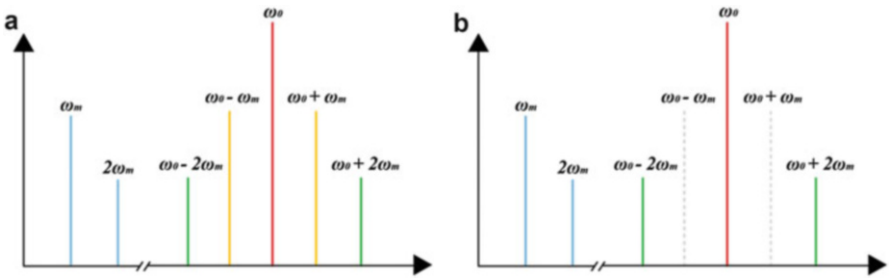


Fig. 4.3 Amplitude versus frequency plot when potential feedback is (**a**) off and (**b**) on in FM-KPFM. Applied modulation bias with frequency f_m on cantilever, which is vibrating at its resonance frequency f_0, modulates the force gradient at both f_m and $2f_m$, leading to side peaks at $f_0 \pm f_m$ and $f_0 \pm 2f_m$. When potential feedback working normally, side peaks at $\omega_0 \pm \omega_m$ will disappear

When a conductive cantilever is oscillating in an electric field, the effective spring constant of the cantilever is changed by electric force gradient; thus

$$k_{eff} = k - \frac{\partial F_e}{\partial z} \tag{4.24}$$

Therefore, for small force gradient (if $\frac{\partial F_e}{\partial z} \ll k$), the resonant frequency shift is

$$\Delta\omega \approx -\frac{\omega_0}{2k}\frac{\partial F_e}{\partial z} \tag{4.25}$$

An AC bias is applied onto a cantilever which is vibrating at its resonance frequency, driving by tapping piezo. The applied AC bias modulates the electric force gradient, which means it also modulates the cantilever resonance frequency. According to Eqs. 4.21 and 4.22, the electrical force gradient is modulated at both AC bias frequency ω_m and the second harmonic $2\omega_m$, so if one mechanically drive the cantilever oscillation at the resonance frequency ω_0, ω_0 is also modulated at both AC bias frequency ω_m and the second harmonic $2\omega_m$, and it will generate four side peaks at $\omega_0 \pm \omega_m$ and $\omega_0 \pm 2\omega_m$. Figure 4.3a shows the side peaks in FM-KPFM when potential feedback is off and Fig. 4.3b indicates side peaks at $\omega_0 \pm \omega_m$ disappear when potential feedback is on. The amplitude of the side peaks indicates the resonance frequency modulation amplitude. In Eq. 4.21, we notice that when V_{dc} is adjusted to exactly the same as ΔV, the electrical force gradient at ω_m, $\frac{\partial F_\omega}{\partial z}$, drops to zero. It will result in the amplitude of side peak at $\omega_0 \pm \omega_m$ also going to zero. Using amplitude or phase of side peak at frequency $\omega_0 \pm \omega_m$ as KPFM feedback and adjusting V_{dc} until the side peak disappear is the core idea of "nulling" electric force gradient to measure the local surface potential in FM-KPFM.

Similar with the AM-KPFM, the FM-KPFM also can be done via both single pass and dual pass procedure.

4.5 KPFM Without Potential Feedback

In typical instrument settings, the KPFM measurement covers the potential range up to $\pm$ 10V, which is adequate for work function difference measurement. However, for the study of trapped charges on an insulating surface, it is totally a different story. Electrostatic charge may lead to very high voltage; if we still use "nulling" method to measure the voltage difference between tip and sample by Kelvin probe method, a high voltage source must be required. It needs to modify current instruments and is dangerous for operation. An alternative way to realize high voltage measurement in current KPFM instruments is calculation method. In this way, the KPFM potential feedback is turned off, and no additional high voltage source is involved.

The first way for calculating high voltage difference between tip and sample is called "KPFM-HV" mode. According to Eq. 4.17, when KPFM potential feedback is off, e.g., V_{dc} does not change with surface potential change, the electrical force at AC bias frequency ω_m can be expressed as follows:

$$F_\omega = \frac{\partial C}{\partial z}(\Delta V)V_{ac}\sin(\omega_m t) \tag{4.26}$$

The cantilever will be forced oscillated by the driving force F_ω at the modulation frequency ω_m, and the equation for cantilever motion can be written as

$$m^*\frac{d^2x}{dt^2} = -kx - \gamma m\frac{dx}{dt} + F_\omega \tag{4.27}$$

where x is the position of end of cantilever and γ is the damped coefficient. The solution of Eq. 4.27 is

$$A = \frac{F_0}{m^*\sqrt{\left(\omega_0^2 - \omega^2\right)^2 - \left(\gamma^2\omega^2\right)}} \tag{4.28}$$

where A is the amplitude of the cantilever and $F_\omega = F_0\sin(\omega_m t)$. The above result indicates the amplitude of cantilever is proportional to the driving force. So if we note the amplitude at AC bias frequency ω_m as A_ω, we can get

$$A_\omega \propto \frac{\partial C}{\partial z}(\Delta V)V_{ac} \tag{4.29}$$

The similar process can be used for Eq. 4.18; if we note the amplitude at AC bias second harmonic frequency $2\omega_m$ as $A_{2\omega}$, we can get

$$A_{2\omega} \propto \frac{1}{4}\frac{\partial C}{\partial z}V_{ac}^2 \tag{4.30}$$

If we vibrate the AC bias at a frequency very far away from the cantilever resonance frequency, e.g., both ω_m and $2\omega_m$ are far away from ω_0, the $A_{2\omega}$ can be considered that it has the same pre-factor as A_ω. So, ΔV can be written as

$$\Delta V = \frac{1}{4} V_{ac} \frac{A_\omega}{A_{2\omega}} \tag{4.31}$$

Using lock-in amplifiers, SPM can measure both A_ω and $A_{2\omega}$; consequently, we can get the potential difference ΔV.

In this method, we can also get $\frac{\partial C}{\partial z}$, which reflects the dielectric constant variations across the sample.

$$\frac{\partial C}{\partial z} = \frac{4A_{2\omega}}{V_{ac}^2} \tag{4.32}$$

The second way for calculating high voltage difference between tip and sample is extrapolation method. This method only uses the linear relationship between cantilever amplitude A_ω at AC bias frequency ω_m and potential difference between tip and sample $V_{dc} - \Delta V$, according to Eq. 4.17. If we change $V_{dc} - \Delta V$ by applying DC bias on sample or tip, the amplitude A_ω will also change with it linearly. If we plot A_ω versus V_{dc}, A_ω will drop to zero when $\Delta V = V_{dc}$, and at this point, the applied bias V_{dc} nulls the original potential difference between tip and sample. In this case, the idea is exactly the same as AM-KPFM, and we will get a fold line in A_ω versus V_{dc} relationship. However, in the voltage operating range -10 V to +10 V, this will not always happen. If the potential difference between tip and sample is larger than $\pm$ 10V and the potential difference between tip and sample cannot be nulled, we will get a straight line in A_ω versus V_{dc} relationship. If we extrapolate the line intersect at $A_\omega = 0$, the value of V_{dc} at the crossover point equals to ΔV.

5 KPFM Measurement

5.1 Lock-In Settings for KPFM Measurement

In current SPM equipment, lock-in amplifiers are very important for KPFM measurement. Lock-in amplifier is a phase-sensitive detector, which can extract a signal with known frequency from an extremely noisy background. It can be understood as a mixer followed by an integrator. The two signals with frequencies f_{ref} and f_{sig} get multiplied in the mixer. If $f_{\text{ref}} = f_{\text{sig}}$, the output of the mixer is a DC voltage with a magnitude proportional to the amplitudes of f_{ref} and f_{sig}; if $f_{\text{ref}} \neq f_{\text{sig}}$, the output signals of the mixer are with two frequencies $f_{\text{ref}} - f_{\text{sig}}$ and $f_{\text{ref}} + f_{\text{sig}}$. An integration with a long time constant suppresses the new frequencies and the output is zero. In other words, lock-in amplifier can pick up amplitude and phase signal at certain frequency f_{ref} . Figure 4.4 is the schematic diagram of the lock-in amplifier.

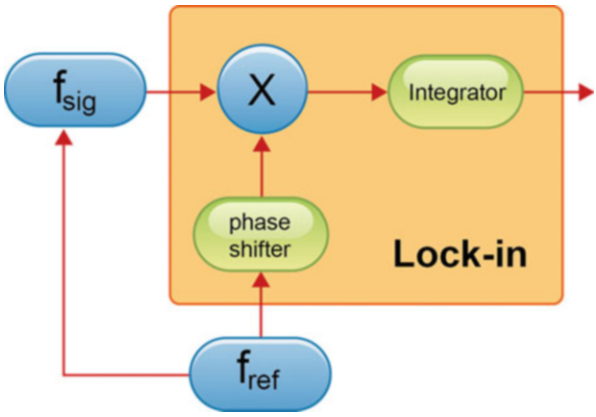


Fig. 4.4 Schematic diagram of a lock-in amplifier

In AM-KPFM, a single lock-in is used to read the amplitude and phase at AC bias frequency ω_m for KPFM measurement. The reference frequency f_{ref} of lock-in is set to AC bias frequency ω_m; consequently, the cantilever oscillation at frequency ω_m can be detected by the lock-in. Signals at other frequencies, such as deflection at DC, which is indicated by Eq. 4.16, and cantilever oscillation at second harmonic 2 ω_m, which is indicated by Eq. 4.18, are averaged to zero. A potential feedback loop uses cantilever amplitude at ω_m as lock-in input and adjusts the feedback signal V_{dc} until the amplitude at ω_m drops to zero. Figure 4.5 illustrates the AM-KPFM method. However, cantilever amplitude at ω_m is not enough for lock-in to adjust the feedback signal V_{dc}. According to Eq. 4.15, the relationship between electrical force F_e and total potential difference V ($V = V_{dc} - \Delta V + V_{ac} \sin(\omega_m t)$) is not a monotonic function. It means F_e may have the same value when the potential difference V between tip and sample is negative or positive. On the negative side, when V increases, the electrical force F_e will decrease, e.g., F_e is out of phase with V_{ac}; on the positive side, when V increases, the electrical force F_e will also increase, e.g., F_e is in phase with V_{ac}. So, the cantilever oscillation will have a different phase, relative to the reference signal V_{ac}, depending on whether the tip voltage is larger or smaller than the sample voltage. Both the cantilever amplitude and phase are needed for the feedback loop to correctly adjust V_{dc}. In fact, the input signal to the potential feedback loop is the cantilever amplitude multiplied by the sine of its phase. It means we have to adjust lock-in phase to get correct feedback direction. In the full range of lock-in phase $\pm 180\,^\circ$, there is a half range which can lead to correct feedback direction and a half range which can result in wrong feedback direction.

In FM-KPFM, the situation is a little complex. It usually uses two cascaded lock-in amplifiers for KPFM measurement, which is shown in Fig. 4.6.

To understand the lock-in setup, we should understand the signal that comes into lock-ins first. According to Eqs. 4.21 and 4.25, the electrical force gradient change at AC bias frequency ω_m will lead to frequency shift $\Delta\omega$

$$\Delta\omega \approx -\frac{\omega_0}{2k}\frac{\partial F_\omega}{\partial z} = \frac{\omega_0}{2k}\frac{\partial^2 C}{\partial z^2}(V_{dc} - \Delta V)V_{ac}\sin(\omega_m t) \tag{4.33}$$

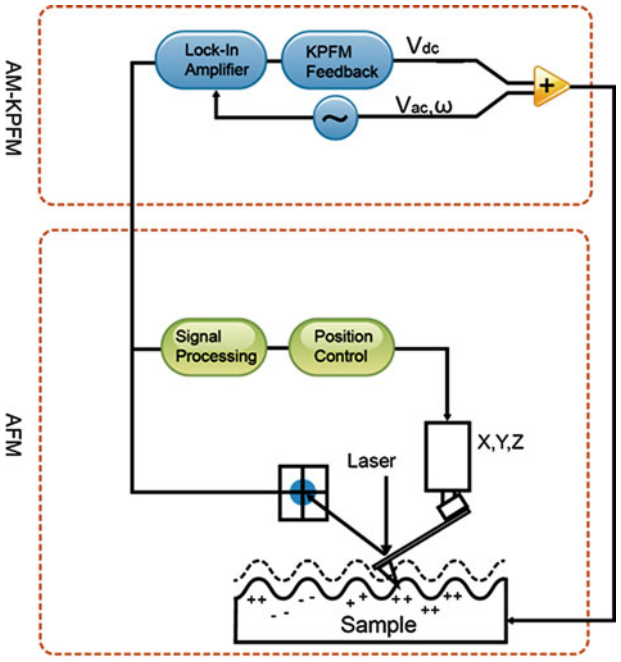


Fig. 4.5 Schematic diagram of AM-KPFM

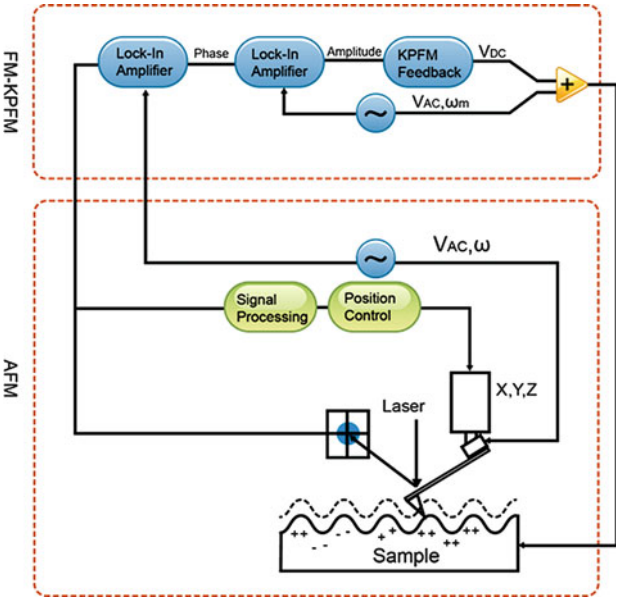


Fig. 4.6 Schematic diagram of FM-KPFM

To simplify the analysis, we note the frequency-modulated amplitude as δf

$$\delta f = \frac{\omega_0}{2k}\frac{\partial^2 C}{\partial z^2}(V_{dc} - \Delta V)V_{ac} \tag{4.34}$$

In FM-KPFM, the cantilever is oscillated at its resonance frequency ω_0; if AC bias modulates the frequency at ω_m, the cantilever motion can be written as

$$x(t) = A\sin\left\{\int_0^t [\omega_0 + \delta f \sin(\omega_m \tau)]d\tau\right\} = A\sin\left[\omega_0 t - \frac{\delta f}{\omega_m}\cos(\omega_m t)\right] \tag{4.35}$$

where A is the amplitude of cantilever. $\delta f \ll \omega_m$ if the above equation can be recast as the following form:

$$x(t) = A\sin(\omega_0 t) - A\frac{\delta f}{\omega_m}\sin(\omega_m t)\cos(\omega_0 t) \tag{4.36}$$

After further transformation, we can get

$$x(t) = A\sin(\omega_0 t) + \frac{A}{2}\frac{\delta f}{\omega_m}\sin[(\omega_0 - \omega_m)t] - \frac{A}{2}\frac{\delta f}{\omega_m}\sin[(\omega_0 + \omega_m)t] \tag{4.37}$$

The above equation indicates that under frequency modulation conditions, cantilever will oscillate at three different frequencies (if $\delta f \ll \omega_m$), e.g., cantilever resonance frequency ω_0 and modulated frequencies $\omega_0 \pm \omega_m$. Using Eq. 4.37, we can easily understand the two side peaks with frequencies at $\omega_0 \pm \omega_m$. Here we only deal with force gradient at ω_m. In real situation, higher-order side peaks $\omega_0 \pm n\omega_m$ will appear.

The cantilever motion signal $x(t)$ goes into the first lock-in amplifier, which reference frequency f_{ref} equals to the cantilever resonance frequency ω_0. Because the amplitude of the side peaks is hard to be detected directly, the phase output at cantilever resonance frequency will be fed into the second lock-in amplifier for further demodulation. From Eq. 4.36, we know the phase signal can be expressed as

$$\varnothing = \arctan\left(-\frac{\delta f}{\omega_m}\sin(\omega_m t)\right) \tag{4.38}$$

For small angle approximation (if $\delta f \ll \omega_m$),

$$\varnothing = -\frac{\delta f}{\omega_m}\sin(\omega_m t) \tag{4.39}$$

The reference frequency of the second lock-in amplifier is set to AC bias modulation frequency ω_m; thus the amplitude output of the second lock-in amplifier

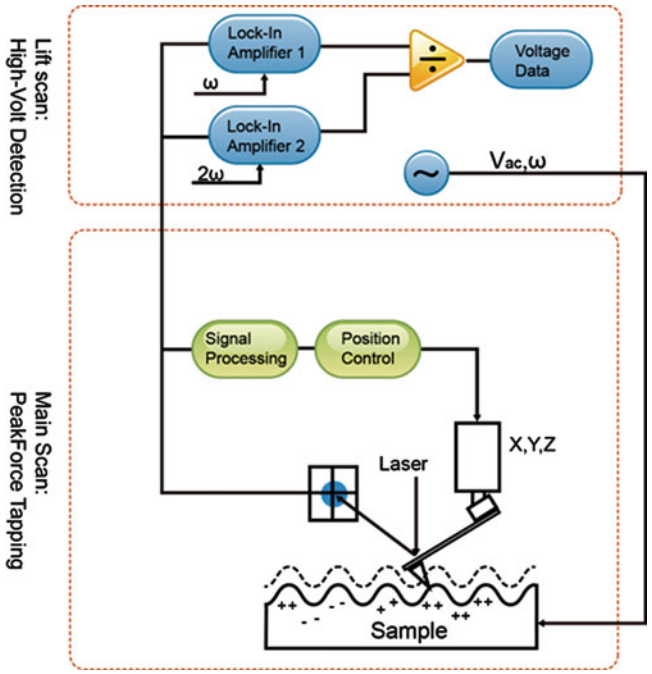


Fig. 4.7 Schematic diagram of KPFM-HV mode

is proportional to $\frac{\delta f}{\omega_m}$, which is also proportional to the amplitude sum of side peaks at $\omega_0 \pm \omega_m$. This signal is then used for KPFM feedback. System adjusts V_{dc} until $\frac{\delta f}{\omega_m}$ drops to zero; at this point, the V_{dc} equals to the potential difference of tip and sample.

In KPFM-HV mode, the potential feedback is turned off, and we use the amplitude of cantilever at AC bias frequency ω_m and the second harmonic $2\omega_m$ to calculate the potential difference. The cantilever motion signal is sent to two separate lock-in amplifiers simultaneously. Reference frequency of one lock-in amplifier is set to AC bias frequency ω_m to detect cantilever amplitude and phase at drive frequency, and reference frequency of the other lock-in amplifier is set to $2\omega_m$ to detect cantilever amplitude and phase at second harmonic. Calculation is done in background to get the potential difference ΔV and $\frac{\partial C}{\partial z}$. The lock-in setting of KPFM-HV mode is shown in Fig. 4.7.

5.2 KPFM Resolution

Let us consider a metal sphere with radius R above an infinite metal plate, the separation is Z. This model is shown in Fig. 4.8. The metal sphere serves as KPFM probe and the infinite metal plate serves as KPFM sample.

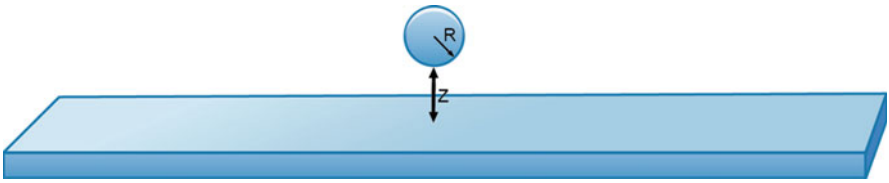


Fig. 4.8 A simple model to study KPFM spatial resolution

If the potential difference between the sphere and the part of plate just below is ΔV, the electrical force between the two objects can be written as

$$\mathrm{F(z)} = -\pi\epsilon_0\left[\frac{R^2}{z(z+R)}\right]\Delta V^2 \tag{4.40}$$

And the electrical force gradient is

$$\frac{\partial F}{\partial z} = -\pi\epsilon_0\left(\frac{1}{z}+\frac{1}{z+R}\right)\left[\frac{R^2}{z(z+R)}\right]\Delta V^2 \tag{4.41}$$

For AM-KPFM, the spatial resolution depends on the relationship between F(z) and z, and for FM-KPFM, the spatial resolution depends on the relationship between $\frac{\partial F}{\partial z}$ and z. Obviously, the electric force gradient has a steeper dependence on Z than the electric force. It also has a steeper dependence on X and Y. It is the reason why FM-KPFM has better resolution than AM-KPFM.

Some experiments were done to study KPFM spatial resolution [13]. The result shows FM-KPFM has higher resolution than AM-KPFM, because larger than half of the FM-KPFM signal is contributed by the foremost 0.3 % of the tip cone; but for AM-KPFM, the contribution from the tip cone never reaches 50 %. It indicates the lateral resolution of FM-KPFM can achieve about 50 nm but AM-KPFM often several micrometers.

So in KPFM, the measured potential in KPFM is actually an average of the sample potential, especially in AM-KPFM. The convolution always happens. The measurements of the potential will be distorted due to the nonuniform capacitive coupling between the tip and various parts of the surface. The measured potential by KPFM is not the real local potential, but a weighted potential. The substrate can be modeled as n electrodes of constant potential V_i, and the relationship between measured potential and real local potential can be expressed as [14]

$$V_{dc} = \frac{\sum_{i=1}^{n}\left(\frac{\partial C_{it}}{\partial z}V_i\right)}{\sum_{i=1}^{n}\left(\frac{\partial C_{it}}{\partial z}\right)} \tag{4.42}$$

where V_{dc} is the measured potential, V_i is the local surface potential at point i on the substrate, and $\frac{\partial C_{it}}{\partial z}$ is the change rate of the capacitance with respect to the distance

between the tip and point i on the substrate. The weighting factors are the derivatives in z of tip–surface capacitances, which can be defined as follows:

$$h_i = \frac{\frac{\partial C_{it}}{\partial z}}{\sum_{i=1}^{n}\left(\frac{\partial C_{it}}{\partial z}\right)} \tag{4.43}$$

Although the potential is averaged, the total charge still can be calculated by the potential image.

5.3 KPFM Sensitivity

Usually the FM-KPFM has less sensitivity in air than AM-KPFM, and this is a major reason why FM-KPFM is usually performed in vacuum. However, the sensitivity of FM-KPFM can be improved if we know the factors which affect its sensitivity. According to Eq. 4.25, the frequency shift induced by force gradient is proportional to the cantilever resonance frequency ω_0 and inversely proportional to the cantilever spring constant k. Consider the cantilever as a simple harmonic oscillator; near its resonance frequency, if frequency changes $\frac{\omega_0}{Q}$, the phase will change $\frac{\pi}{2}$. Consequently, if frequency shifts $\Delta\omega$, the phase shift can be written as

$$\Delta\varphi = \frac{\frac{\pi}{2}\Delta\omega}{\frac{\omega_0}{Q}} = -\frac{\pi}{4}\frac{Q}{k}\frac{\partial F_e}{\partial z} \tag{4.44}$$

So the FM-KPFM sensitivity is proportional to $\frac{Q}{k}$. This result also applies to AM-KPFM. However, it is of particular significance to FM-KPFM, which has lower signal as only the front part of the tip contributes. For AM-KPFM in air, the KPFM signal comes from not only the tip but also cantilever. The signal is usually large enough to get sufficient sensitivity.

From another viewpoint, the force gradient can be considered as an additional spring constant. If cantilever nature spring constant k is small, the same force gradient will lead to relative large change of it, so smaller spring constant indicates higher sensitivity. Furthermore, if the quality factor Q is large, the phase versus frequency plots steeper, and around the cantilever resonance frequency, phase change directly reflects frequency shift (almost linear), so large quality factor also indicates higher sensitivity.

For FM-KPFM, to improve its sensitive, we can increase Q or decrease k. Putting the system into a vacuum environment can dramatically increase Q factor; thus sufficient sensitivity can be achieved. Using probes with large Q and small k also can improve FM-KPFM sensitivity, but for tapping mode, Q cannot be very large and k cannot be very small; for PeakForce tapping,

this limitation is gone, so PeakForce KPFM can work very well in air with high sensitivity.

5.4 KPFM Repeatability

There are several factors that can affect KPFM repeatability. The major reason is the work function of the probe. If the work function of the probe is different from each other, the experiment results are different. Probe made by single materials with unique work function is vital for KPFM repeatability.

Another factor which can affect the KPFM repeatability is the separation between tip and sample. This separation includes the lift height and cantilever amplitude.

Besides above, sometimes there is current flow between tip and sample, which can lead to electrochemical reactions. This factor also makes surface potential change.

Sample or probe surface oxidation, adsorption of molecules, and so on will also result in bad KPFM repeatability.

6 Applications of KPFM in Nanoscale Characterization

Based on the above discussion, KPFM plays an important role in material electrical property mapping. In this section, we will discuss the applications of KPFM in characterization of inorganic nanostructure and nanomaterials. We will mainly focus on five KPFM applications including surface charge detection, work function and doping level study, charge transfer study, FETs, and atomic resolution KPFM.

6.1 Surface Charge

By measuring the surface potential of the sample with KPFM, the electric quantity can be obtained. A quantitative method was developed to count the electric quantity formed when an AFM tip rubs against a SiO_2/Si substrate [9]. The measured potential by KPFM is not the real local potential, but a weighted potential. By using Eqs. 4.43 and 4.44 mentioned above, the real surface potential can be obtained by summing up the measured potential V_{DC} at each point. The capacitance is calculated to be 8.96×10^{-18} F. The electric quantity formed in contact and friction process can be estimated by converting the surface potential from the system capacitance.

Then, the nanotriboelectrification between the tip and the substrate can be investigated quantitatively [9]. As shown in Fig. 4.9b–e, the loaded force between the tip and substrate caused the charge sign reversal, i.e., when applying large loaded force, positive charge formed in the friction or contact areas, and when

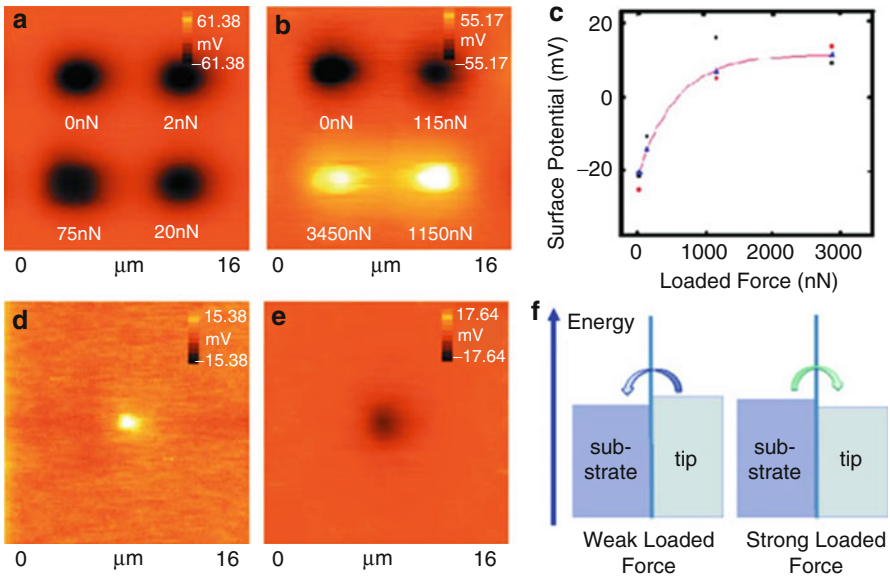


Fig. 4.9 (**a**) and (**b**) The potential images obtained by using different tips on SiO_x substrates. The corresponding loaded forces are shown under each charge pattern. (**c**) The loaded force dependence of surface potential when scanning over the SiO_x surface. (**d**) and (**e**) The potential images of contact experiments obtained by applying different loaded forces. (**d**) 3,450 nN and (**e**) 115 nN. (**f**) The scheme of charge sign reversal model. The *arrow* shows the direction of the electron flow (Reprinted with permission from [9]. Copyright (2010), AIP Publishing LLC)

applying small loaded force, negative charge formed in the friction or contact areas. This charge reversal was attributed to the pressure-induced surface state change.

Nanotriboelectrification can be used to realize high-speed dip-pen nanolithography (DPN) [15]. As stated above, KPFM measurements show the region on the substrate where the AFM tip rubbed was charged. Then, the electrostatic interaction resulting from the charge can be employed to fabricate nanopatterns. The nanoparticles loaded on the tip were transported onto the substrate as the AFM tip moved at a speed as high as hundreds of μm/s. The so-called nanoxerography [16–19] has emerged as a versatile method for assembling nanoparticles from solution onto solid templates. It uses the strong electric fields generated by charge patterns written onto substrate to trap charged or polarizable nanomaterials via electrostatic interactions.

KPFM has also been used to investigate charging and discharging of graphene sheets [20, 21]. Charge can transfer between reduced graphene oxide (rGO) sheets separated in hundreds of nanometers on insulating substrates [20]. Figure 4.10a shows a selected rGO sheet on SiO_2 surface which was cut into four pieces (labeled with 4, 5, 6, and 7, respectively) by an AFM tip. The separation distances between the rGO-4 and rGO-5, rGO-6, and rGO-7 are 150, 150, and 300 nm, respectively, while the corresponding gap lengths are 2,000 nm, 650 nm, and 2,000 nm, respectively. After rGO-4 is charged by an AFM tip bias, KPFM image (Fig. 4.10b)

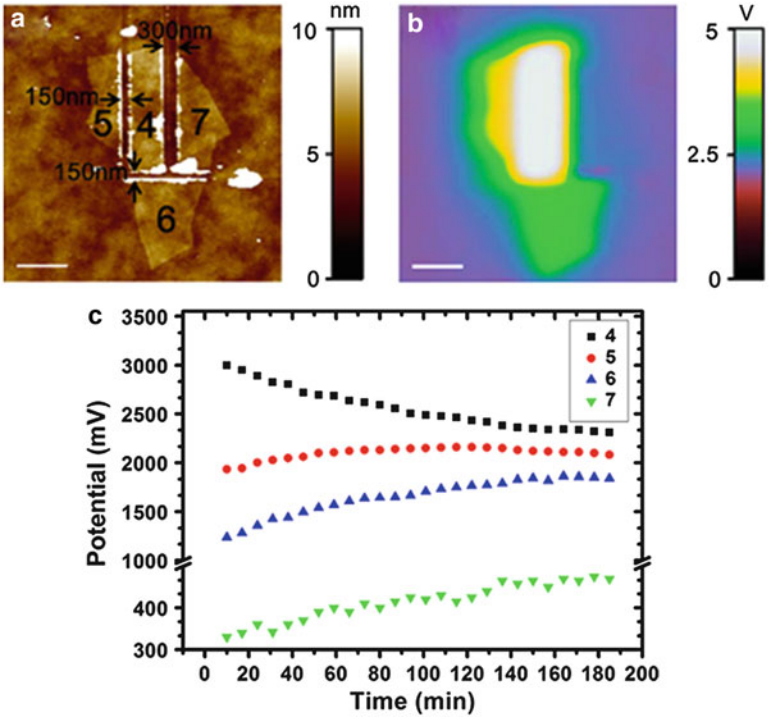


Fig. 4.10 (**a**) Topological image of an rGO sheet that was cut into four separated pieces on SiO_2. The four rGO sheets were indicated with number 4–7, respectively. (**b**) KPFM image taken after the rGO-4 was charged with an AFM tip biased at 12 V for 5 min. (**c**) The time evolution of the surface potentials of the rGO sheets shown in (**a**) and (**b**) (Reprinted with permission from [20]. Copyright (2013), AIP Publishing LLC)

revealed that rGO sheets 4–7 had surface potentials of 3.04, 1.93, 1.24, and 0.33 V, respectively. Obviously, the charges transferring from the rGO-4 to rGO-6 were less than to the rGO-5 due to the smaller gap length, while charges transferring from the rGO-4 to rGO-7 were less than to the rGO-5 due to larger separation. The surface potential of rGO-4 decreased from 3,000 mV to 2,300 mV in 180 min, implying that the charges transferred to its surroundings, so the surface potentials of rGO-5, rGO-6, and rGO-7 increased. This automatic discharging and charging is very slow in a time scale of hours (Fig. 4.10c). When the surface potentials reached equilibrium after about 3 h, there were still distinct differences between their values, reflecting approximately the threshold potential that limited further charge transfer. Apparently, threshold potential increases along with the increase of the separation distance and decrease of the gap length between the rGO sheets.

Humidity in ambient conditions can affect the discharging process [21]. The time evolution of KPFM images of a few-layered graphene (FLG) film indicates the main discharge process is through water molecules adsorbed on the FLG film itself and the water film on the SiO_2 substrate [22]. In fact, water adsorption layers play a

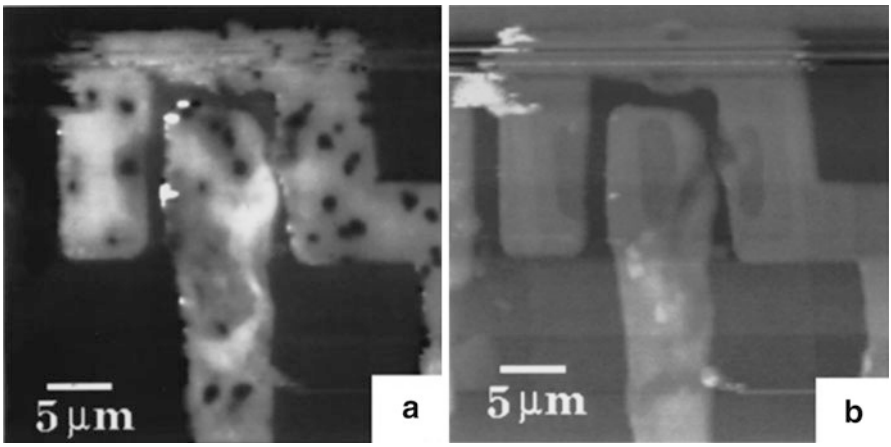


Fig. 4.11 (**a**) KPFM image of Al/Cu film showing contrast between Al and the Al/Cu intermetallic (Al_2Cu). (**b**) AFM topography image of the Al/Cu film in (**a**), recorded simultaneously with the KPFM image (Reprinted with permission from [6]. Copyright (1999), AIP Publishing LLC)

very important role in KPFM measurements [23]. It was found that the thickness of water adsorption layer on the metal surfaces of chromium, copper, and gold increases with the rise of humidity. The surface potential measured by KPFM decreases with the increasing humidity due to water adsorption on the metal. And the reduction of surface potential with the rise of relative humidity is different for these three samples, resulting from the different thickness of adsorbed water layer on their surfaces, which is determined by the different surface properties, such as the roughness and contact angle.

6.2 Work Function and Doping Level

6.2.1 Metallic Nanostructures

KPFM was first developed to investigate contact potential difference (CPD) between metallic materials including gold, platinum, and palladium surfaces [5]. The CPD between two materials depends on a variety of parameters such as the work function, adsorption layers, oxide layers, dopant concentration in semiconductors, or temperature changes on the sample [5, 24].

KPFM is capable of distinguishing different intermetallics in a metal alloy due to the different work functions [6]. As shown in Fig. 4.11b, the topographic image shows the regular topography of the lines with no other contrast. However, the corresponding CPD image (Fig. 4.11a) shows strong contrast that dark patches are observed within the bright background. These are regions which contain intermetallic compound Al_2Cu, which are known to decorate the grain boundaries. The contact potential difference in these regions was 150 mV lower than that of the surrounding Al regions. The spatial resolution reached in these experiments is around 50 nm and the sensitivity to the CPD measurement was

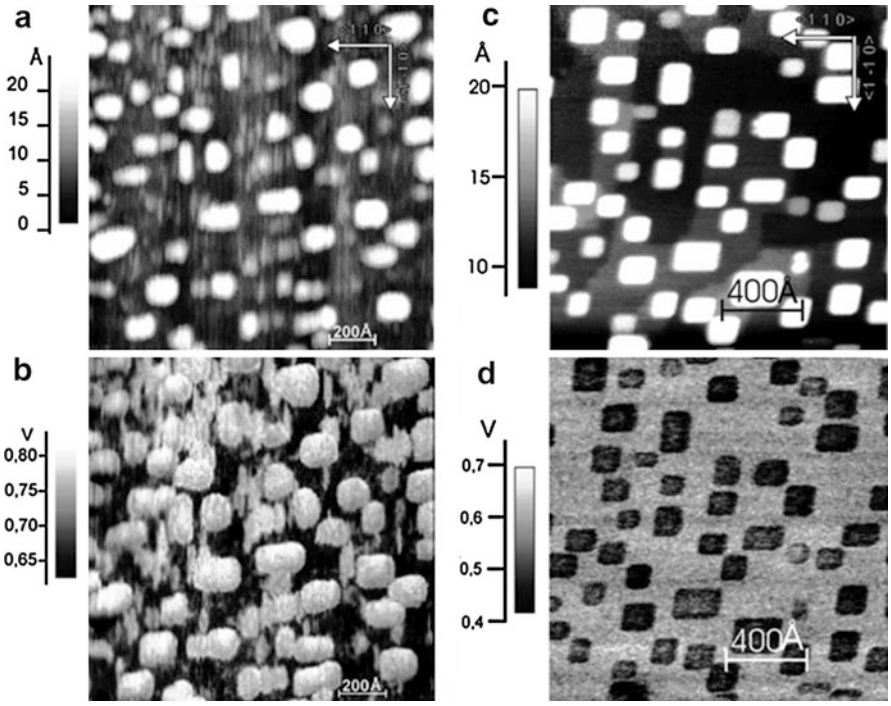


Fig. 4.12 Topography and CPD images of Au nanostructures on InSb (001) surface before and after annealing. Topographical image (**a**) and corresponding CPD image (**b**) of Au/InSb (001) system. Topographical image (**c**) and corresponding CPD image (**d**) of Au/InSb (001) system after annealing at 650 K for 2 h (Reprinted with permission from [25]. Copyright (2005), AIP Publishing LLC)

approximately 0.12 mV. It is obvious that KPFM is capable of detecting sample work function especially on the nanometer scale [6].

Au nanostructures deposited on InSb (001) surface were carefully studied [25, 26]. Au nanostructures were predominantly to form rectangular islands, and the typical height of the islands corresponds to a few monolayers (MLs) of gold. And it was found that the work function was independent on the size of the Au nanostructure. Figure 4.12a and b shows the topography and corresponding CPD mapping of Au nanostructures [25]. The CPD mapping provides more details than surface topography. As shown in Fig. 4.12b, both the islands and the features between the islands have the same higher work function than the one corresponding to the substrate material. Accordingly, it is known that the work function of pure gold is higher than the one for clean InSb. However, the contrast between the Au nanostructures and InSb substrate is reversed after high temperature annealing (Fig. 4.12d), indicating that the nanostructures assembled after the annealing process have the lower work function than the substrate. This is most likely due to indium alloying with gold to form the nanostructures, which results in the Sb-rich substrate between the islands.

6.2.2 Semiconducting Nanostructures

KPFM has been used to study the quantum effect of nanostructures locally. By comparing the topographic and CPD images of InAs quantum dots (QDs) with the size varying from 1.3 to 7.2 nm, it was found that CPD decreases with increasing height. This dependence is governed by quantum size effects, i. e., the amount of charges accumulated in the QD are determined by the confinement energy levels [7].

Topographic and CPD images of ~40 nm InSb nanodots grown on GaAs substrates were measured [27]. Though an obvious correlation between the two images is observed, the dark rings around the dots observed in the CPD image and the CPD peak heights do not match the work function difference between InSb and GaAs, indicating the composition changes. An additional CPD peak on each side outside the dot area is also measured by the KPFM, which is consistent with the estimated CPD signal variations by taking into account the strain and the composition changes within and around individual nanodots.

KPFM is a powerful technique in characterizing two-dimensional (2D) materials such as MoS_2 [28, 29]. For MoS_2 nanoflakes annealed at 350 °C in Ar atmosphere, their Fermi levels can be measured with KPFM as shown in Fig. 4.13 [30]. The Fermi-level shift exhibits exponential decay with the thickness of flakes, indicating the interlayer screening effect exists. The CPD between three layers and two layers was ~170 mV, but the CPD does not change much when the thickness varied from 2.5 nm (about three layers) to 8.7 nm (about ten layers), suggesting that the screening length of MoS_2 flakes is about three or four layers. The screening effect is also observed in graphene [8, 31] and graphene oxide [32].

6.2.3 Carbon Nanostructures

Work function of carbon nanotubes (CNTs) was normally measured by ultraviolet photoelectron spectroscopy (UPS) and found to be ~4.8 eV [33–35]. In fact, KPFM is also capable to detect work function of CNTs [36]. Different treatment or modification (treated with nitric acid, UV, and X-ray, or decorated with metal nanoparticles) will obviously change the CPD of metallic single-walled carbon nanotube (SWCNT) networks, indicating the change of work function. However, comparing the UPS and KPFM measurements both before and after UV exposure reveals that the work functions from UPS measurements are generally lower than those measured by KPFM. The reason is that KPFM measures the local work function difference over a relative small scan area, whereas UPS measures the lowest work function patch on the surface.

It is known that SWCNT field effect transistors (FETs) show p-type characteristics in air [37, 38] and n-type characteristics in ultra-high vacuum (UHV) or inert gases [39, 40]. KPFM and electrostatic force microscopy (EFM) were used to study the mechanism [41]. As shown in Fig. 4.14b and c, the CPDs between the Au substrate and the adsorbed SWCNTs are about −0.06 V for Au (111) in air, whereas they are 0.05 V for Au (111) in UHV. The CPD measurements indicate that the energy-level alignment at SWCNT/Au interfaces is strongly sensitive to the presence of oxygen, suggesting that the vacuum level of the SWCNT is lower than that

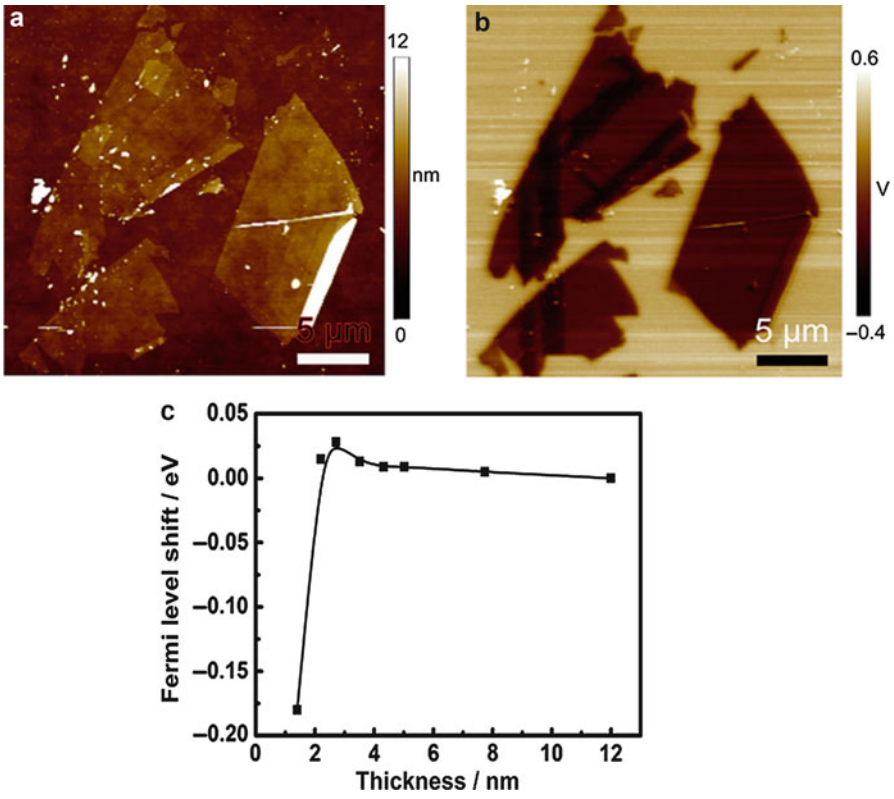


Fig. 4.13 (**a**) Topography of annealed MoS_2 nanoflakes and (**b**) corresponding KPFM image of MoS_2 nanoflakes. (**c**) Fermi-level shift of annealed MoS_2 nanoflakes as a function of thickness (Reprinted with permission from [30]. Copyright (2013), AIP Publishing LLC)

of Au in air but is higher in UHV. EFM measurements show that the interface dipole at the SWCNT/Au interface points from SWCNT (+) to Au (−) in air but reverses its direction in UHV or in a clean N_2 atmosphere. From the EFM measurements, it can be deduced that the SWCNTs on Au are negatively charged with a line density of about 0.1–0.05 e/nm in oxygen-free environments but positively charged with approximately 1 e/nm in air. Therefore, the Au Fermi level lies above the SWCNT mid-gap in vacuum or in inert gases and below the mid-gap in air.

The work function of graphene can also be studied by KPFM. For epitaxial graphene grown on 6*H*-SiC (0001), KPFM was used to distinguish graphene layers from substrate [42]. As shown in Fig. 4.15a, carbon-rich interface layer (IFL) of SiC substrate, single-layer graphene (1LG), and bilayer graphene (2LG) regions were measured. These regions are hardly visible in the topography image due to coincidence with a compensating step of the SiC substrate; however, the work function difference between 1LG and 2LG is 135 ± 9 meV. Bilayer films are found to have the higher work function than single-layer films due to the doping-induced shift of Fermi level. This method allows an unambiguous distinction between IFL, 1LG,

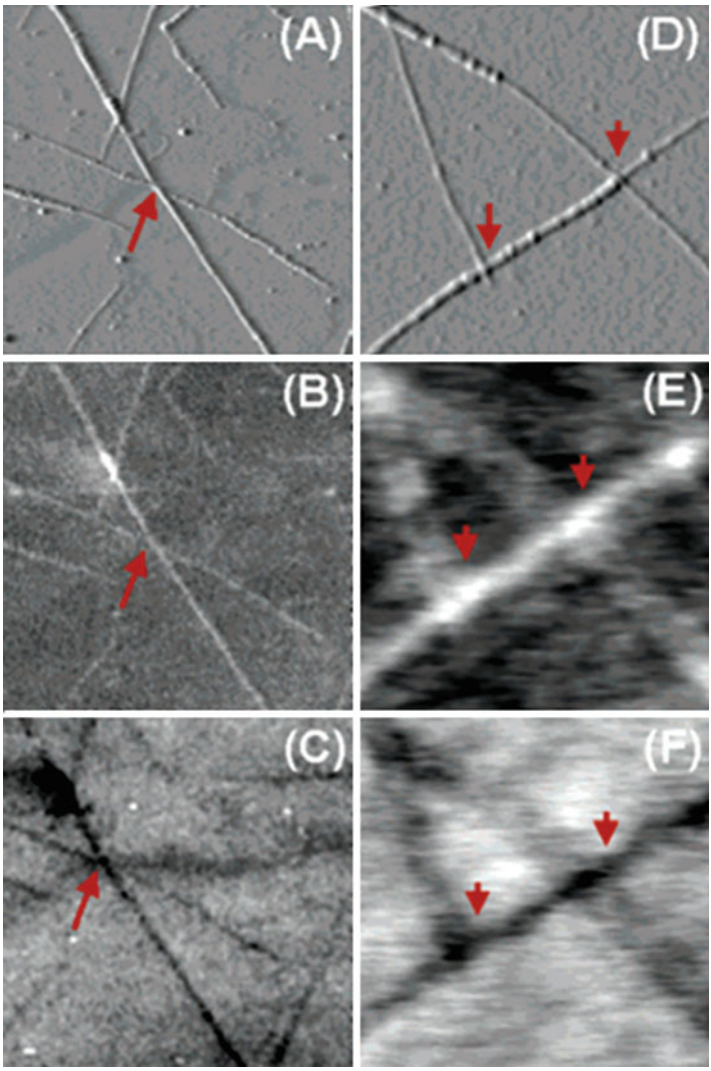


Fig. 4.14 AFM, KPFM, and EFM images of SWCNTs on Au (111) substrates in controlled environments. (**a**, **d**) Topographic images of nanotubes deposited on flame-annealed Au surfaces. (**b**, **c**) KPFM images obtained in air and after a long period in UHV, respectively. (**e**, **f**) EFM images taken in air and in an ambient N_2 environment, respectively (Reprinted with permission from [41]. Copyright (2003) American Chemical Society)

and 2LG. In combination with high-resolution topographic imaging (Fig. 4.15d, e), the complex step structure of epitaxial graphene can be resolved with respect to substrate and graphene layer steps.

Graphene samples can be p-doped when depositing on SiO_2 substrates [43]. KPFM is able to evaluate the doping level [8]. As shown in Fig. 4.16d, the

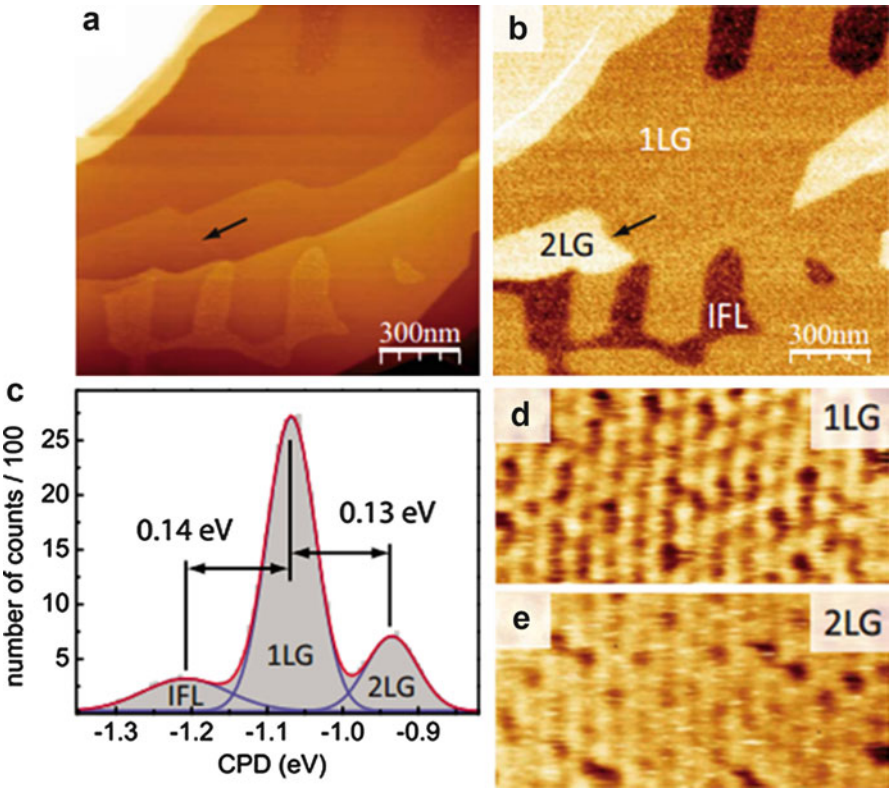


Fig. 4.15 (**a**) Topography image of a graphene film epitaxially grown on SiC (0001). (**b**) CPD map identifying the IFL, 1 LG, and 2 LG. The *arrows* in (**a**) and (**b**) indicate the position of a boundary between single and bilayer regions of graphene. (**c**) Histogram of the CPD map. (**d**) and (**e**) High-resolution topography images of single and bilayer films, respectively (Reprinted with permission from [42]. Copyright (2008), AIP Publishing LLC)

surface potential difference between the 1LG and 2LG region is ~68 meV. The KPFM measurements revealed significant work function variations as a function of the number of graphene layers, in quantitative agreement with ab initio density functional theory (DFT)-calculated work functions for substrate-induced p-doped multilayer graphene (Fig. 4.16g). Work function variation between 1LG and 2LG is mainly due to the shift of the Fermi energy, while for more than two layers, the interlayer screening effects begin to stand out [31]. Raman G band frequency is a function of doping level n [44, 45]. Combining with the Raman data shown in Fig. 4.16g, 1LG has the hole doping level of $n \approx -(2.5 \pm 1) \times 10^{12}\ \mathrm{cm}^{-2}$ and 2LG $n \approx -(7.5 \pm 1.5) \times 10^{12}\ \mathrm{cm}^{-2}$.

As described above, doping level of graphene can be deduced from the work function of graphene, indicating KPFM might be a valid method to evaluate the doping level [46–51].

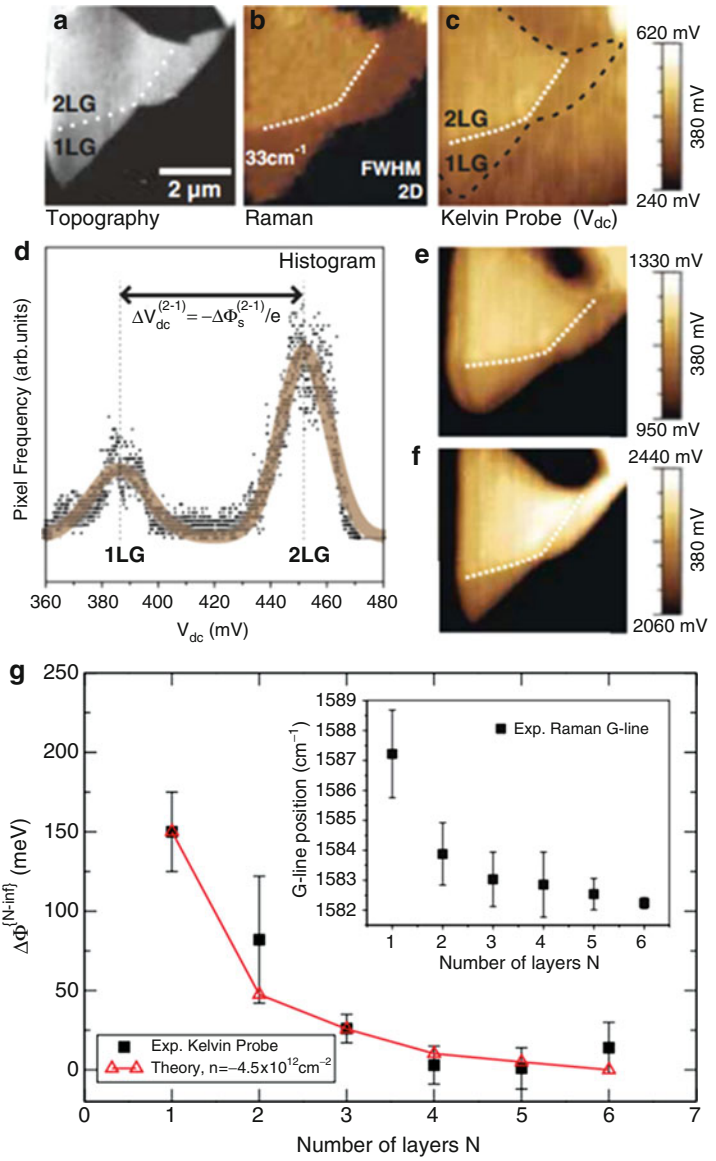


Fig. 4.16 (**a**) AFM topography image of an isolated graphitic flake consisting of single- and bilayer regions (**b**) showing the FWHM of the 2D Raman line (**c**), (**e**), and (**f**) surface potential data. (**d**) Histogram analysis of the acquired surface potential data. The two peaks can be attributed to the 1LG and 2LG regions and a surface potential difference of $\Delta V_{dc}{}^{(2-1)} \approx 66$ mV is observed. (**g**) Work function differences as a function of the layer thickness, extracted by histogram analysis of the acquired surface potential data. (*Inset*) Raman G-line shift (Reprinted with permission from [8]. Copyright (2011) by the American Physical Society)

Using the electric field effect, the work function of graphene can be adjusted as the gate voltage tunes the Fermi level across the charge neutrality point, so the intrinsic work function without any doping can be measured by KPFM [11]. The work function of pristine single-layered graphene (SLG) and bilayer graphene (BLG) without any doping is 4.57 ± 0.05 eV and 4.69 ± 0.05 eV, respectively. These values are in reasonable agreement with theoretical estimations [52].

6.3 Charge Transfer

Charge transfer is very important in photovoltaic, electroluminescence, and photo catalysis processes. KPFM is a powerful technique in studying charge transfer in situ.

KPFM can be used to study the interaction between QDs and silicon substrates and the effect of substrate on photoionization. For example, the photoionization of CdSe/CdS core/shell nanocrystals on n- and p-type silicon substrates with 2 nm surface oxide was investigated by KPFM [53]. The measured work function difference between the two substrates is substantially lower (on the order of 300 meV) than flat band degenerately doped n- and p-type silicon (∼1 eV). This creates upward or downward band bending in the n- and p-type silicon, respectively, and causes Fermi-level pinning at the surface [54]. This band bending influences photoionization by controlling the concentration of photogenerated electrons at the Si/SiO_2 interface, indicating that ultimate control over photoionization is possible.

Platinum-loaded titanium dioxide (TiO_2) is well known for applications in photocatalysis toward water cleavage [55]. The work functions of Pt adatoms [56] and Pt clusters [57] deposited on TiO_2 surface were carefully studied by KPFM. Topographic images identify Pt atoms adsorbed at three different sites: on the Ti atom rows, on the O atom rows, and in O atom vacancies. Most Pt adatoms were observed on Ti atom rows. And successively recorded images show that the Pt adatoms on Ti atom rows (adatoms A) and O atom rows are mobile, while the adatoms in the O atom vacancies (adatoms B) are not. Adatoms A and adatoms B were identified in KPFM images. However, adatoms on O atom rows were not visualized in KPFM images because they moved quickly or were swept out by the tip. Figure 4.17a and b shows a simultaneously recorded topography image and a work function map of the Pt-evaporated surface, respectively. In the topographic image, both the adatoms and O atom rows are resolved. The positions of the Pt adatoms are darker than the surrounding TiO_2 surface, indicating a work function decrease on the Pt adatoms. Figure 4.17e shows that the most probable work function decrease lies in the section between 0.24 and 0.26 eV. The distribution for adatoms B is centered at a larger work function decrease, between 0.26 and 0.28 eV. The work function of Pt on Ti atom row is larger than that on the O atom row by 0.02 eV. The work function of the Pt adatoms is always smaller than that of surrounding TiO_2 surface, indicating that the electron transfer from the adatoms to the surface was induced by an electric dipole moment directed from the substrate to

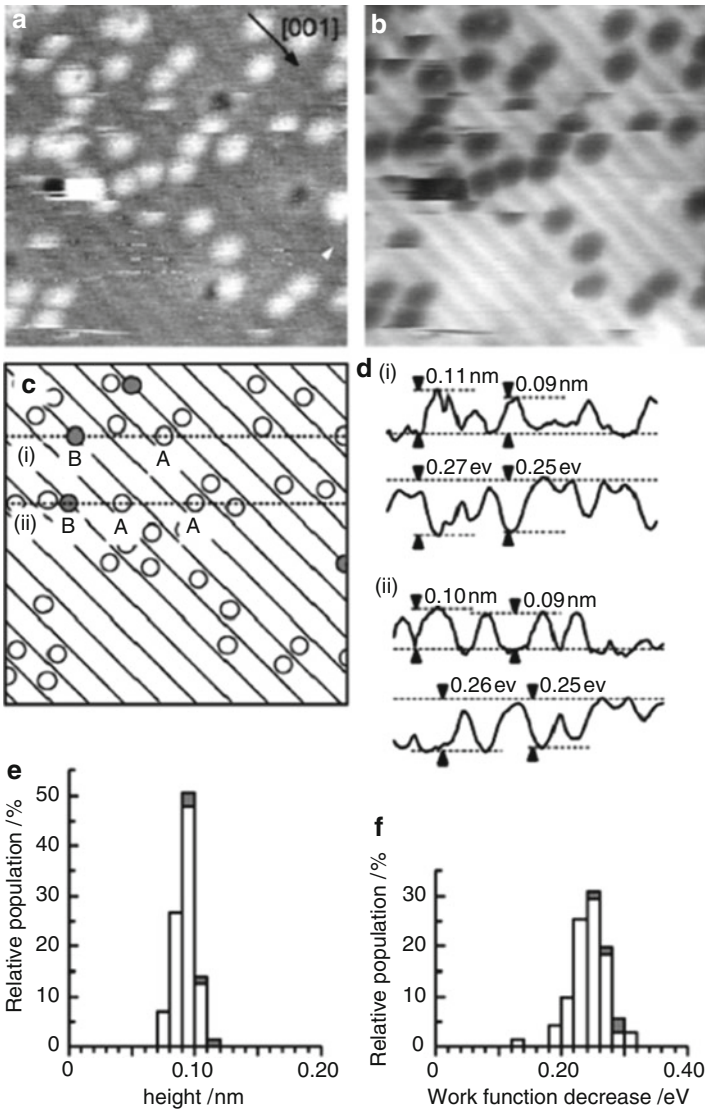


Fig. 4.17 Simultaneously obtained (**a**) topography and (**b**) work function map of the Pt-evaporated TiO_2 surface. (**c**) Model of the surface in (**a**). (**d**) Cross sections along the lines in (**c**). Distribution of the (**e**) heights from the O atom rows and (**f**) work function decrease on the Pt adatoms (Reprinted with permission from [56]. Copyright (2006) American Chemical Society)

the vacuum. The difference in work function decrease between adatoms A and B is presumably due to the number of Ti atoms which receive the electrons. Electrons from adatoms A are received by one Ti atom which is originally coordinated to five O atoms. However, it is geometrically possible for an adatom B to have two neighboring Ti atoms, which may enhance the electron transfer.

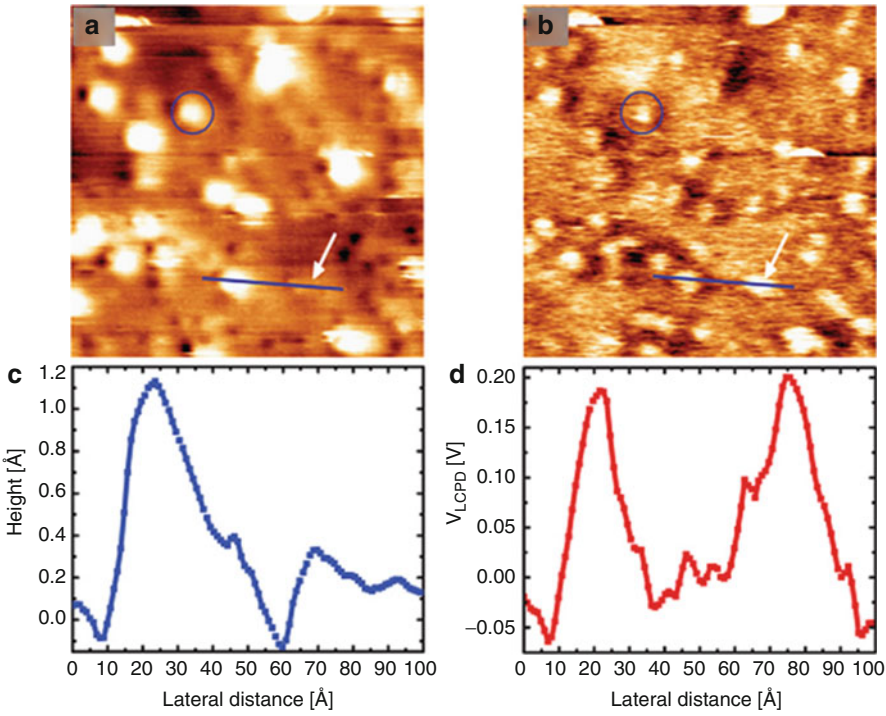


Fig. 4.18 (**a**) Topography and (**b**) KPFM image of the Au adsorbed hydroxylated TiO_2 (110) surface. (**c**) Height and (**d**) CPD profiles are taken along the line drawn in (**a**) and (**b**), respectively. The *circle* indicates the Au nanocluster (Reprinted with permission from [59]. Copyright (2011), AIP Publishing LLC)

Similar observation of lower work function of Pt than TiO_2 support was found in the system of Pt cluster on TiO_2 [57]. And the work function on the clusters decreases as the interface area increases no matter the clusters were on terraces or at step edges. This might be caused by the electric dipoles formed at the interface of Pt cluster and TiO_2.

Rutile TiO_2 (110)-(1 × 1)-supported gold (Au) nanoclusters have been anticipated to fulfill their potential in catalysis and sensor applications, particularly due to the unique size-dependent characteristics of Au clusters and the photocatalytic properties of the supporting TiO_2 surface [58]. Hydroxylated TiO_2 (110) supported Au nanoclusters was carefully studied using KPFM [59]. Figure 4.18a and b shows Au nanoclusters evaporated on TiO_2 surface. The KPFM image in Fig. 4.18b exhibits an increase in the CPD contrast of the surface over the Au nanoclusters compared to the supporting TiO_2 surface. Some atomic species in faint contrast in the topographical image (highlighted by an arrow) are also clearly visible in the CPD image. Figure 4.18d shows Au nanocluster has an average CPD of ∼200 mV higher than the TiO_2 substrate. Similarly to Pt/TiO_2 system described above, it was believed that the main contribution to the observed CPD shift over the Au clusters

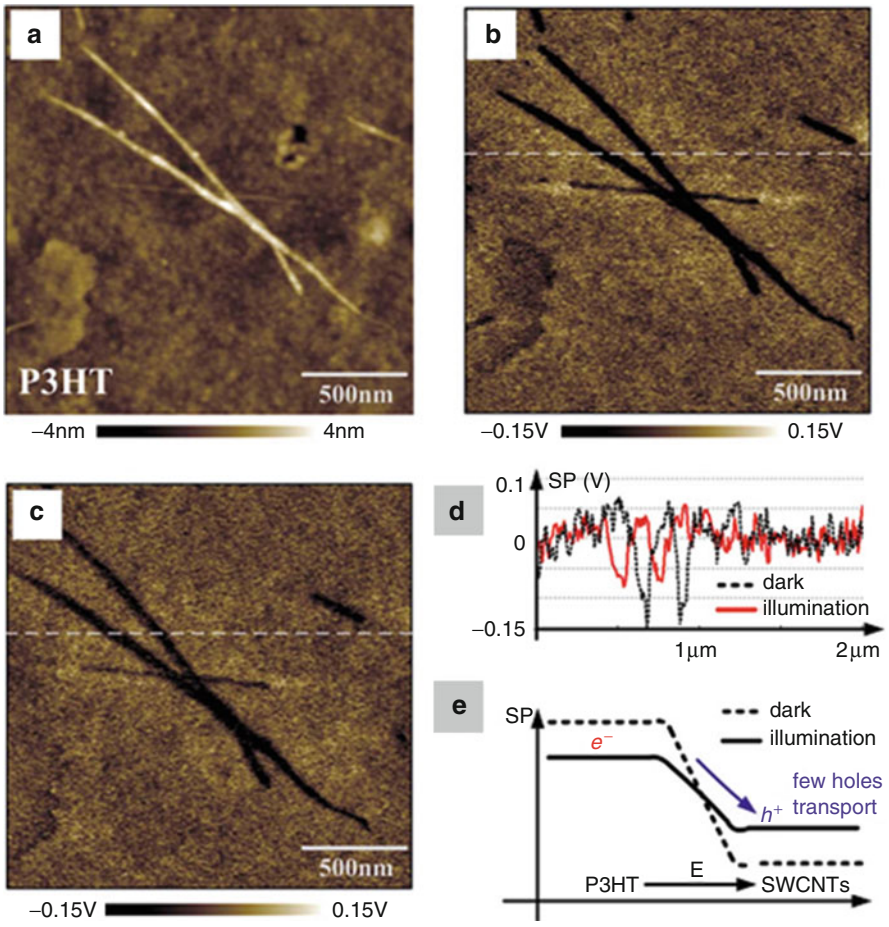


Fig. 4.19 (**a**) Topography of SWCNTs on *top* of P3HT in the dark. (**b**) KPFM image in the dark. (**c**) KPFM image under illumination. (**d**) Surface potential values of the cross section indicated by the *dash line* in KPFM images. (**e**) Schematic to show the charge transport (Reprinted with permission from [10]. Copyright (2010), AIP Publishing LLC)

originated from the electric dipole formed between an Au nanocluster and the TiO_2 interface induced by the Au–TiO_2 charge transfer.

Organic solar cells (OSCs) have drawn much attention because of the low cost and high-throughput solution processes [60–62]. It was reported that introducing carbon nanotubes into active layer of OSCs improves the power conversion efficiency [63, 64] and possesses high open-circuit voltage [65, 66]. Photoinduced holes transported from active layer to SWCNTs was observed using KPFM when SWCNTs fabricated on poly(3-hexylthiophene) (P3HT) film as well as on P3HT and 6,6-phenyl-C61-butyric acid methyl ester (PCBM) blended film [10, 67]. SWCNTs were carefully coated on top of P3HT in order to expose both P3HT and SWCNTs (Fig. 4.19a). Compared with Fig. 4.19b (obtained in the dark)

and c (obtained under illumination), surface potential contrast between SWCNTs and P3HT slightly decreased from 0.14 V in the dark to 0.08 V under illumination, indicating the transport of photoexcited carriers from active layer (P3HT) to SWCNTs, which is illustrated in Fig. 4.19e. In the dark, surface potential of P3HT is higher than that of SWCNTs, suggesting the direction of local electric field is from P3HT to SWCNTs. After light absorption by P3HT, photoexcited holes are driven to SWCNTs by the local electric field at the interface between P3HT and SWCNTs while electrons tend to remain in P3HT. The reduced surface potential contrast under illumination is attributed to the induced electric field by photoexcited electrons in P3HT and holes in SWCNTs, which has opposite direction as the local electric field in the dark. Compared with SWCNTs on P3HT, decrease of surface potential contrast between SWCNTs and P3HT/PCBM under illumination is more significant, indicating more holes transport from active layer P3HT/PCBM to SWCNTs. KPFM study on P3HT/PCBM/SWCNTs demonstrates that photoinduced holes are present in SWCNTs and thus SWCNTs work as donor, which is coincident with the macroscopic fact that introducing SWCNTs in P3HT/PCBM solar cells can increase the power conversion efficiency.

6.4 Field Effect Transistors

Experimental techniques providing valuable electrical, mechanical, and processing properties are critical to the development of FETs. KPFM provides a two-dimensional profile of surface potentials, ideal for characterizing transistor structures.

The performance of thin-film field effect transistors (TFTs) based on conjugated organic materials as the active semiconducting component has experienced impressive improvement in recent years [68]. Bottom-contact polymer FETs made from P3HT were studied by KPFM [69]. Figure 4.20 shows the abrupt voltage drops ΔV_s and ΔV_d caused by source and drain contact resistance, respectively. As illustrated in Fig. 4.20a, very small contact voltage losses occurred, suggesting Cr–Au electrodes form a relatively good contact for P3HT. However, ΔV_s and ΔV_d, and therefore the source and drain contact resistance, are nearly equal in the case of P3HT/Cr–Au. For FETs with a relatively large Schottky barrier for injection, the situation is different as can be seen in Fig. 4.20b, which shows the potential profiles taken of a P3HT transistor with Cr electrodes. They show pronounced asymmetry between the source and drain, i.e., a considerably larger voltage is needed to inject the holes at the source than to extract them at the drain ($\Delta V_s > \Delta V_d$). And this asymmetry is not due to one of the two electrodes forming better contact with the polymer than the other, since upon switching the source and drain electrodes, nearly identical result can be verified by comparing the 300 K profile in Fig. 4.20b with the profile in the inset.

Charge carriers trapped in polystyrene (PS) were investigated with KPFM [70]. Lateral heterojunctions of pentacene/PS were scanned using KPFM, as shown in Fig. 4.21a, exhibiting polarization along a side view of a lateral nonvolatile organic field effect transistor (OFET) dielectric interface. Figure 4.21b shows

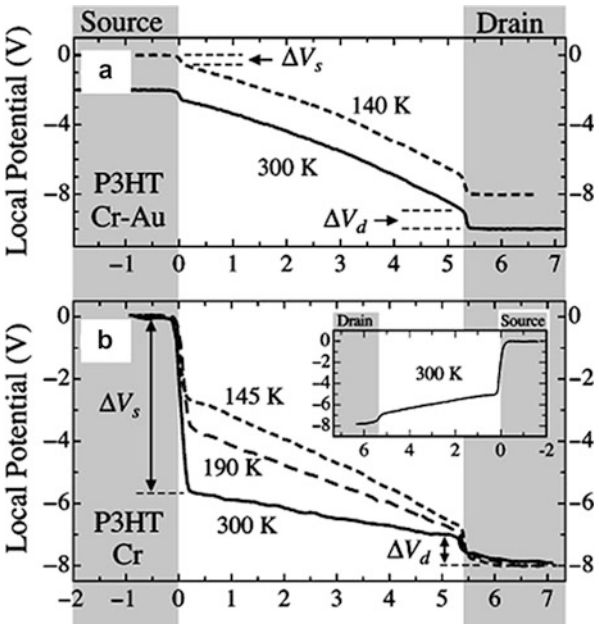


Fig. 4.20 Profiles of the electrostatic potential across the channel of operating transistors. (**a**) P3HT transistor with Cr–Au source/drain electrodes ($L \approx 5.3$ μm, $V_g = -20$ V, $V_d = -8$ V). (**b**) Profiles of an $L \approx 5.5$ μm P3HT transistor with Cr electrodes taken at three different temperatures ($V_g = -40$ V, $V_d = -8$ V). The *inset* of (**b**) shows a profile obtained after switching the source and drain on the same TFT ($V_g = -40$ V, $V_d = -8$ V) (Reprinted with permission from [69]. Copyright (2003), AIP Publishing LLC)

KPFM line scans which were performed on the samples as the bias applied to the pentacene was varied, showing the potential drop across pentacene, PS, and the interface. Figure 4.21c illustrates the measured surface potential after the sample being charged at +200 V to pentacene for 10 min. Before charging, the surface potential on the pentacene side can be raised to higher value than the PS side by applying a small voltage, while after being charged at +200 V, the surface potential on the PS side remains higher than that on the pentacene side, indicating that charges are injected into the PS dielectric layer from the pentacene. When replacing pentacene with gold, a greater shift in surface potential can be observed, due to the higher conductivity of gold compared to pentacene. The charged samples have an offset difference in surface potential when compared to uncharged samples. This offset in surface potential is a result of the stored charges in the PS layers.

Carbon nanotubes (CNTs) have attracted much attention for their unique properties and numerous demonstrations of FETs based on semiconducting CNTs have been reported [71, 72]. KPFM has been applied to study FETs at different bias voltage. Surface potentials along a SWCNT in FETs were studied [73]. The gradual changes in contrast along the SWCNT bundle indicate the current flowing between the two electrodes. The fact that the potential was partially increased by applying a gate bias voltage indicates that the bundle probably includes semiconducting-like nanotubes in addition to metallic ones in this region. When the CNTFET is in the ON state, it shows uniform potential distribution along the CNT. However, when the CNTFET is in the OFF state, nonuniform potential image with dark spots is obtained, probably due to the defects in the CNTs [74].

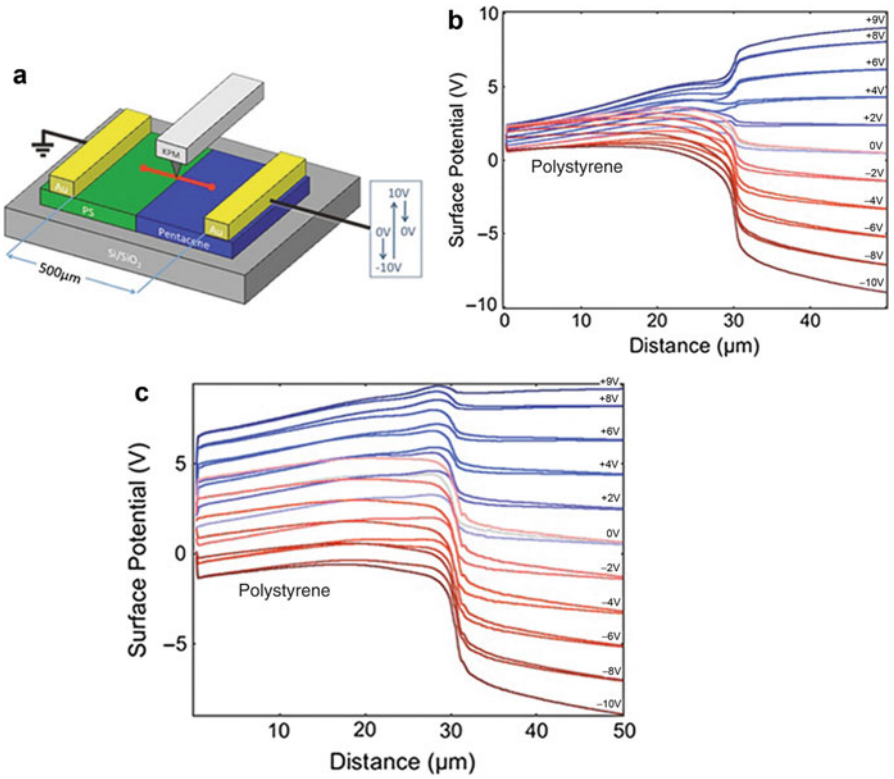


Fig. 4.21 (**a**) The schematic of the heterojunction. (**b**) The uncharged sample surface potential at various applied biases. The sample was initially scanned in the negative direction to −10 V and then the bias was stepped up to +9 V and finally back to 0 V. (**c**) The sample was removed from the KPFM and charged at +200 V for 10 min and then returned to the KPFM and rescanned (Reprinted with permission from [70]. Copyright (2012), AIP Publishing LLC)

Contact resistance of individual Cr–Au electrodes contacting graphene in a graphene device was studied using KPFM [11]. Figure 4.22a shows the current (I) versus V_{SD} characteristics at a fixed gate voltage. The slope of I-V_{SD} yields a resistance of 3.44 kΩ, which includes the contributions of contact resistances between each electrode and the graphene channel. As shown in Fig. 4.22b, the surface potential of the biased drain electrode shifts upward as V_{SD} increases, as drain electrode was grounded. From Fig. 4.22c, linearly increasing V_{CPD} in the channel and kinks in V_{CPD} at the junctions can be found. These sudden potential drops are attributed to the contact resistance between the electrodes and graphene. The vertical ratios between the kinks and the slope correspond to the source and drain contact resistances (r_s and r_d) and graphene channel resistance (r_c). Considering the total resistance of this device is 3.44 kΩ, $r_d : r_c : r_s = 0.5 : 1.7 : 1.24$ kΩ is obtained.

KPFM can also be used to study the interlayer screening effect of graphene sheets in graphene-based FETs [75]. The surface potential decreases exponentially

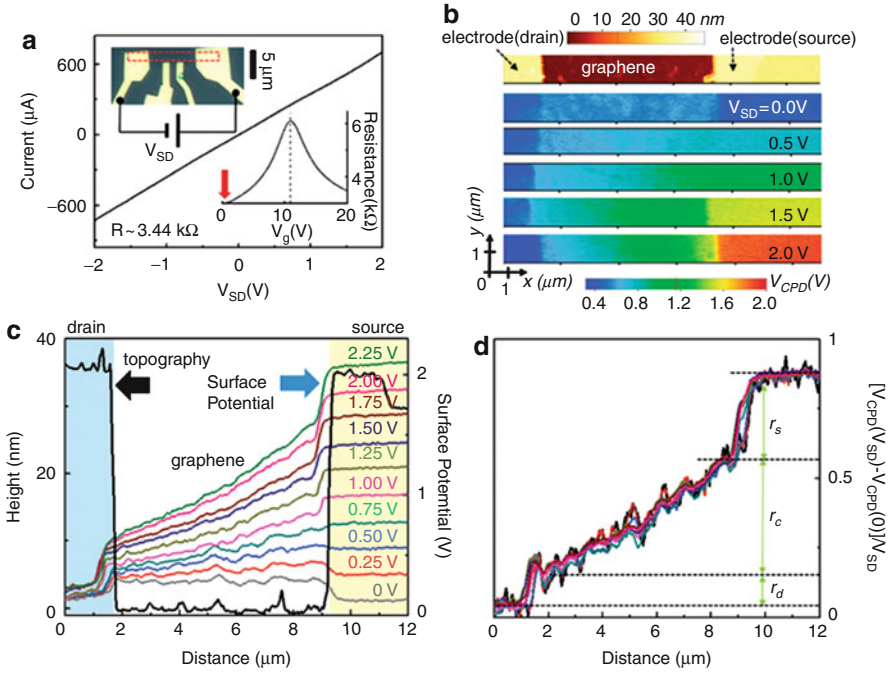


Fig. 4.22 (**a**) Current (I) and bias voltage (V_{SD}) characteristic of a SLG device. *Upper inset* shows the optical microscope image of the device. *Lower inset* shows the resistance as a function of V_g. The *vertical arrow* indicates the gate voltages and *dotted line*, V_D. (**b**) Topographic image (*top*) and surface potential images of the area marked by the rectangular box in (**a**). The drain electrode is grounded, while the source electrode is biased by V_{SD} as indicated in each panel. The gate voltage is fixed to $V_g = 0$. (**c**) Surface potential profiles at different V_{SD}. (**d**) Normalized and referenced surface potential profiles shown in (**c**) (Reprinted with permission from [11]. Copyright (2009) American Chemical Society)

with the number of layers, demonstrating the graphene independently screens the surface potential layer by layer.

6.5 Atomic Resolution KPFM

In atomically resolved KPFM, the measured CPD is defined as local contact potential difference (LCPD), which depends on the electrostatic interaction on an atomic scale. The LCPD is based on the Wandelt's concept of a local work function, which illustrates the short-ranged atomic-scale variation of work function on surfaces [76, 77]. Similar to the local work function concept, atomic-scale KPFM measurements of the total electrostatic force include a new term (a bias-dependent short-range force), which induces the atomic LCPD contrast. The atomic-scale contrast of CPD is attributed to a short-range force, due to the microscopic interaction between the apex of the tip and surface atoms.

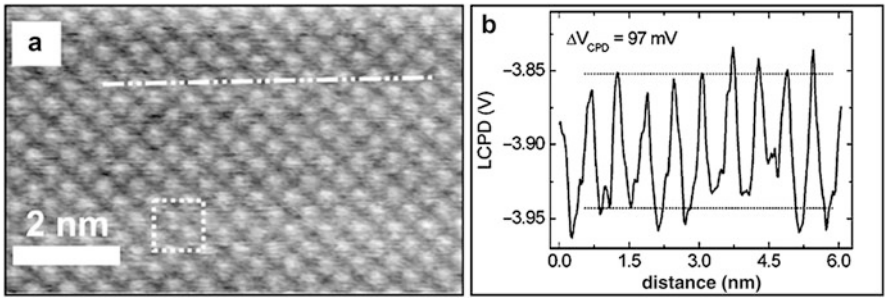


Fig. 4.23 (**a**) CPD image of KBr (001) surface by KPFM. (**b**) CPD profile along the *dashed line* in (**a**) (Reprinted with permission from [78]. Copyright (2008) by the American Physical Society)

Atomic resolution KPFM results of KBr (001) surface in UHV were obtained [78]. As shown in Fig. 4.23, the image exhibits atomic features, the measured period of which is 0.63 nm, which is visible in the joint cross section. This value is in good agreement with the lattice constant of KBr, 0.66 nm. The vertical contrast yields about 100 mV between K^+ and Br^- around an average value of −3.9 V. The expression of the electrostatic force can be split into two major contributions: the first stands for the coupling between the microscopic structure of the tip apex and the capacitor formed between the tip, the ionic crystal, and the counter electrode, while the second term depicts the influence of the Madelung surface potential on the mesoscopic part of the tip, independent of its microscopic structure. The former has the lateral periodicity of the Madelung surface potential, whereas the latter only acts as a static component and shifts the total force. Beyond the dielectric properties of the crystal, the ionic polarization of the sample resulting from the influence of the tip/counter electrode capacitor is responsible for the atomic contrast of the KPFM signal.

Sub-nanometer resolution LCPD has also been observed on a variety of surfaces including Si [79–83], TiO_2 [84], and InSb [26]. Atomic-scale variations in the electronic surface potential on TiO_2 (110) surface were studied [84]. As shown in Fig. 4.24a, the dark-bright striped pattern visibly reflects the normal appearance of the TiO_2 (1 × 1) surface, with alternating rows of bridging oxygen atoms [O(2*c*)] and in-plane titanium atoms [Ti(5*c*)], which are also observed in LCPD image, suggesting the KPFM setup is able to detect atomic-scale variation in the surface charge densities. In LCPD image, the dark rows (more negative) are assigned to O (2*c*) rows, and those bright are assigned to Ti(5*c*) rows. This identification is also supported by the topography image (Fig. 4.24a), where the contrast is observed to be reversed. The results confirm the concepts applied for the interpretation of the LCPD image and furthermore demonstrate that LCPD images can be used for a chemical identification of the surface structure.

KPFM can be used to distinguish atom charge state [85] and measure the charge distribution within single molecules [86–88]. KPFM can be used to detect charge states of metallic atoms by measuring the LCPD between metallic and substrate [85]. The local contact potential difference is shifted depending

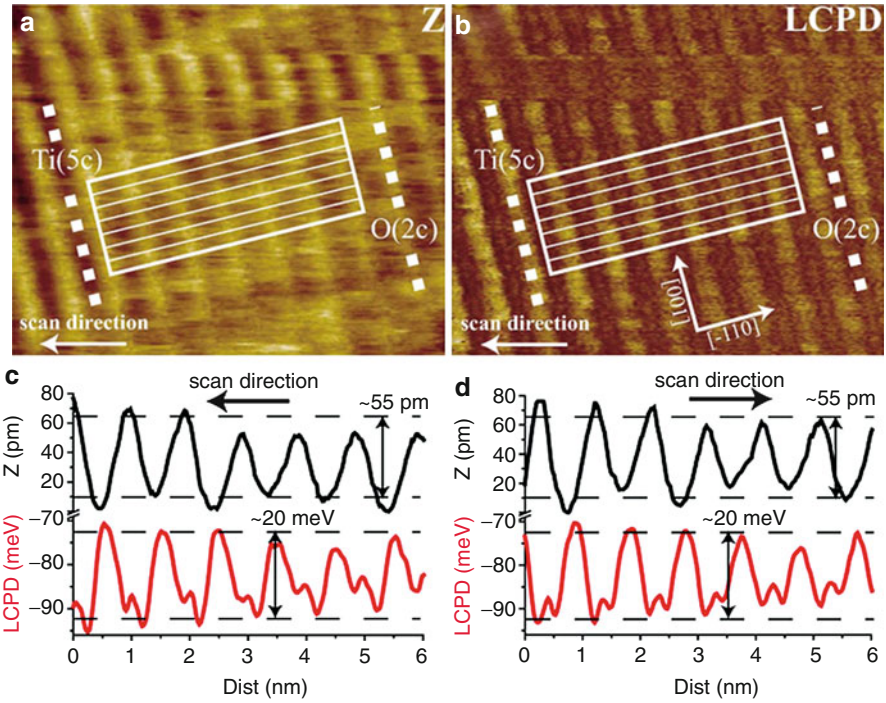


Fig. 4.24 (**a**) The AFM topography image (*Z*). (**b**) Simultaneously recorded LCPD. (**c**) The 99-line average twin cross sections of *Z* and LCPD, as indicated by the *white boxes* in (**a**) and (**b**). (**d**) The 99-line average twin cross sections of *Z* and LCPD recorded in the forward fast-scan direction (Reprinted with permission from [84]. Copyright (2008) by the American Physical Society)

on the sign of the charge and allows the discrimination of positively charged, neutral, and negatively charged atoms.

Charge distribution within naphthalocyanine molecules, which have been reported as molecular switches [89], on a thin insulating layer of NaCl on Cu (111), was studied using KPFM [87]. Figure 4.25b and c shows the LCPD images recorded before and after switching the tautomerization state of a single naphthalocyanine molecule. An obvious asymmetry between the H-lobes and the N-lobes can be observed, with greater values of V^* above the N-lobes. The asymmetry is even more clearly visible in the difference image (Fig. 4.25d) obtained by subtracting the LCPD images of the initial and switched configurations. The DFT-calculated results (Fig. 4.25e) reveal that the submolecular resolution in the LCPD images reflects the total charge distribution within the molecule.

In this chapter, various aspects of KPFM including theory, instrumentation (AM and FM mode), and application have been discussed. KPFM is a powerful technique for high spatial resolution electrical property measurement and has shown to be a feasible method widely applicable in nanoscience and nanotechnology.

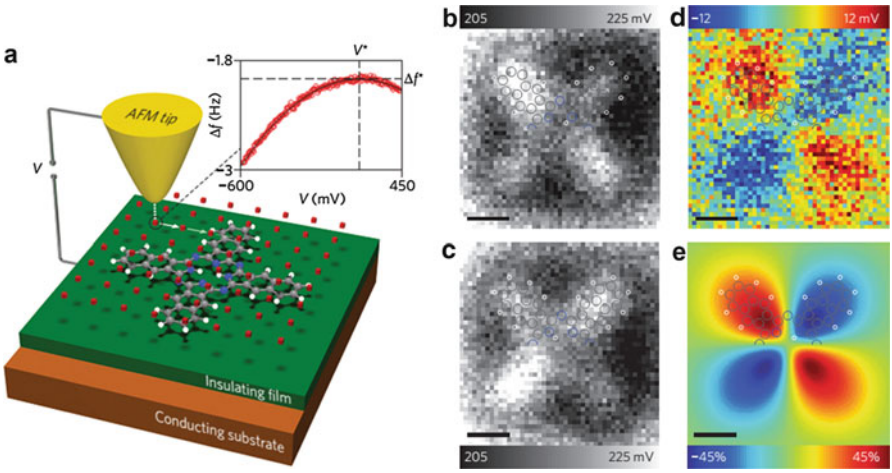


Fig. 4.25 LCPD images of the tautomerization switching of naphthalocyanine. (**a**) Schematic of the measurement principle. (**b**) and (**c**), LCPD images of naphthalocyanine before (**b**) and after (**c**) switching the tautomerization state of the molecule. (**d**) Difference image obtained by subtracting (**c**) from (**b**). (**e**) DFT-calculated asymmetry of the z-component of the electric field above a free naphthalocyanine molecule at a distance $d = 0.5$ nm from the molecular plane (Reprinted by permission from Macmillan Publishers Ltd: Nat Nanotechnol [87], copyright (2012))

References

1. Kelvin L (1898) V. contact electricity of metals. London, Edinburgh, Dublin Philos Mag J Sci 46(278):82–120
2. Zisman W (1932) A new method of measuring contact potential differences in metals. Rev Sci Instrum 3(7):367–370
3. Melitz W, Shen J, Kummel AC, Lee S (2011) Kelvin probe force microscopy and its application. Surf Sci Rep 66(1):1–27
4. Sadewasser S, Glatzel T (2012) Kelvin probe force microscopy. Springer, Heidelberg
5. Nonnenmacher M, O'Boyle M, Wickramasinghe H (1991) Kelvin probe force microscopy. Appl Phys Lett 58:2921
6. O'Boyle M, Hwang T, Wickramasinghe H (1999) Atomic force microscopy of work functions on the nanometer scale. Appl Phys Lett 74(18):2641–2642
7. Yamauchi T, Tabuchi M, Nakamura A (2004) Size dependence of the work function in Inas quantum dots on Gaas (001) as studied by Kelvin force probe microscopy. Appl Phys Lett 84(19):3834–3836
8. Ziegler D, Gava P, Güttinger J, Molitor F, Wirtz L, Lazzeri M, Saitta A, Stemmer A, Mauri F, Stampfer C (2011) Variations in the work function of doped single-and few-layer graphene assessed by Kelvin probe force microscopy and density functional theory. Phys Rev B 83(23):235434
9. Sun H, Chu H, Wang J, Ding L, Li Y (2010) Kelvin probe force microscopy study on nanotriboelectrification. Appl Phys Lett 96(8):083112–083112-3
10. Liu L, Li G (2010) Electrical characterization of single-walled carbon nanotubes in organic solar cells by Kelvin probe force microscopy. Appl Phys Lett 96:083302
11. Yu Y-J, Zhao Y, Ryu S, Brus LE, Kim KS, Kim P (2009) Tuning the graphene work function by electric field effect. Nano Lett 9(10):3430–3434

12. Colchero J, Gil A, Baró A (2001) Resolution enhancement and improved data interpretation in electrostatic force microscopy. Phys Rev B 64(24):245403
13. Zerweck U, Loppacher C, Otto T, Grafström S, Eng LM (2005) Accuracy and resolution limits of Kelvin probe force microscopy. Phys Rev B 71(12):125424
14. Jacobs H, Leuchtmann P, Homan O, Stemmer A (1998) Resolution and contrast in Kelvin probe force microscopy. J Appl Phys 84(3):1168–1173
15. Ding L, Li Y, Chu H, Li C, Yang Z, Zhou W, Tang ZK (2007) High speed atomic force microscope lithography driven by electrostatic interaction. Appl Phys Lett 91(2):023121–023121-3
16. Mesquida P, Stemmer A (2001) Attaching silica nanoparticles from suspension onto surface charge patterns generated by a conductive atomic force microscope tip. Adv Mater 13(18):1395–1398
17. Lee G, Shin Y-H, Son JY (2009) Formation of self-assembled polyelectrolyte multilayer nanodots by scanning probe microscopy. J Am Chem Soc 131(5):1634–1635
18. Seemann L, Stemmer A, Naujoks N (2007) Local surface charges direct the deposition of carbon nanotubes and fullerenes into nanoscale patterns. Nano Lett 7(10):3007–3012
19. Palleau E, Sangeetha NM, Viau G, Marty J-D, Ressier L (2011) Coulomb force directed single and binary assembly of nanoparticles from aqueous dispersions by Afm nanoxerography. ACS Nano 5(5):4228–4235
20. Yue S, Xueqiang Z, Ying W, Xuejiao Z, Jun H, Shouwu G, Yi Z (2013) Charge transfer between reduced graphene oxide sheets on insulating substrates. Appl Phys Lett 103(5):053107 (4 pp)–053107 (4 pp)
21. Verdaguer A, Cardellach M, Segura J, Sacha G, Moser J, Zdrojek M, Bachtold A, Fraxedas J (2009) Charging and discharging of graphene in ambient conditions studied with scanning probe microscopy. Appl Phys Lett 94(23):233105–233105-3
22. Moser J, Verdaguer A, Jimenez D, Barreiro A, Bachtold A (2008) The environment of graphene probed by electrostatic force microscopy. Appl Phys Lett 92(12):123507–123507-3
23. Guo LQ, Zhao XM, Bai Y, Qiao LJ (2012) Water adsorption behavior on metal surfaces and its influence on surface potential studied by in situ Spm. Appl Surf Sci 258(22):9087–9091
24. Craig PP, Radeka V (1970) Stress dependence of contact potential: the Ac Kelvin method. Rev Sci Instrum 41(2):258–264
25. Goryl M, Kolodziej J, Krok F, Piatkowski P, Such B, Szymonski M (2005) Epitaxial nanostructures assembled on Insb (001) by submonolayer deposition of gold. Microelec Eng 81(2):394–399
26. Krok F, Sajewicz K, Konior J, Goryl M, Piatkowski P, Szymonski M (2008) Lateral resolution and potential sensitivity in Kelvin probe force microscopy: towards understanding of the sub-nanometer resolution. Phys Rev B 77(23):235427
27. Shusterman S, Raizman A, Sher A, Paltiel Y, Schwarzman A, Lepkifker E, Rosenwaks Y (2007) Nanoscale mapping of strain and composition in quantum dots using Kelvin probe force microscopy. Nano Lett 7(7):2089–2093
28. Wang QH, Kalantar-Zadeh K, Kis A, Coleman JN, Strano MS (2012) Electronics and optoelectronics of two-dimensional transition metal dichalcogenides. Nat Nanotechnol 7(11):699–712
29. Xu M, Liang T, Shi M, Chen H (2013) Graphene-like two-dimensional materials. Chem Rev 113(5):3766–3798
30. Li Y, Xu C-Y, Zhen L (2013) Surface potential and interlayer screening effects of few-layer Mos 2 nanoflakes. Appl Phys Lett 102(14):143110–143110-4
31. Datta SS, Strachan DR, Mele EJ, Johnson ATC (2009) Surface potentials and layer charge distributions in few-layer graphene films. Nano Lett 9(1):7–11
32. Jaafar M, López-Polín G, Gómez-Navarro C, Gómez-Herrero J (2012) Step like surface potential on few layered graphene oxide. Appl Phys Lett 101(26):263109
33. Ago H, Kugler T, Cacialli F, Salaneck WR, Shaffer MS, Windle AH, Friend RH (1999) Work functions and surface functional groups of multiwall carbon nanotubes. J Phys Chem B 103(38):8116–8121

34. Shiraishi M, Ata M (2001) Work function of carbon nanotubes. Carbon 39(12):1913–1917
35. Suzuki S, Bower C, Watanabe Y, Zhou O (2000) Work functions and valence band states of pristine and Cs-intercalated single-walled carbon nanotube bundles. Appl Phys Lett 76(26):4007–4009
36. Spadafora EJ, Saint-Aubin K, Celle C, Demadrille R, Grévin B, Simonato J-P (2012) Work function tuning for flexible transparent electrodes based on functionalized metallic single walled carbon nanotubes. Carbon 50(10):3459–3464
37. Martel RA, Schmidt T, Shea H, Hertel T, Avouris P (1998) Single-and multi-wall carbon nanotube field-effect transistors. Appl Phys Lett 73:2447
38. Tans SJ, Verschueren AR, Dekker C (1998) Room-temperature transistor based on a single carbon nanotube. Nature 393(6680):49–52
39. Derycke V, Martel R, Appenzeller J, Avouris P (2001) Carbon nanotube inter-and intramolecular logic gates. Nano Lett 1(9):453–456
40. Derycke V, Martel R, Appenzeller J, Avouris P (2002) Controlling doping and carrier injection in carbon nanotube transistors. Appl Phys Lett 80:2773
41. Cui X, Freitag M, Martel R, Brus L, Avouris P (2003) Controlling energy-level alignments at carbon nanotube/Au contacts. Nano Lett 3(6):783–787
42. Filleter T, Emtsev K, Seyller T, Bennewitz R (2008) Local work function measurements of epitaxial graphene. Appl Phys Lett 93(13):133117–133117-3
43. Casiraghi C, Pisana S, Novoselov K, Geim A, Ferrari A (2007) Raman fingerprint of charged impurities in graphene. Appl Phys Lett 91(23):233108–233108-3
44. Yan J, Henriksen EA, Kim P, Pinczuk A (2008) Observation of anomalous phonon softening in bilayer graphene. Phys Rev Lett 101(13):136804
45. Yan J, Zhang Y, Kim P, Pinczuk A (2007) Electric field effect tuning of electron–phonon coupling in graphene. Phys Rev Lett 98(16):166802
46. Shi Y, Kim KK, Reina A, Hofmann M, Li L-J, Kong J (2010) Work function engineering of graphene electrode via chemical doping. ACS Nano 4(5):2689–2694
47. Wang R, Wang S, Zhang D, Li Z, Fang Y, Qiu X (2010) Control of carrier type and density in exfoliated graphene by interface engineering. ACS Nano 5(1):408–412
48. Bußmann BK, Ochedowski O, Schleberger M (2011) Doping of graphene exfoliated on Srtio3. Nanotechnology 22(26):265703
49. Wang X, Xu J-B, Xie W, Du J (2011) Quantitative analysis of graphene doping by organic molecular charge transfer. J Phys Chem C 115(15):7596–7602
50. Pearce R, Eriksson J, Iakimov T, Hultman L, Lloyd Spetz PA, Yakimova R (2013) On the differing sensitivity to chemical gating of single and double layer epitaxial graphene explored using scanning Kelvin probe microscopy. ACS Nano 7:4647–4656
51. Zhou X, He S, Brown KA, Mendez-Arroyo J, Boey F, Mirkin CA (2013) Locally altering the electronic properties of graphene by nanoscopically doping it with rhodamine 6 g. Nano Lett 13(4):1616–1621
52. Sque SJ, Jones R, Briddon PR (2007) The transfer doping of graphite and graphene. Phys Status Solidi (a) 204(9):3078–3084
53. Cherniavskaya O, Chen L, Islam MA, Brus L (2003) Photoionization of individual Cdse/Cds core/shell nanocrystals on silicon with 2-Nm oxide depends on surface band bending. Nano Lett 3(4):497–501
54. Ludeke R, Cartier E (2001) Imaging of trapped charge in Sio 2 and at the Sio 2–Si interface. Appl Phys Lett 78(25):3998–4000
55. Linsebigler AL, Lu G, Yates JT Jr (1995) Photocatalysis on Tio_2 surfaces: principles, mechanisms, and selected results. Chem Rev 95(3):735–758
56. Sasahara A, Pang CL, Onishi H (2006) Probe microscope observation of platinum atoms deposited on the Tio_2 (110)-(1 × 1) surface. J Phys Chem B 110(27):13453–13457
57. Sasahara A, Pang CL, Onishi H (2006) Local work function of Pt clusters vacuum-deposited on a Tio_2 surface. J Phys Chem B 110(35):17584–17588

58. Haruta M, Yamada N, Kobayashi T, Iijima S (1989) Gold catalysts prepared by coprecipitation for low-temperature oxidation of hydrogen and of carbon monoxide. J Catal 115(2):301–309
59. Chung HJ, Yurtsever A, Sugimoto Y, Abe M, Morita S (2011) Kelvin probe force microscopy characterization of Tio_2 (110)-supported Au clusters. Appl Phys Lett 99(12):123102
60. Kim JY, Lee K, Coates NE, Moses D, Nguyen T-Q, Dante M, Heeger AJ (2007) Efficient tandem polymer solar cells fabricated by all-solution processing. Science 317(5835):222–225
61. Li G, Shrotriya V, Huang J, Yao Y, Moriarty T, Emery K, Yang Y (2005) High-efficiency solution processable polymer photovoltaic cells by self-organization of polymer blends. Nat Mater 4(11):864–868
62. Yu G, Gao J, Hummelen JC, Wudl F, Heeger AJ (1995) Polymer photovoltaic cells – enhanced efficiencies via a network of internal donor-acceptor heterojunctions. Science 270(5243):1789–1791
63. Li C, Chen Y, Wang Y, Iqbal Z, Chhowalla M, Mitra S (2007) A fullerene–single wall carbon nanotube complex for polymer bulk heterojunction photovoltaic cells. J Mater Chem 17(23):2406–2411
64. Liu L, Stanchina WE, Li G (2009) Effects of semiconducting and metallic single-walled carbon nanotubes on performance of bulk heterojunction organic solar cells. Appl Phys Lett 94(23):233309–233309-3
65. Kymakis E, Alexandrou I, Amaratunga G (2003) High open-circuit voltage photovoltaic devices from carbon-nanotube-polymer composites. J Appl Phys 93(3):1764–1768
66. Ren S, Bernardi M, Lunt RR, Bulovic V, Grossman JC, Gradecak S (2011) Toward efficient carbon nanotube/P3ht solar cells: active layer morphology, electrical, and optical properties. Nano Lett 11(12):5316–5321
67. Lan F, Li G (2013) Direct observation of hole transfer from semiconducting polymer to carbon nanotubes. Nano Lett 13(5):2086–2091
68. Dimitrakopoulos CD, Malenfant PR (2002) Organic thin film transistors for large area electronics. Adv Mater 14(2):99–117
69. Burgi L, Richards T, Friend R, Sirringhaus H (2003) Close look at charge carrier injection in polymer field-effect transistors. J Appl Phys 94(9):6129–6137
70. Dawidczyk T, Johns G, Ozgun R, Alley O, Andreou A, Markovic N, Katz H (2012) Kelvin probe microscopic visualization of charge storage at polystyrene interfaces with pentacene and gold. Appl Phys Lett 100(7):073305
71. Avouris P (2002) Carbon nanotube electronics. Chem Phys 281(2):429–445
72. McEuen PL, Fuhrer MS, Park H (2002) Single-walled carbon nanotube electronics. Nanotechnol, IEEE Trans 1(1):78–85
73. Miyato Y, Kobayashi K, Matsushige K, Yamada H (2007) Surface potential investigation on single wall carbon nanotubes by Kelvin probe force microscopy and atomic force microscope potentiometry. Nanotechnology 18(8):084008
74. Okigawa Y, Umesaka T, Ohno Y, Kishimoto S, Mizutani T (2008) Potential profile measurement of carbon nanotube fets based on the electrostatic force detection. Nano 3(01):51–54
75. Lee N, Yoo J, Choi Y, Kang C, Jeon D, Kim D, Seo S, Chung H (2009) The interlayer screening effect of graphene sheets investigated by Kelvin probe force microscopy. Appl Phys Lett 95(22):222107–222107-3
76. Küppers J, Wandelt K, Ertl G (1979) Influence of the local surface structure on the 5p photoemission of adsorbed xenon. Phys Rev Lett 43(13):928
77. Wandelt K (1997) The local work function: concept and implications. Appl Surf Sci 111:1–10
78. Bocquet F, Nony L, Loppacher C, Glatzel T (2008) Analytical approach to the local contact potential difference on (001) ionic surfaces: implications for Kelvin probe force microscopy. Phys Rev B 78(3):035410
79. Arai T, Tomitori M (2004) Observation of electronic states on Si (111)-(7 $\times$ 7) through short-range attractive force with noncontact atomic force spectroscopy. Phys Rev Lett 93(25):256101

80. Kitamura S, Iwatsuki M (1998) High-resolution imaging of contact potential difference with ultrahigh vacuum noncontact atomic force microscope. Appl Phys Lett 72(24):3154–3156
81. Kitamura SI, Suzuki K, Iwatsuki M, Mooney C (2000) Atomic-scale variations in contact potential difference on Au/Si (111) 7 × 7 surface in ultrahigh vacuum. Appl Surf Sci 157(4):222–227
82. Okamoto K, Sugawara Y, Morita S (2002) The elimination of the 'Artifact' in the electrostatic force measurement using a novel noncontact atomic force microscope/electrostatic force microscope. Appl Surf Sci 188(3):381–385
83. Okamoto K, Yoshimoto K, Sugawara Y, Morita S (2003) Kpfm imaging of Si(111)5 root 3 × 5 root 3-Sb surface for atom distinction using Nc-Afm. Appl Surf Sci 210(1–2):128–133
84. Enevoldsen GH, Glatzel T, Christensen MC, Lauritsen JV, Besenbacher F (2008) Atomic scale Kelvin probe force microscopy studies of the surface potential variations on the Tio(2) (110) surface. Phys Rev Lett 100(23):236104
85. Gross L, Mohn F, Liljeroth P, Repp J, Giessibl FJ, Meyer G (2009) Measuring the charge state of an adatom with noncontact atomic force microscopy. Science 324(5933):1428–1431
86. Leoni T, Guillermet O, Walch H, Langlais V, Scheuermann A, Bonvoisin J, Gauthier S (2011) Controlling the charge state of a single redox molecular switch. Phys Rev Lett 106(21):216103
87. Mohn F, Gross L, Moll N, Meyer G (2012) Imaging the charge distribution within a single molecule. Nat Nanotechnol 7(4):227–231
88. Walch H, Leoni T, Guillermet O, Langlais V, Scheuermann A, Bonvoisin J, Gauthier S (2012) Electromechanical switching behavior of individual molecular complexes of Cu and Ni on Nacl-covered Cu (111) and Ag (111). Phys Rev B 86(7):075423
89. Liljeroth P, Repp J, Meyer G (2007) Current-induced hydrogen tautomerization and conductance switching of naphthalocyanine molecules. Science 317(5842):1203–1206

Field Ion Microscopy for the Characterization of Scanning Probes

5

William Paul and Peter Grütter

Contents

1 Definition of the Topic 160
2 Overview 160
3 Field Ion Microscopy for the Characterization of Scanning Probes 161
3.1 Introduction 161
3.2 Experimental and Instrumental Methodology 164
3.3 Key Research Findings 182
3.4 Conclusions and Future Perspective 192
References 193

Abstract

Scanning probe microscopy (SPM) is a widely used tool for investigating the nanoscale structure of materials, as well as their electronic and mechanical properties with its related spectroscopic modes of operation. In SPM experiments, the sharp tip which probes the material under investigation is usually uncharacterized; however, its geometry and chemical composition play a large role in the SPM's lateral imaging resolution and the features recorded in electronic and force spectroscopies. To carry out comparisons with modeling, one must consider a set of plausible tip structures and choose the one which best reproduces the experimental data recorded with the uncharacterized tip.

With an atomically defined tip prepared by FIM, the electronic and mechanical properties of the SPM probe are predetermined before the experiment, permitting

W. Paul (✉)
IBM Research Division, Almaden Research Center, San Jose, CA, USA
e-mail: wmppaul@gmail.com

P. Grütter
Physics Department, McGill University, Montréal, QC, Canada

© Springer-Verlag Berlin Heidelberg 2015

C.S.S.R. Kumar (ed.), *Surface Science Tools for Nanomaterials Characterization*,
DOI 10.1007/978-3-662-44551-8_5

direct comparison with theory, as well as the quantitative determination of parameters which depend on tip radius, such as stresses during indentation.

Here we describe the implementation of FIM for the characterization of scanning probe apices. This includes topics of tip integrity, characterization, advanced preparation methodologies, and key research findings from experiments which combine FIM and SPM techniques.

Keywords

Field ion microscopy (FIM) • Scanning probe microscopy (SPM) • Scanning tunneling microscopy (STM) • Atomic force microscopy (AFM) • Field emission • Single-atom tips • Tip characterization • Nanoelectronics • Nanomechanics

1 Definition of the Topic

The field ion microscope (FIM) can image the atomic structure of sharp metal tips with nanometer-sized radii and is notable as being the earliest technique to produce atomically resolved images of matter in real space. Using FIM, one can atomically characterize, and even engineer, the sharp tips used in scanning probe microscopy (SPM). In this chapter, we address the technical aspects of implementing these tips in SPM experiments and review their application to scanning tunneling microscopy (STM), atomic force microscopy (AFM), and SPM-based nanoindentation experiments.

2 Overview

Scanning probe microscopy (SPM) is a widely used tool for investigating the nanoscale structure of materials, as well as their electronic and mechanical properties with its related spectroscopic modes of operation. In SPM experiments, the sharp tip which probes the material under investigation is usually uncharacterized; however, its geometry and chemical composition play a large role in the SPM's lateral imaging resolution and the features recorded in electronic and force spectroscopies. To carry out comparisons with modeling, one must consider a set of plausible tip structures and choose the one which best reproduces the experimental data recorded with the uncharacterized tip.

With an atomically defined tip prepared by FIM, the electronic and mechanical properties of the SPM probe are predetermined before the experiment, permitting direct comparison with theory, as well as the quantitative determination of parameters which depend on tip radius, such as stresses during indentation.

Here we describe the implementation of FIM for the characterization of scanning probe apices. This includes topics of tip integrity, characterization, advanced preparation methodologies, and key research findings from experiments which combine FIM and SPM techniques.

3 Field Ion Microscopy for the Characterization of Scanning Probes

3.1 Introduction

The utility of the FIM for preparing and characterizing tips destined for SPM experiments was considered by Hans-Werner Fink of IBM Zürich in the context of STM shortly after its invention [1]. The main advantage of an atomically defined tip apex is that if the exact atomic arrangement of the apex is known, the electronic structure of the tip and the lateral resolution of the STM are predetermined. The same detailed knowledge of the apex termination, as well as the tip radius, is useful for atomic force microscopy (AFM) experiments and important in the interpretation of results from combined STM and AFM experiments.

Largely unknown, the atomic-scale tip structure is directly responsible for image contrast [2, 3], as well as the details of the measured electronic properties by scanning tunneling spectroscopy [4, 5], chemical bonding forces by force spectroscopy [6, 7], and yield point of materials by indentation [8, 9]. In order to obtain quantitative and reproducible data, which could be considered as a benchmark for computational simulations, one requires a tip with known atomic structure. For example, FIM-characterized tips could act as atomically defined electrodes to build junctions to single molecules, where transport properties are sensitive to the atomic arrangement of the contact electrodes [10].

One must first sort out the technical challenges surrounding the experiment, starting with the reliable transfer of an atomically defined FIM tip to an SPM experiment: this involves moving the tip and sample from an initial separation of the order of meters to a working distance of some angstroms in a brief period of time and without crashing one into the other. Many questions need to be addressed concerning the implementation of FIM tips in SPM: Will the atomically defined tip be modified by impurities in the FIM imaging gas? If so, can this be avoided? Although UHV is very clean, it still has a finite rest gas pressure – how long will the atomically defined tip remain atomically defined in vacuum? How much time do we have to perform our atomically defined SPM experiment? How can we approach the tip to the sample and ensure that it doesn't crash or become modified upon interaction with the substrate?

This chapter begins with a brief introduction to FIM and SPM, and then in Sect. 3.2, we focus on the experimental methodologies of FIM which are most relevant to the characterization of SPM tips. Section 3.3 reviews research findings from STM, AFM, and nanoindentation experiments with atomically defined probes.

3.1.1 Field Ion Microscopy (FIM)

The field ion microscope was invented in 1951 by Erwin W. Müller [11] and by 1956 had achieved the first real-space images of matter with atomic resolution. The first FIM images were of the atomic arrangement of the apex of very sharp tungsten needles. By 1957, the surfaces of other refractory metals had also been imaged [12]. Although the atomic resolution of FIM is no longer unique among microscopes

(TEM, SEM, STM, and AFM have all demonstrated atomic spatial resolution), there still exist distinctive experimental applications of FIM. Particularly well suited to FIM is the study of diffusion of single atoms or clusters on crystal surfaces, and this technique has generated most of the existing experimental data about the diffusion of atoms and clusters on metal surfaces [13].

Another unique feature of the FIM is the possibility of integrating a time-of-flight (ToF) mass spectrometer to enable chemical analysis with single-atom sensitivity and a spatial resolution of several angstroms. The combined technique is known as atom probe field ion microscopy (AP-FIM) or more simply as the atom probe [14–17]. In AP-FIM, a pulsed field is applied to the FIM specimen to field evaporate a small amount of material from its surface to be chemically analyzed in the ToF unit; it is a destructive technique, consuming the sample as data is collected. Tien T. Tsong, a colleague of Müller's from the beginning of FIM, wrote in his book on AP-FIM [12] that the technique provides the "ultimate sensitivity in chemical analysis" because of its exquisite single-atom sensitivity.[1] Unlike scanning probe methods, AP-FIM can access the chemical composition in the bulk of samples, and technique development remains very active today in the computational reconstruction of the data into 3D element-specific atomic maps. Applications of AP-FIM include the investigation of chemical segregation of elements at crystalline defects (steels and semiconductors), local studies of grain boundaries in nanocrystalline materials (with grains too small for techniques like electron backscatter diffraction (EBSD) [20]), and short-range order in materials (e.g., in high-temperature superconductors).

3.1.2 Scanning Probe Microscopy

Scanning probe microscopy uses a physical probe to image surfaces by raster scanning the surface and monitoring some type of interaction between the probe's apex and the sample. In STM, a small current tunneling between the tip and the sample, on the order of pA to nA, is used as an imaging mechanism [21–23]. Due to the current's exponential dependence on the tip-sample distance, with one decade of variation per angstrom, excellent spatial resolution is possible. In AFM, the force or force gradient between the tip and sample is responsible for image contrast [24, 25]. Electrostatic, van der Waals, and chemical bonding forces all contribute to the force-distance profile, so the AFM's resolution depends on which particular force interaction is dominant.

STM and AFM are usually operated under feedback to maintain either constant current or force (or force gradient) while the tip scans the surface. This procedure traces out an isosurface of constant tip-sample interaction, often termed the "topography" of the sample. In particularly stable instruments, often at cryogenic

[1] We note that single-atom chemical sensitivity has also been achieved recently in STM and AFM techniques: inelastic electron tunneling spectroscopy in STM allows for measurement of the vibrational energies of individual chemical bonds, which is a form of chemical sensitivity – for example one can distinguish between hydrogen and deuterium bonds [18, 19]. In the case of AFM, however, it is more of a *relative* chemical sensitivity obtained by comparing force-distance interaction curves from different atomic species with the same tip. Absolute chemical identification relies on the specifics of the tip apex which is usually unknown [6].

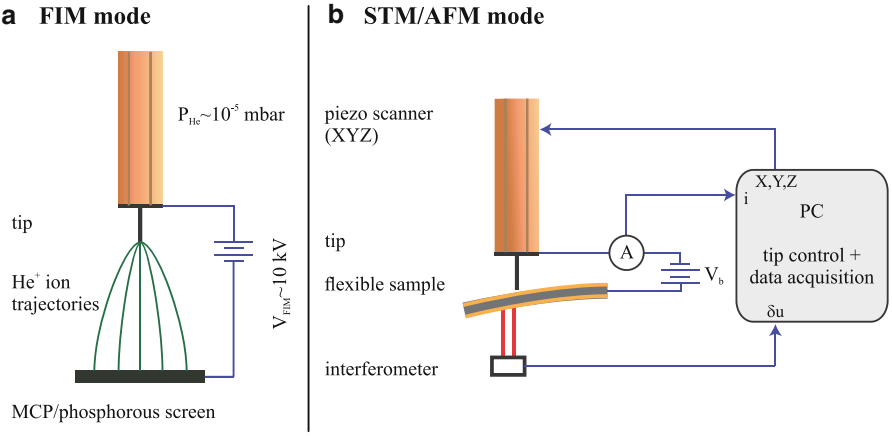


Fig. 5.1 Schematic of the microscope's two principle modes of operation: (**a**) FIM mode; (**b**) STM/AFM mode

temperatures, a constant height scan over the sample can be performed while the variations of current or force are recorded as a function of tip position, forming an "image" of these interactions. SPM can also be used to perform spectroscopy, in which one parameter is modified and the response of another is measured, such as force versus distance, current versus voltage, etc.

In all SPM experiments, the tip structure has a crucial role in contrast formation and data interpretation. Surface science has progressed to the point where the SPM community is able to study exquisitely well-defined surfaces, but the tip of the SPM remains mostly uncharacterized – often one must turn to atomistic modeling to guess at possible structures [7, 26]. Exceedingly few SPMs exist with in situ tip characterization facilities – in this chapter, we consider FIM as a characterization tool for the sharp SPM tips.

3.1.3 Combined STM/AFM/FIM

As an example of an apparatus which combines STM, AFM, and FIM, we describe the system used in our group's experiments [27–29]. The combined STM/AFM/FIM is operated in two modes illustrated in Fig. 5.1. In FIM mode, the apex of the sharp tip is imaged with atomic resolution. As illustrated in Fig. 5.1a, the measurement chamber is backfilled with He gas to $\sim 10^{-5}$ mbar, and a high positive voltage of ~10 kV is applied to the tip. The ionized He gas atoms, reporting on the atomic arrangement of the tip apex, are detected by a microchannel plate (MCP) and phosphor screen.

In the STM/AFM mode shown schematically in Fig. 5.1b, a cantilevered sample is placed under the tip.[2] The tip is approached to tunneling interaction under applied

[2] An unconventional setup which allows tungsten probes, compatible with the high electric fields in FIM, to be used as SPM tips. The development of new AFM force sensors such as the qPlus [30] and length extension resonator [31, 32] conveniently allow tungsten probes to be used for AFM.

bias V_B, while current I is measured by an ammeter [33]. A computer monitors the current and regulates the tip height with the piezo tube actuator to maintain a constant current. Meanwhile, a dual-beam interferometer is used to record the deflection of the cantilevered samples [34], which permits the measurement of forces acting in the tip-sample junction.

3.2 Experimental and Instrumental Methodology

3.2.1 Operating Principle of the FIM

FIM is a particularly simple microscopy technique in comparison to the complexities of electron optics in SEM and TEM, or the control systems and vibration isolation required for SPMs. In its most basic implementation, FIM requires a sample in the shape of a sharp tip, a phosphor screen at a distance of ~10 cm from the tip, a vacuum system backfilled with $\sim 10^{-5}$ mbar of He, and a high voltage supply.

In FIM, a high positive voltage is applied to the tip, and when the electric field approaches ~4 V/Å at the tip, He gas atoms will be ionized and accelerated toward the screen. The ionization of He atoms occurs with the highest rate near surface sites on the tip where the electric field is largest: the field is locally enhanced in positions of reduced radius of curvature such as at atoms located at the edges of atomic planes, individual atoms adsorbed in the middle of atomic planes, and over atoms contained in highly corrugated planes (such as the W(111) plane). The image which forms on the phosphor screen reflects the spatial distribution of the He ionization rate and thus gives atomically resolved information regarding the tip shape.

It is important to point out that the specimen must be shaped like a needle with a very sharp apex in order to achieve a sufficient geometric enhancement of the electric field at its apex.[3] Another important consideration in dealing with such high electric fields is that not all materials can withstand such fields. The destruction of the tip under the applied field can be avoided to some extent by cooling the tip to low temperatures in order to inhibit thermally activated field desorption. Another strategy for imaging softer materials is to employ a different imaging gas such as Ar or Ne which ionizes at lower electric fields, 2.2 and 3.75 V/Å, respectively, compared to 4.4 V/Å for He [10]. Tungsten is the only metal which can withstand room temperature He ion FIM without field evaporating during imaging. Iridium tips, for example, cannot be imaged by He ion FIM at room temperature, but can withstand the fields required to form a Ne ion FIM image [35].

The process of field ionization is illustrated in Fig. 5.2. The dipole attraction of gas atoms occurs near the apex in the presence of the strong field. If the tip is cooled, the gas atoms will thermalize to the tip as they hop over its surface – this contributes to a lower initial random thermal velocity when the gas atom ionizes and helps improve lateral spatial resolution (Sect. 3.2.2). The He gas atom has the highest probability of

[3]These fields are the highest achievable by laboratory techniques and are comparable in magnitude to those inside ionic crystals [10].

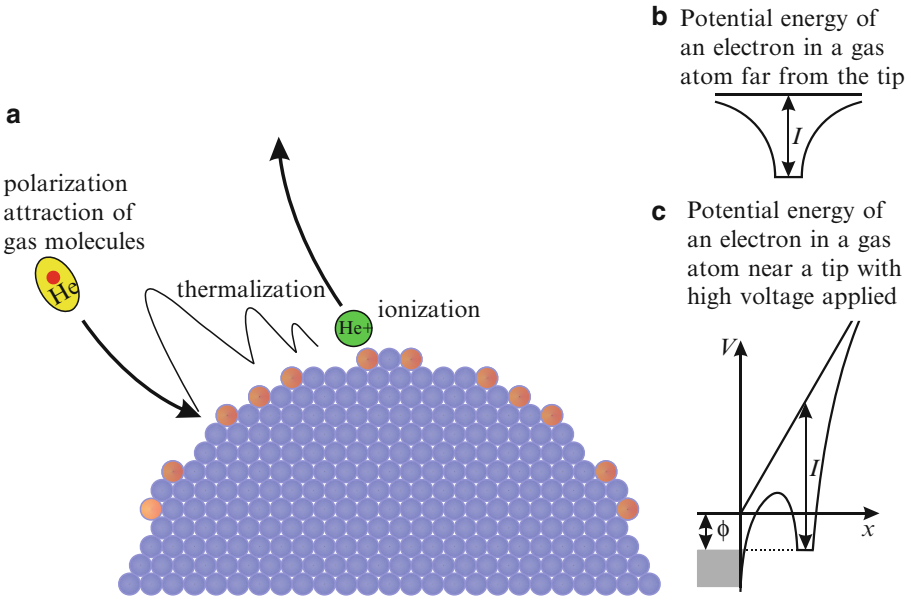


Fig. 5.2 (**a**) Side view of a tip apex showing schematically the dipole attraction of imaging gas atoms, thermal accommodation to the tip, and ionization over an atomic site of locally enhanced field (*orange*). (**b**) Potential energy diagram of a valence electron in a gas atom. (**c**) Potential energy diagram when the atom is within tunneling distance of the metal tip and in a large electric field

being ionized over a protruding atom where the field is locally enhanced, such as those indicated in orange. Once ionized, the He^+ ion is accelerated by the field toward a microchannel plate and phosphor screen for detection.

The loss of an electron from the gas atom to the tip happens by quantum mechanical tunneling. The potential energy landscape of a valence electron in a gas atom with ionization energy I is shown in Fig. 5.2b. In an applied field, the potential becomes sloped. When brought sufficiently close to a metal tip, as illustrated by Fig. 5.2c, the barrier between the electron state in the gas atom and an available electron state in the tip becomes small enough to tunnel through. Applying the WKB method to an equilateral triangle potential well, it is possible to calculate the barrier penetration probability at the critical distance of field ionization as [12]

$$D(F) = \exp\left\{-\left(\frac{8m}{\hbar^2}\right)^{\frac{1}{2}}\frac{2}{3}\left(I - 2\sqrt{e^3F}\right)^{\frac{1}{2}}\frac{I-\phi}{F}\right\}, \tag{5.1}$$

where m is the free electron mass, $\hbar$ is the reduced Planck's constant, e is the elementary charge, I is the ionization energy of the gas atom, F is the magnitude of the applied electric field, and φ is the work function of the tip. It is clear from the illustration of the barrier in Fig. 5.2c and by the result of Eq. 5.1 that the tunneling rate is strongly dependent on the ionization energy of the gas itself (increases with

decreasing ionization energy), as well as the magnitude of the applied field (increases with increasing applied field).

3.2.2 Spatial Resolution of the FIM

The excellent spatial resolution of the FIM allows us to resolve individual atoms on the W(111) plane, where the tip is sufficiently corrugated so that substantial variations in the electric field occur over the surface. We are often asked how it is possible to obtain atomic resolution images of tips at room temperature since most implementations of FIM are cryogenic – at least at liquid nitrogen temperatures, if not below. The answer has two components: Firstly, the extraordinary sharpness of our tips, compared to most used in traditional FIM, enhances the microscope's resolution. Secondly, low temperature, while necessary for studying the diffusion of adsorbed atoms (used to "freeze" their position on the tip's surface during high-field imaging), is not required for characterizing a stable tungsten tip.

We will now discuss the origins of the spatial resolution and show that for tips with sufficiently small radii, the expected spatial resolution is adequate for atomic resolution imaging. In the imaging process, helium atoms are ionized over specific sites on the tip – we consider what effects will broaden the projection of these ionization sites when the helium ions are visualized on the screen. Three factors affect this resolution [12]: the ionization disk size, Heisenberg's uncertainty principle, and thermal broadening. Since these effects are statistically uncorrelated, they are added in quadrature to give the total resolution broadening as a quadrature sum of the components listed above (in order):

$$\delta = \sqrt{\delta_0^2 + \delta_u^2 + \delta_T^2}. \tag{5.2}$$

The ionization disk size reflects an intrinsic diameter of the ionization zone above each surface atom and is approximated to be a constant on the order of $\delta_0 = 2.5$ Å [36]. The subsequent terms in Eq. 5.2 contribute to a broadening beyond this baseline resolution. The second term considers the Heisenberg uncertainty contribution on the tangential velocity component of the gas atom when it is ionized:

$$\delta_u = 2\left(\frac{\beta^2 r_t \hbar^2}{2kem_{\text{gas}}F_0}\right)^{\frac{1}{4}}. \tag{5.3}$$

In the above equation, β is a geometric factor taking into account image compression due to the fact that the tip is not a perfect hemisphere but has a shank. β is on the order of 1.5–1.8 [12] and is taken to be 1.65 in the following calculation. r_t is the tip radius, k is a geometric field reduction factor of ~6 (depends on tip shape, usually $3 < k < 8$ [37]), m_{gas} is the atomic mass of the imaging gas, and F_0 is the magnitude of the ionizing electric field.

The last term represents the broadening due to the initial thermal velocity of the imaging gas atoms:

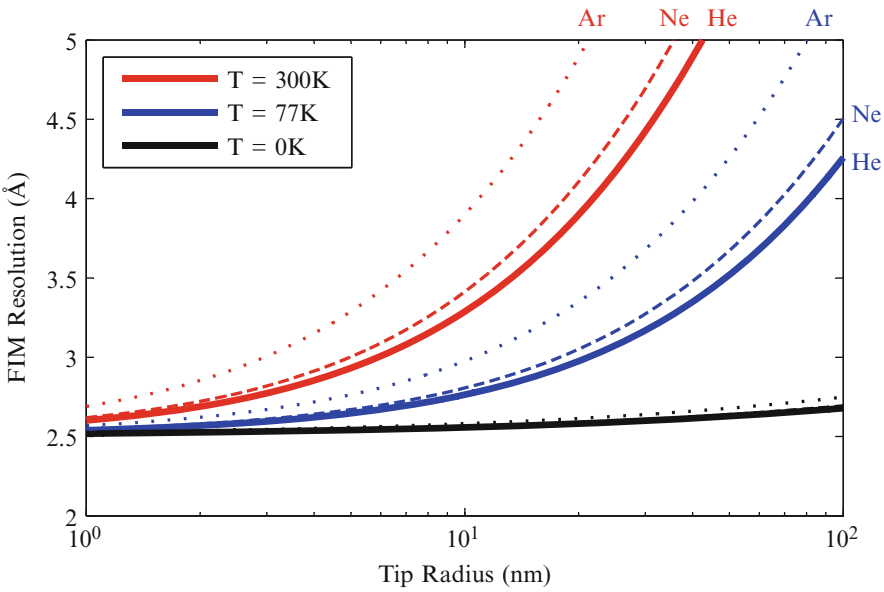


Fig. 5.3 Resolution of FIM as a function of tip radius at room temperature, liquid nitrogen temperature, and absolute zero. Curves for ionization fields corresponding to He, Ne, and Ar imaging gases are shown as *solid*, *dashed*, and *dotted lines*

$$\delta_T = 4\left(\frac{\beta^2 k_B T r_t}{KeF_0}\right)^{\frac{1}{2}}, \tag{5.4}$$

where k_B is the Boltzmann constant and T is the temperature of the gas atom; the other variables have been described previously.

The parameters over which one has practical experimental control are temperature, tip radius, and species of imaging gas. The choice of imaging gas affects the mass term in Heisenberg broadening, Eq. 5.3, but this is generally outweighed by the modification of best imaging field which enters more strongly into Eq. 5.4 for thermal broadening ($F_0 = 4.4$, 3.7, 2.2 V/Å for He, Ne, and Ar, respectively). The combined resolution of FIM, given by Eqs. 5.2, 5.3, and 5.4, is plotted in Fig. 5.3 as a function of tip radius. Temperatures of 300, 77, and 0 K are shown in red, blue, and black, respectively. For each temperature, the resolution achieved by He, Ne, and Ar is indicated by solid, dashed, and dotted lines. Our FIM tip radii mostly fall in the range of 3–12 nm, where for room temperature (and below), the resolution is sufficient to image atoms on the W(111) plane spaced by ~4.5 Å. Larger tips in the range of tens to hundreds of nanometers clearly require low temperatures to achieve atomic resolution.

A last comment on resolution is that the preceding discussion applies to the smallest distance between surface atoms that can be resolved in an image. However, when an adatom is deposited on a surface for diffusion studies in FIM, one can fit

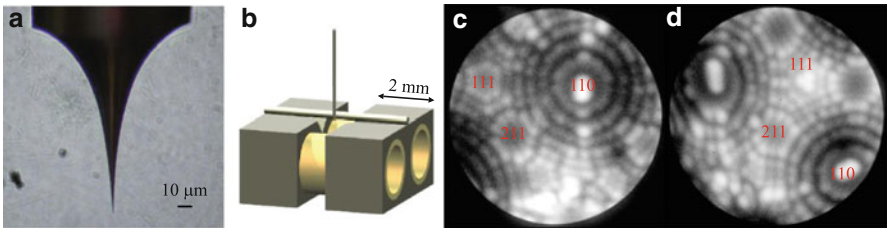


Fig. 5.4 (**a**) Optical microscope image of an electrochemically etched 0.125 mm diameter tungsten wire; (**b**) tip holder design; (**c**) W(110) tip with a radius of 9.4 ± 0.8 nm; (**d**) W(111) tip with a radius of 9.6 ± 0.7 nm

the image intensity distribution and locate its centroid to ~0.3 Å [12]. Another important effect that doesn't enter into the resolution equation is the selective imaging of atoms where the electric field is enhanced by local corrugation and the suppression of imaging on large flat planes of atoms. On smooth, densely packed planes such as the W(110), FIM resolution is effectively nonexistent because surface atoms are not imaged.

3.2.3 Tip Etching and Preparation

Tungsten tips for FIM and SPM experiments are etched in a 9.8 M KOH solution by electrochemical etching at 3 V_{DC}, along the lines of standard procedures found in the STM literature [38–40]. The procedure and design of an electrochemical bath was recently reported by our group [41], and very detailed accounts related to tip preparation can be found in the PhD thesis of Till Hagedorn [28] and the MSc work of Anne-Sophie Lucier [37, 42]. In this section, we will focus on tungsten tips because of the simplicity with which they can be fabricated and imaged in room temperature FIM. For an account of etching iridium tips for FIM/SPM in $CaCl_2$, we refer the reader to Ref. [35].

The typical concave shape of tungsten STM tips is shown in an optical microscope image in Fig. 5.4a. This shape forms automatically during the etching process, having to do with the meniscus shape and currents in the etching solution around the tip shank. Routine success in creating sharp tips during etching is mostly dependent on obtaining a meniscus around the wire which is undisturbed by vibrations, bubbles, or debris in the etching solution and a reliable electronic circuit which removes the applied bias when a sudden drop in electrochemical current is detected.

The etched tips are transferred to UHV and are annealed to an orange glow to remove the tungsten oxide layer and any physisorbed gas on their surfaces. The tip holder design, shown in Fig. 5.4b, is particularly well suited for heating and degassing the entire tip wire. The tungsten tip wire is spot welded to a 0.25 mm diameter annealed 304 stainless steel wire (Alfa Aesar), which is in turn spot welded to the two electrically isolated halves of the tip holder. The stainless steel wire acts as a filament to resistively heat and degas the entire tungsten wire. Mounting tips to a filament is common in conventional FIM, implemented not

only to clean the tips but also in order to rapidly warm them momentarily from cryogenic temperatures to study diffusion of adatoms on their surfaces [12, 13].

After annealing, tips are field emitted against a copper anode placed several mm from their apices. The voltage at which field emission occurs gives a good indication of their sharpness. Since electron emission necessitates a field of ~5 V/nm and ionization of helium gas requires ~5 V/Å, when an appreciable field emission current (~100 nA) is observed at an applied voltage of <1 kV, one can be confident that the tip is sufficiently sharp that an ion image can be obtained in FIM at an applied voltage of <10 kV (the limit of our high voltage supply). Our experience with field emission indicates sensitivity to the placement of the anode electrode and the geometric details of mounting the tip to the holder (long or short tip wire) – these observations are supported and explained by a recent paper by Setvín et al. [43]. We therefore only use field emission as a rough guide to tip sharpness.

Tungsten tips with (110) and (111) apex orientations are commonly used in our studies. W(110) tips result from etching 0.1 mm diameter polycrystalline wire (Alfa Aesar). Polycrystalline tungsten wire is highly textured from the cold drawing process and consists of long and thin ~1 × 50 μm grains oriented in the (110) direction to within a few degrees of its axis [44]. This strong crystallographic texture is common to all cold drawn bcc metals [45]. For our tips having typical apex radii of a few nm, the relevant part of the "polycrystalline" tip is effectively a single crystal. W(111) tips are etched from 0.125 mm diameter single crystal wire oriented to within 2° of the axis (Applied Physics Technologies).

FIM images of W(110) and W(111) tips are presented in Fig. 5.4c, d, respectively. Low-index crystal planes are identified in the micrographs. The planes can be visually identified by their symmetry (twofold or threefold in these cases), their relative size, and placement with respect to each other. Stereographic projection maps, such as the one published in Fig. 3.6 of Ref. [12], are helpful to identify the planes with respect to each other. The radii of the tips shown in Fig. 5.4 are 9.4 ± 0.8 nm and 9.6 ± 0.7 nm, respectively, as determined by averaging results from ring counting between all visible (110), (211), and (111) planes. The gray scale images were created using the green channel (the phosphor screen glows green) of an RGB image obtained by averaging many individual photographs. Image contrast is adjusted using a logarithmic curve to help bring out features which are not otherwise visible in the dynamic range of print or computer displays. This processing technique lends our FIM data a remarkably high printed quality.

3.2.4 Radius Determination by Ring Counting

The most straightforward way to determine the radius of an FIM tip is to use the "ring counting" method [12, 37, 46]. With the assumption that the apex of the tip has spherical envelope, one can count the number of atomic steps between crystallographic planes, which show up as "rings" in the FIM micrograph, and determine the radius by simple geometry (to follow). A spherical envelope is a good approximation within the region of the tip in which we are interested – ball models of tips created by cutting a bcc crystal in a hemisphere give good correspondence to the features seen in FIM images. It is worth noting that more elaborate techniques have

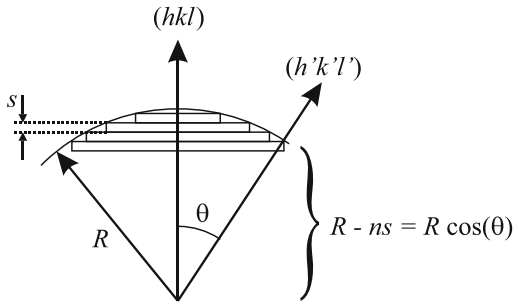


Fig. 5.5 FIM tip apex with radius R showing geometry for ring counting. Planes of interlayer spacing *s* are normal to direction *(hkl)*, and *n* rings are counted between poles *(hkl)* and $(h'k'l')$. The angle between these poles is θ

been developed to extract the surface profile of FIM tips from features in micrographs [47, 48], essentially by using ring counting between various crystallographic poles to extract Cartesian (x, y, z) coordinates of the surface atoms. These are particularly useful if one is interested in determining the cross-sectional profile out into the far edges of the FIM image (which in our case is blocked by an aperture).

The ring counting method can be described as follows [12]: Assuming a spherical envelope of the tip apex, the local radius of curvature, R, between two crystallographic poles separated by angle θ can be found by counting the number of visible rings, n, between them. Using the interlayer spacing, s, corresponding to the appropriate crystal plane, the local radius of curvature is given by

$$R = \frac{ns_{(hkl)}}{1 - \cos\theta}. \tag{5.5}$$

This equation describes the geometry illustrated in Fig. 5.5.

For the ring counting estimations to be accurate, each counted ring must correspond to a *single* atomic step of type *(hkl)*. We will soon demonstrate that in FIM micrographs, a single "ring" can correspond to multiple atomic planes of height s – counting rings is not equivalent to counting steps. The underestimation of FIM tip radii can occur when the rings appearing in the micrograph correspond to *more than one* atomic plane. The standard description of ring counting could be more precisely expressed in the following way: assuming a spherical envelope of the tip apex, the local radius of curvature is determined by counting the number of steps, n, of height s between crystallographic poles with angle θ between them.

The ring counting method can be applied to different choices of *(hkl)* pole, but the rings of the (110) plane are the most straightforward to identify because they have the largest step height in the bcc crystal. The (110) plane also happens to be the apex of most polycrystalline tungsten tips as a consequence of the wire's manufacturing by cold drawing [44].

In Fig. 5.6, we present ball models of tungsten tip apices of radii 3.0, 4.7, 6.0, and 9.0 nm. The models were created by carving a hemispherical shell from a bcc crystal with a (110) apex. The atoms in the outermost 0.05 nm shell are shaded lighter in

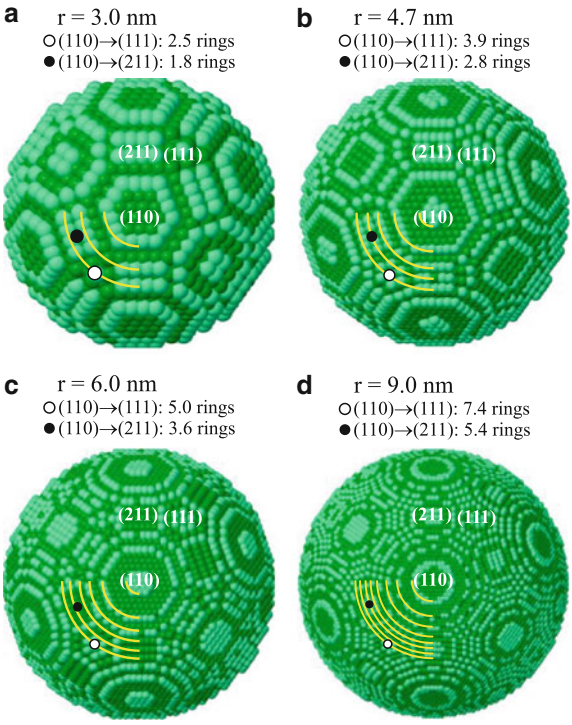


Fig. 5.6 Top view (looking toward the apex) of ball models of W(110) tips with radii (**a**) 3.0 nm, (**b**) 4.7 nm, (**c**) 6.0 nm, and (**d**) 9.0 nm. Quarter-circle lines highlight the (110) rings at step edges. The center of the (111) and (211) poles are indicated by *white* and *black circles*, respectively

order to highlight the atoms at terrace edges which would be imaged brightly in FIM (a common method of visualizing atomic geometry with ball models [49, 50]).

As the tip radius increases, the size of crystallographic facets increases – for example, the (211) facet has just two rows of atoms in Fig. 5.6a but has five rows of atoms in Fig. 5.6c. Correspondingly, the number of rings increases between the centers of crystallographic poles. From Eq. 5.1, we have calculated the expected number of rings n between the (110) apex and the (111) and (211) poles, indicated in Fig. 5.6 with corresponding white and black circles. The centers of these planes are indicated by circles on the ball models.

The expected number of rings corresponds well with the number of rings counted from the tip apex to the center of the crystallographic poles (the rings are indicated by concentric quarter circle lines at the edge of the (110) steps). The number of rings can be thought of as the number of (110) steps that must be descended from the (110) apex in order to reach the center of the $(h'k'l')$ pole in question. For these tips of relatively small radii and for the small angles between the apex and the (111) and (211) directions, there is a single (110) plane for each ring; therefore, the estimation of ring counting is accurate.

Comparing the calculated number of rings to the rings visible in the ball models, it is apparent that a better estimation of the tip radius is obtained using a count of n–1 instead of n: this off-by-one error can be explained in Fig. 5.5 where it is the

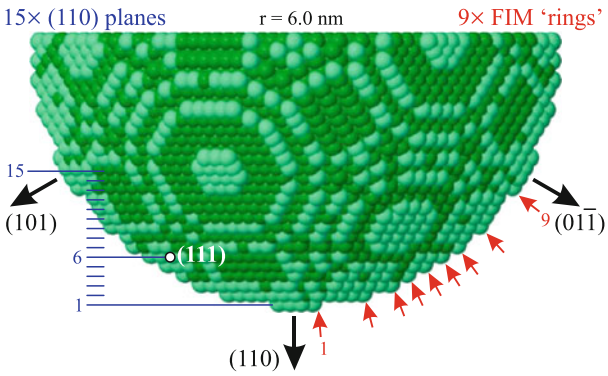


Fig. 5.7 Side view of the 6.0 nm radius W(110) tip presented in Fig. 5.6c. There are 15 layers of (110) planes between the apex and the (101) facet (*dark blue lines*), but only 9 "rings" apparent in the micrograph (*red arrows*). The estimation based on 14 × 0.446 nm yields a radius of 6.2 nm, whereas 9 × 0.446 nm yields an underestimated radius of 4.0 nm. The (111) apex is shown at layer #6 from the (110) apex. The angle between (110) and (111) is sufficiently small that the number of rings corresponds exactly to the number of (110) steps

number of steps crossed to get from *(hkl)* to $(h'k'l')$ that matters (one less than the total number of rings). This is usually a small correction but becomes increasingly important with decreasing tip radius. This concern is equivalently expressed by starting to count rings at 0 rather than 1, as done by Webber [46].

The first serious error that can occur in ring counting consists of counting FIM rings which correspond to more than one atomic plane of type *(hkl)*. This becomes problematic when rings are counted between planes of large angular separation (e.g., (110) type planes that are 60° apart [51]). Shown in Fig. 5.7 is the side view of the 6.0 nm tip presented in Fig. 5.6c. Counting the rings between (110) and $(01\bar{1})$ yields nine rings, indicated by red arrows on the right half of the image. As the angle from the apex increases, the visible rings begin to correspond to more than one (110) plane. This is illustrated by the blue "ruler" on the left half of the image where we have counted 15 atomic planes between the (110) apex and the center of the (101) plane. Using $n = 9$, we obtain a radius of 4.0 nm, whereas a more accurate estimate is obtained using $n–1 = 14$, yielding a radius of 6.2 nm.

A second common ring counting error arises from the use of the wrong interlayer spacing. The interlayer spacing s must correspond to that of the *(hkl)* pole – the initial pole – not $(h'k'l')$, the final pole. Using the (111) plane spacing rather than (110), Urban et al. [52] deduced a tip radius of 14.4 nm, whereas we estimate a radius of the order ∼32 nm by counting ∼21 rings from (110) to (211). These problems are again seen in Pitters et al. [53] where the 3 and 5 nm radii tips determined by the authors are actually of the order 6 and 10 nm, and also in Rezeq et al. [54] where the 1.4 nm radius apex should be ∼4.8 nm (although the image resolution makes the identification of (110) and (111) planes difficult).

To summarize, the key elements to proper radius determination by ring counting are as follows:

- n must be accurately determined – its value must correspond to the number *single* steps of type s.
- s must correspond the plane spacing of (hkl), not $(h'k'l')$.
- n should be replaced by n–1 for a more accurate radius estimation for small tips (or equivalently, counting should begin at zero)

We also urge the use of (110) planes for ring counting due to their large step height and not (111): rings corresponding to single (111) steps are very difficult to discern because of the small (111) step height. The routine construction of ball models of FIM tips also helps to familiarize the experimenter with the appearance of tips with different radii.

Finally, to quickly estimate a tungsten tip radius in nm, one can simply multiply the number of rings from (110) to (211) by 1.66 nm · ring^{-1} or multiply the number of rings from (110) to (111) by 1.21 nm · ring^{-1} (these factors are $s_{(110)}/(1–\cos\theta)$).

3.2.5 Advanced Tip Preparation: Etching and Faceting

In this section, we mention other tip preparation techniques beyond the standard procedure of tungsten tip etching and FIM characterization. Gas etching and tip faceting are well established in the FIM community and offer exciting opportunities to atomically engineer the apices of SPM tips.

The sharpening of tips using nitrogen gas is rather straightforward and has been well studied in the context of building sharp tips for field ion emission in helium ion microscopes or electron emission for coherent electron sources and point projection microscopes. The nitrogen sharpening process was first reported by Rezeq et al. [54] and patented by the same authors in 2008 [55].

The process occurs by adsorption of nitrogen on the tungsten tip shank, illustrated in Fig. 5.8. The nitrogen cannot bind to the very apex of the tip because the electric field there is too large – the gas is ionized and repelled before it can reach the tip surface. Nitrogen can, however, bind to the shank of the tip where the field is not as high. This happens by dissociative adsorption in which a single nitrogen atom forms a chemical bond to a tungsten atom on the tip's surface (this reaction is discussed in Sect. 3.2.6 and is addressed specifically in Refs. [56, 57]). The W-N bond weakens the W atom's bond to its neighbors and lowers the field necessary to evaporate the W-N complex, shown schematically in the patent illustration reproduced in Fig. 5.8a, b.

The weakened tungsten atoms are thus preferentially etched by field evaporation from the tip shank. The resulting reduction in the local radius of curvature of the tip apex is illustrated in Fig. 5.8c. The final profile of the tip is somewhat different than the original: a shoulder is formed where the field on the shank is no longer strong enough to evaporate the W-N (this shape has been experimentally verified by SEM in Ref. [52]). At its apex, the radius is much reduced and can be etched to terminate in a single atom.

One distinct advantage of this tip sharpening technique is that it can be monitored by helium ion FIM imaging during the etching process. Figure 5.9a–e shows a sequence of FIM images during nitrogen sharpening of a W(111) tip at room temperature, beginning at a radius of ~4.3 nm and ending with a radius of ~2.5 nm

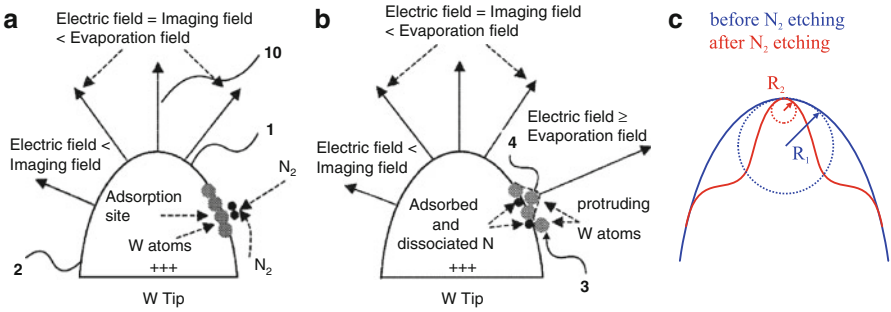


Fig. 5.8 Schematic description of the sharpening process. (**a**) N_2 can only adsorb to the tip shank where the field is lower than at the apex. (**b**) The W-N bond weakens the bonding of the W atoms to the tip, and they field evaporate, leading to a preferential loss of material around the tip shank. (**a**) and (**b**) public domain illustration from Ref. [55]. (**c**) Tip profile before etching (*blue*), and after (*red*), illustrating a reduction in local radius of curvature at the apex and the final "shouldered" shape of the tip

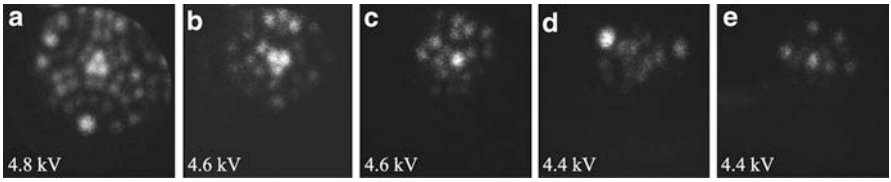


Fig. 5.9 (**a**–**e**) Sequence of FIM images during nitrogen etching at 5×10^{-7} Torr N_2, constant pressure

by image (d). The applied voltage was reduced as necessary to slow evaporation of the tip apex atoms while the apex radius decreased. In this experiment, the nitrogen pressure was constant at 5×10^{-7} Torr. The atomic geometry of the apex could not be completely stabilized due to the nonadjustable nitrogen pressure and the lack of cryogenic cooling during this experiment. However, it demonstrates the impressive efficiency of the technique.

Nitrogen etching may serve as a useful technique to produce tips of varying radii for nanomechanics studies; however, the uncharacterizable shape of the tip shoulder (Fig. 5.8c) could present difficulties in predicting the mechanical properties of the apex. The technique is certainly applicable to experiments with atomically defined SPM junctions provided that single-atom tips can be stabilized (which it can be, with proper control).

Faceting of crystal surfaces is another valuable technique for obtaining single-atom sharp tips. Many crystal surfaces can exhibit faceting – the general methodology is to anneal the surface in the presence of an adsorbed thin layer of another material or in an applied electric field. The ad-layer or applied field is chosen to alter the relative surface energies of the tip's atomic planes in a specific way.

Then, annealing the tip under such conditions allows the low energy planes to expand and intersect, forming an atomically-sharp nano-pyramid at the tip apex.

Much of the initial surface science investigation of faceting systems such as the W(111) surface under adsorbed Pd (as well as other noble metals), W(111) under oxygen, and Ir(210) under oxygen was conducted by Ted Madey's group under LEED and STM investigation of the surfaces of bulk crystals [58–60]. Tien T. Tsong, who worked on FIM from its inception, has succeeded in transferring many of Madey's surface science systems to the apices of sharp FIM tips in order to engineer faceted single-atom tips [61–68]. All of these studies (with exception of the Ir(210) tips) involve the expansion of the (211) planes on a W(111) tip until its apex becomes a three-sided pyramid formed by the intersecting (211) planes (for reference, a W(111) tip can be seen in Fig. 5.4d). The faceting of the Ir(210) surface under oxygen exposure forms a pyramid from the (311), $(31\overline{1})$, and (110) planes with a single-atom apex pointed in the (210) direction [64].

Tip faceting by thermofield annealing (annealing under a large electric field) favors the growth of large (110) terraces. Applied to a W(111) tip, it can be used to create a pyramid in the opposite manner as described for noble metal plating – the (110) terraces expand until they intersect to form a three-sided pyramid at the expense of the (211) planes [69–72]. Thermofield annealing has the advantage of being carried out without the need for an adlayer of oxygen or metal on the tip surface.

The pyramidal geometry of faceted tips would be of considerable interest not only for atomically defined SPM experiments but also in atomic-scale nanoindentation experiments due to the simple relationship between their projected contact area and penetration depth (a desirable feature which is exploited in traditional nanoindentation testing [73]).

3.2.6 Tip Integrity: "Force Field" Protocol and Rest Gases

In order to carry out an SPM experiment with an atomically defined FIM tip, it is necessary to address issues of tip integrity. This is to ensure that when used in SPM, the apex is identical to that characterized in FIM. We will first discuss what is known about the reaction of gas molecules with the surface atoms of tungsten tips and then present a protocol to ensure that the tip structure remains intact between FIM and SPM. Another matter to be considered is how long the atomic structure of the tip is expected to last due to the finite rest gas pressure in UHV – this will determine how promptly an experiment must be performed such that the atomic configuration of the apex is known with reasonable statistical confidence.

The interaction of gases with metal surfaces was studied extensively in FIM by Erwin Müller (the inventor of FIM) at Penn State University, Gert Ehrlich at the University of Illinois at Urbana-Champaign, and Holscher and Sachtler at Shell Research in the Netherlands in the early 1960s. Here, we review the experimental findings for the adsorption of typical rest gases found in a UHV system (N_2, CO, O_2, H_2O, and H_2) on tungsten tips.

Nitrogen adsorbs on tungsten by dissociation, that is, as a single N atom chemically bound to a W tip atom [57]. When imaged, it appears brighter and larger than regular tip atoms [74]. However, the N-W bond is very strong and weakens the W's

bond to its neighbors. Due to the weakened substrate bonding, the N-W complex may field evaporate (as a unit [16]) at fields lower than those necessary for imaging [56]. Missing W atoms in an FIM image could therefore be an indication of N adsorption.

Carbon monoxide is less corrosive than N_2 [57]; however, it was still found to remove substrate atoms when field desorbed, leaving behind vacancies [75]. Oxygen corrodes tungsten in a manner similar to nitrogen, though less aggressively [57]. Again, the presence of oxygen is inferred by missing atoms [76]. Water was shown to remove tungsten atoms down to liquid He temperatures [57].

The adsorption of hydrogen has no corrosive effect on tungsten tips, nor can it be detected in FIM imaging [57, 77]. However, changes in field emission are detectable upon hydrogen adsorption.

In summary, the bonding of gas molecules to tungsten tips often occurs by dissociation of the molecule and a weakening of the bonding of the underlying W atom to its neighbors. The weakened backbonding leads to the phenomenon of adsorbate-induced field desorption during imaging. Therefore, both bright spots and missing W atoms in an FIM image are evidence of gas adsorption. For the interested reader, Table 5.1 recounts in more detail the results of adsorption studies of several types of gases on both tungsten and iridium tips.

Dedicated FIM systems have very stringent vacuum requirements due to their intended application to adatom diffusion. They are designed for high-temperature bakeout (limited to 300 °C by the microchannel plate (MCP)), and extreme procedures are carried out in order to minimize gas evolution [79].[4] In less ideal systems where the FIM is combined with other instrumentation (i.e., an SPM), one will likely have a larger concentration of corrosive gas molecules in the system during FIM imaging than under normal UHV conditions [80].[5]

Figure 5.10 demonstrates the rapid modification of an FIM tip by imaging gas impurities. Starting with the clean tip apex prepared by field evaporation (Fig. 5.10a), we momentarily lower the imaging voltage from 5.1 kV to 0 V and back (this procedure took 40 s). The image in Fig. 5.10b shows the changes that have occurred to the tip's atomic structure in this short time. This image is a color superposition image[6] in which the initial image appears in green and the subsequent image appears in red. Atoms which have been removed from the initial image are colored green, and those that have appeared in the second image are colored red. Both red and green sites are evidence of gas adsorption, and the ~30 changes visible on the tip's 120 nm^2 surface area are certainly not encouraging to

[4]For example, the MCP is bombarded by 200 eV electrons for many days to remove gas atoms trapped in the channels.

[5]Even in the case of admitting ultrapure He through a heated quartz tube, the normal pumping speed of the UHV system may have to be sacrificed during FIM. In our case, the turbo pump must be valved off as the heated quartz cannot provide a sufficient flux of He to reach 10^{-5} mbar.

[6]A technique used by Müller with film and color photographic printing to identify individual changes among the many atomic sites on a FIM tip [81]. Here, it is done digitally.

the prospect of maintaining the atomic-scale tip structure long enough to do an SPM experiment with it!

Thankfully, all is not lost: due to the much higher ionization energy of He compared to all other gases [82], when large fields are applied to the tip (in the vicinity of the FIM imaging voltage), impinging gas molecules are easily ionized and will be repelled from the tip before they can chemically react with the tungsten atoms on its apex. We have found experimentally that reducing the tip voltage to ~80 % of the FIM imaging voltage is sufficient to prevent contaminant gases from reacting with tip atoms over extended periods of time. We call this the "force field" method and demonstrate its efficacy in Fig. 5.10b and c where no changes to the atomic structure of the tip can be identified.

Table 5.1 Adsorption and corrosion behavior of various gases on tungsten and iridium FIM tips

Gas	Tungsten tips	Iridium tips
N_2	Adatoms appear bright, larger. Adatoms observed on highly corrugated planes and at steps – not within the close packed (110), but at the edges. More adatoms near (310) rather than (111) – this anisotropy is attributed to difference in N_2 dissociation rate [74]	N2 adsorbs as a molecule (without dissociation) between Ir atoms. Much less corrosive to Ir than it is to W (weaker bond) [57]
	Nitrogen binds strongly to W. Perturbed by the act of adsorption, the W can be field evaporated at regular imaging fields [56]	
	N binds on top of W sites (the N_2 molecule is dissociated, measured by mass spectrometry). Most N field desorbs before the ion emission is bright enough to be photographed (missing atoms could be sites of previously adsorbed N). W atoms were removed at fields lower than useful for imaging [57]	
	W-N complexes field desorb as a unit, reported in the first paper on the time-of-flight atom probe [16]	
CO	Found to be less corrosive than N_2. During FIM, CO is most corrosive when dissociated due to O adsorption on W which removes W substrate atoms. CO is dissociated by the energetic electrons removed from the He+ during the FIM process. Adding H_2, as a source of even higher energy electrons (in addition to the He imaging gas) enhanced the dissociation rate of CO [57]	Much less corroded than W [57]
	CO adsorption was found to rearrange substrate atoms. At 300 K, this leads to surface corrosion leading to vacancies underneath adsorbed molecules. Chemisorbed CO leads to "promoted field desorption" whereby the adsorbed species evaporates before it can be imaged, leaving behind a vacancy [75]	

(*continued*)

Table 5.1 (continued)

Gas	Tungsten tips	Iridium tips
O_2	Seems to be less corrosive than N2, but not as extensively studied [57]	
	W-O complexes are field desorbed together, observed in Ar ion FIM [78]	
	W-O complexes field desorb as a unit, reported in the first paper on the time-of-flight atom probe [16]	
	In He ion FIM, adsorbed oxygen cannot be directly observed on the surface; its presence is inferred from corrosion damage [76]	
H_2O	Studied in J. F. Mulson PhD thesis. Shown to remove W surface atoms (as well as Pt), even when surface is kept at liquid He temperature [57]	
H_2	Adsorption causes significant changes to the field emission pattern of the tip. However, no change can be detected in FIM. During FIM, a perturbation of the adsorbed H_2 layer is attributed to the bombardment of electrons coming from ionized He+ imaging gas [77]	H_2 could not be imaged, but removal of atoms, particularly in the bright (110) zone boundary, is attributed to H_2 adsorption [57]
	H_2 did not have a corrosive effect and could also not be detected [57]	

The following "force field" protocol is therefore suggested to preserve the tip apex from gas impurities in FIM/SPM experiments:

1. Prepare a clean tip by field evaporation in FIM.
2. Reduce applied voltage to ∼80 % ("force field").
3. Pump imaging gas, refill liquid nitrogen cold traps, flash TSP while "force field" is on.
4. Ramp down "force field" voltage when base pressure has recovered.
5. SPM experiment.

Finally, we must consider the fact that during the interval of the SPM experiment, the FIM tip will be subjected to contaminants in the UHV rest gas. We will consider the likelihood of rest gas molecules impinging on a 1.16 nm^2 area which corresponds to the area of the W(111) tip trimmer apex, plus the perimeter of the second layer of atoms on which it is supported [80]. The following estimations establish an upper bound on tip contamination as adsorption probabilities are considered to be unity.

The gas composition of the UHV rest gas was measured by a residual gas analyzer (RGA) (located in a different – but similarly pumped – UHV chamber used for sample preparation) yielding pressure fractions of the individual rest gas species, n_i. Using the total pressure reading of our measurement

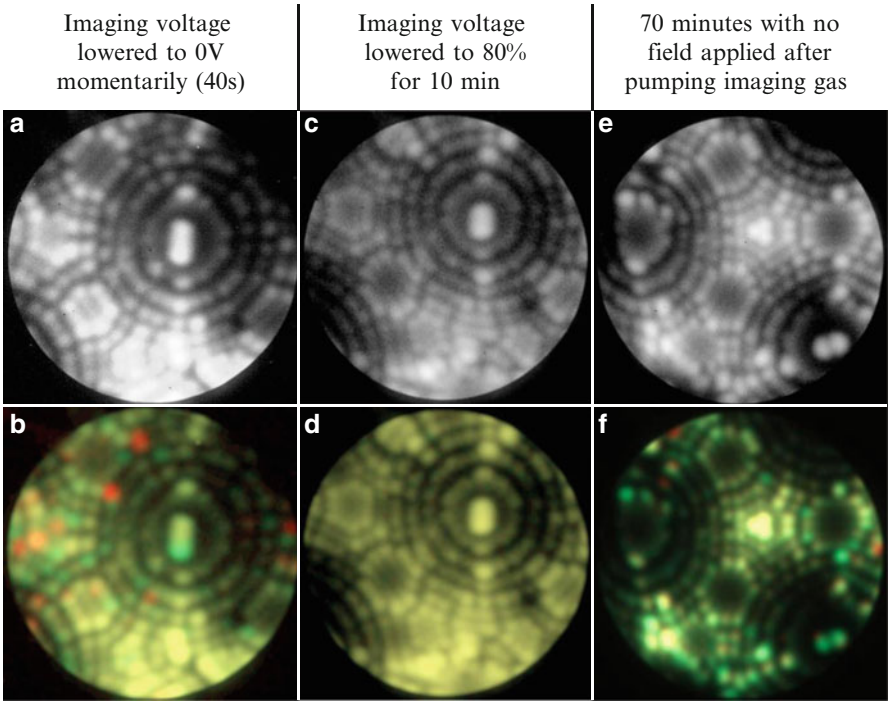


Fig. 5.10 (**a**) (110) tip at 5.1 kV; (**b**) color superposition image of (**a**) with the FIM image after the imaging voltage was momentarily lowered and raised – about 30 atomic sites show modifications; (**c**) (110) tip at 5.0 kV; (**d**) color superposition image of (**c**) with the FIM image after waiting 10 min with the voltage lowered to 4.0 kV – no changes are observed to the atomic structure; (**e**) (111) tip at 6.0 kV; (**f**) color superposition image of (**e**) with the FIM image after waiting 70 min in UHV (From Ref. [80] © IOP Publishing. Reproduced with permission. All rights reserved)

chamber gauge, $P_{\text{gauge}} = 5 \times 10^{-11}$ mbar, the partial pressures, p_i, of the component gases can be calculated from

$$p_i = n_i \frac{P_{\text{gauge}}}{\sum_i \frac{K_i}{K_{N_2}} n_i}, \tag{5.6}$$

where K_i/K_{N_2} is the ionization sensitivity of individual gas species relative to that of N_2 [83]. Combining the Maxwell-Boltzmann velocity distribution of the gas particles with the ideal gas law [84], we obtain the flux of each species as

$$F_i = \frac{p_i}{\sqrt{2\pi m_i k_B T}}, \tag{5.7}$$

where m_i is the atomic mass of the gas species, k_B is the Boltzmann constant, and T is the temperature.

The probability of k gas molecules arriving in area A on the tip during time τ is given by a Poisson distribution (assumes arrival is independent of time and location) [85]:

$$P(k) = \frac{e^{-FA\tau}(FA\tau)^k}{k!}. \tag{5.8}$$

The probability of obtaining more than one arrival on the tip apex area (i.e., $k > 1$) can be easily obtained using the property that the distribution is normalized:

$$P(k > 1) = \sum_{k=1}^{\infty} P_k = 1 - P_0 = 1 - e^{-FA\tau}. \tag{5.9}$$

The rate of tip contamination is described in two ways: In the first way, we calculate the duration of an experiment such that in 5 % of experiments of this duration, more than one gas molecule would have impinged on the apex (i.e., on average, 1 in 20 experiments having this duration would be carried out with a modified tip). In the second way, we calculate the probability of more than one gas molecule impinging on the apex during a 60 min delay (chosen as a minimum reasonable SPM experiment duration which must include tip transfer, sample approach, etc.). The results of these calculations are shown in Table 5.2. Note that other unidentified gases (not listed) make up 2.2 % of the gas composition, meaning they have approximately the same statistics as N_2.

We notice immediately that hydrogen is problematic because of its high pressure fraction and flux (the latter due to its low mass). However, its presence goes undetected in the methods employed here – FIM characterization is blind to hydrogen, and it is known to have no corrosive behavior to tungsten tips [57]. After hydrogen, the next most common gases (H_2O, N_2, and CO) are at a nearly acceptable background level if an experiment is completed within a short period of time ($\sim$1 h).

Figure 5.10e illustrates the typical rest gas contamination of our tungsten tips which have been preserved with a "force field" until the UHV system had returned to base pressure. The tip was left in UHV for 70 min after the "force field" was turned off. The color superposition image in Fig. 5.10f shows changes to $\sim$30 atomic sites. (The number of changes is overestimated due to contamination during the FIM start-up procedure [80].) Assuming an approximate mass of 28 amu, the changes to the tip during this time interval indicate an effective contaminant pressure of $\sim 2 \times 10^{-11}$ mbar. This number is consistent with the calculations presented in Table 5.2 and the expected overestimation of contamination due to the FIM start-up procedure.

Experiments with atomically defined tips must be performed quickly, even in a clean UHV environment. This has important consequences for the design of a combined FIM/SPM experiment: since the sample should also not be subjected to contamination from the imaging gas, the tip (or sample) must be transferred from a separate vacuum chamber in a reasonable time frame, and the coarse approach of the tip to the sample surface must be done with minimal delay.

Table 5.2 Table of typical UHV rest gas species, their partial pressures, fluxes, and calculated contamination times and probabilities for a 1.16 nm^2 tip apex. H_2O is likely overestimated due to the RGA location in the sample preparation chamber which is not as thoroughly baked and is subjected to the regular introduction of new samples (From Ref. [86]. © IOP Publishing. Reproduced with permission. All rights reserved)

Species	Mass, m (amu)	Ionization sensitivity, K_i/K_{N_2}	Pressure fraction, n_i	Partial pressure, p_i (mbar)	Flux, F (nm^{-2} s^{-1})	1:20 apex contamination time (min)	P(k > 1) gas atom on apex during a 60 min delay
H_2	2	0.42	88.0 %	9.4E-11	1.0E-03	0.7	98.5 %
H_20	18	0.9	4.6 %	4.9E-12	1.8E-05	41	7.1 %
N_2	28	1	2.3 %	2.4E-12	7.0E-06	100	2.9 %
CO	28	1.2	1.7 %	1.8E-12	5.2E-06	140	2.1 %
CO_2	44	1.4	1.1 %	1.2E-12	2.7E-06	270	1.1 %
He	4	0.16	0.1 %	1.1E-13	8.1E-07	890	0.3 %

3.3 Key Research Findings

3.3.1 Review of Combined FIM/SPM Experiments

A handful of groups pioneered the combination of FIM and SPM from the mid-1980s to the late 1990s. Here, we review the work of the principal groups in this field in an approximately chronological order.

The first report of combined FIM and STM techniques was from Kuk and Silverman working at AT&T Bell Laboratories in New Jersey. Their investigation focused on the observed corrugation height (constant current STM topography) of the rows of the (1 × 5) reconstructed Au(100) surface using a W(100) tip at room temperature [87]. The same results also appear in a well-cited paper about STM instrumentation published in 1989 [88]. We are not aware of any further publications containing FIM results from these authors.

Toshio Sakurai's group from Tohoku University in Sendai, Japan, published quite extensively about combined FIM and STM in a technique they refer to as field ion-scanning tunneling microscopy (FI-STM). By 1989, Sakurai had built a series of room-temperature FI-STMs [89]. A review article on the FI-STM technique appeared in Progress in Surface Science in 1990 [90]. In the early 1990s, the group focused on silicon surfaces and worked to study the surface bonding of C_{60} molecules [91–93] and alkali metals [94]. In these studies, the FIM was used to confirm tip cleanliness and sharpness in order to help obtain reliable atomic resolution in STM. The role of the tip's atomic structure in STM imaging was not an explicit concern in this work. The group of Yukio Hasegawa, who worked with Sakurai, later demonstrated FIM characterization of a tip mounted to a length extension resonator for AFM [95].

Some very diligent combined FIM/STM work was carried out by Masahiko Tomitori et al. while based at the Tokyo Institute of Technology, Yokohama, Japan, between ∼1990 and 1996. The first work investigating STM tip approach was performed in air on freshly cleaved highly oriented pyrolytic graphite (HOPG), and the Pt-Ir alloy tips were transferred to and from vacuum for FIM characterization [96]. The goal was *not* to implement atomically defined tips in air; they wanted to ensure that the tip apex did not crash into the substrate inadvertently during coarse approach. Tomitori underlined the necessity in performing the tip approach within the bandwidths of the STM feedback loop and current preamplifier – exceeding these bandwidths could result in crashing the tip without any sign of a current spike arising from mechanical contact. Approaching the tips too quickly was found to render the tip apex nonobservable in FIM; a large amount of carbon, hydrogen, and oxygen had also been transferred to the tip apex, detected by a time-of-flight (ToF) mass spectrometer.

In 1996, Tomitori published scanning tunneling spectroscopy (STS) results with a "buildup" pyramidal tip in UHV [97]. The motivation here was to try to develop an experimental procedure to obtain reproducible STS data by controlling the tip geometry – that way, the STS technique could be more straightforwardly applied to unknown samples. STS was carried out on the Si(111)-7 × 7 surface in 64 × 64 point arrays in order to average over the surface unit cell, and spectra were found to be reasonably repeatable with the tips as long as the bias range was kept within

−2 to +2 V. Tips retained similar patterns in field emission microscopy (FEM)[7] with slightly modified voltage thresholds for imaging (perhaps indicating slight tip changes). Expanding the STS bias range to −3 to +3 V altered the STS spectra radically, and FEM showed large changes present on the tip, attributed to the transferral of Si atoms from the substrate.

These two studies by Tomitori provided valuable early insights into the implementation of atomically defined tips in STM: feedback and current detection bandwidths must be respected to avoid tip crashing on approach, FEM might be a less awkward way than FIM to check for tip changes due to the absence of potentially corrosive imaging gas, and STS can be implemented without significant tip changes as long as the bias voltages are kept within a small enough range (±2 V).

At the University of Arizona, a combined STM with a ToF atom probe was built by Uwe Weierstall and John Spence in the mid-1990s. They called the instrument the scanning tunneling atom probe (STAP), and it was intended to be a means of supplementing the STM with chemical identification in a kind of "atomic tweezer." The goal of this instrument was to transfer a chemically unknown species from the sample to the tip, say by pulsing the STM bias voltage, and then switch over to ToF mode to identify the chemical species ejected from the tip. Their first report in 1996 demonstrated the proof of concept of the STAP [98]. The atom probe's mass-to-charge detection was calibrated by W^{3+} and W^{4+} field evaporated from tungsten tips, and the authors presented a preliminary result measuring a handful of Si atoms transferred from an Si(111)-7 × 7 surface to a tip apex, as identified both in STM imaging and ToF mass spectrometry.

A second and final paper from this instrument was published in Surface Science in 1998 [99]. Although FIM-characterized tip apices were not an objective of their work, some aspects of this second paper are relevant to the implementation of atomically defined tips in current endeavors. ToF revealed that some care had to be taken in order to not overshoot the tunneling current set point upon initial approach and transfer Si atoms from mechanical contact (also noted by Tomitori). The authors report statistics on an impressive number of experiments: after improving their tip approach procedure, in ∼80 % of about 50 experiments, W tips could be scanned and returned for ToF analysis without having picked up Si atoms. In ∼20 % of cases, a tip change occurred while scanning, often accompanied by a sudden improvement in STM resolution, and this correlated with the ToF detection of Si transferred to the probe tip.

Although single-ion sensitivity is possible with their chevron microchannel plate, the open area of the detection channels is only ∼60 %. Nevertheless, the statistics are quite convincing that W tips can be approached to tunneling proximity in STM without the transferral of atoms from the substrate, but tip changes seen during STM scanning correlate with atom transfer. FIM imaging of the tip was not a

[7]FEM operates in a similar manner to FIM, but a field emission current is detected rather than field ionized gas atoms. A spatial map of the field emission current is visualized on an MCP/phosphor screen when the tip is negatively biased. The technique does not allow the atomic structure of the tip to be imaged.

goal of this work, but the studies are valuable from the standpoint of considerations of material transfer which would modify atomically defined FIM tip apices when they are used in STM.

Manfred Leisch's group at the Graz Institute of Technology, Graz, Austria, built a position-sensitive atom probe detector to be used in conjunction with a commercial Omicron STM-1. The goal of this system was to investigate the mechanical interaction between materials on the atomic scale [100]. This was essentially an experimental realization of the systems studied in early molecular dynamics simulations to address atomic-scale contact formation, wetting, adhesive bonding, connective neck formation, and plastic deformation [101]. The experimental investigation of mechanical interactions between tips defined in FIM and other specimens was not particularly new – this had been investigated to some extent in the 1960s and 1970s by Müller and Nishikawa [102], but the lack of control over interaction forces between the tip and contacting specimen made it difficult to avoid destroying the delicate FIM tip. Leisch's group identified that the techniques developed for SPM (e.g., piezoelectric transducers, force, and current feedback methods) were ideal for controlling mechanical interactions with FIM tips at atomic length scales. Using STM control of the tip and a time-of-flight mass spectrometer incorporated into the FIM, the number of atoms transferred from the substrate to the tip during indentation could be counted. The authors also made interesting observations about changes to the tip structure induced by STM imaging [103].

3.3.2 Atomically Defined Tips in STM

In Sect. 3.2.6, we introduced the "force field" protocol to ensure that tip apices remain unchanged between FIM and SPM, and we have also determined that they can be kept atomically clean for a reasonable length of time for use in the SPM experiment. Now, we report experimental results on bringing tips into tunneling proximity with SPM samples.

Tomitori identified the necessity to keep the tip approach speed within the detection bandwidth to avoid set point overshoot (which would result in tip crashing; Sect. 3.3.1) [96]. In the case of STM where the tunneling current increases at a rate of about one decade per angstrom, dangerous overshoot can be avoided by limiting the approach speed to a maximum of ~1,000 Å/s. This is to allow sufficient time for the distance regulation feedback loop to respond to regulate the tip distance (a standard tunneling current amplifier has a bandwidth of a couple kHz, and typical SPM feedback loops are tuned to respond in about ~1 ms). We approach tips at a speed of 200 Å/s, resulting in negligible overshoot.

It turns out that the choice of substrate is very important in maintaining tip integrity. We have investigated tip integrity after approaching FIM tips to several types of STM samples: after reaching the tunneling set point and maintaining this distance for a few minutes, tips were retracted and imaged again in FIM [80]. With confidence that relatively few tip changes occur under this time delay due to the rest gas (Sect. 3.2.6), we can study the effect of the interaction with the sample on the tip structure.

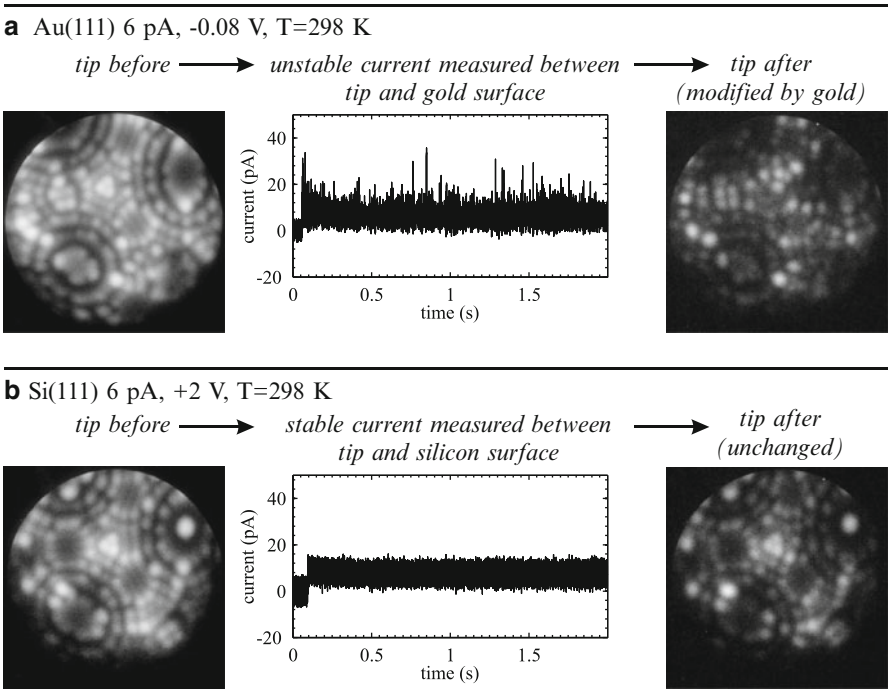


Fig. 5.11 FIM images before and after tunneling experiments with (**a**) Au(111) and (**b**) cleaved Si(111) at room temperature. Tunneling current snapshot shows the initial moment of approach of the tip to the sample surface

We summarize the approach of W(111) FIM tips to Au(111) and cleaved Si(111) surfaces in Fig. 5.11. In both cases, the tip is approached to a tunnel current set point of 6 pA. In the case of the Au(111) surface (Fig. 5.11a), the measured current is very unstable – many spikes are apparent up to ~40 pA throughout the experiment. The tip is imaged again in FIM and reveals changes to the atomic structure in approximately the entire field of view. Note that the underlying threefold symmetry is still visible which indicates that the tip did not suffer mechanical damage during the experiment (the large flat W(110) planes are mostly intact).

The observation of spikes and correlated FIM tip changes for Au(111) is consistent with many other experiments on Au(111), as well as cleaved HOPG, sputter-annealed InSb(001), and cleaved GaAs(001) [29].[8] The presence of changes to the tip apex must be due to interaction with the sample – the "force field" protocol is very successful – but do the atoms which change the tip structure come from the sample itself? Or could they be gas atoms physisorbed on the tip

[8]Though the frequency of spikes was very much less on some of these substrates, their presence was still correlated with changes to the FIM tip.

shank that migrate to the apex under the electric field gradient in STM? In order to understand where the changes come from, we turned to cleaved Si(111), the most reactive surface that could be easily prepared on our system [86].

Figure 5.11b shows that the tunneling current is exquisitely stable between FIM tip and Si(111) surface. It also confirms that very little overshoot occurs when the sample surface is first detected at 0.1 s. The tip apex is unchanged in the image taken after the experiment. The strong correlation between spikes in the tunneling current and tip changes visible in FIM suggests that material is transferred from the sample surface to the tip. The changes to the tip are not due to gas molecules from the shank – if this were the case, the experiments with a Si(111) surface would be equally affected.

The temperature dependence of the tunnel current spikes and tip changes has also been investigated for Au(111) by cooling the entire microscope (sample and tip) to 158 K [104]. As Fig. 5.12 indicates, the magnitude of the current spikes is much higher at low temperature (the vertical scale is the same in both Fig. 5.12a, b). Interestingly, at low temperature, the modifications to the tip apex are confined to the very center of the tip. The thermally activated diffusion of adatoms on the tip is expected to be quenched at this temperature due to the large corrugation of the W(111) surface [104]; therefore, the transferred atoms stay in place.

Though the result of localized tip modifications precludes Au(111) at 158 K as a possible substrate for atomically defined tips in STM, it is a useful result for two reasons: Firstly, it provides additional evidence that the changes to the tip, which are localized to the very apex, originate from atoms transferred from the sample rather than the tip shank.[9] Secondly, it indicates that the expected W(111) crystal plane is indeed the part of the tip which interacts with the sample (i.e., the (111) direction is pointed along the tip wire axis, even after tip fabrication/etching/preparation procedures).

In order to carry out an experiment with an atomically defined tip, it is also important to be able to identify events indicative of tip changes. In experiments on cleaved Si(111), where the tunneling current is mostly stable, occasional tip changes can take place while scanning. These tip changes are characterized by simultaneous spikes in the tunneling current of order 50–100 pA (at 8 pA set point), accompanied by changes in topographic scan height on the order of 10 pm (up to 130 pm), and often changes in the lateral resolution of the STM image [29]. We expect that the $\sim$10 pm changes, which are very much smaller than interatomic distances in crystals, may arise from a transferred atom which diffuses to a site slightly off-center and weakly modifies the electronic density of states of the apex atoms which are involved in tunneling.

Point defects on the cleaved Si(111) surface also provide an opportunity to study tip changes because they image the tip itself in the form of an image convolution. The tip structure is reflected in features repeated throughout the image.

[9] If the latter were the case, tip changes would be seen all over the apex region from chemically bound atoms.

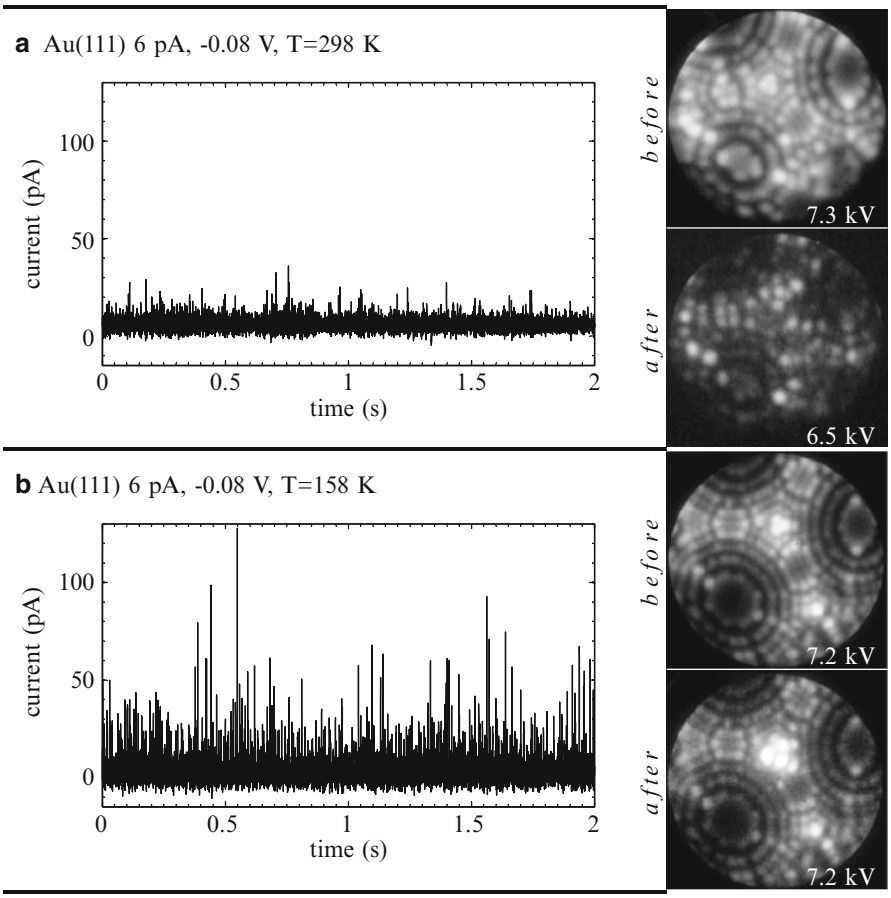


Fig. 5.12 FIM tip apices before and after, as well as a snapshot of the measured tunneling current when approached to Au(111) at temperatures of (**a**) 298 K and (**b**) 158 K

For example, in Fig. 5.13a, b, a 2-lobed feature recurs in the constant current STM image. We can draw a ball-and-stick model of this feature to scale (and in the correct orientation) with the initial FIM image of the tip (Fig. 5.13e). This gives some appreciation of where the STM imaging atoms (added by tip changes) might be located with respect to the original tip geometry. The tip convolution features change as STM scanning is continued, and another repeated motif is shown in Fig. 5.13c, d for negative and positive biases, respectively.

As expected from the changing tip convolutions, the STM tip appears highly modified when it is returned to FIM for imaging (Fig. 5.13f). It is imperative to realize that the image displayed in (f) is just *one* image of many that are taken of the tip structure which evolves during imaging due to field evaporation. FIM carried out on a highly modified tip is a very unstable process for several reasons: the added atoms protrude from the surface, so the electric field is locally enhanced at their

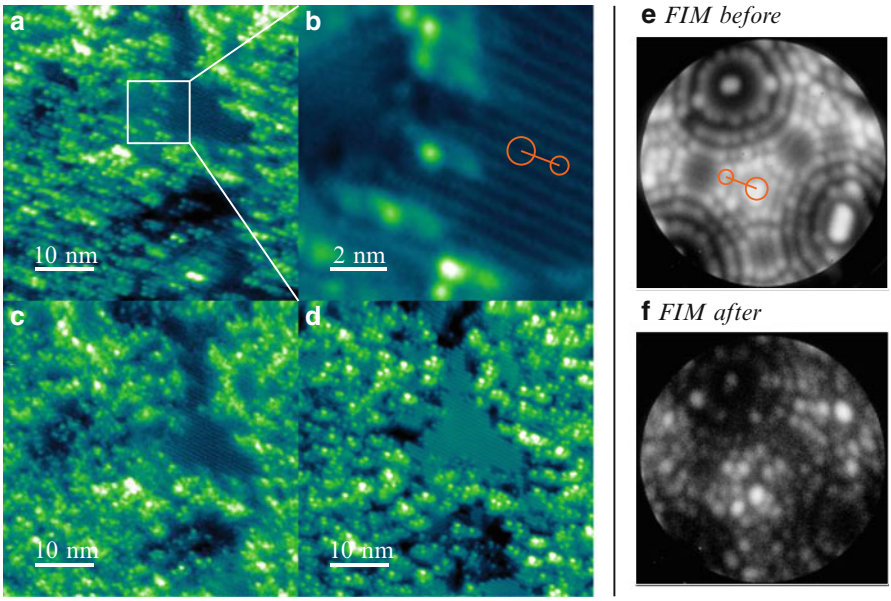


Fig. 5.13 (**a**) STM image showing a partially reconstructed Si(111) terrace. (15 pA, +2 V) (**b**) higher magnification image of a region shown in (**a**) highlighting the tip convolution feature. (15 pA, +2 V) (**c**) Filled-state STM image of the same area after tip changes. (15 pA, −2 V) (**d**) Empty state STM image of the same area. (15 pA, +2 V) Lines running in the 10-o'clock to 4-o'clock direction correspond to the 2 × 1 surface reconstruction. (**e**) FIM image before STM experiments with tip convolution model scaled to the appropriate size and direction. (6.4 kV) (**f**) FIM image after extensive STM experiments. (6.2 kV)

positions, leading to their facilitated field desorption.[10] Because of their different chemical nature, they will be subject to ionization and desorb at lower voltages than tungsten would (the ionization field of almost every other atomic species is lower than that of tungsten [12]). Because of the unstable atomic structure during FIM imaging of a modified tip, it would be inappropriate to compare the image in Fig. 5.13f to the features of the topographic STM images.

A concluding word of caution when inspecting FIM tips after STM experiments: the tip is made from a crystal and is therefore self-similar. After field evaporating three atomic layers from the apex, it will appear nearly indistinguishable from the original tip.[11] It is possible for the experimenter to be misled into thinking that the

[10]The images of modified tips that we display are taken at as low a voltage as possible to minimize tip changes, but it is impossible to determine how many atoms desorb before the onset of imaging. Numerous images are acquired while the voltage is slowly increased; they are averaged together in sets where the tip structure remains constant. The stability of modified tips may increase with decreasing temperature. However, changing the temperature will not change the ionization field of the adsorbed atoms relative to tungsten or the imaging gas.

[11]It takes many layers of field evaporation to increase the radius significantly.

post-STM tip is unchanged when he or she is in fact observing a new layer of atoms. With the present availability of digital cameras and plentiful data storage, it should be possible to acquire many frames and carefully assess the results.[12] We urge caution in the interpretation of early combined FIM/SPM studies which do not discuss the fragility of tungsten tip apices due to their reactivity, the stability of the tunneling current in STM, or the FIM imaging process after STM [87, 105].

At the time of writing, we are confident that STM imaging with pristine FIM tips can be carried out, albeit for a very short period of time (∼1 min to first tip change on cleaved Si(111)). Tip changes are identified during STM scanning by discontinuities in tip height, spikes in the tunneling current, and changes to STM resolution. At room temperature, highly reactive sample surfaces are needed to reduce the population of mobile adatoms on the surface which can transfer to and alter the tip. Operating the experiment at a sufficiently low temperature to freeze out adatom motion on the sample is another promising route to achieve atomically defined FIM tips in SPM.

3.3.3 Long-Range Force Interactions in Noncontact AFM

The advent of new force sensors for noncontact AFM, namely, the qPlus [30] and the length extension resonator [31, 32], has allowed tungsten FIM tips to be used in noncontact AFM where until recently, microfabricated silicon cantilevers had been most popular. FIM imaging of tip apices on length extension transducers has been demonstrated by An et al. [95, 106], noting that field evaporation is a very effective tip preparation technique for removing the surface oxides from tungsten. The successful FIM characterization of a tip on a qPlus transducer was recently reported by Falter et al. in 2013 [51]. This work constitutes a substantial advance in the use of well-characterized tips because the authors use the FIM data in a quantitative way to understand noncontact AFM results.

Falter et al. use the overall tip radius (from FIM) and cone angle (from supplemental SEM measurements) as input to models for electrostatic [107] and van der Waals forces [108] acting between a spherically capped conical tip and a flat surface. The authors were able to identify a strong variation of the contact potential with distance at tip-sample separations less than 2 nm, indicating that the inhomogeneous work function of the faceted tip surface contributes localized patch charges to the electrostatic force response. Detailed electrostatic models of SPM tips based on FIM characterization may also help to elucidate atomic-scale contrast in the contact potential measured by Kelvin probe force microscopy (KPFM) [109, 110].

3.3.4 FIM Tips for Atomic-Scale Nanoindentation

In order to understand the mechanics of deformation during indentation, atomistic simulations are often employed to provide a view "inside" materials while an

[12] In order to screen for tip changes during the STM experiment itself, one may want to acquire a higher bandwidth version of the tunneling current signal throughout the entire experiment to scrutinize carefully for spikes. By higher bandwidth, we mean the several kHz bandwidth of the current preamplifier, rather than the ∼100 Hz pixel STM scan rate.

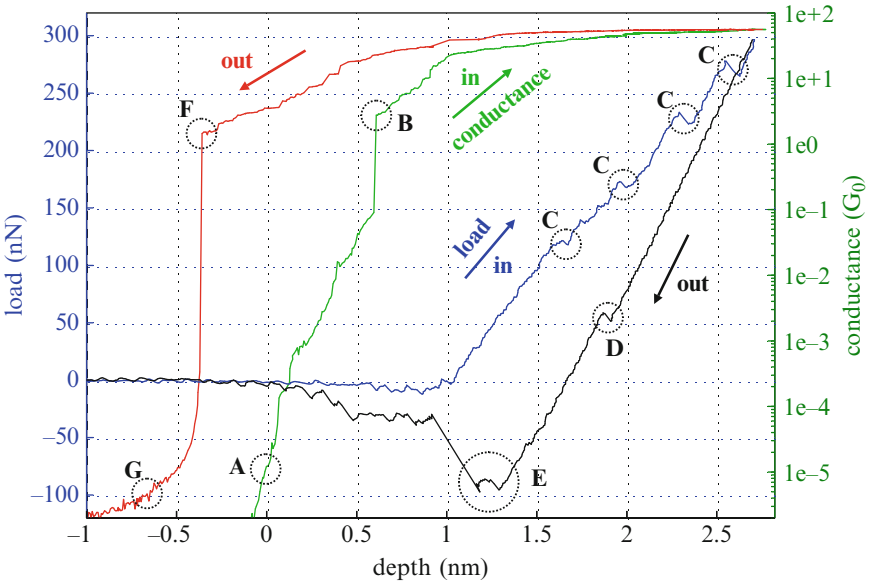


Fig. 5.14 A load-displacement curve showing important features in atomic-scale nanoindentation response (see text). Load is *blue* and conductance is *green* upon loading the contact (in-direction), load is *black* and conductance is red upon unloading the contact (out-direction)

indentation stress is applied [111]. These computer simulations are typically limited to some millions of atoms and thus probe a much smaller volume than in traditional nanoindentation. To close the length scale gap, the lateral size of indentation experiments must be diminished by about three orders of magnitude. Nanometer-sized indenters are also fundamentally interesting due to the breakdown of continuum mechanics at this length scale – spherically shaped crystals contain stepped facets which are expected to modify the contact pressure distribution when used for indentation [112].

Preparation of tips by FIM is an ideal way to obtain a clean, atomically characterized spherical apex with a radius of several nanometers. The strong covalent bonding of tungsten gives the material stable performance under the high electric fields of He ion FIM and makes it exceptionally hard [113]. High hardness is essential to ensure that deformation occurs in the substrate rather than the indenter.

Using a combination of FIM, STM, and AFM (introduced in Fig. 5.1), we have investigated the indentation response of Au(111) under indentation by FIM-characterized tips [27, 29, 114–118]. We now discuss results of recent experiments.

Referring to Fig 5.14, we now present typical features of an atomic-scale nanoindentation curve in which a W(111) FIM tip is indented into a Au(111) single crystal. The zero point of the indentation depth is set to the crossing of the 1 GΩ resistance of the conductance data ($1 \times 1\,0^{-5}$ G_0 in the example shown). This is a

semi-arbitrary zero point because zero separation is not well defined at these length scales. A jump-to-contact is observed in the current (green) at point B where the junction conductance suddenly increases to $\sim 3G_0$. At the points labeled C, abrupt mechanical rearrangements occur in which the load decreases and depth increases simultaneously (the slope of these changes corresponds to the stiffness of the force transducer). These events are known as pop-ins and are attributed to the sudden nucleation of plastic damage in the sample [119]. A pop-out is registered at point D, interpreted as an event which partially reverses the plasticity created during loading. The large adhesion force of the metallic contact is shown at point E. The conductance upon unloading (red) shows a large hysteresis indicative of wire drawing. This atomic-sized wire finally breaks at a conductance of just over 1 G_0 at point F. G is an artifact from the long settling time of the current preamplifier and should not be interpreted physically.

The adhesion of clean nanoscale contacts is remarkable in magnitude and is a key factor differentiating response in these experiments from those of a traditional nanoindenter. The two reasons for this are the exceptional cleanliness of the indenter/surface system prepared in UHV and the large surface-to-volume ratio at small length scales where energies required to create new surfaces are comparable to those required to deform volumes [120]. Using FIM prepared tips, a strong dependence of adhesion on the state of the tip has been observed [117]. After preparing an atomically clean tungsten surface by field evaporation in FIM, the tip was repeatedly indented into the pristine surface of a Au(111) single crystal. As indentation progressed, the adhesive force dropped by a factor of 6× with a 1/e rate of 11–14 indentation cycles, indicating that the surface composition of the tip (in this case, wetted by the gold substrate) strongly affects the measured mechanical behavior. The FIM is therefore an ideal tool to create an experimental indentation system with a well-defined surface composition for quantitative comparison with atomistic simulations.

The determination of contact area and stresses during indentation depends on accurate indenter characterization. With FIM-characterized W(111) indenters, the minimum threshold for plasticity was investigated in Au(111) [116]. The indenter is pictured in Fig. 5.15a, and stochastically initiated plasticity on the Au(111) single crystal surface is shown in Fig. 5.15c before and d after indentation. The broad distribution of yield-point shear stress suggested that dislocations were heterogeneously nucleated in this system. The resolution of very low forces and displacements in AFM also permitted the extraction of energies required to produce defects in the gold substrate: surprisingly, permanent impressions are left in the substrate by a mechanical energy expenditure of only ~70 eV.

The contact area during indentation, which can be inferred from the FIM tip geometry, also yields important insights about electronic transport through the indentation-formed nanocontact [115]. Experiments using a W(111) tip and Au(111) sample yield a highly variable conductance in the range of 0.02–4.9 G_0/nm^2, which is much less than a Sharvin estimation of $\sim 13.8\ G_0/nm^2$. (The latter is expected when each atom in the metallic contact contributes $\sim 1\ G_0$ to the conductance.) The reason for the much reduced conductance between the W(111) and

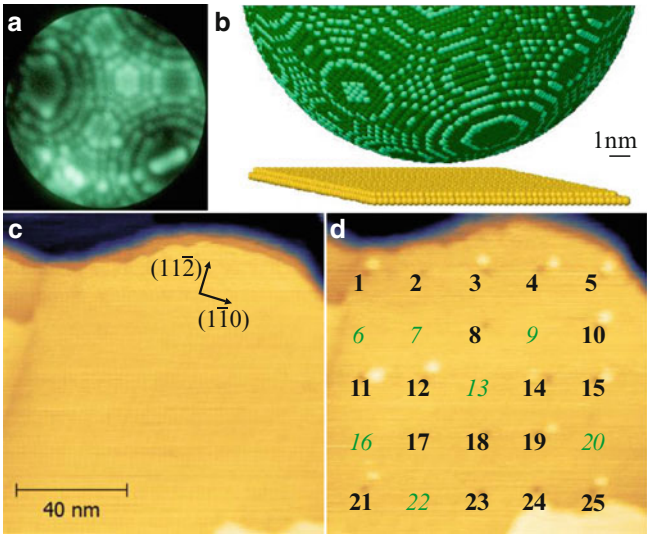


Fig. 5.15 (**a**) FIM image of the W(111) indenter (5.5 kV tip voltage); (**b**) ball model of a W(111) with a 9.5 nm radius and Au(111) substrate to scale; (**c**) Au(111) terrace before and (d) after a 5 × 5 indentation array with 20 nm spacing between indents (20 pA, −0.05 V sample bias). *Bolded numbers* indicate plastic sites, and *italicized numbers* indicate elastic sites (From Ref. [116]. Copyright 2013 by the American Physical Society)

Au(111) metals was clarified by first-principles density functional theory calculations: the d-wave electron modes of tungsten are poorly approximated by the *s*-wave modes of gold, resulting in backscattering of electrons at the interface. Furthermore, disorder and vacancies are also expected to diminish electron conduction. Electronic transport across interfaces has obtained considerable attention in theoretical work [121–124], but the experiments are rare due to the challenge in determining the contact area in nanoscale systems [125, 126]. Because the geometry of FIM tips can be easily modified by starting with wires of different crystal orientations and can be rotated with respect to SPM substrates, one might expect them to find use in the study of the electronic transparency of interfaces and disorder structures.

3.4 Conclusions and Future Perspective

Atomic-scale characterization of SPM tips by FIM provides a detailed view of the tip structure which is usually unknown in SPM experiments. We have discussed the operating principle and resolution of FIM, the preparation and radius determination of the probes, and advanced tip preparation by techniques such as gas etching and surface faceting.

In the implementation of FIM tips in SPM, we considered tip integrity with regard to modifications due to chemical reaction with impurities in the imaging gas and with UHV rest gases. We outlined the “force field” protocol which inhibits

changes to the tips, guaranteeing the transferral of a pristine apex to the SPM tip-sample junction.

At the moment, STM with a stable atomically defined tip has yet to be demonstrated: at room temperature, tip changes occur within a short period of time on many kinds of substrates. We expect that stable tips should be obtainable with the construction of a stable cryogenic SPM with in situ FIM or with the use of very reactive samples, such as Si(111)-7 $\times$ 7, at room temperature. Resolving the issues of tip changes is an essential challenge to overcome in order to move the field into more ambitious experiments such as the characterization of atomically defined molecular junctions, quantitative understanding of local electrostatic forces from faceted tips, and their use as benchmarking probes for materials with exotic electronic properties (e.g., oxide electronics).

Their well-defined radii and chemical composition makes FIM tips ideal for atomic-scale indentation. There are many open questions in this area which can be experimentally addressed in detail, such as indentation by stepped indenters of different geometries and surface chemistries. There is ample opportunity to borrow techniques of advanced tip preparation (such as faceting) from the FIM community and apply them to the study of nanomechanics, as well as the study of electronic transport through mechanically formed nanocontacts.

References

1. Fink H-W (1986) Mono-atomic tips for scanning tunneling microscopy. IBM J Res Dev 30(5):460–465
2. Giessibl FJ, Hembacher S, Mannhart J (2004) Force microscopy with light-atom probes. Science 305(5682):380–383
3. Campbellová A, Ondrácek M, Pou P, Pérez R, Klapetek P, Jelínek P (2011) 'Sub-atomic' resolution of non-contact atomic force microscope images induced by a heterogeneous tip structure: a density functional theory study. Nanotechnology 22(29):295710
4. Hofer WA, Redinger J (1998) Electronic structure of a realistic STM tip: the role of different apex atoms. Philos Mag Part B 78(5):519–525
5. Kwapinski T, Jalochowski M (2010) Signature of tip electronic states on tunneling spectra. Surf Sci 604(19–20):1752–1756
6. Sugimoto Y, Pou P, Abe M, Jelínek P, Pérez R, Morita S, Custance O (2007) Chemical identification of individual surface atoms by atomic force microscopy. Nature 446(7131):64–67
7. Ternes M, González C, Lutz CP, Hapala P, Giessibl FJ, Jelínek P, Heinrich AJ (2011) Interplay of conductance, force, and structural change in metallic point contacts. Phys Rev Lett 106(1):016802
8. Wagner RJ, Ma L, Tavazza F, Levine LE (2008) Dislocation nucleation during nanoindentation of aluminum. J Appl Phys 104(11):114311
9. Shin C, Osetsky Y, Stoller R (2012) Dislocation nucleation and defect formation in copper by stepped spherical indenter. Philos Mag 92(25–27):3158–3171
10. Mehrez H, Wlasenko A, Larade B, Taylor J, Grütter P, Guo H (2002) I-V characteristics and differential conductance fluctuations of Au nanowires. Phys Rev B 65(19):195419
11. Müller EW (1951) Das Feldionenmikroskop. Z Phys 131(1):136–142
12. Tsong TT (1990) Atom-probe field ion microscopy. Cambridge University Press, New York

13. Antczak G, Ehrlich G (2010) Surface diffusion. Cambridge University Press, New York
14. Gault B, Moody M, Cairney JM, Ringer SP (2012) Atom probe crystallography. Mater Today 15(9):378–386
15. Miller MK, Kelly TF, Rajan K, Ringer SP (2012) The future of atom probe tomography. Mater Today 15(4):158–165
16. Müller EW, Panitz JA, McLane SB (1968) The atom-probe field ion microscope. Rev Sci Instrum 39(1):83
17. Panitz JA (1973) The 10 cm atom probe. Rev Sci Instrum 44(8):1034
18. Lee HJ, Ho W (1999) Single-bond formation and characterization with a scanning tunneling microscope. Science 286(5445):1719–1722
19. Stipe BC, Rezaei MA, Ho W (1998) Single-molecule vibrational spectroscopy and microscopy. Science 280(5370):1732–1735
20. Zhou W, Wang ZL (eds) (2006) Scanning microscopy for nanotechnology. Springer, New York
21. Binnig G, Rohrer H (1987) Scanning tunneling microscopy – from birth to adolescence. Rev Mod Phys 59(3):615–625
22. Chen CJ (2008) Introduction to scanning tunneling microscopy, 2nd edn. Oxford University Press, Oxford
23. Stroscio JA, Kaiser WJ (eds) (1993) Scanning tunneling microscopy, 1st edn. Academic, San Diego
24. Sarid D (1994) Scanning force microscopy. Oxford University Press, New York
25. Giessibl FJ (2003) Advances in atomic force microscopy. Rev Mod Phys 75(3):949–983
26. Hauptmann N, Mohn F, Gross L, Meyer G, Frederiksen T, Berndt R (2012) Force and conductance during contact formation to a C 60 molecule. New J Phys 14(7):073032
27. El Ouali M (2010) Nanometre scale indentation: effect of very sharp indenters on adhesion, plasticity, and electronic transport. PhD thesis, McGill University
28. Hagedorn T (2010) Atomic contacts characterized by force and current. PhD thesis, McGill University
29. Paul W (2013) Atomically defined tips in scanning probe microscopy. PhD thesis, McGill
30. Giessibl FJ (1998) High-speed force sensor for force microscopy and profilometry utilizing a quartz tuning fork. Appl Phys Lett 73(26):3956
31. Bartzke K, Antrack T, Schmidt K-H, Dammann E, Schatterny CH (1993) Needle sensor-a micromechanical detector for atomic force microscopy. Int J Optoelectron 8:669
32. Michels A, Meinen F, Murdfield T, Göhde W, Fischer UC, Beckmann E, Fuchs H (1995) 1 MHz quartz length extension resonator as a probe for scanning near-field acoustic microscopy. Thin Solid Films 264(2):172–175
33. Dürig U, Novotny L, Michel B, Stalder A (1997) Logarithmic current-to-voltage converter for local probe microscopy. Rev Sci Instrum 68(10):3814
34. Schönenberger C, Alvarado SF (1989) A differential interferometer for force microscopy. Rev Sci Instrum 60:3131
35. Lalanne J-B, Paul W, Oliver D, Grütter PH (2011) Note: electrochemical etching of sharp iridium tips. Rev Sci Instrum 82(11):116105
36. Miller MK, Cerezo A, Hetherington MG, Smith GDW (1996) Atom probe field ion microscopy. Oxford University Press, Oxford
37. Lucier A-S, Mortensen H, Sun Y, Grütter PH (2005) Determination of the atomic structure of scanning probe microscopy tungsten tips by field ion microscopy. Phys Rev B 72(23):235420
38. Ibe JP, Bey PP, Brandow SL, Brizzolara RA, Burnham NA, DiLella DP, Colton RJ, Lee KP, Marrian CRK (1990) On the electrochemical etching of tips for scanning tunneling microscopy. J Vacuum Sci Technol A 8(4):3570
39. Melmed AJ (1991) The art and science and other aspects of making sharp tips. J Vacuum Sci Technol B Microelectron Nanometer Struct 9(2):601

40. Ekvall I, Wahlström E, Claesson D, Olin H, Olsson E (1999) Preparation and characterization of electrochemically etched W tips for STM. Meas Sci Technol 10(1):11–18
41. Hagedorn T, El Ouali M, Paul W, Oliver D, Miyahara Y, Grütter PH (2011) Refined tip preparation by electrochemical etching and ultrahigh vacuum treatment to obtain atomically sharp tips for scanning tunneling microscope and atomic force microscope. Rev Sci Instrum 82(11):113903
42. Lucier A-S (2004) Preparation and characterization of tungsten tips suitable for molecular electronics studies. Master's thesis, McGill University
43. Setvin M, Javorský J, Turcinková D, Matolinová I, Sobotik P, Kocán P, Ošt'ádal I (2012) Ultrasharp tungsten tips-characterization and nondestructive cleaning. Ultramicroscopy 113:152–157
44. Greiner M, Kruse P (2007) Recrystallization of tungsten wire for fabrication of sharp and stable nanoprobe and field-emitter tips. Rev Sci Instrum 78(2):026104
45. Verlinden B, Driver J, Samajdar I, Doherty RD (2007) Thermo-mechanical processing of metallic materials. Elsevier, Oxford
46. Webber RD, Walls JM, Smith R (1978) Ring counting in field-ion micrographs. J Microsc 113(3):291–299
47. Bolin PL, Ranganathan BN, Bayuzick RJ (1976) Determination of field ion tip shapes. J Phys E Sci Instrum 9(5):363–365
48. Webber RD, Walls JM (1979) The shape of field-ion emitters. J Phys D Appl Phys 12(9):1589–159
49. Moore AJW (1962) The structure of atomically smooth spherical surfaces. J Phys Chem Solid 23(7):907–912
50. Rao PVM, Jensen CP, Silver RM (2004) Enhanced model for scanning tunneling microscope tip geometry measured with field ion microscopy. J Vacuum Sci Technol B Microelectron Nanometer Struct 22(2):636–641
51. Falter J, Langewisch G, Hölscher H, Fuchs H, Schirmeisen A (2013) Field ion microscopy characterized tips in noncontact atomic force microscopy: quantification of long-range force interactions. Phys Rev B 87(11):115412
52. Urban R, Wolkow RA, Pitters JL (2012) Field ion microscope evaluation of tungsten nanotip shape using He and Ne imaging gases. Ultramicroscopy 122:60–64
53. Pitters JL, Urban R, Wolkow R (2012) Creation and recovery of a W(111) single atom gas field ion source. J Chem Phys 136(15):154704
54. Rezeq M, Pitters J, Wolkow R (2006) Tungsten nanotip fabrication by spatially controlled field-assisted reaction with nitrogen. J Chem Phys 124(20):204716
55. Rezeq M, Pitters J, Wolkow R (2008) Nano-tip fabrication by spatially controlled etching. US Patent 7431856 B2, Dec 2008
56. Ehrlich G, Hudda FG (1962) Direct observation of individual adatoms: nitrogen on tungsten. J Chem Phys 36(12):3233
57. Mulson JF, Müller EW (1963) Corrosion of tungsten and iridium by field desorption of nitrogen and carbon monoxide. J Chem Phys 38(11):2615
58. Ermanoski I, Pelhos K, Chen W, Quinton JS, Madey TE (2004) Oxygen-induced nanofaceting of Ir(210). Surf Sci 549(1):1–23
59. Song K-J, Dong C-Z, Madey TE (1991) Faceting of W (111) induced by Ultrathin Pd films. Langmuir 6:3019–3026
60. Szczepkowicz A, Ciszewski A, Bryl R, Oleksy C, Nien C-H, Wu Q, Madey TE (2005) A comparison of adsorbate-induced faceting on flat and curved crystal surfaces. Surf Sci 599(1–3):55–68
61. Chang C-C, Kuo H-S, Tsong TT, Hwang I-S (2009) A fully coherent electron beam from a noble-metal covered W(111) single-atom emitter. Nanotechnology 20(11):115401
62. Fu T-Y, Lin Y-C, Kuo H-S, Hwang I-S, Tsong TT (2007) Study of two types of Ir or Rh covered single atom pyramidal W tips. Surf Sci 601(18):3992–3995

63. Hwang I-S, Kuo H-S, Chang C-C, Tsong TT (2010) Noble-metal covered W(111) single-atom electron sources. J Electrochem Soc 157(2):7
64. Kuo H-S, Hwang I-S, Fu T-Y, Hwang Y-S, Lu Y-H, Lin C-Y, Tsong TT, Hou J-L (2009) A single-atom sharp iridium tip as an emitter of gas field ion sources. Nanotechnology 20(33):335701
65. Kuo H-S, Hwang I-S, Fu T-Y, Lin Y-C, Chang C-C, Tsong TT (2006) Noble Metal/W(111) single-atom tips and their field electron and ion emission characteristics. Jpn J Appl Phys 45(11):8972–8983
66. Kuo H-S, Hwang I-S, Fu T-Y, Lin Y-C, Chang C-C, Tsong TT (2006) Preparation of single-atom tips and their field emission behaviors. e-J Surf Sci Nanotechnol 4(February):233–238
67. Kuo H-S, Hwang I-S, Fu T-Y, Lu Y-H, Lin C-Y, Tsong TT (2008) Gas field ion source from an Ir/W <111> single-atom tip. Appl Phys Lett 92(6):063106
68. Nomura K, Rokuta E, Itagaki T, Oshima C, Kuo H-S, Tsong TT (2008) Electron emission characteristics of Au-covered tungsten <111> Nanotips. e-J Surf Sci Nanotechnol 6(January):25–28
69. Golubok A, Masalov S, Tarasov N (1992) Thermofield tip formation in UHV/STM combined with field-emission microscope. Ultramicroscopy 42–44:1574–1579
70. Pavlov VG (2005) Field-desorption microscopy study of the deformation of a tungsten tip subjected to thermal treatment in an electric field. Phys Solid State 47(11):2180
71. Pavlov VG (2006) Variations in shapes of outgrowths on a tungsten tip during growth in an electric field. Phys Solid State 48(5):969–972
72. Pavlov VG (2007) Atomically sharp <111> trihedral angle of a tungsten tip. Phys Solid State 49(8):1579–1582
73. Fischer-Cripps AC (2011) Nanoindentation, volume 1 of mechanical engineering series. Springer, New York
74. Ehrlich G, Hudda FG (1960) Observation of adsorption on an atomic scale. J Chem Phys 33(4):1253
75. Holscher AA, Sachtler WMH (1966) Chemisorption and surface corrosion in the tungsten + carbon monoxide system, as studied by field emission and field ion microscopy. Discuss Faraday Soc 41:29
76. Cranstoun GKL, Anderson JS (1972) Field ion microscope studies of very low coverage low temperature oxygen adsorption on tungsten. Surf Sci 32(2):397–421
77. Ehrlich G, Hudda FG (1963) Promoted field desorption and the visibility of adsorbed atoms in the ion microscope. Philos Mag 8(93):1587–1591
78. Lewis RT, Gomer R (1971) Adsorption studies in the field ion microscope with argon imaging. Surf Sci 26(1):197–229
79. Müller EW, Tsong TT (1974) Field ion microscopy, field ionization and field evaporation. Prog Surf Sci 4(i):1–139
80. Paul W, Miyahara Y, Grütter PH (2012) Implementation of atomically defined field ion microscopy tips in scanning probe microscopy. Nanotechnology 23(33):335702
81. Müller EW (1957) Study of atomic structure of metal surfaces in the field ion microscope. J Appl Phys 28(1):1
82. Lias SG (2011) Ionization energies of gas-phase molecules. In: CRC Handbook of chemistry and physics, 92nd edn. CRC Press, Boca Raton
83. Singleton JH (2001) Practical guide to the use of Bayard-Alpert ionization gauges. J Vacuum Sci Technol A Vacuum Surf Films 19(4):1712
84. Weston GF (1985) Ultrahigh vacuum practice. Butterworth, Toronto
85. Zelterman D (2006) Models for discrete data. Oxford University Press, New York
86. Paul W, Miyahara Y, Grütter PH (2013) Simple Si(111) surface preparation by thin wafer cleavage. J Vacuum Sci Technol A Vacuum Surf Films 31(2):023201
87. Kuk Y, Silverman PJ (1986) Role of tip structure in scanning tunneling microscopy. Appl Phys Lett 48(23):1597

88. Kuk Y, Silverman PJ (1989) Scanning tunneling microscope instrumentation. Rev Sci Instrum 60(2):165
89. Sakurai T, Hashizume T, Hasegawa Y, Kamiya I, Sano N, Yokoyama H, Tanaka H, Sumita I, Hyodo S (1990) New versatile room-temperature field ion scanning tunneling microscopy. J Vacuum Sci Technol A Vacuum Surf Films 8(1):324
90. Sakurai T, Hashizume T, Kamiya I, Hasegawa Y, Sano N, Pickering H, Sakai A (1990) Field ion-scanning tunneling microscopy. Prog Surf Sci 33(1):3–89
91. Hashizume T, Sakurai T (1997) FI-STM Investigation of fullerenes adsorbed on the semiconductor and metal surfaces (STM-C60), science reports of the research institutes, Tohoku University. Ser A Phy Chem Metall A44:17
92. Hashizume T, Wang X-D, Nishina Y, Shinohara H, Saito Y, Kuk Y, Sakurai T (1992) Field ion-scanning tunneling microscopy study of C 60 on the Si(100) surface. Jpn J Appl Phys 31(Part 2, No. 7A):L880–L883
93. Wang X-D, Hashizume T, Shinohara H, Saito Y, Nishina Y, Sakurai T (1992) Scanning tunneling microscopy of C 60 on the Si(111)7 × 7 surface. Jpn J Appl Phys 31(Part 2, No. 7B):L983–L986
94. Hashizume T, Sumita I, Murata Y, Hyodo S, Sakurai T (1991) Cs adsorption on the Si(100) 2 × 1 surfaces. J Vacuum Sci Technol B Microelectron Nanometer Struct 9(2):742
95. An T, Eguchi T, Akiyama K, Hasegawa Y (2005) Atomically-resolved imaging by frequency-modulation atomic force microscopy using a quartz length-extension resonator. Appl Phys Lett 87(13):133114
96. Tomitori M, Hirano N, Iwawaki F, Watanabe Y, Takayanagi T, Nishikawa O (1990) Elaboration and evaluation of tip manipulation of scanning tunneling microscopy. J Vacuum Sci Technol A Vacuum Surf Films 8(1):425
97. Tomitori M, Sugata K, Okuyama G, Kimata H (1996) Reproducibility of scanning tunneling spectroscopy of Si(111)7 × 7 using a build-up tip. Surf Sci 355(1–3):21–30
98. Spence JCH, Weierstall U, Lo W (1996) Atomic species identification in scanning tunneling microscopy by time-of-flight spectroscopy. J Vacuum Sci Technol B Microelectron Nanometer Struct 14(3):1587
99. Weierstall U, Spence JCH (1998) Atomic species identification in STM using an imaging atom-probe technique. Surf Sci 398(1–2):267–279
100. Fian A, Ernst C, Leisch M (1999) Combined atom probe and STM study of tip-substrate interactions. Fresenius J Anal Chem 365(1–3):38–42
101. Landman U, Luedtke WD, Burnham NA, Colton RJ (1990) Atomistic mechanisms and dynamics of adhesion, nanoindentation, and fracture. Science 248(4954):454–461
102. Nishikawa O, Walko R (1971) Field ion microscopical observation of twinning in iridium induced by a mechanical contact. Acta Metall 19(11):1163–1168
103. Fian A, Leisch M (2003) Study on tip-substrate interactions by STM and APFIM. Ultramicroscopy 95(1–4):189–197
104. Paul W, Oliver D, Miyahara Y, Grütter P (2014) FIM tips in SPM: Apex orientation and temperature considerations on atom transfer and diffusion. Appl Surf Sci 305:124–132
105. Schirmeisen A, Cross G, Stalder A, Grütter PH, Dürig U (2000) Metallic adhesion forces and tunneling between atomically defined tip and sample. Appl Surf Sci 157(4):274–279
106. An T, Nishio T, Eguchi T, Ono M, Nomura A, Akiyama K, Hasegawa Y (2008) Atomically resolved imaging by low-temperature frequency-modulation atomic force microscopy using a quartz length- extension resonator. Rev Sci Instrum 79(3):033703
107. Hudlet S, Saint JM, Guthmann C, Berger J (1998) Evaluation of the capacitive force between an atomic force microscopy tip and a metallic surface. Eur Phys J B 2(1):5–10
108. Argento C, French RH (1996) Parametric tip model and force-distance relation for Hamaker constant determination from atomic force microscopy. J Appl Phys 80(11):6081
109. Sadewasser S, Jelinek P, Fang C-K, Custance O, Yamada Y, Sugimoto Y, Abe M, Morita S (2009) New insights on atomic-resolution frequency-modulation kelvin-probe force-microscopy imaging of semiconductors. Phys Rev Lett 103:266103

110. Mohn F, Gross L, Moll N, Meyer G (2012) Imaging the charge distribution within a single molecule. Nat Nanotechnol 7(4):227–231
111. Sinnott SB, Heo S-J, Brenner DW, Harrison JA, Irving DL (2011) Computer simulations of nanometer-scale indentation and friction. In: Nanotribology and Nanomechanics I. Springer, Berlin/Heidelberg, chapter 10
112. Luan B, Robbins MO (2005) The breakdown of continuum models for mechanical contacts. Nature 435(7044):929–932
113. Lassner E, Schubert W-D (1999) Tungsten. Springer US, New York (DOI: 10.1007/978-1-4615-4907-9)
114. Cross GLW, Schirmeisen A, Grütter PH, Dürig U (2006) Plasticity, healing and shakedown in sharp- asperity nanoindentation. Nat Mater 5(5):370–376
115. Oliver DJ, Maassen J, El Ouali M, Paul W, Hagedorn T, Miyahara Y, Qi Y, Guo H, Grütter PH (2012) Conductivity of an atomically defined metallic interface. Proc Natl Acad Sci U S A 109(47):19097–19102
116. Paul W, Oliver D, Miyahara Y, Grütter PH (2013) Minimum threshold for incipient plasticity in the atomic-scale nanoindentation of Au(111). Phys Rev Lett 110(13):135506
117. Paul W, Oliver D, Miyahara Y, Grütter P (2013) Transient adhesion and conductance phenomena in initial nanoscale mechanical contacts between dissimilar metals. Nanotechnology 24(47):475704
118. Oliver D, Paul W, El Ouali M, Hagedorn T, Miyahara Y, Qi Y, Grütter P (2014) One-to-one spatially matched experiment and atomistic simulations of nanometre-scale indentation. Nanotechnology 25:025701
119. Lawn BR, Cook RF (2012) Probing material properties with sharp indenters: a retrospective. J Mater Sci 47(1):1–22
120. Agraït N, Yeyati AL, van Ruitenbeek JM (2003) Quantum properties of atomic-sized conductors. Phy Rep 377(2–3):81–279
121. Feldman B, Park S, Haverty M, Shankar S, Dunham ST (2010) Simulation of grain boundary effects on electronic transport in metals, and detailed causes of scattering. Phys Status Solidi (B) 247(7):1791–1796
122. Srivastava MK, Wang Y, Zhang X-G, Nicholson DMC, Cheng H-P (2012) Plane-wave transport method for low-symmetry lattices and its application. Phys Rev B 86(7):075134
123. Zhou B-H, Xu Y, Wang S, Zhou G, Xia K (2010) An ab initio investigation on boundary resistance for metallic grains. Solid State Commun 150(29–30):1422–1424
124. Xu P, Xia K, Zwierzycki M, Talanana M, Kelly P (2006) Orientation-dependent transparency of metallic interfaces. Phys Rev Lett 96(17):176602
125. Kim T-H, Zhang X-G, Nicholson DM, Evans BM, Kulkarni NS, Radhakrishnan B, Kenik EA, Li A-P (2010) Large discrete resistance jump at grain boundary in copper nanowire. Nano Lett 10(8):3096–3100
126. Clark KW, Zhang X-G, Vlassiouk IV, He G, Feenstra RM, Li A-P (2013) Spatially resolved mapping of electrical conductivity across individual domain (Grain) boundaries in graphene. ACS Nano 9:7956–7966

Scanning Conductive Torsion Mode Microscopy

6

Ling Sun and Elmar Bonaccurso

Contents

1 Definition of the Topic 200
2 Overview 200
3 Introduction 201
3.1 Motivations 201
3.2 Technical Challenges for Nondestructive Conductive AFM 202
4 Experimental and Instrumental Methodology 203
4.1 How Does SCTMM Work? 203
4.2 Experimental Demonstration of SCTMM 204
4.3 How Does the Tip–Sample Interaction Relate to the Current Measurement in SCTMM? 205
4.4 Is SCTMM Destructive or Nondestructive? 209
5 Key Research Findings 211
5.1 Understanding Structure–Properties Relationship by SCTMM 211
5.2 Mapping of Local Conductivity Variations on Fragile Nanopillar Arrays 216
5.3 Monitoring Electropolymerization of Conjugated Polymers 218
5.4 Understanding Molecular Orientation of Self-Assembly Structures 220
6 Conclusions and Future Perspective 221
6.1 Frequency Modulation SCTMM 221
6.2 Maximum Force-Modulated Current-Sensing Techniques 222
References 223

L. Sun (✉)
Department of Micro- and Nanotechnology, Technical University of Denmark, Kgs. Lyngby, Denmark
e-mail: lisu@nanotech.dtu.dk

E. Bonaccurso
Center of Smart Interfaces, Technische Universität Darmstadt, Darmstadt, Germany

Airbus Group Innovations, Metallic Technologies and Surface Engineering – TX2, Munich, Germany
e-mail: bonaccurso@csi.tu-darmstadt.de; elmar.bonaccurso@airbus.com

© Springer-Verlag Berlin Heidelberg 2015

C.S.S.R. Kumar (ed.), *Surface Science Tools for Nanomaterials Characterization*,
DOI 10.1007/978-3-662-44551-8_6

Abstract

In this chapter, we introduce a special non-contact scanning probe based current sensing technique: scanning conductive torsion mode microscopy (SCTMM), which allows for simultaneous topography and electrical current mapping on solid samples. Due to the low interacting force between the probe and sample surface, this new technique is particularly indicated for and usually applied to measurements on soft materials and fragile structures. We first describe the working principle and discuss the advantages of the technique and its limitations. We also review recent applications of this technique, including studies of structure-properties relationship, local conductivity of nanopillar arrays, electropolymerization of conjugated polymers, and molecular orientation of self-assembly structures. In the end, we discuss some potential improvements of future scanning probe based current sensing techniques.

Keywords

Scanning probe microscopy • Atomic force microscopy • Torsional resonance mode • Non-contact mode • Current sensing • Topography • Soft materials and fragile structures • Organic electronics • Conducting polymers • Self-assembly molecules

1 Definition of the Topic

Scanning conductive torsion mode microscopy allows for simultaneous topography and electrical current mapping on solid samples. Due to the low interacting force between the probe and sample surface, this new technique is particularly indicated for and usually applied to measurements on soft materials and fragile structures. In this chapter we describe the working principle and review recent applications of this technique.

2 Overview

Organic–inorganic hybrid materials or devices have attracted extensive interests in fabricating electronic devices of high efficiency and low costs. These materials and devices usually contain heterogeneous structures on the microscopic or nanoscopic scales. Thus, understanding of the structure–properties relationship of these materials or devices is of paramount importance. Scanning probe microscopy (SPM) or atomic force microscopy (AFM) is one promising technique that allows for simultaneous topography and materials properties mapping. Among them, contact mode conductive AFM (c-AFM) provides simultaneous topography and electric current mapping of materials on the nanoscale. However, in conventional c-AFM, contact mode is used for topographic feedback, which applies relatively high tip–sample contact force during the measurement. Contact mode c-AFM is thus not suitable for applications, where soft materials or fragile structures are concerned. To overcome

such limitations, a scanning probe technique that can be operated at low tip-loading force is highly desired.

Scanning conductive torsion mode microscopy (SCTMM) is a method that provides current mapping with low tip-loading force. In SCTMM, the torsional resonance signal of the cantilever is used as topographic feedback. The vertical (flexural) oscillation amplitude of the cantilever is less than 2 nm in the torsional resonance mode. This distance is small enough for electric current to tunnel from the cantilever tip to the sample, while the sample topography is being recorded. As in SCTMM the cantilever is not in permanent mechanical contact with the sample surface, the tip–sample contact force is smaller than in c-AFM. This method has thus been used to study electrical properties of soft materials or fragile structures. For instance, researchers carried out studies on gold nanoparticles electrostatically immobilized on silicon substrates, DNA on graphite, or chemical vapor-deposited carbon nanotubes on crystalline silicon substrates. Nevertheless, a systematic description of the instrumental methodology is currently missing, while the number of applications is constantly growing. We therefore think that the time is ripe for a first review of the technique and of the work published in the past few years.

In this chapter, we start with introducing the instrumental methodology of the torsional resonance mode-based current-sensing technique, i.e., SCTMM. We highlight the advantages of SCTMM and also discuss some potential limitations. In addition, we review recent development and applications of using SCTMM to unravel structure–property relationships of materials and devices. At the end, we discuss some future perspective in the field of scanning probe-based current-sensing techniques.

3 Introduction

3.1 Motivations

Organic electronic materials have attracted extensive interests in the past decades due to their low cost, chemical tunability, easy processability, and light weight. One application of these materials is to combine organic electronic materials with inorganic semiconductors or metal oxides to fabricate hybrid electronic devices of high efficiency and low cost [1, 2]. These materials could also be used in whole organic electronic devices, solar cells, and organic sensors or detectors [3, 4]. For further improvement of the device efficiency and lifetime, a thorough understanding of structure–properties relationship of applied materials and devices is of vital importance. These devices or hybrid materials typically have heterogeneous structures on the microscopic or even nanoscopic scales. Therefore, characterization tools that could provide simultaneous morphology and materials properties, especially electronic properties of samples on the nanoscale, are highly demanded.

Conductive atomic force microscopy (c-AFM) has been widely used to map simultaneous topography and electrical conductivity of samples since its introduction in the late 1990s [5, 6]. In c-AFM, the cantilever tip is in direct (ohmic) contact

with the sample surface (grounded), and a DC bias voltage is applied to the cantilever, or vice versa. The electronic current is measured by a current-sensing device, and the electric properties of the sample can be thus characterized. Although this technique was first demonstrated on organic molecular crystals on gold surface, its application field was later on extended, i.e., to studies of ion diffusion in batteries [7], interfaces of metal oxides [8], crystalline structures and conducting properties of organic semiconducting molecules [9, 10], inter- and intra-charge transport of polymer nanofibers [11], and more.

During a contact mode c-AFM measurement, the cantilever tip is in permanent contact with the sample surface, which results in a non-negligible lateral force due to sliding friction. This lateral force may induce mechanical wear to the sample surface, which becomes critical when soft materials such as polymers or loosely bounded structures such as self-assembled molecular structures or carbon nanotubes on the substrate are investigated by c-AFM. The mechanical damage could be minimized by reducing the tip-loading force. However, the reduced loading/contact force also results in a smaller tip–sample contact area, leading to poorer electrical contact between the tip and the sample. Appropriate contact forces would typically be 1 nN–1 μN. Such forces are large enough to ensure good ohmic contact between tip and surface, but they are still small enough to avoid damage to the sample. Nevertheless, for some critical applications, morphological modification or materials destruction is observed even when a small contact force is applied in c-AFM. Examples are gold nanoparticles electrostatically immobilized on silicon substrates [12, 13], DNA on graphite [14], or chemical vapor-deposited carbon nanotubes on crystalline silicon substrates [15]. In addition, some researchers also observed changes of material electrical properties after the c-AFM measurement [16]. Thus, techniques that enable both low-force imaging and reliable current sensing are needed for characterizing soft materials or fragile structures.

3.2 Technical Challenges for Nondestructive Conductive AFM

In scanning probe-based techniques, like atomic force microscopy, topographic feedback is required for a stable scanning of the cantilever over the sample surface. In contact mode, the deflection of the cantilever is used as the topographic feedback signal. In intermittent or non-contact mode, the oscillation amplitude or frequency of the cantilever is used as the topographic feedback. Intermittent or non-contact imaging modes allow minimizing the lateral tip–sample interaction. However, in non-contact mode, there is no mechanical contact between the tip and the sample at all, thus no current can be measured. In intermittent contact mode (also known as tapping mode), the vertical oscillation amplitude of the cantilever is approximately 10–100 nm. During only 1 % of the oscillation cycle, the tip is in contact with the sample [14]. The typical oscillation frequency of a cantilever is >50 kHz in intermittent contact mode, and the typical noise level in current-sensing devices is around 50 fA. Therefore, to obtain a current signal with a reasonable signal-to-noise ratio, a current amplifier with a bandwidth above 5 MHz at a gain of 10^7–10^{10} V/A is

necessary. This is challenging with current technology [14, 17]. Thus, to be able to perform nondestructive current mapping on fragile samples, the tip–sample contact should be in the regime between direct contact and intermittent contact.

4 Experimental and Instrumental Methodology

We have discussed the technical challenges of using contact mode, intermittent contact mode, or non-contact mode to characterize electrical properties of samples and to measure currents between them and the cantilever tip. A solution to these issues would be a mode that allows the cantilever to be employed somewhere in between direct contact and intermittent contact. In this section, we will introduce a new scanning probe-based current-sensing technique: scanning conductive torsion mode microscopy (SCTMM).

4.1 How Does SCTMM Work?

It has been demonstrated recently that the torsional resonance (TR) signal of the cantilever could be used as topographic feedback [18, 19]. In the TR mode, the cantilever is excited at its first torsional resonance frequency by two antiparallel-driven piezoelectric crystals fixed to the cantilever holder (Fig. 6.1 inset). When the tip is scanning over a sample surface, the tip–sample interaction causes changes in the torsional oscillation amplitude. By adjusting the tip–sample distance, the TR amplitude can be kept constant (so-called amplitude modulation) [18], and the topography of the sample is acquired. Like in intermittent contact mode, the tip–sample contact force could be minimized by adjusting the TR amplitude set point. In TR mode, the cantilever tip is not in mechanical contact with the sample surface and the tip–sample contact force is thus much smaller than in c-AFM.

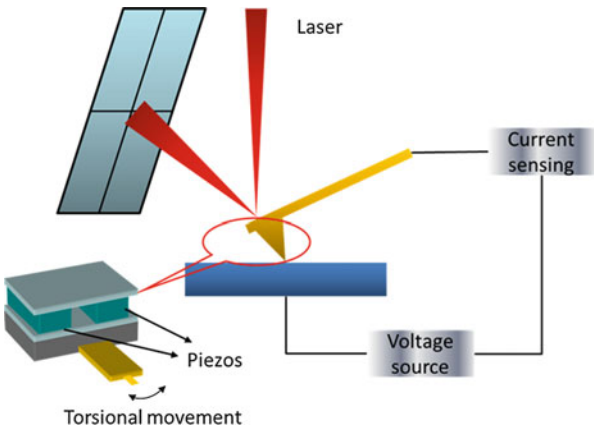


Fig. 6.1 The configuration of a SCTMM setup. *Inset*: cartoon of two piezoelectric crystals fixed to the cantilever holder for torsional mode excitation of the cantilever

The vertical (flexural) oscillation amplitude (perpendicular to the sample surface) of the cantilever is less than 2 nm in the TR mode. This distance is small enough for electric current to tunnel from the cantilever tip to the sample, while the sample topography is being recorded. Recently, by combining TR mode AFM and current-sensing devices, Harris et al. reported simultaneous topography and current mapping on fragile structures [14]. This method was named torsional TUNA® or scanning conductive torsional mode microscopy (SCTMM) [12–14, 20].

The setup of SCTMM is very similar to conventional c-AFM, as shown in Fig. 6.1. The cantilever tip is brought in proximity to the sample surface (grounded), and a DC bias voltage is applied to the cantilever, or vice versa. The electrical current measured in SCTMM is the tunneling of electrons across the air gap between the cantilever tip and the sample. The tunneling current I decays exponentially with increasing tip–sample distance z [21]:

$$I \propto V\rho \exp(-2\kappa z), \text{ with } \kappa = \frac{\sqrt{2mE}}{\hbar}, \tag{6.1}$$

Here ρ represents the local density of states of a sample, m is the electron mass, E is the barrier height for electron tunneling, and $\hbar$ is the reduced Planck constant. If all other parameters (tip conductivity, sample conductivity, and applied voltage) are kept constant, the current measured by SCTMM is generally several orders of magnitude lower than that measured by contact mode c-AFM [20, 22]. The much lower current measured in SCTMM results from the small (approx 2 nm) but finite tip–sample distance in SCTMM measurements compared with c-AFM measurements (see Eq. 6.1). On the other side, since the contact force can be controlled and minimized in SCTMM, the technique allows for nanoscopic current measurements on nanoparticles, conjugated polymer blends, nanorods, and other conducting and semiconducting soft materials or fragile structures [12, 13, 15, 20, 23–27].

4.2 Experimental Demonstration of SCTMM

Harris et al. demonstrated SCTMM in the Bruker Corporation application note [14]. In this study, Harris et al. casted a carbon nanotube (CNT) suspension onto a silicon substrate with gold patterns. The CNTs were loosely bounded to the substrate. When contact mode c-AFM was applied, the CNTs were swept off the scanned area due to the high lateral force applied during scanning. High-quality topography of the CNT could only be acquired in intermittent contact mode or TR mode. Due to the short dwell or contact time of the tip on the sample (Sect. 3.2), no electrical signal could be detected in intermittent contact mode. In TR mode, stable topography and current images could be obtained simultaneously (Fig. 6.2). Interestingly, the current image did not completely resemble the topographic one: only nanotubes (yellowish fibers) that were in contact with the gold layer were detected in the current image, while the rest of the area appeared nonconductive. The silicon substrate was covered by a native oxide layer, which acted as an insulator, thus

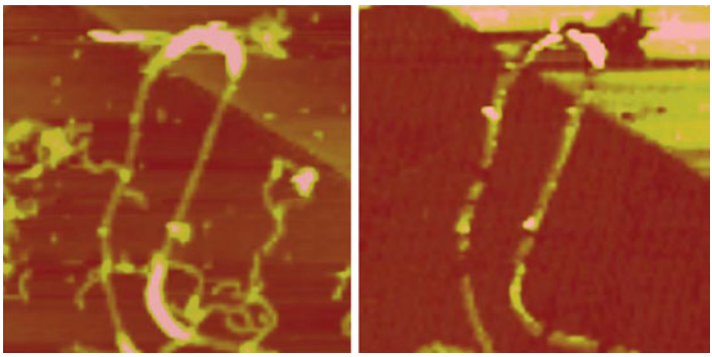


Fig. 6.2 Carbon nanotubes deposited from solution onto a gold grid (connected to the bias voltage) are shown as topography (*left*) and current (*right*) images. The SCTMM data shows only those nanotubes that are electrically connected to the gold grid and not to each other (Reprinted with permission from Ref. [14]. Copyright 2010, Bruker Corporation)

preventing electrons from being transported from the conductive CNT to the semiconducting silicon substrate. The mismatch of the topography and the current images also proves that there was no cross talk between the topographic and current signals during the measurement.

Another example is found in Berger's review [20]. Berger et al. used focused ion beam to deposit a cross consisting of a conducting platinum bar and an insulating silicon oxide bar (Fig. 6.3) onto highly oriented pyrolytic graphite (HOPG). Electrical properties of such a structure are known. Thus measurements by contact mode c-AFM (Fig. 6.3a, b) and SCTMM (Fig. 6.3c, d) could be directly compared. The images obtained by both techniques were very similar. However, stripe noise could be observed on the topography image measured by contact mode c-AFM, whereas no such noise was observed on that obtained by SCTMM. The horizontal stripes are typically caused by sudden increase or decrease of the lateral force (stick–slip of the cantilever tip) that results in changes of contact time, contact force, or contact area. The maximum current measured by SCTMM on the same platinum bar was 5 pA, which was several orders of magnitude lower than that measured by c-AFM (380 nA) with a similar applied bias voltage [20]. The lower measured current in SCTMM resulted from the exponential decay of the tunneling current with the tip–sample distance (see Eq. 6.1).

4.3 How Does the Tip–Sample Interaction Relate to the Current Measurement in SCTMM?

The measured tunneling current by SCTMM depends on the tip–sample distance. The tip–sample distance could be adjusted by adjusting TR amplitude set point, which alters the tip–sample interaction. Thus, it is necessary to understand the tip–sample distance with respect to the tip–sample interaction in SCTMM.

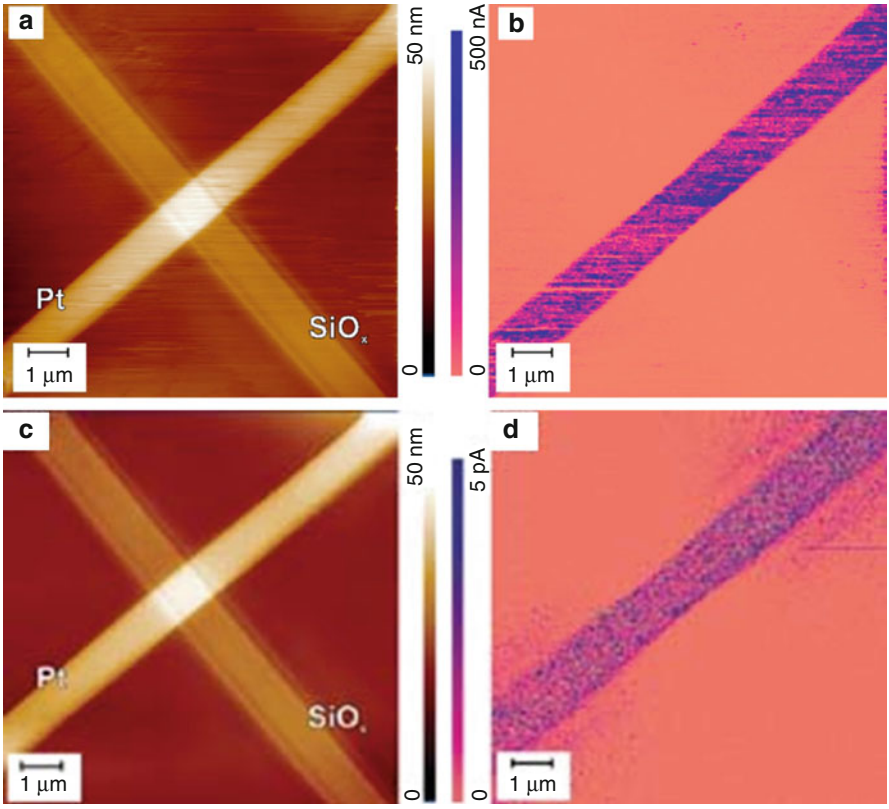


Fig. 6.3 (**a**, **b**) Contact c-AFM of a cross Pt and SiOx stripes deposited by focused ion beam on HOPG. The Pt was deposited on top of SiOx: (**a**) topography and (**b**) corresponding c-AFM current image obtained at a bias of 38 mV. (**c**) Topography of the same cross as imaged in Fig. 6.3a obtained in TR mode. (**d**) The corresponding SCTMM current map. The Pt was deposited on top of SiOx and therefore a continuous conductive area was measured (Adapted with permission from Ref. [20]. Copyright 2009, Macromolecular Rapid Communications)

As SCTMM is a current-sensing technique based on TR mode AFM, we first introduce the tip–sample interaction in TR mode.

In TR mode, the feedback error is modulated by TR amplitude change with respect to tip–sample distance in amplitude-modulated (AM) mode [18, 28] or by TR frequency shift with respect to tip–sample distance in frequency-modulated (FM) mode [29, 30]. As the topographic feedback in current SCTMM is modulated by TR amplitude, we will only discuss AM-TR mode in this chapter. Studies of TR amplitude change in response to tip–sample distance were pioneered by Su et al. by measuring TR amplitude versus tip–sample distance on a silicon surface (Fig. 6.4) [28]. The flexural deflection of the cantilever versus tip–sample distance curve was acquired simultaneously with the TR amplitude–distance curve. The TR amplitude started to decrease when the cantilever tip entered the attractive

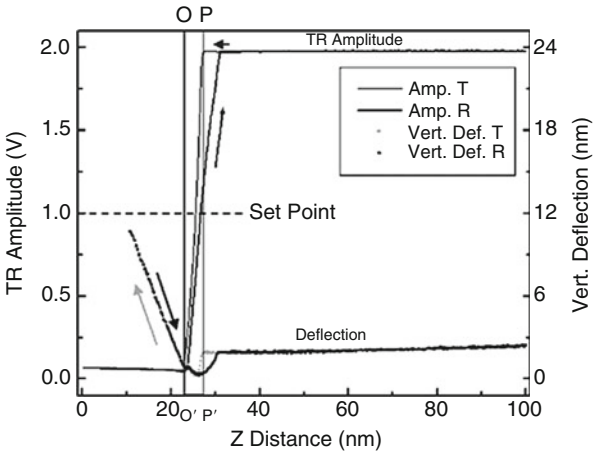


Fig. 6.4 Torsional resonance amplitude as a function of the tip–sample distance on a Si sample. The *horizontal axis* is the *z* ramp size. The vertical axis on the *left* and *right* represent amplitude and vertical (flexural) deflection, respectively. The line marked "TR amplitude" represents approaching (trace, marked as T) and retracting (retrace, marked as R) curves of the torsional resonance amplitude. Deflection curves shown are vertical deflections during approach and retraction (Reprinted with permission from Ref. [28]. Copyright 2007, Springer Science + Business Media)

zone (negative constant flexural deflection). Interestingly, the decrease of the TR amplitude with respect to tip–sample distance was monotonic in the entire attractive force regime and the TR amplitude was nonzero in both attractive and repulsive force regimes. Although the TR amplitude–distance curve is rather illustrative, the results obtained by Su et al. demonstrated unique features of TR mode from intermittent contact mode or contact mode [28]. The monotonic decrease of TR amplitude in the attractive force regime indicates that in TR mode stable images could be obtained in this regime, which is not possible in intermittent contact mode or in contact mode [28]. On the other hand, the nonzero TR amplitude at full contact (repulsive contact) makes it possible for the TR mode to be operated in a situation where tip and sample are in close proximity and in the extreme case also in contact mode [31]. By controlling the TR amplitude set point, TR mode could thus be applied in the near field [28]. As a result, in SCTMM, it is possible to maintain a small tip–sample vertical separation (<2 nm) and in the meantime modulate the tip–sample interaction from attractive to repulsive without introducing strong lateral forces. Such features make SCTMM a unique tool to measure electrical properties of soft materials – like polymers – and of structures loosely bound to the substrate, like nanoparticles, nanotubes, or DNA chains.

A similar study on tip–sample contact in SCTMM was carried out recently by Weber et al. [26]. In their work, Weber et al. performed distance and bias spectroscopy on poly(3,4-ethylenedioxythiophene) poly(styrene sulfonate) (PEDOT:PSS), a conducting polymer widely used in polymer electronics.

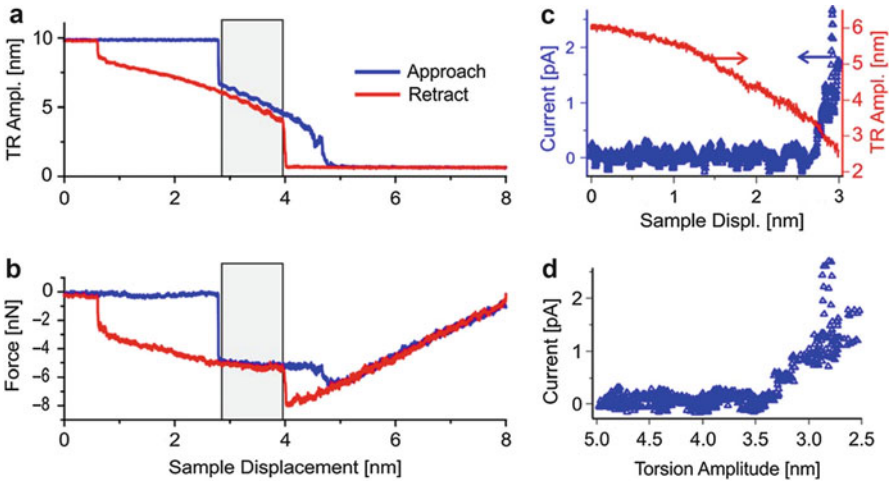


Fig. 6.5 Distance spectroscopy experiments. (**a**) Simultaneously recorded torsion amplitude versus sample displacement and (**b**) vertical force versus sample displacement. (**c**) The torsion amplitude (*red line*) and the tip–sample current (*blue triangles*) versus sample displacement, and (**d**) the same data replotted as current versus torsion amplitude (Reprinted with permission from Ref. [26]. Copyright 2013, AIP Publishing)

Weber et al. observed two discontinuous jumps (snap-in) in both amplitude–distance and deflection–distance curves (Fig. 6.5). The first snap-in happened when the tip was brought into close proximity to the sample surface, in an attractive region, as proved by the downward bending of the cantilever. The second snap-in indicated that a repulsive tip–sample interaction was established, as proved by the upward bending of the cantilever. Similar to results of Su et al., the TR amplitude remained nonzero in the repulsive regime. The current started to be measurable when the amplitude decreased to ~3.5 nm (where the tip was in the attractive regime) and increased exponentially. The exponential increase of the current with decreasing tip–sample distance indicated that the measured current was the tunneling current, as explained in Sect. 4.1 Eq. 6.1. This study demonstrated that electrical current can be measured in the near field with a low tip–sample force (~5.2 nN in the experiment) in SCTMM.

It is worth mentioning that the resonance frequency of the cantilever shifts when the tip–sample interaction changes from attractive to repulsive. In the intermittent contact mode, this shift is so large that there is no overlap between the free flexural resonance frequency and the contact resonance frequency. Thus, in the intermittent contact mode, the amplitude reduces to zero when a constant contact is established between tip and sample. The free TR frequency and the contact TR frequency, on the other hand, have enough overlap to keep amplitude nonzero throughout the attractive and repulsive regimes, which is consistent with experimental observations [26, 28].

We have here discussed the contact dynamics in SCTMM. As SCTMM is often used to study polymers or other soft materials, the special surface properties of

polymers should be taken into account. It is relatively difficult to define the surface of a polymer, as density of polymer chains is different at the surface and in the bulk. In addition, longer chains tend to repel shorter chains, leading to a thin layer of shorter polymer chains at the polymer–air interface. Yurtsever et al. have observed that, by reducing frequency set point in a FM-TR measurement, the dissipation energy was also reduced [29, 30]. Yurtseer et al. attributed the observation to materials property variations from the surface to the bulk: with decreasing tip–sample distance (reducing frequency set point), the cantilever tip probes the surface of the polymer and gradually moves into the bulk of the polymer. Therefore, when conducting polymers are studied, different electrical properties at the surface or in the bulk of these polymers should be considered.

4.4 Is SCTMM Destructive or Nondestructive?

In SCTMM, both topographic and electric properties are characterized. Thus, when discussing whether SCTMM is destructive or nondestructive, it is important to consider both mechanical wear and electrical wear of the sample after one or several scans. We discussed in the previous section (Sect. 4.2) that the contact force in SCTMM is much smaller than in c-AFM; thus, SCTMM is typically considered mechanically nondestructive. Here we will discuss whether SCTMM is also electrically nondestructive [13, 26].

4.4.1 Reduced Electrical Conductivity After SCTMM Measurements

Weber et al. observed that the electrical conductivity of PEDOT:PSS decreased after one SCTMM measurement was performed [26]. Weber et al. first performed SCTMM measurement with a scan size of $1 \times 1\ \mu m^2$ and then enlarged the scan area to a size of $3 \times 3\ \mu m^2$. A slightly reduced current from 1.3 ± 0.7 pA to 1.1 ± 0.6 pA with similar applied voltage of 7 V was observed, while topography remained almost unchanged. The reduced current at similar applied bias voltage indicated that the conductivity of PEDOT:PSS in that area decreased slightly. We could thus conclude that SCTMM causes minor conductivity changes to some materials. Interestingly, a similar observation was also reported by Dang et al. using contact mode c-AFM [16]. However, in Dang et al.'s study, the electrical conductivity of PEDOT:PSS decreased by more than one order of magnitude after one c-AFM scan. In addition, when the applied bias voltage was increased to more than 9 V, topographic change of the scanned area was observed, which was not observed in Weber et al.'s study even with higher applied voltages and more SCTMM scans [16, 26]. Apparently, for PEDOT:PSS, conductivity decrease caused by SCTMM is significantly smaller compared with that caused by c-AFM.

4.4.2 Changes of Surface Potential After SCTMM Measurements

We have observed in our previous study that surface potential of gold nanoparticles (AuNPs) covered by a thin polystyrene (PS) film changed after a SCTMM

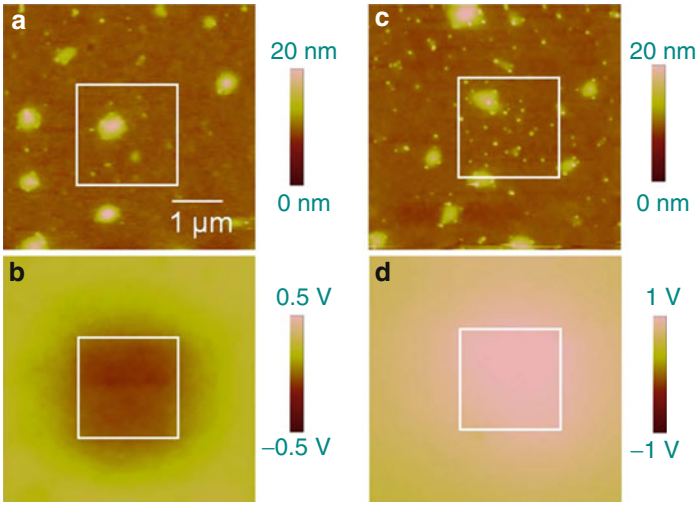


Fig. 6.6 Height (**a** and **c**) and surface potential (**b** and **d**) images of individual AuNPs embedded in a PS film of $t = 40$ nm: (**a** and **b**) after a positive bias of 12 V was applied, (**c** and **d**) after a negative bias of 12 V was applied. Areas inside the *white squares* are positions where SCTMM measurements were performed

measurement [12]. We first performed SCTMM measurements on AuNPs/PS over an area of 2×2 μm^2, with both positive and negative bias voltages of 12 V applied to the sample. We used relatively high voltages, as we were interested in the extreme situation of a complete electrical wearing-out of the sample. Next, we performed surface potential mapping immediately after each SCTMM measurement on the same area but on a larger scale of 5×5 μm^2 by Kelvin probe force microscopy (KPFM, Fig. 6.6) [12]. We observed changes of surface potential in the area where SCTMM was performed, while the topography remained almost unchanged. The surface potential of where SCTMM was performed increased when a negative bias was applied in SCTMM and decreased when a positive bias was applied. The magnitude of the potential variation was dependent on that of the applied bias during the SCTMM measurement. We also noticed that surface potential variation was less pronounced on thinner PS films compared with thicker PS films.

The sign of the applied voltage in SCTMM correlates to different directions of the current flow. With a positive voltage applied to the sample, electrons tunnel from the tip to the sample and vice versa for a negative applied voltage. As a nonconductive polymer, the thick PS layer limits the electrons to tunnel through. The electrons thus accumulated on the PS surface during the SCTMM measurement and polarized the PS film. Hence, the surface potential decreased when a positive voltage was applied to the sample and vice versa. The dielectric effect of PS is weaker when a thinner PS covers the conducting AuNPs. Therefore, changes of the surface potential were smaller if the PS layer was thinner. The experiment indicated

that electrical wear could be introduced during SCTMM measurements even if no apparent topographic variations are observed. This electrical wear could be minimized by minimizing the bias voltage applied to the sample, i.e., a voltage that is just high enough for electrons to tunnel between the conducting tip and the sample. On the other hand, as in SCTMM the cantilever tip is not in constant contact with the sample surface, a higher voltage is usually required for measuring a current at all. In conclusion, when a material of poor electrical conductivity like PS is characterized by SCTMM, the measurement is prone to cause an electric degradation of the sample.

5 Key Research Findings

In this section, we will introduce some applications of SCTMM. We will show that SCTMM could be used beyond measuring electrical conductivity of conducting or semiconducting samples. In fact, we would like to provide some examples where SCTMM was used in understanding structure–properties relationships, defect checking, electropolymerization monitoring, and molecular structure studies.

5.1 Understanding Structure–Properties Relationship by SCTMM

Due to the important role of conjugated polymer blends in organic semiconductor industry, many studies have been carried out on this group of materials. Conjugated polymer blends possess nanoscopic heterogeneity in both morphological and electrical properties. Thus, it is necessary to understand the correlation of nanoscopic heterogeneity and macroscopic properties of conjugated polymer blends. In this section we will present some of our own work on how to use SCTMM to understand structure–properties relationships of complex systems. We start from a model AuNPs/PS system and continue with a more complex system, i.e., polypyrrole: polystyrene sulfonate (PPy/PSS) blends.

5.1.1 SCTMM Analysis on Individual AuNPs

Although c-AFM and SCTMM are widely used to study conjugated polymer blends, both have limitations. The resolution and accuracy of c-AFM or SCTMM are influenced by the nanoscopic heterogeneity of the materials. For instance, with c-AFM or SCTMM, information on conducting domains is not always accessible if they are embedded inside a nonconducting matrix and do not form a conducting channel (percolation path) through the sample. To overcome such limitations, we carried out SCTMM measurements on a model system with controlled nanoscopic morphology and known electric properties [12, 13]. This model system is a mimic of conjugated polymer blends. We coated thin PS films of controlled thickness (t) on top of gold particles with diameters of around 20–30 nm. We chose this size as it is similar to that of the conducting domains of conjugated polymer blends [32, 33]. Gold is chemically inert in air and its electronic properties are well known.

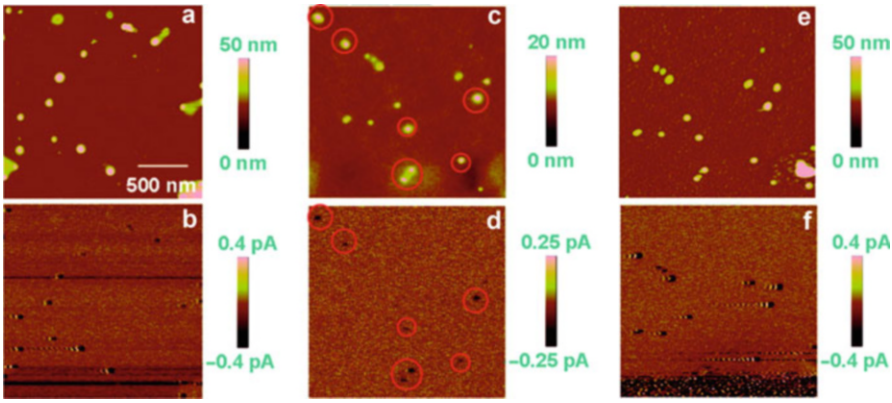


Fig. 6.7 SCTMM measurements on the Au/PS system: (**a** and **b**) height and current images of AuNPs on treated silicon wafer, current bias = −9 V; (**c** and **d**) height and current images of AuNPs with 25 nm PS layer, current bias = −12 V; (**e** and **f**) height and current images of AuNPs (same position as (**c** and **d**)) after 10 min plasma etching, current bias = −8 V (Reprinted with permission from Ref. [12]. Copyright 2010, American Chemical Society)

The negatively charged AuNPs were only electrostatically bonded to a silicon substrate of a monolayer of NH^{4+}. Therefore, we selected SCTMM to study the AuNPs/PS system. Otherwise AuNPs would have been swept away by the cantilever tip if a contact mode c-AFM had been applied.

Figure 6.7 is a representative series of topography and current images of individual AuNPs and AuNPs/PS before and after plasma etching. Here we applied negative bias to the sample; thus, a more negative current corresponded to a percolation/conducting path of higher conductivity. The naked AuNP on the bare silicon surface corresponded to a current of around 6 pA with a bias voltage of −9 V. The height of AuNPs reduced from 20–30 nm to 7–17 nm after a layer of 25 nm PS film was coated onto them. Only half of them (marked by red circles) still corresponded to a current, which reduced to only 0.4–0.8 pA despite that a higher voltage of −12 V was applied. After plasma etching, AuNPs were completely exposed to the conductive tip, and the measured current increased to 5 pA at a voltage of −8 V.

Both topographic and SCTMM results of naked AuNPs and AuNPs/PS after plasma etching were very similar, indicating that both morphological and electrical properties of AuNPs remained unchanged during the SCTMM measurements. The PS layer on the AuNPs acted as a tunneling barrier, leading to reduced and, in the extreme case, undetectable current signal (beyond the resolution of the current amplifier of 50 fA. [14]). To extrapolate our experimental results to real conjugated systems, we would conclude that if a conducting domain is deeply embedded inside the insulating matrix material, it may not be detected by SCTMM.

As not all conducting domains would be detected by SCTMM, it is necessary to study the maximum tunneling distance or the tunneling threshold of individual system. The tunneling threshold could be calculated using results obtained in this

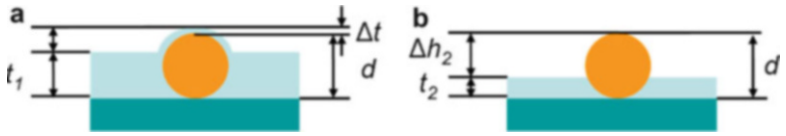


Fig. 6.8 Schematic sketches of geometries of an AuNP embedded in a PS film ($t = 25$ nm) before (**a**) and after (**b**) the plasma etching

experiment [13]. Figure 6.8 is a geometric illustration of an AuNP covered by a thin PS film before and after the plasma etching. The diameter of the AuNP can be determined as

$$d = \Delta h_1 + t_1 - \Delta t = \Delta h_2 + t_2. \tag{6.2}$$

Here Δh_1 and Δh_2 are the height differences between the apex of the AuNP and the PS surface before and after the plasma etching, and t_1 and t_2 are the thicknesses of the PS film on silicon surface before and after the plasma etching. Both Δh and t in Eq. 6.2 are measurable.

With $t = 25$ nm, 2 nm $< \Delta t <$ 4 nm for smaller particles, and $\Delta t <$ 2 nm for bigger particles. Here the smaller particles are those that did not conduct current after being covered by the PS film, while the big particles are those that still conducted current after being covered by the PS film (Fig. 6.7). Therefore, for this AuNPs/PS system and experimental setup, the maximum tunneling distance was 2 nm. To further prove our conclusion, we carried out similar experiments on AuNPs covered by a thicker PS layer, i.e., 70 nm, as a control experiment [13]. No current could be detected at applied bias of 12 V, although these particles were proved to be conductive by SCTMM after plasma etching. For PS layer of 70 nm, the thickness Δt of PS layer on top of them was larger than 2 nm, which is beyond the maximum tunneling distance of the system we studied. In this study, we aimed at understanding AuNPs/PS system and SCTMM. Therefore, we used relatively high voltage, i.e., −12 V, to determine the maximum tunneling distance. However, to avoid any potential electrical damage induced by SCTMM, a minimum bias voltage should be used for electrical characterization on real systems. Thus, the actual vertical detection limit of SCTMM could be smaller than 2 nm for a system similar to AuNPs/PS.

5.1.2 SCTMM Analysis of Au Clusters

SCTMM could also be performed on a more complex system, i.e., Au clusters/PS system. Here we present one example on how we used SCTMM to study conductivity variations of the system by ex situ plasma (50 % argon) treatment [12, 13]. We first casted a layer of PS of 56 nm onto some Au clusters and imaged them by SCTMM (Fig. 6.9a, b). Then we removed the PS stepwise by plasma etching and examined the system on the same position by SCTMM (Fig. 6.9c–f). We marked similar features/areas on both topography and current images by red and white circles. Topography of the clusters became clearer and particles inside the red

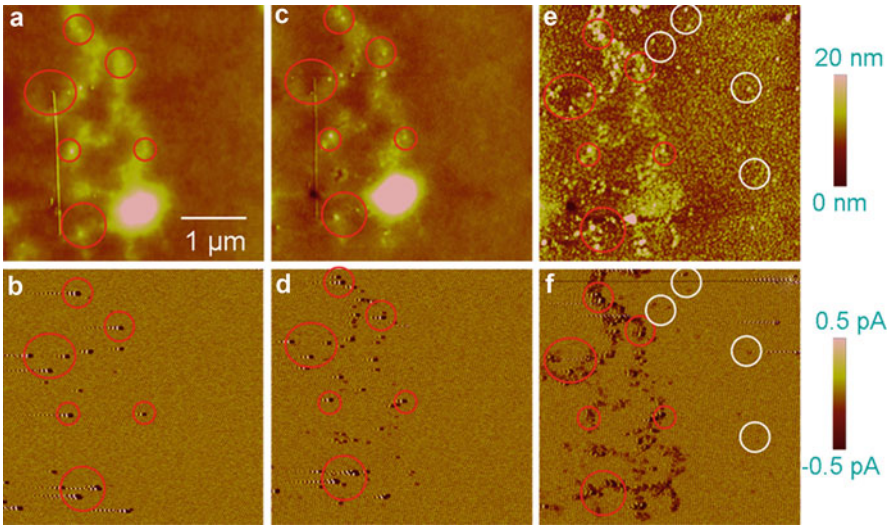


Fig. 6.9 Thickness dependence of the Au/PS system by SCTMM: (**a** and **b**) height and current images of Au clusters with $t = 56$ nm PS layer, current bias $= -10.5$ V; (**c** and **d**) height and current images of Au clusters after 4 min plasma etching, residual PS layer thickness $t \sim 50$ nm, current bias $= -8.5$ V; (**e** and **f**) height and current images of Au clusters after 12 min plasma etching, PS layer thickness $t \sim 24$ nm, current bias $= -6.0$ V (Reprinted with permission from [12]. Copyright 2010, American Chemical Society)

circles protruded out more than the others after the first plasma treatment (Fig. 6.9c). The surface became rougher and new particles started to appear inside the white circled areas after the second plasma treatment (Fig. 6.9e). The measured current also changed accordingly. To minimize electrical damage to the sample, we reduced the applied voltage when examining the sample after each plasma etching step, due to the increased conductivity of each measuring spot after the plasma treatment. The measured current of each step was around 10 pA while the applied voltage was reduced from -10 V to -6 V after each plasma etching. The number of conducting/percolation channels also increased after each plasma etching step. Additionally, after the second plasma etching, we measured a current of around 2 pA on particles (marked in white circles) that were previously not visible on either height or current images inside the white circles (Fig. 6.9f).

In Sect. 5.1.1 we have shown that electrons could only tunnel through a nonconducting PS layer of up to 2 nm thickness. Thus, for a system of a nonconducting PS film of around 56 nm before the plasma etching, the conducting channels could only be formed by two AuNPs stacked vertically. In this case, the tunneling barrier decreased to less than 1 nm. The increasing number and the increasing conductivity of the conducting channels after each plasma etching step indicated that the PS film was progressively removed. In addition, some individual AuNPs started to be exposed to the conductive tip after the plasma etching. These particles were still partially covered by PS as the measured current of these particles

was smaller (around 2 pA) than that of the naked AuNPs (around 6 pA). The existence of these individual AuNPs was also confirmed by potential mapping before the SCTMM measurement [12]. In this system, the individual AuNPs could only be detected after the plasma etching, which is not always feasible when an unknown system is studied. Therefore, complementary techniques might be needed in understanding structure–properties relationship of real systems.

5.1.3 Understanding the Nanoscopic Structure of Conjugated Polymer Blends

During SCTMM measurements, current is flowing through between an individual percolation channel of the sample and the cantilever tip. This flowing path is not influenced by other percolation channels nearby. Hence, SCTMM allows imaging with relatively high lateral resolution and is capable of distinguishing among different conducting channels and measuring their distributions across the sample. Such information is essential for a quantitative analysis of the charge transport routes and of their distribution in conjugated polymers on the nanoscale [34, 35]. However, the trace of the conducting domains is completely lost in SCTMM when they are too deeply buried by the nonconducting matrix, which results in a missing puzzle in understanding nanoscopic morphology of complex systems, i.e., conjugated polymer blends. One solution is to obtain supplementary information from other techniques. Here we present one example of studies on nanoscopic morphology of PPy/PSS blends using combined KPFM and SCTMM measurements.

Figure 6.10 represents topography, surface potential, and current images acquired on the PPy/PSS film of 80 nm. There are some domains of a diameter of 20–30 nm on the topography image (yellowish areas on Fig. 6.10a), which corresponded to a lower surface potential than the surroundings on the potential image (brownish areas on Fig. 6.10b). The surface potential of each domain was rather uniform and of similar size. The current signal of these domains, on the other hand, was rather discontinuous, i.e., several conducting channels of smaller dimension were formed inside each single domain.

During the synthesis, PPy formed aggregates rather than being homogeneously dispersed in PSS [13, 32, 33]. Therefore, in the polymer film there must be regions with a higher PPy concentration, i.e., PPy-rich phase/domains, and regions with a higher PSS concentration, i.e., a PSS-rich phase. The two phases are not completely separated; in fact, we have proved in other studies that there is also PPy in the PSS-rich phase and PSS in the PPy domains [36]. The domains on the topography images are thus PPy phase, as supported by the current image. The diameter of the PPy domains measured here is consistent with that measured by dynamic light scattering (approx. 26 nm) [13]. Thus, together with KPFM and SCTMM results, we could conclude that each individual conductive PPy domain with diameter of 20–30 nm consists of several PPy sub-domains with diameters smaller than 10 nm. The PPy sub-domains embedded in the PSS matrix form the actual percolation paths through the PPy/PSS film. By combining SCTMM and KPFM, we were able to understand nanoscopic morphology and electronic properties of PPy/PSS, which is essential in materials optimization.

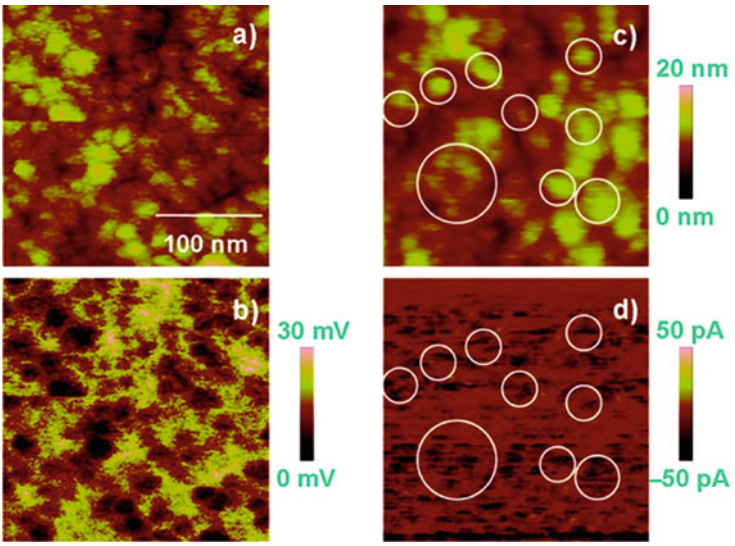


Fig. 6.10 KPFM and SCTMM images of PPy/PSS thin films: (**a** and **b**) topography and potential images by KPFM; (**c** and **d**) topography and current images by SCTMM, current bias = −4.1 V, current sensitivity = 10 pA/V. All images are scans of 250 × 250 nm. The current image was flattened without modifying the current data (Reprinted with permission from Ref. [12]. Copyright 2010, American Chemical Society)

5.2 Mapping of Local Conductivity Variations on Fragile Nanopillar Arrays

Conductive nanopillars made of polymers have been considered as a promising candidate for organic photovoltaic industry. The high aspect ratio of the pillar structure makes it suitable for an electron donor/acceptor layer in an organic solar cell when they are arranged in an array [27, 37]. Moreover, arrays of nanopillars could be easily prepared using anodized aluminum oxide (AAO) [38], for instance. Therefore, understanding the electrical properties with respect to the nanoscopic morphology of these nanopillar arrays has attracted extensive interests recently. Nevertheless, it is very challenging to study the morphological and electrical properties of the freestanding nanopillar arrays by contact mode c-AFM. The lateral force induced by contact mode imaging would damage the fragile nanopillar arrays when the cantilever is scanning over the surface.

Weber et al. reported a simultaneous measurement of morphological and electrical properties of the freestanding nanopillars by SCTMM [27]. In their study, Weber et al. prepared semiconducting freestanding polymer nanopillar arrays using AAO templates and performed SCTMM on freshly prepared arrays and aged ones. Figure 6.11a, b represents topography and current images of freshly prepared nanopillar arrays. Individual nanopillars could be observed on the topography

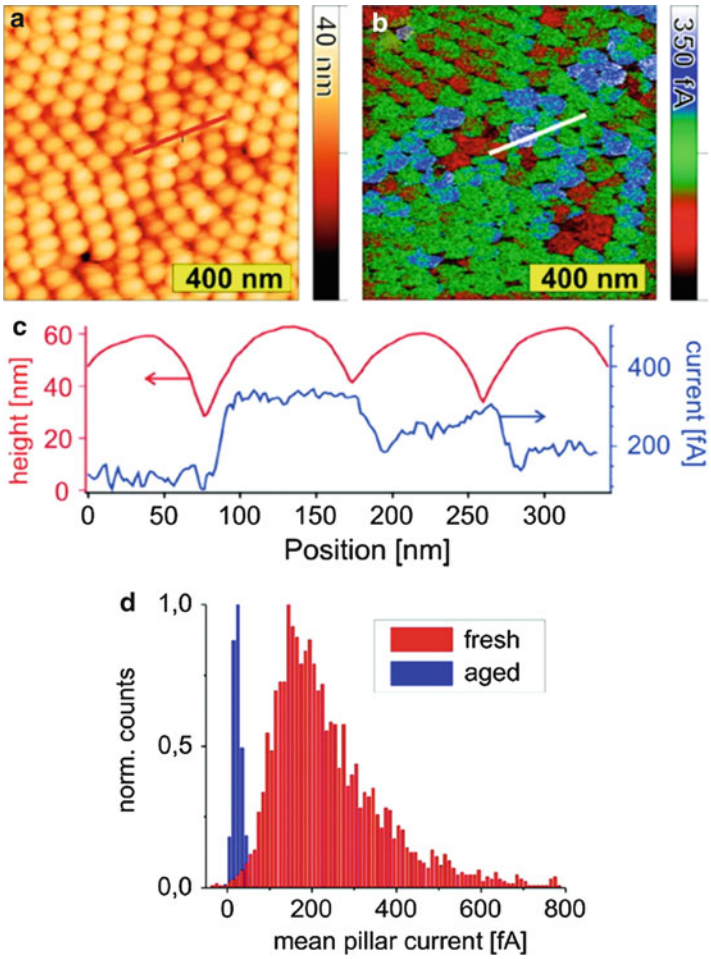


Fig. 6.11 Topography (**a**) and current map (**b**) measured simultaneously with scanning conductive torsion mode microscopy. (**c**) Averaged line sections in topography (*red*) and current (*blue*) obtained from six parallel lines at the positions marked with a *red line* in the topography (**a**) and *white line* in the current map (**b**). (**d**) Histogram of the mean pillar currents. *Red bars*: fresh sample measured on 2,660 rods on an area of 5 μm × 5 μm within 24 h after preparation. *Blue bars*: the same sample after 15 days exposed to air and light (514 rods on 2 μm × 2 μm) (Adapted with permission from Ref. [27]. Copyright 2010, American Chemical Society)

image. Each nanopillar corresponded to one conducting domain with a current measured up to 340 fA. For a more clear presentation, both topography and current profiles were plotted along indicated lines in Fig. 6.11a, b. A depth of 30–40 nm of gaps between two adjacent nanopillars could be measured, which is lower than the length (165 ± 5 nm) of the nanopillars measured by scanning electron microscopy [27]. The reduced measured depth of gaps could be attributed to the geometrical effect of the cantilever tip during the scanning. Additional current mapping was

conducted on a larger scale of 5 × 5 μm^2 for a statistical analysis on the electrical conductivity of 2,660 nanopillars. The analysis resulted in an average current of 240 ± 140 fA. Of all the measured nanopillars, less than 2 % of the nanopillars corresponded to current lower than 50 fA. (noise threshold of the current amplifier). The distribution of the measured current of the freshly prepared nanopillars was rather broad according to the current histogram (Fig. 6.11d). Nanopillars are extremely sensitive to light, oxygen, or humidity, resulting in electrical degradation [39]. Thus the nonconducting nanopillars could be degraded ones or ones with defects that inhibited electrons from transporting through the conducting channels, since the experiment was carried out in air. This explains the broad current distribution of the nanopillars: some of the nanopillars might degrade partially while others were more electrically stable. To examine electrical degradation of nanopillars, Weber et al. performed similar statistic SCTMM analyses on aged nanopillars. The average current measured on aged nanopillars was 24 ± 11 fA, which was below the noise level of the current amplifier of 50 fA. The current histogram of the aged nanopillars was rather narrow compared to the fresh ones, indicating complete degradation. The significantly lower current on the aged nanopillars further proved that nanopillars could lose their conductivity dramatically after being exposed to air. This study also demonstrated that SCTMM could be used to check defects of nanopillars or other similar structures and their electrical degradation.

5.3 Monitoring Electropolymerization of Conjugated Polymers

Conjugated polymers are difficult to process due to their rigid molecular structure, which limits their applications in organic electronics. Thus, conjugated polymers are usually blended with insulating polyelectrolytes to increase the solubility in water for better processability [40]. The disadvantage of blending is that the electronic properties of the blend are strongly dependent on the distribution of conducting polymer domains inside the insulating matrix. Another solution is to use in situ electropolymerization to incorporate conjugated polymers directly into prefabricated electrodes or devices. It is well known that polymers synthesized under different electropolymerization procedures can have different morphologies and electrical properties [41–43]. Therefore, in situ studies of electropolymerization procedure have attracted researchers' attention.

Musumeci et al. have reported in their recent study that SCTMM could be used to assist monitoring of electropolymerization process of 3,4-ethylenedioxythiophene (EDOT) [24]. In their work, Musumeci et al. first applied a voltage of 10 V between two gold microelectrodes immersed in EDOT solution. PEDOT fibers gradually grew and bridged the two electrodes. The residual EDOT was washed away. EDOT itself is not conducting, while its polymer, PEDOT, is conducting. A way to check the polymerization of EDOT is to measure the conductivity of fibers grown between two adjacent electrodes. As the gold electrodes were patterned on an insulating SiO_2 substrate, only fibers that connected

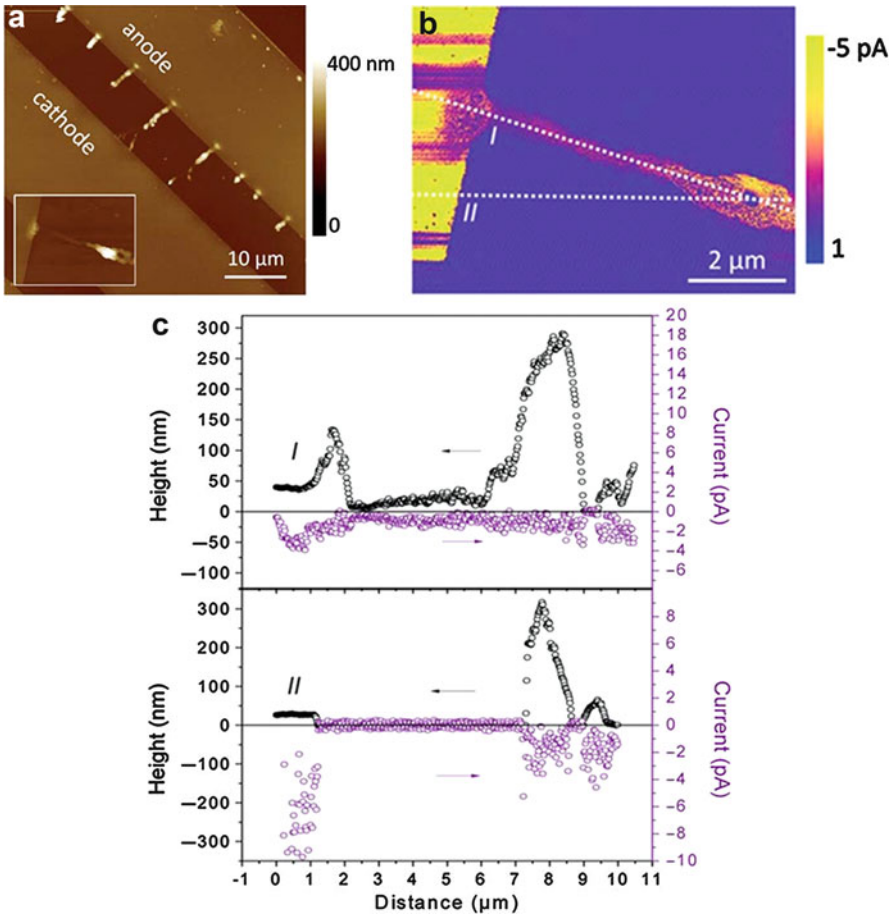


Fig. 6.12 PEDOT fibers obtained by electropolymerization of EDOT, solution 0.1 M in MeCN at 10 V, 5 s crossing a 10 mm wide gap. (**a**) AFM topographical image showing aligned fibers growing from the anode and bridging the gap. In the *inset* a single fiber connected to an electrode is shown, the current map of which obtained by SCTMM is reported in (**b**). (**c**) Height and current profiles along the marked lines (I and II) in (**b**): I refers to the fiber connected to the electrode and II considers also the bare SiO_2 substrate (Reprinted with permission from Ref. [24]. Copyright 2013, The Royal Society of Chemistry)

the gold electrodes could conduct the current. Therefore, by comparing individual fibers on topography and current images, it resulted possible to monitor defects in the synthesized polymer fibers. The PEDOT fibers fabricated this way were very thin – in the range of 5–350 nm. Conventional contact mode c-AFM would scrap these fibers off the surface, leading to permanent mechanical damage of the thin fibers. SCTMM succeeded in this purpose. Figure 6.12 represents topography and current images of PEDOT fibers between two gold microelectrodes [24]. All PEDOT fibers were connected to the anode, while only some were also connected

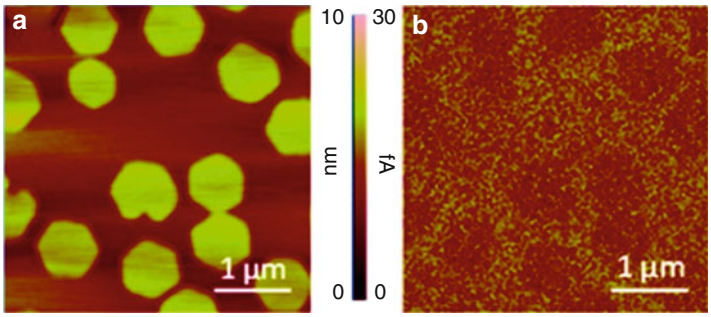


Fig. 6.13 Surface morphology measured in torsional resonant mode (**a**) and corresponding current map (**b**) of 1-DMDOA deposited onto Si with its thin native oxide layer (thickness 1.5 ± 0.3 nm) (Reprinted with permission from Ref. [25]. Copyright 2011, American Chemical Society)

to the cathode, indicating that the growth of PEDOT started from the anode. For a clearer presentation, two profiles were plotted along dotted lines on Fig. 6.12b (Fig. 6.12c, d). Apparently, only fibers and gold electrodes contributed to the current signal while the SiO_2 substrate was insulating. The results of Musumeci et al. demonstrated that SCTMM could be a precious tool for monitoring electropolymerization processes and assessing the quality of the synthesized polymers.

5.4 Understanding Molecular Orientation of Self-Assembly Structures

Polyoxometalates (POM) are complex metal oxide molecules, whose structural and electronic properties have attracted extensive interest [44]. Studies have shown that POM nanostructures formed from solution can be strongly influenced by the selection of counter ions as well as by substrates on which they are deposited [45]. To better control the self-assembly process, it is very important to understand the structure formation process, especially the molecular orientation of POM and its counter ions. AFM has been extensively used in studying the morphology of self-assembly structures [46]. As the self-assembly structures are stabilized by weak van der Waals forces or electrostatic forces, contact mode is usually not suitable for this purpose. Musumeci et al. have shown in their recent studies that SCTMM could be used to understand molecular orientation of self-assembly structures [25]. In their studies, Musumeci et al. formed 2D hexagonal nanostructures made of POM anions and dioctadecyldimethylammonium (DMDOA) cations on silicon substrates through Langmuir–Blodgett deposition. When a positive bias voltage higher than 6 V was applied to the silicon substrate, a current image could be acquired by SCTMM (Fig. 6.13). The hexagons corresponded to a lower current and were thus less conductive than the silicon substrate. When the applied bias exceeded 8 V,

damage of the hexagons was observed. However, when the sign of the applied bias was reversed, i.e., a negative bias was applied to the substrate, no current could be observed even at a bias of −8 V. In SCTMM, when a positive bias is applied to the substrate, electrons tunneled through the cantilever tip to the sample surface, and electrons tunneled through the sample to the cantilever tip when a negative bias is applied to the substrate. If the surface of the sample is positively charged, tunneling of the electrons from the cantilever tip to the sample surface would be easier and vice versa. If the surface ions are only weakly attached to their counter ions (anions), increasing of the positive bias might result in removal of the cations from their counter ions. The experimental observation of Musumeci et al. demonstrated that the top layer of the hexagons was covered by DMDOA cations, which was consistent with their assumption [25]. In this study, via mapping the current on POM:DMDOA, the molecular orientation of POM:DMDOA was determined. This study broadened the application of SCTMM.

6 Conclusions and Future Perspective

One goal in scanning probe-based atomic force microscopy techniques is to increase spatial resolution of topography imaging and sensitivity of mapping physical properties, like the electrical conductivity. We have thus introduced the technical background of SCTMM and discussed its advantages in applications of characterizing soft materials and fragile structures. We also introduced some recent applications of SCTMM. Many of the studies mentioned could only be conducted by SCTMM, since it combines current sensing with low contact force imaging, which is a major advantage of SCTMM compared with c-AFM. One drawback of SCTMM is the larger tip–sample separation compared with contact mode c-AFM, which means that a higher bias voltage must be applied. This is not favorable for more fragile materials of low conductivity. Further, in SCTMM the tip–sample contact area is not well defined, leading to difficulties in interpreting the measured point current [17]. We would thus like to address possible improvements of future scanning probe-based current-sensing techniques.

6.1 Frequency Modulation SCTMM

The SCTMM technique we have discussed in this chapter is based on amplitude-modulated torsional resonance (AM-TR) mode. It has been demonstrated that a more sensitive technique, i.e., frequency modulation technique, could also be used in TR mode (FM-TR) for stable imaging [30, 47]. FM-TR mode has been shown to be highly sensitive and could be used to map dissipation energy of samples if a constant TR amplitude is maintained [30, 47]. Thus, combination of current sensing and FM-TR mode may result in a new technique that offers simultaneous mechanical and electric properties mapping, which could be highly interesting.

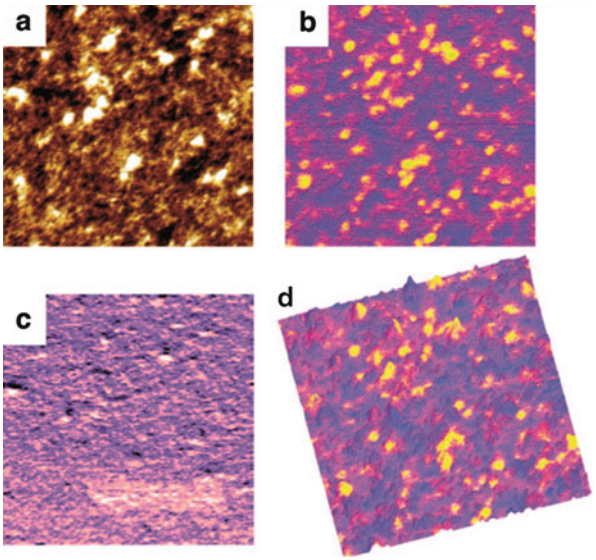


Fig. 6.14 PeakForce TUNA images of P3HT thin film spin-coated on glass/ITO/PEDOT substrate and annealed at 120 °C. Shown are (**a**) topography, scale 10 nm; (**b**) peak current, scale 300pA; (**c**) DMT modulus, scale 15 MPa; and (**d**) the overlay of conductivity map on topography. Image size is 2 × 2 μm, taken at 1 nN PeakForce, 3 V DC bias, using Bruker's PeakForce TUNA probe (Au coating, spring constant of 0.4 N/m) on a MultiMode 8 AFM in a glove box with below 1 ppm O_2 and H_2O (Reprinted with permission from Ref. [17]. Copyright 2011, Bruker Corporation)

6.2 Maximum Force-Modulated Current-Sensing Techniques

As explained in Sect. 3.2, the intermittent contact mode is not suitable for simultaneous current and topography mapping due to technical limitations of the current amplifier. Typical oscillation frequency of a cantilever in intermittent contact mode is above 50 kHz, which is too fast for the current amplifier to obtain a reasonable signal-to-noise ratio [14]. However, if the oscillation frequency of the cantilever could be reduced by an order of magnitude, i.e., down to 1–2 kHz, current amplifiers with bandwidths of 10–20 kHz at a gain of 10^7–10^{10} V/A can be used [17]. PeakForce tapping, introduced by Bruker Corporation, is an imaging mode in which a cantilever is oscillated at a frequency of 1–2 kHz [17]. In this mode, the cantilever performs force–distance curves on each measuring pixel. The maximum tip–sample force is used as topographic feedback and can be properly adjusted. Although the cantilever tip is in direct contact with the sample surface at each pixel, it is not in contact with the sample when moving from one pixel to the next. Therefore, the lateral force in PeakForce tapping is reduced to nearly zero. Current mapping with low tip-loading force can be achieved by combining current-sensing devices with PeakForce tapping (so-called PeakForce TUNA by Bruker

Corporation) [17, 48]. Figure 6.14 is a representative example, where current of poly(3-hexylthiophene) (P3HT) film was measured by PeakForce TUNA. As the maximum tip–sample force is used as the topographic feedback, the tip–sample force could be minimized, which is beneficial for measuring soft materials or fragile structures. However, it is still under discussion whether the spatial (XY) resolution of PeakForce TUNA is comparable to SCTMM. In addition, with increasing and decreasing tip–sample distance, the tip–sample contact area changes as well. Changes of contact area may result in changes of current flowing through the ohmic contact. A still open question with this technique is how to define at which time of the oscillation cycle the current should be measured.

References

1. Sessolo M, Bolink HJ (2011) Hybrid organic–inorganic light-emitting diodes. Adv Mater 23(16):1829–1845
2. Xu T, Qiao Q (2011) Conjugated polymer-inorganic semiconductor hybrid solar cells. Energy Environ Sci 4(8):2700–2720
3. Baeg K-J, Binda M, Natali D, Caironi M, Noh Y-Y (2013) Organic light detectors: photodiodes and phototransistors. Adv Mater 25(31):4267–4295
4. Ameri T, Khoram P, Min J, Brabec CJ (2013) Organic ternary solar cells: a review. Adv Mater 25(31):4245–4266
5. Kelley TW, Granstrom E, Frisbie CD (1999) Conducting probe atomic force microscopy: a characterization tool for molecular electronics. Adv Mater 11(3):261–264
6. Loiacono MJ, Granstrom EL, Frisbie CD (1998) Investigation of charge transport in thin, doped sexithiophene crystals by conducting probe atomic force microscopy. J Phys Chem B 102(10):1679–1688
7. Zhu J, Lu L, Zeng K (2013) Nanoscale mapping of Lithium-Ion diffusion in a cathode within an all-solid-state Lithium-Ion battery by advanced scanning probe microscopy techniques. ACS Nano 7(2):1666–1675
8. Hou J, Rouxel B, Qin W, Nonnenmann SS, Bonnell DA (2013) Tip loading effects on AFM-based transport measurements of metal–oxide interfaces. Nanotechnology 24(39):395703
9. Yang H, Shin TJ, Ling M-M, Cho K, Ryu CY, Bao Z (2005) Conducting AFM and 2D GIXD studies on pentacene thin films. J Am Chem Soc 127(33):11542–11543
10. Hendriksen BLM, Martin F, Qi Y, Mauldin C, Vukmirovic N, Ren J, Wormeester H, Katan AJ, Altoe V, Aloni S, Fréchet JMJ, Wang L-W, Salmeron M (2011) Electrical transport properties of oligothiophene-based molecular films studied by current sensing atomic force microscopy. Nano Lett 11(10):4107–4112
11. Jean-Christophe B, Wibren DO, Laurence L, Dirk V, Jean M (2013) The importance of bridging points for charge transport in webs of conjugated polymer nanofibers. Adv Funct Mater 23(7):862–869
12. Sun L, Wang J, Bonaccurso E (2010) Nanoelectronic properties of a model system and of a conjugated polymer: a study by Kelvin probe force microscopy and scanning conductive torsion mode microscopy. J Phys Chem C 114(15):7161–7168
13. Sun L (2010) Nanoscopic studies of conjugated polymer blends by (electric) scanning probe microscopy. Dissertation, Johannes Gutenberg-Universität
14. Harris P, Huang L, Su C (2010) Electrical testing of soft delicate samples using Torsional Resonance Mode and TUNA. Application note, Bruker Corporation
15. Vetushka A, Itoh T, Nakanishi Y, Fejfar A, Nonomura S, Ledinsky M, Kocka J (2012) Conductive atomic force microscopy on carbon nanowalls. J Non Cryst Solids 358(17):2545–2547

16. Dang X-D, Dante M, Nguyen T-Q (2008) Morphology and conductivity modification of poly (3,4-ethylenedioxythiophene):poly(styrene sulfonate) films induced by conductive atomic force microscopy measurements. Appl Phys Lett 93(24):241911
17. Li C, Stephen M, Pittenger, B, Mednick, A, Michele G, Nguyen, T-Q (2011) Simultaneous electrical and mechanical property mapping at the nanoscale with PeakForce TUNA. Application note, Bruker Corporation
18. Huang L, Su C (2004) A torsional resonance mode AFM for in-plane tip surface interactions. Ultramicroscopy 100(3–4):277–285
19. Kasai T, Bhushan B, Huang L, Su C (2004) Topography and phase imaging using the torsional resonance mode. Nanotechnology 15(7):731–742
20. Berger R, Butt HJ, Retschke MB, Weber SAL (2009) Electrical modes in scanning probe microscopy. Macromol Rapid Commun 30(14):1167–1178
21. Binnig G, Quate CF, Gerber C (1986) Atomic force microscopy. Phys Rev Lett 56(9):930–933
22. Binnig G, Rohrer H (1982) Scanning tunneling microscopy. Helv Phys Acta 55(6):726–735
23. Berger R, Domanski AL, Weber SAL (2013) Electrical characterization of organic solar cell materials based on scanning force microscopy. Eur Polym J 49(8):1907–1915
24. Musumeci C, Hutchison JA, Samori P (2013) Controlling the morphology of conductive PEDOT by in situ electropolymerization, from thin films to nanowires with variable electrical properties. Nanoscale 5(17):7756–7761
25. Musumeci C, Rosnes MH, Giannazzo F, Symes MD, Cronin L, Pignataro B (2011) Smart high-κ nanodielectrics using solid supported polyoxometalate-rich nanostructures. ACS Nano 5(12):9992–9999
26. Weber SAL, Berger R (2013) Electrical tip-sample contact in scanning conductive torsion mode. Appl Phys Lett 102(16):163105
27. Weber SAL, Haberkorn N, Theato P, Berger R (2010) Mapping of local conductivity variations on fragile nanopillar arrays by scanning conductive torsion mode microscopy. Nano Lett 10(4):1194–1197
28. Su C, Huang L, Prater C, Bhushan B (2007) Torsional resonance microscopy and its applications. In: Bhushan B, Kawata S, Fuchs H (eds) Applied scanning probe methods series, Series V: nanoscience and technology. Springer, Berlin/Heidelberg, pp 113–148
29. Yurtsever A, Gigler AM, Dietz C, Stark RW (2008) Frequency modulated torsional resonance mode atomic force microscopy on polymers. Appl Phys Lett 92(14):143103
30. Yurtsever A, Gigler AM, Stark RW (2009) Amplitude and frequency modulation torsional resonance mode atomic force microscopy of a mineral surface. Ultramicroscopy 109(3):275–279
31. Rabe U, Kopycinska M, Hirsekorn S, Arnold W (2002) Evaluation of the contact resonance frequencies in atomic force microscopy as a method for surface characterization (invited). Ultrasonics 40(1–8):49–54
32. Wang J, Sun L, Mpoukouvalas K, Fassbender B, Bonaccurso E, Brunklaus G, Muehlebach A, Rime F, Butt H, Wegner G (2009) Facile synthesis of spherical polyelectrolyte brushes as carriers for conducting polymers to be used in plastic electronics. Macromol Chem Phys 210(18):1504–1509
33. Wang J, Sun L, Mpoukouvalas K, Lienkamp K, Lieberwirth I, Fassbender B, Bonaccurso E, Brunklaus G, Muehlebach A, Beierlein T, Tilch R, Butt H, Wegner G (2009) Construction of redispersible polypyrrole core-shell nanoparticles for application in polymer electronics. Adv Mater 21(10–11):1137–1141
34. Cornil J, Beljonne D, Calbert JP, Brédas JL (2001) Interchain interactions in organic π-conjugated materials: impact on electronic structure, optical response, and charge transport. Adv Mater 13(14):1053–1067
35. Pingree LSC, Reid OG, Ginger DS (2009) Scanning probe microscopy: electrical scanning probe microscopy on active organic electronic devices. Adv Mater 21(1):19–28
36. Sun L, Wang J, Butt H-J, Bonaccurso E (2011) Influence of relative humidity on the nanoscopic topography and dielectric constant of thin films of PPy:PSS. Small 7(7):950–956

37. Yang X, Loos J (2007) Toward high-performance polymer solar cells: the importance of morphology control. Macromolecules 40(5):1353–1362
38. Haberkorn N, Lechmann MC, Sohn BH, Char K, Gutmann JS, Theato P (2009) Templated organic and hybrid materials for optoelectronic applications. Macromol Rapid Commun 30(14):1146–1166
39. Jørgensen M, Norrman K, Krebs FC (2008) Stability/degradation of polymer solar cells. Solar Energy Mater Solar Cells 92(7):686–714
40. Moons E (2002) Conjugated polymer blends: linking film morphology to performance of light emitting diodes and photodiodes. J Phys Condens Matter 14(47):12235
41. Gao W, Sattayasamitsathit S, Uygun A, Pei A, Ponedal A, Wang J (2012) Polymer-based tubular microbots: role of composition and preparation. Nanoscale 4(7):2447–2453
42. Branzoi F, Branzoi V, Musina A (2013) Coatings based on conducting polymers and functionalized carbon nanotubes obtained by electropolymerization. Prog Org Coat 76(4):632–638
43. Sarac AS, Ozgul SE, Gencturk A, Schulz B, Gilsing HD, Faltz H (2010) Morphological and impedance studies on electropolymerized 3,4-(2,2-dibenzylpropylenedioxy)thiophene nanostructures on micron sized single carbon fiber. Prog Org Coat 69(4):527–533
44. Miras HN, Yan J, Long D-L, Cronin L (2012) Engineering polyoxometalates with emergent properties. Chem Soc Rev 41(22):7403–7430
45. Rosnes MH, Musumeci C, Pradeep CP, Mathieson JS, Long D-L, Song Y-F, Pignataro B, Cogdell R, Cronin L (2010) Assembly of modular asymmetric organic–inorganic polyoxometalate hybrids into anisotropic nanostructures. J Am Chem Soc 132(44):15490–15492
46. Loos J (2005) The art of SPM: scanning probe microscopy in materials science. Adv Mater 17(15):1821–1833
47. Yurtsever A, Gigler AM, Macias E, Stark RW (2007) Response of a laterally vibrating nanotip to surface forces. Appl Phys Lett 91(25):253120
48. Desbief S, Hergue N, Douheret O, Surin M, Dubois P, Geerts Y, Lazzaroni R, Leclere P (2012) Nanoscale investigation of the electrical properties in semiconductor polymer-carbon nanotube hybrid materials. Nanoscale 4(8):2705–2712

Field Ion and Field Desorption Microscopy: Principles and Applications

7

Yuri Suchorski

Contents

1 Definition of the Topic 228
2 Overview 228
3 Introduction 229
4 Experimental and Instrumental Methodology 232
4.1 Field Ion Microscopy 232
4.2 Imaging with Field-Desorbed Ions 234
4.3 Probe-Hole Analysis of Emitted Ions 238
4.4 Field Ion Appearance Energy Spectroscopy 238
5 Key Research Findings and Applications 241
5.1 FIM Applications and Findings 241
5.2 Field Desorption Microscopy 250
5.3 Probe-Hole Ion Analysis and Field Ion Appearance Energy Spectroscopy 256
5.4 Carbon Nanotubes 262
6 Summary and Future Perspective 263
References 266

Abstract

The chapter describes the basic principles of the field ion (FIM) and field desorption (FDM) microscopies and of the probe-hole spectroscopic analysis of imaging species, as well as their applications for the studying of dynamic surface processes on the atomic scale.

Although the field ion microscopy is the oldest technique resolving individual atoms, it remains preeminent in their ability to prepare the atomically perfect surfaces and to persuade the dynamic surface processes such as catalytic

Y. Suchorski (✉)
Institute of Materials Chemistry, Vienna University of Technology, Vienna, Austria
e-mail: yuri.suchorski@tuwien.ac.at

© Springer-Verlag Berlin Heidelberg 2015

C.S.S.R. Kumar (ed.), *Surface Science Tools for Nanomaterials Characterization*,
DOI 10.1007/978-3-662-44551-8_7

reactions on the nanoscale using the parallel imaging principle. This has led, despite of the great success of the scanning electron microscopy and scanning tunneling microscopy (STM), to the revival of the FIM based techniques and to developing of new versions, such as Lithium Field Desorption Microscopy (Li-FDM) in last decades. The present chapter is focused on the recent surface chemistry applications, especially on the in situ imaging of catalytic reactions. The newest results in studying the local reaction kinetics in the nanosized reaction systems by FIM are presented and the fluctuation-induced deviations from the behaviour predicted by macroscopic rate laws revealed by FIM are discussed.

Especially emphasized is the possibility to analyze via probe-hole the species emitted from the individual surface sites. Such an analysis provides the basis for the Field Ion Appearance Energy Spectroscopy (FIAES). This technique and its practical applications, particularly in catalysis, are explicitly analyzed in the chapter.

Keywords

Field ion microscopy • Field desorption microscopy • Probe-hole analysis • Field ion appearance energy spectroscopy • Field-effects • Reaction induced fluctuations

1 Definition of the Topic

The chapter describes the principles of the field ion (FIM) and field desorption (FDM) microscopies and their applications for the nanoscale imaging of the solid surfaces and dynamic surface processes as well as probe-hole analysis of imaging species.

2 Overview

The field ion microscope (FIM) was the first device to image surfaces on an atomic scale (E.W. Müller, 1951). Although many techniques, such as scanning electron microscopy or scanning tunneling microscopy, can nowadays visualize surfaces with atomic resolution, the FIM remains inimitable in their ability to prepare the atomically perfect surfaces and to persuade the dynamic processes such as diffusion of individual atoms using the parallel imaging principle. In last 50 years, FIM had a significant impact mainly on materials research and on studies of the behavior of individual atoms on metal surfaces which are well illustrated in the existing literature. Therefore the present chapter is rather focused on the recent surface chemistry applications, such as in situ imaging of catalytic reactions (since 1990s). These novel applications have significantly contributed to the revival of the FIM-based techniques and to developing of new versions, such as lithium field

desorption microscopy (Li-FDM), which is in detail described in the present contribution.

Especially emphasized is the possibility to analyze via probe hole the species emitted atom by atom from the individual surface sites. Such an analysis provides the basis for the atom-probe applications, such as atom-probe tomography (APT), which are also comprehensively reviewed elsewhere. In turn, much less attention in the literature is paid to the laterally resolved retarding potential analysis of emitted ions which serves as a basis for the field ion appearance energy spectroscopy (FIAES). This technique and its practical applications, particularly in catalysis, are explicitly analyzed in the chapter.

3 Introduction

The modern *electron microscopy* (EM) summarizes the decades of the discoveries and the evolutionary developments, providing now the unique possibilities to study the condensed matter structure and to reveal its properties on an atomic scale. This allows the manifold applications from the physical to the biological sciences. In turn, the *scanning probe microscopy* (SPM) introduced by Binning and Rohrer in the 1980s as a result of a revolutionary invention provides a possibility to position a local probe near the studied surface with a sub-ångström precision and to obtain the local spatial and spectroscopic information in a single-atom limit or even beyond. As a result, many SPM techniques have emerged during the last 30 years, with the *scanning tunneling microscopy* (STM) and *atomic force microscopy* (AFM) as most important and most widely used.

These techniques provide not only a static, time-integrated imaging, but allow also in situ surface visualization [1, 2] suffering however from the principle-caused limitations such as a relatively poor time resolution. The attempts to provide the chemical resolution on the atomic scale using the STM-based methods, such as *scanning atom probe* (SAP, [3]) do not allow yet an operation under realistic conditions.

Unfortunately, the rapid development of the SPM techniques has outshined the technique, using which men first saw atoms, namely, *field ion microscopy* (FIM). Although in last decades new FIM applications, especially for surface chemistry and particularly for catalysis were developed, no monograph in existence covers these new developments. This chapter attempts to fill this gap and to chart these new developments so that the reader may better compare the SPM and FIM-based techniques.

The FIM achieves its extraordinary magnification by the radial projection of positively charged ions originated close to the nanosized apex of a sharp specimen (field emitter tip, Fig. 7.1a). This basic principle holds also for all the FIM-based techniques, such as the *field emission microscopy* (FEM) and *lithium field desorption microscopy* (Li FDM). Distinguishing feature of these microscopies is the parallel imaging, i.e., all the surface atoms provide the information (via ions or

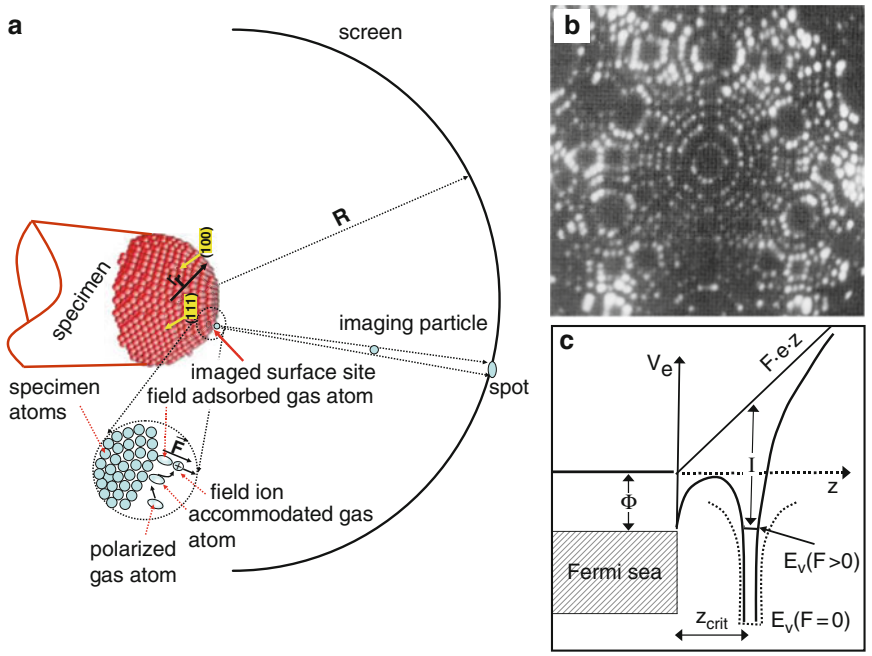


Fig. 7.1 Principles of the field emission-based microscopies. (**a**) Geometry of the point projection. The surface of the specimen apex is projected on a screen by imaging particles with a magnification M ≈ R/r. Imaging particles are electrons (in FEM), imaging gas ions (in FIM), or Li^+ ions (in Li FDM). The tip apex is shown as a spherical fcc ball model (From [5]). The inset illustrates the mechanism of the ion formation in FIM. Imaging gas ions are generated over the protruding surface atoms covered by field-adsorbed gas atoms, field-ionized atoms are replaced by highly mobile accommodated gas atoms (see text). (**b**) Ne^+ field ion image of a [111]-oriented Rh field emitter tip (From [6]). (**c**) Potential energy diagram for field ionization over a metal surface

electrons) simultaneously, in contrary to, e.g., STM where the collecting of the information occurs sequentially, via scanning from one surface atom to another. Therefore, all these microscopies allow in situ imaging of dynamic surface processes on the nm- or even sub-nm scale with a time resolution limited by the data collection rate only [4]. The FIM-based techniques utilize the particles (electrons in FEM, metal (Li) ions in Li FDM or gas ions in FIM) radially emitted in high electrostatic field from the surface. The studied area, i.e., the apex of a field emitter tip is usually prepared by electrochemical etching of a thin (few tenths of a mm) wire and consists, due to its small size, mainly on a single crystal exhibiting differently oriented nanofacets (Fig. 7.1a, b). The heterogeneity of the surface and presence of differently oriented nanofacets recommend such tips as suitable models for, e.g. catalytic particles of comparable dimensions [7].

Since the tip surface can be prepared in a reproducible manner by field evaporation and subsequently characterized with atomic resolution, this provides a

unique possibility to study surface reactions on well-defined nanosizes samples. FIM, as well as the FEM and Li FDM has been successfully used then to visualize in situ on the nanoscale such fast surface processes as catalytic CO oxidation or NO reduction on the platinum metal nanofacets [8–10]. The most serious limitation of the field emission-based microscopies had been their inability to identify the chemical identity of the individual surface atoms. A breakthrough was achieved in 1967 by a combination of a probe-hole FIM with a mass spectrometer having single-particle sensitivity, named *atom-probe field ion microscope* (APFIM) by its inventor E.W. Müller [11]. During FIM operation, an atomic site of interest could be selected by placing it (by adjusting the position of the tip) over a probe hole in the image screen. Pulsed field evaporation extracted the chosen surface atom and passed it through the hole into the spectrometer. Time-of-flight spectroscopy allowed measuring one-dimensional "in-depth" compositional maps (1D *atom probe*, AP). A three-dimensional nm-scale reconstruction of a sample composition was possible by moving the sample relatively to the probe hole. Later on, the necessity to move the tip was avoided by developing the *imaging atom probe* (IAP, [12, 13]) where the ions emitted from the surface were analyzed with a 2D detector. Application of short laser pulses (first applied by Drachsel [14], Kellogg and Tsong [15]) in combination with the *local-electrode atom probe* (LEAP®, [16]) where the microminiaturized counterelectrode is placed in an immediate proximity (μm scale) to the specimen made the atom probe to an ultimate analytic tool where the 3-D position of each detected specimen atom and its identity including all the isotopes could be resolved.

In this way the first part of the ingenious prediction of the principal inventor of these techniques, E.W. Müller, was realized to a full extent: "Further experimental work will be centered around two objectives: One is the straightforward application of the atom-probe FIM as a microanalytical tool of ultimate sensitivity. The chemical identity and the location with respect to the lattice structure of impurities, segregations, precipitates and alloy constituents are immediate goals" [17]. Mainly by the efforts of groups at Oxford University, University of Rouen and Materials Science Center at the University of Wisconsin–Madison (Director Prof. Tom Kelly) the commercial LEAP® devices were developed and produced and are widely used in materials science [18, 19]. The second part of Müller's prediction: "The second aim of atom-probe research will be to shed new light on the complex situation at specific atomic sites of the surface....where the surface-gas interaction data carry a new dimension of reliability by the identification of the particles involved" [17], i.e., application of the AP techniques to in situ surface chemistry and catalysis, has been, unfortunately, only partially realized, despite significant experimental effort during the last decades. Correspondingly, existing FIM literature has been dominated by pure materials science applications such as metallurgy. In turn, as already mentioned, surface chemistry applications of the FIM/AP instruments as well as other atom-probe-like techniques combined with FIM such as *pulsed field desorption mass spectrometry* (PFDMS, [20]) and *field ion appearance energy spectroscopy* (FIAES, [21, 22]) have experienced much less attention. The aim of the present contribution is to account, at least partially, for this imbalance and to discuss the novel surface chemistry applications of the FIM-based techniques.

4 Experimental and Instrumental Methodology

4.1 Field Ion Microscopy

The FIM, invented by E.W. Müller in 1951 [23], is in its principle a right simple projection microscope which permitted for the first time true atomic resolution enabling men to see individual atoms already in 1955 [24]. Since then FIM contributed significantly to surface science, in particular to materials research [25, 26] and to studying the behavior of individual atoms on metal surfaces [27, 28]. In the present chapter the principles and the basics of the instrumentation are summarized, only briefly, due to the limited space and with emphasis of recent novel insights, such as the role of the weakly bounded field-adsorbed layer of imaging gas atoms. For more instrumental details, including the specimen preparation techniques, the comprehensive monographs by Müller and Tsong [29, 30] are recommended.

In a typical FIM a cryogenically cooled specimen of the shape of a sharp tip (Fig. 7.1a) with a radius of curvature in the sub-μm range is positioned a few centimeters away from an image intensifier (usually a micro-channel-plate/phosphor-screen assembly). The tip, usually prepared by electrochemical polishing (see the recipes in Ref. [29]), is exposed to a high positive voltage in the presence of an imaging gas at 10^{-3}–10^{-5} mbar. In a sufficiently high field (tens of V/nm) the atoms or molecules of the imaging gas (usually He, Ne or reactive gases like oxygen) become polarized and are attracted to the specimen surface where they accommodate at cryogenic temperatures losing their kinetic energy in a thermal accommodation process [29]. The accommodated gas atoms follow the local field gradient across the surface, arrive at local field maxima above the prominent surface atoms and become, in the case of the usually used He or Ne as imaging gas, field adsorbed on protruding surface atoms. The following accommodated gas atoms become steadied over those field-adsorbed species, whereas the local field distribution plays a decisive role [30–34]. Steadied gas atoms being free and at rest are then field ionized by electron tunneling through the field-adsorbed atoms into the specimen [29]. A collision-induced exchange process between the field-adsorbed and "arriving" accommodated gas atoms is also possible close prior the field ionization event [34].

At the instance of field ionization, the gas atom is localized at the critical distance z_{crit} (see inset in Fig. 7.1c) to specimen surface. This distance is necessary to allow lifting the atom's valence electron level over the Fermi level of the specimen by applied field, a tunneling at smaller than z_{crit} distances is not possible since it would mean a tunneling into occupied states below the Fermi level (Fig. 7.1c). The gas ions formed at (or beyond) z_{crit} are accelerated in the applied field projecting in the narrow ion beams the surface atoms on a screen and creating thus a field ion image (Fig. 7.1b). An extremely high degree of the spatial localization of the imaging gas atoms at the instant of field ionization provides atomic resolution in the FIM images. The essential role of the field-adsorbed layer of the imaging gas atoms for atomic resolution in FIM is illustrated for Ne gas atoms ionized over an Rh tip in Fig. 7.2 [33]. Increasing the temperature of the tip

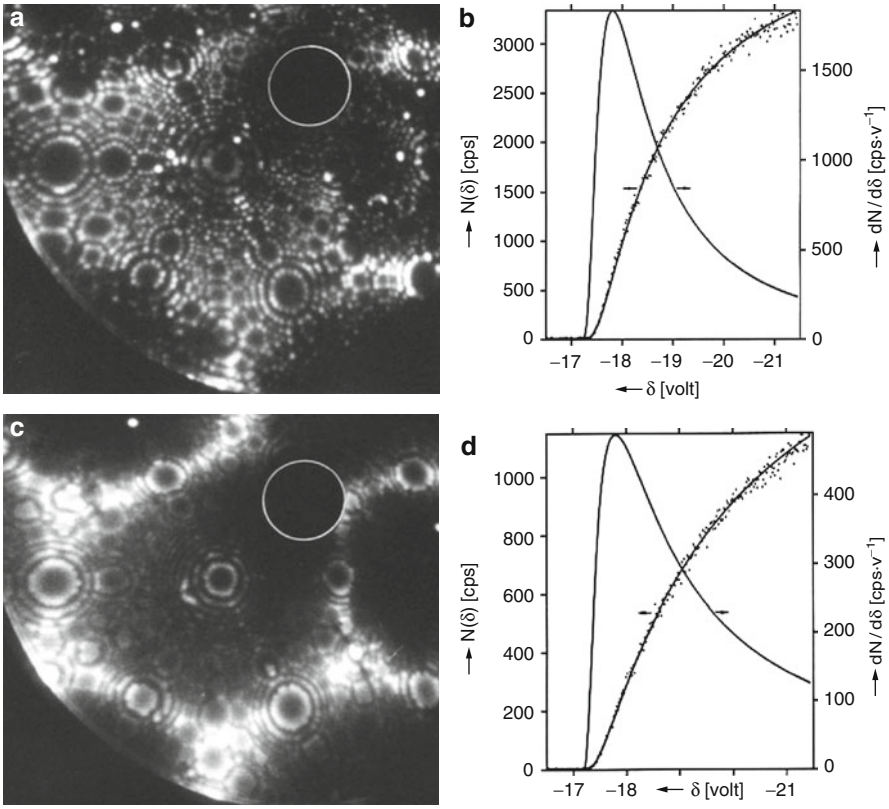


Fig. 7.2 Field adsorbed Ne atoms in localized field ionization. (**a**) Ne field ion image of a [111]-oriented Rh emitter kept at 79 K and at 35 V/nm (field-adsorbed Ne layer is present). The area encircled in *white* represents the probe hole. (**b**) The locally measured Ne^+ retardation curve N(δ) and the differentiated curve, $dN/d\delta$ (**c**) The same as in (**a**), at 107 K (field-adsorbed Ne layer is depleted) (**d**) Corresponding Ne^+ retardation curve N(δ) and the differentiated curve, $dN/d\delta$. One observes: (i) the field ion image become blurred, (ii) the field ionization rate at the probed surface sites decreases drastically, (iii) the value of field ion appearance energy derived from the field ion retardation curves decreases and becomes equal to the ionization energy of the free gas atom, and (iv) the full width at half maximum of the field ion energy distribution increases significantly (from 1.45 V to 2.08 V) (Adapted from [33])

or enhancing the field over the BIF (best image field), the field-adsorbed layer is depleted and following features are observed for noble imaging gas atoms such as Ne or He: (i) the field ion image become blurred, (ii) the field ionization rate at the probed surface sites decreases drastically, (iii) the value of field ion appearance energy (FIAE) derived from the field ion retardation curves decreases and becomes equal to the ionization energy of the free gas atom (meaning of the FIAE is discussed in Sect. 4.4), and (iv) the full width at half maximum of the field ion energy distribution increases significantly. A wide range of conducting

samples can be studied by FIM: metals including alloys, semiconductors, and even oxides [26–30]. The natural limit of the FIM applicability is the field evaporation process (i.e., field desorption of the specimen lattice atoms) in which the surface atoms of the specimen are field ionized and removed from the surface. This process is used for controlled fine shaping and cleaning the tip: it can however lead to the destruction of the specimen when the imaging field is equal or higher than the onset of field evaporation of the particular sample. The values of the evaporation field strength are listed in the reviews [29, 36]: for the details of the field desorption and field ionization process, we address the reader to the literature [28–30, 34–36].

FIM operation with reactive imaging gases, like O_2, CO, and N_2, occurs mainly by field desorption of the adsorbed gas molecules which are subsequently replaced by a diffusion supply from the tip shank where the mobile gas molecules are adsorbed [37–39]. Thus, an FIM operating with a reactive imaging gas is basically a field desorption microscope. Figure 7.3 shows an example of the imaging with O_2^+ ions, where initial stages of the oxidation of Rh surface are visualized in situ [40].

Such studies provide a unique possibility to reveal the effect of high electric field in order of few volt per angström on the surface oxidation [40] and generally allow to study the interaction of gas molecules such as nitrogen with the solid-state surface in high electric fields [39].

4.2 Imaging with Field-Desorbed Ions

It is also possible to obtain images with metal ions field emitted directly from the specimen surface. Such a mode is based on the fact that a field of a few volts per angstrom can remove metal atoms from a surface even at low temperatures where field-free thermal desorption is inefficient [41]. This effect is called *field desorption* (in the case the *preadsorbed* atoms are removed by field) and field evaporation (in the case the *substrate* atoms are field removed). In both possible cases, namely, when ionized specimen atoms are used as imaging species or when the adsorbed metal atoms are exploited, the corresponding technique is called field desorption microscopy (FDM, [42]). While in the first case the imaging process is rather instable because of evaporation of the specimen during the visualization [43], in the second one, especially when using Li^+ ions supplied by diffusion from the specimen shank, stable images comparable with those obtained by FIM can be obtained [44].

The corresponding device, lithium field desorption microscope (Li FDM) developed by Medvedev and Suchorski in the 1990s [44, 45], is based on the principle that the surface sites are visualized by radial projection of the Li^+ ions field desorbed from these sites themselves. Desorbed Li atoms are continuously replaced via surface diffusion from the long-lasting multilayer Li deposit on the shank of the tip (Fig. 7.4). When the diffusion supply along the surface is sufficient (desorption rate does not exceed the diffusion supply) the surface can be imaged in a continuous

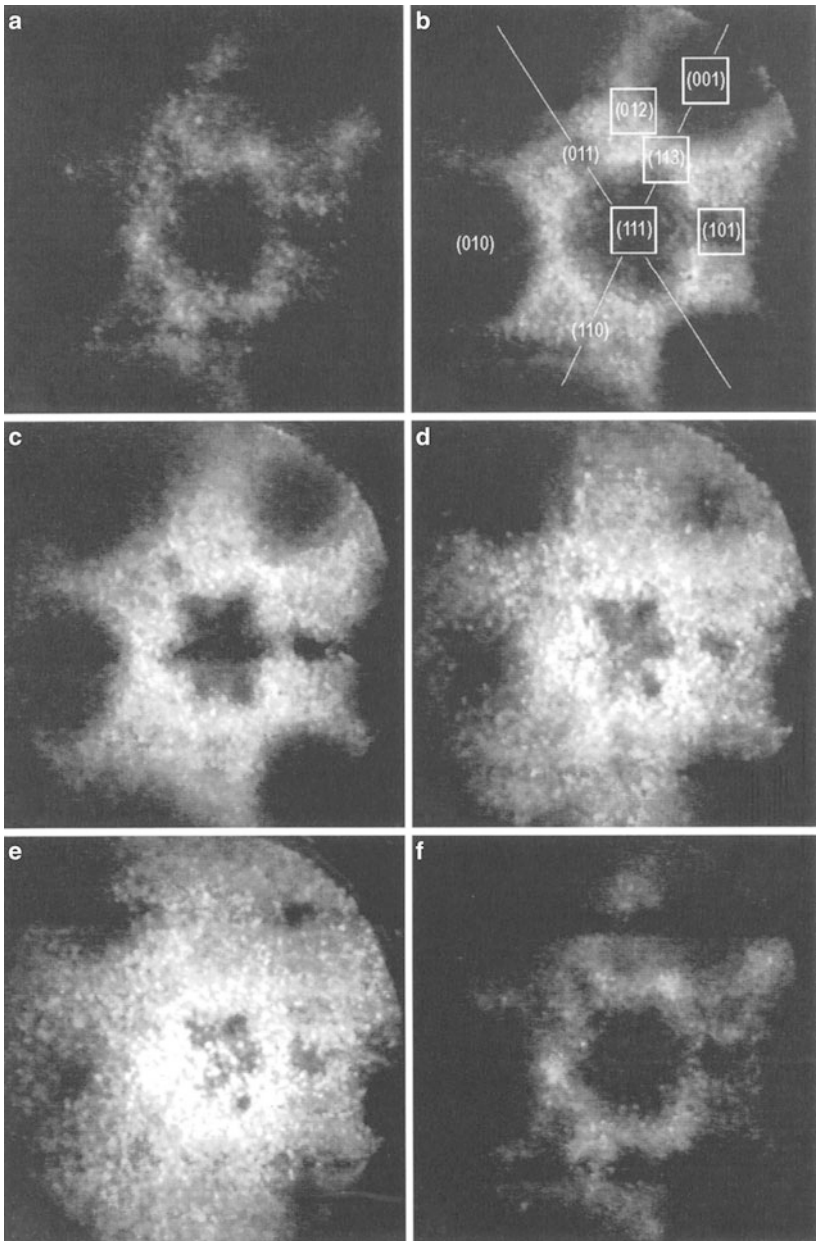


Fig. 7.3 FIM imaging with reactive imaging gases: (**a**) O_2^+-field ion image of the initial stage of the oxygen interaction with Rh at 375 K. (**b–e**) O_2^+-field ion micrographs showing the sequential stages of the interaction of oxygen at 5.2×10^{-5} mbar in the presence of an external field of 15 V/nm; (**f**) O_2^+-field ion micrograph showing the result of reduction the oxidized surface by CO in the presence of an external field of 15 V/nm (Adapted with permission from [40]. Copyright 1998 ACS)

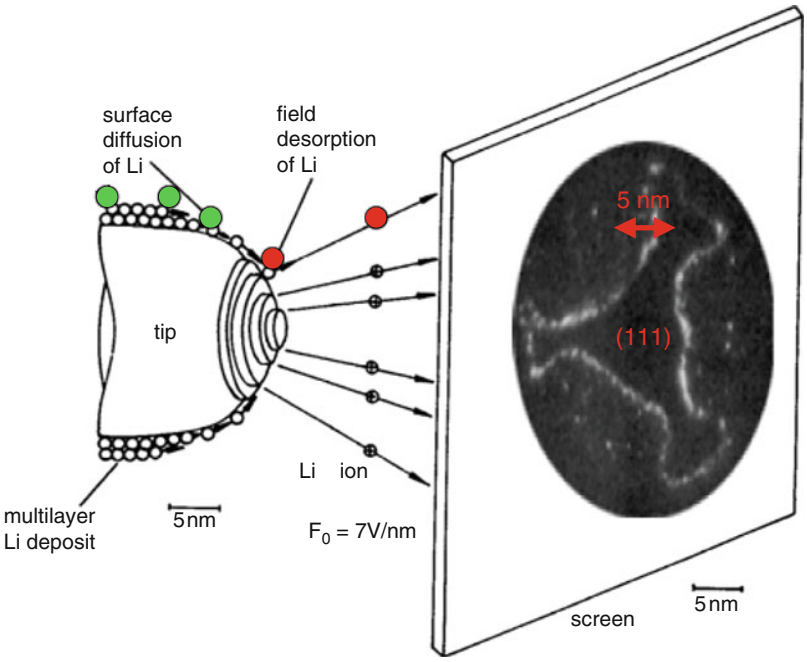


Fig. 7.4 Lithium field desorption microscope: principle of the image formation in Li FDM. Li atoms diffuse from the multilayer deposit on the shank of the tip towards the apex. Li^+ ions field desorbed from the apex on the tip create a projection image on the screen

imaging mode. However, in the case, the diffusion supply does not provide sufficient number of Li atoms in the desorption zone, the pulsed mode can be used: the image is then created by Li^+ ions desorbed by periodic high-voltage pulses. Between the pulses, sufficient Li coverage is collected on the imaged surface via the surface diffusion supply. Since the surface diffusion is a field-dependent process, the rate of the diffusion supply can be adjusted by a high-field bias, when a constant field is applied which is sufficient for an accelerated surface diffusion of Li, but not sufficient for the field desorption.

Thus varying the temperature and the applied field values, the relation between the diffusion supply and desorption rate can be adjusted to obtain the optimal image intensity.

The initial development of Li-FDM was concerned with the imaging of different clean and adsorbat-covered metal surfaces, investigations of mechanisms of Li FDM image formation [44, 45], and visualization of dynamic diffusion–reaction processes [9, 46–48]. As a result, the Li FDM is capable of operating in the presence of CO and oxygen (up to 10^{-3} mbar) and of imaging at these conditions the dynamic processes on metal surfaces with a time resolution of 0.01 s. Figure 7.5 shows an example of such visualization for the [110]-oriented Pt tip.

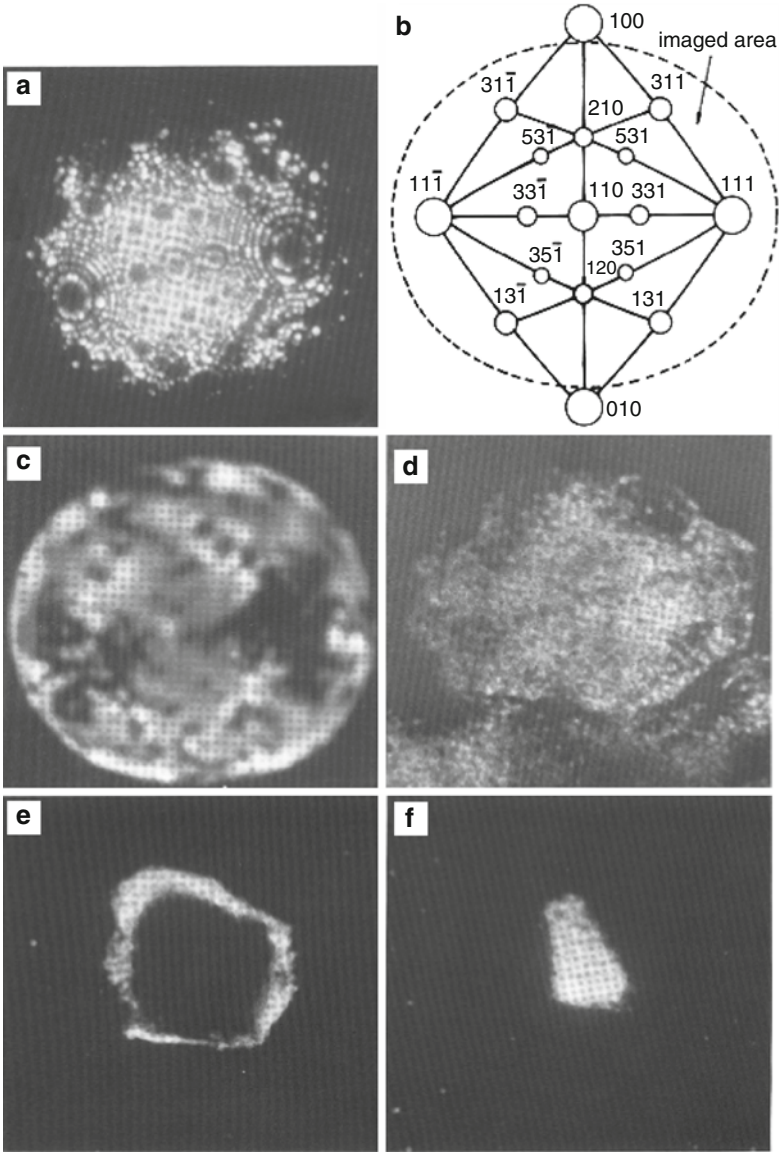


Fig. 7.5 Surface of the [110]-oriented Pt tip as imaged by field-desorbed Li^+ ions. (**a**) Ne FIM image, 78 K, 10,380 V (35 V/nm); (**b**) crystallographic map; (**c**) Li-FDM image of the same surface as in (**a**), 446 K, V_{const} = 1,145 V (3.8 V/nm), V_{pulse} = 1,600 V (5.4 V/nm) f = 9,260 Hz; (**d**) the same as in (**c**) but the surface is CO covered, 417 K, V_{const} = 969 V (3.8 V/nm), V_{pulse} = 3,000 V (5.1 V/nm) f = 333 Hz; (**e**) the same as in (**c**) but the surface is oxygen covered, 417 K, V_{const} = 5,000 V (8.4 V/nm), V_{pulse} = 3,000 V (5.1 V/nm) f = 540 Hz (**f**) the same as in (**e**) but imaged with V_{const} = 2,541 V (4.3 V/nm), V_{pulse} = 5,000 V (8.4 V/nm) f = 54 Hz (Based on [45])

Since in the temperature range of 400–450 K, lithium can be desorbed from the Pt surface by an applied field less than 1 V/Å, the adsorbed layers, such as oxygen or CO, remain intact during the Li-FDM operation, i.e., they can be imaged by Li^+ ions (Fig. 7.5c–f). During the pulsed mode of imaging, surface diffusion of Li occurs between the pulses, only those regions are imaged, where Li diffusion has provided a sufficient Li coverage, thus the size of the imaged region can be adjusted by varying the frequency and duration of single pulses (compare Fig. 7.5e, f). Many of catalytic reactions, such as CO oxidation reaction, occur via Langmuir–Hinshelwood mechanism, i.e., the reacting species are adsorbed on the surface prior and during the reaction. Therefore, the reaction process can be imaged in situ by Li FDM, as will be in details described in Sect. 5.2.

4.3 Probe-Hole Analysis of Emitted Ions

Since the emitted ions are originating directly from the imaged surface sites, where an interaction with surface atoms occurs, they may contain additional information, apart of the visible spots projected on the screen. While the sample is imaged with atomic resolution by FIM, the selected surface area can be positioned over the probe hole in the screen, usually of few mm aperture (corresponding to few angström on the specimen surface, Fig. 7.6). The ions projected into the probe-hole can then be detected and identified by different mass spectrometries, e.g., by time-of-flight mass spectrometry. This is the idea behind the *time-of-flight atom probe* (TOF AP). As already mentioned in the Introduction, this technique, invented by Müller [11] and continuously developed over decades (see, e.g., reviews [25, 26, 49–51]), culminated in the *local-electrode atom probe* (LEAP) [16, 52]. Since the AP and LEAP techniques are well illuminated in the literature, the focus in the present contribution is directed to the less-known technique which is also based on the probe-hole analysis of the locally emitted ions, namely, *field ion appearance energy spectroscopy* (FIAES).

4.4 Field Ion Appearance Energy Spectroscopy

Although the mentioned above E.W. Müller's vision of the atom probe as a nano-analytical tool of ultimate sensitivity became true with AP and especially with LEAP techniques, in surface chemistry, the surface–gas interaction data, such as binding energies of adsorbed atoms or molecules are of great interest, in addition to the identity of specimen atoms. Already in early experiments by Müller and Bahadur [53], the indications were achieved that thermodynamic information about the energetics of processes at the surface can be derived by measuring the onset of the field ion energy distribution. Historically, the FIAES instrumentation has grown from the *field ion mass spectrometry* (FIMS, [54]) and *magnetic sector field atom-probe* (MSAP) devices (see, e.g., Ref. [55]) in which the field-desorbed surface species having different masses are selected by probe hole and mass to

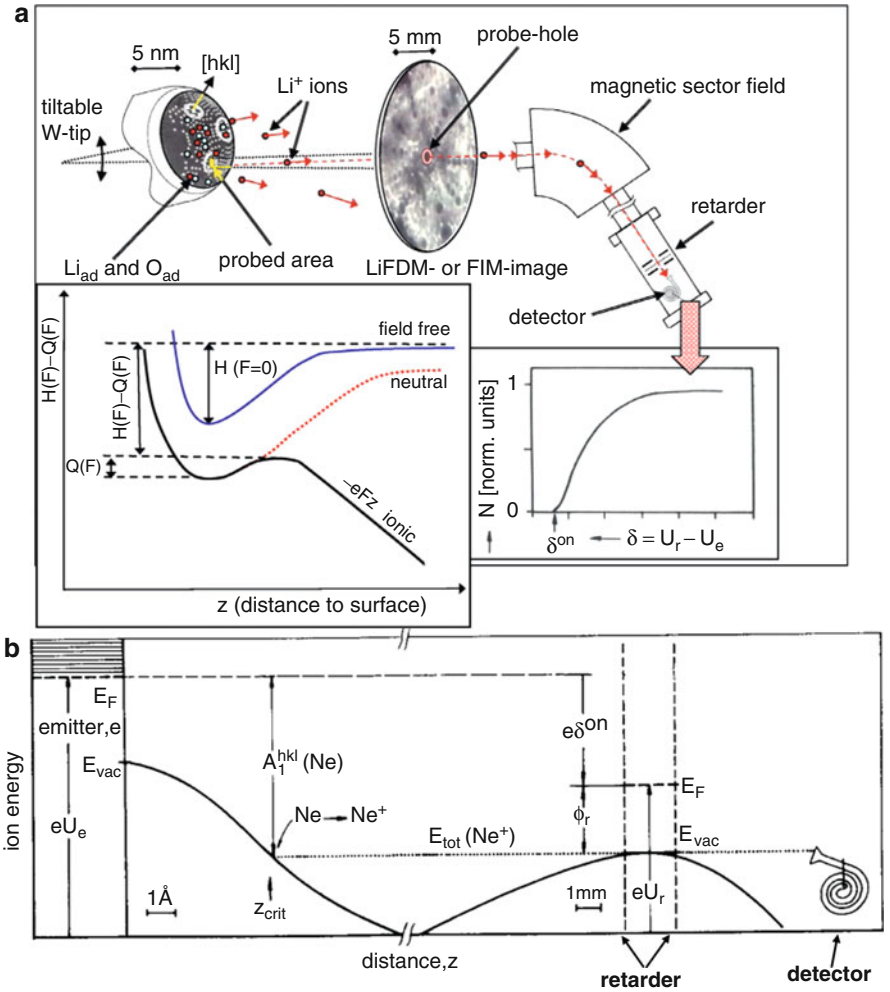


Fig. 7.6 Principle of FIAES. (**a**) Mass-to-charge resolved retarding potential analysis of locally emitted ions: Field desorbed surface species (e.g., CO^+ ions) laterally selected by a probe hole are mass-to-charge separated using magnetic sector field, pass a retarding potential analyser and are detected by a single particle detector. *Left-side inset* explains the Eq. 7.2, *right-side inset* shows schematically a retardation curve (Adapted from [4]). (**b**) Energy diagram: the appearance energy A_1^{hkl} represents the total energy of a single charged ion (e.g., Ne^+) created over a particular (hkl) surface site at the critical distance z_{crit}. Value E_F is the Fermi energy of the emitter (tip) and the retarder (collector), respectively, potential difference $U_r - U_e$ provides $\delta^{\circ n}$, the onset voltage at which the ion is just collected. The *inset* shows schematically a retardation curve N(δ) (Adapted from [34])

charge analyzed using a magnetic sector field. Corresponding FIAES instruments are often similar and differ solely by an energy analyzer: however, also linear arrangements (without magnetic field) are possible [21, 22]. Such an FIAES instrument with a 60° magnetic sector field ending in a retarding potential analyzer

with a single-particle detector is schematically shown in Fig. 7.6a. The current of ions reaching the detector is measured as a function of the voltage δ^{on}, applied between retarder electrode and emitter to vary the height of the retarding electrostatic barrier. The appearance energy A, as was introduced by Goldenfeld et al. [56], is derived for a singly charged ion:

$$A_1 = \Phi_{ret} - e\delta^{on}, \tag{7.1}$$

where Φ_{ret} is the work function of the retarder, e is the charge of the ion, and δ^{on} is the onset voltage for ion collection ($\delta^{on} = U_r - U_e$, see explanation in Fig. 7.6b). In principle A_1 is the energy to remove an electron of a given molecule (ground state) to create an ion at its surface position. By conducting a closed thermionic cycle proposed by Forbes [57], the appearance energy for a field-desorbed molecule can be derived:

$$A_1 = I + H(F_{loc}) - Q(F_{loc}) \tag{7.2}$$

if temperature-dependent terms are neglected.

In this expression I means the ionization potential of the ionized species, $H(F_{loc})$ means the adsorption energy at the local field, and $Q(F_{loc})$ is the activation energy for field desorption of this species. An extended discussion of the energy terms involved in field ion appearance spectroscopic measurements is given in references [21, 22]. The concept of the field ion appearance energy is closely related to the term *critical energy deficit* (since the atom/molecule is going to be ionized at certain distance from the emitter surface, z_{crit}, it experiences not the whole acceleration potential of the emitter, i.e., has an energy deficit) [30].

Crucial for the use of FIAES in surface chemistry was the possibility to calibrate the work function of the retarder in situ, e.g., from the onset voltage for rare gas ions, e.g., Ne using Eq. 7.2, as was proposed already in Ref. [27]. Unfortunately, initially it was not possible to measure the absolute A_1 values inclusive the field-dependent terms: these terms were first measured in the 1990s [22]. It was also detected, that at elevated temperatures ($T > 100$ K) when the field-adsorbed imaging gas layer is depleted, field-dependent terms for noble gas atoms like Ne or Ar do not contribute essentially (thus $A_1 \equiv I$) [22, 33]. Since that time, the work function of the retarder could routinely be determined in situ from the known ionization potential of a noble test gas as $\Phi_{ret} = e\delta_{testgas} + I_{testgas}$. Replacing the test gas by a reactive one, e.g., CO, its appearance energy can be obtained from the calibrated Φ_{ret} and measured δ_{CO} values. First successful measurements of such type are dated by 1995 [58].

Using Eqs. 7.1 and 7.2 the field dependence of $H(F) - Q(F)$ can be obtained from the measured $\delta^{\circ n}$ values. The $Q(F)$ value can be estimated from the temperature dependence of the ion rate, thus the binding energy H(F) from chosen atomic surface sites is available. This procedure can also be used during a reaction to provide in situ data about the binding energy of the reactants. Also aside of surface chemistry, the method can be used for determination of local electrostatic fields

over individual atoms [22], distinguishing between the localized and delocalized field ionization (see Fig. 7.2, [6]), determination of binding energy of metal adsorbates [59] or even sublimation energy of metals by direct measuring the appearance energy of field evaporated atoms [60]. Two reviews summarize these rather physical applications [34, 36]; the surface chemistry applications are discussed in Sect. 5.3.

5 Key Research Findings and Applications

5.1 FIM Applications and Findings

Till the 1990s, the most important applications of FIM took place in materials science, especially in metallurgy, where the segregation of impurities, grain-boundary segregation, decomposition of alloys, role of lattice defects and other surface effects were studied on an atomic scale [25, 26, 28–30]. In a parallel way, a great contribution to the surface physics has been accomplished by FIM, especially in studying the diffusion processes and behavior of individual atoms on metal surfaces [27–30, 61] long before as such studies became routine for STM [62, 63]. First evidences of a substrate-mediated indirect interaction of adatoms were obtained by FIM for Re adatoms on W(110) [64], as well as for W–Pd and Re–Pd and Re–Pd atom pairs on W(110) [65, 66]. A compilation of this early development including the dipole–dipole and elastically mediated non-oscillatory interactions is given in a comprehensive review [67]. First experiments on a directional walk of adsorbed atoms in an externally applied field gradient [68] and on field desorption of single adatoms by a voltage pulse [69] were direct predecessors of the atom manipulation in STM [70]. However, since the 1990s, with the progressing domination of the STM-based techniques, the FIM contribution to the surface physics became less meaningful, but to the same time, a revival of the FIM in surface chemistry begun initiated by first in situ observations of a catalytic surface reaction on a nanoscale in Block's group in Berlin [8]. Important role in this development played an increasing understanding of the importance of the parallel imaging principle (which distinguishes the FIM from STM with its sequentially scanning imaging mechanism) for such real-time observations. This advantage was convincingly demonstrated by use of the *photoemission electron microscope* (PEEM) for the real time surface chemistry studies on the macroscopic (∼μm) scale. Various spatiotemporal phenomena as target patterns, island formation, spirals, standing waves, etc., were observed and are summarized in reviews [71, 72] and in the Nobel Prize Lecture by G. Ertl [73].

5.1.1 FIM in Surface Chemistry

In the early 1990s, it was demonstrated that such spatiotemporal phenomena occurring on the catalytically active metal surfaces can be also imaged in situ by FIM with a nanometer resolution using the platinum metals tip specimens, which served as models for the catalytically active precious metal particles. Similarly to a

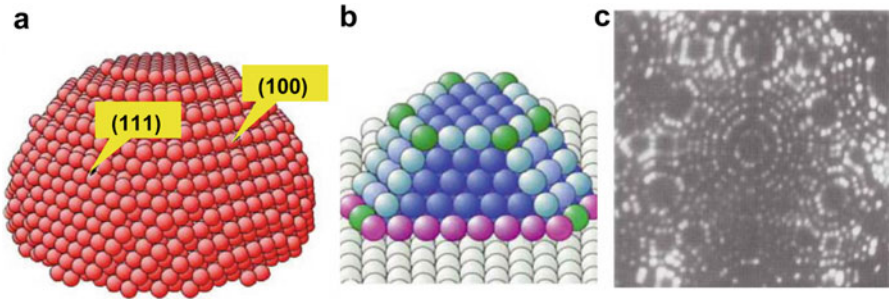


Fig. 7.7 (**a**) Ball model of the apex of a spherical fcc tip. (**b**) Metal aggregate on an oxide substrate. (**c**) Field ion image of the [111]-oriented Rh field emitter tip (From Ref. [4])

catalytic particle of comparable dimensions, the apex of a field emitter tip exhibits a heterogeneous surface formed by differently oriented nanofacets (compare Fig. 7.7a, b).

However, in contrast to a catalyst particle, the tip surface can be prepared reproducibly by field evaporation and subsequently characterized with atomic resolution by imaging in the FIM (Fig. 7.7c). Such well-defined surface can be used to catalyze a surface reaction and the process can be followed by FIM in real time. Another benefit of the FIM based methods is the possibility to study the structural changes on an atomic scale caused by molecular adsorption or by the catalyzed reaction itself. Reconstruction phenomena on nanofacets which are hardly accessible by other analytic techniques are well observable in FIM [40], the reaction-induced morphological changes are described in the present chapter below.

The breakthrough in the visualization of catalytic reactions was achieved by using of the reactive gases such as oxygen as imaging gas instead of traditionally used noble gases such as neon. Figure 7.8 shows an example of such an in situ visualization, where CO oxidation on a Rh tip is imaged by O_2^+ ions [48]. Such imaging allows deep insights into the microscopic mechanisms of the processes occurring during the reaction, e.g., the coarsening of the image (Fig. 7.8b) indicates the formation of RhO_x granules during the kinetic transition from an inactive (CO covered) to the catalytically active (oxygen covered) Rh surface, an effect which was not observed to that time on the macroscopic single-crystal surfaces. The size of the formed granules depends on the tip temperature: a decrease of the tip temperature leads to a rather fast decrease of the granules size (Fig. 7.8c, d). In turn, the transition from the oxygen- to the CO-covered Rh surface which starts near the centers of the {111} and {100} planes is accompanied with disappearing of the RhO_x granules (Fig. 7.8e, f).

Using FIM, important questions concerning the surface reactions could be answered: (i) the role of the of the applied electric field on the reaction mechanism [74], (ii) the influence of the structural heterogeneity of the field emitter tip surface (dynamic coupling effects between the individual planes) [75], and

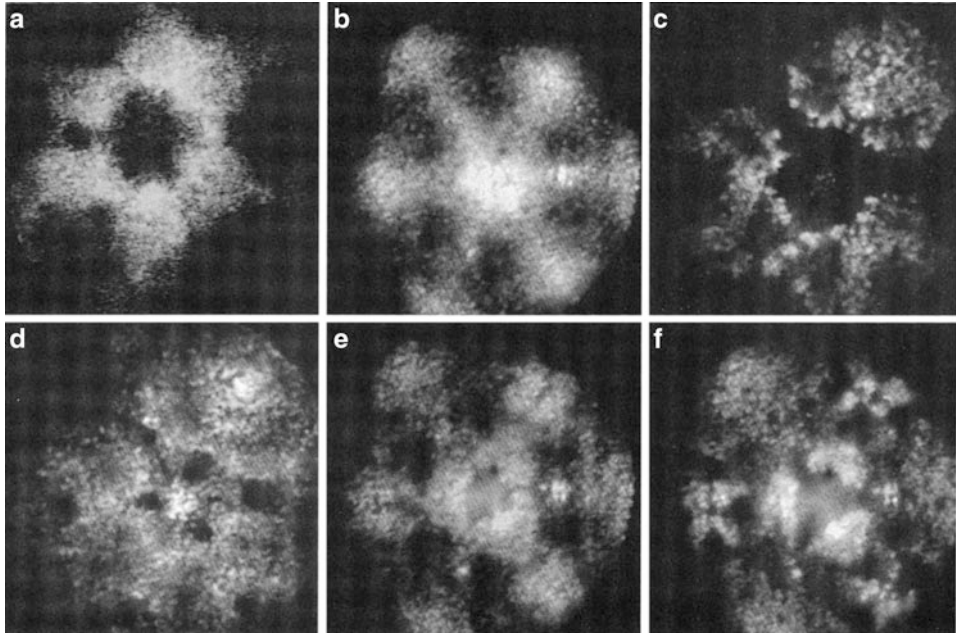


Fig. 7.8 Field ion imaging with O_2^+ ions. (**a**–**f**) O_2^+ images of the CO oxidation reaction on a [111]-oriented Rh tip. (**a**–**d**) Transition from the CO- to the oxygen-covered surface. (**a**) The initial stage, 350 K, (**b**) begin of the transition, coarsening of the image, 410 K, (**c**) further granulation of the surface due to RhO_x formation, 483 K, (**d**) after fast drop of temperature in from 483 to 370 K. (**e**, **f**) The sequential stages of a reverse process (After [48])

(iii) the role of fluctuations on the reaction kinetics and possible fluctuation-induced deviations from the behaviour predicted by macroscopic (mean-field) rate laws [76, 77].

To prove experimentally the effect of the imaging electrostatic field the unique feature of FIM was used, namely, the possibility to switch from the FIM imaging by O_2^+ ions (applied field $\sim$12 V nm^{-1}) to the imaging with field-emitted electrons (FEM = field emission microscopy, applied field $\sim$4 V $\cdot$ nm^{-1}) just by reversing the applied voltage polarity. In this way, the reactive kinetic phase diagram of CO oxidation on Pt can be obtained by FEM and FIM for the same sample. In FIM the different ionization probabilities for oxygen (used as imaging gas) over the oxygen- and CO-covered surface [78] and in FEM the local work function variations create the image contrast, respectively. This allows to identify the catalytically active state and to measure the kinetic phase diagram by monitoring the local field emission current (or image brightness) while varying the external parameters such as p_{CO}, $p_{O2,}$ and T. Figure 7.9a shows the kinetic phase diagrams obtained with both, FIM and FEM, for the same Pt tip and the same oxygen partial pressure 4×10^{-4} Torr. Since additional FEM measurements performed with pulsed high-voltage supply varying the duty cycles factor showed no influence of the duration of the pulses on the catalytic CO oxidation [74], the FEM results can be interpreted as quasi-field-free. In turn, the phase diagram obtained by FIM appeared as shifted significantly to lower p_{CO} values in comparison to the field-free one. The physical reason for this effect was revealed by FIAES measurements and is described in the next chapter.

Under certain conditions, CO oxidation reaction exhibits self-sustained oscillations [73]. Figure 7.9b illustrates the local and "global" oscillatory behavior of the reaction on the tip apex shown in Fig. 7.9a. Although different facets are exhibited, the whole tip area undergoes synchronous transitions from a CO-covered to an oxygen-covered surface and vice versa at the transition points (bifurcation points) of the bistability region (compare variation of the local and total image intensity in Fig. 7.9b).

The comparison of FEM measurements with data for catalytic CO oxidation on a macroscopic Pt(110) surface reveals influence of the structural heterogeneity of the field emitter tip surface: the single-crystal studies by Eiswirth et al. (open circles in Fig. 7.9a, [79]) and Moldenhauer (filled circles, [80]) suggest the position for the bifurcation point which is significantly shifted in respect to the FEM results. These differences can be directly attributed to the size of the system and to dynamic coupling effects of the {110} facets with neighboring orientations.

The CO oxidation reaction is especially suitable for the FEIM/FIM studies since the difference in the work function of the CO and oxygen layers adsorbed on platinum-group metals is big enough to provide a sufficient contrast on both, FEM and FIM imaging modes. Of course, CO oxidation is not a sole reaction that can be studied in FIM. Other reactions like H_2 oxidation [75, 81, 82] or NO reduction with H_2 [10, 83–85] (which are relevant in the sense of automotive catalytic converters) were studied using video FEM/FIM, often in combination atom-probe techniques to get an insight into the chemical composition of the

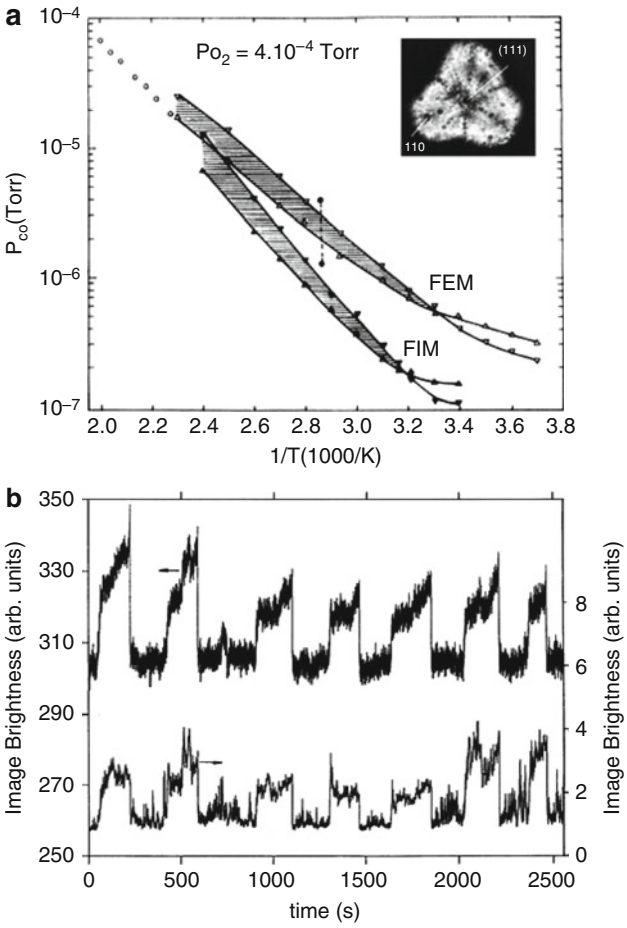


Fig. 7.9 CO oxidation on a [111]-oriented Pt tip. (**a**) Kinetic phase diagrams for CO oxidation on Pt nanofacets determined with FEM ($F_0 = 4$ Vnm^{-1}) and FIM ($F_0 = 12$ Vnm^{-1}). The *shaded areas* mark the existence ranges for the oscillations. Below their crossing point, the boundary lines for instabilities enclose a region of bistability. The *open circles* are Pt(110) single-crystal data indicating the existence range for oscillations; the bistability range of reaction on Pt(110) at $T = 349$ K is indicated by *filled circles*. The *insert* shows the geometry of the [111]-oriented Pt tip used in our experiments (clean Pt surface imaged at 78 K with FIM using Ne as imaging gas, $F_0 = 35$ Vnm^{-1}); the central (111) and one of three {110} planes are indicated (Adapted from [74]). (**b**) Oscillatory behavior of CO oxidation on the Pt tip apex displayed in the insert of (**a**). *Upper curve* total FEM image intensity; *lower curve*, local FEM intensity of the (110) plane. $T = 398$ K, $p_{CO} = 6.2 \times 10^{-6}$ Torr, $p_{O2} = 4.3 \times 10^{-4}$ Torr (Adapted from [74])

surface and intermediate species. Mostly the Pt, Rh, and Pd tips were used as specimens in these studies due to the importance of these metals in the automotive exhaust converters. NO reduction with hydrogen on Pd was the most studied reaction apart of the CO oxidation, whereas the FIM imaging was combined with

the local chemical probing by PFDMS, i.e., the structural transformations of the Pd specimen were correlated with the direct local information on the surface composition. FIM brightness analysis provided data about the hysteresis behavior and a corresponding kinetic phase diagram consisting on the NO-covered steady state, hysteresis region, and H_2-covered steady state in the temperature region 450–575 K was determined [85]. Local chemical probing suggests that processes in the subsurface region play a significant role: e.g., exchange of the hydrogen atoms between the adsorbed layer and palladium bulk and Pd surface oxidation (PdO_2^+ ions were detected) [85]. On the NO side of the reaction, N_2O^+ ions were observed, suggesting the presence of N_2O_{ad} species on the surface. Detection of small amounts of $(NO)_2^+$ in turn indicates that the appearance of N_2O is caused mainly by the formation of $(NO)_2$ dimers and their dissociation towards N_2O and O_{ad} [86] similarly as it was observed earlier for Au tips [87].

An important process which accompanies often the surface reactions is the change of the oxidation state of the sample. Here, FIM allows again a direct in situ observation, whereas a direct comparison of the local behaviour of crystallographically differently oriented facets is possible (Fig. 7.10, [40]). In particular, the stepped regions between the low-index poles appear to be most susceptible to oxidation. This is different from the behavior of the central Rh(111) plane and of the {001} peripheral planes which seem to be rather reluctant to oxidation. Quite interestingly, the {011} planes seem to undergo slower oxidation than the {113} planes. Following the results of previous field-free measurements, both planes are not expected to be reconstructed at 375 K. For the quantitative evaluation, the local FIM intensity for different facets was extracted from the corresponding video sequence [40]. As is clearly visible in the Fig. 7.9b, after a considerable time delay a steep increase of local FIM brightness, related to the RhO_x formation, occurs.

The time dependence of the local image brightness shown in Fig. 7.10b demonstrates the high activity of the stepped planes {113} and {012} towards the surface oxidation. In contrast, the low-index planes are much less active, while (011) presents an intermediate case. Assuming a pseudo-first-order reaction kinetics, the rate constants can be estimated from the initial slopes of the curves shown in Fig. 7.10b. The values of 1.7 s^{-1} at 350 K and 2.3 – 2.4 s^{-1} at 375 K for both (113) and (012) planes were found and a rather crude estimation of the activation energies leads to values in the range of 5–17 kJ/mol.

The reaction-induced structural, morphological and chemical changes of the catalytic specimens are relevant for the function of a catalyst therefore, the studies of such reaction-caused modifications becomes increasingly important. This led to the development of a dedicated three-dimensional atom probe combined with a high pressure/high-temperature reaction cell [88]. This new instrument, called the *catalytic atom probe* (CAP), can be used for studying the interaction of gases with surfaces typical for use in commercial, e.g. automotive catalysts. It allows to study a wide variety of gas–surface interactions [89] and other effects accompanying catalytic reactions, such as oxidation-driven surface segregation and transport on Pt alloys. Exemplarily, the reaction of nitric oxide (NO) and oxygen (O_2) on Pt and

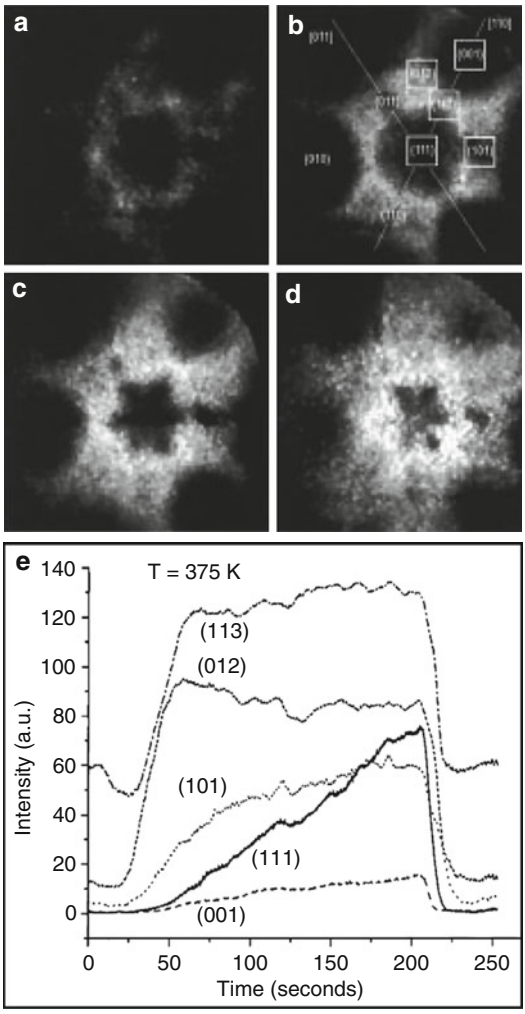


Fig. 7.10 FIM monitoring of the Rh surface oxidation. (**a**) O_2^+-field ion image of the initial stage of the oxygen interaction with Rh at 375 K. (**b–d**) O_2^+- FIM video frames showing the sequential stages of the surface oxidation of Rh at 5.2×10^{-5} mbar of oxygen in the presence of an external field of 15 V/nm; (**e**) Corresponding local image intensity for (111), (001), (011), (113), and (012) planes as a function of the oxidation time (Adapted with permission from [40]. Copyright 1998 ACS)

Pt–17.4 at % Rh/FIM specimens were studied, revealing a range of surface restructuring and segregation effects, which depend sensitively on catalyst composition, orientation, temperature, and gas chemistry [90].

5.1.2 Fluctuation-Induced Effects

Nanofacets on the specimen apex can serve as an excellent model of nanosized systems where a significant influence of fluctuations is potentially expected. Such expectations are based on the $1/N^{1/2}$ (N being the number of fluctuating particles, e.g., reacting molecules) scaling of the relative amplitude of fluctuations. The number of the reacting particles on a nanofacet varies in the 10^2–10^3 range, thus one may observe deviations from the behavior predicted by macroscopic rate laws, such as fluctuation-induced transitions in a bistable system [91]. The "parallel"

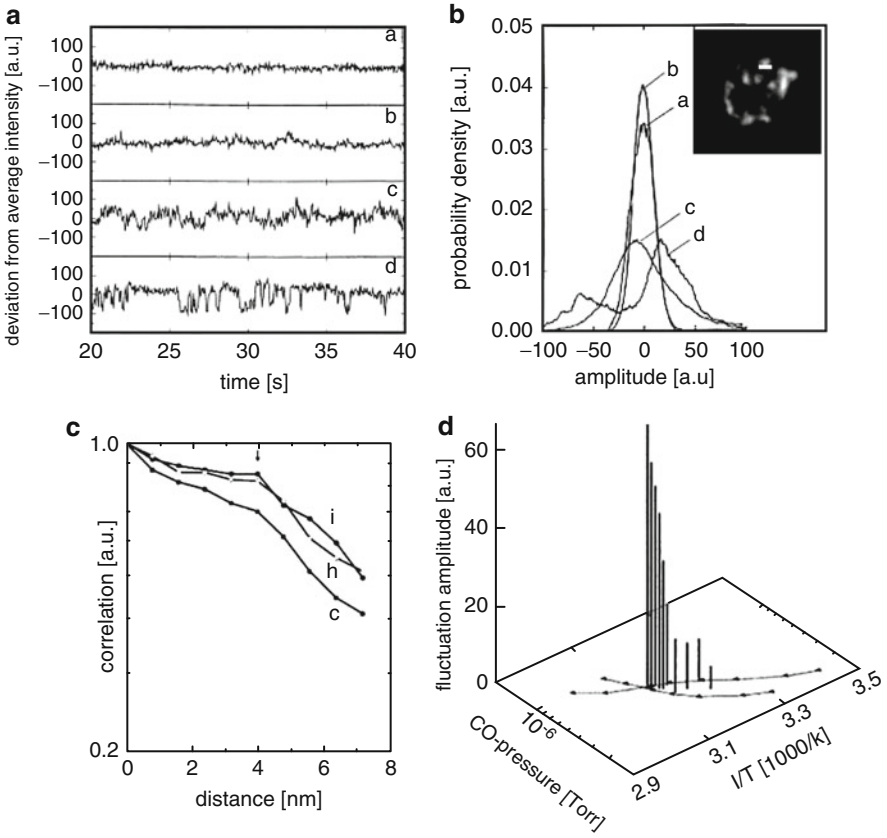


Fig. 7.11 Fluctuation-induced transitions in catalytic CO oxidation on a Pt field emitter tip. (**a**) Time series of the local (2×2 nm^2) FEM brightness and (**b**) correspondent probability distributions (*right-hand side*). The inset shows a FEM image with marked rectangular area where the local FEM brightness was analyzed (Adapted from [76]). (**c**) Break of the spatial correlation of the first atomic step (marked by an *arrow*) confining the individual (112) facet. The letters refer to different reaction conditions and the distance zero refers to edge of the facet. (**d**) Increase in the average amplitude of the local FEM brightness fluctuations on a Pt(112) facet at approaching the critical point given by the crossing point of the two boundary lines of the bistability range (Adapted from [94])

imaging principle of the FIM makes this technique naturally suitable for monitoring fluctuations: the processes proceeding on the different surface regions can be analyzed simultaneously and the time resolution is limited just by the features of the used video technique. Processing of the corresponding video frames allows to study the dynamic processes within the ROIs (regions of interest in digitized video frames and which correspond to the selected surface regions of few nm^2) arbitrarily located on the surface [92].

Figure 7.11 shows the local time series recorded for a small 2×2 nm^2 area in the vicinity of the (110) facet of a Pt tip. The small amplitude fluctuations caused mainly

by the CO diffusion and characterized by a Gaussian probability distribution were observed in the *monostable* range on the inactive branch of the reaction. This is illustrated by the time series *a* (Fig. 7.11a) and a corresponding probability distribution (Fig. 7.11b). Similar time series but with somewhat higher magnitude of fluctuations were also observed in the monostable range on the active branch (curves *b* in Fig. 7.11a). Unexpectedly, in the bistable range of the reaction, the probability distribution becomes broad and asymmetric and turns even into a bimodal probability distribution (curves c and d in Fig. 7.11a and corresponding distributions in Fig. 7.10b). The bimodal distribution d in Fig. 7.11b evidences the fluctuation-induced transitions between the two possible states in the bistability region [76].

Another unexpected result was the absence of the synchronization between the fluctuations on the neighboring facets [77]. This is unexpected because the tip is known to behave as one synchronized dynamic system during kinetic transitions from the active to inactive state (marked by lines in crossshaped diagrams in Fig. 7.9) the spatial coupling occurs apparently due to the fast CO diffusion.

More detailed studies using the Haar wavelet analysis detected that such fluctuation-induced transitions occur spatially correlated over the flat facet surface (the mentioned region in the vicinity of Pt(110) was identified as a small (331) facet) [93] and are confined by the first atomic step due to the disturbed diffusional coupling over the stepped surface. We note that this effect cannot be predicted within the mean-field theory. The Monte Carlo simulations naturally incorporating the stochastic nature of the modelled processes can, in turn, predict such an effect provided the modelled system is sufficiently small and in close proximity to a bifurcation (critical) point where bistability vanishes and fluctuations diverge [94].

The lack of the synchronization in respect to fluctuations between the various orientations can be understood if one takes into account that differently oriented facets may own different intrinsic bifurcation diagrams at the same external p, T, parameters. The stepped regions around the individual facets disturb the diffusive coupling via CO so much that it is not sufficient to synchronize the fluctuations on different facets. Figure 7.10c illustrates this by showing the break in the spatial correlation of the fluctuation at the position of the first atomic step confining the individual facet. We note that within the individual facet the reaction-induced fluctuations are generally well correlated as was demonstrated by the corresponding POD (*proper orthogonal decomposition*) and Haar wavelet analysis of the FEM video sequences [77, 93]. In addition, the degree of the spatial coherence increases at approaching the critical point (crossing point in the phase diagram in Fig. 7.11d) simultaneously with the amplitude of fluctuations (Fig. 7.10d) [94]. Similar behavior is well known for the equilibrium systems where the correlation length diverges (in an infinite system). In our case the correlation length seems to be simply limited by the size of the facets.

The noise-induced transitions in the CO oxidation detected first on the Pt nanofacets allowed to explain the vanishing bistability during CO oxidation on a Pd model catalyst consisting of small Pd particles [95]. For the model system consisting of particles of $\sim$500 nm size a pronounced bistability is observed which vanishes when the particle size becomes smaller than 6 nm (approximately

the size of an individual facet of the field emitter tip). The fluctuation-induced transitions, which occur in an unsynchronized way lead to the apparent disappearance of the bistability as observed by an averaging method (total CO_2 rate for many particles was measured in Ref. [95]).

Another promising FIM application that exploits the fluctuation effects is monitoring the surface diffusion by "virtual probe-hole" technique. The idea that the local image brightness fluctuations in the recorded FIM video images can provide the surface diffusion parameters is based on Onsager's hypothesis about the applicability of macroscopic diffusion laws to the microscopic density fluctuations [96] and on the finding that such brightness fluctuations reflect microscopic concentration deviations in an apparently homogeneous adsorbed layer and can thus be analyzed via the density fluctuation method, proposed by Kleint and Gomer [97, 98]. The "parallel" imaging principle of FIM allows the simultaneous analysis of processes on many chosen surface regions of only a few nm^2 size, in contrast to the "real probe-hole" measurements, where the emission from just one or two regions (in a "two probe-holes" experiment [99]) can be recorded. Particularly promising is the use of the field desorbed Li^+ ions in such an application (see Sect. 5.2) [100].

5.2 Field Desorption Microscopy

In the most of applications of the *field desorption microscopy* (FDM), the parallel imaging principle (the same advantage as in the FIM) is exploited: the fast dynamic processes and the spatial correlation of the events occurring simultaneously on spatially separated regions of the sample can be monitored. In the case of the Li FDM, an additional important advantage becomes relevant: an exceptionally low value of the applied field necessary to desorb Li atoms from the most of solid surfaces. Even at cryogenic temperatures this value hardly exceeds 10 V/nm, i.e., it is at least by factor 3.5 lower than the best imaging field for Ne^+ ions. This allows using of the Li^+ ions for imaging of the field-sensitive processes, such as surface reactions.

It was, e.g., possible to image by Li^+ ions the sole reaction front in the CO oxidation on a [111]-oriented Rh tip and the propagation of this front during the extension of the oxygen-covered, respectively, CO-covered surface. The illustration of such imaging is presented in Fig. 7.12 where different reaction states and reaction front shapes are imaged [46]. It is also possible to adjust the applied field to a value which is sufficient for the field desorption of Li from the CO-covered surface, but not sufficient to remove Li from the oxygen-covered surface (due to the higher binding energy of Li in the Li/O coadsorption system). This allow to create unique situations where an alkali promoter is added only to one reactant (oxygen) in the catalytic CO oxidation and to observe in situ the result of such spatially separated reaction promotion. Since the surface density of Li adatoms in the imaged area (reaction zone) can be adjusted by the field and temperature-dependent surface diffusion of Li from the shank of the tip, the degree of the local alkali-induced modification of the surface can be controlled in a reproducible way.

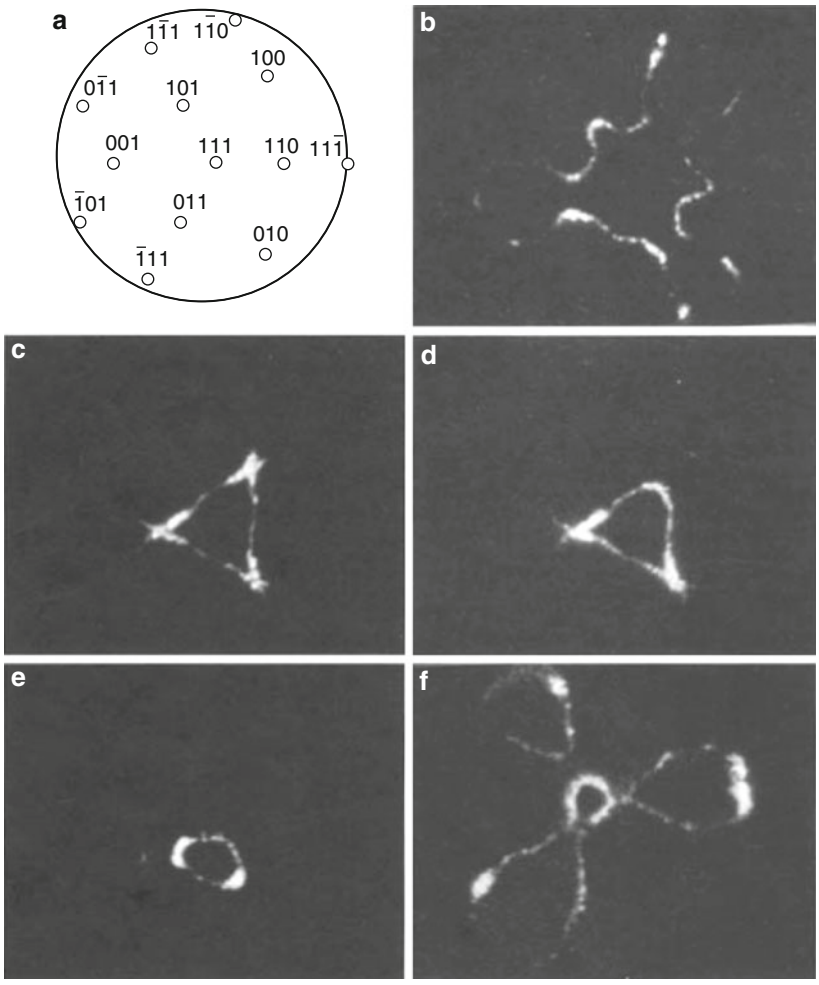


Fig. 7.12 Visualization of the CO-oxidation reaction on a [111]-oriented Rh tip by Li^+ ions, (**a**) crystallographic map; (**b**) steady state at 417 K, $p_{CO} = 1.5 \times 10^{-5}$ Torr, $p_{O2} = 7.5 \times 10$–5 Torr, $F_{const} = 0.85$ V/A, $F_{pulse} = 0.70$ V/A, f = 526 Hz; (**c**–**e**) the extension of the oxygen-covered surface caused by reducing of the CO pressure from 1.5×10^{-5} Torr to 1.3×10^{-5} Torr, (**f**) the initial stage of a reverse process (From [46])

Using the coadsorption of Li, even a reaction mode can be induced which does not exist in a Li-free case: oscillating CO oxidation on Rh [9, 47]. The prerequisites necessary for the oscillating behavior of the isothermal CO oxidation reaction on catalyst surfaces are (i) the existence of a bistability region in the phase diagram of the CO/Oad-Pt(Pd) adsorption system and (ii) involvement of a feedback mechanism. In the present case of the Li-induced oscillations, the reversible formation of surface oxide serves as a feedback mechanism (Fig. 7.12, [39]). The imaged reaction front (bright line in Fig. 7.12b, c) marks the spatial separation

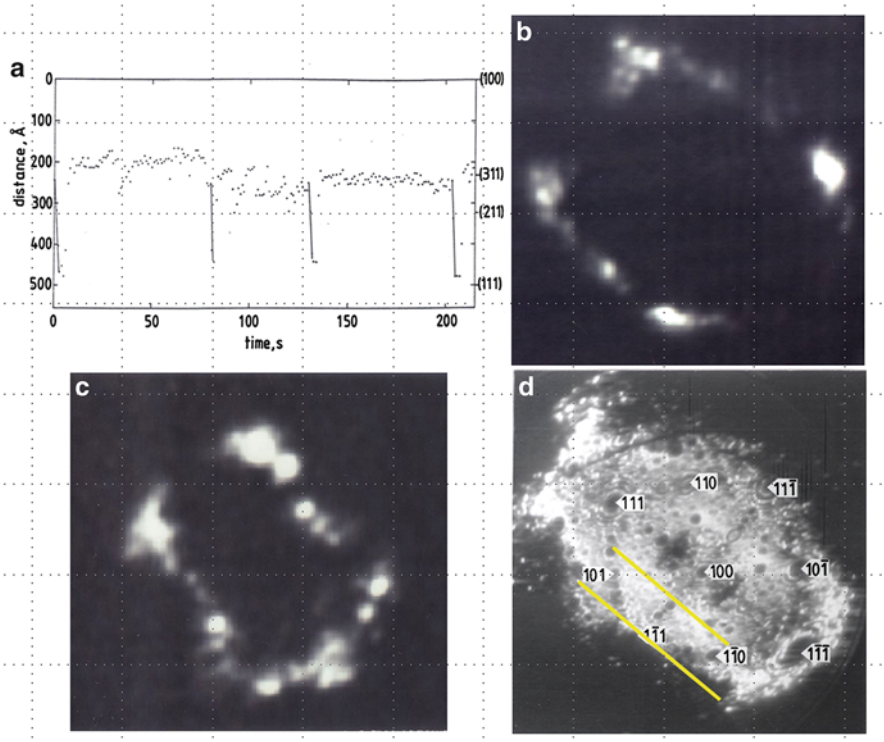


Fig. 7.13 (**a**) Li-mediated oscillations in CO oxidation on a [100]-oriented Rh tip: time dependence of the reaction front propagation. The current position of the front is measured from the center of the apex (100) plane along the [001] zone line. (**b**, **c**) Li-FDM images of the maximum (**b**) and minimum (**c**) extent of the reaction/diffusion front. (**d**) Ne-F1M image of the [100]-oriented Rh tip at 78 K. Part of the zone in which the oscillating motion of the reaction/diffusion front was observed is marked (From [47])

between the CO-covered surface and the area covered with oxygen (and Li). Such separation is a consequence of the increased rate of oxygen adsorption on the alkali-precovered surface [9, 47]. The exposure of Rh to oxygen in high-field conditions leads to morphological changes of the Rh surface (see Fig. 7.10 above) increasing its roughness due to RhO_x formation. The field desorption of Li is extremely sensitive to surface roughness because of the strong influence of this effect on the local field. Thus the variation of the surface roughness modulates the field desorption of Li. Increased local field due to the RhO_x formation leads to the avalanche-like field desorption of Li from the roughened surface. This causes a sudden motion of the border between the oxygen- and Li-covered part of the surface (compare Fig. 7.13b, c). The progressive reversal of the oxygen caused roughness by CO should lead in turn to the gradual motion of the Li desorption borderline (reaction front) towards the top of the tip. Under certain conditions this process begins to oscillate, as is in fact observed in the experiment (Fig. 7.13a).

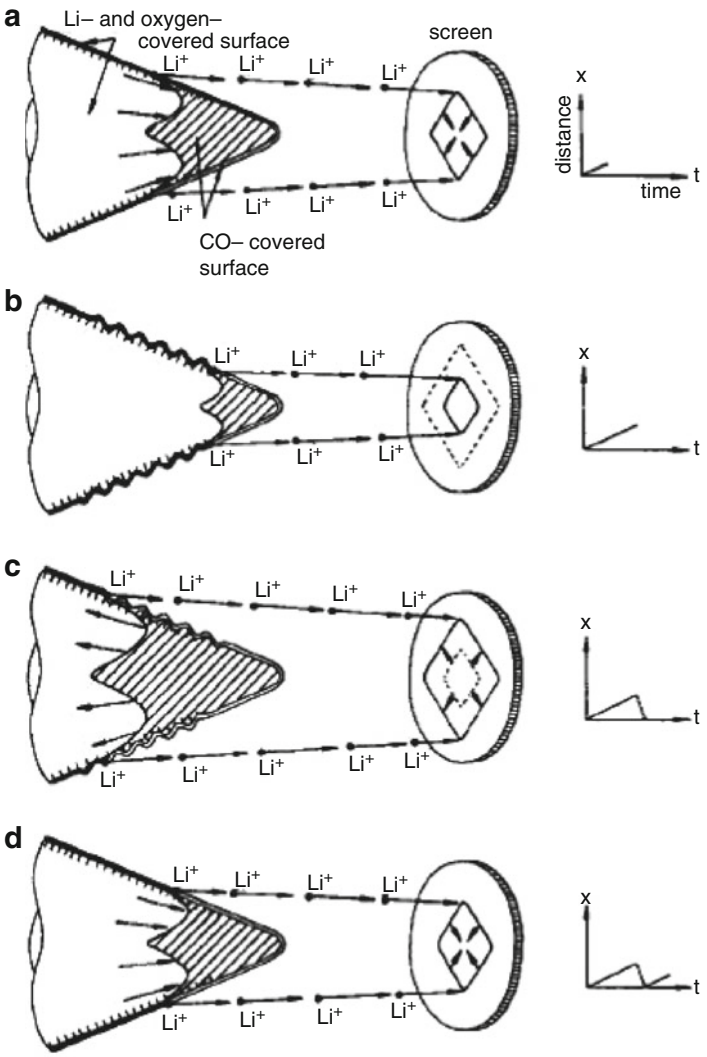


Fig. 7.14 Mechanism of the Li-mediated oscillations. (**a**) Initial state: oxygen is being stored in a "reservoir". (**b**) Growth of oxide granules resulting in increased roughness of the Rh surface. (**c**) Avalanche-like Li field desorption and consequent removal of the oxygen layer. (**d**) Final state; oscillatory cycle may start again (From [47])

The individual steps of the oscillating mechanism are shown in Fig. 7.14a–d, where the particular processes, such as storage of oxygen via Li-accelerated oxidation of Rh (Fig. 7.13a), Li desorption due to the roughness-enhanced local field (Fig. 7.14b) and subsequent reduction of the stored oxygen (Fig. 7.14c), are depicted. The drawings in the Fig. 7.14a, b corresponds to the micrographs in the Fig. 7.13b and c respectively.

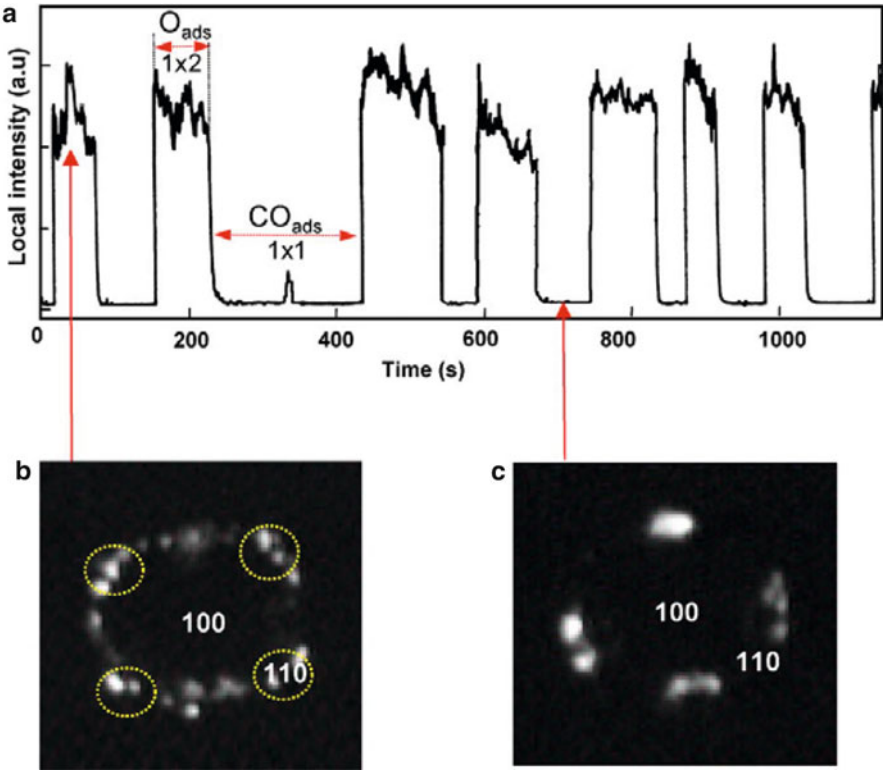


Fig. 7.15 The oscillating CO oxidation reaction on Pt nanofacets monitored with field-desorbed Li^+ ions at 490 K, $p_{CO} = 1.8 \times 10^{-5}$ mbar, $p_{O2} = 2 \times 10^{-4}$ mbar. (**a**) Local intensity of the Li-FDM image in the (110) region versus time. (**b**) Li-FDM image of the oxygen-covered apex of the [100]-oriented Pt tip. The dotted circles indicate the (110) regions. (**c**) The same for the CO-covered surface. The (110) regions remain dark (no field desorption of Li from those regions under these conditions) (From [101])

The use of Li as imaging medium has allowed also for the first direct evidence of the surface reconstruction as a feedback mechanism in the oscillating reactions on the nm-sized Pt facets [101]. Despite the tacit assumption that the "macro"-oscillating reaction kinetics, including the reconstruction driven feedback mechanism, should also be valid for the nm-sized facets of "real catalyst" Pt particles, no experimental evidence has been provided till 2006 (a kind of a "materials gap" problem). It means, it could not be excluded, that oscillations on a nanosized small metal particle with its differently oriented facets which are confined by stepped regions might also be induced by reaction–diffusion processes coupled in a complex manner [75].

The extreme sensitivity of Li to the atomic structure of the surface was exploited to prove the feedback mechanism of oscillations on Pt(110) nanofacets of a Pt tip [101]. In Fig. 7.15a the time dependence of the local Li^+ image brightness within a ROI placed in a (110) region during the oscillating CO oxidation is shown. During the self-sustained oscillations in the reaction, the Li-FDM image switches periodically, with a period of ~120 s, between a circular (Fig. 7.15b) and a crossshaped pattern (Fig. 7.15c).

The surface reconstruction of the Pt(110) facets from the (1 × 1) to (1 × 2) structure provides, due to the different corrugations of the reconstructed and unreconstructed surfaces, different local field enhancements "felt" by adsorbed Li atoms. When the externally applied field is adjusted to the value which is just sufficient for the field desorption of Li from the oxygen-covered (1 × 2) surface (Fig. 7.15b), the desorption of Li from the CO-covered much smoother (1 × 1) surface does not take place (Fig. 7.15c), since the local field is not sufficient (corrugation caused field enhancement is too low, see Sect. 5.3 and Fig. 7.18) for desorption of Li. This evidences for two different structures of the same (110) facet caused by different CO coverages. The switching between the (1 × 1) and (1 × 2) structures modifies the sticking coefficient for oxygen on the nm-sized Pt (110) facets, thus providing the same feedback mechanism as is known for the macroscopic single-crystal surfaces [73].

As already mentioned above, the analysis of intensity fluctuations in the Li-FDM images can be used for the study of the surface diffusion of Li. This may shed light on an important, but often overlooked, factor in catalysis, namely, the mobility of the catalytic (alkali) promoter itself. The first successful attempt to measure in situ the diffusivity of an alkali coadsorbat in a catalytic reaction was undertaken 2007 by use of the fluctuation method described in [92] and applied to Li in CO oxidation on Pt [100]. Figure 7.16 shows the Li-FDM images taken at similar conditions as in Fig. 7.15 and corresponding locally measured intensity series. With the corresponding calibration, the current fluctuations can be related to the fluctuations of the number of Li adatoms N_{Li} in the probed area.

The corresponding autocorrelation function is related to the diffusion coefficient which can be obtained from the comparison of the experimental and theoretical autocorrelation functions [92, 102, 103]. The results shown in Fig. 7.16c demonstrate the differences in the diffusivity of Li on the CO-covered Pt(111) surface along and across the atomic steps and indicate a "slowing" effect of the coadsorbed CO on the Li diffusion.

The lithium field desorption microscope can also be operated by making use of a supply mechanism in which Li diffuses as species intercalated in the region between a Rh metal and a surface carbon layer created by graphitizing of a Rh tip [104]. Figure 7.17 shows a [111]-oriented Rh tip which was field evaporated (Fig. 7.17a) and annealed in UHV at 1,000 K in a subsequent step. During this step carbon segregated to the surface producing a graphite-like overlayer structure in which the further field evaporation created occasionally two circular windows which could be imaged either by Li^+ (Fig. 7.17b) or O_2^+ (Fig. 7.17c) ions. Bright rings in the Fig. 7.17b appear as a result of Li^+ desorption at the border between the clean Rh and the surrounding graphite-like overlayer. Obviously, Li is continuously supplied from the shank reservoir to the tip apex. This evidences the mobile Li atoms to be intercalated between the Rh surface and the graphite-like layer.

Such mode of imaging allows to study quantitatively the diffusivity of the intercalated Li layer using e.g., a pulsed mode of imaging and adjusting the pulse frequency to the diffusion rate, as it was demonstrated in [48]. Additionally the formation of subsurface oxygen within the circular windows was detected by comparison of the O_2^+ FIM image intensity fort the CO-and oxygen-covered surface [104].

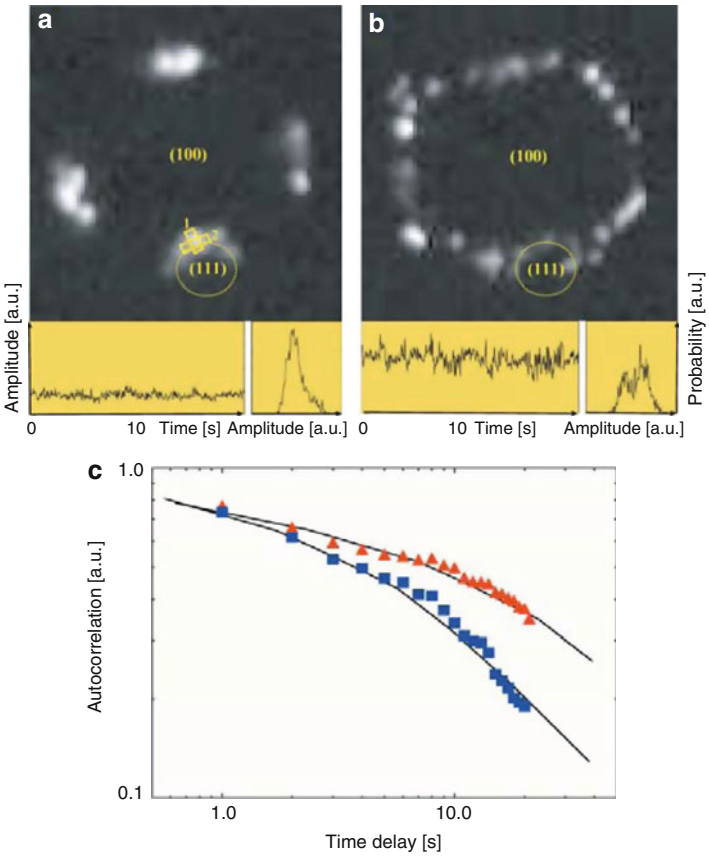


Fig. 7.16 Li^+ intensity fluctuations in the CO oxidation on a [100]-oriented Pt tip (at the same conditions as in the Fig. 7.14). (**a**) In the inactive (CO-covered) state, fluctuations of the image originate from Li diffusion. The ROI in the position 1 allows to monitor the diffusion along the atomic steps which confine the (111) facet, the ROI in position 2 across the steps, correspondingly. An example of a locally measured time series and a corresponding (Gaussian-like) amplitude distribution is shown below. (**b**) In the active (oxygen-covered) state, fluctuations of the image are caused by the reaction itself. The corresponding local time series exhibits a bimodal (non-Gaussian) distribution. (**c**) Autocorrelation functions which demonstrate the differences in the diffusivity of Li on the CO-covered Pt(111) surface along (■) and across (▲) the atomic steps. The diffusion coefficients ($D = 8 \times 10^{-13}$ and 2×10^{-13} cm^2/s, respectively) are derived from the theoretical autocorrelation functions fitting the experimental data (Based on [100])

5.3 Probe-Hole Ion Analysis and Field Ion Appearance Energy Spectroscopy

The applications of techniques based on the analysis of ions emitted through a probe hole, which corresponds to a microscopically small area of surface, are based on the pioneering work of Ingram and Gomer in the 1950s [105, 106].

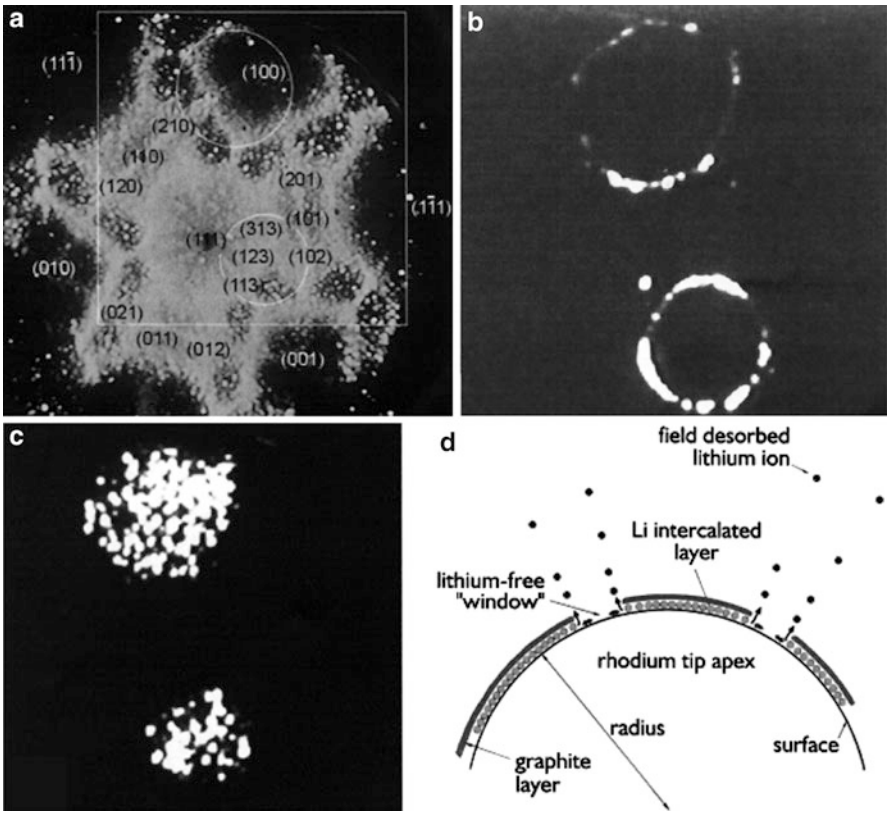


Fig. 7.17 Li layer intercalated between the Rh (**a**) Ne^+ FIM image of a [111]-oriented Rh tip ($F \approx 35$ V/nm, $T = 78$ K, note that field evaporation does not remove surface carbon quantitatively) (**b**) Li^+ FDM image ($F = 9.5$ V/nm, $T = 407$ K,) of the section indicated by the square in (**a**) after the Rh tip was heated to ~1,000 K to produce a graphite-like overlayer. *Two circle*-like windows of the clean surface contain Rh(100) (*top*) and Rh(123) (*bottom*) planes, see white circles in (**a**). (**c**) is the same as in (**b**) but imaged with O_2^+ ions at 78 K, $F = 12.2$ V/nm. (**d**) Scheme of the mechanism leading to the formation of bright ring patterns in (**b**). Li supply is provided by interlayer diffusion of the intercalated Li layer (Based on [104])

Since these early attempts, basic contributions to the *field ion mass spectrometry* (FIMS) which was used mainly to study the gaseous compounds ionized by a strong electric field at surfaces, were made by Beckey [107], Block [54] and few other groups. A version of this technique, *pulsed field desorption mass spectrometry* (PFDMS, [20]) which combines FIM with the time-of-flight (TOF) analysis of surface species field desorbed as ions offers a unique method to study the reaction intermediates or products which can be sampled far below the temperatures that would normally be required for their unassisted thermal desorption.

As already mentioned in the Introduction, the FIM principle was first applied for the chemical identification of single surface atoms by the *atom-probe field ion microscope* (AP-FIM), developed by Müller et al. [11, 108]. Since that time, this

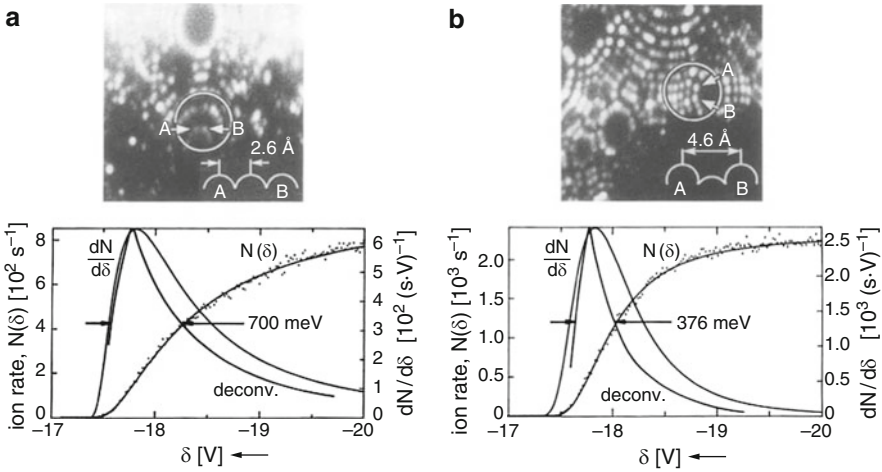


Fig. 7.18 Determination of the local electric field above the individual surface atoms. (**a**) Section of a Ne^+ field ion image at 79 K. The probe hole (*white circle*) is placed over steps of the Rh(001) facet. Below the corresponding locally measured retardation curve N(δ) for the selected site and differentiated (non- and deconvoluted) curves dN/dδ are shown. (**b**) The same as in (**a**) but for a more corrugated step on Rh(113) (From [34])

technique, commonly called *atom probe* (AP), has evolved to a *3-D atom-probe tomography* (APT) which allows 3-D reconstructions of the sample on an atomic scale. Due to a wide use of this commercially available techniques, an abundance of reviews and monographs dedicated to various versions of AP and 3-D APT is available [25–27, 30, 49, 51, 109], including the descriptions of the recently developed *local-electrode atom probe* ($LEAP^R$) [18, 19, 110]. A combination of the $LEAP^R$ design with laser pulsing provides up-to-date due to its high mass resolution and high data collection rate the wide field of possible applications.

In contrary to the AP techniques, the spectroscopies based on the measurements of the energy distributions of field ions have found much less applications till now. Present chapter is dedicated to the applications of the *field ion appearance energy spectroscopy* (FIAES). The main strength of FIAES is the ability to obtain locally the binding energy of adsorbed (or field-adsorbed) atoms or molecules on chosen surface sites by direct measuring of appearance energy of corresponding field ions [20, 57]. This has allowed e.g., measurements of the local electric fields above the individual surface atoms [22, 34]. Figure 7.18 shows the sections of the Ne^+ field ion image for the more Rh(113) and less Rh(001) corrugated surface of a [111]-oriented Rh tip and corresponding Ne^+ field ion retardation curves below.

From the onsets of the retardation curves, the absolute (based on the independent calibration of the retarder) field ion appearance energies were obtained and the values of the local field at distances of ~0.3 nm from surface atoms were obtained from the field-dependent term of the appearance energy [57] (see Table 7.1, from Ref. [34]). These values were compared to the values obtained independently from the local electron energy spectroscopy (i.e., at the distance of about 1.5 nm to

Table 7.1 Local probe-hole FIAES measurements for chosen Rh(001) and Rh(113) surface sites

	Closed-packed steps of Rh(001)	Steps across the chains of Rh(113)
A_1^{hkl} (eV)	21.77 ± 0.03	1.79 ± 0.02
F_{loc}^{hkl} (V/A)	4.04 ± 0.29	3.95 ± 0.18
F_0^{hkl} (V/A)	3.12 ± 0.03	2.57 ± 0.02
F_{loc}^{hkl}/F_0^{hkl}	1.27 ± 0 13	1.54 ± 0.08
$FWHM_{deconvolved}$ (meV)	700	376

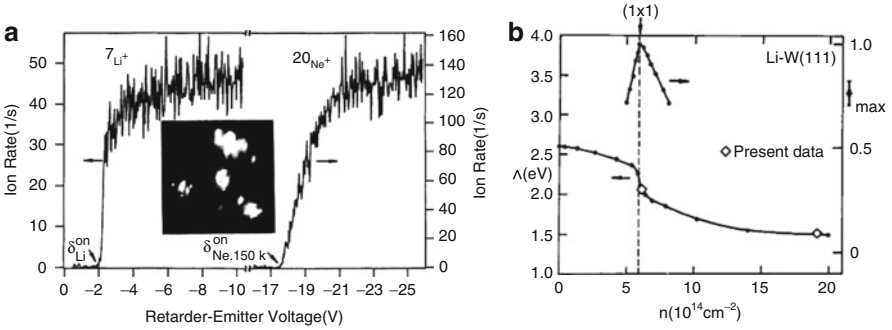


Fig. 7.19 FIAES of the Li^+ ions emitted from few atomic sites of the apex plane of a [111]-oriented W tip. (**a**) Li^+ retardation curves measured at T = 352 K and F = 7.9 V/nm and corresponding curves for the Ne^+ ions emitted from the same surface sites at T = 150 K and 36 V/nm. The *inset* shows the Li FDM image of a[111]-oriented W tip (From [111]). (**b**) Binding energy of Li atoms derived from the FIAES data in comparison with the field-free binding energy, Λ, of Li adatoms on a W(111) single-crystal surface shown as a dependence on the surface density of Li adatoms. Maximum of the intensity of low-energy electron diffraction spots, *I*/*I*max, corresponds to the structure 1 × 1 of the Li adlayer (From [59])

the surface) at the same position of the probe hole and the local field enhancement factors (also listed in Table 7.1) were obtained.

As an example of use of FIAES for the direct determination of the binding energy of adsorbed atoms, the binding energy of Li adatoms on W(111) can be mentioned, which was obtained from energy analysis of locally desorbed Li^+ ions [59, 111] (Fig. 7.19a) in a good agreement with the known thermo-desorption data (Fig. 7.19b). Also the binding energy values of Rh atoms, field evaporated from Rh (110) obtained in this way agree well with the sublimation energy of Rh [60].

Especially promising is the application of this method to the coadsorption systems, where the properly chosen values of the field and the temperature of the sample (far below the thermodesorption threshold) allow to extract selected adatoms from the coadsorbed layers and to derive their binding energy. As an example, the recent FIAES measurements of the binding energy of Li atoms coadsorbed with oxygen on W(112) surface can serve, where the binding energy of Li adatoms was measured for different coverages of coadsorbed oxygen [112].

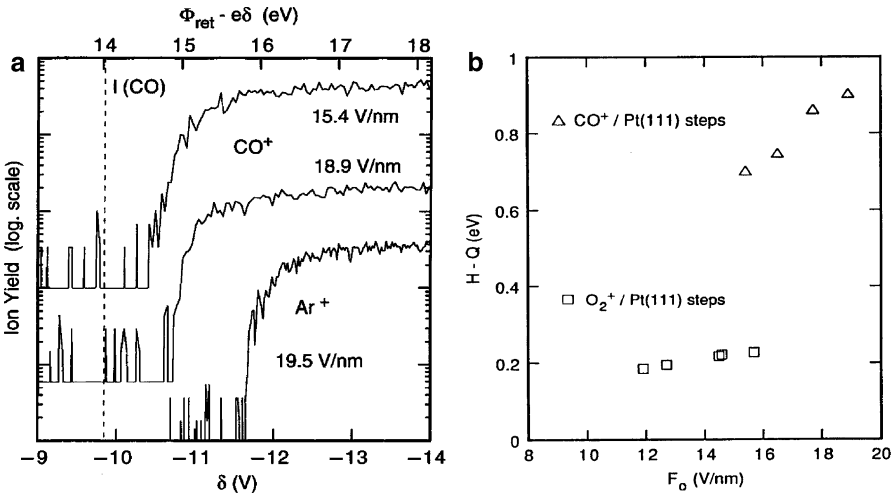


Fig. 7.20 FIAES of reactants in catalytic CO oxidation reaction on Pt. (**a**) O_2^+ retardation curves measured at 11.9 V/nm from oxygen-covered step sites on Pt(111) at T = 79 K. The *dashed line* indicates the ionization energy for a free O_2 molecule. The Ar^+ retardation curve used for calibration of Φ_{ret} is also shown. (**b**) The *H-Q* term (see Eq. 7.2) as a function of applied field F_0. The *upper* (*lower*) results have been obtained from CO^+ (O_2^+)-field ion appearance energies measured at 79 K for stepped Pt(111) surfaces covered with CO_{ad} (O_{ad}) (Taken from [114])

It is also possible to use the FIAES during a surface reaction to determine in situ the binding energy of reactants and also the field dependence of this energy. This allows to shed light on the role of perturbances of local electron density distributions as they occur, e.g., on the oxide/metal interface in supported catalysts [113]. Figure 7.20 shows the experimentally measured field-dependences of the binding energy for the CO and O_2 molecules on chosen step sites of the Pt(111) nanofacet [114]. The plots show that the binding energy of adsorbed CO increases quite strongly with the electric field strength, whereas adsorbed O_2 displays a relatively weak dependence on the applied field, in agreement with the self-consistent calculations by Kreuzer and Wang [78]. These results allow to explain the field effect in the CO oxidation on Pt described in Sect. 5.1.1. The effect on the binding strength of adsorbed species results from the additional charge transfer caused by a field-induced redistribution of the electronic charge at the surface: the "positive" field applied in FIM reduces the electronic density outside the geometric surface plane as compared to the field-free case [34].

The corresponding changes in the binding energies of the molecular adsorption states of O_2 and CO on Pt shift the adsorption/desorption equilibria of the molecular O_2 species and of CO. Enhanced binding strength of CO modifies the supply rate of CO into the reaction zone whereas the considerably lower binding energy of O_2 molecules leads to an insignificant additional supply of O_2 molecules under reaction conditions. Both effects taken together lead to a shift of the FIM diagram towards the smaller p_{CO} values in comparison to the (quasi-field-free) FEM diagram.

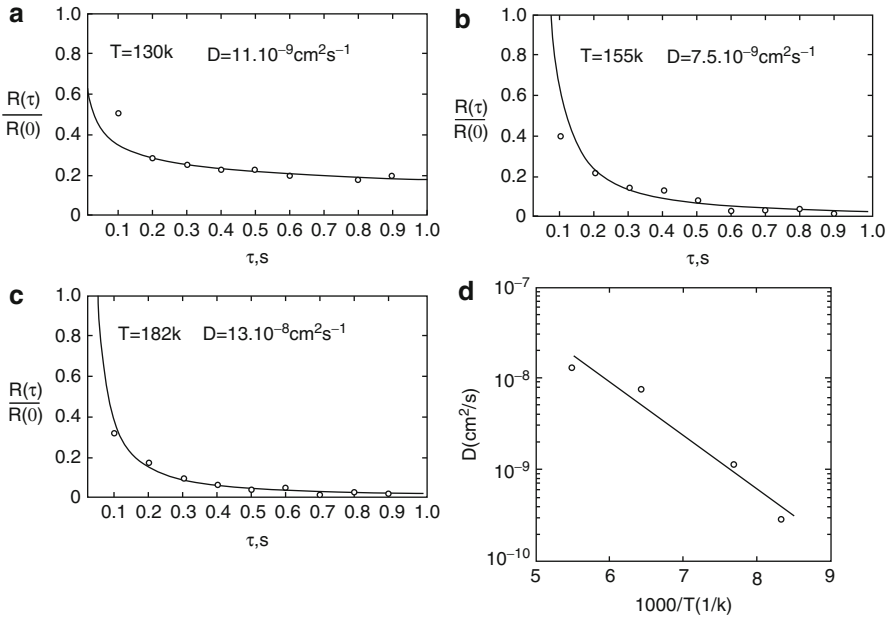


Fig. 7.21 Autocorrelation function, *R(r)/R(O),* for the ion rate fluctuations of CO^+ emitted from the few selected surface site on the apex plane of the [111]-oriented W tip at: (**a**) 130 K, (**b**) 155 K, and (**c**) 182 K. *Solid lines*: theoretical functions, *circles*: experimental values. (**d**) Temperature dependence of D, the diffusivity of CO on W(111) at FIM experimental conditions (Pco = 2×10^{-5} Torr, F = 20 V/nm) (Based on [102])

It has to be noted, that weakly bound highly mobile CO species detected with FIAES under UHV conditions are apparently present on the catalyst surface under high pressure conditions as results from the comparison of *high-field* and *high-pressure* studies [115]. In this way the high-field experiments allow to mimic the high-pressure conditions on catalytic metal nanoparticles thus bridging (at least partially) both the materials and pressure gap.

The mass-to-charge resolved local (probe-hole) ion rate measurements of ions desorbed from particular surface sites can be used to obtain the diffusivity of corresponding adsorbed atoms: since the number of ions, emitted from the defined area of the surface, reflects the local surface coverage and the fluctuations of the ion rate reflect the fluctuations in the surface density of adatoms [102]. Thus, the autocorrelation analysis of rate fluctuations can be applied, similarly as it was used earlier for the fluctuations of the field emission current [92].

Figure 7.21 shows such analysis for the CO^+ field ions originating from the apex plane of a [111]-oriented W tip and the corresponding temperature dependence of the diffusion coefficient, obtained in this way (Fig. 7.21c, [102]).

The slope of this dependence yields a value of 0.12 eV for the activation energy of CO in a weakly bound layer formed at elevated coverages. This value is in qualitative agreement with diffusivities reported by Gomer from shadowing

measurements [116] for higher coverages of CO on W [107]. It is also to be noted that such measurements can be in principle performed also for coadsorption layers, since the ion rate is measured in a mass-to-charge resolved way. In principle, using the retarding energy analyzer, also the fluctuations of the energy-resolved ion rate can be measured, i.e., the diffusivity of particular species (e.g., weakly bound with the energy smaller than particular chosen value) can be obtained.

5.4 Carbon Nanotubes

Cylindrical *carbon nanotubes* (CNTs) with their extraordinary mechanical and electrical properties can be considered as natural field emitters, since they possess all the necessary prerequisites for an effective field emission: a nanometer-scale radius of curvature, high mechanical stiffness, chemical inertness and electrical conductivity. Therefore, much attention has recently been paid to the CNTs as possible highly effective electron sources for flat-panel displays.

Indeed, field emission was obtained from individual single-wall carbon nanotubes (SWNTs) [117] and multiwall nanotubes (MWNTs) [118, 119] as well as from nanotube films [120] and from nanotube assemblies [121]. These studies have shown that CNTs are excellent field emitters, with operating voltages that are far lower than those for diamond or amorphous carbon film emitters. Furthermore, the nanotube field electron sources have shown a high degree of coherence of the field emission current and appeared to be less affected by self-sputtering degradation, unlike metal field emitters [122]. As a result, field emission displays with nanotube cold cathodes have been fabricated, and their performance appeared to be good enough for a practical use [123].

In contrary to above FEM studies, where the atomic structure cannot be resolved, the use of CNTs as ion sources and correspondingly the FIM observations of nanotubes, both SWNTs and MWNTs, are rather scarce, despite a great interest. This is caused mainly by the relatively low evaporation field of carbon, which appears lower than the applied field necessary for the ionization of usual FIM imaging gases as Ne or He. In addition, unlike metallic samples exposed to high electric fields, carbon materials evaporate not atom by atom but rather in the form of nm-sized complexes [124]. This leads to unraveling of the nanotubes under the FIM conditions. This shortcoming can be circumvented by using of mixture of helium and hydrogen as imaging gas [125]. In such mixtures, local field enhancement over the field-adsorbed atoms of one component of the mixture allows the field ionization of another component at lower applied fields [126].

Alternatively, the nanotube specimen can be cooled down, e.g., to 4.2 K. In this case the field evaporation, which is a thermally activated process, is effectively suppressed [29, 30, 36] and FIM visualization of samples sensitive to field evaporation becomes possible [25, 30]. In this way, a full atomic resolution of the end cap of closed carbon nanotubes was achieved recently for the first time [127].

Such observations are of particular interest since the cap of a closed nanotube, being half of a fullerene molecule, is characterized by a particular electronic structure, the so-called cap electronic states [128, 129], which are manifested, e.g., in an increased reactivity and emissivity in comparison with the smooth lateral surface of the nanotube. The FIM observations [127] have shown that the atomic structure of the upper layer of the caps of subnanometer carbon tubes consists predominantly of hexagonal rings in contrary to the lateral surface which consists of carbon hexagons only [130]. The FIM studies are particularly important, since the nanotubes become often deformed during field emission. Such deformation contributes to the emission characteristics of the nanotubes. Actually, the deformation mechanism is not understood in all details, but it can be explained, at least partially, by the heterogeneous nucleation mechanism for the closed nanotube, and by the change in the bonding state from an sp^2- to sp^3-like bonding state for the opened nanotube [131].

Generally, it has to be noted that the potential of the FIM techniques relatively to the CNTs is not really exploited yet only few atomically resolved structures are published up to date.

6 Summary and Future Perspective

Exploring solid surface, two aspects are dominating: (i) imaging, if possible with atomic resolution and (ii) laterally resolved chemical identification of surface species. The field ion microscope (FIM) equipped with the atom probe (AP) was historically the first technique able to handle both aspects on an atomic scale. FIM, AP and their "descendants" such as 3-D AP and LEAP are widely applied since the 1960s in materials science, particularly in the study of metallurgical problems [25, 26, 29, 30, 109]. Apart of this, FIM has stimulated the development of other atomic resolution microscopies, especially scanning probe microscopy (SPM). Before the SPM-techniques accrued from the adolescence (i.e., before the 1990s), FIM has contributed significantly to such important developments as the study of surface diffusion of single atoms and of small atomic clusters by direct observation of particle displacements [28, 29]. The random walk of individual atoms and their movement under a driving force produced by, e.g., a field gradient or by atomic interactions could be comprehensively studied in FIM [27, 61, 132]. Later on, the random walk analysis provided finding that the interaction potential between two adatoms may exhibit both repulsive and attractive regions, i.e., that the pair potential is nonmonotonic in distance [66, 133]. This was first observation of the indirect adatom–adatom interaction which discussed intensively till now [69, 134, 135].

Clustering of atomic species, stability of cluster ions, and field dissociation of compound atoms are topics among others where FIM contributed significantly [136]. With the development of SPM in the 1980s, the leading role of the FIM in revealing the surface phenomena on an atomic scale moved to this new technique, since it provides also direct observation of the motion of single atoms or molecules

on a surface, but the material caused limitations are much less stringent. In addition, the specimens do not need to be sharp tips and the surface area can also be much larger.

Since the 1990s, the experimental efforts of several FIM groups became focused on using the FIM-based techniques to study catalytic reactions and other dynamic phenomena on the surface of field emitter tips used as models of catalytic particles. The chamber of the field emission/field ion microscope is exploited in such studies as a flow reactor with a controlled supply of the gas reactants, which react on the surface of the catalytically active specimen. Using the digital video technique, the breakthrough was achieved in the sense that the reaction fronts, self-sustaining oscillations and other evidences of the spatially temporal self-organization, known for the macroscopic flat surfaces [73] became visible in situ for the first time on the nanometer scale. Mainly the CO oxidation reaction [8, 9], but also other reactions like H_2 oxidation [75, 81] or NO reduction with H_2 [10, 82–84] on Pt, Rh, and Pd surfaces (which are relevant in the sense of automotive catalytic converters), was visualized, and kinetic phase diagrams for the nanosized samples were published. Effects, which are basically not observable on the macroscopic surfaces, such as fluctuation-induced kinetic transitions [76] or size-dependent phase diagrams [94], were detected and described. Corresponding reviews [4, 137, 138] were published recently, where also the role of the size effects, applied electric field, and reaction-induced fluctuations are analyzed.

It has to be emphasized that this renaissance of FIM occurred in the 1990s, i.e., in times, when the probe-hole analysis of emitted ions and atom-probe techniques including 3-D tomography was fully established, this allowed to exploit these additional possibilities for the local chemical probing and even create a *catalytic atom probe* (CAP) [88]. This new instrument consists on an FIM, a 3-D atom probe, and a reaction cell (allowing to expose specimens to reactive pressures of up to 1 bar) and is constructed specifically to investigate the properties of heterogeneous catalysts. It allows to study a wide variety of gas–surface interactions [89] and other effects accompanying catalytic reactions, such as oxidation-driven surface segregation and transport on Pt alloys [90].

Development of such and similar techniques stimulated the theoretical analysis of the problems of the field evaporation of nonmetallic materials, such as oxides. A quantum-mechanical theory of field desorption and field evaporation was developed in the 1980s and 1990s for atoms and molecules on metal tips and also for the understanding of field-induced chemistry [36, 139]. A similar first principles approach was developed newly for oxides [140], important components in microelectronics and in catalysis. This allows to improve the interpretation of 3-D tomography images which was rather difficult due to a lack in the understanding of the different evaporation mechanisms involved in semiconductors and oxides [141].

Despite of the snowballing development of the SPM-based studies, the niche for the FIM application is still sufficiently big due to the possibility of parallel imaging which is inherent to FIM functional principle. Especially such in situ studies of the dynamic processes where a direct comparison of individual behavior of atoms or

molecules on crystallographically different facets of the same specimen (i.e., in the exactly same conditions) is desired are suitable for the FIM. FIM is also a native technique to study the field effects and especially to understand the field-induced chemistry: in fields of the order of volt per angström, chemical effects come into play because the electronic orbitals get field modified to such a degree that the chemical characteristics of an atom or molecule become altered, e.g., by establishing new bonding orbitals [36, 139]. Still a lot can be done by FIM in this direction, especially for nonmetallic systems.

Distinguishing atoms of different chemical nature in a nondestructive way, e.g., just from imaging remains a great challenge in FIM. Already in the early days of FIM, such attempts were undertaken for binary alloys [142]. Today, the improved calculation possibilities may provide much better basis for such identification as was shown in the STM studies of ordered alloys [143] where different chemical species provide differing STM image intensity. A breakthrough in such identification would allow to characterize the surface composition just by counting the number of atoms of the particular species. Alternatively, as proposed already in 1993 [144], the FIAES of the noble gases from the individual surface sites may reveal the 3-D distribution of the local field and thus the local electron density distribution over the individual atoms. This could open the way to a nondestructive atom probe.

A promising fields of possible FIM applications are nanotubes and nanowires. Whereas both nanotubes (e.g., CNTs) and nanowires (e.g., ZnO [145]) are often used as electron emission sources, difficulties caused by low evaporation field hinder up to now wide application of FIM to such nanostructures. Cooling down to 4 K or using mixtures of imaging gases might circumvent these problems thus one may expect a breakthrough in the near future. A very promising future application of field ionization over the carbon nanotubes seems to be the use of the planar array of CNTs as a high-efficiency detector for the neutral supersonic helium beams [146]. The need for such a compact high-sensitivity detector results from the perspective of a helium atom microscope (de Broglie microscope) with nm resolution, where the supersonic helium beams would be used as surface probes [147]. However, lot of difficulties has to be overcome for such a development, since field ionization of non-accommodated He atoms occurs in this case, i.e., the ionization mechanism differs from that in the FIM during the imaging. Both experimental and theoretical efforts are necessary to achieve optimal spatial localization of the field ionization event [148].

The wide use of the scanning tunneling microscopy and other scanning probe techniques rose the problem of the atomic-scale definition of the STM tips used as probes. The advantage of an atomically well-defined tip is evident: the known atomic structure predetermines the electronic structure and thus the lateral resolution of the STM. Particularly important is the knowledge of the tip structure in the combined STM and AFM experiments [149]. The best way to characterize and to shape the scanning tip (including the possibility to create a one-atom tip [150]) is to combine the FIM and the STM in one device and to create the common protocols which could be used for comparison the results obtained in different

experimental setups. First successful steps in this direction are already done [151] the corresponding theory linking the atomic and the electronic structure may follow soon.

Summarizing, it can be said that there are many advantages of the scanning probe techniques in surface applications, as compared to the FIM. Not only much more surface atomic sites appear in the image but also the spectrum of materials applicability is much wider in case of STM. However, the potential of the FIM and the FIM-based spectroscopies is not yet totally exploited: there are still many possible applications where the FIM can be used as a complementary tool and even few of those, where the FIM is still the only technique of choice.

References

1. Wintterlin J, Volkening S, Janssens TVW, Zambelli T, Ertl G (1997) Atomic and macroscopic reaction rates of a surface-catalyzed reaction. Science 278:1931
2. Hendriksen BLM, Bobaru SC, Frenken JWM (2005) Looking at heterogeneous catalysis at atmospheric pressure using tunnel vision. Top Catal 36:43
3. Nishikawa O, Kimoto M (1994) Toward a scanning atom probe – computer simulation of electric field. Appl Surf Sci 76/77:424
4. Suchorski Y, Drachsel W (2007) Catalytic reactions on platinum nanofacets: bridging the size and complexity gap. Top Catal 46:201, and references therein
5. http://www.fhi-berlin.mpg.de/th/personal/hermann/pictures.html
6. Suchorski Y, Schmidt WA, Block JH (1993) Enhanced local electric fields in field ionization at steps of clean and Au-covered Rh(111). Appl Surf Sci 67:124
7. Freund H-J, Baumer M, Libuda J, Kuhlenbeck H, Al-Shamery K, Hamann H (1998) Metal aggregates on oxide surfaces: structure and adsorption. Cryst Res Technol 33:977
8. Gorodetski VV, Drachsel W, Block JH (1993) Imaging the oscillating CO-oxidation on Pt-surfaces with field ion microscopy. Catal Lett 19:223
9. Medvedev VK, Suchorski Y, Block JH (1995) Oscillations of the CO oxidation on Rh induced by field-controlled Li coadsorption. Surf Sci 343:169
10. Voss C, Kruse N (1995) Field ion microscopy during an oscillating surface reaction: NO/H_2 on Pt. Appl Surf Sci 87/88:127
11. Müller EW, Panitz JA, McLane SB (1968) The atom probe field ion microscope. Rev Sci Instr 39:83
12. Panitz JA (1974) The 10 cm atom probe. Rev Sci Instrum 44:1034
13. Panitz JA (1978) The imaging atom-probe mass spectroscopy. Progr Surf Sci 8:219
14. Drachsel W, Nishigaki S, Block JH (1980) Photon-induced field ionization mass spectroscopy. Int J Mass Spectrom Ion Phys 32:333
15. Kellog GL, Tsong TT (1980) Pulsed-laser atom-probe field-ion microscopy. J Appl Phys 51:1184
16. Kelly TF, Kamus PP, Larson DJ, Holzman LM, Bajikar SS (1996) On the many advantages of local-electrode atom probes. Ultramicroscopy 62:29
17. Müller EW (1970) The atom-probe field ion microscope. Naturwissenschaften 57:222
18. http://www.imago.com/ (IMAGO Scientific Instruments Corporation, Madison)
19. http://www.cameca.fr (Cameca Sa, Paris)
20. Kruse N (1999) Surface reaction kinetics on the atomic scale: studies by means of pulsed field desorption mass spectrometry. Mater Sci Eng A270:75; (2001) Dynamics of surface reactions studied by field emission microscopy and atom-probe mass spectrometry. Ultramicroscopy 89:51

21. Ernst N (1993) Appearance energy spectroscopy of field ions. Appl Surf Sci 67:82
22. Schmidt WA, Ernst N, Suchorski Y (1993) Local electric fields at individual atomic surface sites: field ion appearance energy measurements. Appl Surf Sci 67:101
23. Müller EW (1951) Das Feldionenmikroskop. Z Physik 131:136
24. Müller EW (1956) Das Auflösungsvermögen des Feldionenmikroskopes. Z Naturforsch 11a:88; (1956) Resolution of the atomic structure of a metal surface by the field ion microscope. J Appl Phys 27:474
25. Miller MK, Cerezo A, Hetherington MG, Smith GDW (1996) Atom probe field ion microscopy. Oxford University Press, Oxford
26. Seidman DN (1976) Study of radiation damage in metals with the field-ion and atom-probe microscopes. In: Peterson NL, Harkness SD (eds) Radiation damage in metals. American Society for Metals, Materials Park
27. Ernst N, Ehrlich G (1986) Field ion microscopy. In: Gonser U (ed) Microscopic methods in metals. Springer, Berlin Heidelberg
28. Tsong TT (1988) Experimental studies of the behaviour of single adsorbed atoms on solid surfaces. Rep Progr Phys 51:759, and references therein
29. Müller EW, Tsong TT (1969) Field ion microscopy, principles and applications. American Elsevier, New York
30. Tsong TT (1990) Atom-probe field ion microscopy, field ion emission and surfaces and interfaces at atomic resolution. Cambridge University Press, Cambridge, NY
31. Rendulic KD (1971) Measurements on field adsorption of neon and helium and the field ionization of a helium-neon mixture. Surf Sci 28:285; ibidem, (1973) On field adsorption, ionization rates and gas supply. Surf Sci 34:581
32. Ernst N, Block JH (1982) Field adsorption of neon on tungsten studied by electron-stimulated field desorption. Surf Sci 117:561
33. Schmidt WA, Suchorski Y, Block JH (1994) New aspects of field adsorption and accommodation in field ion imaging. Surf Sci 301:52
34. Suchorski Y, Schmidt WA, Ernst N, Block JH, Kreuzer HJ (1995) Electrostatic fields above individual atoms. Progr Surf Sci 48:121
35. Gomer R (1994) Field emission, field ionization, and field desorption. Surf Sci 299/300:129, and references therein
36. Suchorski Y, Ernst N, Schmidt WA, Medvedev VK, Kreuzer HJ, Wang RLC (1996) Field desorption and field evaporation of metals: in memoriam professor J.H. Block. Progr Surf Sci 53:135
37. Suchorski Y, Schmidt WA, Block JH, Medvedev VK (1995) Appearance energy spectroscopy of CO^+ field ions emitted from W(111). Surf Sci 331/333:277
38. Suchorski Y (1998) Field ionization of O_2 on oxygen-covered Pt(111) and W(111) as studied using field ion appearance energy spectroscopy. Ultramicroscopy 73:139
39. Suchorski Y, Medvedev VK, Block JH (1996) Noble-gas-like mechanism of localized field ionization of nitrogen as detected by field ion appearance energy spectroscopy. Appl Surf Sci 94/95:217
40. Medvedev VK, Suchorski Y, Voss C, Visart de Bocarme T, Bar T, Kruse N (1998) Oxygen-induced reconstruction and surface oxidation of rhodium. Langmuir 14:6151
41. Müller EW (1941) Abreißen adsorbierter Ionen durch hohe elektrische Feldstärken. Naturwissenschaften 29:533
42. Walko RJ, Müller EW (1972) Self-imaging of a surface by field desorption. Phys Stat Sol A9:K9
43. Waugh AR, Boyes ED, Southon MJ (1976) Investigations of field evaporation with a field-desorption microscope. Surf Sci 61:109
44. Medvedev VK, Suchorski Y, Block JH (1994) Lithium field desorption microscope: a new tool for surface investigations. Ultramicroscopy 53:27
45. Medvedev VK, Suchorski Y, Block JH (1994) Investigations of the CO-oxidation on Pt with lithium field desorption microscopy. Appl Surf Sci 76/77:136

46. Medvedev VK, Suchorski Y, Block JH (1995) Non-linear dynamics of CO oxidation reaction on Pt and Rh as studied with the lithium field desorption microscope. Vacuum 46:563
47. Medvedev VK, Suchorski Y, Block JH (1996) Li-mediated feedback mechanism of oscillations in CO oxidation on a Rh field emitter tip. Appl Surf Sci 94/95:200
48. Medvedev VK, Suchorski Y, Block JH (1995) Investigation of adsorption and coadsorption of O_2 and CO on Rh by O_2^+ field ion and Li^+ field desorption microscopies. Appl Surf Sci 87/88:159
49. Miller M (2000) Atom probe tomography: analysis at the atomic level. Kluwer/Plenum, New York
50. Bunton J, Lenz D, Olson J, Thompson K, Ulfig R, Larson D, Kelly T (2006) Instrumentation developments in atom probe tomography: applications in semiconductor research. Microsc Microanal 12:1730
51. Suchorski Y, Drachsel W (2011) Field ion microscopy (FIM) and atom probe (AP). In: Friedbacher G, Bubert H (eds) Surface and thin film analysis. Wiley-VCH, Weinheim
52. Larson DJ, Prosa TJ, Ulfig RM, Geiser BP, Kelly TF (2013) Local electrode atom probe tomography. Springer, New York, p 344
53. Müller EW, Bahadur K (1956) Field ionization of gases at a metal surface and the resolution of the field ion microscope. Phys Rev 102:624
54. Block JH, Chanderna AW (1975) Field ionization at surfaces investigated by mass spectrometry. In: Chanderna AW (ed) Methods and phenomena, vol 1. Elsevier, Amsterdam, p 379
55. Tsong TT, Block JH, Nagasaka M, Viswanathan B (1976) Photon stimulated field ionization. J Chem Phys 65:2469
56. Goldenfeld IV, Korostyshewsky IZ, Mischanchuk BG (1974) Analysis of field ion energies in a mass spectrometer. Int J Mass Spectrom Ion Phys 13:297
57. Forbes RG (1976) A generalised theory of standard field ion appearance energies. Surf Sci 61:221
58. Schmidt WA, Suchorski Y, Block JH, Kreuzer HJ, Wang RLC (1995) Field ion appearance energy spectroscopy of CO^+ originated from Rh(111) and Au(111) surface step sites. Surf Sci 326:243
59. Suchorski Y, Medvedev VK, Block JH, Wang RL, Kreuzer HJ (1996) Field desorption of lithium. Phys Rev B 53:4109
60. Schmidt WA, Ernst N (1994) On the binding strength of surface metal atoms in a high electric field–face-specific appearance energy measurements of field evaporated rhodium ions. Vacuum 45:255
61. Ehrlich G (1966) Atomic displacements in one- and two-dimensional diffusion. J Chem Phys 44:1050
62. Barth JV (2000) Transport of adsorbates at metal surfaces: from thermal migration to hot precursors. Surf Sci Rep 40:75
63. Hwang IS, Ho MS, Tsong TT (2001) Scanning tunneling microscope study of dynamic phenomena on clean Si(111) surfaces: Si magic clusters and their role. J Phys Chem Solids 62:1655
64. Tsong TT (1973) Field-ion microscope observations of indirect interaction between adatoms on metal surfaces. Phys Rev Lett 31:1207
65. Fink H-W, Faulian K, Bauer E (1980) Evidence for nonmonotonic long-range interactions between adsorbed atoms. Phys Rev Lett 44:1008
66. Watanabe F, Ehrlich G (1991) Direct observations of pair interactions on a metal: heteropairs on W(110). J Chem Phys 95:6075
67. Braun OM, Medvedev VK (1989) Interaction between particles adsorbed on metal surfaces. Sov Phys Usp 32:328
68. Tsong TT, Kellog GL (1975) Direct observation of the directional walk of single adatoms and the adatom polarizability. Phys Rev B 12:1343
69. Tsong TT (2006) Fifty years of seeing atoms. Phys Today 59:31, and references therein

70. Eigler DM, Schweizer EK (1990) Positioning single atoms with a scanning tunnelling microscope. Nature 344:524
71. Ertl G (2008) Non-linear dynamics: oscillatory kinetics and spatio-temporal pattern formation. In: Ertl G, Knözinger H, Schüth F, Weitkamp J (eds) Handbook of heterogeneous catalysis, vol 8, 2nd edn. Wiley-VCH, Weinheim, pp 1492–1516
72. Ertl G (2002) Spiers memorial lecture. Dynamics of surface reactions. Farad Discuss 121:1
73. Ertl G (2008) Reactions at surfaces: from atoms to complexity (nobel lecture). Angew Chem Int Ed 47:3524–3535
74. Suchorski Y, Imbihl R, Medvedev VK (1998) Compatibility of field emitter studies of oscillating surface reactions with single crystal measurements: catalytic CO oxidation on Pt. Surf Sci 401:392
75. Gorodetskii V, Lauterbach J, Rotermund HH, Block JH, Ertl G(1994) Coupling between adjacent crystal planes in heterogeneous catalysis by propagating reaction-diffusion waves. Nature 370:276
76. Suchorski Y, Beben J, James EW, Evans JW, Imbihl R (1999) Fluctuation-induced transitions in a bistable surface reaction: catalytic CO oxidation on a Pt field emitter tip. Phys Rev Lett 82:1907
77. Suchorski Y, Beben J, Imbihl R (1998) Fluctuations during catalytic CO oxidation on different crystal planes of a Pt field emitter. Progr Surf Sci 59:343
78. Kreuzer HJ, Wang RLC (1997) Resonant field ionization: a new imaging mechanism in the field ion microscope. Z Phys Chem 202:127
79. Eiswirth M, Möller P, Wetzel K, Imbihl R, Ertl G (1989) Mechanisms of spatial self-organization in isothermal kinetic oscillations during the catalytic CO oxidation on Pt single crystal surfaces. J Chem Phys 90:510
80. Moldenhauer S (1996) In situ FTIR Spektroskopie der katalytischen CO Oxidation auf Platinmetallen. PhD thesis, Freie Universität, Berlin
81. McEwen J-S, Gaspard P, Visart De Bocarme T, Kruse N (2009) Oscillations and bistability in the catalytic formation of water on rhodium in high electric fields. J Phys Chem C 113:17045
82. Visart De Bocarme T, Beketov G, Kruse N (2004) Water formation from O_2 and H_2 on Rh tips: studies by field ion microscopy and pulsed field desorption mass spectrometry. Surf Interface Anal 36:522
83. McEwen J-S, Gaspard P, De Decker Y, Barroo C, Visart De Bocarme T, Kruse N (2010) Catalytic reduction of NO_2 with hydrogen on Pt field emitter tips: kinetic instabilities on the nanoscale. Langmuir 26:16381
84. Chau T-D, Visart De Bocarme T, Kruse N (2004) Kinetic instabilities in the NO/H_2 reaction on platinum. Surf Interface Anal 36:528
85. Visart de Bocarme T, Kruse N (2011) Field emission techniques for studying surface reactions: applying them to NO–H_2 interaction with Pd tips. Ultramicroscopy 111:376
86. McEwen J-S, Garcia Cantu Ros A, Gaspard P, Visart de Bocarme T, Kruse N (2010) Non-equilibrium surface pattern formation during catalytic reactions with nanoscale resolution: investigations of the electric field influence. Catal Today 154:75
87. Chau TD, Visart de Bocarme T, Kruse N (2004) Formation of N_2O and $(NO)_2$ during NO adsorption on Au 3D crystals. Cat Lett 98:85
88. Bagot PAJ, Visart de Bocarme T, Cerezo A, Smith GDW (2006) 3D atom probe study of gas adsorption and reaction on alloy catalyst surfaces I: instrumentation. Surf Sci 600:3028
89. Bagot PAJ, Cerezo A, Smith GDW (2007) 3D atom probe study of gas adsorption and reaction on alloy catalyst surfaces II: results on Pt and Pt–Rh. Surf Sci 601:2245
90. Bagot PAJ, Kreuzer HJ, Cerezo A, Smith GDW (2011) A model for oxidation-driven surface segregation and transport on Pt-alloys studied by atom probe tomography. Surf Sci 605:1544
91. Horsthemke W, Lefever R (1983) Noise-induced transitions: theory and applications in physics, chemistry, and biology. Springer series in synergetics, vol 15, 1st edn

92. Suchorski Y, Beben J (2003) Surface diffusion by adsorbate density fluctuation measurements. Prog Surf Sci 74:3
93. Suchorski Y, Beben J, Weiss H (2004) Noise-induced transitions in CO oxidation on Pt: Haar-Wavelet analysis. In: Aumayr F, Varga P (eds) Symposium on surface science 3S'04. St. Christoph am Arlberg, Austria, Contributions, p 145
94. Suchorski Y, Beben J, Imbihl R, James EW, Liu D-J, Evans JW (2001) Fluctuations and critical phenomena in catalytic CO oxidation on nanoscale Pt facets. Phys Rev B 63:165417
95. Johánek V, Laurin M, Grant AW, Kasemo B, Henry CR, Libuda J (2004) Fluctuations and Bistabilities on Catalyst Nanoparticles. Science 304:1639
96. Onsager L (1931) Reciprocal relations in irreversible processes. II. Phys Rev 38:2265
97. Kleint C, Gasse H-J (1960) Schrot und Funkelrauschen bei kalter Elektronen-Emission. Z Naturfor 15a:87
98. Gomer R (1973) Current fluctuations from small regions of adsorbate covered field emitters: a method for determining diffusion coefficients on single crystal planes. Surf Sci 38:373
99. Beben J, Kleint C, Meclewski R (1989) Improved adsorbate fluctuation measurements and their explanation by different diffusion mechanisms: I. Arguments in favour of single adatoms surface diffusion. Surf Sci 213:438
100. Suchorski Y, Beben J, Frac A, Medvedev V, Weiss H (2007) The mobility of an alkali promoter as probed in situ during a catalytic reaction: Li in the CO oxidation on Pt. Surf Interface Anal 39:161
101. Suchorski Y, Drachsel W, Gorodetskii VV, Medvedev VK, Weiss H (2006) Lifted reconstruction as a feedback mechanism in the oscillating CO oxidation on Pt nanofacets: microscopic evidences. Surf Sci 600:1579
102. Suchorski Y, Beben J, Medvedev VK, Block JH (1996) Study of CO surface diffusion on CO/W(111) by analysis of CO^+ field ion rate fluctuations. Appl Surf Sci 94/95:207
103. Suchorski Y, Beben J, Imbihl R (1998) Surface diffusion measurements from digitized FEM images: analysis of local brightness fluctuations. Ultramicroscopy 73:67
104. Medvedev VK, Suchorski Y, Visart de Bocarme T, Bar T, Kruse N (1999) FIM studies of clean and graphitized rhodium using lithium and oxygen as imaging species. Ultramicroscopy 79:239
105. Ingram MG, Gomer R (1954) Mass spectrometric analysis of ions from the field microscope. J Chem Phys 22:1279
106. Ingram MG, Gomer R (1955) Massenspektrometrische Untersuchungen der Feldemission positiver Ionen. Z Naturforsch A 10:863
107. Beckey HD (1971) Field ionization mass spectrometry. Regamon Press, Oxford
108. Müller EW (1975) Atom-probe field ion microscopy. In: Chanderna AW (ed) Methods of surface analysis, vol 1. Elsevier, Amsterdam, p 329
109. Kelly TF, Larson DJ (2012) Atom probe tomography 2012. Annu Rev Mater Res 42:1
110. Kelly TF, Larson DJ (2000) Local electrode atom probes. Mater Charact 44:59
111. Suchorski Y, Medvedev V, Block J (1995) Absolute appearance energy of Li^+ ions field-desorbed from W(111). Phys Rev B 51:4734
112. Suchorski Y, Hupalo M (2011) Coadsorption of lithium and oxygen on W(1 1 2): nanosized facets versus single crystals. Ultramicroscopy 111:381
113. Suchorski Y, Wrobel R, Becker S, Weiss H (2008) CO oxidation on a CeOx/Pt(111) inverse model catalyst surface: catalytic promotion and tuning of kinetic phase diagrams. J Phys Chem C 112:20012
114. Sieben B, Suchorski Y, Bozdech G, Ernst N (1997) Interaction of CO and O_2 with Pt studied by field ion appearance energy spectroscopy. Z Phys Chem 202:103
115. Suchorski Y, Drachsel W, Rupprechter G (2009) High-field versus high-pressure: weakly adsorbed CO species on Pt(111). Ultramicroscopy 109:430
116. Gomer R (1990) Diffusion of adsorbates on metal surfaces. Rep Prog Phys 53:917, and references therein

117. Dean KA, Chalamala BR (2003) Experimental studies of the cap structure of single-walled carbon nanotubes. J Vac Sci Technol B 21:868
118. Saito Y, Hamaguchi K, Hata K, Uchida K, Tasaka Y, Ikazaki F, Yumura M, Kasuya A, Nishina Y (1997) Conical beams from open nanotubes. Nature 389:554
119. Saito Y, Uemura S (2000) Field emission from carbon nanotubes and its application to electron sources. Carbon 38:169
120. Bonard J, Salvetat J, Stockli T, de Heer WA, Forro L, Chatelain A (1998) Field emission from single-wall carbon nanotube films. Appl Phys Lett 73:918
121. Wang QH Corrigan TD, Dai JY, Chang RPH and Krauss AR (1997) Field emission from nanotube bundle emitters at low fields. Appl Phys Lett 70:3308
122. Schmid H, Fink H-W (1997) Carbon nanotubes are coherent electron sources. Appl Phys Lett 70:2679
123. Choi WB, Chung DS, Kang JH, Kim HY, Jin YW, Han IT, Lee YH, Jun JE, Lee NS, Park GS, Kim JM (1999) Fully sealed, high-brightness carbon-nanotube field-emission display. Appl Phys Lett 75:3129
124. Hata K, Ariff M, Tohji K, Saito Y (1999) Selective formation of C_{20} cluster ions by field evaporation from carbon nanotubes. Chem Phys Lett 308:343
125. Saito Y, Hata K, Takakura A, Yotani J, Uemura S (2002) Field emission of carbon nanotubes and its application as electron sources of ultra-high luminance light-source devices. Phys B 323:30
126. Suchorski Y, Schmidt W, Block J (1994) Local electric fields above individual surface atoms in the presence of field-adsorbed rare gas atoms: an additional field enhancement. Appl Surf Sci 76/77:101
127. Ksenofontov VA, Gurin VA, Gurin IV, Kolosenko VV, Mikhailovskij IM, Sadanov EV, Mazilova TI, Velikodnaya OA (2007) Low-temperature field ion microscopy of carbon nanotubes. Low Temp Phys 33:858
128. Carroll DL, Redlich P, Ajayan PM, Charlier JC, Blase X, DeVita A, Car R (1997) Electronic structure and localized states at carbon nanotube tips. Phys Rev Lett 78:2811
129. Kim P, Odom TW, Huang J-L, Lieber CM (1999) Electronic density of states of atomically resolved single-walled carbon nanotubes: Van Hove singularities and end states. Phys Rev Lett 82:1225
130. Han S, Ihm J (2000) Role of the localized states in field emission of carbon nanotubes. Phys Rev B 61:9986
131. Kuzumaki T, Takamura Y, Ichinose H, Horike Y (2001) Structural change at the carbon-nanotube tip by field emission. Appl Phys Lett 78:3699
132. Ehrlich G, Hudda FG (1966) Atomic view of surface self-diffusion: tungsten on tungsten. J Chem Phys 44:1039
133. Tsong TT (1972) Direct observation of interactions between individual atoms on tungsten surfaces. Phys Rev B 6:417
134. Knorr N, Brune H, Epple M, Hirstein A, Schneider MA, Kern K (2002) Long-range adsorbate interactions mediated by a two-dimensional electron gas. Phys Rev B 65:115420
135. Fichthorn KA, Scheffler M (2000) Island nucleation in thin-film epitaxy: a first-principles investigation. Phys Rev Lett 84:5371
136. Tsong TT (2007) Field ion microscopy and beyond in some aspects of surface and nanoscience applications. Surf Interface Anal 39:111, and references therein
137. Gorodetskii VV, Elokhin VI, Bakker JW, Nieuwenhuys BE (2005) Field electron and field ion microscopy studies of chemical wave propagation in oscillatory reactions on platinum group metals. Catal Today 105:183
138. Kruse N, Visart de Bocarme T (2008) Heterogeneous catalysis in high electric fields. In: Ertl G, Knözinger H, Schüth F, Weitkamp J (eds) Handbook of heterogeneous catalysis, 2nd edn. Wiley-VCH, Weinheim, p 870
139. Kreuzer HJ (2004) Physics and chemistry in high electric fields. Surf Interface Anal. 36:372

140. Karahka M, Kreuzer HJ (2013) Field evaporation of oxides: a theoretical study. Ultramicroscopy 132:54
141. Mazumder B, Vella A, Deconihout B, Al-Kassab T (2011) Evaporation mechanisms of MgO in laser assisted atom probe tomography. Ultramicroscopy 111:571
142. Tsong TT, Muller EW (1967) Evaporation mechanisms of MgO in laser assisted atom probe tomography. Appl Phys Lett 9:7
143. Schmid M, Stadler H, Varga P (1993) Direct observation of surface chemical order by scanning tunneling microscopy. Phys Rev Lett 70:1441
144. Suchorski Y, Schmidt WA, Block JH (1993) Local electric fields above individual surface atoms in the presence of field-adsorbed rare gas atoms: an additional field enhancement. In: Okuyama F, Yamamoto M (eds) 40th field emission symposium, Nagoja, p 26
145. Zhao CX, Li YF, Chen J, Deng SZ, Xu NS (2013) Tunable field emission characteristics of ZnO nanowires coated with varied thickness of lanthanum boride thin films. Ultramicroscopy 132:36
146. O'Donnell KM, Fahy A, Barr M, Allison W, Dastoor PC (2012) Field ionization detection of helium using a planar array of carbon nanotubes. Phys Rev B 85:113404
147. Holst B, Allison W (1997) An atom-focusing mirror. Nature 390:244
148. Holst B, Piskur J, Kostrobiy PP, Markovych BM, Suchorski Y (2009) Field ionization of helium in a supersonic beam: kinetic energy of neutral atoms and probability of their field ionization. Ultramicroscopy 109:413
149. Welker J, Giessibl FJ (2012) Revealing the angular symmetry of chemical bonds by atomic force microscopy. Science 336:444
150. Fink HW (1986) Point source for electrons and ions. IBM J Res Develop 30:460
151. Paul W, Miyahara Y, Grütter P (2012) Implementation of atomically defined field ion microscopy tips in scanning probe microscopy. Nanotechnology 23:335702

Noncontact Atomic Force Microscopy for Atomic-Scale Characterization of Material Surfaces

8

Mehmet Z. Baykara

Contents

1 Definition of the Topic 274
2 Overview 274
3 Introduction 275
4 Experimental and Instrumental Methodology 278
5 Key Research Findings 282
5.1 Atomic-Resolution Imaging 282
5.2 Atomic-Resolution Force Spectroscopy 290
6 Conclusions and Outlook 303
References 304

Abstract

Among the large variety of scanning probe microscopy techniques, noncontact atomic force microscopy (NC-AFM) stands out with its capability of atomic-resolution imaging and spectroscopy measurements on conducting, semiconducting as well as insulating sample surfaces. In this chapter, we review the fundamental experimental and instrumental methodology associated with the technique and present key results obtained on different classes of material surfaces. In addition to atomic-resolution imaging, the use of NC-AFM towards the goal of atomic-resolution force spectroscopy is emphasized.

Keywords

Atomic Force Microscopy • Atomic Force Spectroscopy

M.Z. Baykara (✉)
Department of Mechanical Engineering and UNAM – Institute of Materials Science and Nanotechnology, Bilkent University, Ankara, Turkey
e-mail: mehmet.baykara@bilkent.edu.tr

© Springer-Verlag Berlin Heidelberg 2015

C.S.S.R. Kumar (ed.), *Surface Science Tools for Nanomaterials Characterization*,
DOI 10.1007/978-3-662-44551-8_8

1 Definition of the Topic

Since its invention in 1994, noncontact atomic force microscopy (NC-AFM) is routinely being used to image a multitude of material surfaces with atomic resolution. In this chapter, we review the fundamental experimental and instrumental methodology associated with the technique, as well as key results obtained on different classes of material surfaces in the last two decades. In addition to atomic-resolution imaging, the use of NC-AFM towards the goal of atomic-resolution force spectroscopy is also emphasized.

2 Overview

Scanning probe microscopy (SPM) techniques based on the detection of various types of interactions experienced by a sharp probe tip in the vicinity of a sample surface have been used with great success towards high-resolution imaging and measurement of various physical properties since the 1980s. Today, with a large number of manifestations tailored towards different applications, atomic force microscopy (AFM) is one of the most widely used SPM techniques in research and industrial laboratories around the world.

Due to the fact that traditional AFM experiments rely on a *light* contact of the probe tip with the sample surface to detect nanometer-scale topographical features, the interactions of the tip apex with the sample surface are averaged over a finite area, preventing true atomic-resolution imaging. In order to obtain true atomic-resolution imaging on a multitude of material surfaces using an AFM-based approach, the method of noncontact atomic force microscopy (NC-AFM) has been developed. The NC-AFM technique, based on the detection of minor changes in the resonance frequency of an oscillating cantilever due to force interactions between the tip apex atoms and the atoms of the sample surface, does not result in the formation of a finite contact so that experiments can be performed using atomically sharp probe tips. Thus, utilizing NC-AFM, it is possible to image material surfaces with true atomic-resolution *without the formation of a contact* provided that sufficiently sharp probe tips are utilized in conjunction with appropriate experimental procedures.

In addition to its capability of atomic-resolution imaging, NC-AFM has also been employed successfully to perform force spectroscopy (i.e., measure the interaction force acting between the probe tip and the sample surface as a function of tip-sample distance) on well-defined atomic sites on a number of relevant surfaces. Combined with its capability of atomic-resolution imaging, the capability of performing atomic-scale force spectroscopy makes NC-AFM a very powerful tool for the physical and chemical characterization of scientifically and technologically relevant material surfaces for diverse fields of research such as catalysis, adhesion and friction, among others.

Here we provide an introduction to the method of noncontact atomic force microscopy, briefly review the associated experimental and instrumental fundamentals, and report key results in atomic-resolution imaging and force spectroscopy

obtained with the method in the past. Being a subject of continuing research and development, NC-AFM will certainly be used towards a number of different scientific goals in the near future. As such, we will conclude the chapter with a brief outlook regarding future perspectives.

3 Introduction

Despite the fact that properties of solids are largely determined by their atomic structure as well as the associated interatomic interactions has been known for a long time, imaging the atomic structure of material surfaces in real space was first made possible by the relatively recent invention of the scanning tunneling microscope (STM) in the early 1980s by G. Binnig and colleagues [1, 2]. Due to its basic operational principle, which essentially relies on the *quantum tunneling* effect involving the flow of electrons over a vacuum gap between the material surface and a sharp metal probe tip in its vicinity, STM has been extensively used since its invention to image a large number of material surfaces with atomic resolution and measure their electronic properties [3]. Even though a new era in surface science has effectively been started with the introduction of the STM method, due to its fundamental working principle, the technique can only be utilized towards the investigation of conducting and semiconducting surfaces. As such, atomic-scale investigation of insulating material surfaces – such as the majority of metal oxides, a large number of which are scientifically and technologically very relevant – has not been realized with STM. Moreover, STM effectively probes the electronic density of states at the Fermi level associated with the material surface under investigation and therefore, a detailed investigation of various interatomic forces acting between the probe tip and the sample surface is not possible using the technique.

In order to overcome the limitations regarding sample conductivity in STM and the inability of the technique to measure interaction forces, an alternative scanning probe microscopy [4] method – atomic force microscopy (AFM) – has been introduced by Binnig and colleagues at Stanford in 1986 [5]. The operation of the traditional AFM method in the so-called contact mode is based on the controlled approach of a sharp probe tip attached to a micro-machined Si, SiO_2 or SiN cantilever [6–9] to the sample surface under investigation and the subsequent formation of a light contact (Fig. 8.1). While the tip apex is *lightly* touching the sample surface, the tip is raster-scanned in a precisely controlled fashion using piezoelectric scanners and topographic maps of the surface are obtained by detecting the deflection of the cantilever in the vertical direction using techniques such as laser beam deflection [10, 11] and interferometry [12, 13]. Using such an approach, nanoscale topographical maps of various kinds of surfaces have been successfully recorded [14, 15]. Additionally, by simultaneously detecting cantilever twisting around the longitudinal axis in addition to the deflection in the vertical direction, lateral forces experienced by the probe tip can be detected [16, 17], leading to a variation of the method known as *friction force microscopy* (FFM) useful for tribology studies performed on the nanoscale [18].

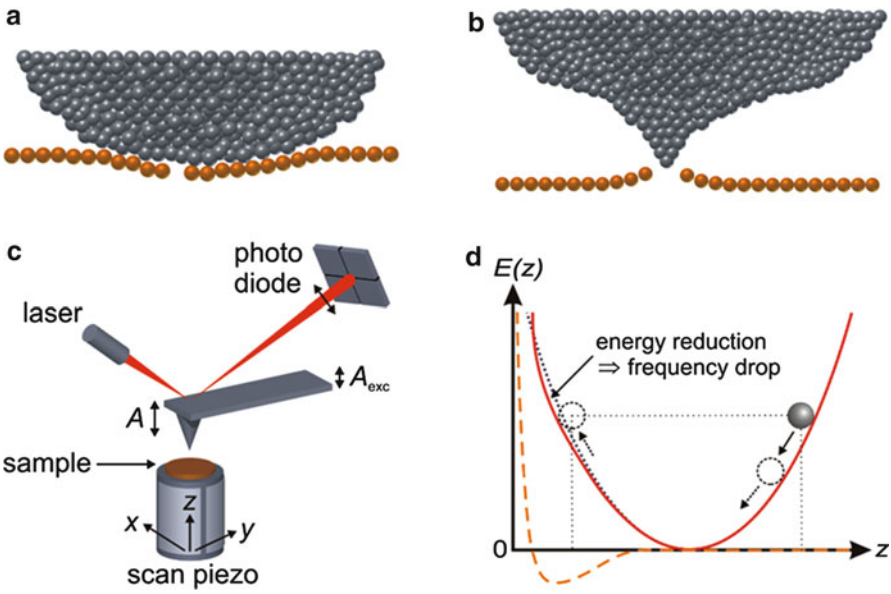


Fig. 8.1 (**a**) Model of an AFM tip in contact with the sample surface. Due to interaction averaging over the finite contact area, the single vacancy is not detected. (**b**) Model of an atomically sharp AFM tip in noncontact operation. Note that the attractive interaction is emphasized by the exaggerated relaxation of the surface around the defect. (**c**) Schematic setup of a typical AFM experiment. During dynamic operation, the cantilever base is excited with an amplitude A_{exc}, leading to an oscillation of the tip with amplitude A. Utilization of a laser source and a photo diode allow detection of cantilever motion whereas the sample is positioned under the tip via a piezoelectric tube (the *scan piezo*). (**d**) The physical origin of the frequency shift during NC-AFM operation is based on the modification of the harmonic oscillation potential of the tip (the *dotted blue line*) due to tip-sample interaction (the *dashed orange line*) at small tip-sample distances, leading to an overall reduction of oscillation frequency (as represented by the *red line*). The gray ball is used to represent the oscillatory motion of the tip based on symmetric (*dotted blue line*) and modified (*straight red line*) potentials (Figure reproduced from Ref. [22])

Despite the success of contact-mode AFM in imaging the nanoscale structure of a number of material surfaces [19], the technique naturally requires the formation of a permanent, albeit *light* contact between the probe tip apex and the sample surface comprising of tens to hundreds of atoms (Fig. 8.1a). Since an initially atomically sharp probe tip apex becomes considerably more blunt due to the formation of the contact, averaging of the force interactions occurring between the atoms of the probe apex and the sample surface over the contact area consequently prevents *true* atomic resolution imaging, leading to an inability to detect single atomic defects such as individual vacancies on the material surface. Instead, apparent atomic-scale images obtained in contact-mode AFM shortly after its introduction have been later understood to demonstrate only the lattice periodicity of the surface under investigation [20, 21].

In order to achieve true atomic resolution imaging using an AFM-based approach, a new *dynamic* operation mode has been introduced in 1995 [23–26]. As opposed to the *static* operation associated with contact-mode AFM, the micromachined cantilever to which the tip apex is attached is oscillated at its resonance frequency in the new, *noncontact AFM* mode (NC-AFM) [27–33]. In typical NC-AFM operation, the tip is brought into close proximity of the surface in the attractive interaction regime while the cantilever is oscillating and changes in the resonance frequency induced by atomic-scale force interactions between the probe apex and the sample surface are detected as the oscillation amplitude is kept constant using a feedback loop in the so-called *frequency-modulation* (FM) operation [34]. As actual contact with the surface is prevented, the tip apex remains atomically sharp (Fig. 8.1b) and site-specific variations in frequency shift detected during precise raster-scanning over the sample surface result in the acquisition of true atomic-resolution maps reflecting the structure of the surface. Since its first successful application for atomic-resolution imaging in 1995 [23–26], the method of NC-AFM has delivered atomically resolved maps of a large number of surfaces, including semiconductors [35–46], metals [47–50], and insulators [51–60]. Moreover, in recent years, well-defined functionalization of the probe tip apex with adsorbed molecules such as CO and partial operation in the repulsive interaction regime have resulted in the acquisition of very high-resolution spatial maps on adsorbed organic molecules on surfaces so that individual atoms and bonds inside the molecules have been clearly observed [61–64].

Since NC-AFM directly utilizes the effect of chemical interactions acting between the probe tip and the sample surface on the oscillation characteristics of a micromachined cantilever to perform atomic-resolution imaging, it is natural to expect that the method can also be used towards the quantification of those interactions in terms of forces and energies. Unfortunately, despite the fact that the connection between frequency shifts (the main parameter relevant for NC-AFM imaging) and interaction forces and energies can be expressed mathematically, the associated calculations require acquisition of the frequency shift values from the point of interest above the surface all the way to a distance where the cantilever oscillation is unaffected by interactions with the surface [65–70]. As such, the determination of interaction forces and energies quantitatively above a given atomic site on the material surface starts with the recording of a frequency shift-distance curve in the vertical direction. Consequent conversion of the acquired frequency shift data mathematically into a force/energy curve using the above-mentioned methods thus forms the essence of force spectroscopy, which has been demonstrated in a number of studies in the past [71–77]. As a natural extension of the described technique, combination of a large number of spectroscopy curves acquired at different locations on a given sample surface into 2D and 3D maps of interaction forces and energies has been realized as well [78–87], thanks to advancements in instrumentation and acquisition methods [88].

In the following sections of the present chapter, an overview regarding experimental and instrumental methodology associated with the NC-AFM technique will

be provided, followed by a review of key research findings associated with atomic-resolution imaging of various material surfaces, as well as atomic-resolution force spectroscopy. The chapter will conclude with an outlook regarding potential directions for future NC-AFM research. While the NC-AFM community was initially small, it is growing with each passing year and as such, the number of reported results rapidly increases, as well. While an effort has been made to include a majority of published results regarding various aspects of NC-AFM research in this chapter, we apologize for any unintended omissions.

4 Experimental and Instrumental Methodology

Shortly after the introduction of the STM, it was apparent that interaction forces acting between the metallic probe tip apex and the sample surfaces under investigation led to certain distortions in acquired data [89]. As such, the possibility of detecting interaction forces between atoms at such small length scales has been investigated, resulting in the invention of the AFM [5]. As described in the previous section, it became ultimately apparent that AFM in its traditional manifestation of contact-mode was unable to achieve true atomic-resolution due to the finite contact area that forms between the probe apex and the sample surface, leading to the introduction of *dynamic* operation modes, where the cantilever is oscillated at or near its resonance frequency as opposed to static operation in the contact mode [29]. Dynamically operating an atomic force microscope can be accomplished in two different ways: amplitude modulation (AM) or frequency modulation (FM). AM-AFM – where the cantilever is oscillated with a fixed driving frequency near resonance and changes in its amplitude and phase characteristics based on changing tip-sample distance are used as the detection signal [90, 91] – has been mainly used in the literature towards the goal of nanometer-scale imaging in liquid and ambient conditions due to the relatively long timescales associated with the response of high quality factor (Q) cantilevers which are needed for atomic resolution imaging with low imaging noise [29, 92]. As opposed to AM-AFM, during FM-AFM operation the cantilever is oscillated at resonance (f_0) and the magnitude of the oscillation amplitude (A) is kept constant by the utilization of a feedback loop [34]. As the cantilever base is approached to the sample surface under investigation, the resonance frequency of the cantilever shifts to a new value f due to the interactions of the tip apex atoms with the atoms of the surface, and the associated shift in resonance frequency (referred to as *frequency shift*, $\Delta f = f - f_0$) is used as the main imaging signal. A second feedback loop is utilized to keep the frequency shift at a fixed value by changing the vertical position of the cantilever base accordingly while the surface is being raster-scanned by the probe tip with picometer resolution and so atomic-resolution topographical maps of any flat sample surface irrespective of electrical conductivity (as opposed to STM) can be obtained. As atomic-resolution NC-AFM studies have been almost exclusively performed in the FM mode in the literature (with the exception of a few cases [93]), the use of the term "NC-AFM" in the AFM community is usually taken to imply FM operation.

Interactions of the probe tip with the sample surface leading to the frequency shift can be classified as long-range and short-range. While electrostatic interactions occurring due to potential differences between the probe tip and the samples surface as well as the ubiquitous van der Waals interaction due to spontaneous fluctuations leading to dipoles act at long range and cause generally a diffuse background signal in NC-AFM images, the site-specific chemical interactions relevant for atomic-resolution imaging (usually described by empirical models such as those by Morse and Lennard-Jones) [94] are generally of short-range character [73, 77, 84]. It needs to pointed out that while atomic-resolution imaging with NC-AFM has been traditionally performed mainly in the attractive interaction regime [27], recently it has been demonstrated that partial operation in the repulsive regime with small amplitudes results in the acquisition of very high-resolution images on adsorbed organic molecules, revealing the intramolecular structure with unprecedented precision based on minute differences in site-specific Pauli repulsion forces [61, 95].

Mechanical properties of cantilevers employed in NC-AFM (spring constant k, resonance frequency f_0 and quality factor Q) affect oscillation characteristics and consequently, the acquired data. While in the initial manifestation of NC-AFM, cantilevers with relatively low stiffness values (few tens of N/m or less) have been employed with large oscillation amplitudes ($\sim$10 nm) to perform atomic resolution imaging [23, 47, 96, 97], the use of tuning forks with much higher stiffness ($\sim$2,000 N/m) in conjunction with lower oscillation amplitudes ($\sim$1 nm) in the so-called *q-Plus* mode has emerged as an exciting alternative [80, 84, 86, 98–101]. The main advantages associated with the use of tuning forks in NC-AFM experiments can be summarized as the ability to operate at low amplitudes without instabilities related to the *jump-to-contact* phenomenon due to increased stiffness, increased sensitivity to short range interaction forces due to reduced amplitudes [102], the ability to freely choose the tip material by utilizing cleaved or electrochemically etched thin metallic wires attached to one of the prongs, as well as the electrical detection of the oscillating signal based on the piezoelectric character of quartz, eliminating the need for optical detection equipment in the microscope [30].

As indicated in the previous section, one of the main strengths of NC-AFM is based on the fact that it can be utilized towards performing site-specific interaction force and energy spectroscopy on the material surface of interest [71–88]. The acquisition of individual curves of frequency shift versus tip-sample distance and the consequent conversion into force and energy follows established procedures. At this point, it should be indicated that various mathematical approaches have been put forward in the literature to describe the relation between frequency shifts measured in NC-AFM spectroscopy experiments as a function of tip-sample distance and the interaction forces that cause them [65–70]. While some of the methods used to calculate interaction forces from measured frequency shift data are valid only for relatively large amplitudes (>5 nm), the method of Sader and Jarvis is usually preferred due to the fact that it provides a good approximation for all amplitude regimes and that its solution is relatively easy to implement

computationally [68]. According to this approach, the interaction force F acting between the tip and sample in the vertical direction at a distance of z is given by

$$F(z) = 2k\int_{z}^{\infty}\left(1+\frac{\sqrt{A}}{8\sqrt{\pi(u-z)}}\right)\frac{\Delta f(u)}{f_0} - \frac{A^{3/2}}{\sqrt{2(u-z)}}\frac{d}{du}\left(\frac{\Delta f(u)}{f_0}\right)du$$

Once again, it should be pointed out that the calculation of the interaction force at a given tip-sample distance requires knowledge of all frequency shifts form the distance of interest all the way to a separation where tip-sample interactions are negligibly small, as seen from the mathematical expression above. After conversion to force F has been performed for a single spectroscopy curve, interaction energy values are simply obtained by numerically integrating the force data. Since short-range chemical forces are mainly thought to be responsible for atomic-resolution imaging and spectroscopy in NC-AFM experiments on reactive surfaces [103, 104], appropriate methods have been proposed to eliminate the contribution of long-range interactions from the experimentally measured total force [105, 106]. Accordingly, compensating for the contact potential difference between the tip and sample by the application of a bias voltage and subsequent subtraction from the total force interaction eliminates the long-range electrostatic force contribution. Moreover, the fitting of a Hamaker-type interaction model to the long-range part of measured force spectroscopy curves assuming a sphere-plane geometry (where the radius of the sphere represents the radius of curvature associated with the apex of the tip employed in the experiments) and subsequent subtraction from the total force interaction eliminates the effect of van der Waals interactions.

Based on the methods established in the literature regarding spectroscopic data acquisition and subsequent conversion into forces and energies, various approaches have been suggested and utilized for the acquisition of two/three-dimensional interaction force and energy data [88]: While the *curve-by-curve* acquisition method depends on recording multiple spectroscopy curves one by one and their subsequent combination into a single two/three-dimensional map, i.e., Refs. [78, 79, 87, 107–110] the *layer-by-layer* method involves the recording of several NC-AFM images with slow topography feedback at various semi-constant heights above the sample surface (Fig. 8.2) i.e., Refs. [84, 86, 87, 111, 112]. The individual layers of data can be then manually drift-corrected and combined into a single three-dimensional map of interaction forces or energies. While both techniques feature certain advantages and disadvantages, it should be stated that the *curve-by-curve* method necessitates the use atom-tracking/feedforward methods [113, 114] in order to collect drift-corrected data, while the layer-by-layer method allows post-acquisition drift correction, which is additionally facilitated at low temperatures [88].

As expected, atomic resolution imaging and force spectroscopy experiments performed using NC-AFM are readily affected by the structural and chemical

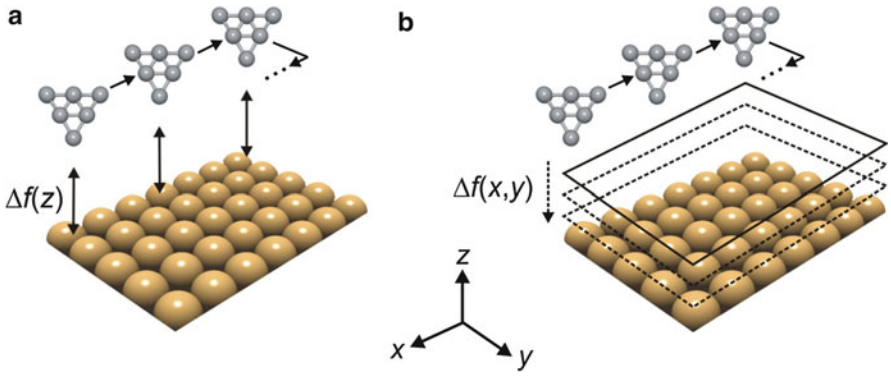


Fig. 8.2 Schematic illustrations describing acquisition procedures used to collect site-specific frequency shift data on material surfaces: While the *curve-by-curve* approach is based on the recording of individual $\Delta f(z)$ curves (**a**), separate NC-AFM images at semi-constant heights above the surface are collected in the *layer-by-layer* approach (**b**) (Figure reproduced from Ref. [88])

properties of the tip apices employed in the experiments [31, 61, 115–121]. While the effect of tip asymmetry and elasticity on NC-AFM experiments have been the subject of a few numerical studies in recent years [88, 122], more effort needs to be spent in this direction if a standardization of atomic-resolution imaging and especially spectroscopy experiments is to be achieved. An interesting experimental approach towards standardization of the chemical and structural properties have been realized through the adsorption of a well-defined single molecule such as CO on the tip apex, delivering several very promising results in terms of increased spatial resolution [61, 62, 123].

It should also be noted that atomic resolution imaging and spectroscopy experiments on material surfaces of interest using NC-AFM are significantly facilitated by the utilization of low temperatures (achieved by the use of liquid nitrogen or helium) and operation under ultrahigh vacuum (UHV) conditions [73, 124]. While operation at low temperatures delivers higher levels of stability with decreased thermal drift and piezo nonlinearity effects as well as improved quality factors leading to high signal-to-noise ratios, ultrahigh vacuum conditions ensure the atomic-scale cleanliness of the sample surface for long durations by dramatically reducing the number of adsorbed molecules on the sample surface [27]. Despite the advantages provided by low temperature operation under UHV for NC-AFM experiments, the development of methods such as atom tracking [113] in combination with the feedforward methodology [114] now allow virtually drift-free imaging and spectroscopy experiments at room temperature [87, 107, 108, 125]. Additionally, it should be stated that in recent years, the relatively small niche area of atomic-resolution experiments in UHV conditions has been expanded by successful demonstration of atomic-resolution imaging and spectroscopy under liquids as well as ambient conditions via major advances in instrumentation and methodology [126–133].

5 Key Research Findings

5.1 Atomic-Resolution Imaging

5.1.1 Semiconductor Surfaces

Due to their wide-spread use in the electronics industry, silicon and related semiconductor materials are of great scientific, technological and industrial importance. Therefore, it is only natural that the prototypical Si(111)-7×7 surface has been the focus of initial NC-AFM studies where atomic-resolution was demonstrated in 1995 under UHV conditions by the utilization of a frequency modulation approach [23, 25]. During the same year, research efforts by the group of S. Morita in Osaka University culminated in the atomic-resolution imaging of the InP(110) surface and the observation of point defect motion at room temperature [24, 26]. Following these spectacular results constituting a "proof-of-principle" for true atomic-resolution imaging via NC-AFM, multiple research groups have succeeded in obtaining atomic-resolution images of the Si(111)-7×7 surface using different microscope setups [134–136]. Despite the fact that the Si(111)-7×7 surface was one of the first to be imaged with atomic-resolution via NC-AFM and is nowadays frequently employed as a "test sample" to investigate the capabilities of custom-built and commercial instruments, several interesting results continue to be reported on this sample system, such as the observation of subsurface atoms [137] as well as differences in contrast formation mechanisms observed during combined NC-AFM/STM studies [138].

Another sample system based on the semiconducting Si(111) surface that has been characterized to a certain extent by NC-AFM experiments is the $Ag:Si(111)-\left(\sqrt{3}\times\sqrt{3}\right)R30^{o}$ surface obtained by deposition of Ag atoms on a Si(111) surface under UHV conditions and at elevated temperatures [40, 43, 46]. The atomic-scale investigations on this sample are motivated by a general interest in metal–semiconductor interfaces as well as the fact that the precise atomic structure of the surface has remained a matter of debate in the scientific community. Earlier investigations at room temperature have revealed that the atomic-scale contrast observed in NC-AFM experiments changes based on varying tip-sample distance and it was concluded that a so-called *honeycomb-chained-trimer* (HCT) model describes the surface structure satisfactorily [40, 46]. However, an extensive study of combined NC-AFM and STM experiments performed at variable temperatures have later revealed that the ground state surface structure is explained by an *inequivalent trimer* (IET) model at low temperatures and the appearance of a HCT-type structure at room temperature is due to a thermal averaging (fluctuation) effect [43]. Thus, the exciting potential of the NC-AFM method in atomic-scale structural characterization of semiconducting surfaces is clearly demonstrated.

Due to its importance for the electronics industry and micro-fabrication technologies, the Si(100) surface has also been targeted by NC-AFM measurements aimed at uncovering its atomic-scale structure in real space [35, 41, 44, 139–143].

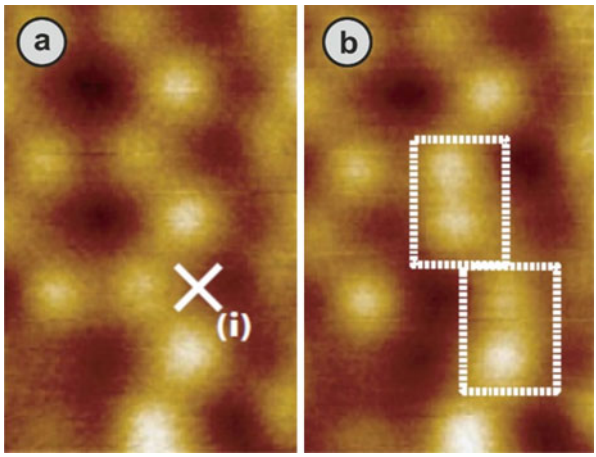


Fig. 8.3 NC-AFM images of the semiconducting Si(100) surface acquired at a temperature of 5 K. While atomic arrangement of the surface in the $c(4\times2)$ reconstruction is imaged in (**a**), controlled approach of the tip to the location indicated by (*i*) leads to *dimer flipping*, as indicated by the rectangles in (**b**) (Figure reproduced from Ref. [141]. Copyright (2011) by the American Physical Society)

While measurements performed at low temperatures have confirmed that the ground state of the surface is characterized by buckled Si dimers with tilted bonds leading to a $c(4\times2)$ reconstruction [139], thermal fluctuations between stable buckling positions for each dimer lead to an apparent $p(2\times1)$ surface structure at room temperature [35]. Even more interestingly, Li et al. have determined that tip-induced interaction forces at small tip-sample distances during NC-AFM imaging induce dimer flipping, leading to the occasional observation of a $p(2\times1)$ reconstruction during low temperature experiments [44]. Further, careful experiments by Sweetman et al. have culminated in the deliberate flipping of single dimers on the Si(100) surface at zero bias voltage and low temperatures by controlling the magnitude of the tip-sample interaction, essentially demonstrating pure mechanical toggling of an atomic scale switch (Fig. 8.3) [140, 141].

In order to evaluate the ability of NC-AFM to discriminate the chemical identity of multiple atomic species on a given surface, semiconductor alloy surfaces consisting of combinations of Si, Sn, In, Ge and Pb atoms have been investigated via imaging experiments [144–147]. The results remarkably show that the NC-AFM method is clearly able to distinguish one type of atom from the other by detecting differences in measured topographic height (Fig. 8.4). Evaluating the recorded images in conjunction with careful force spectroscopy measurements then allows the assignment of the detected height difference to atomic scale relaxations as well as differences in short-range interaction forces exhibited by each type of atom with the probe tip. Finally, by utilizing a combination of experimental results and ab initio calculations, a procedure for chemical identification of individual atoms regardless of the specifics of experimental parameters and tip apex properties has been introduced (for details, see Sect. 5.2.1; [77]).

Results related to atomic-resolution imaging of semiconductor surfaces are not limited to the examples discussed above. Indeed, excellent atomic-scale structural data has been presented on Ge(111) [39, 148] and Ge(001) [45], GaAs(110) [38], and InAs (110) [149]. Based on the discussion in this section, it is clearly seen that NC-AFM has

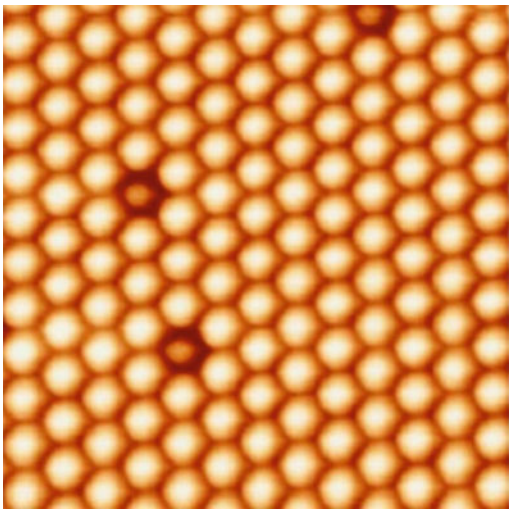


Fig. 8.4 Topographic NC-AFM image of a Sn/Si (111) alloy surface (8.5 nm^2 × 8.5 nm^2) where differences in the chemical identity of individual atoms lead to clear changes in image contrast (Figure reproduced from Ref. [147]. Copyright (2006) by the American Physical Society)

been established as a prominent tool for atomic-scale characterization of semiconductor surfaces. In the following sections, application of the NC-AFM method to other surfaces of scientific interest (metal oxides, ionic crystals, etc.) will be covered.

5.1.2 Metal Oxide Surfaces

Shortly after the first demonstration of the atomic-resolution capability of NC-AFM on the surface of Si(111)-7×7, efforts have been directed at resolving the atomic structure of surfaces associated with other materials. Of the different classes of materials that have been investigated with NC-AFM, metal oxides are of particular interest due to (a) their wide application in diverse fields such as electronics, heterogeneous catalysis and biomedical engineering and (b) the fact that most metal oxides of technological interest are electrical insulators and as such, the associated surfaces cannot be probed with ease using standard surface science techniques relying on the utilization of freely moving electrons [150]. Therefore, prior to the introduction of NC-AFM as a surface characterization tool with atomic-resolution imaging capability, experimental studies aimed at atomic-resolution imaging of metal oxide surfaces using STM have been closely restricted to partially reduced, semiconducting metal oxide samples (e.g., rutile TiO_2(110) [151]) and thin films on conducting substrates [152].

Based on growing scientific and technological interest in the surface structure and properties of metal oxides, NC-AFM has been utilized towards atomic-resolution imaging of surfaces associated with a number of insulating and semiconducting metal oxides (including thin oxide films) such as TiO_2 [96, 115, 118, 120, 121, 153–156], Al_2O_3 [52, 157–163], CeO_2 [57, 164–169], NiO [170–174], MgO [162, 175–177], ZnO [178], MoO_3 [179], and $MgAl_2O_4$ [59, 180, 181], as well as thin layers formed through oxidation of metal substrates [86, 182] in the past two decades. While an excellent and exhaustive review of the subject has been published previously [183], in

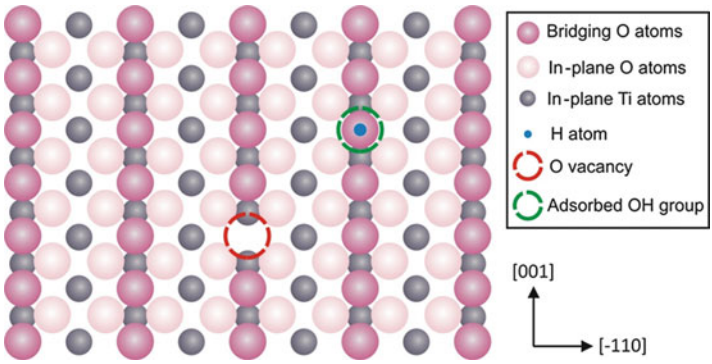


Fig. 8.5 Structural model of the rutile $TiO_2(110)$ surface with *regular* defects. In-plane oxygens are threefold coordinated, whereas bridging oxygens are twofold coordinated. Ti sites under the bridging oxygens are sixfold, and the exposed ones are fivefold coordinated

this chapter we will present the development of atomic-resolution imaging on metal oxide surfaces via NC-AFM with the example of rutile $TiO_2(110)$, which is by far the most widely studied metal oxide surface via a host of surface science techniques, in addition to being of high importance for photocatalysis applications [151, 184].

Even though the anatase form of TiO_2 is more relevant for practical catalysis applications, rutile $TiO_2(110)$ has been the focus of most NC-AFM imaging experiments due to the fact that its structure and the types of common defects encountered are very well known and have been well documented in the literature [151]. As shown in Fig. 8.5, the rutile $TiO_2(110)$ surface is composed of alternating rows of five and sixfold coordinated Ti^{4+} cations and threefold coordinated *in-plane* O^{2-} anions, as well as rows of *bridging* O^{2-} anions that are twofold coordinated. Whereas the bulk unit cell has a tetragonal structure with $a = b = 0.4584$ nm and $c = 0.2953$ nm [151], the distance between two rows of *bridging* O^{2-} anions or fivefold coordinated Ti^{4+} cations on the (110) face is 0.65 nm, while a monoatomic step is 0.325 nm high [185]. The types of defects which are commonly encountered on the rutile (110) surface after conventional UHV preparation (involving sputter/anneal cycles) include O vacancies on *bridging* O^{2-} rows, as well as OH groups forming on such vacancies due to H_2O dissociation a few hours after sample preparation, even under very good UHV conditions [121, 186].

While the contrast observed in typical STM images of $TiO_2(110)$ [185–188] has been well understood (bright stripes coinciding with rows of fivefold Ti^{4+} ions, and bright protrusions in between corresponding either to O vacancies or OH groups) [151]. NC-AFM images have shown a much larger variety of contrasts ever since the first atomic-resolution measurements have been performed on $TiO_2(110)$ using this technique [96]. The overall consensus in the literature so far is that there are three most common contrast types observed in NC-AFM measurements of $TiO_2(110)$ [120, 121]: (1) The *protrusion* mode, where Ti rows are imaged as bright stripes and O vacancies and OH groups are imaged as bright protrusions between the stripes. (2) The *hole* mode, where bridging O^{2-} rows are imaged as

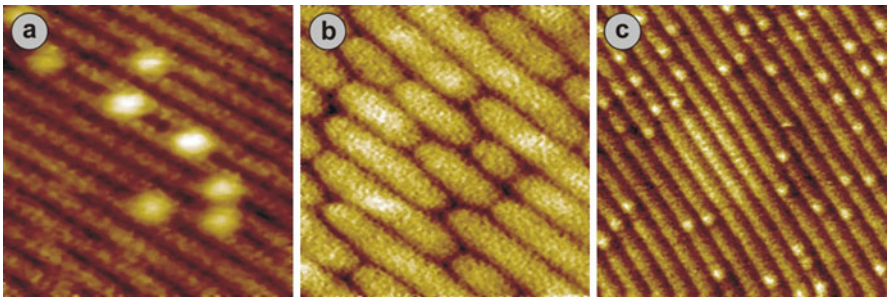


Fig. 8.6 The three common imaging modes that are frequently encountered in NC-AFM measurements: the *protrusion* (**a**), *hole* (**b**), and *neutral* (**c**) modes. In the protrusion mode, bright stripes coincide with fivefold Ti^{4+} sites on the surface and regular defects are imaged as protrusions between the stripes. For both hole and neutral modes, bright stripes coincide with bridging oxygen sites. Whereas the hole mode displays regular defects as depressions on bright stripes, the neutral mode resembles the *real* topography of the oxide surface (Figure reproduced from Ref. [121]. Copyright (2007) by the American Physical Society)

bright and O vacancies/OH groups as dark depressions on these rows. (3) The *neutral* mode where AFM images tend to reflect the real topography of the sample surface: In this imaging mode, bridging O^{2-} rows are imaged as bright stripes, OH groups as bright protrusions on top of these rows and O vacancies as dark depressions on the same rows. The extensive NC-AFM work performed in F. Besenbacher's group at Aarhus University in collaboration with DFT simulations has led to the conclusion that these contrast types can be generally explained by the different electronic *polarities* of the tip apices used in the experiments: [120, 121] (1) A negatively charged anion at the tip apex (e.g., O^{2-}) would interact more strongly with the positively charged Ti^{4+} ions on the surface due to local electrostatic interaction and produce images where rows of Ti^{4+} ions are imaged as bright stripes. Moreover, since O vacancies and OH groups might be thought of as electrostatically *less negative* than regular O^{2-} anions, they are imaged as bright protrusions on dark O^{2-} rows (*protrusion* mode). (2) Similarly, a positively charged cation at the tip apex (e.g. Ti^{4+}) would interact more strongly with the negatively charged O^{2-} ions on the surface due to electrostatic interaction and produce images where rows of O^{2-} ions are imaged as bright stripes, with O vacancies/OH groups as depressions on these rows due to weaker electrostatic attraction to the tip apex (the *hole* mode). (3) Lastly, a *neutral* tip apex (such as a pure Si tip that has not been pre-treated by light crashes with the TiO_2(110) surface, thus terminated by Si atoms), would interact mostly via covalent bonds with the surface atoms and produce images representing the true topography of the sample surface, as corroborated by DFT simulations (the *neutral* mode) [121, 189]. A comparison of all contrast modes discussed here for NC-AFM imaging is given in Fig. 8.6.

It should be noted here that a few additional NC-AFM studies performed by other research groups have revealed the existence of additional, more *exotic* imaging modes. Specifically, Yurtsever et al. have been able to observe bright rows of O^{2-} ions with no apparent OH groups that usually cover TiO_2(110) surfaces a few hours

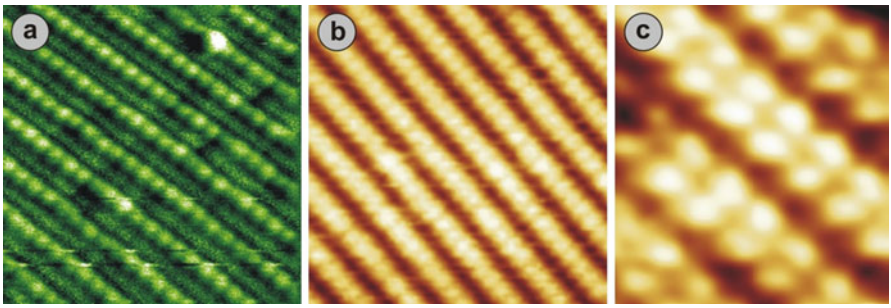


Fig. 8.7 A summary of the more *exotic* imaging modes associated with NC-AFM experiments on TiO_2(110). (**a**) The so-called *all-inclusive* mode where both bridging oxygens as well as fivefold Ti^{4+} sites are imaged as bright protrusions. (**b**) The *hidden* mode where adsorbed OH groups are not detected in NC-AFM images showing bright protrusions associated with bridging oxygen sites. (**c**) A rather rare NC-AFM image exhibiting in-plane oxygens as bright protrusions. ((**a**) reproduced from reference [118]. (**b**) and (**c**) reproduced from Ref. [155]. © IOP Publishing. Reproduced with permission. All rights reserved.)

after cleaning in UHV (the so-called *hidden* mode) [155]. Additional imaging modes observed in NC-AFM include the imaging of *in-plane* oxygens as bright protrusions [155], as well as an *all-inclusive* mode observed by Bechstein et al. [118], where both bridging O^{2-} as well as fivefold Ti^{4+} ions are imaged simultaneously as bright protrusions in NC-AFM. The all-inclusive imaging mode might be explained by the existence of a Si(100) tip with a dimer-like apex including an adsorbed O atom or OH group [116]. Regardless of the specific details associated with each of the experiments discussed in this paragraph, the results presented (and summarized in Fig. 8.7) lead to the conclusion that a simple electrostatic view of tip apices (positive, negative, or neutral) might not always be sufficient to explain all contrast types observed in NC-AFM imaging of metal oxide surfaces such as TiO_2(110). In fact, a combination of force spectroscopy experiments and ab initio simulations have been recently utilized to identify the tip apex structures responsible for commonly observed contrast modes on TiO_2(110), with the conclusion that flexible tip apices contaminated with clusters from the surface quantitatively explain the experimental imaging and spectroscopy results [156].

Finally, combined NC-AFM/STM studies have been performed on the TiO_2(110) surface to elucidate the role of the tip in contrast formation for both imaging channels [115]. Specifically, all three general modes of NC-AFM imaging (the protrusion, hole, and neutral modes) are observed in the AFM channel, with simultaneous STM images showing either *in-phase* (bright rows in AFM correspond with bright rows in STM) or *out-of-phase* character (bright rows in AFM correspond with dark rows in STM). Figure 8.8 can be consulted in order to compare the various contrasts that are obtainable in simultaneous AFM/STM imaging of TiO_2(110). Having such a variety of image contrasts available, identification of tip apices associated with each mode using DFT simulations requires considerable effort [190]. Additionally, simultaneous NC-AFM/STM

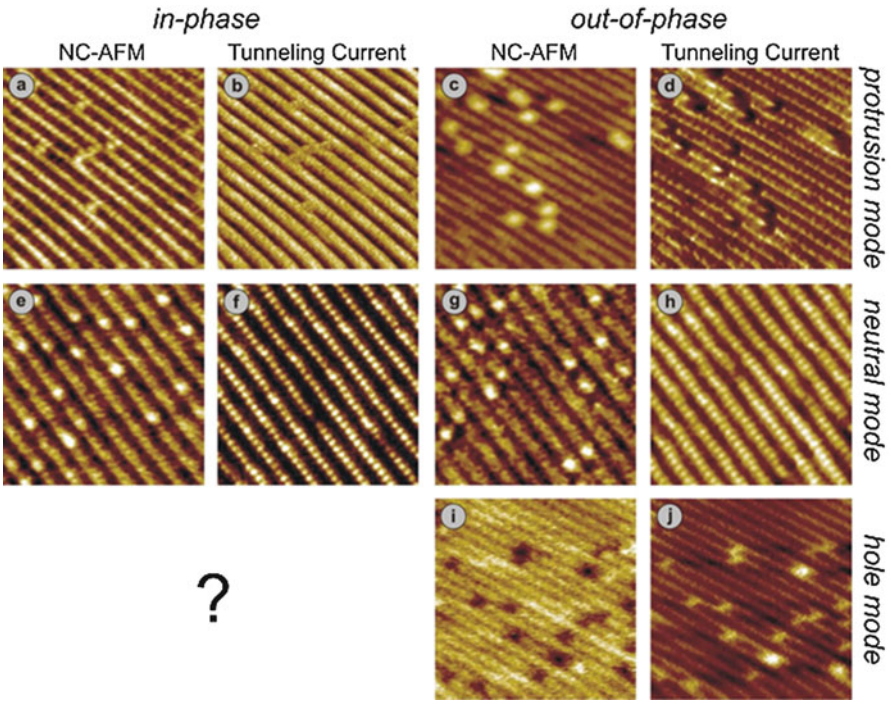


Fig. 8.8 Various imaging modes attainable in simultaneous NC-AFM/STM measurements on the TiO_2(110) surface. All combinations of the typical NC-AFM imaging modes (protrusion (**a**–**d**), hole (**i**–**j**), and neutral (**e**–**h**)) with in-phase and out-of-phase tunneling current imaging are attained in this study, except for the in-phase recording of tunneling current data for hole mode NC-AFM imaging (Figure reproduced from Ref. [115]. Copyright (2008) by the American Physical Society)

measurements have revealed the existence of a subsurface defect in the form of an interstitial H atom, which has a characteristic electronic signature in the STM channel, but is practically undetectable with AFM [154].

Overall, the key role that NC-AFM plays in atomic-resolution characterization of metal oxide surfaces is clearly demonstrated by the representative example of the rutile TiO_2(110) surface presented in this section, together with the significant effect of tip structure and chemistry on the experiments. Taking into account that metal oxide surfaces continue to be an integral component of technical development in a number of fields, it is natural to expect that in the near future, the application of NC-AFM imaging will spread to new metal oxides beyond the classic examples of TiO_2, Al_2O_3, CeO_2, NiO, etc. mentioned previously.

5.1.3 Ionic Crystal Surfaces

Another class of materials that have been studied in detail via NC-AFM imaging experiments are ionic crystals such as NaCl, KBr, and CaF_2 [53, 54, 60, 74, 111, 191–201]. The main interest in studying the atomic structure of ionic crystal surfaces is based on three factors: (i) Ease of sample preparation through simple

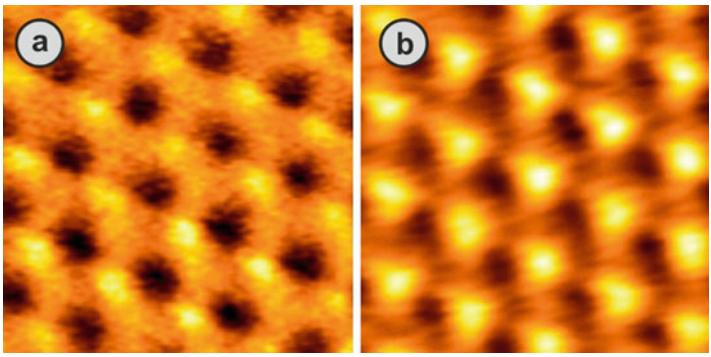


Fig. 8.9 Constant height NC-AFM images of the ionic $CaF_2(111)$ surface acquired with a tuning fork sensor in the *qPlus* configuration (1.36 nm × 1.36 nm). The image contrast reflects the frequency shift. While (**a**) has been acquired in the attractive interaction regime, (**b**) has been recorded in the repulsive regime, resulting in a reversal of contrast (Figure reproduced from Ref. [198]. © IOP Publishing. Reproduced with permission. All rights reserved.)

cleaving, (ii) the fact that the physical properties associated with their bulk structure have been studied for a very long time and (iii) the fact that they constitute model insulating substrate systems for the growth of metallic thin films as well as organic layers for molecular electronics.

Motivated by the mentioned factors, the first atomic resolution image of an ionic crystal surface (NaCl(001)) demonstrating the detection of point defects obtained via NC-AFM was published in 1997 [191]. NC-AFM work performed on fluoride surfaces such as $CaF_2(111)$ have later revealed the mobility of defects at room temperature and the alleviation of associated kinetics based on interaction with oxygen molecules leading to the formation of chemisorbed species, [53] as well as atomic-resolution imaging of step edges where individual ions and vacancies have been resolved [194]. Moreover, it was determined that the contrast exhibited by the imaged ions on $CaF_2(111)$ during NC-AFM experiments strongly depends on the polarity of the tip apex employed (which may spontaneously change during experiments by means of material transfer in the form of small clusters to or from the surface) by utilizing a combination of experimental results and theoretical calculations [54, 192]. The fundamental idea that contrast formation on ionic surfaces during NC-AFM experiments is dominated by atomic-scale variations in electrostatic interactions exhibited by the surface ions with the probe tip have been later supported by experimental studies aimed at imaging the $CaF_2(111)$ surface with well-characterized tip apices [119]. Finally, lateral manipulation of point defects on this sample surface were achieved via NC-AFM [197, 199] and individual surface ions were imaged using a tuning fork based detection scheme (Fig. 8.9; [198]).

Due to the fact that the cations and anions on binary ionic crystal surfaces (such as KBr and NaCl) are arranged in equivalent surface unit cells, their identification during NC-AFM imaging experiments via symmetry arguments is not possible and often considerable support from theoretical calculations is needed to achieve this goal. In order to overcome this difficulty, two main methods have been proposed where (i) the

ionic crystal is doped to a known ratio by a given impurity (such as Cl^- ions replacing a certain portion of Br^- ions in a KBr crystal) such that differences in topography between the two types of anions in NC-AFM images can be used to identify the type of ion imaged [196]. It is interesting to note that the two types of anions interact differently with the probe tip despite the fact that their formal charge states should be equivalent. Alternatively, (ii) the binary ionic crystal may be doped with divalent cations such that a new phase on the surface forms together with the introduction of point defects compensating for the charge imbalance caused by doping leading to facilitation of chemical identification of ions in NC-AFM images [202–204].

Aside from the surfaces obtained by cleaving of bulk ionic crystal samples, ultrathin films of alkali halides and fluorides grown on metal and semiconductor substrates have been targeted by atomic-resolution NC-AFM studies as well, primarily due to their potential applications in fields such as catalysis and molecular electronics [205–207]. Moreover, ultrathin films of alkali halides have been used as substrates for very high-resolution imaging of adsorbed organic molecules in studies conducted by tips functionalized with single molecules such as CO [61].

5.1.4 Other Material Surfaces and Adsorbed Molecules

In addition to semiconductors, metal oxides and ionic crystals, NC-AFM has been used to perform atomic-resolution imaging experiments on a number of other material surfaces. Examples include, but are not limited to: Surfaces of single crystal metal samples [47–50], highly oriented pyrolithic graphite (HOPG) [84, 97, 208–210], carbon nanotubes and associated metallofullerene peapods [83, 211], a film of Xe adsorbed on graphite [51], and more recently, thin films of silica (SiO_2) showing crystalline as well as vitreous structure grown on Ru(0001) substrates [212, 213], silicene grown on Ag(111) [214], and finally, graphene [215–218].

Despite the fact that the review presented in this chapter is mainly oriented towards NC-AFM based imaging and spectroscopy of bare material surfaces, the key role that the method has played in resolving the structural, physical and chemical details of single molecules and molecular layers adsorbed on various substrates should be emphasized. In addition to recent reports of unprecedented intramolecular resolution on single molecules achieved through deliberate functionalization of tip apices [61, 62, 64, 110], earlier efforts in this direction include the imaging of formate and acetate ions, terephthalic acid, perylene derivatives, C_{60}, Co-Salen, truxene, porphyrin derivatives, water, etc. adsorbed on various substrates [219–232]. As such, the potential of NC-AFM as a powerful characterization tool capable of resolving atomic-scale structural properties extends from various classes of bare material surfaces to individual molecules.

5.2 Atomic-Resolution Force Spectroscopy

5.2.1 Pioneering Studies in Atomic-Resolution Force Spectroscopy

Surfaces play a key role for a large number of scientifically and technologically relevant phenomena including friction, adhesion, corrosion, thin film growth and

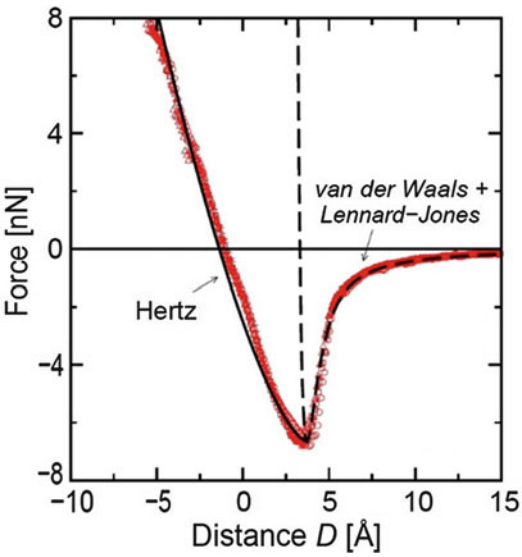


Fig. 8.10 A force spectroscopy curve obtained experimentally via the recording of frequency shift as a function of tip-sample distance using a Si tip on the HOPG surface at a temperature of 80 K. While the interaction up to the turning point is nicely approximated by the Hamaker-type van der Waals and the Lennard-Jones interaction models (*dashed line*), the interaction at closer separations obeys the Hertz contact law (*straight line*) (Figure reproduced from Ref. [71]. Copyright (2000) by the American Physical Society)

heterogeneous catalysis, among others. Considering that the interactions exhibited by atoms at the surfaces of various materials with other atoms, molecules or surfaces in their vicinity direct the physical laws that govern the processes mentioned above, the need for an experimental technique that would allow direct measurement of such interactions at atomic length scales arises. As mentioned earlier in this chapter, the method of NC-AFM, when utilized in conjunction with appropriate experimental equipment and protocols, allows to perform atomic-resolution force (and consequently, energy) spectroscopy in all three spatial dimensions above sample surfaces of interest. As such, we will review in this section key results that have been obtained with NC-AFM with regards to atomic-resolution force spectroscopy.

Shortly after the demonstration of atomic-resolution imaging on semiconductor surfaces using a frequency modulated NC-AFM approach [23–26], efforts have been directed by several research groups around the world to perform atomic-resolution force spectroscopy by measuring the tip-sample interaction force as a function of tip-sample distance above individual locations on sample surfaces [71–73, 233]. Specifically, an extensive analysis of force spectroscopy data obtained on HOPG at liquid nitrogen temperatures found good agreement between the experimental measurement and specific force laws (Hamaker-type van der Waals interaction law, Lennard-Jones type interaction law and Hertz-type contact law) (Fig. 8.10) [71]. Moreover, in a seminal work published in 2001, the scanning probe microscopy research group at University of Basel have succeeded in quantifying the short-range interaction forces associated with the onset a covalent bond between a Si tip and a Si(111)-7×7 surface using a low temperature atomic force microscope with high-stability, whereby minute differences in interactions between inequivalent atoms of the surface have also been detected [73].

The pioneering force spectroscopy experiments described above have been complemented by additional studies where force spectroscopy data obtained on different atomic sites on ionic crystal surfaces such as KBr(001), NaCl(001) and CaF_2(111) have been utilized in conjunction with ab initio simulation studies to (a) characterize in detail the structure and polarity of tip apices, (b) determine the identity of imaged ionic species, and (c) study the effects associated with atomic-scale relaxation and asymmetry of the tip apex utilized in the experiments [74, 200, 234, 235]. Moreover, the simultaneous recording of multiple data channels (such as frequency shift and tunneling current) during spectroscopy experiments have revealed varying distance dependence for the observed variables and allowed comparisons to be made regarding the physical mechanisms responsible for each [236]. In an interesting experiment, Sugimoto et al. have demonstrated that enhanced signal-to-noise ratio for frequency shift spectroscopy curves acquired at room temperature can be achieved by the use of higher flexural modes of cantilevers in conjunction with decreasing oscillation amplitudes [76]. Finally, in 2007, the goal of unambiguous chemical identification of individual atoms that form a material surface has been realized [77]: The authors, by utilizing a combination of a large number of force spectroscopy curves on alloy surfaces consisting of Si, Sn, In and Pb atoms and ab initio density functional theory calculations, have demonstrated that the largest force interactions always occur on Si atoms and the relative ratio of the maximum force interaction values between different types of atoms remains constant, despite the fact that absolute values of measured interactions do change considerably based on measurement parameters as well as chemical and structural properties of the tip apex (Fig. 8.11).

5.2.2 Three-Dimensional Force Spectroscopy with Atomic Resolution

As demonstrated by the experiments described above, the procedures for recording and processing frequency shift spectroscopy curves to obtain atomic-resolution force and energy data as a function of tip-sample distance on individual lattice sites has been well-established in the decade following the achievement of atomic-resolution imaging in NC-AFM. Consequently, the idea of combining thousands of such $\Delta f(z)$ curves to form three-dimensional data sets that allow recovering forces and energies as a function of position (x, y, z) above the sample surface seems straightforward. Performing this task with a sufficiently high number of $\Delta f(z)$ curves such that high-quality volumetric maps of interaction force and energy are obtained, is however a very challenging aim. Considering that acquiring a low-noise $\Delta f(z)$ curve takes typically about 5 s, collecting individual curves for each point on a data set consisting of 256 $\times$ 256 pixels laterally (a resolution common for NC-AFM images) should take about 90 h [237]. Due to the fact that most NC-AFM instruments operate at room temperature, thermal drift becomes an important issue, making it impossible to image the same area of the sample surface for such extended measurement times unless atom-tracking/feedforward techniques [113, 114] are employed (note that based on the microscope design and associated stability characteristics, even microscopes operating at low temperatures may feature levels of thermal drift that are not suitable for three-dimensional

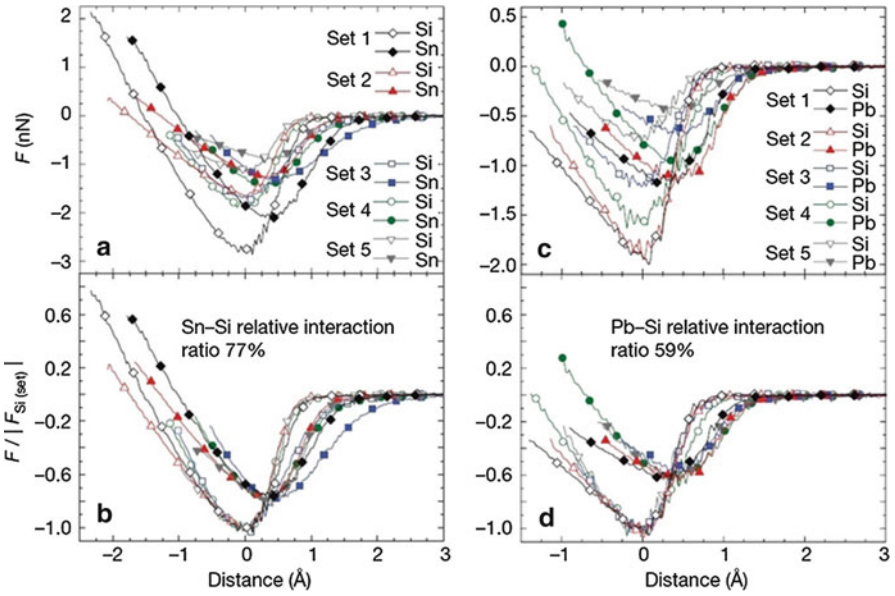


Fig. 8.11 Sets of force spectroscopy curves recorded on Si and Sn (**a**) as well as Si and Pb atoms (**c**) using NC-AFM. Despite the fact that significant differences between individual force curves can be observed due to the use of different tips, normalizing the data in each set with respect to the absolute maximum force recorded on Si $|F_{Si(set)}|$ reveals a distinct chemical signature associated with each type of atom in terms of the maximum normalized interaction force (**b**, **d**), irrespective of the specifics of the tip apex employed (Figure reproduced from Ref. [77] by permission from Macmillan Publishers Ltd, copyright (2007))

spectroscopy). Moreover, extended measurement times also increase the chance of permanent tip changes occurring at the apex, rendering the data collected up to the point of tip change unusable [237].

Due to the challenges described above, most experiments aimed at collecting full three-dimensional (volumetric) maps of interaction forces and energies above sample surfaces using NC-AFM have initially resulted in two-dimensional maps, describing the tip-sample interaction as a function of distance and lateral position in a defined crystallographic direction [78–82, 238]. While these experiments provided very useful physical information regarding, e.g., potential energy barriers [79] and lateral in addition to vertical force interactions [81], the goal of full three-dimensional atomic-resolution force spectroscopy was reached in 2009 [84]. The scanning probe microscopy group at Yale University utilized the combination of a home-built, ultrahigh vacuum and low-temperature noncontact atomic force microscope with very high stability and low drift rates (as low as 2–3 Å per day at liquid helium temperature as opposed to a typical value of a few Å per minute at room temperature) [101] and a new data acquisition and processing method to obtain a virtually drift-free map of interaction forces in three-dimensions on a 1750 pm × 810 pm area on HOPG [22, 84]. While the details of the data acquisition and

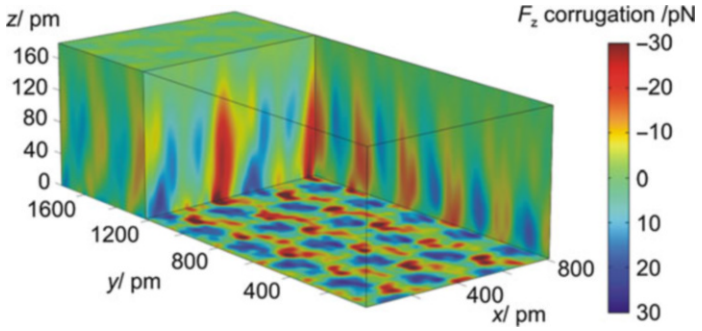


Fig. 8.12 Three-dimensional representation of the interaction force field acquired via NC-AFM based spectroscopy on HOPG. Atomic-scale corrugation on the plane of closest approach as well as the gradual weakening of interactions with increasing tip-sample distance are clearly observed. More negative values indicate more attractive interaction (Figure reproduced from Ref. [22])

processing steps as well as experimental parameters have been described elsewhere [237], the main advantage of the method lies in the fact that a *layer-by-layer* approach has been utilized instead of the typical *curve-by-curve* data collection procedure, allowing post-acquisition correction of the remaining drift to be performed manually after the experiment is finished. In the layer-by-layer approach, as described in Sect. 4 of this chapter, a series of regular, topographic NC-AFM images (together with the error signal in terms of deviations from the Δf setpoint) is collected at semi-constant heights above the sample surface with slow topography feedback, manual correction of lateral drift (which has been dramatically reduced thanks to the stable microscope design and low temperature operation) is performed image by image by cropping the part of each image that is common to all layers, and the resulting layers of topography and Δf information are combined to form a full three-dimensional set of spectroscopy data. The post-acquisition drift correction procedures also eliminates artifacts associated with the overall elastic deflection of asymmetric tip apices with increasing vertical forces as the tip-sample distance is decreased [237].

Once a full, drift-free three-dimensional map of frequency shifts is acquired as described above (in ∼40 h, at $T = 6$ K and under UHV conditions, using a tuning fork in the *qPlus* configuration with an etched Pt/Ir tip and featuring a data density of 6.8 pm laterally and ∼2 pm vertically), the data are converted to interaction force using appropriate mathematical procedures [68]. A three-dimensional visualization of the vertical interaction force field obtained in this way is presented in Fig. 8.12 (please note that the average force value for each height has been subtracted to enhance the contrast). The average interaction force observed in the bottom plane is ∼2.35 nN and the total corrugation is ∼70 pN. One can also clearly observe atomic resolution in the bottom plane as well as the gradual weakening of the interaction with increasing tip-sample distance.

For a more detailed analysis, *cuts* of forces along any direction can now be produced to study the evolution of interaction forces as a function of lateral position on the surface using horizontal cuts as well as tip-sample distance using vertical

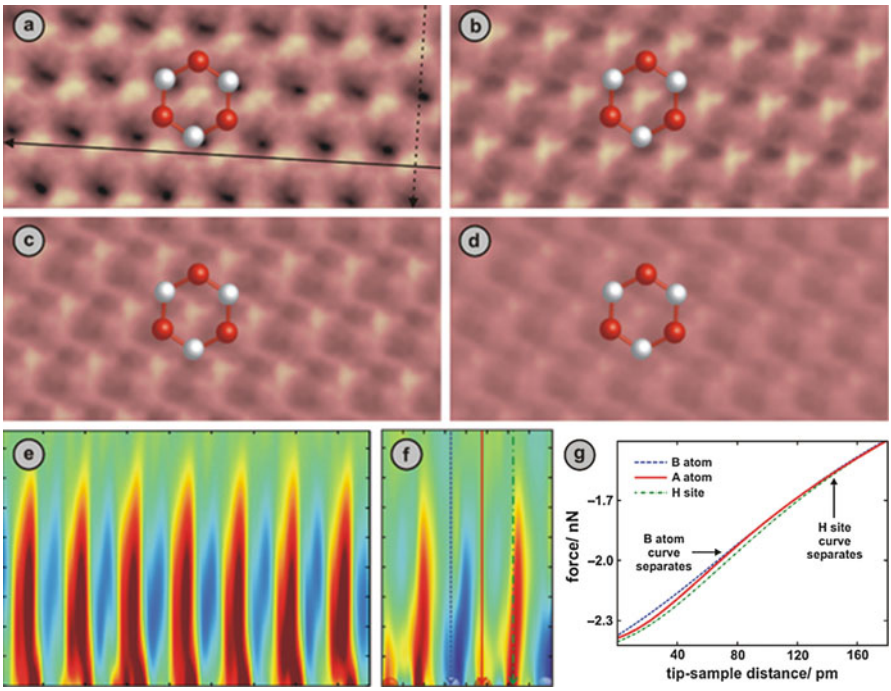


Fig. 8.13 (**a**–**d**) Horizontal force maps at 12 pm (**a**), 52 pm (**b**), 97 pm (**c**), and 132 pm (**d**) above the plane of closest approach reproduced from the three-dimensional data in Fig. 8.12. The hexagon designates the positions of the two types of inequivalent C atoms on the top layer of HOPG (A (red) and B (white) atoms). (**e**–**f**) Vertical force maps along the *straight* (**e**) and *dashed* (**f**) arrows in (**a**). (**g**) Three force spectroscopy curves recorded on the hollow lattice site (H site) as well as on top of the A and B atoms indicated in (**f**), highlighting site-specific differences in interaction forces (Figure reproduced from Ref. [22])

cuts (Fig. 8.13). Despite the fact that the horizontal maps presented in Fig. 8.13 resemble regular, *topographical* NC-AFM images, they differ significantly from these due to the fact that the image contrast now directly reflects the *magnitude of the interaction force* as a function of lattice position at a given height above the sample surface. In contrast, individual images obtained using NC-AFM only reflect a "topography" associated with a constant frequency shift, which is of limited physical significance. It is also interesting to note that the locations of largest attractive interaction with the probe tip are situated above the *hollow* sites (H sites) of the graphite lattice (i.e., the centers of the hexagons formed by the carbon atoms) [84, 239] essentially due to the fact that the relatively small atomic spacing between carbon atoms on the top layer of graphite leads to an increased interaction with the probe tip apex om hollow locations where the apex is closely surrounded by six carbon atoms.

As described above, an alternative way to study the three-dimensional interaction force data is to produce vertical maps along crystallographic directions of

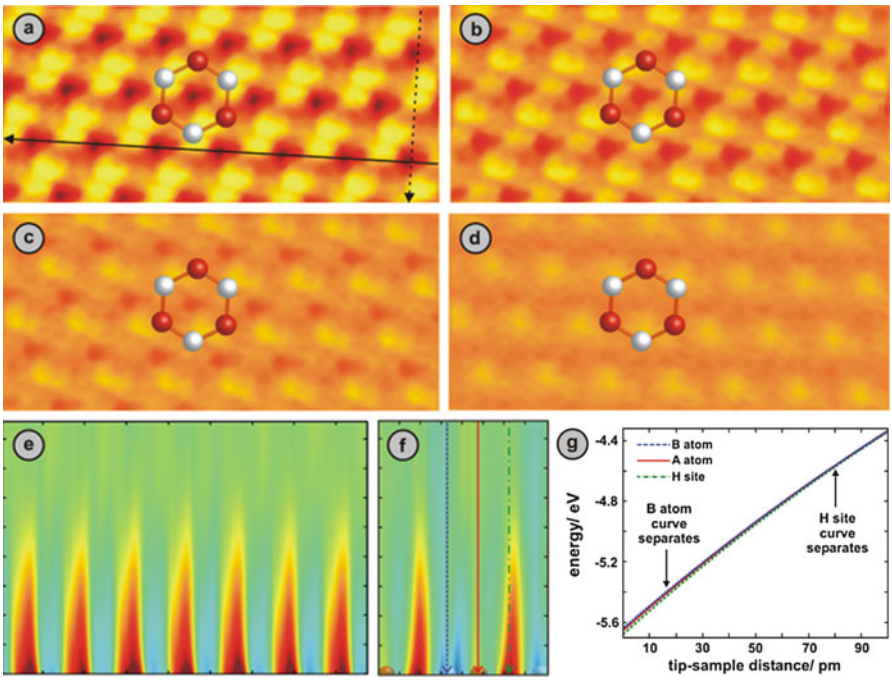


Fig. 8.14 (**a**–**d**) Horizontal maps of interaction energy corresponding to the tip-sample distances indicated in Fig. 8.13. (**e**–**f**) Vertical energy maps along the *straight* (**e**) and *dashed* (**f**) arrows in (**a**). (**g**) Three energy spectroscopy curves recorded on the hollow lattice site (H site) as well as on top of the A and B atoms indicated in (**f**). Note that the site-specific variation of interaction energy is less pronounced than force (Figure reproduced from Ref. [22])

interest. Studying the vertical force maps presented in Fig. 8.13, one can see that the atomic scale variations of the normal force on different lattice sites gradually weaken with increasing tip-sample distance and disappear at ∼150 pm above the plane of closest approach for both crystallographic directions of interest (Fig. 8.13e, f). Moreover, by extracting individual force-distance curves from the three-dimensional data on different lattice sites, the magnitude of the interactions exhibited by those sites with the probe apex can be quantified and compared as a function of tip-sample separation (see Fig. 8.13g).

As indicated before, integration of the three-dimensional interaction force data in the vertical direction results in a three-dimensional map of interaction energies, assuming that the magnitude of energy dissipation during experiments is negligible or significantly smaller than the total interaction. Analogous to Fig. 8.13, horizontal as well as vertical maps of interaction energies are presented in Fig. 8.14, together with representative curves of interaction energy versus tip-sample distance for three lattice positions of interest. It is observed that the total energy corrugation (∼0.05 eV) is less than 1 % of the maximum interaction energy observed in the bottom plane (5.7 eV). Within this context, care should be taken when comparing

quantitative results in terms of interaction forces and energies between different experiments, as the exact structure and chemistry of the tip apex have been previously found to affect NC-AFM results significantly [115–117]. The maximum interaction energy value discovered here is more than those reported for NiO (4 eV) [240] and NaCl (1.3 eV) [79], which is indicative of a rather blunt tip apex considering that graphite is a van der Waals surface and should be expected, as such, to exhibit relatively weak interactions with the probe apex. Moreover, the potential corrugation value of ~0.05 eV is smaller than the one observed for NiO (0.3 eV) [240], but similar to the one found for NaCl [79].

An important area of scientific inquiry with great technological implications is friction [241]. Despite the fact that friction is ubiquitous in our daily lives and a major source of energy dissipation in industrial processes, the basic physical laws that govern this particular phenomenon at the nanometer scale are still not well known [242]. As such, the capability of NC-AFM to perform atomic-resolution force spectroscopy to measure lateral forces acting between the probe tip and various material surfaces is of great importance. A significant advantage of NC-AFM as opposed to traditional, contact-based FFM in terms of tribological studies is that atomic-resolution information about lateral forces can be obtained thanks to the fact that the probe tip remains atomically sharp during the experiments. In contrast, since NC-AFM based force spectroscopy experiments typically probe the attractive interaction regime, direct conclusions regarding processes occurring during actual sliding events between two surfaces in contact (i.e., in the repulsive regime) cannot be made in a straightforward fashion. Still, NC-AFM has been used in the past to either directly probe frequency shifts caused by lateral forces by oscillating the tip parallel to the sample surface [243–245] or to perform two- or three-dimensional spectroscopy and then take the derivative of the resulting interaction energy field in the lateral directions x and/or y to obtain the lateral force field [81, 82, 87, 240, 246]. Moreover, in a powerful demonstration of the technique, Ternes et al. used a similar approach to calculate the magnitude of lateral forces needed for lateral manipulation of atoms and molecules on a metal surface [247]. Very recently, Weymouth et al. have utilized a tip apex terminated by a single CO atom to quantify the vertical and lateral forces experienced by the probe tip during imaging of another CO molecule adsorbed on a copper surface and have impressively managed to calculate the torsional stiffness associated with the CO molecule adsorbed on the tip apex in conjunction with a deceptively simple mechanical model [248]. Within this general context, an analysis of lateral forces in the 2009 study by Albers et al. (obtained by derivation of the interaction energy data in the lateral x and y directions) is presented in Fig. 8.15 [84, 85]. As one can clearly observe from the presented data, the structure of lateral forces detected on a horizontal plane at a fixed height above the sample surface is very different than the vertical force data: Lateral forces experienced by the atomically sharp probe tip are heavily localized around the hollow sites of the graphite lattice (where the maximum vertical forces are detected) in asymmetric rings, while the lateral force values outside of the localized rings are comparably very small. This interesting observation is further supported by zoomed images of a lateral force ring (Fig. 8.15e, f)

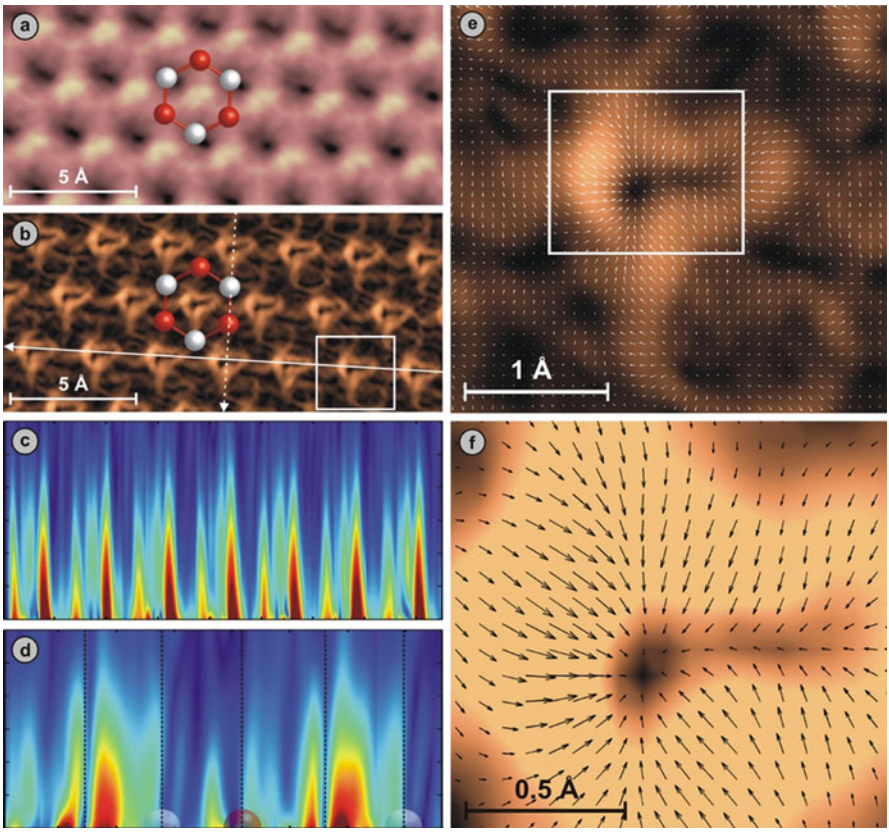


Fig. 8.15 Horizontal maps of normal (**a**) and lateral (**b**) interaction forces above the HOPG surface. The color scale in (**b**) ranges from 0 to 120 pN. Note the localization of lateral forces around the hollow sites of the HOPG lattice. (**c**) and (**d**) visualize the evolution of lateral forces as a function of tip-sample distance along the *straight* and *dashed arrows* in (**b**) while (**e**) and (**f**) describe in very high resolution the distribution of lateral force vectors around the hollow sites (Figure reproduced from Ref. [85] © IOP Publishing. Reproduced with permission. All rights reserved)

where depicted vectors (separated by ∼7 pm) indicate the direction and magnitude of the measured lateral force at each data point. The authors have argued that this remarkable localization of lateral forces might help explain the exceptional frictional properties of HOPG as a solid lubricant [84, 85].

Additionally, using vertical cuts of lateral forces along crystallographic directions of interest, it is shown that atomic-scale corrugation in terms of lateral forces disappears at about 120 pm above the plane of closest approach (corresponding to a vertical force magnitude of about 1.6 nN) and the maximum lateral force detected in the bottom plane is ∼0.2 nN, a comparable value to some of the previously published results on KBr [81] and Si [82].

After atomic-resolution force spectroscopy in three dimensions has been demonstrated as a proof of principle on the model surface of HOPG [84], several other

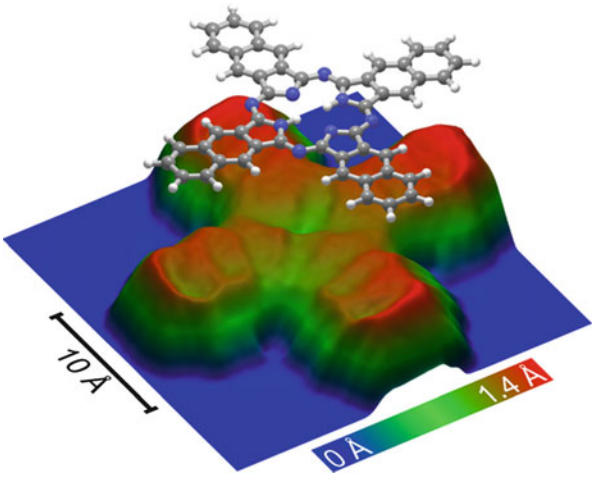


Fig. 8.16 A three-dimensional representation of the topography associated with a single naphthalocyanine molecule at constant tip-sample interaction. The data has been extracted from a full three-dimensional set of frequency shifts utilized for force spectroscopy (Figure reproduced from Ref. [110]. Copyright (2011), AIP Publishing LLC)

experiments have shown the feasibility of the technique on other sample systems. Specifically, in a groundbreaking experiment, Gross et al. have been able to image the intramolecular structure of a pentacene molecule using a tip apex functionalized with a CO molecule, whereby they have also performed three-dimensional force spectroscopy [61]. Again using a CO-modified tip apex, Mohn et al. have measured the three-dimensional short-range force field over a naphthalocyanine molecule (Fig. 8.16) [110]. Moreover Such et al. have utilized the technique to show that significant tip relaxation based on changing tip-sample distance is observable for specific tip apices during spectroscopy experiments [111] and that a height-dependent contrast reversal occurs during spectroscopy experiments on Cu(111) [112]. Fremy et al. have compared the advantages and disadvantages of the *curve-by-curve* and *layer-by-layer* data acquisition methods for three-dimensional force spectroscopy on a model ionic crystal surface (KBr) [87], while Kawai et al. have studied interaction induced atomic relaxations [107] and Sugimoto et al. have simultaneously performed three-dimensional force and tunneling current spectroscopy on Si(111)-7×7 [108]. Furthermore, using three-dimensional force spectroscopy, Pawlak et al. have investigated the mechanical properties of C_{60} molecules [225] as well porphyrin derivatives [228]. It is important to note that a significant number of three-dimensional spectroscopy experiments mentioned here have been performed at room temperature thanks to the use of atom-tracking/feedforward methods [87, 107, 108]. Finally, Giessibl et al. have performed a combined three-dimensional study of interaction forces and tunneling current on a single CO molecule adsorbed on a copper surface, whereby they were able to observe angular dependence of measured chemical interaction forces on changing crystallographic orientation of a tungsten tip apex [249]. While all force spectroscopy experiments mentioned here have been performed under UHV conditions, attention should be drawn to the fact that the technique has recently been extended to liquid conditions thanks to certain

developments in instrumentation and methodology, an important step towards broadening the application areas of NC-AFM based spectroscopy experiments [128, 129, 250, 251].

5.2.3 Combined Three-Dimensional Force and Tunneling Current Spectroscopy with Atomic Resolution

One of the important advantages associated with the three-dimensional force spectroscopy technique performed via NC-AFM is that additional data channels such as dissipated energy and tunneling current may be recorded during the experiments [22]. Simultaneous recording of interaction forces and tunneling currents is of particular interest due to the fact that information about atomic-scale chemical interactions exhibited by surface atoms with the tip apex and at the same time, clues regarding the electronic properties of the surface are collected concurrently such that the data in the two channels can be contrasted and compared. Moreover, the complementary information included in the two channels can be used towards identification of lattice sites on sample surfaces consisting of more than one type of atom where symmetry arguments in a single channel do not allow for an unambiguous assignment of lattice sites to observed maxima. Additionally, chemical and structural identification of the tip apex used in specific experiments remains a significant issue, which can be facilitated by the additional data available in the tunneling current channel, especially if the experimental data is interpreted with help from ab initio simulations.

To illustrate the points described above, a simultaneously recorded data set of interaction forces and tunneling currents on a surface-oxidized Cu(100) sample will be presented as a representative example [86] (keeping in mind that other studies exist where combined three-dimensional force and tunneling current spectroscopy have been performed, as well [108, 249]). The monolayer-thick surface oxide layer investigated in the experiments described here features a missing-row reconstruction where one in every four copper rows of the underlying substrate forms a trough, with filled rows between the troughs consisting of nearly co-planar Cu and O atoms in an alternating configuration (Fig. 8.17a). The spectroscopy experiments have been performed using the same instrument [101] utilized for acquiring the pioneering three-dimensional force spectroscopy data on HOPG [84] at liquid helium temperatures and a quartz tuning fork in the *qPlus* configuration with an etched and field-ion beam treated Pt/Ir tip as the force sensor. While the tuning fork is oscillating with a an amplitude of $\sim$1.0 nm above the sample surface, frequency shift and tunneling current data (averaged over the oscillatory motion of the tip) are acquired *layer-by-layer* in a dense grid above the surface. After drift correction, the region of the surface over which the spectroscopy data is displayed remains 2.89 nm $\times$ 2.89 nm, featuring 221 $\times$ 221 pixels.

The three-dimensional map of interaction forces collected as described above is displayed in Fig. 8.17b, where the average force value at each height has been subtracted to enhance the contrast. The magnitude of the maximum interaction force measured in the bottom plane is $\sim$1.34 nN whereas the contrast between atomically defined lattice sites is $\sim$23 pN.

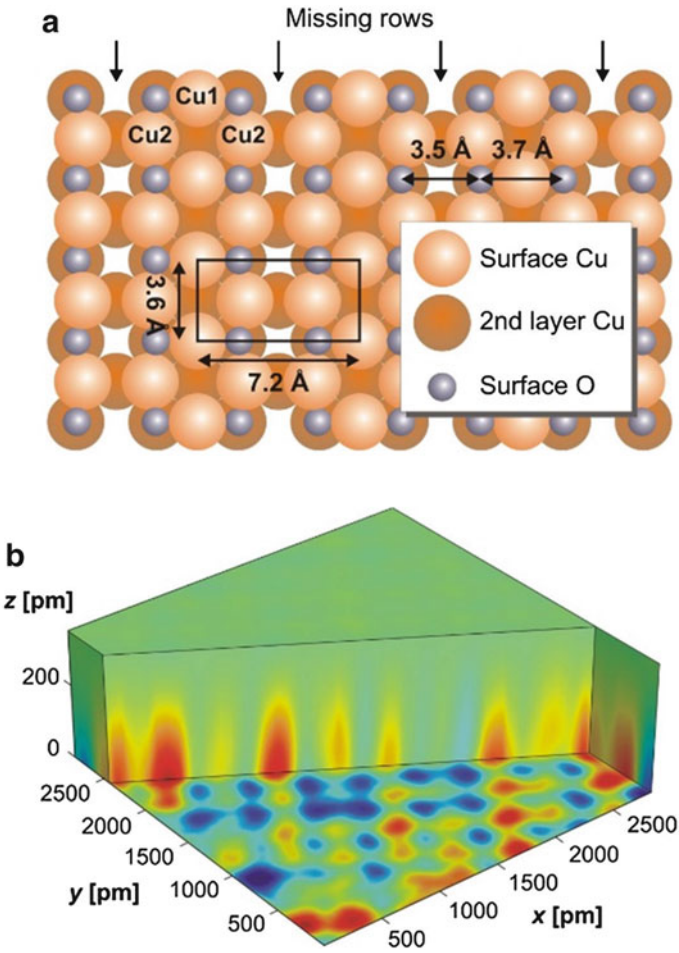


Fig. 8.17 (**a**) Reconstructed missing-row model of the surface oxide layer on Cu(100). Cu1 atoms are located at the centers of filled rows while Cu2 atoms are at the edges. (**b**) Three-dimensional representation of interaction forces obtained on the sample surface using NC-AFM based spectroscopy. Atomic corrugation is clearly observable on the plane of closest approach (Figure reproduced from Ref. [86]. Copyright (2013) by the American Physical Society)

Studying the atomic-scale arrangement of interaction forces on a *horizontal* cut produced from the three-dimensional map allows an unambiguous determination of force maxima as the O atoms on the surface (Fig. 8.18a), based on symmetry arguments. Interestingly, the interaction force observed on each O atom is different, with the values measured for each atom differing by as much as 40 % of the total force contrast at that distance. On the other hand, the corresponding tunneling current map obtained at the same fixed height features a *ladder-like* symmetry, with the occasional appearance of linear defects imaged as partially *nonmissing rows* (Fig. 8.18b). Comparison of the obtained experimental data with ab initio

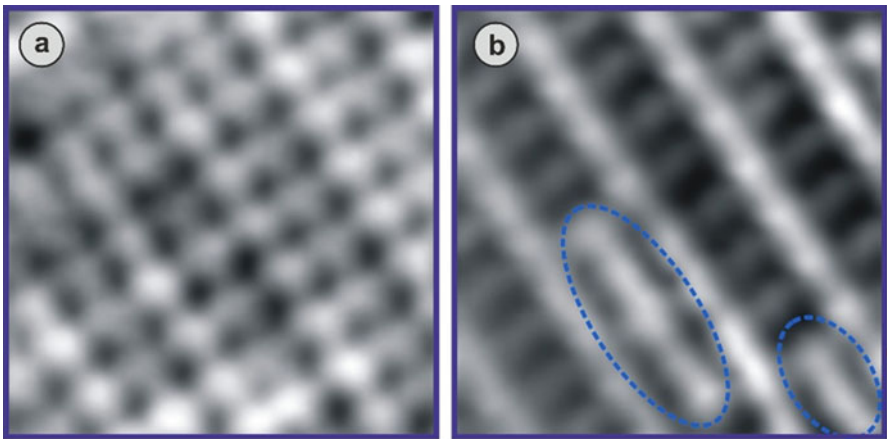


Fig. 8.18 (**a**) Horizontal force map (2.89 nm × 2.89 nm) extracted from the data in Fig. 8.17b at the plane of closest approach. Maxima are observed to coincide with the oxygen atoms on the surface. (**b**) Simultaneously acquired image of average tunneling current at the same height. A *ladder-type* contrast coinciding with the copper atom arrangement on the surface is observed, together with highlighted surface defects (Figure reproduced from Ref. [86]. Copyright (2013) by the American Physical Society)

density functional theory calculations involving model tip apices consisting of Cu and O atoms (selected due to the fact that tips have been treated by gentle crashes into the sample surface prior to data acquisition to improve imaging resolution) then allows to (a) identify the structure and chemistry of the tip apex used in the experiments by a comparison with simulated force curves and tunneling current images, and (b) identify the linear defects observed in the tunneling current channel. Consequently, the tip apex used in the experiments is predicted to be terminated by a Cu atom with an O atom adsorbed on the side, which successfully reproduces the experimentally obtained contrast in the tunneling current channel (where Cu1 atoms located at the centers of filled rows are imaged as bright protrusions and faint bridges of tunneling current are formed by Cu2 atoms on both sides of the missing rows) and interacts most favorably with the O atoms on the surface in the investigated height regime. Simultaneous imaging of two different chemical species via multichannel NC-AFM is thus demonstrated. Moreover, after investigating a number of defect models and the resulting simulations of tunneling current contrast, the atomic-scale origin of the linear defect observed in the current channel can be determined to involve the displacement of two pairs of Cu2 atoms into the missing rows (Fig. 8.19a, b). The authors eventually conclude that the variation of interaction force observed on each O atom is due to the variability in the chemical and electronic environment induced by the existence of surface defects, thereby providing a direct, real-space evidence that surface defects affect chemical reactivity on the atomic scale [86].

As seen by the representative example presented here, the combination of three-dimensional force and tunneling current spectroscopy performed via NC-AFM

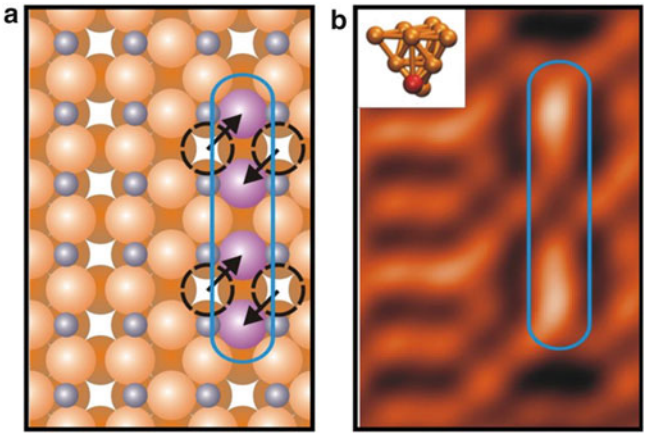


Fig. 8.19 A surface defect model involving the displacement of two pairs of Cu_2 atoms into the missing row (**a**) is predicted to result in the observation of a linear defect in the tunneling current channel (**b**) via ab initio simulations, in alignment with experimental data displayed in Fig. 8.18b. The *inset* in (**b**) represents the structural model of the tip apex used in the simulations (Figure reproduced from Ref. [86]. Copyright (2013) by the American Physical Society)

exhibits a tremendous potential for atomic-scale characterization of surfaces featuring multiple chemical species and even defects. As such, in addition to its atomic-resolution imaging capabilities, NC-AFM emerges as a very powerful tool for ultra-high resolution physical, chemical and mechanical characterization of material surfaces.

6 Conclusions and Outlook

The immense application potential of NC-AFM as an ultra-high resolution characterization tool for nanoscience and nanotechnology has been demonstrated by the results presented in this chapter. With NC-AFM, researchers now have the capability to characterize the structure of various material surfaces including semiconductors, metal oxides, ionic crystals, etc. with atomic resolution, while force spectroscopy experiments allow the site-specific quantification of chemical interactions, paving the way towards full atomic-scale characterization of surface reactivity – a topic of fundamental importance for numerous fields including tribology and heterogeneous catalysis.

While atomic-resolution NC-AFM experiments have been restricted to ultrahigh vacuum conditions for a long time, advances in instrumentation and experimental methodology now allow molecular- and atomic-resolution imaging studies to be performed in ambient conditions as well as liquids. As such, it is expected that the application of NC-AFM will expand in the near future towards high resolution characterization of different types of functional biological materials under liquid environment, where the structural integrity of investigated molecules and molecular structures are conserved.

As demonstrated throughout the chapter via numerous experimental and theoretical studies, results obtained by NC-AFM strongly depend on the structural and chemical properties of the tip apex. While tip apex standardization has been reached to some extent via functionalization through adsorbed molecules such as CO, the next step in this direction could involve the functionalization of tip apices via molecules that are of particular importance with regards to certain applications such as catalysis. Within this context, the ability to fully map the potential energy landscape experienced by particular molecules in the vicinity of single crystal substrates of catalytic importance would result in the acquisition of much needed data in terms of the effect of defects (such as step edges, kinks as well as vacancies, etc.) on site-specific chemical reactivity.

Last but not least, the demonstrated capability of the method to simultaneously acquire structural, physical, chemical as well as electronic information regarding material surfaces on the atomic scale via the recording of multiple data channels holds great potential for future applications of nanotechnology. Combined with the fact that NC-AFM can now be used to perform atomic manipulation experiments on surfaces [252, 253], the vision of true bottom-up engineering on the nanoscale involving the rational construction and subsequent characterization of atomic-scale, functional structures may be realized in the near future.

References

1. Binnig G, Rohrer H (1982) Scanning tunneling microscopy. Helv Phys Acta 55(6):726–735
2. Binnig G, Rohrer H, Gerber C, Weibel E (1983) 7x7 Reconstruction on Si(111) resolved in real space. Phys Rev Lett 50(2):120–123
3. Chen CJ (2007) Introduction to scanning tunneling microscopy. Oxford University Press, Oxford
4. Bonnell DA, Basov DN, Bode M, Diebold U, Kalinin SV, Madhavan V, Novotny L, Salmeron M, Schwarz UD, Weiss PS (2012) Imaging physical phenomena with local probes: from electrons to photons. Rev Mod Phys 84(3):1343
5. Binnig G, Quate CF, Gerber C (1986) Atomic force microscope. Phys Rev Lett 56(9):930–933
6. Albrecht TR, Quate CF (1988) Atomic resolution with the atomic force microscope on conductors and nonconductors. J Vac Sci Technol Vac Surf Films 6(2):271–274
7. Albrecht TR, Akamine S, Carver TE, Quate CF (1990) Microfabrication of cantilever styli for the atomic force microscope. J Vac Sci Technol-Vac Surf Films 8(4):3386–3396
8. Akamine S, Barrett RC, Quate CF (1990) Improved atomic force microscope images using microcantilevers with sharp tips. Appl Phys Lett 57(3):316–318
9. Wolter O, Bayer T, Greschner J (1991) Micromachined silicon sensors for scanning force microscopy. J Vac Sci Technol B 9(2):1353–1357
10. Meyer G, Amer NM (1988) Novel optical approach to atomic force microscopy. Appl Phys Lett 53(12):1045–1047
11. Alexander S, Hellemans L, Marti O, Schneir J, Elings V, Hansma PK, Longmire M, Gurley J (1989) An atomic-resolution atomic-force microscope implemented using an optical-lever. J Appl Phys 65(1):164–167
12. Rugar D, Mamin HJ, Guethner P (1989) Improved fiber-optic interferometer for atomic force microscopy. Appl Phys Lett 55(25):2588–2590
13. Moser A, Hug HJ, Jung T, Schwarz UD, Guntherodt HJ (1993) A miniature fiber optic force microscope scan head. Meas Sci Technol 4(7):769–775

14. Binnig G, Gerber C, Stoll E, Albrecht TR, Quate CF (1987) Atomic resolution with atomic force microscope. Europhys Lett 3(12):1281–1286
15. Meyer G, Amer NM (1990) Optical-beam-deflection atomic force microscopy – the nacl (001) surface. Appl Phys Lett 56(21):2100–2101
16. Marti O, Colchero J, Mlynek J (1993) Friction and forces on an atomic-scale. Nanosour Manip Atoms Under High Fields Temp Appl 235:253–269
17. Meyer G, Amer NM (1990) Simultaneous measurement of lateral and normal forces with an optical-beam-deflection atomic force microscope. Appl Phys Lett 57(20):2089–2091
18. Mate CM, McClelland GM, Erlandsson R, Chiang S (1987) Atomic-scale friction of a tungsten tip on a graphite surface. Phys Rev Lett 59(17):1942–1945
19. Eaton PJ, West P (2010) Atomic force microscopy. Oxford University Press, Oxford
20. Giessibl FJ, Binnig G (1992) Investigation of the (001) cleavage plane of potassium-bromide with an atomic force microscope at 4.2-k in ultra-high vacuum. Ultramicroscopy 42:281–289
21. Ohnesorge F, Binnig G (1993) True atomic-resolution by atomic force microscopy through repulsive and attractive forces. Science 260(5113):1451–1456
22. Baykara MZ, Schwendemann TC, Altman EI, Schwarz UD (2010) Three-dimensional atomic force microscopy – taking surface imaging to the next level. Adv Mater 22(26–27):2838–2853
23. Giessibl FJ (1995) Atomic-resolution of the silicon (111)-(7x7) surface by atomic-force microscopy. Science 267(5194):68–71
24. Sugawara Y, Ohta M, Ueyama H, Morita S (1995) Defect motion on an InP(110) surface observed with noncontact atomic-force microscopy. Science 270(5242):1646–1648
25. Kitamura S, Iwatsuki M (1995) Observation of 7x7 reconstructed structure on the silicon (111) surface using ultrahigh-vacuum noncontact atomic-force microscopy. Jpn J Appl Phys Part 2 Lett 34(1B):L145–L148
26. Ueyama H, Ohta M, Sugawara Y, Morita S (1995) Atomically resolved InP(110) surface observed with noncontact ultrahigh-vacuum atomic-force microscope. Jpn J Appl Phys Part 2 Lett 34(8B):L1086–L1088
27. Morita S, Wiesendanger R, Meyer E (2002) Noncontact atomic force microscopy. Springer, Berlin
28. Morita S, Giessibl FJ, Wiesendanger R (2009) Noncontact atomic force microscopy, vol 2. Springer, Berlin
29. Garcia R, Perez R (2002) Dynamic atomic force microscopy methods. Surf Sci Rep 47(6–8):197–301
30. Giessibl FJ (2003) Advances in atomic force microscopy. Rev Mod Phys 75(3):949–983
31. Hofer WA, Foster AS, Shluger AL (2003) Theories of scanning probe microscopes at the atomic scale. Rev Mod Phys 75(4):1287–1331
32. Barth C, Foster AS, Henry CR, Shluger AL (2011) Recent trends in surface characterization and chemistry with high-resolution scanning force methods. Adv Mater 23(4):477–501
33. Morita S (2013) Atomically resolved force microscopy. J Vac Sci Technol A 31(5):050802
34. Albrecht TR, Grutter P, Horne D, Rugar D (1991) Frequency-modulation detection using high-q cantilevers for enhanced force microscope sensitivity. J Appl Phys 69(2):668–673
35. Yokoyama K, Ochi T, Yoshimoto A, Sugawara Y, Morita S (2000) Atomic resolution imaging on Si(100)2x1 and Si(100)2x1: H surfaces with noncontact atomic force microscopy. Japanese J Appl Phys Part 2 Lett 39(2A):L113–L115
36. Schwarz A, Allers W, Schwarz UD, Wiesendanger R (2000) Dynamic-mode scanning force microscopy study of n-InAs(110)-(1x1) at low temperatures. Phys Rev B 61(4):2837–2845
37. Kitamura S, Iwatsuki M (1996) Observation of silicon surfaces using ultrahigh-vacuum noncontact, atomic force microscopy. Jpn J Appl Phys Part 2-Lett 35(5B):L668–L671
38. Sugawara Y, Uchihashi T, Abe M, Morita S (1999) True atomic resolution imaging of surface structure and surface charge on the GaAs(110). Appl Surf Sci 140(3–4):371–375
39. Sawada D, Sugimoto Y, Morita K, Abe M, Morita S (2010) Simultaneous atomic force and scanning tunneling microscopy study of the Ge(111)-c(2x8) surface. J Vac Sci Technol B 28(3):C4D1

40. Yokoyama K, Ochi T, Sugawara Y, Morita S (1999) Atomically resolved silver imaging on the Si(111)-$\left(\sqrt{3} \times \sqrt{3}\right)$-Ag surface using a noncontact atomic force microscope. Phys Rev Lett 83(24):5023–5026
41. Sweetman A, Gangopadhyay S, Danza R, Berdunov N, Moriarty P (2009) qPlus atomic force microscopy of the Si(100) surface: buckled, split-off, and added dimers. Appl Phys Lett 95(6):063112
42. Sweetman A, Danza R, Gangopadhyay S, Moriarty P (2012) Imaging and manipulation of the Si(100) surface by small-amplitude NC-AFM at zero and very low applied bias. J Phys Condens Matter 24(8):084009
43. Sweetman A, Stannard A, Sugimoto Y, Abe M, Morita S, Moriarty P (2013) Simultaneous noncontact AFM and STM of Ag:Si(111)-$\left(\sqrt{3} \times \sqrt{3}\right)$R30°. Phys Rev B 87(7):075310
44. Li YJ, Nomura H, Ozaki N, Naitoh Y, Kageshima M, Sugawara Y, Hobbs C, Kantorovich L (2006) Origin of p(2 x 1) phase on Si(001) by noncontact atomic force microscopy at 5 k. Phys Rev Lett 96(10):106104
45. Naitoh Y, Ma ZM, Li YJ, Kageshima M, Sugawara Y (2010) Simultaneous observation of surface topography and elasticity at atomic scale by multifrequency frequency modulation atomic force microscopy. J Vac Sci Technol B 28(6):1210–1214
46. Minobe T, Uchihashi T, Tsukamoto T, Orisaka S, Sugawara Y, Morita S (1999) Distance dependence of noncontact-AFM image contrast on Si(111)$\sqrt{3} \times \sqrt{3}$-Ag structure. Appl Surf Sci 140(3–4):298–303
47. Orisaka S, Minobe T, Uchihashi T, Sugawara Y, Morita S (1999) The atomic resolution imaging of metallic Ag(111) surface by noncontact atomic force microscope. Appl Surf Sci 140(3–4):243–246
48. Loppacher C, Bammerlin M, Guggisberg M, Schar S, Bennewitz R, Baratoff A, Meyer E, Guntherodt HJ (2000) Dynamic force microscopy of copper surfaces: atomic resolution and distance dependence of tip-sample interaction and tunneling current. Phys Rev B 62(24):16944–16949
49. Caciuc V, Holscher H, Weiner D, Fuchs H, Schirmeisen A (2008) Noncontact atomic force microscopy imaging mechanism on Ag(110): experiment and first-principles theory. Phys Rev B 77(4):045411
50. Konig T, Simon GH, Rust HP, Heyde M (2009) Atomic resolution on a metal single crystal with dynamic force microscopy. Appl Phys Lett 95(8):083116
51. Allers W, Schwarz A, Schwarz UD, Wiesendanger R (1999) Dynamic scanning force microscopy at low temperatures on a noble-gas crystal: atomic resolution on the xenon (111) surface. Europhys Lett 48(3):276–279
52. Barth C, Reichling M (2001) Imaging the atomic arrangements on the high-temperature reconstructed alpha-Al_2O_3(0001) surface. Nature 414(6859):54–57
53. Reichling M, Barth C (1999) Scanning force imaging of atomic size defects on the CaF_2(111) surface. Phys Rev Lett 83(4):768–771
54. Barth C, Foster AS, Reichling M, Shluger AL (2001) Contrast formation in atomic resolution scanning force microscopy on CaF(2)(111): experiment and theory. J Phys-Condens Matter 13(10):2061–2079
55. Hoffmann R, Lantz MA, Hug HJ, van Schendel PJA, Kappenberger P, Martin S, Baratoff A, Guntherodt HJ (2003) Atomic resolution imaging and frequency versus distance measurements on NiO(001) using low-temperature scanning force microscopy. Phys Rev B 67(8):085402
56. Ruschmeier K, Schirmeisen A, Hoffmann R (2009) Site-specific force-vector field studies of KBr(001) by atomic force microscopy. Nanotechnology 20(26):264013
57. Gritschneder S, Namai Y, Iwasawa Y, Reichling M (2005) Structural features of CeO_2(111) revealed by dynamic SFM. Nanotechnology 16(3):S41–S48
58. Ostendorf F, Torbrugge S, Reichling M (2008) Atomic scale evidence for faceting stabilization of a polar oxide surface. Phys Rev B 77(4):041405
59. Rasmussen MK, Foster AS, Canova FF, Hinnemann B, Helveg S, Meinander K, Besenbacher F, Lauritsen JV (2011) Noncontact atomic force microscopy imaging of atomic

structure and cation defects of the polar $MgAl_2O_4(100)$ surface: experiments and first-principles simulations. Phys Rev B 84(23):235419
60. Hoffmann R, Weiner D, Schirmeisen A, Foster AS (2009) Sublattice identification in noncontact atomic force microscopy of the NaCl(001) surface. Phys Rev B 80(11):115426
61. Gross L, Mohn F, Moll N, Liljeroth P, Meyer G (2009) The chemical structure of a molecule resolved by atomic force microscopy. Science 325(5944):1110–1114
62. Gross L, Mohn F, Moll N, Meyer G, Ebel R, Abdel-Mageed WM, Jaspars M (2010) Organic structure determination using atomic-resolution scanning probe microscopy. Nat Chem 2(10):821–825
63. Meyer G, Gross L, Mahn F, Repp J (2012) Scanning probe microscopy of atoms and molecules on insulating films: from imaging to molecular manipulation. Chimia 66(1–2):10–15
64. Mohn F, Schuler B, Gross L, Meyer G (2013) Different tips for high-resolution atomic force microscopy and scanning tunneling microscopy of single molecules. Appl Phys Lett 102(7):073109
65. Gotsmann B, Anczykowski B, Seidel C, Fuchs H (1999) Determination of tip-sample interaction forces from measured dynamic force spectroscopy curves. Appl Surf Sci 140(3–4):314–319
66. Durig U (1999) Relations between interaction force and frequency shift in large-amplitude dynamic force microscopy. Appl Phys Lett 75(3):433–435
67. Giessibl FJ (2001) A direct method to calculate tip-sample forces from frequency shifts in frequency-modulation atomic force microscopy. Appl Phys Lett 78(1):123–125
68. Sader JE, Jarvis SP (2004) Accurate formulas for interaction force and energy in frequency modulation force spectroscopy. Appl Phys Lett 84(10):1801–1803
69. Giessibl FJ (1997) Forces and frequency shifts in atomic-resolution dynamic-force microscopy. Phys Rev B 56(24):16010–16015
70. Durig U (2000) Extracting interaction forces and complementary observables in dynamic probe microscopy. Appl Phys Lett 76(9):1203–1205
71. Holscher H, Schwarz A, Allers W, Schwarz UD, Wiesendanger R (2000) Quantitative analysis of dynamic-force-spectroscopy data on graphite(0001) in the contact and noncontact regimes. Phys Rev B 61(19):12678–12681
72. Gotsmann B, Fuchs H (2001) Dynamic force spectroscopy of conservative and dissipative forces in an Al-Au(111) tip-sample system. Phys Rev Lett 86(12):2597–2600
73. Lantz MA, Hug HJ, Hoffmann R, van Schendel PJA, Kappenberger P, Martin S, Baratoff A, Guntherodt HJ (2001) Quantitative measurement of short-range chemical bonding forces. Science 291(5513):2580–2583
74. Hoffmann R, Kantorovich LN, Baratoff A, Hug HJ, Guntherodt HJ (2004) Sublattice identification in scanning force microscopy on alkali halide surfaces. Phys Rev Lett 92(14):146103
75. Abe M, Sugimoto Y, Custance O, Morita S (2005) Room-temperature reproducible spatial force spectroscopy using atom-tracking technique. Appl Phys Lett 87(17):173503
76. Sugimoto Y, Innami S, Abe M, Custance O, Morita S (2007) Dynamic force spectroscopy using cantilever higher flexural modes. Appl Phys Lett 91(9):093120
77. Sugimoto Y, Pou P, Abe M, Jelinek P, Perez R, Morita S, Custance O (2007) Chemical identification of individual surface atoms by atomic force microscopy. Nature 446(7131):64–67
78. Langkat SM, Holscher H, Schwarz A, Wiesendanger R (2003) Determination of site specific interatomic forces between an iron coated tip and the NiO(001) surface by force field spectroscopy. Surf Sci 527(1–3):12–20
79. Schirmeisen A, Weiner D, Fuchs H (2006) Single-atom contact mechanics: from atomic scale energy barrier to mechanical relaxation hysteresis. Phys Rev Lett 97(13):136101
80. Heyde M, Simon GH, Rust HP, Freund HJ (2006) Probing adsorption sites on thin oxide films by dynamic force microscopy. Appl Phys Lett 89(26):263107

81. Ruschmeier K, Schirmeisen A, Hoffmann R (2008) Atomic-scale force-vector fields. Phys Rev Lett 101(15):156102
82. Sugimoto Y, Namikawa T, Miki K, Abe M, Morita S (2008) Vertical and lateral force mapping on the Si(111)-(7x7) surface by dynamic force microscopy. Phys Rev B 77(19):195424
83. Ashino M, Obergfell D, Haluska M, Yang SH, Khlobystov AN, Roth S, Wiesendanger R (2008) Atomically resolved mechanical response of individual metallofullerene molecules confined inside carbon nanotubes. Nat Nanotechnol 3(6):337–341
84. Albers BJ, Schwendemann TC, Baykara MZ, Pilet N, Liebmann M, Altman EI, Schwarz UD (2009) Three-dimensional imaging of short-range chemical forces with picometre resolution. Nat Nanotechnol 4(5):307–310
85. Baykara MZ, Schwendemann TC, Albers BJ, Pilet N, Monig H, Altman EI, Schwarz UD (2012) Exploring atomic-scale lateral forces in the attractive regime: a case study on graphite (0001). Nanotechnology 23(40):405703
86. Baykara MZ, Todorovic M, Monig H, Schwendemann TC, Unverdi O, Rodrigo L, Altman EI, Perez R, Schwarz UD (2013) Atom-specific forces and defect identification on surface-oxidized Cu(100) with combined 3D-AFM and STM measurements. Phys Rev B 87(15):155414
87. Fremy S, Kawai S, Pawlak R, Glatzel T, Baratoff A, Meyer E (2012) Three-dimensional dynamic force spectroscopy measurements on KBr(001): atomic deformations at small tip-sample separations. Nanotechnology 23(5):055401
88. Baykara MZ, Dagdeviren OE, Schwendemann TC, Monig H, Altman EI, Schwarz UD (2012) Probing three-dimensional surface force fields with atomic resolution: measurement strategies, limitations, and artifact reduction. Beilstein J Nanotechnol 3:637–650
89. Pethica JB (1986) Interatomic forces in scanning tunneling microscopy – giant corrugations of the graphite surface – comment. Phys Rev Lett 57(25):3235
90. Martin Y, Williams CC, Wickramasinghe HK (1987) Atomic force microscope force mapping and profiling on a sub 100-a scale. J Appl Phys 61(10):4723–4729
91. Zhong Q, Inniss D, Kjoller K, Elings VB (1993) Fractured polymer silica fiber surface studied by tapping mode atomic-force microscopy. Surf Sci 290(1–2):L688–L692
92. Castro García R (2010) Amplitude modulation atomic force microscopy. Wiley-VCH, Weinheim
93. Erlandsson R, Olsson L, Martensson P (1996) Inequivalent atoms and imaging mechanisms in ac-mode atomic-force microscopy of Si(111)7x7. Phys Rev B 54(12):R8309–R8312
94. Israelachvili JN (2011) Intermolecular and surface forces. Academic, Burlington
95. Moll N, Gross L, Mohn F, Curioni A, Meyer G (2010) The mechanisms underlying the enhanced resolution of atomic force microscopy with functionalized tips. New J Phys 12(12):125020
96. Fukui K, Onishi H, Iwasawa Y (1997) Atom-resolved image of the TiO_2(110) surface by noncontact atomic force microscopy. Phys Rev Lett 79(21):4202–4205
97. Allers W, Schwarz A, Schwarz UD, Wiesendanger R (1999) Dynamic scanning force microscopy at low temperatures on a van der Waals surface: graphite (0001). Appl Surf Sci 140(3–4):247–252
98. Giessibl FJ (2000) Atomic resolution on Si(111)-(7x7) by noncontact atomic force microscopy with a force sensor based on a quartz tuning fork. Appl Phys Lett 76(11):1470–1472
99. Giessibl FJ, Hembacher S, Bielefeldt H, Mannhart J (2000) Subatomic features on the silicon (111)-(7x7) surface observed by atomic force microscopy. Science 289(5478):422–425
100. Giessibl FJ, Hembacher S, Herz M, Schiller C, Mannhart J (2004) Stability considerations and implementation of cantilevers allowing dynamic force microscopy with optimal resolution: the qPlus sensor. Nanotechnology 15(2):S79–S86
101. Albers BJ, Liebmann M, Schwendemann TC, Baykara MZ, Heyde M, Salmeron M, Altman EI, Schwarz UD (2008) Combined low-temperature scanning tunneling/atomic force microscope for atomic resolution imaging and site-specific force spectroscopy. Rev Sci Instrum 79(3):033704

102. Giessibl FJ, Bielefeldt H, Hembacher S, Mannhart J (1999) Calculation of the optimal imaging parameters for frequency modulation atomic force microscopy. Appl Surf Sci 140(3–4):352–357
103. Perez R, Payne MC, Stich I, Terakura K (1997) Role of covalent tip-surface interactions in noncontact atomic force microscopy on reactive surfaces. Phys Rev Lett 78(4):678–681
104. Perez R, Stich I, Payne MC, Terakura K (1998) Surface-tip interactions in noncontact atomic-force microscopy on reactive surfaces: Si(111). Phys Rev B 58(16):10835–10849
105. Bennewitz R, Bammerlin M, Guggisberg M, Loppacher C, Baratoff A, Meyer E, Guntherodt HJ (1999) Aspects of dynamic force microscopy on NaCl/Cu(111): resolution, tip-sample interactions and cantilever oscillation characteristics. Surf Interface Anal 27(5–6):462–466
106. Guggisberg M, Bammerlin M, Loppacher C, Pfeiffer O, Abdurixit A, Barwich V, Bennewitz R, Baratoff A, Meyer E, Guntherodt HJ (2000) Separation of interactions by noncontact force microscopy. Phys Rev B 61(16):11151–11155
107. Kawai S, Glatzel T, Koch S, Baratoff A, Meyer E (2011) Interaction-induced atomic displacements revealed by drift-corrected dynamic force spectroscopy. Phys Rev B 83(3):035421
108. Sugimoto Y, Ueda K, Abe M, Morita S (2012) Three-dimensional scanning force/tunneling spectroscopy at room temperature. J Phys Condens Matter 24(8):084008
109. Braun DA, Weiner D, Such B, Fuchs H, Schirmeisen A (2009) Submolecular features of epitaxially grown PTCDA on Cu(111) analyzed by force field spectroscopy. Nanotechnology 20(26):264004
110. Mohn F, Gross L, Meyer G (2011) Measuring the short-range force field above a single molecule with atomic resolution. Appl Phys Lett 99(5):053106
111. Such B, Glatzel T, Kawai S, Koch S, Meyer E (2010) Three-dimensional force spectroscopy of KBr(001) by tuning fork-based cryogenic noncontact atomic force microscopy. J Vac Sci Technol B 28(3):C4B1
112. Such B, Glatzel T, Kawai S, Meyer E, Turansky R, Brndiar J, Stich I (2012) Interplay of the tip-sample junction stability and image contrast reversal on a Cu(111) surface revealed by the 3D force field. Nanotechnology 23(4):045705
113. Abe M, Sugimoto Y, Custance O, Morita S (2005) Atom tracking for reproducible force spectroscopy at room temperature with non-contact atomic force microscopy. Nanotechnology 16(12):3029–3034
114. Abe M, Sugimoto Y, Namikawa T, Morita K, Oyabu N, Morita S (2007) Drift-compensated data acquisition performed at room temperature with frequency modulation atomic force microscopy. Appl Phys Lett 90(20):203103
115. Enevoldsen GH, Pinto HP, Foster AS, Jensen MCR, Kuhnle A, Reichling M, Hofer WA, Lauritsen JV, Besenbacher F (2008) Detailed scanning probe microscopy tip models determined from simultaneous atom-resolved AFM and STM studies of the TiO(2)(110) surface. Phys Rev B 78(4):045416
116. Oyabu N, Pou P, Sugimoto Y, Jelinek P, Abe M, Morita S, Perez R, Custance O (2006) Single atomic contact adhesion and dissipation in dynamic force microscopy. Phys Rev Lett 96(10):106101
117. Pou P, Ghasemi SA, Jelinek P, Lenosky T, Goedecker S, Perez R (2009) Structure and stability of semiconductor tip apexes for atomic force microscopy. Nanotechnology 20(26):264015
118. Bechstein R, Gonzalez C, Schutte J, Jelinek P, Perez R, Kuhnle A (2009) 'All-inclusive' imaging of the rutile TiO_2(110) surface using NC-AFM. Nanotechnology 20(50):505703
119. Arai T, Gritschneder S, Troger L, Reichling M (2010) Atomic resolution force microscopy imaging on a strongly ionic surface with differently functionalized tips. J Vac Sci Technol B 28(6):1279–1283
120. Lauritsen JV, Foster AS, Olesen GH, Christensen MC, Kuhnle A, Helveg S, Rostrup-Nielsen JR, Clausen BS, Reichling M, Besenbacher F (2006) Chemical identification of point defects and adsorbates on a metal oxide surface by atomic force microscopy. Nanotechnology 17(14):3436–3441

121. Enevoldsen GH, Foster AS, Christensen MC, Lauritsen JV, Besenbacher F (2007) Noncontact atomic force microscopy studies of vacancies and hydroxyls of TiO(2)(110): experiments and atomistic simulations. Phys Rev B 76(20):205415
122. Uluutku B, Baykara MZ (2013) Effect of lateral tip stiffness on atomic-resolution force field spectroscopy. J Vac Sci Technol B 31(4):041801
123. Sun ZX, Boneschanscher MP, Swart I, Vanmaekelbergh D, Liljeroth P (2011) Quantitative atomic force microscopy with carbon monoxide terminated tips. Phys Rev Lett 106(4):046104
124. Schwarz A, Schwarz UD, Langkat S, Holscher H, Allers W, Wiesendanger R (2002) Dynamic force microscopy with atomic resolution at low temperatures. Appl Surf Sci 188(3–4):245–251
125. Rahe P, Schutte J, Schniederberend W, Reichling M, Abe M, Sugimoto Y, Kuhnle A (2011) Flexible drift-compensation system for precise 3D force mapping in severe drift environments. Rev Sci Instrum 82(6):063704
126. Fukuma T, Ichii T, Kobayashi K, Yamada H, Matsushige K (2005) True-molecular resolution imaging by frequency modulation atomic force microscopy in various environments. Appl Phys Lett 86(3):034103
127. Fukuma T, Kobayashi K, Matsushige K, Yamada H (2005) True atomic resolution in liquid by frequency-modulation atomic force microscopy. Appl Phys Lett 87(3):034101
128. Fukuma T, Ueda Y, Yoshioka S, Asakawa H (2010) Atomic-scale distribution of water molecules at the mica-water interface visualized by three-dimensional scanning force microscopy. Phys Rev Lett 104(1):016101
129. Herruzo ET, Asakawa H, Fukuma T, Garcia R (2013) Three-dimensional quantitative force maps in liquid with 10 piconewton, angstrom and sub-minute resolutions. Nanoscale 5(7):2678–2685
130. Asakawa H, Fukuma T (2009) Spurious-free cantilever excitation in liquid by piezoactuator with flexure drive mechanism. Rev Sci Instrum 80(10):103703
131. Asakawa H, Fukuma T (2009) The molecular-scale arrangement and mechanical strength of phospholipid/cholesterol mixed bilayers investigated by frequency modulation atomic force microscopy in liquid. Nanotechnology 20(26):264008
132. Mitani Y, Kubo M, Muramoto K, Fukuma T (2009) Wideband digital frequency detector with subtraction-based phase comparator for frequency modulation atomic force microscopy. Rev Sci Instrum 80(8):083705
133. Fukuma T (2009) Wideband low-noise optical beam deflection sensor with photothermal excitation for liquid-environment atomic force microscopy. Rev Sci Instrum 80(2):023707
134. Guthner P (1996) Simultaneous imaging of Si(111) 7x7 with atomic resolution in scanning tunneling microscopy, atomic force microscopy, and atomic force microscopy noncontact mode. J Vac Sci Technol B 14(4):2428–2431
135. Luthi R, Meyer E, Bammerlin M, Baratoff A, Lehmann T, Howald L, Gerber C, Guntherodt HJ (1996) Atomic resolution in dynamic force microscopy across steps on Si(111)7x7. Z Physik B-Condens Matter 100(2):165–167
136. Nakagiri N, Suzuki M, Okiguchi K, Sugimura H (1997) Site discrimination of adatoms in Si (111)-7x7 by noncontact atomic force microscopy. Surf Sci 373(1):L329–L332
137. Sawada D, Sugimoto Y, Abe M, Morita S (2010) Observation of subsurface atoms of the si (111)-(7x7) surface by atomic force microscopy. Appl Phys Express 3(11):116602
138. Sugimoto Y, Nakajima Y, Sawada D, Morita K, Abe M, Morita S (2010) Simultaneous AFM and STM measurements on the Si(111)-(7x7) surface. Phys Rev B 81(24):245322
139. Uozumi T, Tomiyoshi Y, Suehira N, Sugawara Y, Morita S (2002) Observation of Si(100) surface with noncontact atomic force microscope at 5 K. Appl Surf Sci 188(3–4):279–284
140. Sweetman A, Jarvis S, Danza R, Bamidele J, Gangopadhyay S, Shaw GA, Kantorovich L, Moriarty P (2011) Toggling bistable atoms via mechanical switching of bond angle. Phys Rev Lett 106(13):136101

141. Sweetman A, Jarvis S, Danza R, Bamidele J, Kantorovich L, Moriarty P (2011) Manipulating Si(100) at 5 K using qPlus frequency modulated atomic force microscopy: role of defects and dynamics in the mechanical switching of atoms. Phys Rev B 84(8):085426
142. Sweetman A, Jarvis S, Danza R, Moriarty P (2012) Effect of the tip state during qPlus noncontact atomic force microscopy of Si(100) at 5 K: probing the probe. Beilstein J Nanotechnol 3:25–32
143. Naitoh Y, Li YJ, Nomura H, Kageshima M, Sugawara Y (2010) Effect of surface stress around the sa step of Si(001) on the dimer structure determined by noncontact atomic force microscopy at 5 K. J Physical Soc Japan 79(1):013601
144. Sugimoto Y, Abe M, Yoshimoto K, Custance O, Yi I, Morita S (2005) Non-contact atomic force microscopy study of the Sn/Si(111) mosaic phase. Appl Surf Sci 241(1–2):23–27
145. Yi I, Sugimoto Y, Nishi R, Morita S (2006) Study on topographic images of Sn/Si(111)-$\left(\sqrt{3}\times\sqrt{3}\right)$R30° surface by non-contact AFM. Surf Sci 600(17):3382–3387
146. Yi I, Nishi R, Sugimoto Y, Morita S (2007) Non-contact AFM observation of the $\left(\sqrt{3}\times\sqrt{3}\right)$ to (3x3) phase transition on Sn/Ge(111) and Sn/Si(111) surfaces. Appl Surf Sci 253(6):3072–3076
147. Sugimoto Y, Pou P, Custance O, Jelinek P, Morita S, Perez R, Abe M (2006) Real topography, atomic relaxations, and short-range chemical interactions in atomic force microscopy: the case of the alpha-Sn/Si(111)-$\left(\sqrt{3}\times\sqrt{3}\right)$R30° surface. Phys Rev B 73(20):205329
148. Abe M, Sugimoto Y, Morita S (2005) Imaging the restatom of the Ge(111)-c(2x8) surface with noncontact atomic force microscopy at room temperature. Nanotechnology 16(3): S68–S72
149. Schwarz A, Allers W, Schwarz UD, Wiesendanger R (2000) Detection of doping atom distributions and individual dopants in InAs(110) by dynamic-mode scanning force microscopy in ultrahigh vacuum. Phys Rev B 62(20):13617–13622
150. Henrich VE, Cox PA (1994) The surface science of metal oxides. Cambridge University Press, Cambridge
151. Diebold U (2003) The surface science of titanium dioxide. Surf Sci Rep 48(5–8):53–229
152. Freund HJ, Pacchioni G (2008) Oxide ultra-thin films on metals: new materials for the design of supported metal catalysts. Chem Soc Rev 37(10):2224–2242
153. Raza H, Pang CL, Haycock SA, Thornton G (1999) Non-contact atomic force microscopy imaging of TiO_2(100) surfaces. Appl Surf Sci 140(3–4):271–275
154. Enevoldsen GH, Pinto HP, Foster AS, Jensen MCR, Hofer WA, Hammer B, Lauritsen JV, Besenbacher F (2009) Imaging of the hydrogen subsurface site in rutile TiO(2). Phys Rev Lett 102(13):136103
155. Yurtsever A, Sugimoto Y, Abe M, Morita S (2010) NC-AFM imaging of the TiO(2)(110)-(1x1) surface at low temperature. Nanotechnology 21(16):165702
156. Yurtsever A, Fernandez-Torre D, Gonzalez C, Jelinek P, Pou P, Sugimoto Y, Abe M, Perez R, Morita S (2012) Understanding image contrast formation in TiO_2 with force spectroscopy. Phys Rev B 85(12):125416
157. Pang CL, Raza H, Haycock SA, Thornton G (2002) Noncontact atomic force microscopy imaging of ultrathin Al_2O_3 on NiAl(110). Phys Rev B 65(20):201401
158. Wang J, Howard A, Egdell RG, Pethica JB, Foord JS (2002) Arrangement of rotational domains of the $\left(\sqrt{31}\times\sqrt{31}\right)$ R +/− 9° reconstruction of Al_2O_3(0001) revealed by non-contact AFM. Surf Sci 515(2–3):337–343
159. Simon GH, Konig T, Nilius M, Rust HP, Heyde M, Freund HJ (2008) Atomically resolved force microscopy images of complex surface unit cells: ultrathin alumina film on NiAl(110). Phys Rev B 78(11):113401
160. Simon GH, Konig T, Rust HP, Heyde M, Freund HJ (2009) Atomic structure of the ultrathin alumina on NiAl(110) and its antiphase domain boundaries as seen by frequency modulation dynamic force microscopy. New J Phys 11(9):093009

161. Lauritsen JV, Jensen MCR, Venkataramani K, Hinnemann B, Helveg S, Clausen BS, Besenbacher F (2009) Atomic-scale structure and stability of the $\left(\sqrt{31} \times \sqrt{31}\right)$R9° surface of Al_2O_3(0001). Phys Rev Lett 103(7):076103
162. Heyde M, Simon GH, Lichtenstein L (2013) Resolving oxide surfaces – from point and line defects to complex network structures. Phys Status Solidi B-Basic Solid State Phys 250(5):895–921
163. Simon GH, Konig T, Heinke L, Lichtenstein L, Heyde M, Freund HJ (2011) Atomic structure of surface defects in alumina studied by dynamic force microscopy: strain-relief-, translation- and reflection-related boundaries, including their junctions. New J Phys 13(12):123028
164. Fukui K, Namai Y, Iwasawa Y (2002) Imaging of surface oxygen atoms and their defect structures on CeO_2(111) by noncontact atomic force microscopy. Appl Surf Sci 188(3–4):252–256
165. Namai Y, Fukui KI, Iwasawa Y (2003) Atom-resolved noncontact atomic force microscopic and scanning tunneling microscopic observations of the structure and dynamic behavior of CeO_2(111) surfaces. Catal Today 85(2–4):79–91
166. Namai Y, Fukui K, Iwasawa Y (2003) Atom-resolved noncontact atomic force microscopic observations of CeO_2(111) surfaces with different oxidation states: surface structure and behavior of surface oxygen atoms. J Phys Chem B 107(42):11666–11673
167. Gritschneder S, Reichling M (2007) Structural elements of CeO_2(111) surfaces. Nanotechnology 18(4):044024
168. Gritschneder S, Reichling M (2008) Atomic resolution imaging on CeO_2(111) with hydroxylated probes. J Phys Chem C 112(6):2045–2049
169. Pieper HH, Derks C, Zoellner MH, Olbrich R, Troger L, Schroeder T, Neumann M, Reichling M (2012) Morphology and nanostructure of CeO_2(111) surfaces of single crystals and Si(111) supported ceria films. Phys Chem Chem Phys 14(44):15361–15368
170. Hosoi H, Sueoka K, Hayakawa K, Mukasa K (2000) Atomic resolved imaging of cleaved NiO(100) surfaces by NC-AFM. Appl Surf Sci 157(4):218–221
171. Allers W, Langkat S, Wiesendanger R (2001) Dynamic low-temperature scanning force microscopy on nickel oxide (001). Appl Phys Mater Sci Process 72:S27–S30
172. Kaiser U, Schwarz A, Wiesendanger R (2007) Magnetic exchange force microscopy with atomic resolution. Nature 446(7135):522–525
173. Schmid M, Mannhart J, Giessibl FJ (2008) Searching atomic spin contrast on nickel oxide (001) by force microscopy. Phys Rev B 77(4):045402
174. Kaiser U, Schwarz A, Wiesendanger R (2008) Evaluating local properties of magnetic tips utilizing an antiferromagnetic surface. Phys Rev B 78(10):104418
175. Barth C, Henry CR (2003) Atomic resolution imaging of the (001) surface of UHV cleaved MgO by dynamic scanning force microscopy. Phys Rev Lett 91(19):196102
176. Heyde M, Sterrer M, Rust HP, Freund HJ (2005) Atomic resolution on MgO(001) by atomic force microscopy using a double quartz tuning fork sensor at low-temperature and ultrahigh vacuum. Appl Phys Lett 87(8):083104
177. Heyde M, Sterrer M, Rust HP, Freund HJ (2006) Frequency modulated atomic force microscopy on MgO(001) thin films: interpretation of atomic image resolution and distance dependence of tip-sample interaction. Nanotechnology 17(7):S101–S106
178. Torbrugge S, Ostendorf F, Reichling M (2009) Stabilization of zinc-terminated ZnO(0001) by a modified surface stoichiometry. J Phys Chem C 113(12):4909–4914
179. Suzuki S, Ohminami Y, Tsutsumi T, Shoaib MM, Ichikawa M, Asakura K (2003) The first observation of an atomic scale noncontact AFM image of MoO_3(010). Chem Lett 32(12):1098–1099
180. Rasmussen MK, Foster AS, Hinnemann B, Canova FF, Helveg S, Meinander K, Martin NM, Knudsen J, Vlad A, Lundgren E, Stierle A, Besenbacher F, Lauritsen JV (2011) Stable cation inversion at the $MgAl_2O_4$(100) surface. Phys Rev Lett 107(3):036102

181. Rasmussen MK, Meinander K, Besenbacher F, Lauritsen JV (2012) Noncontact atomic force microscopy study of the spinel $MgAl_2O_4(111)$ surface. Beilstein J Nanotechnol 3:192–197
182. Kishimoto S, Kageshima M, Naitoh Y, Li YJ, Sugawara Y (2008) Study of oxidized Cu(110) surface using noncontact atomic force microscopy. Surf Sci 602(13):2175–2182
183. Lauritsen JV, Reichling M (2010) Atomic resolution non-contact atomic force microscopy of clean metal oxide surfaces. J Phys Condens Matter 22(26):263001
184. Irie H, Sunada K, Hashimoto K (2004) Recent developments in TiO_2 photocatalysis: novel applications to interior ecology materials and energy saving systems. Electrochemistry 72(12):807–812
185. Onishi H, Iwasawa Y (1994) Reconstruction of $TiO_2(110)$ surface – STM study with atomic-scale resolution. Surf Sci 313(1–2):L783–L789
186. Wendt S, Matthiesen J, Schaub R, Vestergaard EK, Laegsgaard E, Besenbacher F, Hammer B (2006) Formation and splitting of paired hydroxyl groups on reduced $TiO_2(110)$. Phys Rev Lett 96(6):066107
187. Schaub R, Thostrup P, Lopez N, Laegsgaard E, Stensgaard I, Norskov JK, Besenbacher F (2001) Oxygen vacancies as active sites for water dissociation on rutile TiO(2)(110). Phys Rev Lett 87(26):266104
188. Wendt S, Schaub R, Matthiesen J, Vestergaard EK, Wahlstrom E, Rasmussen MD, Thostrup P, Molina LM, Laegsgaard E, Stensgaard I, Hammer B, Besenbacher F (2005) Oxygen vacancies on $TiO_2(110)$ and their interaction with H_2O and O-2: a combined high-resolution STM and DFT study. Surf Sci 598(1–3):226–245
189. Foster AS, Pakarinen OH, Airaksinen JM, Gale JD, Nieminen RM (2003) Simulating atomic force microscopy imaging of the ideal and defected $TiO_2(110)$ surface. Phys Rev B 68(19):195410
190. Pinto HP, Enevoldsen GH, Besenbacher F, Lauritsen JV, Foster AS (2009) The role of tip size and orientation, tip-surface relaxations and surface impurities in simultaneous AFM and STM studies on the TiO(2)(110) surface. Nanotechnology 20(26):264020
191. Bammerlin M, Lüthi R, Meyer E, Baratoff A, Lü J, Guggisberg M, Gerber C, Howald L, Güntherodt HJ (1997) True atomic resolution on the surface of an insulator via ultrahigh vacuum dynamic force microscopy. Probe Microsc 1:3
192. Foster AS, Barth C, Shluger AL, Reichling M (2001) Unambiguous interpretation of atomically resolved force microscopy images of an insulator. Phys Rev Lett 86(11):2373–2376
193. Foster AS, Barth C, Shluger AL, Nieminen RM, Reichling M (2002) Role of tip structure and surface relaxation in atomic resolution dynamic force microscopy: $CaF_2(111)$ as a reference surface. Phys Rev B 66(23):235417
194. Barth C, Reichling M (2000) Resolving ions and vacancies at step edges on insulating surfaces. Surf Sci 470(1–2):L99–L103
195. Bennewitz R, Schar S, Barwich V, Pfeiffer O, Meyer E, Krok F, Such B, Kolodzej J, Szymonski M (2001) Atomic-resolution images of radiation damage in KBr. Surf Sci 474(1–3):L197–L202
196. Bennewitz R, Pfeiffer O, Schar S, Barwich V, Meyer E, Kantorovich LN (2002) Atomic corrugation in nc-AFM of alkali halides. Appl Surf Sci 188(3–4):232–237
197. Fujii S, Fujihira M (2007) Atomic contrast on a point defect on $CaF_2(111)$ imaged by non-contact atomic force microscopy. Nanotechnology 18(8):084011
198. Giessibl FJ, Reichling M (2005) Investigating atomic details of the $CaF_2(111)$ surface with a qPlus sensor. Nanotechnology 16(3):S118–S124
199. Hirth S, Ostendorf F, Reichling M (2006) Lateral manipulation of atomic size defects on the $CaF_2(111)$ surface. Nanotechnology 17(7):S148–S154
200. Hoffmann R, Lantz MA, Hug HJ, van Schendel PJA, Kappenberger P, Martin S, Baratoff A, Guntherodt HJ (2002) Atomic resolution imaging and force versus distance measurements on KBr(001) using low temperature scanning force microscopy. Appl Surf Sci 188(3–4):238–244

201. Bammerlin M, Luthi R, Meyer E, Baratoff A, Lu J, Guggisberg M, Loppacher C, Gerber C, Guntherodt HJ (1998) Dynamic SFM with true atomic resolution on alkali halide surfaces. Appl Phys Mater Sci Process 66:S293–S294
202. Barth C, Henry CR (2008) Imaging Suzuki precipitates on NaCl: Mg(2+)(001) by scanning force microscopy. Phys Rev Lett 100(9):096101
203. Barth C, Henry CR (2009) NaCl(001) surfaces nanostructured by Suzuki precipitates: a scanning force microscopy study. New J Phys 11(4):043003
204. Foster AS, Barth C, Henry CR (2009) Chemical identification of ions in doped NaCl by scanning force microscopy. Phys Rev Lett 102(25):256103
205. Bennewitz R, Foster AS, Kantorovich LN, Bammerlin M, Loppacher C, Schar S, Guggisberg M, Meyer E, Shluger AL (2000) Atomically resolved edges and kinks of NaCl islands on Cu(111): experiment and theory. Phys Rev B 62(3):2074–2084
206. Klust A, Ohta T, Bostwick AA, Yu QM, Ohuchi FS, Olmstead MA (2004) Atomically resolved imaging of a CaF bilayer on Si(111): subsurface atoms and the image contrast in scanning force microscopy. Phys Rev B 69(3):035405
207. Filleter T, Paul W, Bennewitz R (2008) Atomic structure and friction of ultrathin films of KBr on Cu(100). Phys Rev B 77(3):035430
208. Holscher H, Allers W, Schwarz UD, Schwarz A, Wiesendanger R (2000) Interpretation of "true atomic resolution" images of graphite (0001) in noncontact atomic force microscopy. Phys Rev B 62(11):6967–6970
209. Hembacher S, Giessibl FJ, Mannhart J, Quate CF (2003) Revealing the hidden atom in graphite by low-temperature atomic force microscopy. Proc Natl Acad Sci U S A 100(22):12539–12542
210. Kawai S, Kawakatsu H (2009) Surface-relaxation-induced giant corrugation on graphite (0001). Phys Rev B 79(11):115440
211. Ashino M, Schwarz A, Behnke T, Wiesendanger R (2004) Atomic-resolution dynamic force microscopy and spectroscopy of a single-walled carbon nanotube: characterization of interatomic van der Waals forces. Phys Rev Lett 93(13):136101
212. Loffler D, Uhlrich JJ, Baron M, Yang B, Yu X, Lichtenstein L, Heinke L, Buchner C, Heyde M, Shaikhutdinov S, Freund HJ, Wlodarczyk R, Sierka M, Sauer J (2010) Growth and structure of crystalline silica sheet on Ru(0001). Phys Rev Lett 105(14):146104
213. Lichtenstein L, Heyde M, Freund HJ (2012) Atomic arrangement in two-dimensional silica: from crystalline to vitreous structures. J Phys Chem C 116(38):20426–20432
214. Majzik Z, Tchalala MR, Svec M, Hapala P, Enriquez H, Kara A, Mayne AJ, Dujardin G, Jelinek P, Oughaddou H (2013) Combined AFM and STM measurements of a silicene sheet grown on the Ag(111) surface. J Phys Condens Matter 25(22):225301
215. Sun ZX, Hamalainen SK, Sainio J, Lahtinen J, Vanmaekelbergh D, Liljeroth P (2011) Topographic and electronic contrast of the graphene moire on Ir(111) probed by scanning tunneling microscopy and noncontact atomic force microscopy. Phys Rev B 83(8):081415
216. Boneschanscher MP, van der Lit J, Sun ZX, Swart I, Liljeroth P, Vanmaekelbergh D (2012) Quantitative atomic resolution force imaging on epitaxial graphene with reactive and nonreactive AFM probes. ACS Nano 6(11):10216–10221
217. Hamalainen SK, Boneschanscher MP, Jacobse PH, Swart I, Pussi K, Moritz W, Lahtinen J, Liljeroth P, Sainio J (2013) Structure and local variations of the graphene moire on Ir(111). Phys Rev B 88(20):6
218. Dedkov Y, Voloshina E (2014) Multichannel scanning probe microscopy and spectroscopy of graphene moire structures. Phys Chem Chem Phys 16(9):3894–3908
219. Fukui K, Onishi H, Iwasawa Y (1997) Imaging of individual formate ions adsorbed on TiO_2(110) surface by non-contact atomic force microscopy. Chem Phys Lett 280(3–4):296–301
220. Rahe P, Nimmrich M, Nefedov A, Naboka M, Woll C, Kuhnle A (2009) Transition of molecule orientation during adsorption of terephthalic acid on rutile TiO_2(110). J Phys Chem C 113(40):17471–17478

221. Schutte J, Bechstein R, Rahe P, Rohlfing M, Kuhnle A, Langhals H (2009) Imaging perylene derivatives on rutile TiO_2(110) by noncontact atomic force microscopy. Phys Rev B 79(4):045428
222. Loske F, Bechstein R, Schutte J, Ostendorf F, Reichling M, Kuhnle A (2009) Growth of ordered C_{60} islands on TiO_2(110). Nanotechnology 20(6):065606
223. Fremy S, Schwarz A, Lammle K, Prosenc M, Wiesendanger R (2009) The monomer-to-dimer transition and bimodal growth of Co-salen on NaCl(001): a high resolution atomic force microscopy study. Nanotechnology 20(40):405608
224. Lammle K, Trevethan T, Schwarz A, Watkins M, Shluger A, Wiesendanger R (2010) Unambiguous determination of the adsorption geometry of a metal-organic complex on a bulk insulator. Nano Lett 10(8):2965–2971
225. Pawlak R, Kawai S, Fremy S, Glatzel T, Meyer E (2011) Atomic-scale mechanical properties of orientated C(60) molecules revealed by noncontact atomic force microscopy. ACS Nano 5(8):6349–6354
226. Pawlak R, Kawai S, Fremy S, Glatzel T, Meyer E (2012) High-resolution imaging of C_{60} molecules using tuning-fork-based non-contact atomic force microscopy. J Phys Condens Matter 24(8):084005
227. Such B, Trevethan T, Glatzel T, Kawai S, Zimmerli L, Meyer E, Shluger AL, Amijs CHM, de Mendoza P, Echavarren AM (2010) Functionalized truxenes: adsorption and diffusion of single molecules on the KBr(001) surface. ACS Nano 4(6):3429–3439
228. Pawlak R, Fremy S, Kawai S, Glatzel T, Fang HJ, Fendt LA, Diederich F, Meyer E (2012) Directed rotations of single porphyrin molecules controlled by localized force spectroscopy. ACS Nano 6(7):6318–6324
229. Sasahara A, Uetsuka H, Onishi H (2001) NC-AFM topography of HCOO and CH(3)COO molecules co-adsorbed on TiO(2)(110). Appl Phys Mater Sci Process 72:S101–S103
230. Gritschneder S, Iwasawa Y, Reichling M (2007) Strong adhesion of water to CeO_2(111). Nanotechnology 18(4):044025
231. Burke SA, Mativetsky JM, Fostner S, Grutter P (2007) C_{60} on alkali halides: epitaxy and morphology studied by noncontact AFM. Phys Rev B 76(3):035419
232. Burke SA, Ledue JM, Topple JM, Fostner S, Grutter P (2009) Relating the functional properties of an organic semiconductor to molecular structure by nc-AFM. Adv Mater 21(20):2029–2033
233. Gotsmann B, Seidel C, Anczykowski B, Fuchs H (1999) Conservative and dissipative tip-sample interaction forces probed with dynamic AFM. Phys Rev B 60(15):11051–11061
234. Lantz MA, Hoffmann R, Foster AS, Baratoff A, Hug HJ, Hidber HR, Guntherodt HJ (2006) Site-specific force-distance characteristics on NaCl(001): measurements versus atomistic simulations. Phys Rev B 74(24):245426
235. Hoffmann R, Barth C, Foster AS, Shluger AL, Hug HJ, Guntherodt HJ, Nieminen RM, Reichling M (2005) Measuring site-specific cluster-surface bond formation. J Am Chem Soc 127(50):17863–17866
236. Hembacher S, Giessibl FJ, Mannhart J, Quate CF (2005) Local spectroscopy and atomic imaging of tunneling current, forces, and dissipation on graphite. Phys Rev Lett 94(5):056101
237. Albers BJ, Schwendemann TC, Baykara MZ, Pilet N, Liebmann M, Altman EI, Schwarz UD (2009) Data acquisition and analysis procedures for high-resolution atomic force microscopy in three dimensions. Nanotechnology 20(26):264002
238. Holscher H, Langkat SM, Schwarz A, Wiesendanger R (2002) Measurement of three-dimensional force fields with atomic resolution using dynamic force spectroscopy. Appl Phys Lett 81(23):4428–4430
239. Ashino M, Schwarz A, Holscher H, Schwarz UD, Wiesendanger R (2005) Interpretation of the atomic scale contrast obtained on graphite and single-walled carbon nanotubes in the dynamic mode of atomic force microscopy. Nanotechnology 16(3):S134–S137

240. Schwarz A, Holscher H, Langkat SM, Wiesendanger R (2003) Three-dimensional force field spectroscopy. AIP Conf Proc 696:68–78
241. Bhushan B (2002) Introduction to tribology. Wiley, New York
242. Bhushan B (2005) Nanotribology and nanomechanics: an introduction. Springer, Berlin
243. Giessibl FJ, Herz M, Mannhart J (2002) Friction traced to the single atom. Proc Natl Acad Sci U S A 99(19):12006–12010
244. Atabak M, Unverdi O, Ozer HO, Oral A (2009) Sub-Angstrom oscillation amplitude non-contact atomic force microscopy for lateral force gradient measurement. Appl Surf Sci 256(5):1299–1303
245. Weymouth AJ, Meuer D, Mutombo P, Wutscher T, Ondracek M, Jelinek P, Giessibl FJ (2013) Atomic structure affects the directional dependence of friction. Phys Rev Lett 111(12):126103
246. Kawai S, Glatzel T, Koch S, Such B, Baratoff A, Meyer E (2010) Ultrasensitive detection of lateral atomic-scale interactions on graphite (0001) via bimodal dynamic force measurements. Phys Rev B 81(8):085420
247. Ternes M, Lutz CP, Hirjibehedin CF, Giessibl FJ, Heinrich AJ (2008) The force needed to move an atom on a surface. Science 319(5866):1066–1069
248. Weymouth AJ, Hofmann T, Giessibl FJ (2013) Quantifying molecular stiffness and interaction with lateral force microscopy. Science 343:1120–1122
249. Welker J, Giessibl FJ (2012) Revealing the angular symmetry of chemical bonds by atomic force microscopy. Science 336(6080):444–449
250. Kimura K, Ido S, Oyabu N, Kobayashi K, Hirata Y, Imai T, Yamada H (2010) Visualizing water molecule distribution by atomic force microscopy. J Chem Phys 132(19):194705
251. Asakawa H, Yoshioka S, Nishimura K, Fukuma T (2012) Spatial distribution of lipid headgroups and water molecules at membrane/water interfaces visualized by three-dimensional scanning force microscopy. ACS Nano 6(10):9013–9020
252. Sugimoto Y, Jelinek P, Pou P, Abe M, Morita S, Perez R, Custance O (2007) Mechanism for room-temperature single-atom lateral manipulations on semiconductors using dynamic force microscopy. Phys Rev Lett 98(10):106104
253. Sugimoto Y, Pou P, Custance O, Jelinek P, Abe M, Perez R, Morita S (2008) Complex patterning by vertical interchange atom manipulation using atomic force microscopy. Science 322(5900):413–417

Applications of Synchrotron-Based X-Ray Photoelectron Spectroscopy in the Characterization of Nanomaterials

9

W. H. Doh, V. Papaefthimiou, and S. Zafeiratos

Contents

1 Definition of the Topic 318
2 Overview 318
3 Introduction 320
4 Experimental and Instrumental Methodology 321
4.1 The Fundamentals of XPS 321
4.2 Advantages in X-Ray Photoelectron Spectroscopy by Synchrotron Radiation 336
5 Key Research Findings 344
5.1 Scanning Photoelectron Microscopy: XPS with High Lateral Resolution 344
5.2 Ambient Pressure X-Ray Photoelectron Spectroscopy: XPS Under Pressure 349
5.3 Hard X-Ray Photoemission Spectroscopy: XPS in the Bulk 356
6 Conclusions and Future Perspective 362
References 363

Keywords

Review • Near ambient pressure XPS (NAP-XPS) • Hard X-ray photoelectron Spectroscopy (HXPES) • Depth profile • Nanocrystals • Catalysis • Batteries • Fuel cells

Abbreviations

AES	Auger electron spectroscopy
AL	Attenuation length
APPES or APXPS	Ambient pressure photoelectron spectroscopy
ASF	Atomic sensitivity factor

W.H. Doh • V. Papaefthimiou • S. Zafeiratos (✉)
Institut de chimie et procédés pour l'énergie, l'environnement et la santé (ICPEES), UMR 7515 du CNRS-Université de Strasbourg, ECPM, Strasbourg, France
e-mail: spiros.zafeiratos@unistra.fr

© Springer-Verlag Berlin Heidelberg 2015

C.S.S.R. Kumar (ed.), *Surface Science Tools for Nanomaterials Characterization*,
DOI 10.1007/978-3-662-44551-8_9

E_B	Binding energy
EDX	Energy dispersive X-ray spectroscopy
EELS	Energy electron loss spectroscopy
E_k	Kinetic energy
ESCA	Electron spectroscopy for chemical analysis
EXAFS	Extended X-ray absorption fine structure
FWHM	Full width at half maximum
HXPES	Hard X-ray photoemission spectroscopy
IMFP	Inelastic mean free path
LECBD	Low-energy cluster beam deposition
MEA	Membrane electrode assembly
NPs	Nanoparticles
PES	Photoemission spectroscopy
RPES	Resonant X-ray photoemission spectroscopy
SEI	Solid electrolyte interface
SEM	Scanning electron microscopy
SPEM	Scanning photoelectron microscopy
SPI	Solid permeable interface
SR	Synchrotron radiation
SR-XPS	Synchrotron radiation X-ray photoelectron spectroscopy
TEM	Transmission electron microscopy
UHV	Ultrahigh vacuum
XPS	X-ray photoelectron spectroscopy
Φ	Work function

1 Definition of the Topic

X-ray photoelectron spectroscopy (XPS) has proved to be one of the most powerful experimental techniques for the chemical analysis of solid surfaces and nanomaterials. The use of synchrotron radiation (SR) as the excitation source of photoelectrons offers particular advantages compared to the conventional laboratory X-ray tubes and extends the capabilities of the technique. In this chapter we intend to give an overview of the synchrotron-based X-ray photoelectron spectroscopy (SR-XPS), giving emphasis to applications related to nanomaterials and, in particular, to nanoparticles (NPs).

2 Overview

Nanomaterials have attracted tremendous attention in the last 20 years due to their size- and shape-dependent properties, which are usually different than those of their bulk counterparts. Their unique electronic, optical, magnetic, and reactivity characteristics have led to a wide range of applications in several technological

fields, including electronics, photonics, catalysis, chemical sensing, etc. [1]. Today's research aims to identify and develop innovative nanomaterials with tailored properties and improved performance. To this direction several methods have been proposed and applied for the fabrication of nanomaterials [1–3]. Along with the progress in the synthesis and fabrication methods, numerous characterization techniques have been developed in order to better *understand* the chemical, physical, and mechanical properties of the produced nanomaterials [2, 4]. The main challenge is to find and optimize techniques with a capacity to characterize nanomaterials with the highest possible precision and specificity [4].

Traditionally, material's characterization employs techniques with electrons as a probe, like transmission electron microscopy (TEM) and energy electron loss spectroscopy (EELS), or photons such as UV−visible absorption spectroscopy, extended X-ray absorption fine structure (EXAFS), Raman spectroscopies, etc. Most of these techniques probe the overall volume of the nanomaterials (*bulk characterization techniques*) and are not particularly sensitive to the surface. Since the surface to volume ratio of nanomaterials is high, bulk techniques can also provide information for the surface, if nano-objects with very small sizes (<5 nm) are probed.[1] Alternatively, for larger and less uniform objects, or if surface characterization is of major interest for the application (i.e., in catalysis), it is preferential that methods with high surface sensitivity or specificity are employed. Usually techniques utilizing low- and medium-energy electrons are better suited for surface-sensitive studies, due to the strong interaction of electrons with matter. Among these techniques, XPS is probably the most powerful, since it can be used to perform elemental and chemical analysis of the nanomaterials, while under certain conditions it can also quantify their composition.

Several excellent essays describe in detail theoretical and practical aspects of X-ray photoelectron spectroscopy (see, e.g., [5, 6]), and we propose referring to these sources for more details about the technique. The objective of this chapter is to discuss synchrotron-based XPS and describe the particular aspects and the capabilities this technique can profit by using SR. Although the information presented here can be applied for the analysis of both extended and any type of nanoscale solid materials, the presented examples are selected from the field of nanoparticles' research, in order to make the discussion more cohesive. We start by introducing the necessary background of the technique, including basic phenomena and instrumentation aspects. In the next section we focus on the presentation of the main advantages to perform XPS at synchrotrons, and we demonstrate some characteristic examples. In the last part, we refer to relatively recent developments in SR-XPS, by presenting three variations of the technique, while we discuss some selected examples to indicate the potential of these methods in the nanomaterials' research.

[1]Of course the number of surface atoms depends very much on the shape of the nano-object.

3 Introduction

X-ray photoelectron spectroscopy (XPS), also known as electron spectroscopy for chemical analysis (ESCA) or photoemission spectroscopy (PES), is a characterization technique with high surface sensitivity often employed to study solid surfaces. Although the theoretical background of the technique (*photoelectric effect*) was described already since 1905 by Albert Einstein, it was not since 1954 that the first high-energy-resolution XPS spectrum was reported by Kai Siegbahn and his group in Uppsala (Sweden) [7, 8]. The first commercial XPS instruments became available in the early 1970s by Varian, vacuum generators (VG), and other manufactures, and since then the technique has been applied to several research domains. Nowadays, XPS has been well established as a standard surface characterization technique both in industry and academia.

The technique measures the kinetic energy (E_k) of photoelectrons originating from core or valence band energy levels and is particularly sensitive to atoms at or near the surface of the solid specimen. The energy of the photoelectrons (peak position in the kinetic or binding energy scale) is used for elemental analysis, while the technique can be easily employed in order to identify the valence state of the element (i.e., oxidation state). In addition, from the relative number of detected photoelectrons (peak height or area of the spectrum), quantitative analysis of the surface composition can be performed.

Typically the radiation used for the excitation of photoelectrons is produced by laboratory X-ray sources, with or without the use of quartz crystal monochromators. The radiation produced by these X-ray sources has certain energies (commonly 1,253.6 eV (MgKα) or 1,486.6 eV (AlKα)), while the energy resolution can vary from about 0.3 to 0.7 eV depending on the instrument. The development of large-scale SR facilities, and especially third-generation synchrotrons, significantly increased the spectral resolution, but more importantly the photon flux per unit area (related to brilliance) by at least 10 orders of magnitude. This is of major importance when low-density systems (such as atomic adsorbates or supported nanoparticles[2]) are to be studied, especially if fast processes have to be monitored in real time, e.g., surface reactions [9].

An overview of the production of synchrotron radiation is out of the scope of the present chapter, and the reader can refer to excellent reviews on this topic [8, 10]. Here we briefly recall the basic principles of radiation production in synchrotron facilities, in order to facilitate the comprehension. In a synchrotron, bunches of relativistic electrons are kept on a circular path inside an evacuated storage ring. Radiation is emitted whenever these bunches of electrons are transversely accelerated in bending magnets or insertion devices (usually called *wigglers* and *undulators*). The produced radiation beam is transferred to the experimental station by several meters long tube called the *beamline*. Besides the aforementioned high brilliance and energy

[2]Nanoparticles or nanopowders or nanoclusters or nanocrystals are microscopic particles with at least one dimension less than 100 nm.

resolution, synchrotron radiation also offers a broad, tunable energy range (from IR to hard X-rays) selected by the user, polarized light (linear and circular) and finally the possibility of producing extremely short pulses at frequencies as high as a MHz. Due to the advantages of SR, several variations of the XPS technique have been developed during the last few years. Among them, the most promising for studies on nanomaterials are *(i)* scanning photoelectron microscopy (SPEM), *(ii)* ambient pressure X-ray photoelectron spectroscopy (APXPS), and *(iii)* hard X-ray photoemission spectroscopy (HXPES). These methods will be explained in detail in Sect. 5.

4 Experimental and Instrumental Methodology

4.1 The Fundamentals of XPS

4.1.1 The Physical Principles

The fundamentals of X-ray photoelectron spectroscopy have been previously explained in numerous reports [5, 11]. The photoelectric effect (a schematic view of which is shown in Fig. 9.1a) was observed by Hertz in 1887 and theoretically explained by Einstein in 1905. The basic equation that describes this effect for condensed phase systems is[3]

$$E_K = hv - E_B - \varphi \tag{9.1}$$

where E_K is the kinetic energy of the emitted photoelectron, hv the energy of the incident photons, E_B the binding energy that the ejected photoelectron had in the solid relative to the Fermi level of the sample, and φ is the work function of the sample, which is defined as the minimum energy which is required to remove an electron from the surface to infinity (see Fig. 9.1b). In practice, in a photoemission experiment over metallic and semiconducting samples, E_K and φ are replaced by the kinetic energy of the electron as measured by the spectrometer and the work function of the spectrometer (φ_{sp}), respectively (Fig. 9.1b). Since the spectrometer remains under ultrahigh vacuum (UHV), the φ_{sp} term is constant (typically around 4.5 eV), for a given instrument, and can be easily compensated by the application of an equivalent potential. Therefore, the measurement of the photoelectron E_K via the electron analyzer and the knowledge of the incoming photon energy allow the calculation of the binding energy according to Eq. 9.2. For electrical insulating samples, the above description is complicated, since the reference Fermi level is neither well defined nor in electrical contact with the spectrometer (this problem is usually referred to as electrostatic charging). In that case a well-known internal reference is needed [12]:

[3]Please note that this formula is slightly modified when applied to gasses, since the work function is not defined in that case.

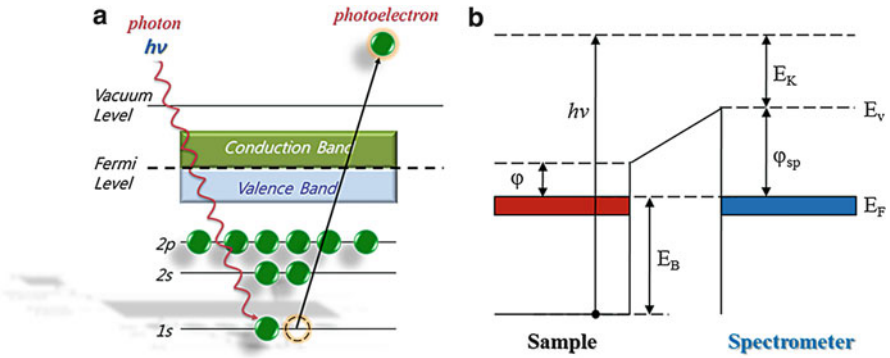


Fig. 9.1 (**a**) Schematic illustration of the core-level photoelectron emission by the photoelectric effect in a metal. (**b**) Energy-level diagram of the sample and the spectrometer in a core-level photoemission experiment of a metallic sample

$$E_B = hv - E_K \tag{9.2}$$

Photoelectron spectroscopy can equally probe core-level and valence band electrons. However, the valence band spectra are typically quite complex because of the large number of valence levels overlapping in a small energy region. On the other hand, in the core-level spectra, the position of atoms from different chemical elements is distinct and usually easy to distinguish. At the same time, differences up to several eV in the binding energy of a specific element allow identifying its local chemical environment and the electronic structure. Therefore, in most cases core-level photoelectrons are used for elemental analysis, while small shifts in their E_B (known as *chemical shifts*) can be used to determine the oxidation state. The number of photoelectrons (in other words the photoelectron peak intensity) is proportional to the amount of the presented elements, and therefore core-level spectra can be used for quantitative analysis as well. In order to do so, the possibility for each element to produce photoelectrons should be taken into account, by using measured, empirical, or theoretically calculated atomic sensitivity factors (ASF), which are also sometimes called photoelectron cross sections. The ASF strongly depend on the element, the specific core-level shell, and the excitation photon energy. For laboratory X-ray source experiments, empirically derived ASF are usually used [11], while for synchrotron-based experiments, calculated values are typically employed since they take into account the photon energy dependence of the ASF [13].

4.1.2 The Contribution of Initial and Final State Effects to the Photoelectron Energy

Photoelectron spectroscopy is a well-established technique to directly investigate the electronic structure of nanomaterials. This is due to the fact that the binding energy of core-level electrons is strongly related to the electron distribution around the core of the atom. This means that, ideally, the E_B found in a photoemission

experiment using Eq. 9.2 can be employed as a probe to distinguish differences in the electron distribution around the atom. The problem in the use of E_B as a probe for the electron distribution is that after photoemission all the remaining electrons are not "frozen" but are influenced by the removal of the photoelectron. Following this picture the E_B calculated in a photoemission experiment does not directly reflect the state of the atom before photoemission, but is also affected by the redistribution of all the surrounding electrons, the so-called initial and final state effects [14]. In particular, the *initial state* contribution to the measured E_B reflects differences in the charge density, which arise from changes in the electronic structure (due to the chemical or the geometric environment), while *final state* effects are due to differences in the screening of the core hole created after photoemission. As will be discussed below, the removal of an electron from a particular shell of the atom may induce several types of final states. The effectiveness of the core hole screening depends not only on the particular element (intra-atomic screening) but also on the surrounding environment, i.e., atom coordination number and interaction with the support (extra-atomic screening). It is evident that in the case of supported nanosized particles, changes in the extra-atomic screening could have a significant contribution to the E_B, due to electronic interaction with the support. Since in that case the core hole screening is not so effective compared to that in the bulk equivalent, an increase in the core-level binding energy is usually observed for supported NPs [15]. However, initial state effects associated to the intrinsic electronic structure of the NPs may also contribute, but to a lesser extent, to the E_B shift. Apart from the extra-atomic screening of the photo-hole, the interaction with the support can in principal induce charge transfer and hybridization of the NP/support electronic states, which can alter the electron orbital energy *(initial state)* as well. The initial and final state contribution in the binding energy shifts can be in principle distinguished using the so-called Auger parameter method [14, 15].

The above discussion can explain the binding energy shifts observed in photoemission experiments where *soft* X-ray[4] photons are used. However, in the case of *hard* X-ray photoelectron spectroscopy (excitation energy of 4–8 keV), the part of the kinetic energy of the photoelectron is being imparted to the emitting atom, due to the momentum conservation. As a result, the binding energy determined by Eq. 9.2 is greater than the true binding energy. This effect, better known as *recoil effect*, is too small and can be neglected for soft X-ray XPS experiments, but in the case of hard X-ray XPS, it can induce asymmetric broadening and high E_B shift of the photoelectron peak [16]. A characteristic example of peak shift and broadening due to the recoil effect is given in Fig. 9.2. The C 1s core-level spectra of the same graphite (HOPG) sample were measured in two different beamlines using soft (340 and 870 eV) and hard (5,950 and 7,940 eV) X-ray SR. Both instruments had similar energy resolution, and the binding energy scale was carefully calibrated.

[4]The distinction between soft and hard X-rays is not well defined in the literature. *Soft X*-rays are the lower-energy X-rays, while the higher-energy ones are referred to as *hard X*-rays. In this text soft X-rays are those with energies less than 1,500 eV, while those with grater energies are considered as hard X-rays.

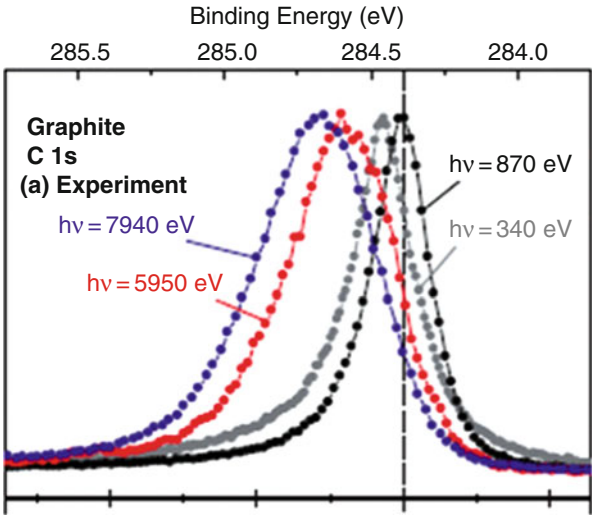


Fig. 9.2 Photon energy dependence of C 1s core-level spectra of graphite (HOPG) measured at room temperature. The total instrument resolution for the soft X-ray (340 and 870 eV) and hard X-ray (5,950 and 7,940 eV) experiments was 100 and 120 meV, respectively (From Ref. [16])

The comparison of the photoelectron peaks recorded with hard and soft X-rays indicates that the C 1s E_B shifts up to 0.3 eV and is significantly broader for high-energy photons. These differences are attributed to the recoil effect and should be taken into account when photoelectron spectra are recorded using high-energy photons (e.g., hv > 2,000 eV).

4.1.3 Instrumentation Aspects

Below a few salient points of the basic instrumentation used in a photoemission experiment are given, while for more details one can refer to more specialized literature [5, 8]. Figure 9.3 shows the basic parts of a photoelectron experiment, which consists of the *photon source*, the *electron lenses*, the electron *energy analyzer*, and the *electron detector*. All the above parts should be operated under UHV conditions, so as reliability and long lifetime requirements of the spectrometer are fulfilled. As a *photon source,* a gas discharge lamp, an X-ray tube, or SR has been used. Each of these sources provides different photon energies and fluxes. Owing to its high photon flux density and continuous frequency distribution, an SR source is undoubtedly the most versatile light source at present.

The incident photons are absorbed by the sample, and the emitted photoelectrons (but also Auger and stray electrons) enter the *electron lenses*, where they are focused by means of electrostatic fields. The electron lenses physically separate the sample from the electron analyzer, and their main function is to retard or accelerate the electrons to a fixed energy (*pass energy*) and focus them to the analyzer entrance (*slit*). In laboratory experiments, the probed sample area and the electron acceptance angle (usually few degrees) are typically defined by the lenses' settings.

Consequently the electrons enter into the analyzer, where only those with a given pass energy can pass through the electrostatic field created between the outer and

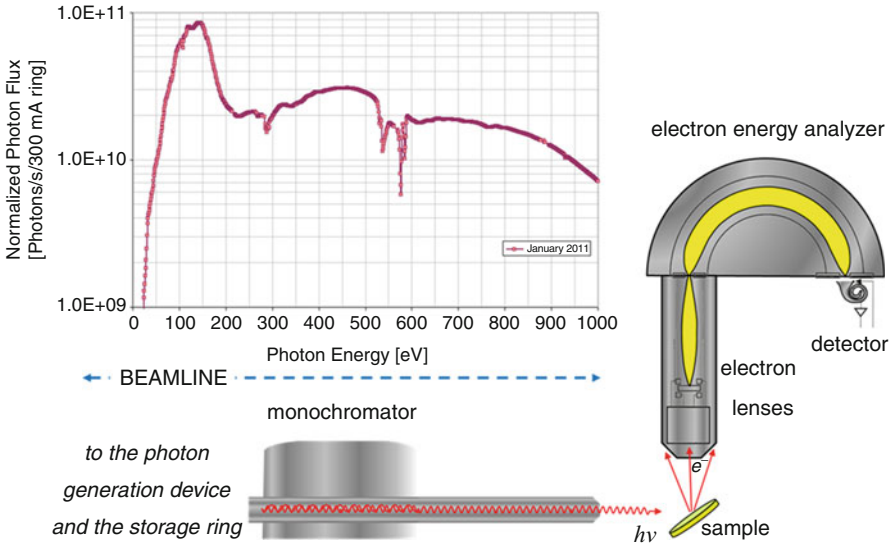


Fig. 9.3 A schematic diagram of a photoemission experiment using synchrotron radiation. A typical experimental photon flux curve, collected with a photodiode, is shown at the *top left* part

inner (hemi)spheres. Although several different types of *electron energy analyzers* have been developed and used through the years, the electrostatic hemispherical analyzer is the one most frequently used in today's commercial instruments. The analyzer defines, to a large extent, the energy resolution, which is practically the ability to resolve peaks with small energy differences.

Finally, at the exit slit of the analyzer, the number of photoelectron is multiplied and counted by the electrode detection system. Two main types of electron detectors are in use today, namely, channel electron multiplier and charge-coupled device (CDD) camera detectors. The latter type can be also position sensitive in two dimensions, which makes possible the determination of the position (usually with accuracy of microns) or the angular direction of the photoelectrons.

The above description applies both in laboratory and synchrotron-based photoemission experiments. The only difference between the two is the photon source. As mentioned above, in a synchrotron experiment, the radiation is produced in the storage ring and carried to the experimental station (*end station*) through a several meters long tube, called the *beamline*. Every synchrotron facility has several beamlines, the design of which depends very much on the desired energy range and the intensity of the transferred radiation. A beamline for a photoemission experiment is practically a long vacuum tube equipped with several focusing mirrors, slits to control the physical width of the beam, and the radiation monochromator. Commonly, the preferred photon energy is selected by changing the settings of the monochromator (by mechanical movement of the diffraction crystals within it), a procedure which

usually takes from few seconds to a couple of minutes. The number of incident photons, or in other words the *photon flux* on the sample, is very much dependent on the photon energy. This in turn is related to factors, such as the specifications of the monochromator, or possible contamination on the focusing mirrors. In Fig. 9.3 a typical experimental photon flux curve, collected with a photodiode inserted at the end of the beamline, is shown[5]. It is evident that the difference in the photon flux can vary up to an order or magnitude with the photon energy (of course this might also vary a lot in different beamlines). Sharp decrease in the photon flux (e.g., ca.280 and 530 eV) is usually related to the absorption of radiation on the beamline elements by unwanted contaminates.

4.1.4 Basic Characteristics of an XPS Spectrum

An XPS spectrum is displayed as a plot of the number of electrons versus their kinetic energy or more frequently their binding energy as is calculated by Eq. 9.2. Usually the XPS analysis starts with a survey spectrum, which is a scan in a wide energy region (typically for soft X-ray XPS from 1,200 to −2 eV) and with low spectral resolution, which is received in order to identify all elements present on the sample. In Fig. 9.4a survey spectrum recorded on nickel nanoparticles with mean size of 50 nm is shown. The spectrum was recorded in a synchrotron facility using two different photon energies (1,000 and 1,200 eV). Both photoelectron and Auger electron peaks are dominating the survey scan, while other peak types like shake-up and energy loss lines have much less intensity and will not be discussed here. The photoelectron and Auger electron peaks in the survey spectrum can be easily distinguished in synchrotron-based photoemission experiments by using different excitation photon energies. In particular, when the survey scan is presented in the binding energy scale, the Auger electron peaks are shifted with photon energy, while the photoelectron peaks are not[6]. This is shown in Fig. 9.4, where only the Ni LMM Auger peaks are shifted in the survey spectrum, when different photon energies are used.

After all elements have been identified (*elemental analysis*), detailed spectra (which are sometimes called high-resolution scans) of the more intense peak of the element(s) of interest are recorded. The detailed spectra (see inset of Fig. 9.4) allow the precise determination of the binding energy and the chemical shift (*chemical state analysis*), as well as the accurate estimation of the peak areas to be used for the *quantitative analysis* of the sample. When selecting the excitation photon energy, one should be particularly careful that the Auger peaks do not overlap with useful photoelectron peaks. In the selected example of Fig. 9.4, the Ni LMM Auger peak is overlapping with the C 1s peak at about 285 eV, when 1,000 eV excitation photon

[5]Data are taken from the specifications of the materials science beamline, at Elettra Sincrotrone facility in Trieste, and are recorded in January 2011 (http://www.elettra.trieste.it/lightsources/elettra/elettra-beamlines/msb/beamline-description).

[6]Here it is more appropriate to say that the kinetic energy of the Auger electrons does not depend on the photon energy, while when higher photon energy is used, it is offered as excess kinetic energy to the photoelectron peaks.

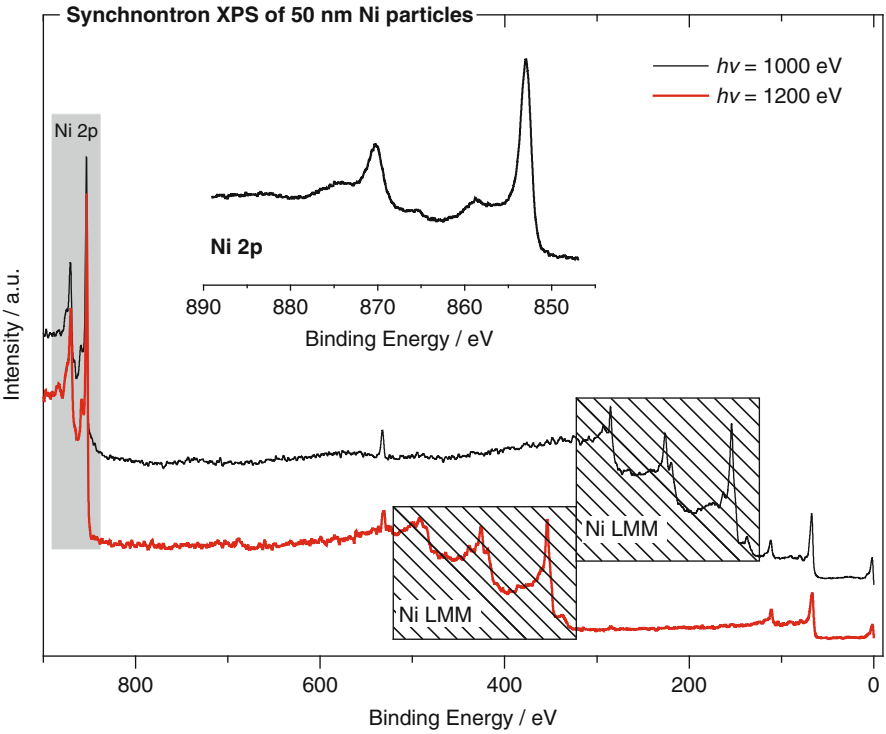


Fig. 9.4 Synchrotron X-ray photoelectron survey scan spectra of 50 nm Ni particles excited by two different photon energies (1,000 and 1,200 eV). The dashed box indicates the Ni LMM Auger electron peaks, while the *gray box*, the Ni 2p photoelectron peak. In the *inset* the high-resolution Ni 2p spectrum is shown

energy is used. This makes this particular photon energy (1,000 eV) not a good choice for recording carbon species in nickel-containing samples.

For the quantification of laboratory XPS results, the intensities of the spectra should be normalized to the atomic sensitivity factors [13], which describe the probability of photoelectron emission from a particular core level, as well as to the electron inelastic mean free path (IMFP), which expresses the kinetic energy dependence of the probing region [17]. In addition to that, for quantitative analysis of SR-XPS results (see Sect. 4.1.6), differences in the *photon flux* between various excitation energies should be taken into account. When spectra are recorded in different time periods, the calculations might be also influenced by differences in the storage ring electron current, especially for synchrotrons not operating in the *top-up* mode[7]. Therefore, for quantitative analysis of SR-XPS results, it is indispensable that the photon flux is constantly monitored in the course of the experiment.

[7]In this operation mode, the current in the storage ring is steady, while in the periodic injection operating mode, the ring current decays monotonically, between two electron injections.

4.1.5 Analysis Depth (or Surface Sensitivity)

X-ray photoelectron spectroscopy is usually referred to as an analytical method with high surface specificity or more commonly as a *surface-sensitive* method. Practically this means that only a very thin layer of the outermost surface is probed by the technique, which is typically referred to in textbooks as "within a few atomic layers of the surface." However, the analysis depth is rarely quantified with precision, and in general 2–5 nm is assumed as the analysis depth of the technique. In this paragraph we will try to explain why this is happening and show how we can significantly modify the analysis depth of the technique by using SR.

The physical origin behind the surface sensitivity of XPS is the high probability of low-kinetic-energy electrons to undergo inelastic scattering and loose energy when they traverse into matter. One should stress here that the interaction of X-rays with solids is much weaker, so X-rays employed in XPS can penetrate a substantial distance into the sample (few μm). This means that photoelectrons are created not only within the first few nm of the sample but also in much deeper layers. However, photoelectrons emitted from atoms deep into the solid will lose energy due to scattering and probably never escape from the sample, or in the best case will just contribute to the spectral background. Thus photoelectrons that are created at, or near, the surface will have a smaller possibility for inelastic collisions and will be the main contribution to the XPS spectra. Two terms are commonly used to describe and quantify this effect: the so-called inelastic mean free path (IMFP or λ) and the (effective) attenuation length (AL) [5]. Although the definition of these two terms is not the same, they are both used to describe the average distance that a photoelectron with a given energy travels within the solid. For the estimation of the IMFP, it is assumed that the photoelectron can lose energy only due to inelastic scattering with atoms or electrons, while in the AL term, elastic scattering is also considered. For simplicity in this text, we will assume that only inelastic scattering is responsible for electron attenuation, and we will use the IMFP to describe the surface sensitivity, unless otherwise stated. The IMFP has been calculated for practically all the elements and many organic and inorganic compounds, using several algorithms. We propose here the QUASES-IMFP-TPP2M software which has been developed by S. Tougaard using the Tanuma Powell and Penn algorithm [17] and can be currently downloaded free of charge.[8] This database is quite complete and easy to use.

The evolution of the IMFP as a function of the photoelectron kinetic energy, calculated by the Tanuma Powell and Penn algorithm, is shown in Fig. 9.5 for three selected cases. The graph shows that the IMFP is strongly dependent on the electron kinetic energy, with shorter IMFP as the electron energy decreases. As is evident by comparing the curves for electron traversing though Ni (8.9 g/cm^3), NiO (7.45 g/cm^3), and carbon (2.26 g/cm^3) matrixes, the IMFP is also material dependent, especially at high kinetic energies. As a rule of thumb, the higher the

[8] http://www.quases.com/products/quases-imfp-tpp2m/

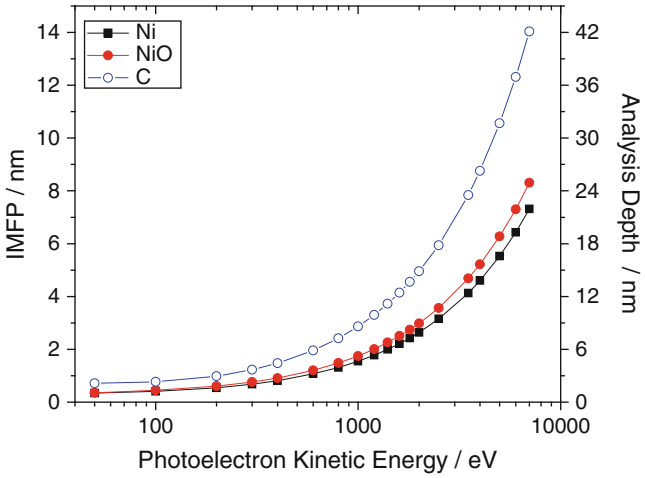


Fig. 9.5 The evolution of the IMFP as a function of photoelectron kinetic energy inside Ni, NiO, and C matrixes. The *curves* are calculated using the algorithm proposed by Tanuma Powell and Penn [17]. The analysis depth indicated in the right y-axis is calculated as three times the IMFP

bulk density of the material (values in the parentheses above), the lower the IMFP. The IMFP values are directly related to the information depth of the XPS method.

The results of Fig. 9.5 can also explain why it is not possible to give a single value to define the analysis depth or, in other words, the surface sensitivity of the XPS method. The information depth of the technique is not constant but varies among different materials and for diverse photon sources. However, the IMFP, and thus the analysis depth, dependence on photoelectron energy may be turned to advantage. When SR is available, it is possible to select the incident photon energies that give the same photoelectron energy for each of the photoelectron peaks of interest. This means that the depth into the sample from which these electrons escape is similar for each element. By selecting more than one photoelectron energy, it is possible to get some information about the depth distribution of elements or chemical species [18]. This type of measurements is called *depth-dependent* measurements or simply *depth profile*.

The number of electrons that can escape from a distance (or depth) d inside the solid without losing energy will contribute to the peak signal of the XPS spectrum, while all the others will be part of the spectrum background. The intensity I, of the signal emitted from atoms in a depth d, is exponentially attenuated with the depth as described in Eq. 9.3 [11, 19]:

$$I = I^{\infty} \exp\left(-\frac{d}{\lambda \cos\theta}\right) \tag{9.3}$$

where λ is the IMFP, I^{∞} is the intensity of an infinitively thick sample (usually calculated ASF are used as the I^{∞}), and θ is the angle of electron emission with

respect to the surface normal. As is evident by Eq. 9.3, about 95 % of the photoelectrons escaping from the sample without loss of energy will come from a distance 3 (λ cos θ). It is therefore usual when referring to the *sampling or analysis depth* of the XPS technique, to use 3 (λ cos θ) as an indicative value.

4.1.6 Quantitative XPS Analysis

In the quantitative analysis of the XPS results, the intensities of the photoelectron peaks are used to obtain the elemental composition of the sample. Before a quantification method is applied, the raw spectral intensities are calculated after proper background subtraction and are subsequently corrected for factors like the transmission function of the analyzer and the sensitivity to photoemission. Typically for routine quantification, the sample is assumed as planar (flat). However, when models developed for planar samples are applied on spherical particles, significant deviations of the calculated and the real compositions are observed, especially for very small particles [20]. In that case more complex quantitative analysis methods should be applied. In some cases quantitative calculations using XPS intensities can be indispensable to obtain information about nanomaterials, especially when other methods are difficult to apply. For example, in the case of core–shell (c-s) nanostructures, the determination of the thickness of the overlayer by microscopy techniques (e.g., TEM) might be difficult, if the boundary between core and shell or shell and surroundings is not clearly distinguishable or the surface layer is too thin. In addition, quantitative XPS analysis may also be used to provide more detailed information on the way that the surface composition varies with depth.

Since the quantitative analysis of XPS spectra for nanomaterials is more complicated than for planar surfaces, we discuss in detail in this section quantitative analysis dedicated to spherical c-s nanoparticles. Two different theoretical models for the determination of shell thickness will be introduced, together with the generally applied model for planar substrates. Before applying the mathematical equations presented below, it is necessary to fulfill two main prerequirements. The first is that the experimental XPS intensities are normalized by the photon flux, especially if the measurement for different elements was performed by using different photon energies. The second is that the diameters of the particles are smaller than the XPS probing depth, that is to say, at about 5–10 nm.

Approach for Planar Model

The equations that are used to calculate the theoretical XPS intensity for a flat surface (B) covered by one or more overlayers (S_i) are well described in the literature [11]. As an example, the equations for two successive overlayers (S_1, S_2) on a substrate (B) are ([21] and references there in)

$$I_i^{S_1} = I_i^{\infty}\left[1 - \exp\left(-\frac{d_1}{\lambda_i^{S_1}\cos\theta}\right)\right] \qquad \text{outermost layer}$$

$$I_j^{S_2} = I_j^{\infty}\exp\left(-\frac{d_1}{\lambda_j^{S_1}\cos\theta}\right)\left[1-\exp\left(-\frac{d_2}{\lambda_j^{S_2}\cos\theta}\right)\right] \quad \text{intermediate layer}$$

$$I_k^{B} = I_k^{\infty}\exp\left(-\frac{d_1}{\lambda_k^{S_1}\cos\theta}\right)\exp\left(-\frac{d_2}{\lambda_k^{S_2}\cos\theta}\right) \quad \text{bulk}$$

where I is the photoelectron intensity, I^{∞} is the intensity of an infinitive thick sample, λ is the IMFP, d is the layer thickness, and θ is the angle of electron emission with respect to the surface normal. The S_1, S_2, and B denote the surface layers and the bulk, which are composed of the chemical elements or compounds i, j and k, respectively. The $\lambda_i^{S_1}$ of the photoelectron emitted from element (i) in the medium (S_1) can be found by, e.g., using Ref. [17].

Let's now consider the simple case of a single overlayer S_1 on the substrate B. Then the XPS intensities from the overlayer and the substrate are simplified:

$$I_i^{S_1} = I_i^{\infty}\left[1-\exp\left(-\frac{d_1}{\lambda_i^{S_1}\cos\theta}\right)\right] \tag{9.4}$$

$$I_k^{B} = I_k^{\infty}\exp\left(-\frac{d_1}{\lambda_k^{S_1}\cos\theta}\right) \tag{9.5}$$

Since the absolute XPS intensity values are very difficult to simulate without accurate knowledge of I^{∞}, usually the XPS peak intensity ratio between the substrate and the overlayer, as provided by dividing Eq. 9.5 by Eq. 9.4, is used. The mathematical equation can be greatly simplified if the IMFPs of photoelectrons emitted from the substrate and the overlayer are equal (i.e., $\lambda_k^{S_1} = \lambda_i^{S_1}$):

$$d_1 = \lambda_i^{S_1}\ln\left(\frac{I_k^{\infty}}{I_i^{\infty}}\frac{I_i^{S_1}}{I_k^{B}}-1\right) \tag{9.6}$$

Taking into account that the IMFP predominantly depends on the photoelectron E_K, in SR-XPS it is feasible to select the photon energies according to Eq. 9.2, so as photoelectron peaks of different elements to have the same E_K and Eq. 9.6 can be applied.

In laboratory-based XPS, Eq. 9.6 is used to estimate the thickness of native oxide layers formed on transition metals [22–24]. In this particular case, the IMFP of substrate and overlayer is very similar, since the chemical shift between metals and their oxides does not excess few eV. As an example, the thickness of an Al_2O_3 layer on an Al foil (see schematics of Fig. 9.6) was calculated by XPS and compared to the thickness estimated by TEM cross-sectional images. The oxide layer was formed by anodic polarization of a pure aluminum foil in a mixture of ethanol and perchloric acid [24]. In the Al 2p spectra presented in Fig. 9.6a, two oxidation

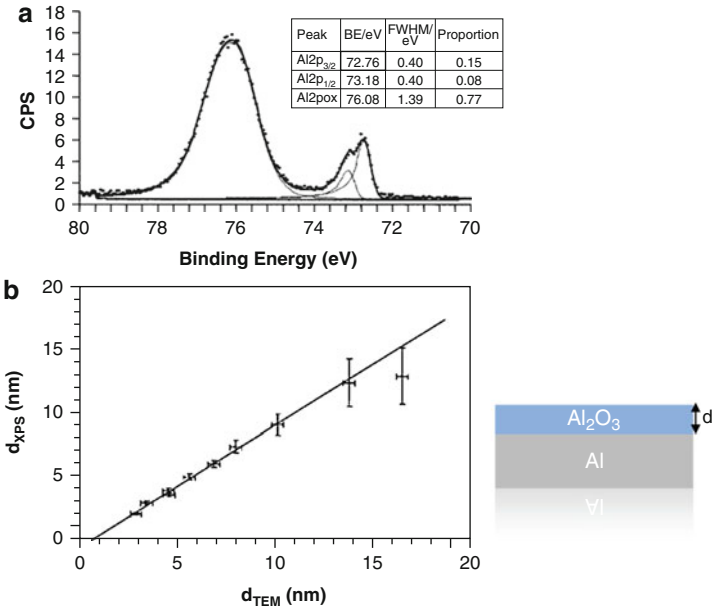


Fig. 9.6 (**a**) The XPS Al 2p peak obtained from a 5.65 nm thick anodic oxide formed on pure aluminum foil using an AlKα source, and (**b**) the film thicknesses estimated by the XPS intensity (d_{XPS}) versus the ones measured by TEM (d_{TEM}) (From Ref. [24])

states of Al are clearly distinguished. In particular, metallic and oxidized Al 2p peaks are found at about 72.5 and 76 eV, respectively. The thicknesses of the oxide layer calculated by using the XPS intensity (d_{XPS}) are very close to the TEM results (d_{TEM}) as shown in Fig. 9.6b. The estimation of the thickness by the XPS measurement is reasonably good up to 10 nm of overlayer thickness, while it deviates after that due to the much higher surface sensitivity of XPS compared to TEM [23]. This is also the expected behavior taking into account that the IMFP of Al 2p photoelectrons ($E_K \sim 1{,}410$ eV) in Al_2O_3 is 3.27 nm and therefore the estimated information depth is about 9.8 nm (3 times the IMFP).

Using the Geometry Correction Factor for Spherical Nanoparticles

As shown above, in the case of flat/planar samples, quantitative calculations can become relatively simple. However, it is reported that applying the equations derived for planar samples to calculate layers of spherical shaped core–shell NPs may lead to overestimation of the overlayer thickness values [21, 20, 25]. An approach to overcome this problem is to introduce the *effective thickness* of the layer, d^{eff}, which represents the depth on the sample surface "seen" by the electron analyzer. Although for flat samples d^{eff} is the same in all parts of the sample, for curved surfaces (i.e., NPs), d^{eff} varies at different positions across the diameter of the particle, as shown in Fig. 9.7a. The hemisphere of the particle is therefore divided into 9 segments of 10° each, and the d^{eff} is represented by its middle angle;

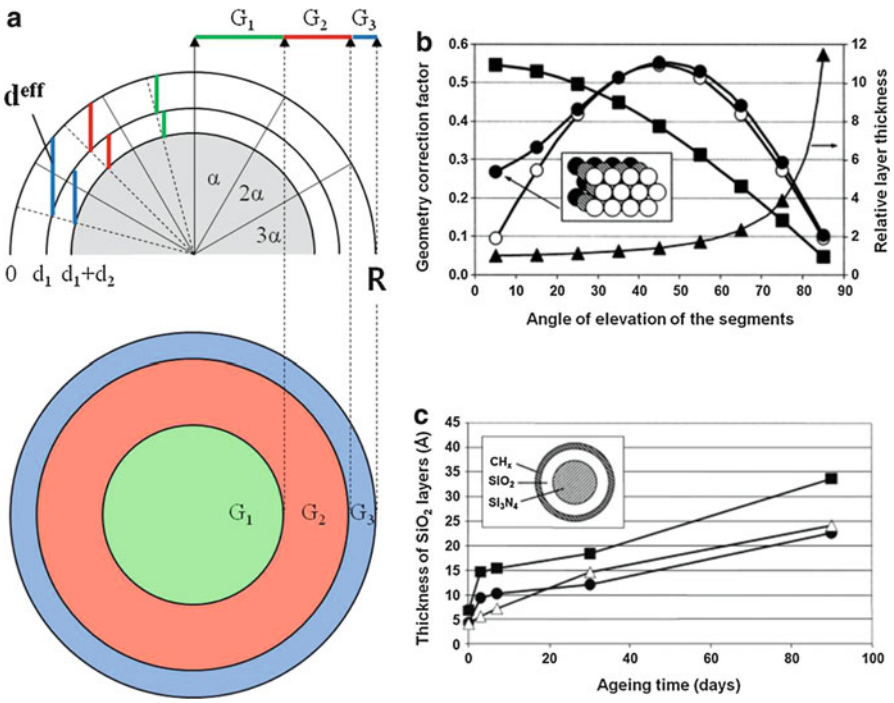


Fig. 9.7 (**a**) Schematic drawing of the axial cross section and *top* view of projected area for a core–shell nanoparticle. (**b**) The geometry correction factors of the segments as a function of the angle of elevation for spherical model with (*filled circles*) and without (*open circles*) contribution of the lower rows of spheres (*inset*), cylindrical model (*squares*), and the relative virtual thickness of the layer (*triangles*). (**c**) The thickness of the growing oxide layer on silicon nitride nanodispersed powder aged in air of 80 % relative humidity, calculated from XPS intensity by the spherical (*circles*) and the planar model (*squares*) and bulk chemical analysis data (*triangles*) (The figures are taken from Ref. [21])

$d_i^{eff} = d_i \cos\theta$. The intensity is calculated at each position, and it should be weighted by the geometric correction factor depending on the zone (G_1, G_2, etc.), which is proportional to the projected area of the segments of the sphere. The geometry correction factor of the segment is shown in Fig. 9.7b as a function of the angle. The experimental intensity can then be corrected by summing all the intensities from the weighted zones.

It is evident that by using the geometry correction factors for spherical particles, the calculations become much more complex than the planar model. Nevertheless, a simple estimation can be done if the XPS measurement is performed at the detection angle of 55° (so-called the magic angle). Figure 9.7c shows the calculated evolution of the Si oxide layer grown over a monodispersed silicon nitride powder (40 nm in diameter) as a function of the aging time in air of 80 % relative humidity [21]. The model is even more complicated by the presence of an adventitious carbon layer on the surface of the particles. According to these results, the ratio between

the overlayer thickness, d_{cal}, calculated by the planar model (Eq. 9.6) to the apparent thickness, d_o, estimated by chemical analysis is constant; $d_{cal}/d_o = 1.6$. However the accuracy of the model is very much improved when the measurements are performed using the spherical model at the magic angle, as shown in Fig. 9.7c [21]. The above discussion indicates that when Eq. 9.6, which is originally derived for flat surfaces, is applied for calculations of core–shell spherical NPs, the calculated thickness is overestimated and for better accuracy should be divided by the factor 1.6. However the above discussion also shows that the error in the thickness estimation by Eq. 9.6 does not depend on the layer thickness and therefore can be used to compare core–shell samples with different shell thickness, even if a large uncertainty in the absolute shell thickness value remains.

General Equation for the Core–Shell Nanoparticles

An alternative theoretical approach for the determination of the shell thickness of the c-s NPs by using XPS intensity has been proposed by Gillet et al. [26, 27]. In their model, they assume that the c-s NP has a spherical symmetry and the core is in the center. They consider an individual particle where the radius of the core is r and the shell thickness is d. The general equation of the theoretical XPS intensity $I(\lambda,d,r)$ from the core is expressed as follows:

$$I(\lambda, d, r) = n\, S(\lambda, r) \exp\left(-\frac{d}{\lambda}\right) h\left(\frac{d}{\lambda}, \frac{r}{\lambda}\right) F_1\left(\frac{r}{\lambda}\right) \tag{9.7}$$

with $S(\lambda, r) = \frac{I_0 \lambda \pi r^2}{n}$

$$h(\delta, \rho) = \frac{k(\rho)\delta + 1}{\delta + 1} \quad \text{with} \quad k(\rho) = \frac{\beta_1 \rho^2 + \beta_2 \rho + 1}{\beta_1 \rho^2 + \beta_3 \rho + 1}$$

$$F_1(\rho) = 1 + \frac{(2\rho + 1)\exp(-2\rho) - 1}{2\rho^2}$$

where $I(\lambda, d, r)$ is the photoelectron intensity from the core which has three variables; λ in this model is not the IMFP but the "effective attenuation length" (EAL) of the photoelectron from the core, d is the *shell* thickness, and r the *core* radius. The EAL values can be substituted for the IMFP provided that the photoemission angle does not exceed 60°, but in any case can be found in the NIST standard reference database 82. The ASF is given by the equation $S(\lambda, r) = I_0 \lambda \pi r^2/n$, where n is the density of the atom and I_0 is the XPS intensity from the uncoated bulk material, which is proportional to the atomic cross-sectional factor under specific incident photon energy. Alternatively, the photoionization cross sections can be found online[9]. The $h(\delta, \rho)$ and $k(\rho)$ are fitting functions with the three given

[9]Atomic calculation of photoionization cross sections and asymmetry parameters, http://ulisse.elettra.trieste.it/services/elements/WebElements.html.

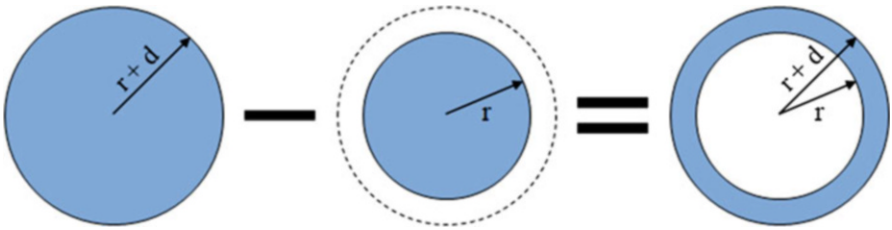


Fig. 9.8 Schematic drawing of the calculation of the theoretical XPS intensity from the shell

constants: $\beta_1 = 0.002\,889\,84$, $\beta_2 = 0.051\,355\,94$, and $\beta_3 = 0.459\,824\,62$. The $F_1(\rho)$ is the 1-dimensional factor of the individual NP.

If the theoretical XPS intensity from the core is expressed as $I_c(\lambda_c, d, r)$, where λ_c is the EAL of the photoelectron from the core element, then the theoretical XPS intensity from the shell can be expressed as $I_s = I(\lambda_s, d = 0, r + d) - I(\lambda_s, d, r)$, where the λ_s is EAL of the photoelectron from the shell component. The $I(\lambda_s, d = 0, r + d)$ is the theoretical XPS intensity of a sphere of an uncovered NP of the same chemical component with the shell with radius r + d, while the $I(\lambda_s, d, r)$ is the theoretical XPS intensity from the core as shown in Fig. 9.8. The theoretical XPS intensity ratio between the core and the shell can be then calculated from the equation:

$$\frac{I_s}{I_c} = \frac{I(\lambda_s, d = 0, r + d) - I(\lambda_s, d, r)}{I(\lambda_c, d, r)} \tag{9.8}$$

This method was applied to calculate the growth of an oxide shell on Si spherical nanoparticles (with initial diameter of about 5 nm) that were exposed to air at room temperature [28, 29]. The relative SiO_x concentration of the oxidized shell can be found as follows [27]:

$$C_{SiOx} = \frac{I_s}{I_s + \mu I_c} \tag{9.9}$$

where μ is the ratio of the atomic densities of Si (4.96×10^{22} cm^{-3}) and SiO_2 (2.27×10^{22} cm^{-3}). Figure 9.9a shows the Si 2p spectra, while Fig. 9.9b the % SiO_x concentration (C_s) and the core and shell thicknesses (r and d, respectively) for the five Si 2p spectra calculated from Eqs. 9.8 and 9.9. It is interesting that after the formation of about 3 nm of surface SiO_x shell, no signal of the core is detected. As we will discuss later in this chapter, in that case the interior of the particles can be detected by increasing the excitation photon energy.

Although this mathematical approach is based on a single NP, it is possible to be expanded for a layer of NPs dispersed on a substrate. If one considers more than one layer of spherical NPs closely packed on a substrate, then Eq. 9.8 will not correspond to the experimental XPS intensities. This is due to the contribution of the second and

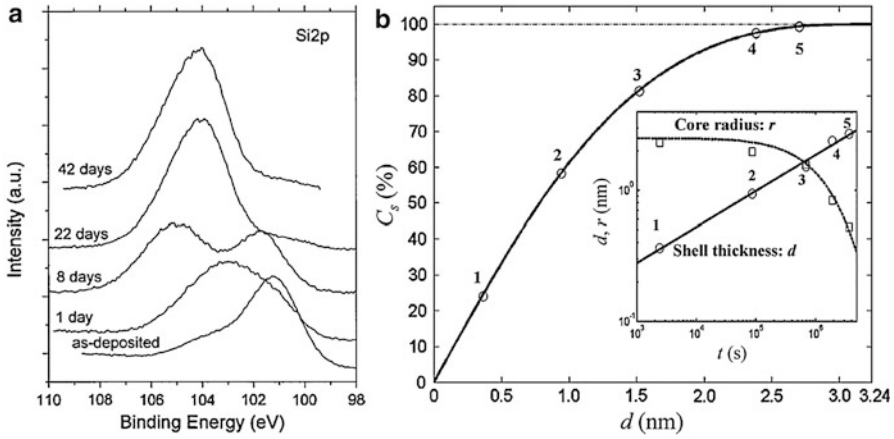


Fig. 9.9 (**a**) Evolution of the XPS Si 2p peak of Si nanoparticles on HOPG, after exposure to air at room temperature, (**b**) the curve of C_s versus the thickness of SiO_2 shell calculated by Eq. 9.9. *Inset*: log–log plots of d versus t and r versus t (The figures are taken from Refs. [27] and [26] respectively)

third row of spheres to the signal detected by XPS through the empty space between the spheres. The shell thickness of the NPs in such a complex system can be alternatively simulated by using the available software, e.g., XPS MultiQuant.[10] In this program it is possible to estimate the XPS intensity and overlayer thickness by changing the surface model, referring to the surface morphology found, for example, by TEM results. Obviously in order to obtain reliable results, homogeneity of the particles' size and shape is required.

4.2 Advantages in X-Ray Photoelectron Spectroscopy by Synchrotron Radiation

X-ray photoelectron spectroscopy experiments at synchrotrons can be benefited by the unique characteristics of the SR compared to laboratory X-ray sources. When it comes to the characterization of nanomaterials, the most important advantages are the high intensity and brightness (or brilliance), the energy tunability, and the high spectral resolution. Below, we will further explain each of these characteristics and indicate some representative examples where they are utilized for the advanced characterization of NPs.

4.2.1 Intense and Bright Radiation

Third-generation synchrotron facilities use bending magnets and insertion devices to produce **intense and bright radiation**. *Brilliance* is a term that describes both

[10]Mohai M., XPS MultiQuant user manual, 2012.

the brightness and the angular spread of the beam, or simply how many photons can be squeezed in a very small area. Synchrotron sources produce radiation with brilliance that is more than a billion times higher than the common laboratory sources (X-ray tubes). Due to the high brilliance and the small spot size of the beam, SR can provide XPS spectra with significantly higher lateral resolution and signal-to-noise ratio, compared to conventional X-ray sources. This may be essential when spatially well-isolated NPs with low coverage densities are studied.

4.2.2 Energy Tunability

The **tunability** of SR over a wide energy range gives the opportunity to perform photoemission experiments with variable photon energy. Bending magnets and insertion devices emit radiation in a broad energy range, from which specific energies are extracted using a suitable monochromator. Therefore, in contrast to the standard laboratory X-ray sources which produce up to two fixed photon energies, SR can be easily varied in a broad photon energy region (e.g., 5–2,000 eV) with a precision better than 0.1 eV. In photoemission, this allows tuning the kinetic energy of the produced photoelectrons for a specific atomic energy level, therefore modifying the analysis depth from sub-nanometer up to several nm. When hard X-rays are available, the highest depth can reach 20 nm or more. This unique flexibility in the analysis depth makes the technique suitable to determine characteristics of NPs, for example, the formation of core–shell morphologies [30]. In addition, when the concentration of different constituents (elements) within the sample needs to be compared, the photon energy can be properly selected so as the kinetic energy of the ejected photoelectrons from different elements to be the same. This assures that the probing depth of the technique is identical for all particle constituents. What is more, the measurements are independent of the transmission function of the energy analyzer, and the influence of any surface contamination layer can be neglected, since they equally contribute to the attenuation of the signal of all elements. These two aspects are important for more reliable quantitative analysis of the XPS results.

4.2.3 High Energy Resolution

The **energy resolution** in a photoemission experiment is a measure of the ability to resolve peaks with small energy difference [5, 11]. Although there are many different terms to define the resolution (*absolute, relative resolution, resolving power*, *etc.*), in most of the cases, in this chapter we will use the peak width or more precisely the full width at half maximum (FWHM) of the core-level photoelectron peak, as an indicator of the energy resolution. The resolving power of the technique (ability to distinguish between two peaks with close E_B) is improving when the width of the photoelectron peaks becomes narrower.

In general, the overall width of a photoelectron peak is a convolution of three main factors: the *natural line width* of the peak, the resolution of the *electron analyzer* (spectrometer), and the *line width* of the incident *X-rays* [5, 11]. The natural line width is related to the photoelectric effect and is the ultimate down limit of the spectral width. This value varies with the element type and the specific atomic lever, but is usually between 0.13 and 0.7 eV (0.33 eV for Ag $3d_{5/2}$ typically

used for comparison of different instruments). The analyzer resolution mainly depends on the dimensions of the hemispheres and the quality of the electrostatic lenses. Since laboratory and synchrotron-based experiments use identical electron analyzers, it is the *line width* of the incident *X-rays* which makes the difference in resolution between the two. Although the absolute photon energy resolution varies among different beamlines, and even within the same beamline as a function of the photon energy, it is noticeably smaller than that of the laboratory spectrometers. This allows to monitor fine chemical shifts (i.e., small difference in the binding energy) related to the different chemical species. In the case of very small nanoparticles, the width of the photoemission peaks can also carry important information about the homogeneity of the size distribution [31]. In particular, taking into account size-dependent binding energy shifts (see below), broader peaks are expected to form by the convolution of peaks derived from particles with differences in the particle size. This practically means that samples containing NPs with low size distribution will in general have photoelectron peaks with small FWHMs. However, as will be shown in the next paragraph, very small particles (with sizes in the sub-nm scale) might have core-level photoelectron peaks which are significantly broader than the bulk material.

4.2.4 Characteristic Examples

Below are given three representative examples where the unique characteristics of SR are employed to study the electronic and chemical state as well as the composition of NPs.

High Resolution and Brilliance to Distinguish Particle Size-Dependent Core-Level Shifts in Photoelectron Spectroscopy

Since the early days of XPS, it has been demonstrated that nanometer-sized metallic or semiconducting particles can exhibit significant binding energy shifts, normally at higher E_B in respect to their bulk equivalents [32]. The observed shifts, commonly referred to as *size-dependent* E_B shifts, typically decrease toward the E_B of the bulk phase when the particles' size increases. Size-dependent shifts are usually observed at very small nanoparticles with sizes below 2 nm. Therefore, one should be cautious when E_B shifts are observed at larger NPs, since they might be due to other phenomena such as chemical shift or electrostatic charging. Size-dependent E_B shifts have been extensively studied in laboratory XPS experiments (e.g., [33]). However, when SR is used, there are two main advantages; first the high photon flux allows recording spectra with good signal-to-noise ratio even for very low NP coverage (around 1 % atomic coverage), and second it also allows the collection of high-resolution spectra and therefore permits to distinguish certain characteristics and the fine structure of the spectrum.

S. Peters and coworkers recently published a very rigorous study of the size dependence modifications of the XPS spectra for mass-selected Au, Ag, and Cu nanoparticles supported on SiO_2 [34, 35]. The synthesis of the particles was made by physical methods (using a cluster deposition source) which allowed preparation of extra small particles down to few atoms, with variable sizes and very narrow size

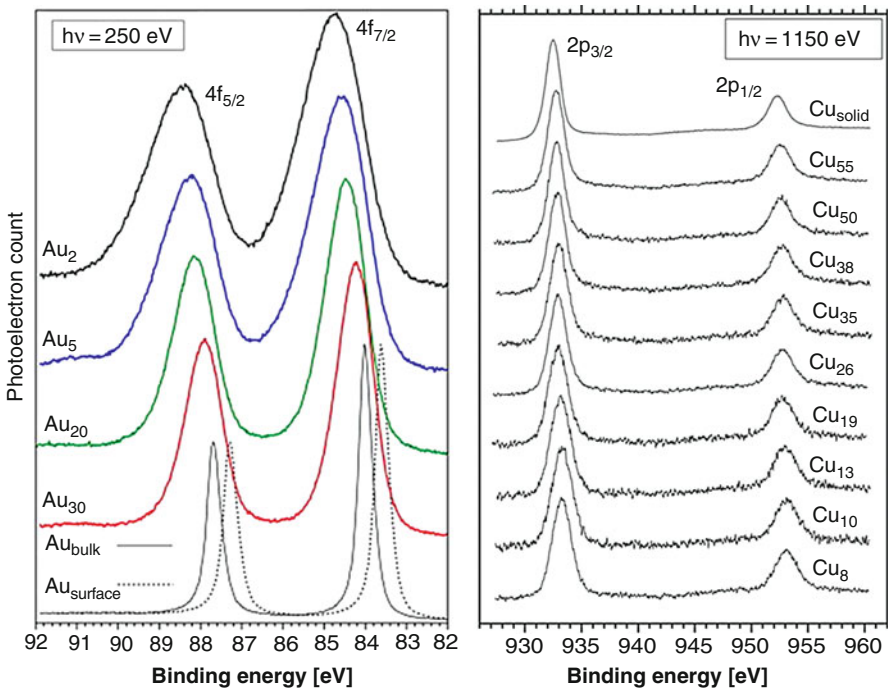


Fig. 9.10 Au 4f (*left*) and Cu 2p *(right)* SR-PES spectra of monodispersed Au and Cu NPs, respectively, supported on thin silica layer naturally grown on a Si wafer (SiO_2/Si). For comparison, the peaks of bulk Au and Cu taken under the same experimental conditions are included. The surface peak of a macroscopic Au crystal is indicated by the *dotted line*. The indices in Au and Cu indicate the number of atoms in each NP (From Refs. [34, 35])

distribution. It is obvious that the uniformity of the particle size is indispensable in studies where size-dependent phenomena are investigated [36]. Figure 9.10 shows the Au 4f core-level spectra of supported Au_N nanoparticles of various sizes (where N is the number of atoms in each particle) [35]. We can estimate the size of the nanoparticles by using the formula proposed in Ref. [37] to be between 0.4 (Au_2) and 1 nm (Au_{30}). In the same figure, the Au 4f photoelectron peaks derived from bulk and surface gold samples were included for comparison.

Three main differences are evident when comparing the Au 4f peaks recorded on bulk and NP gold: when the particle size decreases, (i) the E_B, (ii) the peak width (FWHM), and (iii) the asymmetry in the peak shape increase. In particular, compared to the E_B of bulk Au, Au_2 dimmers (ca. 0.4 nm) are shifted of about 0.8 eV, while the shift drops to 0.2 eV for the 1 nm particles (Au_{30}). On the other hand, the FWHM of the NP spectra is considerably increasing from 0.4 eV measured on the bulk Au to 1.7 eV for Au_2. According to the authors of this study, final state effects are mainly responsible for the high E_B shift of the peak, while the asymmetry in the low binding energy side of the peak is interpreted as an initial state effect due to under-coordinated Au atoms within the NPs.

In the case of Cu particles, the Cu 2p photoelectron peak has characteristics similar to those observed for Au that is broadening and shifting to higher E_B with respect to the bulk as the particle size decreases [34]. The magnitude of E_B shift is comparable with the one observed for Au (0.9 eV shift compared to the bulk for Cu_8 particles). However, in contrast to Au, in the case of Cu, the spectral shape is not influenced by the particle size.

Overall, the high brilliance and high energy resolution obtained in a synchrotron-based photoemission experiment can be beneficial to distinguish fundamental characteristics in the spectra of NPs with sizes down to a single atom. From these studies, the high binding energy shift of supported metal particles was confirmed, together with a remarkable broadening of the peak width. However, it was also shown that these spectral modifications are dominant for particles with very small sizes (up to 1 or 2 nm) and fade for larger particles which have practically similar spectral characteristics to the bulk material. Therefore, as mentioned, one should be extremely cautious before interpreting binding energy shifts and peak broadening of NP spectra as size-dependent sifts, since similar spectral modifications can have a different origin, as, for example, differential electrostatic charging.

It is interesting here to refer to a study by Anderson et al. [38, 39], concerning size-dependent shifts of similar particle-sized Au NPs. They used a liquid phase colloidal synthesis method to prepare their Au NPs with narrow size distributions that were afterward deposited onto commercial high-surface-area TiO_2 powder. The supported Au NPs produced by the colloidal synthesis are capped into the organic surfactant, and for that reason the samples had to be posttreated in order to remove the organic ligands. Evidently, this synthesis method provides less control of the supported Au particles, than the physical method used in the work of S. Peters et al., but has a high technical relevance since it better resembles the fabrication methods used for the preparation of technical heterogeneous catalysts. E_B shifts to higher energy and peak broadening for small Au NPs were observed in this study, similar to the work of S. Peters et al. This indicates that the SR-XPS method can be equally effective to study both model and realistic, more complex, NP systems.

Energy Tunability for Nondestructive Depth Profiling

As mentioned above, the probing depth of the PES measurements depends on the kinetic energy of the emitted photoelectrons. Therefore, the use of different excitation energies enables variation in the depth sensitivity. Conventional XPS laboratory sources (AlKα and MgKα as well as He I and He II lines) provide fixed photon energies. Therefore, when the analysis of the depth distribution is required, ion sputtering methods or angle resolved measurements are employed [5]. These methods have been developed for the analysis of macroscopically planar samples, and their applications on nanoscaled materials might give unreliable results. Consistent depth profile analysis can be only done by using the tunable SR, where the different excitation energies enable the variation of the depth sensitivity of the measurement from sub-nm up to tenths of nm (in case of excitation by hard X-rays). Evidently, the contribution of surface components is less as the electron kinetic energy increases.

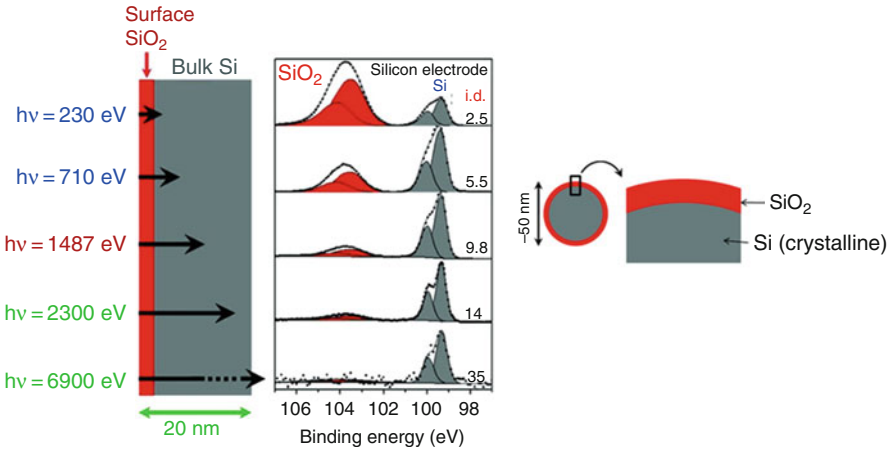


Fig. 9.11 Influence of the photon energy on the Si 2p spectrum of 50 nm silicon NPs. Schematic view of the evolution of the information depth (*arrow*) as a function of the photon energy (hν) (From Ref. [40]). The i.d. number in each spectrum denotes the information depth calculated by the method proposed in Ref. [17]

Note, however, that the photon energy not only influences the information depth but also the ASF of photoemission. Therefore, when photoelectron peaks from different elements are compared, care should be taken that the differences in the photon energy-dependent ASF have been taken into account. A tutorial example of nondestructive depth profile measurements over silicon nanoparticles with core–shell morphology follows [40]. Silicon is a benchmark material for such studies, since a stable oxide passivation layer is formed upon air exposure of metallic silicon, while the E_B of Si 2p core-level peaks between the oxide and the metallic state are well separated.

Figure 9.11 shows the Si 2p XPS spectra of a silicon nanopowder with ~50 nm mean diameter recorded using various photon energies (hν). The Si 2p spectra consist of 2 peak doublets, with E_B characteristic for metallic and oxide silicon. In particular, the first Si 2p peak at about 99.5 eV (deconvoluted into $2p_{3/2}$ and $2p_{1/2}$ due to spin−orbit coupling) is typically assigned to metallic silicon (in gray), while the peak at about 103.5 eV is due to the native SiO_2 oxide (in red). Spectra recorded in three instruments using SR soft X-rays (100–800 eV), a laboratory source (1,486.6 eV), and SR hard X-rays (2,000–7,000 eV) are summarized in Fig. 9.11. It is evident that the relative intensity between the Si and SiO_2 peaks is dramatically influenced by the variations in the photon energy. In particular, the relative intensity of the SiO_2 peak is decreasing with the increase of the photon energy, indicating that the Si NPs have a core–shell morphology with SiO_2 forming a thin shell over the Si core.

This example can be also used to illustrate the importance of using surface-sensitive methods, like XPS (with soft X-rays), in nanomaterials characterization. When a photon energy of 2,300 eV is used (estimated information depth, i.d. = 14 nm), the surface SiO_2 peak is hardly seen, while for 6,900 eV (i.d. = 35 nm), the

SiO_2 signal is in the noise level. Therefore, the assumption that bulk characterization techniques can provide information for the surface state of nanomaterials due to the high surface to bulk atom percentage is limited to very small sizes. In this example, when the detection depth (or equally the particle size) exceeds to 20–30 nm, the surface signal is practically "invisible" by the experimental method.

Resonant Photoemission Spectroscopy

Resonant X-ray photoemission spectroscopy (RPES) is a very sensitive tool for studying electronic states of atoms within solids and interfaces. In an RPES experiment, valence band spectra are measured using several photon energies tuned across a narrow energy range. An increase in the photoemission intensity of a certain electronic state is observed at a specific photon energy (on resonance) compared to all the other energies (off resonance). To select the resonant frequency (energy) of the photons, the X-ray absorption spectrum is used, where the resonant energy is linked to the absorption peak maximum. Once the resonant energy has been found, the photon energy is fixed and the XPS spectrum is recorded. Information from the RPES experiments can be used in order to conclude about the hybridization of electronic states between neighboring atoms in the solid, as, for example, for the type of metal–oxygen bond in an oxide. Detailed explanation of the physical phenomena governing resonant photoemission is out of the scope of this chapter, and extensive reviews can be found elsewhere [41].

T. Kataoka and coworkers [42] utilized RPES to study the electronic structure of Fe-doped ZnO NPs with mean size of about 7 nm. In this study, the determination of the valence of iron ion was of major importance, in order to rationalize the magnetic properties of the mixed oxide. In order to better visualize the Fe 3d states in the valence band region, the authors studied resonant spectra of both the Fe 3p–Fe 3d and Fe 2p–Fe 3d cores' excitation. Since the excitation photon energy within the two cases differs of about 650 eV, the iron electronic state in two different probing depths could be examined. This permits studying the electronic structure in both the core and surface region of the NPs in a single experiment.

In Fig. 9.12a the RPES results from the Fe 3p–Fe 3d core excitation (surface region of the NPs) are shown. The difference between valence band spectra measured on and off resonance was used to extract the resonantly enhanced Fe 3*d* contributions to the valence band region. From the X-ray absorption spectra of the Fe 3p (or Fe $M_{3,2}$ in the Siegbahn notation) shown in Fig. 9.12b, the authors could determine the on-resonance photon energies for Fe^{3+} (at 58 eV) and Fe^{2+} ions (at 57 eV). The off-resonance spectrum using 53 eV photon energy was recorded as a reference. As is evident by directly comparing off- and on-resonance spectra (Fig. 9.12c), there are slight intensity differences between them, particularly at about 3 eV. This is better visualized in the difference curves between off- and on-resonance spectra (see at the bottom of Fig. 9.12a). New features at about 3 eV appear when the valence band spectrum is recorded using the 58 eV photon energy, while for 57 eV there is no evidence of new valence band states. Since, as mentioned above, only Fe^{3+} species give resonance at 58 eV, these results indicate the Fe^{3+} ions are dominant in the surface region of the ZnO:Fe NPs.

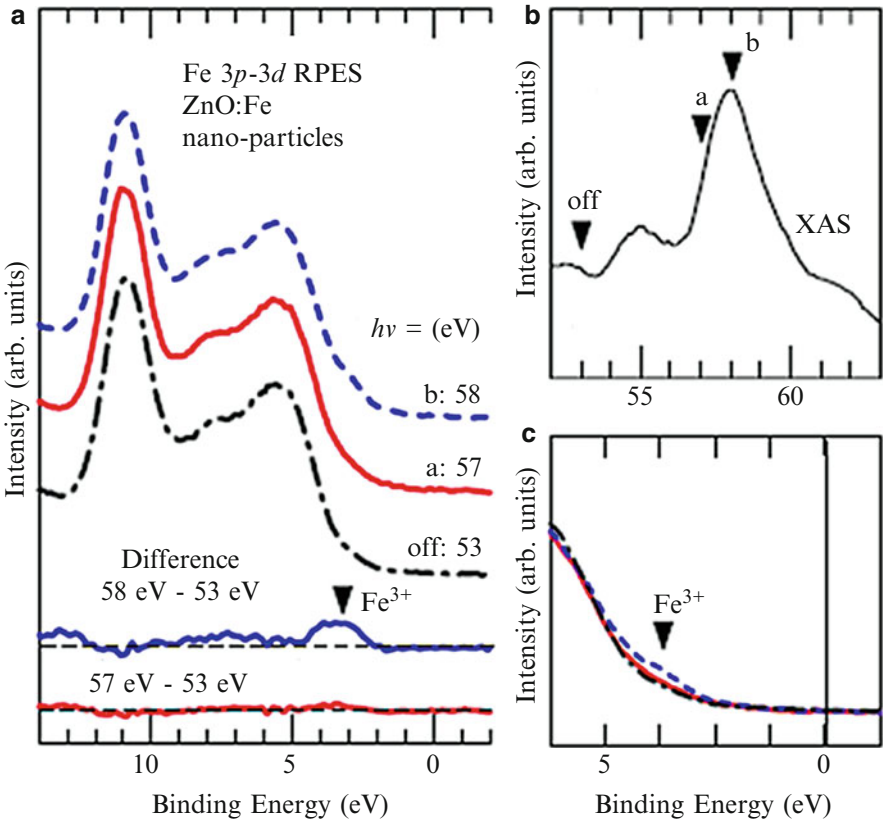


Fig. 9.12 (**a**) Resonance valence band photoemission spectra of the Fe:ZnO nanoparticles taken with photon energies in the Fe 3p–3d core-excitation region. The difference curves at the bottom represent the Fe^{3+} states. (**b**) X-ray absorption spectra on the Fe 3p (Fe $M_{3,2}$) edge. (**c**) Detail of the valence band spectra close to the Fermi edge (From Ref. [42])

Similar resonant results can be also recorded for the Fe 2p–Fe 3d core excitation (not shown). However, in that case the Fe 2p (or Fe $L_{3,2}$ in the Siegbahn notation) absorption threshold is at about 705 eV, which is much higher compared to that corresponding about 53 eV in the case of the Fe 3p. Therefore, much higher photon energies should be used to monitor resonance spectra in the valence band, also inducing higher photoelectron energies. According to the discussion in paragraph 2.5, this will be also related to the higher probing depth. From these results the authors concluded that iron is in a mixed $Fe^{2+}$and Fe^{3+} state, but the Fe^{2+} ions dominate the deeper layers, supporting a core–shell morphology of the iron ions in the Fe:ZnO NPs (Fe^{2+} core/ Fe^{3+} shell). In this example RPES experiments were used to reveal the layer morphology of mixed oxide NPs, by distinguishing features related to Fe^{2+} and Fe^{3+} oxidation states. It should be noted that in this particular case, the Fe 2p core-level spectra are

much less informative than the RPES results. This is due to the complex shape and the peak overlapping of Fe^{2+} and Fe^{3+} 2p core-level peaks [43], which cause difficulties in the peak analysis by spectral deconvolution.

5 Key Research Findings

In the early years of SR-XPS, the majority of the experiments were performed in conventional UHV experiment setups (*end stations*) where just the X-ray tube was substituted by the synchrotron source (e.g., [44]). The aforementioned advantages of SR were sufficient enough to provide more detailed information compared to a laboratory experiment. However in the last 10–15 years, synchrotron-based apparatuses were redesigned, and/or new concepts were used so as to take full advantage of the exceptional capabilities of SR. New approaches of the XPS technique have been developed and implemented in many synchrotrons worldwide. Below we will describe three relatively newly developed photoelectron spectroscopy methods, which are becoming increasingly popular experimental tools for the characterization of nanomaterials. Selected examples from the application of these techniques to NP research are given.

5.1 Scanning Photoelectron Microscopy: XPS with High Lateral Resolution

The photon beam in a focused soft X-ray SR beamline has a typical diameter in the order of few microns. However, if a focusing element is introduced, like a Fresnel zone plate, the beam diameter on the sample can be focused down to the nanometer size (Fig. 9.13). The photoelectrons excited from this area are then collected by the electron analyzer, like in any other XPS experiment. If the sample is scanned with respect to the photon beam, an XPS spectrum is acquired at each point, and a two-dimensional distribution of the photoelectron intensity can be constructed (image). The lateral resolution of the instrument is given by the size of the focused X-ray beam on the sample. This combined system is called a scanning photoelectron microscope (SPEM). The advantage of SPEM compared to other microscopic techniques, like scanning electron microscopy (SEM), is the ability to provide elemental and chemical state information, as well as quantitative elemental compositions, with considerably higher surface sensitivity. Still the main drawback of the SPEM technique remains the low lateral resolution of about 50 nm, which is much inferior compared to electron (SEM, TEM) or atomic probe microcopies (AFM, STM). A schematic representation of the SPEM technique is given in Fig. 9.13 [45]. More details and information about the technical aspects can be found in specialized reviews [46–48]. Below we will present a recent example of the application of the SPEM technique to study electrochemical interfaces.

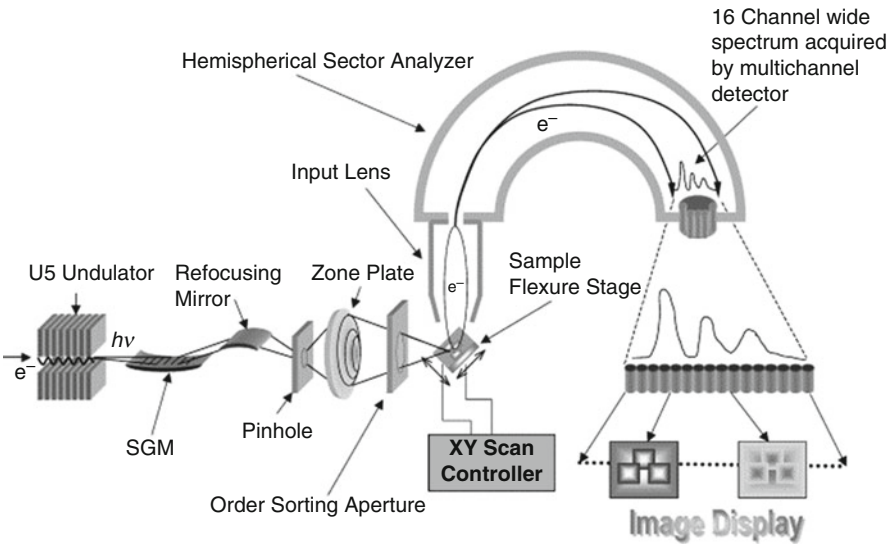


Fig. 9.13 Schematic diagram of a SPEM experiment [45]

5.1.1 Case Study 1: Monitor the Characteristics of Membrane/Pt NP Interfaces Under Polarization with SPEM

In this work, E. R. Savinova and coworkers investigated a model membrane/electrode assembly (MEA) under polarization conditions by using SPEM [49]. It was shown that by this method it is possible to monitor the morphology, the surface composition, and the chemical state of electrode constituents in a single experiment. The model MEA shown in Fig. 9.14a was composed by a phosphoric acid-doped polymer electrolyte membrane, a Pt nanostructured film as the working electrode (WE), and a Pt/C layer as the counter electrode (CE). As shown by SEM microscopy performed in another instrument, the Pt film covers most of the membrane with some fractures (darker areas in Fig. 9.14b, c) where the polymer electrolyte membrane is exposed. This morphology was chosen since it is beneficial for probing simultaneously the electrode, the membrane, and their interface. The Pt film consists of approximately 20–30 nm aggregates, each made up of Pt NPs about 3 nm in diameter (Fig. 9.14d).

Practically, each pixel in a SPEM image reflects the number of photoelectrons (or the integrated spectrum area) of the specific photoelectron core-level peak excited by the selected photon energy. For example, assuming that the photon energy is kept fixed in the course of the experiment (e.g., hv = 690 eV) and one is interested on the Pt 4f peak (binding energy ~71 eV), then the electron analyzer should be set so as to record photoelectrons with kinetic energy 619 eV (in practice a short energy window of few eVs around this energy is recorded). It is therefore evident that areas rich in Pt will appear brighter compared to areas deficient in Pt. Please note that compared to all other high-lateral-resolution elemental analysis techniques, SPEM is the only one which gives information exclusively from the

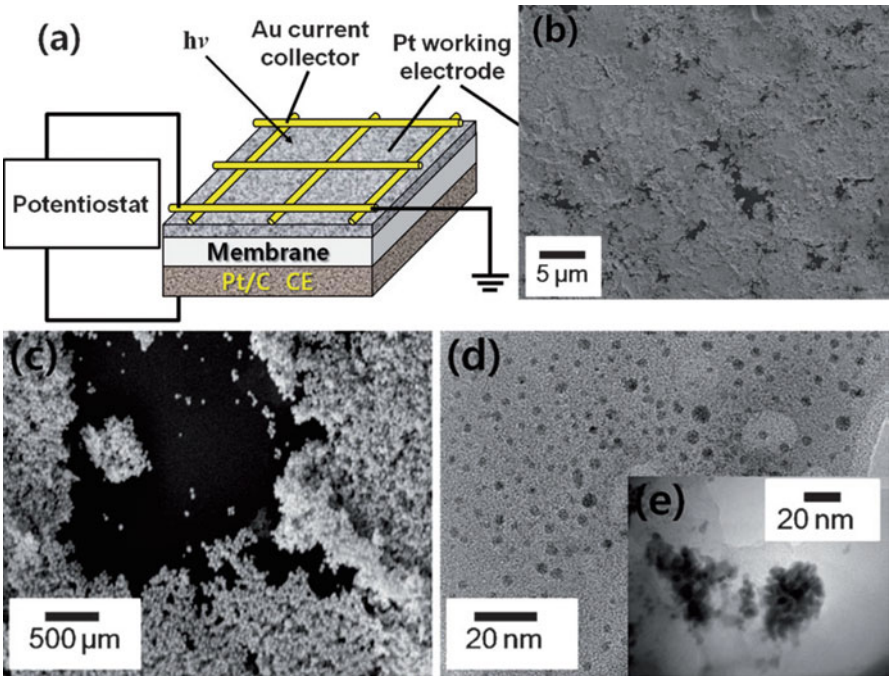


Fig. 9.14 (**a**) Schematic diagram of the model MEA. (**b**, **c**) Postmortem SEM images of the WE side of the MEA at different magnifications. (**d**, **e**) TEM images obtained by suspending Pt film from the WE in ethanol and drop casting on a TEM grid [49]

first 1 to 4 nm. As mentioned above, the model electrode consists of a Pt aggregated layer over the membrane, and as such, it is not atomically smooth. Therefore, the contrast in the SPEM image is not only due to concentration contrast between P and Pt but also due to topographic features (like in a SEM image). S. Gunther et al. [50] developed a method to remove the contribution of the topographic features from SPEM images, and after the application of this method, images of Fig. 9.15 exclusively reflect the real concentration contrast between P and Pt. It is evident that the brightness of the two images is reversed when P 2p or Pt 4f photoelectrons are recorded, highlighting in this way the areas dominated by platinum or phosphorous species. A very important feature of the technique is that the SPEM images can be easily transformed to individual spectra, and therefore it is possible to acquire spectra from selected areas in the image by integration of the individual pixel/spectra within this area (please keep in mind that each pixel in the image represents an individual spectrum). At the bottom of Fig. 9.15, reconstructed Pt and P spectra from four selected areas of the SPEM images (1–4) are presented. As is evident, Pt and P are present all over the electrode, which means that traces of Pt are found within the cracked areas, while phosphorous species are also detected in areas dominated by Pt. This last information is extremely valuable, taking into account the high surface sensitivity of this technique. Non-surface-sensitive

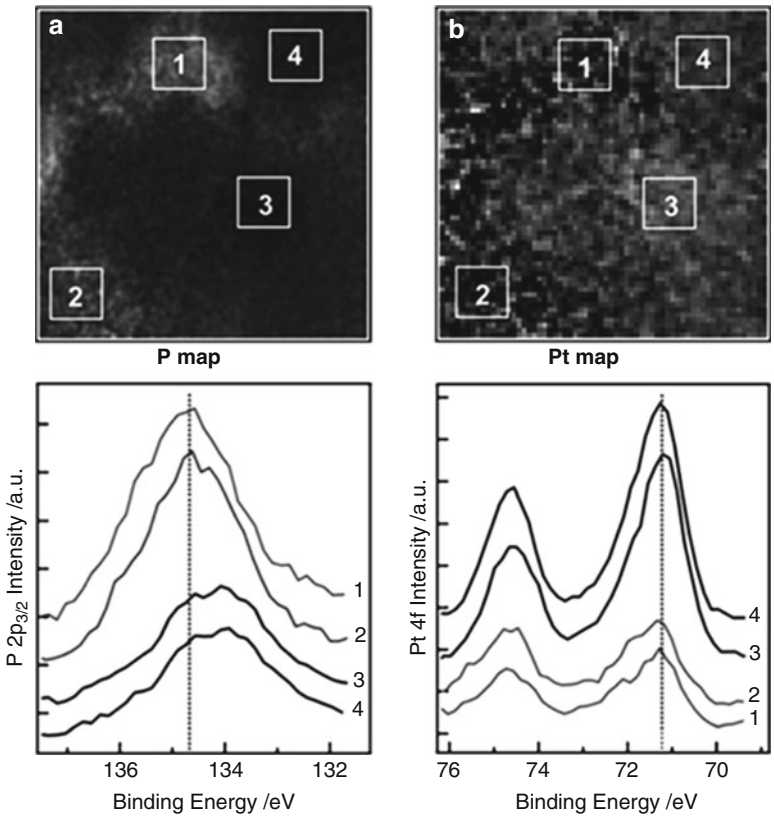


Fig. 9.15 Top: SPEM images of the same area taken by tuning the analyzer to the P $2p_{3/2}$ (**a**) and Pt 4f (**b**) photoelectron emission at the OCP, under 1×10^{-5} mbar water vapor atmosphere obtained after processing to remove the contribution of the topographic features. Bottom: reconstructed P $2p_{3/2}$ and Pt 4f spectra from the selected areas marked 1–4 in the SPEM images and concentration maps [49]

methods (e.g., EDX mapping) cannot distinguish if phosphorous species are located over or under the Pt nano-layer. However the SPEM results clearly show that phosphorous species are adsorbed over the Pt layer. In addition, the chemical specificity of the technique was employed to distinguish between possible differences of the phosphorous species on the membrane and on the electrode (Pt) areas. Indeed, the P $2p_{3/2}$ binding energy in the fractured zones (mainly on the polymer membrane) is 134.7 eV, which was attributed to ortho-, pyro-, or polyphosphoric acid. On the other hand, the line shapes of the P $2p_{3/2}$ spectra over the Pt areas (3, 4) are broader and shifted to lower E_B. The difference of the P $2p_{3/2}$ spectra in the two areas was attributed to differences in the polarization of the phosphoric acid electrolyte residing in the polymer membrane and in the Pt film.

The positioning of the sample gave the possibility to work under bias conditions, i.e., measure SPEM spectra when a potential is applied between the working (top side)

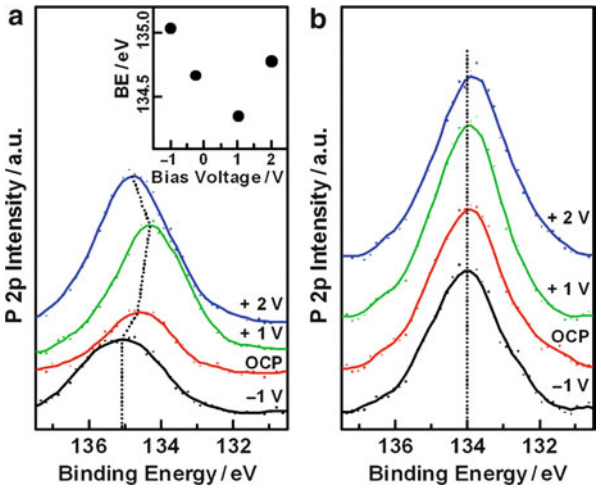


Fig. 9.16 Spectra extracted from SPEM P2$p_{3/2}$ images corresponding to the Pt film fracture (**a**) and to the Pt film (**b**). The respective MEA zones are marked in Fig. 9.15 with labels 4 (for Pt film) and 1 (for the film fracture). The *inset* shows the BE shifts of the P 2p peaks as a function of the bias voltage (From Ref. [49])

and the counter (back side) electrodes. As shown in Fig. 9.14a, a gold mesh attached on the Pt nano-layer was used as the current collector, whereas the small beam size allowed to record SPEM images within the holes of the mesh. The Au mesh was connected to the ground (and so is the Fermi level of the analyzer), and therefore in bias experiments the potential of the mesh and the parts of Pt electrode in electrical contact with it remain constantly to the ground (zero voltage). On the other hand, parts of the Pt electrode which are not in contact with the Au mesh, for example, isolated Pt islands on the membrane or the membrane itself, should "feel" part of the potential applied to the counter electrode. These potential changes are easy to detect with high accuracy in a photoemission experiment, since they will induce a shift on the emitted photoelectron kinetic energy. Therefore, the SPEM technique can be used as a very sensitive local probe for the study of differences in potential between the electrode and the electrolyte (polymer membrane or solid oxide) in electrochemistry [51]. Here we focus on the P 2$p_{3/2}$ peak, since as shown above, it can be detected both on the membrane and on Pt areas. To facilitate the discussion, we distinguish between areas corresponding to the membrane (area 1, within the Pt film fractures) and those corresponding to the Pt film (area 4, please refer to Fig. 9.15).

Figure 9.16a shows that the P 2p peak on the membrane systematically shifts toward lower E_B with increasing bias voltage from −1 to +1 V. When the bias voltage increases toward positive values, the surface of the phosphoric acid-doped membrane becomes negatively charged relative to the Pt WE, because protons in the membrane move toward the Pt/C CE. This negative charging naturally leads to an increase of the P 2p photoelectron kinetic energy, which is translated into a decrease of the apparent E_B. The extent of the membrane polarization relative to the Pt WE can be estimated from the E_B shift (see inset in Fig. 9.16a). For $\Delta V_{Cell} = \pm 1$ V, $\Delta E_B = \pm 0.5$ eV, which suggests a polarization relative to the open-circuit potential (OCP) of about ±0.5 V. Apparently, the E_B shifts are smaller

than the applied bias voltage, which can be explained by the ohmic losses in the membrane (related to the decreased proton conductivity under dry experimental conditions) and possibly some polarization losses at the CE. The P 2p E_B shift has the reverse trend, with further increase of the bias voltage to +2 eV. Such a nonlinear behavior may be explained by the hydrogen evolution at the CE and a concomitant negative shift of the OCP (note that the CE in our two-electrode cell also acts as the reference electrode).

Figure 9.16b shows P 2p spectra of phosphorus species present on the continuous Pt layer reconstructed from the SPEM image. They do not exhibit any shift with the bias voltage, and this suggests that phosphoric acid located on top of the Pt film is not polarized. In order to explain this fact, it was proposed that because of the low water vapor pressure, phosphoric acid rests on the surface of the nanostructured Pt film in the form of droplets that are disconnected from the bulk of the electrolyte. Since Pt is grounded, this would explain the independence of the P 2p peak positions from the bias voltage. In general, this work demonstrated the ability of SPEM to simultaneously probe the morphology, the surface composition, and the chemical state with high lateral resolution. It is also manifesting the potential of the method to analyze complex samples under conditions which simulate these of the operational conditions.

5.2 Ambient Pressure X-Ray Photoelectron Spectroscopy: XPS Under Pressure

Both SR and laboratory-based X-ray photoelectron spectroscopy experiments are traditionally applied under ultrahigh vacuum conditions (UHV). However, in most of their applications (e.g., in catalysis), nanomaterials are operating under much higher pressures like atmospheric pressure or above. This pressure difference implies that the phase (structure and chemical state) that is monitored under UHV conditions may undergo significant changes at higher pressures, as a consequence of dynamic phase rearrangements induced by the interaction with the gas environment. The earlier attempts to bridge this pressure gap were by ex situ experiments, allowing direct transfer of samples between a UHV station and a high-pressure reaction cell; in that manner, UHV surface-science techniques were coupled with reaction experiments carried out under realistic conditions [52]. This strategy permits the determination of the structure and composition of nanomaterials before and after interaction with the gas phase, but is relatively limited since the measurements are not performed in equilibrium with the gas phase and important modifications might take place during UHV characterization and transfer (i.e., segregation of specific components, etc.) [53]. These limitations were lifted by the development of new class of photoelectron spectrometers able to operate at the mbar pressure range [54]. This technique is usually called "ambient pressure" photoelectron spectroscopy (APXPS)[11] in order to be distinguished from vacuum-based X-ray

[11] Also known as high-pressure XPS or (near) ambient pressure photoelectron spectroscopy (PES).

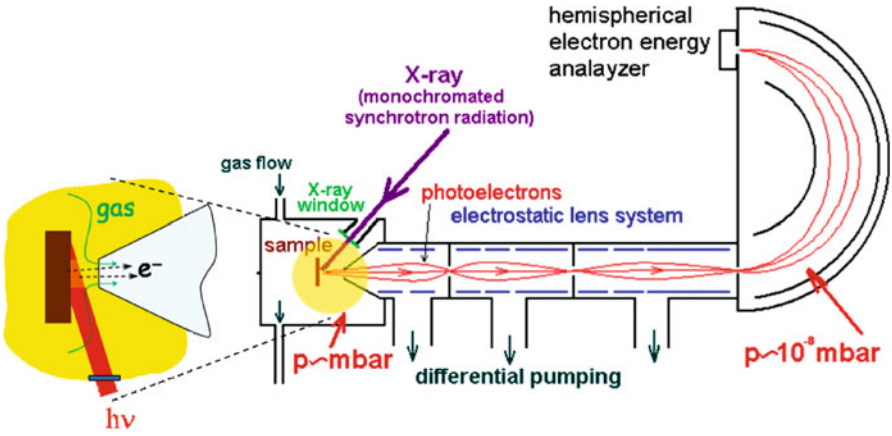


Fig. 9.17 Schematic representation of an APXPS setup and close up of the analyzer nozzle-sample area (From ref. [57])

photoelectron spectroscopy. Although the first application of APXPS was reported by K. Siegbahn's group in the early 1970s [55], it took almost 30 years before the development of an improved SR-APXPS instrument by D. F. Ogletree et al. [54] and the installation of the two first prototypes at the ALS (Berkeley) and BESSY II (Berlin) [56]. Today, more than 10 SR-APXPS instruments have been or are about to be installed in several synchrotrons around the world, and tutorial reviews about the subject can be found in recent publications of the pioneers in the field [56–58].

Briefly, the unique elements of an ambient pressure instrument, compared to a conventional XPS setup, are (a) the X-ray window, which separates the beamline (which is under UHV conditions) from the sample cell (which is under mbar pressure), and (b) the long, differentially pumped electron lenses, which separate the sample cell from the electron analyzer (Fig. 9.17). The maximum pressure in the sample cell is limited by the scattering of photoelectrons by gas phase molecules, which leads to a decrease of the photoelectron signal. Typically the operation pressure of APXPS instruments is in the order of few mbars, while with further optimization, it can reach up to 130 mbar [58].

Here we attempt to demonstrate the capabilities of the technique, by presenting two characteristic examples from research on nanoalloys. We focus the discussion on cobalt–platinum-based NPs in equilibrium with various gas atmospheres. Bimetallic PtCo NPs are of large and growing interest because of potential applications in fields such as magnetism [59], catalysis [60], and electrocatalysis [61]. It will be shown that depending on the ability of the gas to oxidize or reduce the NPs, the morphology, composition, and oxidation states of the NPs are altered considerably. Photoemission spectroscopy is well suited to study these modifications and could be beneficial to other spectroscopic and microscopic methods (e.g., electron microscopy or X-ray absorption spectroscopy), due to its high surface sensitivity that helps to retrieve important information about the gas/solid interface.

5.2.1 Case Study 2: The Oxidation State and the Morphology of PtCo Bimetallic Nanoparticles Under Reducing (H_2) and Oxidizing (O_2) Environments

Monodispersed PtCo alloyed NPs with mean size of 3 nm were studied in oxidizing and reducing conditions by APXPS [36]. The PtCo NPs were prepared by the low-energy cluster beam deposition technique (LECBD) [62] and exhibited a mean diameter of $Dm = 3$ nm, as derived from TEM measurements (Fig. 9.18). A PtCo foil (bulk stoichiometry 1:1) prepared by conventional metallurgy was also studied as an internal reference, in order to detect, if any, differences in the redox behavior between the bulk and the nanoparticle's system.

Characteristic photoemission spectra of the PtCo NPs and foil recorded in 0.2 mbar of O_2 and H_2 at 520 K are shown in Fig. 9.19. In H_2, the Pt $4f_{7/2}$ peak for both NPs and foil (Fig. 9.19a) was found at 71.4 ± 0.1 eV, a value that is reported for PtCo alloys. The Pt 4f peak of the NPs does not change in O_2 ambience, while it vanishes in the PtCo foil (hν = 1,290 eV, estimated information depth ca. 5.5 nm [17]). Cobalt and oxygen peaks dominate the foil's survey spectra, indicating extensive de-alloying and Pt migration into the inner layers. In the PtCo foil (Fig. 9.19, *bottom spectra*), cobalt switches from Co_3O_4 to metallic Co [63] in H_2 atmosphere. In the case of PtCo NPs (*upper spectra*), in O_2 the Co $2p_{3/2}$

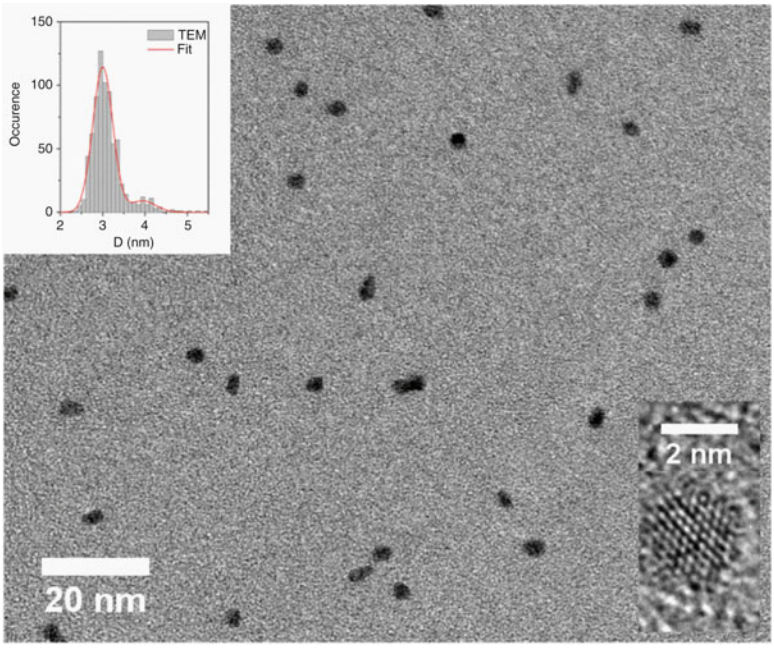


Fig. 9.18 TEM image of PtCo clusters prepared by the LECBD method and the corresponding size distribution (*up left corner*). Characteristic high-resolution TEM image of a 2 nm PtCo particle (*down right image*) (From Ref. [36])

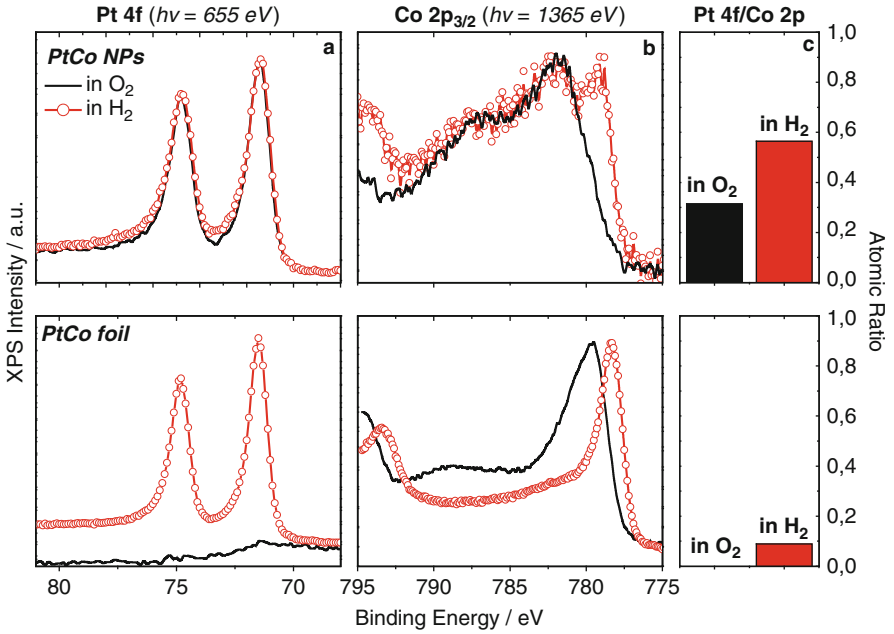


Fig. 9.19 (**a**) The relative Pt 4f and (**b**) the Co $2p_{3/2}$ photoelectron peaks of 3 nm PtCo NPs (*top*) and polycrystalline foil (*bottom*) recorded at 520 K in 0.2 mbar O_2 (*solid lines*) and H_2 (*open circles*). The spectra are normalized in height to facilitate comparison. (**c**) The Pt 4f/Co 2p atomic ratio (photoelectron KE = 580 eV) calculated for NPs and foil samples under the same temperature and gas atmosphere conditions (From Ref. [36])

spectrum is characteristic of CoO [63], while in H_2, reduced cobalt species appear as an additional component at low E_B. What is important to note here is that the CoO oxide formed over NPs is more difficult to reduce compared to the foil, an unexpected result given the small size of the NPs. The Pt/Co atomic ratio (Fig. 9.19c) increases in H_2 as compared to O_2 atmosphere, showing clearly that reduction favors surface segregation of Pt.

The depth distribution of Pt and Co over the first few atomic layers was investigated by nondestructive depth profile measurements. The relative Pt 4f/Co 2p atomic ratios, normalized to the photon flux, and the experimental photoionization cross section in four different information depths are shown in Fig. 9.20a. In H_2, the Pt/Co intensity ratio decreases when deeper layers are probed for both PtCo NPs and foil, indicating that Pt is preferentially localized on the surface and Co in the subsurface region. The stable Pt/Co ratio observed for the NPs for $h\nu > 370$ eV (i.d. ca. 2.5 nm [17]) is reasonable, due to the fact that practically the entire NP volume is probed. On the other hand, the inverse trend is observed in O_2 ambience, indicating the enrichment of cobalt (oxide) on the NP surface. A schematic model of the surface arrangement of PtCo NPs and foil under oxidizing and reducing conditions is given in Fig. 9.20b. The redox behavior of both NPs and the foil can be clearly designated from

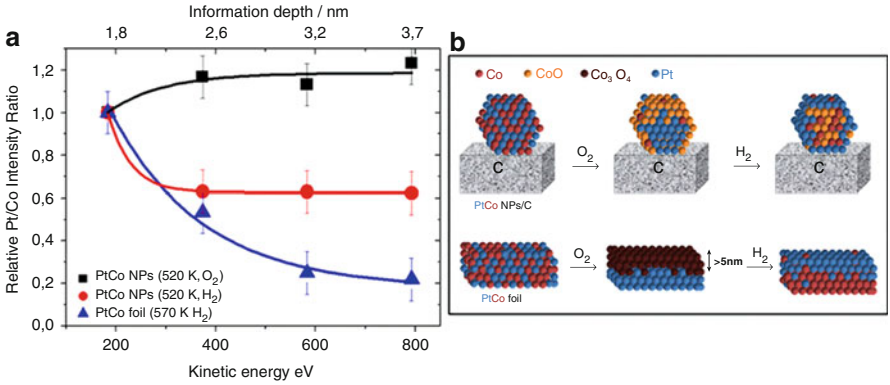


Fig. 9.20 (**a**) The Pt/Co atomic ratio calculated from the Pt4*f* and Co2*p* photoelectron peaks, as a function of the electron KE, measured at 520 K for PtCo NPs in O_2 and in H_2 and for the PtCo foil in H_2. On the upper x-axis the estimated average information depth for each electron KE is given. (**b**) Schematic model illustration of the proposed PtCo atom arrangement in NPs and foil under oxidative and reductive environments (From Ref. [36])

the XPS results; in O_2, cobalt is oxidized to Co_3O_4 at the foil or to CoO-like oxide at NPs and encapsulates Pt, while in H_2, cobalt oxides reduce to the metallic state at the foil or to a mixed CoO/Co state at NPs, while Pt segregates back to the surface.

5.2.2 Case Study 3: Studying the Redox Behavior of a Realistic PtRuCo Electrocatalyst with APXPS

In this work, unsupported PtRuCo nanopowder with nominal composition $Pt_{0.375}Ru_{0.375}Co_{0.25}$ was studied under various gas environments [64]. The material was prepared by combustion synthesis, which is one of the chemical synthesis techniques proposed for electrocatalyst's preparation. In contrast to the well-controlled LECBD technique used in the example above, chemical synthesis techniques typically lead to a mixture of different nanostructures, rather than a well-defined particular nanostructure with defined size and properties. By this example we demonstrate the capability of APXPS to characterize relatively complex nanopowders, which resemble very much the catalysts and electrocatalysts used in applications. TEM images showed the formation of soft agglomerates composed of nanocrystallined highly dispersed PtRuCo particles in the range of 10–17 nm, while the X-ray diffraction (XRD) patterns revealed Pt-based alloy formation with Ru and/or Co in the bulk [64].

The sample was analyzed in equilibrium with various gas atmospheres at 0.5 mbar overall pressure and at 670 K temperature. In Fig. 9.21, the C 1s, Ru $3d_{5/2}$, Pt 4f, and Co $2p_{3/2}$ APXPS spectra recorded under pure O_2 or H_2 atmospheres and CH_3OH/H_2O reaction mixture are presented. The Pt 4f spectra recorded in reducing H_2 atmosphere show a narrow peak centered at 71.1 eV, indicating that Pt is present in the zero-valence state. In contrast, in O_2 ambient, two new doublets appear in the Pt 4f spectra in addition to the metallic state, with Pt $4f_{7/2}$ centered at

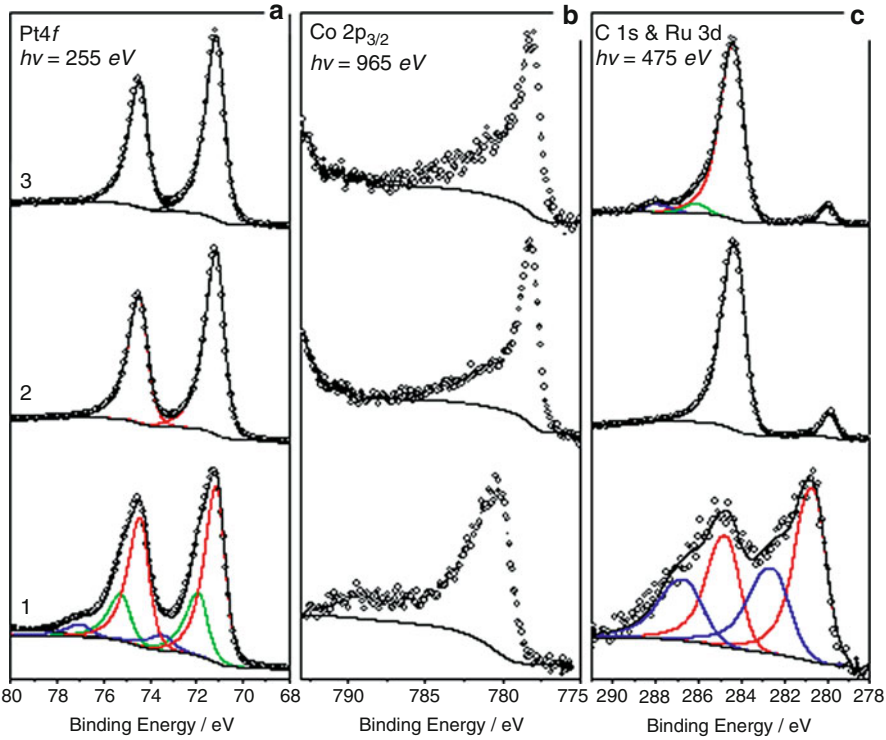


Fig. 9.21 APXPS spectra of (**a**) Pt 4f, (**b**) Co $2p_{3/2}$, (**c**) C 1s and Ru 3d, recorded on Pt–Ru–Co in situ at 570 K and in 0.5 mbar (*1*) O_2 ambient (*2*) H_2 ambient (*3*) $CH_3OH:H_2O = 1:2$ (From Ref. [64])

71.9 and 73.5 eV, due to the formation of two Pt oxide species [65]. Under CH_3OH/H_2O mixture Pt is reduced back to zero valence, which indicates that although the reaction mixture contains 0.35 mbar H_2O, the reducing effect of CH_3OH is dominant, preventing the Pt oxidation.

The oxidation state of cobalt is also very much affected by the gas atmosphere over the sample, as is shown in Fig. 9.21b, where the Co $2p_{3/2}$ peaks are presented. In H_2, cobalt is metallic as demonstrated from the Co $2p_{3/2}$ peak at 778.2 eV and the characteristic peak shape asymmetry at the high BE site. In O_2 ambient, Co $2p_{3/2}$ is shifted at 780.4 eV and an intense shake-up satellite is formed, indicating Co^{2+} formation due to CoO or CoOOH [63]. Due to the complex nature of the Co $2p_{3/2}$ peak, deconvolution of the spectra was done using reference spectra recorded at the same experimental setup. Comparison of the peak recorded under reaction with the reference spectra (*not shown*) indicates that during methanol oxidation cobalt is mainly metallic at 778.2 eV, with possible traces of ionic Co^{2+} appearing as a shoulder at about 780.4 eV.

The analysis of the Ru 3d spectra is obscured due to the overlapping with the strong C 1s signal induced by adsorbed carbon species. However, due to the high

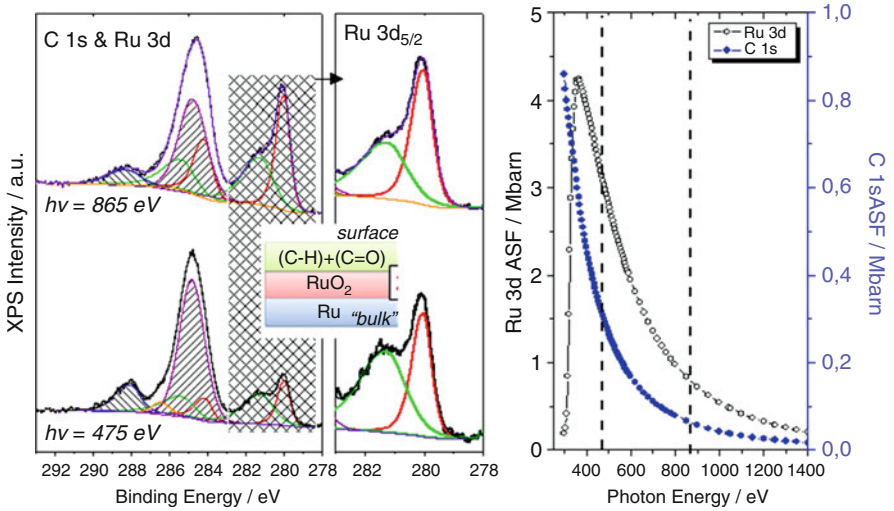


Fig. 9.22 (*Left*) APXPS C 1s and Ru 3d (in *shaded peak*) core-level photoelectron peaks of PtRuCo catalyst, recorded in $CH_3OH:H_2O$= 1:2 reaction mixtures in a total pressure of 0.5 mbar, at 570 K, with two photon energies. A magnification of the Ru 3d $_{5/2}$ peak is presented in the center. (*Right*) The evolution of Ru 3d and C 1s atomic sensitivity factors as a function of the excitation photon energy derived from Ref. [13]

energy resolution obtained in synchrotron radiation, the overlapping mainly concerns the Ru $3d_{3/2}$ component, while the Ru $3d_{5/2}$ one is clearly distinguishable, as is shown in Fig. 9.21c, where the energy region for both C 1s and Ru 3d is presented. Under reaction conditions, hydrocarbons and/or graphitic carbon species located at 284.4 eV dominate the C 1s region [66], while two additional species at 286.2 and 288.0 eV were also observed. The C 1s peaks at 286.2 and 288.0 eV correspond to carbon bound to oxygen – most probably alcohol or carbonyls groups (C–O) and formate-carbonate groups (C=O), respectively [66]. The Ru $3d_{5/2}$ peak is centered at 280.0 eV, very close to the binding energy measured for clean metallic Ru (0001) in the same setup [67]. Reference spectra recorded under pure H_2 ambient show only metallic Ru and the main C 1s component at 284.4 eV, while oxygen-bonded carbon species were not found. The origin of the C 1s peak recorded in pure H_2 ambient is most likely hydrocarbon species from the reactor walls which are adsorbed and decompose on the sample. As expected, carbon is completely removed under O_2 ambient at 570 K, and two Ru 3d doublets at 280.7 and 282.7 eV, indicative of the RuO_2 and RuO_3 oxides, respectively, were found [67].

By simple comparison of depth-dependent spectra, one can get useful information about the adsorbed species and the surface arrangement, in this relatively complex nanopowder system. In Fig. 9.22 the C 1s and Ru 3d region recorded for two different depths is shown. It is evident that the C 1s peak is much more intense for the 475 eV excitation photon energy (hv) spectrum compared to that of the

Table 9.1 Variation of the surface atomic ratios for two different probing depths

	C 1s/Ru 3d (raw data)	C 1s/Ru 3d (ASF)	C 1s/Ru 3d (norm. to the ASF)
hν = 475 eV	3.6	0.099	36.4
hν = 875 eV	2.2	0.079	27.9

865 eV one. In particular, the C 1s/Ru 3d raw area ratio varies from 3.6 at 475 eV to 2.2 at 875 eV (see Table 9.1). The observed difference in the relative intensity between the Ru 3d and C 1s peaks when the spectra are recorded with different photon energies has two possible origins; either it reflects the photon energy-dependent ASF differences between the C 1s and Ru 3d levels, or it is caused by the arrangement of Ru and C in layers (e.g., formation of core–shell structure). The inelastic mean free path should not have significant contribution, since it is known to vary almost linearly with the photoelectron kinetic energy [17]. Therefore, in order to be able to compare results recorded with different photon energies, the raw data should be normalized by the ASF. As is shown in Fig. 9.22, where the ASF of both core levels are presented, the difference in the ASF becomes very important when photon energies below 320 eV are used. As shown in the last column of Table 9.1, after normalization the C 1s/Ru 3d ratio in two depths differs of about 25 %, which indicates that carbon species are mainly adsorbed on the surface (most probably due to methanol decomposition). If we focus on the Ru $3d_{5/2}$ spectra shown in the middle of Fig. 9.22, the RuO_x component is more pronounced at hν = 475 eV. This reflects the layered structure of ruthenium species, with RuO_x located over the Ru metal core. A schematic representation of the arrangement of C and Ru species is inserted in the figure.

In general it was shown that APXPS can give a detailed picture of the surface state of NPs under reactive gas environment, which is essential for the comprehension and design of materials with better performance. It is also demonstrated that the surface state of nanomaterials is not static but dynamic and is readily transformed under reaction with gas phase environments. The recognition of this fact, which is a common ground in almost all APXPS characterization studies, may act as the stimuli for the reconsideration and redefinition of our present understanding on the behavior of nanomaterials in their applications.

5.3 Hard X-Ray Photoemission Spectroscopy: XPS in the Bulk

Traditionally XPS is developed and utilized as a method for surface analysis of solids. As we discussed before, the surface sensitivity is due to the low kinetic energy of the photoelectrons, which in turn is directly related to the energy of the excitation photons as described by Eq. 9.1. It is therefore evident that when high photon energies are used, the method becomes less surface sensitive, or in other terms *bulk sensitive*. However, photoemission using high-energy X-rays (hard X-rays) produces extremely low spectrum signals. This is due to the fact that the probability of photoemission (as this is expressed by the ASF) is rapidly decreasing

with increasing the photon energy. For example, for the Cr 3d core level, the probability of photoemission at 8 keV is almost one million times lower than that at 100 eV ([68] and references therein). Therefore high brilliance synchrotron-based light sources are needed in order to produce as many photoelectrons as possible and overcome the strong reduction of photoionization cross section in the hard X-ray regime (up to ~10 keV). The development of third-generation synchrotron facilities and elaboration of modified high-energy electron energy analyzers established hard X-ray photoemission spectroscopy (HXPES)[12] as a method to analyze the electronic structure and the chemical state in the first 10–20 nm of the sample surface. Another very prominent feature of HXPES, especially if combined with soft X-ray SR-XPS, is the possibility of the analysis of the atomic composition and chemical state of the sample with depth by using depth-dependent measurements.

The design of the beamlines and experimental end stations for an HXPES experiment uses similar concepts with soft X-ray XPS. In the beamline design, care should be taken to ensure that the maximum of the radiation produced in the synchrotron is used, in order to enhance the photoelectron signal. The electron analyzer is the typical hemispherical type, but is properly modified for high transmission and high resolution at electron kinetic energies up to 10 keV. In order to match the photon penetration depth with the electron escape depth, grazing X-ray incidence should be employed. In addition, electrons should be detected at normal emission to maximize the bulk contribution in the detected signal ([69] and references therein). Comprehensive overviews in the field of HXPES can be found in recent literature [68, 70–72]. Below we will present some selected examples, which describe recent important results in the area of battery research.

5.3.1 Case Study 4: Analysis of Li-Ion Batteries by HXPES

In the field of energy storage, batteries play a key role. Among the numerous battery technologies, the lithium-ion battery (Li-ion) is probably the most widely used rechargeable battery type [73]. In a Li-ion battery, Li ions move from the anode to the cathode producing current to an external circuit, while the battery can be recharged when the ions follow the reverse route. Carbonaceous materials, and most commonly graphite, are used as the anode electrode, while Li-containing compounds (like Li-metal oxides and phosphates) as the cathode. Silicon is a promising candidate to replace carbon in battery electrode, since it has almost 10 times higher maximum theoretical capacity as compared to carbon. However, the large volume expansion that takes place upon lithiation of Si can cause electrode cracking and deterioration of the battery performance. A possible solution is to use nanostructured Si materials, as, for example, NPs, to limit volume expansion and improve the stability of Si-based batteries. The nonaqueous electrolyte is placed between the two electrodes and typically consists of a mixture of organic carbonates containing complexes with lithium ions. Since the commercialization of the Li-ion

[12] In the literature there are many other terms for HXPES, such as HEPES, HAXPES, and HIKE.

batteries at the beginning of the 1990s [74], numerous studies have been devoted to the development of new electrode and electrolyte materials with improved performance.

The electrode/electrolyte interface (also referred to as the solid electrolyte interface (SEI) and the solid permeable interface (SPI) for the anode and the cathode, respectively) is recognized as one of the key factors that influence the performance of the device, and several analytical methods have been used for its characterization (including nuclear magnetic resonance and Raman spectroscopies). Photoelectron spectroscopy is frequently used to characterize solid interfaces, since it is sensitive to the element type and its chemical state, while it provides also quantitative information about the composition. This is a combination of information that very few analytical techniques can provide. However, the high surface sensitivity of the XPS technique (<5 nm) when soft X-rays are used (<1,500 eV), which is usually an advantage for most of the applications, becomes a drawback in the case of the Li-ion batteries studies. This is due to the fact that in batteries the electrode/electrolyte interface is 3 dimensional (3D) and extends up to several tens of nanometers into the electrodes, exceeding by far the detection depth of soft X-ray photoelectron spectroscopy.

In the early days, destructive depth profiling techniques (through the sputtering of thin sections of the sample's surface by energetic ion bombardment and subsequent AES/XPS characterization) have been used to observe deeper parts of the interface [75]. However, sputtering induces changes (e.g., preferential sputtering of one element or compound compared to another) that limit the potential of this method. One solution to this problem is to use hard X-rays (usually from 2 up to 8 keV) in order to increase the kinetic energy of the ejected photoelectrons and thus their escape depth, so as the effective electrode/electrolyte interface to be within the probing depth. Therefore, HXPES has been established as an effective method to investigate the electrode interfaces in batteries and give depth information in tens of nanometers range.

In a series of recent publications, K. Edstrom and coworkers used HXPES to study Li-ion batteries using composite electrodes containing about 80 % of crystalline silicon nanoparticles with diameters of about 50 nm [40, 76, 77]. Their aim was to associate the interface reactions with the battery characteristics upon charging and de-charging. A very critical step in the performance of the battery is the incorporation of Li ions into Si nanoparticles (alloy formation) that takes place during the first discharge cycle and the reversibility of this process. The pristine electrode was a mixture of silicon NPs, carbon black, and the binder (CMC). Initially the battery cell was fully charged and subsequently was monitored by XPS upon different discharging and recharging stages. In particular after each electrochemical treatment, the battery cell was dismounted and the interface of interest was monitored by XPS, employing three different photon sources (MaxIV Laboratory, Lund, Sweden, and Bessy II, Helmholtz Centre, Berlin, Germany synchrotron facilities, as well as an AlKa laboratory source) and a wide range of photon energies (from 100 to 7,000 eV). In order to avoid air contamination, the samples were stored and transferred under inert atmosphere.

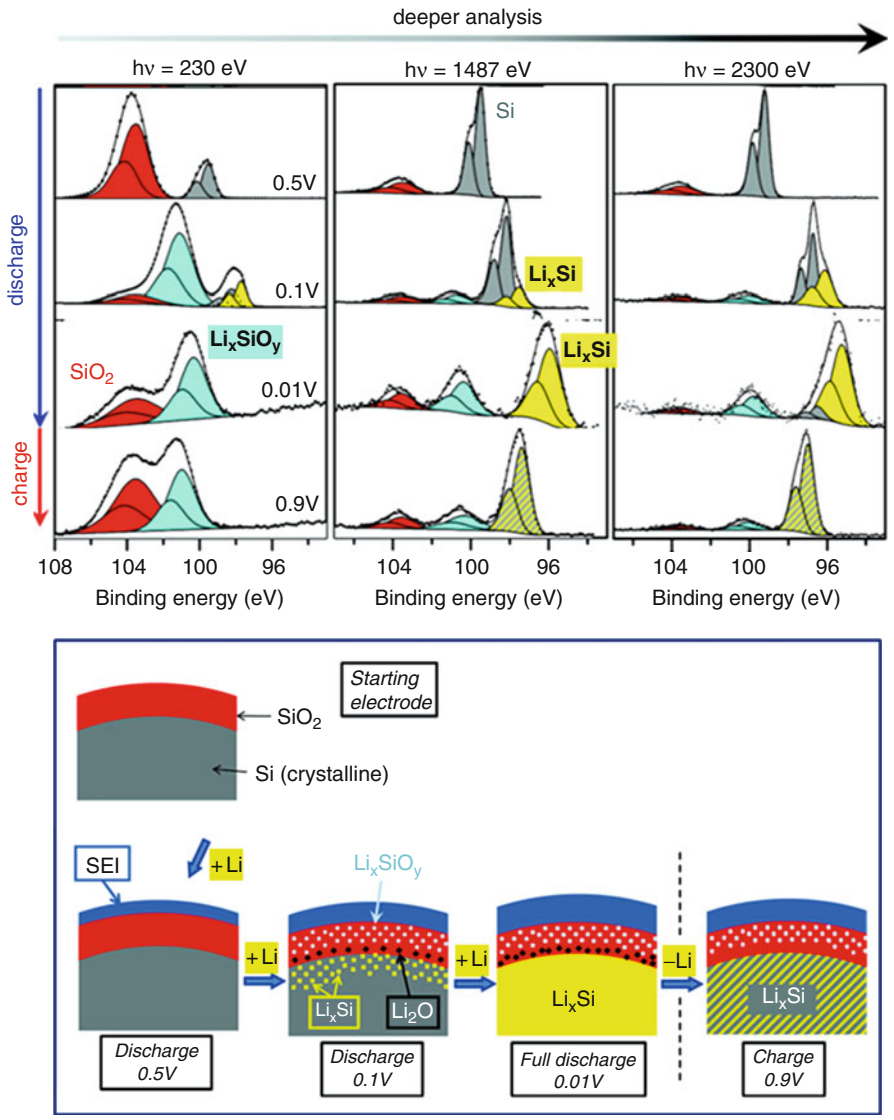


Fig. 9.23 (*Top*) Si 2p spectra of the Si/C/CMC composite electrodes upon the first discharge/charge cycle. From left to the right: evolution as a function of the photon energy. (*Bottom*) Schematic view of the mechanisms occurring at the surface of the silicon NPs: Formation of the SEI at the beginning of the discharge. Formation of the Li–Si alloy upon further discharge, together with Li_2O and Li_xSiO_y interfacial phases. Partial reversibility upon charge (Adapted from Ref. [40])

Figure 9.23 shows the Si 2p spectra of the Si/C/CMC composite electrode upon the first discharge/charge cycle and their dependence on the photon energy (hν) and thus on the analysis depth [40]. The E_B of different Si components obtained after deconvolution of the Si 2p spectra are summarized in Table 9.2. Initially, for the

Table 9.2 The binding energies of the Si 2p components corresponding to the deconvolution process presented in Fig. 9.23

BE (eV)	Silicon type	Color code in the figure
99.5	Si	Gray
97.5	Li_xSi alloy	Yellow
100–101	Li_xSiO_y	Blue
103.5	SiO_2	Red

fully charged battery (spectra not shown here), the characteristic metallic and oxide Si 2p peaks are recorded, similar to those presented in Fig. 9.11. At the beginning of discharge (0.5 V), no changes were found with respect to the pristine electrode, indicating that the reaction of lithium toward silicon has not yet started. The first changes are observed after discharge at 0.1 V where two additional components appear in the Si 2p spectrum. The Si $2p_{3/2}$ component at 97.5 eV (yellow in the figure) is attributed to a Li_xSi alloy, indicating that the formation of the Li–Si alloy has just started at 0.1 V. The Si $2p_{3/2}$ component at 100–101 eV appears after discharge to 0.1 V and corresponds to Li_4SiO_4 located at the extreme surface of the particles, as shown by depth profiling measurements.

Upon further discharge (0.01 V), the Si 2p component assigned to silicon disappears, except for the largest analysis depth (2,300 eV); therefore, the Li–Si alloying process is almost complete, at least in the probed depth region. Please note that the Li_xSi alloy component cannot be observed when using the lowest analysis depth (230 eV), indicating that the core of the particles is covered by a thin layer of SiO_2 and Li_xSiO_y phases. When the battery is recharged to 0.9 V, only small changes are observed concerning the SiO_2 and Li_xSiO_y surface phases. Contrary to the discharge process, no separate Li–Si and Si peaks are observed, while an important broadening of the Li–Si alloy component is evident with respect to the pristine silicon material, even though most of the lithium has been extracted. This broadening may be either due to the amorphization process or due to a nonuniform lithium extraction caused by the loss of electrical contact between Si particles upon charging.

Based on these spectroscopic results, details about the formation and the composition of the SEI upon the first discharging and charging battery cycle were revealed (illustrated at the bottom of Fig. 9.23). At the very beginning of discharge (0.5 V), lithium has not yet reacted with silicon, but a thin SEI layer has been already formed. After further discharge (0.1 V), the thickness of the SEI has increased, but its composition has not changed significantly. At the same time, lithium has started to react with the silicon nanoparticle. Reaction with the surface SiO_2 layer leads to the formation of Li_2O and Li_xSiO_y, most probably Li_4SiO_4, whereas reaction with silicon leads to the formation of the Li–Si alloy. After full discharge (0.01 V), the Li–Si alloying process is almost complete, but some remaining unreacted silicon may be found in the core of the particles. The amount of Li_2O continuously increases until the end of the discharge, but some unreacted SiO_2 still remains on the surface. The thickness of the SEI has increased, but its

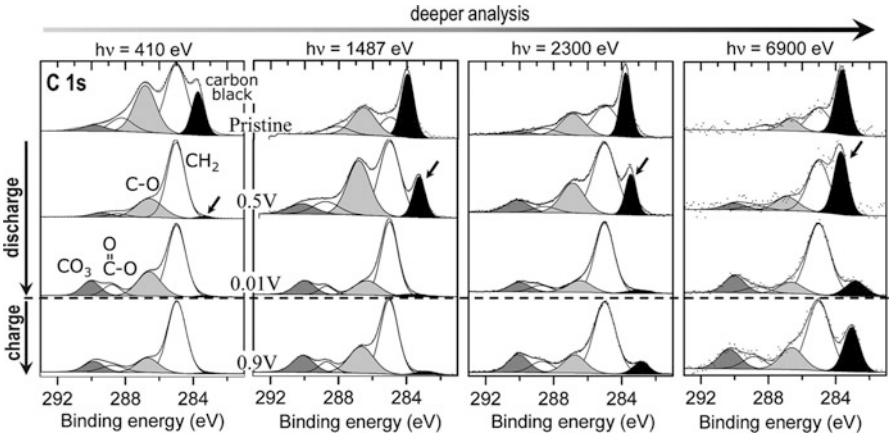


Fig. 9.24 C 1s spectra of the Si/C/CMC composite electrodes upon the first discharge/charge cycle. Evolution as a function of the photon energy (Adapted from Ref. [40])

Table 9.3 The binding energies and the origin of the C 1s components corresponding to the spectra presented in Fig. 9.24

BE (eV)	Carbon type	Color code in the figure	Origin
284	Carbon black	Black	Component of the electrode
285	C–H	White	Contamination
286.5	C–O	Gray	CMC binder
288.5	O═C–O	White	CMC binder
290	CO_3	Dark gray	Li carbonates

composition has not changed significantly. After recharging (0.9 V), lithium has been almost fully extracted from the core of the particles ($Li_\varepsilon Si$ with ε going down to zero); in addition, the thickness of the SEI has only slightly decreased, and Li_2O has disappeared.

The chemistry of the carbon black and the binder species intergraded in the electrode were also studied. Figure 9.24 shows the C 1s spectra of the Si/C/CMC composite electrode upon the first discharge/charge cycle. The complexity of the spectral shape indicates that several carbon species coexist on the electrode. In an attempt to distinguish if these species are localized close or far from the electrode/electrolyte interface, the C 1s peak was recorded by using 4 characteristic photon energies (ranging from 410 to 6,900 eV). Literature data and reference experiments were mainly used to distinguish the origin of each C 1s component, as presented in Table 9.3.

As shown in the figure, all five carbon species are present on the near surface of the pristine sample, while depth-dependent measurements clearly show that carbon black is preferentially located at the inner layers (please note the relative increase of

this component with the increase of photon energy). As discussed above, the solid electrolyte interface is already formed after 0.5 V discharge. This has a direct effect on the C 1s signal of carbon black, which can be hardly detected for the lowest analysis depth, while it still remains observable for higher photon energies (indicated by an arrow). When the device is almost completely discharged (0.01 V), a thick SEI layer has formed, and carbon black can be detected only in the higher photon energy spectra. In addition, carbonate species (Li_2CO_3 and/or lithium alkyl carbonates) at 290 eV are clearly evident not only at the surface (hv = 410 eV) but also in the inner (hv = 6,900 eV) SEI layers. After recharge of the device at 0.9 V, the C 1s component at 284 eV due to carbon black gains part of its initial intensity due to the decrease of the SEI layer thickness. However, its intensity never reaches the one of the pristine sample (before discharge), indicating that the formation of the SEI layer is irreversible.

The comparison of the C 1s spectra recorded with different photon energies at a given potential can give information about the homogeneity of the SEI film. In order to do so, the C 1s component originating from the SEI film but not from the electrode underneath (actually all C 1s components apart from the carbon black and the contamination at 284 and 285 eV, respectively) should be compared using spectra recorded with different photon energies (i.e., different depths of the SEI film analyzed). It is evident that there are no major differences in the spectra (regarding carbonaceous compounds) of the surface-sensitive and bulk-sensitive modes at a given potential. Therefore, one can deduce that there is no major difference in the composition of the SEI film, at least as a function of depth. This example nicely shows that depth-dependent measurements can be used not only to indicate core–shell structures and segregation effects but also to evidence the opposite, i.e., homogeneity of the surface layers in the first few nanometers.

6 Conclusions and Future Perspective

Our intention in this chapter was to give an overview of the SR X-ray photoelectron spectroscopy and the main applications in the characterization of nanomaterials and in particular nanoparticles. The presented examples clearly showed that SR-XPS presents an appropriate tool for the investigation of nanomaterials, providing detailed information on the chemical state and the composition of the surface. Although using SR-XPS apparatuses is far more complicated and costly than the laboratory-based experiments, the technique gradually becomes increasingly popular not only in the academic but also in the industrial community. This is due to the enormous capabilities and flexibility of the SR-XPS methods, which can provide high-quality results and improve our knowledge on nanomaterials. Currently, many synchrotron radiation facilities are available worldwide and allow access to the different variations of the SR-XPS technique. This greatly expands the limits of laboratory-based XPS systems even further and provide the scientific community with a great choice of powerful and versatile tools in the field of nanoscience and nanotechnology research.

Acknowledgments S.Z. and V.P. gratefully acknowledge financial support from EU project IRAFC (Project Number 245202) and FRC (International Center for Frontier Research in Chemistry, Strasbourg). W. H. Doh thanks the EU-FP7 FreeCats project (NMP3-SL-2012-280658) for financial support.

References

1. Cao G, Wang Y (2011) Nanostructures and nanomaterials: synthesis, properties, and applications. World Scientific, Singapore
2. Wang ZM (2009) Toward functional nanomaterials. Springer, New York, USA
3. Saka M (2011) Metallic micro and nano materials: fabrication with atomic diffusion. Springer, New York, USA
4. Fesenko O, Yatsenko L, Brodin M (2013) Nanomaterials imaging techniques, surface studies, and applications: selected proceedings of the FP7 international summer school nanotechnology: from fundamental research to innovations, Bukovel, 26 Aug–2 Sept 2012. Springer, London
5. Briggs D, Grant JT (2003) Surface analysis by Auger and X-ray photoelectron spectroscopy. IMPublications, Chichester, UK and SurfaceSpectra, Manchester, UK
6. Watts JF, Wolstenholme J (2003) An introduction to surface analysis by XPS and AES. John Wiley & Sons Ltd, Chichester, UK
7. Siegbahn K, Edvarson K (1956) β-ray spectroscopy in the precision range of 1: 105. Nucl Phys 1(3):137–159
8. Wiedemann H (2003) Synchrotron radiation. Springer, Heidelberg, Germany
9. Yamamoto S, Matsuda I (2013) Time-resolved photoelectron spectroscopies using synchrotron radiation: past, present, and future. J Physical Soc Japan 82(2):021003
10. Duke P (2008) Synchrotron radiation: production and properties. Oxford University Press, Oxford
11. Briggs D, Seah P (1990) Practical surface analysis: Auger and X-ray photoelectron spectroscopy. John Wiley & Sons Ltd, Chichester, UK
12. Kelly MA (2010) Historical perspectives on charging issues in XPS. J Electron Spectrosc Relat Phenom 176(1–3):5–7
13. Yeh JJ, Lindau I (1985) Atomic subshell photoionization cross-sections and asymmetry parameters – 1 less-than-or-equal-to Z less-than-or-equal-to 103. Atomic Data Nucl Data Tables 32(1):1–155
14. Moretti G (2013) The Wagner plot and the Auger parameter as tools to separate initial- and final-state contributions in X-ray photoemission spectroscopy. Surf Sci 618:3–11
15. Zafeiratos S, Kennou S (1999) A study of gold ultrathin film growth on yttria-stabilized ZrO_2(100). Surf Sci 443(3):238–244
16. Takata Y, Kayanuma Y, Yabashi M, Tamasaku K, Nishino Y, Miwa D, Harada Y, Horiba K, Shin S, Tanaka S, Ikenaga E, Kobayashi K, Senba Y, Ohashi H, Ishikawa T (2007) Recoil effects of photoelectrons in a solid. Phys Rev B 75(23):233404
17. Tanuma S, Powell CJ, Penn DR (1994) Calculations of electron inelastic mean free paths.5. data for 14 organic-compounds over the 50–2000 ev range. Surf Interface Anal 21(3):165–176
18. Merzlikin SV, Tolkachev NN, Strunskus T, Witte G, Glogowski T, Woell C, Gruenert W (2008) Resolving the depth coordinate in photoelectron spectroscopy – comparison of excitation energy variation vs. angular-re solved XPS for the analysis of a self-assembled monolayer model system. Surf Sci 602(3):755–767
19. Powell CJ, Jablonski A (2010) Progress in quantitative surface analysis by X-ray photoelectron spectroscopy: current status and perspectives. J Electron Spectrosc Relat Phenom 178:331–346
20. Baer DR, Engelhard MH (2010) XPS analysis of nanostructured materials and biological surfaces. J Electron Spectrosc Relat Phenom 178:415–432
21. Mohai M, Bertoti I (2004) Calculation of overlayer thickness on curved surfaces based on XPS intensities. Surf Interface Anal 36(8):805–808

22. Gunter PLJ, Dejong AM, Niemantsverdriet JW, Rheiter HJH (1992) Evaluation of take-off-angle-dependent xps for determining the thickness of passivation layers on aluminum and silicon. Surf Interface Anal 19(1–12):161–164
23. Cole DA, Shallenberger JR, Novak SW, Moore RL, Edgell MJ, Smith SP, Hitzman CJ, Kirchhoff JF, Principe E, Nieveen W, Huang FK, Biswas S, Bleiler RJ, Jones K (2000) SiO_2 thickness determination by x-ray photoelectron spectroscopy, Auger electron spectroscopy, secondary ion mass spectrometry, Rutherford backscattering, transmission electron microscopy, and ellipsometry. J Vac Sci Technol B 18(1):440–444
24. Alexander MR, Thompson GE, Zhou X, Beamson G, Fairley N (2002) Quantification of oxide film thickness at the surface of aluminium using XPS. Surf Interface Anal 34(1):485–489
25. Martin JE, Herzing AA, Yan W, Li X-Q, Koel BE, Kiely CJ, Zhang W-X (2008) Determination of the oxide layer thickness in core-shell zerovalent iron nanoparticles. Langmuir 24(8):4329–4334
26. Gillet JN, Meunier M (2005) General equation for size nanocharacterization of the core-shell nanoparticles by X-ray photoelectron spectroscopy. J Phys Chem B 109(18):8733–8737
27. Yang DQ, Gillet JN, Meunier M, Sacher E (2005) Room temperature oxidation kinetics of Si nanoparticles in air, determined by x-ray photoelectron spectroscopy. J Appl Phys 97(2):24303
28. Patrone L, Nelson D, Safarov VI, Sentis M, Marine W, Giorgio S (2000) Photoluminescence of silicon nanoclusters with reduced size dispersion produced by laser ablation. J Appl Phys 87(8):3829–3837
29. Hofmeister H, Huisken F, Kohn B (1999) Lattice contraction in nanosized silicon particles produced by laser pyrolysis of silane. Eur Phys J D 9(1–4):137–140
30. Bernardi F, Fecher GH, Alves MCM, Morais J (2010) Unraveling the formation of core-shell structures in nanoparticles by S-XPS. J Phys Chem Lett 1(6):912–917
31. Zharnikov M (2010) High-resolution X-ray photoelectron spectroscopy in studies of self-assembled organic monolayers. J Electron Spectrosc Relat Phenom 178:380–393
32. Mason MG (1983) Electronic-structure of supported small metal-clusters. Phys Rev B 27(2):748–762
33. Kuhrt C, Harsdorff M (1991) Photoemission and electron-microscopy of small supported palladium clusters. Surf Sci 245(1–2):173–179
34. Peters S, Peredkov S, Neeb M, Eberhardt W, Al-Hada M (2013) Size-dependent Auger spectra and two-hole Coulomb interaction of small supported Cu-clusters. Phys Chem Chem Phys 15(24):9575–9580
35. Peters S, Peredkov S, Neeb M, Eberhardt W, Al-Hada M (2013) Size-dependent XPS spectra of small supported Au-clusters. Surf Sci 608:129–134
36. Papaefthimiou V, Dintzer T, Dupuis V, Tamion A, Tournus F, Teschner D, Haevecker M, Knop-Gericke A, Schloegl R, Zafeiratos S (2011) When a metastable oxide stabilizes at the nanoscale: Wurtzite CoO formation upon dealloying of PtCo nanoparticles. J Phys Chem Lett 2(8):900–904
37. Liu X, Atwater M, Wang J, Huo Q (2007) Extinction coefficient of gold nanoparticles with different sizes and different capping ligands. Colloids Surf B-Biointerfaces 58(1):3–7
38. Anderson DP, Alvino JF, Gentleman A, Al Qahtani H, Thomsen L, Polson MIJ, Metha GF, Golovko VB, Andersson GG (2013) Chemically-synthesised, atomically-precise gold clusters deposited and activated on titania. Phys Chem Chem Phys 15(11):3917–3929
39. Anderson DP, Adnan RH, Alvino JF, Shipper O, Donoeva B, Ruzicka J-Y, Al Qahtani H, Harris HH, Cowie B, Aitken JB, Golovko VB, Metha GF, Andersson GG (2013) Chemically synthesised atomically precise gold clusters deposited and activated on titania. Part II. Phys Chem Chem Phys 15(35):14806–14813
40. Philippe B, Dedryvere R, Allouche J, Lindgren F, Gorgoi M, Rensmo H, Gonbeau D, Edstrom K (2012) Nanosilicon electrodes for lithium-ion batteries: interfacial mechanisms studied by hard and soft X-ray photoelectron spectroscopy. Chem Mater 24(6):1107–1115

41. Menzel D (2008) Ultrafast charge transfer at surfaces accessed by core electron spectroscopies. Chem Soc Rev 37(10):2212–2223
42. Kataoka T, Kobayashi M, Sakamoto Y, Song GS, Fujimori A, Chang FH, Lin HJ, Huang DJ, Chen CT, Ohkochi T, Takeda Y, Okane T, Saitoh Y, Yamagami H, Tanaka A, Mandal SK, Nath TK, Karmakar D, Dasgupta I (2010) Electronic structure and magnetism of the diluted magnetic semiconductor Fe-doped ZnO nanoparticles. J Appl Phys 107(3):033718
43. Fujii T, de Groot FMF, Sawatzky GA, Voogt FC, Hibma T, Okada K (1999) In situ XPS analysis of various iron oxide films grown by NO_2-assisted molecular-beam epitaxy. Phys Rev B 59(4):3195–3202
44. Peden CHF, Rogers JW, Shinn ND, Kidd KB, Tsang KL (1993) Thermally grown si_3n_4 thin-films on si(100) – surface and interfacial composition. Phys Rev B 47(23):15622–15629
45. Hong IH, Lee TH, Yin GC, Wei DH, Juang JM, Dann TE, Klauser R, Chuang TJ, Chen CT, Tsang KL (2001) Performance of the SRRC scanning photoelectron microscope. Nucl Instrum Methods Phys Res A 467:905–908
46. Kiskinova M, Marsi M, Di Fabrizio E, Gentili M (1999) Synchrotron radiation scanning photoemission microscopy: instrumentation and application in surface science. Surf Rev Lett 6(2):265–286
47. Gunther S, Kaulich B, Gregoratti L, Kiskinova M (2002) Photoelectron microscopy and applications in surface and materials science. Progr Surf Sci 70(4–8):187–260
48. Horiba K, Nakamura Y, Nagamura N, Toyoda S, Kumigashira H, Oshima M, Amemiya K, Senba Y, Ohashi H (2011) Scanning photoelectron microscope for nanoscale three-dimensional spatial-resolved electron spectroscopy for chemical analysis. Rev Sci Instrum 82(11):113701
49. Doh WH, Gregoratti L, Amati M, Zafeiratos S, Law YT, Neophytides SG, Orfanidi A, Kiskinova M, Savinova ER (2014) Scanning photoelectron microscopy study of the pt/phosphoric-acid-imbibed membrane interface under polarization. ChemElectroChem 1(1):180–186
50. Gunther S, Kolmakov A, Kovac J, Kiskinova M (1998) Artefact formation in scanning photoelectron emission microscopy. Ultramicroscopy 75(1):35–51
51. Bozzini B, Abyaneh MK, Amati M, Gianoncelli A, Gregoratti L, Kaulich B, Kiskinova M (2012) Soft X-ray imaging and spectromicroscopy: new insights in chemical state and morphology of the key components in operating fuel-cells. Chem Eur J 18(33):10196–10210
52. Rodriguez JA, Goodman DW (1991) High-pressure catalytic reactions over single-crystal metal-surfaces. Surf Sci Rep 14(1–2):1–107
53. Zafeiratos S, Piccinin S, Teschner D (2012) Alloys in catalysis: phase separation and surface segregation phenomena in response to the reactive environment. Catal Sci Technol 2(9):1787–1801
54. Ogletree DF, Bluhm H, Lebedev G, Fadley CS, Hussain Z, Salmeron M (2002) A differentially pumped electrostatic lens system for photoemission studies in the millibar range. Rev Sci Instrum 73(11):3872–3877
55. Asplund L, Kelfve P, Siegbahn H, Goscinski O, Fellnerfeldegg H, Hamrin K, Blomster B, Siegbahn K (1976) Chemical-shifts of Auger-electron lines and electron-binding energies in free molecules – sulfur-compounds. Chem Phys Lett 40(3):353–356
56. Salmeron M, Schlogl R (2008) Ambient pressure photoelectron spectroscopy: a new tool for surface science and nanotechnology. Surf Sci Rep 63(4):169–199
57. Knop-Gericke A, Kleimenov E, Haevecker M, Blume R, Teschner D, Zafeiratos S, Schloegl R, Bukhtiyarov VI, Kaichev VV, Prosvirin IP, Nizovskii AI, Bluhm H, Barinov A, Dudin P, Kiskinova M (2009) X-ray photoelectron spectroscopy for investigation of heterogeneous catalytic processes. Adv Catal 52(52):213–272
58. Starr DE, Liu Z, Havecker M, Knop-Gericke A, Bluhm H (2013) Investigation of solid/vapor interfaces using ambient pressure X-ray photoelectron spectroscopy. Chem Soc Rev 42(13):5833–5857

59. Chin TS (2000) Permanent magnet films for applications in microelectromechanical systems. J Magn Magn Mater 209(1–3):75–79
60. Chu W, Chernavskii PA, Gengembre L, Pankina GA, Fongarland P, Khodakov AY (2007) Cobalt species in promoted cobalt alumina-supported Fischer-Tropsch catalysts. J Catal 252(2):215–230
61. Stamenkovic VR, Mun BS, Arenz M, Mayrhofer KJJ, Lucas CA, Wang G, Ross PN, Markovic NM (2007) Trends in electrocatalysis on extended and nanoscale Pt-bimetallic alloy surfaces. Nat Mater 6(3):241–247
62. Perez A, Dupuis V, Tuaillon-Combes J, Bardotti L, Prevel B, Bernstein E, Melinon P, Favre L, Hannour A, Jamet M (2005) Functionalized cluster-assembled magnetic nanostructures for applications to high integration-density devices. Adv Eng Mater 7(6):475–485
63. Zafeiratos S, Dintzer T, Teschner D, Blume R, Haevecker M, Knop-Gericke A, Schloegl R (2010) Methanol oxidation over model cobalt catalysts: influence of the cobalt oxidation state on the reactivity. J Catal 269(2):309–317
64. Zafeiratos S, Paloukis F, Papakonstantinou G, Teschner D, Havecker M, Vass E, Schnorch P, Knop-Gericke A, Schlogl R, Moreno B, Chinarro E, Jurado JR, Neophytides SG (2010) A comparative in situ XPS study of PtRuCo catalyst in methanol steam reforming and water gas shift reactions. Catal Today 157(1–4):250–256
65. Butcher DR, Grass ME, Zeng Z, Aksoy F, Bluhm H, Li W-X, Mun BS, Somorjai GA, Liu Z (2011) In situ oxidation study of Pt(110) and its interaction with CO. J Am Chem Soc 133(50):20319–20325
66. Rodriguez NM, Anderson PE, Wootsch A, Wild U, Schlogl R, Paal Z (2001) XPS, EM, and catalytic studies of the accumulation of carbon on Pt black. J Catal 197(2):365–377
67. Blume R, Havecker M, Zafeiratos S, Teschner D, Kleimenov E, Knop-Gericke A, Schlogl R, Barinov A, Dudin P, Kiskinova M (2006) Catalytically active states of Ru(0001) catalyst in CO oxidation reaction. J Catal 239(2):354–361
68. Kobayashi K (2009) Hard X-ray photoemission spectroscopy. Nucl Instrum Methods Phys Res A 601(1–2):32–47
69. Granroth S, Olovsson W, Holmstrom E, Knut R, Gorgoi M, Svensson S, Karis O (2011) Understanding interface properties from high kinetic energy photoelectron spectroscopy and first principles theory. J Electron Spectrosc Relat Phenom 183(1–3):80–93
70. Kover L (2010) X-ray photoelectron spectroscopy using hard X-rays. J Electron Spectrosc Relat Phenom 178:241–257
71. Claessen R, Sing M, Paul M, Berner G, Wetscherek A, Mueller A, Drube W (2009) Hard x-ray photoelectron spectroscopy of oxide hybrid and heterostructures: a new method for the study of buried interfaces. New J Phys 11:125007
72. Panaccione G, Kobayashi K (2012) Hard X-ray photoemission spectroscopy: variable depth analysis of bulk, surface and interface electronic properties. Surf Sci 606(3–4):125–129
73. Goodenough JB, Kim Y (2010) Challenges for rechargeable Li batteries. Chem Mater 22(3):587–603
74. Shimotake H (1990) Progress in batteries and solar cells. JEC Press
75. Edstrom K, Gustafsson T, Thomas JO (2004) The cathode-electrolyte interface in the Li-ion battery. Electrochim Acta 50(2–3):397–403
76. Philippe B, Dedryvere R, Gorgoi M, Rensmo H, Gonbeau D, Edstrom K (2013) Improved performances of nanosilicon electrodes using the salt LiFSI: a photoelectron spectroscopy study. J Am Chem Soc 135(26):9829–9842
77. Philippe B, Dedryvere R, Gorgoi M, Rensmo H, Gonbeau D, Edstrom K (2013) Role of the $LiPF_6$ salt for the long-term stability of silicon electrodes in Li-Ion batteries – a photoelectron spectroscopy study. Chem Mater 25(3):394–404

Exploration into the Valence Band Structures of Organic Semiconductors by Angle-Resolved Photoelectron Spectroscopy

10

Yasuo Nakayama and Hisao Ishii

Contents

1 Definition of the Topic 368
2 Overview 368
3 Introduction 369
4 Experimental and Instrumental Methodology 370
4.1 Essential Principles of the Photoelectron Spectroscopy (PES) 370
4.2 History of Problems with PES on Organic Solids 376
4.3 Solution I: Photoelectron Yield Spectroscopy (PYS) 377
4.4 Solution II: PES Assisted by Photoconduction 379
5 Key Research Findings 381
5.1 Valence Bands of Crystalline Thin Films of an Organic Semiconductor: Pentacene 381
5.2 Rubrene Single Crystal: Demonstration of the Band Dispersion on an "Insulating" Material 383
5.3 Novel Nano-organic Interaction: π-Conjugated Molecules on Quantum Wells 389
6 Conclusions and Future Perspective 397
7 Acknowledgments 399
References 399

Y. Nakayama (✉)
Graduate School of Advanced Integration Science, Chiba University, Chiba, Japan
e-mail: nkym@restaff.chiba-u.jp

H. Ishii
Graduate School of Advanced Integration Science, Chiba University, Chiba, Japan

Center for Frontier Science, Chiba University, Chiba, Japan

© Springer-Verlag Berlin Heidelberg 2015

C.S.S.R. Kumar (ed.), *Surface Science Tools for Nanomaterials Characterization*,
DOI 10.1007/978-3-662-44551-8_10

Abstract

In this chapter, we describe technical essences and several example works of angle-resolved photoelectron spectroscopy (ARPES) that is a surface science methodology to map out the electronic band structures of the matters. Successful results of demonstrating the valence band dispersion relations of crystalline organic semiconductor materials are introduced, which were acquired through resolution of inherent "sample charging" problems in photoelectron spectroscopy techniques. The effective mass of the valence hole and intermolecular transfer integral values of van-der-Waals molecular solids were directly derived as fundamental physical properties regulating the charge carrier transport in these solids. In addition, recent ARPES works on novel interface electronic structures of organic semiconducting molecules in contact with "quantum wells" in nanometer-thick metal thin-films are also reviewed.

Keywords

Angle-resolved photoelectron spectroscopy (ARPES) • Energy-momentum (*E-K*) dispersion relation • Sample charging • Photoelectron yield spectroscopy • Rubrene • Pentacene • Transfer integral • Mobility • Quantum well • Phthalocyanine

1 Definition of the Topic

Angle-resolved photoelectron spectroscopy (ARPES) is a powerful tool to demonstrate the valence band structures of crystalline solids. In this chapter, we describe technical essences of this methodology, in particular special tactics which are necessary to adopt this method for organic materials, with some examples of successful illustration of the valence band structures of π-conjugated organic molecular crystals and novel hetero-interfaces between organic molecules and metal thin-film "quantum wells."

2 Overview

Present electronics are built up onto a basis of fundamental knowledge on the electronic band structures of semiconductor materials by which the electron motion inside the devices can be explained and controlled. Accordingly, the photoelectron spectroscopy (PES) and its related techniques possess notable importance for progress in the electronics technologies by revealing novel electronic properties as well as providing experimental evidences to rationalize known electric phenomena.

Organic electronics is a currently emerging technology which potentially brings about drastic reformation of our daily life through its inherent flexibility, light weight, material diversity, ubiquity, and cost-effectiveness. These technologies utilize molecules (or supra-molecules) with π-conjugated orbitals, which are generally categorized as "organic semiconductors," as electronically active materials.

A striking characteristic of the organic semiconductors as opposed to their inorganic counterparts is that they are condense themselves by the weak van der Waals interaction rather than covalent or ionic bonding. However, generalized principles taking this point thoroughly into account to describe the charge carrier transport natures in such molecular solids have not been established satisfactorily. This situation is caused mostly by technical difficulties to conduct the (AR)PES measurements on the organic single crystal samples for directly demonstrating the intrinsic electronic structures of the materials themselves.

In the present chapter, we review recent advances in PES-related methodologies that have enabled one to measure the valence bands of the organic semiconductor single crystals. In particular, an accurate energy-momentum dispersion relation of the valence band was successfully acquired through ARPES measurements on the single crystal of a representative organic semiconductor, rubrene, which led to the determination of several essential physical properties, the effective mass of the valence holes, and anisotropic intermolecular transfer integrals, in relevance to the charge carrier transport. Meanwhile, there are still largely untouched rooms for development toward future nanotechnology applications in the present organic electronics field. Several scientific attempts however have been commenced for this direction. As an example, discovery of novel nano-organic hybridization by means of ARPES is also introduced in addition to the *pure* organic cases.

3 Introduction

It is a Japanese saying that semiconductors are "rice" of industries. Indeed, semiconductor electronics is one of the most fundamental social infrastructures of the present age. The word "semiconductor" instantaneously evokes an image of silicon to our mind. In practice, electronic devices pervading our daily life are functionalized predominantly by silicon or some other inorganic semiconducting solids. Besides these mature electronics of such *hard* materials, π-conjugating organic materials are now attracting growing anticipation as a new class of semiconductors toward more ubiquitous and sustainable applications of the electronic devices owing to their inherent *softness*. It is commonly known that the spectacular development of the present semiconductor technologies arises from invention of a point-contact transistor on the single crystal of germanium by Bardeen, Brattain, and Shockley in 1947. The history of "organic semiconductors" is as old as that of these inorganic counterparts; studies in electric conduction characteristics in several solid-state aromatic hydrocarbon dyes were initiated no later than 1950 [1, 2], which led to the discovery of their "semiconductivity" by Eley [3], Vertanyan [4], Inokuchi, and Akamatsu [5–7]. Through divers epoch-making innovations to assemble these organic matters into practical electronic devices [8–12], for instance, an invention of the first *realistic* organic light-emitting diode (OLED) with a donor–acceptor bilayer structure made by Tang and VanSlyke in 1987, the organic electronics are now rapidly catching up the conventional semiconductor electronics.

No matter whether it is organic or inorganic, functionalities of the electronic devices are based on behaviors of electrons inside their constituent semiconductor

solids. In other words, development of the electronic devices is nothing but contriving more and more efficient ways to manipulate the electrons in the devise as one intends. Accurate knowledge on the electronic states, or more concretely the electronic band structures, is accordingly an elemental basis for the semiconductor devices as a guideline of the electron motion. Actually, the progress in conventional semiconductor electronics has been underpinned by preestablished paradigms of the solid-state physics. On the other hand, a generalized principle describing transport phenomena in the organic semiconductors has not accomplished yet despite half-century-long continuous scientific efforts since their discovery. A key of this problem is just insufficiency of precise and comprehensive information about the electronic structures of the organic solids based on experimental evidences. While a most direct and commonly used experimental method to measure the electronic (band) structure of the solids is (angle-resolved) photoelectron spectroscopy, some technical hurdles have restricted the widespread application of this methodology for the miscellaneous organic materials.

Recently, progress in photoemission-based experimental techniques has opened up the possibilities to directly measure the valence band of the organic semiconductors. In the next section, these advanced methodologies are described after a general explanation on essential principles of the photoelectron spectroscopy (PES). Several examples for successful demonstration of the valence band measurements on organic semiconductor crystals and novel nano-organic hetero-structures by means of the angle-resolved PES (ARPES) are also introduced in Sect. 5.

4 Experimental and Instrumental Methodology

4.1 Essential Principles of the Photoelectron Spectroscopy (PES)

Photoelectron spectroscopy (PES) is an experimental technique to measure the kinetic energy and momentum of "photoelectrons" ejected out of the sample by an external photoemission event [13]. In the case of solid-state specimens, this event can expediently be regarded as the following successive three processes (the three-step model): (1) the electron excitation by photon absorption of the specimen, (2) migration of the photoexcited electron inside the solid, and (3) an escape of the electron out of the solid surface. In addition, one has to take the fourth process into account for *practical* PES measurements, that is, (4) flight of the photoelectron through a vacuum gap from the sample surface to the electron analyzer at which the energy and momentum of an electron are *measured*. Conservation of energy and momentum is required throughout these four processes, where the former condition is schematically illustrated in Fig. 10.1. The essential principles of PES are described step-by-step hereafter.

The first step is an electric dipole transition whose probability P_{fi} is expressed by the Fermi's golden rule as follows:

$$P_{\mathrm{fi}} \propto |< \psi_{\mathrm{f}}|\boldsymbol{e}\cdot\boldsymbol{r}|\psi_{\mathrm{i}} >|^2 \delta(h\nu - E_{\mathrm{f}} + E_{\mathrm{i}}) \tag{10.1}$$

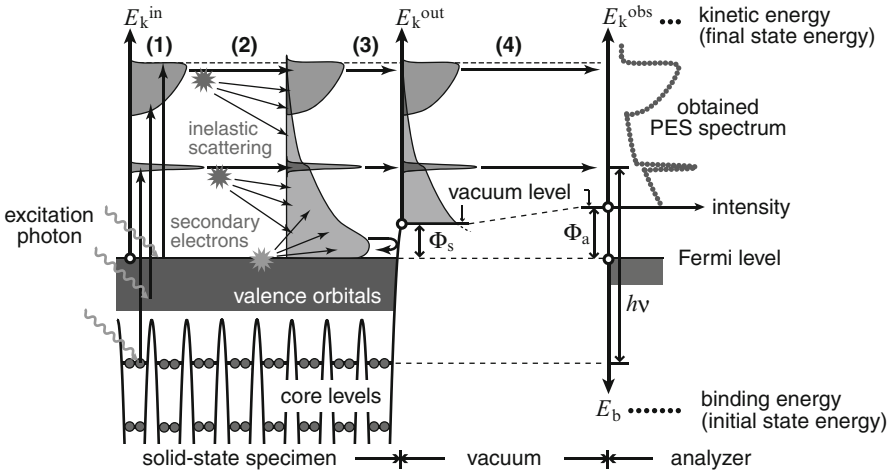


Fig. 10.1 A schematic drawing representing the energy conservation relation throughout the PES measurement. The zero points of four energy scales (E_k^{in}, E_k^{out}, E_k^{obs}, and E_b) in this diagram are indicated with open circles at respective arrowheads

where ψ_i and ψ_f are wave functions of the initial and final states, respectively; $\boldsymbol{e}$ and $h\nu$ are the electric vector and energy, respectively, of the excitation photon; $\boldsymbol{r}$ is the coordination of the electron; and E_f and E_i are the electron energies at the final and initial states, respectively.

Equation 10.1 indicates that the photoemission intensity is proportional to the square of the term $<\psi_f|\boldsymbol{e}\cdot\boldsymbol{r}|\psi_i>$ which is called as the transition dipole moment. For the sake of estimating this value, simple approximation to treat ψ_i and ψ_f as one-electron wave functions is generally taken. For example, they were regarded to be atomic wave functions to calculate the photoionization cross sections for core-level electrons. On the other hand, the ultraviolet photoelectron spectroscopy (UPS) spectra are often considered to be a "replica" of the density-of-state (DOS) distribution as a function of the initial state energy $D(E_i)$ for an elementary interpretation. This simplification is based on the following two assumptions: Firstly, the right term of Eq. 10.1 can be replaced by $D(E_f)\cdot D(E_i)$ where $E_f - E_i = h\nu$. Secondly, the final state can be approximated as a free electron-like state in which $D(E_f)$ varies proportional to the square root of the electron energy and thus can be considered to be a constant when the energy range is not too wide.

Not only a rough profile of the DOS but also fine characters of ψ_i are accessible through further accurate measurement and analysis of PES. For crystalline samples, ψ_i and ψ_f are expressed as Bloch functions. Since the momentum of the vacuum-ultraviolet or soft x-ray photons is sufficiently small in comparison to that of electrons, the momentum conservation requires a "vertical" excitation, in which an electron is kicked up keeping their wave number in the reduced zone. This allows one to approach an energy-momentum (E–k) dispersion relation of the valence electrons in the solid state from angle-resolved photoelectron spectroscopy (ARPES)

measurements. Details of the methodology will be described later. On the other hand, if the final state can be well approximated to be a free electron-like plane wave, the transition dipole moment is equivalent to Fourier transformation of ψ_i by a plane wave $e^{i\boldsymbol{k}\cdot\boldsymbol{r}}$, where $\boldsymbol{k}$ is the wave vector of the photoelectron. Hence the spatial distribution of ψ_i can be illustrated by the inverse Fourier transformation of the two-dimensional photoemission intensity profile that corresponds to the electron distribution in the reciprocal space. Whereas going into the details of this type of ARPES is beyond the scope of this article, an example is shortly introduced in Sect. 5.1. In the meantime, the characters of ψ_f for organic molecular specimens can be approximated as a sum of photoelectron contributions from individual atoms constructing the molecule. This approach is known as the independent atomic center (IAC) model [14], which has been developed to take single and multiple scattering events into account [15, 16]. Precise knowledge about the molecular orientation is accessible by simulating the angular dependence of the photoemission intensity with respect to the polarization vector of the excitation light under this model.

Meanwhile, the delta function in Eq. 10.1 represents the required energy conservation, that is, $E_i + h\nu = E_f$. For simplicity, we adopt the one-electron model hereafter. In this approximation, the transition energy $(E_f - E_i)$ is equal to $(E_b + E_k^{in})$ where E_b and E_k^{in} are the electron binding energy and kinetic energy in the solid, respectively, with respect to the Fermi level.

The second essential step of the photoemission event is migration of the photoexcited electrons inside the solid. During this process, the photoelectrons may experience "collision" to another electron in a certain probability, which punches the victim electron (secondary electron) up to a moderate excited state in expense of a part of the primary energy of the photoelectron. Since information about the energy and momentum of the initial state conveyed by the photoelectron is lost by this inelastic scattering incident, a distance how long the photoelectrons can travel in the solid before the first scattering event is a criterion how deep inside from the solid surface one can probe by the photoemission spectroscopy. The average value of this distance, which is known as the inelastic mean free path (IMFP), strongly depends on the kinetic energy of the electron but exhibits a "universal" trend, as shown in Fig. 10.2, irrespective of the materials [17]. This indicates that IMPF of electrons whose energy is in the range of 10–1,000 eV is at most several nanometers; in other words, ultraviolet PES (UPS) or soft x-ray PES (XPS) which detects the photoelectrons in such energy range is in principle surface-sensitive methodology. The surface sensitiveness is further emphasized as tilting the photoelectron takeoff angle from the surface normal direction. By utilizing this property, one can highlight the surface components from overlapping bulk species by changing the probing angle [13, 18–20]. This type of ARPES is often adopted as an optional tactic for the core-level PES analysis.

A portion of the photoexcited electrons then reach the surface of the specimen. Ejection of the photoelectron from the solid to the vacuum is the third step of the external photoemission event. Any matters possess an electrostatic potential barrier at the surface to confine the electrons inside. The top of this barrier is called the vacuum level E_{vac} which corresponds to the energy zero point of the

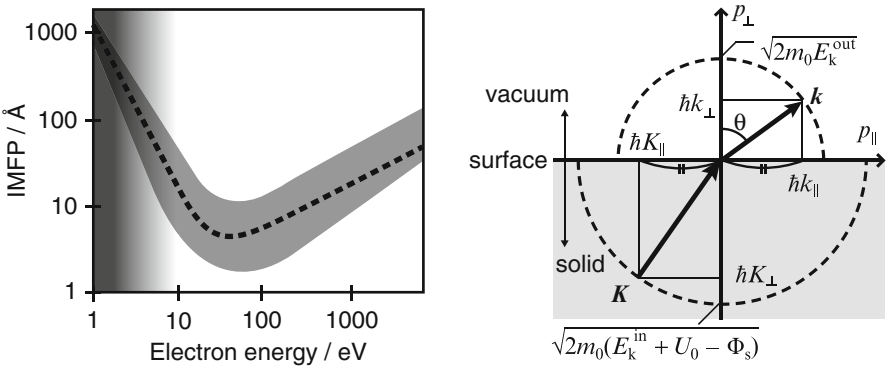


Fig. 10.2 (*Left*) The "universal curve" of the photoelectron IEMP. A *dotted line* and *gray band* are retraced from the data reported in a literature (Seah and Dench 1979). It should be additionally noted that the IMFP in the low-energy region (<10 eV) is controversial, which is shaded in the graph. (*Right*) A schematic drawing of the momentum conservation relationship during the external photoemission event

photoelectrons in the vacuum close to the sample surface. An energy offset between E_{vac} and the Fermi level is known as the work function of the sample Φ_s. This is the minimum necessary energy to surmount this barrier to pick an electron out of the matter; in other words, the photoelectrons lose this energy when they pass through the sample surface. Accordingly, the energy conservation in this step is written as

$$E_k{}^{out} = E_k{}^{in} - \Phi_s = h\nu - E_b - \Phi_s, \tag{10.2}$$

where $E_k{}^{out}$ is the kinetic energy of a photoelectron ejected out of the sample.

The photoelectrons flying through the vacuum fulfill the energy-momentum relationship of the free electron:

$$E_k^{out} = \frac{\hbar^2|\boldsymbol{k}|^2}{2m_0}, \tag{10.3}$$

where $\boldsymbol{k}$ is the wave vector of the photoelectron in the vacuum and m_0 is the electron rest mass. This equation can be rewritten as

$$\hbar\boldsymbol{k} = \left(\hbar k_\parallel, \hbar k_\perp\right) = \left(\sqrt{2m_0E_k{}^{out}}\cdot\sin\theta,\ \sqrt{2m_0E_k{}^{out}}\cdot\cos\theta\right), \tag{10.4}$$

where subscripts "$\parallel$" and "$\perp$" hereafter represent the surface parallel and normal components, respectively, and θ is the electron takeoff angle with respect to the surface normal direction. ARPES allows one to measure $\boldsymbol{k}$ *of* the photoelectrons through this relationship. On the other hand, the photoelectrons inside the solid as well can be assumed as free electrons when the excitation

energy is sufficiently large ($E_k^{in} > 10$ eV). Thus, the energy-momentum dispersion relation is expressed as follows:

$$E_k^{in} - (U_0 - \Phi_s) = \frac{\hbar^2 |\boldsymbol{K}|^2}{2m^*}, \tag{10.5}$$

where $\boldsymbol{K}$ and m^* are the momentum and effective mass of a photoelectron inside the sample and U_0 is called as the inter-potential that corresponds to the bottom energy of the pseudo-parabolic dispersion with respect to the vacuum level. As mentioned above, $\boldsymbol{K}$ conserves the initial state electron wave vector of matter that is what we want to access. The target $\boldsymbol{K}$ is connected to the observable $\boldsymbol{k}$ as follows:

$$\hbar\boldsymbol{K} = (\hbar K_{\parallel}, \hbar K_{\perp}) = \left(\hbar k_{\parallel}, \sqrt{\hbar^2 K_{\perp}^2 + U_0}\right). \tag{10.6}$$

This relationship is geometrically illustrated in Fig. 10.2. Since the surface parallel component of the momentum is conserved throughout the third step of the external photoemission event, it can be directly derived from the ARPES spectra of various θ through the following relation:

$$K_{\parallel} = \frac{\sqrt{2m_0(h\nu - E_b - \Phi_s)}}{\hbar} \times \sin\theta \approx 5.11\sqrt{h\nu - E_b - \Phi_s}\sin\theta\left[\mathrm{nm}^{-1}\right], \tag{10.7}$$

where the unit of energy is taken in eV for the rightest side. For the sake of accessing the surface normal component $K_{\perp}$, an ordinary way is changing $h\nu$ at the normal emission geometry ($\theta = 0$):

$$K_{\perp} = \frac{\sqrt{2m_0(h\nu - E_b - \Phi_s) + U_0}}{\hbar}. \tag{10.8}$$

In practice, the photoelectrons are detected with an electron analyzer, i.e., what we observe is not the energy of the photoelectrons just out of the sample (E_k^{out}) but that at the analyzer (E_k^{obs}). In standard measurement setups of PES, the analyzer is electrically connected to the sample. It means that the Fermi levels of the sample and analyzer align and a contact potential difference (CPD) is usually generated at the gap of these two due to mismatch of their work functions. The photoelectron gains/loses its energy by this CPD when passing through the vacuum gap from the sample to the analyzer:

$$E_k^{obs} = E_k^{out} - (\Phi_a - \Phi_s) = h\nu - E_b - \Phi_a, \tag{10.9}$$

where E_k^{obs} is the observable kinetic energy of the photoelectron at the analyzer position and the CPD is given by ($\Phi_a - \Phi_s$). Note that the rightest side of Eq. 10.9 does not contain Φ_s. This indicates that we need not care about the work function value of the sample for achieving the initial state E_b from the observed kinetic energy of the photoelectrons E_k^{obs}. The work function of the analyzer is a

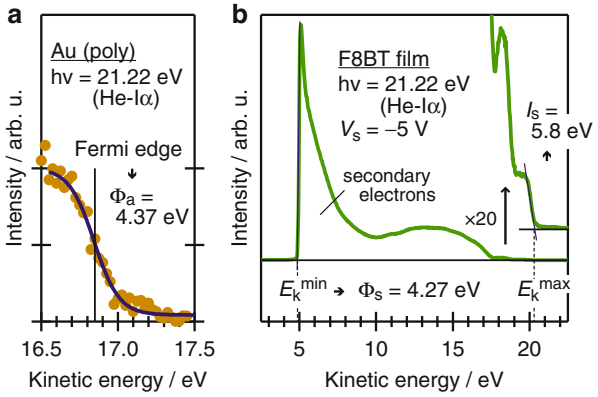


Fig. 10.3 (**a**) A PES spectrum of a polycrystalline Au film. A fitting curve by the Fermi–Dirac distribution function is displayed as a blue line. From the Fermi edge position ($E_k = 16.85$ eV) and excitation photon energy ($h\nu = 21.22$ eV), $\Phi_a = 4.37$ eV is derived. (**b**) A PES spectrum of a F8BT film taken with the identical electron analyzer to (**a**) under a negative sample bias of $V_s = -5$ V. $E_k^{min} = 4.90$ eV leads $\Phi_s = 4.27$ eV, and thus $I_s = 5.8$ eV is obtained from $E_k^{max} = 20.3$ eV

sample-independent value and usually easy to be calibrated from, e.g., the Fermi edge position obtained by a known excitation energy (Fig. 10.3a). Contrariwise, this also means that Φ_s is not always accessible by the standard PES measurements. In order to determine this value, a common way is to apply a negative sample bias V_s (<0) and measure the minimum kinetic energy E_k^{min} of the photoelectrons at that condition:

$$\Phi_s = \Phi_a + \left(E_k^{min} + eV_s\right), \tag{10.10}$$

where e is the elementary charge. Since the photoemission signal of this low kinetic energy range mostly originates from the secondary electrons, E_k^{min} is generally called as the secondary electron cutoff (SECO). Figure 10.3b shows an example of PES spectrum of a thin film of a light-emitting polymer material, poly (dioctylfluorene-*alt*-benzothiadiazole) (F8BT), under a negative sample bias of $V_s = -5$ V [21], where $\Phi_s = 4.27$ eV was derived from $E_k^{min} = 4.9$ eV and $\Phi_a = 4.37$ eV. For the organic semiconducting materials, the vacuum level rather than the Fermi level is often used as an energy standard to describe their energy-level positions. For instance, the solid-state ionization energy I_s, which corresponds to the binding energy of the highest occupied molecular orbital (HOMO) or valence band maximum with respect to E_{vac}, is regarded as the first criterion to judge an "aptitude" of a material for a hole conductor. Although this value can be determined by another specialized experimental technique that will be introduced in Sect. 4.3, PES measurements also derive Is through the following relationship;

$$I_s = h\nu - \left(E_k^{max} - E_k^{min}\right), \tag{10.11}$$

where E_k^{max} is the maximum kinetic energy of the photoelectrons. In the case of Fig. 10.3b, $I_s = 5.8$ eV was obtained for this polymer material from $E_k^{max} = 20.3$ eV at $h\nu = 21.22$ eV.

4.2 History of Problems with PES on Organic Solids

The explication given in the previous section requires the charge neutrality throughout the sample; to express in concrete terms, positive charges (i.e., a deficiency of the electrons) at the sample surface resulting from photoelectron ejection have to be canceled immediately. Otherwise, the energy and momentum of the photoelectrons are disturbed by an unknown electrostatic field caused by these remaining charges. This requirement is automatically fulfilled for metal samples. For less conductive specimens, however, one has to mind whether or not the electrostatic potential at the "front" surface of the sample is really equal to that of the "backside." In a simple viewpoint to regard the whole measurement system as a closed electric circuit, a potential drop ΔV_s across a sample to the thickness direction can be phenomenologically simulated as

$$\Delta V_s \sim j_s \rho d, \tag{10.12}$$

where j_s is the total current density accompanied with the PES measurement, ρ is the electric resistivity of the sample material, and d is the vertical distance between the surface and metallic substrate behind the sample. Although this assumption neglecting a capacitance component and charge traps inside the sample is too simplified to reproduce any accurate magnitude of ΔV_s, still this can be a criterion to estimate a necessary condition for conducting meaningful PES measurements by maintaining ΔV_s small enough (practically less than the energy resolution of the measurement system). On the contrary, distortion and/or suppression of the PES spectra caused by unsatisfaction of this requirement for insulating samples are known as the "sample charging problem" or "charge-up" [22].

To avoid the sample charging, at least one of these three parameters in the right side of Eq. 10.12 has to be sufficiently reduced. The most commonly adopted tactic is shrinkage of d, i.e., preparation of a nanometer-scale ultrathin film as a sample. Since standard UPS and XPS are surface-sensitive techniques as mentioned above, a few nanometer-thick overlayer is enough to conceal the substrate signal from the spectra, and thus, this approach has been utilized for figuring out the electronic structures of various kinds of insulating materials. However, the solid-state properties (e.g., crystal structures) of such ultrathin films are not always identical to those of the bulk. For the sake of conducting the PES measurement on less conductive materials in their bulk phase, another widely applied method is substantial cancelation of j_s by a reverse electric current, that is, compensation of the photoemission-induced positive charge by using a low-energy electron beam from a "flood gun." This is also an established scheme that has revealed the electronic structures of many inorganic insulating materials.

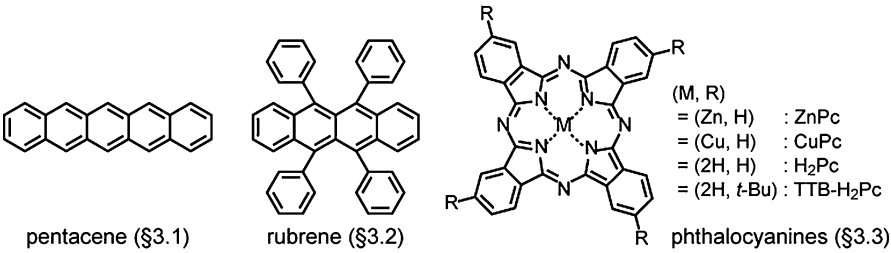


Fig. 10.4 Molecular structures of organic materials being discussed in this article

The first tactic is useful also for organic solids; the electronic properties of various organic materials are routinely examined in this approach [23]. Although most organic molecular solids are poor electric conductor where their typical electric resistivity is several orders of magnitude greater than that of standard metals, intermolecular valence band structures were successfully discovered on well-crystalline ultrathin films of several organic molecules by means of ARPES. A series of the ARPES works conducted on crystalline thin films of pentacene (Fig. 10.4) is introduced in Sect. 5.1 as typical cases. The second method is, however, generally not suitable for organic samples because these materials are easily damaged by the electron irradiation via chemical decomposition or polymerization. Hence the PES measurement for a bulk organic crystal requires a third way to reduce its electric resistivity ρ. Challenges so far along this course of action are briefly summarized in Sect. 4.4.

As described above, the substance of the sample charging problem is nothing but violation of the one-to-one correspondence of E_k^{obs} to E_b due to an unidentified ΔV_s. From the opposite point of view, this problem can be evaded if one chooses another parameter, uninfluenced by the electrostatic potential as a variable rather than E_k^{obs}. In this context, photoelectron yield spectroscopy (PYS), where the total photoelectron yield from a negatively biased sample is counted as a function of the excitation photon energy $h\nu$, is a promising solution for the sake of characterizing the electronic structures of bulk insulating materials. While it is an ancestor version of the modern PES techniques [24–26] and is not an angle-resolvable technique in principle, still it is worthwhile to devote a space to introduce this experimental method owing to its great advantage of applicability for universal materials. Then technical essences of PYS will be described in the next subsection.

4.3 Solution I: Photoelectron Yield Spectroscopy (PYS)

PYS is a technique to detect the overall amount of the ejected photoelectrons from the sample irradiated by monochromatized ultraviolet light. There are several variants with methods to count the photoelectrons; representative ones are detection

of the electrons themselves with an electron multiplier [27–29] and measuring the drain current flowing into the sample to cancel the photoemission-induced positive charge with a precise ammeter [30–32]. Either has benefits and drawbacks; the former provides extremely high sensitivity (theoretically the single photoemission event can be detected) but can be operated only in vacuum condition, while the latter is available in any atmosphere (even in the ambient condition) but is not free from a sensitivity limit of $\sim 10^4$ electrons per second (several fA). In this article, we introduce some results of the latter PYS technique.

Photoelectron yield Y for the excitation photon energy $h\nu$ is derived by dividing the total photoemission-induced current J by a photon flux F:

$$Y(h\nu) = \frac{J(h\nu) - \delta}{F(h\nu)}. \tag{10.13}$$

Here, δ represents an electric "dark current" overlapping to the real photocurrent for some reasons, which has to be subtracted adequately for practical data processing. Although the physical substance of Y is complex, the following simplified relationship is widely accepted for a standard analysis to determine I_s:

$$Y(h\nu) = A(h\nu - I_s)^n S(h\nu - I_s), \tag{10.14}$$

where A is a material-dependent constant and $S(x)$ is an appropriate step function to give zero when x is negative or unity when x is positive. The exponent n is thought to depend on the material types; empirically, $n = 2$ is adopted for, e.g., indirect gap inorganic semiconductors [33], whereas $n = 3$ is proposed for organic materials [34]. This equation is known to reproduce the experiment when $h\nu$ is not far greater than I_s.

On practical PYS measurements, the sample is negatively biased with respect to an electron collector (or anode). As long as the potential drop across the sample is sufficiently smaller than the applied sample bias, the whole of the emitted photoelectrons is pushed away from the sample, and the drain current supplies the same amount of electrons to the surface. In this condition, the measured photocurrent is independent of the actual surface potential of the sample, i.e., magnitude of the sample charging. In a typical measurement condition, the sample bias and total photocurrent are -10 V and 1 pA, respectively. Hence, if the vertical resistance of the sample is less than 10^{13} Ω, the potential drop resulted from a leakage current across the sample is still kept below the applied sample bias. For a 1 mm-thick bulk sample, since the spot area of the excitation photon is normally about 10 mm^2, the PYS measurement is possible on insulating materials of the electric resistivity up to 10^{12} Ωm. Furthermore, even for extreme insulators of greater resistivity, still one has a chance to conduct the PYS measurements with a mechanism so-called capacitor mode where the sample itself behaves as a capacitor to maintain the potential drop smaller than the applied bias [35]. Figure 10.5 shows the PYS spectra taken on electrically isolated Au patches by two types of

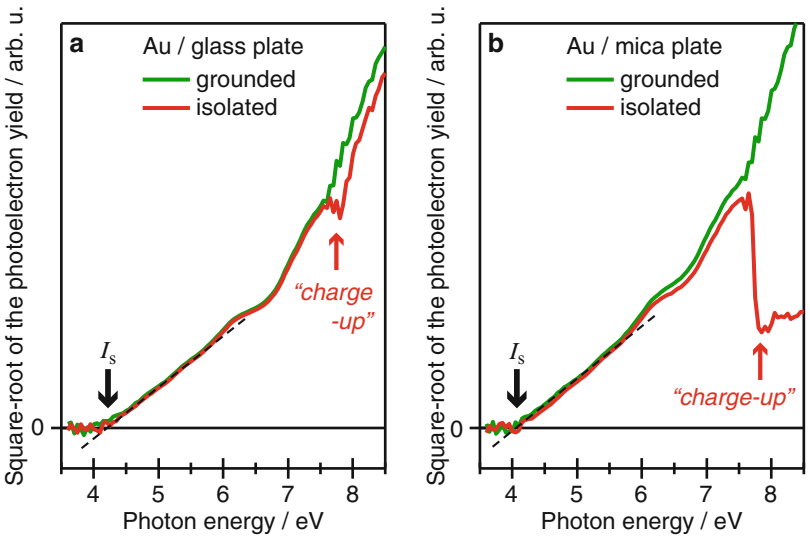


Fig. 10.5 PYS spectra of an electrically isolated (*red line*) and grounded (*green*) Au island film formed onto a (**a**) glass or (**b**) mica (*muscovite*) plate. All samples were biased at −33 V from a collector. The vertical axis of each plot is scaled with a square root of the photoelectron yield, where a horizontal intercept of the linear fit of each spectral onset gives the ionization energy value. Deviation of the red line from the green one in the high energy side represents the "charge-up" of the isolated sample due to very intense photoemission

insulators: a glass ($\sim 10^{10}$ Ω) or mica ($\sim 10^{15}$ Ω) plate. Although spectral distortion ascribed to the sample charging appears in the high energy side, it does not influence the photoemission threshold range, and thus, the I_s values are reasonably defined for both samples. Another example of PYS demonstration on an undoped (gem) diamond, that is, a bulk insulator itself, is also represented in Fig. 10.6. Two thresholds are clearly resolved, which should be assigned to the ionization energy and band-gap width, namely, the vacuum-level position and overlying conduction band minimum, respectively, toward the valence band edge [36, 37].

4.4 Solution II: PES Assisted by Photoconduction

Though PYS is a useful tool to characterize the top edge of the occupied electronic state of bulk insulating materials, it is not suitable to probe any detailed structures inside the valence band. While single crystals of π-conjugated organic semiconductors have been a fascinating target as benchmark samples for the sake of resolving long-term mysteries about electric transport behaviors in such class of materials, experimental demonstration of the electronic structures, especially band mapping by means of ARPES, on bulk organic crystalline samples has been

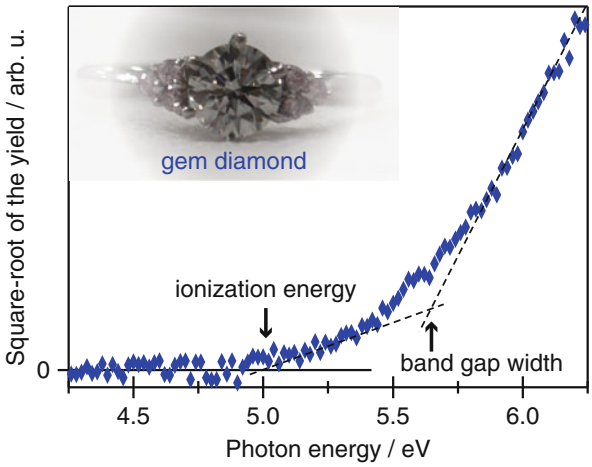


Fig. 10.6 A PYS spectrum of a bulk *gem* (undoped) diamond. Since the diamond is known as a negative electron affinity material, the spectral threshold and breakpoint are assigned as the vacuum-level position (ionization energy) and conduction band minimum (band-gap width), respectively, toward the valence band maximum. (*Inset*) A photograph of the specimen. The sample was mounted onto a Pt "sample holder"

challenged against the sample charging problem. The key strategy is lessening of the electric resistance of the sample ρ as mentioned in Sect. 4.2.

The first successful photoemission results on organic single crystal samples were achieved by Sato and co-workers in the early 1980s [38]. They capped the single crystal surface of polyacene and related materials by a very thin metal (Au) film to produce a side path and also shined the crystal by white light to make use of the photoconductivity. Later on, Vollmer and co-workers conducted PES measurement on the single crystal of pentacene by illuminating the sample with a green laser to inject the cancelation charge from a backside electrode through internal photoemission [39]. Although angular-integrated density-of-state (DOS) distributions of organic single crystal samples were successfully resolved by their tactics, detailed structures of the valence band still had been left untouched.

Our group attempted the PES measurement on the single crystal of rubrene (see Fig. 10.3) under illumination of blue or violet laser light. Figure 10.7 shows the spectra depending on the laser wavelength [40]. The spectral profile reproduced by molecular orbital distribution is clearly resolved under the violet ($\lambda = 405$ nm; 3.06 eV) light while it transforms into featureless and lift-weighted one for the blue (445 nm; 2.79 eV) light case indicating unsuccessful relief of the sample charging. Taking the energy gap width between the HOMO and lowest unoccupied molecular orbital (LUMO) of rubrene (2.8 eV [41]) into consideration, this implies that it is important to select an adequate wavelength for the support light to over-exceed the bandgap of the sample for the sake of conducting the PES measurement on insulating materials. Through this approach, successful PES measurements on the single crystals of rubrene [42–44], derivatives of rubrene [45], tetracene [44], pentacene [46], and picene [47] have been reported so far. In the present article, a series of results taken for the rubrene single crystal is presented in Sect. 5.2.

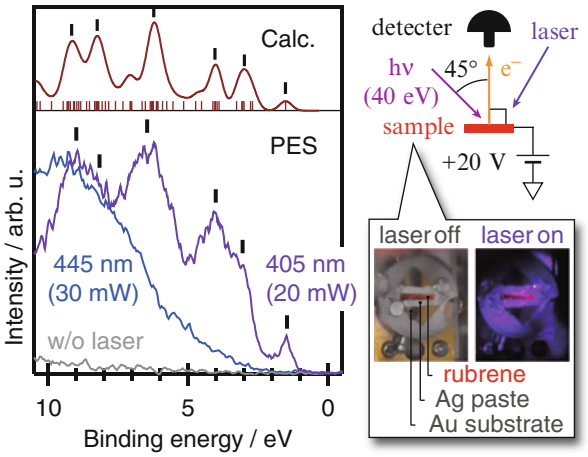


Fig. 10.7 PES spectra of a bulk rubrene single crystal sample taken with and without *violet* (405 nm) or *blue* (445 nm) laser light illumination. A simulated DOS curve from a calculated molecular orbital distribution is also represented in the top panel. A schematic drawing and photographs of a sample with and without violet laser light illumination are shown in the right panel

5 Key Research Findings

5.1 Valence Bands of Crystalline Thin Films of an Organic Semiconductor: Pentacene

ARPES characterization of an ultrathin film formed onto a conductive substrate is the most established methodology to determine its intermolecular valence band structure if one can prepare a well-ordered crystal sample in this course. Actually, the observation of intermolecular valence band structures for the organic semiconductors was initially attempted on well-crystalline thin films. The first successful demonstration was accomplished by Hasegawa and co-workers on bis-(1,2,5-thiadiazolo)-*p*-quinobis(1,3-dithiole) (BTQBT) which assembles itself into well-ordered crystalline packing of π-orbital stacking perpendicular to the surface onto a highly oriented pyrolytic graphite (HOPG) substrate [48]. They conducted the excitation energy-dependent PES at the normal emission geometry to find out the valence band dispersion of around 0.4 eV wide toward the thickness direction of the film at room temperature (290 K). A relatively light effective mass ($\sim 3\ m_0$) was derived from the valence band structure.

Koch and co-workers applied this method to a crystalline thin film of pentacene [49]. Since a charge carrier mobility over 1 $cm^2V^{-1}\ s^{-1}$ was discovered for the first time in the organic field-effect transistor (OFET) of this molecule [50], pentacene has attracted notable attention as a prototype material of high-mobility organic semiconductors. Pentacene, as BTQBT, also forms a crystalline thin film of a flat-lying molecular orientation with the perpendicular π-stacking onto HOPG; the valence band dispersion can be mapped out through the *hv* dependence of the normal emission PES spectra. They observed a valence band dispersion of 0.24 (±0.05) eV at 120 (±10) K, which exhibited a shrinkage into 0.19 (±0.05) eV at room temperature presumably due to increased population of intra- and intermolecular phonons.

For ordinary OFET devices, since charge carriers mainly transport in the conductive channel parallel to the surface, a crystal structure of an upright-standing molecular orientation is more favorable rather than the flat lying. Sakamoto and co-workers succeeded in demonstrating the valence band dispersion of a crystalline monolayer of upright-standing pentacene molecules covering over a Bi(100)/Si(111) substrate by means of ARPES [51]. They conducted the measurements at 140 K along three symmetric directions of the surface Brillouin zone (SBZ) to illustrate a two-dimensional band structure, where the maximum energy dispersion was found to be 0.33 (±0.04) eV along the Γ-M direction and the effective mass of the holes m_h* was evaluated as 1.26 m_0 under the one-dimensional tight-binding (1D-TB) approximation. Later on, the valence band structure of the bulk phase pentacene crystalline film was more precisely investigated by Hatch and co-workers, where they figured out a significant anisotropy of the intermolecular transfer integral and hole effective mass based on the two-dimensional tight-binding (2D-TB) approximation [52]. They also analyzed their PES results of sample temperature dependence carefully for the sake of inquiring into the natures of electron–phonon coupling to ascertain that it enhances the effective mass by 36 % and its origin has to be ascribed to the intermolecular vibrations taking a smaller Einstein energy (∼0.01 eV) in comparison to the cutoff for the intramolecular ones into consideration [53].

In practice, pentacene is known to exhibit several crystalline polymorphs. The crystalline film formed onto Bi(100) exhibits one called as the "bulk phase," while another structure, the "thin-film phase," is obtained on gate dielectric surfaces such as SiO_2 [54]. Since it has been theoretically predicted that the valence band dispersion of pentacene is sensitively affected by its molecular packing structures [55], the ARPES measurement on this crystalline phase was of the highest anticipation. Shimada and co-workers succeeded in the preparation and ARPES demonstration of a "single-domain" thin-film phase crystalline film of pentacene onto a Bi-passivated Si(111) substrate with regularly bunching steps [56]. A light and relatively isotropic m_h* (ranging in between 0.8 and 0.9 m_0) was derived from the valence band mapping results at 130 K, whereas anisotropic declination of the band dispersion with increasing sample temperature to 300 K was observed, suggesting possible orientation dependence of decoherence of the molecular wave functions [57].

As described above, ARPES is a useful technique to unveil essential electronic properties, such as the transfer integral and effective mass, in direct relevance to the charge carrier transport nature in molecular solids. I would like to conclude this subsection by introducing another variant of ARPES methodologies, in which variation of the photoemission intensity rather than the energy is a matter to be mapped out as a function of the probing angle. Puschnig and co-workers carefully traced the azimuthal-angular dependence of the HOMO-derived photoemission intensity from the (022) face of a crystalline thin film of pentacene over a hemispherical region [58]. Under the approximation to treat the final state ψ_f as a plane wave (PW), the Fermi's golden rule (Eq. 10.1) is equivalent to the Fourier transform of the initial state wave function ψ_i by the PW; in other words, the orbital shape of the initial state can, in principle, be retrieved from the inverse Fourier transform of an experimental intensity pattern of the photoemission intensity. They compared their

angular distribution pattern with a simulated one from the density functional theory to corroborate satisfactory agreement with each other. The method "orbital tomography" is indeed useful to visualize the character (e.g., symmetry) of unidentified orbitals. One example was reported by Reinert and co-workers for 3,4,9,10-perylenetetracarboxylic dianhydride (PTCDA) molecules on Ag(111), where they mapped the angular distribution of the photoemission intensity from the HOMO and partially occupied LUMO of PTCDA to ascertain modification of the latter orbital due to the hybridization with the metal electronic state [59].

5.2 Rubrene Single Crystal: Demonstration of the Band Dispersion on an "Insulating" Material

The aforementioned achievements on the crystalline thin films have pioneered a way to access the valence bands of the organic molecular crystals. This approach is, however, not always applicable onto every material because we often face difficulties to prepare thin films of satisfactory crystalline quality. One example is the case of rubrene (5,6,11,12-tetraphenyltetracene). This material has been fascinating researchers of both application and fundamental fields since the invention of its notably high and anisotropic charge carrier mobility in a "transistor stamp" device of its single crystal [60]. Currently, the rubrene single crystal is known as the champion material of the hole mobility for all organic semiconductors [61]. Hence its electronic structure, or more concretely the valence band structure, has been of keen interest. However, the rubrene molecules exhibit a dissimilar conformation in the bulk single crystals with respect to the "ground state" one in ordinary thin films or in the gas phase. This situation makes it difficult to prepare thin films of rubrene of the identical structure with its single crystal [62].

Our group adopted PYS as a suitable technique to probe electronic properties of bulk insulating samples such as the rubrene single crystal [63]. Figure 10.8 shows the PYS spectra of a single crystal and amorphous film of rubrene. As seen, these two spectra revealed remarkable discrepancy in the photoemission threshold. Each ionization energy was derived through least-squares fitting of the photoelectron yield $Y(h\nu)$ with Eq. 10.13 (Fig. 10.7b), or by linear fit for the cube root of the photoelectron yield $\sqrt[3]{Y(h\nu)}$ (Fig. 10.7c), to be 4.85 and 5.3 eV for the single crystal and amorphous film, respectively. The latter value agrees with previous results by PES [64, 65], whereas the present ionization energy of the single crystal is about a half eV smaller than the known value for rubrene. A similar phenomenon, i.e., a better crystallinity lifts the upper edge of the HOMO up toward the vacuum level, was also reported for several forms of pentacene thin films [66], where principal reasons of this trend can be attributed to an energy dispersion of the valence band and a "dipole layer" caused by C–H polar bonds at the topmost part of the molecular solids for the well-crystalline samples [67]. For rubrene, the true nature should be more complex to quantitative comprehension of this discrepancy in the ionization energies between the single crystal and amorphous film at the present stage; the switching of the molecular conformation may lead a change in the molecular orbital

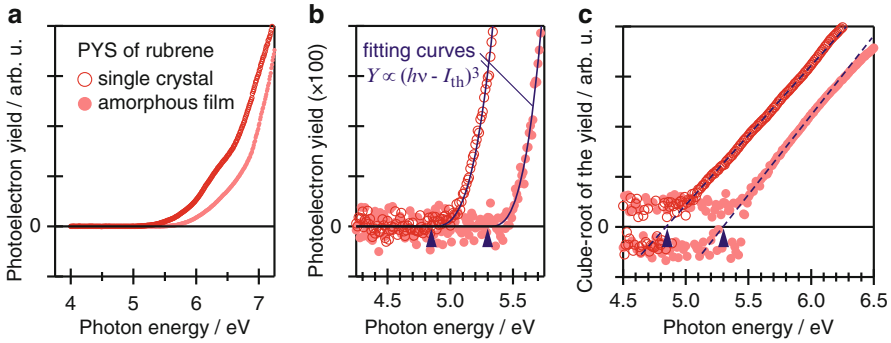


Fig. 10.8 (**a**) PYS spectra of a single crystal and amorphous film (formed onto an indium-tin-oxide substrate) of rubrene. (**b**) Magnified spectra of (**a**). Least-squares fitting curves with Eq. 10.13 ($n = 3$) are also displayed. (**c**) The spectra plotted in a cube root of the photoelectron yield scale, where its line fit in the threshold region gives each ionization energy value for organic samples. The wedge marks represent the ionization energy positions derived from the present results

energies [68], and a probable existence of some oxidized species on the ex situ single crystal surface may cause an additional vacuum-level shift. Nevertheless, it should be emphasized that, in terms of the carrier injection, a smaller ionization energy is a great advantage for "*p*-type" organic semiconductors as rubrene.

As mentioned above, a reduced ionization energy, or a shallower onset energy of the HOMO, implies that the molecular HOMO transforms into a valence band with a considerable energy dispersion width. However, further details of the valence band structure are in principle inaccessible by means of PYS as an angle-integrated measurement technique. For the next step, we attempted the ARPES measurement on the rubrene single crystal by a tactic mentioned in Sect. 4.4.

Firstly, an appropriate measurement condition was surveyed [42]. As shown in Fig. 10.9, the HOMO-derived peak in the PES spectra became narrower and shifted to the low binding energy (BE) side upon raising the illumination power of the continuous-wave violet (405 nm) laser, while the sample charging made the peak very broad and push it away leftward. No further change was found even when the laser power was further increased beyond 7 mW, which suggests complete cancelation of the sample charging. The ARPES measurements described hereafter were conducted under the laser light illumination at 14 mW. It should be noted that the laser light was somewhat defocused over several cm^2 area in order not to induce any mechanical damage onto the specimen.

Figure 10.10 shows the ARPES spectra of a rubrene single crystal sample taken along the crystalline ***b***-axis (Γ-Y direction), for which the largest hole mobility was experimentally discovered [60] and the widest energy dispersion of the valence band was predicted by theoretical calculations [69, 70]. The HOMO-derived peak revealed a prominent energy shift depending on the electron takeoff angle θ. The peak positions were plotted in the E_b–$K_{\parallel}$ plane as shown in Fig. 10.10c, where θ is transposed into $K_{\parallel}$ by Eq. 10.7. A periodic alternation in the peak position is thought

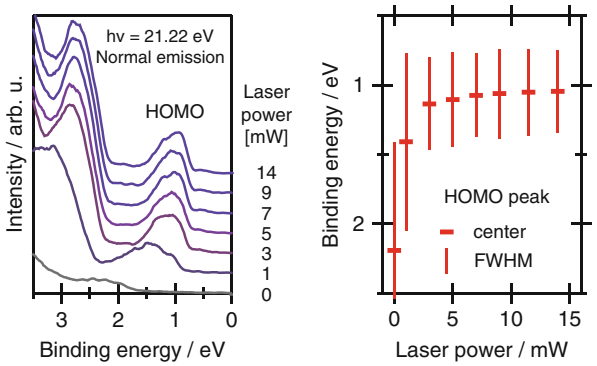


Fig. 10.9 (*left*) Evolution of the PES spectra of a rubrene single crystal depending on the illumination power of the 405 nm laser. (*right*) The peak position and width of the HOMO of rubrene depending on the laser power

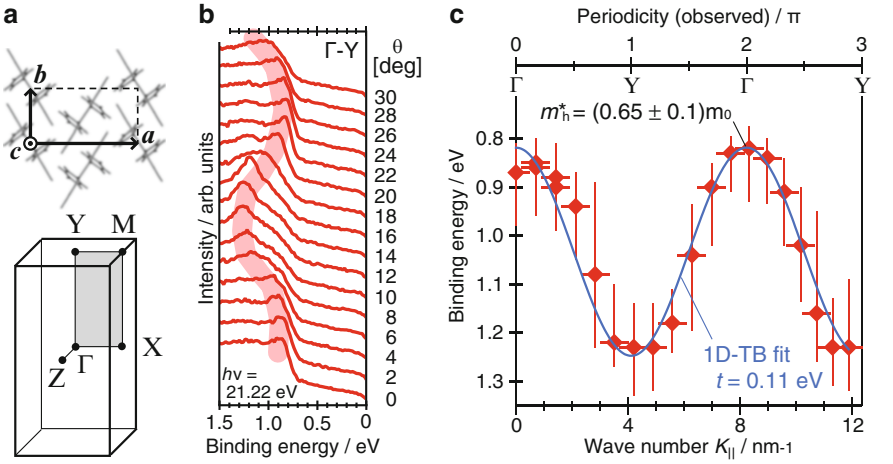


Fig. 10.10 (**a**) Schematic drawings of the crystal lattice and Brillouin zone of the rubrene single crystal. The hatched area represents the SBZ. The molecular arrangement in the ***ab*** plane (parallel to the surface) is also shown. (**b**) ARPES spectra of a rubrene single crystal sample taken along the Γ-Y direction, where the electron takeoff angle θ was tilted from the surface normal within the crystalline ***bc*** plane. (**c**) An E–$K_{\|}$ plot of the valence band derived from the HOMO peak position depending on θ of the ARPES spectra. The 1D-TB fitting result is also shown

to be a clear experimental evidence of the valence band of a considerable energy dispersion. The present E–K dispersion relation can be reproduced by the 1D-TB relation, where the electron energy E is connected to the wave number K as

$$E = E_c - 2t\cos(LK), \tag{10.15}$$

where E_c is the energy of the band center, L is the lattice constant, and t is the intermolecular transfer integral toward the adjacent unit. In the present case, t was

estimated to be 0.11 eV from the experimental E–K relation. The hole effective mass m_h* at the valence band top was thereupon derived to be $(0.65 \pm 0.1)m_0$ from the band curvature. This remarkably light value for organic semiconductors is consistent to a previous proposition based on infrared absorption results [70].

As an extension of this accomplishment, we demonstrated the valence band mapping of the rubrene single crystal in a three-dimensional manner [43]. For the surface normal direction, no energy shift of the HOMO-derived peak was corroborated independent of the excitation energy $h\nu$, which evince an absence of the E–$K_\perp$ dispersion as expected. Meanwhile, ARPES measurements were conducted toward three symmetry points of the SBZ as shown in Fig. 10.11 (left). To the Γ-X direction, which is orthogonal to the most conductive axis (Γ-Y), the valence band is substantially flat without any notable energy dispersion. In contrast, significant energy dispersion was observed to the diagonal direction of the SBZ (Γ-M); in comparison to the Γ-Y direction, the dispersion width was equivalent, whereas the turnaround angle was farther from the normal emission reflecting a wider Brillouin zone size. From these ARUPS spectra, the 2D valence band E–$K_\parallel$ relation can instantaneously be mapped out as shown in Fig. 10.11 (right). The hole effective mass at the Γ point can be estimated to be 0.63 and 0.84 m_0 toward the Y and M points, respectively, whereas that toward the X point was no lighter than 2 m_0. Furthermore, the intermolecular transfer integrals to four nonequivalent adjacent molecules (as seen in the inset of Fig. 10.11) can be extracted from these dispersion relationships under the 2D-TB approximation that is expressed in the case of the rubrene single crystal as

$$E = E_c - 2t_a \cos\left(L_a K_x\right) - 2t_b \cos\left(L_b K_y\right) - \sqrt{4{t_d}^2\left[\cos\left(\frac{L_a K_x}{2} + \frac{L_b K_y}{2}\right) + \cos\left(\frac{L_a K_x}{2} - \frac{L_b K_y}{2}\right)\right]^2 + \frac{\Delta E}{2}}, \tag{10.16}$$

where t_a, t_b, t_d are the nearest-neighbor intermolecular transfer integral values to the crystallographic $\boldsymbol{a}$, $\boldsymbol{b}$, and diagonal directions, respectively; L_a and L_b are lattice constants to the respective direction; K_x and K_y are two independent components of $\boldsymbol{K}$ along the Γ-X and -Y directions, respectively; and ΔE is the energy difference between two inequivalent sites in the unit cell. As seen, this reproduces the experimental valence band structure satisfactory, and the transfer integral values were derived as given also in the figure, which also agree with the theoretical calculations fairly well [71–73]. This result indicates that the intermolecular charge carrier transport efficiency is strongly anisotropic, which has to be the electronic origin of the orientation-dependent μ_h discovered for the rubrene single crystal field-effect transistor.

These two physical properties, the effective mass and transfer integral, determined above are essential values which dominate charge carrier transport inside the organic molecular solids. In a commonly adopted model to ordinary organic semiconductors, the carrier conduction phenomena are treated as charge exchange reactions between a molecular ion and its adjacent neutral species. In this model,

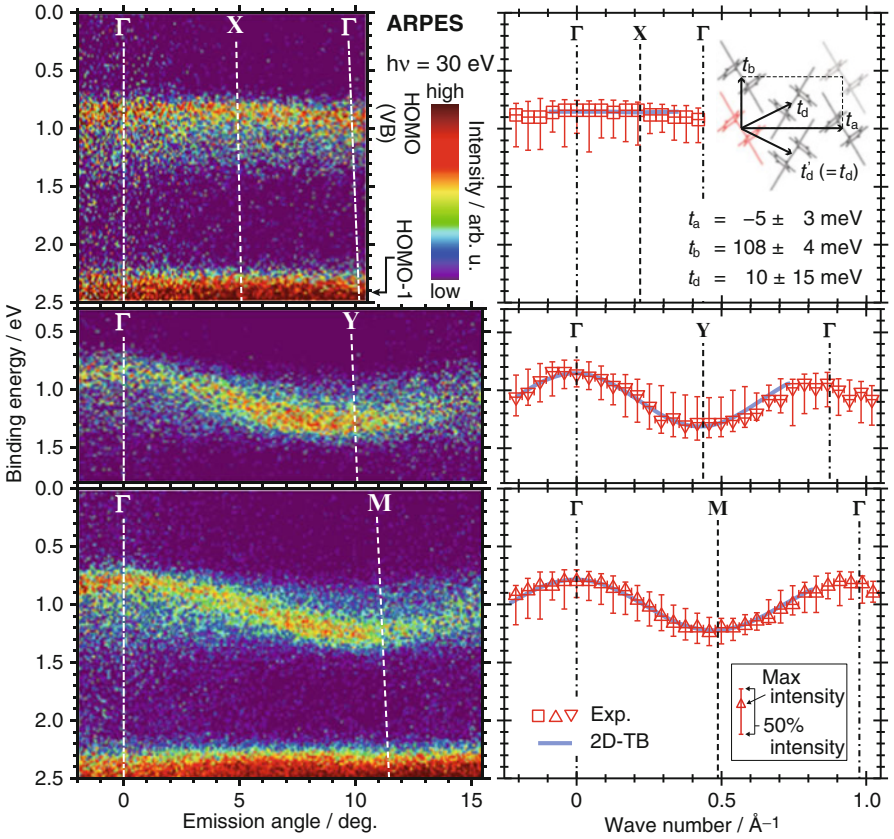


Fig. 10.11 (*left*) ARPES spectra of the rubrene single crystal taken along three symmetric direction of the SBZ. The excitation energy was 30 eV. The horizontal and vertical axes of these two-dimensional spectral images correspond to the electron takeoff angle and binding energy, respectively, while the color tone indicates the photoelectron intensity. The angles corresponding to the critical points of the SBZ are also indicated. (*right*) The E–$K_{\parallel}$ maps derived from the ARPES spectra. The blue lines represent the best fit curves of the E–$K_{\parallel}$ relations under the 2D-TB approximation. (*Inset*) The intermolecular transfer integral values derived under the 2D-TB approximation toward the four inequivalent adjacent molecules (where $t_d' = t_d$ by symmetry)

the hopping mobility μ_M of the charge carriers can be expressed by the Marcus electron transfer theory as

$$\mu_M = \left(\frac{eL^2}{k_B T}\right) k_{ET}, \tag{10.17}$$

where k_B and T are the Boltzmann constant and temperature, respectively. k_{ET} represents the rate of the electron transfer reaction, which is described as a function of the intermolecular transfer integral t:

$$k_{\mathrm{ET}} = \frac{2\pi\, t^2}{\hbar}\sqrt{\frac{1}{4\pi\lambda_{\mathrm{r}} k_{\mathrm{B}} T}}\,\exp\left(\frac{-\lambda_{\mathrm{r}}}{4k_B T}\right), \tag{10.18}$$

where λ_{r} is the reorganization energy [74]. Since λ_{r} of rubrene was previously proposed to be 0.16 eV both theoretically and experimentally, the hopping mobility at room temperature can be estimated to be $\sim$20 $\mathrm{cm^2V^{-1}\,s^{-1}}$ from the present t_{b} of the rubrene single crystal. It has to be emphasized that this mobility value should be regarded as the highest limit which can be achieved in an *ideal* condition without any drawback factors for carrier transport (such as impurities and defects) within the crystal. Nonetheless, comparable or even greater hole mobility has been reported in *actual* OFET devices of the rubrene single crystal [61, 75]. This strongly suggests that the hopping transport model is insufficient to explain such a large mobility exhibited by the rubrene single crystal.

On the other hand, in a framework of "band transport" as standard inorganic semiconductors or metals, the electric conduction is considered as a current of "free" charge carriers with continuous scattering events. Within this classical Drude model, the drift mobility μ_{D} can be written as a function of the effective mass m^* of the charge carrier to be

$$\mu_{\mathrm{D}} = \frac{e\tau}{m^*}. \tag{10.19}$$

Here τ is the relaxation time of the charge carriers, which is determined as a result of several extrinsic (e.g., impurities and defects) and intrinsic (e.g., intramolecular vibrations and lattice phonons) scattering factors, and is an unknown parameter in the present stage. Conversely, one can phenomenologically estimate τ from an experimental mobility value through Eq. 10.19. For instance, the mobility value of 40 $\mathrm{cm^2V^{-1}\,s^{-1}}$ reported by Takeya and co-workers [61] corresponds to the relaxation time of 16 fs, where the aforementioned m_{h}^* value along the Γ-Y direction is substituted to m^*. Since the energy uncertainly being equivalent to this τ is $\sim$0.04 eV which is still one order of magnitude smaller than the valence band width, a prerequisite condition for the band transport framework is fulfilled. A conducting carrier keeps its coherence between two successive scattering events. The mean coherent length $\bar{l}$ of the holes is therefore given as

$$\bar{l} = \bar{u}\tau = \sqrt{\frac{3k_{\mathrm{B}}T}{m_{\mathrm{h}}^*\tau}} \approx 2.1[\mathrm{nm}] \sim 3\ L_{\mathrm{b}}, \tag{10.20}$$

where we assume the Maxwell–Boltzmann distribution for the mean speed of the carrier $\bar{u}$. Again, these $\bar{l}$ and τ values were ones derived from a practical mobility, and thus the fundamental physical properties of this material have to be no smaller than these. The present results manifest that the coherence of the conductive holes is preserved as far as a few crystalline lattice units along the ***b***-axis, or in other words, the charge carriers delocalize over a couple of molecules in the rubrene single crystal even at room temperature.

5.3 Novel Nano-organic Interaction: π-Conjugated Molecules on Quantum Wells

PES is a useful technique also for revealing the fundamental physics inside nanomaterials, for instance, monatomic sheets [76, 77], atomic wires [78–80], and quantum dots [81–84]. In this article, we pick up "quantum wells" (QWs) of nanometer-thick and atomically flat metal thin films as an example [85, 86]. While this type of nanostructure is somewhat a *classical* representative of the low-dimensional matters, its exotic physical properties, that is, atomic layer-by-layer variations of, e.g., work function [87], surface reactivity [88], electric conductivity [89], and superconducting transition temperature [90], have been attracting notable attention in the surface science research fields. In a viewpoint of the electronics application, especially for the organic electronics, the nanotechnology will provide an additional possibility for us to optimize the characters of electrodes making use of the quantum size effect, whereas the electronic properties of conventional bulk metals are given inherently in the materials. We herein introduce the characteristic electronic structures of the QWs and their interactions with organic molecules recently discovered by means of ARPES.

When the thickness of a metal shrinks into a few nanometers, confinement of the electrons toward the thickness direction leads to the quantization of the electronic states, while a free electron-like character is preserved to rest two dimensions. In other words, an electronic band of a three-dimensional paraboloid shape eventually splits into a series of parabolic "sub-bands" because of the quantum size effect, which is clearly resolvable by means of ARPES as shown in Fig. 10.12 (left) [91]. In a textbook "particle-in-a-box" framework, the nth quantization energy E_n of the quantum wells can be connected to the well width d as

$$E_n = \frac{\hbar^2 {k_n}^2}{2m^*} = \frac{\hbar^2}{2m^*}\left(\frac{n\pi}{d}\right)^2, \tag{10.21}$$

where k_n represents the wave number of the nth standing wave within the well and m^* is the effective mass of electrons. As this simplest quantization rule assumes an infinite potential barrier at both "walls" of the well, the boundary conditions have to be modified for the practical systems according to the actual characters of the potential walls. In a model called as "phase shift accumulation rule" or "Bohr–Sommerfeld quantization rule," any details of the potential walls are included into the phase shifts of the electron wave reflected at the respective boundaries. For example, in Fig. 10.12, the quantization condition switches on crossing the band edge of the Ge substrate (indicated with a dotted line); there is no permitted state at the either end of the well for the upper side, whereas electrons can exist in the substrate part for the lower side, so that the electronic states in this region are called as "quantum well resonance (QWR) states" making distinction with the fully confined quantum well state (QWS). Although accurate properties of the potential barriers that the electrons in the well feel are not easy to be defined,

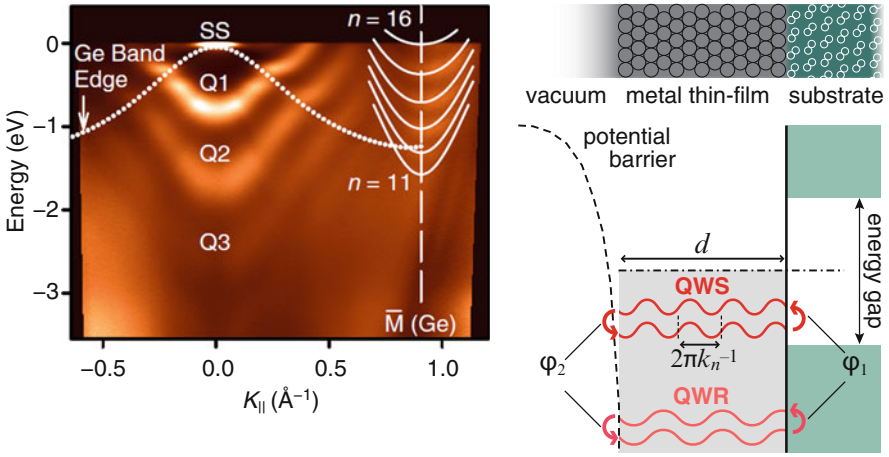


Fig. 10.12 (*Left*) ARPES spectra of a 13 ML-thick Ag thin film on Ge(111). Q1, Q2, and Q3 are QWSs, and SS is a Shockley surface state. Singularities in free electron-like dispersion of these QWSs appear at intersection points with the Ge valence band edge. A set of parabolic band around the M(Ge) point is called as QWSs of the "second kind" (whose details are beyond the scope of this article). Reproduced from Tang et al. (2006) (http://prl.aps.org/abstract/PRL/v96/i21/e216803) with permission of the copyright holder (American Physical Society). (*Right*) Schematic illustrations of a metal thin-film QW and the quantization rule within this QW

such difference in the boundary conditions can be taken into account as a modification in the phase shift, which is schematically illustrated in Fig. 10.12 (right). In this model, the quantization condition is expressed as

$$2k_n d + \varphi_1 + \varphi_2 = 2\pi n, \tag{10.22}$$

where φ_1 and φ_2 are the phase shift magnitude at the first and second boundaries, which corresponds the right-side interface (with the substrate) and the left-side surface (with the vacuum) for the metal thin-film QWs, respectively. This indicates that the electronic structure of a metal thin film is affected by two additional parameters besides the thin-film thickness d. In other words, we have two more freedoms to regulate the electronic properties of a QW electrode, that is, the interface characteristics with the substrate φ_1 and adsorbate-mediated surface condition φ_2.

We first examined the latter factor φ_2 independently from the other two by utilizing an organic insulator material physisorbed onto the surface of the QW [92]. Figure 10.13 shows the normal emission PES spectra of a nine monolayer (ML)-thick Ag thin film formed on a Ge(111) substrate and its evolution upon coverage by a *normal* alkane $C_{44}H_{90}$ (tetratetracontane; TTC). The work function was brought down as the TTC overlayer grew, which was eventually followed by saturation at ~0.6 eV below the primary position after the thickness of ~0.2 nm. The spectral profile exhibited notable variation which can be attributed to transition

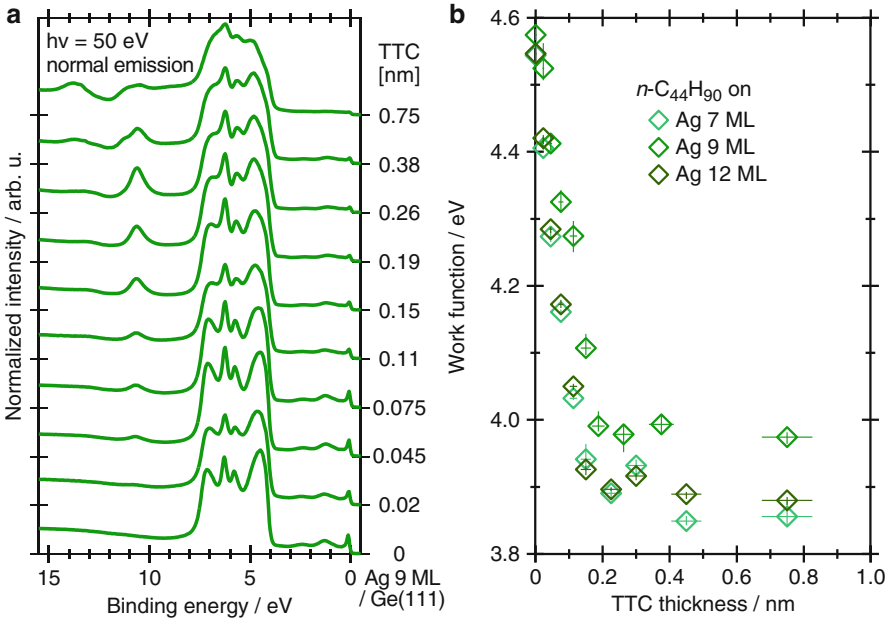


Fig. 10.13 (**a**) A normal emission PES spectrum of a 9 ML-thick Ag thin film and its evolution depending on the thickness of TTC overlayers. The excitation energy was 50 eV. (**b**) Variation of the work function of Ag thin films of 7, 9, and 12 MLs plotted as a function of the thickness of the TTC overlayers

of the averaged molecular orientation of TTC. A feature arising at the binding energy of ~10 eV is a sign of the flat-lying TTC molecule [93]. We can therefore decide that the overlayer thickness of ~0.2 nm corresponds to completion of one monolayer of the flat-lying TTC molecules.

The ARPES spectra for the pristine and 1 ML TTC-covered Ag thin film are presented in Fig. 10.14. Two QWR sub-bands are resolved in this energy range as parabolas of the downward convex. The bottom of the upper parabola moved up by ~0.1 eV toward the Fermi level upon TTC coverage, where the lower one also showed the same trend. It was reported that physisorption of rare-gas molecules onto noble metal surfaces lifts the Shockley surface state (SS) up toward the Fermi level and the origin of this behavior is ascribed to the Pauli repulsion that pushes the electron density spilling out of the surface back inside the solid [94]. Indeed lessening of the SS after TTC coverage suggests that it was also raised beyond the Fermi level by the identical mechanism. It should be noted that the curvature of the sub-bands was preserved upon the TTC coverage; e.g., the electron effective mass of the upper sub-band after the TTC coverage (0.47 m_0) was actually equal to that of the pristine Ag thin film (0.45 m_0). This strongly suggests that the observed energy shift of QWR is not caused by any chemical interaction between the adsorbate and Ag thin film but by a modulation of the boundary condition at the surface side.

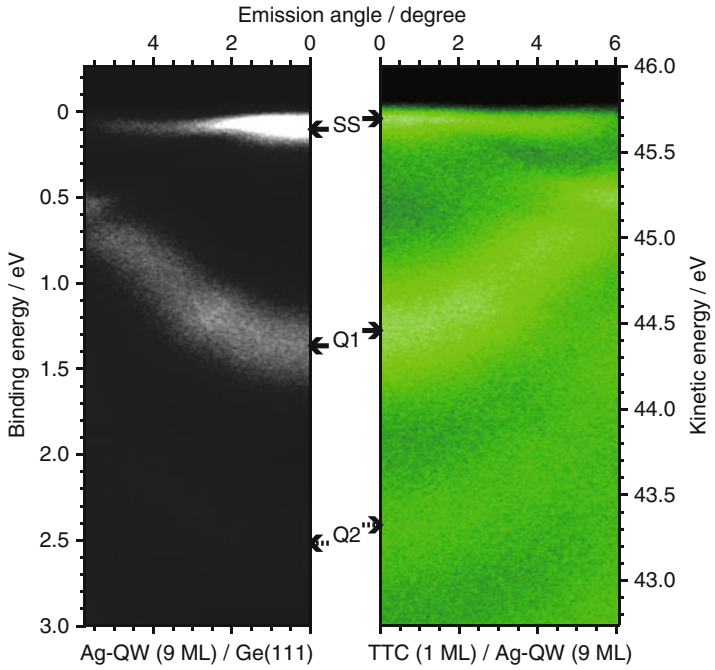


Fig. 10.14 ARPES spectra of the pristine (*left*) and 1 ML TTC-covered (*right*) Ag-QW (9 ML). The vertical axes are common for both spectra, where the binding energy and corresponding photoelectron kinetic energy are displayed in the left and right scales, respectively

As a more quantitative treatment, the change of the boundary condition induced by the physisorbed TTC molecules can be expressed as a modification of Eq. 10.22:

$$2(k_n + \mathrm{d}k)Nt + \varphi_1 + (\varphi_2 + \mathrm{d}\varphi_2) = 2\pi n, \tag{10.23}$$

where t is the atomic layer thickness (0.236 nm for the present Ag thin film) and N is the number of the atomic layer (thus, $Nt \equiv d$). This means that a slight variation of the phase shift $\mathrm{d}\varphi_2$ makes an adjustment of the wave number of the standing wave by $\mathrm{d}k$. Note that this change in the wave number is independent of the quantum number n because the following relation is derived from Eqs. 10.22 and 10.23:

$$\mathrm{d}k_\perp = \frac{\mathrm{d}\varphi_2}{2Nt}. \tag{10.24}$$

(Hereafter we put a subscript symbol $\perp$ onto k just in order to clarify that this is the vertical component of the electron wave vector.) This equation can be further modified into a relationship between $\mathrm{d}\varphi_2$ and the quantized energy shift $\mathrm{d}E$ as

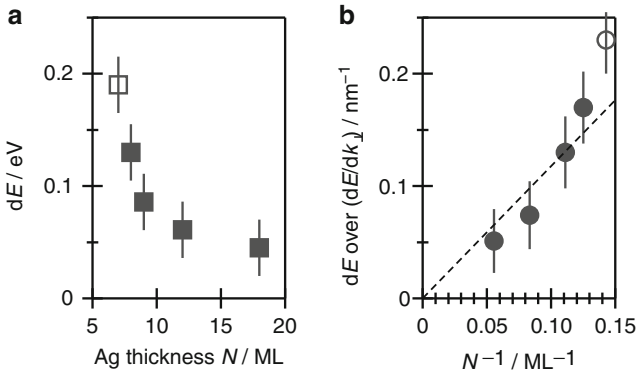


Fig. 10.15 (**a**) The energy shift dE of the bottom of the "Q1" state on coverage of the 1 ML TTC overlayers plotted as a function of the Ag-QW thickness N. (**b**) dE normalized with (dE/d$k_\perp$) plotted as a function of inverse Ag thickness N^{-1}. A least-squares fitting line of these data points except the rightest one (7 ML; an open symbol) by Eq. 10.24 is displayed as a dashed line

$$\mathrm{d}E = \frac{-\mathrm{d}\varphi_2}{2Nt(\mathrm{d}E/\mathrm{d}k_\perp)}. \tag{10.25}$$

Since the surface crystalline lattice of the Ag thin film is identical to the (111) face of the bulk Ag crystal, we can use a known value of the bulk Ag for dE/d$k_\perp$ [85]. Therefore, dφ_2 can be evaluated from a dependence of dE onto the layer number N of the Ag thin film. In practice, dE is decided from the shifting magnitude of the bottom of the uppermost QWR upon coverage by the 1 ML-thick TTC overlayer, which reveals apparent monotonous dependence on the Ag thickness as shown in Fig. 10.15a. In Fig. 10.15b, these values are normalized by dE/d$k_\perp$ and plotted versus the inverse-thickness N^{-1} to derive dφ_2 directly. Except the thinnest one, the data points align on a line fairly well as expected from Eq. 10.25. The reason why the 7 ML result did deviate is currently undefined but might be ascribed to a possible impact of the adsorbates onto the other boundary through the extremely thin QW. In any case, it can be concluded from this plot that the TTC molecules change the phase shift of the electron wave in the metal film by $-0.18(\pm 0.02)\pi$ with respect to the vacuum.

In the case of more reactive molecules, e.g., π-conjugated ones, touching the metal surface, some chemical interaction is likely to bring about at the contact. As representatives of the organic semiconductors, we adopted phthalocyanine family materials (see Fig. 10.4) to explore peculiar metal–organic coupling which possibly brings about on the QWs. Preliminary trial was conducted on a system that zinc-phthalocyanine (ZnPc) molecules were deposited onto a 10 ML-thick Ag thin-film QW [95]. Figure 10.16 displays evolution of the ARPES spectra depending on the ZnPc coverage. Two QWS sub-bands with apparent energy dispersion was resolved in the spectra of the pristine Ag thin film (Fig. 10.16a), whereas angular dependence of the peak position was, if any, negligibly small for the thick

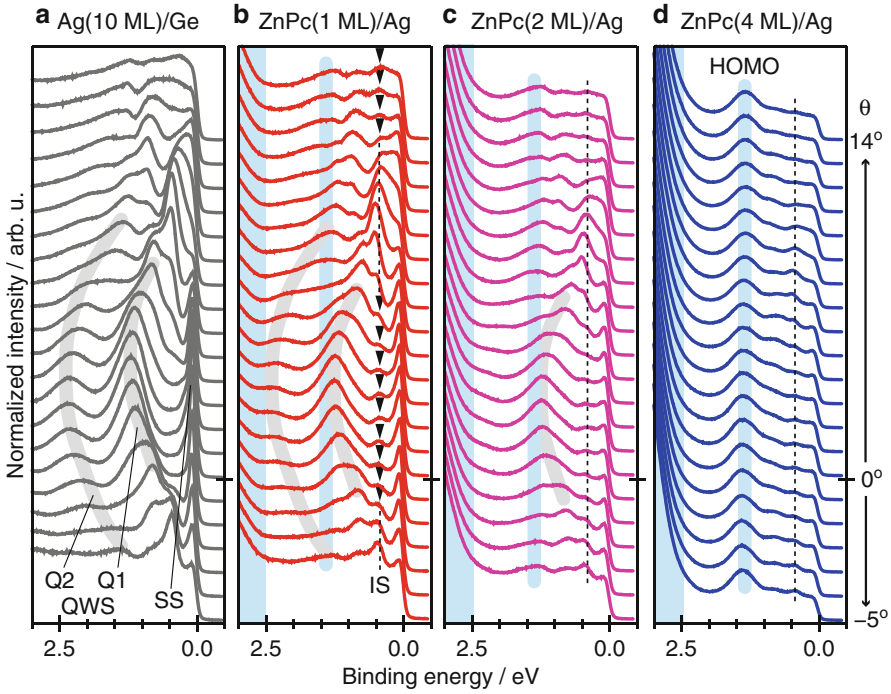


Fig. 10.16 Series of the ARPES spectra of (**a**) a pristine Ag thin film of 10 ML-thick and ZnPc overlayers of (**b**) 1 ML, (**c**) 2 ML, and (**d**) 4 ML thick. Each spectrum is obtained by averaging over the electron takeoff angle of ±0.44°. Thick light gray and light blue lines are guide for eyes indicating the energy positions of the QWSs (Q1 and Q2) and HOMO of ZnPc, respectively. Peak positions of the interface state (IS) are pointed by wedge marks in (**b**), where the same energy position is guided by dashed lines also in (**c**) and (**d**)

ZnPc overlayers (Fig. 10.16d). This flat-band characteristic of the latter represents a localized nature of that electronic state within individual ZnPc molecules. In a glance, the spectra for the intermediate thicknesses seem to be superposition of those two. However, as indicated with downward wedge marks in Fig. 10.16b, an additional peaky structure emerged nearby the Fermi level. This new feature has to be regarded as an interface state (IS) which localizes at the metal–organic contact because this peak was most intense for the 1 ML ZnPc overlayer. The IS peak looked flat as the ZnPc-HOMO, suggesting that it retains a molecular orbital (MO) character rather than a continuum state of metals.

Emergence of the IS itself is nothing special by usage of the QW as a substrate but rather a common phenomenon for the interfaces between phthalocyanines and metals [96–99]. Indeed, it has been reported that ZnPc yields an IS on the bulk Ag surfaces [99]. Nevertheless, there is a noteworthy discrepancy in the energy position of the IS for the present ZnPc–QW interface with respect to its bulk counterpart; it is located at $E_b = 0.45$ eV for the present ZnPc on the Ag thin-film contact, whereas the reported energy position of the IS is $E_b \sim 0.3$ eV for the ZnPc/Ag(110) system.

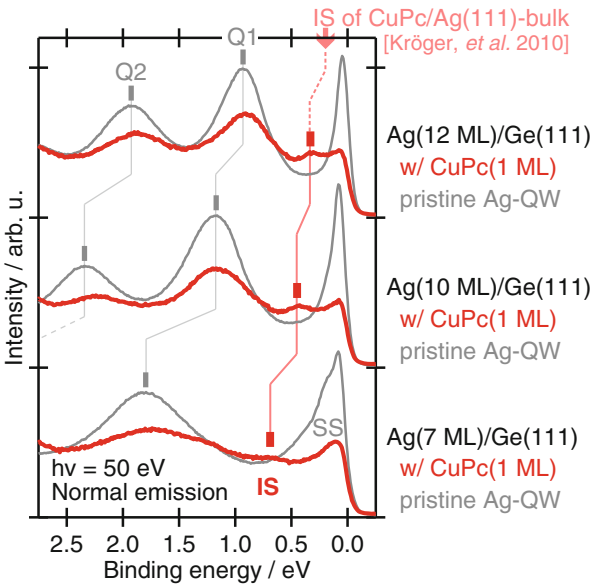


Fig. 10.17 Normal emission PES spectra of pristine Ag thin films (*gray*) and 1 ML-thick CuPc overlayers (*red*) of various QW thicknesses. The energy position of the IS for each Ag thickness is marked with a thick red line, while that formed onto the bulk Ag(111) substrate, which taken from a literature (Krörger, et al. 2010), is also indicated at the top

In fact, modification of the IS energy through the quantum size effect (QSE) was evinced for copper-phthalocyanine (CuPc), a one-electron-loss "brother" of ZnPc, attached onto the Ag thin films of various thicknesses [100]. Figure 10.17 shows the normal emission PES spectra of the pristine Ag thin films and 1 ML CuPc overlayers of various well widths. This clearly manifests that the energy position of the IS moved toward the high binding energy side as the thickness of the Ag-QW shrank. Also it is noteworthy that the reported IS position of the bulk counterpart of this system, CuPc/Ag(111), is further closer to the Fermi level ($E_b \sim 0.2$ eV [98]) than the case of the thickest QW (12 ML) of the present series. An intriguing notion that one can regulate the metal–organic interaction by means of QSE is accordingly evolved from the present results.

The origin of this IS has to be attributed into hybridization of the electronic states of the metal thin film with a *certain* MO, presumably frontier or adjacent-frontier orbitals. The orbital characters of such MOs of CuPc and ZnPc can roughly be categorized into two types: *d*-states of the center metal cation or π-orbitals distributing mainly on the surrounding ligand part. For the sake of discriminating these two possibilities, we replaced the molecule into hydrogenated phthalocyanine (H_2Pc) which has no center metal therefore no *d*-state. As shown in Fig. 10.18a, neither the intensity nor energy position of the IS revealed apparent change by switching or removing the center metal. This strongly suggests that the *d*-state of the metal species makes no contribution onto the IS. Meanwhile, coupling of the molecular π-orbital with the substrate can be weakened by *spatially* separating these two. Switching the adsorbate molecule from H_2Pc into its tetra-tertiary-butyl substituent (TTB-H_2Pc), for which the four bulky side groups at each corner of the

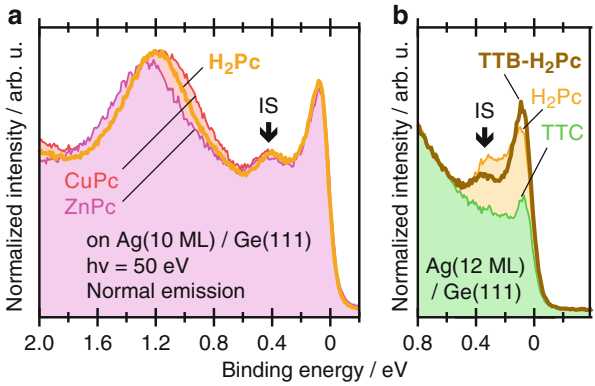


Fig. 10.18 (**a**) Normal emission PES spectra of approximately 1 ML-thick overlayers of ZnPc (*purple*), CuPc (*red*), and H_2Pc (*orange*) covering over the 10 ML-thick Ag thin film. (**b**) Normal emission PES spectra of approximately 1ML-thick overlayers of TTC (*green*), H_2Pc (*orange*), and TTB-H_2Pc (*brown*) covering over the 12 ML-thick Ag thin film

molecular frame physically lift the π-orbitals up from the Ag surface, significantly reduced the IS intensity as shown in Fig. 10.18b. Furthermore, we recall the readers to an absence (or at least negligibility if any) of the IS for the aforementioned TTC/Ag-QW systems. As a consequence, it is concluded that the molecular π-orbitals do participate into this peculiar IS.

As described above, for the present Ag thin films formed onto the Ge substrate, the QW-derived sub-bands cross the valence band edge of Ge. As seen in Fig. 10.12, the sub-bands split upward and downward at these intersections, and the DOS exhibits its local maxima at these singularity points. It is interesting to note that the energy position of the IS shows well accordance to the uppermost singularity point. Actually, Ag thin films formed onto Au(111), where no such DOS singularity occurs but only QWSs are generated within an electron "pocket" around the Γ point of the substrate, did not yield any clear IS even on coverage of the CuPc overlayer [100]. These results imply that not only the topmost interface but also the buried one between the Ag thin film and substrate, which is the bottom boundary condition (φ_1), can impact the interaction between the metal nanostructures and organic molecules.

As discussed above, it has been unveiled that a chemical interaction between π-conjugated molecules and nanometer-thick metal thin films can be regulated by the quantum size effect. Conversely, the quantization energy in metal thin films is also influenced by contact with organic molecules; for instance, as seen in Fig. 10.17, coverage by CuPc also shifts the QWS energy positions. Besides the aforementioned case of TTC where the overlayer can be simply regarded as a dielectric medium to modulate the phase shift at the top surface of the QWs [92], shifting tendencies of the QWSs induced by the present cases of phthalocyanines or other π-conjugated molecules have to be more complex because hybridization of the molecular orbitals into the QWSs interactively impacts the quantization conditions. It is currently left as an open question to build up a *modified* quantization rule under such metal–organic chemical interactions. Systematic accumulation of experimental insights with wide variety of molecules

as well as adequate theoretical formulation is strongly anticipated toward a breakthrough of this novel nano-organic interaction into next-generation electronic devices.

6 Conclusions and Future Perspective

In this article, we have provided an overview of recent achievements in exploring the valence electronic structures of organic semiconductors by means of experimental techniques based on photoemission. While a longtime problem caused by sample charging impedes standard ways to access the electronic states of organic solids as poor electric conductors in general, PYS and laser-assisted PES allow one to directly measure the valence band of the organic materials even in their bulk states. The valence band dispersion of several hundred meV width was mapped out successfully on the single crystal of a molecular semiconducting material, rubrene, by means of ARPES as a result. Furthermore, ARPES is useful technique to characterize the electronic properties of straight relevance to transport phenomena on nanomaterials also. As an example application, novel interacting systems consisting of nanometer-thick metal film "quantum wells" and organic molecules were investigated by ARPES, which led to the discovery of a peculiar nano-organic coupling.

Establishment of the experimental methodologies to demonstrate the electronic structures of the bulk organic single crystal samples will accelerate the research progress toward achievement of generalized understanding about the transport nature in the organic semiconductor solids. One remaining subject of a keen demand is discrimination of the intrinsic transport nature separately from any extrinsic factors. Since the organic semiconductor molecules condense themselves into solids by the weak intermolecular van der Waals (vdW) bonding, the charge carriers typically exhibit localizing tendencies within a single molecule, and thus, in comparison to the case of the conventional covalent solids, intramolecular vibration or lattice phonon *intrinsically* impacts the intermolecular charge transfer. However, there is a well-known drawback of ordinary organic semiconductors of their insufficient purity; the organic materials as the sources of the electronic devices are ordinarily not purer than the three-nine grade, while the purity of the conventional semiconductors has normally reached the seven or eight order of magnitude higher level. Such uncontrolled impurities make serious perturbations to overwhelm the intrinsic properties of the materials. Efforts to pursuit ultra-purification of the organic semiconductors up to the seven-nine grade are now unveiling the unique characteristics of their own [101]. As an extension of this direction, comprehensive understanding describing the transport mechanisms, in which all the intrinsic phenomena are taken into account, can be achieved through temperature-dependent ARPES on ultra-purified organic single crystals. In this context, accurate demonstration of "narrow" bands in common organic semiconductors is also an important task [102]. The aforementioned example materials that exhibited fairly wide band widths of several hundred meV are rather exceptional cases. The band width of most organic semiconductors is expected to be at most a few 10 meV as a

representative of weakly coupling nature of the vdW solids. In order to approach the fundamental insight into the charge carrier behaviors in the practical organic electronic devices, it is highly anticipated to accumulate careful experiments on such ordinary narrowband structures and their evolution depending on the temperature by means of the state-of-the-art ARPES apparatuses.

In another aspect, the advanced ARPES technique applicable to the organic bulk single crystal samples opens a new possibility to cut into interface characterization through the mature "surface science" paradigm. As the practical OLEDs have been realized just by the invention of the donor–acceptor bilayer structures, functionalities of the organic electronic devices are yielded from their embedded interfaces. Here in the case of the organic devices, the substance of the interfaces is actually abrupt bimolecular contacts, which is strikingly in contrast to the conventional inorganic p-n heterojunctions where "donor" and "acceptor" regions face each other across a neutral region of numerous atomic layers thick. Whereas the essential electronic processes are occurring at individual molecular contacts, the practical interfaces formed onto polycrystalline or amorphous organic thin films are not homogeneous at all in a macroscopic viewpoint. The surface science approach on a stage of the organic single crystal surfaces will allow one to access the properties of a specific molecular contact through a well-ordered and uniform interface. We have commenced this course of research at a model interface between the rubrene single crystal and an overlayer of a dielectric molecule to figure out the valence band structure of the channel region of an organic field-effect transistor [103]. Photoemission characterization of well-ordered donor–acceptor contacts is now being undertaken.

Throughout this article, we have taken up the valence band structures only. This does never mean that the conduction bands of the organic semiconductors are unworthy of discussion. The electron conduction behaviors in the conduction bands are as important as the hole cases. In principle, such unoccupied states can be probed by inverse photoelectron spectroscopy (IPES) which utilizes the reverse process of the external photoemission event; speak plainly, light emission resulting from de-excitation of electrons injected into the specimen from its exterior. An utmost difficulty in applying this technique to organic samples is caused by another weak point of the organic materials: fragility against the *hot* electrons. Actually, even for the *forward* PES measurements, reduction of the excitation photon flux at the sacrifice of the signal intensity is often required in order to avoid the radiation damage of the organic samples. The situation is much more severe for the IPES measurements due to an extremely low quantum efficiency of the light emission. Recently, a technical breakthrough against this difficulty was innovated by Yoshida [104]. He adopted considerably low-energy (<5 eV) electrons as the excitation source and found out that damage-less IPES measurements are possible even for half-a-day continuous electron beam irradiation as high as 1 μA, which is utterly impossible by the conventional IPES setup. This may be a big leap toward realization of the conduction band mapping of the crystalline organic semiconductors by means of angle-resolved IPES in future, though further technical upgrading is requisite.

To close this chapter, we make a brief comment on the nano-organic systems. As introduced above, shrinkage of the metal substrate into the nanometer scale leads to novel electronic hybridization with organic molecules in contact through the quantum size effect. This suggests that the nanotechnology may potentially renovate the architectures of future organic electronics. In the reverse direction, organic molecules can provide additional functionalities onto nanomaterials. One remarkable example was reported by Noguchi and co-workers where the optical response of an organic dye molecule switches the mesoscopic conduction behavior of a metal nanoparticle single electron transistor [105]. The accurate physics behind these novel phenomena exhibited in the nano-organic hybrid systems is still unestablished. The (AR)PES has been and will keep being an essential tool to challenge these mysteries of these exotic electronic properties.

7 Acknowledgments

The authors would like to thank Prof. Nobuo Ueno, Prof. Satoshi Kera, Dr. Yutaka Noguchi, and Dr. Kaveenga Rasika Koswattage of Chiba University (CU), Prof. Steffen Duhm of Soochow University, Dr. Takeo Minari and Dr. Kazuhito Tsukagoshi of the National Institute for Materials Science, Prof. Kazuhiko Mase of the High Energy Accelerator Research Organization, Dr. Tun-Wen Pi of the National Synchrotron Radiation Research Center, and Prof. Shu-Jung Tang of the National Tsing Hua University (NTHU) for a fruitful collaboration. We also appreciate all graduate students of Prof. Tang's group (NTHU) as well as of our group (CU) for their helpful participation to these works. YN thank Ms. Kana Nakayama for providing the diamond sample and her critical reading of this manuscript. Financial support from the Grant-in-Aid for Young Scientists (B) [23750209] from the Japan Society for the Promotion of Science (JSPS), TEPCO Memorial Foundation, the Yazaki Memorial Foundation for Science and Technology, the Sasagawa Scientific Research Grant of the Japan Science Society, Summer Visiting Program of Interchange Association Japan, the Izumi Science and Technology Foundation, the JSPS-FIRST program initiated by the Council for Science and Technology Policy through Kyushu University, and the G-COE Program (Advanced School for Organic Electronics; G-3) of CU is gratefully acknowledged.

References

1. Pope M, Swenberg CE (eds) (1999) Electronic processes in organic crystals and polymers, 2nd edn. Oxford University Press, New York
2. Inokuchi H (2006) The discovery of organic semiconductors. Its light and shadow. Org Electron 7(2):62–76
3. Eley DD (1948) Phthalocyanines as semiconductors. Nature 162(4125):819–819
4. Vartanyan A (1948) Semiconductor properties of organic dyes. 1. Phthalocyanines. Zhurnal Fizicheskoi Khimii 22(7):769–782

5. Akamatu H, Inokuchi H (1950) On the electrical conductivity of violanthrone, iso-violanthrone, and pyranthrone. J Chem Phys 18(6):810–811
6. Akamatu H, Inokuchi H (1952) Photoconductivity of violanthrone. J Chem Phys 20(9):1481–1482
7. Inokuchi H (1954) Photoconductivity of the condensed polynuclear aromatic compounds. Bull Chem Soc Jpn 27(I):22–27
8. Kudo K, Yamashina M, Moriizumi T (1984) Field effect measurement of organic dye films. Jpn J Appl Phys 23(1):130–130
9. Tang C (1986) Two-layer organic photovoltaic cell. Appl Phys Lett 48(2):183–185
10. Tang C, VanSlyke S (1987) Organic electroluminescent diodes. Appl Phys Lett 51(12):913–915
11. Hiramoto M, Fujiwara H, Yokoyama M (1991) Three-layered organic solar cell with a photoactive interlayer of codeposited pigments. Appl Phys Lett 58(10):1062–1064
12. Halls JJM, Walsh CA, Greenham NC, Marseglia EA, Friend RH, Moratti SC, Holmes AB (1995) Efficient photodiodes from interpenetrating polymer networks. Nature 376:498–500
13. Hüfner S (2003) Photoelectron spectroscopy, 3rd edn. Springer, Berlin
14. Grobman WD (1978) Angle-resolved photoemission from molecules in the independent-atomic-center approximation. Phys Rev B 17(12):4573–4585
15. Ueno N, Kitamura A, Okudaira KK, Miyamae T, Harada Y, Hasegawa S, Ishii H, Inokuchi H, Fujikawa T, Miyazaki T, Seki K (1997) Angle-resolved ultraviolet photoelectron spectroscopy of thin films of bis (1,2,5-thiadiazolo)-p-quinobis(1,3-dithiole) on the MoS2 surface. J Chem Phys 107(6):2079–2089
16. Nagamatsu S, Kera S, Okudaira K, Fujikawa T, Ueno N (2005) Multiple-scattering approach to angle-resolved ultraviolet photoelectron spectroscopy of large molecules. e-J Surf Sci Nanotechnol 3:461–465
17. Seah MP, Dench WA (1979) Quantitative electron spectroscopy of surfaces: a standard data base for electron inelastic mean free paths in solids. Surf Interface Anal 1(1):2
18. Nakayama Y, Kondoh H, Ohta T (2004) Structure-dependent mixed valence of Sm on Cu (111) studied by XPS and STM. Surf Sci 552(1–3):53–62
19. Yoshida H, Sato N (2012) A precise analysis of the core-level energy difference between the surface and bulk region of organic semiconductor thin films. J Phys Chem C 116(18):10033–10038
20. Yoshida H, Ito E, Hara M, Sato N (2012) Core level energy differences between the surface and bulk of organic semiconductor films: the effect of electrostatic polarization energy. Synth Met 161(23–24):2549–2553
21. Nakayama Y, Morii K, Suzuki Y, Machida H, Kera S, Ueno N, Kitagawa H, Noguchi Y, Ishii H (2009) Origins of improved hole-injection efficiency by the deposition of MoO_3 on the polymeric semiconductor poly(dioctylfluorene-alt -benzothiadiazole). Adv Funct Mater 19(23):3746–3752
22. Cazaux J (1999) Mechanisms of charging in electron spectroscopy. J Electron Spectrosc Relat Phenomena 105(2–3):155–185
23. Ueno N, Kera S (2008) Electron spectroscopy of functional organic thin films: deep insights into valence electronic structure in relation to charge transport property. Prog Surf Sci 83(10–12):490–557
24. Kazda C (1925) The photo-electric threshold for mercury. Phys Rev 26(5):643–654
25. Morris L (1931) Certain photoelectric properties of gold. Phys Rev 37(10):1263–1268
26. Fowler R (1931) The analysis of photoelectric sensitivity curves for clean metals at various temperatures. Phys Rev 38(1):45–56
27. Sebenne C, Bolmont D, Guichar G, Balkanski M (1975) Surface states from photoemission threshold measurements on a clean, cleaved, Si (111) surface. Phys Rev B 12(8):3280–3285
28. Miyazaki S, Maruyama T, Kohno A, Hirose M (1999) Photoelectron yield spectroscopy of electronic states at ultrathin SiO_2/Si interfaces. Microelectron Eng 48:63–66

29. Szuber J (2000) New procedure for determination of the interface Fermi level position for atomic hydrogen cleaned GaAs(100) surface using photoemission. Vacuum 57(2):209–217
30. Watanabe I (1994) Optical oxidation potential: a new measure for reducing power. Anal Sci 10:229–239
31. Inumaru K, Okubo Y, Fujii T, Yamanaka S (2000) Effects of organic vapour adsorption on the photoelectron emission from Au thin films in atmospheric air. Phys Chem Chem Phys 2:3681–3685
32. Honda M, Kanai K, Komatsu K, Ouchi Y, Ishii H, Seki K (2007) Atmospheric effect of air, N_2, O_2, and water vapor on the ionization energy of titanyl phthalocyanine thin film studied by photoemission yield spectroscopy. J Appl Phys 102(10):103704
33. Kane EO (1962) Theory of photoelectric emission from semiconductors. Phys Rev 127(1):131–141
34. Kochi M, Harada Y, Hirooka T, Inokuchi H (1970) Photoemission from organic crystal in vacuum ultraviolet region. IV. Bull Chem Soc Jpn 43(9):2690–2702
35. Nakayama Y, Machida S, Tsunami D, Kimura Y, Niwano M, Noguchi Y, Ishii H (2008) Photoemission measurement of extremely insulating materials: capacitive photocurrent detection in photoelectron yield spectroscopy. Appl Phys Lett 92(15):153306
36. Himpsel F, Knapp J, VanVechten J, Eastman D (1979) Quantum photoyield of diamond (111) – a stable negative-affinity emitter. Phys Rev B 20(2):624–627
37. Ley L, Ristein J, Meier F, Riedel M, Strobel P (2006) Surface conductivity of the diamond: a novel transfer doping mechanism. Phys B Condens Matter 376–377:262–267
38. Sato N, Inokuchi H, Schmid B, Karl N (1985) Ultraviolet photoemission spectra of organic single crystals. J Chem Phys 83(11):5413–5419
39. Vollmer A, Jurchescu OD, Arfaoui I, Salzmann I, Palstra TTM, Rudolf P, Niemax J, Pflaum J, Rabe JP, Koch N (2005) The effect of oxygen exposure on pentacene electronic structure. Eur Phys J E 17(3):339–343
40. Nakayama Y, Machida S, Duhm S, Xin Q, Kera S, Ishii H, Ueno N (2011) Shed laser light on the valence band structures of organic semiconductor single crystals. J Jap Laser Process Soc 18(3):202–206 [in Japanese]
41. Sai N, Tiago M, Chelikowsky J, Reboredo F (2008) Optical spectra and exchange-correlation effects in molecular crystals. Phys Rev B 77(16):161306
42. Machida S, Nakayama Y, Duhm S, Xin Q, Funakoshi A, Ogawa N, Kera S, Ueno N, Ishii H (2010) Highest-occupied-molecular-orbital band dispersion of rubrene single crystals as observed by angle-resolved ultraviolet photoelectron spectroscopy. Phys Rev Lett 104(15):156401
43. Nakayama Y, Uragami Y, Machida S, Koswattage KR, Yoshimura D, Setoyama H, Okajima T, Mase K, Ishii H (2012) Full picture of the valence band structure of rubrene single crystals probed by angle-resolved and excitation energy dependent photoelectron spectroscopy. Appl Phys Expr 5(11):111601
44. Vollmer A, Ovsyannikov R, Gorgoi M, Krause S, Oehzelt M, Lindblad A, Mårtensson N, Svensson S, Karlsson P, Lundvuist M, Schmeiler T, Pflaum J, Koch N (2012) Two dimensional band structure mapping of organic single crystals using the new generation electron energy analyzer ARTOF. J Electron Spectrosc Relat Phenomena 185(3–4): 55–60
45. Xie W, Prabhumirashi PL, Nakayama Y, Mcgarry KA, Geier ML, Uragami Y, Mase K, Douglas CJ, Ishii H, Hersam MC, Frisbie CD (2013) Utilizing carbon nanotube electrodes to improve charge injection and transport in bis(trifluoromethyl)-dimethyl-rubrene ambipolar single crystal transistors. ACS Nano 7(11):10245–10256
46. Nakayama Y, Uragami Y, Yamamoto M, Machida S, Kinjo H, Mase K, Koswattage KR, Ishii H (2014) Determination of the highest occupied molecular orbital energy of pentacene single crystals by ultraviolet photoelectron and photoelectron yield spectroscopies. Jpn J Appl Phys 53(1S):01AD03

47. Xin Q, Duhm S, Bussolotti F, Akaike K, Kubozono Y, Aoki H, Kosugi T, Kera S, Ueno N (2012) Accessing surface brillouin zone and band structure of picene single crystals. Phys Rev Lett 108(22):226401
48. Hasegawa S, Mori T, Imaeda K, Tanaka S, Yamashita Y, Inokuchi H, Fujimoto H, Seki K, Ueno N (1994) Intermolecular energy-band dispersion in oriented thin films of bis(1,2,5-thiadiazolo)-p-quinobis(1,3-dithiole) by angle-resolved photoemission. J Chem Phys 100(9):6969–6974
49. Koch N, Vollmer A, Salzmann I, Nickel B, Weiss H, Rabe J (2006) Evidence for temperature-dependent electron band dispersion in pentacene. Phys Rev Lett 96(15):156803
50. Lin Y-Y, Gundlach DJ, Nelson SF, Jackson TN (1997) Stacked pentacene layer organic thin-film transistors with improved characteristics. IEEE Electron Device Lett 18(12):606–608
51. Kakuta H, Hirahara T, Matsuda I, Nagao T, Hasegawa S, Ueno N, Sakamoto K (2007) Electronic structures of the highest occupied molecular orbital bands of a pentacene ultrathin film. Phys Rev Lett 98(24):247601
52. Hatch R, Huber D, Höchst H (2009) HOMO band structure and anisotropic effective hole mass in thin crystalline pentacene films. Phys Rev B 80(8):081411(R)
53. Hatch RC, Huber DL, Höchst H (2010) Electron–phonon coupling in crystalline pentacene films. Phys Rev Lett 104(4):047601
54. Bouchoms IPM, Schoonveld WA, Vrijmoeth J, Klapwijk TM (1999) Morphology identification of the thin film phases of vacuum evaporated pentacene on SiO2 substrates. Synth Met 104(3):175–178
55. Yoshida H, Sato N (2008) Crystallographic and electronic structures of three different polymorphs of pentacene. Phys Rev B 77(23):235205
56. Ohtomo M, Suzuki T, Shimada T, Hasegawa T (2009) Band dispersion of quasi-single crystal thin film phase pentacene monolayer studied by angle-resolved photoelectron spectroscopy. Appl Phys Lett 95(12):123308
57. Shimada T, Suzuki T, Ohtomo M, Hasegawa T (2009) Epitaxial growth and photoelectron spectroscopy of pentacene. Hyomen Kagaku (J Surf Sci Soc Jpn) 30(1):7–10 [in Japanese]
58. Puschnig P, Berkebile S, Fleming AJ, Koller G, Emtsev K, Seyller T, Riley JD, Ambrosch-Draxl C, Netzer FP, Ramsey MG (2009) Reconstruction of molecular orbital densities from photoemission data. Science 326(5953):702–706
59. Ziroff J, Forster F, Schöll A, Puschnig P, Reinert F (2010) Hybridization of organic molecular orbitals with substrate states at interfaces: PTCDA on silver. Phys Rev Lett 104(23):233004
60. Sundar VC, Zaumseil J, Podzorov V, Menard E, Willett RL, Someya T, Gershenson ME, Rogers JA (2004) Elastomeric transistor stamps: reversible probing of charge transport in organic crystals. Science 303(5664):1644–1646
61. Takeya J, Yamagishi M, Tominari Y, Hirahara R, Nakazawa Y, Nishikawa T, Kawase T, Shimoda T, Ogawa S (2007) Very high-mobility organic single-crystal transistors with in-crystal conduction channels. Appl Phys Lett 90(10):102120
62. Käfer D, Ruppel L, Witte G, Wöll C (2005) Role of molecular conformations in rubrene thin film growth. Phys Rev Lett 95(16):166602
63. Nakayama Y, Machida S, Minari T, Tsukagoshi K, Noguchi Y, Ishii H (2008) Direct observation of the electronic states of single crystalline rubrene under ambient condition by photoelectron yield spectroscopy. Appl Phys Lett 93(17):173305
64. Sato N, Seki K, Inokuchi H (1981) Polarization energies of organic solids determined by ultraviolet photoelectron spectroscopy. J Chem Soc Faraday Trans 2(77):1621–1633
65. Wang L, Chen S, Liu L, Qi D, Gao X, Wee ATS (2007) Thickness-dependent energy level alignment of rubrene adsorbed on Au(111). Appl Phys Lett 90(13):132121
66. Fukagawa H, Yamane H, Kataoka T, Kera S, Nakamura M, Kudo K, Ueno N (2006) Origin of the highest occupied band position in pentacene films from ultraviolet photoelectron spectroscopy: hole stabilization versus band dispersion. Phys Rev B 73(24):245310

67. Duhm S, Heimel G, Salzmann I, Glowatzki H, Johnson RL, Vollmer A, Rabe JP, Koch N (2008) Orientation-dependent ionization energies and interface dipoles in ordered molecular assemblies. Nat Mater 7(4):326–332
68. Duhm S, Xin Q, Hosoumi S, Fukagawa H, Sato K, Ueno N, Kera S (2012) Charge reorganization energy and small polaron binding energy of rubrene thin films by ultraviolet photoelectron spectroscopy. Adv Mater 24(7):901–905
69. Da Silva Filho DA, Kim E-G, Brédas J-L (2005) Transport properties in the rubrene crystal: electronic coupling and vibrational reorganization energy. Adv Mater 17(8):1072–1076
70. Li ZQ, Podzorov V, Sai N, Martin MC, Gershenson ME, Di Ventra M, Basov DN (2007) Light quasiparticles dominate electronic transport in molecular crystal field-effect transistors. Phys Rev Lett 99(1):016403
71. Coropceanu V, Cornil J, da Silva Filho DA, Olivier Y, Silbey R, Brédas J-L (2007) Charge transport in organic semiconductors. Chem Rev 107(4):926–952
72. Troisi A (2007) Prediction of the absolute charge mobility of molecular semiconductors: the case of rubrene. Adv Mater 19(15):2000–2004
73. Girlando A, Grisanti L, Masino M, Bilotti I, Brillante A, Della Valle R, Venuti E (2010) Peierls and holstein carrier-phonon coupling in crystalline rubrene. Phys Rev B 82(3):035208
74. Kera S, Yamane H, Ueno N (2009) First-principles measurements of charge mobility in organic semiconductors: valence hole–vibration coupling in organic ultrathin films. Prog Surf Sci 84(5–6):135–154
75. Hulea IN, Fratini S, Xie H, Mulder CL, Iossad NN, Rastelli G, Ciuchi S, Morpurgo AF (2006) Tunable Fröhlich polarons in organic single-crystal transistors. Nat Mater 5(12):982–986
76. Hsieh D, Qian D, Wray L, Xia Y, Hor YS, Cava RJ, Hasan MZ (2008) A topological Dirac insulator in a quantum spin hall phase. Nature 452(7190):970–974
77. Fleurence A, Friedlein R, Ozaki T, Kawai H, Wang Y, Yamada-Takamura Y (2012) Experimental evidence for epitaxial silicene on diboride thin films. Phys Rev Lett 108(24):245501
78. Chen P, Wu X, Sun X, Lin J, Ji W, Tan K (1999) Electronic structure and optical limiting behavior of carbon nanotubes. Phys Rev Lett 82(12):2548–2551
79. Ago H, Kugler T, Cacialli F, Salaneck WR, Shaffer MSP, Windle AH, Friend RH (1999) Work functions and surface functional groups of multiwall carbon nanotubes. J Phys Chem B 103(38):8116–8121
80. Himpsel FJ, Altmann KN, Crain JN, Kirakosian A, Lin J-L, Liebsch A, Zhukov VP (2002) Photoelectron spectroscopy of atomic wires. J Electron Spectrosc Relat Phenomena 126(1):89–99
81. Colvin V, Alivisatos A, Tobin J (1991) Valence-band photoemission from a quantum-dot system. Phys Rev Lett 66(21):2786–2789
82. Konchenko A, Nakayama Y, Matsuda I, Hasegawa S, Nakamura Y, Ichikawa M (2006) Quantum confinement observed in Ge nanodots on an oxidized Si surface. Phys Rev B 73(11):113311
83. Nakayama Y, Matsuda I, Hasegawa S, Ichikawa M (2006) Quantum regulation of Ge nanodot state by controlling barrier of the interface layer. Appl Phys Lett 88(25):253102
84. Nakayama Y, Matsuda I, Hasegawa S, Ichikawa M (2008) Growth, quantum confinement and transport mechanisms of Ge nanodot arrays formed on a SiO2 monolayer. e-J Surf Sci Nanotechnol 6(August):191–201
85. Chiang T-C (2000) Photoemission studies of quantum well states in thin films. Surf Sci Rep 39(7):181–235
86. Matsuda I, Tanikawa T, Hasegawa S, Yeom HW, Tono K, Ohta T (2004) Quantum-well states in ultra-thin metal films on semiconductor surfaces. e-J Surf Sci Nanotechnol 2(May):169–177
87. Kim J, Qin S, Yao W, Niu Q, Chou MY, Shih C-K (2010) Quantum size effects on the work function of metallic thin film nanostructures. Proc Natl Acad Sci U S A 107(29): 12761–12765

88. Aballe L, Barinov A, Locatelli A, Heun S, Kiskinova M (2004) Tuning surface reactivity via electron quantum confinement. Phys Rev Lett 93(19):196103
89. Miyata N, Horikoshi K, Hirahara T, Hasegawa S, Wei C, Matsuda I (2008) Electronic transport properties of quantum-well states in ultrathin Pb(111) films. Phys Rev B 78(24):245405
90. Guo Y, Zhang Y-F, Bao X-Y, Han T-Z, Tang Z, Zhang L-X, Zhu W-G, Wang EG, Niu Q, Qiu ZQ, Jia J-F, Zhao Z-X, Xue Q-K (2004) Superconductivity modulated by quantum size effects. Science 306(5703):1915–1917
91. Tang S-J, Lee Y-R, Chang S-L, Miller T, Chiang T-C (2006) Umklapp-mediated quantization of electronic states in Ag films on Ge(111). Phys Rev Lett 96(21):216803
92. Lin M-K, Nakayama Y, Wang C-Y, Hsu J-C, Pan C-H, Machida S, Pi T-W, Ishii H, Tang S-J (2012) Interfacial properties at the organic-metal interface probed using quantum well states. Phys Rev B 86(15):155453
93. Yoshimura D, Ishii H, Ouchi Y, Ito E, Miyamae T, Hasegawa S, Okudaira KK, Ueno N, Seki K (1999) Angle-resolved ultraviolet photoelectron spectroscopy and theoretical simulation of a well-ordered ultrathin film of tetratetracontane (n-$C_{44}H_{90}$) on Cu(100). Phys Rev B 60(12):9046–9060
94. Forster F, Hüfner S, Reinert F (2004) Rare gases on noble-metal surfaces: an angle-resolved photoemission study with high energy resolution. J Phys Chem B 108(38):14692–14698
95. Nakayama Y, Lin M-K, Wang C-Y, Pi T-W, Ishii H, Tang S-J (2012) Interface electronic structure of zinc-phthalocyanine on the silver thin-film quantum-well. e-J Surf Sci Nanotechnol 10:149–152
96. Häming M, Scheuermann C, Schöll A, Reinert F, Umbach E (2009) Coverage dependent organic–metal interaction studied by high-resolution core level spectroscopy: SnPc (sub) monolayers on Ag(111). J Electron Spectrosc Relat Phenomena 174(1–3):59–64
97. Gargiani P, Angelucci M, Mariani C, Betti MG (2010) Metal-phthalocyanine chains on the Au(110) surface: interaction states versus d-metal states occupancy. Phys Rev B 81(8):085412
98. Kröger I, Stadtmüller B, Stadler C, Ziroff J, Kochler M, Stahl A, Pollinger F, Lee T-L, Zegenhagen J, Reinert F, Kumpf C (2010) Submonolayer growth of copper-phthalocyanine on Ag(111). New J Phys 12(8):083038
99. Giovanelli L, Amsalem P, Angot T, Petaccia L, Gorovikov S, Porte L, Goldoni A, Themlin J-M (2010) Valence band photoemission from the Zn-phthalocyanine/Ag(110) interface: charge transfer and scattering of substrate photoelectrons. Phys Rev B 82(12):125431
100. Lin M-K, Nakayama Y, Chen C-H, Wang C-Y, Jeng H-T, Pi T-W, Ishii H, Tang S-J (2013) Tuning gap states at organic-metal interfaces via quantum size effects. Nat Commun 4:2925
101. Ishiyama N, Kubo M, Kaji T, Hiramoto M (2013) Tandem organic solar cells formed in co-deposited films by doping. Org Electron 14(7):1793–1796
102. Yamane H, Kosugi N (2013) Substituent-induced intermolecular interaction in organic crystals revealed by precise band-dispersion measurements. Phys Rev Lett 111(8):086602
103. Nakayama Y, Niederhausen J, Machida S, Uragami Y, Kinjo H, Vollmer A, Rabe JP, Koch N, Ishii H (2013) Valence band structure of rubrene single crystals in contact with an organic gate dielectric. Org Electron 14(7):1825–1832
104. Yoshida H (2012) Near-ultraviolet inverse photoemission spectroscopy using ultra-low energy electrons. Chem Phys Lett 539–540:180–185
105. Yamamoto M, Terui T, Ueda R, Imazu K, Tamada K, Sakano T, Matsuda K, Ishii H, Noguchi Y (2012) Photoinduced conductance switching in a dye-doped gold nanoparticle transistor. Appl Phys Lett 101(2):023103

Band Bending at Metal-Semiconductor Interfaces, Ferroelectric Surfaces and Metal-Ferroelectric Interfaces Investigated by Photoelectron Spectroscopy

11

Nicoleta Georgiana Apostol and Cristian-Mihail Teodorescu

Contents

1 Definition of the Topic 406
2 Overview 406
3 Introduction 407
3.1 Band Bending in Solids: Metal–Semiconductors and Ferroelectric Surfaces 407
4 Experimental and Instrumental Methodology 410
4.1 X-Ray Photoelectron Spectroscopy Method: Basic Aspects and Data Analysis 410
4.2 Preparation Methods 415
5 Key Research Findings 417
5.1 X-Ray Photoelectron Spectroscopy in Analysis of Band Bendings: A Short Review 417
5.2 Theoretical Aspects 424
5.3 Experimental Examples 434
6 Conclusions and Future Perspective 454
References 455

Abstract

X-ray photoelectron spectroscopy is nowadays a well-established technique for the determination of chemical compounds with surface sensitivity. To the atomic and chemical specificity and surface sensitivity, recently a new functionality was added to this technique, the ability to identify energy band bendings near surfaces and interfaces. Two standard cases are represented by Schottky metal–semiconductor structures and by ferroelectric surfaces

N.G. Apostol • C.-M. Teodorescu (✉)
National Institute of Materials Physics, Magurele-Ilfov, Romania
e-mail: nicoleta.apostol@infim.ro; teodorescu@infim.ro

© Springer-Verlag Berlin Heidelberg 2015

C.S.S.R. Kumar (ed.), *Surface Science Tools for Nanomaterials Characterization*,
DOI 10.1007/978-3-662-44551-8_11

exhibiting out-of-plane polarization. The case of metal–ferroelectric interfaces is more difficult to assess, but elements of a suitable theory start to be sketched nowadays and in short time a consistent model is expected to emerge. This chapter analyzes the recent progresses in the derivation of band bendings at surfaces and interfaces by X-ray photoelectron spectroscopy. A critical review of the literature will be presented, together with basic aspects of the theory of band bending. The experimental section will review some quite recent results, going from "standard" cases of Schottky contacts to usual semiconductors and to free ferroelectric surfaces, analyzing also the preferential adsorption of dipole molecules on some ferroelectrics, and ending with metal–ferroelectric cases, where sometimes unexpected phenomena occur, connected to a competition between Schottky barrier formation and loss of ferroelectric out-of-plane polarization by the grounding of the surface due to the deposited metal layer.

1 Definition of the Topic

A survey of the ability of X-ray photoelectron spectroscopy to be used in the determination of band bendings at surfaces and interfaces. A review of the existing literature will be connected with some very basic theoretical aspects of band bendings in semiconductors and with an overview of recent experimental results.

2 Overview

X-ray photoelectron spectroscopy is nowadays a well-established technique for the determination of chemical compounds with surface sensitivity. To the atomic and chemical specificity and surface sensitivity, recently a new functionality was added to this technique, the ability to identify energy band bendings near surfaces and interfaces. Two standard cases are represented by Schottky metal–semiconductor structures and by ferroelectric surfaces exhibiting out-of-plane polarization. The case of metal–ferroelectric interfaces is more difficult to assess, but elements of a suitable theory start to be sketched nowadays and in short time a consistent model is expected to emerge. This chapter analyzes the recent progresses in the derivation of band bendings at surfaces and interfaces by X-ray photoelectron spectroscopy. A critical review of the literature will be presented, together with basic aspects of the theory of band bending. The experimental section will review some quite recent results, going from "standard" cases of Schottky contacts to usual semiconductors and to free ferroelectric surfaces, analyzing also the preferential adsorption of dipole molecules on some ferroelectrics, and ending with metal–ferroelectric cases, where sometimes unexpected phenomena occur, connected to a competition between Schottky barrier formation and loss of ferroelectric out-of-plane polarization by the grounding of the surface due to the deposited metal layer.

3 Introduction

3.1 Band Bending in Solids: Metal–Semiconductors and Ferroelectric Surfaces

Materials generally have different work functions (Φ), i.e., energies required to extract electrons from them. The work function is defined, in a first approximation, as the energy difference between the vacuum level and the Fermi energy. When two materials are contacted such as to form an interface, the Fermi energy of both materials becomes equal, at thermodynamic equilibrium. This is achieved via a charge transfer, namely, electrons are transferred from the material with an initially higher value of the Fermi energy (lower work function) towards the material with higher work function. When two metals are put in contact, this gives rise to the contact (Volta) potential; two semiconductors (e.g., with different dopings) brought in contact form a junction (or a diode); the same happens also when a metal with higher work function is contacted with an n-doped semiconductor with lower work function, and in this case the junction is called also a Schottky diode [1]. It follows that the band bendings occurring at surfaces and interfaces are fundamental phenomena for a wide range of applications, practically for the whole field of nowadays microelectronics.

Figure 11.1 presents the typical energy band dependence on the coordinate perpendicular to the plane of the contact for Schottky diodes. We shall discuss in more details the case when the work function of the metal is lower than that of the semiconductor, $\Phi_M < \Phi_S$, Fig. 11.1a. By achieving the contact between the metal and the semiconductor, electrons are transferred from the metal into the whole semiconductor, yielding to the rising of its Fermi energy. (An entity – atom, molecule, or solid – with bound electrons which receive some excess electrons moves its energy levels at higher energy position, or lower binding energy, because the escape of bound electrons will require less energy than from a neutral state.) The excess electrons injected into the semiconductor accumulate in larger quantity near the interface and, in this area, an electric field oriented from the metal towards the semiconductor is developed to prevent further migration of electrons from the metal (more details about this mechanism will be discussed in Sect. 4). This interface electric field is described also by an energy variation (or *band bending*) towards lower energies. This structure, for electrons, does not present a steep potential barrier, e.g., by applying a negative voltage on the metal to inject further electrons into the semiconductor, progressively the current increases. On contrary, the structure from Fig. 11.1b, realized between a metal and a semiconductor with $\Phi_M < \Phi_S$, presents a well-defined barrier for electrons; if one applies a negative voltage on the metal, one has to exceed an energy value equal to $(\Phi_M - \Phi_S) + (E_C - E_F)$ to ensure convenient electron injection into the semiconductor. This energy value is called the Schottky barrier and is defining the main conduction characteristics $I(V, T)$ of the junction (I = current, V = voltage, T = temperature).

The values of band bendings and the shape of bands near interfaces are usually determined by $I(V, T)$ measurements combined with simulations [2]. However, the

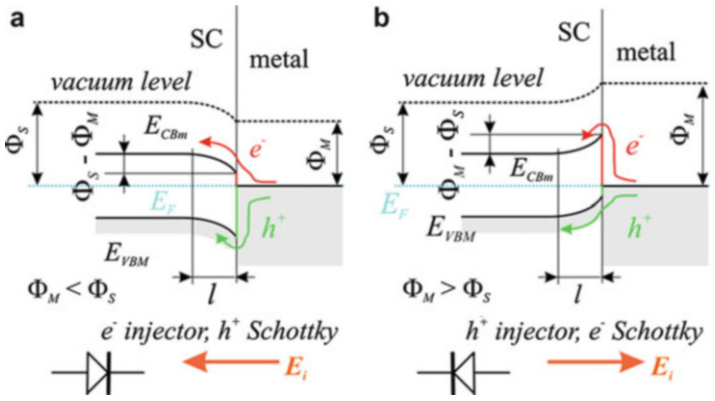


Fig. 11.1 Schematics of band bending occurring at a metal/semiconductor interface. The work function of the metal is lower (**a**) or higher (**b**) than that of the semiconductor. In the first case, the contact is ohmic for electrons and rectifying for holes. In the second case, the contact is rectifying for electrons and ohmic for holes

characterization of a pure Schottky diode will be affected also by the other metal–semiconductor contact needed to ensure the electrical connection. Clearly this second contact must be ohmic, but sometimes at this second interface undesired effects, such as interface ionized (defect) states, thin oxide layers yielding to additional junctions, or adsorbed molecules, will bias the result. It follows immediately that the determination of band bending and Schottky barriers by "noninvasive" methods, other than typical electrical measurements, will be welcome. In the following, we will discuss the ability of X-ray photoelectron or X-ray photoemission spectroscopy (XPS) to achieve this task. The key to understand the way photoemission may be used to investigate band bendings is represented in Fig. 11.2. It is assumed that, within a good approximation, the core levels follow the spatial variation of the valence and conduction bands [3, 4]. Therefore, if the binding energies (BE) of these core levels are determined with sufficient resolution, one may be able to quantify the interface band bending. This is an easy task in two cases: (a) the spatial range of the band bending, l, is much larger than the photoelectron inelastic mean free path, λ (see the next paragraph for more details); (b) the reverse, i.e., $l << \lambda$, but when XPS is able to discriminate clearly, the surface core-level shifts. In the intermediate case, the situation is somehow more complicated, and quite often the band bending effect results in a broadening of the core-level signature [5–8]. However, even in this case an accurate modeling may yield to the band bending dependence near the investigated interfaces.

Band bendings occur also near free semiconductor surfaces, especially when the semiconductor presents ferroelectric properties. Ferroelectrics are another class of materials widely used nowadays, owing to their piezoelectric, pyroelectric, variable capacitance, and ability for nonvolatile data storage [9]. The interesting case in the following is represented by ferroelectrics whose permanent polarization is oriented perpendicular to the sample surface. Let us consider that this polarization vector, $\boldsymbol{P}$,

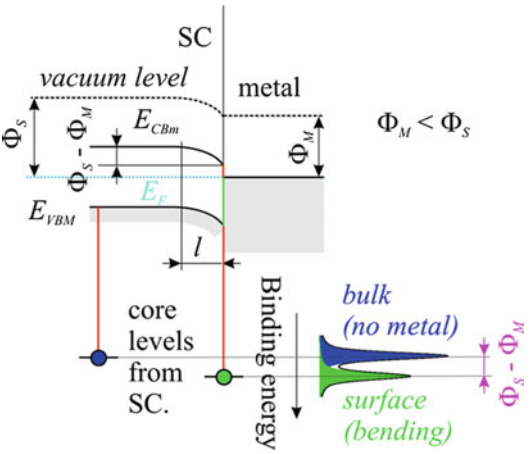


Fig. 11.2 Band bending effect on core-level position. The Fermi energy is constant; therefore, the vacuum level follows the conduction and valence band bending; so does the position of core levels. An increase in the binding energy of a core level near the surface implies band bending downwards, towards lower (negative) energies

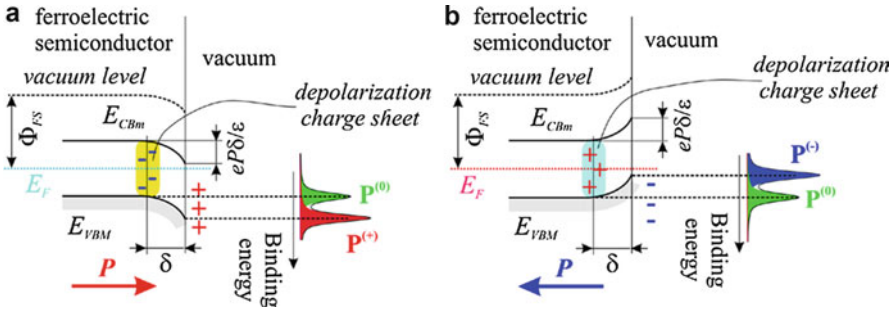


Fig. 11.3 Schematics of band bendings occurring at free, insulating ferroelectric surfaces: (**a**) outward and (**b**) inward static polarization. The bound polarization charges develop the depolarization field, which induces migration of the mobile charges near surface, such as to compensate the electric field inside the sample. The "depolarization charge sheet" is formed by electrons for outward polarized surfaces (**a**) and by holes for inward polarized surfaces (**b**). The figure depicts also the evolution of core levels from surface atoms belonging to these polarized surfaces. Binding energies increase for outward polarized surfaces

is oriented *outwards,* from the ferroelectric towards the vacuum (it is assumed that the right-hand side of the film is free and this will be investigated by photoelectron spectroscopy). This polarization is formed by an assembly of microscopic dipoles, (−) → (+); (−) → (+); (−) → (+)..., such as the net result is that at the surface of the considered ferroelectric layer, there will be uncompensated (+) charge, and at the bottom of the film, there will be uncompensated (−) charge, both of atomic (ionic) origin. These uncompensated fixed charges produce an electric field oriented in opposite direction with respect to ***P***. This is called *depolarization field* and its first effect on the mobile carriers (electrons and holes) will be to push electrons towards the surface with (+) fixed charge and holes towards the opposite direction. This situation is represented in Fig. 11.3a. If the compensation is perfect, namely, if the layer is neutral, the sheets of electrons and holes have a total charge which

compensate the fixed charge, then the electric field in the bulk of the ferroelectric will vanish (no further drift of mobile charges occur) and near the surface the bands will be bended according to Fig. 11.3a. Figure 11.3b presents simply the opposite situation, when the polarization of the ferroelectric is oriented *inwards* (from the vacuum towards the ferroelectric). Figure 11.3 presents also the way these ferroelectric surfaces will be visible by photoelectron spectroscopy.

The situation of metal contacts on ferroelectric is even more complicated. More details on the band bending characterization of ferroelectrics and of metal–ferroelectric systems will be discussed from both theoretical and experimental points of view in this chapter.

The chapter starts with a short description of the experimental and instrumental methods used, particularly for XPS and for sample preparation techniques. Special emphasis will be given to the XPS data analysis, since accurate data analysis is crucial for deriving tiny effects, such as band bendings reflected in sub-eV shifts in the core-level binding energies. Next, the key research findings from recent works will be presented in Sect. 5, starting with a brief overview of recent literature (Sect. 5.1), and then a short presentation of the theoretical aspects connected to band bendings at Schottky contacts and at ferroelectric surfaces will be outlined (Sect. 5.2), and in the following paragraphs several experimental examples will be given, starting from "school cases" of Schottky contacts until the more sophisticated problematic of metal/ferroelectric interfaces, where depolarization, overcompensation, and interplays between ferroelectricity and charge carrier density manifest and may sometimes be investigated quantitatively by XPS. Finally, Sect. 6 presents some conclusions and perspectives of this new functionality of X-ray photoelectron spectroscopy.

4 Experimental and Instrumental Methodology

4.1 X-Ray Photoelectron Spectroscopy Method: Basic Aspects and Data Analysis

X-ray photoelectron spectroscopy (XPS) is nowadays a widely used technique in the characterization of surfaces and interfaces [10]. The main features of this technique, used since four decades, are (i) the ability to derive the chemical compositions through both the ability to detect the signatures of all atomic species (with the exception of hydrogen) and the sensitivity of the chemical states of the constituents via the XPS chemical shifts, well documented in literature and in databases [11, 12], and (ii) the surface sensitivity of this method, which is due to the relatively low value of the inelastic mean free path of the photoelectrons escaping from the sample [10, 13]. The inelastic mean free path (λ) as function on the photoelectron kinetic energy (KE) ranges from ~4–5 Å for KE ~40–60 eV to ~15–20 Å for KE ~1.2–1.5 keV. The photoemitted intensity from a material at a depth z is recorded at the sample surface as attenuated by a factor $\exp(-z/\lambda)$; therefore, ~95 % of the photoemission signal originates from a layer with depth equal to 3λ.

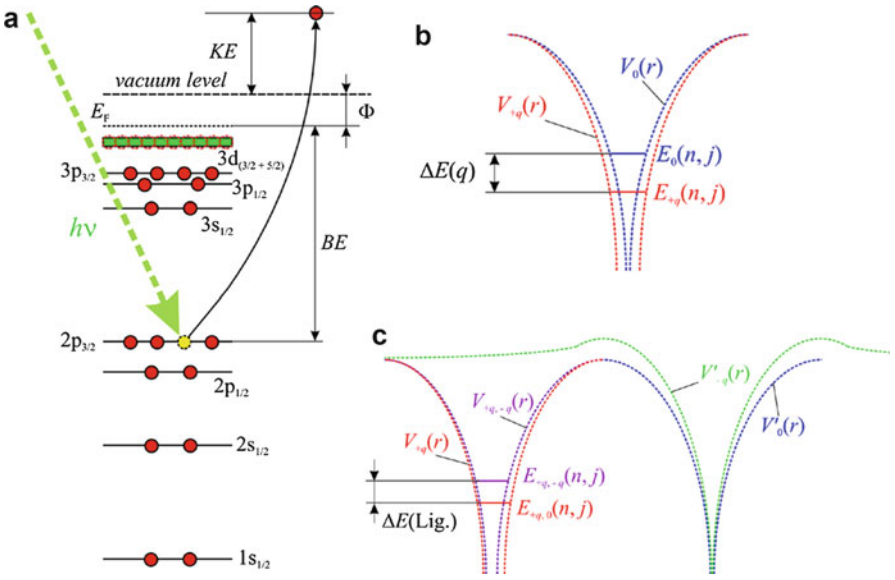


Fig. 11.4 Basics of X-ray photoelectron spectroscopy: (**a**) the inner shell photoemission process, (**b**) potentials and energy difference of core-level states between a neutral atom and a positively charged ion (origin of the binding energy increase), and (**c**) the case when the excited cation has an anionic neighborhood: the binding energy decreases owing to the ligand field

The XPS method, which was awarded in 1981 by the Nobel Prize to Kai M. Siegbahn, stems simply to the photoelectric effect applied to atomic inner shells (Fig. 11.4). By identifying the peaks in the kinetic energy (*KE*) of emitted photoelectrons and knowing the energy of the absorbed photons, one is able to derive the binding energies (*BE*) of all atoms from the sample, via the photoelectric effect equation:

$$BE = hv - KE - \Phi \tag{11.1}$$

where hv is the photon energy and Φ is the work function of the material. Binding energies are atomic specific [10–13]; additionally, the charge state of the atom which emitted the photoelectron manifests in some changes in binding energies, named "chemical shifts." It is easy to understand why, according to Fig. 11.4b, a positively ionized species will exhibit higher binding energies than the same atomic species in a neutral state. The situation in condensed matter is more complicated since, to the positive chemical shifts of pure atomic origin (for a cation), the crystal field (mainly due to surrounding anions) acts with an overall negative potential ($V_c < 0$), yielding shifts of the energy levels towards larger values ($-eV_c$); therefore, the binding energy decreases, according to Fig. 11.4c. It follows that the derivation of ionization states and of compounds formed is not that easy even in the above rough approximations (purely additive potentials) and sometimes an ionic compound will exhibit, e.g., similar or even lower binding energies for a

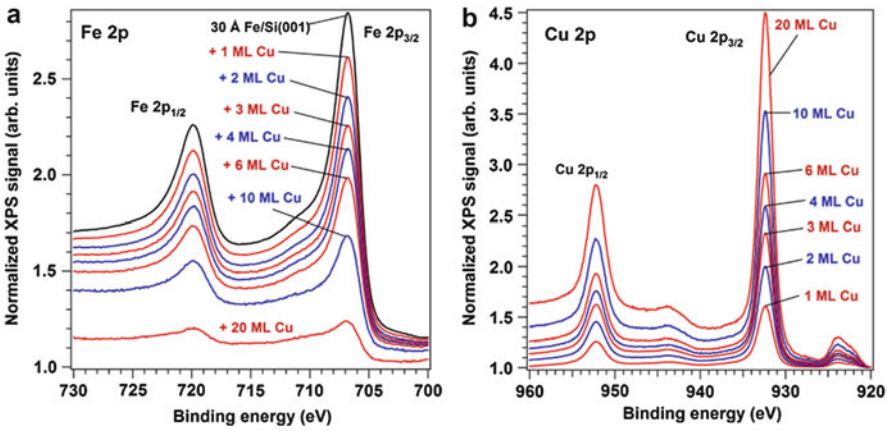


Fig. 11.5 Effects of surface sensitivity on core levels for Cu single atomic layers grown by molecular beam epitaxy on Fe deposited on Si(001): (**a**) the decrease of the Fe 2p signal and (**b**) the increase of the Cu 2p signal

cation than for its neutral correspondent (e.g., in metallic state). For instance the Pb 4f binding energy of PbO is similar to that of metal Pb [11, 12, 14]. Nevertheless, binding energies may be found in databases [11, 12] and quite often the derivation of chemical compounds formed at the surface is tractable. The comparison between the line intensity originating from different atomic species, normalized by known "atomic sensitivity factors" [15], also helps, together with the estimate of chemical shifts, to establish the nature of chemical compounds formed near the surface of a sample [14–16].

A second specificity of the XPS method is its extreme surface sensitivity, mentioned also previously. Figure 11.5 presents Cu 2p and Fe 2p XPS spectra obtained for a fresh Fe layer deposited in ultrahigh vacuum on Si(001), then after sequential deposition of copper single atomic layers ("monolayers," ML). As expected, the Fe 2p signal decreases exponentially $\exp(-d_{CU}/\lambda)$, whereas the Cu 2p signal increases in intensity following a law such as $[1 - \exp(-d_{CU}/\lambda)]$, where the inelastic mean free path $\lambda \approx 9$ ML Cu ≈ 16 Å, a value in line with the "universal curve" tabulated in most textbooks [10, 13]. Sometimes, angle-resolved XPS is utilized to increase the surface sensitivity, because when photoelectrons are detected at a takeoff angle θ (measured with respect to the direction normal to the surface), the inelastic mean free path has to be replaced in the attenuation equation by $\lambda \cos \theta$.

It follows that a requisite to investigate the individual compounds formed at a surface is the ability to simulate XPS spectra with individual components, attributed to the same atomic species forming different bonds, belonging either to the volume or to the surface, etc. [10, 13]. Such procedure, sometimes called "deconvolution" (without, anyway, having anything in common with deconvolution in mathematics), is based by proper simulation of lineshapes, whose profiles must integrate core-level broadenings, which are Lorentz functions, with instrumental broadenings, mainly due to electron energy analyzers, which are simulated by Gauss

lineshapes. Therefore, the "real" line profile is simulated by Voigt or pseudo-Voigt profiles [18], with associated inelastic tails towards higher binding energies (lower kinetic energies) which simulate the electrons having lost part of their kinetic energies by inelastic collisions before leaving the sample [10]. Associating separate inelastic backgrounds to each individual component allows one to derive the "bulk" or "surface" (or "outermost atomic shell") nature of the components in question [19, 20]. For a singlet, the function used to simulate it is a combination of Voigt profile and its integral, as follows:

$$F_S(W_L, W_G, BE, b, x) = V\left(W_L, W_G, x - BE\right) + b \times I(W_L, W_G, x - BE) \quad (11.2)$$

where $V(W_L, W_G, x) = \int_{-\infty}^{\infty} L(W_L, y)G(W_G, y - x)dy$ is the Voigt profile, written as convolution of area normalized Lorentz and Gauss functions with full widths at half maximum, W_L and W_G, respectively, and $I(W_L, W_G, x) = \int_{-\infty}^{x} V(W_L, W_G, y)dy$ is the primitive of the Voigt function [18]. For spin-orbit split doublets, the simulation is performed with combination of Voigt profiles with fixed ratio of their integrals (which is called the "branching ratio") and is given by $(l + 1)/l$, l being the orbital quantum number of the investigated doublet [19]:

$$F_D(W_L, W_G, \Delta E_{SOS}, BR, BE(j_{\max}), b, x) = \frac{BR \times F_S(W_L, W_G, BE(j_{\max}), b, x) + F_S(W_L, W_G, BE(j_{\max}) + \Delta E_{SOS}, b, x)}{BR + 1} \quad (11.3)$$

where BR is the branching ratio and ΔE_{sos} is the spin-orbit splitting of the level in $j_{\max} = l + 1/2$ and $j_{\min} = l - 1/2$ sublevels.

A third feature of the XPS method, which is the subject of the actual chapter, is the derivation of band bendings at free surfaces and metal/semiconductor surfaces. "Textbook" cases are discussed in Refs. [3, 21–25]. Figure 11.6 presents a demonstration of the rigid shift of a core level with the valence band maximum for a PZT sample subject to annealing at increasing temperature. One clearly observes that successive annealing, which produces progressive n doping of the surface (owing to oxygen depletion), yields at the same time an increase of the $E_F - E_V$ energy difference, manifested by a shift of the valence band maximum (E_V) towards higher binding energies, and that the Pb $5d_{5/2}$ core (or shallow) level follows this evolution. For a free surface, therefore, core-level spectroscopy does not bring so much information as compared with valence band spectroscopy. But, when a metal is deposited onto a semiconductor or an insulator, the valence band region will be dominated by the metal states, with high density of states, and one cannot extract the valence band of the substrate alone, because the valence band of semiconductors or insulators has low density of states and, at the same time, this signal is attenuated by the overlayer. Therefore, in this case, the band bending in the substrate may be investigated by core-level spectroscopy only.

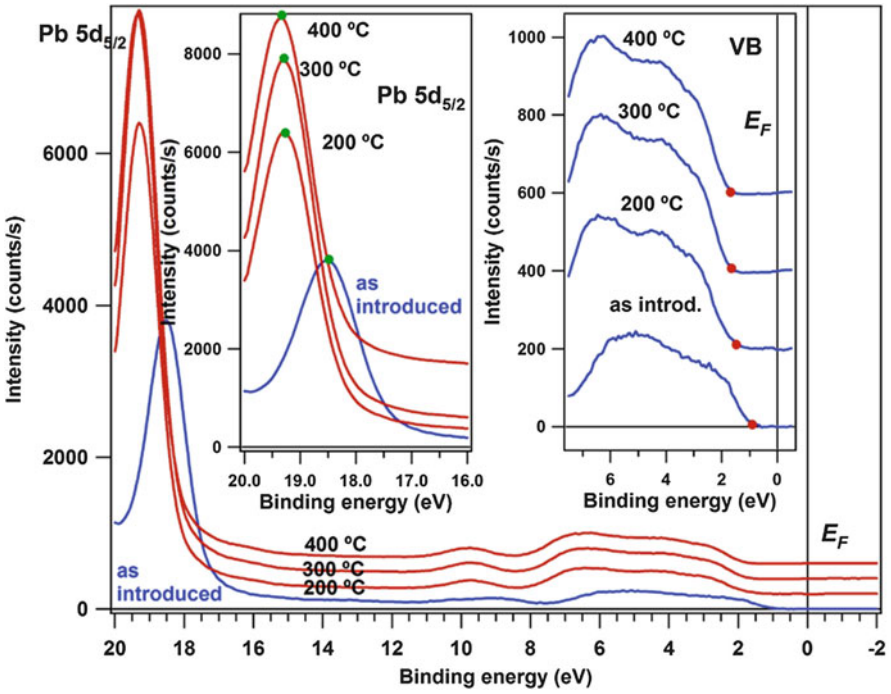


Fig. 11.6 Region of low binding energies (valence band + Pb 5d5/2) recorded for a Pb(Zr,Ti)O3 sample as introduced and after several annealings in ultrahigh vacuum. Annealing induces oxygen vacancies formation near the surface; therefore, the sample becomes progressively n doped in this region, with the difference between the Fermi energy and the valence band maximum increasing with annealing temperature. The core-level Pb $5d_{5/2}$ follows the onset of the valence band; therefore, the assumption of rigid core-level shifts with band bendings from Figs. 11.2 and 11.3 is confirmed (Adapted from Ref. [21])

A fourth feature of the XPS spectroscopy is the relatively low interaction with the sample. It was demonstrated that, for semiconductor single crystals, XPS produces a much lower contamination when compared with techniques involving electron probing of the sample, such as electron diffraction or Auger electron spectroscopy [26, 27]. It is true that in some cases X-ray interaction with the sample produces defects acting at traps at interfaces and affecting the band bending [28]. In other cases, charging effects may severely affect the ability to derive XPS chemical shifts and band bendings [29]. A method to overcome these undesired charging effects is the use of an electron flood gun whose parameters (electron energy and emission) are adjusted such as to compensate the charging effect due to photoemission processes. This was achieved in Refs. [14, 16, 21, 30–33] and implied detailed investigation of several surfaces of similar natures by adjusting the X-ray intensity and the flood gun parameters until several levels (the C 1s from the inherent contamination, together with core levels originating from the substrate) are found to lie at their tabulated values in literature.

Alternatively, e.g., for ferroelectric layers, the samples are heated until sufficient oxygen vacancies are produced near the surface, such as to ensure a surface conductivity in order to eliminate excess charge due to the photoemission [16, 21, 34–38]. However, in this case the ferroelectric polarization near the surface may also be affected, when one needs to investigate free ferroelectric surfaces or metals grown on them. Most of the data discussed throughout this chapter are obtained by using the flood gun, i.e., the first procedure.

4.2 Preparation Methods

Metal deposition is achieved by various methods: molecular beam epitaxy, pulsed laser deposition, magnetron sputtering, thermionic vacuum arc, etc. In the following, we shall concentrate on the molecular beam epitaxy (MBE) method, which is softer, is cleaner (it operated in ultrahigh vacuum, 10^{-10}–10^{-11} mbar), and is supplemented with several in situ analysis methods. These methods are used to determine (a) sample compositions by XPS and Auger electron spectroscopy (AES), eventually also by secondary ion mass spectroscopy (SIMS), low- or medium-energy ion scattering (LEIS and MEIS); (b) sample surface structure by electron diffraction techniques, such as low-energy electron diffraction (LEED) and reflection high-energy electron diffraction (RHEED); and (c) surface morphology by scanning tunneling microscopy (STM) or atomic force microscopy (AFM). A comprehensive review of these techniques may be found in Ref. [39].

In Fig. 11.7, a photograph is given of such a system, which includes (i) an MBE chamber, equipped with LEED, AES, RHEED, residual gas analysis, allowing one to record also SIMS, a sample manipulator which may be cooled down up to liquid nitrogen temperature (77 K) or heated up to 1,500 K, several effusion cells (resistive heating or electron bombardment), an ion sputter gun for cleaning, and a quartz thickness monitor for calibration of the evaporation rates; (ii) a variable temperature (77–600 K) scanning tunneling microscopy (STM) chamber, with a sample garage allowing one also sample preparation by heating and another sputter gun for sample treatment or tip sharpening; and (iii) a photoemission chamber, equipped with the same kind of sample manipulator as the MBE chamber, with two X-ray sources: a dual anode Al/Mg K_α allowing one to probe the sample with unmonochromated radiation whose main peak energies is at 1,486.7 eV for the Al anode or 1,253.6 eV for the Mg anode and a monochromated X-ray source Al $K_{\alpha 1}$/Ag $L_{\alpha 1}$, with excitation energies 1,486.74 eV and 2,984.31 eV, respectively. Electrons are detected by using a 150 mm radius hemispherical energy analyzer, and there is also the possibility to record spin-resolved photoelectron spectroscopy, by using a mini-Mott detector. AES may be recorded also by using an additional high-energy electron gun, whereas the low-energy flood gun is used for sample neutralization. There is also the possibility to record ultraviolet photoelectron spectroscopy (UVS) spectra by using a high power (300 W) UV lamp. The construction of the analyzer allows angle-resolved experiments, and the

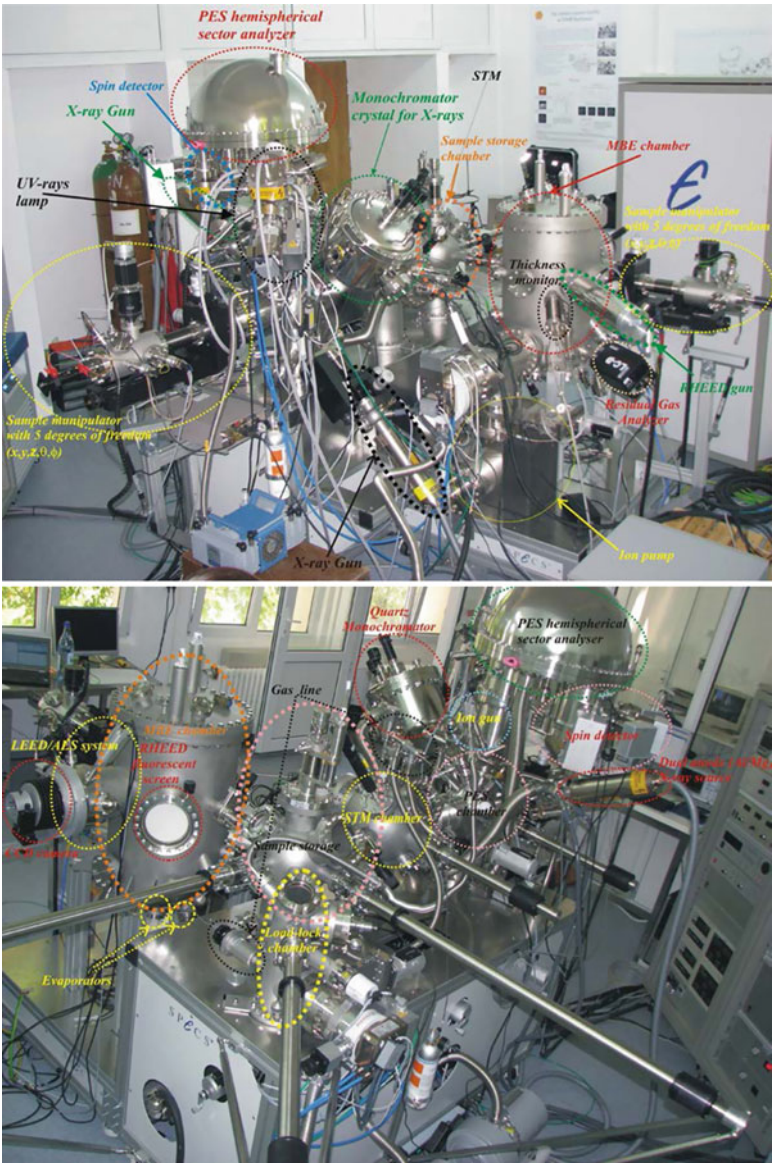


Fig. 11.7 Two views of a complex surface science installation comprising a molecular beam epitaxy (*MBE*), a variable temperature scanning tunneling microscopy facility (*STM*), and an analysis chamber by photoelectron spectroscopies (XPS, UPS, ARUPS, XPD, spin-resolved PES)

manipulator is equipped such as to allow angle-resolved XPS or UPS (ARXPS or ARUPS), the latter method allowing one to trace the valence band structure of single crystal samples [10], while the first method is useful for photoelectron diffraction experiments [17, 40–44].

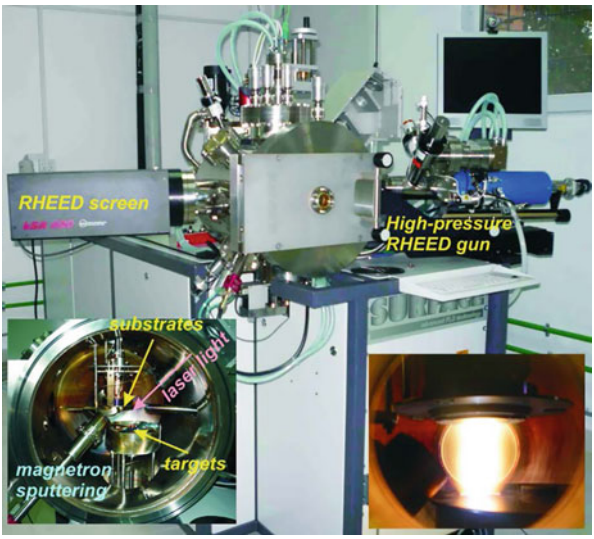


Fig. 11.8 A pulsed laser deposition (PLD) system, equipped with a magnetron sputtering auxiliary cathode and with a high pressure reflection high-energy electron diffraction (*RHEED*) system. Inserts represent an inside view of the deposition chamber and a photograph of the laser-induced plasma plume during deposition

Ferroelectric thin layers must be produced by a method allowing one to transfer the composition of a target onto a substrate. The pulsed laser deposition (PLD) method is the most suitable to achieve this task, especially for complicated compounds [17, 30, 45, 46]. This method uses pulsed high power lasers (excimers or solid state) directed onto a target to sputter atoms from this target and transfer them onto a substrate. This is achieved in an inert gas (Ar) atmosphere, where a plasma plume is formed when the laser interacts with the target. Eventually, the atmosphere is supplemented with oxygen, to compensate for oxygen deficit which may occur in the synthesized sample, going up to a complete change of the nature of the compounds formed [30]. Such a system is represented in Fig. 11.8, equipped with a RHEED system able to operate in the high pressure conditions during the depositions. This RHEED analysis allows one to extract exactly the number of layers synthesized on the substrate [32, 39]. Especially in Refs. [14, 21, 47] a quite accurate surface composition of PZT layers was derived by XPS to reproduce in some cases the target composition.

5 Key Research Findings

5.1 X-Ray Photoelectron Spectroscopy in Analysis of Band Bendings: A Short Review

It was recognized since two decades that, with a good approximation, core-level XPS may be used to assess band bendings in various semiconductor–semiconductor and metal–semiconductor systems. Hudson et al. reported in 1993 a surface band bending of 0.4 eV observed for Ba 4d in $BaTiO_3$ [48]. Woll and coworkers recognized in 1994 band bendings associated with surface metal formation in InP(001) [49].

Band bendings at diamond surfaces were reported also in 1994 by Lau and coworkers [50] and then by Diederich and coworkers in 1998 [51, 52]. Schlaf and coworkers, in 1998, by analyzing LiF interfaced with Al or Pt, evidenced a strong band bending for the Pt case and no band bending for the Al case [22]. This was also one of the rare cases in which a separate contribution of interface dipole layers formed by chemisorbed water (between LiF and Al in this case) was taken into account. School cases yielding a large band bending are discussed for a junction involving organic semiconductors (PTCDA/SnS_2 [23] and Ga q_3/Pt [24]). A key stone to the band bending assessment by XPS was the Waldrop–Grant simple equation [3]:

$$\Delta E_V = (E_{CL} - E_V)_{1,\,\text{bulk}} - (E_{CL} - E_V)_{2,\,\text{bulk}} + (\Delta E_{CL})_{\text{junction}} \tag{11.4}$$

where ΔE_V represents the valence band offset, the first two energy differences in the right-hand side are measured in the bulk states of materials Eqs. 11.4 and 11.1, respectively, and the last term represents the energy difference between the corresponding core levels measured when the two materials are in contact. E_{CL} refers to core-level binding energies, and E_V refers to the binding energy corresponding to the valence band maximum (all energy levels in photoemission spectroscopy are related to the Fermi energy).

Another demonstration of the XPS ability for quantifying band bendings was provided in Ref. [53] for ITO treated with several kinds of plasmas. It was shown that, for samples initially n doped, after plasma treatment, E_F is pushed towards the middle of the bandgap, the work function increases, and the core levels shift towards lower binding energy. In a detailed study [54], the analysis of Pt/SiO_2/SiC(0001) 6H subject to bias voltage evidenced four kinds of charges giving rise to band bendings: (a) interface charges, (b) depleted layers, (c) oxide fixed, and (d) counter charges at the metal/SiO_2 interface.

Starting with 2008, there was an explosion of works related to quantification of band bendings by XPS. It is better to organize this presentation according to the category of systems investigated:

5.1.1 "Standard" Systems

(a) *Si-based heterostructures and/or new methodologies of measurements*. The effect of X-ray-induced traps in Si/SiO_2 structures by performing also time-dependent measurements was discussed in Ref. [28]. It was shown that the Si 2p BE increases with the X-ray dose. Time-dependent measurements for HfO_2/SiO_2/Si interface are presented also in Ref. [29], where one proposes a correction procedure based on a permanent comparison between the first scan (lasting 10 s) and the scan performed when charge is stabilized. The fact that in the above structure the band alignment between Si/SiO_2 is affected by the HfO_2 layer thickness is discussed in Ref. [55]. Inserting a La_2O_3 layer between the HfO_2 and the silica layer was found to produce flat-band conditions [56]. The fact that laser irradiated Si samples exhibit different band bendings as function

on their initial dopings was evidenced in Refs. [4, 57, 58]. Additionally, in Ref. [58] it was shown how band bending at a buried Si/SiO_2 interface, under a thick silica layer such as this interface is not directly accessible by XPS, can be probed by combining optical pumping of carriers (generating a surface photovoltaic effect) at this interface with investigation of the surface Si 2p core-level shift. A noticeable shift of the Si 2p core levels is reported for interfaces involving p-doped Si only, and this allows one to retrieve the band bending evolution at the Si/SiO_x interface beneath the SiO_2 layer. Water adsorption on Si(001) 2×1, n^+ doped induces a band bending of 0.46 eV, despite the close values of the Si 2p core levels for the clean and water adsorbed surface. This was explained by a net negative charge density of $\sim 10^{-2}$ electrons per surface Si atom transferred from the adsorbate, while the width of the bending is about 5 nm [59].

(b) *III–V semiconductor heterostructures*. In/indium tin oxide (ITO)/p-GaN heterostructures exhibited an increase of the Ga 2p BE by 0.5 eV upon annealing [60]. Surface upward band bendings of GaN(0001) were reported to be as 0.9 eV for Ga faces and 0.4 eV for N faces [61]; therefore, band bendings are highly sensitive to the surface termination. In InN(0001) 2×2, a downward band bending is reported in Ref. [62, 63], and this band bending is reduced by O_2 or H_2O adsorption. AlN/GaN or GaN/AlN heterojunctions were investigated, and a direct proportionality of the valence band offsets with the density of the two dimensional electron gas formed at the interface was inferred [64]. A strong band bending was reported at the InN, for both a-plane and c-plane crystals, due to electron accumulation layers [65]. A good agreement between the surface barrier height obtained by XPS and electrical measurements (1.5 eV) was reported for InN/GaN heterostructures [66]. Also, GaN($000\overline{1}$) grown on $Al_2O_3(0001)$ exhibited a noticeable band bending of 0.4 eV, whereas the spatial extent of the band bending is quite low (3 nm) [67].

The wide variety of areas where XPS investigated band bendings on the systems discussed above were listed in Ref. [4] as

> (1) Nature of the dopant, as well as band bending in n- and p-doped Si samples; (2) Interfacial charges and band-bending in SiO_2/Si interfaces for n and p-Si samples; (3) Surface photovoltage development on In and Ga atoms in an InGaN sample; (4) External bias polarity dependence and photoillumination in thin (~4 nm) SiO_2 layers; (5) Effect of forward and reverse biasing on n- and p-domains of an operating Si p-n junction; (6) Dynamics of electron and photoinduced charge accumulation and dissipation in: (i) a Si p-n junction, (ii) an ~4- nm-thick SiO_2 layer, and (iii) a CdS film.

(c) *ZnO-based structures*. Sulfur passivation of a Zn0($000\overline{1}$) single crystal manifested in an upward band bending of 0.1–0.3 eV, explained by the displacement by the sulfur of surface hydroxyl species [68]. An unexpected low band bending (0.06 eV) is found for Pt/ZnO(0001) despite the large difference between the Pt and ZnO work functions (5.65 [69] and 4.08 eV, respectively) [70]. New experiments performed on Pt deposited on Zn-terminated ZnO(001) exhibited a Schottky barrier height of 1.11 eV, while the calculated value was of 1.35 eV.

The discrepancy was explained by the setup of an interlayer Pt-O compound [71]. For ZnO layers produced by spin coating on SiO_2/Si, a different behavior was observed as function on the annealing temperature: low temperature annealing (300 °C) induces a band bending upwards by 0.7 eV, whereas higher temperature annealing induced a band bending in the opposed direction (downwards) by 1.4 eV [72]. An explanation was sketched starting with the balance between the concentrations of oxygen and zinc vacancies. The ZnO case is interesting also because there were recent progresses in synthesis of ZnO nanowires. Such nanowires, grown by chemical vapor deposition with Au catalysts exhibited a band bending of 0.2 eV upwards when contamination water is removed, and this shift was found to be reversible [73].

(d) *TiO_2- and SnO_2-based heterostructures, with applications in photocatalysis and gas sensing*. A clear chemical effect on surface band bendings of NO and O_2 adsorption on TiO_2 (and not on SiO_2, for instance) was reported in Ref. [74]. The interplay between oxygen vacancies and band diagrams was discussed in Ref. [75] for TiO_x/Pt/TiO_x produced by oxidation of Ti/Pt/Ti layers. Deposition of Cu and of Cu_2O onto TiO_2 was analyzed in Ref. [76]. It was found that titania with a high amount of surface defects is subject to smaller valence band offsets and Cu deposition onto surfaces without defects results in lower BE (band bending upwards), whereas Cu2O depositions result in band bending downwards. Gold deposition on n-doped SnO_2 induced Schottky barriers, when the surface was plasma treated, and ohmic contacts, when the surface was not treated before deposition [77]. The extent of the band bending was found to be quite low, about 3 nm. Band bending evolution as function on the dopant (In or Sb) concentration in SnO_2(101) exhibited a considerable band bending for In doping only [65].

(e) *Carbon-based materials, molecules, and organic semiconductors*. We already mentioned pioneering work performed on diamond [50]. CVD diamond (001) exhibited a band bending downwards [78]. In C_{60}, a shift towards lower binding energies which may be attributed to a band bending effect in the highest occupied molecular orbital (HOMO), analogous to EV, was reported when molecules are brought in contact with SiO_2 or SiON [79]. Benzanthracene deposited on Au(111) and Ag(111) exhibited a band bending upwards of 0.57 eV (Ag) and 0.15 eV (Au) [80], respectively, and the pinning factor S was found to differ essentially from unity ($S = 0.39$). (For the meaning of the S factor, see Ref. [14] or the brief discussion below.) Adsorbed self-assembled monolayers (SAM) onto 3C-SiC surfaces are reported to reduce the magnitude of the surface band bending, suggesting passivation of active surface states [81].

(f) *High-k dielectrics and different other oxides.* Observable band bending is reported at the interface between Hf aluminate and GaAs. Treating the GaAs wafer with $(NH_4)_2S$ reduces the band bending [82]. Annealing WO_3 induces an upward surface band bending of 0.3 eV, due to oxygen migration from the bulk to the surface [83]. Interfacing an oxidized Fe with PCAT (phenyl-capped

aniline tetramer) induces a band bending of 0.7 eV towards higher BE (i.e., downwards) [84]. In In_2O_3, photoemission studies combined with I–V characteristics evidenced the removal of the surface charge accumulation layer by plasma treatment [25]. The surface accumulation layer manifests by a downward band bending near the surface, the presence of a weak conduction band peak (E_F pinning), and a linear I–V characteristic. Plasma treatment induced an upward band bending, the disappearance of the conduction band peak, and a nonlinear I–V characteristic. Pt deposited on $SrTiO_3$(001) evidence an inversion of the evolution of the substrate core levels with Pt deposition, depending on the initial state of the surface: when the surface was just annealed, the shifts were towards higher BE, and when the surface is etched, the shift reverses its sign. This is explained by an alteration mechanism of band bending by introduction of surface layer hydroxyl groups.

By summarizing all these investigations, one may notice that band bending investigations by XPS of "standard" Schottky diodes are missing (e.g., Au/Si, Ag/Si, Cu/Si, etc.). One of the reasons is that metal deposition on semiconductors proceeds via the formation of interface compounds of complicated compositions and structures, with no information available, e.g., about their work functions. For instance, it was shown that strong reaction and intermixing occurs when incomplete 3d shell metals are deposited on semiconductors: Fe/Si(001) [85, 86], Fe/Si(111) [40, 41], Fe/GaAs(001) [87], Fe/InAs(001) [88–90], and Co/GaAs(011) [42–44]. In all these papers, the effects of band bending are avoided by using the following procedure: the core levels are deconvoluted, the bulk component is identified in all of them, and then all the other components, including the whole spectrum, are aligned to the bulk component "in order to compensate the band bendings." It is maybe time to revisit all these data and to try to extract also the band bending evolution, e.g., with metal thickness. Note, however, that recently an assessment of band bending was presented for Au/Ge(001) in Refs. [91, 92], where a band bending upwards of 0.15 eV was derived, close to the value expected from the difference of work functions between Au (5.1–5.3 eV) and Ge (5.0 eV). Later on in this chapter (Sect. 5), we will discuss other "school cases," that of copper deposited on Ge (001) and that of Au deposited on unpoled lead zirco-titanate $Pb(Zr,Ti)O_3$ (PZT).

5.1.2 Ferroelectric Systems

Ferroelectric thin films are widely studied nowadays, owing to a tremendous number of applications [9, 93]. The details of charge distribution near the surface in the presence of a polarization perpendicular to the surface started to be elucidated only recently [14, 16, 21, 47]. Charge accumulation near surfaces may induce surface depolarization in the films and the relaxation of the tetragonal distortion, responsible for the occurrence of ferroelectricity. The interplay between the two phenomena (charge accumulation and lattice relaxation towards the cubic geometry) is still a subject of debates. Recent experiments exhibited a partial lattice relaxation in the first few layers of the ferroelectric [17], and one must notice that most older experiments were performed on polycrystalline samples, where grain

boundary effects intervene in a complicated manner. At the same time, modern synthesis methods, such as pulsed laser deposition, allow the controlled growth of single crystal ferroelectric films with well-defined stoichiometry and minimum surface roughness [14, 30]. Such samples are well suited for the detailed study of the aforementioned phenomena.

For most applications, the active ferroelectric material is contacted with metals in order to apply the necessary voltages. Interfaces formed by metals with ferroelectrics imply not only band bendings but also phenomena such as surface disruption, charge accumulation, oxygen depletion, etc. Surface layers can have quite different composition with respect to bulk [30, 31] and the early stages of metal deposition proceed via complicated processes, involving sometimes formation of undesirable compounds by uptaking the inherent (mainly carbon) contamination of the ferroelectric layer [94, 95].

It is clear that many properties useful for application are strongly dependent on the Schottky barrier formed at these interfaces [45, 96]. In Ref. [45] it was demonstrated that the short circuit photocurrent strongly depends on the work function of the metal deposited on PZT; it is more elevated by several orders of magnitude when the work function of the metal (Pt: 5.65 eV [69]) exceeds that of PZT (5.1 eV [9]). In conclusion, the investigation of the barrier formed at metal/ferroelectric interface is of prime importance.

Although the bulk atomic structure, polarization, and ferroelectric domains are nowadays known with high accuracy [97], complicated depolarization phenomena, including lattice relaxation [98, 99] and strong depolarization fields [100, 101], occur at ferroelectric surfaces, affecting the band bending of free ferroelectric surfaces. Therefore, obtaining reliable experimental data allowing one to quantify the surface band bending is crucial. The band bending induced by the ferroelectric polarization (Fig. 11.3) may be expressed as $e\,P\delta/\in$, where e is the elementary charge, P is the static polarization, δ is the distance between the surface and the polarization charge sheet, and $\in = \in_0 \in_r$ is the dielectric constant of the ferroelectric [101]. Therefore, a method to extract this ferroelectric band bending was proposed [44], implying ferroelectric hysteresis loops and C–V and I–V characteristics measurements. Typical values obtained for epitaxial $PbZr_{0.2}Ti_{0.8}O_3$ are $P = 95\ \mu C/m^2$ [102], $\delta = 3.0$ nm, and $\in_r = 180$ [44]. This implies a maximum downward band curvature of 1.8 eV induced by the ferroelectric film only.

Metal deposition induces further band bending whose curvature depends on the difference between the work function of the metal and that of the semiconductor (Fig. 11.1). The Schottky barrier height is influenced by charge transfer induced by the ferroelectric surface states via the S pinning factor, such that for electrons $\Phi_{bi} = S\ \mathrm{x}\ (\Phi_M - \Phi_S) + (\Phi_S - \chi_S)$, where $S = 1$ corresponds to the pure Schottky case (band alignment), whereas $S = 0$ corresponds to the Bardeen case, where the charge transferred fully compensates the interface band bending [103]. For holes, $\Phi_{bi} = S\ \mathrm{x}\ (\Phi_S - \Phi_M) + (\chi_S - \Phi_S + E_g)$, where Φ_M and Φ_S are work functions for the metal and for the semiconductor, χ_S is the semiconductor's electronic affinity, and E_g is the bandgap. The S factor can be expressed by using the surface density of interface states N_S, the penetration of these states into the semiconductor δ, and the

dielectric constant of the semiconductor $\in$: $S^{-1} = 1 + e^2 N_S \delta / \in$and S is found to lie between 0.31 for $PbTiO_3$ and 0.4 for $PbZrO_3$ [103].

Other complementary methods to investigate the surface charge and/or band bending we should mention are (i) scanning tunneling spectroscopy (STS): for example, the interface barrier potential at a free $BiFeO_3$ surface was found to vary between 0.62 and 1.0 eV when the sample was poled upwards $P^{(+)}$ [104]; (ii) mirror electron microscopy (MEM) investigations on piezoresponse force microscopy (PFM) written domains exhibited a relative low difference between $P^{(+)}$ and $P^{(-)}$ written domains for the transition between the MEM regime (electrons completely deflected) and the low-energy electron microscopy (LEEM) regime (electrons penetrating into the sample) [105]. However, in view of all the description from above, XPS seems to be one of the most suitable methods to quantify band bendings at free ferroelectric surfaces and at metal/ferroelectric interfaces; (iii) electrical measurements are quite often used to derive surface band bendings at Schottky contacts [1, 2]; however, some assumptions need to be done to derive the Schottky barrier height, such as to model the interaction of electrons with image charges, yielding the Simmons–Schottky model [106] or the uniformity of the electric field inside a ferroelectric thin film [107]. Additionally, as mentioned above, the "other" contact also influences the $I(V)$ curve of a Schottky contact, which may sometimes affect the conclusions drawn for the contact of interest.

Metal–semiconductor band bending spatial ranges are on the order of $(\in k_B T/N)^{1/2}/e$, 16–160 nm at room temperature (T) for PZT ($\in_r \approx 180$) with the density of ionized impurities $N = 10^{18} - 10^{16}$ cm^{-3} (see Sect. 4 for more details). For larger doping levels, the extent of the band bending approaches the surface sensitivity range for XPS: therefore, an appropriate simulation of the XPS peaks should yield the band bending also in this case.

The main problem is that XPS evaluation of simple surface charging and/or band bending may be hindered by interface reactions [16, 34–38]. For instance, in the case of PZT, Pb segregation was detected in several metal/PZT interfaces [34, 35]; interfaces with indium tin oxides (ITO) [36] or with RuO_2 [37] were also found to have a complicated surface chemistry. A procedure for derivation of ionization potentials was proposed in Ref. [38]. However, none of the above Refs. [34–38] identified a real effect of the ferroelectric polarization. Only recently, the same group published outstanding results where all core levels of $BaTiO_3$ (BTO) were found to vary as function on the polarization voltage applied in situ on the sample [16]. A difference of about 1 eV in binding energy was found between $P^{(+)}$ and $P^{(-)}$ poled samples; therefore, the band bending occurring at the BTO surface due to the ferroelectric polarization is about 0.5 eV.

On PZT, the band bending effect was found to be bigger, owing to the larger polarization of PZT (in the range of 100 μC/cm^2) as compared with BTO (in the range of 25 μC/cm^2). In Ref. [14] a band bending of 0.94 eV was detected between PZT with outward ($P^{(+)}$) polarization and surfaces with no polarization perpendicular to the plane. $P^{(-)}$ polarized areas were detected only on quite freshly prepared PZT surfaces, by a band bending of the same order of magnitude (∼1 eV) in opposite directions, according to Fig. 11.3 [21].

Deposition of Au on PZT was found to proceed via a standard Schottky barrier formation, with a band bending ranging from 0.2 eV up to about 0.45 eV, depending on the initial state of the substrate [14, 21]. Deposition of Cu on PZT was found to produce a non-monotonous evolution of binding energies, which is explained by a competition between the Schottky barrier formation and the progressive loss of the surface ferroelectric band bending, owing to the shortcut realized by the Cu layer [32, 33].

5.2 Theoretical Aspects

In this section we will revisit the basic aspects of band bending for metal/semiconductor interfaces and for free ferroelectric surfaces. We will develop a formalism which is valid for both cases, we will sketch the way the differential equations may be solved numerically, and we will finish with some considerations for the more complicated metal/ferroelectric case.

5.2.1 Metal–Semiconductor Schottky Contacts

In the following, we shall treat only systems where electrons are the important mobile charges, i.e., n-doped semiconductors. The case of p-doped semiconductor is quite similar and is left to the reader as an exercise. When a metal is brought into contact with the semiconductor, electrons migrate from one material to the other, from the one with lower work function into the one with larger work function. This happens until at the interface a field is developed which stops further migration. There will be therefore a balance between the diffusion current due to spatial variations of electron density, and the drift current, promoted by the interface field via the Ohm law. This provides a first relation between the electron density and the potential. The second relation is the Poisson equation.

The diffusion equation may be written as follows:

– with particle current density:

$$\boldsymbol{j}_{\text{part., diff.}} = -D_n \nabla n \tag{11.5a}$$

where D_n is the diffusion coefficient for electrons and n their density
– with charge (electrons) current density:

$$\boldsymbol{j}_{\text{diff.}} = eD_n \nabla n \tag{11.5b}$$

The drift equation is

$$\boldsymbol{j}_{\text{drift}} = \sigma \boldsymbol{E} = en\mu_n \boldsymbol{E} = -en\mu_n \nabla \phi \tag{11.6}$$

where $\boldsymbol{E}$ is the electric field, ϕ is the electrostatic potential, σ is the conductivity, and μ_n is the electron mobility.

The equilibrium equation

$$\boldsymbol{j}_{\text{diff.}} + \boldsymbol{j}_{\text{drift}} = 0 = eD_n \nabla_n - en\mu_n \nabla\phi \tag{11.7}$$

implies

$$\nabla\phi = \frac{D_n}{\mu_n} \cdot \frac{\nabla_n}{n} = \frac{k_B T}{e} \nabla(\log n) \tag{11.8}$$

where the Einstein equation was considered: $D_n/\mu_n = k_B T/e$.

In the following, we will work in terms of potential energy, not electric potential. For electrons, the potential energy yields

$$V = -e\phi = -k_B T \log \frac{n}{n_0} \tag{11.9}$$

where n_0 is the bulk electron density (when $x \to \infty$). V and n are functions on the distance from the interface x, $V(x)$ and $n(x)$.

The Poisson equation is written as

$$\Delta\phi = -\frac{\rho}{\in} = -\frac{eN_D{}^{(+)} - en}{\in} \tag{11.10}$$

where $N_D{}^{(+)}$ is the density of ionized donors, which is also a function on the distance from the interface $N_D{}^{(+)}(x)$. In absence of this term, we would just consider the case of metal/metal contacts (Seebeck effect).

In terms of potential energy, the Poisson equation yields

$$\Delta V = \frac{e\rho}{\in} = \frac{e^2}{\in} \left(N_D{}^{(+)} - n \right) \tag{11.11}$$

The creation of the interface field is produced by the fact that the donor levels near the interface will also follow the band bending $E_D = E_D{}^{(0)} + V(x)$ [108]. Therefore, the density of ionized donors will vary, since the energy difference between the Fermi energy E_F and the donor levels E_D will also be a function on the distance to the interface. The density of ionized donors is written as [1]:

$$N_D{}^{(+)} = \frac{N_D}{1 + 2\exp\left(\frac{E_F - E_D}{k_B T} \right)} = \frac{N_D}{1 + 2\exp\left(\frac{E_F - E_D{}^{(0)}}{k_B T} - \frac{V}{k_B T} \right)} \tag{11.12}$$

where $E_D{}^{(0)}$ is the donor impurity level in absence of band bending $V(x)$. In the following, we shall work in reduced units $v = V/(k_B T)$, $y = n/n_0$, and the length will be measured in units of l, where

$$l = \left(\frac{\in k_B T}{e^2 n_0}\right)^{1/2} \tag{11.13}$$

This will be called *diffusion length* in the following. It yields, e.g., 3.8 nm for $\in_r = 10$ $T = 300$ K and $n_0 = 10^{24}$ m^{-3}.

Furthermore, we note $\alpha = \exp\left(\frac{E_F - E_D{}^{(0)}}{k_B T}\right)$ and $\beta = \frac{N_D}{n_0}$. The diffusion equation yields $y = \exp(-v)$, and the Laplace equation, combined with the diffusion equation, yields

$$\frac{d^2 v}{dx} = \frac{\beta}{1 + 2\alpha \exp(-v)} - \exp(-v) \tag{11.14}$$

In all the above considerations, we did not consider the electrical neutrality in the bulk of the semiconductor, namely, n_0 and N_D are considered independent variables. That means that the actual model may be applied also for charged semiconductors, e.g., in presence of optical pumping. If, in addition, one considers $n_0 = N_D{}^{(+)}$, from Eq. 11.12, it follows $\beta = 1 + 2\alpha$ and $v_\infty = 0$ from Eq. 11.14.

The boundary conditions are $v(0) = (\Phi_M - \Phi_S)/(k_B T)$, whereas $\left(\frac{dv}{dx}\right)_0$ must be chosen such that $\lim_{x \to \infty} v(x)$ is finite. This equation is solved by iterations, i.e., starting with a function $v_0(x)$, one computes the right-hand side of the Eq. 11.14, integrate it with the boundary conditions, obtain a first order function $v_1(x)$, reintroduce it in the right-hand side, reintegrate it, obtain a second order function $v_2(x)$, and so on. The procedure converges after 10–20 iterations, irrespective on the initial function $v_0(x)$. One has to choose with great care $\left(\frac{dv}{dx}\right)_0$, such that the (reduced) potential energy remains finite when $x \to \infty$. Figure 11.9 presents some examples, when one may also notice that slight deviations in the initial derivative of the potential energy may yield serious divergence of the $v(x)$ function for large values of x. Let us remark that the procedure converges for $v(0) > 0$, which correspond to the Schottky contact between the metal and the n-type semiconductor ($\Phi_S < \Phi_M$), according to Fig. 11.1b.

This procedure allows one to derive the electric field at the interface:

$$E(0) = \left(\frac{n_0 k_B T}{\in}\right)^{1/2} \cdot \left(\frac{dv}{dx}\right)_0 \tag{11.15}$$

Another immediate consequence of the Poisson equation is the derivation of the temperature dependence of the Schottky barrier. Indeed, as $x \to \infty$, the Laplacian $\Delta v \to 0$; therefore, one may compute v_∞:

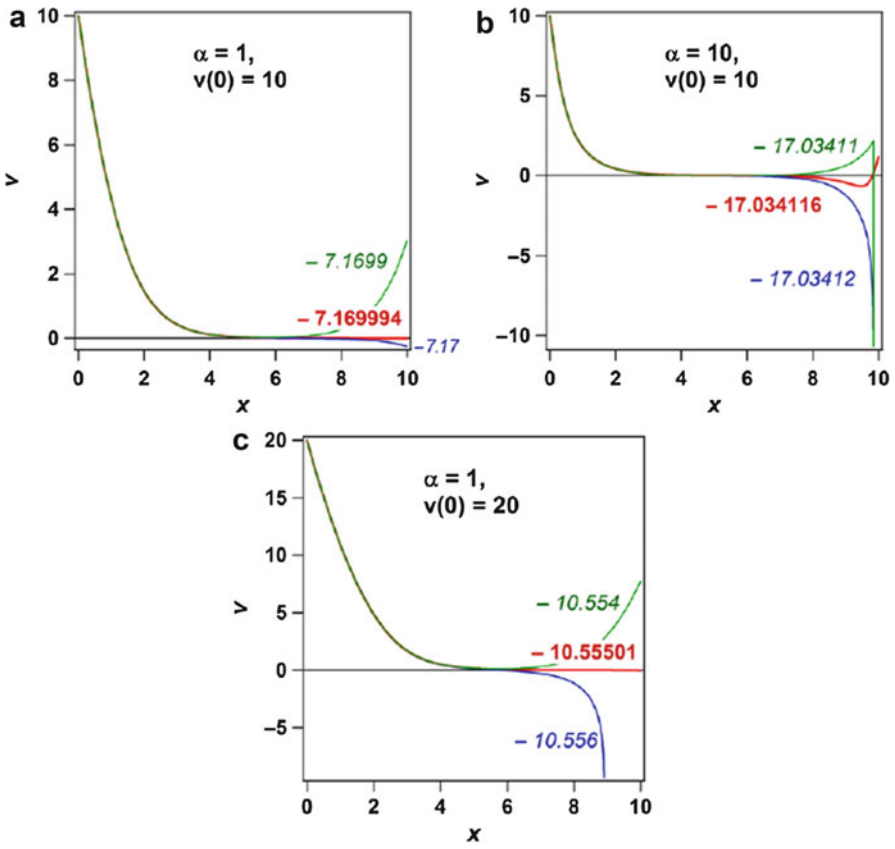


Fig. 11.9 Solutions of Eq. 11.12 for the potential energy inside a semiconductor contacted with a metal, as function on the Schottky barrier at the interface (10 k_BT units) and on the parameter α and β. Note that the neutrality condition $\beta = 1 + 2\alpha$ was employed in Eq. 11.12

$$v_\infty = \log \frac{4\alpha}{\sqrt{1 + 8\alpha\beta} - 1}, \quad \text{i.e.,}$$
$$V_\infty = k_B T \log \frac{4\exp\left(\frac{E_F - E_D{}^{(0)}}{k_B T}\right)}{\sqrt{1 + 8\frac{N_D}{n_0}\exp\left(\frac{E_F - E_D{}^{(0)}}{k_B T}\right)} - 1} \tag{11.16}$$

This value is always positive. When $T \to 0$, it yields $(E_F - E_D{}^{(0)})/2$. The total Schottky barrier is expressed as

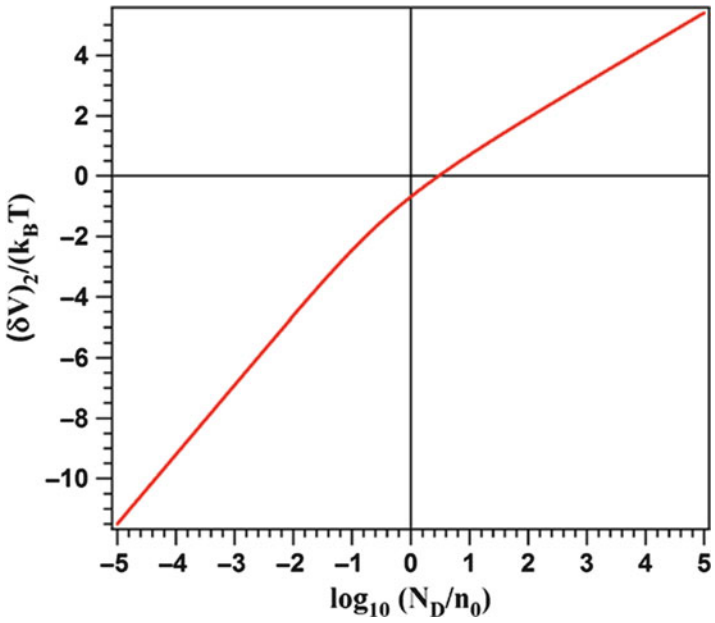


Fig. 11.10 The deviation from the case of a simplified Schottky barrier in the case of Fermi level pinning at the donor level $(\delta V)_1 = \Phi_S - \Phi_M$, Eq. 11.19

$$\delta V(T) \equiv V(0) - V_\infty$$

$$= \Phi_M - \Phi_S - k_B T \log \frac{4 \exp\left(\frac{E_F - E_D{}^{(0)}}{k_B T}\right)}{\sqrt{1 + 8\frac{N_D}{n_0}\exp\left(\frac{E_F - E_D{}^{(0)}}{k_B T}\right)} - 1} \tag{11.17}$$

with the limit as $T \to 0$:

$$\delta V(0) = \Phi_S - \Phi_M - \frac{E_F - E_D{}^{(0)}}{2} \tag{11.18}$$

Another interesting case is that when the Fermi energy is pinned to the donor levels, $E_F = E_D{}^{(0)}$. The Schottky barrier is a simple function on N_D/n_0:

$$\delta V(T) = \Phi_M - \Phi_S - k_B T \log \frac{4}{\sqrt{1 + 8\frac{N_D}{n_0}} - 1} \equiv (\delta V)_1 + (\delta V)_2 \tag{11.19}$$

This function is represented in Fig. 11.10.

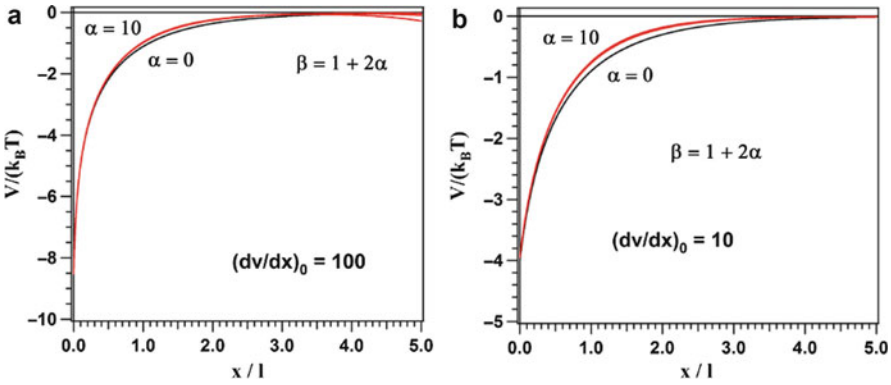


Fig. 11.11 Simulation of potential energy curves near a free ferroelectric surface placed at the *left-hand* side of the graph, for two values of the electric field near the origin and for several values of the α parameter, with the neutrality condition fulfilled

5.2.2 The Case of Free Ferroelectric Surfaces

The same formalism applies in the case of free ferroelectric surfaces, with, however, a change in the paradigm. In the metal/semiconductor case, the boundary conditions were: (a) the potential energy in $x = 0$ is fixed to the difference between the two work functions $v(0) = (\Phi_S - \Phi_M)/(k_B T)$ and (b) the derivative of v in the origin is adjusted such as to produce a solution $v(x)$ which is finite everywhere. This produces the electric field at the interface.

In the case of free ferroelectric surfaces, the field at the surface is known, being the polarization of the ferroelectric divided by the permittivity. By inverting Eq. 11.15 and introducing the polarization of the crystal, the result is

$$\left(\frac{dv}{dx}\right)_0 = \frac{P_0}{(\in n_0 k_B T)^{1/2}} \tag{11.20}$$

The denominator in Eq. 11.18 is on the order of 2 mC/m^2 for $\in_r = 100$, $T = 300$ K, and $n_0 = 10^{24}$ m^{-3}. Consequently, one will have to set the derivative at $x = 0$ to the known value for the physical system in question and adjust the value of the potential in origin such that the whole function $v(x)$ remains finite. The procedure is quite similar to the case of a metal/semiconductor Schottky contact, where one sets the value of the potential at the origin and adjusts its derivative. Some results are represented in Fig. 11.11; for systems with the neutrality condition, $\beta = 1 + 2\alpha$ fulfilled. Note that the direction of the electric field is positive (i.e., oriented inwards) when $(dv/dx)_0 > 0$. But this is the depolarizing field [32, 33]; the orientation of the static ferroelectric polarization will be outwards. It is clear that up to now the position of donor levels and the concentration of doping atoms seem not to be critical. The most critical parameter is the value of the derivative in the origin (i.e., the polarization).

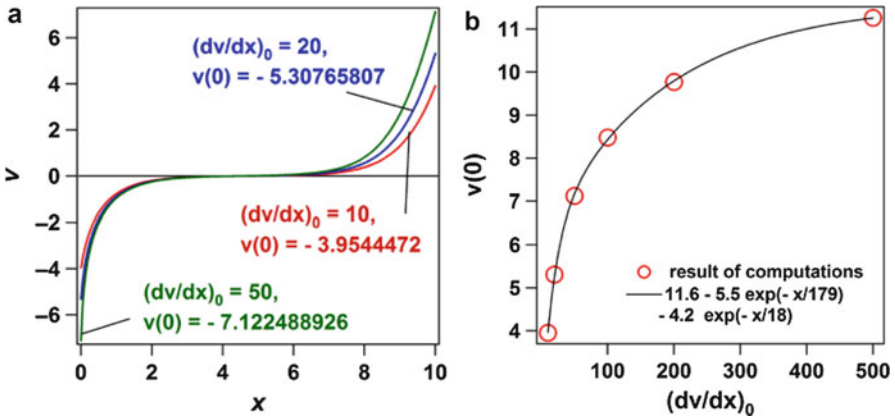


Fig. 11.12 (**a**) Simulation of the potential energy curve for electrons inside a finite ferroelectric layer of thickness $10 \times (\in k_B T/e^2 n_0)^{1/2}$, for three values of the polarization, in units of $(\in n_0 k_B T)^{1/2}$. (**b**) Initial band bending required to achieve a convenient potential energy dependence, as in (**a**), represented as function of the derivative in origin (polarization) (see text for units)

A ferroelectric layer of finite thickness $x \in (0, d)$ may be simulated by the following procedure:

(i) Adjusting the derivative in the origin to the known value via Eq. 11.18
(ii) Choosing the value of the potential in the origin (i.e., the band bending) such that

$$\left(\frac{dv}{dx}\right)_d = \left(\frac{dv}{dx}\right)_0 \tag{11.21}$$

and, eventually, $v(d) = -v(0)$. Some results are presented in Fig. 11.12a. The resulting curves should be antisymmetric with respect to the middle of the layer $x = d/2$. Deviations from antisymmetry are to be connected with numerical integration errors. Nevertheless, there is an important consequence of the computations represented in Fig. 11.12a: the band bending at the surface of the ferroelectrics, for thin ferroelectric layers, is not proportional to the value of the polarization. The dependence of the band bending derived by the procedure described above on the polarization (i.e., the electric field at the interface) is represented in Fig. 11.12b, together with a simulation by a sum of exponentials. Alternatively, if this band bending is expressed as $e\ P\ \delta/\in$, the parameter δ may be computed, in units of l, defined by Eq. 11.13, as being $|v(0)|/(dv/dx)_0$; it is found that this depends on the polarization P and weakly on the thickness of the ferroelectric layer. By using the simulation function from Fig. 11.12b, one may derive the parameter δ as

$$\delta \approx \frac{\in k_B T}{e^2 n_0}\left\{11.6 - 5.5\exp\left[-\frac{P_0}{179(\in n_0 k_B T)^{1/2}}\right] - 4.2\exp\left[\frac{P_0}{18(\in n_0 k_B T)^{1/2}}\right]\right\} \tag{11.22}$$

The two limiting cases are $\delta \approx 2l$ for vanishing polarization and $\delta \approx 12l$ for infinite polarization. Therefore, with increase of the polarization, the parameter δ increases as well, for systems with similar equilibrium density of carriers n_0.

5.2.3 Metal Contacts on Ferroelectrics

Up to now, the Poisson equation with the charge density integrated in it was solved in two conditions: (i) by fixing the initial value of the potential and adjusting its derivative in the origin (the interface electric field) in order to obtain finite solutions at infinity, case which corresponds to Schottky barriers, and (ii) by fixing the derivative of the potential and adjusting its value in order to obtain either finite solutions at infinity or convenient solutions at the other border of the ferroelectric layer; this case was attributed to the free ferroelectric surface with known value of the polarization and of the dielectric constant. When treating the metal–ferroelectric Schottky contact, one encounters the problem that both the potential and its derivative must be fixed: the potential by the fixed potential of the electrode and the derivative by the known value of the polarization. This will yield for sure inconvenient solutions at infinity or at the other border of the ferroelectric thin layer. There is a need for an additional degree of freedom.

More than one decade ago, Matsuura proposed a modified Poisson equation, in which the polarization of the ferroelectric is allowed to vary as function on x. The Poisson equation written by Matsuura is [108]

$$\Delta\phi = -\frac{1}{\in}(\rho - \operatorname{div} \boldsymbol{P}) \tag{11.23}$$

and one has to add a modified drift-diffusion (Eq. 11.8). When the polarization is variable across the layer, a third equation is needed. Intuitively, when excess charges (electrons) are provided by the metal, the ferroelectric polarization should decrease as a function on electron density. In a first approximation, this may be represented by a law such as

$$P = P_{\text{max.}} - \tilde{p} \cdot n \tag{11.24}$$

where $\tilde{p}$ has the dimensions of a dipole moment and should be not far away from the dipole moment corresponding to an elementary cell of the ferroelectric. Equations such as Eq. 11.24 may be derived by various assumptions, the simpler being the following. We consider the polarization oriented upwards. When some excess negative charge is provided to a ferroelectric elementary cell, part of this

charge reduces the ionization state of the Ti^{4+} cation, and part of it is distributed on the upper and lower faces of the cell, by taking into account that the electrons already present on these faces are strongly hybrid O 2p and Pb 6p electrons. Thus, these faces can be seen as being occupied by delocalized electrons, similar to metals and additional electrons may be seen in a first approximation as being distributed uniformously on these faces. The new equilibrium condition may be calculated and connected to a reduced value of polarization, as function on the excess electron charge density. Equation 11.24 simulates well the obtained curve. More sophisticated Landau–Ginsburg–Devonshire theory gives similar results for the interplay between the remanent ferroelectric polarization and the charge density [100]. Now, the drift-diffusion equation together with the modified Poisson equation 11.23 and with the relation Eq. 11.24 may be combined into a single, slightly more complicated, differential equation, with similar notations and units as Eq. 11.14:

$$\frac{d^2v}{dx^2}+\gamma\exp(-v)\frac{dv}{dx}=\frac{\beta}{1+2\alpha\exp(-v)}-\exp(-v),\quad \text{where } \gamma = \tilde{p}\left(\frac{n_0}{\in k_B T}\right)^{1/2} \tag{11.25}$$

The parameter γ may be seen as the ratio between ionic displacements (mostly for Ti^{4+}) from their centrosymmetric position, giving rise to the dipole moment of the elementary cell, and the diffusion length. Solving the above differential equation indeed yields reduced band bending when the γ parameter is increased towards a few percents.

Matsuura in Ref. [108] proceeded to some approximations which will not be discussed in detail, yielding to the conclusion that the ferroelectric behaves as a high dielectric constant material and it is highly depleted from charge carriers. In this case, the existence of two conditions for each border of the ferroelectric thin film is not too restrictive. However, in the following we shall not deal with a so complicated formalism, but prefer to present some intuitive potential energy curves, aiming to interpret the experimental data which will be commented in the next section.

In most cases, ferroelectric thin layers are grown epitaxially on a bottom electrode; therefore, a first band bending occurs at the bottom interface. For the practical cases which will be discussed in Sect. 5, the bottom electrode is $SrRuO_3$ (SRO) grown epitaxially by PLD on $SrTiO_3$ (STO).

Figure 11.13 represents a schematic of a 150-nm thick ferroelectric layer grown on SRO. The left panels represent the case where the outward surface of the ferroelectric is completely isolated and may have a different potential energy than that of the bottom electrode. The right panels represent the case when the conductivity of the outward surface suffices to ensure the grounding of the surface to the same potential as that of the bottom electrode. Blue curves represent smoothed versions of the red curves, and, by comparison with the general aspects

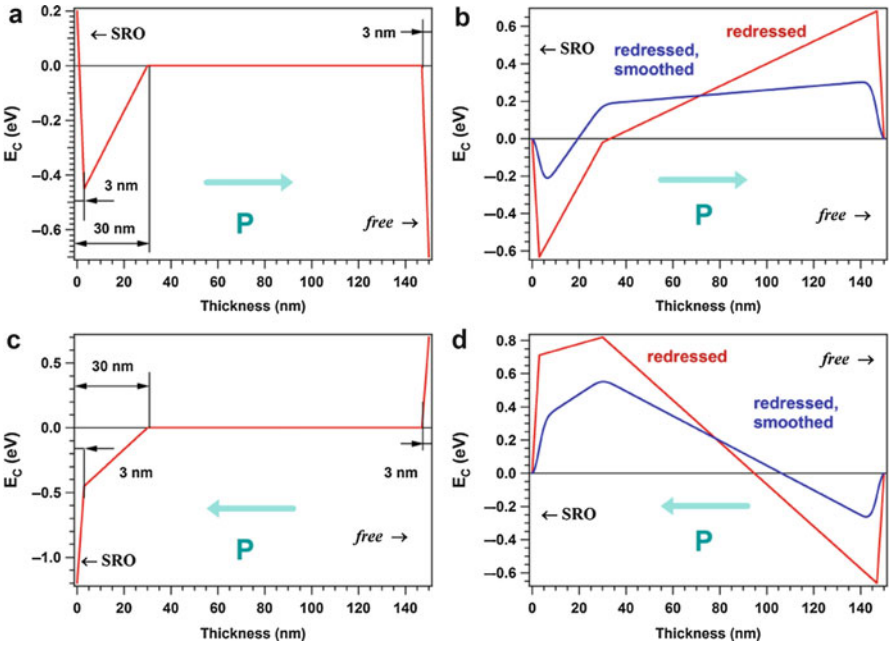


Fig. 11.13 Conduction band dependence vs. film thickness for a ferroelectric layer (PZT, BTO) deposited on an SRO metal buffer layer. The barrier height at the interface with SRO is considered 0.5 eV and the ferroelectric band bending is considered 0.7 eV. (**a**) Represents the case of ferroelectric polarization oriented from the SRO substrate towards the free surface of the film (outward polarization); (**b**) represents the same case, but when one imposes that the potential of the surface is the same as that of the bottom electrode (red curve). The blue curve is obtained by several smoothings of the red curve. (**c**, **d**) Similar plots, but for inward polarization. The extent of the Schottky band bending is considered 30 nm, and the distance to the depolarization charge sheet is $\delta = 3$ nm

of the computed curves from the previous paragraph, one may notice that the discrepancy is not that important. Grounding the outward surface yields a non-vanishing field inside the volume of the ferroelectric thin films owing to an overcompensation of the mobile charges stabilized near both interfaces (see also Fig. 11.3) [32, 33].

The next two figures represent the cases when a metal with lower work function (Cu, Fig. 11.14) or higher work function (Pt, Fig. 11.15) is deposited on the ferroelectric layer. By taking also the case of Au, whose work function is only slightly larger than that of the ferroelectric, all cases when both surfaces of the ferroelectric thin layer are at the same potential are represented in Fig. 11.16. One can therefore see that detectable shifts may be obtained from layers not so deep inside the outward surface, when analyzed by XPS. In the following, we shall discuss in more details the experimental results obtained in all these cases.

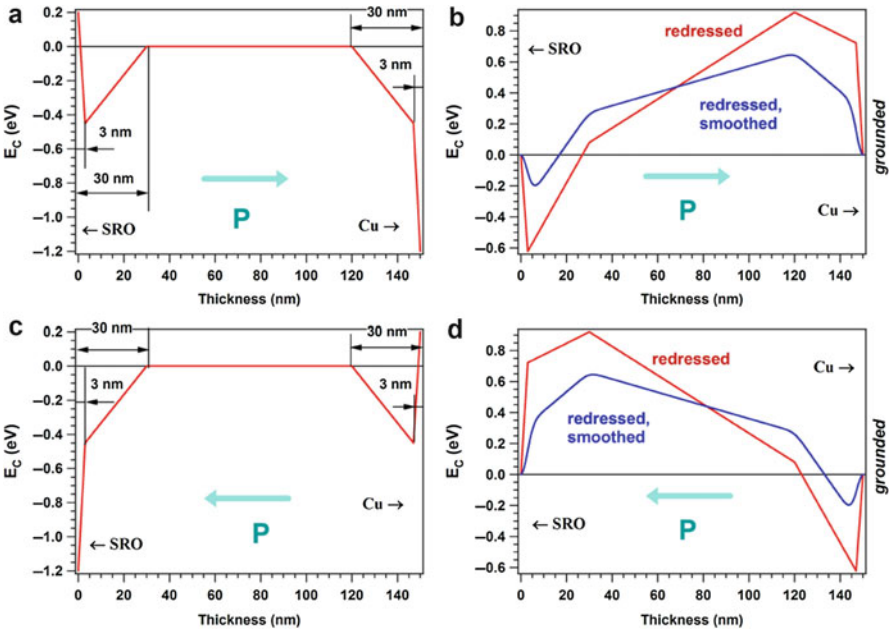


Fig. 11.14 Same as Fig. 11.13, but for a Cu layer deposited on top of the ferroelectric layer, with the work function of the metal lower by 0.5 eV than that of the ferroelectric

5.3 Experimental Examples

5.3.1 Standard Cases of Schottky Barriers

Cu/Ge(001)

Figure 11.17 presents XPS results obtained on Cu layers deposited on Ge(001) $(2 \times 1) - (1 \times 2)$. The continuity of the Cu layer may be easily derived from the analysis of integral intensities of Ge and Cu peaks. Especially the Ge 3d levels are attenuated according to an exponentially decreasing law, with an inelastic mean free path of 14.5 Å. The early stages of Cu growth proceed by epitaxy, such as good LEED patterns may be seen up to 8 Å of Cu deposited, and then the LEED pattern degrades, which is a sign of a Stranski–Krastanov type of growth.

The binding energies of the Ge surface components (for both Ge 3d and Ge 2p levels) follow a saturation law, with a maximum shift of 0.37 eV for Ge 3d and of 0.46 eV for Ge 2p towards higher binding energies, i.e., the bands are shifted downwards, as expected from Fig. 11.1a, by taking into account that $\Phi_{Ge} \approx 5.0$ eV (depending on doping) and $\Phi_{Cu} = 4.65$ eV [69]. One may therefore say that this is a "school case"; however, there are two important remarks:

(a) The Ge "bulk" component has a quite low shift. This implies that the band bending extends over the very first few layers of the Ge(001) crystal or,

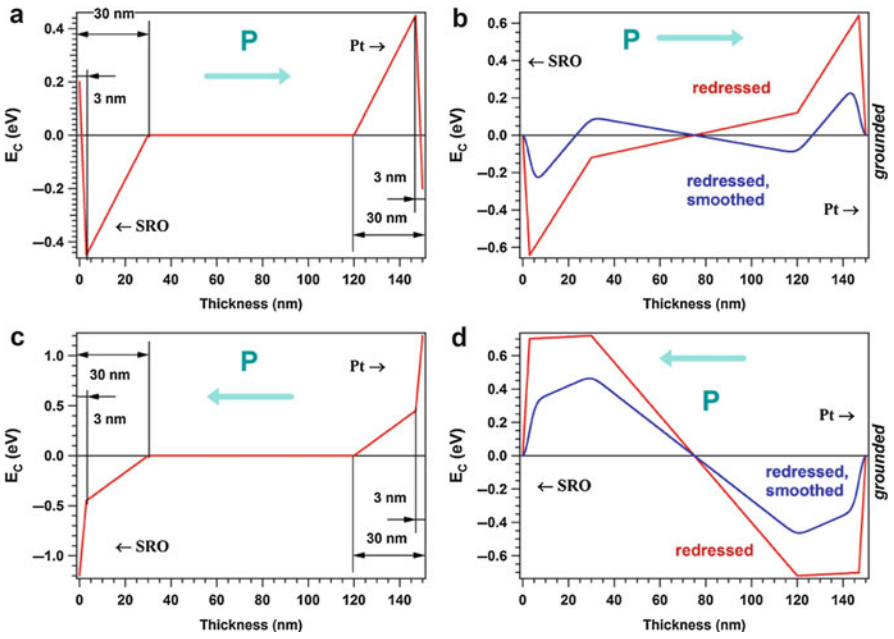


Fig. 11.15 Same as the two figures above, but for the case of the deposition of a metal (Pt) whose work function exceeds by 0.5 eV that of the ferroelectric

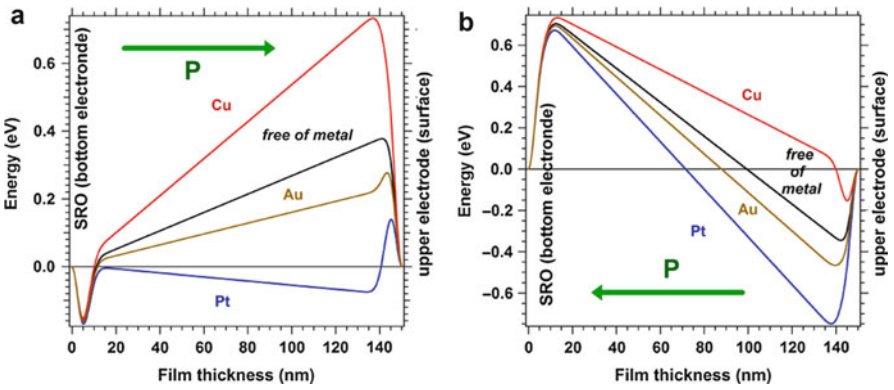


Fig. 11.16 Band bending for a free PZT surface and for Cu, Au, and Pt deposited on it, as resulted from the procedure outlined in the above graphs. The work functions are considered 5.1 eV for the ferroelectric thin film, 4.6 eV for Cu, 5.3 eV for Au, and 5.7 eV for Pt. The Schottky barrier region is considered 10 nm and $\delta = 3$ nm. (**a**) Outward polarization and (**b**) inward polarization

equivalently, the parameter l from Eq. 11.13 is quite low (below 1 nm). This implies that the density of electrons inside the Ge layer is at least $n_0 \sim 2 \times 10^{25}$ m^{-3}, which implies a high level of doping. The as-introduced sample had a much lower degree of doping (10^{21}–10^{22} m^{-3});

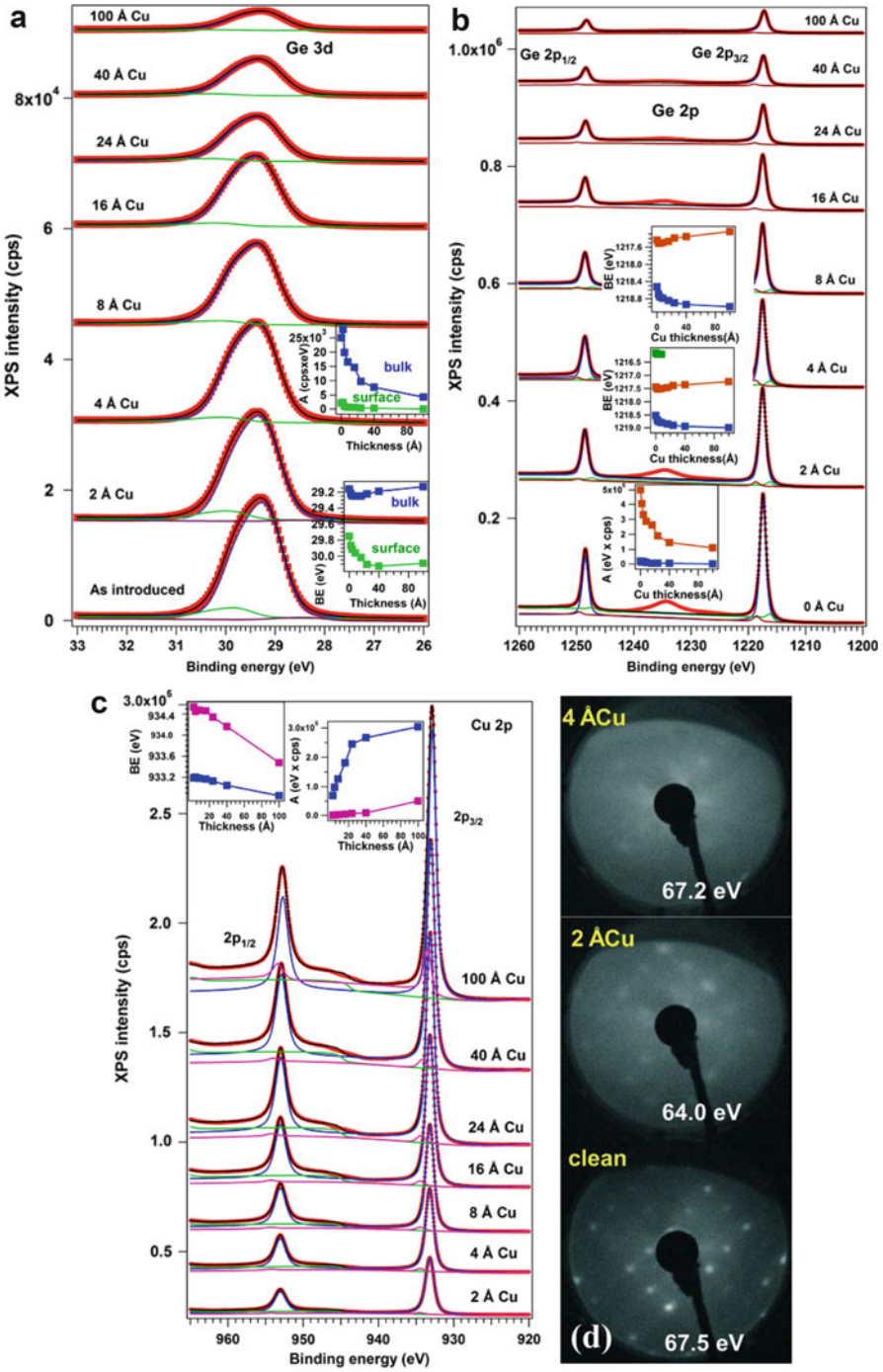


Fig. 11.17 (continued)

therefore, the high doping level in the near surface region is probably due to the Cu deposition.

(b) The Ge 2p shift is larger than that of Ge 3d. This could eventually be connected to the different probing depth of the two core-level spectroscopies, knowing that Ge 2p photoelectrons have lower kinetic energies (about 250 eV, to be compared with about 1,450 eV for Ge 3d). However, a fit of the exponential decay of the Ge 2p bulk component yields an inelastic mean free path of 12.7 Å, not much lower than that obtained for Ge 3d. On the other hand, the relative amplitude of the surface component for Ge 2p is about 4.4 % of the bulk component, whereas in the case of Ge 3d, it is about 8.6 %, almost the double, despite the fact that the latter spectrum is supposed to be less surface sensitive.

Therefore, an actual interpretation might be that the Ge 2p surface component really represents the outermost layer of Ge interacting with Cu, whereas the surface component used in the simulation of the Ge 3d spectrum represents at least two layers of Ge. Therefore, the progressive band bending with a low value of the parameter l affects the average binding energy obtained for Ge 3d, yielding a lower value of the band bending. Therefore, the most reliable value of the band bending is 0.46 eV, as was obtained from the Ge 2p spectrum. By assuming that the band bending obtained for Ge 3d is an average of two Ge layers, the second Ge layer should exhibit a band bending equal to $2 \times 0.37–0.46 = 0.28$ eV. The first two Ge layers are separated by about 1.4 Å. Therefore, a minimal value of the l parameter (assuming a linear decay) is $1.4 \times 0.46 / (0.46–0.28) = 3.6$ Å. By assuming that the surface Ge 3d component is obtained by averaging over three Ge layers, the decrease from one layer to the next is found to be 0.09 eV, and $l \approx 7.2$ Å. Also, one may derive that the initial work function of the Ge(001) crystal was $4.65 + 0.46 = 5.11$ eV, as expected from the moderate p-doping of the as-introduced crystal.

The lesson one can learn from this "school case" is that the band bending is not always extending over tens or hundreds of nanometers, as obtained from basic considerations and by using the bulk density of charge carriers, and that the "deconvolution" yields sometimes as "surface component" a component which may represent several atomic layers. Less problems are encountered when using high resolution photoelectron spectroscopy [109].

Au/PZT(001), Contaminated, Without Thermal Treatment: Standard Schottky Mechanism in Case of a Ferroelectric Surface

Figure 11.18 presents all core-level photoemission spectra obtained when Au is deposited onto a PZT layer. In the following, we will state a bit on the history of this layer, since it was proven that the history of a ferroelectric surface is crucial for its properties [47]. This layer was synthesized several months before Au deposition

Fig. 11.17 Core-level spectroscopy, together with analysis of integral intensities and binding energies of individual components for Cu deposited on Ge(001): (**a**) Ge 3d, (**b**) Ge 2p, and (**c**) Cu 2p. (**d**) Represents LEED patterns of clean Ge(001) $(2 \times 1) - (1 \times 2)$ and of the thinnest layers of Cu deposited on this substrate

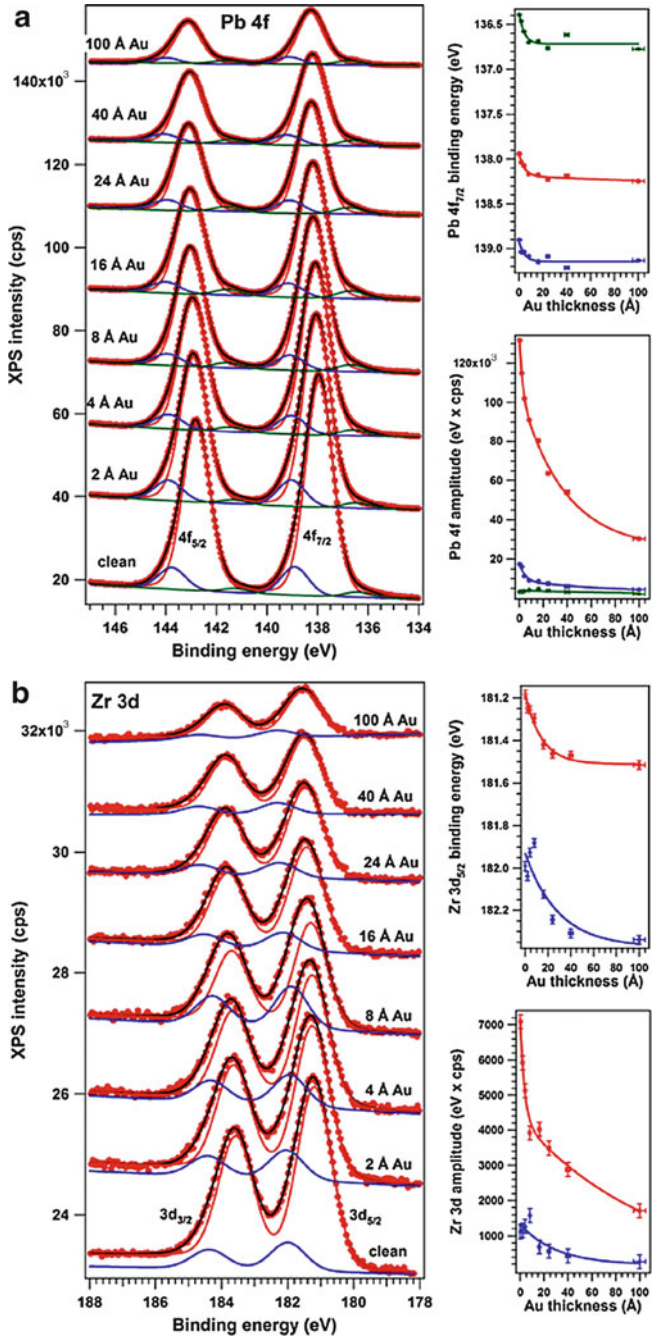


Fig. 11.18 (continued)

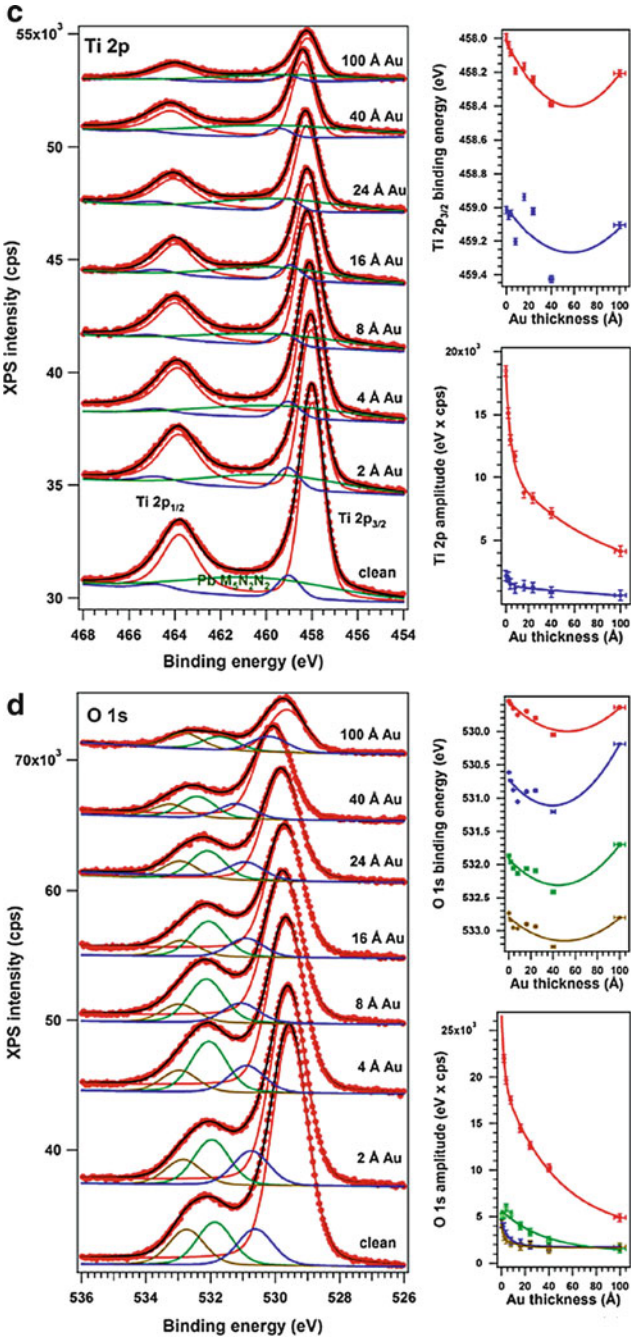


Fig. 11.18 (continued)

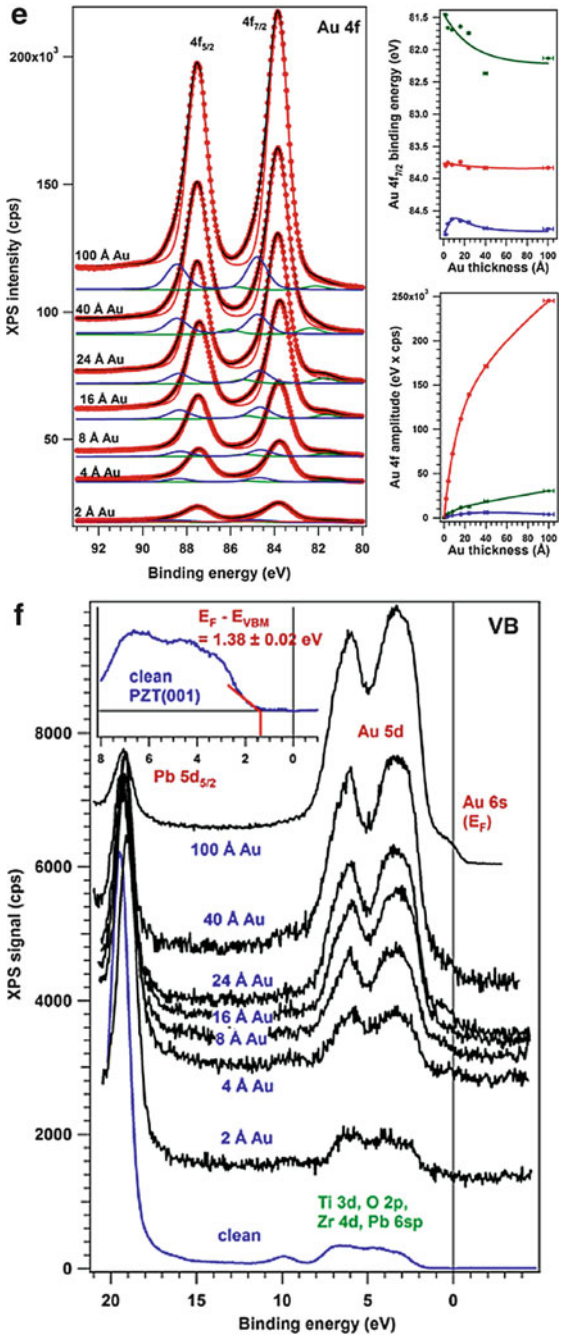


Fig. 11.18 (continued)

and XPS analysis, and its preparation conditions are reported to result in surfaces with outward polarization [110]. Although it was stored in clean conditions, one may infer that a large part of the surface is contaminated and the contaminant inhibits the out-of-plane polarization. Moreover, as can be seen from Fig. 11.19, Au is forming unconnected nano-islands of more than 10 nm typical dimensions. This manifests also in the XPS spectra by non-negligible signals of the substrate components (Pb, Zr, Ti) even when 100 Å of Au are deposited, which is about 6–8 times the inelastic mean free path and, therefore, the levels should have been attenuated by $\exp(-8) - \exp(-6) \approx 0.03$–$0.2$ %. Therefore, in this case we speak about the deposition of a discontinuous Au film on a contaminated PZT surface.

The binding energies obtained for the clean sample for the red component are 137.94 eV for Pb $4f_{7/2}$, 181.18 eV for Zr $3d_{5/2}$, 457.99 eV for Ti $2p_{3/2}$, and 529.54 eV for O 1s (±0.01 eV). These values are in fair agreement with the NIST XPS database [11] and with more recent work [111, 112]. The evolution of binding energies for all core levels investigated is consistent with a band bending towards lower energies (higher binding energies) of 0.45 ± 0.05 eV [14]; therefore,

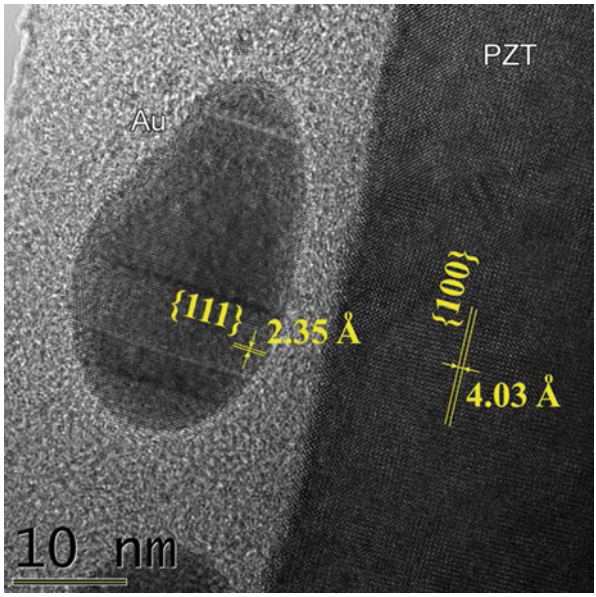


Fig. 11.19 High resolution transmission electron microscopy image of an isolated Au nanoparticle formed by gold deposition on PZT(001) (Unpublished material, courtesy of Dr. Corneliu Ghica)

Fig. 11.18 X-ray photoelectron spectroscopy for Au deposited on $Pb(Zr,Ti)O_3$ without thermal treatment of the substrate: (**a**) Pb 4f, (**b**) Zr 3d, (**c**)7 Ti 2p, (**d**) O 1s, and (**e**) Au 4 f. The valence band is represented in (**f**). Each series of spectra (with the exception of the valence bands) has been analyzed with Voigt lineshapes, and binding energies and integral amplitudes are plotted aside of each series of spectra. When the analyzed level is a doublet, the integral amplitude refers to the whole doublet, and the binding energy is that of the most intense line, i.e., that with $j = l + 1/2$ (Adapted from Ref. [14])

a model such as the one in Fig. 11.1a is valid also in this case, and $\Phi_{PZT} = \Phi_{Au} + 0.45$ eV ≈ 5.55 eV. In this case, the PZT layer seems to be p-doped, with a lower difference between E_F and E_V than half of the bandgap (1.7 eV). This is demonstrated also by the valence band spectra of Fig. 11.18f, where $E_f - E_V \approx 1.38$ eV. Moreover, all (Pb 4f, Zr 3d, Ti 2p, O 1s) spectra exhibit basically into two components attributed to the PZT layer, with similar relative intensity, of about 12–13 %. The smaller component, shifted towards a higher binding energy of about 0.94 eV, is attributed to areas from the PZT surface exhibiting outward polarization, according to the diagram of Fig. 11.3a. This shift of 0.94 eV is in range of the expected surface band bending of PZT, by taking into account that for BTO it was found as being close to 0.5 eV [16] and that PZT has a higher polarization than BTO. Note that there is a factor of 4 between the polarization of PZT and that of BTO, whereas the obtained experimental ration of band bending is only ~ 2. This result is in line with the theoretical simulations represented in Fig. 11.12 and commented in the previous section.

Interestingly, also the Au 4f spectrum exhibits this higher binding energy component; therefore, it is attributed to unconnected Au islands placed on the areas with outward $P^{(+)}$ polarization. Note also that, for Au 4f, simulations provided that within the experimental resolution (0.6 eV for both Lorentz $4f_{7/2}$ component and Gauss full widths at half maximum), it is almost impossible to resolve the surface component, shifted by about 0.4 eV towards higher binding energy [113].

Other features of the spectra presented in Fig. 11.18 include (a) the presence in the Pb 4f spectrum of a low binding energy component, which was attributed to a small amount (fraction of monolayer) of Pb or PbO at the surface, and (b) the presence in the Au 4f spectrum of a component of quite low binding energy, which was attributed to the formation of negative Au islands. The apparition of these islands is counterintuitive, by taking into account that we just inferred that PZT has a higher work function than Au; therefore, one expects electron transfer from the Au islands towards the PZT surface, leaving the islands positively ionized. However, smaller Au islands may have considerably increased work function (or ionization energies) [114]; therefore, these islands may pump electrons from the PZT layer and become negatively ionized. The overall charge transmitted to the PZT is, however, negative, and this is the origin of the observed band bending.

The O 1s spectra contain two additional lines at higher binding energies, which are attributed to hydrocarbon contamination [11]. The fact that there are two lines has to be connected to the presence of this contamination on areas of the sample with no out-of-plane polarization and with $P^{(+)}$ polarization. The fact that the ratio between the component with the highest binding energy and the other contamination component (the second in order of decreasing binding energy) is larger than 12–13 % (the ratio found for the core-level components from the substrate) is to be connected with the presence of a higher amount of contaminants on $P^{(+)}$ areas; this will be commented in the next paragraph.

Putting everything together, this case of Au discontinuous layer deposited on a contaminated PZT surface exhibited all features of the standard Schottky model; additionally, independent mechanisms with similar band bendings are

found to coexist for areas with outward ferroelectric polarization and for areas with no out-of-plane polarization.

5.3.2 Free Ferroelectrics: PZT(001), Sample History and Contamination

The fact that the sample history is important is reflected in Fig. 11.20, where core-level photoemission spectroscopy was recorded for freshly introduced samples (immediately after their preparation by PLD), 1 week after the preparation, and after annealing in ultrahigh vacuum [115]. The main observation is the presence of a well-defined component attributed to areas with $P^{(-)}$ polarization (inwards, oriented from the vacuum towards the ferroelectric layer) in Ti 2p and O 1s spectra, while for the same sample the C 1s core level is shifted by about 1 eV towards higher binding energy.

In XPS data analysis, quite often the "adventitious" carbon contamination is taken as reference for binding energies: its value is set to 284.6 eV [11], and all the other core-level binding energies are calibrated with the shift derived for C 1s between the experimental value and the above value. However, in this case this procedure cannot yield accurate results for Ti 2p and O 1s. Not only these lines are found to unusually low binding energies, but shifting them further towards lower energies yields binding energies which cannot be explained at all.

Figure 11.21 presents piezoresponse force microscopy (PFM) data, showing the progressive contamination of a PZT(001) layer, and it may be seen in Fig. 11.21b that the contamination seems to adhere preferentially on areas of one given orientation of polarization.

This puzzle was solved by Stoflea et al. in Ref. [115], by noting that all other C 1s level spectra had maxima at the generally accepted value for "adventitious contamination," 284.6 $\pm$ 0.1 eV. Therefore, for the particular case of the "fresh" sample, it may be supposed that a large majority of contamination carbon is found on areas with $P^{(+)}$ polarization, whereas areas with $P^{(-)}$ polarization are free of carbon. Owing to inelastic mean free path effects, the intensities of the substrate core levels originating from the $P^{(+)}$ areas are attenuated and the spectra of the "fresh" sample are dominated by signals originating from $P^{(-)}$ areas, shifted towards lower binding energies. The mechanism is schematized in Fig. 11.22, where it is shown how contamination adhering on $P^{(+)}$ areas quench the substrate signal originating from these areas and how, once the contamination affects also the $P^{(-)}$ areas, it realizes a shortcut between surface with different charges, yielding to the loss of the out-of-plane polarization. In Fig. 11.22d the contaminant was considered a fatty acid molecule, with an anionic head and with the positive charge distributed over the whole alkyl chain. It is understandable that a much stronger interaction is expected to occur between the anionic head and a positively charged surface than between the cationic tail and a negatively charged surface.

Note also that the shifting towards lower BE for $P^{(-)}$ areas is much more visible in the O 1s and Ti 2p spectra than in the Pb 4f and Zr 3d spectra. This was connected in Ref. [115] to the ionicity of the $Ti^{4+}O^{2-}$ bonds, which may accommodate additional charge, whereas more covalent bonds (PbO, ZrO) have a lower affinity to accommodate additional electrons.

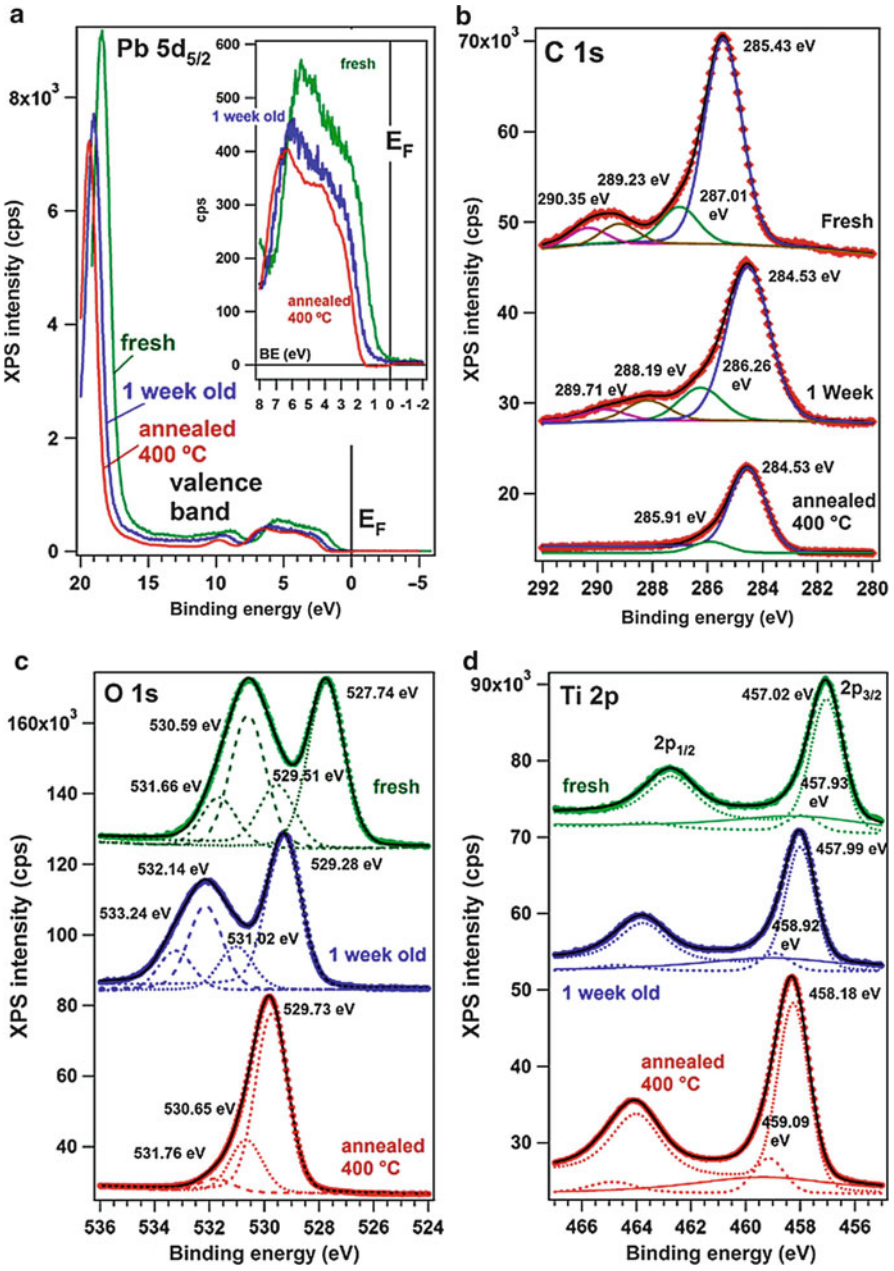


Fig. 11.20 (continued)

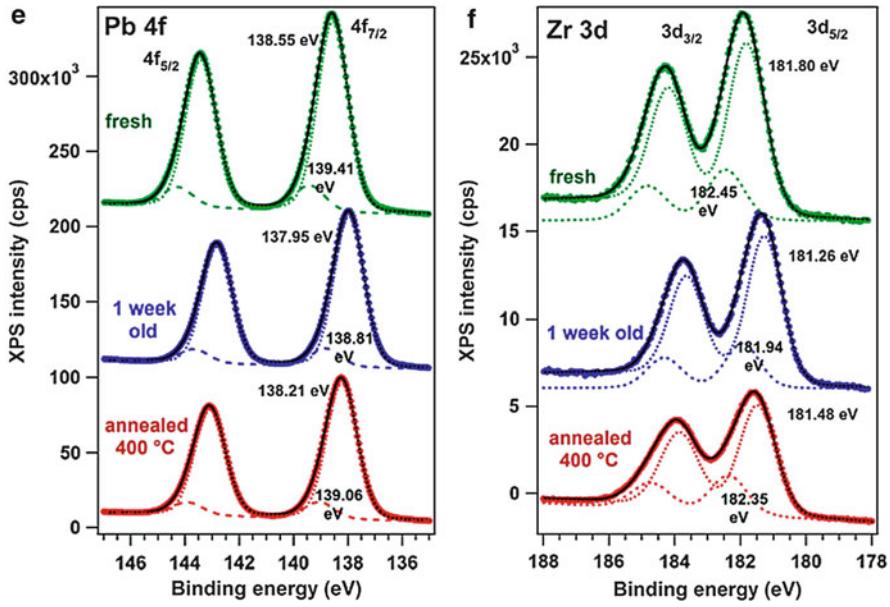


Fig. 11.20 Photoemission analysis of three samples: the fresh one (*green curves*), the "1-week-old" sample (*blue curves*), and a sample annealed at the highest temperature from the series (400 °C). (**a**) Represents valence band spectra, (**b**) C 1s, (**c**) O 1s, (**d**) Ti 2p, (**e**) Pb 4f, and (**f**) Zr 3d core-level spectra. The increase in binding energy is clearly seen for Ti 2p and O 1s, together with the decrease in binding energy for C 1s (Reproduced from Ref. [115])

Similar observations were recently reported, by using mainly the temperature programmed desorption technique [116–119]. Differences of 100 K are observed between the desorption temperatures of polar molecules (2-propanol [116] or acetic acid [117]), from $LiNbO_3$(0001) exhibiting outward ($P^{(+)}$) or inward ($P^{(-)}$) polarization. For nonpolar molecules (dodecane [117]), no dependence on the initial polarization state of the substrate is reported. Dissociative adsorption on polar surfaces (e.g., 2-fluoroethanol) may occur, with differences in the activation energies of product formation (acetaldehyde) between different substrate ($BaTiO_3$) polarization state [118]. Similar results (15–20 K desorption temperature differences) are reported on water and methanol on $LiNbO_3$ [119]. However, the actual data promote XPS as a suitable method to investigate surface reactions at ferroelectric surfaces.

5.3.3 Continuous Metal Layers Deposited on Ferroelectrics

We remember that Au produced nano-islands when deposited on PZT(001), whereas the Cu layers obtained on Ge(001) are continuous. Cu deposited on PZT(001) without thermal treatment results also in a continuous layer, as can be seen from the substrate core levels represented in Fig. 11.23a–d.

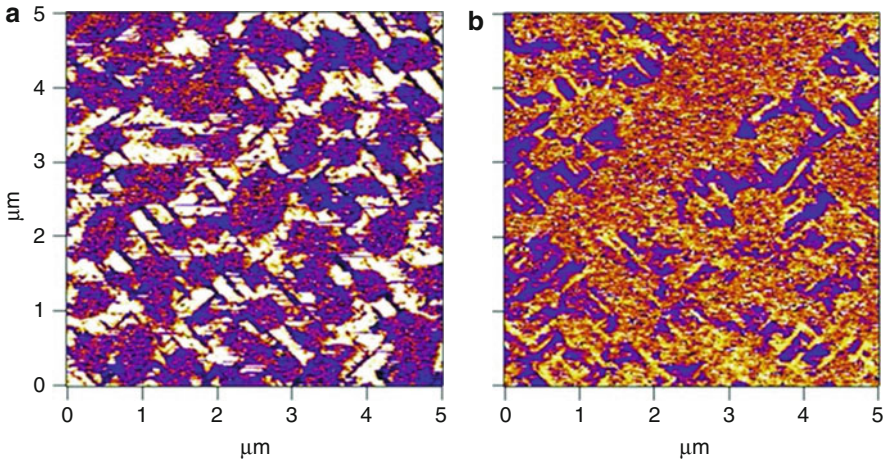


Fig. 11.21 Piezoresponse force microscopy (PFM) on clean PZT samples: (**a**) a fresh surface; (**b**) a surface after a few days of supporting ambient environment (Adapted from Ref. [53])

For a 100 Å Cu layer, the substrate levels are severely attenuated, which was not the case for Au/PZT(001) (see Fig. 11.18).

The binding energy evolution in this case exhibits a non-monotonous behavior: for thinnest layers of Cu deposited, the BE increases; therefore, the bands are bended towards lower energies, as expected from a Schottky contact when the work function of the metal is lower than that of the semiconductor, Fig. 11.1a. Starting with a thickness θ_0 of about 8 Å, the BE evolution reverses its sign; the shifts are now towards lower BE, i.e., higher energies. Apostol and coworkers [33] solved this problem by supposing that at the thickness θ_0 the Cu layer, which forms unconnected islands at the early stages of growth (just like Au), percolates into a continuous layer and it ensures the grounding of the surface of the ferroelectric layer [32, 33]. Therefore, the potential of the surface will be fixed for thicker layers of Cu, to the same value as that of the bottom electrode. This implies a band bending such as that represented in Fig. 11.16, with the existence of a nonvanishing electric field inside the ferroelectric thin film. At the end, one recovers the situation of a standard Schottky diode formed by a layer with no polarization perpendicular to the surface with an electrode with lower work function.

There are two hypothesis to be confirmed: the first one is that, indeed, the initial surface presents $P^{(+)}$ polarization on its area. This was confirmed by PFM recorded on a "witness" sample prepared simultaneously with the one covered by Cu and analyzed by XPS, represented in Fig. 11.24. The scans represented are obtained after PFM writing on the substrate of a well-defined pattern, consisting on a larger square of $P^{(+)}$ orientation (negative tip voltage) surrounding a smaller square with $P^{(-)}$ orientation (positive tip voltage), as shown in the insert of Fig. 11.24. The scan after PFM writing showed only the $P^{(-)}$ area; therefore, the remaining parts of the surface exhibit $P^{(+)}$ polarization.

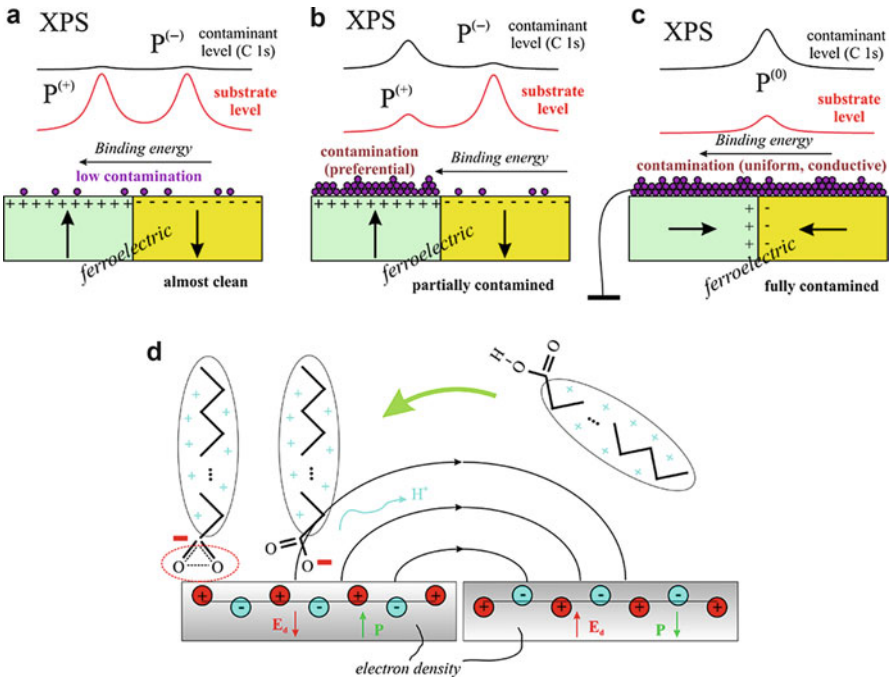


Fig. 11.22 Mechanism proposed to justify the observations from XPS spectra of Fig. 11.20 (**b–d**). In (**a**), an almost clean surface is represented, with different signatures of outward and inward polarized areas. In (**b**), the outward polarized area starts to get contaminated; therefore, the corresponding core levels from the substrate are attenuated, whereas the contaminant's core level experiences the positive charge state of the surface. In (**c**), the sample is fully contaminated. The contaminant grounds the sample and the weak core levels from the substrate correspond to a situation with no polarization perpendicular to the sample surface. In (**d**), a mechanism is schematized yielding to preferential adsorption of fatty acids on areas with outward polarization (Adapted from Ref. [115])

The second hypothesis to be checked is the presence of Cu nano-islands, and this was tested by high resolution transmission electron microscopy, represented in Fig. 11.25. One may notice that both isolated and coalescing Cu islands exist on the 100 Å Cu film. Therefore, the hypothesis of an initial growth of isolated islands, then, after a critical thickness, of an electrically continuous Cu film is reasonable.

Detailed analysis, presented in Ref. [33], supposes a basic mechanism of purely electronic origin for compensation of band bending at the PZT surface covered by Cu. The presence of the metal contacted to the ground allows one to inject inside the ferroelectric layer excess electrons which contribute to the "depolarization charge sheet" represented in Fig. 11.3a. This allows the "rectification" of the energy bands, as represented also in Fig. 11.26. This mechanism was named by Apostol, Stoflea, and coworkers "overcompensation."

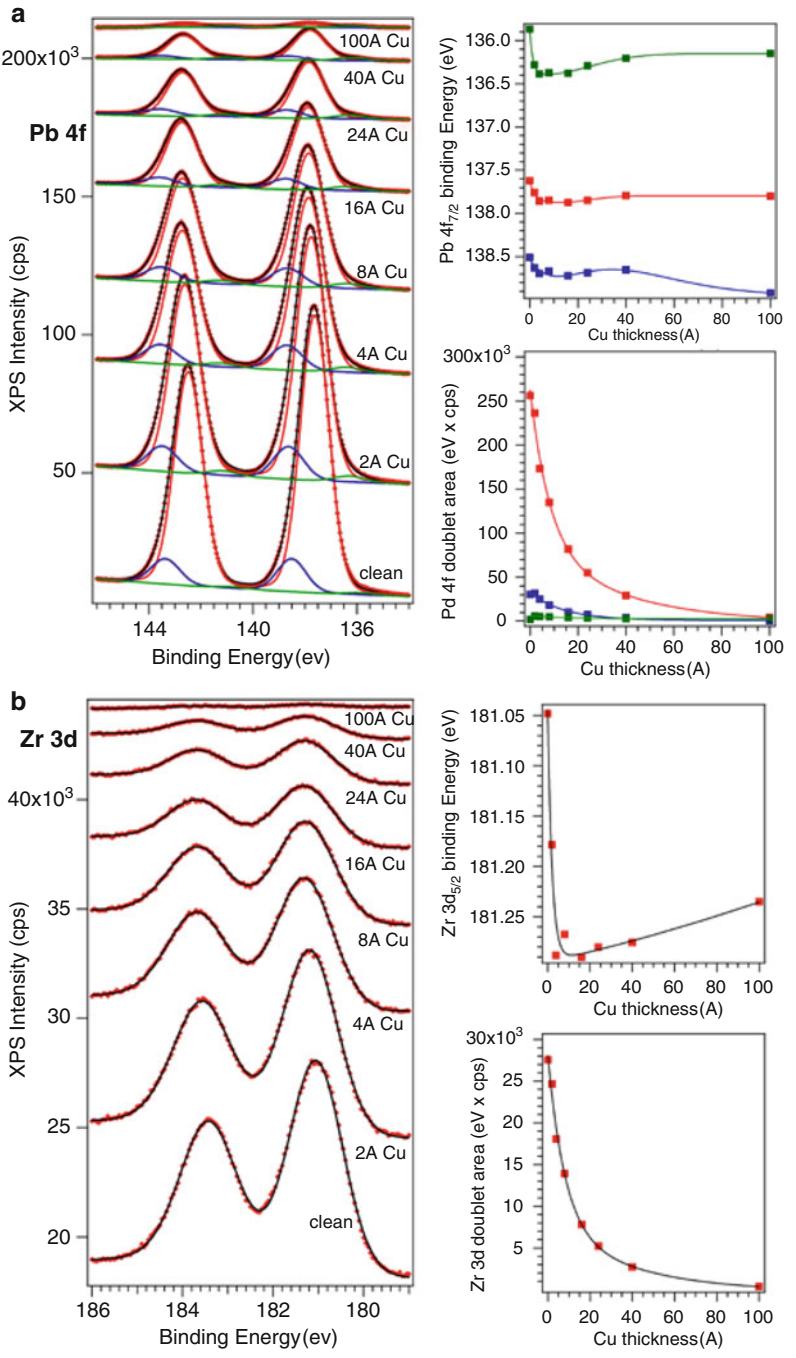


Fig. 11.23 (continued)

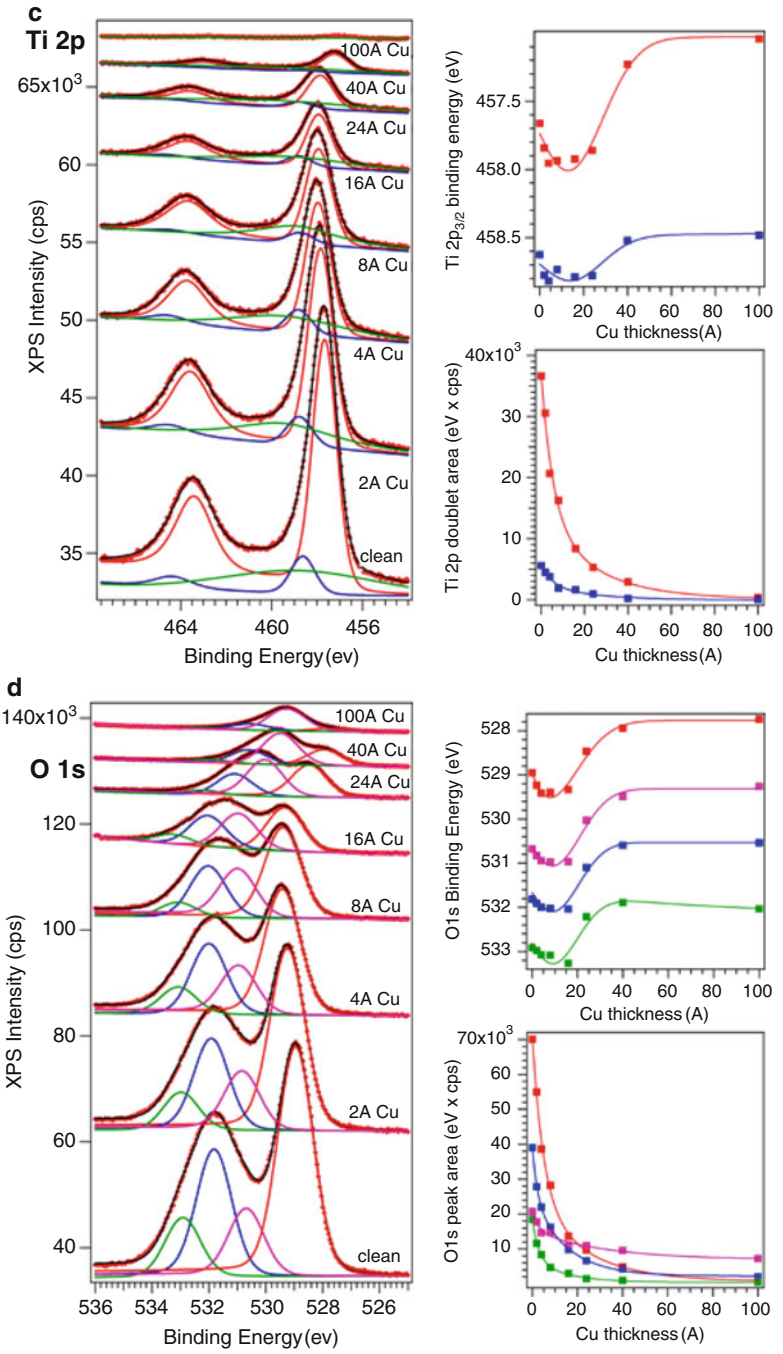


Fig. 11.23 (continued)

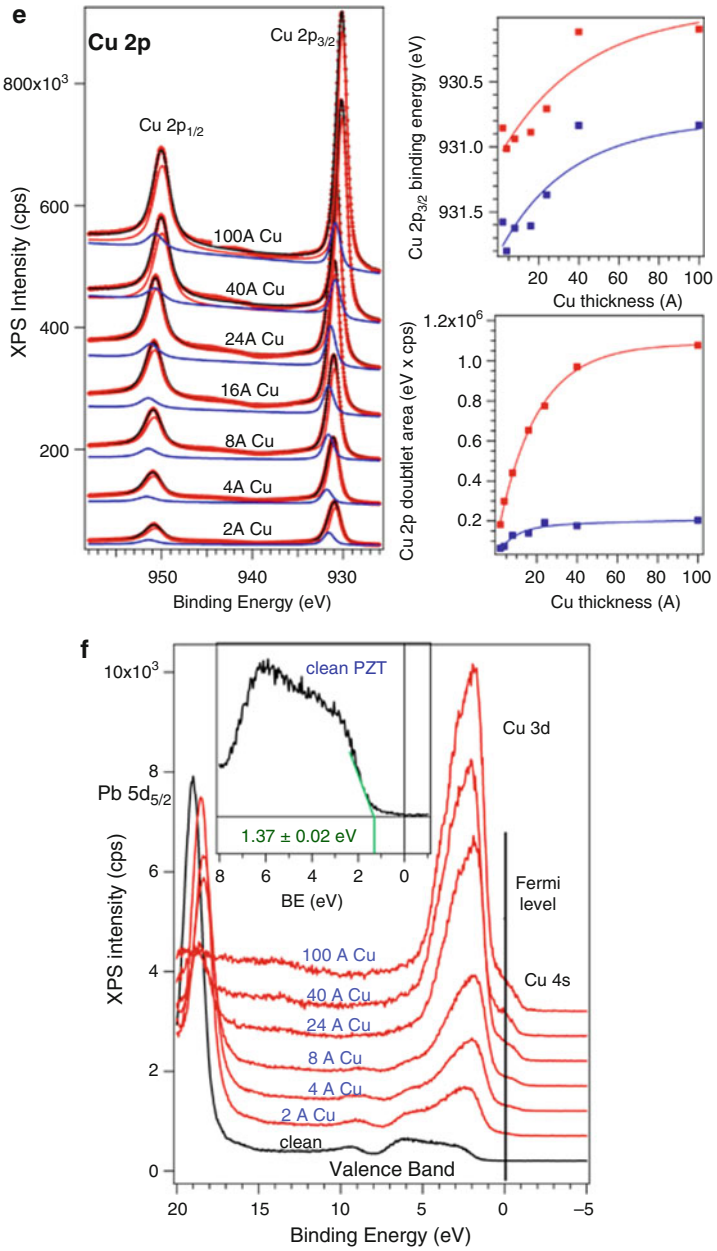


Fig. 11.23 Photoelectron spectroscopy analysis of Cu deposited on PZT without thermal treatment: (**a**) Pb 4f, (**b**) Zr 3d, (**c**) Ti 2p, (**d**) O 1s, (**e**) Cu 2p, and (**f**) valence band. For core-level spectra, two panels are added to represent the binding energy and integral intensity evolutions (see the caption of Fig. 11.17) (Adapted from Ref. [33])

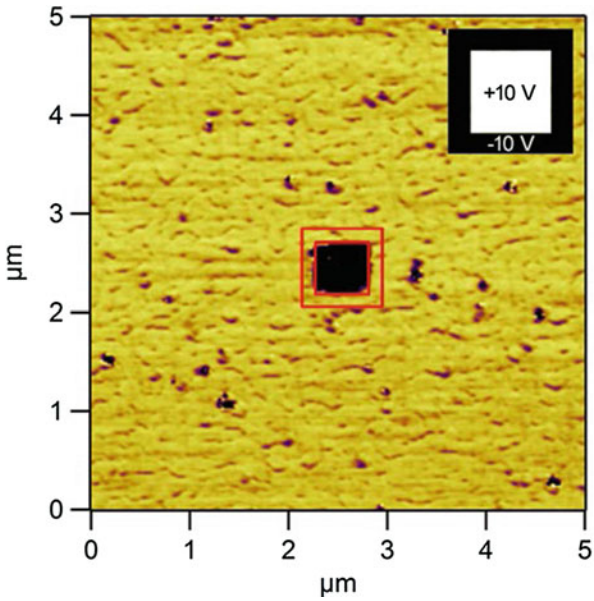


Fig. 11.24 Piezoresponse force microscopy of a PZT film from the same generation as the one used for Cu depositions. The scans are performed after poling the surface according to the represented pattern in the corner of the image (a small square with inward polarization inside a larger square with outward polarization). The fact that no contrast can be seen between the $P^{(+)}$ written area and the remaining part of the surface is attributed to the $P^{(+)}$ polarization imprint of the whole surface (Extracted from Ref. [33])

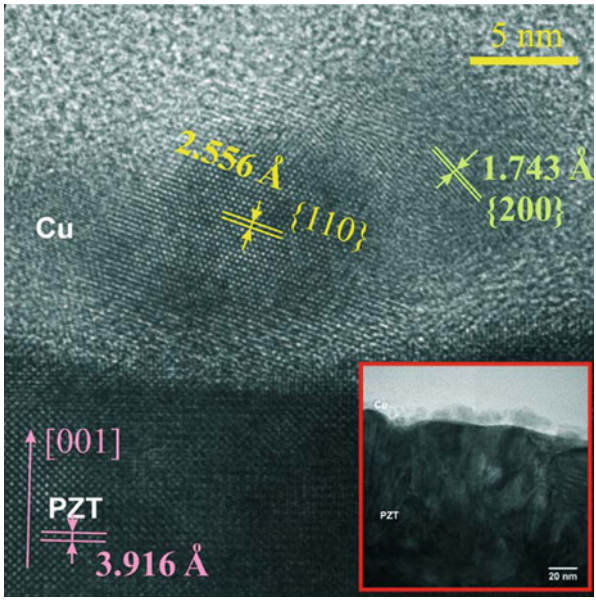


Fig. 11.25 High resolution transmission electron microscopy of a Cu/PZT film of 10-nm nominal thickness. The formation of Cu nanoparticles is clearly seen. Also, the *inset* represents a lower resolution image showing the coalescence of these nanoparticles

Nevertheless, though all phenomena presented before are intuitive enough, other mechanisms of pure ionic origin may be proposed to assess this loss of band bending at the surface of the ferroelectric by metal deposition. Knowing that there is an interplay between the distortion from the cubic symmetry yielding the

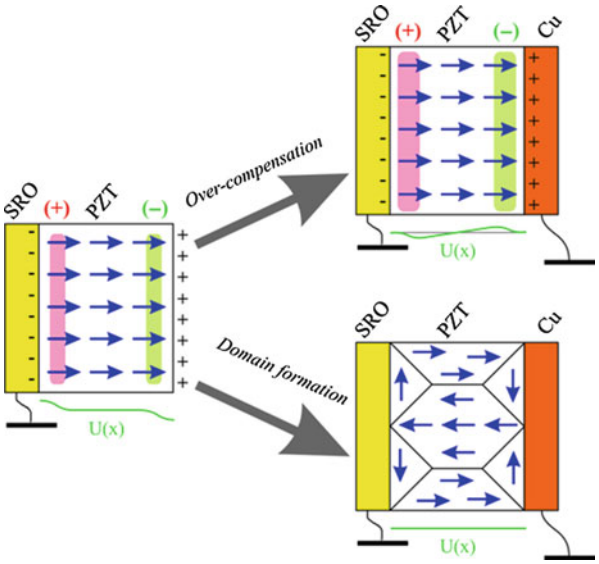


Fig. 11.26 Two proposed mechanisms for losing the polarization-induced band bending at the surface of the ferroelectric. The first one (**a**) is the overcompensation due to additional electrons provided by the grounded metal electrode in order to equalize the potential of the surface with that of the buffer metal layer. The second one implies formation of 90° domains with in-plane polarization

ferroelectric polarization and the local charge density and fields created by its inhomogeneity, it may happen that, upon Cu deposition yielding to the grounding of the surface of the ferroelectric, 90° domains are formed, such as the surface ferroelectric is oriented in plane. There are several theoretical computations [120, 121] yielding such behavior. The key experiments that have to be performed to check all these theoretical assumptions are X-ray photoelectron diffraction experiments, which, when analyzed properly, are able to detect lattice relaxation and rumpling over the first few atomic layers [76]. This will help to validate one of the two mechanisms sketched in Fig. 11.26.

A third mechanism proposed by Apostol et al. in Ref. [33] is represented by Eq. 11.24 and stems in the decrease of the ferroelectric polarization when excess electrons are provided by the Cu contact connected to the ground of the system. As mentioned above, additional experiments are needed to confirm which one of the three proposed mechanisms is the dominant one.

5.3.4 Metal Layers Deposited on Ferroelectrics Subject to Thermal Treatments

As mentioned in Sects. 4 and 4.1, quite often ferroelectric layers are thermally treated in order to produce surface oxygen vacancies, which act as n-type dopants, to improve the conductivity properties of the surfaces and to eliminate charging effects yielding undesired shifts of photoemission peaks. By taking into account the considerations from Sect. 5.2.3, together with the recently discussed case of continuous Cu layers grown on PZT(001), it results that the band bendings obtained for conductive surfaces, whose surface potential is fixed to that of the bottom electrode, may differ from that obtained for more insulating surfaces.

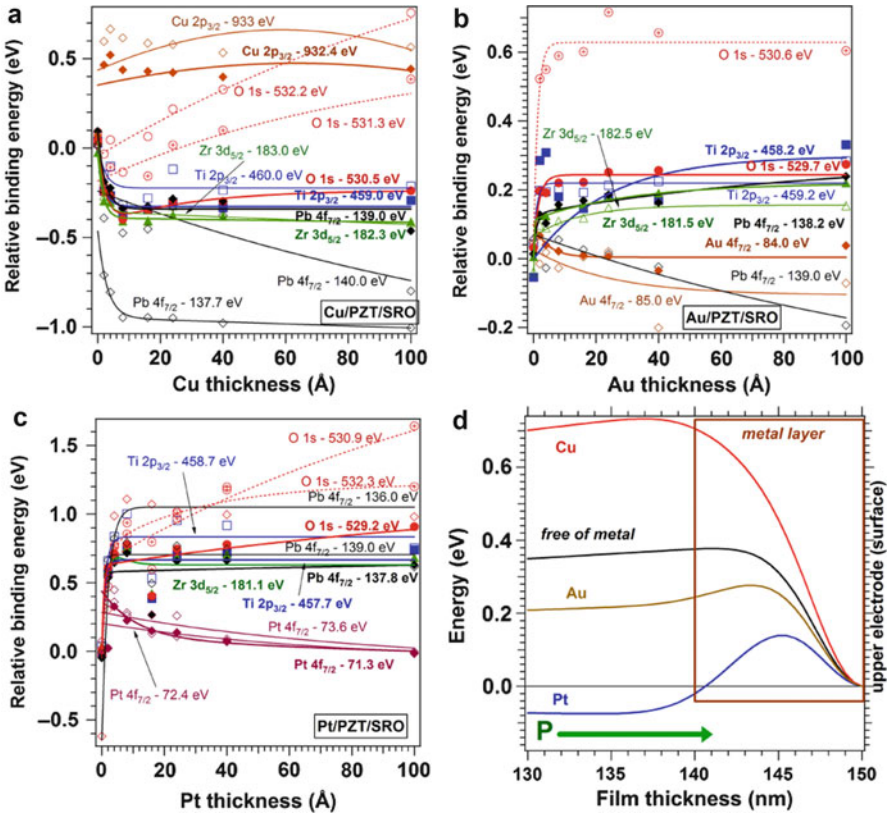


Fig. 11.27 Overview of binding energies for Cu, Au, and Pt deposited on PZT subject to thermal treatment: (**a**) the Cu/PZT case, (**b**) the Au/PZT case, and (**c**) the Pt/PZT case. *Thicker lines* represent the major components of each spectrum. (**d**) Represents a cut from Fig. 11.16a, limited to the outermost 20 nm of the ferroelectric layer

Figure 11.27 presents an overview of all binding energy dependences obtained for several thicknesses of Cu (a), Au (b), and Pt (c) grown on PZT [122]. Achieving these dependencies was a considerable amount of work, including the deconvolutions of over 100 spectra. The main component for each spectrum is represented by thicker lines. The net result of the whole analysis is expressed in three numbers: the band bending of Cu/PZT(001) is by 0.45 eV upwards (lower BE), whereas for Au and Pt, it is downwards (higher BE) by 0.24 eV and 0.65 eV, respectively. From the very beginning we must state that counterintuitive results are obtained if one takes into consideration just a simple Schottky model (assume that $\Phi_{PZT} \approx 5.1$ eV): thus, the band bending should have been by about 0.4 eV downwards for Cu, negligible or upwards by 0.2 eV for Au, and by about 0.6 eV upwards for Pt, according to the models sketched in Fig. 11.1. One obtains experimentally, within a good approximation, the opposite of the computed band bendings by differences in work functions.

The key to understand these dependencies are, again, related to the interplay between the ferroelectric-induced band bending and the Schottky effect. The band bending for copper is within a good approximation the final band bending from the previous case (Cu deposited onto PZT without thermal treatment, Fig. 11.23). This might be due to the fact that the substrates investigated in this paragraph are cleaner and exhibit more conductive surfaces; probably, Cu forms more easily continuous layers starting with the lowest amounts of Cu deposited. Similar behaviors are expected for Pt and, to some extent, also for Au.

In Fig. 11.27d we reproduced partially the energy curves from Fig. 11.16a for the outermost 20 nm of the layer, and one may notice that the shifts observed actually may be well simulated by these energy curves provided the *biggest band curvature (towards zero potential energy) takes place inside the deposited metal layer*. Therefore, the potential is zero at the metal's surface only; going deeper inside the metal layer, one obtains nonzero potential energy, probably because the metal is not continuous and has reacted with the semiconductor and probably has also to some grain boundaries or inclusions of contaminants. The polarization of the ferroelectric may also play a role in establishing the finite resistivity of the metal layer.

Alternatively, a similar result may be obtained by inferring quite low values of the δ and l typical bending length parameters, owing to the charge transferred from the metal into the ferroelectric, in a similar way it was detected for Cu/Ge(001).

Another mechanism which may be proposed to explain this unusual behavior of band bendings on thermally treated surfaces is the *overcompensation* in case of Cu with lower work function (discussed in Sect. 5.3) and the *under-compensation* in case of Au and Pt with higher work functions (which will pump electrons from the surface of the PZT layer, reducing the charge of the depolarization sheet). Therefore, in this case a strengthening of the band bending is, in fact, observed. In any case, both hypotheses formulated here: (i) extent of the most important variation of the band bending inside the metal and (ii) overcompensation vs. under-compensation of depolarization charge sheets point on the unusual behavior of band bendings when ferroelectrics are interfaced with metals and support the high interest dedicated during the last decade to their heterostructures.

6 Conclusions and Future Perspective

The ability of X-ray photoelectron spectroscopy to quantify band bendings at surfaces and interfaces was reviewed, together with some theoretical sketches of the basic principles of band bendings. The typical cases, which may now be explained quite easily, are metal–semiconductor Schottky contacts and free ferroelectric surfaces. The case of metal–ferroelectric interfaces present intriguing phenomena involving mechanism related to the charge redistribution owing to the presence of the metal, which may yield overcompensation or under-compensation of the depolarization charge sheet, without forgetting also the interplay between this charge redistribution and the ferroelectric polarization due to ion displacement in the lattice.

Experimentally, we have shown that XPS is able in some cases to estimate also the spatial extent of the band bending. For instance, in the case of Cu/Ge(001) it was found that this spatial extent is much lower than the computed value by using the equilibrium charge density. For free ferroelectric surfaces, we have seen how areas with outward and inward polarization can be identified via the binding energies of the atomic constituents of the samples and how one can evidence new surface phenomena, such as the preferential adsorption of contaminants on areas with outward polarization. Metal/ferroelectric interfaces exhibit also a wide variety of phenomena, going from the standard Schottky behavior up to the loss of the ferroelectric polarization due to the grounding of the sample surface due to the metal layer. Finally, for ferroelectric surfaces with slightly conductive properties, it is found that the observed band bending is opposed to the one expected by the Schottky model, and some hypotheses are formulated to explain this unusual behavior.

The field is rapidly growing, especially in what concerns ferroelectric surfaces and their interaction with adsorbates and with metals deposited on them. One expects that in the near future new structural data will be available, possibly also from XPS-based techniques (such as X-ray photoelectron diffraction), to elucidate clearly the interplay between the charge redistribution and the possible structural changes at these surfaces.

Also, quite recently, the scientific community started to be aware on the enormous potential presented by charged surfaces and by ferroelectrics for catalysis. To this functionality, the fact that on ferroelectric surfaces negatively charged noble metal clusters may be stabilized may act in a synergistic way. Therefore, a completely new area is expected to emerge pointing on the interplay between the ferroelectric or the surface charge state with molecular reactions at surfaces and interfaces. It is clear that one of the principle techniques which will be used to investigate such processes will be photoelectron spectroscopy, especially by using synchrotron radiation and near ambiental pressure setups. In order to correctly assess all the data expected to emerge from these studies, reliable derivation of band bending effects will be of prime importance.

Acknowledgements This work was supported by the RO-FR contract "chemical switching of surface ferroelectric topology" (CHEM-SWITCH), which started in 2013. Discussions with Lucian Pintilie are gratefully acknowledged. We acknowledge also contributions from Laura Stoflea, who participated in the XPS data acquisition and analysis on ferroelectrics; Cristina Chirila with the ferroelectrics sample preparation; Lucian Trupina with the PFM analysis; George A. Lungu, Liviu C. Tanase, and Cristina I. Bucur who participated in the Cu/Ge(001) experiment; and Raluca Negrea and Corneliu Ghica for the high-resolution transmission electron microscopy.

References

1. Sze SM (1981) Physics of semiconductor devices. Wiley, Hoboken
2. Cowley AM, Sze SM (1965) Surface states and barrier height of metal–semiconductor systems. J Appl Phys 36(10):3212–3220

3. Waldrop JR, Grant RW (1996) Measurement of AlN/GaN(0001) heterojunction band offsets by x-ray photoemission spectroscopy. Appl Phys Lett 68(20):2879–2881
4. Sezen H, Suzer S (2013) XPS for chemical- and charge-sensitive analyses. Thin Solid Films 534:1–11
5. Duan TL, Pan JS, Ang DS (2013) Interfacial chemistry and valence band offset between GaN and Al_2O_3 studied by X-ray photoelectron spectroscopy. Appl Phys Lett 102(20):201604:1–201604:4
6. Kakushima K, Okamoto K, Tachi K, Song J et al (2008) Observation of band bending of metal/high-k Si capacitor with high energy x-ray photoemission spectroscopy and its application to interface dipole measurement. J Appl Phys 104(10):104908:1–104908:5
7. Akazawa M, Gao B, Hashizume T, Hiroki M et al (2011) Measurement of valence-band offsets of InAlN/GaN heterostructures grown by metal-organic vapor phase epitaxy. J Appl Phys 109(1):013703:1–013703:8
8. Chiam SY, Liu ZQ, Pan JS, Manippady KK et al (2012) Effects of electric field in band alignment measurements using photoelectron spectroscopy. Surf Interface Anal 44(8): 1091–1095
9. Scott JF (2000) Ferroelectric memories. Springer, Berlin
10. Hüfner S (2003) Photoelectron spectroscopy: principles and applications. Springer, Berlin
11. NIST XPS database. http://srdata.nist.gov/xps
12. Crist BV (2004) Handbook of monochromatic XPS spectra. The elements and native oxides, vol 1. Commercially pure binary oxides, vol 2. XPS International, Mountain View
13. Ibach H (1977) Electron spectroscopy for surface analysis. Springer, Berlin
14. Apostol NG, Stoflea LE, Lungu GA, Chirila C et al (2013) Charge transfer and band bending at Au/Pb(Zr, Ti)O3 interfaces investigated by photoelectron spectroscopy. Appl Surf Sci 273:415–425
15. Wagner CD, Davis LE, Zeller MV, Taylor JA et al (1981) Empirical atomic sensitivity factors for quantitative analysis by electron spectroscopy for chemical analysis. Surf Interface Anal 3(5):211–225
16. Chen F, Klein A (2012) Polarization dependence of Schottky barrier heights at interfaces of ferroelectrics determined by photoelectron spectroscopy. Phys Rev B 86(9): 094105:1–094105:7
17. Pancotti A, Wang J, Chen P, Tortech L et al (2013) X-ray photoelectron diffraction study of relaxation and rumpling of ferroelectric domains in $BaTiO_3$(001). Phys Rev B 87(18):184116:1–184116:10
18. Teodorescu CM, Esteva JM, Karnatak RC, El Afif A (1994) An approximation of the voigt I profile for the fitting of experimental X-ray absorption data. Nucl Instrum Methods Phys Res, Sect A 345(1):141–147
19. Mardare D, Luca D, Teodorescu CM, Macovei D (2007) On the hydrophilicity of nitrogen-doped TiO_2 thin films. Surf Sci 601(18):4515–4520
20. Luca D, Teodorescu CM, Apetrei R, Macovei D et al (2007) Preparation and characterization of increased-efficiency photocatalytic $TiO_{2-2x}N_x$ thin films. Thin Solid Films 515(24): 8605–8610
21. Apostol NG, Stoflea LE, Lungu GA, Tanase LC et al (2013) Band bending in Au/Pb(Zr, Ti)O3 investigated by X-ray photoelectron spectroscopy: dependence on the initial state of the film. Thin Solid Films 545:13–21
22. Schlaf R, Parkinson BA, Lee PA, Nebesny KW et al (1998) Photoemission spectroscopy of LiF coated Al and Pt electrodes. J Appl Phys 84(12):6729–6736
23. Schlaf R, Schroeder PG, Nelson MW, Parkinson BA et al (1999) Observation of strong band bending in perylene tetracarboxylic dianhydride thin films grown on SnS_2. J Appl Phys 86(3):1499–1509
24. Schlaf R, Merritt CD, Crisafulli LA, Kafafi ZH (1999) Organic semiconductor interfaces: discrimination between charging and band bending related shifts in frontier orbital line-up measurements with photoemission spectroscopy. J Appl Phys 86(10):5678–5686

25. Bierwagen O, Speck JS, Negata T, Chikyow T et al (2011) Depletion of the In_2O_3(001) and (111) surface electron accumulation by an oxygen plasma surface treatment. Appl Phys Lett 98(17):172101:1–172101:3
26. Gheorghe NG, Lungu GA, Costescu RM, Popescu DG et al (2011) Enhanced contamination of Si(001) when analyzed with AES with respect to XPS. Optoelectron Adv Mater-Rapid Commun 5(5–6):499–504
27. Gheorghe NG, Lungu GA, Costescu RM, Teodorescu CM (2011) Significantly different contamination of atomically clean Si(001) when investigated by XPS and AES. Phys Status Solidi (b) – Basic Solid State Phys 248(8):1919–1924
28. Hirose K (2010) XPS time-dependent measurement of SiO_2/Si and $HfAlO_x$/Si interfaces. J Electron Spectrosc Relat Phenomena 176(1–3):46–51
29. Bersch E, Di M, Consiglio S, Clark RD et al (2010) Complete band offset characterization of the HfO_2/SiO_2/Si stack using charge corrected X-ray photoelectron spectroscopy. J Appl Phys 107(4):043702:1–043702:13
30. Dragoi C, Gheorghe NG, Lungu GA, Trupina L et al (2012) X-ray photoelectron spectroscopy of pulsed laser deposited Pb(Zr, Ti)O3−δ. Physica Status Solidi (a) – Appl Mater Sci 209(6):1049–1052
31. Galca AC, Stancu V, Husanu MA, Dragoi C et al (2011) Substrate-target distance dependence of structural and optical properties in case of Pb(Zr, Ti)O3 films obtained by pulsed laser deposition. Appl Surf Sci 257(14):5938–5943
32. Apostol NG (2013) Surfaces of elemental and oxide semiconductors and interfaces of them with metals deposited by molecular beam epitaxy. PhD thesis, "I.G. Murgulescu" Institute of Chemical Physics Bucharest (in Romanian; unpublished)
33. Stoflea LE, Apostol NG, Chirila C, Trupina L et al (2013) Schottky barrier versus surface ferroelectric depolarization at Cu/Pb(Zr,Ti)O_3 interfaces. J Mater Sci (resubmitted with minor revisions)
34. Chen F, Schafranek R, Wu WB, Klein A (2009) Formation and modification of Schottky barriers at the PZT/Pt interface. J Phys D Appl Phys 42(21):215302:1–215302:5
35. Chen F, Schafranek R, Wu WB, Klein A (2011) Reduction-induced Fermi level pinning at the interfaces between Pb(Zr, Ti)O_3 and Pt, Cu and Ag metal electrodes. J Phys D Appl Phys 44(25):255301:1–255301:7
36. Li SY, Ghinea C, Bayer TJM, Motzko M et al (2011) Electrical properties of (Ba, Sr)TiO_3 thin films with Pt and ITO electrodes: dielectric and rectifying behaviour. J Phys Condens Matter 23(33):334202:1–334202:9
37. Chen F, Schafranek R, Li S, Wu WB et al (2010) Energy band alignment between Pb(Zr,Ti)O_3 and high and low work function conducting oxides-from hole to electron injection. J Phys D Appl Phys 43(29):295301:1–295301:6
38. Schafranek R, Li SY, Chen F, Wu WB et al (2011) $PbTiO_3/SrTiO_3$ interface: energy band alignment and its relation to the limits of Fermi level variation. Phys Rev B 84(4):045317:1–045317:7
39. Vickerman JC, Gilmore IS (eds) (2000) Surface analysis, the principal techniques, 2nd edn. Wiley, Chichester
40. Avila J, Mascaraque A, Teodorescu C, Michel EG, Asensio MC (1997) Fe/Si (111) interface formation studied by photoelectron diffraction. Surf Sci 377–379:856–860
41. Mascaraque A, Avila J, Teodorescu CM, Asensio MC, Michel EG (1997) Atomic structure of the reactive Fe /Si (111) 7 × 7 interface. Phys Rev B 55(12):R7315–R7318
42. Teodorescu CM, Chrost J, Ascolani H, Avila J et al (1998) Growth of epitaxial Co layers on Sb-passivated GaAs(110) substrates. Surface Rev Lett 5(1):279–283
43. Teodorescu CM, Martin MG, Franco N, Ascolani H et al (1999) Epitaxial growth of bcc Co films on Sb-passivated GaAs(110) substrates. J Electron Spectrosc Relat Phenomena 101–103:493–499
44. Izquierdo M, Dávila ME, Avila J, Ascolani H et al (2005) Epitaxy and magnetic properties of surfactant-mediated growth of bcc cobalt. Phys Rev Lett 94(18):187601(1–4)

45. Pintilie L, Dragoi C, Pintilie I (2011) Interface controlled photovoltaic effect in epitaxial Pb(Zr, Ti)O_3 films with tetragonal structure. J Appl Phys 110(4):044105:1–044105:6
46. Pintilie L, Boerasu I, Gomes MJM, Zhao T et al (2005) Metal-ferroelectric-metal structures with Schottky contacts. II. Analysis of the experimental current–voltage and capacitance-voltage characteristics of Pb(Zr,Ti)O_3 thin films. J Appl Phys 98(12):124104:1–124104:9
47. Apostol NG, Stoflea LE, Lungu GA, Tache CA et al (2013) Band bending at free Pb(Zr, Ti)O3 surfaces analyzed by X-ray photoelectron spectroscopy. Mater Sci Eng B – Adv Funct Solid-State Mater 178:1317–1322
48. Hudson LT, Kurtz RL, Robey SW, Temple D et al (1993) Surface core-level shifts of barium observed in photoemission of vacuum-fractured $BaTiO_3$(100). Phys Rev B 47(16):10832–10838
49. Woll J, Allinger T, Polyakov V, Schaefer JA et al (1994) Electronic effects of surface in atoms at clean and hydrogenated InP(100) 4 × 2 surfaces. Surf Sci 315(3):293–301
50. Lau WM, Huang LJ, Bello I, Yiu YM et al (1994) Modification of surface band bending of diamond by low-energy argon and carbon ion-bombardment. J Appl Phys 75(7):3385–3391
51. Diederich L, Kuttel OM, Ruffieux P, Pillo T et al (1998) Photoelectron emission from nitrogen- and boron-doped diamond (100) surfaces. Surf Sci 417(1):41–52
52. Diederich L, Kuttel O, Aebi P, Schlapbach L (1998) Electron affinity and work function of differently oriented and doped diamond surfaces determined by photoelectron spectroscopy. Surf Sci 418(1):219–239
53. Yu HY, Feng XD, Grozea D, Lu ZH et al (2001) Surface electronic structure of plasma-treated indium tin oxides. Appl Phys Lett 78(17):2595–2597
54. Kobayashi H, Sakurai T, Takahashi M, Nishioka Y et al (2003) Interface states at SiO_2/6H- SiC(0001) interfaces observed by x-ray photoelectron spectroscopy measurements under bias: comparison between dry and wet oxidation. Phys Rev B 67(11):115305:1–115305:8
55. Wang XL, Han K, Wang WW, Xiang JJ et al (2012) Band alignment of HfO_2 on SiO_2/Si structure. Appl Phys Lett 100(12):122907:1–122907:4
56. Kakushima K, Okamoto K, Adachi M, Tachi K et al (2008) Band bending measurement of HfO_2/SiO_2/Si capacitor with ultra-thin La_2O_3 insertion by XPS. Appl Surf Sci 254(19):6106–6108
57. Sezen H, Suzer S (2011) Communication: enhancement of dopant dependent x-ray photoelectron spectroscopy peak shifts of Si by surface photovoltage. J Chem Phys 135(14):141102:1–141102:4
58. Copuroglu M, Sezen H, Opila RL, Suzer S (2013) Band-bending at buried SiO_2/Si interface as probed by XPS. ACS Appl Mater Interfaces 5(12):5875–5881
59. Gallet JJ, Bournel F, Rochet F, Köhler U et al (2011) Isolated Silicon dangling bonds on a water-saturated n + −doped Si(001)-2 × 1 surface: an XPS and STM study. J Phys Chem C 115(15):7686–7693
60. Oh JH, Kim KK, Hong HG, Byeon KJ et al (2010) Electrical characteristics of In/ITO p-type ohmic contacts for high-performance GaN-based light-emitting diodes. Mater Sci Semiconduct Process 13(4):272–275
61. Lorenz P, Haensel T, Gutt R, Koch RJ, Schaefer JA, Krischok S (2010) Analysis of polar GaN surfaces with photoelectron and high resolution electron energy loss spectroscopy. Phys Status Solidi B 247(7):1658–1661
62. Eisenhardt A, Reiss S, Himmerlich M, Schaefer JA et al (2010) Changes in the valence band structure of as-grown InN(0001)-2 × 2 surfaces upon exposure to oxygen and water. Phys Status Solidi (a) – Appl Mater Sci 207(5):1037–1040
63. Eisenhardt A, Himmerlich M, Krischok S (2012) Characterization of as-grown and adsorbate-covered N-polar InN surfaces using in situ photoelectron spectroscopy. Phys Status Solidi (a) – Appl Mater Sci 209(1):45–49

64. Xu XQ, Liu XL, Guo Y, Wang J et al (2010) Influence of band bending and polarization on the valence band offset measured by x-ray photoelectron spectroscopy. J Appl Phys 107(10):104510:1–104510:6
65. Nagata T, Koblmuller G, Bierwagen O, Gallinat CS, Speck JS (2009) Surface structure and chemical states of a-plane and c-plane InN films. Appl Phys Lett 95(13): 132104:1–132104:3
66. Kim KT, Lee K, Oh MS, Park CH et al (2009) Surface-induced time-dependent instability of ZnO based thin-film transistors. Thin Solid Films 517(23):6345–6348
67. Hamsen C, Lorenz P, Schaefer JA, Krischok S et al (2010) Analysis of the band offsets between ultrathin GaN(0001) layers and sapphire (0001) by photoelectron spectroscopy. Phys Status Solidi (c) – Curr Top Solid State Phys 7(2):268–271
68. Uhlrich JJ, Franking R, Hamers RJ, Kuech TF et al (2009) Sulfide treatment of ZnO single crystals and nanorods and the effect on P3HT-ZnO photovoltaic device properties. J Phys Chem C 113(50):21147–21154
69. Lide DL (ed) (1995) CRC Handbook of chemistry and physics, 75th edn. CRC Press, Boca Raton
70. Kim T, Yoshitake M, Yagyu S, Nemsak S et al (2010) XPS study on band alignment at Pt-O-terminated ZnO(000_1) interface. Surf Interface Anal 42(10–11):1528–1531
71. Blumentrit P, Yoshitake M, Nemsak S, Kim T et al (2011) XPS and UPS study on band alignment atPt-Zn-terminated ZnO(0001) interface. Appl Surf Sci 258(2):780–785
72. Ericsson LKE, Zhang HM, Magnusson KO (2013) Photoemission study of ZnO nanocrystals: thermal annealing in UHV and induced band bending. Surf Sci 612:10–15
73. Maffeis TGG, Penny MW, Castaing A, Guy OJ et al (2012) XPS investigation of vacuum annealed vertically aligned ultralong ZnO nanowires. Surf Sci 606(1–2):99–103
74. Herranz T, Deng XY, Cabot A, Liu Z et al (2011) In situ XPS study of the adsorption and reactions of NO and O_2 on gold nanoparticles deposited on TiO_2 and SiO_2. J Catal 283(2):119–123
75. Chung YL, Lai PY, Chen YC, Chen JS (2011) Schottky barrier mediated single-polarity resistive switching in Pt layer-included TiO_x memory device. ACS Appl Mater Interfaces 3(6):1918–1924
76. Huang L, Peng F, Ohuchi FS (2009) "In situ" XPS study of band structures at Cu_2O/TiO_2 heterojunctions interface. Surf Sci 603(17):2825–2834
77. Nagata T, Bierwagen O, White ME, Tsai MY et al (2010) Study of the Au Schottky contact formation on oxygen plasma treated n-type SnO_2 (101) thin films. J Appl Phys 107(3):033707:1–033707:7
78. Kono S, Saito T, Kang SH, Jung WY et al (2010) Band diagram for chemical vapor deposition diamond surface conductive layer: presence of downward band bending due to shallow acceptors. Surf Sci 604(13–14):1148–1165
79. Cho SW, Yi Y, Chung KB, Kang SJ et al (2010) The interfacial electronic structure of fullerene/ultra thin dielectrics of SiO_2 and SiON. Chem Phys Lett 499(1–3):136–140
80. Manandhar K, Parkinson BA (2012) Photoemission study of the morphology and barrier heights at the interface between Benz[a]anthracene and noble metal (111) surfaces. J Phys Chem C 116(36):19379–19384
81. Schoell SJ, Sachsenhauser M, Oliveros A, Howgate J et al (2013) Organic functionalization of 3C-SiC surfaces. ACS Appl Mater Interfaces 5(4):1393–1399
82. Aguirre-Tostado FS, Milojevic M, Choi KJ, Kim HC et al (2008) S passivation of GaAs and band bending reduction upon atomic layer deposition of HfO_2/Al_2O_3 nanolaminates. Appl Phys Lett 93(6):061907:1–061907:3
83. Maffeis TGG, Yung D, LePennec L, Penny MW et al (2007) STM and XPS characterisation of vacuum annealed nanocrystalline WO_3 films. Surf Sci 601(21):4953–4957
84. Greiner MT, Festin M, Kruse P (2008) Investigation of corrosion-inhibiting aniline oligomer thin films on iron using photoelectron spectroscopy. J Phys Chem 112(48): 18991–19004

85. Gheorghe NG, Husanu MA, Lungu GA, Costescu RM et al (2010) Atomic structure and reactivity of ferromagnetic Fe deposited on Si(001). J Mater Sci 47:1614–1620
86. Gheorghe NG, Husanu MA, Lungu GA, Costescu RM et al (2012) Reactivity, magnetism and local atomic structure in ferromagnetic Fe layers deposited on Si(001). Dig J Nanomater Biostruct 7(1):373–384
87. Teodorescu CM, Luca D (2006) Comparative study of magnetism and interface composition in Fe/GaAs(100) and Fe/InAs(100). Surf Sci 600(18):4200–4204
88. Teodorescu CM, Chevrier F, Richter C, Ilakovac V et al (2000) Structure of Fe layers grown on InAs(100). Appl Surf Sci 166(1–4):137–142
89. Teodorescu CM, Chevrier F, Brochier R, Richter C et al (2001) X-ray magnetic circular dichroism, photoemission and RHEED studies of Fe/InAs(100) interfaces. Surf Sci 482–485:1004–1009
90. Teodorescu CM, Chevrier F, Brochier R, Richter C et al (2002) Reactivity and magnetism of Fe/InAs(100) interfaces. Eur Phys J B 28(3):305–313
91. Popescu DG, Husanu MA (2013) Au–Ge bonding on a uniformly Au-covered Ge(001) surface. Phys Status Solidi RRL 7(4):274–277
92. Popescu DG, Husanu MA (2014) Epitaxial growth of Au on Ge(001) surface: photoelectron spectroscopy measurements and first-principles calculations. Thin Solid Films. doi:10.1016/j.tsf.2013.12.049
93. Rabe KM, Dawber M, Lichtensteiger C, Ahn CH et al (2007) Modern physics of ferroelectrics: essential background. In: Rabe KM, Ahn CH, Triscone JM (eds) Physics of ferroelectrics: a modern perspective. Topics in applied physics, vol 105. Springer, Berlin, pp 1–30
94. Kurasawa M, McIntyre PC (2005) Surface passivation and electronic structure characterization of $PbTiO_3$ thin films and $Pt/PbTiO_3$ interfaces. J Appl Phys 97(10):104110:1–104110:9
95. Chen Y, McIntyre PC (2007) Lead zirconate titanate ferroelectric thin film capacitors: effects of surface treatments on ferroelectric properties. Appl Phys Lett 91(7):072910:1–072910:3
96. Pintilie L, Stancu V, Trupina L, Pintilie I (2010) Ferroelectric schottky diode behavior from a $SrRuO_3$-$Pb(Zr_{0.2}Ti_{0.8})O_3$-Ta structure. Phys Rev B 82(8):085319:1–085319:8
97. Jia CL, Mi SB, Urban K, Vrejoiu I et al (2008) Atomic-scale study of electric dipoles near charged and uncharged domain walls in ferroelectric films. Nat Mater 7(1):57–61
98. Jia CL, Nagarajan V, He JQ, Houben L et al (2007) Unit-cell scale mapping of ferroelectricity and tetragonality in epitaxial ultrathin ferroelectric films. Nat Mater 6(1):64–69
99. Li CR, Cui SF, Liu BT, Zhu AJ et al (1998) Dependence of lattice constant on layer thickness of $Pb(Zr_{0.52}Ti_{0.48})O_3$ thin films. J Mater Sci Lett 17(15):1263–1266
100. Zubko P, Jung DJ, Scott JF (2006) Space charge effects in ferroelectric thin films. J Appl Phys 100:114112:1–114112:10
101. Pintilie L, Alexe M (2005) Metal-ferroelectric-metal heterostructures with Schottky contacts. I. Influence of the ferroelectric properties. J Appl Phys 98(12):124103:1–124103:8
102. Vrejoiu I, Alexe M, Hesse D, Gösele U (2008) Functional Perovskites – from epitaxial films to nanostructured arrays. Adv Funct Mater 18(24):3892–3906
103. Robertson J, Chen CW (1999) Schottky barrier heights of tantalum oxide, barium strontium titanate, lead titanate, and strontium bismuth tantalate. Appl Phys Lett 74(8):1168–1170
104. Huang BC, Chen YT, Chiu YP, Huang YC et al (2012) Direct observation of ferroelectric polarization-modulated band bending at oxide interfaces. Appl Phys Lett 100(12):122903:1–122903:4
105. Krug I, Barrett N, Petraru A, Locatelli A et al (2010) Extrinsic screening of ferroelectric domains in $Pb(Zr_{0.48}Ti_{0.52})O_3$. Appl Phys Lett 97(22):222903:1–222903:3
106. Simmons JC (1967) Poole-Frenkel effect and Schottky effect in metal-insulator-metal systems. Phys Rev 155(3):657–660

107. Chai FK, Brews JR, Schrimpf RD, Birnie DP III (1995) Limitations of the uniform effective field approximation due to doping of ferroelectric thin-film capacitors. J Appl Phys 78(7):4766–4775
108. Matsuura H (2000) Calculation of band bending in ferroelectric semiconductor. New J Phys 2:8.1–8.11
109. Zhang HM, Hirvonen Grytzelius J, Johansson LSO (2013) Thin Mn germanide films studied by XPS, STM, and XMCD. Phys Rev B 88(4):045311:1–045311:7
110. Arenholz E, van der Laan G, Fraile-Rodríguez A, Yu P et al (2010) Probing ferroelectricity in $PbZr_{0.2}Ti_{0.8}O_3$ with polarized soft x rays. Phys Rev B 82(14):140103:1–140103:4
111. Takatani S, Miki H, Kushida-Abdelghafar K, Torii K (1999) $Pt/PbZr_xTi_{1-x}O_3$ interfacial reaction and Schottky barrier formation studied by x-ray photoelectron spectroscopy: effect of H2 and O_2 annealing. J Appl Phys 85(11):7784–7791
112. Zhu TJ, Lu L (2004) X-ray diffraction and photoelectron spectroscopic studies of (001)- oriented $Pb(Zr_{0.52}Ti_{0.48})O_3$ thin films prepared by laser ablation. J Appl Phys 95(1):241–247
113. Hsieh TC, Shapiro AP, Chiang T-C (1985) Core-level shifts for Au epitaxial overlayers on Ag. Phys Rev B 31(4):2541–2544
114. Svanqvist M, Hansen K (2010) Non-jellium scaling of metal cluster ionization energies and electron affinities. Eur Phys J D 56(2):199–203
115. Ştoflea LE, Apostol NG, Trupină L, Teodorescu CM (2014) Selective adsorption of contaminants on Pb(Zr,Ti)O3 surfaces shown by X-ray photoelectron spectroscopy. Journal of Materials Chemistry A 2:14386–14392
116. Yun Y, Kampschulte L, Li M, Liao D, Altman EI (2007) Effect of ferroelectric poling on the adsorption of 2-Propanol on $LiNbO_3$(0001). J Phys Chem C 111:13951–13956
117. Yun Y, Altman EI (2007) Using ferroelectric poling to change adsorption on oxide surfaces. J Am Chem Soc 129:15684–15689
118. Zhao MH, Bonnell DA, Vohs JM (2009) Influence of ferroelectric polarization on the energetics of the reaction of 2-fluoroethanol on $BaTiO_3$. Surf Sci 603:284–290
119. Garra J, Vohs JM, Bonnell DA (2009) The effect of ferroelectric polarization on the interaction of water and methanol with the surface of $LiNbO_3$(0001). Surf Sci 603:1106–1114
120. Bellaiche L, Garcia A, Vanderbilt D (2000) Finite-temperature properties of $Pb(Zr_{1-x}Ti_x)O_3$ alloys from first principles. Phys Rev Lett 84(23):5427–5430
121. Stengel M, Vanderbilt D (2009) Berry-phase theory of polar discontinuities at oxide-oxide interfaces. Phys Rev B 80(24):241103:1–241103:4
122. Pintilie I, Teodorescu CM, Ghica C, Chirila C et al (2014) Polarization-control of the potential barrier at the electrode interfaces in epitaxial ferroelectric thin films, ACS Advanced Materials and Interfaces 6:2929–2939

Higher Resolution Scanning Probe Methods for Magnetic Imaging

12

S. N. Piramanayagam and Binni Varghese

Contents

1 Definition of the Topic 463
2 Overview 464
3 Introduction 464
4 Experimental and Instrumental Methodology 464
5 Key Research Findings 466
5.1 Applications of Magnetic Force Microscopy 466
5.2 Advanced Techniques 479
6 Conclusions and Future Perspectives 484
References 484

1 Definition of the Topic

With the emergence of nanotechnology, the feature size of devices is getting smaller and smaller and the demand for higher resolution imaging tools is growing. For the visualization of magnetic domains of nanostructures and thin films, magnetic force microscopy is the feasible and most utilized technique. The resolution of MFM is about 20–30 nm in the current instruments and efforts to improve the resolution in the sub-10 nm range are in progress. In this chapter, an overview of key research findings of several researchers and recent advances in the direction of improving the MFM resolution is provided.

S.N. Piramanayagam (✉) • B. Varghese
Data Storage Institute, A*STAR (Agency for Science, Technology and Research), Singapore, Singapore
e-mail: prem@ieee.org

© Springer-Verlag Berlin Heidelberg 2015

C.S.S.R. Kumar (ed.), *Surface Science Tools for Nanomaterials Characterization*,
DOI 10.1007/978-3-662-44551-8_12

2 Overview

MFM is a versatile tool for imaging the domain structure of magnetic materials. However, the MFM resolution needs to be improved for characterizing sub-10 nm features. Generally resolution of MFM can be improved by reducing the magnetic interaction volume between the tip and sample. Several strategies were implemented to reduce the magnetic interaction volume including usage of ultra-sharp tip, selective removal of magnetic coating from the MFM tip and by using magnetic coating with perpendicular anisotropy. In this chapter, recent developments towards high resolution MFM imaging are summarized.

3 Introduction

Characterization of magnetic properties of materials and nanostructures is not only useful in advancing science, but is also key in understanding and improving the performance of magnetic materials and devices in real life applications [1]. Magnetic properties can be tested in various ways. For measuring the bulk or thin film magnetic properties, magnetometric techniques such as vibrating sample magnetometer, alternating gradient force magnetometer etc. are used [2, 3]. At a microscopic level, techniques such as Bitter pattern, Kerr microscopes can be used to understand the magnetic domain patterns [4, 5]. To achieve magnetic imaging at nanometer scales, techniques such as Lorentz transmission electron microscopy (TEM), and magnetic force microscopy (MFM) can be used [6]. Tedious sample preparation for Lorentz TEM poses a hurdle in making it a popular choice for nano-scale magnetic imaging. On the other hand, MFM is a versatile tool to characterize magnetic nanostructures with sub-30 nm resolution, due to the ease of use and a reasonable resolution for most applications [7–15]. Moreover; MFM has the additional advantage of ambient imaging without the need of a vacuum atmosphere.

This chapter provides an overview of MFM technique and the recent developments in improving this technique. Section 4 discusses the fundamental principles of MFM. In Sect. 5.1, some examples of the ways in which MFM has been used by researchers for various applications are provided. Section 5.2 describes the advances in MFM characterization technique. Section 6 concludes the chapter with a description of future possibilities.

4 Experimental and Instrumental Methodology

MFM is a special type of scanning probe microscopy whereby the stray magnetic field from the sample is imaged to provide an insight on the magnetic properties of the sample. MFM operation is similar to that of AFM, which uses the atomic forces to interpret the topography [9]. In MFM, the force of attraction or repulsion between magnets (tip and the probed surface) is used to obtain information on the

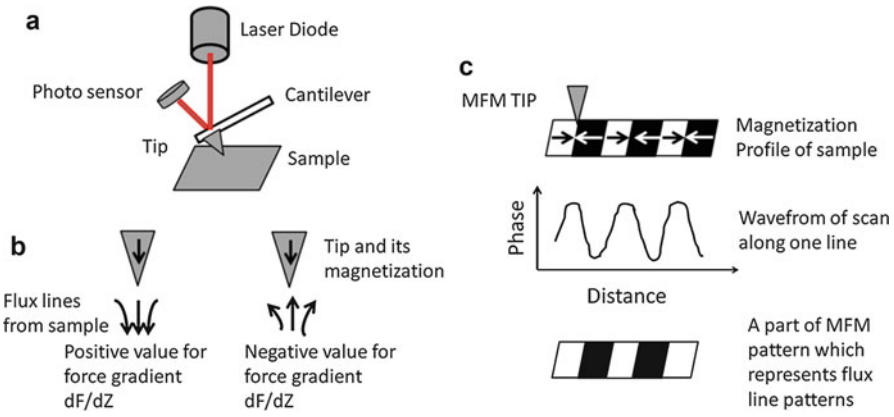


Fig. 12.1 A schematic of working principle of magnetic force microscopy (**a**) Illustration of the tip-sample stage and the laser geometry (**b**) Illustration of the interaction between the flux lines and the magnetized tip and (**c**) illustration of the magnetization, flux lines and the resultant MFM pattern

magnetic flux pattern from the probed surface. For this purpose, a cantilever with a coating of ferromagnetic material is typically employed to capture magnetic images using AFM instruments.

The working principle of MFM is based on the magnetostatic interaction of the sample stray field and/or its gradient with a magnetic tip at the free end of the cantilever probe. Either magnetostatic force or its gradient between the magnetic tip and sample stray field is sensed using the cantilever and laser probe combination to obtain contrast image of the sample stray field. Figure 12.1a shows the schematic of the MFM setup. A laser beam is incident on the cantilever, which is set to deflect it to the photo-sensor diode. In the widely accepted dynamic mode, the cantilever set to vibrate near its resonance frequency and the changes in the phase or amplitude of cantilever oscillation (due to magnetostatic force gradients) is sensed to form the MFM contrast image. Figure 12.1b, c illustrate this point. The MFM signal (shift in phase) can be approximated to be [7],

$$\Delta w \cong \frac{Q}{k}\frac{dF}{dz} \tag{12.1}$$

Where Q is the quality factor, k is the spring constant of the cantilever, $\frac{dF}{dz}$ is the force gradient in the z-direction. It has to be noticed that the dF/dz is mainly due to the divergence of the flux from the samples. Therefore, it may or may not represent the magnetization. In Fig. 12.1c, the magnetization patterns typical of a longitudinal recording medium are shown. In this case, the magnetic flux emerges only at the magnetization transitions. Therefore, the MFM indicates mainly the magnetization transitions. In the case of a film with perpendicular magnetic anisotropy (such as a perpendicular recording medium), the magnetization direction and the flux directions are the same and hence MFM indicates the magnetization pattern in the sample.

In principle, the sensitivity can be increased by using cantilevers of low spring constant and large Q values. However, there are some practical limitations while using very low spring constant and large Q value of cantilevers. Reduction in spring constant causes large cantilever deflection and may lead to the undesirable jump-to-contact effects. For this reason, cantilevers with spring constant 1–5 nN/nm are routinely employed for MFM imaging. Likewise, a large Q value may results in extremely slow scanning.

To eliminate or reduce the effect of strong short range forces, the tip is usually kept at a distance above the sample surface during the magnetic imaging. A two pass scanning method is commonly used. With this method, the topography of the sample is recorded in the first pass by scanning the tip in close proximity to the surface. Then, the magnetic image is recorded in the subsequent scanning at a fixed distance above the sample surface whereby retracing the recorded topography. The topography and magnetic imaging is carried out in a line by line fashion and the complete image is captured by raster scanning over the entire selected area of the sample.

However, it is worthwhile to note that the magnetic images also include contributions from other long range interactions such as electrostatic forces. The effect of electrostatic forces can be minimised by applying a bias to the tip, which is equal to the contact potential between the tip and sample materials [8]. A detailed description of the principles of MFM are provided in a review article [7].

5 Key Research Findings

5.1 Applications of Magnetic Force Microscopy

Since its invention, MFM has been used for various applications [6]. One of the important applications of MFM is in the field of magnetic recording technology. MFM is routinely used to characterize magnetization information of the recording media, field distribution in recording head and also to probe noise in the recording media [7, 8]. In fact, first demonstration of MFM was made using hard disk head. In magnetic recording media, MFM can be used to examine recorded patterns and to study the switching field distribution. MFM has also been used to make fundamental understanding on several magnetic systems. Furthermore, MFM has also been applied to study rock magnetism and even biological cells. This section makes an attempt to describe some of the applications of magnetic force microscopy, without dwelling on the details of the technique itself.

5.1.1 Magnetic Recording

In magnetic recording, the reader, the writer as well as the recording media can be tested using magnetic force microscopy. In order to propose and demonstrate the advantages of MFM, Martin and Wickramasinghe used a thin film recording head [9]. In their first report, two modes of MFM operation were discussed. In the first mode of operation, dynamic fields were imaged by placing the magnetized tip at a constant height above the recording head. The recording head was then driven

with a sinusoidal voltage at a frequency of 20 kHz. This set the magnetic probe to oscillate at the same frequency and its amplitude was monitored by a laser heterodyne probe. By raster scanning the sample using the tip and estimating the amplitude of the signal from the laser probe, magnetic image of the sample was obtained. In the second mode, a low spring constant magnetic probe was vibrated by using a piezoelectric bimorph element. As the tip approaches the sample surface the force gradient (which includes the van der Wall's, electric and magnetic force contributions) will change the effective spring constant and thereby shift the resonance frequency which can be measured using the laser probe. A resolution of 100 nm was achieved using these techniques. Since then, MFM technique has evolved significantly over the years to reach a resolution close 30 nm using commercially available probes. The imaging time has also been significantly reduced. As of now, the most popular mode of operation is the tapping-lift scan method where the topography information is captured and stored in the first pass at a lower/contact scan height and the tip is lifted to a user-set height before scanning the second pass. In the second pass, the probe traces the topography stored in the first scan and obtains the magnetic signal. Thus the magnetic signals can be separated from the topographic signal.

MFM has also been used to image field and field gradient from the perpendicular recording head. Recording heads are designed to have higher field gradient in order to achieve sharper bit transitions. Normally engineers relied upon simulations to aid the head design and fabrication process. MFM is proven to be an effective tool to experimentally obtain several head parameters. For example, quantitative MFM studies have shown that shielded heads exhibited higher field gradients than the unshielded heads [10].

Miniaturization of recording head necessitates higher MFM resolution to image the field distribution. Main pole of current heads have feature size in sub-ten nm range, which is far below the resolution of commercial MFM tools. In addition, the magnetization of the MFM tip must be stable and should not flip due to the high field emanating from the head. Tips coated with high anisotropy (K_u) materials like $L1_0$ FePt or CoPt are required to image the high field from recording head. Few attempts were found effective in improving MFM resolution and imaging the head field distribution, e.g. frequency modulated- MFM [11].

Longitudinal Magnetic Recording Medium

Magnetic recording medium is one area where magnetic force microscopy was utilized in a significant way. In the beginning of 1990's, MFM has been used just as an additional tool to show individual bits recorded in the media. Groenland et al., have pointed out several issues of MFM with regards to the imaging of recorded pattern including scanning height dependent resolution, overlapping of magnetic signal from adjacent tracks and difficulties to obtain quantitative data using MFM [12]. In their paper, the authors employed a constant force gradient mode of MFM operation whereby the distance between the tip and sample was constantly adjusted. They proposed that several of aforementioned issues may be surpassed by scanning the surface a second time at constant height and measuring the phase variation.

In mid and late nineties, MFM found several applications from being an additional tool to highlight areal density demonstrations to being a tool to understand the noise sources of recording media. MFM has played a major role in the study of magnetic recording medium. Glijer et al., demonstrated the ability of MFM to reveal the magnetic microstructures of longitudinal recording media at different magnetic states [13]. Studies on CoCrPt/Cr media showed that the distance between magnetic transitions was close to the Cr underlayer grain size which are equivalent to nearly 20–30 magnetic grains. This suggests that the magnetic grains on each Cr grains were strongly exchange coupled to function as a single magnetic unit. Their studies also revealed the presence of magnetic vortices in the ac demagnetized state of longitudinal recording media. In addition, these studies demonstrated a correlation between 'magnetic roughness' measured from the magnetic force images with media noise. A decrease in magnetic roughness with decrease in the media noise was observed.

Madabhushi et al., have studied inter-track interference in longitudinal recording media using MFM [14]. The cross-track interference was found to sensitively depend on several parameters including relative phase difference of nearby tracks, the track width and linear recording density. It was shown at higher densities that the tracks were largely unaffected by the inter-track interference as long as the phase offset between the adjacent tracks remains lower. However, low density tracks were significantly affected by inter-track interference for almost all phase offsets. MFM was also used to obtain understanding on transition noise by studying the magnetization fluctuation at the transition region [15, 16].

Abarra et al., studied the SNR and thermal stability characteristics of written transitions in longitudinal recording media using MFM [17]. CoCrTa and CoCrPtTa medium were investigated in this study (Fig. 12.2). The magnetic signal was estimated from the averaged MFM profiles of the written track. The power spectrum of the MFM profile was used to obtain the media noise. Both these parameters, estimated using MFM, were found comparable to the MR read head measurements. In their study, the thermal stability of written bits in a longitudinal recording media were evaluated by collecting MFM images of the written tracks after subjecting the samples to thermal annealing. Although energy barrier against thermal activation is considerably lower than the theoretically predicted value of $60k_BT$ for thermal stability, no significant degradation of the written pattern were observed after moderate temperature annealing. This observation was attributed to the larger size of the magnetic reversal unit relative to the grain size due to the exchange coupling between the grains. However degradation of the magnetic patterns was observed in the MFM images of longitudinal media samples annealed at a higher temperature.

Several studies on longitudinal media using MFM have been attempted for obtaining the correlation between the magnetic clustering of grains with medium noise [18]. Chen et al., studied the dependence of cluster size on the recording density and medium noise by analysing MFM images [19]. In this procedure, the signal profile of recording patterns was retrieved from the power spectrum of the averaged MFM profile. The signal profile obtained this way was subtracted

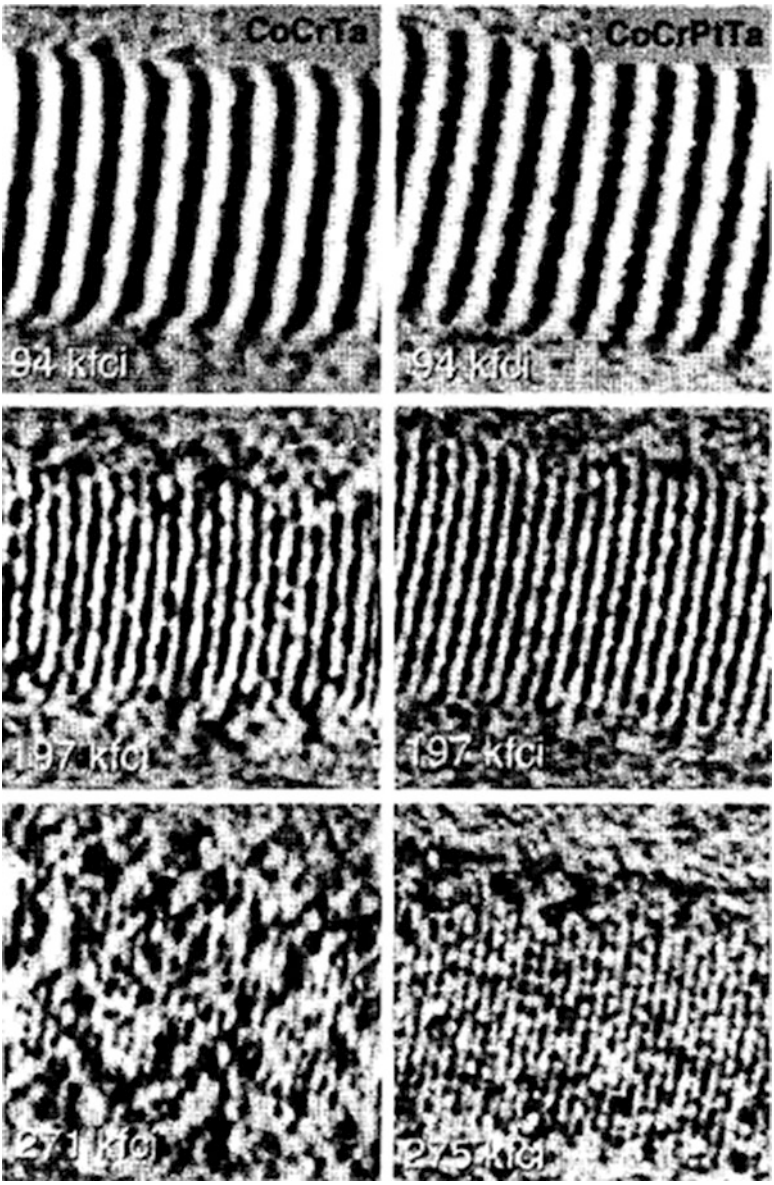


Fig. 12.2 MFM images of CoCrTa and CoCrPtTa based longitudinal recording media with bits transitions of different linear density. Even at higher densities, the bit transition can be seen in the CoCrPtTa media (Reprinted from Journal of Magnetism and Magnetic Materials vol.175, E.N. Abarra, P. Glijer, H. Kisker, I. Okamoto and T. Suzuki, "Thermal Stability and Micromagnetic Properties of High Density CoCrPtTa Longitudinal Media", pp.148–158 (1997), with permission from Elsevier)

from the average profile and the MFM recording pattern to obtain the noise profile and noise image. The cluster size measured from the MFM noise image was found to increase with recording density of the longitudinal medium. In addition, the SNR of the medium decreased with increase in magnetic cluster size.

Perpendicular Media

MFM technique continued to find widespread application in magnetic recording as the technology evolved from longitudinal to perpendicular recording. Higher resolution of MFM was exploited to demonstrate the high density capability of perpendicular recording. Zhu et al., studied the recorded magnetization patterns and track edge overwrite properties of perpendicular recording media using MFM [20]. Their studies revealed sharp track edges and absence of edge erasure of single pole written tracks on keepered perpendicular media. Studies on FePt media at the ac demagnetized state and recorded patterns revealed the correlation of recording resolution with the domain size observed at the ac demagnetized state [21].

Mei et al., studied the effect of intergranular exchange interaction in Pt/Co and Pt/CoCrTa multilayer recording media with perpendicular magnetic anisotropy using MFM [22]. The strong coupling in Pt/Co multilayer film resulted in the formation of large virgin domains in the unwritten regions. The higher coupling also affected the regions of written transitions by domain wall motion into the nearby regions of opposite magnetization and increased the noise in the media. Such effects can be directly observed in MFM images in the form of irregular boundaries at the written transitions. On the other hand, in Pt/CoCrTa multilayers formed at elevated temperature, smaller domains were observed due to Cr segregation at the grain boundary and the relatively lower exchange coupling as its consequence. Better recording performance of such optimum exchange coupled multilayers was demonstrated by revealing the high linear density patterns written on these samples by MFM.

Several works have been focused on obtaining a reliable correlation between the magnetic domain size measured using MFM with various noise mechanisms in a perpendicular recording medium. Typically the MFM imaging is carried out at the ac demagnetized state and the average cluster/domain size and its distribution is estimated. Generally it was noticed that the SNR of the recording media decreases as the cluster size increased [23]. This is understandable, as the cluster size represents grains that will reverse together. Such clusters, if they are big, will be bigger than the bits themselves leading to bit-error-rates. Even when they are smaller, but bigger than the grains, they might cause transition noise.

Most of the studies as of now focused on the average cluster size measurement using MFM at the ac demagnetized state to assess the noise level in perpendicular recording media. Although the average cluster size at the demagnetized state do provide some information, key factors related to the media noise could not be easily retrieved from such a study. For instance, bit error rate (BER) and transition jitter noise of such granular recording medium are determined primarily by relatively larger clusters. In addition, clusters with lower thermal stability could flip due to thermal effects and cause issues such as media noise, wide area track erasure (WATER) etc.

The MFM images collected at the ac demagnetized state might not selectively reveal clusters of these two categories. To address some these issues a new methodology is proposed where cluster size measurements of the perpendicular recording media were carried out at three magnetic remanence states, including the ac demagnetized state, to better correlate the MFM cluster size with medium noise [24]. The other two remanent states (besides ac demagnetized state) were designed to probe the smaller/low thermal stability and much bigger clusters. For probing lower thermal stability grains/clusters, a saturated sample was subjected to a reverse field close to the nucleation field and subsequently cluster size measurements were carried out at the remanent state. MFM images at this condition could provide information about wide-area adjacent track erasure (WATER). For probing irreversible clusters that cause BER, the saturated sample was subjected to a reverse field close to saturation field and the magnetic clusters were examined at the corresponding remanent state. MFM images at this condition may reveal presence of clusters that could not be written using the field arising out of the head in a recording process. Figure 12.3 shows MFM images collected at these three magnetic states from perpendicular recording media samples fabricated at different conditions.

In addition, SNR and transition noise in perpendicular recording were also be obtained by analysing MFM images collected from areas of tracks written at various linear density. The medium noise can be estimated by analysing the Fourier transform of the MFM image of the track region after excluding the signal peak. On the other hand, transition noise can be estimated from a noise image formed by subtracting the average signal profile from the original MFM profile collected from the track region in a line by line fashion [25].

It is worthwhile to note that the lateral resolution of commercial MFM is currently ~30 nm, which is adequate enough to resolve a maximum of 800 kfci tracks (bit size ~31 nm). However the bit density in hard disk drives has increased at a rapid pace, which demands higher resolution in MFM techniques.

Patterned Media

Patterned media, or bit-patterned media (BPM), where the magnetic bits are stored in isolated magnetic islands, is one area of research where MFM has been used intensively. The reasons for this are manifold: (1) Patterning is usually carried out in a small area and most often, the conventional magnetometric techniques, such as vibrating sample magnetometer (VSM) or alternating gradient magnetometer (AGM) which require samples of more than tens of mm^2 area, cannot be used for small samples that were obtained by performing lithography over a small area. (2) The features fabricated for patterned media are small (few tens to hundreds of nm) and hence MFM is one of the few techniques that can resolve the small features. Even though MFM cannot completely replace the information provided by magnetometric techniques, it has been proved to be useful.

Group of Terris et al., have carried out numerous investigations on the understanding of BPM since their earlier studies in 2001 [26, 27]. Their studies on patterned magnetic nanostructures of different sizes using MFM revealed that nanostructures of Co/Pd multilayers with sizes below 50 nm show single domain

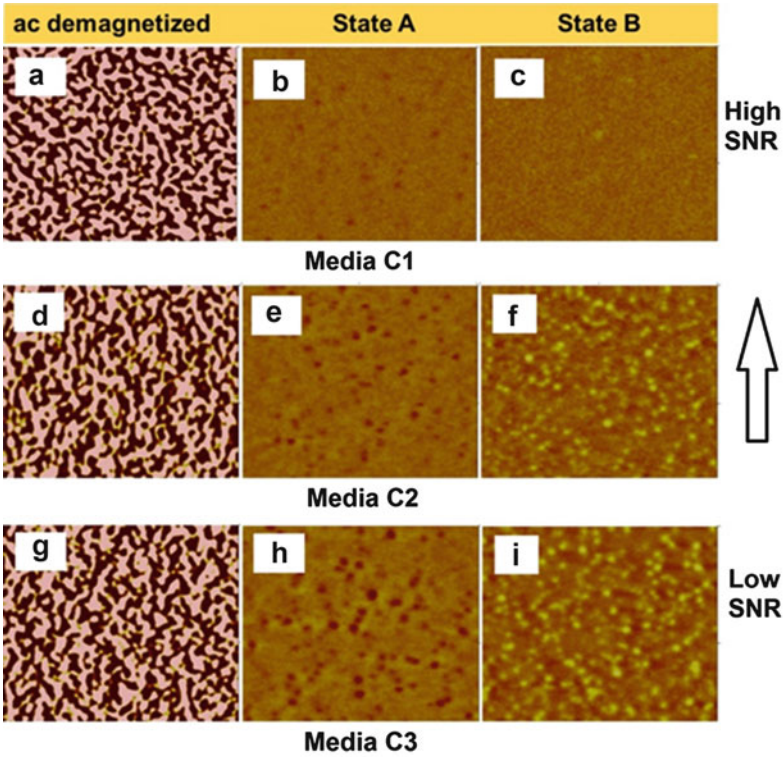


Fig. 12.3 MFM images of different perpendicular recording media (unpublished, Ref. 24). Four media samples (C1, C2, and C3) were fabricated at different deposition conditions and MFM image were collected at the three different remnant magnetic states. The number of clusters appeared in the MFM images recorded after the media is subjected to reverse fields close to nucleation and saturation fields increases with decrease in SNR. Scan size is 2 × 2 μm for all the images

structures [28]. However, relatively bigger elements with size above 200 nm were found to support the multidomain structure (Fig. 12.4). In addition, these studies pointed out that the Co/Pd multilayers would show a huge switching field, when patterned [29]. With the support of magnetometric studies, such a huge increase in switching field was attributed to the change of reversal mechanism from domain wall propagation in thin film to Stoner-Wohlfarth (SW) type rotation in nanostructures.

One important concern associated with bit patterned media for practical applications is the large switching field distribution (SFD) of the array of magnetic island. The SFD of the bit patterned media depends on intrinsic and extrinsic factors. The intrinsic factors arise due to the dispersion in magnetic properties of magnetic island due to variation in crystal orientation, composition and other microstructures. The edge damage during the fabrication, variation in size and shape of the magnetic elements and the magnetostatic interactions between nearby islands set the extrinsic factors determining the SFD of the patterned media.

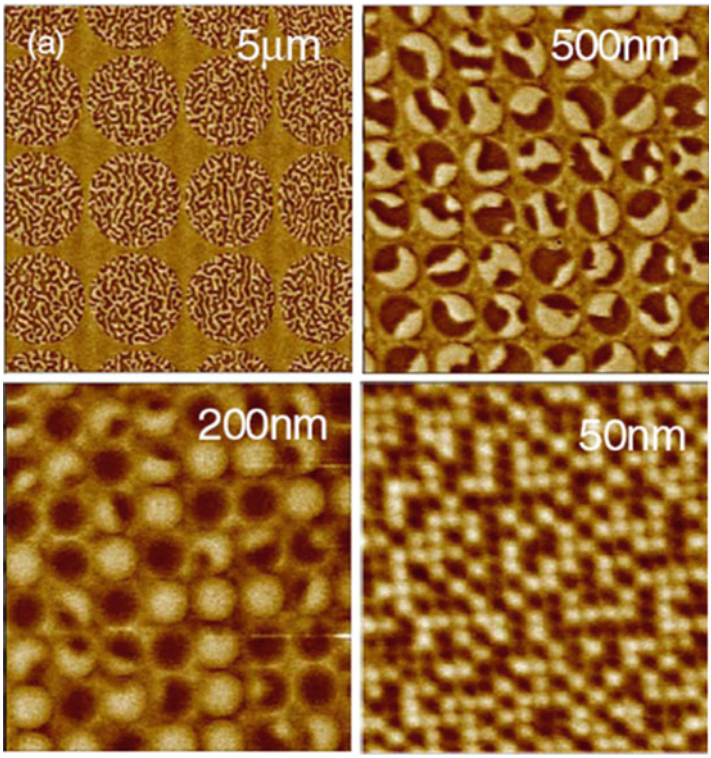


Fig. 12.4 MFM images of patterned magnetic island of different feature sizes (Reproduced figure with permission from T. Thomson, B.D. Terris and G. Hu, Phys. Rev. Lett. 96, 257204, (2006) Copyright (2006) by the American Physical Society). Multidomain structure is clearly revealed in the MFM images of islands with size above 200 nm. However array of island with size 50 nm showed single domain structure

In this connection, MFM has been widely used to systematically investigate the reversal mechanisms and SFD in patterned media.

In order to understand the switching mechanisms in nanodot arrays, Shaw et al., carried out MFM studies on nanodot arrays fabricated using two different methods [30]. In the first case, the nanodot arrays were fabricated by lithography and followed by milling on Co/Pd multilayer thin films. In the second approach, multilayers were deposited on a pre-patterned substrate to form separated nanodot without edge damage. Different trends in the dependence of switching field on size of the nanodots of these two types of nanodot arrays were noted. For the milled sample, a significant reduction in switching field was observed for smaller structures. However for arrays fabricated on pre-patterned sample, an increase in switching field was noted as feature size reduces. This result suggests that the edge damage in the milled samples largely determine its switching characteristics. The reversed domains near the edges of these samples can be seen in the MFM images of the nanodot arrays taken at the remanent state after applying a large in-plane field.

Piramanayagam et al., have carried out significant investigations on the understanding of SFD and ways to control the switching field distribution in BPM. As a way to reduce the SFD of BPM, an antiferromagnetically coupled (AFC) structure was proposed [31, 32]. In AFC structure, a very thin Ru layer (<1 nm) is inserted between two magnetic layers to form an AFC magnetic film. The AFC structure reduces the remnant magnetization (Mr) and thereby decreases the magnetostatic interaction between the individual bits. Such changes in magnetostatic interactions will also modify the SFD of the array of magnetic dots (Fig. 12.5). By recording a series of MFM images at the remnant state of the BPM after subjecting to different external fields, SFD can be estimated from the remanent hysteresis curve obtained by counting the number of reversed bits/dots. For BPM with smaller magnetic feature size and spacing, a significant reduction in SFD was observed for AFC structures compared to single layer structures. Similar MFM studies on square and hexagonal lattice configuration of nanodot arrays were carried out to understand the relative magnetostatic interactions [33]. This study revealed the wider SFD of the hexagonal lattice configuration of nanodot array relative to the square lattice configuration, probably arises from the difference in the magnetostatic interaction.

Chen et al., have reported switching probability and probability distribution of nanodots using MFM [34]. In their study, statistical reversal behaviour of each dots in an array of nanodots was obtained by repeated switching tests and MFM imaging under identical conditions. The switching probability of each nanodots was assessed from the MFM images. At a reverse field close to remnant coercivity of the nanodots, ~60 % of nanodots showed a switching probability in the range $0 < p < 1$ and such switching behaviour was attributed to the thermal effects.

Gaur et al., have used MFM, in association with X-ray diffraction and other Magnetometric measurements, to highlight the changes associated with the ion-implantation of thin films. When FePt was covered with a patterned mask and implantation was carried out using Sb + ions in the uncovered portion, the FePt in the masked region lost its magnetic anisotropy significantly. This resulted in the observation of a weaker MFM signal from the unimplanted regions in contrast to a high signal when implantation was not carried out. The MFM results were further confirmed by Magnetometric measurements [35].

The potential of BPM technology is in the high density recording and speculated density exceed beyond 10 Tbits/in^2. At such high density, the feature size of the bit islands and its pitch will be in sub ten nm range. In order to characterize the properties of such high density BPM samples significant improvements in the resolution of MFM techniques is required. Section 5.2 of this chapter describes such attempts by various researchers.

5.1.2 Physics of Magnetic Materials

MFM provided an efficient platform for understanding fundamental physics of several magnetic materials. In particular, MFM studies were applied to understand the manifold phenomenon associated with magnetic thin films, micro and nanostructures. Key advantages of MFM technique over other techniques include

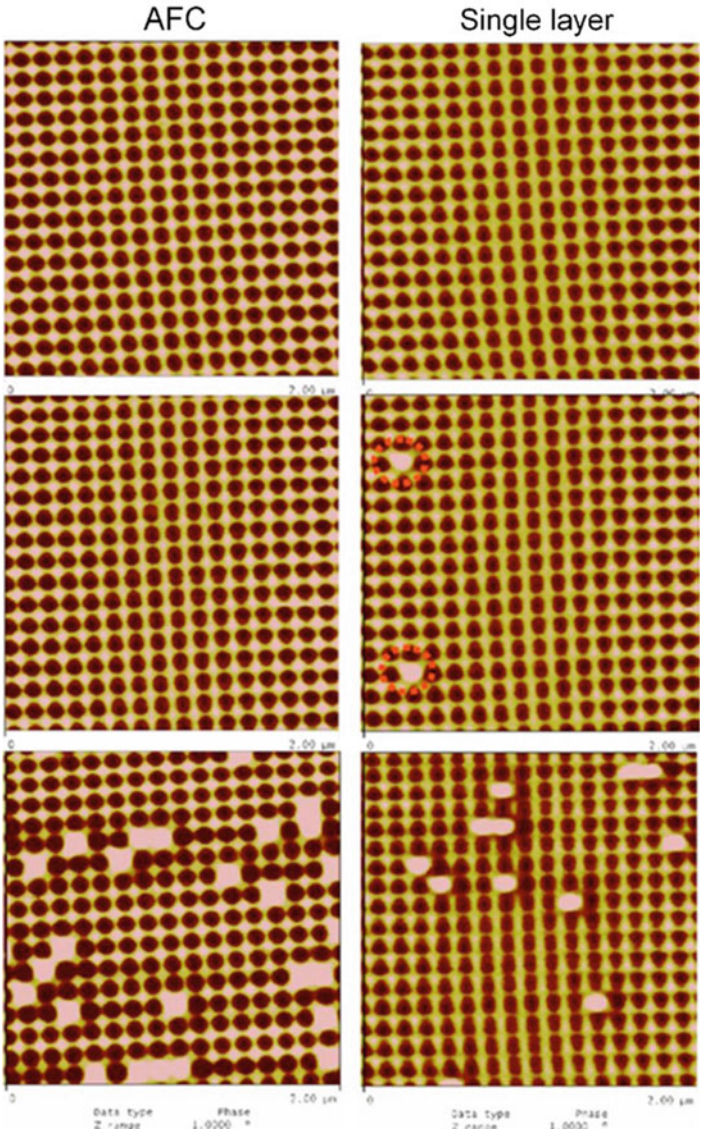


Fig. 12.5 MFM images collected at the remanence of magnetic dots with AFC and single layer structures (Reprinted with permission from S.N. Piramanayagam, K.O. Aung, S. Deng, R. Sbiaa, J. Appl. Phys. 105, 07C118 Copyright (2009), AIP publishing LLC). In single layer dot arrays, the switching starts at a relatively lower field when compared to the AFC structured dots

minimal sample preparation, possibility of application of magnetic field during imaging, ambient and vacuum operating capability and so on.

MFM was widely used to visualize magnetic vortex presented in thin ferromagnetic discs (circular dots) of diameter in the range of submicron to micron level.

A magnetic vortex is a curling magnetic structure with perpendicular magnetization at the core region. Such magnetic structures are commonly observed in circularly patterned cobalt or permalloy (NiFe alloy) structure with thickness less than 50 nm. The theoretically predicted magnetic vortex with perpendicular magnetization at the core region is experimentally visualized using MFM [36]. The perpendicular magnetization in the core region of the vortex appeared as bright or dark contrast in MFM images. For the imaging of such magnetic vortex using MFM, care should be taken to ensure that the stray field from the MFM tip should not alter the magnetization state of the sample. This is achieved by either using tip coated with low magnetization materials or by scanning the sample at relatively higher lift scan height. Magnetic switching characteristics of magnetic vortex arrays can be obtained following a similar approach described earlier for BPM, whereby collecting a series of MFM images at the remanent state after subjecting the samples to different reverse fields [37].

Hehn et al., studied the thickness dependent domain structure of epitaxial cobalt film using MFM [38]. For films with thickness less than 50 nm, in plane magnetization was found to be the major component. M-H curves and MFM studies of MBE grown Co films showed fully perpendicular anisotropy characteristics for thicknesses above 50 nm. In demagnetized samples, stripes or labyrinthine stripe like domain structure were observed in thicker Co films depending on the in plane or perpendicular demagnetization, respectively. Moreover the ordered stripe domain can be aligned along the in plane field direction. The width of the stripe domain (D) was found to vary with thickness of the film (d) and it was found that $D \propto \sqrt{d}$ as predicted by Kittel. Elliptical bubble like domain structure was observed in the MFM images of samples which are perpendicularly magnetized. Similar crossover from in-plane to perpendicular domain magnetization was noted in MFM studies of several other magnetic thin films including permalloy [39] and the technologically important FePt film [40] (Fig. 12.6).

MFM Studies on (Co/Pd) multilayers revealed that the domain size and structure depends on the number of repeat of bilayer units [41]. MFM images, collected at the ac demagnetized state of the multilayer film, indicated larger domains in multilayer films with less number of repeats, while smaller domains appeared in films with large number of repeats. Such thickness dependent domain size of (Co/Pd) multilayer is explained on the basis of magnetostatic energy aroused due to the interaction between different magnetic layers.

In CoCrPt-SiO_2 based thin films for recording media applications, Gaur et al., have used MFM to understand the effect of ion-implantation on the movement of magnetic elements and the resultant changes in exchange coupling [42]. When such films were implanted with low mass ions such as B+, the changes in the exchange coupling were not significant. However, when Ar + ions were used for implantation, due to their heavy mass, the lateral movements of magnetic elements caused an increase in exchange coupling, leading to the observation of larger clusters. Such information cannot be gained only from Magnetometric measurements and MFM plays an important role in adding another dimension to the understanding.

Domain wall structures of synthetic antiferromagnetically (AFC) coupled multilayers of different thickness have also been studied using MFM [43]. Here,

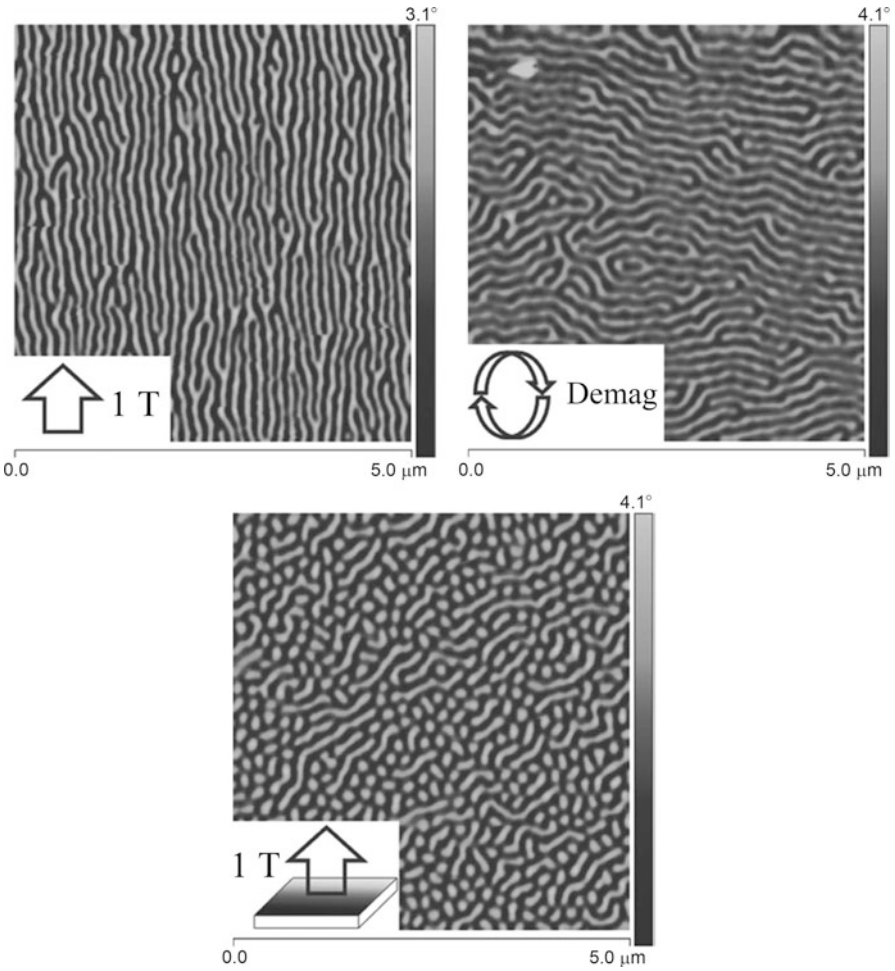


Fig. 12.6 MFM images showing the domain structure of FePt thin film at remanence with different field history (Reproduced figure with permission from E.S. Leva, R. C. Valente, F. M. Tabares, M. V. Mansilla, S. Roshdestwensky and A. Butera, Phys. Rev. B 82, 144410 (2010) Copyright (2010) by the American Physical Society). With an in-plane field of 1T the stripe domains are more or less aligned along the field direction. The demagnetized samples showed a more disordered stripe (labyrinthine) domain patterns. Magnetic bubbles were visible in the sample which is subjected to a field normal to the film surface

multilayers of the form $([Co/Pt]_{X-1}/Co/Ru)_N$, which are analogous to the A-type antiferromagnetic materials was fabricated and its domain structure was examined using MFM. A transition from nonmagnetic to ferromagnetic domain wall structure was observed in these films as thickness increases (Fig. 12.7). The observed transition in domain wall structure was explained on the basis of the competition between the dipolar and exchange energy as thickness increases.

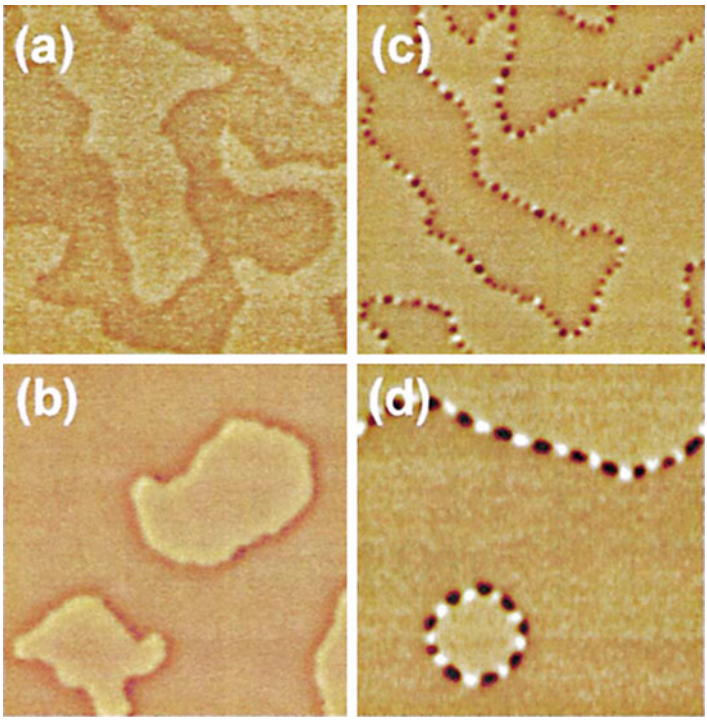


Fig. 12.7 MFM images of $([Co/Pt]_{X-1}/Co/Ru)_N$ multilayers with different thickness (Reproduced figure with permission from O. Hellwing, A. Berger,and E. E. Fullerton, Domain Walls in Antiferromagnetically Coupled Multilayer Films, Phys. Rev. Lett., 2003, 91(19): 197203 Copyright (2003) by the American Physical Society). The multilayer structure were (**a**) N = 4, X = 5; (**b**) N = 10, X = 5; (**c**) N = 12, X = 7; (**d**) N = 18, X = 8. A transition from non-magnetic to magnetic domain wall structure is noted for the AFC coupled multilayers

In addition to the domain structure characterization, MFM technique was found effective in probing and characterizing the magnetic defects that exist in magnetic thin films and other nanostructures. Magnetic defects in perpendicular anisotropic thin films, for example, include dispersion in crystal orientation, presence of stacking faults, inhomogeneity in local chemical composition and so forth. Such defects could function as nucleation centres and largely determine the magnetization reversal characteristics of magnetic films and hence functionalities of the devices made using these films. For instance, studies on (Co/Pd) multilayers demonstrated that the defects sites can be selectively revealed using MFM imaging after the application of a critical in-plane field [44].

5.1.3 Geological Applications

MFM has also been applied to study the domain structure and stray field from natural rock samples. The remanent magnetization in rocks and other geological

substances is due to the presence of strongly magnetic mineral like magnetite (Fe_3O_4). During the rock formation, process like rapid cooling results the magnetic minerals to get precipitated and could magnetized due to earth's magnetic field. Studies on rock magnetism could provide significant information on our planet's history. So far, a few studies were employed MFM as a characterization tool to reveal the domain structure of geological samples. Frandsen et al., studied the domain structure of rock samples with magnetite lamellae in clinopyroxane crystals using MFM [45]. Shaar et al., studied the magnetic properties of dendrites in basaltic glass and synthetic glass samples using MFM [46]. Their studies showed that the domains in dendrites depend on its geometry and size of the branches.

5.1.4 Biological Applications

MFM is also found useful in characterizing and imaging some biological specimens. For example, magnetic crystals inside the magnetotactic bacteria were imaged using MFM [47]. Magnetotactic bacteria could mineralize magnetic crystal like Fe_3O_4, Fe_3S_4 inside their cell, which help them navigate along the earth's magnetic field lines. Magnetic dipole moments of such bacteria were estimated from the MFM line scan.

5.2 Advanced Techniques

For the past two decades, magnetic force microscopy (MFM) has remained as a common technique to resolve fine magnetic features. In order to image fine nanomagnetic patterns, an improved resolution is desired. The simplest path to improve resolution from sub-100 nm as reported first to sub-30 nm was to exploit the magnetic properties by coating a non-magnetic tip with a suitable magnetic material. Coating techniques have evolved from single-layer coating of CoCrPt alloys to antiferromagnetically coupled layer structures which act like point-dipoles to layers with a perpendicular magnetic anisotropy. Magnetic force microscopy in vacuum has also been employed to provide better resolution. Improvements have also been made using techniques such as focused ion beam (FIB) trimming, carbon nanotubes coated with magnetic films as MFM tips etc. This section describes such developments that helped to advance MFM technique in imaging of magnetic nanostructures.

5.2.1 Focused Ion Beam Etching

As the MFM resolution depends on the interaction volume, one way to reduce the interaction volume is to make the MFM coating to smaller dimensions. This can be achieved by top-down techniques, such as focused ion beam etching. Phillips et al., fabricated MFM tips with high aspect ratio cobalt coating by focused ion beam etching [48]. In their work, Co film was deposited to one face of the pyramidal tip and the focused ion beam was employed to remove majority of the Co film leaving thin bars with high aspect ratio. Such tips with high aspect ratio of magnetic bars could function as magnetic monopoles as the magnetic stray fields

from the samples hardly reach the farther end of the bar. Thus fabricated tips with Co bars of aspect ratio higher than 30:1 and an end radius of about 25 nm exhibited a MFM resolution of ~30 nm.

Gao et al., have carried out MFM studies using CoPt permanent magnetic film coated tips after focused ion beam modifications [49]. In this study, majority of the CoPt film from the tip was removed by ion beam milling, leaving only a 30 nm diameter magnetic particle at the very end of the tip. With such special tips, the area from which the magnetic flux emanating from the tip can be limited and hence the magnetic interaction volume can be reduced. They have used Fourier transformation to estimate the resolution and have claimed a lateral resolution of 11 nm in ambient conditions. The error in estimation of the resolution is reported to be around 2 nm.

Although high resolution MFM imaging can be realized using ion beam modified tips, the complicated and expensive instrumentation required for the fabrication of tips is major disadvantage of this technique. In addition, serial nature of the fabrication procedure further reduces the wide applicability of this method.

5.2.2 Carbon Nanotubes

Carbon nanotubes provide an additional avenue to achieve low physical interaction volume. Deng et al. [50] coated carbon nanotubes with magnetic thin films and achieved a resolution of 20 nm. Their process consists of the growth of carbon nanotubes using wafer-scale chemical vapor deposition on commercial silicon tips for tapping mode atomic force microscopy, followed by a shortening of nanotube and deposition of metal films. They report that the tapping mode cantilevers are not as damaging to the sample or the tip as contact mode cantilevers, and allow a fine control over the tip–sample separation. Their process involves complex growth and electrical cutting of the nanotubes and the resolution depends on the thickness of the carbon nanotube. While short carbon nanotubes provide a good stiffness, the magnetic material from the cantilever starts interacting with the sample for too short lengths of carbon nanotube. Deng et al., have used Co as the coating material.

Kuramochi et al. [51] have used CoFe as a coating material over carbon nanotube. By ensuring uniform coating over the carbon nanotube, they claim that their MFM tip could resolve a density of 1,100 kfci (kilo-flux-cycles-per inch) of recorded bits. They also claim an ultimate resolution of about 10 nm using such tips. Winkler et al. [52] have carried out MFM using carbon nanotubes filled with Fe particles. In their study, MFM probes were prepared by pinning iron-filled multiwall carbon nanotubes to conventional scanning force microscopy probes. The authors claim that these nanotube MFM probes reveal a great potential for high spatial resolution of both topography and magnetic stray field. The ends of the high aspect ratio iron nanowires within the nanotubes can be considered as stationary effective magnetic monopole moments, which open the possibility of quantitative stray field measurements in a straightforward manner. The carbon shells around the iron nanowires provide wear resistance and oxidation protection. Although their results showed improvement in both topography and magnetic resolution, the improvement in resolution is not stated in numbers. This is due to the fact that they did not use a high-density recording media as is a common practice with most MFM related work.

Carbon nanotube or other one dimensional nanostructures based tips provide an opportunity for improving the MFM resolution. However, feasible approaches to integrate these nanostructures to the cantilever are essential. Direct and site specific growth of nanostructure at the tip apex is likely an option to tackle this issue.

5.2.3 Fine Tips by Other Methods

While Carbon nanotubes provide one way of achieving thin MFM probes, commercial Si tips with a fine radius are available in the recent past. Futamoto et al., have made use of commercially available Si tips of 4 nm diameter to achieve improved resolution [53]. They have carried out coating of various types of materials on such Si tips and have observed that a resolution of less than 10 nm can be achieved by using materials such as CoFe and CoFeB as coatings.

5.2.4 MFM Tips with Antiferromagnetically Coupled (AFC) Magnetic Layers

All the approaches described in the previous subsections were based on the principle of reducing the interaction volume in a physical manner, such as by using sharp tips such as carbon nanotubes or tips trimmed by other physical methods. Of late, there is an interest to reduce the interaction volume using magnetic principles. Wu et al. [54] have carried out experimental work on tips coated with antiferromagnetic layers. Although their work is similar to the simulation work of Oti et al. [55] who had proposed tips with antiferromagnetic coupling, the approaches and objectives of the two appear to be different. Oti et al., proposed tips with antiferromagnetic coupling (AFC) in order to stabilize the magnetic configuration of the tip. This will help in the probe magnetization being unaffected by the sample's stray field. Oti et al., also suggested that the AFC tip would not produce a stray field; thus preventing the sample magnetization being affected by the tip magnetic field.

In an alternative manner, Wu et al., have proposed that a tip in the AFC configuration can be helpful in achieving a point-dipole. In their experiments, they tried various coatings and ultimately used CoCrPt/Ru/CoCrPt structure, as this provided the required stability of magnetization. The magnetic layers had a nominal thickness (as measured from deposition on wafers) of 4 nm and Ru had a nominal thickness of 0.8 nm. They describe that the point dipole can be very small, where the Ru thickness is different from 0.8 nm. Thus, a higher resolution can be achieved using such structures. Figure 12.8 shows the illustration of their AFC tip and its point-dipole nature.

Amos et al. [56] have achieved similar effect by using two FePt layers sandwiching a MgO layer of 8 nm thickness. In these tips, the antiparallel arrangement of magnetization of the two FePt layers was achieved by magnetostatic coupling, rather than the synthetic antiferromagnetism as induced by Ru.

5.2.5 MFM Tips with a Perpendicular Magnetic Anisotropy

All the MFM tips discussed until the previous section, were coated with a magnetic material that does not have a magnetic anisotropy other than the shape anisotropy. The magnetization in all those studies and that in the commercial tips lies along the tip surface. As the interaction between the tip and the sample is caused by the

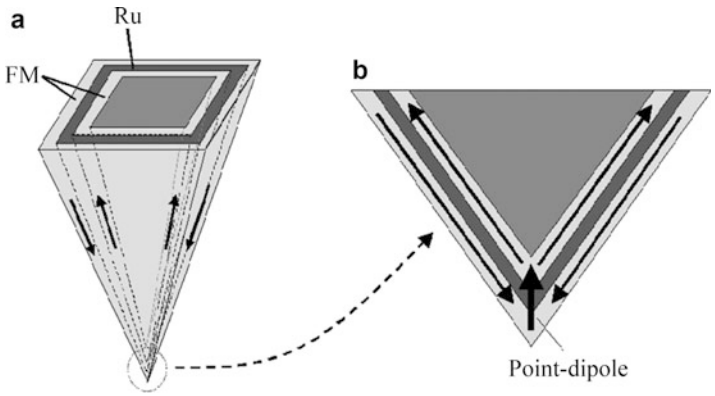


Figure 12.8 (**a**) Illustration of the synthetic antiferromagnetically coupled MFM tips and (**b**) enlarged view of the tip apex, depicting the point-dipole (Reprinted with permission from Y.H. Wu, Y. Shen, Z. Liu, K. Li, and J. Qiu, Appl. Phys. Lett., 82, 1748–1751 Copyright (2003), AIP Publishing LLC)

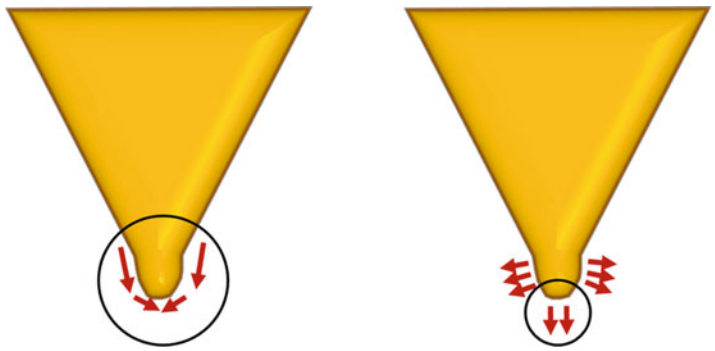


Fig. 12.9 Illustration of stray field from the sample and the magnetization in (**a**) tips with conventional coating and (**b**) tips with a layer of perpendicular magnetic anisotropy

perpendicular component of magnetization, a larger interaction volume is expected in the case of tips coated with conventional coating procedure Fig 12.9a.

On the other hand, if the tip is coated with a material that has a good perpendicular magnetic anisotropy (PMA), the magnetization would lie perpendicular to the plane as shown by the arrows in Fig. 12.9b. In this case, the vertical magnetic field from the sample is in the easy axis direction for the circled region and in the hard axis direction for the rest of the magnetization. The part of the tip that has a horizontal magnetization does not contribute much to the force. Therefore, the interaction volume is only around the circled region, which is expected to be smaller than the conventional MFM tip with in-plane magnetic anisotropy of the same tip size and shape. Therefore, the resolution that is possible with the

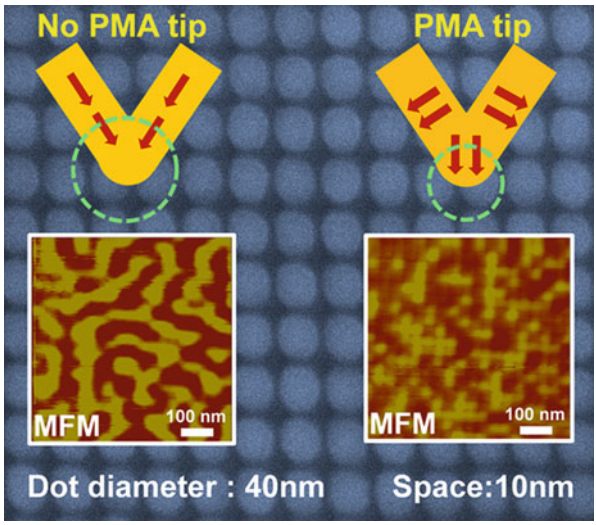


Fig 12.10 MFM images of bit-patterned media obtained with a conventional MFM tip and a tip with PMA

perpendicular magnetic anisotropic tip is expected to be better. Perpendicular magnetic anisotropy can be obtained using several magnetic films such as TbFeCo, Co/Pd multilayers or CoCrPt alloys with specific seedlayers.

Piramanayagam et al. [57] have fabricated tips with perpendicular magnetic anisotropy, using a layer structure adapted from perpendicular recording media [58]. In these tips, the tip coating material is an alloy of CoCrPt-SiO_2, similar to the recording layer used in perpendicular magnetic recording. A perpendicular magnetic anisotropy is generated in this system, by utilizing heteroepitaxial growth on Ta/Ru (00.2) seedlayers [59]. By using these tips, Piramanayagam et al., have shown a significant improvement in the resolution of these tips over commercial tips and the reference tips that were prepared without any induced magnetocrystalline anisotropy. The X-Ray diffraction (XRD) and polar Kerr rotation measurements of the samples (deposited at a similar condition as the tips) confirmed the presence of perpendicular magnetic anisotropy in the deposited layers.

Piramanayagam et al. [60] have also used such tips to demonstrate their advantage in characterizing bit-patterned media. Magnetic dots separated from each other at 10 nm spacing can be resolved using MFM tips coated with a magnetic film possessing a perpendicular magnetic anisotropy (PMA). Compared to MFM tips with no special magnetic anisotropy, MFM tips with PMA can resolve the bits clearly, because of a smaller magnetic interaction volume. Figure 12.10 shows the images of bit-patterned media obtained with conventional tips and tips with a PMA. This improved resolution is achieved despite the fact that the physical radius of the tip with PMA being larger. Further improvements along this line are possible by reducing the coating thickness of tips with PMA, but still maintaining PMA.

Ranjbar et al. [61] have used PMA tips in an AFC configuration. In comparison to the experiments of Wu et al., where the AFC layers had an in-plane magnetization

configuration, the magnetization in the tips of Ranjbar et al., had a perpendicular configuration. However, in comparison to the PMA configuration (single layer), the AFC-PMA configuration did not provide any significant improvement in performance.

5.2.6 MFM Imaging in Vacuum

Techniques like frequency modulation (FM) detection schemes offers high sensitivity and yet faster AFM imaging at a high vacuum atmospheres [62]. Similar techniques could offer higher resolution for MFM in a vacuum atmosphere. The MFM signal according to Eq. 12.1 increases with the increase in Q-factor value of the cantilever. The Q-factor is given by,

$$Q = \frac{m\omega}{\eta_{\text{eff}}} \tag{12.2}$$

where m is the mass of the cantilever, η_{eff} is the effective damping factor. The Q-factor increases in vacuum due to the decrease of effective damping factor and help improving the MFM sensitivity. Lim et al., used MFM in vacuum to characterize high density bit patterns on recording media written using the shingle-write scheme [63].

It is worthwhile to note that the ultimate sensitivity and hence resolution of MFM is limited by the fluctuations due to thermal vibrations. In fact maximum sensitivity of MFM required a high vacuum and low temperature operation [64].

6 Conclusions and Future Perspectives

Over the years MFM has advanced as a versatile technique for studying several key properties of magnetic materials and devices. To meet the growing demand for characterizing smaller features, several approaches have been implemented in effort to improve MFM resolution. The developed techniques are based on either the reduction of physical tip size or by reducing the magnetic interaction volume using advanced magnetic material coating. Although reduction of physical tip via etching methods are promising, expensive instrumentations required is a disadvantage. In addition, techniques like focused ion beam modification are serial in nature and might not be suitable for batch fabrication of tips. Refinements on the approaches, which are based on reducing the magnetic interaction volume via coating specially designed magnetic material structures on the tips, would be an alternative to fabricate advanced MFM tips which can be batch fabricated at a lower cost.

References

1. Lau JW, Shaw JM (2011) Magnetic nanostructures for advanced technologies: fabrication, metrology and challenges. J Phys D Appl Phys 44:303001
2. Foner S (1956) Vibrating sample magnetometer. Rev Sci Instrum 27(7):548–548

3. Flanders PJ (1990) A vertical force alternating-gradient magnetometer. Rev Sci Instrum 61(2):839–847
4. Xu XT, Moses AJ, Hall JP, Williams PI, Jenkins K (2011) A Comparison of magnetic domain images using a modified bitter pattern technique and the Kerr method on Grain-oriented electrical steel. IEEE Trans Magn 47(10):3531–3534
5. Barman A, Kimura T, Otani Y, Fukuma Y, Akahane K, Meguro S (2008) Benchtop time-resolved magneto-optical Kerr magnetometer. Rev Sci Instrum 79(12):123905
6. Budruk A, Phatak C, Petford-Long AK et al (2011) In situ Lorentz TEM magnetization studies on a Fe–Pd–Co martensitic alloy. Acta Materiialia 59(17):6646–6657
7. Hartmann U (1999) Magnetic force microscopy. Annu Rev Mater Sci 29:53–87
8. Schwartz A, Wiesendager R (2008) Magnetic sensitive force microscopy. Nano Today 3(1–2):28
9. Martin Y, Wickramasinghe HK (1987) Magnetic imaging by "force microscopy" with 1000 Å resolution. Appl Phys Lett 50(20):1455
10. Chen YJ, Leong SH, Huang TL, Ng KW, Hu SB, Yuan ZM, Ng V (2008) A comparative study of write field distribution of trailing-edge shielded and unshielded perpendicular write heads by quantitative magnetic force microscopy. Appl Phys Lett 92:162505
11. Lu W, Li Z, Hatakeyama K, Egawa G, Yoshimura S, Saito H (2010) High resolution magnetic imaging of perpendicular magnetic recording head using frequency-modulated magnetic force microscopy with a hard magnetic tip. Appl Phys Lett 96(14):143104
12. Groenland JPJ, van Engelen GJP, Bernards JPC, Cramer HAJ (1993) Investigating recording patterns using magnetic force microscopy. J Magn Magn Mater 120:327–329
13. Glijer P, Sivertsen JM, Judy JH (1995) Magnetic force microscopy (MFM) studies of micromagnetic structures of high coercivity CoCrPt/Cr and CoCrPtB/Cr thin films. IEEE Trans Magn 31(6):2842
14. Madabhushi R, Gomez RD, Burke ER, Mayergoyz ID, Orloff J (1997) Inter-track interference studies using MFM image reconstruction. IEEE Trans Magn 33(5):4053
15. Takekuma I, Haseyama M, Sueoka K, Mukasa K, Yasui M (1999) A study of magnetization fluctuations in transition region using MFM image analysis. IEEE Trans Magn 35(5):2685
16. Moser A, Rubin KA, Best ME (2001) Transition position jitter in longitudinal magnetic recording media. IEEE Trans Magn 37(4):1872
17. Abarra EN, Glijer P, Kisker H, Okamoto I, Suzuki T (1997) Thermal stability and micromagnetic properties of high-density CoCrPtTa longitudinal media. J Magn Magn Mater 175(1–2):148
18. Murayama A, Hyomi K, Ohshima K, Miyamura M, Maekawa M, Kondoh S (1997) Grain structure and magnetic clustering in SiO2 added CoNiPt granular films. J Appl Phys 81(8):3925
19. Chen J, Saito H, Ishio S, Kobayashi K (1998) Analysis of two-dimensional medium noise and magnetic cluster with MFM for $Co_{82}Cr_{13}Ta_5$ longitudinal magnetic recording media. J Magn Magn Mater 188(1–2):260
20. Zhu JG, Luo YS, Ding JR, Ye XG, Louis EA (1994) MFM study of edge overwrite in perpendicular thin film recording media. IEEE Trans Magn 30(5):2755
21. Suzuki T, Honda N, Ouchi K (1999) Fe-Pt media for perpendicular magnetic recording. IEEE Trans Magn 35(5):2748
22. Mei L, Liu WH, Ho K, Lairson BM, Dunning FB (1998) Magnetic force microscopy of high-density perpendicular magnetic recording media. J Magn Magn Mater 187:268
23. Takenoiri S, Sakai Y, Enomoto K, Watanabe S, Uwazumi H (2003) Magnetic properties, magnetic cluster size, and read-write performance of CoPtCr-SiO_2 perpendicular recording media. IEEE Trans Magn 39:2279
24. Varghese B, Piramanayagam SN, Lee WK, Tan HK (2014) Noise characterization of perpendicular recording media by cluster size measurements. IEEE Trans magn 50: 3201606
25. Svedberg EB, Khizroev S, Litvinov D (2002) Magnetic force microscopy study of perpendicular media: signal-to-noise determination and transition noise analysis. J Appl Phys 91(8):5365

26. Rettner CT, Best ME, Terris BD (2001) Patterning of granular magnetic media with a focused ion beam to produce single-domain islands at >140 Gbit/in^2. IEEE Trans Magn 37(4):1649
27. Lohau J, Moser A, Rettner CT, Best ME, Terris BD (2001) Writing and reading perpendicular magnetic recording media patterned by a focused ion beam. Appl Phys Lett 78(7):990
28. Thomson T, Hu G, Terris BD (2006) Intrinsic distribution of magnetic anisotropy in thin films probed by patterned nanostructures. Phys Rev Lett 96:257204
29. Hu G, Thomson T, Albrecht M, Best ME, Terris BD, Rettner CT, Raoux S, McClelland GM, Hart MW (2004) Magnetic and recording properties of Co/Pd islands on prepatterned substrates. J Appl Phys 95(11):7013
30. Shaw JM, Russek SE, Thomson T, Donahue MJ, Terris BD, Hellwig O, Dobisz E, Schneider ML (2008) Reversal mechanisms in perpendicularly magnetized nanostructures. Phys Rev B 78:024414
31. Piramanayagam SN, Aung KO, Deng S, Sbiaa R (2009) Antiferromagnetically coupled patterned media. J Appl Phys 105:07C118
32. Mojtaba R, Piramanayagam SN, Deng S, Aung KO, Sbiaa R, Kay YS, Wong SK, Chong TC (2010) Antiferromagnetically coupled patterned media and control of switching field distribution. IEEE Trans Magn 46(6):1787
33. Ranjbar M, Tavakkoli KGA, Piramanayagam SN, Tan KP, Sbiaa R, Wong SK, Chong TC (2011) Magnetostatic interaction effects in switching field distribution of conventional and staggered bit-patterned media. J Phys D Appl Phys 44:265005
34. Chen YJ, Ding J, Deng J, Huang T, Leong SH, Shi J, Zong B, Hnin YY, Chun KA, Hu S, Liu B (2010) Switching probability distribution of bit Islands in bit patterned media. IEEE Trans Magn 46(6):1990
35. Gaur N, Kundu S, Piramanayagam SN, Maurer SL, Tan HK, Wong SK, Steen SE, Yang H, Bhatia CS (2013) Lateral displacement induced disorder in $L1_0$-FePt nanostructures by ion-implantation. Sci Rep 3:1907
36. Raabe J, Pulwey R, Sattler R, Schweinbock T, Zweck J, Weiss D (2000) Magnetization pattern of ferromagnetic nanodisks. J Appl Phys 88(7):4437
37. Okuno T, Shigeto K, Ono T, Mibu K, Shinjo T (2002) MFM study of magnetic vortex cores in circular permalloy dots: behavior in external field. J Magn Magn Mater 240:1–6
38. Hehn M, Padovani S, Ounadjela K, Bucher JP (1996) Nanoscale magnetic domain structures in epitaxial cobalt films. Phys Rev B 54(5):3428
39. Amos N, Fernandez R, Ikkawi R, Lee B, Lavrenov A, Krichevsky A, Litvinov D, Khizroev S (2008) Magnetic force microscopy study of magnetic stripe domains in sputter deposited permalloy thin films. J Appl Phys 103:07E732
40. Leva ES, Valente RC, Tabares FM, Mansilla MV, Roshdestwensky S, Butera A (2010) Magnetic domain crossover in FePt thin films. Phys Rev B 82:144410
41. Sbiaa R, Bilin Z, Ranjbar M, Tan HK, Wong SK, Piramanayagam SN, Chong TC (2010) Effect of magnetostatic energy on domain structure and magnetization reversal in (Co/Pd) multilayers. J Appl Phys 107:103901
42. Gaur N, Piramanayagam SN, Maurer SL, Nunes RW, Steen S, Yang H, Bhatia CS (2011) Ion implantation induced modification of structural and magnetic properties of perpendicular media. J Phys D Appl Phys 44:365001
43. Hellwing O, Berger A, Fullerton EE (2003) Domain walls in antiferromagnetically coupled multilayer films. Phys Rev Lett 91(19):197203
44. Shaw JM, Olsen M, Lau JW, Schneider ML, Silva TJ, Hellwig O, Dobisz E, Terris BD (2010) Intrinsic defects in perpendicularly magnetized multilayer thin films and nanostructures. Phys Rev B 82:144437
45. Frandsen C, Stipp SLS, McEnroe SA, Madsen MB, Knudsen JM (2004) Magnetic domain structures and stray fields of individual elongated magnetite grains revealed by magnetic force microscopy (MFM). Phys Earth Planet In 141:121–129

46. Shaar R, Feinberg JM (2013) Rock magnetic properties of dendrites: insights from MFM imaging and implications for paleomagnetic studies. Geochem Geophys Geosyst 14:407
47. Proksch RB, Schaffer TE, Moskowitz BM, Dahlberg ED, Bazylinski DA, Frankel RB (1995) Magnetic force microscopy of the submicron magnetic assembly in a magnetotactic bacterium. Appl Phys Lett 66(19):2582
48. Phillips GN, Siekman M, Abelmann L, Lodder JC (2002) High resolution magnetic force microscopy using focused ion beam modified tips. Appl Phys Lett 81:865
49. Gao L, Yue LP, Yokota T, Skomski R, Liou SH, Takahoshi H, Saito H, Ishio S (2004) Focused ion beam milled CoPt magnetic force microscopy tips for high resolution domain images. IEEE Trans Magn 40:2194
50. Deng Z, Yenilmez E, Leu J, Hoffman JE, Straver EW, Dai H, Moler KA (2004) Metal-coated carbon nanotube tips for magnetic force microscopy. Appl Phys Lett 85:6263
51. Kuramochi H, Uzumaki T, Yasutake M, Tanaka A, Akinaga H, Yokoyama H et al (2005) A magnetic force microscope using CoFe-coated carbon nanotube probes. Nanotechnology 16:24
52. Winkler A, M¨uhl T, Menzel S, Kozhuharova-Koseva R, Hampel S, Leonhardt A, B¨uchner B (2006) Magnetic force microscopy sensors using iron-filled carbon nanotubes. J Appl Phys 99:104905
53. Futamoto M et al (2013) Improvement of magnetic force microscope resolution and application to high-density recording media. IEEE Trans Magn 49(6):2748
54. Wu Y, Shen Y, Liu Z, Li K, Qiu J (2003) Point-dipole response from a magnetic force microscopy tip with a synthetic antiferromagnetic coating. Appl Phys Lett 82:1748–1751
55. Oti JO, Rice P, Russek SE (1994) Proposed antiferromagnetically coupled duallayer magnetic force microscope tips. J Appl Phys 75:6881
56. Amos N, Ikkawi R, Haddon R, Litvinov D, Khizroev S (2008) Controlling multidomain states to enable sub-10-nm magnetic force microscopy. Appl Phys Lett 93:203116
57. Piramanayagam SN, Ranjbar M, Tan EL, Tan HK, Sbiaa R, Chong TC (2011) Enhanced resolution in magnetic force microscropy using tips with perpendicular magnetic anisotropy. J Appl Phys 109:07E326
58. Piramanayagam SN (2007) Perpendicular recording media for hard disk drives. J Appl Phys 102:011301
59. Piramanayagam SN, Shi JZ, Zhao HB, Mah CS, Zhang J (2005) Stacked CoCrPt: SiO_2 layers for perpendicular recording media. IEEE Trans Magn 41(10):3190–3192
60. Piramanayagam SN, Ranjbar M, Sbiaa R, Tavakkoli AKG, Chong TC (2012) Characterization of high-density bit-patterned media using ultra-high resolution magnetic force microscopy. Phys Status Solidi-Rapid Res Lett 6(3):141–143
61. Ranjbar M, Piramanayagam SN, Sbiaa R, Chong TC (2012) Advanced magnetic force microscopy for high resolution magnetic imaging. Nanosci Nanotechnol Lett 4(6):628–633
62. Albrecht TR, Grutter P, Horne D, Rugar D (1991) Frequency modulation detection using high-Q cantilevers for enhanced force microscope sensitivity. J Appl Phys 69:668
63. Lim F, Wilson B, Wood R (2010) Analysis of shingle-write readback using magnetic-force microscopy. IEEE Trans Magn 46:1548
64. Volodin A, Temst K, Van Haesendonck C, Bruynseraede Y (2000) Low temperature magnetic force microscopy with enhanced sensitivity based on piezoresistive detection. Rev Sci Instrum 71:4468

Imaging and Characterization of Magnetic Micro- and Nanostructures Using Force Microscopy

13

Stephan Block

Contents

1 Introduction and Definition of the Topic 490
2 General Experimental Methodology: Principles of Magnetic AFMs 491
2.1 Basic Setup 491
2.2 AFM Cantilevers: Micromechanical Resonators Acting as Force Sensors 492
2.3 Detection of Cantilever Oscillation 497
3 Specific Experimental Methodology: Implementations of Magnetic AFM Approaches 498
3.1 Magnetic Force Microscopy (MFM) 499
3.2 Magnetic Resonance Force Microscopy (MRFM) 509
3.3 Magnetic Exchange Force Microscopy (MExFM) 515
4 Conclusions and Outlook 517
References 518

Abstract

This chapter introduces into the principles of different force microscopic approaches that sense a magnetic probe-sample force to study magnetism of micro- and (sub)nanometer-sized objects. Although all of them are capable to characterize magnetic properties on small length scales, their applicability depends strongly on the object (e.g., nm-thin magnetic films, magnetic nanoparticles, electronic and nuclear spins) to be investigated. A comparison of their application range will be given, which allows identifying the method most suitable for the intended measurement. Finally, the discussion of each approach is complemented by an overview about current exemplary applications.

S. Block (✉)
Department of Physics, Ernst–Moritz–Arndt University of Greifswald, Greifswald, Germany
Applied Physics, Chalmers University of Technology, Gothenburg, Sweden

© Springer-Verlag Berlin Heidelberg 2015

C.S.S.R. Kumar (ed.), *Surface Science Tools for Nanomaterials Characterization*,
DOI 10.1007/978-3-662-44551-8_13

Keywords
Spin • Magnetic moment • Magnetization • Scanning probe microscopy • Atomic force microscopy • Magnetic force microscopy • Magnetic resonance force microscopy • Magnetic exchange force microscopy

1 Introduction and Definition of the Topic

The past decades have seen a tremendous development of new magnetic microscopy techniques; many of them are able to provide direct, real-space imaging of magnetic structures allowing extraction of different magnetic properties [1–3]. The development of some of these new imaging techniques was directly triggered by the development of the first scanning probe microscopes (SPM), the scanning tunneling microscope (STM) [4, 5], and the atomic force microscopy (AFM) [6, 7], which demonstrated the measurement of material properties on the nanoscale by using nm-sharp probes. This concept of localizing the measurement process by using probes was immediately adopted in the field of magnetic microscopes and resulted in the development of very different SPM approaches capable of measuring magnetic properties from the μm scale down to the sub-nm length scale [8–11].

These developments had an enormous impact, as they satisfied the demand for methods that allow to characterize small magnetic structures, which is essential to understand the fundamentals of magnetism. In applied research, they were immediately applied to questions in the field of data storage technologies (to enhance the performance of magnetic recording media) to create nanostructured media with unique magnetic properties. However, their field of applications broadened dramatically over the years, e.g., toward magnetic resonance imaging on the nanoscale, characterization of magnetization reversal, and measurement of spin dynamics for spintronics (to name only very few examples).

In this review, some of the recent advances in the field of magnetic microscopy will be given. Due to the vast amount of available techniques, this chapter will focus only on methods based on "magnetic atomic force microscopes" (magnetic AFMs), i.e., approaches that use force microscopy to measure a magnetic probe-sample interaction. It will not include optical approaches (e.g., Kerr and Kerr scanning near-field optical microscopy) [12, 13], electron microscopic approaches (e.g., Lorentz microscopy, electron holography) [14–17], and other non-force sensing SPM-based magnetic microscopes (e.g., scanning squid microscopy [18], scanning hall microscopy [19, 20], optical sensing using nitrogen vacancy probes mounted on SPM setups [21–23], spin-polarized scanning tunneling microscopy [11], etc.). The reader is referred to Refs. [17, 18, 24–26] for detailed reviews on some of these techniques.

A brief introduction in the basic concepts and the basic instrumentation of magnetic AFM approaches will be given, which is complemented by a review of recent applications of these approaches.

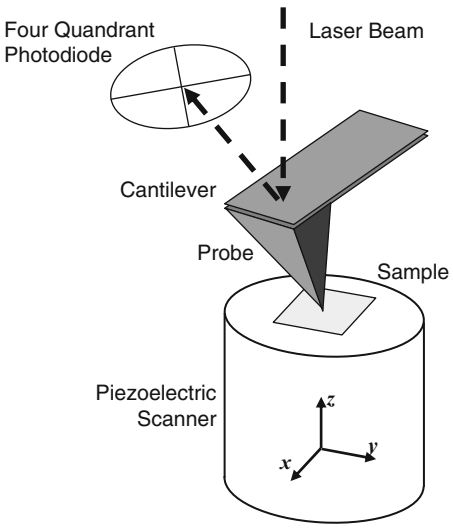


Fig. 13.1 Exemplary design of an atomic force microscopy (*AFM*) setup. A piezoelectric scanner is used to position a probe relative to the sample, while the forces (originating from the probe-sample interaction) are detected either by a deflection of the cantilever or by changes in the resonance properties of the cantilever

2 General Experimental Methodology: Principles of Magnetic AFMs

2.1 Basic Setup

Atomic force microscopy (AFM) uses the interaction of a probe with a sample to measure certain material properties (e.g., sample topology, friction, (electrical) resistance, elasticity, etc.). As the probe can be scanned over the sample surface, it is possible to record maps containing the spatial distribution of the measured material property. The resolution of such maps depends on the range of the probe-sample interaction, i.e., by choosing very short-ranged interactions, atomic resolution can be achieved using SPM approaches [4, 5].

AFMs evaluate the forces arising between probe and sample to determine material properties [6, 7]. It was successfully applied in the past to quantify electrostatic [27], van der Waals [27–29], friction [30–32], steric [33–36], and magnetic forces [8–10], allowing to extract various material properties including the sample's surface potential, magnetization, and work function [37–41].

Typically each AFM setup consists of at least four parts (Fig. 13.1): (ι) the sample; (ιι) the probe, which is mounted on a cantilever beam (acting as micromechanical force sensor); (ιιι) a piezoelectric crystal that allows to change the relative position between probe and sample (typically with sub-nm precession); and (ιυ) a deflection detection system that measures the cantilever deflection induced by the probe-sample forces. This probe-on-cantilever setup is the most common AFM implementation, but it should be noted that certain special implementations (e.g., some MRFM designs described in Sect. 3.2) employ an inverted scheme (the so-called sample-on-cantilever setup), in which probe and sample switch the position.

Hence, the actual design and implementation depend strongly on the requirements and constraints of the desired measurement. Depending on the magnetic property to be investigated, it might be necessary to extent the "basic AFM setup" by additional components (e.g., external magnetic/electromagnetic fields), which can lead to very sophisticated setups. All these issues will be discussed more in detail in the sections, describing different approaches to measure magnetic effects on the μm down to the sub-nm scale.

2.2 AFM Cantilevers: Micromechanical Resonators Acting as Force Sensors

Cantilever Properties – Virtually all AFM approaches sense probe-sample forces using a micromechanical beam in cantilever configuration, i.e., with one end fixed to a rigid body. As the remaining free end is equipped with the AFM probe, probe-sample forces F lead to a deflection z of the cantilever's free end. For static forces F, this deflection follows Hook's law [42]:

$$F = k \cdot z, \quad \text{(static mode)} \tag{13.1}$$

in which the spring constant k is given by

$$k = \frac{3 \cdot E \cdot I}{l^3} \tag{13.2}$$

(with E denoting the Young's modulus, I the moment of inertia of the bar, and l the length of the cantilever) [43]. For a rectangular cantilever with width b and thickness h, the moment of inertia is given by $I = h^3\ b\ /\ 12$, and Eq. 13.2 reads $k = E\ h^3\ b\ /\ (4\ l^3)$.

Employing very soft cantilevers ($k \approx 1$ mN/m) allows to measure pN forces [39]. However, much smaller forces can be detected if resonance properties of the AFM cantilever are incorporated into the measurement setup, i.e., if the cantilever is understood as a micromechanical resonator driven by a periodic force instead of a static force sensor (*dynamic mode*). The resonance properties can be calculated by solving the differential equation

$$E \cdot I \cdot \frac{\partial^4 z(x,t)}{\partial x^4} + \mu \cdot \frac{\partial^2 z(x,t)}{\partial t^2} = F(x,t), \tag{13.3}$$

which assumes that there is no internal friction within the cantilever and that the amplitude of vibrations is small compared to any length scale in the system [44, 45]. In this equation, μ denotes the mass per unit length of the beam, F the externally applied force per unit length, x the spatial coordinate, and t the time. Using the constraints of one fixed end and absence of any friction (i.e., placement in vacuum), one can show that Eq. 13.3 has several oscillatory solutions

(flexural modes of cantilever movement), each associated with a resonance frequency (of the *i*th mode) [45, 46]:

$$\omega_i = \frac{\alpha_i^2}{\alpha_1^2}\omega_1 \quad \text{with} \quad \omega_1 = \sqrt{\frac{E \cdot I}{\mu}} \cdot \frac{\alpha_1^2}{l^2}. \tag{13.4}$$

Equation 13.4 is given in terms of the angular frequency ω_i, which is connected via $\omega_i = 2\pi \cdot f_i$ to the resonance frequency f_i of the *i*th mode. For this described geometry, the coefficients α_i have to fulfill the equation

$$\cos\alpha_i \cosh\alpha_i = -1, \tag{13.5}$$

which leads to the following values: $\alpha_1 = 1.88$, $\alpha_2 = 4.69$, $\alpha_3 = 7.85$, $\alpha_4 = 11.00$, and $\alpha_i = (i - 0.5)\pi$ for $i > 4$. Each flexural mode has a certain linewidth $\delta\omega_i$ of the resonance peak (centered at ω_i), which is a measure for the quality Q_i of the *i*th mode:

$$Q_i = \frac{\delta\omega_i}{\omega_i}. \tag{13.6}$$

Friction and other dissipative losses shift these frequencies ω_i and decrease the quality factor Q_i, which can be calculated using sophisticated methods for some systems [45, 47, 48].

Magnetic AFM cantilevers typically have higher-quality factors ($Q_i \gg 10$), which allow to approximate the mode spectrum by a superposition of independent, damped, harmonic oscillators (one for each flexural mode; see Fig. 13.2a, b for an exemplary mode spectrum of a usual magnetic cantilever) [45]. This simplifies Eq. 13.3 for the *i*th mode into

$$\frac{d^2}{dt^2}z(t) + \frac{\omega_i}{Q_i}\frac{d}{dt}z(t) + \omega_i^2 \cdot z(t) = \frac{1}{m_i^*}F(t) \quad \text{with} \quad m_i^* = \frac{3}{\alpha_i^4}m. \tag{13.7}$$

For a pure harmonic excitation (with angular frequency ω)

$$F_{\text{harm}}(t) = F_0 \cos(\omega \cdot t), \tag{13.8}$$

the *i*th mode contributes to the steady-state solution of the deflection $z(t)$ with a harmonic oscillation, which is characterized by amplitude Z_i and phase ϕ_i: [49]

$$Z_i(\omega) = \frac{F_0}{m_i^*} \cdot \left[\left(\omega^2 - \omega_i^2\right)^2 + \left(\omega \cdot \omega_i/Q_i\right)^2\right]^{-1/2} \tag{13.9}$$

$$\tan\varphi_i(\omega) = \frac{\omega_i \cdot \omega}{Q_i\left(\omega^2 - \omega_i^2\right)}. \tag{13.10}$$

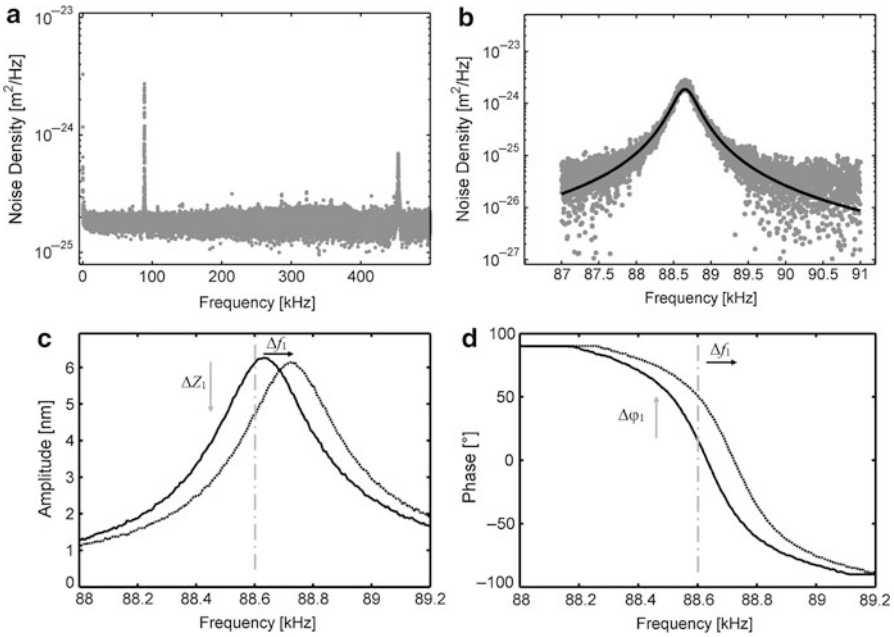


Fig. 13.2 Resonance properties of a representative cantilever used for magnetic force microscopy (MFM; type MESP from Bruker AXS, Mannheim, Germany). (**a**) The noise spectrum of the MESP cantilever shows resonant oscillation modes (flexural modes) at 86.62 kHz and 452.2 kHz with quality factors $\gg$10 (leading to sharp peaks in the spectrum). (**b**) The fundamental mode (*gray dots*; zoom of *a*) is well described by the response function of a harmonic oscillator (*line*; Eq. 13.9). (**c**, **d**) The resonance properties are affected by changes in the probe-sample forces, leading to shifts Δf_i in the resonance frequencies and/or changes in the quality factor. These changes can be quantified by either directly tracking the resonance frequencies (dynamic AFM) or indirectly by exciting a cantilever oscillation at a fixed frequency and by measuring changes in cantilever oscillation amplitude ΔZ_i or phase $\Delta\varphi_\mathrm{i}$ due to the shift Δf_i

Equation 13.9 further simplifies for large quality factors $Q_\mathrm{i} \gg 10$ and $\omega = \omega_\mathrm{i}$ (resonant excitation) to

$$Z_i(\omega) = Q_i \cdot \frac{F_0}{k}, \tag{13.11}$$

which shows the enhancement in force sensitivity due to resonance properties (cf. Eq. 13.1).

In practice the AFM cantilever will be subject to a superposition of a harmonic excitation $F_\mathrm{harm}(t)$ and a distance-dependent probe-sample force $F_\mathrm{D}(d)$. However, the calculations remain valid, if $F_\mathrm{D}(d)$ can be well approximated by the first term of a Taylor series expansion. In this case, Eqs. 13.7, 13.8, 13.9, and 13.10 can be directly reused if the resonance frequency of the *i*th mode is replaced by [50]

$$\omega_{i,\,\mathrm{force}}^2 = \omega_i^2 - \frac{1}{m_i^*}\frac{\partial F_\mathrm{D}(d)}{\partial d}. \tag{13.12}$$

Hence, the presence of a force gradient shifts the resonance properties of the AFM cantilever, which allows to quantitatively reconstruct the distance-dependent probe-sample forces $F_\mathrm{D}(d)$ [51–56], if the cantilever is well characterized (see Refs. [46] and [57–63] for detailed information on cantilever calibration procedures).

A comparison of Eq. 13.11 with Eq. 13.1 shows that using the oscillatory behavior of the cantilever enhances the force sensitivity by the cantilever's quality factor Q_i. As magnetic AFM setups employ high-quality cantilevers ($Q_\mathrm{i} \gg 10$), this corresponds to a tremendous increase in force sensitivity by up to several orders of magnitude. Therefore, it is no surprise that all state-of-the-art magnetic AFM approaches extract the magnetic probe-sample force indirectly by measuring changes in the oscillatory properties of the cantilever.

For usage in SPM, a vast amount of differently designed cantilevers have been reported. Spring constants can be as small as 10^{-6} N/m and quality factors as large as 100'000 (in vacuum), and the fundamental resonance frequency may vary between 1 kHz up to 1 GHz.

Operation Modes of AFMs and How to Measure Forces by Recording Changes in Cantilever Oscillation – Based on the kind of probe-sample contact occurring during the measurement process, the operation mode of an AFM is typically categorized in terms of contact, intermittent contact, and noncontact mode AFM.

In *contact mode AFM* [6, 7], the probe is pressed into the sample leading to probe-sample contact during the majority of the measurement, while in *intermediate contact AFM approaches* [64, 65], the cantilever is oscillated close to a resonance frequency, and the probe touches the sample only over a certain period of the cantilever oscillation, leading to intermittent probe-sample contact (sometimes called tapping). One should keep in mind that probe-sample contact adds a hardcore repulsion as force contribution to the total probe-sample interaction. Hence, using contact or intermittent contact mode for the measurement of magnetic forces leads always to a superposition of the magnetic force with nonmagnetic contributions, which makes a quantitative interpretation difficult. Hence, both modes are usually not used for the measurement of magnetic forces by current magnetic AFMs. However, intermittent contact mode has relevance in magnetic force microscopy (MFM, see Sect. 3.1), where it is often used in a first scan to determine the sample morphology, which allows to keep (in a second scan) the probe-sample distance constant during the actual magnetic measurement.

In *noncontact mode* AFM [66–70], changes of the oscillation properties of the AFM cantilevers are used to measure the force acting on the probe. Ideally, the probe never touches the sample surface, and the oscillation of the cantilever is only subject to the forces sensed by the probe. Virtually all magnetic AFMs use noncontact mode AFM approaches to extract magnetic interactions from the measurement.

Several approaches have been published in the past to extract probe-sample forces $F_\mathrm{D}(d)$ from such measurements [51–56]. All of them induce a cantilever

oscillation of one or several flexural modes by applying a periodic force on the cantilever (typically using a piezoelectric crystal placed close to it) and measure changes in this forced oscillation. The approaches can be roughly divided into methods, which excite an oscillation at a *fixed* frequency or which track the cantilever's resonance frequency using a *variable* excitation frequency controlled by a feedback loop.

Approaches employing a *fixed excitation frequency* ω_{fix} (which is usually chosen within the resonance curve of a certain mode ω_{i}) sense changes in the resonance frequency indirectly by recording changes in cantilever oscillation amplitude $Z_{\mathrm{i}}(\omega_{\mathrm{fix}})$ or phase $\varphi_{\mathrm{i}}(\omega_{\mathrm{fix}})$ [68]. A shift $\Delta\omega_{\mathrm{i}}$ in the resonance frequency ω_{i} also shifts the resonance curve, leading to changes in $Z_{\mathrm{i}}(\omega_{\mathrm{fix}})$ and $\varphi_{\mathrm{i}}(\omega_{\mathrm{fix}})$, which can be calculated using Eqs. 13.9 and 13.10 (see Fig. 13.2c, d). Inversion of these equations allows in principle to determine the shift of ω_{i} and hence (according to Eq. 13.12) the probe-sample force. For small shifts $\Delta\omega_i = 2\pi \cdot \Delta f_{\mathrm{i}}$, it is feasible to choose an excitation frequency ω_{fix} at the edges of the resonance curve, where the slopes $\mathrm{d}Z_{\mathrm{i}}(\omega)/\mathrm{d}\omega$ or $\mathrm{d}\varphi_{\mathrm{i}}(\omega)/\mathrm{d}\omega$ become steepest. At these points, maximum sensitivity is obtained, and changes Z_{i} or φ_{i} depend almost linearly on $\Delta\omega_{\mathrm{i}}$ for sufficiently small forces (*slope detection method*). It was calculated that the minimum detectable force gradient is given by [66, 70]

$$\min(F_{\mathrm{D}}') = \sqrt{\frac{2 \cdot k \cdot k_{\mathrm{B}} \cdot T \cdot B}{\omega_i \cdot Q \cdot < Z_i^2 >}}. \tag{13.13}$$

Here, B denotes the bandwidth of the measurement, $k_{\mathrm{B}} \cdot T$ the thermal energy (product of Boltzmann's constant k_{B} and the temperature T), and $< Z_i^2 >$ is the mean squared displacement of the cantilever during the oscillation.

However, as also the quality factor Q_{i} enters into the equations for the extraction of F_{D} and as Q might be altered due to additional energy losses (i.e., dissipative effects due to probe-sample interaction), care must be taken in quantitative interpretations of such measurements. Moreover, one should also keep in mind that the settling time (i.e., the time interval, which is necessary for the cantilever to settle on changes of the probe-sample force) of such *fixed frequency* approaches scales with the quality factor Q_{i} of the resonance mode [50]. As typically cantilevers with high-quality factors are employed in magnetic AFM setup (to enhance the force resolution by the factor of Q_{i}), this feature leads to large settling times, pushing the bandwidth of the measurement below 1 Hz [50], which is much too slow for reasonable measurement times.

Such (and other problems) are circumvented by using a cantilever excitation with a *variable excitation frequency* [50]. Here, the cantilever is driven all the time at the resonance frequency of a certain resonance mode (e.g., $\omega = \omega_{\mathrm{i}}$), which can be achieved by using phase-locked loops (PLLs) or positive feedback networks that keep the phase shift $\varphi_{\mathrm{i}}(\omega)$ between excitation and cantilever oscillation at the resonance condition of $\pi/2$. In this case, the shift $\Delta\omega_{\mathrm{i}}$ of the excitation frequency (which can be directly extracted from the PLL) is a direct measure for the gradient in the probe-sample force (according to Eq. 13.12). As the excitation frequency is locked at the resonance frequency and therefore variable during the measurement,

such approaches are also termed *frequency modulation AFM*, *dynamic mode AFM*, or *dynamic force microscopy*.

Interestingly, *frequency modulation* approaches can be extended using a second control loop, keeping the oscillation amplitude at the fixed value (*constant amplitude mode*). Such setups have the advantage that the probe-sample forces can be decomposed into non-dissipative and dissipative components, as the former class affects only the resonance frequency, while the latter one can be extracted from the force required to maintain a constant value of the excited amplitude. Moreover, in *frequency modulation*, the bandwidth is dominated by the characteristics of the electronics and not by the quality factor of the cantilever, leading for high-Q cantilevers to much higher bandwidths compared to the slope detection method [50]. Albrecht and co-workers calculated the minimum detectable force gradient in FM AFM: [50]

$$\min(F_{\mathrm{D}}{}') = \sqrt{\frac{4 \cdot k \cdot k_{\mathrm{B}} \cdot T \cdot B}{\omega_i \cdot Q \cdot < Z_i^2 >}}. \tag{13.14}$$

2.3 Detection of Cantilever Oscillation

Several approaches have been described to measure the cantilever deflection, which is a prerequisite for measuring force-induced changes in the cantilever oscillation. The majority of these approaches can be roughly divided into implementations having an *electric* or *optical* readout system.

Electric readout requires that certain electric cantilever properties change, if the cantilever is deflected. For example, cantilevers made out of *piezoelectric* materials (e.g., quartz crystals) create a voltage upon deflection, which can be used for both, sensing the deflection but also to induce a cantilever oscillation by application of an oscillating voltage. Hence, this *tuning fork* approach has the advantage that excitation and sensing can be achieved with the same unit. Recent designs achieved a deflection noise floor on the order of $5 \cdot 10^{-14}$ m $\mathrm{Hz}^{-1/2}$ [71].

Other examples are cantilevers made out of *piezoresistive* materials, which change their resistance upon deflection [72, 73]. Current implementations reach deflection sensitivities on the order of 10^{-11} m $\mathrm{Hz}^{-1/2}$ and force sensitivities down to 250 aN $\mathrm{Hz}^{-1/2}$ (both at room temperature) [74]. Both examples have the advantage that the cantilever deflection is directly converted into an electric signal.

In contrast to this, implementations using *optical readout* systems have to convert the light (used to detect the cantilever deflection) using photodiodes into an electric signal, which may give rise to additional noise. However, it turns out in practice that the performance of optical deflection detection is in most cases (despite this fact) comparable or even better than that of electronic deflection detection. Hence, it is no surprise that most setups reported so far rather use optical than electronic deflection detection. Depending on the sensitivity, two different implementations are mostly used.

The so-called light lever method uses the fact that a laser beam (which is reflected by the cantilever) changes its direction if the cantilever is deflected [75, 76]. Typically, the laser beam is such aligned that the reflected beam hits (in the absence of any cantilever deflection) the center of a four-quadrant photodiode, leading to equal illumination of all quadrants (see Fig. 13.1). A deflection shifts the reflected beam, causing an unequal illumination, which can be quantified by measuring the photocurrents of the different quadrants. Current implementations reach deflection sensitivities on the order of 10^{-12} m $Hz^{-1/2}$ [77]. The adjustment of the light lever method is very convenient and user-friendly, and the setup is relatively robust and cheap, making this implementation the most used one reported in literature.

Higher sensitivities can be achieved using *optical interferometry* [78–80], which is (on the other hand) more complex and more challenging than the light lever method. However, this method is very established in magnetic AFM designs operating under extreme conditions (e.g., at very low temperatures) or requiring the highest possible sensitivity. Hence, almost all designs made for MRFM and MExFM employ this deflection detection method. In optical interferometry, the cantilever forms one mirror of an optical cavity. Using mirrors with sufficiently high reflectivities makes such cavities optically transparent only at certain wavelengths, which fulfill a resonance condition set by the distance between the two mirrors. Cantilever deflection changes the mirror-to-mirror distance and shifts the resonance wavelengths, allowing to measure the deflection by tracking the resonance condition of the optical cavity. Current implementations reach deflection sensitivities on the order of 10^{-14} m $Hz^{-1/2}$ at room temperature, which makes optical interferometry to the most sensitive deflection detection reported so far [80]. The combination of optical interferometry, high-Q cantilevers, and low measurement temperatures results in force sensitivities on the order of 1 aN Hz-1/2 [81].

3 Specific Experimental Methodology: Implementations of Magnetic AFM Approaches

The following sections discuss how the "basic AFM setup" can be extended to measure magnetic properties at the μm down to the sub-nm scale. The discussion starts with the simplest and most widely used magnetic AFM technique, the magnetic force microscopy (MFM) [8–10], which is capable to study the lateral distribution of the (static) sample's magnetization with imaging resolutions down to 10 nm. Afterward, the so-called magnetic resonance force microscopy (MRFM) is introduced [82, 83], which combines concepts of magnetic resonance with AFM. Although single electron spin resolution was already demonstrated using MRFM, the lateral imaging resolution is currently still not sufficient to measure spin maps with true atomic resolution. However, this outstanding resolution was recently demonstrated on antiferromagnetic samples by the last magnetic AFM technique to be discussed, the magnetic exchange force microscopy (MExFM), which uses the quantum mechanical effect of exchange interaction to yield atomically resolved spin maps [84].

All approaches differ in the constituents creating the magnetic probe-sample force and/or the kind of magnetic interaction used to generate this force. MRFM senses the magnetic moments of electronic or nuclear spins, which are resonantly excited (and thus subject to permanent manipulation) by external magnetic fields. Hence, MRFM measures dynamic magnetic interactions arising between the sample's spins and the magnetic probe and allows to elucidate the spin dynamics of para- and ferromagnets. Similarly, MExFM also senses an exchange interaction between probe and sample spins, but (in contrast to MRFM) these spins are stably aligned by the antiferromagnetic order of the sample and spin dynamics are hardly accessible. In contrast to this, MFM measures a magnetostatic interaction arising between the ferromagnetic probe and a sample containing stably align magnetic moments. It is therefore mostly applied to ferromagnetic or superparamagnetic samples (if necessary, magnetized in an external magnetic field).

Table 13.1 gives a general overview over a part of the available literature on these approaches by describing the concepts, the first experiments, and recent applications. Some of these topics will be discussed in more detail in the following sections.

3.1 Magnetic Force Microscopy (MFM)

3.1.1 General Remarks

Soon after the invention of AFM, it was realized by several groups that the magnetic stray field of a sample can be investigated with an AFM-based setup, if the nonmagnetic probe is replaced by a magnetic one. The approach was termed magnetic force microscopy (MFM) and represents the first realization of a magnetic AFM [8–10]. MFM senses magnetostatic probe-sample interactions and can therefore be applied to almost any sample that exhibits stably magnetized parts. Hence, the majority of the publications demonstrate measurements of ferromagnetic materials and structured magnetic materials containing ferromagnetic constituents.

Application of MFM requires the usage of a magnetic AFM probe and the possibility to scan the sample in a so-called dual-pass or two-pass fashion (which will be described below in detail). In comparison to other magnetic AFM methods, these are rather simple requirements on the basic MFM design. Hence, few years after the first demonstration of MFM, commercial MFM solutions became available, making this technology widely accessible. MFM is therefore the mostly used magnetic AFM method to date. The application of MFM has been reported in ultrahigh vacuum (UHV), in air, and even in liquids [146], which demonstrates the broad feasibility of the approach.

3.1.2 Origin of Magnetic Force

MFM was originally designed to measure the magnetostatic interactions arising between the magnetic probe (mounted onto the cantilever) and a magnetic stray field $\boldsymbol{B}_{\text{sample}}$, created by the sample of interest. This field might be generated by a

Table 13.1 Publications giving detailed information about the concepts, instrumentation, theory, and application of the different magnetic AFM approaches

Topic	References
Magnetic force microscopy (MFM)	
Concept	Refs. [8–10]
Reviews	Refs. [85–90]
Theory/data analysis	Refs. [91–98]
Calibration	Refs. [99–105]
Probes	Refs. [106–113]
Applications	
Magnetic recording	Refs. [85–88]
Micromagnetic investigations	Refs. [86, 114–116]
Nm-thin multilayered systems	Refs. [117–120]
Magnetization reversal and domain structure: nanodisks, nanodots, etc.	Refs. [121–139]
Properties magnetic nanoparticles	Refs. [140–147]
Superconductor vortices	Refs. [148–150]
Magnetic resonance force microscopy (MRFM)	
Concept	Refs. [82, 83]
Reviews	Refs. [81, 163–169]
Theory/data analysis	Refs. [170–174]
Instrument design	Refs. [175–181]
Cantilever/probes	Refs. [182–187]
Applications	
ESR spectroscopy/imaging	Refs. [188–194]
NMR spectroscopy/imaging	Refs. [195–201]
FMR spectroscopy/imaging	Refs. [202–209]
Manipulating small spin ensembles	Refs. [210–212]
Magnetic exchange force microscopy (MExFM)	
Concept	Refs. [84]
Reviews	Refs. [89, 229]
Theory/data analysis	Refs. [230–234]
Instrument design	Refs. [84, 235]
Applications on antiferromagnets	
NiO(001)	Refs. [84, 235]
Fe on W(001)	Refs. [236–238]

sample magnetization $\boldsymbol{M}_{\text{sample}}$ (e.g., by magnetized Weiss domains of a ferromagnetic material [86, 88] or by (super)paramagnetic materials, which are magnetized inside an external magnetic field) [143–146] or equivalently by magnetic moments $\boldsymbol{m}_{\text{sample}}$ (e.g., generated by an electrical current or by flux lines within superconductors) [148–150] incorporated in the sample (Fig. 13.3). It is important that the sample magnetization can be regarded as magnetostatic, i.e., the magnetic sample

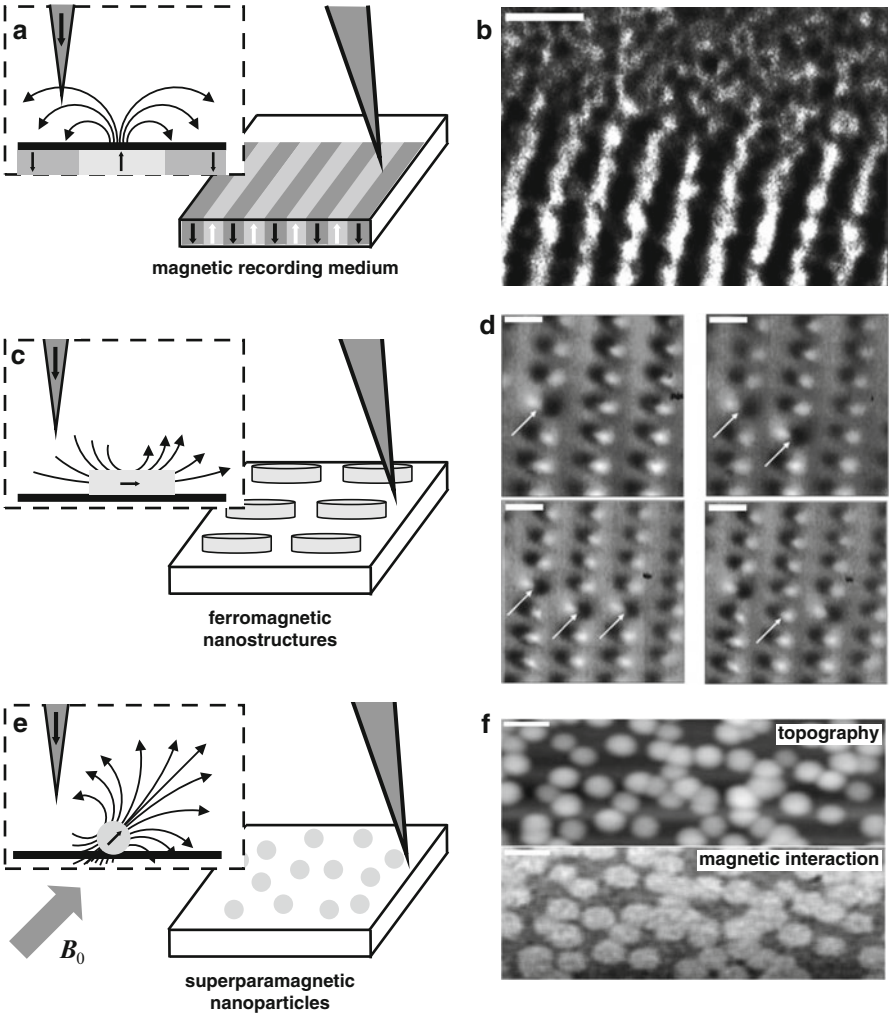


Fig. 13.3 Examples for MFM applications as indicated in the schematics in the left column. The right column gives typical experimental results. Scale bar: (*top*) 2 μm, (*middle*) 1 m, (*bottom*) 250 nm. Strong changes in the stray fields give high contrast in MFM measurements (e.g., caused by changes in the direction of the magnetization, or by dipolar fields of isolated magnetic domains). The images in **d** show magnetization reversal of single magnetic nanostructures (*white arrows*) in dependence of the applied magnetic field strength [131]. Imaging of superparamagnetic nanoparticles often requires an external magnetic field B_0 to stabilize the nanoparticle magnetization. In **f**, this field was oriented almost perpendicular to the sample surface, so that only one side of the dipolar field is imaged in the magnetic chanel (**d** is taken with permission from Ref. [131])

properties must be stable on the timescale of the MFM measurement (which is typically on the order of some minutes).

The magnetostatic interaction of the probe (having a magnetization $\boldsymbol{M}_{\text{probe}}$) with the sample's stray field $\boldsymbol{B}_{\text{sample}}$ leads to the interaction energy U

$$U\left(\boldsymbol{r}_{\text{probe}}\right) = -\int\limits_{\text{probe}} \boldsymbol{M}_{\text{probe}}(\boldsymbol{r}) \cdot \boldsymbol{B}_{\text{sample}}(\boldsymbol{r}) dV$$
$$= -\int\limits_{\text{sample}} \boldsymbol{M}_{\text{sample}}(\boldsymbol{r}) \cdot \boldsymbol{B}_{\text{probe}}(\boldsymbol{r}) dV \tag{13.15}$$

which can (due to reciprocity) [151] also be understood as the interaction of the sample's magnetization $\boldsymbol{M}_{\text{sample}}$ with the stray field of the magnetic probe $\boldsymbol{B}_{\text{probe}}$ [95, 96]. This interaction gives rise to the magnetic probe-sample force $\boldsymbol{F}(\boldsymbol{r}_{\text{probe}})$

$$\boldsymbol{F}\left(\boldsymbol{r}_{\text{probe}}\right) = -\text{grad}\, U\left(\boldsymbol{r}_{\text{probe}}\right) \tag{13.16}$$

acting on the cantilever.

It should be noted that although Eq. 13.15 has a simple appearance at first sight, the underlying calculations are often complex even if several approximations are included (e.g., restricting to only mono- and dipole components of the tip magnetization) [86, 92]. The reader is referred to Refs. [91–98] for a detailed discussion of the mathematics behind MFM.

3.1.3 Instrumentation

In principle, every AFM is capable in conducting MFM experiments if it is equipped with a cantilever carrying a magnetic probe and if it is able to be operated in a dual-pass/two-pass fashion.

Probes – As MFM is a highly established technique (i.e., it is routinely performed in a vast number of laboratories), many different kinds of MFM probes are commercially available. The probe's magnetic moment (of commercial solutions) is typically created by a nm-thick ferromagnetic coating (often made of Cr or Fe), which is evaporated onto Si, SiO_2, or Si_3N_4 probes. The underlying cantilever usually offers quality factors and spring constants on the order of 100 and 1 N/m (fundamental mode; $i = 1$), respectively. Softer cantilevers are rarely fabricated as they tend to "jump into contact" during the measurement. Unfortunately, the exact composition of the ferromagnetic coating in commercial MFM probes is often undisclosed by the manufacturer and hence not known, which complicates the modeling process of the measurement.

The shape of the magnetic probe strongly affects the resolution of the MFM measurements, which triggered the development of different protocols to enhance their spatial properties. They range from etching/milling techniques to sharpen the magnetization volume [106, 107, 110], mounting of ferromagnetically filled carbon nanotubes onto cantilevers [108, 111–113], to attaching ferromagnetic nanospheres onto the cantilever [109]. These examples show impressively that a spatial confinement of the magnetic probe's volume may drastically increase the lateral resolution of MFM measurements [86]. As carbon nanotube probes can often be treated as magnetic monopoles, they offer not only high-spatial resolutions but also simplify the quantitative data analysis [112, 113].

The MFM setup might be complemented by an additional external magnetic field $\boldsymbol{B}_0$, which can be used to control the sample's magnetization $\boldsymbol{M}_{\text{sample}}$. This is, for example, useful if the sample exhibits a stable magnetization only in the presence of a polarizing magnetic field (e.g., for superparamagnetic materials) [143–146] or if the dependence of $\boldsymbol{M}_{\text{sample}}$ on externally applied fields should be investigated (e.g., for switching experiments/study of magnetization reversal, for visualizing the movement of domain walls, etc.) [121–139].

Dual-Pass/Two-Pass Capabilities – MFM takes advantage of the fact that the range of magnetic forces is typically much larger than that of "ordinary" surface forces (like van der Waals attraction, electrostatic interaction, etc.), which are usually restricted to the very first 10 nm close to the surface. Hence, the magnetic interaction can be extracted (without disturbance from other surface forces) if the sample is imaged at probe-sample distances larger than few 10 nm. Hence, the AFM setup needs to be able to keep a constant probe-sample distance (on the order of few 10 nm up to some 100 nm) during the MFM imaging process, which is often solved by so-called dual-pass/two-pass implementations.

In these implementations, the sample is scanned at least twice. During the first scan (the *first pass*), the MFM is operated in a conventional AFM imaging mode, which allows to extract the sample morphology/topography. In the actual MFM measurement (the *second pass*), the previously measured sample morphology is taken "as a reference," and a displacement is introduced between the measured track (on the sample) and the actual track of the probe, which keeps the probe-sample distance fairly constant. To avoid errors due to drifts, a line-wise switching is often preferred between the two scans. This means that in the first pass one line of the sample morphology is scanned; a constant displacement is added to the height profile of this line, which then defines the track that is used to scan the probe in the second pass (the actual MFM measurement).

Hence, to conduct MFM measurements, it must be possible to operate the AFM in such a dual-pass/two-pass fashion, which is fulfilled for every commercially available AFM built in the last decade.

3.1.4 Measurement Procedure

In MFM the magnetic probe is typically raster-scanned above the sample in a dual-pass/two-pass fashion (see Sect. 3.1.3 for more details), giving both the sample morphology (*first pass*) as well as the spatial distribution of the magnetic interaction (*second pass*) as data channels. Hence, the *first pass* typically employs an AFM imaging method like intermittent contact or noncontact mode imaging approaches (see Sect. 2.2).

To avoid artifacts caused by nonmagnetic forces during the actual MFM measurement [94, 152], the magnetic probe is then (*second pass*) "lifted" from the sample surface by introducing a user set probe-sample distance, which is kept constant during the magnetic measurement. To allow a quantitative extraction of the magnetic force, it is necessary to operate the AFM in a *noncontact mode* (see Sect. 2.2) during this step. Both fixed frequency excitation (readout = changes in the induced cantilever oscillation amplitude or phase, *slope detection method*) and

variable frequency excitation (readout = tracking of the cantilever's resonance frequency, *dynamic force AFM*) have been reported. Newer implementations use (sometimes simultaneous) excitation at several resonance frequencies [153, 154], which may enhance the resolution [146].

Depending on the properties of the sample and the required spatial resolution, the sample morphology (first pass) is typically recorded at very small probe-sample distances (less than or only very few nm), while it increases in the actual MFM scan (second pass) to values ranging between some 10 nm and few 100 nm. This means that the two scans (yielding sample morphology and magnetic interaction) are typically recorded at completely different probe-sample distances, which has the advantage that only (relatively long-ranged) magnetic forces contribute to the second scan, that the sample morphology introduces only a relatively small cross talk into the measurement of the magnetostatic interaction, and that this interaction may be quantified, if the magnetic properties of the probe and the oscillation properties of the cantilever are known. Decreasing the probe-sample distance in the second pass increases not only the lateral resolution but also the risk of having morphological cross talks.

3.1.5 Image Formation

MFM is obviously an imaging approach, i.e., spatial changes in the sample's magnetization $\boldsymbol{M}_{\text{sample}}$ (or the related stray field $\boldsymbol{B}_{\text{sample}}$) are reconstructed from lateral changes of the magnetostatic force acting on the cantilever (indirectly extracted from changes of the cantilever oscillation as described above). A qualitative assessment can be done directly from these images, e.g., if the focus is set on the spatial distribution and arrangement of Bloch walls and magnetic/Weiss domains, or on the quality of a magnetic pattern written into a ferromagnetic thin film (Fig. 13.3) [85, 86].

Despite advances in the modeling of the MFM measurement process, a quantitative data analysis is still challenging and is only possible if cantilever and probe properties (like resonance frequency, quality factor, spring constant, the probe's curvature radius, and magnetic moment) have been determined by calibration [46, 57–63, 99–105]. Several models have been proposed to relate these properties with the measured changes in the cantilever oscillation to yield quantitative information about the spatial distribution of the magnetic force and finally of the sample magnetization. However, the real spatial distribution of the probe's magnetization is usually not known and is often replaced by an "effective" value. Moreover, different sample magnetizations may lead to the same results after applying Eq. 13.16, showing that further knowledge is necessary to unambiguously extract the sample magnetization from MFM measurements. Please refer to Refs. [91–98] for more detailed information about these quantification approaches.

It should be noted that calibration of the magnetic probe should be done on reference samples having similar dimensions like the sample of interest [102]. This is mainly due to the fact that it is difficult for magnetic interactions to define a priori a clear cutoff value for the distance, at which magnetic interactions can be neglected. This is different to exponential decays, in which such a cutoff distance

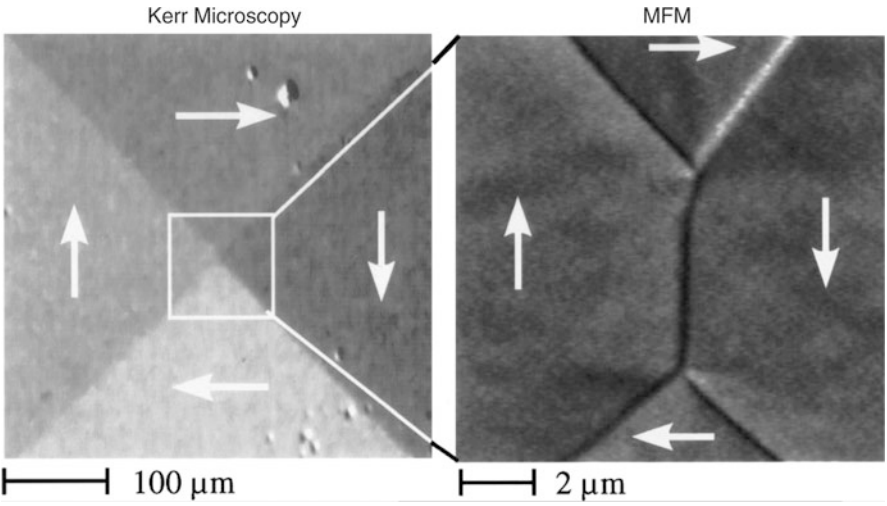


Fig. 13.4 Comparison of (optical) Kerr microscopy and MFM applied to a single crystal Fe film (500 nm thickness). Micromagnetic details are hardly accessible in Kerr microscopy, while they can be visualized using MFM. Moreover, it demonstrates again that changes in the stray field are necessary to achieve a contrast in the MFM images; the domain walls create a good contrast, while the domain itself shows only small variations (Taken with permission from Ref. [155])

is given by the decay length. In the experiments, this is reflected by the observation that the probe's magnetic moment, which is extracted from magnetometric measurements using planar, µm-sized coils, depends on the size of the coils used for calibration; larger coils suggest larger magnetic moments, which shows that the probe's volume that participates in the magnetic interaction increases with the size of the coil [102, 104]. To minimize these effects, either monopole-like MFM probes should be employed [112, 113], or the probe should be calibrated using reference samples having a similar size like the sample of interest.

3.1.6 Applications

Magnetic Thin Films/Magnetic Recording – As it was realized that MFM can be used to investigate near-surface stray-field variations caused by changes in sample magnetization, MFM became a standard tool for investigation and optimization of magnetic recording media and thin magnetic films. MFM has been applied to study the quality, density, and stability of the data patterns written in such media. Excellent reviews on this topic can be found in Refs. [85–90], which makes a repetition of findings in this field dispensable. Latest research concentrates on thin magnetic bi- and multilayered films, which allows to study the scaling behavior of such complex structures as the physical dimensions are reduced [117–120].

Magnetic Micro- and Nanostructures – In parallel to its application on magnetic recording media, MFM was also applied to image magnetic domain structures (Fig. 13.4) in dependence of the material composition, internal organization (structure), and an externally applied magnetic field (used to induce a reordering

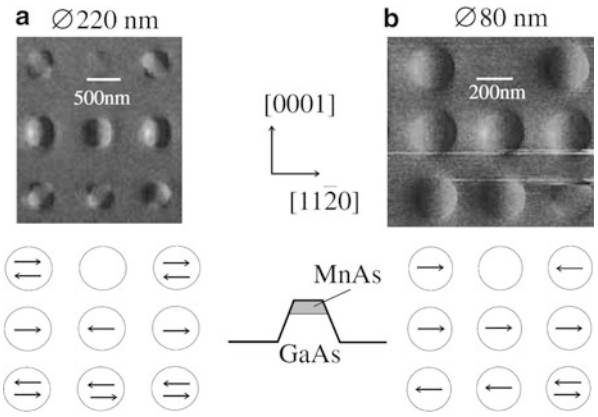


Fig. 13.5 Magnetization of epitaxial MnAs nanodisks on GaAs (diameters: a = 220 nm, b = 80 nm; thickness = 50 nm). MFM imaging allows to distinguish nanodisks containing the ferromagnetic α-MnAs phase (containing a single or two ferromagnetic domains at these dimensions) and the paramagnetic β-MnAs phase (no MFM contrast, open circles in the schematics), which can be correlated with methods that average overall disks (e.g., X-ray diffraction) (Taken with permission from Ref. [133])

of the magnetic domain). Instrumentation and methods were further improved to reduce the length scale of stray-field variations resolvable with this AFM technique. Moreover, the achievements in micro- and nanolithography and thin film deposition techniques allowed to produce magnetic micro- and nanostructured layers having well-defined geometries and highly crystalline structures, which contain very few or only a single magnetic domain (Fig. 13.5). MFM was applied to such micro- and nanostructures to investigate the connection between properties like the chemical composition and anisotropy (e.g., shape, surface, and, if applicable, crystal anisotropy) and the measured magnetization, giving the intriguing possibility to study magnetization reversal processes on well-defined, single domains and to correlate microscopically and macroscopically resolved magnetization curves (Fig. 13.6) [121–139].

Characterization of Superparamagnetic Nanoparticles – Superparamagnetic materials are formed, if the size of a ferromagnetic domain is decreased to such small values that the sample magnetization is no longer stabilized (e.g., by crystal and shape anisotropy) against thermal fluctuations [156, 157]. Hence, in the absence of a polarizing magnetic field, the sample's average magnetic moment vanishs. However, there is still (due to the strong exchange interaction) a strong sample magnetization, which can be aligned in a magnetic field. Several protocols have been published, which allow to synthesize superparamagnetic particles with nm-sized radii (so-called nanoparticles), which may serve (due to their remarkable magnetic properties) as contrast agent in magnetic resonance imaging (MRI), or which may allow a (magnetically induced) local heating of tissue, which is, e.g., employed in hyperthermal cancer treatment [158–161].

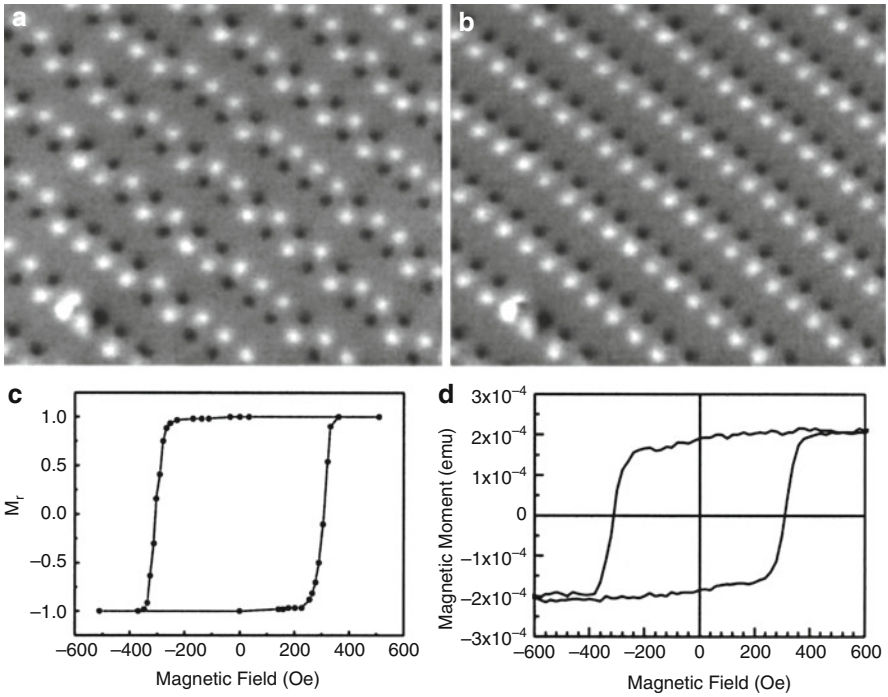


Fig. 13.6 MFM magnetization reversal study of a nanorod (240 × 90 × 10 nm) array by recording MFM images at different field strength of an external magnetic field (applied parallel to the long axis of the nanorods). (**a**, **b**) Increasing the field strength switches the orientation of the nanorod magnetization preferentially parallel to the external field. (**c**) Calculating the fractions of nanorods with parallel and antiparallel orientation allows to determine the magnetization curve of the sample and (**d**) enables a direct comparison with (averaging techniques like) alternating gradient magnetometry (Taken with permission from Ref. [137])

Several groups employed MFM to determine magnetic properties of single superparamagnetic nanoparticles. In most cases these measurements are conducted on iron-oxide-based nanoparticles, which have (due to their nontoxicity) the highest pharmacological relevance. Schreiber et al. conducted MFM experiments and simulations of such nanoparticles and concluded that in a conventional MFM setup (using commercially available MFM probe, measuring in air), only nanoparticles larger than 10 nm in diameter can be accessed, a conclusion which triggered several new developments in this field [143]. In 2011, several groups succeeded (by enhancing the measurement sensitivity using modified versions of MFM) in stray-field imaging of single, isolated iron-oxide-based nanoparticles being as small as 5 nm in diameter [145, 146].

Some methods have been published, which allow to extract the nanoparticle's magnetic moment from such MFM measurements [147]. Usually, the dipole-dipole approximation is employed, i.e., the magnetic properties of both nanoparticle and MFM probe are approximated by simple magnetic dipoles m_{NP} and

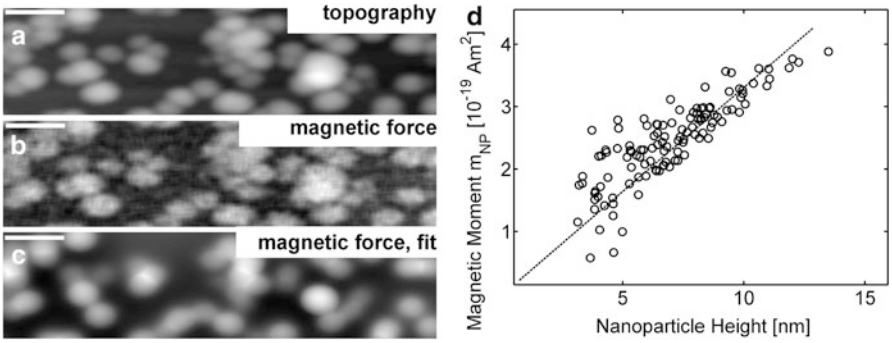


Fig. 13.7 Extraction of the magnetic moment distribution of superparamagnetic maghemite nanoparticles using an MFM approach employing an external magnetic field that oscillates with the cantilever's fundamental resonance frequency (termed NIOMI; see Ref. [145] for details on the method). The approach gives (**a**) the sample topography and (**b**) the spatial distribution of the magnetic force arising from the probe-nanoparticle-interaction. Using a magnetic dipole-dipole interaction allows to individually extract the magnetic moment for each nanoparticle and (**c**) gives the theoretically calculated force map for the magnetic moment distribution shown in (**d**), which matches well the measured force map in (**b**). The distribution of the magnetic moments follows rather a straight line than a cubic law (as expected for spherical nanoparticle shape), indicating that the nanoparticle shape is rather an ellipsoid than a sphere. Scale bar = 100 nm

m_{Probe}, respectively, which interact at a certain probe-sample distance h. These measurements are currently extended to extract full distribution histograms of the nanoparticle magnetic moments (Fig. 13.7) and to localize superparamagnetic nanoparticles specifically bound to proteins of interest (on or within cells) [144, 145].

Flux Line Mechanics – As stated above, MFM can be applied to almost any sample that contains magnetostatic moments. Technically it makes no difference, if these moments are created by magnetic domains in a sample or by ring currents [162]. The latter are, for example, formed in type II superconductors, which are subject to an externally applied magnetic field. In this case it is well known that exceeding a certain external field strength, flux lines of the external field enter into the type II superconductor and that the superconductor "reacts" by creating a lattice of so-called vortices surrounding and partially shielding the flux lines. Recently, it was demonstrated that MFM is not only capable to localize vortices within type II superconductors, but that it is also possible to manipulate the position of these vortices using the magnetic interaction of an MFM. This opens up very interesting possibilities like in situ probing of the dynamic and mechanic behavior of single vortices (which is not achievable by conventional bulk techniques) and probing, how the structure of type II superconductors affects vortex pinning [148–150].

3.2 Magnetic Resonance Force Microscopy (MRFM)

3.2.1 General Remarks

Magnetic resonance imaging (MRI) had a tremendous impact on biology, life, and material science as it allows noninvasive imaging and differentiation of soft tissues without producing ionizing radiation like X-ray imaging or computed tomography [213–216]. It (and all other methods employing magnetic resonance) uses the fact that a magnetic moment, which is aligned by an external magnetic field, rotates with the (so-called) Larmor frequency around the direction of its initial alignment once it is tilted out of alignment (e.g., by a second magnetic field, applied perpendicular to the first one). Due to dissipative effects, the tilted moment will evolve back to its initial alignment (typically on the ms timescale). All commercially available MRI implementations use an inductive detection method involving a coil to manipulate and measure the state of the magnetic moments within the sample, leading to spatial resolutions (so-called voxel volumes) down to 40 μm^3 corresponding to lateral resolutions on the μm length scale [217, 218].

In the 1990s, it was realized by J. A. Slides that the spatial resolution of MRI could be substantially enhanced from the μm to the nm scale if microfabricated cantilevers are employed for mechanical detection of magnetic resonance (MR) [82, 83], which was a fundamental change in the basic concepts of MR. This resulted in the development of magnetic resonance force microscopy (MRFM), which combines ideas of MRI with AFM. Reducing the spatial resolution of MRI down to the size of single atoms would allow to analyze molecules in an atom-by-atom fashion, leading to a three-dimensional atomic structure of the analyzed molecules [81].

MRFM typically requires complex instrument designs (in comparison to the other magnetic AFM methods discussed in this manuscript), and up to now the author is not aware of any commercially available MRFM implementation. This might be the reason for the observation that the majority of publications using MRFM are created by less than ten independent labs. MRFM has been applied for magnetic resonance spectroscopy and imaging using nuclear magnetic resonance (NMR), electron spin resonance (ESR), and ferromagnetic resonance (FMR). During the time this manuscript was written, the sensitivity of MRFM was sufficient to achieve detection of a single electron spin and of approximately 100 nuclear spins, which corresponds to a 10^7-fold increase in the sensitivity compared to the first MRFM experiment [81]. Additionally, MRFM allows to manipulate the spins in the sample, which can be used to gain fascinating insights into the dynamic behavior of spin systems, strongly extending the scope of the approach from MRI to spintronics, material sciences, and even the application in quantum computing was proposed [219–221].

3.2.2 Origin of Magnetic Force

Subject of MRFM measurements is the interaction of the magnetic probe with magnetic moments that are created by resonantly excited nuclear or electronic spins. Typically, the sample's spins are aligned by a strong external magnetic

field $\boldsymbol{B}_0$ giving rise to a sample magnetization $\boldsymbol{M}_{\text{sample}}$, which is in the static case parallel to $\boldsymbol{B}_0$. However, if the spins are tilted out of this direction, a precessional motion of the spins around $\boldsymbol{B}_0$ occurs. The angular frequency of this precession is the Larmor frequency ω_{L}:

$$\omega_{\text{L}} = \gamma \cdot B_{\text{eff}} \tag{13.17}$$

with γ denoting the gyromagnetic ratio of the spin and B_{eff} being the effective magnetic flux sensed by the spin [213]. The gyromagnetic ratio of nuclear spins is typically 1,000 times smaller than that of an electron ($\gamma_{\text{e}}/2\pi$ = 28.024 GHz/T).

In magnetic resonance experiments, precession of $\boldsymbol{M}_{\text{sample}}$ is induced by applying an electromagnetic field which is oriented perpendicular to $\boldsymbol{B}_0$ and which meets the resonance condition, i.e., whose oscillation frequency equals ω_{L}. Due to this precessional motion, $\boldsymbol{M}_{\text{sample}}$ is composed of a time-dependent and time-independent term $\boldsymbol{M}_0$ and $\delta\boldsymbol{M}$, respectively:

$$\boldsymbol{M}_{\text{sample}}(\boldsymbol{r}, t) = \boldsymbol{M}_0(\boldsymbol{r}) + \delta\boldsymbol{M}(\boldsymbol{r}, t) \tag{13.18}$$

The interaction of this magnetization with the magnetic field $\boldsymbol{B}_{\text{probe}}$ (created by the magnetic probe) gives rise to a time-dependent component of the magnetic force $\boldsymbol{F}$ acting on the MRFM cantilever: [168]

$$\boldsymbol{F}\left(\boldsymbol{r}_{\text{probe}}, t\right) = \int\limits_{\text{sample}} (\delta\boldsymbol{M}(\boldsymbol{r}, t) \cdot \text{grad})\boldsymbol{B}_{\text{probe}}(\boldsymbol{r})dV. \tag{13.19}$$

It should be noted that MRFM employs at least two resonance conditions: (ι) resonant excitation of the spins requires that the frequency of the electromagnetic field equals the Larmor frequency ω_{L}, which is typically on the order of radio frequency (rf) fields (i.e., few 100 MHz to some GHz), and (ιι) to enhance force sensitivity, $\boldsymbol{F}$ has to be modulated at the resonance frequency of the MRFM cantilever, which typically ranges between 1 and 100 kHz. These requirements triggered the development of dedicated spin manipulation protocols (i.e., modulation protocols for the rf field), which are described in detail in the Refs. [165] and [166].

Moreover, one has to regard that the Larmor frequency depends on the effective magnetic flux sensed by the spins (Eq. 13.17), which varies spatially (due to the probe's inhomogeneous magnetic field) in MRFM measurements. Strikingly, it is possible to restrict the volume having resonant spin excitation to a small zone in the vicinity of the probe, the so-called *resonant slice* (Fig. 13.8) [165, 172, 222]. The volume and shape of this zone determines the spatial resolution of the MRFM measurement, which is enhanced if probes with large magnetic gradients are employed. Interestingly, this feature allows to magnetically control the interaction volume in MRFM measurements, which is, for example, not possible in MFM.

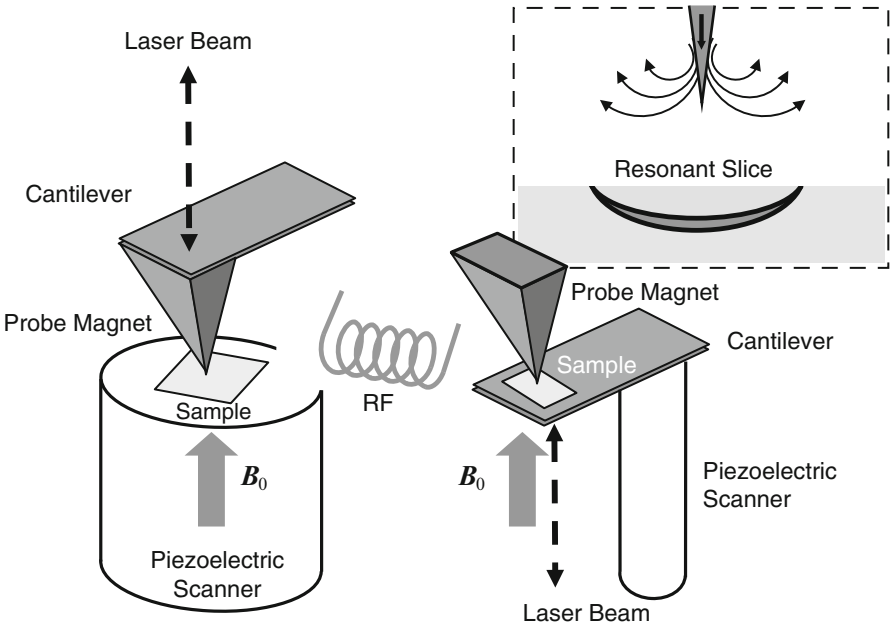


Fig. 13.8 Exemplary scheme of a magnetic resonance force microscopy (*MRFM*) setup. The *left* implementation shows the probe-on-cantilever geometry (similar to usual AFM designs), while the sample-on-cantilever geometry is given on the *right* side, which is currently often found in high-resolution NMR-MRFM designs. The basic AFM setup is complemented by an external magnetic field $\boldsymbol{B}_0$ and a rf field (used for spin manipulation and detection)

Moreover, as the resonant slice extends well in front of the probe, it can be positioned inside the sample without having any mechanic contact between the probe and the sample. Hence, MRFM inherits from MRI the very intriguing feature of allowing noninvasive MR measurements within the sample (e.g., imaging of spin densities within a specimen).

3.2.3 Instrumentation

MRFM has the most complex instrumentation of all magnetic AFM approaches discussed in this chapter (Fig. 13.8). Initial alignment of the spins requires a *strong external magnetic field* $\boldsymbol{B}_0$, which is complemented by an rf magnetic field $\boldsymbol{B}_{\mathrm{rf}}$ (applied perpendicular to $\boldsymbol{B}_0$) necessary to achieve spin manipulation (in conjunction with the magnetic probe). The usage of conventional rf coils (NMR) or microwave cavities (ESR and FMR) to generate $\boldsymbol{B}_{\mathrm{rf}}$ is technically challenging if not impossible, as it would require to place the sample and the microscope within these structures. Therefore, new designs have been developed including microcoils and microstripe resonators to place the sample as close as possible to the generator of $\boldsymbol{B}_{\mathrm{rf}}$ [223, 224].

Sensing of changes in the sample's magnetization is again achieved by magnetic probes (possessing large field gradients). The may be formed by μm-sized ferromagnetic spheres [180], whose aspect ratio is further enhanced (to gain higher field gradients and to improve the spatial resolution) by modification techniques like focused ion beam milling (FIB) [168].

To place the probe, two different approaches have been reported for MRFM. In the first design, the probe is mounted (like in the other magnetic AFM approaches) on the cantilever (*probe-on-cantilever*, Fig. 13.8, left). However, higher sensitivities have been reported by inverting this conventional setup, i.e., by placing the probe onto a microstripe resonator while mounting the sample onto the cantilever (Fig. 13.8, right) [197, 199, 200].

Depending on the question, the usage of conventional AFM cantilevers (with $Q \sim 100 \ldots 1{,}000$ and $k \sim 0.01$ N/m) might be sufficient to achieve reasonable signal-to-noise ratios. However, to enhance the sensitivity, many MRFM designs employ *dedicated MRFM cantilevers*, which yield very high Q values ($Q > 10{,}000$), have very low spring constants ($k \ll 0.001$ N/m), and typically deviate from the flat cantilever design (so-called mass-loaded cantilevers, which possess better noise characteristics than their flat counterparts) [182, 183]. The author is not aware of any commercial supplier for such MRFM cantilevers. It should be noted that the high Q values often reduce by up to two orders of magnitude due to the interaction with the strong, external magnetic field (required for the alignment of the spins) during the actual MRFM experiments. The majority of the reported designs excited normal vibration mode in the cantilever, while few publications describe also the usage of torsional vibration [225, 226].

MRFM experiments have been reported in vacuum and in air. However, the improvement of the sensitivity (especially if small volumes containing few spins are investigated) requires measurements in ultrahigh vacuum (UHV) and at low temperature. All these difficulties make the overall design of the MRFM challenging.

3.2.4 Measurement Procedure

The measurement procedure of MRFM depends very strongly on the magnetic properties of the sample under investigation. There are several reviews available giving a very detailed introduction into the different operation modes and especially the different spin manipulation and detection protocols used in MRFM [165, 166]. Hence, this paragraph gives only a very brief introduction into the procedure of MRFM measurements.

MRFM can be used to measure magnetic resonance spectra as function of the probe-sample position, i.e., to choose a certain position of the probe above the sample and to measure (force-induced) changes in the cantilever oscillations by varying the external magnetic fields. To couple the cantilever movement to the changes in the sample's magnetization, the rf magnetic field $\boldsymbol{B}_{\mathrm{rf}}$ is often modulated at the cantilever's resonance frequency.

As MRFM is sensitive only within the resonant slice, this procedure yields resonance spectra only for the part of the sample that is located within the resonant slice. Displacing the MRFM probe enables to control the location of the resonant

slice in three dimensions allowing spatial recording of such resonance spectra. Imaging is usually conducted by locking onto a certain magnetic resonance condition, yielding magnetic three-dimensional images of the sample. For paramagnetic samples, spin density maps are extracted, while for ferromagnetic samples the analysis is more challenging (due to the creation of collective magnetic modes). However, it should be noted that MRFM imaging with spatial resolutions below 20 nm required the usage of dedicated deconvolution algorithms to correct the measured spin density maps from artifacts introduced by the shape of the resonant slice [199, 200].

3.2.5 Applications

Electron Spin Resonance Experiments – Using MRFM, the first mechanically detected electron spin resonance (ESR) spectrum was recorded in 1992 by Rugar and co-workers, who deposited 30 ng of the paramagnetic chemical diphenylpicrylhydrazyl (DPPH) onto a cantilever [188]. In this experiment (which was the first MRFM measurement at all), the apparatus was operated at room temperature in UHV. At resonance a change in cantilever oscillation of approximately 2.8 Å was induced, which is equivalent to a force of only 10^{-14} N.

This success was directly followed by the first demonstration of ESR imaging on the μm scale in 1993 by Züger and Rugar, who achieved resolutions of 5 μm (laterally) and 1 μm (axially) on μm-sized DPPH drops [191]. Modifications in the MRFM design and the usage of dedicated spin manipulation protocols allowed to increase the sensitivity of the approach, leading to an enhancement of the voxel size resolution (<100 nm) and finally the detection of a single electron spin using MRFM in 2004 (Fig. 13.9) [194].

Nuclear Magnetic Resonance Experiments – The first mechanical detection of nuclear magnetic resonance (NMR) was achieved by Rugar and co-workers in 1994 on an ammonium nitrate sample [195]. This first NMR-MRFM measurement reached a single shot sensitivity of 1.6 10^{13} protons and a spatial resolution of 2.6 μm. Enhancing the sensitivity of NMR MRFM pushed this resolution below the μm scale. The first MRI image with a resolution better than 100 nm was achieved by Mamin et al. on a nanostructured CaF_2 sample in 2007 [197]. The MRFM was operated at a temperature of 600 mK in UHV, achieving a detection sensitivity of roughly 1200 ^{19}F nuclear moments. Only 2 years later, the same group further enhanced the spatial resolution, as they imaged features of tobacco mosaic virus particles and carbon nanotubes with resolutions better than 10 nm [199, 200]. This and similar experiments showed impressively that MRFM allows to perform MRI at the true nanoscale.

However, in contrast to single electron spin detection described above, it was (at the time this manuscript was written) not yet possible to detect a single nuclear spin using MRFM. This follows mainly from the fact that nuclear magnetic moments are typically a factor 1,000 smaller than that of a single electron, which makes the detection of a single nuclear spin much more challenging.

Ferromagnetic Resonance Experiments – A fundamental difference between ferromagnetic resonance (FMR) and ESR/NMR is the feature that an exchange

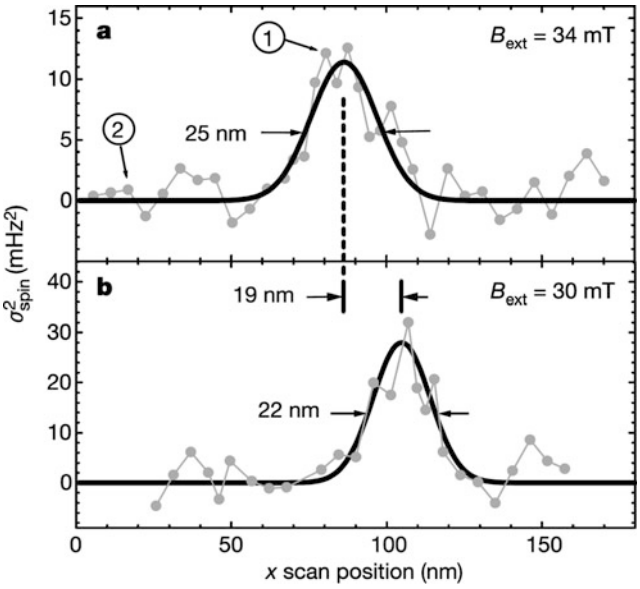


Fig. 13.9 Spin signal (*gray dots + line*) of an MRFM probe scanned in x-direction over a single electron spin for two different strengths of the external magnetic field $\boldsymbol{B}_0$ (called $\boldsymbol{B}_{ext}$ in the original work). The *solid black line* represents a Gaussian fit as guide to the eye. As the shape of the resonant slice is modulated by the external field $\boldsymbol{B}_0$, the small change in the field strength leads to an apparent shift in the spin's position (Taken with permission from Ref. [194])

interaction exists between adjacent spins, which correlates them over much large distances [227, 228]. Or (in other words), the strong interaction between the adjacent spins leads in ferromagnets to the creation of extended collective modes, whose length scale can reach macroscopic values, making the resonance frequency a property of the whole sample [168]. Hence, the concept of the resonant slice is not generally valid for FMR MRFM.

At first sight, it might be counterintuitive to apply imaging approaches to such material. However, as almost all scientifically and technologically important materials are created by layered magnetic systems, it is obvious that there is a strong need for imaging techniques (like MRFMs operated in FMR imaging mode) that are able to resolve such structured materials or other buried systems on the μm and nm scale. Moreover, a theoretical treatment of ferromagnetism in complex media is often a challenging process, which can be well supported by the insights gained from MRFM-based FMR experiments.

The first demonstration of MRFM-based FMR was presented by Zhang and co-workers, who investigated a μm-sized yttrium iron garnet in air [202]. As the magnetic field strength of the probe was not high enough to allow for local imaging, the observed resonance peaks were attributed to collective magnetostatic modes of

the whole sample, which was also confirmed by other groups [204]. The imaging resolution of MRFM-based FMR was then further improved, as demonstrated by the characterization of spin dynamics in ferromagnetic $Ni_{80}Fe_{20}$ disks (diameter = 1.5 μm, layer thickness = 50 nm) by Mewes and co-workers [205]. This study intriguingly showed the capability of MRFM to collect spatially resolved FMR spectra (in dependence of the probe-sample distance), which allowed to analyze the data in terms of global (with respect to the whole sample) and local dynamic properties. Using probes with even higher magnetic field strengths finally allowed to excite localized spin wave states, which further enhanced the lateral resolution of the approach down to 200 nm [207, 208].

3.3 Magnetic Exchange Force Microscopy (MExFM)

3.3.1 General Remarks

Magnetic exchange force microscopy (MExFM) was designed to yield an AFM approach combining atomic resolution and single spin sensitivity [229]. In MExFM, the measured force is generated by an exchange interaction between the spins of the probe and the sample, which is much more short ranged than the magnetic interactions used in MFM or MRFM. This is, for example, reflected in the typical probe-sample distance, which is below 1 nm in MExFM and ranges between few 10 nm and some 100 nm in MFM or MRFM.

Although calculations in the 1990s suggested the possibility of MExFM [239–241], the first trails were not successful [242–244], and it took several years to find a suitable setup and system to experimentally demonstrate the concept of MExFM [84]. These measurements already showed the impressive capability of MExFM to create spin maps with true atomic resolution. This feature makes MExFM unique among all other magnetic AFM approaches discussed in this chapter.

MExFM uses a noncontact mode AFM setup and is typically conducted in ultrahigh vacuum and at low temperatures. Although the first experimental demonstration required a strong external magnetic field to stabilize the spin(s) at the probe's apex [84], recent experiments reported working designs without this field [235]. Up to now, the published literature contains only MExFM measurements of antiferromagnetic materials. However, this method opens the possibility to study spin ordering with sub-nm resolutions, especially (but not limiting) on insulators, which are inaccessible by alternative approaches like SP-STM [229].

3.3.2 Force Generation

To achieve atomic resolution, MExFM exploits a quantum mechanical effect known as *exchange interaction*, which arises between two single spins at very short distances [245]. As there is no classical analogy for this effect, it is not straightforward to write down a simple expression to directly calculate the force acting on the AFM cantilever. To quantitatively analyze the measured forces, the

usage of quantum mechanical calculations like density functional approaches (DFT) is often reported [231, 232, 236, 237]. However, it should be (qualitatively) noted that the exchange interaction between the two spins becomes strongest, if the spins are aligned parallel or antiparallel to each other.

3.3.3 Instrumentation

Most MExFM experiments reported so far used a probe, which is formed by in situ evaporation of a very thin layer of a ferro- or antiferromagnetic material onto a Si probe [229]. Such thin layers ensure that during the measurement only very few spins of the probe interact with the spins of the sample, which is a requirement for recording atomically resolved spin maps. However, restricting the interaction to few spins also leads to very small forces. Hence, MExFM also requires high force sensitivity, which is achieved (ι) by performing the measurement in ultrahigh vacuum (UHV) and at low temperatures and (ιι) by using a *noncontact mode* AFM approach to measure the probe-sample forces and to control the small probe-sample distance (typically <1 nm). Finally, to align the spins in the MExFM probe, a strong magnetic field (up to several teslas) is applied perpendicular to the sample surface, enabling sensing of the out-of-plane spin components [84].

However, recent demonstrations of MExFM on NiO(001) used a SmCo probe mounted on a tuning fork sensor. This allowed to record spin maps without the necessity of the strong, external magnetic field, which was attributed to the much higher magnetocrystalline anisotropy energy of SmCo with respect to Fe [235].

3.3.4 Measurement Procedure

In MExFM, the probe is raster-scanned over the sample surface in a *noncontact mode* AFM, i.e., the probe-sample distance is adjusted during scanning, so that the shift $\Delta\omega$ in resonance frequency is kept constant. For probe-sample distances on the nm scale (small $\Delta\omega$), the obtained images arise mostly from a chemical contrast (between different atomic species in the sample), while at smaller probe-sample distances (larger $\Delta\omega$), an additional contrast due to the exchange interaction arises, which can be used to extract spin maps. The minimum probe-sample distance necessary to observe exchange forces depends strongly on the investigated sample: stronger localization of the electron orbitals (which create the exchange interaction) also decreases the minimum probe-sample distance, making the observation of exchange interaction more challenging [229]. Hence, MExFM is (in contrast to MFM) a single pass approach, and the recorded force maps contain information about both the chemical contrast and the exchange interaction (if measurable).

The (distance-dependent) exchange interaction can be extracted from these force maps by comparing the (distance-dependent) forces between atoms that differ in the orientation of the spins (parallel versus antiparallel) but exhibit the same chemical contrast. This approach was termed magnetic exchange force spectroscopy (MExFS) [237].

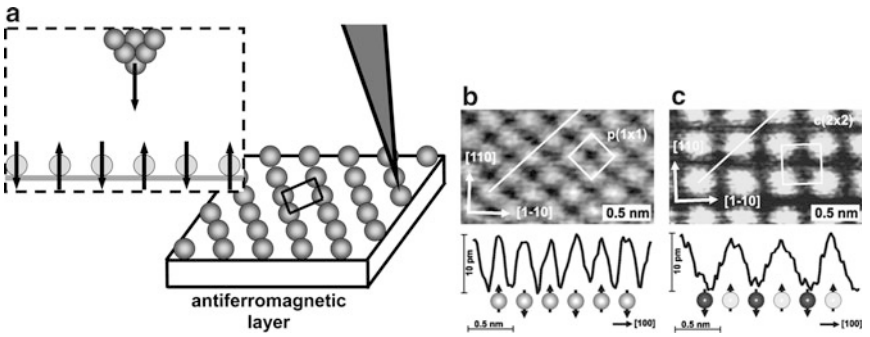


Fig. 13.10 MExFM uses the short-ranged exchange interaction (arising between few spins of the probe and the sample) to record spin maps of antiferromagnetic materials with atomic resolution. (**a**) The MExFM probe (covered with a very thin ferromagnetic layer) is scanned using noncontact mode AFM over the sample. Often, a strong external magnetic field is used to align the spin at the probe's apex perpendicular to the sample surface, enabling out-of-plane sensitivity of the measurement. (**b**, **c**) show MExFM applied to a Fe monolayer, which exhibits antiferromagnetic ordering on a W(001) surface. (**b**) Locking to small frequency shifts (absence of exchange interaction) leads to atomically resolved AFM images, in which the protrusions correspond to single Fe atoms. (**c**) Larger frequency shifts decrease the probe-sample distance, leading to an additional force contribution in the image arising from the exchange interaction. Comparison of the line section shows that now only every second Fe atoms create a protrusion, which is interpreted by the different spin orientations of neighboring Fe atoms (Taken with permission from Ref. [236])

3.3.5 Applications

Spin Mapping of Antiferromagnets – MExFM achieved atomically resolved spin maps of antiferromagnetic insulators (NiO) and conductors (single Fe monolayer on a W(001) surface) in the past, which enabled the investigation of antiferromagnetic spin ordering in materials with sub-nm precision (Fig. 13.10). Using MExFM at different probe-sample distances (MExFS) allowed to quantitatively extract the Fe-Fe and the SmCo-Ni exchange interaction [235, 237, 238].

Single Spin Switching – Recent theoretical considerations suggest that MExFM can be used to dynamically switch the state of a single spin [246].

4 Conclusions and Outlook

This chapter reviewed some recent advances in the field of magnetic AFMs, which was the subject of a tremendous development over the past 20 years. Each of the methods discussed here aims at answering different questions and differs therefore in the magnetic interactions used for force generation between probe and sample and by the length scales, which can be resolved by the method.

MFM, developed itself in an established technique in the 1990s, and since then, the majority of the publications show MFM applications to characterize ferromagnetic materials. However, there is a noticeable amount of literature describing

modifications of the original MFM design, in order to simplify the process of extracting quantitative information from the measurement, to make this process more reliable, or to increase the lateral resolution of MFM. For example, using such modifications, imaging and characterization of single, isolated superparamagnetic nanoparticles (having a characteristic sizes smaller than 10 nm) was demonstrated by several groups. Future work will probably push this limit to even smaller values.

MRFM showed a strong development in the instrumentation in the last 20 years, which is impressively underlined by the detection of single electron spin resonance in 2004, by the possibility to study fluctuations in small spin ensembles, and by the demonstration of ferromagnetic resonance imaging using localized spin waves (to mention only few examples). To achieve the sensitivity necessary to detect single nuclear spin resonance, several issues still have to be solved, and it is currently not clear if this goal will be reached using mechanical detection of nuclear resonance. However, its capability to study spin dynamics will be very valuable in fields like spintronics.

Very recently, the MExFM demonstrated the impressive capability to measure atomically resolved spin maps on antiferromagnetic insulators and metals and to extract the distance-dependent exchange interaction between spins. This opens up fascinating possibilities to manipulate and probe spin excitations at atomic length scales.

References

1. Freeman MR, Choi BC (2001) Advances in magnetic microscopy. Science 294(5546):1484–1488
2. Dan Dahlberg E, Proksch R (1999) Magnetic microscopies: the new additions. J Magn Magn Mater 200(1):720–728
3. Allenspach R (1994) Ultrathin films: magnetism on the microscopic scale. J Magn Magn Mater 129(2):160–185
4. Binnig G, Rohrer H, Gerber C, Weibel E (1982) Tunneling through a controllable vacuum gap. Appl Phys Lett 40(2):178–180
5. Binnig G, Rohrer H, Gerber C, Weibel E (1982) Surface studies by scanning tunneling microscopy. Physical Rev Lett 49(1):57
6. Binnig G, Quate CF, Gerber C (1986) Atomic force microscope. Phys Rev Lett 56(9):930
7. Binnig G, Gerber C, Stoll E, Albrecht TR, Quate CF (1987) Atomic resolution with atomic force microscope. Surf Sci 189:1–6
8. Saenz JJ, Garcia N, Grutter P, Meyer E, Heinzelmann H, Wiesendanger R, Guntherodt HJ et al (1987) Observation of magnetic forces by the atomic force microscope. J Appl Phys 62(10):4293–4295
9. Martin Y, Wickramasinghe HK (1987) Magnetic imaging by “force microscopy” with 1000 Å resolution. Appl Phys Lett 50(20):1455–1457
10. Rugar D, Mamin HJ, Guethner P, Lambert SE, Stern JE, McFadyen I, Yogi T (1990) Magnetic force microscopy: general principles and application to longitudinal recording media. J Appl Phys 68(3):1169–1183
11. Wiesendanger R, Güntherodt HJ, Güntherodt G, Gambino RJ, Ruf R (1990) Observation of vacuum tunneling of spin-polarized electrons with the scanning tunneling microscope. Phys Rev Lett 65(2):247

12. Betzig E, Trautman JK, Wolfe R, Gyorgy EM, Finn PL, Kryder MH, Chang CH (1992) Near-field magneto-optics and high density data storage. Appl Phys Lett 61(2):142–144
13. Silva TJ, Schultz S, Weller D (1994) Scanning near-field optical microscope for the imaging of magnetic domains in optically opaque materials. Appl Phys Lett 65(6):658–660
14. Chapman JN, McFadyen IR, McVitie S (1990) Modified differential phase contrast Lorentz microscopy for improved imaging of magnetic structures. Magn, IEEE Trans 26(5):1506–1511
15. Kirk KJ, Chapman JN, Wilkinson CDW (1999) Lorentz microscopy of small magnetic structures. J Appl Phys 85(8):5237–5242
16. Lichte H (1986) Electron holography approaching atomic resolution. Ultramicroscopy 20(3):293–304
17. Tonomura A (1987) Applications of electron holography. Rev Mod Phys 59(3):639
18. Kirtley JR, Wikswo JP Jr (1999) Scanning SQUID microscopy. Annu Rev mater Sci 29(1):117–148
19. Chang AM, Hallen HD, Harriott L, Hess HF, Kao HL, Kwo J, Chang TY et al (1992) Scanning hall probe microscopy. Appl Phys Lett 61(16):1974–1976
20. Oral A, Bending SJ, Henini M (1996) Real-time scanning hall probe microscopy. Appl Phys Lett 69(9):1324–1326
21. Balasubramanian G, Chan IY, Kolesov R, Al-Hmoud M, Tisler J, Shin C, Wrachtrup J et al (2008) Nanoscale imaging magnetometry with diamond spins under ambient conditions. Nature 455(7213):648–651
22. Kolkowitz S, Unterreithmeier QP, Bennett SD, Lukin MD (2012) Sensing distant nuclear spins with a single electron spin. Phys Rev Lett 109(13):137601
23. Grinolds MS, Hong S, Maletinsky P, Luan L, Lukin MD, Walsworth RL, Yacoby A (2013) Nanoscale magnetic imaging of a single electron spin under ambient conditions. Nat Phys 9:215–219
24. Bode M (2003) Spin-polarized scanning tunnelling microscopy. Rep Prog Phys 66(4):523
25. Wiebe J, Zhou L, Wiesendanger R (2011) Atomic magnetism revealed by spin-resolved scanning tunnelling spectroscopy. J Phys D Appl Phys 44(46):464009
26. Wiesendanger R (2011) Single-atom magnetometry. Curr Opin Solid State Mater Sci 15(1):1–7
27. Butt HJ (1991) Measuring electrostatic, van der Waals, and hydration forces in electrolyte solutions with an atomic force microscope. Biophys J 60(6):1438–1444
28. Hartmann U (1991) van der Waals interactions between sharp probes and flat sample surfaces. Phys Rev B 43(3):2404
29. Argento C, French RH (1996) Parametric tip model and force–distance relation for Hamaker constant determination from atomic force microscopy. J Appl Phys 80(11):6081–6090
30. Erlandsson R, Hadziioannou G, Mate CM, McClelland GM, Chiang S (1988) Atomic scale friction between the muscovite mica cleavage plane and a tungsten tip. J Chem Phys 89:5190
31. Mate CM, McClelland GM, Erlandsson R, Chiang S (1993) Atomic-scale friction of a tungsten tip on a graphite surface. In: Scanning tunneling microscopy. Springer Netherlands, pp 226–229. ISBN: 978-0-7923-2065-4
32. Vanossi A, Manini N, Urbakh M, Zapperi S, Tosatti E (2013) Colloquium: modeling friction: from nanoscale to mesoscale. Rev Mod Phys 85:529–552
33. Borkovec M, Papastavrou G (2008) Interactions between solid surfaces with adsorbed polyelectrolytes of opposite charge. Curr Opin Colloid Interface Sci 13(6):429–437
34. Block S, Helm CA (2007) Measurement of long-ranged steric forces between polyelectrolyte layers physisorbed from 1 M NaCl. Phys Rev E 76(3):030801
35. Block S, Helm CA (2008) Conformation of poly (styrene sulfonate) layers physisorbed from high salt solution studied by force measurements on two different length scales. J Phys Chem B 112(31):9318–9327
36. Drechsler A, Synytska A, Uhlmann P, Elmahdy MM, Stamm M, Kremer F (2009) Interaction forces between microsized silica particles and weak polyelectrolyte brushes at varying pH and salt concentration. Langmuir 26(9):6400–6410

37. Quate CF (1994) The AFM as a tool for surface imaging. Surf Sci 299:980–995
38. Meyer E, Hug HJ, Bennewitz R (2004) Scanning probe microscopy: the lab on a tip. Springer, Berlin
39. Butt HJ, Cappella B, Kappl M (2005) Force measurements with the atomic force microscope: technique, interpretation and applications. Surf Sci Rep 59(1):1–152
40. Bhushan B (ed) (2010) Springer handbook of nanotechnology. Springer-Verlag Berlin Heidelberg, ISBN: 978-3-642-02524-2
41. Barth C, Foster AS, Henry CR, Shluger AL (2011) Recent trends in surface characterization and chemistry with high-resolution scanning force methods. Adv Mater 23(4):477–501
42. Senden TJ (2001) Force microscopy and surface interactions. Curr Opin Colloid Interface Sci 6(2):95–101
43. Stokey WF (1989) Shock and vibration handbook. McGraw-Hill, New York, pp 7.1–7.44
44. Landau LD, Lifshitz EM (1986) Theory of elasticity, 3rd edn. Oxford, Pergamon
45. Sader JE (1998) Frequency response of cantilever beams immersed in viscous fluids with applications to the atomic force microscope. J Appl Phys 84(1):64–76
46. Butt HJ, Jaschke M (1995) Calculation of thermal noise in atomic force microscopy. Nanotechnology 6(1):1
47. Salapaka MV, Bergh HS, Lai J, Majumdar A, McFarland E (1997) Multi-mode noise analysis of cantilevers for scanning probe microscopy. J Appl Phys 81(6):2480–2487
48. Green CP, Lioe H, Cleveland JP, Proksch R, Mulvaney P, Sader JE (2004) Normal and torsional spring constants of atomic force microscope cantilevers. Rev Sci Instrum 75(6):1988–1996
49. Chester W (1979) Oscillations. In: Mechanics. George Allen & Unwin London, pp 136–173
50. Albrecht TR, Grütter P, Horne D, Rugar D (1991) Frequency modulation detection using high-Q cantilevers for enhanced force microscope sensitivity. J Appl Phys 69:668
51. Giessibl FJ (1997) Forces and frequency shifts in atomic-resolution dynamic-force microscopy. Phys Rev B 56(24):16010
52. Guggisberg M, Bammerlin M, Loppacher C, Pfeiffer O, Abdurixit A, Barwich V, Güntherodt HJ et al (2000) Separation of interactions by noncontact force microscopy. Phys Rev B 61(16):11151
53. Giessibl FJ (2001) A direct method to calculate tip–sample forces from frequency shifts in frequency-modulation atomic force microscopy. Appl Phys Lett 78(1):123–125
54. Sader JE, Jarvis SP (2004) Accurate formulas for interaction force and energy in frequency modulation force spectroscopy. Appl Phys Lett 84(10):1801–1803
55. Sader JE, Uchihashi T, Higgins MJ, Farrell A, Nakayama Y, Jarvis SP (2005) Quantitative force measurements using frequency modulation atomic force microscopy – theoretical foundations. Nanotechnology 16(3):S94
56. Welker J, Illek E, Giessibl FJ (2012) Analysis of force-deconvolution methods in frequency-modulation atomic force microscopy. Beilstein J Nanotechnol 3(1):238–248
57. Cleveland JP, Manne S, Bocek D, Hansma PK (1993) A nondestructive method for determining the spring constant of cantilevers for scanning force microscopy. Rev Sci Instrum 64(2):403–405
58. Hutter JL, Bechhoefer J (1993) Calibration of atomic-force microscope tips. Rev Sci Instrum 64:1868
59. Sader JE, Larson I, Mulvaney P, White LR (1995) Method for the calibration of atomic force microscope cantilevers. Rev Sci Instrum 66(7):3789–3798
60. Sader JE, Chon JW, Mulvaney P (1999) Calibration of rectangular atomic force microscope cantilevers. Rev Sci Instrum 70:3967
61. Chon JW, Mulvaney P, Sader JE (2000) Experimental validation of theoretical models for the frequency response of atomic force microscope cantilever beams immersed in fluids. J Appl Phys 87(8):3978–3988

62. Burnham NA, Chen X, Hodges CS, Matei GA, Thoreson EJ, Roberts CJ, Tendler SJB et al (2003) Comparison of calibration methods for atomic-force microscopy cantilevers. Nanotechnology 14(1):1
63. Cook SM, Schäffer TE, Chynoweth KM, Wigton M, Simmonds RW, Lang KM (2006) Practical implementation of dynamic methods for measuring atomic force microscope cantilever spring constants. Nanotechnology 17(9):2135
64. Hansma PK, Cleveland JP, Radmacher M, Walters DA, Hillner PE, Bezanilla M, Elings V et al (1994) Tapping mode atomic force microscopy in liquids. Appl Phys Lett 64(13):1738–1740
65. Garcia R, San Paulo A (1999) Attractive and repulsive tip-sample interaction regimes in tapping-mode atomic force microscopy. Phys Rev B 60(7):4961
66. Martin Y, Williams CC, Wickramasinghe HK (1987) Atomic force microscope–force mapping and profiling on a sub 100 Å scale. J Appl Phys 61(10):4723–4729
67. Anselmetti D, Luthi R, Meyer E, Richmond T, Dreier M, Frommer JE, Guntherodt HJ (1994) Attractive-mode imaging of biological materials with dynamic force microscopy. Nanotechnology 5(2):87
68. Garcia R, Perez R (2002) Dynamic atomic force microscopy methods. Surf Sci Rep 47(6):197–301
69. Higgins MJ, Riener CK, Uchihashi T, Sader JE, McKendry R, Jarvis SP (2005) Frequency modulation atomic force microscopy: a dynamic measurement technique for biological systems. Nanotechnology 16(3):S85
70. Grütter P, Mamin HJ, Rugar D (1992) Magnetic Force Microscopy (MFM). In: Wiesendanger R, Güntherodt H-J (eds) Scanning tunneling microscopy II. Springer series in surface sciences 28. Springer, Berlin, pp 151–207
71. Giessibl FJ, Pielmeier F, Eguchi T, An T, Hasegawa Y (2011) Comparison of force sensors for atomic force microscopy based on quartz tuning forks and length-extensional resonators. Phys Rev B 84(12):125409
72. Yuan CW, Batalla E, Zacher M, De Lozanne AL, Kirk MD, Tortonese M (1994) Low temperature magnetic force microscope utilizing a piezoresistive cantilever. Appl Phys Lett 65(10):1308–1310
73. Giessibl FJ, Trafas BM (1994) Piezoresistive cantilevers utilized for scanning tunneling and scanning force microscope in ultrahigh vacuum. Rev Sci Instrum 65(6):1923–1929
74. Arlett JL, Maloney JR, Gudlewski B, Muluneh M, Roukes ML (2006) Self-sensing micro- and nanocantilevers with attonewton-scale force resolution. Nano Lett 6(5):1000–1006
75. Alexander SLOJVPKM, Hellemans L, Marti O, Schneir J, Elings V, Hansma PK, Gurley J et al (1989) An atomic-resolution atomic-force microscope implemented using an optical lever. J Appl Phys 65(1):164–167
76. Putman CA, De Grooth BG, Van Hulst NF, Greve J (1992) A detailed analysis of the optical beam deflection technique for use in atomic force microscopy. J Appl Phys 72(1):6–12
77. Colchero J, Cuenca M, Martinez JF, Abad J, García BP, Palacios-Lidón E, Abellán J (2011) Thermal frequency noise in dynamic scanning force microscopy. J Appl Phys 109(2):024310–024310
78. Erlandsson R, McClelland GM, Mate CM, Chiang S (1988) Atomic force microscopy using optical interferometry. J Vacuum Sci Technol A Vacuum Surf Films 6(2):266–270
79. Rugar D, Mamin HJ, Erlandsson R, Stern JE, Terris BD (1988) Force microscope using a fiber-optic displacement sensor. Rev Sci Instrum 59(11):2337–2340
80. Hoogenboom BW, Frederix PLTM, Yang JL, Martin S, Pellmont Y, Steinacher M, Hug HJ et al (2005) A Fabry–Perot interferometer for micrometer-sized cantilevers. Appl Phys Lett 86(7):074101–074101
81. Poggio M, Degen CL (2010) Force-detected nuclear magnetic resonance: recent advances and future challenges. Nanotechnology 21(34):342001

82. Sidles JA, Garbini JL, Drobny GP (1992) The theory of oscillator coupled magnetic resonance with potential applications to molecular imaging. Rev Sci Instrum 63(8):3881–3899
83. Sidles JA, Rugar D (1993) Signal-to-noise ratios in inductive and mechanical detection of magnetic resonance. Phys Rev Lett 70(22):3506
84. Kaiser U, Schwarz A, Wiesendanger R (2007) Magnetic exchange force microscopy with atomic resolution. Nature 446(7135):522–525
85. Porthun S, Abelmann L, Lodder C (1998) Magnetic force microscopy of thin film media for high density magnetic recording. J Magn Magn Mater 182(1):238–273
86. Hartmann U (1999) Magnetic force microscopy. Ann Rev Mater Sci 29(1):53–87
87. Koblischka MR, Hartmann U (2003) Recent advances in magnetic force microscopy. Ultramicroscopy 97(1):103–112
88. Zhu X, Grütter P (2004) Imaging, manipulation, and spectroscopic measurements of nanomagnets by magnetic force microscopy. MRS Bull 29(07):457–462
89. Schwarz A, Wiesendanger R (2008) Magnetic sensitive force microscopy. Nano Today 3(1):28–39
90. Agarwal G (2009) Characterization of magnetic nanoparticles using magnetic force microscopy. Nanotechnologies for the life sciences. In: Kumar CSSR (ed) Nanotechnologies for the life sciences, vol 4, Magnetic Nanomaterials. Wiley, Weinheim
91. Wadas A, Grütter P (1989) Theoretical approach to magnetic force microscopy. Phys Rev B 39(16):12013
92. Hartmann U (1989) The point dipole approximation in magnetic force microscopy. Phys Lett A 137(9):475–478
93. Hartmann U (1990) Theory of magnetic force microscopy. J Vacuum Sci Technol A Vacuum Surfaces Films 8(1):411–415
94. Schönenberger C, Alvarado SF (1990) Understanding magnetic force microscopy. Zeitschrift für Physik B Condensed Matter 80(3):373–383
95. Wright CD, Hill EW (1995) Reciprocity in magnetic force microscopy. Appl Phys Lett 67(3):433–435
96. Hubert A, Rave W, Tomlinson SL (1997) Imaging magnetic charges with magnetic force microscopy. Phys Status Solidi B Basic Res 204:817–828
97. Hug HJ, Stiefel B, Van Schendel PJA, Moser A, Hofer R, Martin S, OHandley RC et al (1998) Quantitative magnetic force microscopy on perpendicularly magnetized samples. J Appl Phys 83(11):5609–5620
98. Häberle T, Haering F, Pfeifer H, Han L, Kuerbanjiang B, Wiedwald U, Koslowski B et al (2012) Towards quantitative magnetic force microscopy: theory and experiment. New J Phys 14(4):043044
99. Babcock KL, Elings VB, Shi J, Awschalom DD, Dugas M (1996) Field-dependence of microscopic probes in magnetic force microscopy. Appl Phys Lett 69(5):705–707
100. Kong L, Chou SY (1997) Quantification of magnetic force microscopy using a micronscale current ring. Appl Phys Lett 70(15):2043–2045
101. Goddenhenrich T, Lemke H, Muck M, Hartmann U, Heiden C (1990) Probe calibration in magnetic force microscopy. Appl Phys Lett 57(24):2612–2614
102. Lohau J, Kirsch S, Carl A, Dumpich G, Wassermann EF (1999) Quantitative determination of effective dipole and monopole moments of magnetic force microscopy tips. J Appl Phys 86(6):3410–3417
103. Van Schendel PJA, Hug HJ, Stiefel B, Martin S, Guntherodt HJ (2000) A method for the calibration of magnetic force microscopy tips. J Appl Phys 88(1):435–445
104. Kebe T, Carl A (2004) Calibration of magnetic force microscopy tips by using nanoscale current-carrying parallel wires. J Appl Phys 95(3):775–792
105. Jaafar M, Asenjo A, Vazquez M (2008) Calibration of coercive and stray fields of commercial magnetic force microscope probes. Nanotechnol IEEE Trans 7(3):245–250

106. Ruhrig M, Porthun S, Lodder JC, McVitie S, Heyderman LJ, Johnston AB, Chapman JN (1996) Electron beam fabrication and characterization of high-resolution magnetic force microscopy tips. J Appl Phys 79(6):2913–2919
107. Leinenbach P, Memmert U, Schelten J, Hartmann U (1999) Fabrication and characterization of advanced probes for magnetic force microscopy. Appl Surf Sci 144:492–496
108. Arie T, Nishijima H, Akita S, Nakayama Y (2000) Carbon-nanotube probe equipped magnetic force microscope. J Vacuum Sci Technol B Microelectron Nanometer Struct 18(1):104–106
109. Ono T, Esashi M (2003) Magnetic force and optical force sensing with ultrathin silicon resonator. Rev Sci Instrum 74(12):5141–5146
110. Gao L, Yue LP, Yokota T, Skomski R, Liou SH, Takahoshi H, Ishio S et al (2004) Focused ion beam milled CoPt magnetic force microscopy tips for high resolution domain images. Magn IEEE Trans 40(4):2194–2196
111. Kuramochi H, Uzumaki T, Yasutake M, Tanaka A, Akinaga H, Yokoyama H (2005) A magnetic force microscope using CoFe-coated carbon nanotube probes. Nanotechnology 16(1):24
112. Wolny F, Weissker U, Muhl T, Leonhardt A, Menzel S, Winkler A, Buchner B (2008) Iron-filled carbon nanotubes as probes for magnetic force microscopy. J Appl Phys 104(6):064908–064908
113. Wolny F, Mühl T, Weissker U, Lipert K, Schumann J, Leonhardt A, Büchner B (2010) Iron filled carbon nanotubes as novel monopole-like sensors for quantitative magnetic force microscopy. Nanotechnology 21(43):435501
114. Foss S, Proksch R, Dahlberg ED, Moskowitz B, Walsh B (1996) Localized micromagnetic perturbation of domain walls in magnetite using a magnetic force microscope. Appl Phys Lett 69(22):3426–3428
115. Pokhil TG, Moskowitz BM (1997) Magnetic domains and domain walls in pseudo-single-domain magnetite studied with magnetic force microscopy. J Geophys Res 102(B10):22681–22
116. McVitie S, White GS, Scott J, Warin P, Chapman JN (2001) Quantitative imaging of magnetic domain walls in thin films using Lorentz and magnetic force microscopies. J Appl Phys 90(10):5220–5227
117. Asenjo A, García D, García JM, Prados C, Vázquez M (2000) Magnetic force microscopy study of dense stripe domains in Fe-B/Co-Si-B multilayers and the evolution under an external applied field. Phys Rev B 62(10):6538
118. Donzelli O, Palmeri D, Musa L, Casoli F, Albertini F, Pareti L, Turilli G (2003) Perpendicular magnetic anisotropy and stripe domains in ultrathin Co/Au sputtered multilayers. J Appl Phys 93(12):9908–9912
119. Ehresmann A, Krug I, Kronenberger A, Ehlers A, Engel D (2004) In-plane magnetic pattern separation in NiFe/NiO and Co/NiO exchange biased bilayers investigated by magnetic force microscopy. J Magn Magn Mater 280(2):369–376
120. Gottwald M, Hehn M, Lacour D, Hauet T, Montaigne F, Mangin S, Berger A et al (2012) Asymmetric magnetization reversal in dipolarly coupled spin valve structures with perpendicular magnetic anisotropy. Phys Rev B 85(6):064403
121. Gibson GA, Schultz S (1993) Magnetic force microscope study of the micromagnetics of submicrometer magnetic particles. J Appl Phys 73(9):4516–4521
122. Kleiber M, Kümmerlen F, Löhndorf M, Wadas A, Weiss D, Wiesendanger R (1998) Magnetization switching of submicrometer Co dots induced by a magnetic force microscope tip. Phys Rev B 58(9):5563
123. Lohau J, Carl A, Kirsch S, Wassermann EF (2001) Magnetization reversal and coercivity of a single-domain Co/Pt dot measured with a calibrated magnetic force microscope tip. Appl Phys Lett 78(14):2020–2022
124. Raabe J, Pulwey R, Sattler R, Schweinbock T, Zweck J, Weiss D (2000) Magnetization pattern of ferromagnetic nanodisks. J Appl Phys 88(7):4437–4439

125. Pulwey R et al (2001) Switching behavior of vortex structures in nanodisks. Magn IEEE Trans 37.4:2076–2078
126. Garcıa JM, Thiaville A, Miltat J (2002) MFM imaging of nanowires and elongated patterned elements. J Magn Magn Mater 249(1):163–169
127. Pulwey R, Zolfl M, Bayreuther G, Weiss D (2002) Magnetic domains in epitaxial nanomagnets with uniaxial or fourfold crystal anisotropy. J Appl Phys 91(10):7995–7997
128. Rahm M, Schneider M, Biberger J, Pulwey R, Zweck J, Weiss D, Umansky V (2003) Vortex nucleation in submicrometer ferromagnetic disks. Appl Phys Lett 82(23):4110–4112
129. Rahm M, Biberger J, Umansky V, Weiss D (2003) Vortex pinning at individual defects in magnetic nanodisks. J Appl Phys 93(10):7429–7431
130. Garcia-Martin JM, Thiaville A, Miltat J, Okuno T, Vila L, Piraux L (2004) Imaging magnetic vortices by magnetic force microscopy: experiments and modelling. J Phys D Appl Phys 37(7):965
131. Chang J, Mironov VL, Gribkov BA, Fraerman AA, Gusev SA, Vdovichev SN (2006) Magnetic state control of ferromagnetic nanodots by magnetic force microscopy probe. J Appl Phys 100(10):104304–104304
132. Takagaki Y, Jenichen B, Herrmann C, Wiebicke E, Däweritz L, Ploog KH (2006) First-order phase transition in MnAs disks on GaAs (001). Phys Rev B 73(12):125324
133. Jenichen B, Kaganer VM, Takagaki Y, Herrmann C, Ploog KH, Dudzik E, Feyerherm R (2007) First order phase transition in MnAs nanodisks. Phys Status Solidi (a) 204(8):2772–2777
134. Hanson M, Bručas R, Kazakova O (2007) Effects of size and interactions on the magnetic behaviour of elliptical (001) Fe nanoparticles. J Magn Magnetic Mater 316(2):181–183
135. Zhu X, Grutter P, Metlushko V, Hao Y, Castano FJ, Ross CA, Smith HI et al (2003) Construction of hysteresis loops of single domain elements and coupled permalloy ring arrays by magnetic force microscopy. J Appl Phys 93(10):8540–8542
136. Roy PE, Lee JH, Trypiniotis T, Anderson D, Jones GAC, Tse D, Barnes CHW (2009) Antivortex domain walls observed in permalloy rings via magnetic force microscopy. Phys Rev B 79(6):060407
137. Weissker U, Loffler M, Wolny F, Lutz MU, Scheerbaum N, Klingeler R, Buchner B et al (2009) Perpendicular magnetization of long iron carbide nanowires inside carbon nanotubes due to magnetocrystalline anisotropy. J Appl Phys 106(5):054909–054909
138. Mironov VL, Ermolaeva OL, Gusev SA, Klimov AY, Rogov VV, Gribkov BA, Petrashov VT et al (2010) Antivortex state in crosslike nanomagnets. Phys Rev B 81(9):094436
139. Mironov VL, Ermolaeva OL, Skorohodov EV, Klimov AY (2012) Field-controlled domain wall pinning-depinning effects in a ferromagnetic nanowire-nanoislands system. Phys Rev B 85(14):144418
140. Suzuki H, Tanaka T, Sasaki T, Nakamura N, Matsunaga T, Mashiko S (1998) High-resolution magnetic force microscope images of a magnetic particle chain extracted from magnetic bacteria AMB-1. Jpn J Appl Phys 37:L1343–L1345
141. Albrecht M, Janke V, Sievers S, Siegner U, Schüler D, Heyen U (2005) Scanning force microspy study of biogenic nanoparticles for medical applications. J Magn Magn Mater 290:269–271
142. Krishna H, Miller C, Longstreth-Spoor L, Nussinov Z, Gangopadhyay AK, Kalyanaraman R (2008) Unusual size-dependent magnetization in near hemispherical Co nanomagnets on SiO2 from fast pulsed laser processing. J Appl Phys 103(7):073902–073902
143. Schreiber S, Savla M, Pelekhov DV, Iscru DF, Selcu C, Hammel PC, Agarwal G (2008) Magnetic force microscopy of superparamagnetic nanoparticles. Small 4(2):270–278
144. Moskalenko AV, Yarova PL, Gordeev SN, Smirnov SV (2010) Single protein molecule mapping with magnetic atomic force microscopy. Biophys J 98(3):478–487
145. Block S, Glöckl G, Weitschies W, Helm CA (2011) Direct visualization and identification of biofunctionalized nanoparticles using a magnetic atomic force microscope. Nano Lett 11(9):3587–3592

146. Dietz C, Herruzo ET, Lozano JR, Garcia R (2011) Nanomechanical coupling enables detection and imaging of 5 nm superparamagnetic particles in liquid. Nanotechnology 22(12):125708
147. Sievers S, Braun KF, Eberbeck D, Gustafsson S, Olsson E, Schumacher HW, Siegner U (2012) Quantitative measurement of the magnetic moment of individual magnetic nanoparticles by magnetic force microscopy. Small 8(17):2675–2679
148. Yuan CW, Zheng Z, De Lozanne AL, Tortonese M, Rudman DA, Eckstein JN (1996) Vortex images in thin films of YBa 2 Cu 3 O 7-x and Bi 2 Sr 2 Ca 1 Cu 2 O 8+ x obtained by low-temperature magnetic force microscopy. J Vacuum Sci Technol B Microelectron Nanometer Struct 14(2):1210–1213
149. Auslaender OM, Luan L, Straver EW, Hoffman JE, Koshnick NC, Zeldov E, Moler KA et al (2008) Mechanics of individual isolated vortices in a cuprate superconductor. Nat Phys 5(1):35–39
150. Schwarz A, Liebmann M, Pi UH, Wiesendanger R (2010) Real space visualization of thermal fluctuations in a triangular flux-line lattice. New J Phys 12(3):033022
151. Brown JWF (1962) Magnetostatic principles in ferromagnetism, vol 112. North-Holland Publ. Co, Amsterdam
152. Wadas A, Guntherodt HJ (1990) The topography effect on magnetic images in magnetic force microscopy. J Appl Phys 68(9):4767–4771
153. Giessibl FJ (2006) Higher-harmonic atomic force microscopy. Surf Interface Anal 38(12–13):1696–1701
154. Garcia R, Herruzo ET (2012) The emergence of multifrequency force microscopy. Nat Nanotechnol 7(4):217–226
155. Schneider M, Müller-Pfeiffer S, Zinn W (1996) Magnetic force microscopy of domain wall fine structures in iron films. J Appl Phys 79(11):8578–8583
156. Fannin PC, Scaife BKP, Charles SW (1993) Relaxation and resonance in ferrofluids. J Magn Magn Mater 122(1):159–163
157. Kötitz R, Fannin PC, Trahms L (1995) Time domain study of Brownian and Néel relaxation in ferrofluids. J Magn Magn Mater 149(1):42–46
158. Hao R, Xing R, Xu Z, Hou Y, Gao S, Sun S (2010) Synthesis, functionalization, and biomedical applications of multifunctional magnetic nanoparticles. Adv Mater 22(25):2729–2742
159. Jun YW, Huh YM, Choi JS, Lee JH, Song HT, Kim S, Cheon J et al (2005) Nanoscale size effect of magnetic nanocrystals and their utilization for cancer diagnosis via magnetic resonance imaging. J Am Chem Soc 127(16):5732–5733
160. Huh YM, Jun YW, Song HT, Kim S, Choi JS, Lee JH, Cheon J et al (2005) In vivo magnetic resonance detection of cancer by using multifunctional magnetic nanocrystals. J Am Chem Soc 127(35):12387–12391
161. Kim J, Kim HS, Lee N, Kim T, Kim H, Yu T, Hyeon T et al (2008) Multifunctional uniform nanoparticles composed of a magnetite nanocrystal core and a mesoporous silica shell for magnetic resonance and fluorescence imaging and for drug delivery. Angew Chem Int Ed 47(44):8438–8441
162. Hoffmann B, Houbertz R, Hartmann U (1998) Eddy current microscopy. Appl Phys A Mater Sci Process 66:S409–S413
163. Sidles JA, Garbini JL, Bruland KJ, Rugar D, Züger O, Hoen S, Yannoni CS (1995) Magnetic resonance force microscopy. Rev Mod Phys 67(1):249
164. Hammel PC, Pelekhov DV, Wigen PE, Gosnell TR, Midzor MM, Roukes ML (2003) The magnetic-resonance force microscope: a new tool for high-resolution, 3-D, subsurface scanned probe imaging. Proc IEEE 91(5):789–798
165. Suter A (2004) The magnetic resonance force microscope. Prog Nucl Magn Reson Spectrosc 45(3):239–274
166. Borgonovi F, Gorshkov VN, Tsifrinovich VII (2006) Magnetic resonance force microscopy and a single-spin measurement. World Scientific, Hackensack

167. Wigen PE, Roukes ML, Hammel PC (2006) Ferromagnetic resonance force microscopy. In: Spin dynamics in confined magnetic structures III. Springer, Berlin/Heidelberg, pp 105–136
168. Hammel PC, Pelekhov DV (2007) The magnetic force microscope. In: Kronmuller H, Parkin S (eds) Handbook of magnetism and advanced magnetic materials, vol 5, Spintronics and magnetoelectronics. Wiley, Chichester
169. Kuehn S, Hickman SA, Marohn JA (2008) Advances in mechanical detection of magnetic resonance. J Chem Phys 128:052208
170. Zhang Z, Roukes ML, Hammel PC (1996) Sensitivity and spatial resolution for electron-spin-resonance detection by magnetic resonance force microscopy. J Appl Phys 80(12):6931–6938
171. Dougherty WM, Bruland KJ, Chao SH, Garbini JL, Jensen SE, Sidles JA (2000) The Bloch equations in high-gradient magnetic resonance force microscopy: theory and experiment. J Magn Reson 143(1):106–119
172. Suter A, Pelekhov DV, Roukes ML, Hammel PC (2002) Probe–sample coupling in the magnetic resonance force microscope. J Magn Reson 154(2):210–227
173. Charbois V, Naletov VV, Youssef JB, Klein O (2002) Influence of the magnetic tip in ferromagnetic resonance force microscopy. Appl Phys Lett 80(25):4795–4797
174. Mozyrsky D, Martin I, Pelekhov D, Hammel PC (2003) Theory of spin relaxation in magnetic resonance force microscopy. Appl Phys Lett 82(8):1278–1280
175. Wago K, Zuger O, Kendrick R, Yannoni CS, Rugar D (1996) Low-temperature magnetic resonance force detection. J Vacuum Sci Technol B Microelectron Nanometer Struct 14(2):1197–1201
176. Garbini JL, Bruland KJ, Dougherty WM, Sidles JA (1996) Optimal control of force microscope cantilevers. I. Controller design. J Appl Phys 80(4):1951–1958
177. Bruland KJ, Garbini JL, Dougherty WM, Sidles JA (1996) Optimal control of force microscope cantilevers. II. Magnetic coupling implementation. J Appl Phys 80(4):1959–1964
178. Zhang Z, Hammel PC, Moore GJ (1996) Application of a novel rf coil design to the magnetic resonance force microscope. Rev Sci Instrum 67(9):3307–3309
179. Dougherty WM, Bruland KJ, Garbini JL, Sidles JA (1996) Detection of AC magnetic signals by parametric mode coupling in a mechanical oscillator. Meas Sci Technol 7(12):1733
180. Zhang Z, Hammel PC (1998) Magnetic resonance force microscopy with a ferromagnetic tip mounted on the force detector. Solid State Nucl Magn Reson 11(1):65–72
181. Nazaretski E, Graham KS, Thompson JD, Wright JA, Pelekhov DV, Hammel PC, Movshovich R (2009) Design of a variable temperature scanning force microscope. Rev Sci Instrum 80(8):083704–083704
182. Streckeisen P, Rast S, Wattinger C, Meyer E, Vettiger P, Gerber C, Güntherodt HJ (1998) Instrumental aspects of magnetic resonance force microscopy. Appl Phys A Mater Sci Process 66:S341–S344
183. Rugar D, Stipe BC, Mamin HJ, Yannoni CS, Stowe TD, Yasumura KY, Kenny TW (2001) Adventures in attonewton force detection. Appl Phys A 72(1):S3–S10
184. Jenkins NE, DeFlores LP, Allen J, Ng TN, Garner SR, Kuehn S, Marohn JA et al (2004) Batch fabrication and characterization of ultrasensitive cantilevers with submicron magnetic tips. J Vacuum Sci Technol B Microelectron Nanometer Struct 22(3):909–915
185. Barbic M, Scherer A (2005) Composite nanowire-based probes for magnetic resonance force microscopy. Nano Lett 5(1):187–190
186. Mamin HJ, Rettner CT, Sherwood MH, Gao L, Rugar D (2012) High field-gradient dysprosium tips for magnetic resonance force microscopy. Appl Phys Lett 100(1):013102–013102
187. Longenecker JG, Mamin HJ, Senko AW, Chen L, Rettner CT, Rugar D, Marohn JA (2012) High-gradient nanomagnets on cantilevers for sensitive detection of nuclear magnetic resonance. ACS Nano 6(11):9637–9645
188. Rugar D, Yannoni CS, Sidles JA (1992) Mechanical detection of magnetic resonance. Nature 360(6404):563–566

189. Wago K, Zuger O, Wegener J, Kendrick R, Yannoni CS, Rugar D (1997) Magnetic resonance force detection and spectroscopy of electron spins in phosphorus-doped silicon. Rev Sci Instrum 68(4):1823–1826, ESR-Spectr mit Hyperfeinsplitting
190. Wago K, Botkin D, Yannoni CS, Rugar D (1998) Force-detected electron-spin resonance: adiabatic inversion, nutation, and spin echo. Phys Rev B 57(2):1108
191. Züger O, Rugar D (1993) First images from a magnetic resonance force microscope. Appl Phys Lett 63(18):2496–2498
192. Züger O, Rugar D (1994) Magnetic resonance detection and imaging using force microscope techniques. J Appl Phys 75(10):6211–6216
193. Hammel PC, Zhang Z, Moore GJ, Roukes ML (1995) Sub-surface imaging with the magnetic resonance force microscope. J Low Temp Phys 101(1–2):59–69
194. Rugar D, Budakian R, Mamin HJ, Chui BW (2004) Single spin detection by magnetic resonance force microscopy. Nature 430(6997):329–332
195. Rugar D, Züger O, Hoen S, Yannoni CS, Vieth HM, Kendrick RD (1994) Force detection of nuclear magnetic resonance. Science 264(5165):1560–1563
196. Züger O, Hoen ST, Yannoni CS, Rugar D (1996) Three-dimensional imaging with a nuclear magnetic resonance force microscope. J Appl Phys 79(4):1881–1884
197. Mamin HJ, Poggio M, Degen CL, Rugar D (2007) Nuclear magnetic resonance imaging with 90-nm resolution. Nat Nanotechnol 2(5):301–306
198. Eberhardt KW, Degen CL, Hunkeler A, Meier BH (2008) One- and Two-Dimensional NMR spectroscopy with a magnetic-resonance force microscope. Angew Chem Int Ed 47(46):8961–8963
199. Degen CL, Poggio M, Mamin HJ, Rettner CT, Rugar D (2009) Nanoscale magnetic resonance imaging. Proc Natl Acad Sci 106(5):1313–1317
200. Mamin HJ, Oosterkamp TH, Poggio M, Degen CL, Rettner CT, Rugar D (2009) Isotope-selective detection and imaging of organic nanolayers. Nano Lett 9(8):3020–3024
201. Joss R, Tomka IT, Eberhardt KW, van Beek JD, Meier BH (2011) Chemical-shift imaging in micro-and nano-MRI. Phys Rev B 84(10):104435
202. Zhang Z, Hammel PC, Wigen PE (1996) Observation of ferromagnetic resonance in a microscopic sample using magnetic resonance force microscopy. Appl Phys Lett 68(14):2005–2007
203. Zhang Z, Hammel PC, Midzor M, Roukes ML, Childress JR (1998) Ferromagnetic resonance force microscopy on microscopic cobalt single layer films. Appl Phys Lett 73(14):2036–2038
204. Wago K, Botkin D, Yannoni CS, Rugar D (1998) Paramagnetic and ferromagnetic resonance imaging with a tip-on-cantilever magnetic resonance force microscope. Appl Phys Lett 72(21):2757–2759
205. Mewes T, Kim J, Pelekhov DV, Kakazei GN, Wigen PE, Batra S, Hammel PC (2006) Ferromagnetic resonance force microscopy studies of arrays of micron size permalloy dots. Phys Rev B 74(14):144424
206. Urban R, Putilin A, Wigen PE, Liou SH, Cross MC, Hammel PC, Roukes ML (2006) Perturbation of magnetostatic modes observed by ferromagnetic resonance force microscopy. Phys Rev B 73(21):212410
207. Lee I, Obukhov Y, Xiang G, Hauser A, Yang F, Banerjee P, Hammel PC et al (2010) Nanoscale scanning probe ferromagnetic resonance imaging using localized modes. Nature 466(7308):845–848
208. Lee I, Obukhov Y, Hauser AJ, Yang FY, Pelekhov DV, Hammel PC (2011) Nanoscale confined mode ferromagnetic resonance imaging of an individual Ni81Fe19 disk using magnetic resonance force microscopy. J Appl Phys 109(7):07D313–07D313
209. Pigeau B, Hahn C, De Loubens G, Naletov VV, Klein O, Mitsuzuka K, Montaigne F et al (2012) Measurement of the dynamical dipolar coupling in a pair of magnetic nanodisks using a ferromagnetic resonance force microscope. Phys Rev Lett 109(24):247602

210. Mamin HJ, Budakian R, Chui BW, Rugar D (2003) Detection and manipulation of statistical polarization in small spin ensembles. Phys Rev Lett 91(20):207604
211. Budakian R, Mamin HJ, Chui BW, Rugar D (2005) Creating order from random fluctuations in small spin ensembles. Science 307(5708):408–411
212. Mamin HJ, Budakian R, Chui BW, Rugar D (2005) Magnetic resonance force microscopy of nuclear spins: detection and manipulation of statistical polarization. Phys Rev B 72(2):024413
213. Magnetic resonance imaging: physical principles and sequence design. Wiley-Liss, New York 1999
214. Belliveau JW, Kennedy DN, McKinstry RC, Buchbinder BR, Weisskoff RM, Cohen MS, Vevea JM, Brady TJ, Rosen BR (1991) Functional mapping of the human visual cortex by magnetic resonance imaging. Science 254(5032):716–719
215. Kwong KK, Belliveau JW, Chesler DA, Goldberg IE, Weisskoff RM, Poncelet BP, Turner R et al (1992) Dynamic magnetic resonance imaging of human brain activity during primary sensory stimulation. Proc Natl Acad Sci 89(12):5675–5679
216. Huettel SA, Song AW, McCarthy G (2004) Functional magnetic resonance imaging, vol 1. Sinauer Associates, Sunderland
217. Ciobanu L, Seeber DA, Pennington CH (2002) 3D MR microscopy with resolution 3.7 μm by 3.3 μm by 3.3 μm. J Magn Reson 158(1):178–182
218. Weiger M, Schmidig D, Denoth S, Massin C, Vincent F, Schenkel M, Fey M (2008) NMR microscopy with isotropic resolution of 3.0 μm using dedicated hardware and optimized methods. Conc Magn Reson Part B Magn Reson Eng 33(2):84–93
219. Berman GP, Doolen GD, Hammel PC, Tsifrinovich VI (2000) Solid-state nuclear-spin quantum computer based on magnetic resonance force microscopy. Phys Rev B 61(21):14694–14699
220. Berman GP, Doolen GD, Hammel PC, Tsifrinovich VI (2001) Magnetic resonance force microscopy quantum computer with tellurium donors in silicon. Phys Rev Lett 86(13):2894–2896
221. Cerletti V, Coish WA, Gywat O, Loss D (2005) Recipes for spin-based quantum computing. Nanotechnology 16(4):R27
222. Bruland KJ, Dougherty WM, Garbini JL, Sidles JA, Chao SH (1998) Force-detected magnetic resonance in a field gradient of 250 000 Tesla per meter. Appl Phys Lett 73(21):3159–3161
223. Mamin HJ, Budakian R, Rugar D (2003) Superconducting microwave resonator for millikelvin magnetic resonance force microscopy. Rev Sci Instrum 74(5):2749–2753
224. Poggio M, Degen CL, Rettner CT, Mamin HJ, Rugar D (2007) Nuclear magnetic resonance force microscopy with a microwire rf source. Appl Phys Lett 90(26):263111–263111
225. Ascoli C, Baschieri P, Frediani C, Lenci L, Martinelli M, Alzetta G, Pardi L et al (1996) Micromechanical detection of magnetic resonance by angular momentum absorption. Appl Phys Lett 69(25):3920–3922
226. Löhndorf M, Moreland J, Kabos P (2000) Ferromagnetic resonance detection with a torsion-mode atomic-force microscope. Appl Phys Lett 76(9):1176–1178
227. Wilson KG (1975) Renormalization group methods. Adv Math 16(2):170–186
228. Wilson KG (1975) The renormalization group: critical phenomena and the Kondo problem. Rev Mod Phys 47(4):773
229. Wiesendanger R (2009) Spin mapping at the nanoscale and atomic scale. Rev Mod Phys 81(4):1495
230. Kaiser U, Schwarz A, Wiesendanger R (2008) Evaluating local properties of magnetic tips utilizing an antiferromagnetic surface. Phys Rev B 78(10):104418
231. Lazo C, Caciuc V, Hölscher H, Heinze S (2008) Role of tip size, orientation, and structural relaxations in first-principles studies of magnetic exchange force microscopy and spin-polarized scanning tunneling microscopy. Phys Rev B 78(21):214416
232. Lazo C, Heinze S (2011) First-principles study of magnetic exchange force microscopy with ferromagnetic and antiferromagnetic tips. Phys Rev B 84(14):144428

233. Schwarz A, Kaiser U, Wiesendanger R (2009) Towards an understanding of the atomic scale magnetic contrast formation in NC-AFM: a tip material dependent MExFM study on NiO (001). Nanotechnology 20(26):264017
234. Vedmedenko EY, Zhu Q, Kaiser U, Schwarz A, Wiesendanger R (2012) Atomic-scale magnetic dissipation from spin-dependent adhesion hysteresis. Phys Rev B 85(17):174410
235. Pielmeier F, Giessibl FJ (2013) Spin resolution and evidence for superexchange on NiO (001) observed by force microscopy. Phys Rev Lett 110(26):266101
236. Schmidt R, Lazo C, Holscher H, Pi UH, Caciuc V, Schwarz A, Wiesendanger R, Heinze S (2008) Probing the magnetic exchange forces of iron on the atomic scale. Nano Lett 9(1):200–204
237. Schmidt R, Lazo C, Kaiser U, Schwarz A, Heinze S, Wiesendanger R (2011) Quantitative measurement of the magnetic exchange interaction across a vacuum gap. Phys Rev Lett 106(25):257202
238. Schmidt R, Schwarz A, Wiesendanger R (2012) Magnetization switching utilizing the magnetic exchange interaction. Phys Rev B 86(17):174402
239. Ness H, Gautier F (1995) Theoretical study of the interaction between a magnetic nanotip and a magnetic surface. Phys Rev B 52(10):7352
240. Nakamura K, Hasegawa H, Oguchi T, Sueoka K, Hayakawa K, Mukasa K (1997) First-principles calculation of the exchange interaction and the exchange force between magnetic Fe films. Phys Rev B 56(6):3218
241. Foster AS, Shluger AL (2001) Spin-contrast in non-contact SFM on oxide surfaces: theoretical modelling of NiO (001) surface. Surf Sci 490(1):211–219
242. Hölscher H, Langkat SM, Schwarz A, Wiesendanger R (2002) Measurement of three-dimensional force fields with atomic resolution using dynamic force spectroscopy. Appl Phys Lett 81:4428–4430
243. Hoffmann R, Lantz MA, Hug HJ, Van Schendel PJA, Kappenberger P, Martin S, Baratoff A, Güntherodt HJ (2003) Atomic resolution imaging and frequency versus distance measurements on NiO (001) using low-temperature scanning force microscopy. Phys Rev B 67(8):085402
244. Langkat SM, Hölscher H, Schwarz A, Wiesendanger R (2003) Determination of site specific interatomic forces between an iron coated tip and the NiO (001) surface by force field spectroscopy. Surf Sci 527(1):12–20
245. Schwabl F (2005) Advanced quantum mechanics. Springer, Berlin/Heidelberg
246. Wieser R, Caciuc V, Lazo C, Hölscher H, Vedmedenko EY, Wiesendanger R (2013) A theoretical study of the dynamical switching of a single spin by exchange forces. New J Phys 15(1):013011

Combining Micromanipulation, Kerr Magnetometry and Magnetic Force Microscopy for Characterization of Three-Dimensional Magnetic Nanostructures

14

Amalio Fernández-Pacheco, Russell P. Cowburn, Luis E. Serrano-Ramón, M. Ricardo Ibarra, and José M. De Teresa

Contents

1 Definition of the Topic 532
2 Overview 532
3 Introduction 533
4 Experimental and Instrumental Methodology 533
4.1 Experimental Techniques 534
4.2 Combining Micromanipulation, Kerr Magnetometry, and Magnetic Force Microscopy to Characterize Magnetic Nanostructures 536
5 Key Research Findings 538
5.1 Patterning of Three-Dimensional Magnetic Nanostructures Using Focused Electron Beam 538

A. Fernández-Pacheco (✉) • R.P. Cowburn
Cavendish Laboratory, University of Cambridge, Cambridge, UK
e-mail: af457@cam.ac.uk

L.E. Serrano-Ramón
Instituto de Ciencia de Materiales de Aragón (ICMA), Departamento de Física de la Materia Condensada, Universidad de Zaragoza–CSIC, Zaragoza, Spain

M.R. Ibarra
Departamento de Física de la Materia Condensada, Universidad de Zaragoza, Zaragoza, Spain

Laboratorio de Microscopias Avanzadas (LMA), Instituto de Nanociencia de Aragón (INA), Universidad de Zaragoza, Zaragoza, Spain

J.M. De Teresa
Instituto de Ciencia de Materiales de Aragón (ICMA), Departamento de Física de la Materia Condensada, Universidad de Zaragoza–CSIC, Zaragoza, Spain

Laboratorio de Microscopias Avanzadas (LMA), Instituto de Nanociencia de Aragón (INA), Universidad de Zaragoza, Zaragoza, Spain

© Springer-Verlag Berlin Heidelberg 2015

C.S.S.R. Kumar (ed.), *Surface Science Tools for Nanomaterials Characterization*,
DOI 10.1007/978-3-662-44551-8_14

5.2 Direct Magneto-optical Kerr Effect Measurements on Suspended Nanostructures 540
5.3 The "Felling Method" 545
6 Conclusions and Future Perspective 555
References 556

Abstract

In order to characterize the magnetic properties of magnetic suspended nanostructures, we show here a methodology which combines micromanipulation, Kerr magnetometry, and magnetic force microscopy. By following this procedure, we directly measure the magnetization switching of suspended nanowires, we determine the mechanism for magnetization reversal of the wires, and we image their magnetic domain structure.

Keywords

Magneto-optical Kerr effect • Magnetic Force Microscopy • Nanowires • Spintronics • Domain walls • Nanoelectronics • Three-dimensional devices

1 Definition of the Topic

The combination of advanced characterization techniques makes possible an in detail study of three-dimensional magnetic nanostructures.

2 Overview

The recent development of advanced nanolithography techniques which can pattern complex three-dimensional nanostructures is very exciting. The possibility to study physical phenomena in different symmetries or boundary conditions than those currently accessible and the realization of 3D nano-architectures for *Beyond Moore* nanoelectronics are two examples of the novelties that these new tools may bring in the future [1]. In particular, the possibility to create suspended magnetic nanowires is of high interest for the spintronic community, which during the last years has intensely studied the physics behind the controlled motion of domain walls in planar nanowires. The extension of these ideas to three-dimensional structures could make possible the realization of the "vertical racetrack memory" [2], proposed several years ago.

However, together with the possibility to pattern new 3D nanostructures, the development of new characterization techniques or a different use and combination of preexisting ones is required. This chapter shows the methodology we have followed for the characterization of 3D cobalt nanowires grown by focused electron beam-induced deposition. Several techniques and strategies have been used in parallel in order to thoroughly characterize these nanostructures, which growth optimization is still in progress.

3 Introduction

During the last years, there has been an intense research in the area of spintronics to study and control the motion of domain walls in nanowires. A nanowire with a well-defined anisotropy (either magnetocrystalline, surface, or shape anisotropy) can encode binary information in a very efficient way, as the magnetization will only point along one of two possible directions. The boundary between two opposite domains is called a domain wall [3]. It has been shown that magnetic nanowires can act as conduits for domain wall propagation [4], i.e., a domain wall can be moved along a nanowire as a particle inside a pipe [5]. This motion is produced by applying either magnetic fields, spin-polarized electrical currents, or spin currents. Nanowire networks hosting multiple domain walls can therefore be used to store binary information [1, 6–10] and perform logic operations [11, 12]. The possibility to use these systems as a new low-power, fast, high-density storage technology with no mobile parts is very promising, which has made the research based on magnetic nanowires one of the most active ones within spintronics.

However, in order to make these ideas viable, the storage capacity of these devices should compete against coming technologies, implying that densities of $\sim$1 Tbit/in^2 should be reached. Interestingly, a possible way to achieve those capacities consists of growing nanowires perpendicularly to the substrate, and not along it, as currently. So far, conventional growth and lithography methods such as evaporation or sputtering and electron beam lithography have been used to pattern 2D wires. High-aspect ratio nanowires cannot be fabricated using those methods and new lithography techniques are therefore required. For the vertical deposition of magnetic materials, methods such as electrodeposition [13, 14] or atomic layer deposition [15, 16] are very appropriate. Nevertheless, in order to create three-dimensional devices, nanostructures need to be more complex than what these techniques provide.

In order to investigate alternative nanolithography techniques to pattern 3D magnetic nanostructures, we are currently exploring the use of focused electron beam-induced deposition (FEBID), which has the capabilities mentioned before [17–19]. This chapter is focused on studying magnetic nanowires grown by FEBID, using a characterization methodology which combines magneto-optical Kerr effect, micromanipulation, and atomic and magnetic force microscopy.

4 Experimental and Instrumental Methodology

In this section we describe the experimental techniques used for this work. In particular, we give a brief description of focused electron beam-induced deposition, an advanced nanolithography technique which can grow complex three-dimensional magnetic nanostructures, and we also briefly explain the magneto-optical Kerr effect and magnetic force microscopy. In addition, we schematically present the methodology followed to characterize 3D magnetic nanostructures, based on two different routes.

4.1 Experimental Techniques

During the last years, we have been investigating the magnetic properties of nanostructures patterned using focused electron and ion beams [20, 21]. For that we have used a dual beam system such as the one shown in Fig. 14.1a. This setup comprises a scanning electron microscope (SEM) and a focused ion beam (FIB), with the possibility to perform nanolithography processes using both focused beams simultaneously. In addition to normal imaging (using both beams) or milling (using FIB), it is possible to grow nanostructures by using gas injection systems (GIS) as the ones indicated in the figure. A GIS consists of a gas reservoir connected to a needle (see Fig. 14.1b), which is approached up to a few tens of microns from the target place. When the gas is delivered, the molecules get adsorbed on the substrate, being decomposed by using either the SEM or FIB. In particular, the secondary electrons generated during these processes are the main responsible of the molecule decomposition. Usually, the gases used are organometallic, so when the molecular bonds are broken, the heavy metals get deposited on the substrate, whereas the rest, which is usually volatile, is pumped out of the system. Figure 14.2 shows schematically all the processes involved in a FEBID process: adsorption, diffusion, dissociation, and deposition. See refs [17–21] for a more detailed description of the technique.

For the fabrication of magnetic nanostructures, we have used dicobalt octacarbonyl [$Co_2(CO)_8$]. Usually, FEBID produces deposits with around

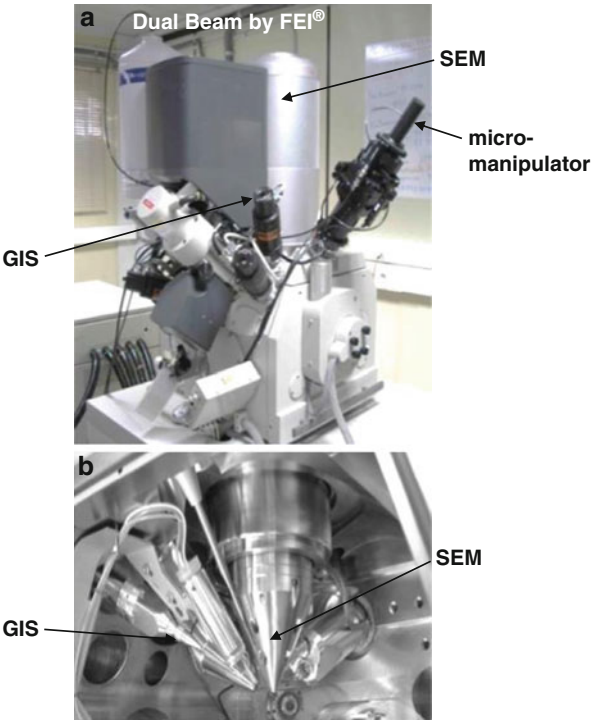


Fig. 14.1 (**a**) Dual beam system combining a SEM and a FIB. The system also comprises a micromanipulator, several GIS to inject gases inside the vacuum chamber and perform local deposition processes, and an EDX detector for spectroscopy measurements. (**b**) Inside of the chamber, where SEM and GIS are marked

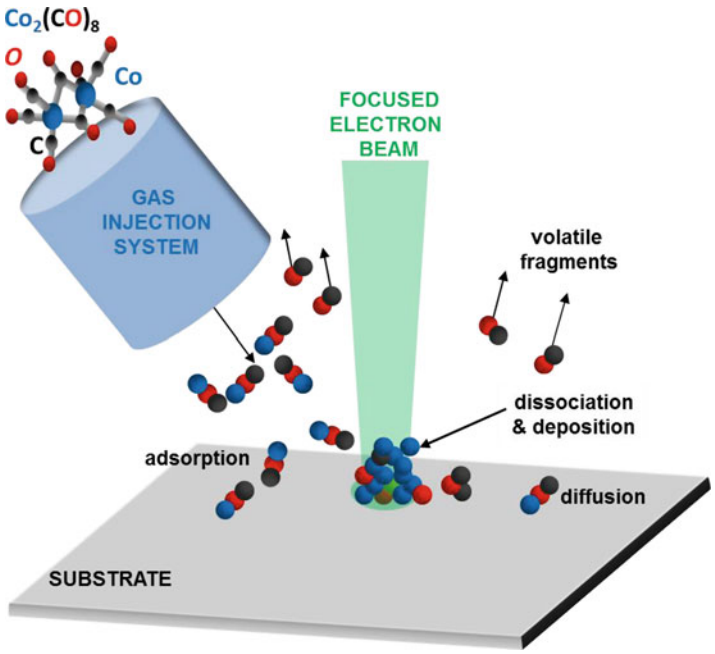


Fig. 14.2 Sketch showing the basics of focused electron beam-induced deposition. The molecule used to grow cobalt nanostructures, $Co_2(CO)_8$, is included

30–40 % metallic composition when using most commercial organometallic gas precursors [17, 18], with the rest being composed by carbon and oxygen. However, FEBID using Co carbonyl results in deposits formed by almost pure polycrystalline Co [22, 23], which makes FEBID a very interesting technique to pattern magnetic nanostructures.

For the magnetic characterization of the nanostructures, we have used two techniques: magneto-optical Kerr effect (MOKE) and magnetic force microscopy (MFM). MOKE is a versatile magnetometry technique to study magnetic nanostructures. For these experiments we have used the system shown in Fig. 14.3a. Polarized light is focused on the sample, being reflected and collected by a detector. Due to the interaction between the incident electromagnetic wave and the magnetic sample, the polarization of the reflected light is rotated with respect to the incident one, and it acquires a small ellipticity [1]. This effect is called longitudinal MOKE when the magnetization component probed is parallel to the plane of incident of the light. Both Kerr rotation and ellipticity can be probed locating an analyzer and a quarter-wave plate before the detector. Our system is a focused MOKE, with the laser spot about 5 μm in diameter, and in-plane fields (in x and y) can be applied on the sample. This type of MOKE system is very sensitive, making possible to measure magnetic nanostructures (nanometric in thickness and in one of the two in-plane dimensions) with magnetic moments as small as 10^{-12} emu [24]. For this, the nanostructure to be probed must be far away (∼50 μm) from any other magnetic element.

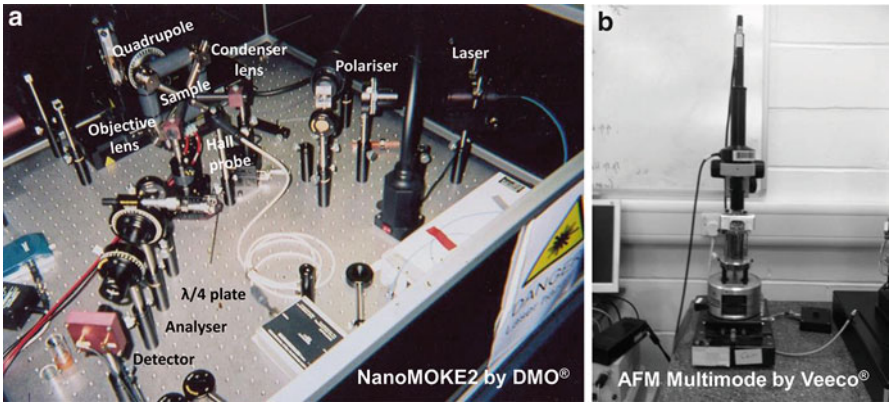


Fig. 14.3 (**a**) Focused MOKE for magnetometry measurements of nanostructures. The sample sits between the poles of a quadrupole, to apply in-plane fields during measurements. The different elements of the system are indicated. (**b**) Probe microscope used in this work

Together with MOKE measurements, in order to get a better insight into the morphology and magnetism of our nanostructures, we have performed AFM and MFM measurements. For these measurements we have used the system shown in Fig. 14.3b operating in tapping mode, with commercial cobalt-chromium-coated tips which have a nominal coercivity of 400 Oe, magnetic moment of 10^{-13} emu, and nominal tip radius of 35 nm. The magnetic and topographic signals were separated using a two-pass scanning method [25]. In the first scan, the tip oscillates at low heights, being mainly sensitive to short-range interactions such as van der Waals forces, and therefore imaging the topography of the sample. A second scan is performed with the tip typically about 80–100 nm above the surface, where the long-range magnetic interactions are detected. The recorded image is then a map of the variation of the magnetic force gradient at constant height above the sample surface.

4.2 Combining Micromanipulation, Kerr Magnetometry, and Magnetic Force Microscopy to Characterize Magnetic Nanostructures

Research based on 3D nanostructures is currently an emerging field, with potential applications in diverse disciplines such as biology, medicine, or nanoelectronics [26–28]. However, great challenges are faced by researchers working in this area, since it does not only require advanced lithography tools to pattern 3D nanostructures, but the characterization of single three-dimensional nanostructures is very challenging. This is due to the fact that most of the current experimental techniques are designed to characterize 2D objects. Probe microscopy is a good example of a technique which is not suitable for suspended nanostructures. In order to overcome these difficulties and thoroughly characterize the magnetic properties of nanowires grown by FEBID, we have developed a protocol which is sketched in

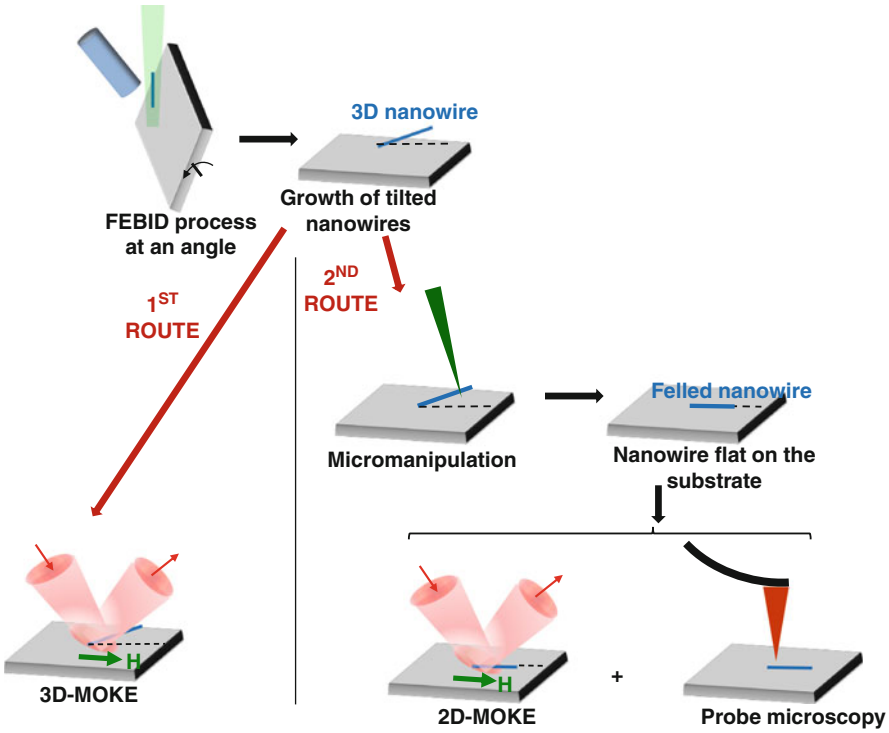


Fig. 14.4 Sketch showing the methodology followed to characterize 3D nanostructures. After the growth of tilted nanowires, two complementary routes are followed for a full characterization

Fig. 14.4. First of all, and as will be explained in detail in Sect. 5.2, the nanowires investigated here were grown forming an angle with the substrate. For that, the sample holder is tilted with respect to the SEM beam, which permits to grow nanostructures at any angle. After the growth, two different routes have been followed to characterize magnetically the nanowires:

- Route 1: Using focused magneto-optical Kerr effect, we have directly probed the magnetic switching of the nanowires. For that, the MOKE laser was placed directly on the wire, and the Kerr signal was measured while applying in-plane x fields. We will refer to this approach as "3D-MOKE."
- Route 2: We have developed a method to place the nanowires flat on the substrate, using a micromanipulator. Once the wires are flat, we have performed conventional (longitudinal) 2D-MOKE, followed by atomic force and magnetic force microscopy of the wires. We will refer to this method as the "felling procedure," since the nanowires, analogously to trees, are felled using the micromanipulator for subsequent investigation.

The two methods presented here are complementary one with the other. The first one allows studying the magnetic switching of nanowires in the configuration

which were grown, i.e., it is a pure 3D magnetic characterization. However, several issues and difficulties are present when using this approach, as is discussed in detail in Sect. 5.2. On the contrary, the second route consists of performing a 2D characterization (on the plane) of 3D objects which have been placed flat on the substrate. As a drawback, by following this procedure you modify the 3D configuration of the structure in order to measure it. On the contrary, there are several advantages: a thorough characterization can be carried out, doing, for instance, magnetic microscopy measurements of the nanostructures. Also and very importantly, the felling method can be applied to 3D structures fabricated by any lithography method.

5 Key Research Findings

5.1 Patterning of Three-Dimensional Magnetic Nanostructures Using Focused Electron Beam

As explained in Sect. 4.1, the work shown here consists of studying magnetic nanostructures patterned by FEBID, using $Co_2(CO)_8$ as gas precursor. This gas is the only one reported so far in FEBID which leads to almost pure metallic deposits in high-vacuum conditions [22]. In the past, our group and others have studied the magnetic properties of 2D planar Co nanostructures grown by FEBID. The high purity of the deposits, their polycrystalline microstructure, and the high resolution of the lithography techniques lead to patterning nanostructures with suitable properties for applications in spintronics [29].

In this work, we have focused our efforts in fabricating high-quality 3D Co nanostructures using FEBID. As shown in Fig. 14.5, the capability of FEBID to grow 3D objects is unique. Complex 3D geometries can be patterned in a few minutes, such as the one shown here, a two-loop spiral erected several microns up the substrate. The ability of FEBID to pattern this type of nanostructures is very exciting, since it opens a new route to develop devices such as the vertical racetrack memory [2], which was proposed years ago but which has not been implemented so far due to the great difficulties of fabricating 3D magnetic nanowires in a controlled manner.

Importantly, and as shown in Fig. 14.5c, the nanowires studied here have circular cross sections and not rectangular, as is the case for nanowires patterned flat on the substrate. This has important implications regarding the type of domain wall present in these wires [30, 31].

Due to the complex processes occurring in FEBID, the microstructure and composition of the wires can substantially change, depending on the growth parameters. We observed that the best conditions to grow high-aspect ratio, smooth, metallic-rich nanowires are achieved with the SEM operating at 3 kV and 21 pA [21, 32]. These conditions also minimize the magnetic halo beneath the nanowire, which can be very large for other growth conditions.

The work presented here consists of studying straight magnetic nanowires such as those shown in Fig. 14.6, where the SEM is focused on the same point during

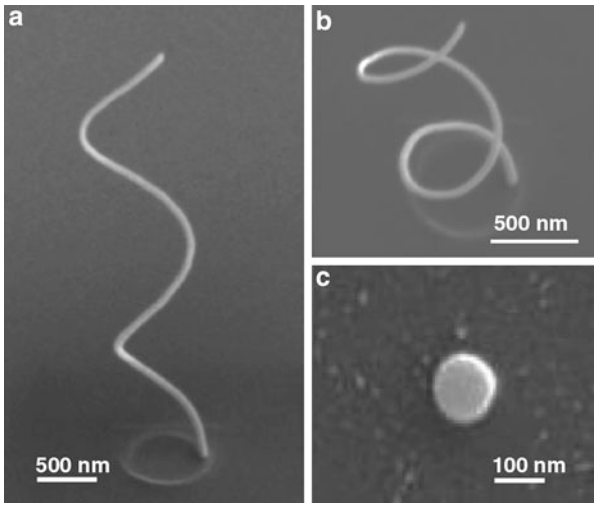


Fig. 14.5 Magnetic nanowires grown by FEBID. (**a**) and (**b**) Nano-spiral erected several microns up the substrate, imaged from different angles. (**c**) Top image of a nanowire, showing a circular cross section (Adapted from ref [32])

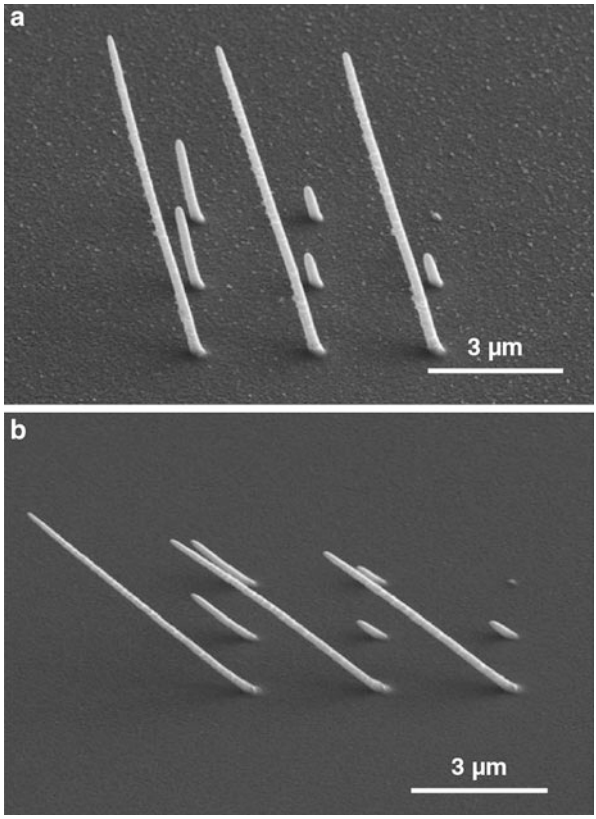


Fig. 14.6 Arrays of nanowires patterned using different growth conditions. The angle formed by the wires with the substrate can be controlled by tilting the substrate during growth

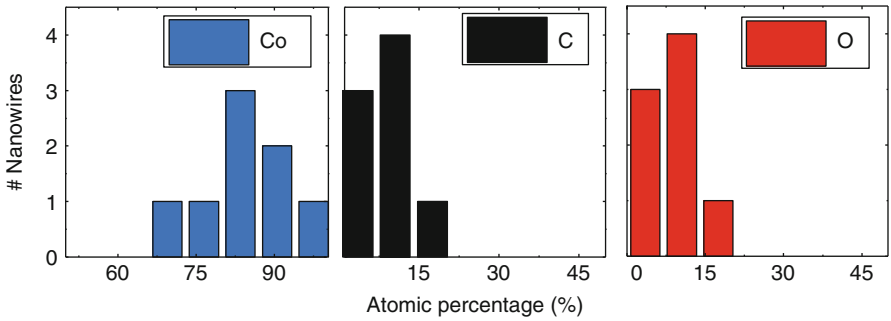


Fig. 14.7 Histograms composed by eight nanowires grown in different batches, indicating the atomic percentages of the wires. The average Co content is 85 %

growth, and the beam is switched on and off alternatively. By following this strategy two goals are achieved: firstly the beam is off during enough time to allow new carbonyl molecules to be adsorbed at the growth area; secondly, heating effects produced by the electron beam are reduced. The different heights in the figure correspond to using different dwell and refresh times. We typically worked with values of 1 ms and 100 ms, respectively, which resulted in growth rates of approximately 3 μm/min [21]. As observed in the two figures, the wires can be grown forming any angle with the substrate plane, by tilting the stage the complementary angle, since the wire grows along the SEM beam (neglecting possible deviations toward the GIS). This method was first used by Gazzadi et al [33]. The nanowire diameter is determined by the SEM beam aperture and the interaction between the beam and gas molecules [17, 18], which also depends on the gas flux. The wires investigated here have typical diameters of 100 nm. Under non-optimized conditions, small grains can grow along the length of the wires, as will be further discussed in Sects. 5.3.3 and 5.3.4.

In Fig. 14.7 histograms compiling the nanowire atomic composition of samples grown in 8 batches, determined by energy-dispersive X-ray spectroscopy (EDX), are shown. Each point in the histograms corresponds to one wire for each batch. The wires are mainly composed of cobalt, the rest being carbon and oxygen. In spite of being nominally identical, a significant dispersion in the composition is observed, with average Co of 85 %. This value is significantly higher than previous results in the literature, where for similar diameters, compositions not higher than 40 % were reported [34, 35].

5.2 Direct Magneto-optical Kerr Effect Measurements on Suspended Nanostructures

As explained in Sect. 4.1, MOKE is a very sensitive magnetometry technique to study the magnetic properties of single nanostructures. This technique is commonly used to study effects such as the magnetic switching of thin films and

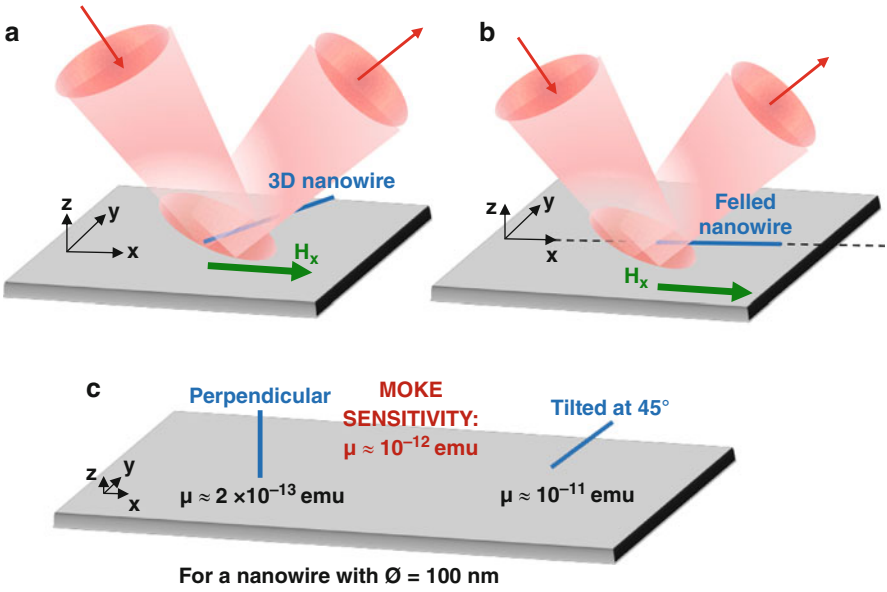


Fig. 14.8 MOKE magnetometry of nanostructures. (**a**) Direct 3D MOKE on suspended tilted nanowires. (**b**) Conventional longitudinal MOKE on a 2D nanowire. (**c**) Comparison of magnetic moments probed by focused MOKE and its sensitivity. Only tilted nanostructures can be directly probed using 3D MOKE

multilayers [36, 37] or laterally patterned nanostructures [24]. By combining different MOKE geometries (longitudinal, transversal, polar) or performing simultaneous magnetoelectrical measurements, it is possible to perform a detailed characterization of magnetic devices [38, 39]. MOKE microscopy also allows observing magnetic domains during the reversal of micron-sized structures [10]. However, so far and to the best of our knowledge, all MOKE measurements had been done in 2D nanostructures. The results shown here, some of them previously published in ref. [32], are the first ones where MOKE is used to directly measure the magnetic switching of 3D nanostructures (3D-MOKE)

Figure 14.8a shows the configuration followed for 3D-MOKE measurements: the laser spot is focused on a 45 degree-tilted suspended nanowire, and fields along the x direction are applied. This MOKE configuration is not standard, since longitudinal (M_x) and polar (M_z) components of the wire magnetization are simultaneously measured. On the contrary, felled nanowires (see Fig. 14.8b) are probed in a conventional magneto-optical geometry: only M_x is measured under fields along the x direction (longitudinal MOKE). In addition to these differences, 3D-MOKE measurements are significantly more complicated than standard ones: a strong diffuse scattering of light is produced when focusing the laser on a suspended nanostructure, which reduces the signal detected. Also, additional sources of noise, such as those due to the mechanical motion of the wires, are present, which reduce significantly the signal-to-noise ratio. In spite of that, as will be shown below,

3D-MOKE can be used as a way to measure directly the magnetic switching of 3D nanostructures.

Together with the two possible MOKE geometries, Fig. 14.3c shows the magnetic moments μ estimated depending on the geometry used. These moments are compared with the MOKE sensitivity of our system. The calculation is done for 100 nm in diameter wires made of Co (M_s = 1,400 emu/cm^3), with a MOKE laser diameter = 5 μm and taking into account that MOKE is a surface technique: only about the top t = 20 nm magnetic thickness is detected for metals [36]. Therefore, from this estimation, it is evident that to perform 3D-MOKE measurements in single nanowires, these have to be tilted enough with respect to the substrate normal to detect their magnetic moments. Growing tilted nanowires is quite straightforward with FEBID, but is not trivial with other techniques such as electrodeposition or atomic layer deposition.

5.2.1 Magnetic Switching of Tilted Nanowires

In order to perform 3D-MOKE measurements, we fabricated 4–20 μm long suspended Co nanowires forming 45° with the substrate, as shown in Fig. 14.9a. Figure 14.9b shows an example of a hysteresis loop measured for this nanowire. The loop detected is squared, presenting abrupt switches for magnetization reversal. As explained before, these are the first results where 3D magnetic nanostructures are directly probed using MOKE. In Co, sharp magnetization switches are due to the reversal of the magnetization mediated by nucleation and propagation of domain walls [40, 41].

It should also be noticed that the loops presented here are the result of averaging hundreds or thousands of loops, which imply measurement times of tens of minutes. In spite of the averaging, we can observe in this case an abrupt single switching at the coercive field, implying that the magnetization is reversed the same way during all these events. This point is relevant for domain wall technologies, where the dispersion in domain wall propagation and depinning fields due to the stochastic nature of these effects must be minimized [42].

5.2.2 Drawbacks: Heating, Mixed Signals, and Sources of Noise

Figure 14.10 shows two nanowires after having been measured by 3D-MOKE for an extended period of time. Whereas the segment closer to the substrate seems unaffected by these measurements, it is evident that the top part has been damaged. The laser used for these measurements provides a power density per unit length of ~10 W/m. So far, in conventional 2D-MOKE we had never observed damage of any probed nanostructure. However, these results show that 3D nanostructures cannot dissipate this power density efficiently enough, bending as a consequence. The severe damage shown for the top part in Fig. 14.10b is probably associated to some structural defect along the wire which makes it deform at that point. Further work is in progress to fully understand how the heat affects 3D magnetic nanowires as those grown here. In order to minimize the deterioration of the nanostructures when probed by 3D-MOKE, we performed subsequent experiments with the laser focused at the base of the wire and reduce the measurement time to the minimum required.

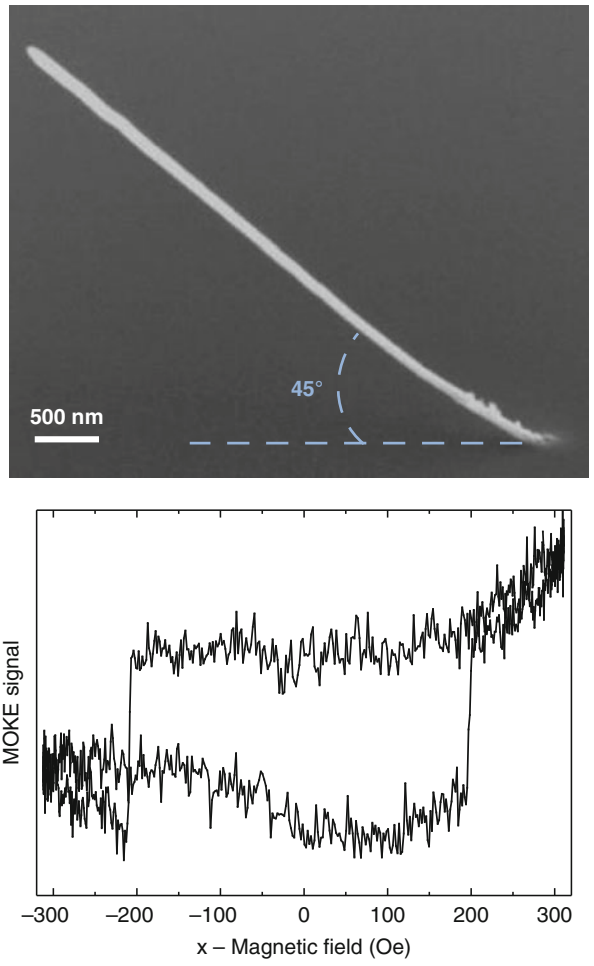


Fig. 14.9 3D-MOKE on single tilted nanostructures. (**a**) Nanowire grown forming 45° with the substrate (**b**) MOKE loop of this nanowire, showing hysteresis and abrupt switching of the magnetization (Adapted from ref. [32])

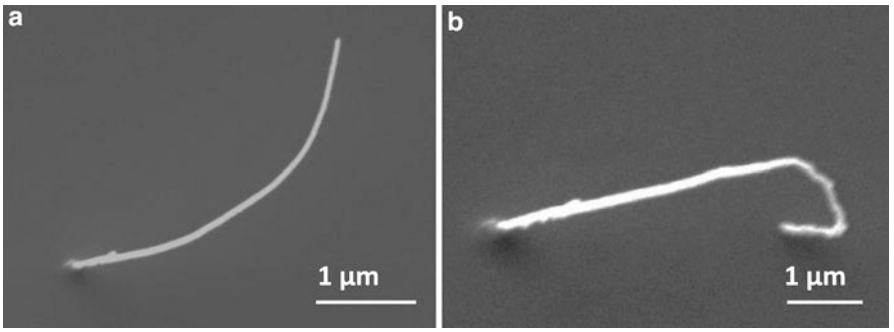


Fig. 14.10 Example of 3D nanowires damaged after measuring with MOKE for a prolonged amount of time

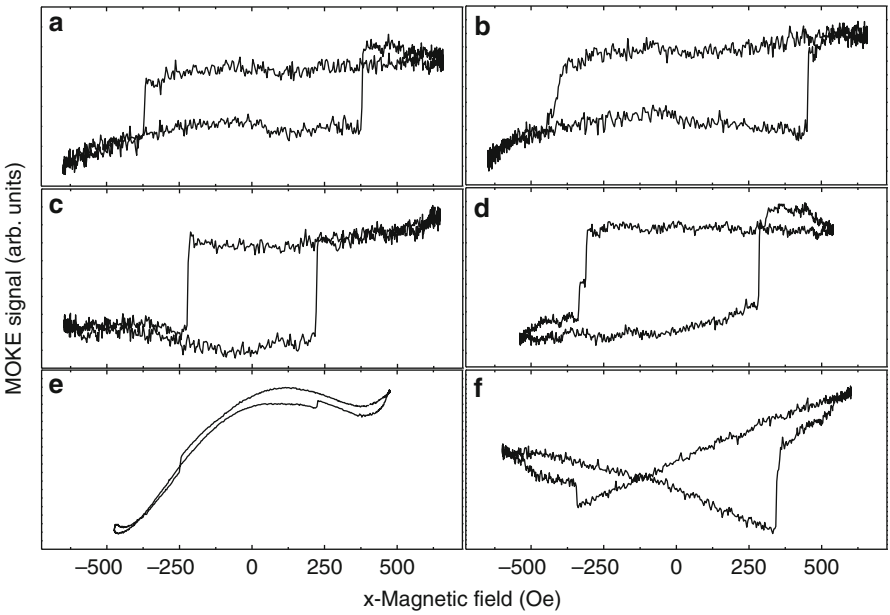


Fig. 14.11 MOKE loops on 3D nanowires. (**a**)–(**d**) show variation of properties from wire to wire: single or multiple switching and different switching fields. (**e**) Loop with a strong proportional-to-the-field quadratic signal. (**f**) Loop with a strong proportional-to-the-magnetization quadratic signal

Figure 14.11 illustrates examples of hysteresis loops of different nanowires grown at 45° with respect to the substrate measured by 3D-MOKE. All the loops are the result of hundreds of averages. The only data treatment performed has been the subtraction of a constant slope to the loops, which is a typical contribution when MOKE measurements are performed in magnetic nanostructures. Typical features of these loops are the dispersion on the switching field values from wire to wire, and that the reversal is in some cases via a single jump, but in other occasions it occurs via multiple jumps. Together with standard MOKE loops (Fig. 14.11a–d), we show two measurements which illustrate the difficulty found for the measurements of 3D nanowires. In Fig. 14.11e a strong quadratic-with-the-field signal superimposes to a normal loop, hindering a clear observation of details during the switching of the magnetization. This type of contribution comes as a result of mechanical noise during the measurements. Focusing the laser closer to the basis of the nanowire was usually effective to diminish this effect. We discuss this effect further in reference [32]. Also, Fig. 14.11f shows a hysteresis loop with a strong quadratic-with-the-magnetization signal. The shape of this type of loops resulted to be strongly dependent on analyzer and quarter-wave plate angles and resembles those found for materials with a strong quadratic MOKE [43, 44]. We are currently studying in detail this effect, since the interpretation of this contribution is complex, due to the nontrivial geometrical configuration of these measurements.

5.3 The "Felling Method"

Due to the disadvantages described below and in order to characterize more thoroughly the grown nanowires, we have developed a method consisting of placing the wires flat in the substrate using a micromanipulator. This process for characterization is denominated route 2 in Fig. 14.4.

5.3.1 Micromanipulation of Suspended Nanostructures

The use of micromanipulators for moving nanowires or nanotubes is currently a quite extended procedure [45–47], and more sophisticated tools such as nano-grippers or nano-tweezers are now used to manipulate nano-objects [48, 49]. Regarding magnetic materials, manipulation methods have made possible the detection of ultra-low magnetic moments of single beads and nanoparticles, by placing them in superconducting quantum interference devices (nano-SQUIDs) or Hall crosses [50–52].

In order to attach a nanostructure and the manipulator, there are mainly three methods, as discussed by Langford et al [45]. The first one consists of approaching the micromanipulator to the object and using the excess of charges in one of the objects to produce electrostatic attraction between both, effect which can be exploited more efficiently by biasing the manipulator. The second is based on depositing additional materials using FEBID which weld the nanowire and the tip. The third is based on pressing the manipulator against the wire to create a pressure weld. Once the nano-object is located at the target area, either a FIB etching process or the addition of a thick FEBID deposit can be used to release the object. In our case, we decided to follow a simple method which cuts the wires, placing them flat on the substrate next to where they were grown. This "felling method" is less invasive than others involving FIB processes or additional deposits, which can alter or even destroy the magnetism of nanostructures [53].

Figure 14.12 shows snapshots of a video recording the felling of a nanowire grown at 45° with respect to the substrate. We used an Omniprobe® micromanipulator made of tungsten, with an initial tip diameter of 500 nm. In some cases we also used previously damaged manipulators with a much larger diameter, as in this case. The micromanipulation speed used for the process is 1 mm/s. The process followed here is quite robust, with a success rate for felling wires of approximately 75 %. The shortest wires that we can place flat are 400 nm high, and as shown in Fig. 14.13, the felling process can be carried out for wires located in relatively dense arrays.

Figure 14.14 shows a similar process, but now in a wire initially grown perpendicular to the substrate. As observed, the wire falls into the substrate at a direction which is approximately 45° with respect to the horizontal. We have observed that this angle can be roughly controlled and depends on the direction of motion of the manipulator while felling, on the specific geometry of the manipulator tip which contacts the wire, and on the elastic properties of the nanowire, which are very dependent on its metallic content.

Figures 14.14 and 14.15 are two felling processes carried out in nanowires with different composition. In the former case, the wire is formed by almost 100 % Co.

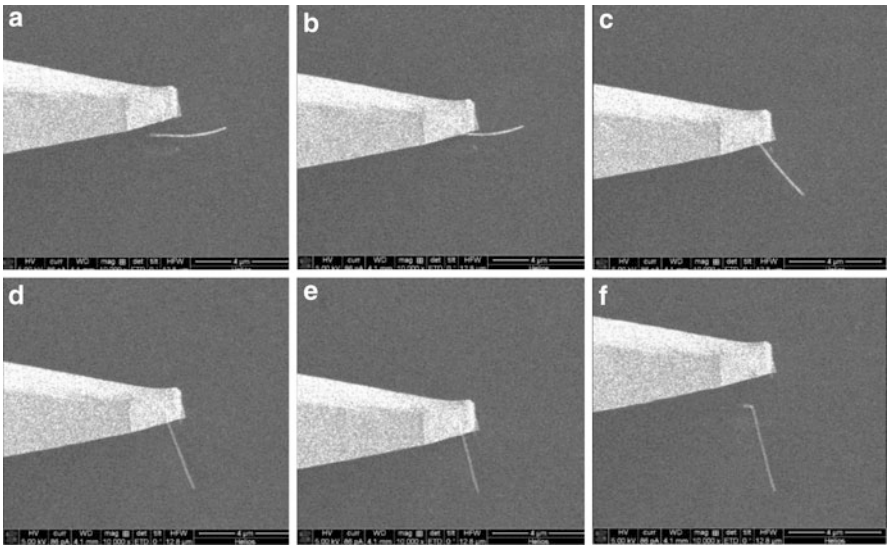


Fig. 14.12 SEM images showing the process to fell a nanowire

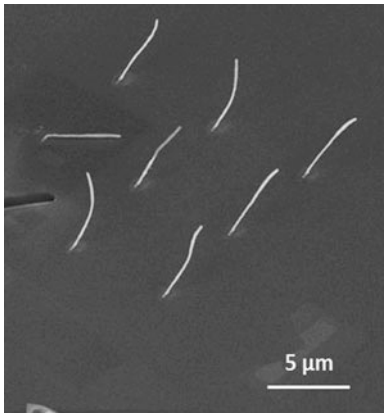


Fig. 14.13 Array of nanowires where the leftmost has been felled using a micromanipulator

As a consequence, the micromanipulator produces a straight and clean cut of the wire, which falls flat on the substrate. On the contrary, in the second case, the wire has a composition of about 70 % Co and 30 % C, which makes it much more resistant to be bent by the manipulator. The wire bends first elastically and then plastically, but it does not finally drop on the substrate, but stays suspended, now forming a different angle with the substrate than at the beginning.

In Fig. 14.16 we show a final example, where we use the manipulator not only to cut a wire, but we reshape it for subsequent measurements. In this case, the wire was pressure welt to the micromanipulator while felling. In order to release it, the

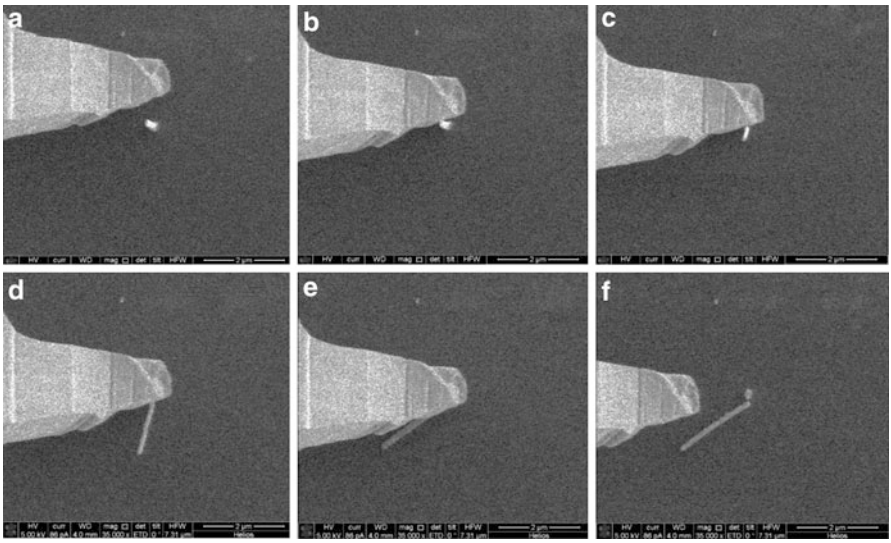


Fig. 14.14 Felling procedure in a nanowire initially grown perpendicular to the substrate

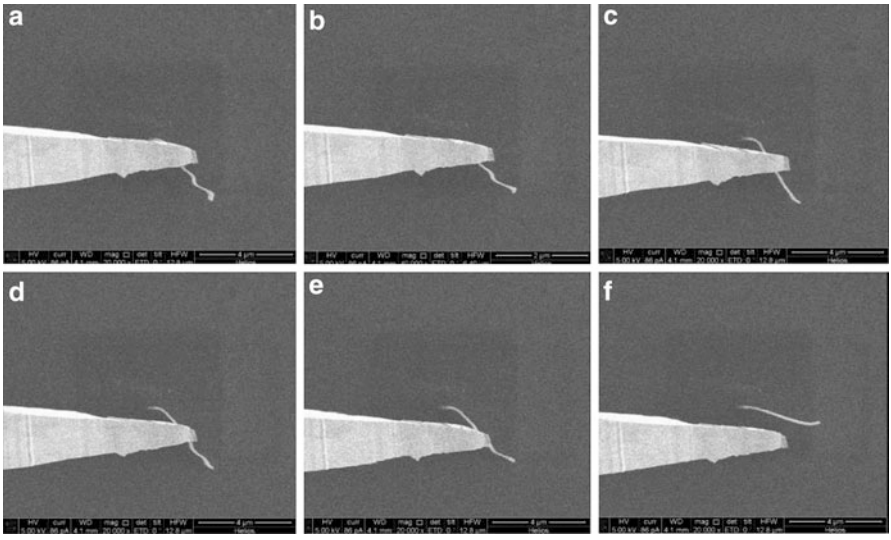


Fig. 14.15 Example of an unsuccessful felling procedure: the nanowire elastically returns to its initial (approximately) position after being bent with the micromanipulator

tip was approached closer and closer to the substrate while moving it backward. The friction created between the wire and the substrate was first used to form an inverted C shape until it was large enough to detach the wire from the manipulator.

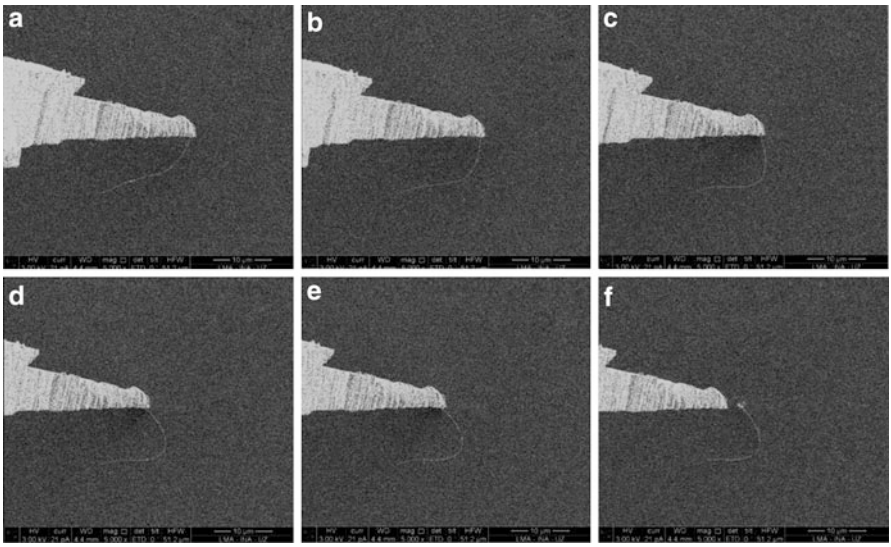


Fig. 14.16 Micromanipulator process to reshape a nanowire. The final configuration is a felled C-shape wire

5.3.2 MOKE on Felled Nanostructures

Once we placed the nanowires flat on the substrate using the felling process described above, we measured them using MOKE. The geometry used in this case is sketched in Fig. 14.8b, i.e., it is conventional longitudinal MOKE. There are no ambiguities, therefore, about what component of the magnetization we are probing: in this case it is exclusively M_x, parallel to the wire axis. Moreover, the particular sources of noise in 3D-MOKE measurements, as described before, are not present in these measurements, implying that the signal-to-noise ratio is orders of magnitude better than in the previous configuration.

Figure 14.17 shows MOKE loops for two different nanowires. The same characteristics discussed before for suspended wires are also observed here: the hysteresis loops are squared, with the wire being single domain at remanence. Also, in some of the wires, as the one on the left of the figure, the switch of the magnetization is very abrupt, suggesting a reversal mediated by domain walls. In other wires, on the contrary, this process is multistepped. However, by performing one-average measurements (inset of this figure) we observe that this multistep behavior is usually due to the switching of the wire magnetization at different fields for different events, not to different areas of the object switching at different fields for the same reversal event. We had observed this behavior previously in Co 2D nanowires grown by FEBID [29].

In addition to single-shot measurements, another big advantage for MOKE measurements in felled nanowires is that we can study the dependence of the switching field with respect to the in-plane angle. Figure 14.18 shows this dependence for one particular nanowire, where the measurement geometry is sketched in the inset. A clear increase of the switching field H_{sw} is observed with the angle θ.

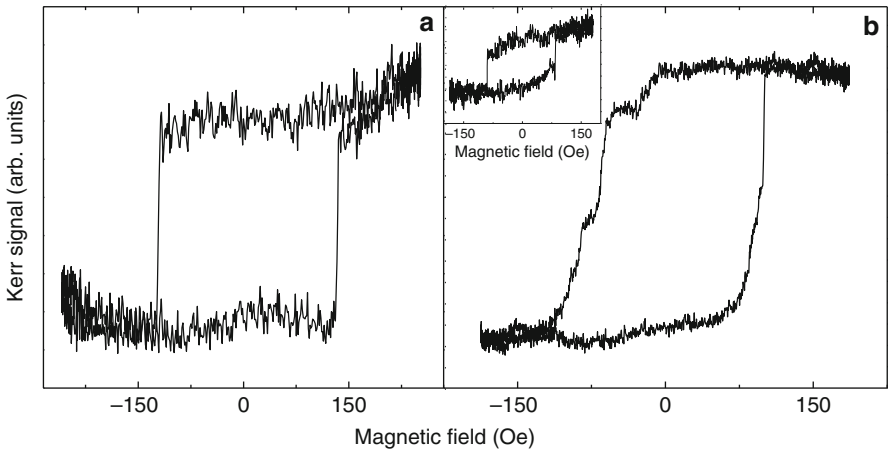


Fig. 14.17 Examples of MOKE loops on two felled nanowires. Single (**a**) and multiple (**b**) switching of the magnetization are observed. The inset in (**b**) is a single-shot measurement of the large loop shown in (**b**), which was averaged hundreds of times (Adapted from ref. [32])

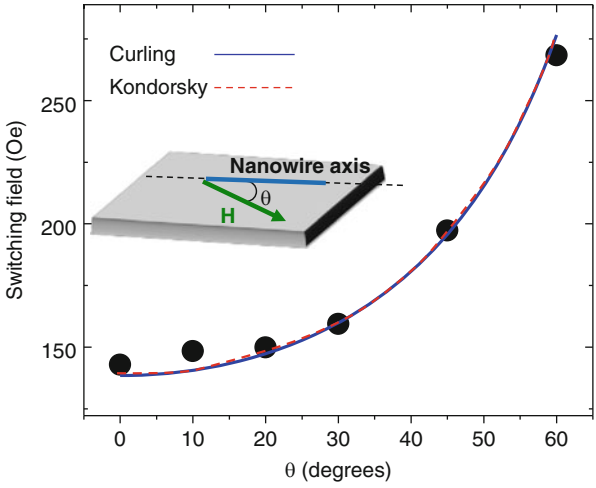


Fig. 14.18 Angular dependence of the switching field with the in-plane field direction. The increase observed can be fitted both to the Curling nucleation model and the Kondorsky propagation model

As expected, this dependence is not the one followed for reversal modes involving coherent rotation of the magnetization [14, 54], since the exchange length of Co is much smaller than the diameter of the nanowires. On the contrary, this type of dependence can be fitted to two types of magnetization reversal:

– Curling of the magnetization:

$$H_{sw} = 2\pi M_s \frac{a(1+a)}{\sqrt{a^2 + (1+2a)\cos^2\theta}} \tag{14.1}$$

where a $= -1.08(Ø_0 /Ø)^2$, with Ø the nanowire diameter and $\varnothing_0 = 2(A/M_s^2)^{1/2} \approx 5\lambda_{ex}$ (A, exchange stiffness; λ_{ex}, exchange length). In this case the magnetization at the edges of the nanowire curls with the applied magnetic field, nucleating a domain which is abruptly propagated along the wire and reverses the magnetization. We obtained a good fit for $\lambda_{ex} = 4$ nm, in good agreement with the value expected for Co [55]. This type of behavior has been observed, for example, for Ni electrodeposited nanowires where the shape anisotropy is dominating the magnetic configuration of the wires [54].

– Kondorsky model for domain wall propagation:

$$H_{sw} = 2\pi M_s \frac{H(\theta = 0)}{\cos(\theta)} \tag{14.2}$$

In this case the switching of the wire is not nucleation dominated, as in the previous model, but propagation dominated: the effective force on a domain wall will be stronger, the closer the field is to the axis of the nanowire, following an inverse cosine dependence [56].

The two models described here fit well our experimental results. Therefore, we cannot discriminate if the switching of the magnetization in our wires is nucleation or propagation dominated. What is clear from this analysis is that the reversal involves the formation of domains. This is confirmed in Sect. 5.3.4, where we image the magnetic structure of the wires using MFM.

5.3.3 Atomic Force Microscopy on Felled Nanostructures

Together with the advantages cited before for MOKE measurements, the felling method makes possible to image 3D nanowires using probe microscopy. This allows us to correlate their magnetic behavior with their geometry and magnetic domain structure. In this work we have performed AFM and MFM measurements of a selection of wires previously measured by MOKE. A study involving a larger amount of wires is in progress. However, the examples shown in this chapter give a good overview of the different behaviors expected for this type of wires.

Figure 14.19 shows the AFM profile along several microns for different felled nanowires. Clear differences are observed in the three wires shown, as a consequence of different growth conditions. Whereas Fig. 14.19a corresponds to a smooth nanowire, with a height deviation around 5 % of the average height, Fig. 14.19b corresponds to a rough wire, with this deviation being higher than 30 %. These two very different roughnesses observed are a consequence of growing these wires under different conditions [17, 18]. In order to get smooth wires, the FEBID process must be performed at the electron-limited regime, defined by a small electron/gas flux ratio, which results in high growth rates and lower metallic concentrations. Rougher and smaller nanostructures are grown at the precursor-limited regime, where the electron/gas ratio is high. In addition to this, heating effects are extremely important when growing suspended nanostructures by FEBID [57]. Strong heating created by the beam will foster the growth of larger Co grains,

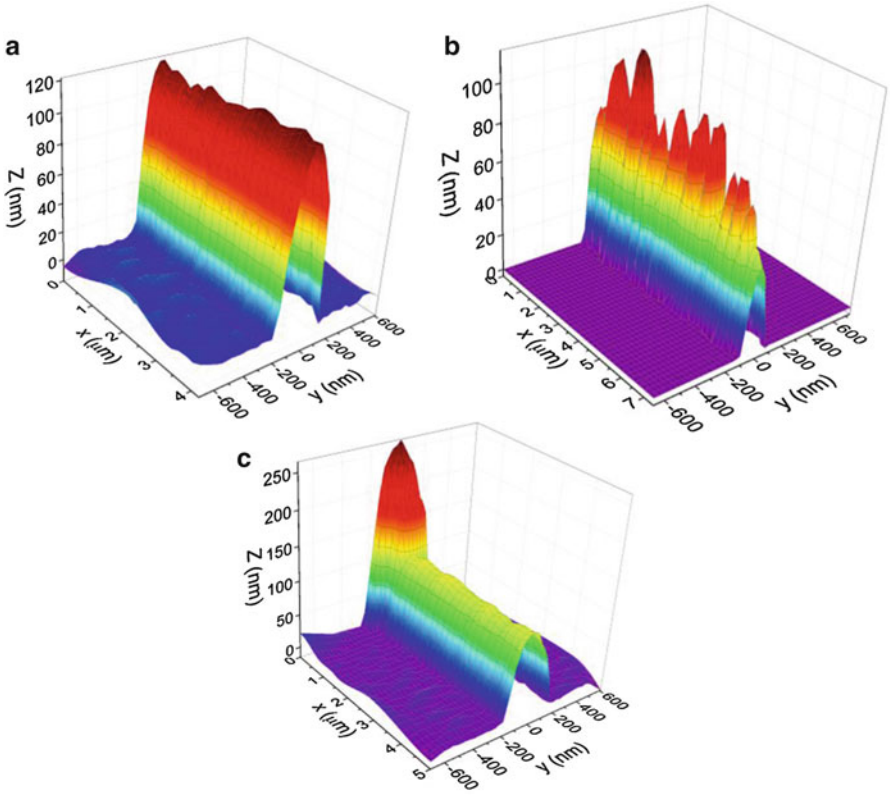


Fig. 14.19 Structural profiles of different nanowires along several microns, measured by AFM. (**a**) Smooth profile. (**b**) Rough profile. (**c**) Profile of a nanowire lifting up the substrate for low x

favoring inhomogeneous growth. As will be shown in the following section, two different profiles as those described here have substantially different remanent states.

In addition to these two extreme cases, Fig. 14.19c shows another AFM profile where we can observe that whereas the wire is very smooth along several microns, with roughnesses again below 5 %, the height probed by AFM increases dramatically for $x < 2$ μm, not being possible to measure its profile for $x < 0$. This is a consequence of the fact that wires grown by FEBID using the method described in Sect. 4.1 are not straight. Especially for high growth rates, the wires do not grow perfectly parallel to the SEM beam, but they tend to deviate toward the GIS axis direction. As a consequence, when they are felled with the micromanipulator, they fall not perfectly flat along their full length, but some sections are lifted from the substrate. The bottom part of the felled nanowire in Fig. 14.12 is an example of this, although SEM images are not as sensitive to height variations as AFM ones.

Another important aspect of the AFM profiles shown in Fig. 14.19 is that the effective width probed by AFM is about twice its height. However, this is a

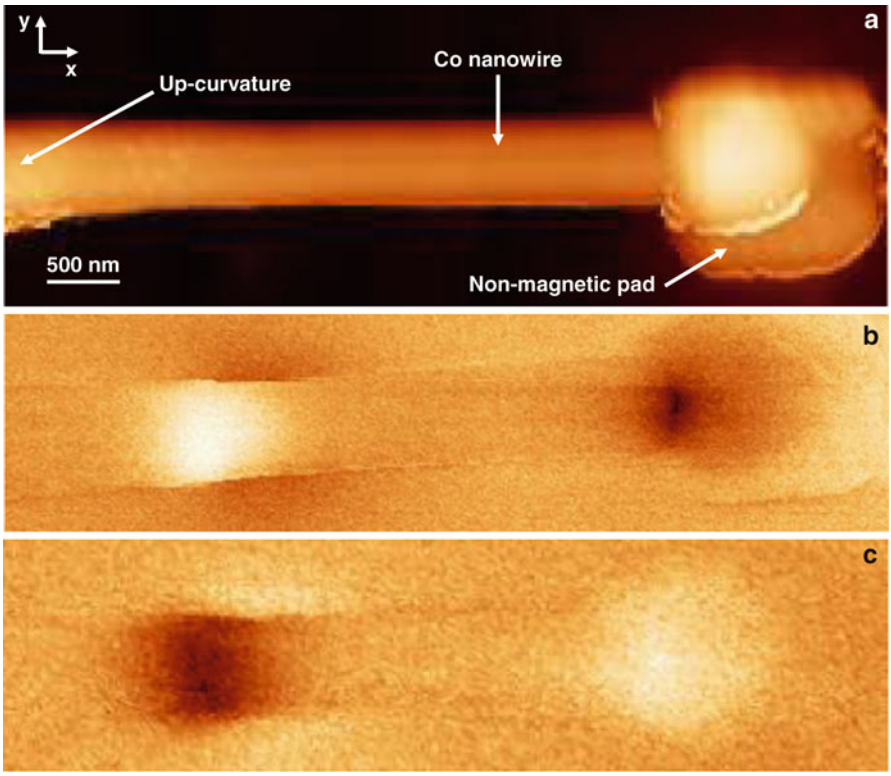


Fig. 14.20 AFM (**a**) and MFM (**b**–**c**) images of a smooth nanowire showing the stray field at one edge and the presence of a single domain wall. (**b**) and (**c**) were taken with the magnetic tip inverted (Adapted from ref. [32])

measurement artifact, since the nanowires have circular cross sections, as determined from SEM images (see Fig. 14.5c). The artificial large wire width measured by AFM is due to the impossibility of the tip to resolve circular profiles [58]. This has been studied by Henry et al [25], where a detailed model of this effect is proposed. In practical terms, the diameter of the wire can be extracted from the height of AFM profiles and not from the measured widths. This effect has also important consequences in the MFM images, as explained in the following section.

5.3.4 Magnetic Force Microscopy on Felled Nanostructures

As discussed in Sect. 4.1, we have performed MFM measurements in selected nanowires. The images shown here are recorded at remanence, after applying a field of about 500 Oe forming a small angle ($<10°$) with the nanowire axis. Figure 14.20 includes topographic and magnetic images for the wire which profile was previously shown in Fig. 14.19c. A nonmagnetic pad was added to one side of the wires after being felled in order to guarantee a good adhesion of the wire to the substrate.

This pad is composed of carbon and platinum and was grown by FEBID using $(CH_3)_3Pt(CpCH_3)$ as gas precursor [1]. Figure 14.20b and c are magnetic images where the MFM tip is magnetized along opposite directions, in order to confirm that the contrast observed is magnetic.

Together with the stray field emanating from the edge of the wire, additional magnetic contrast is observed at the left side of the image. This contrast corresponds to the presence of a domain wall trapped within the wire. A straight magnetic nanowire with these dimensions, formed by a polycrystalline magnetic material, will be monodomain at remanence, due to shape anisotropy [59]. Thus, only magnetic contrast at the edges of the wire would be expected. However, the strong curvature of this wire on the left side of the image makes possible to trap a wall. The use of curved conduits to pin and control motion of domain walls is a strategy widely used in 2D magnetic nanowires [7, 11, 60].

Regarding the structure of the domain wall observed at remanence for this wire, we performed different images at different tip-substrate heights and after applying magnetic fields along slightly different directions. We could not identify any clear wall features, but in all cases the images show a diffuse magnetic contrast. In fact, this is the type of image expected for a Bloch-point vortex domain wall, as computed from micromagnetic simulations [32]. However, as discussed in the previous section, for these images the tip cannot resolve the real profile of the wire, making us impossible to guarantee that this is the type of wall present here. If confirmed, this would be the first experimental observation of a Bloch-point wall, which is a type not present in 2D planar (with rectangular cross section) nanowires. Using high-resolution MFM tips would help to eliminate this ambiguity.

Furthermore, in order to resolve univocally the structure of a domain wall in nanowires with cylindrical symmetry, the best approach consists of recording images of the wire at different angles and performing subsequent 3D reconstruction of the magnetic contrast observed. This is not possible using MFM, so we propose here the following strategy, sketched in Fig. 14.21: the wall structure should be measured multiple times, after applying fields $H_{y,z}$ along different directions perpendicular to the nanowire axis and exploiting the different structures of Bloch-point and transverse domain walls. Whereas a Bloch wall should give in all cases the same magnetic contrast (as is the case here), we should expect a clear change in the MFM signal depending on the relative direction between the tip and the net magnetic charge of a transverse wall, which may be changed by applying the aforementioned external magnetic fields along different directions. This procedure can only be carried out assuming that the wall will always stay pinned at the same position and will not transform after applying this type of field sequences.

For completeness, we should cite that recent results report on the imaging of different types of domain walls in cylindrical nanowires using either transmission electron holography [61] or synchrotron radiation [62].

Finally, Fig. 14.22 shows images of the topography and magnetic contrast of the wire which AFM profile was previously shown in Fig. 14.19b. This wire is narrower than the previous one, with an average diameter (excluding the large

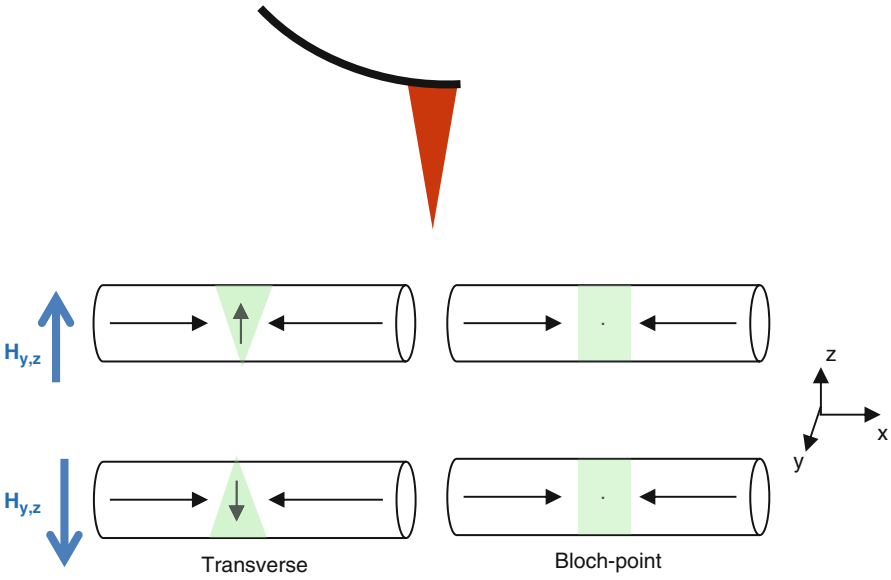


Fig. 14.21 Procedure proposed to distinguish a transverse and a Bloch-point domain wall using MFM measurements at remanence. The blue arrows correspond to the field component applied on the (y,z) plane, which is set to zero before the measurements. The figure compares two cases where the field is applied parallel or antiparallel to the MFM tip axis. The procedure should be followed applying H along multiple directions in the (y,z) plane

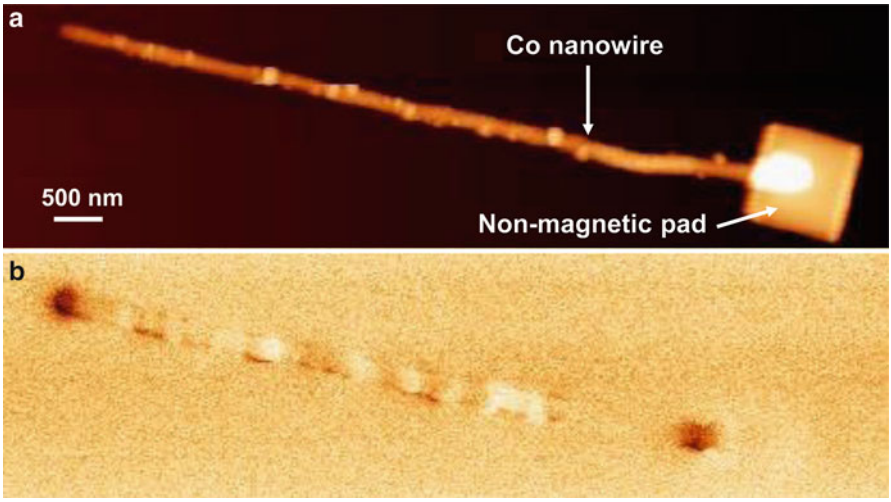


Fig. 14.22 AFM (**a**) and MFM (**b**) images of a rough nanowire at remanence

crystals distributed along its length) of ~75 nm. As explained before, the high roughness and irregularity observed seem to be related to growing this wire under non-optimal conditions. Together with the stray field at the edges of the wire, multiple white-and-dark alternating areas are present, which seem to be associated to magnetic domains with different orientations. A correspondence is observed between some of the large crystals distributed along the wire length and the change of magnetization orientation. The two MFM images shown here exemplify that in order to use 3D nanowires for domain wall applications, where a fine control on the nucleation, propagation, and depinning of single domain walls is required, it is necessary to find appropriate growth conditions where small crystal sizes and homogeneous diameters are achieved. Further work is in progress to achieve a better control on growing smooth nanowires with diameters below 100 nm.

6 Conclusions and Future Perspective

The patterning of 3D magnetic nanostructures is currently an emerging research line with a high potential impact in fields such as nanoelectronics or biomagnetism. Using focused electron beam-induced deposition with $Co_2(CO)_8$ as gas precursor, we are able to pattern high-aspect ratio polycrystalline Co nanowires. By tuning the deposition conditions, we can modify the composition and morphology of the wires, achieving highly metallic structures with low roughnesses and uniform geometry along several microns.

In order to characterize the magnetic properties of the nanowires, we have followed two different routes. In the first one, we have shown that it is possible to measure directly the magnetization switching of the wires in a 3D configuration. This is achieved by growing the wires tilted with respect to the substrate and using focused MOKE. The results shown here, previously published in reference [32], are the first ones where this type of characterization is carried out. Route 2, on the contrary, consists of using a micromanipulator to fell the nanowires, for subsequent standard 2D characterization, which in our case consists of using MOKE and MFM techniques. As described in this chapter, the felling method shown here is flexible, produces small damage in the segment of the wires to be probed, and has a high rate of success. Along this chapter, several aspects of the felling process have been discussed, such as the influence of the nanowire composition or how to use the manipulator to reshape long wires. Once the nanowires are flat on the substrate, systematic MOKE measurements can be performed in order to elucidate what is the mechanism for magnetization reversal of the wires, which in our case has been determined to be domain wall based. In addition, AFM and MFM measurements have been carried out to probe in detail the morphology and magnetic domain structure of selected wires. In this chapter, we have compared two extreme cases: when nanowires are grown under optimized conditions, they are smooth, favoring single domain wall reversal processes. Under different growth conditions, rough nanowires are patterned, with large grains along their

length, which may result in multidomain structures at remanence. Finally, we have proposed a method to distinguish the type of domain walls in cylindrical nanowires using MFM, based on the different symmetry of Bloch-point and transverse domain walls.

The double-route method presented here, involving direct measurements on 3D nano-objects and micromanipulation and combination of magnetometry and magnetic imaging, exemplifies the type of multistep procedure which should be followed when characterizing state-of-the-art 3D magnetic nanostructures.

Acknowledgments This research was supported by an Intra-European Marie Curie Fellowship project No. 251698: 3DMAGNANOW and an ERC Advanced Grant project No. 247368: 3SPIN, both funded by the 7th European Community Framework Programme, by the MAT2011-27553-C02 project funded by the Spanish Ministry of Economy (including FEDER funding), and by the I-LINK0026 project funded by the Spanish CSIC. We would like to thank our collaborators L. O'Brien, D. Petit, J. Lee, R. Mansell, J. M. Michalik, R. Cordoba, and L. Casado.

References

1. Fernández-Pacheco A (2011) Studies of nanoconstrictions, nanowires and Fe_3O_4 thin films, springer theses. Springer, Berlin
2. Parkin SSP, Hayashi M, Thomas L (2008) Magnetic domain-wall racetrack memory. Science 320:190
3. Klāui M (2008) Head-to-head domain walls in magnetic nanostructures. J Phys Condens Matter 20:313001
4. Cowburn RP, Petit D (2005) Spintronics: turbulence ahead. Nat Mater 4:721
5. Ono T, Miyajima H, Shigeto K, Kibu M, Hosoito N, Shinjo T (1999) Propagation of a magnetic domain wall in a submicrometer magnetic wire. Science 284:468
6. Hayashi M, Thomas L, Moriya R, Rettner C, Parkin SSP (2008) Current-controlled magnetic domain-wall nanowire shift register. Science 320:209
7. O'Brien L, Read DE, Zeng HT, Lewis ER, Petit D, Cowburn RP (2009) Bidirectional magnetic nanowire shift register. Appl Phys Lett 95:232502
8. Chiba D, Yamada G, Koyama T, Ueda K, Tanigawa T, Fukami S, Suzuki T, Ohshima N, Ishiwata N, Nakatani Y, Ono T (2010) Control of multiple magnetic domain walls by current in a Co/Ni nano-wire. Appl Phys Express 3:073004
9. Kim K-J, Lee J-C, Yun S-J, Gim G-H, Lee K-S, Choe S-B, Shin K-H (2010) Electric control of multiple domain walls in Pt/Co/Pt nanotracks with perpendicular magnetic anisotropy. Appl Phys Express 3:083001
10. Franken JH, Swagten HJM, Koopmans B (2013) Shift registers based on magnetic domain wall ratchets with perpendicular anisotropy. Nat Nanotechnol 7:499
11. Allwood DA, Xiong G, Faulkner CC, Atkinson D, Petit D, Cowburn RP (2005) Magnetic domain-wall logic. Science 309:1688
12. Lei N, Devolder T, Agnus G, Aubert P, Daniel L, Kim J-V, Zhao W, Trypiniotis T, Cowburn RP, Chappert C, Ravelosona D, Lecoeur P (2012) Strain-controlled magnetic domain wall propagation in hybrid piezoelectric/ferromagnetic structures. Nat Commun 4:1378
13. Fert A, Piraux L (1999) Magnetic nanowires. J Magn Magn Mater 200:338
14. Vivas LG, Escrig J, Trabada DG, Badini-Confalonieri GA, Vázquez M (2012) Magnetic anisotropy in ordered textured Co nanowires. Appl Phys Lett 100:252405

15. Bachmann J, Jing J, Knez M, Barth S, Shen H, Mathur S, Gosele U, Nielsch K (2007) Ordered iron oxide nanotube arrays of controlled geometry and tunable magnetism by atomic layer deposition. J Am Chem Soc 129:9554
16. Lim BS, Rahtu A, Gordon RG (2003) Atomic layer deposition of transition metals. Nat Mater 2:749
17. Utke I, Hofmann P, Melngailis J (2008) Gas-assisted focused electron beam and ion beam processing and fabrication. J Vacuum Sci Technol B 26:1197
18. van Dorp WF, Hagen CW (2008) A critical literature review of focused electron beam induced deposition. Appl Phys Rev 104:081301
19. Koops HW (2003) Rapid prototyping and structure generation using three dimensional nanolithography with electron beam induced chemical reactions. Proc SPIE 5116:393
20. Gabuerac M, Bernau L, Utke I, De Teresa JM, Fernández-Pacheco A (2011) Focused ion and electron beam induced deposition of magnetic structures. In: Russell PE, Utke I, Moshkalev S (eds) Nanofabrication using focused ion and electron beams: principles and applications. Oxford University Press, Oxford
21. Fernández-Pacheco A, Córdoba R, Serrano-Ramón LE, Ibarra MR, De Teresa JM (2013) Direct patterning of cobalt nanostructures using focused electron beam-induced deposition. In: Kobayashi Y, Suzuki H (eds) Cobalt: occurrence, uses and properties. Nova Publishers, New York
22. Fernández-Pacheco A, Córdoba R, Ibarra MR, De Teresa JM (2009) Magnetotransport properties of high-quality cobalt nanowires grown by focused-electron-beam-induced deposition. J Phys D Appl Phys 42:055005
23. Serrano-Ramón LE, Córdoba R, Rodríguez LA, Magen C, Snoeck E, Gatel C, Serrano I, Ibarra MR, De Teresa JM (2011) Ultrasmall functional ferromagnetic nanostructures grown by focused electron-beam-induced deposition. ACS Nano 5:7781
24. Alwood DA, Xiong G, Cooke MD, Cowburn RP (2003) Magneto-optical Kerr effect analysis of magnetic nanostructures. J Phys D Appl Phys 36:2175
25. Henry Y, Ounadjela K, Piraux L, Dubois S, George J-M, Duvail J-L (2001) Magnetic anisotropy and domain patterns in electrodeposited cobalt nanowires. Euro Phys J B 20:35
26. Ke Y, Ong LL, Shih WM, Yin P (2012) Three-dimensional structures self-assembled from DNA bricks. Science 338:1177
27. Schindler M, Nur-E-Kamal A, Ahmed I, Kamal J, Liu HY, Amor N, Ponery AS, Crockett DP, Grafe TH, Chung HY, Weik T, Jones E, Meiners S (2006) Living in three dimensions: 3D nanostructured environments for cell culture and regenerative medicine. Cell Biochem Biophys 45:215
28. Ferry DK (2008) Nanowires in nanoelectronics. Science 319:579
29. Fernández-Pacheco A, De Teresa JM, Córdoba R, Ibarra MR, Petit D, Read DE, O'Brien L, Lewis ER, Zeng HT, Cowburn RP (2009) Domain wall conduit behavior in cobalt nanowires grown by focused electron beam induced deposition. Appl Phys Lett 94:192509
30. Wieser R, Nowak U, Usadel KD (2004) Domain wall mobility in nanowires: transverse versus vortex walls. Phys Rev B 69:064401
31. Yan M, Kakay A, Gliga S, Hertel R (2010) Beating the walker limit with massless domain walls in cylindrical nanowires. Phys Rev Lett 104:057201
32. Fernández-Pacheco A, Serrano-Ramón LE, Michalik JM, Ibarra MR, De Teresa JM, O'Brien L, Petit D, Lee JH, Cowburn RP (2013) Three dimensional magnetic nanowires grown by focused electron-beam induced deposition. Sci Rep 3:1492
33. Gazzadi GC, Frabboni S, Menozzi C (2007) Suspended nanostructures grown by electron beam-induced deposition of Pt and TEOS precursors. Nanotechnology 18:445709
34. Utke I, Hofmann P, Berger R, Scandella L (2002) High-resolution magnetic Co supertips grown by a focused electron beam. Appl Phys Lett 80:4792
35. Utke I, Michler J, Gasser PH, Santschi C, Laub D, Cantoni M, Buffat PA, Jiao C, Hoffmann P (2005) Cross-section investigations of compositions and sub-structures of tips obtained by focused electron beam induced deposition. Adv Eng Mater 7:323–331

36. Qiu ZQ, Bader SD (1999) Surface magneto-optic Kerr effect (SMOKE). J Magn Magn Mater 200:664
37. Hamrle J, Ferre J, Nyvlt M, Visnovsky S (2002) In-depth resolution of the magneto-optical Kerr effect in ferromagnetic multilayers. In-depth resolution of the magneto-optical Kerr effect in ferromagnetic multilayers. Phys Rev B 66:224423
38. Perna P, Rodrigo C, Muñoz M, Prieto JL, Bollero A, Maccariello D, Cuñado JLF, Romera M, Akerman J, Jiménez E, Mikuszeit N, Cros V, Camarero J, Miranda R (2012) Magnetization reversal signatures in the magnetoresistance of magnetic multilayers. Phys Rev B 86:024421
39. Zeng HT, Read DE, Petit D, Jausovec AV, O'Brien L, Lewis ER, Cowburn RP (2009) Combined electrical and magneto-optical measurements of the magnetization reversal process at a domain wall trap. Appl Phys Lett 94:103113
40. Leven B, Dumpich G (2005) Resistance behavior and magnetization reversal analysis of individual Co nanowires. Phys Rev B 71:064411
41. Brands M, Dumpich G (2005) Experimental determination of anisotropy and demagnetizing factors of single Co nanowires by magnetoresistance measurements. J Appl Phys 98:014309
42. Muñoz M, Prieto JL (2011) Suppression of the intrinsic stochastic pinning of domain walls in magnetic nanostripes. Nature. Communications 2:562
43. Hamrle J, Blomeier S, Gaier O, Hillebrands B, Schneider H, Jakob G, Postava K, Felser C (2007) Huge quadratic magneto-optical Kerr effect and magnetization reversal in the Co2FeSi Heusler compound. J Phys D Appl Phys 40:1563
44. Buchmeier M, Schreiber R, Bürgler DE, Schneider CM (2009) Thickness dependence of linear and quadratic magneto-optical Kerr effects in ultrathin Fe(001) films. Phys Rev B 79:064402
45. Langford RM, Wang T-X, Thornton M, Heidelberg A, Sheridan JG, Blau W, Leahy R (2006) Comparison of different methods to contact to nanowires. J Vac Sci Technol B 24:2306
46. Eichfeld CM, Gerstl SSA, Prosa T, Ke Y, Suzanne RJM, Mohney A (2012) Local electrode atom probe analysis of silicon nanowires grown with an aluminum catalyst. Nanotechnology 23:215205
47. Zhang YL, Li J, To S, Zhang Y, Ye X, You L, Sun Y (2012) Automated nanomanipulation for nanodevice construction. Nanotechnology 23:065304
48. Mølhave K, Wich T, Kortschack A, Bøggild P (2006) Pick-and-place nanomanipulation using microfabricated grippers. Nanotechnology 17:2434
49. Cagliani A, Wierzbicki R, Occhipinti L, Petersen DH, Dyvelkov KN, Sukas OS, Herstrøm BG, Booth T, Bøggild P (2010) Manipulation and in situ transmission electron microscope characterization of sub-100 nm nanostructures using a microfabricated nanogripper. J Micromech Microeng 20:035009
50. Hao L, Cox D, See P, Gallop J, Kazakova O (2010) Magnetic nanoparticle detection using nano-SQUID sensors. J Phys D Appl Phys 43:474004
51. Di Michele L, Shelly C, de Marco P, See P, Cox D, Kazakova O (2011) Detection and susceptibility measurements of a single Dynal bead. J Appl Phys 110:063916
52. Bellido E, Domingo N, Ojea-Jiménez I, Ruiz-Molina D (2012) Structuration and integration of magnetic nanoparticles on surfaces and devices. Small 8:1465
53. Romano-Rodríguez A, Hernández-Ramirez F (2007) Dual-beam focused ion beam (FIB): a prototyping tool for micro and nanofabrication. Microelectron Eng 84:789
54. Wernsdorfer W, Doudin B, Mailly D, Hasselbach K, Benoit A, Meier J, Ansermet J-P, Barbara B (1999) Nucleation of magnetization reversal in individual nanosized nickel wires. Phys Rev Lett 77:1873
55. Kläui M, Vaz CAF, Bland JAC, Heyderman LJ, Nolting F, Pavlovska A, Bauer E, Cherifi S, Heun S, Locatelli A (2004) Head-to-head domain-wall phase diagram in mesoscopic ring magnets. Appl Phys Lett 85:5637
56. Shigeto K, Shinjo T, Ono T (1999) Injection of a magnetic domain wall into a submicron magnetic wire. Appl Phys Lett 75:2815

57. Utke I, Bret T, Laub D, Buffat P, Scandella L, Hoffmann P (2004) Thermal effects during focused electron beam induced deposition of nanocomposite magnetic-cobalt-containing tips. Microelectron Eng 73:553
58. Stan G, Ciobanu CV, Parthangal PM, Cook RF (2007) Diameter-dependent radial and tangential elastic moduli of ZnO nanowires. Nano Lett 7:3691
59. Fernández-Pacheco A, De Teresa JM, Córdoba R, Ibarra MR, Petit D, Read DE, O'Brien L, Lewis ER, Zeng HT, Cowburn RP (2009) Magnetization reversal in individual cobalt micro and nanowires grown by focused-electron-beam-induced-deposition. Nanotechnology 20:475704
60. Lewis ER, Petit D, Thevenard L, Jausovec AV, O'Brien L, Read DE, Cowburn RP (2009) Magnetic domain wall pinning by a curved conduit. Appl Phys Lett 95:152505
61. Biziere N, Gatel C, Lassalle-Balier R, Clochard MC, Wegrowe JC, Snoeck E (2013) Imaging the fine structure of a magnetic domain wall in a Ni nanocylinder. Nano Lett 13:2053
62. Fruchart O (2013) 58th Annual magnetism and magnetic materials (MMM) conference, Denver

High Resolution STM Imaging

15

Alexander N. Chaika

Contents

1 Definition of the Topic 562
2 Overview 562
3 Introduction 563
4 Experimental and Instrumental Methodology 564
4.1 Basic Principle and Experimental Realization of STM 564
4.2 Preparation of Tips and Samples for High-Resolution STM Experiments 567
5 Key Research Findings 573
5.1 Atomically Resolved STM Imaging 573
5.2 Role of the Tip Electronic Structure 578
5.3 Distance Dependence of STM Images 582
5.4 Chemical Contrast in STM Experiments 591
5.5 Electron Orbital Resolution in STM Experiments 596
5.6 Conclusions and Future Perspective 609
References 610

Abstract

Scanning tunneling microscopy (STM) is one of the basic techniques for the analysis of surface reconstructions, overlayer growth mechanisms, surface dynamics, and chemistry at the atomic scale. STM is used in physics, chemistry, and biology for high resolution studies of organic and inorganic nanoobjects. This chapter is devoted to STM imaging at the level of individual electron

A.N. Chaika (✉)
Institute of Solid State Physics, Russian Academy of Sciences, Chernogolovka, Moscow District, Russia

Centre for Research on Adaptive Nanostructures and Nanodevices (CRANN), School of Physics, Trinity College Dublin, Dublin, Ireland
e-mail: chaika@issp.ac.ru

© Springer-Verlag Berlin Heidelberg 2015

C.S.S.R. Kumar (ed.), *Surface Science Tools for Nanomaterials Characterization*,
DOI 10.1007/978-3-662-44551-8_15

orbitals which can lead to improvement of the spatial resolution in STM experiments down to the subatomic scale and development of chemical-selective imaging of multi-component surfaces.

Keywords
Scanning tunneling microscopy • Atomic resolution • Electron orbital

1 Definition of the Topic

Scanning tunneling microscopy (STM) is one of the most powerful methods of direct visualization of the surface electronic structure with picometer spatial resolution, chemical- and spin-selective imaging at the atomic scale, manipulations by individual atoms, fabrication of surface structures from atoms and molecules, and investigations of reactions and dynamic processes on surfaces. This chapter is devoted to high-resolution imaging at the level of individual electron orbitals which can lead to improvement of the spatial resolution in STM experiments down to the subatomic scale and development of chemical-selective imaging.

2 Overview

Since its invention at the beginning of the 1980s, scanning tunneling microscopy (STM) has become one of the basic techniques for the analysis of surface reconstructions, overlayer growth mechanisms, surface dynamics, and chemistry at the atomic scale. STM is used in physics, chemistry, and biology for studies of organic and inorganic nanoobjects. However, the limit of the spatial resolution and the mechanisms of the STM image formation are still not completely known. In particular, detailed knowledge of the tip apex structure and control of the relative contribution of different tip and surface electron orbitals are still missing in most STM experiments. The lack of information about the role of different electron orbitals in STM experiments is caused by difficulties in the preparation of probes with well-defined atomic and electronic structure. Furthermore, the electronic structure of tip and surface atoms can be modified by the tip–sample interaction at small tunneling gaps, typical for atomically resolved experiments. This chapter discusses reproducible fabrication of functionalized probes for high-resolution STM imaging, results of experimental and theoretical studies of the relative contribution of different tip and surface electron orbitals, the role of the tunneling parameters in atomically resolved STM imaging of multicomponent surfaces, and selective visualization of certain electron orbitals as well as potential outcomes of this selective orbital imaging capability.

3 Introduction

The invention of scanning probe microscopy (SPM) [1–3] allowed studying the local properties of surface structures with atomic resolution. The SPM methods use sharp (ideally, single-atom terminated) tips for surface imaging [4], fabricating nanostructures from individual atoms and molecules [5–11], studying the vibrational spectra of single molecules [12], identifying the chemical nature of the surface atoms [13, 14], and revealing magnetic contrast on surfaces [15–17]. SPM methods provide unique direct information about the surface structures at the atomic scale without their destruction by a scanning probe.

Scanning tunneling microscopy (STM) is based on quantum tunneling of electrons from atoms at the surface of a sample to the front atom of an STM tip (or vice versa) through the vacuum gap. Due to the strong exponential distance dependence of the electron tunneling probability, most of the current is typically localized on two interacting atoms. This provides unique, atomic-scale spatial resolution of STM. First atomically resolved STM experiments [18, 19] demonstrated the lateral and vertical resolution of the order of 1 nm and 10 pm, respectively. During the last three decades, the vertical and lateral resolution in STM experiments has reached the picometer scale [20–24]. However, the questions related to the limit of the spatial resolution and mechanisms of the STM image formation are still open.

Since the tunneling current usually flows through only several tip and surface atoms, the ultimate resolution of STM can correspond to probing individual electron orbitals of the interacting atoms [22–28]. This can be achieved if the electron orbitals of only one apex atom of a sharp tip collect most of the tunneling current. However, such ultimate, orbital resolution could rarely be reached in experiments because of simultaneous contribution of different electron orbitals of the tip and surface atoms and nonideal geometries of the tips used.

Most serious obstacles for controllable probing individual electron orbitals and getting ultimate resolution in STM experiments are related to the lack of reliable information about the tip atomic structure and possible modifications of the tip and surface atom electronic structure at very small (2.0–5.0 Å) distances between interacting atoms, usually required for STM imaging with atomic resolution. In most studies, the apex structure is unknown and can only be proposed after detailed analysis of the theoretical calculations and experimental results. In this case, researchers cannot define the electronic structure of the front tip atom, responsible for the STM imaging, during the experiments. Although there are several examples of atomically resolved STM imaging with certain tip orbitals [22–27], the control of the orbital structure of the apex atom still has not been reached in general case. In turn, for obtaining information about the modification of the orbital structure of the surface atoms interacting with the tip, extremely high spatial resolution and reliable information about the tip electronic structure are required.

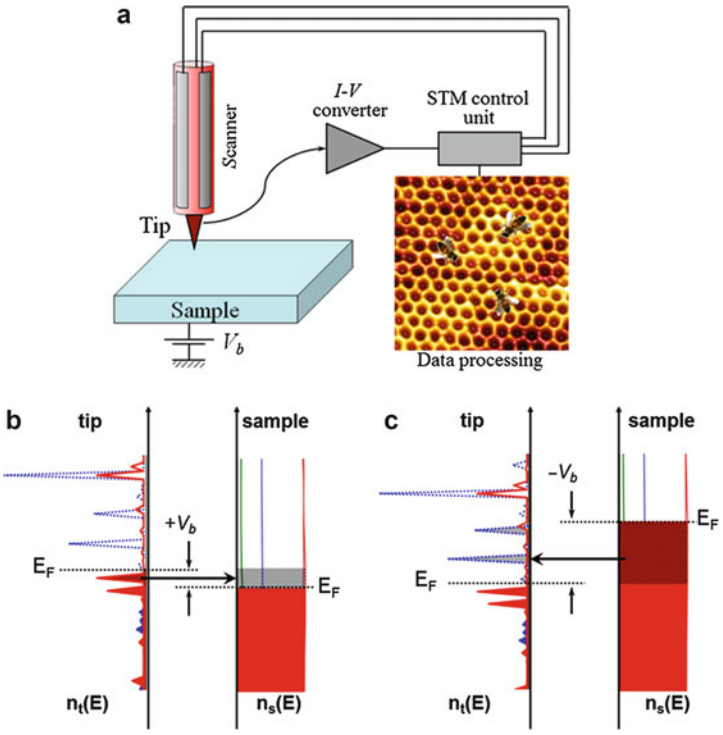


Fig. 15.1 (**a**) Schematic view of an STM unit (**a**) and tunneling of electrons from the occupied tip states to the empty surface states (**b**) and vice versa (**c**)

This chapter is focused on the experimental and theoretical studies aimed at detailed understanding of the role of the tip–sample distance and certain tip and surface electron orbitals in STM experiments and development of high-resolution imaging at the level of individual electron orbitals. The examples of the distance-dependent STM experiments with electron orbital resolution, presented in this chapter, can shed light upon the role of the tip electronic structure and different tunneling parameters in STM experiments and pave the way to controllable probing individual atomic orbitals and surface imaging with the highest, picometer spatial resolution.

4 Experimental and Instrumental Methodology

4.1 Basic Principle and Experimental Realization of STM

Figure 15.1a shows a schematic view of an STM unit: a sharp conducting tip is mounted on a piezodrive, known usually as a scanner, which allows the positioning of the tip along the *x*-, *y*-, and *z*-axes with picometer precision. A conducting sample can be either mounted on a fixed sample holder or on another piezodrive

which allows a coarse approach of the sample to the tip from several millimeters to nanometer-scale distances where the electron tunneling effect can be observed. When a bias voltage V_b is applied to the sample and the gap between tip and sample is of the order of several interatomic distances, electrons can tunnel from the occupied tip electron states to the empty surface states or vice versa, as Fig. 15.1b, c illustrates. The tunneling current is measured using the current–voltage (I–V) converter and can be used as a reference signal in the z-feedback loop controlling the gap between tip and sample.

The tunneling current depends exponentially on the tip–sample distance and can be described by Eq. 15.1:

$$I = G_0 \frac{4\pi^2}{e} \int_0^{eV_b} \rho_t(E_F - eV + \varepsilon)\rho_s(E_F + \varepsilon) \mid M^2 \mid d\varepsilon, \tag{15.1}$$

where $G_0 = 2e^2/h$ is the quantum of conductance, $\rho_t(E)$ and $\rho_s(E)$ are the electron density of states (DOS) of the tip and the surface, respectively, and M is the tunneling matrix element. The tunneling probability depends exponentially on the distance between the electrodes:

$$|M|^2 \sim e^{-kz}, \tag{15.2}$$

$$k = \frac{\sqrt{2m(U-E)}}{\hbar}, \tag{15.3}$$

where k is the inverse decay length of the electron wave functions in the vacuum gap, $\hbar$ is the Plank constant, and m is the mass of electron.

Simple estimations with typical values of the work function in metals and semiconductors show that tunneling current drops approximately by one order of magnitude with every 1-Å increase in the tip–sample separation. This strong distance dependence is the origin of unique high lateral and vertical resolution of STM which can be of the order of 1 pm [21] and even below this value [20], respectively.

A feedback loop usually controls the z-piezodrive to maintain constant tunneling current during scanning across the surface in x- and y-directions. This is the so-called constant current mode (CCM) which is utilized for surface imaging in most STM experiments. The CCM is especially important for surfaces with complicated atomic structure and high density of defects, e.g., stepped surfaces, rippled graphene layers, missing row reconstructions, surfaces with adsorbed atoms and molecules, etc. In the CCM, the tip height z is plotted versus the lateral position ($Z(x,y)$ at $I = \text{const}$). In the constant-height mode (CHM), which is used for some STM experiments on flat surfaces with minimal number of defects (e.g., layered materials and low-index surfaces of metals), a tip is scanned across a surface at nearly constant height while I is measured as a function of the tip lateral position ($I(x,y)$ at $z = \text{const}$). According to Eq. 15.1, images measured in both modes should simultaneously reflect the surface atomic structure and the convolution of the tip

and surface electron local density of states (LDOS) in each point of measurements. In principle, the topographic effects can be eliminated using the scanning tunneling spectroscopy (STS) which is based on measurements of the current–voltage characteristics during scanning. From Eq. 15.1 one can suggest that the surface DOS can be defined from the derivatives of the *I(V)* curves if the tip DOS does not substantially change in the interval between V_b and the Fermi energy (E_F).

It can be assumed from Eq. 15.1 that noise in the tunneling current channel and possible instabilities in the tip–surface distance are two major factors limiting the spatial resolution in STM experiments. The noise in the tunneling current can originate from the *I–V* converter and undesirable signals caused by a proximity of the electric wires connecting the scanner and piezodrives with the control unit. The former origin is usually responsible for very small noise which is well below the values critical for atomically resolved imaging. At the same time, proper wiring of the STM control system is crucial for stabilizing the tunneling current and getting high-resolution images. The mechanical vibrations of the scanner, leading to instability in the tip–surface distance, are usually suppressed by passive or active damping of the whole STM chamber combined with mechanical and magnetic damping of the scanner which can isolate it from possible vibrations of the chamber. Such a multistage damping system usually allows to achieve picometer-scale stability of the tip and sample positions even in room temperature (RT) STMs operated under ultrahigh vacuum (UHV). However, working with RT STM, experimentalists must be very careful in stabilizing the ambient conditions (temperature, sunlight, access to the UHV chamber, etc.) because even minor changes in the scanner temperature can be responsible for large deformations of the piezoscanner along the *x*-, *y*-, and *z*-axes, which are not compatible with atomically resolved experiments.

Stability of the STM scanner, defining the limit of the spatial resolution and reproducibility of the experimental data, can further be increased by cooling the system down to helium temperatures and below. The best contemporary STMs can be operated even at temperatures below 1 K [29] that is crucial for the studies of superconducting properties and temperature-driven phase transitions on surfaces as well as for STS experiments demanding extremely high stability for both the tip and the surface atomic structure which can only be obtained at low temperatures (LTs). Although the picometer lateral resolution can be achieved even using RT UHV STMs [21–24], it is believed that the best resolution, higher reproducibility of the experimental results, and greater control of the tip and surface electronic structure can be obtained using LT UHV STMs.

The spatial resolution can further be improved using special scanning regimes. For example, in the so-called dynamic STM mode [25], the probe tip oscillates at small amplitudes (1.0 Å and below) to reduce the lateral forces acting on the apex atom during scanning because of the presence of the retracting phase. This method increases the tip stability and, therefore, gives exceptional advantages in high-resolution STM experiments demanding very small tunneling gaps [25]. The scanners suitable for dynamic STM studies usually allow combined STM and atomic force microscopy (AFM) studies [30]. In this case, both conducting and insulating surfaces can be studied with atomic resolution.

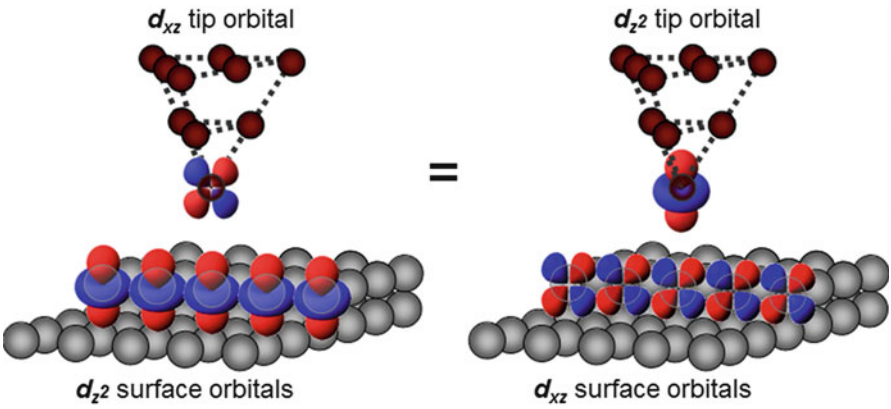


Fig. 15.2 A schematic presentation of the reciprocity principle of STM: imaging of the surface d_{xz} atomic orbitals by the d_z^2 tip orbital is equivalent to imaging of the surface d_z^2 electron orbitals by the tip d_{xz}-orbital

For studies of biological objects, STM should be operated either under ambient conditions or in liquid environment [31, 32]. These conditions, necessary for studying living cells, can limit the spatial resolution and eliminate possibilities to control the tip apex atomic structure and, therefore, will not be considered in this chapter.

According to Eq. 15.1, the tunneling current depends both on the tip and surface electron density of states (DOS). This is the basis of the reciprocity principle of STM introduced by Chen [33]: if the electronic states of the tip and the sample are swapped, the resulting image should be the same. In other words, STM images may be interpreted either as probing the sample electron orbitals by the tip orbitals or as probing the tip orbitals by the sample orbitals. Figure 15.2 shows a situation when electronic structure of the tip and surface atoms is defined just by one particular electron orbital, namely, either d_{xz}- or d_z^2-orbital. In this case, imaging the surface d_{xz}-orbitals by the tip d_z^2-orbital is equivalent to the imaging the surface d_z^2 electron states by the tip d_{xz} state. In most experiments, the tip and surface DOS include contribution from different electron states in the energy range between E_F and V_b. However, even the simplest situations shown in Fig. 15.2 can be realized in STM experiments [26, 34].

4.2 Preparation of Tips and Samples for High-Resolution STM Experiments

The exponential distance dependence of the tunneling current means that in experiments with sharp, geometrically perfect tips, most of the tunneling current flows through the one, front atom of the STM tip. This strong current–distance dependence allows atomically resolved imaging even in experiments, with relatively blunt probes having a nano-tip which collects most of the tunneling current, as

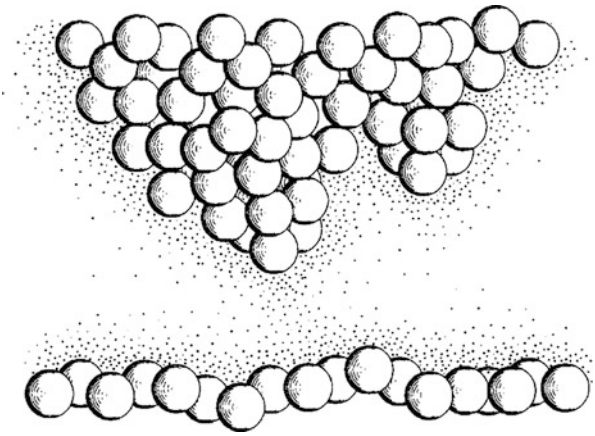


Fig. 15.3 A schematic of STM imaging with a nonideal tip. The tunneling probability decreases exponentially with the tunneling distance, about a factor 10 for 1 Å. For the tip having two apexes separated by two interatomic distances in *z*-direction, this gives approximately one million reduction in the tunneling current flowing through the upper nano-tip. In experiments on highly ordered, flat surfaces, only the lower tip will be responsible for the STM imaging (Reprinted with permission from Ref. [35]. Copyright 1987 by the American Physical Society)

Fig. 15.3 illustrates [35]. However, nonideal shape of the tip apex can be critical for experiments on highly corrugated reconstructions or surfaces with a large number of natural defects which usually demand extremely sharp, single-atom-terminated tips.

Reproducible fabrication of sharp STM tips with stable and well-defined atomic and electronic structure is crucial both for improvement of the spatial resolution and explanation of the atomic-scale contrast in STM and STS experiments. Although even several-atom-terminated tips can produce atomic resolution on metal surfaces [36], the ultimate resolution can be reached only with STM tips collecting most of the tunneling current through the electron orbitals of a single atom closest to the surface. Therefore, reliable preparation of sharp, single-atom-terminated tips is one of the critical issues in high-resolution STM research.

Controllable fabrication of STM probes with well-defined geometry can be achieved only in UHV conditions which are also crucial for preparation of high-quality surface reconstructions. Although defects on surfaces are frequently used to demonstrate the sharpness of the tip, they can impede high-resolution imaging even with relatively sharp tips. Clean and well-ordered surfaces are usually obtained using in-situ cleavage in the STM chamber, high-temperature flashing, or repeated cycles of ion bombardment and annealing. Frequently, preparation of high-quality surfaces suitable for atomically resolved studies continues even longer than the STM experiments.

STM tips are usually fabricated from low-cost polycrystalline noble metal [37, 38] and tungsten [39] wires using electrochemical etching. For specific (superconducting, spin-polarized, etc.) studies, functionalized probes from other materials are fabricated. For example, GaAs [40, 41], InAs [42], Nb [43], MnNi [44], MnPt [45],

Cr [46–49], and magnetic metal-covered tungsten probes [17, 50, 51] were successfully utilized in high-resolution STM/STS experiments. High spatial resolution has been achieved using the *f*-orbitals of an Sm atom at the apex of a Co_6Fe_3Sm tip [25] and *p*-orbitals of the light-element atoms at the apexes of Be [52] and conductive diamond tips [53–57].

In most STM experiments, chemically etched polycrystalline tungsten tips [39] are used because of their low price and high stiffness. For atomically resolved STM experiments, tungsten tips are cleaned and sharpened in situ in UHV using high-temperature annealing [58], electric field restructuring [59–65], coaxial ion milling [66–69], and controllable tip crash using voltage pulses or contact between tip and sample [70, 71]. Sometimes scanning at high tunneling currents and high bias voltages are applied to sharpen STM tips in tunneling regime. The latter method is based on the growth of nanometer-sized needles on tungsten tip apexes at large (~10 V) negative sample bias voltages [64]. The apex quality and spatial resolution in STM experiments are usually higher for the tips cleaned at high electric fields rather than at high tunneling currents, as comparative STM and field ion microscopy (FIM) studies demonstrate [72].

An enhancement of the spatial resolution can be achieved using conducting tips functionalized by carbon nanotubes [73] and molecules consisting on light-element atoms [74–82]. As an example, Fig. 15.4a shows high-resolution images of a pentacene molecule on Au(111) obtained with a tungsten tip in the conventional STM (top) and the so-called scanning tunneling hydrogen microscopy (STHM) modes (bottom) [78]. Submolecular resolution, which could hardly be achieved in the STM mode at $|V_b| > 50$ mV (Fig. 15.4a, top), became feasible in the STHM mode in the presence of the D_2 molecule at the apex (Fig. 15.4a, bottom). The best STHM resolution was achieved in the CHM regime at $|V_b| < 10$ mV. The appearance of the highest resolution STHM imaging after D_2 dosing coincided with the emergence of the inelastic features in dI/dV spectra measured above the pentacene molecule [V_{inel} in Fig. 15.4b]. Imaging could be switched reversibly between the STM and STHM modes by changing the bias voltage in accordance with Fig. 15.4b. Figure 15.4c, d shows different distance dependence of the conductivity measured at different lateral positions of the tip above the pentacene molecule for the bias voltages corresponding to the STM and STHM modes. This is consistent with the visualization of the chemical bonds in the STHM mode (Fig. 15.4a, bottom) and uniform contrast on the pentacene molecule obtained in the conventional STM mode (Fig. 15.4a, top). The $G_{D2}(z)$ and $R_G(z)$ dependences (Figs. 15.4c, d) and STHM images measured at different gap resistances (Fig. 15.4e) show that enhanced spatial resolution in the STHM mode can be achieved at small tunneling gaps where the $G_{D2}(z)$ dependence is nonexponential and the $R_G(z)$ is close to its local minimum.

Although the lateral resolution at the level of intramolecular chemical bonds has been reached in STM experiments using molecule-terminated probes [78, 79], the applied tip treatments are hardly capable of producing stable apexes with well-defined structure. For example, the tungsten tip in STHM mode became unstable and produced substantial noise at small tunneling gaps (Fig. 15.4e).

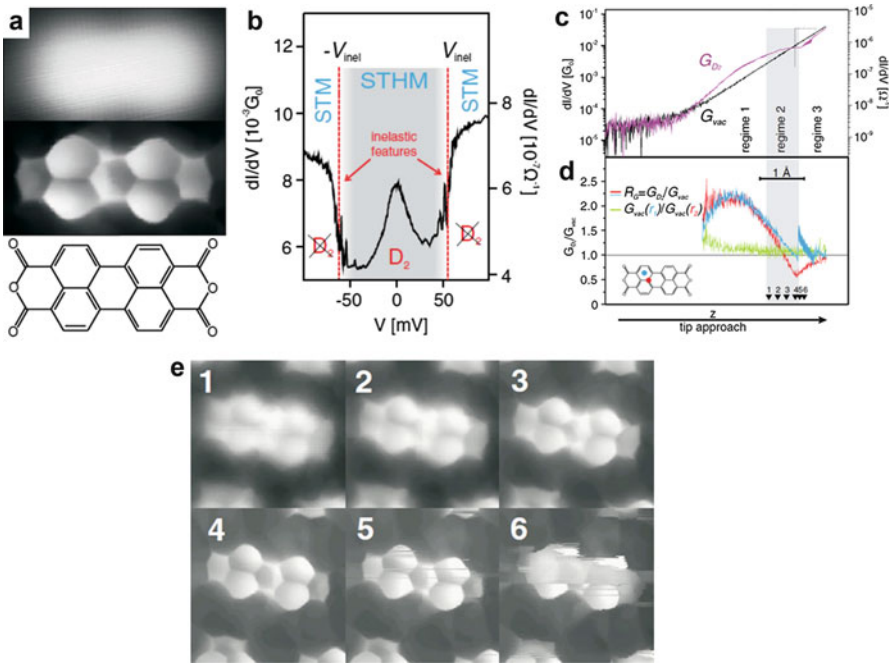


Fig. 15.4 (**a**) STM (*top*) and STHM image (*bottom*) of PTCDA (3,4,9,10-perylenetetracarboxylic-dianhydride) on Au(111): 1.3×0.7 nm^2, constant height, D_2, $V_b = 316$ mV (STM) and $V_b = 5$ mV (STHM). The chemical structure of PTCDA is shown for comparison. (**b**) *dI/dV* spectrum measured in the center of PTCDA/Au(111), recorded with lockin detection (10 mV modulation, frequency 2.3 kHz). $G_0 = 2e^2/h = (12.9\ \text{kOhm})^{-1}$. (**c**) $dI/dV(z)$ spectra recorded at fixed bias, measured with D_2 on PTCDA/Au(111) (z-axis scale given by scale bar). G_{D2} (*magenta*): $V_b = -5$ mV. G_{vac} (*black*): $V_b = -130$ mV. (**d**) $R_G(z)$ curves measured at positions r_1 (*blue*) and r_2 (*red*) marked in the lower *inset*. The ratio $G_{vac}(r_1)/G_{vac}(r_2)$ is shown in *green*. (**e**) STHM images (1.3×1.3 nm^2, CHM, $V_b = -5$ mV) of PTCDA/Au(111) measured with D_2 at different z indicated by *black triangles* in panel (**d**) (Reprinted with permission from Ref. [78]. Copyright 2010 by the American Physical Society)

Besides, STM images measured with the molecule-terminated tips can strongly depend on the precise orientation of the molecule at the apex and the bias voltage [83–85] that can complicate the interpretation of the atomically resolved STM and STS data.

The in situ tip characterization using FIM, field electron emission microscopy (FEEM), or scanning electron microscopy (SEM) may represent one of the ways to control the atomic structure of the tip utilized in high-resolution STM studies, but these combinations can hardly be considered as a routine experimental practice because of difficulties with their technical realization. Therefore, development of reliable procedures for fabrication of well-defined apexes and their refurbishment in the UHV chamber are very important for the STM studies with ultimate, picoscale spatial resolution.

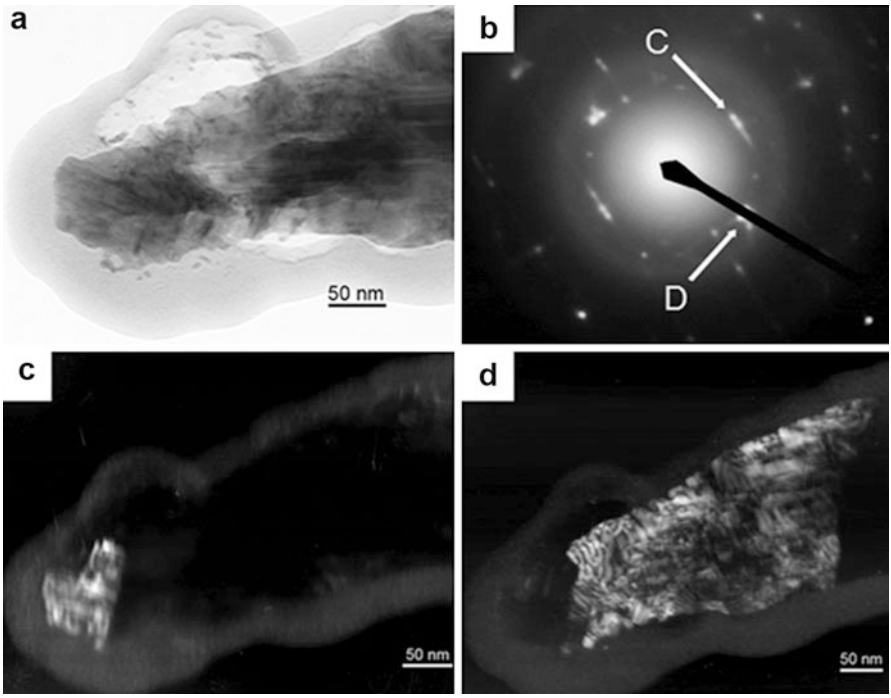


Fig. 15.5 Images of the W[001] tip apex after electron beam heating at 1,000 °C and coaxial ion sputtering with a 600-eV Ar^+ ion beam. (**a**) Bright-field TEM image and (**b**) electron diffraction pattern taken from the apex. (**c** and **d**) Dark-field TEM images of the apex taken with the C and D diffraction spots on panel (**b**) (Reproduced with permission from Ref. [24])

Although it was demonstrated that tungsten tips fabricated from cold-drawn polycrystalline wires are preferentially oriented along the [011] crystallographic direction [66], the precise orientation of the apex and its atomic structure cannot be defined in STM experiments with polycrystalline tips. A better control of the tip structure can be achieved in STM experiments with single crystalline tips. It is known that chemically etched refractory metal single crystalline tips can produce single asperity at the apex [59, 67, 68, 86] instead of multi-tips frequently obtained with polycrystalline wires [66]. Figure 15.5 shows transmission electron microscopy (TEM) images of a typical [001]-oriented tungsten tip apex obtained using chemical etching and sharpening in the UHV STM chamber [24]. The tip was fabricated from a [001]-oriented rectangular single crystalline tungsten ingot ($0.5 \times 0.5 \times 10$ mm^3) by electrochemical etching in 2 M NaOH with controllable cutoff adjusted by the current jump. The use of the derivative of the etching current instead of its cutoff value allowed switching off the voltage between the electrodes with minimal delay reducing the radius of curvature at the apex. The length of the ingot immersed into the etchant was in the range of 2.5–3 mm while the voltage applied between two electrodes was in the range of 4.0–4.5 V. These values correspond to the optimal parameters for fabrication of tungsten tips with minimal radius of

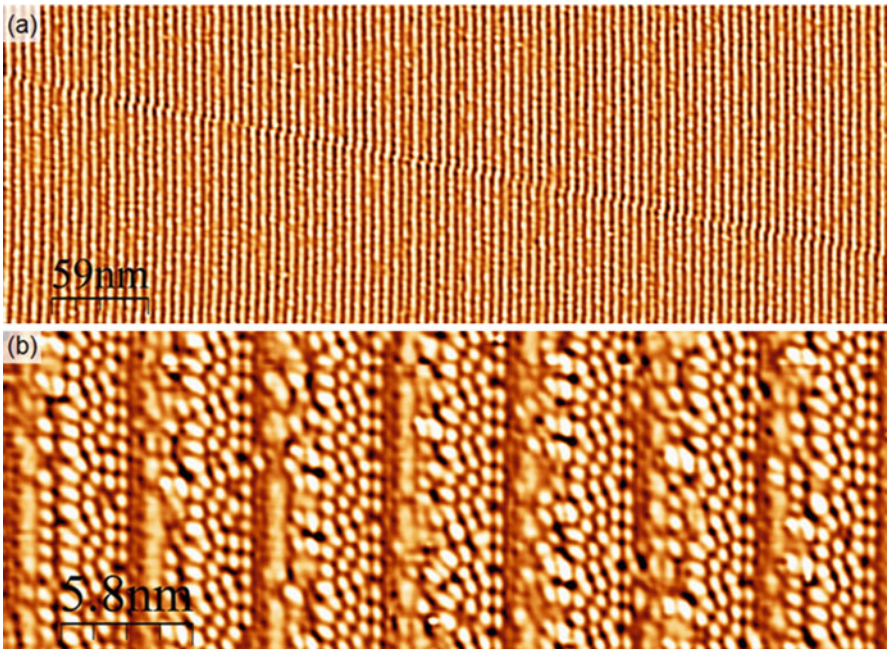


Fig. 15.6 Large area (**a**) and atomically resolved (**b**) STM images of the regular Si(557)7 × 7 step array. To enhance the contrast on steps, the Laplacian filtering using the WSxM software [186] was applied to the image in panel (**b**)

curvature [39]. Prior to electron microscopy characterization and UHV treatments, the etched tip was cleaned in hot distilled water to remove major apex contaminations after the chemical etching. Other cleaning procedures like ultrasonic rinsing in ethanol, isopropanol, or acetone were avoided since they could lead to breaking the tip apex [87]. According to SEM characterization, about 90 % of the tips etched using the above described procedure possessed the apex with radius of curvature below 20 nm. Further sharpening of the tungsten tip apex was achieved using electron beam flash heating and coaxial ion sputtering. The bright-field TEM image in Fig. 15.5a shows the pyramid at the W[001] tip apex formed after UHV sharpening. Electron diffraction pattern taken from the apex (Fig. 15.5b) exhibits characteristic diffraction reflexes, which correspond to the {011} and {001} crystallographic planes forming the apex pyramid [24]. This is further illustrated by the dark-field TEM images taken from two different diffraction spots [marked by C and D in Fig. 15.5b], which allow to achieve better contrast in different regions of the tip. The dark-field image in Fig. 15.5c reveals that the angle at the tip apex is close to 90° that corresponds to the [001]-oriented tungsten apex grained by the {011} planes. Double-spot reflexes (C and D) in Fig. 15.5b indicate the presence of slightly misoriented single crystalline blocks at the apex. This misorientation is presumably caused by the stress applied to the apex at the final stage of the chemical etching and does not exceed several degrees. As a result, even tip orbital

contribution can be controlled in precise distance-dependent STM experiments with such well-defined single crystalline tips [22–24]. An example of high-resolution imaging of a stepped Si(557) surface [88–91] using a single crystalline W[001] tip is shown in Fig. 15.6. The atomic resolution (Fig. 15.6b), reproducibly obtained both on (7 × 7)-reconstructed terraces and steps of the atomically precise triple step array fabricated on an Si(557) surface (Fig. 15.6a), proves extreme sharpness and stability of the W[001] tip used in these experiments. Despite their high cost, the oriented single crystalline tips can be utilized in high-resolution STM experiments demanding picoscale resolution [21] and detailed knowledge of the apex electronic structure.

5 Key Research Findings

5.1 Atomically Resolved STM Imaging

First atomically resolved STM experiments on semiconducting [18] and metallic [19] surfaces have been carried out more than three decades ago. Since then, numerous high-resolution STM studies have been reported. In this section only some representative examples of atomically resolved STM imaging on different samples will be mentioned.

5.1.1 Semiconductors

Atomic resolution in STM experiments on semiconductors was demonstrated for the first time in 1983 [18]. The real space atomically resolved images of the Si(111)7 × 7 reconstruction [18] proved the dimer-adatom-stacking fault (DAS) model [92] shown in Fig. 15.7a, b. The topmost layer of the Si(111)7 × 7 unit cell contains 12 adatoms having p_z dangling bonds. These dangling bonds can usually be visualized in atomically resolved STM experiments (Fig. 15.7c). Six atoms in the second layer (rest atoms), not bound with adatoms, have also dangling bonds which can be resolved only at certain bias voltages using extremely sharp single-atom-terminated tips [93]. An example of the STM image revealing both the adatom and the rest-atom p_z electron states is shown in Fig. 15.7d. Furthermore, the bias voltage-dependent STM and STS experiments [94–96] demonstrated selective visualization of the backbond electron states, rest-atoms' dangling bonds, and even the corner hole p_z states associated with the silicon atoms located in the third layer. As an example, Fig. 15.8 shows spectroscopic images of the Si(111)7 × 7 surface taken at different bias voltages [97]. This example illustrates the role of the bias voltage in STM experiments on semiconducting surfaces. Here, the bias voltage controls the direct visualization of the occupied/empty surface electron states associated with nonequivalent surface atoms.

Figure 15.9 shows an example of the atomic resolution studies of the Si(001) surface [98]. The topmost surface layer of the Si(001)-c(4 × 2) reconstruction contains buckled dimer atoms having one dangling bond [99, 100], as Fig. 15.9i illustrates. As can be seen from Fig. 15.9a–h, either the z-directed orbitals of the

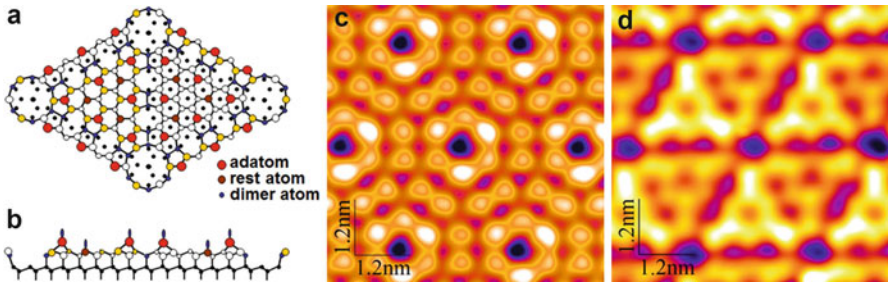


Fig. 15.7 (**a**, **b**) Top (**a**) and side (**b**) view of the DAS model [92]. (**c**, **d**) Empty (**c**) and occupied (d) state CCM STM images of the Si(111)7 × 7 surface. The images were measured with tungsten tips at $V_b = 1$ V and $I = 80$ pA (**c**) and $V_b = -1.4$ V and $I = 50$ pA (**d**)

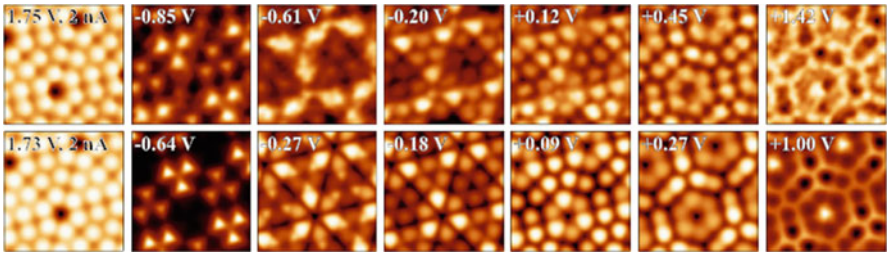


Fig. 15.8 Experimental current-imaging-tunneling spectroscopy maps of the Si(111)7 × 7 surface (*top pictures*) and simulations using a silicon tip (*bottom pictures*). The left panels show CCM STM images at $I = 2$ nA and $V_b = 1.75$ V. The remaining images represent *dI*/*dV maps* as a function of V_b (Reprinted with permission from Ref. [97]. Copyright 2005 by the American Physical Society)

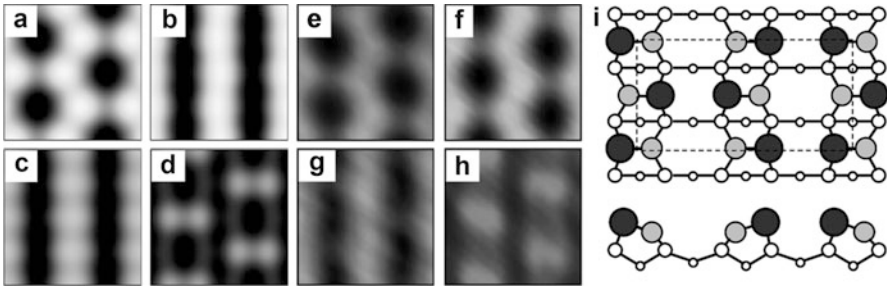


Fig. 15.9 (**a**–**d**) Simulated STM images of the Si(001)–*c*(4 × 2) reconstruction at $V_b = -1.0$ V (**a**), $V_b = 0.7$ V (**b**), $V_b = 1.6$ V (**c**), and $V_b = 2.1$ V (**d**). (**e**–**h**) Experimental STM images measured at $V_b = -1.5$ V (**e**), $V_b = 0.7$ V (**f**), $V_b = 0.7$ V (**g**), and $V_b = 1.5$ V (**h**). (**i**) A schematic model of the Si(001)-c(4 × 2) surface (Reprinted with permission from Ref. [98]. Copyright 2005 by the American Physical Society)

topmost dimer atoms or in-plane aligned bonds can be resolved in STM images at specific tunneling conditions. This example shows that qualitatively the same images can be resolved at different bias voltages (Fig. 15.9e, f). At the same time, the images in Fig. 15.9f, g demonstrate that different patterns can be resolved on the same Si(001) surface reconstruction at fixed bias voltage. Selective visualization of the electron orbitals of the Si(001)-c(4 × 2) reconstruction, presumably, can be controlled by the bias voltage as well as by the combination of the voltage and current defining the tunneling gap at certain tip state.

Atomic resolution was achieved in numerous STM and STS experiments on semiconductors, and even subatomic features were reported in several bias- and distance-dependent studies [28, 101, 102]. In general, atomic resolution can easier be obtained on semiconductors than on metals. A choice of the bias voltage frequently allows selective imaging of certain electronic features which produce regular atomically resolved patterns. Furthermore, STM imaging of semiconducting samples can be slightly simplified because the surface atomic orbitals are further protruded into vacuum region comparing to *d*-orbitals of metal surfaces. The atomic corrugations on semiconductors are usually of the order of 10 pm and above which exceed typical values obtained on metallic surfaces.

5.1.2 Metals

First atomic resolution in STM experiments on metals was achieved at the beginning of 1980s on the reconstructed Au(110) surface [19]. The lateral resolution in these studies was on the order of several Ångströms. Shortly afterward, atomic resolution was obtained on close-packed metal surfaces [62, 103, 104]. Although the origins of the high lateral resolution and large atomic corrugations in the experiments on metals were not clear, STM rapidly showed its ability to resolve the electronic structure of various atomic reconstructions on metallic surfaces. As an example, Fig. 15.10a shows a high-resolution STM image of a Cu(001) surface, while Fig. 15.10b presents the atomic corrugations observed in the experiments as a function of the conductivity of the tunneling junction [105]. These studies show that corrugations in different experiments on the same surface can systematically vary in the ranges of 2–6 pm and 8–20 pm depending on the tip structure [105]. This was ascribed to two different types of tips with different atomic structures. Notably, the image corrugations fall off at small gap resistances (high tunneling conductivity in Fig. 15.10b). This was explained by the tip–surface interaction decreasing the atomic corrugations at very small tip–sample distances. This result can generally be valid for STM experiments on other metallic surfaces. The atomic resolution on metals is usually achieved at small bias voltages and small tip–sample separations where atomic relaxations can modify the observed contrast. The typical atomic corrugations on metals are of the order of several picometers even at small tunneling gaps characterized by strong tip–sample interaction.

5.1.3 Insulators

In accordance with the basic principle, STM is usually considered as a tool for direct imaging of metallic and semiconducting surfaces. Nevertheless, application of nonconventional modes [106] or measurements at elevated temperatures [107]

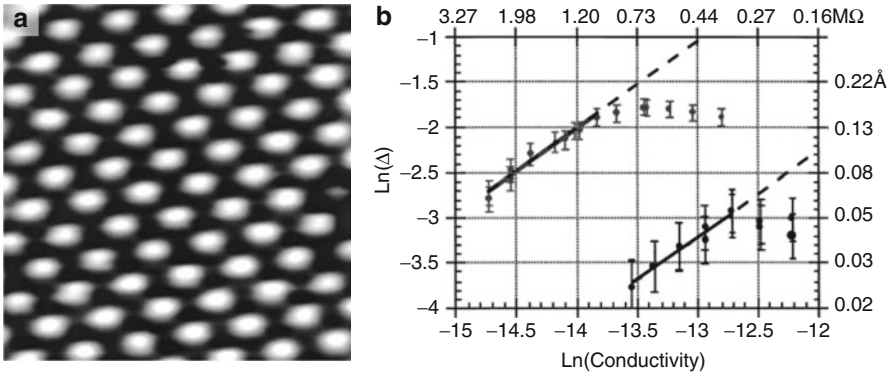


Fig. 15.10 (**a**) A 23 × 23 Å^2 image of a Cu(001) surface taken at $V_b = 28$ mV and $I = 12.5$ nA. (**b**) Ln(Δ) versus ln(*s*) plots illustrating the two general types of tips obtained in this work. Bias voltage: 3 mV for upper and 4 mV for lower plot (Reprinted with permission from Ref. [105]. Copyright 1996 by the American Physical Society)

allow atomically resolved imaging of single crystalline surfaces even on insulators. High-resolution STM imaging is also feasible on insulating thin films deposited on metallic substrates [75, 108–113].

Figure 15.11a demonstrates an example of high-resolution STM imaging achieved on the diamond surface in a resonant electron injection mode [106]. The atomically resolved STM image of the clean diamond C(100)2 × 1 surface (Fig. 15.11a) was recorded at very high sample bias voltage ($V_b = 5.9$ V). In this image, the terraces, rotated by 90° with respect to one another, are clearly visible. The periodic structure of bright and dark lines is observed on every terrace. The periodicity of 0.5 nm (Fig. 15.11b) agrees well with the distance between the carbon dimer rows of the (2 × 1)-reconstructed diamond surface (Fig. 15.11c). The bright lines, joining at the step edges in the STM image shown in Fig. 15.11a, represent the interdimer row valleys, whereas the dark lines correspond to the dimer rows of the (2 × 1)-reconstructed diamond surface.

Atomically resolved STM images of the CoO(001) and NiO(001) surfaces obtained at 200 °C (Fig. 15.11d) show one order of magnitude difference in the atomic corrugations for these two surfaces [107]. According to the electronic structure calculations [107], the lowest unoccupied states of the CoO(001) and NiO(001) surfaces have predominantly d_{xy} and d_z^2 character, respectively. The difference in the symmetry of the unoccupied *d*-orbitals on the CoO(001) and NiO(001) surfaces is responsible for the much lower corrugations observed in the STM images of cobalt oxide.

5.1.4 Molecules

Molecular ensembles on metallic and semiconducting surfaces have been studied extensively because of possible applications in organic-based micro- and nanoelectronics [114–126]. STM studies with high spatial resolution are basically

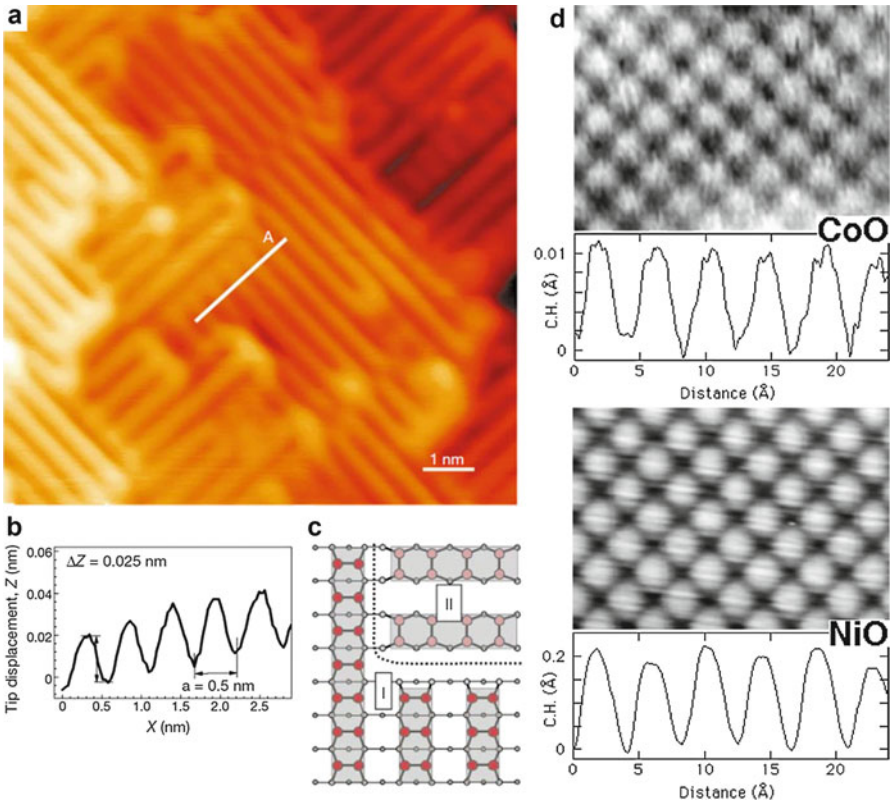


Fig. 15.11 (**a**) The STM topography (10×10 nm^2) of the clean diamond C(100)2 × 1 surface recorded in the near-field emission regime ($V_b = 5.9$ V, $I = 1.1$ nA). (**b**) Cross section along the line A. (**c**) Top view of a monoatomic step on the two-domain (2 × 1)-reconstructed surface. The *colored circles* represent the carbon atoms belonging to the top four surface layers; the *biggest circles* represent the dimers. The domains labeled as I and II represent the upper and lower terrace, respectively. The dimer rows are highlighted by *shading*. The *dashed line* shows the boundary between the domains (Reprinted with permission from Ref. [106]. Copyright 2001 by Macmillan Publishers Ltd). (**d**) Empty states CHM STM image of CoO(001) (V_b =2.7 V, $I = 0.57$ nA) and CCM STM images of NiO(001) ($V_b = 1.3$ V, $I = 1.0$ nA). Corrugation heights (*CH*) are shown as *horizontal line* scans taken through the centers of the corresponding images. The corrugations for the CoO image were calculated from the current variations across the image. Image widths are 24 Å (Reprinted with permission from Ref. [107]. Copyright 1999 by the American Physical Society)

required to understand the dynamic of molecules on surfaces and their bonding with substrates and details of the electronic structure. However, the intramolecular electronic structure at the level of individual atomic orbitals is frequently not resolved in STM experiments. It has been supposed [127] that usual transition metal tips having *d* electron states at the apex are not suitable for submolecular resolution which can only be achieved using functionalized STM probes terminated by an atom of light element [75–82]. STM images of the pentacene molecule shown in Fig. 15.4

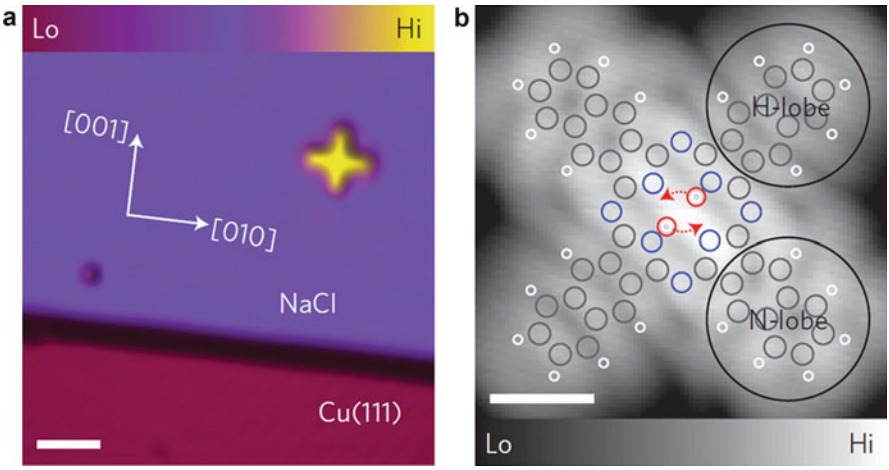


Fig. 15.12 STM imaging of naphthalocyanine molecule on NaCl/Cu(111). (**a**) CCM STM image ($I = 2$ pA, $V_b = 0.25$ V) recorded at the edge of a 2 ML NaCl island on Cu(111). A naphthalocyanine molecule (*yellow*) and a CO molecule (depression near the step edge) can be identified. (**b**) CCM STM image of a naphthalocyanine molecule ($I = 2$ pA, $V_b = 0.6$ V) measured using a CO-terminated tip. The positions of atoms in the molecule are illustrated (Reprinted with permission from Ref. [82]. Copyright 2012 by Macmillan Publishers Ltd)

demonstrate an enhancement of spatial resolution in STM experiments with a metallic probe functionalized by a D_2 molecule. Another example of high-resolution STM imaging of molecular structures is shown in Fig. 15.12 presenting the submolecular contrast in STM images of naphthalocyanine molecule on NaCl/Cu (111) measured using a CO-terminated tip having *p*-orbitals at the apex [82]. It has been demonstrated [78, 79] that tip–sample distance can be one of the crucial factors that define the spatial resolution in STM experiments on molecular structures even with light-element-terminated probes. The resolution can be enhanced significantly at extremely small tunneling gaps when short-range forces dominate in the tip–sample interaction. Therefore, the possibility to fabricate sharp and stable apexes terminated by light-element atoms is crucial for STM imaging of molecular orbitals with ultimate spatial resolution.

5.2 Role of the Tip Electronic Structure

5.2.1 Spatial Resolution with $m = 0$ Tip States

One of the first theoretical explanations of atomic contrast in STM experiments was given by Tersoff and Hamann who considered a spherically symmetric *s*-wave STM tip [128, 129]. In this case the simulated STM images should coincide with the surface DOS maps calculated in the energy range between the bias voltage and E_F. This theory provides a good agreement between the simulated and experimental images for numerous atomically resolved STM studies. However, it cannot explain

high lateral resolution in STM experiments on metal surfaces. The ultimate lateral resolution R within the Tersoff and Hamann approach [128] is given by Eq. 15.4:

$$R = \sqrt{d \cdot 2k^{-1}}, \tag{15.4}$$

where d is the distance between the interacting tip and surface atoms and $k^{-1} \approx 1$ Å.

According to Eq. 15.4, the limit of the lateral resolution for the tip–sample distance of 4.5 Å should be about 3 Å. In contrast, lateral resolution achieved even in first atomically resolved STM experiments on metals [103, 104] was below this value. Equation 15.4 predicts an enhancement of the spatial resolution with decreasing tip–sample distance but cannot explain the experimentally observed lateral resolution below 1 Å [21–24] even at the tunneling gaps in the range of 2.0–2.5 Å. The theory cannot also explain large atomic corrugations observed in STM experiments on metal surfaces [62, 103, 104]. These can be explained either by the tip and surface atom relaxations [130] or by decisive contribution of higher momentum electron states with different momentum projections [131–135]. For example, calculations of Tersoff and Lang performed for different tip atoms (Mo, Na, Ca, Si, C) on a helium surface demonstrate that atomic corrugations on the same surface can vary from 10 to 100 pm depending on the relative contribution of the electron states with different l and m [131].

In the theoretical works of C. J. Chen [132, 133], it was suggested that d_z^2 and p_z tip electron states are responsible for atomic resolution and large corrugations on metallic surfaces. According to the derivative rule [132], the tunneling matrix elements for these states are proportional to the z derivative of the surface atom wave function at the center of the tip apex atom. Therefore, for the $m = 0$ tip electron states, the simulated STM image should correspond to the surface electron density distribution. This assumes that best candidates for STM tips can be d-band metals possessing d_z^2 states at the apex atom and semiconductors with p_z dangling bonds [71]. Taking into account the reciprocity principle (Fig. 15.2), this conclusion agrees with the results obtained on the NiO(001) and CoO(001) surfaces [107] demonstrating higher corrugations for NiO(001) having unoccupied d_z^2 surface states (Fig. 15.11d).

5.2.2 STM Imaging with m ≠ 0 Tip States

In a metallic tip, the electronic structure of the apex is usually defined by a set of electron orbitals with different l and m. The effects related to the presence of the $m \neq 0$ tip states at the apex atom have theoretically been studied by C. J. Chen and W. Sacks [132–135]. The theories predict at least one order of magnitude increase in atomic corrugations and multiple atomic protrusions at small tunneling gaps for the tips with $m \neq 0$ orbitals at the apex (namely, $d_{xz,yz}$ and d_{xy,x^2-y^2}). As an example, Fig. 15.13b shows the LDOS of the surface in proximity to the tips with different orbital structure of the apex atom calculated by W. Sacks [135]. The contours corresponding to the same gap resistance illustrate that $m \neq 0$ electron states (d_{xz}, d_{yz}, d_{xy}, and $d_{x^2-y^2}$) can produce two- and fourfold split subatomic features above the atom positions at very small tunneling gaps and yield enhanced atomic corrugations in comparison with those produced by s and d_z^2 tip orbitals (Fig. 15.13b).

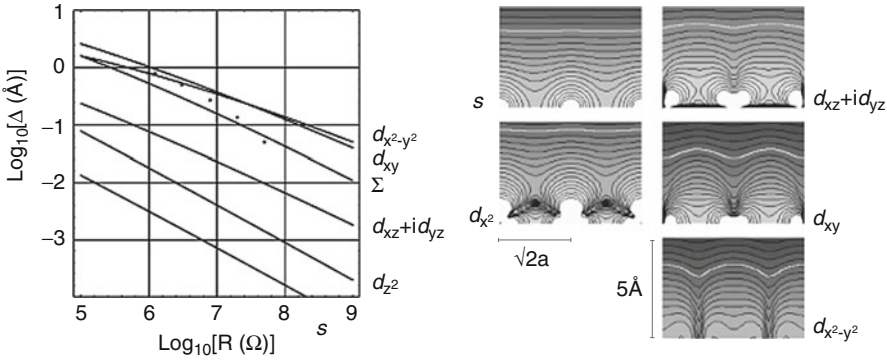


Fig. 15.13 (**a**) Magnitude of the corrugation for *s*- and *d*-orbital tips as a function of the tunneling gap resistance *R*. The corrugation is slightly larger for the $d_x{}^2$-orbital and further enhanced for the orbitals of higher *m*. The curve Σ corresponds to the superposition of only 2 % $d_x{}^2$ with the $d_x{}^2{}_{-y}{}^2$-orbital. (**b**) Gray level representation of the surface LDOS in the plane normal to the surface for the five different tip orbitals. The contours in white correspond to the same value of the gap resistance, $R = 10^5\Omega$ (Reprinted with permission from Ref. [135]. Copyright 2000 by the American Physical Society)

The dependences of the corrugations on the tunneling gap resistance calculated for different electron orbitals [135] demonstrate that $d_z{}^2$- and $m \neq 0$ *d*-orbitals can produce enhanced corrugations in comparison to the *s* state (Fig. 15.13a). Furthermore, the corrugations can increase with decreasing gap resistance. Figure 15.13a shows also more than one and two orders of magnitude enhancement of the corrugations for the $d_{xz,yz}$ and $d_{xy,x}{}^2{}_{-y}{}^2$ tip states, respectively. However, this result may be not fully supported by all existing experimental data (e.g., Fig. 15.11d).

5.2.3 Electronic Structure of Realistic Tips at Small Tunneling Gaps

Although the theories of C. J. Chen and W. Sacks consider simplified models of STM tips with particular electron orbitals at the apex [132–135], they can provide a correlation between experimental and theoretical images in some specific cases. However, they do not take into account the realistic electronic structure of metal tips and its possible changes because of tip–sample interaction at small tunneling gaps. It has been demonstrated in recent theoretical studies [136–139] that electronic structure of the transition metal tips and relative weights of different *d*-orbitals in the tip DOS near E_F are strongly dependent on the tip element, tip cluster size, and local environment around the tip. In particular, it has been shown that $d_z{}^2$-orbital is more sensitive to the local environment and the tip cluster size than $m \neq 0$ *d*-orbitals (d_{xz}, d_{yz}, d_{xy}, and $d_x{}^2{}_{-y}{}^2$) [138]. The theoretical calculations prove that electronic structure of different transition metal tips can non-equally depend on the tip–surface distance [138, 139], indicating that determination of the best tip–surface combination can be crucial for reaching highest spatial resolution on particular surfaces.

The necessity to consider modification of the tip electronic structure by the tip–sample interaction has been exemplified in Ref. [139]. Stimulated by the AFM

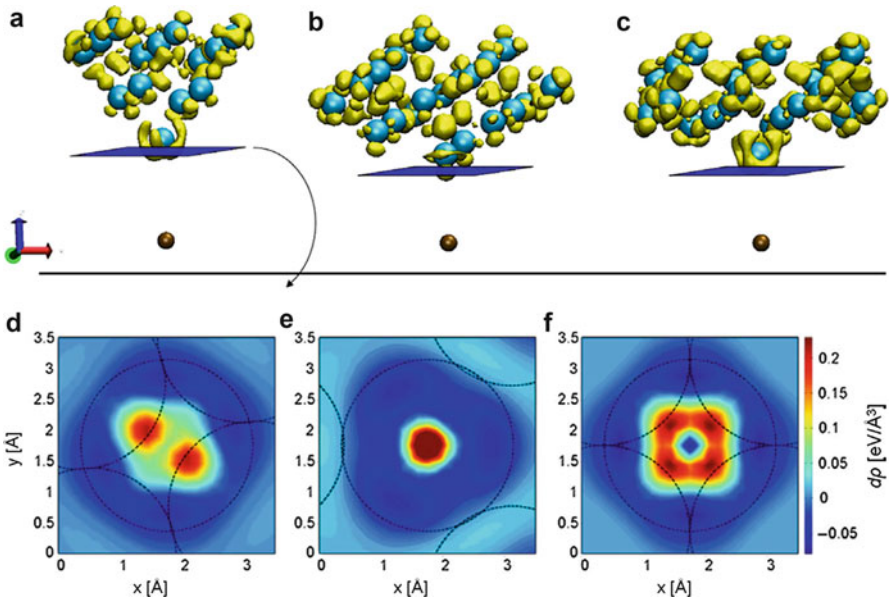


Fig. 15.14 (**a**–**c**) The dρ = 0.08 eV/Å^3 isosurface of the change in electron density for the (**a**) He–W[011], (**b**) He–W[111], and (**c**) He–W[001] systems. The helium atom is positioned directly below the front atom of the tip, with the tip–sample distance of 4.0 Å for the W[011] tip and 3.5 Å for the W[111] and W[001] tips. (**d**)–(**f**) Constant-height slices through the density corresponding to the systems above. The relative sizes and positions of the first two layers of the tips' tungsten atoms are drawn as *black circles* (Reprinted with permission from Ref. [139]. Copyright 2013 by IOP Publishing)

studies revealing subatomic features in high-resolution images of a graphite surface [140], Wright and Solares calculated the electronic structure of tungsten tips with different crystallographic orientations in proximity to different surface clusters [139, 141, 142]. The results showed that image symmetry in the SPM experiments with subatomic, orbital resolution [22–24, 140] can be related to the tip symmetry, but the explanation is not so straightforward as it was originally anticipated [140]. According to the calculations, the appearance of the subatomic features is related to the tip–sample interaction, and the effect can be suppressed with larger or more reactive sample atoms. Notably, the stability of the tungsten tips interacting with the surface clusters was found to be dependent on the crystallographic orientation. In particular, W[001] tip was found to be stable down to a tip–sample distance of 1.50 Å, while [011]- and [111]-oriented tungsten tips were found to be stable at gaps down to 2.25 Å and 2.50 Å, respectively. This result independently proves the feasibility of the orbital resolution STM [22–24] and AFM [140] experiments with tungsten tips demanding the tunneling gaps below 2.5 Å. Figure 15.14a–c shows the isosurfaces of the change in the electron density calculated for the [011]-, [111]-, and [001]-oriented tungsten tips interacting with the helium atom located directly below the front atom of the tips [139]. Figure 15.14d–f illustrates that increased density (dark red) is seen

between the front atom of the W[011] and W[001] tips and the atoms in the second tip layer to which it is bonded. These areas of increased density reveal the two- and fourfold symmetry representative of each tip's crystallographic orientation. However, for the W[111] tip, the areas of increased density do not reveal the threefold symmetry that one would expect [140]. These results suggest that the highest spatial resolution can be achieved in STM experiments using W[111] tips which have symmetrical charge density distribution along the tip axis even at relatively small distances from the surface cluster. At the same time, W[001] tips can produce unusual asymmetric features on a subatomic scale at small tip–sample distances [22–24] but can be more suitable for STS experiments demanding higher tip stability.

5.3 Distance Dependence of STM Images

Atomic resolution in STM experiments is usually achieved at very small tunneling gaps comparable with interatomic distances in solids. At these distances, the interaction between tip and surface atoms can change the tunneling barrier height [143], induce tip and surface atom relaxations [62, 130, 144], and modify their electronic structure [22, 23, 137–139, 145–147]. The interaction can change the orbital structure of the tip and surface atoms and, consequently, the symmetry of the high-resolution STM images. These effects can strongly depend on the distance between interacting tip and surface atoms. One of the first distance dependences of atomically resolved STM images was measured on the gold-sputtered graphite surface [148]. Afterward, the gap resistance dependence of atomically resolved STM images has been studied both theoretically and experimentally in a number of works [22, 23, 27, 28, 36, 130, 149–157]. However, because of complexity of the theoretical calculations for realistic tip–surface systems and experimental studies with precise control of the tunneling gap and the tip state, there is still no detailed knowledge about the role of the tip–sample distance in high-resolution STM experiments.

5.3.1 Enhancement of Lateral Resolution with Decreasing Tunneling Gap

According to the theory [128, 135], an enhancement of the lateral resolution and atomic corrugations should be anticipated with decreasing tip–sample separation. Therefore, small tip–sample separations are crucial for high-resolution STM imaging. It has been demonstrated that extremely sharp atomic features reproducing the atomic orbital distribution maps can be resolved with clean [22, 23] and molecule-terminated [78, 79] tungsten tips at distances below 4 Å. An example of improvement of the spatial resolution with decreasing distance in STM experiments on molecules is shown in Fig. 15.4e [78]. Figure 15.15 demonstrates an enhancement of the atomic contrast with decreasing gap resistance in the experiments on a highly oriented pyrolytic graphite (HOPG) surface using a W[001] tip [22, 23]. The atomic features become sharper with increasing tunneling current (decreasing tip–sample distance). At $I = 3.9$ nA the full diameter of the atomic features at half height is

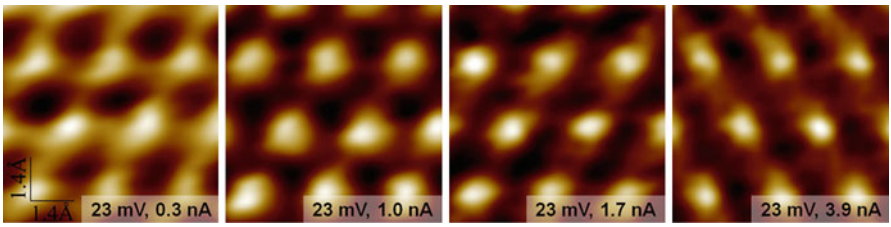


Fig. 15.15 Gap resistance dependence of HOPG(0001) STM images measured using a [001]-oriented tungsten tip. The tunneling parameters are indicated on each frame

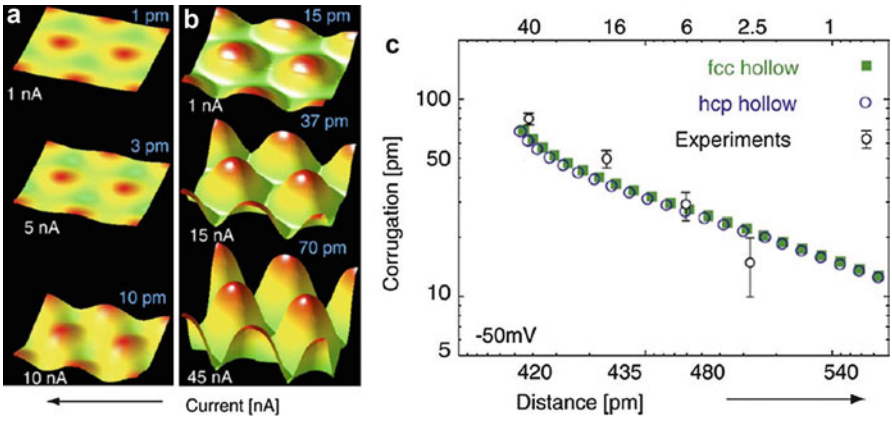


Fig. 15.16 (**a**, **b**) Calculated constant current contours on Al(111) for $V_b = -50$ mV. The surface is slightly corrugated in the contours based on the surface electronic structure calculations (**a**); however, the tip–sample interaction can enhance atomic corrugations up to 70 pm (**b**). The corrugations increase mainly in the range of the gap resistances between 10 and 1 MΩ; its maximum value in the simulations is about 80 pm (**c**) (Reprinted with permission from Ref. [130]. Copyright 2004 by Elsevier)

below 1.0 Å which can correspond to the limit of resolution with a tungsten tip having the $5d_z^2$ electron orbital at the apex.

5.3.2 Atomic Relaxations and Corrugation Enhancement on Metal Surfaces

The role of elastic effects in high-resolution STM imaging on metallic surfaces was thoroughly studied in Ref. [130]. To estimate the corrugation enhancement on different close-packed metal surfaces at different tunneling gaps, the simulations were performed for Cu(111) and Al(111) surfaces at different tip configurations [130]. The dynamic effects were found to be stronger for Al(111) which can be related to the higher elasticity of the aluminum surface. As an example, Fig. 15.16 shows a substantial increase of the corrugation amplitude due to dynamic effects. The atomic relaxations lead to the Al(111) surface corrugation of up to 70 pm

(at $V_b = -50$ mV and $I = 45$ nA). Similar results were obtained for tungsten tips with tungsten and aluminum pyramids at the apex, but the effect was more pronounced for the aluminum-terminated tip. The calculations [130] explain the anomalously high corrugation amplitudes observed in STM experiments on close-packed metal surfaces. The large outward relaxations of the surface atoms under typical tunneling conditions can lead to atomic corrugations which can hardly be explained from the electron density of states (Fig. 15.16a). Combined with the changes of forces, as the tip moves from the on-top to the hollow position, the outward surface atom relaxations give rise to unexpected large corrugation values (Fig. 15.16b). The main increase of corrugations occurs at tunneling resistances between 1 and 10 MOhm (currents between 5 and 50 nA for the images in Fig. 15.16a, b). In this range of the gap resistances, the corrugations increase from 20 to 70 pm, while the gap resistance decreases faster than exponential (Fig. 15.16c). Since the corrugation enhancement was proved on different surfaces, it can be valid for other metals, although the effect can be not so well pronounced as on the aluminum surface.

5.3.3 Contrast Inversion in Gap Resistance-Dependent STM Experiments

The change of the tip and surface atom relaxations at different tunneling gaps and electronic structure effects can lead to the contrast reversal even in STM experiments on the surfaces with relatively simple atomic structure [130, 156, 157]. For example, this effect was predicted for Cu(111) and Pt(111) at tip–sample distances where the short-range attractive atomic force reaches its maximum value [157]. The interaction forces at small distances induce substantial shifts of both the tip and the surface atoms. These relaxations have a decisive impact on the STM contrast increasing the atomic corrugations and shifting the lateral positions of the apparent maxima. As a result, even on (1×1)-reconstructed close-packed metal surfaces, protrusions on STM images can be observed above the hollow sites rather than above the true atomic positions of the surface atoms [157]. For the surfaces with more complicated structure, different vertical and lateral relaxations of nonequivalent surface atoms can produce maxima above different atoms at various tip–sample distances. One of the well-known examples of such contrast reversal is the hexagonal pattern observed on HOPG(0001). The honeycomb lattices in the neighboring layers of graphite crystal are shifted in x-y plane so that only half of the surface carbon atoms (α atoms) are located directly above the atoms of the underlying layer, while the others are located above the hollow sites (β atoms). Because of their nonequivalence, α and β atoms can demonstrate different relaxations interacting with STM tip [158]. As a result, for most tunneling conditions, only one of the two sublattices is resolved [30, 158, 159]. Recent theoretical calculations [156] showed that at small tip–sample distances, due to the tunneling current saturation, bright spots can correspond to hollows instead of atomic site positions even without inclusion of atomic relaxations of the surface atoms. Figure 15.17 illustrates that the multiple electron scattering effects can lead to evolution of the STM contrast on HOPG(0001) with decreasing tunneling gap.

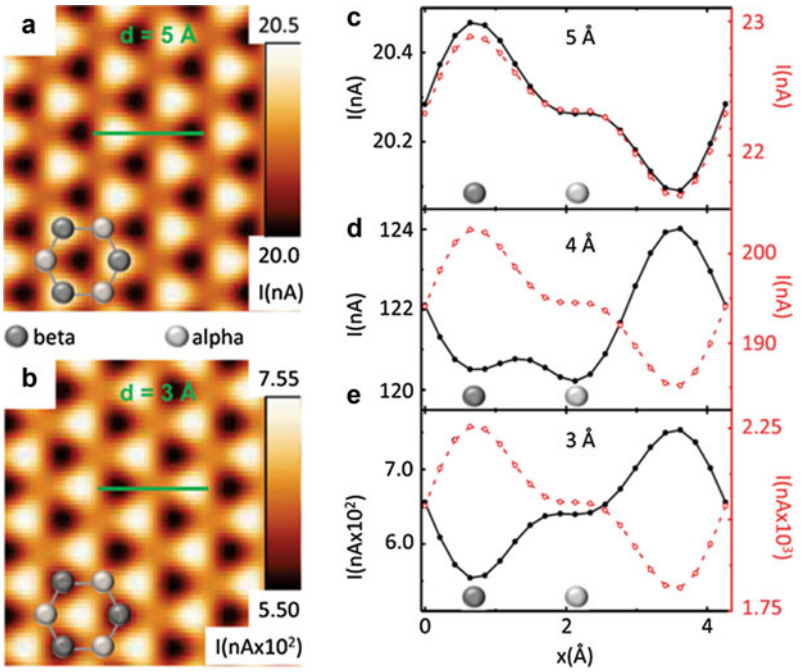


Fig. 15.17 CHM STM images of graphite(0001) ($V_b = -300$ mV), including multiple scattering effects, for a tip–surface distance of 5 Å (**a**) and 3 Å (**b**). The images reveal hexagonal patterns with maxima on either β atoms or hollow sites. (**c**)–(**e**) Line profiles at three distances demonstrate that multiple scattering, not included in the perturbative approach (*red line*), are needed to explain the contrast inversion (*black line*) (Reprinted with permission from Ref. [156]. Copyright 2011 by the American Physical Society)

At tip–sample distances about 5 Å, these calculations show that β atoms yield larger currents that can correspond to the bright features in the STM images (Fig. 15.17a). At the same time, in the near-contact regime, multiple scattering effects become relevant, and at distances below 4 Å, the hollow sites become the brighter spots, leading to a contrast inversion (Fig. 15.17b). The evolution of the STM contrast on HOPG(0001) as a function of the tip–sample distance is emphasized by the calculated line profiles for three different gaps (Fig. 15.17c–e).

5.3.4 Mapping the Surface Wave Functions in Distance-Dependent STM Experiments

Theoretical calculations (e.g., Fig. 15.13b) suggest that strong distance dependence of STM images can be anticipated when higher momentum electron states with $m \neq 0$ are responsible for the tunneling current. This can take place in experiments on clean and adsorbate-reconstructed metal surfaces. The spatial distribution of the tip and surface wave functions can be responsible for the distance dependence of the image symmetry and sometimes for the chemical contrast at the atomic scale.

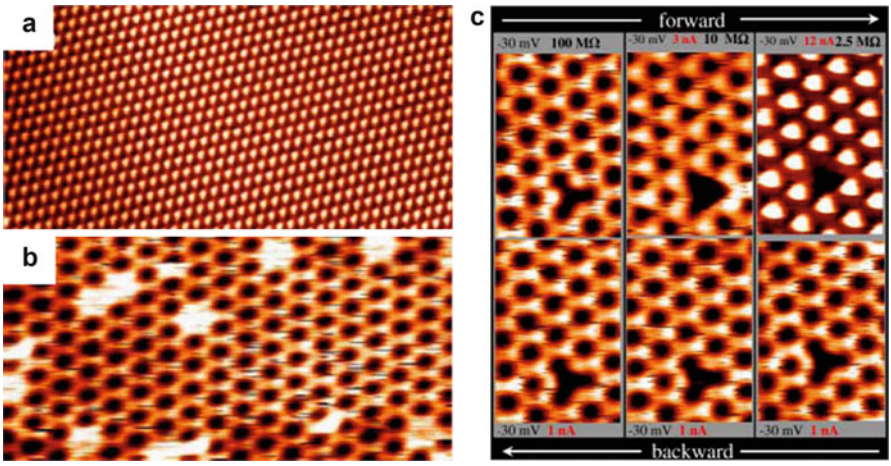


Fig. 15.18 (**a**) 10 × 5 nm^2 STM image of a clean Ru(0001) surface measured at $V_b = -23$ mV with a gap resistance of 2 MΩ. (**b**) 10 × 5 nm^2 image of the O(2 × 2)/Ru(0001) reconstruction recorded at $V_b = -0.1$ V and a gap resistance of 200 MΩ. The oxygen atoms appear as dark holes. (**c**) A series of 2.2 × 3.2 nm^2 dual-mode STM images of the O(2 × 2)/Ru(0001) reconstruction. The upper panels (*forward*) show images recorded at $V_b = -30$ mV and decreasing gap resistances (100, 10, and 2.5 MΩ). The reference images (*backward*) in the lower panels were measured at $V_b = -30$ mV and a constant gap resistance of 30 MΩ to exclude possible tip changes (Reprinted with permission from Ref. [152]. Copyright 2004 by the American Physical Society)

Figures 15.18 and 15.19 show two examples of the gap resistance dependence of atomically resolved STM images observed on oxygen-reconstructed metal surfaces. For the Ru(0001)–O system (Fig. 15.18), the observed gradual transformation of the STM images with increasing current (decreasing distance) was explained by a change of the relative contribution of ruthenium *s*- and p_z-orbitals and oxygen p_{xy}-orbitals. It was suggested [152] that ruthenium orbitals dominate at larger distances (honeycomb pattern), while the oxygen orbitals are responsible for hexagonal pattern observed at small distances (large tunneling currents). Similar results were obtained on the oxygen-reconstructed Pd(111)2 × 2 surface [153]. Note that change of the STM contrast for the Ru(0001)–O system (Fig. 15.18c) was observed in a wide range of the gap resistances. In contrast, STM studies of the stepped Cu(014)–O surface conducted using polycrystalline MnNi tips [27] reveal sharp distance dependence of the atomically resolved images at less than one order of magnitude decrease in the gap resistance (Figure 15.19a). At certain tunneling gaps and tip states, three typical atomically resolved STM images of the Cu(014)–O surface could be measured both with W and MnNi tips [27, 34, 160], as Fig. 15.19b illustrates. The gap resistance dependence in Fig. 15.19a proves that all these images can be measured at the same tip and surface structure varying the tunneling gap. The observed dependence was explained by decisive contribution of d_z^2 electron orbital of the copper atoms at larger distances (preferential visualization of three copper atomic rows), $d_{xy,x}{}^2{}_{-y}{}^2$-orbitals at the smallest distances (imaging two Cu–O atomic rows), and $d_{xz,yz}$ atomic orbitals at intermediate distances (preferential visualization of only one,

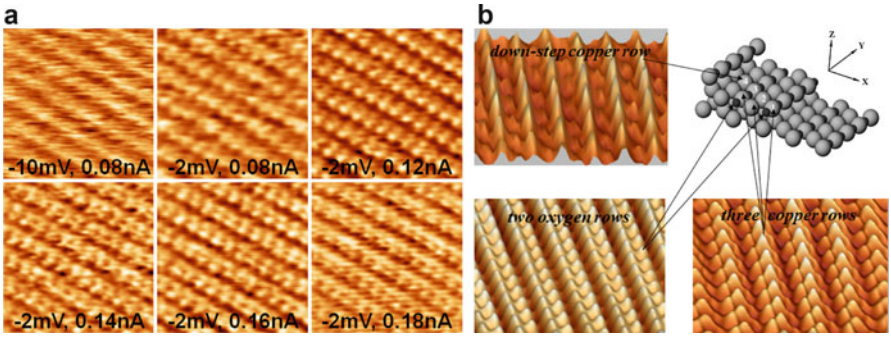


Fig. 15.19 (**a**) Gap resistance dependence of STM images of the Cu(014)–O surface measured with an MnNi tip. The dependence is explained by decisive contribution of the surface atom *d*-orbitals with different *m* at different tip–sample distances [27]. (**b**) Schematic model and 3-D presentations of three typical atomically resolved STM images of the Cu(014)–O reconstruction measured using polycrystalline tungsten tips [160]

down-step copper row within the terraces). This qualitative interpretation, based on the well-known spatial distributions of different *d*-orbitals, was supported by the tight binding (TB) calculations of the Cu(014)–O surface electronic structure and high-resolution STM images measured using tungsten tips [34]. The change of the relative contribution of electron orbitals with different *m* could lead to chemical-selective imaging of copper and oxygen atomic rows of the Cu(014)–O surface at the same bias voltages [34, 160]. As recent experimental and theoretical studies demonstrate [22, 23, 137, 147, 161], the partial contribution of the Cu d_z^2-orbital, dominating at larger distances, could be suppressed at small tunneling gaps because of different decay lengths of the *d*-orbitals with different *m* and modification of the surface electronic structure because of tip–sample interaction.

5.3.5 Interaction-Induced Reduction in Tunneling Current Channels

First indications of the tunneling current channels associated with different electron orbitals have been reported more than a decade ago [162]. However, their role in STM imaging at different gaps is still not clear. Recent theoretical studies show that relative contributions of different electron orbitals can be modified substantially because of tip–sample interaction changing the tip and surface DOS near E_F [136–139, 147, 161, 163]. Figure 15.14 demonstrates the distinct asymmetry of the [001]- and [011]-oriented tungsten probes interacting with a helium atom [139] which appears only at small gaps when overlap of the tungsten tip and helium atoms' orbitals takes place. Figure 15.20 shows a similar effect for the DOS associated with the adatom of the Si(111)7 × 7 reconstruction interacting with the [001]-oriented tungsten tip [147]. The interaction drastically modifies the electronic structure of the surface atom at distances below 4.75 Å reducing the adatom's DOS near E_F, as Fig. 15.20d illustrates. The non-monotonous dependence of the interaction forces (Fig. 15.20b) and the tunneling current (Fig. 15.20c) is observed at the same distances. The theoretical calculations reproduce the exponential current–distance

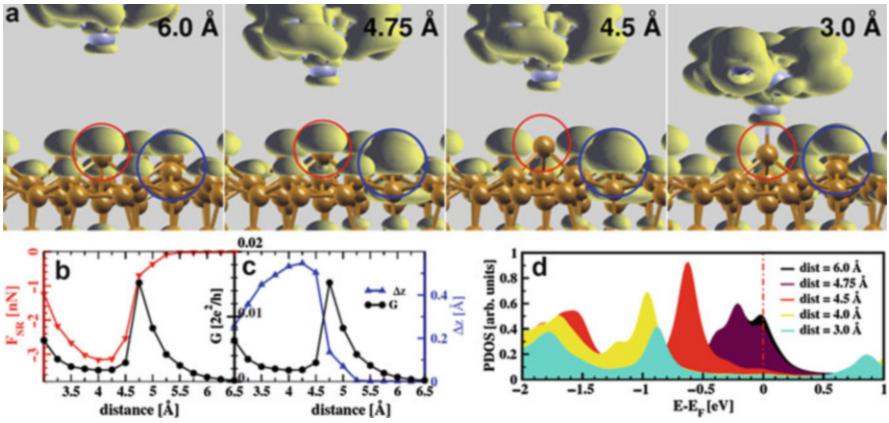


Fig. 15.20 (**a**) Isosurfaces of electron charge density 0.005 $e/Å^3$ integrated in the energy range from E_F to E_F-0.4 eV, for different tip–sample distances. The probe is placed over the corner adatom in the Si(111)7 × 7 faulted unit cell. The adatom and rest atom are marked by *red* and *blue cycles*, respectively. (**b**) Evolution of the quantum conductance G (*right axis*) and the atomic force (*left axis*) as a function of the tip–sample distance. (**c**) The quantum conductance (*left axis*) and the vertical adatom displacement (*right axis*) as a function of the tip–sample distance. (**d**) PDOS of the silicon corner adatom as a function of the tip–sample distance (Reprinted with permission from Ref. [147]. Copyright 2008 by the American Physical Society)

dependence at large distances and reveal the sudden drop of the conductance at a distance of 4.75 Å (Fig. 15.20c). Figure 15.20b, c demonstrates a strong correlation between the upward adatom displacement, the decrease of the conductance, and the formation of the chemical bond between the apex atom and the surface adatom. At large tip–sample distances, there is no significant vertical displacement of the adatom (Fig. 15.20c). A large upward movement of the adatom is observed around the distances of 5 Å. At the same distance, a rapid variation of the short-range chemical force between tip and sample occurs (Fig. 15.20b). Then, the vertical adatom displacement decreases until it reaches its initial value at a tip–sample distance about 3 Å. The electron DOS isosurfaces calculated for different tip–sample distances (Fig. 15.20a) show the characteristic charge density distribution of the Si(111)7 × 7 surface at 6.0 Å, a charge transfer from the adatom to its neighbors at 4.75 Å, the absence of the electron charge corresponding to the adatom dangling bond at 4.5 Å, and the chemical bond formation at 3.0 Å which prevents the electron transport between the tip and the surface at small distances. At the same time, the tip electronic structure remains practically unchanged during the tip to surface approach. First-principles simulations for the tip–sample interaction and transport calculations of Jelinek et al. [147] show that changes in the surface LDOS induce a substantial decrease of the current in the near-contact region at low bias voltages. It is known that p_z states dominate in the Si(111)7 × 7 surface DOS near E_F. Therefore, it can be assumed that suppression of the p_z-orbital result in a strong modification of the tunneling current. Furthermore, one can expect similar phenomena in other systems where the electron transport occurs through p_z electron states near E_F.

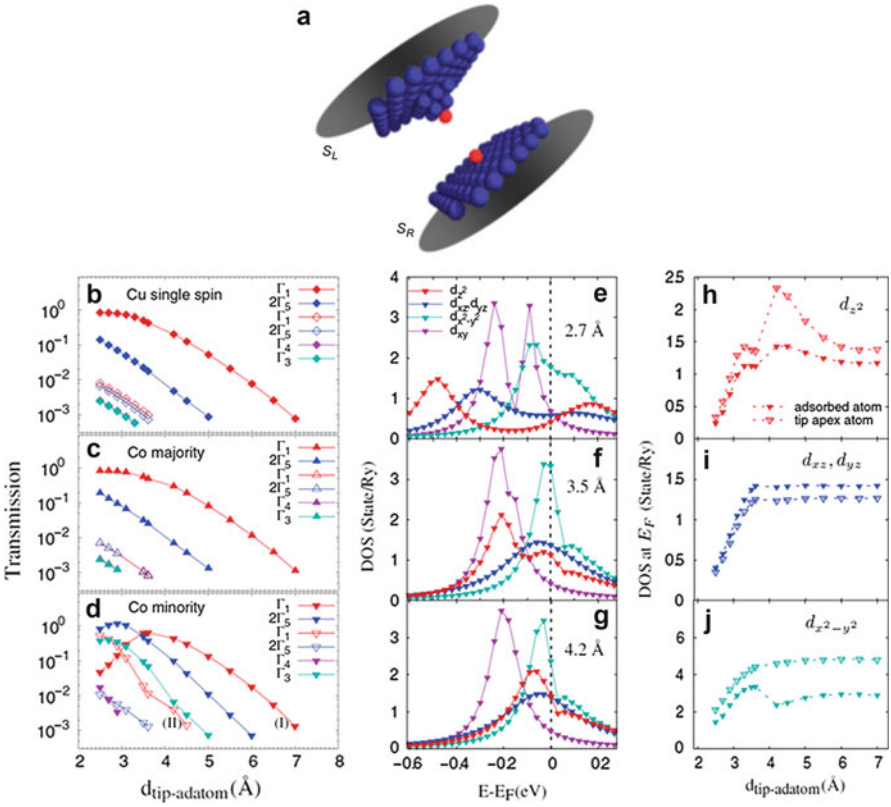


Fig. 15.21 (**a**) A schematic model of the tip–adatom system. The *red atoms* indicate positions of the Cu/Co atoms. The *gray areas* correspond to atomic planes used for the evaluation of the conductance, situated four monolayers above the tip (S_L) and below the adsorbed atom (S_R). (**b–d**) Transmissions of the conduction channels as a function of the distance between the STM tip and the adatom: (**b**) a nonmagnetic Cu system, (**c**) majority spin channel of the magnetic system composed of Cu surface with a Co adatom probed by the Cu tip with a Co apex atom, and (**d**) the corresponding minority spin channel. (**e–g**) Evolution of the minority spin LDOS at the Co adatom as a function of the tip–adatom distance (indicated on each panel). The LDOS of the five *d*-orbitals are shown. (**h–j**) LDOS calculated at the Fermi level for different *d*-orbitals as a function of the tip–adatom distance. The contributions at the adatom (*closed symbols*) are compared with those at the tip atom (*open symbols*) (Reprinted with permission from Ref. [137]. Copyright 2011 by the American Physical Society)

Recent theoretical calculations of the tunneling current between an STM tip and a single Cu/Co atom adsorbed on a Cu(001) surface [137] showed that conductance can be decomposed into several contributions while the tunneling probabilities of these channels can provide the information about the modifications of the adatom's LDOS caused by the tip–adatom interaction. Figure 15.21 shows a schematic model of the tip–adatom system used in the calculations (Fig. 15.21a), the analysis of the channel contributions (Fig. 15.21b–d), and the dependence of the minority spin

LDOS calculated for the Co adatom on a Cu(001) surface as a function of the tip–adatom distance (Fig. 15.21e–j). The tunneling channels in Fig. 15.21 correspond to the one-dimensional Γ_1 (s, p_z, d_z^2 contributions), Γ_3 ($d_{x^2-y^2}$), and Γ_4 (d_{xy}) irreducible representations and to the two-dimensional Γ_5 ($\{p_x, d_{xz}\},\{p_y, d_{yz}\}$) representation. Figure 15.21b demonstrates that in the case of the Cu adatom probed by the Cu tip, only Γ_1 channel contributes considerably to the conductance for all distances relevant to STM experiments. Other contributions are substantially smaller. Similarly, there is only one dominant Γ_1 channel for the majority spin states of a Co adatom interacting with the tip (Fig. 15.21c). In contrast, for the Co minority spin states, almost all contributions play a significant role at small distances where the d-orbitals start to overlap (Fig. 15.21d). At distances around 3 Å, five channels should be considered: two Γ_1 channels, the double degenerate Γ_5 channel, and the Γ_3 channel. The tunneling probability for these channels does not change monotonically with the distance. This is related to the modifications of the LDOS at the Co adatom induced by its interaction with the tip. The d_{xy} states are almost fully occupied (Fig. 15.21e–g), and therefore their contribution to conductance (Γ_4) is minor. The other d-orbitals are partially occupied and contribute to the tunneling current at small distances. The $d_{x^2-y^2}$ states are located in the vicinity to E_F, giving rise to the Γ_3 channel. With increasing distance, the $d_{x^2-y^2}$ states accumulate at E_F (Fig. 15.21j) and support transmission of the Γ_3 channel until it starts to decay exponentially at larger distances. A similar behavior is observed for the minority Γ_5 channel of Co. At small distances, this channel is strongly influenced by the minority d_{xz} and d_{yz} states of the Co adatom. With increasing tip–adatom separation, the d_{xz}, d_{yz} peak, located at 0.3 eV below E_F at small distances (Fig. 15.21e), shifts to lower energies increasing the LDOS at E_F (Fig. 15.21i) and transmission of the Γ_5 channel. The exponential decay for larger distances is driven by the p_x, p_y contributions to this channel. Finally, two minority Γ_1 channels [Γ_1(I) and Γ_1(II) in Fig. 15.21d] can be related to superpositions of the 4 s and $3d_z^2$ states. At the contact point, the Γ_1(I) channel is nearly closed and can be associated with the d_z^2 states, whose weight at E_F is suppressed at small distances (Fig. 15.21e). The Γ_1(II) channel has mainly s-like character and is open at small distances. When the tip is retracted from the adatom, the d_z^2 peak approaches E_F (Fig. 15.21e–h), which leads to the opening of the Γ_1(I) channel. At distances above 3.0 Å, these two Γ_1 channels are hybrids of s- and d_z^2-orbitals. At small tunneling gaps, the Γ_1(I) channel saturates to a transmission value of about 1.0. For large separations, this channel acquires more s weight and decays exponentially similar to the majority spin Γ_1 channel (Fig. 15.21f). At the same time, the Γ_1(II) channel acquires more d_z^2 character and decays faster because of the reduced overlap of the adatom and tip orbitals. The intensities of different d-orbitals at the Fermi level (Fig. 15.21h–j) reveal that d_z^2-orbitals of the interacting atoms are the most sensitive to the tip–adatom distance because they start to overlap at larger distances. At the same time, the intensity of the $d_{x^2-y^2}$-orbitals starts to decrease at smaller tunneling gaps, and the total reduction in the intensity of the $d_{x^2-y^2}$-orbital at distances between 4.0 and 2.5 Å is smaller in comparison with that of the d_{xz}-, d_{yz}-, and d_z^2-orbitals.

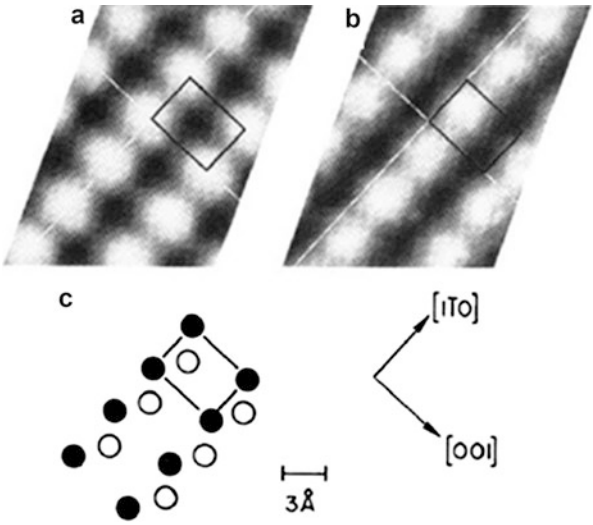


Fig. 15.22 Chemical selective STM imaging of the GaAs(110) surface. (**a**, **b**) CCM STM images measured at $V_b = 1.9$ V (**a**) and $V_b = -1.9$ V (**b**). (**c**) Top view of the surface atoms. As and Ga atoms are represented by *open* and *closed circles*, respectively (Reprinted with permission from Ref. [13]. Copyright 1987 by the American Physical Society)

5.4 Chemical Contrast in STM Experiments

5.4.1 Chemical Contrast on Semiconductors: GaAs(110) and GaTe($10\overline{2}$)

The bias voltage dependence of atomically resolved STM images of multicomponent semiconducting surfaces can lead to chemical-selective imaging [13]. Figure 15.22 shows one of the first examples of atomically resolved chemical discrimination with STM. In this case selective visualization of the electron orbitals associated with either Ga or As atoms of the GaAs(110) surface was achieved at different bias voltage polarities. This is in line with the electronic structure of the GaAs(110) surface.

The voltage-dependent selective imaging was also observed on other semiconductors and even on metal alloys [164]. It can be understood in terms of the surface electronic structure. However, the experimental results obtained on metal oxides [34, 155, 160, 165–168], Pt–Ni, Pt–Co, and Pt–Rh metal alloys [14, 169–172] and GaTe($10\overline{2}$) [173], demonstrate that chemical-selective visualization can be observed on metals and semiconductors at fixed bias voltages. This cannot be explained by the electronic structure of the studied surfaces without consideration of the tip–sample interaction.

Figure 15.23 shows the chemical contrast in atomically resolved STM images of the GaTe($10\overline{2}$) [173]. Three different images measured using the same [001]-oriented single crystalline tungsten tip (Fig. 15.23a–c) qualitatively agree with the structure of the uppermost layers presented in Fig. 15.23d. The images in Fig. 15.23a, b reveal preferential contributions of either Te or Ga sublattices, while the image in Fig. 15.23c represents more complicated structure with contributions from both sublattices. It should be emphasized that all three types of the images shown in Fig. 15.23 were obtained at almost the same negative sample bias voltage. The calculations of the DOS in the valence band of the GaTe($10\overline{2}$) surface [173] showed

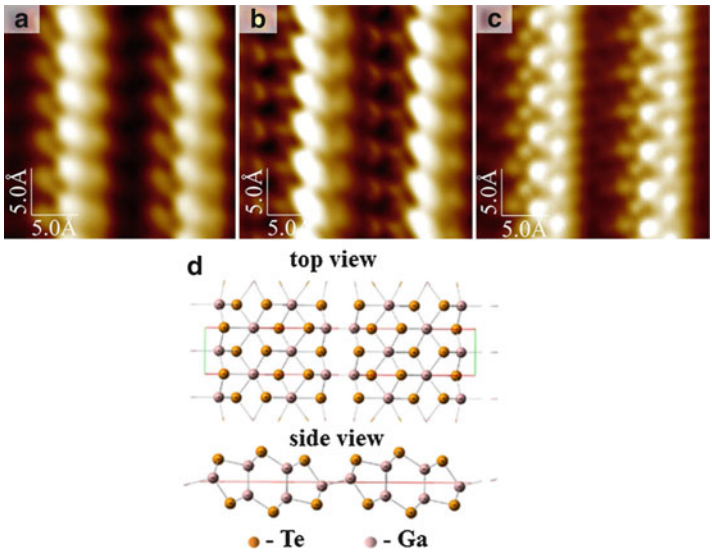


Fig. 15.23 (**a**–**c**) 25×25 Å^2 STM images of the GaTe($10\overline{2}$) [173], surface measured with a W[001] tip at $V_b = -1$ V and $I = 120$ pA (**a**), $V_b = -1$ V and $I = 50$ pA (**b**), and $V_b = -0.9$ V and $I = 40$ pA (**c**). (**d**) A schematic representation of the atomic structure of GaTe(1 0–2) [173]

that Te 5*p* states provide major contribution to the total DOS in a wide range of binding energies relevant to the STM experiments. Therefore, the relative contribution of the Te and Ga atomic orbitals could not be changed by the bias voltage. In turn, the chemical-selective imaging at the same bias voltage can be understood taking into account the interaction-induced modification of the surface DOS and reduction of the relative weights of the tunneling current channels associated with different electron orbitals of the surface atoms. In accordance with the theoretical calculations for other tip–sample systems [137, 147], the role of the channels associated with the Ga and Te atomic orbitals can be modified at different tunneling gaps and the tip states. Presumably, the DOS associated with the Te 5*p*-orbitals near E_F can be modified at small distances similarly to the DOS associated with the Si 2*p* states of the Si(111)7 × 7 surface interacting with the tip atom (Fig. 15.20). The tip–sample interaction can substantially reduce the relative contribution of the Te 5*p*-orbitals and provide selective visualization of the Ga sublattice in the STM experiments on the GaTe($10\overline{2}$) surface (Fig. 15.23b).

5.4.2 Chemical Contrast on Binary Metal Alloys: PtNi, PtCo, PtRh

One of the first examples of the atomic-scale chemical contrast on metal alloys was reported by Schmid et al. [14] who observed the chemical order on the (111) surface of a $Pt_{25}Ni_{75}$ single crystal. The difference of corrugations between Pt and Ni atoms located in the same surface layer was found to be about 0.3 Å. The different heights of the Pt and Ni atoms led to direct visualization of the atomic positions on high-resolution STM topograms [14]. Later on, the chemical contrast was observed on

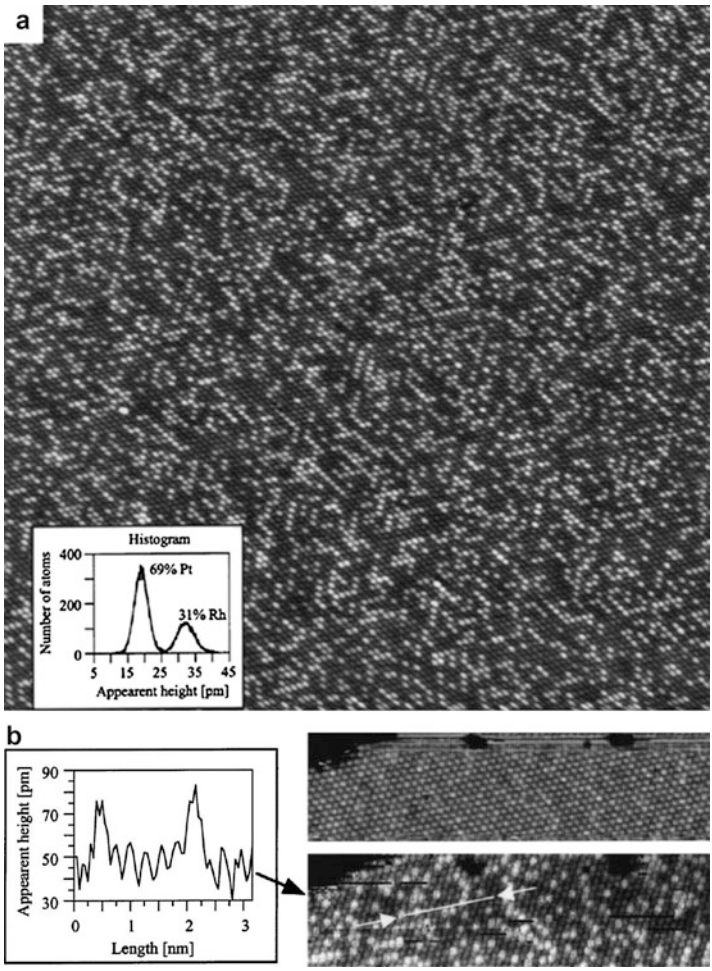


Fig. 15.24 (**a**) STM image of $Pt_{25}Rh_{75}(111)$ with chemical contrast (30×30 nm^2, $V_b = -2$ mV, $I = 0.7$ nA). *Inset*: the histogram of the apparent heights of the surface atoms. (**b**) Two STM images of the same $Pt_{25}Rh_{75}(111)$ surface area demonstrating the sudden appearance of a high chemical contrast explained by an adsorbed atom on the tip (4×15 nm^2; upper frame $V_b = -0.3$ mV, $I = 3$ nA, lower frame $V_b = -0.3$ mV, $I = 4.7$ nA) (Reprinted with permission from Ref. [171]. Copyright 1999 by Elsevier)

the $Pt_{40}Ni_{60}(100)$, $Pt_{50}Ni_{50}(100)$ [170], $Pt_{25}Co_{75}(100)$ [169], $Pt_{25}Rh_{75}(111)$, $Pt_{25}Rh_{75}(110)$, and $Pt_{25}Rh_{75}(100)$ surfaces [171, 172]. An example of the chemical-selective imaging of the $Pt_{25}Rh_{75}(111)$ surface [171] is presented in Fig. 15.24a. The chemical contrast on the binary alloys was originally attributed to the interaction of an adsorbate atom at the tip apex with the individual surface atoms. This could provide chemical selectivity and different atomically resolved STM images at the same bias voltages which cannot be explained by the surface

electronic structure. An example of sudden appearance of the chemical contrast on $Pt_{25}Rh_{75}(111)$ is shown in Fig. 15.24b. More recent theoretical calculations [174, 175] proved the decisive role of the tip–sample interaction in the formation of the chemical contrast on PtX alloys. The chemically resolved STM images of the binary alloys, obtained under specific tip conditions, cannot be only referred to the undisturbed surface electronic structure. However, the first-principles calculations also showed that chemical resolution could be achieved even with stable and clean tungsten tips [174]. In this case, the decay of the surface atomic orbitals in the vacuum region was supposed to play an essential role in the chemical-selective STM imaging of the surfaces.

5.4.3 Chemical Contrast on Metal Oxides

Atomically resolved selective visualization of the oxygen and metal sublattices on metal oxide surfaces has been reported by different groups [34, 155, 160, 165–168]. Similar to metal alloys, the chemical discrimination was frequently achieved at the same bias voltages and could not be explained using only the surface electronic structure. The crucial role of the tip–sample interaction in the appearance of the chemical contrast on oxidized metal surfaces was suggested in Ref. [165] where selective imaging of the oxygen and metal sublattices on the Cu(110)–O and Ni (110)–O surfaces was explained by fabrication of the tungsten- and oxygen-terminated apexes. Recent experimental and theoretical studies demonstrate that the origins of the chemical-selective imaging on metal oxides are not so straightforward, albeit the tip–sample interaction is very important. For example, Fig. 15.19 shows at least three different atomically resolved STM images of the well-ordered Cu(014)–O surface measured using polycrystalline tungsten tips [34, 160]. These cannot be explained by two possible tip terminations (tungsten or oxygen atom at the apex). Furthermore, distant-dependent STM studies carried out using MnNi tips [27] prove that different images can be measured at different tunneling gaps without modifying the tip state (Fig. 15.19a). Similar effects were reported for the Cu(001)–O surface [34, 155].

The model of the missing row $(2\sqrt{2} \times \sqrt{2})R45°$ reconstruction of the Cu(001)–O surface is shown in Fig. 15.25a. The density functional theory (DFT) calculations [155] reveal different electronic structure of the copper atoms in Cu and Cu–O rows (Fig. 15.25b). Moreover, different electron orbitals (namely, s and p_z) provide major contribution to the total DOS of the copper atoms below and above E_F. As a result, different atomically resolved images can be measured on the same surface at different bias voltages and tip–sample distances. These images emerge from a subtle balance between the surface geometry and the different decay lengths of the electron orbitals of nonequivalent atoms. Figure 15.25c–e shows theoretical STM images which can be obtained at different voltages, tip–sample distances, and apex terminations. Notably, at certain tunneling parameters and tip states, selective imaging of nonequivalent surface atoms and chemical-selective imaging can be achieved [155]. This result is in line with the earlier experimental studies [34] where several typical atomically resolved STM images of the Cu(001)–O surface were measured using tungsten probes (Fig. 15.26). The effect was explained by a change of the relative contribution of the surface atomic orbitals at different

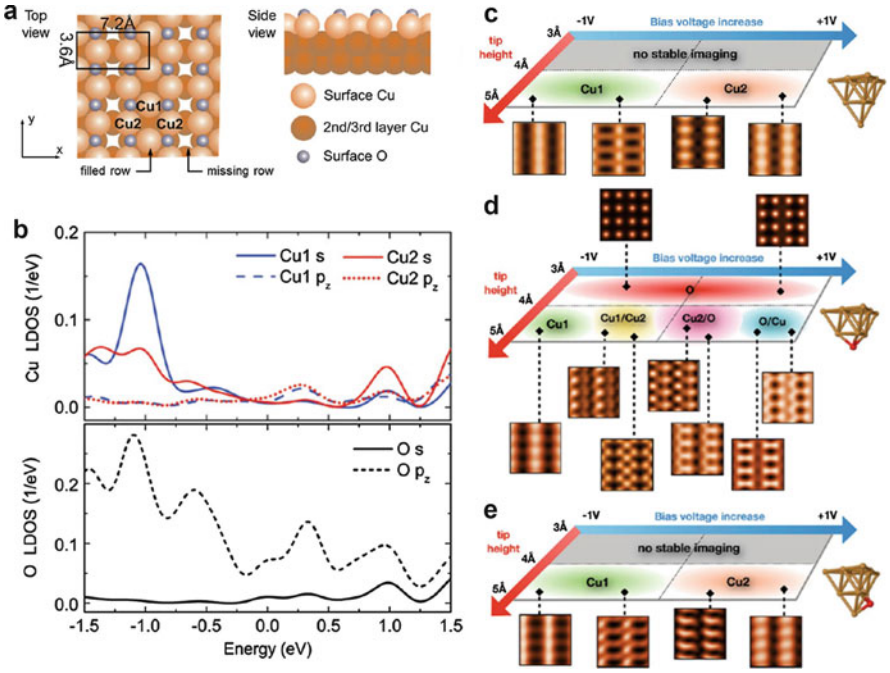


Fig. 15.25 (**a**) Schematic of the oxygen-induced $(2\sqrt{2} \times \sqrt{2})$R45° missing row reconstruction of the Cu(001) surface. Due to the rotational symmetry of the Cu(001) surface, the *x*- and *y*-directions may correspond to either [100] or [010] crystallographic directions of the substrate. The *black rectangle* indicates the unit cell. (**b**) LDOS of the *s* and p_z surface states near E_F, which are associated with current in the *z*-direction. (**c**–**e**) Imaging regimes for the pure copper tip (**c**), the oxygen-terminated copper tip (**d**), and the copper-terminated copper tip contaminated by oxygen atom (**e**) at different bias voltages and tip–sample distances. The labels indicate the atomic features which are preferentially imaged (Reprinted with permission from Ref. [155]. Copyright 2013 by the American Chemical Society)

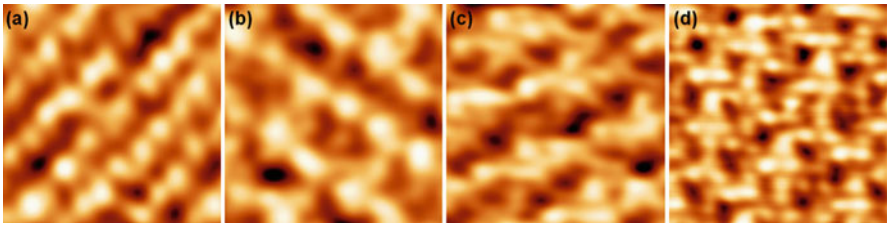


Fig. 15.26 (**a**–**d**) 2×2 nm^2 atomically resolved STM images of the Cu(001)–O surface [34] measured using a polycrystalline tungsten probe at $V_b = -2$ mV and $I = 0.15$ nA (**a**), $V_b = -3$ mV and $I = 0.12$ nA (**b**), $V_b = -1$ mV and $I = 0.1$ nA (**c**), and $V_b = -5$ mV and $I = 0.3$ nA (**d**)

tip–sample distances. For example, the image in Fig. 15.26a can be interpreted as visualization of the oxygen rows, while the other images are, presumably, related to probing different electron orbitals of the surface copper atoms. The STM imaging mechanisms observed on the Cu(001)–O reconstruction [34, 155] are important for

establishing general ways to control element-specific imaging on multicomponent surfaces and, most likely, can be applied to other metal oxides and similar complex compounds (e.g., chalcogenides, pnictides, etc.). However, for developing new strategies for the atomically resolved site-selective imaging, precise control of the tip state and the tip–sample distance becomes crucial.

5.5 Electron Orbital Resolution in STM Experiments

Figures 15.7 and 15.8 represent examples of the electron orbital resolution when particular orbitals of the Si(111)7 × 7 surface atoms are responsible for the STM contrast at different bias voltages. The control of the relative contribution of different electron orbitals on multicomponent metal surfaces is more difficult because of the partial contributions of higher momentum electron states which can produce multiple protrusions in STM experiments at small tunneling gaps (Fig. 15.13). The first experimental observations of the orbital channels in the tunneling conductance between two interacting atoms were reported approximately 15 years ago [162]. However, only several representative STM images which could be identified with particular electron orbitals have been published up to date. Mostly, these features are related to direct visualization of the tip atom electron states by more localized surface atomic orbitals in accordance with the reciprocity principle (Fig. 15.2). However, some STM studies reveal the subatomic electronic features associated with the $m \neq 0$ orbitals of the surface atoms [34, 176]. The STM data with subatomic resolution presented in this section can shed light upon gap resistance dependence of atomically resolved STM images and chemical contrast on metallic and semiconducting surfaces (Figs. 15.19, 15.23, 15.24, and 15.25). They can provide a key for reproducible chemical-selective imaging and control of the tip electronic structure in STM experiments and bring important information about the best tunneling parameters for high-resolution STM imaging of technologically relevant surfaces with complicated atomic and electronic structure.

5.5.1 Atomic Orbitals of the Si-terminated Tip Resolved Using the p_z-Orbitals of the Si(111)7 × 7 Surface Atoms

SPM imaging with subatomic electron orbital resolution was reported for the first time by Giessibl et al. [177]. The AFM images of the Si(111)7 × 7 reconstruction demonstrating regular splitting of the surface atomic features were explained by direct visualization of the two atomic orbitals of a silicon atom at the tip apex by the p_z-orbitals of the Si(111)7 × 7 surface atoms. This is schematically shown in Fig. 15.27b along with the results of distance-dependent STM experiments (Fig. 15.27a) demonstrating the appearance of the subatomic contrast with decreasing tip–sample distance [28]. The tips both for the AFM [177] and the STM experiments (Fig. 15.27) were prepared by a gentle contact of a polycrystalline tungsten probe with a silicon surface. Therefore, the precise structure of the apex responsible for the subatomic contrast [28, 177] was unknown, and the origin of the double features in the Si(111)7 × 7 SPM images was highly

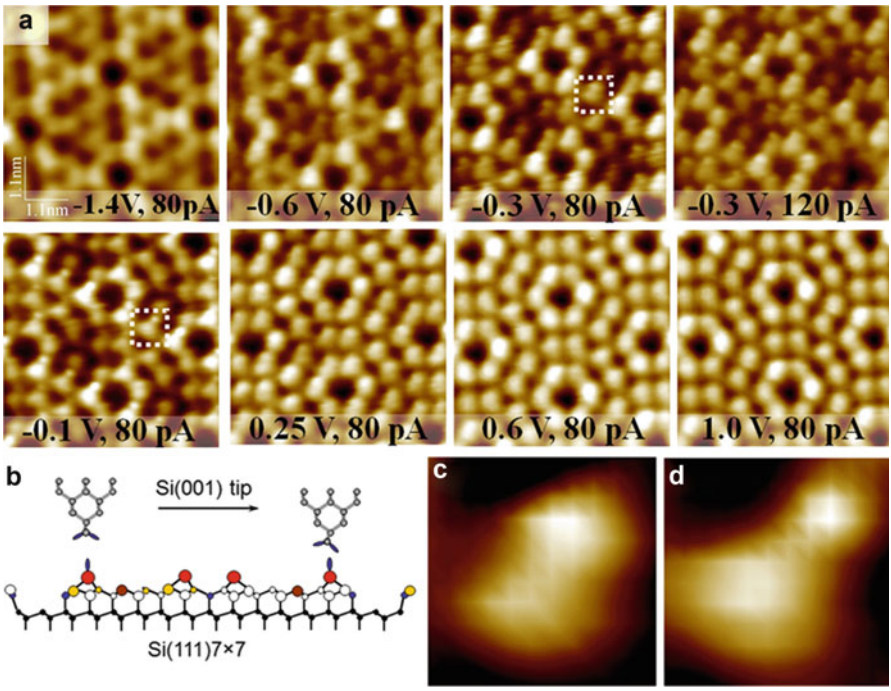


Fig. 15.27 (**a**) 5.5 × 5.5 nm^2 STM images of the Si(111)7 × 7 surface measured at different bias voltages and tunneling currents (shown on each frame) with unchanged silicon-terminated tungsten tip. The fast scanning direction was from *left* to *right*. (**b**) Side view of a [001]-oriented silicon tip over the Si(111)7 × 7 surface; *right panel* depicts a tip bending opposite to the scan direction. (**c**, **d**) 7×7Å^2 images of the double features indicated by the *dotted squares* on images measured at $V_b = -0.3$ V, $I = 80$ pA (**c**) and $V_b = -0.1$ V, $I = 80$ pA (**d**)

disputed [102, 178–182]. Although the explanations based on feedback loop artifacts [178] and the presence of a carbon atom at the apex [182] were proposed, independent theoretical calculations [102, 179, 180] proved that visualization of the asymmetric charge distribution around the apex atom of the [001]-oriented Si tip (Fig. 15.27b) can be achieved at small (2.5–4.0 Å) tip–surface separations.

This is in agreement with the gap resistance-dependent STM experiments carried out with the silicon-terminated tip [28]. Figure 15.27a demonstrates that at large negative bias voltages, a (7 × 7) pattern with well-resolved adatoms, rest atoms, and corner holes is observed which is only possible with extremely sharp single-atom-terminated tips [93]. At small voltages (small distances), the regular splitting of the adatom features becomes discernible. The effect can hardly be explained by a two-atom-terminated tip because deep corner holes, rest atoms, and single-atom defects on the surface were simultaneously resolved in the experiments [28]. The gap resistance dependence demonstrates that the double features become sharper and change their appearance from symmetric to asymmetric with decreasing gap resistance (Fig. 15.27 c, d). The changes of the shapes of the double

features were observed both with varying tunneling current at fixed voltage and decreasing/increasing voltage at the same current [28]. The asymmetry of the double features can be explained by a relaxation of the apex atom at small tip–surface separations, as Fig. 15.27b illustrates. The distance between two maxima within the subatomic features was in the range of 2.2–2.75 Å depending on the gap resistance [28]. The distance between two maxima of the double features decreased from 2.7 to 2.2 Å at gap resistances between 7.5 and 2.5 GΩ and then increased to 2.75 Å at gap resistances between 2.5 and 1.25 GΩ. The decrease of the separation between two subatomic features at gap resistances between 7.5 and 2.5 GΩ is in line with the spatial distribution of the two sp^3 dangling bonds at the [001]-oriented silicon apex [179]. The increase of the distance between the subatomic maxima at smaller gap resistances can be attributed to strong tip–sample interaction modifying the electronic structure of the tip and surface atoms in near-to-contact regime and inducing their lateral relaxations which can shift the apparent maxima on STM images. However, because of uncontrollable modification of the tip apex during the contact with the silicon surface, other interpretations cannot be excluded. For example, splitting of the atomic features at very small distances can even be related to imaging individual tetrahedral hybrid orbital of a silicon atom at the apex which is not ideally aligned with the normal to the surface [181]. Apparently, unambiguous interpretation of the subatomic contrast observed in STM (Fig. 15.27) [28] and AFM experiments on the Si(111)7 × 7 surface [177] can only be given on the basis of experimental data obtained with well-defined single crystalline tips.

5.5.2 Sm $4f_z^3$ Electron Orbital of a Co_6Fe_3Sm Tip Probed by the p_z-Orbitals of the Silicon Atoms

Figure 15.28a shows an example of high-resolution STM imaging of the Si(111)7 × 7 surface using a Co_6Fe_3Sm tip [25]. In these experiments a dynamic STM mode with an oscillating probe was used to decrease the tip–sample distance and improve the spatial resolution. The enhanced stability of the tip apex at extremely small tunneling gaps in this mode is related to the presence of retracting phase during oscillations of the probe reducing the lateral forces in tip–sample contact. The adatoms in Fig. 15.28a are imaged as extremely sharp spherically symmetric features surrounded by lower lying crescents. This asymmetry of atomic features was explained by a convolution of the p_z-orbitals of the surface atoms and the f_z^3-orbital of a Sm atom at the apex (Fig. 15.28b). This interpretation is supported by a good agreement between experimental (Fig. 15.28c, e) and theoretical images (Fig. 15.28d, f) calculated in an assumption of the Sm f_z^3 tip orbital tilted to the surface normal by 37°. The well-resolved single-atom defect on the surface (Fig. 15.28a) proves that the tip is terminated by a single atom at the apex. Therefore, the STM image in Fig. 15.28a revealing the (7 × 7) pattern of the tilted Sm $4f_z^3$ electron orbitals can be explained only by an asymmetric DOS distribution on the Sm apex atom at certain tunneling conditions.

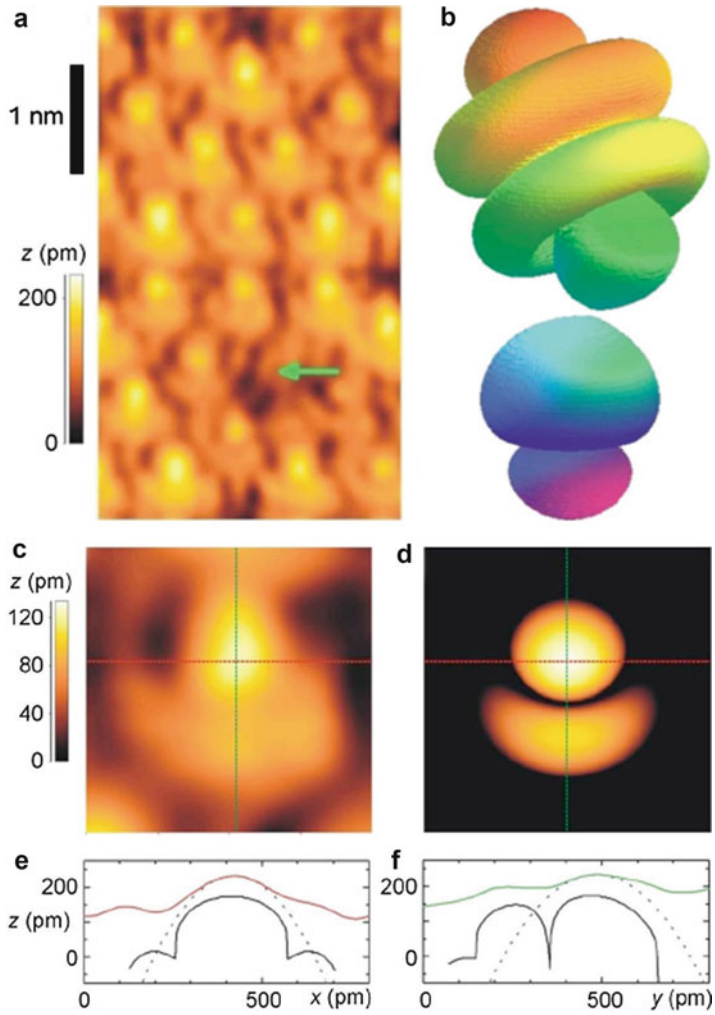


Fig. 15.28 (**a**) Dynamic STM image of an Si(111)7 × 7 surface measured using a Co_6Fe_3Sm tip. The *green arrow* indicates an atomic defect. (**b**) Schematic presentation of the electron states producing the image shown in (**a**). The sp^3 silicon states are tunneling mainly into an Sm $4f_z^3$ tip state tilted by ∼37°. (**c**) Experimental image of a single Si adatom. (**d**) Calculated dynamic STM image for a silicon p_z sample state and an Sm f_z^3 tip state inclined 37° with respect to the z-axis. (**e**) Profile through the maximum of the image in the x-direction (*red line*). The paraboloid fitted to the profile has an apex radius of $R_x = 0.12$ nm. (**f**) Profile through the maximum of the image in the y-direction (*green line*). The paraboloid fitted to the trace has an apex radius of $R_y = 0.15$ nm. The black lines in (**e**) and (**f**) show the corresponding cross sections of the constant current surface at the main peak of the theoretical image (Reprinted with permission from Ref. [25]. Copyright 2003 by the American Physical Society)

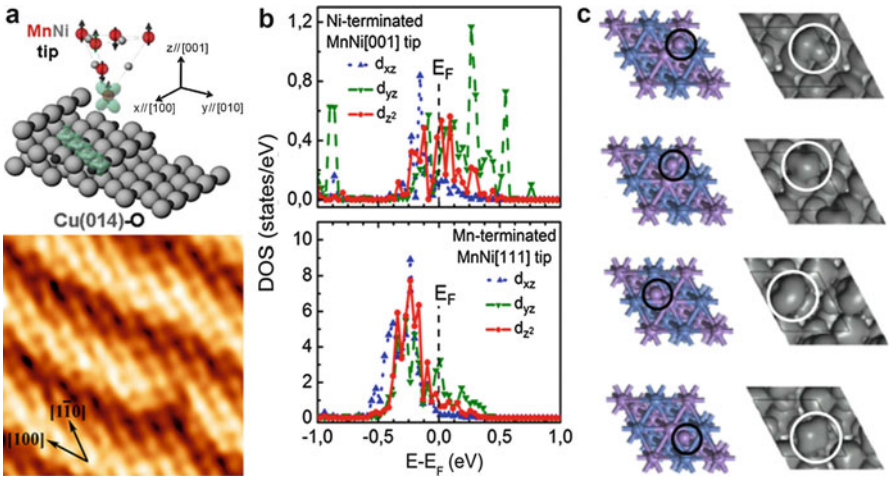


Fig. 15.29 (**a**) Regular doubling of atomic features in STM images of the Cu(014)–O surface measured with an MnNi tip (*lower panel*) and schematic model of the d_{yz} tip orbital scanning over d_z^2-orbitals of the surface atoms (*top panel*). The 2×2 nm^2 image was taken at $V_b = -30$ mV and $I = 80$ pA. (**b**) TB calculation of the PDOS associated with different *d*-orbitals of the apex atoms of the Ni-terminated MnNi[001] tip (*top*) and Mn-terminated MnNi[111] tip (*bottom*). (**c**) Schematic models and calculated electron density isosurfaces for four different [111]-oriented MnNi tip configurations. The model of the tip is presented on the left and shows the relative position of the tip atom on the (111) surface. The corresponding isosurface is shown on the right and displays the calculated electron density at 2.4×10^{-3} electrons/Å^3 in the $E_F \pm 0.22$ eV energy range. The apex atom positions are indicated by *black* and *white* circles on *left* and *right* panels, respectively (Reprinted with permission from Ref. [27]. Copyright 2007 by the American Physical Society)

5.5.3 d_{yz} Electron Orbital of an MnNi Tip Resolved in STM Experiments on the Cu(014)–O Surface

According to the theory [132–135], asymmetric subatomic features with multiple protrusions can be observed in STM experiments with the tips having $m \neq 0$ electron states at the apex. Figure 15.29a shows the STM image of the Cu(014)–O surface measured using a polycrystalline MnNi tip [26, 27]. The image demonstrates regular splitting of the copper atomic features along one of the close-packed <110> directions of the substrate. The experimental image displays the 7.2 ± 0.2 Å wide terraces, step edges along the [100] direction, and an additional fine structure within the terraces. The image in Fig. 15.29a reveals a single-atom defect proving the sharpness of the MnNi tip. The doubling of atomic features was observed at certain tip states and tunneling parameters. In particular, well-resolved images with the subatomic features were measured only in rare experiments at small negative sample bias voltages between −30 and −50 mV in very narrow range of the tunneling currents. This can be explained by the sharp distance dependence of the Cu(014)–O STM images (Fig. 15.19a) and the electronic structure of MnNi tips [26, 27]. Figure 15.29b shows the partial density of electron states (PDOS) associated with the Ni and Mn atoms at the apexes of the [001]- and [111]-oriented MnNi tips calculated using the TB method. The TB calculations demonstrate domination of the d_{yz}-orbital near the Fermi level for the [111]-oriented

MnNi tip terminated by an Mn atom (Fig. 15.29b). The results of the DFT calculations shown in Fig. 15.29c demonstrate that only certain configurations of the Mn-terminated MnNi[111] tips can produce regular doubling with almost symmetric twofold split features [27]. The regular pattern of the double features reproducing the shape of the Mn atom d_{yz} electron orbital (Fig. 15.29a) can be resolved on the Cu (014)–O surface only when the surface d_z^2-orbitals and the tip d_{yz}-orbital provide major contribution to the tunneling current. However, because of the surface complexity and distance dependence of atomically resolved STM images of the Cu(014)–O surface (Fig. 15.19a), the role of the tunneling parameters (voltage and gap resistance) in control of the relative contribution of particular tip and surface electron orbitals could not be studied in detail.

5.5.4 d_{xz}-Orbitals of the Copper and Cobalt Atoms Resolved Using Clean and Iron-Covered Tungsten Tips

STM images shown in Figs. 15.30 and 15.31 correspond to the situations when the surface electronic structure is probed with subatomic electron orbital resolution using "sharper" orbitals of the front tip atoms. The image shown in Fig. 15.30a was measured with a polycrystalline tungsten tip on the stepped Cu(014)–O surface [34]. This image reveals one bright atomic row within the four-atom-wide terraces (see the model in Fig. 15.29a). All atomic features within the well-resolved copper row are essentially asymmetric. The shapes of these features with two maxima separated by approximately 1 Å (Fig. 15.30b) qualitatively reproduce the electron density distribution in the Cu d_{xz} atomic orbital that supports the interpretation of the gap resistance dependence of the Cu(014)–O STM images shown in Fig. 15.19b. According to the TB calculations (Fig. 15.30c), the DOS associated with the d_{xz}-orbitals of the surface copper atoms is maximal for the fourth (down-step) copper terrace row. This means that visualization of one copper row within the terraces can be feasible if the d_{xz}-orbitals yield the largest contribution to the tunneling current at some tunneling parameters. The STM image with one well-resolved row with double features (Fig. 15.30a) can be explained by imaging the d_{xz}-orbitals of the Cu(014)–O surface using the d_z^2-orbital of a tungsten tip atom.

Figure 15.31 presents spin-polarized STM images of the cobalt atoms adsorbed on the Mn/W(110) surface obtained using an iron-covered tungsten tip [176]. As shown at the bottom of Fig. 15.31b, the manganese layer exhibits a robust cycloidal spin spiral induced by the Dzyaloshinskii–Moriya interaction, propagating along the $[1\bar{1}0]$ direction. This spin spiral gives rise to periodic stripes on the manganese layer along the [001] direction (Fig. 15.31a, b). This apparent height contrast vanishes approximately every 6 nm along the $[1\bar{1}0]$ direction where the local manganese moments lie in the plane. Thus, the manganese layer not only has nearly opposite magnetic moments in neighboring sites, but their orientation also varies gradually across the surface. The adsorbed cobalt atoms reside in hollow sites (Fig. 15.31d) and have varying heights and shapes that strongly depend on their lateral position with respect to the underlying spin spiral (Fig. 15.31a, b). The cobalt atoms appear higher when they are located on bright manganese atom rows (top) and lower on dark manganese rows (bottom). At sites where the spin spiral contrast

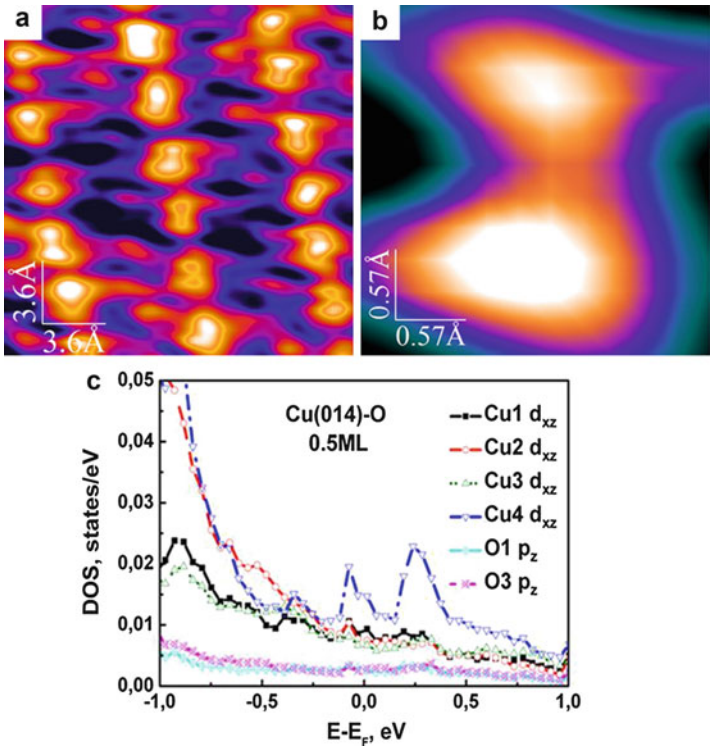


Fig. 15.30 (**a**) A 2.1 × 2.1 nm^2 STM image of the stepped Cu(014)–O surface illustrating the distinct asymmetry of the atomic features associated with the down-step copper row resolved using a polycrystalline W tip at $V_b = -5$ mV and $I = 0.1$ nA [34]. (**b**) A 2.9 × 2.9 Å^2 STM image of a subatomic feature reproducing the shape of the Cu d_{xz} electron orbital. (**c**) PDOS associated with the d_{xz}-orbital of the copper atoms and p_z-orbital of the oxygen atoms of the Cu(014)–O surface. The model of the surface is shown in Fig. 15.29b

vanishes (manganese moments are in plane), the cobalt atoms have an intermediate height (right). The shape of the atoms is different on bright and dark manganese rows. Figure 15.31c shows a magnified view of two cobalt atoms at positions where the manganese magnetic moments underneath point exactly upward and downward. Depending on which of these two possible orientations occur, the cobalt atom appears either rotationally symmetric with its maximum height at its center (Fig. 15.31c, left) or elongated with two lobes along the $[1\bar{1}0]$ direction and a central minimum (Fig. 15.31c, right). The calculated LDOS for the cobalt atom in the vicinity of E_F displays a nearly circular shape for the majority channel, whereas the minority channel demonstrates two lobes along the $[1\bar{1}0]$ direction with a minimum above the atom (Fig. 15.31e, f, top and cross-sectional view), in agreement with the STM images shown in Fig. 15.31c. In the majority channel, the cobalt atom has a state composed of s-, p_z-, and d_z^2-orbitals, all of which are rotationally symmetric along the z-axis, with a maximum above the cobalt atom. For the minority channel, the LDOS is

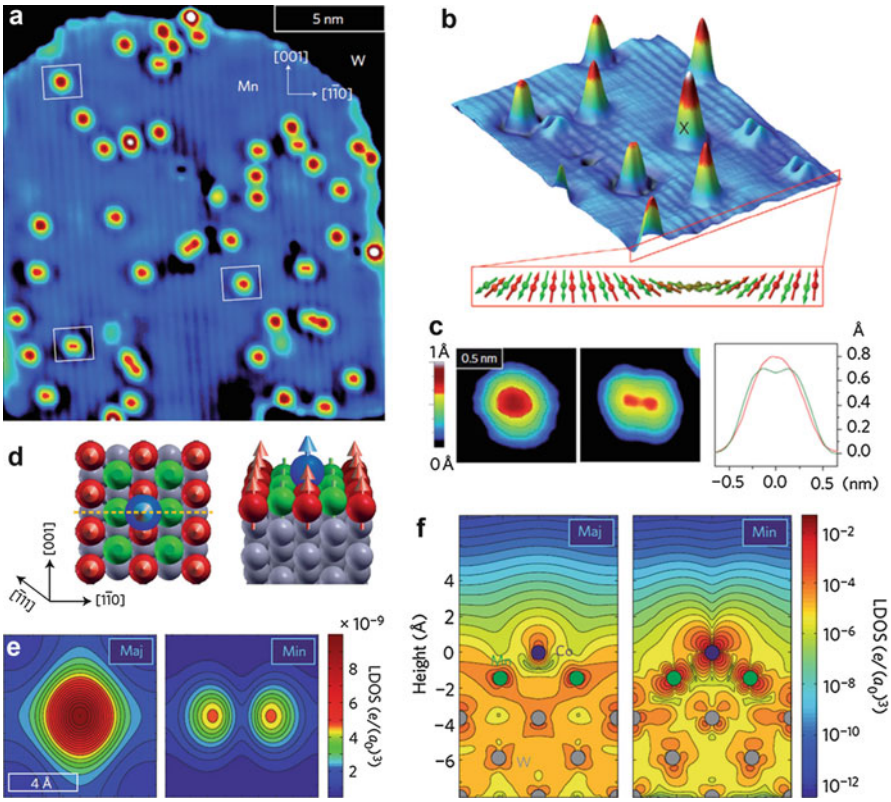


Fig. 15.31 (**a**–**c**) SP-STM measurements of single cobalt atoms on 1ML Mn/W(110), with a tip sensitive to the out-of-plane magnetization. (**a**) CCM STM image ($V_b = -50$ mV, $I = 2$ nA). The height and shape of the cobalt atoms depend on their position on the manganese spin spiral. (**b**) Perspective view of another sample area ($V_b = -10$ mV, $I = 2$ nA) and sketch of the manganese spin spiral (side view). A cobalt dimer is indicated by a *black cross*. (**c**) Two particular cases (cobalt magnetic moment up and down) and the respective line profiles taken along the [110] direction. (**d**–**f**) Calculated spin-resolved LDOS of a cobalt atom on Mn/W(110). (**d**) Top and perspective views of the unit cell. *Red* and *green* spheres represent manganese atoms with magnetization parallel and antiparallel to the cobalt atom (*blue*), respectively. (**e**) LDOS in the energy interval between E_F and E_F + 10 meV for majority (maj) and minority (min) electrons in a plane parallel to the surface 5.2 Å above the cobalt atom (a_0 is the Bohr radius). (**f**) LDOS in a plane perpendicular to the surface along the dashed line in panel (**d**) (Reprinted with permission from Ref. [176]. Copyright 2010 by Macmillan Publishers Ltd)

mainly given by a d_{xz} state, which exhibits a node at the cobalt atom center. The separation between two maxima in the images of the Co d_{xz}-orbitals (Fig. 15.31c, e) exceeds the distance between the subatomic maxima in Fig. 15.30 that can be related to different electronic structure of the probed atoms and different tunneling gaps used in these two experiments. The images in Fig. 15.31 demonstrate that control of the relative contribution of electron orbitals responsible for the STM imaging can produce a spin contrast at the atomic scale for certain systems.

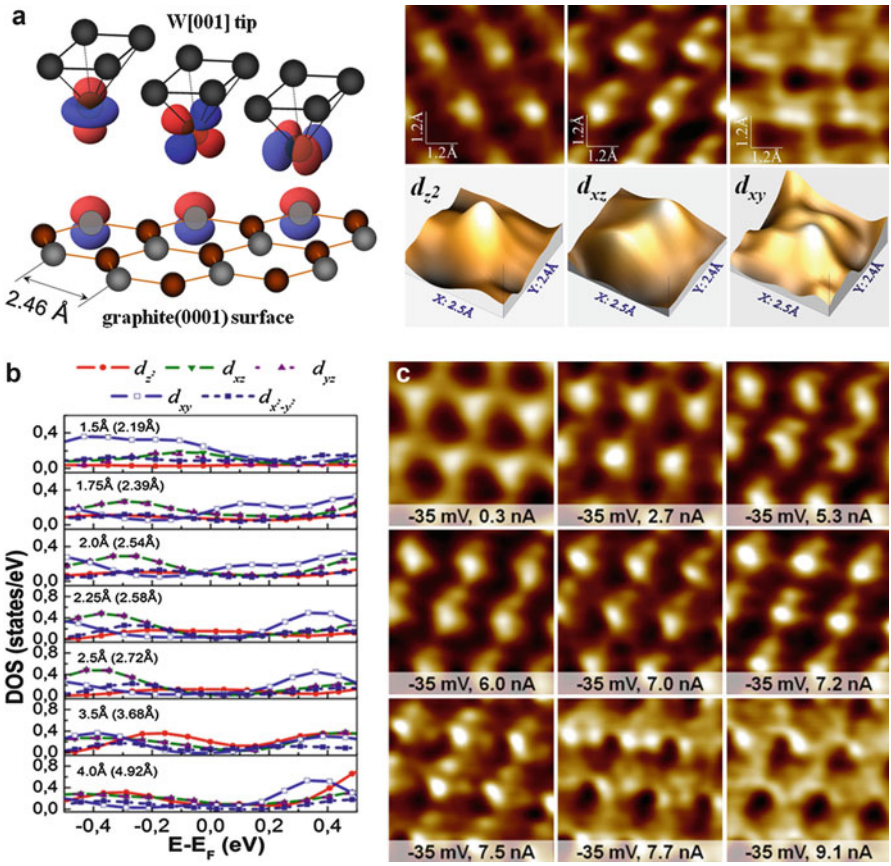


Fig. 15.32 (**a**) *Left*: schematic model of a [001]-oriented W tip over a graphite (0001) surface. *Right*: 6 × 6 Å^2 (*top row*) and 2.5 × 2.4 Å^2 (*bottom row*) STM images measured with single crystalline W[001] tips at $V_b = 23$ mV and $I = 2.7$ nA (*left panels*), $V_b = -35$ mV and $I = 6.8$ nA (*central panels*), and $V_b = -100$ mV and $I = 1.7$ nA (*right panels*). (**b**) PDOS associated with different *d*-orbitals of the W[001] tip apex atom interacting with the graphite (0001) surface. The initial and final distances between interacting tip and surface atom nuclei are indicated on each panel. (**c**) Gap resistance dependence of HOPG(0001) STM images measured using a W[001] tip at $V_b = -35$ mV. Tunneling currents are indicated on each frame

5.5.5 Distance Dependence of the W[001] Tip Atom *d*-orbital Contribution in STM Experiments on HOPG(0001)

The possibility to control the electronic structure of the front tip atom and relative contribution of different *d*-orbitals in high-resolution STM experiments has recently been demonstrated [22–24]. In these studies, electron orbitals of the HOPG(0001) surface atoms were used to study the relative contribution of *d*-orbitals of the [001]-oriented single crystalline tungsten tip at different tunneling parameters (Fig. 15.32). To eliminate possible artifacts caused by the apex contamination, W[001] tips were cleaned by flash heating and ion sputtering in UHV before high-resolution STM

experiments. The TEM images of a W[001] tip shown in Fig. 15.5 prove that this treatment leads to fabrication of nanopyramid with well-defined structure at the apex. Moreover, the electron microscopy studies proved that W[001] tip structure is not modified after the STM experiments on graphite [24].

Figure 15.32c shows a gap resistance dependence of atomically resolved STM images measured with a W[001] tip at a bias voltage of −35 mV. At smaller currents (larger distances), a hexagonal pattern is observed. The atomic features forming this pattern become sharper with increasing tunneling current (decreasing distance). The shape of the features at $I = 2.7$ nA suggests imaging of the surface atomic orbitals by the d_z^2 electron orbital of the tungsten tip atom. With further increase in the tunneling current, the spherically symmetric features are consecutively transformed into two-, three-, and fourfold split subatomic features at currents between 5.3 nA and 9.1 nA. Similar subatomic features were resolved in AFM experiments with polycrystalline tungsten probes [140] and ascribed to the orbital structure of the tungsten tips with three different crystallographic orientations. The gap resistance dependence measured with unchanged [001]-oriented tungsten tip (Fig. 15.32c) demonstrates that these orbital images can belong to the electronic structure of the same atom interacting with a graphite surface at different tip–sample distances. The twofold and fourfold split features in Fig. 15.32 are not related to the electronic structure of the surface which is threefold symmetrical along the tip axis. Therefore, the subatomic features can only be explained by a direct visualization of the tip atom electronic structure modified by the tip–sample interaction at small tunneling gaps. According to Eqs. 15.1, 15.2, and 15.3, the difference in the tunneling currents responsible for the transition from the twofold to fourfold splitting (Fig. 15.32c) can correspond to difference in the tip–sample distance about 0.1–0.2 Å.

At certain tunneling parameters, the shapes of the multiple subatomic features measured in STM experiments on HOPG(0001) with single crystalline W[001] tips reproduce the electron density distribution associated with the d_z^2-, d_{xz}-, and d_{xy}-orbitals in the tungsten atom. This can be explained by a major contribution of particular electron orbitals of the tungsten tip atom at certain tip–sample distances (Fig. 15.32a). According to the gap resistance dependence shown in Fig. 15.32c, the relative contribution of the tungsten d-orbitals with $m \neq 0$ increases with decreasing gap resistance. The DFT calculations (Fig. 15.32b) reveal the origin of the effect observed at small tunneling gaps. PDOS calculations for fully relaxed "W[001] tip–HOPG(0001)" system (Fig. 15.32b) demonstrate a suppression of the tip d_z^2 electron states near E_F at tip–sample separations below 2.5 Å because of overlap of the tungsten d_z^2 electron orbital with the carbon atomic orbitals. The domination of the tip d_{xy} electron orbital near E_F is pronounced in a narrow range of the tip–surface distances between 2.2 and 2.5 Å. This rather narrow range of the tunneling gaps is in agreement with the currents in STM experiments (Fig. 15.32c). The surface imaging by the tungsten d_z^2-orbital can be realized at tunneling gaps between 2.5 and 4.0 Å, while d_{xy} electron orbital can yield a maximum contribution to the tunneling current at distances between 2.2 and 2.5 Å. These distances are in agreement with results of the theoretical calculations

presented in Refs. [141 and 142] proving that asymmetric electronic structure of the W[001] tip interacting with the graphite surface is responsible for the subatomic features observed in the AFM [140] and STM experiments [22–24] at tip–sample distances below 2.5 Å. The appearance of the asymmetric features is related to modification of the PDOS associated with different electron *d*-orbitals of the tungsten tip atom because of strong tip–sample interaction. Note that similar effects at tunneling gaps below 4.0 Å have been predicted theoretically for several tip–surface systems [137, 139, 147, 161].

The DFT calculations and distance-dependent STM experiments on HOPG(0001) show the correlation between the spatial distribution of the atomic orbitals (in particular, extension in *z*-direction) and the order of their suppression with decreasing tip–sample distance. The suppression of the electron orbitals with $m = 0$ can increase the role of the $m \neq 0$ electron states at small gaps. Figure 15.32 demonstrates that picoscale spatial resolution and even direct imaging of the transition metal *d*-orbitals can be achieved using the *p*-orbitals of light elements.

5.5.6 STM Imaging of HOPG(0001) Using a [111]-Oriented Single Crystal Diamond Tip

Conductive (e.g., boron-doped) diamond probes can provide carbon atomic orbitals suitable for STM imaging with picoscale spatial resolution (Fig. 15.32) and high apex stability at small tunneling gaps necessary for high-resolution experiments. It has been demonstrated recently that high spatial resolution can be achieved in STM experiments with single crystal diamond tips [57], which are generally considered for use as probes for atomic force microscopy. Figure 15.33a–d displays a comparison of the spatial resolution which can be achieved with a boron-doped [111]-oriented diamond and [001]-oriented tungsten probes. Note that STM image in Fig. 15.33b was measured with the W[001] tip used for the distance-dependent experiments on HOPG(0001) (Fig. 15.32) and high-resolution studies of other surfaces with complex atomic structures [91, 173]. The images taken with the diamond and W[001] probes (Fig. 15.33a, b) reveal two sublattices corresponding to nonequivalent α and β atoms in the honeycomb lattice. However, the hollow sites are substantially deeper, and individual surface atoms are better resolved in the image measured with the boron-doped diamond probe (see the cross sections on Fig. 15.33c, d). This is related to different spatial distribution of the carbon *p*-orbitals and tungsten *d*-orbitals at the apexes of the STM tips. In particular, carbon atomic orbitals are further protruded in the *z*-direction and more localized in the *x*-*y* plane than tungsten *d*-orbitals. DFT calculations [57] reveal a minor difference in the DOS corresponding to the α and β atoms of the graphite surface (Fig. 15.33e, f). The density of electron states at E_F is larger for β atoms by ~25 % (Fig. 15.33f), and the difference decreases for the DOS integrated over a wider range of the electron energies. This difference is responsible for the two nonequivalent sublattices of carbon atoms in Fig. 15.33a, b. The observed height difference between α and β atoms in STM images correlates well with the minor difference in DOS associated with the nonequivalent atoms (Fig. 15.33f). The smaller height difference in the STM image measured at $V_b = -0.4$ V with

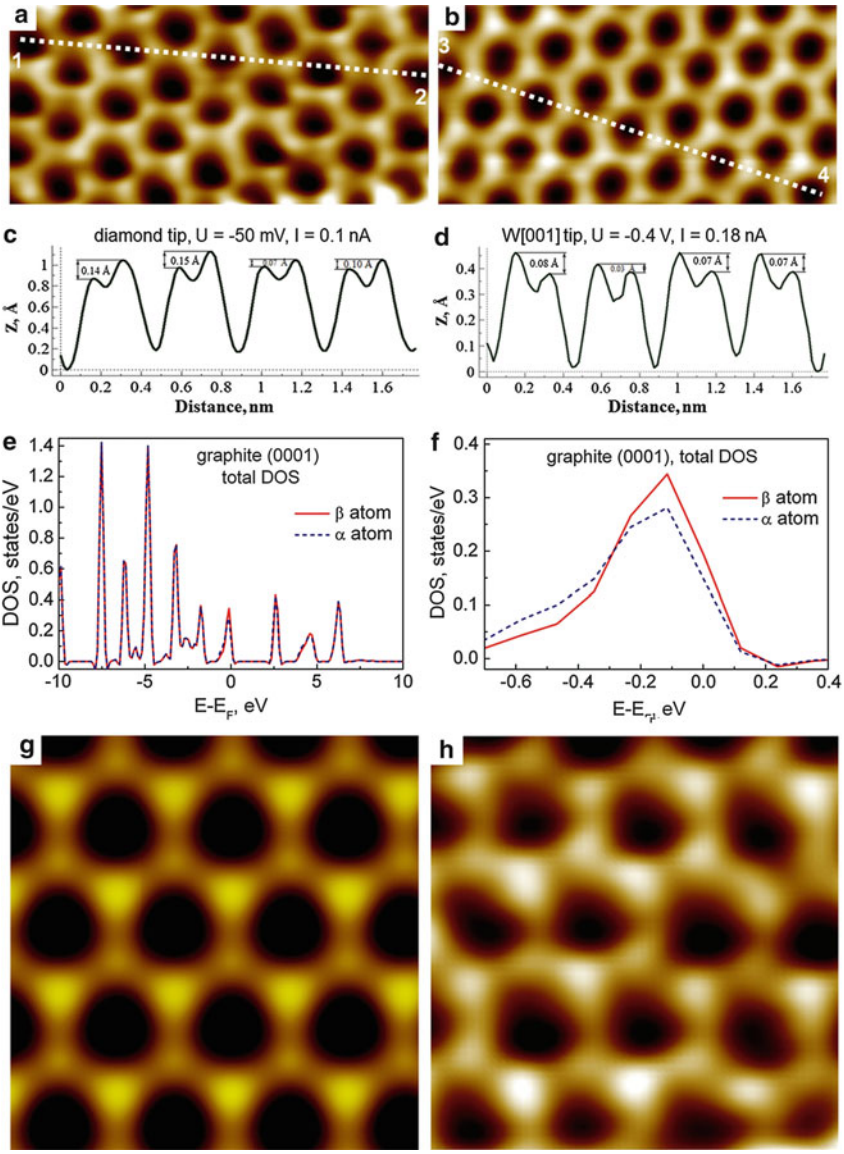


Fig. 15.33 (**a**, **b**) 18 × 9 Å^2 atomically resolved STM images of HOPG(0001) measured with a diamond probe at $V_b = -50$ mV and $I = 0.1$ nA (b) and a [001]-oriented single crystalline W probe at $V_b = -0.4$ V and $I = 0.18$ nA (**b**). (**c**, **d**) Cross sections 1–2 (**c**) and 3–4 (**d**) of the images in panels (**a**) and (**b**), respectively. (**e**, **f**) Total density of electron states associated with the α and β atoms of a graphite (0001) surface. (**g**, **h**) Comparison of the 9 × 9 Å^2 calculated electron density distribution map in the energy range from E_F-0.2 eV to E_F (g) and the experimental STM image measured on HOPG(0001) with the diamond probe at $V_b = -50$ mV and $I = 0.8$ nA (h). Both images show nonequivalence of the α and β atoms in accordance with the DOS shown in panels (**e**) and (**f**) (Panels (**a**–**f**) are reprinted with permission from Ref. [57]. Copyright 2014 by IOP Publishing)

the W[001] tip (Fig. 15.33b, d) is in agreement with the decreasing difference in the DOS integrated over the corresponding energy range.

Figure 15.33g, h shows a comparison of the HOPG(0001) STM image resolved using the conductive diamond tip (Fig. 15.33h) and the calculated charge density map corresponding to the surface electron states near E_F (Fig. 15.33g). Both images demonstrate different contrast on α and β atoms. The DOS (Fig. 15.33e, f) and the charge density map (Fig. 15.33g) were calculated at a tip–sample distance of 4.5 Å where the orbital structure of the tip and surface atoms is not substantially modified by the interaction and relaxations of the tip and surface atoms are minimal [57]. The excellent agreement between experimental and theoretical images (Fig. 15.33g, h) proves that the highest resolution images revealing the honeycomb lattice of the graphite surface were measured with the diamond probe operated at tunneling gaps of 3.5–4.5 Å where the tip did not strongly interact with the surface. This result shows the advantages of the oriented single crystal diamond probes having the *p*-orbitals at the apex: their structure is stable and well defined, while high lateral and vertical resolution can be achieved at larger tunneling gaps comparing to typical tip–sample distances used in experiments with transition metal tips. This allows STM imaging of the surface electronic structure with sub-Ångström lateral and vertical resolution without its modifying by tip–sample interaction.

5.5.7 STM Imaging of the Random Carbon Bond Length Distortions in Quasi-freestanding Graphene Synthesized on SiC(001)

Figure 15.34 demonstrates the picometer lateral resolution achieved in high-resolution STM studies of graphene/SiC(001) system using a [111]-oriented single crystalline tungsten tip [21]. Theoretical calculations performed for the [001]-, [011]- and [111]-oriented tungsten tips interacting with a single helium atom (Fig. 15.14) [139] showed that only front atom of the [111]-oriented tip possesses rotationally symmetric electron density distribution along the tip axis even at small distances between the atoms (Fig. 15.14e). Although the [111]-oriented tungsten tips were found to be the least stable from three possible low-index crystallographic orientations [139], they can produce higher spatial resolution of the surface electronic structure without possible electron orbital structure effects which can be observed with the W[001] tips (Fig. 15.32). Indeed, high spatial resolution has been achieved on the quasi-freestanding graphene grown on SiC(001) with the most stable W[001] tips [24]; however, the highest spatial resolution on this technologically relevant system [183] has been obtained using the [111]-oriented tungsten tip [21].

Atomic resolution STM studies of graphene/SiC(001) reveal the rippled morphology typical of quasi-freestanding graphene weakly interacting with the substrate (Fig. 15.34a). The lateral and vertical dimensions of the ripples are about 30–50 and 1 Å, respectively, which coincide with the theoretically predicted values for a freestanding graphene monolayer [184]. Figure 15.34b, c demonstrates random picoscale distortions of the carbon bond lengths which were also theoretically predicted for the freestanding graphene monolayer [184]. The contrast in atomically resolved STM images shown in Fig. 15.34b, c was adjusted to enhance the bond length distribution in small domain regions. For clarity a distorted hexagon is

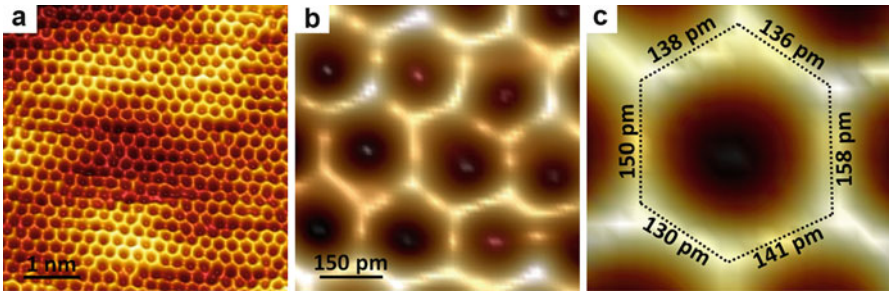


Fig. 15.34 STM images of the graphene synthesized on SiC(001) demonstrating atomic-scale rippling (**a**) and random picoscale distortions of the carbon bond lengths in the graphene honeycomb lattice (**b**, **c**). A distorted hexagon is overlaid on the image; the size of the hexagon sides is indicated for clarity (**c**). The STM images were measured at $V_b = 22$ mV and $I = 70$ pA (**a**) and $V_b = 22$ mV and $I = 65$ pA (**b**, **c**). The images were smoothed by (3 × 3) matrix using the WSxM software [186]

overlaid on the STM image in Fig. 15.34c. The picometer lateral resolution obtained in the RT STM experiments (Fig. 15.34) corresponds to the best standards of SPM research and can be compared with the resolution achieved in the recent AFM studies [185].

5.6 Conclusions and Future Perspective

The spatial resolution on the level of individual electron orbitals corresponds to the ultimate resolution which can be achieved in STM experiments. During the last decade, STM studies demonstrating selective visualization of individual electron orbitals and subatomic spatial resolution have been published. However, most of the SPM studies carried out with subatomic resolution demonstrate probing the tip atomic orbitals by the surface electron orbitals. The distance-dependent experiments carried out using the [001]-oriented tungsten tip on HOPG(0001) [22–24] and the STM data obtained with the diamond [57]- and [111]-oriented tungsten probes [21] suggest the way to reverse the situation and reach higher spatial resolution of the studied surfaces: one can use STM tips having *p*-orbitals at the apex atom or *d*-metal tips with electron states rotationally symmetric along the *z*-axis at the front atom (e.g., [111]-oriented tungsten probes keeping symmetric charge distribution at the apex atom even at small tunneling gaps).

The latest theoretical and experimental results show that direct STM imaging of the intra-atomic orbital structures or selective imaging of the surface electron orbitals can only be achieved at finely adjusted bias voltages and tip–sample distances which can be feasible using stable single crystalline tips producing single asperity at the apex. For further development of the electron orbital imaging capability, stability of the tip–sample separation should be maintained at the level of 1 pm or below.

Finally, several important reasons for developing selective electron orbital imaging capability with precise control of the tunneling gap can be emphasized.

The first is related to developing probes with controllable electron orbital structure for picometer-scale STM imaging. This is especially critical for investigations of the atomic-scale systems of potential practical importance (e.g., graphene or insulating and conducting monolayers on metallic and semiconducting substrates). Then, the ability to perform STM imaging using electron orbitals with certain m can be important for development of spin-polarized STM. Indeed, it has been shown [176] that spin direction of individual atoms can be mapped via spin-polarized orbitals with different orbital momentum projections on the quantization axes (namely, d_z^2- and $d_{xz,yz}$-orbitals). Furthermore, selective imaging of atomic orbitals is related to development of chemical-selective imaging. There are examples of the chemical-selective STM imaging achieved at fixed bias voltages [14, 34, 171, 173]. This could take place because of modification of the PDOS associated with the surface atoms at small tunneling gaps because of overlap of the tip and surface atomic orbitals. The detailed understanding of the PDOS redistributions in a tunneling junction and controlled chemical-selective imaging at the atomic scale can only be achieved with accurate control of the tip–surface distance in STM experiments with well-characterized tips.

Acknowledgments This work was supported by the Russian Academy of Sciences, Russian Foundation for Basic Research (grants № 11-02-01256, 14-02-01234, 11-02-01253, 14-02-00949, 13-02-00781) and Marie Curie International Incoming Fellowship project within the 7th European Community Framework Programme. The author is very grateful to S. N. Molotkov, S. I. Bozhko, S. S. Nazin, V. N. Semenov, A. M. Ionov, V. Yu. Aristov, M. G. Lazarev, N. N. Orlova, A. N. Myagkov, K. N. Eltsov, A. N. Klimov, V. M. Shevlyuga, I. V. Shvets, S. Murphy, S. A. Krasnikov, O. Lübben, B. E. Murphy, K. Radican, A. L. Vazquez de Parga, and F. J. Giessibl for their help and fruitful discussions.

References

1. Binnig G, Rohrer H, Gerber C, Weibel E (1982) Tunneling through a controllable vacuum gap. Appl Phys Lett 40(2):178–180
2. Binnig G, Rohrer H (1982) Scanning tunnelling microscopy. Helv Phys Acta 55(6):726–735
3. Binnig G, Quate CF, Gerber C (1986) Atomic force microscope. Phys Rev Lett 56(9):930–933
4. Binnig G, Rohrer H, Gerber C, Weibel E (1982) Surface studies by scanning tunneling microscopy. Phys Rev Lett 49(1):57–61
5. Eigler DM, Schweizer EK (1990) Positioning single atoms with a scanning tunneling microscope. Nature 344(6266):524–526
6. Crommie MF, Lutz CP, Eigler DM (1993) Confinement of electrons to quantum corrals on a metal surface. Science 262(5131):218–220
7. Stroscio JA, Celotta RJ (2004) Controlling the dynamics of a single atom in lateral atom manipulation. Science 306(5694):242–247
8. Walsh MA, Hersam MC (2009) Atomic-scale templates patterned by ultrahigh vacuum scanning tunnelling microscopy on silicon. Annu Rev Phys Chem 60:193–216
9. Khajetoorians AA, Wiebe J, Chilian B, Wiesendanger R (2012) Realizing all-spin–based logic operations atom by atom. Science 332(6033):1062–1064
10. Khajetoorians AA, Wiebe J, Chilian B, Lounis S, Blügel S, Wiesendanger R (2012) Atom-by-atom engineering and magnetometry of tailored nanomagnets. Nat Phys 8(6):497–503

11. Krasnikov SA, Lübben O, Murphy BE, Bozhko SI, Chaika AN, Sergeeva NN, Bulfin B, Shvets IV (2013) Writing with atoms: oxygen adatoms on the MoO_2/Mo(110) surface. Nano Res 6(12):929–937
12. Stipe BC, Rezaei MA, Ho W (1998) Single-molecule vibrational spectroscopy and microscopy. Science 280(5370):1732–1735
13. Feenstra RM, Stroscio JA, Tersoff J, Fein AP (1987) Atom-selective imaging of the GaAs (110) surface. Phys Rev Lett 58(12):1192–1195
14. Schmid M, Stadler H, Varga P (1993) Direct observation of surface chemical order by scanning tunneling microscopy. Phys Rev Lett 70(10):1441–1444
15. Wiesendanger R, Güntherodt H-J, Güntherodt G, Gambino RJ, Ruf R (1990) Observation of vacuum tunneling of spin-polarized electrons with the scanning tunneling microscope. Phys Rev Lett 65(2):247–250
16. Wiesendanger R, Shvets IV, Bürgler D, Tarrach G, Güntherodt HJ, Coey JMD, Gräser S (1992) Topographic and magnetic-sensitive scanning tunneling microscope study of magnetite. Science 255(5044):583–586
17. Wiesendanger R (2009) Spin mapping at the nanoscale and atomic scale. Rev Mod Phys 81(4):1495–1550
18. Binnig G, Rohrer H, Gerber C, Weibel E (1983) (7 × 7) reconstruction on Si(111) resolved in real space. Phys Rev Lett 50(2):120–123
19. Binnig G, Rohrer H, Ch G, Weibel E (1983) (111) facets as the origin of reconstructed Au (110) surfaces. Surf Sci 131(1):L379–L384
20. Gawronski H, Mehlhorn M, Morgenstern K (2008) Imaging phonon excitation with atomic resolution. Science 319(5865):930–933
21. Chaika AN, Molodtsova OV, Zakharov AA, Marchenko D, Sanchez-Barriga J, Varykhalov A, Shvets IV, Aristov VY (2013) Continuous wafer-scale graphene on cubic-SiC(001). Nano Res 6(8):562–570
22. Chaika AN, Nazin SS, Semenov VN, Bozhko SI, Lübben O, Krasnikov SA, Radican K, Shvets IV (2010) Selecting the tip electron orbital for scanning tunneling microscopy imaging with sub-ångström lateral resolution. EPL 92(4):46003
23. Chaika AN, Nazin SS, Semenov VN, Orlova NN, Bozhko SI, Lübben O, Krasnikov SA, Radican K, Shvets IV (2013) High resolution STM imaging with oriented single crystalline tips. Appl Surf Sci 267:219–223
24. Chaika AN, Orlova NN, Semenov VN, Postnova EY, Krasnikov SA, Lazarev MG, Chekmazov SV, Aristov VY, Glebovsky VG, Bozhko SI, Shvets IV (2014) Fabrication of [001]-oriented tungsten tips for high resolution scanning tunneling microscopy. Sci Rep 4:3742. doi:10.1038/srep03742
25. Herz M, Giessibl FJ, Mannhart J (2003) Probing the shape of atoms in real space. Phys Rev B 68(4):045301
26. Chaika AN, Semenov VN, Nazin SS, Bozhko SI, Murphy S, Radican K, Shvets IV (2007) Atomic row doubling in the STM images of Cu(014)-O obtained with MnNi tips. Phys Rev Lett 98(20):206101
27. Murphy S, Radican K, Shvets IV, Chaika AN, Semenov VN, Nazin SS, Bozhko SI (2007) Asymmetry effects in atomically resolved STM images of Cu(014)-O and W(100)-O surfaces measured with MnNi tips. Phys Rev B 76(24):245423
28. Chaika AN, Myagkov AN (2008) Imaging atomic orbitals in STM experiments on a Si(111)-(7 × 7) surface. Chem Phys Lett 453(4–6):217–221
29. Cren T, Serrier-Garcia L, Debontridder F, Roditchev D (2011) Vortex fusion and giant vortex states in confined superconducting condensates. Phys Rev Lett 107(9):097202
30. Hembacher S, Giessibl FJ, Mannhart J, Quate CF (2005) Local spectroscopy and atomic imaging of tunneling current, forces, and dissipation on graphite. Phys Rev Lett 94(5):056101
31. Grim PCM, De Feyter S, Gesquière A, Vanoppen P, Rücker M, Valiyaveettil S, Moessner G, Müllen K, De Schryver FC (1997) Submolecularly resolved polymerization of diacetylene

molecules on the graphite surface observed with scanning tunneling microscopy. Angew Chem Int Ed Engl 36(23):2601–2603
32. den Boer D, Li M, Habets T, Iavicoli P, Rowan AE, Nolte RJM, Speller S, Amabilino DB, De Feyter S, Elemans JAAW (2013) Detection of different oxidation states of individual manganese porphyrins during their reaction with oxygen at a solid/liquid interface. Nat Chem 5(7):621–627
33. Chen CJ (1988) Theory of scanning tunneling spectroscopy. J Vac Sci Technol A 6(2):319–322
34. Chaika AN, Nazin SS, Bozhko SI (2008) Selective STM imaging of oxygen-induced Cu (115) surface reconstructions with tungsten probes. Surf Sci 602(12):2078–2088
35. Binnig G, Rohrer H (1987) Scanning tunneling microscopy – from birth to adolescence. Rev Mod Phys 59(3):615–625
36. Jurczyszyn L, Mingo N, Flores F (1998) Influence of the atomic and electronic structure of the tip on STM images and STS spectra. Surf Sci 402–404:459–463
37. Nagahara LA, Thundat T, Lindsay SM (1989) Preparation and characterization of STM tips for electrochemical studies. Rev Sci Instrum 60(10):3128–3130
38. Iwami M, Uehara Y, Ushioda S (1998) Preparation of silver tips for scanning tunneling microscopy imaging. Rev Sci Instrum 69(11):4010–4011
39. Ibe JP, Bey PP, Brandow SL, Brizzolara RA, Burnham NA, DiLella DP, Lee KP, Marrian CRK, Colton RJ (1990) On the electrochemical etching of tips for scanning tunneling microscopy. J Vac Sci Technol 8(4):3570–3575
40. Nunes G, Amer NM (1993) Atomic resolution scanning tunneling microscopy with a gallium arsenide tip. Appl Phys Lett 63(13):1851–1853
41. Prins MWJ, Jansen R, Van Kempen H (1996) Spin-polarized tunneling with GaAs tips in scanning tunneling microscopy. Phys Rev B 53(12):8105–8113
42. Sutter P, Zahl P, Sutter E, Bernard JE (2003) Energy-filtered scanning tunneling microscopy using a semiconductor tip. Phys Rev Lett 90(16):166101
43. Kohen A, Noat Y, Proslier T, Lacaze E, Aprili M, Sacks W, Roditchev D (2005) Fabrication and characterization of scanning tunneling microscopy superconducting Nb tips having highly enhanced critical fields. Physica C 419(1–2):18–24
44. Murphy S, Osing J, Shvets IV (1999) Atomically resolved p(3×1) reconstruction on the W(100) surface imaged with magnetic tips. J Magn Magn Mater 198–199:686–688
45. Murphy S, Osing J, Shvets IV (1999) Fabrication of submicron-scale manganese-nickel tips for spin-polarized STM studies. Appl Surf Sci 144–145:497–500
46. Wiesendanger R, Bürgler D, Tarrach G, Schaub T, Hartmann U, Güntherodt H-J, Shvets IV, Coey JMD (1991) Recent advances in scanning tunneling microscopy involving magnetic probes and samples. Appl Phy A-Materials Sci Process 53(5):349–355
47. Shvets IV, Wiesendanger R, Bürgler D, Tarrach G, Günterodt H-J, Coey JMD (1992) Progress towards spin-polarized scanning tunneling microscopy. J Appl Phys 71(11):5489–5499
48. Schlenhoff A, Krause S, Herzog G, Wiesendanger R (2010) Bulk Cr tips with full spatial magnetic sensitivity for spin-polarized scanning tunneling microscopy. Appl Phys Lett 97(8):083104
49. Romming N, Hanneken C, Menzel M, Bickel JE, Wolter B, von Bergmann K, Kubetzka A, Wiesendanger R (2013) Writing and deleting single magnetic skyrmions. Science 341(6146):636–639
50. Bode M (2003) Spin-polarized scanning tunnelling microscopy. Rep Prog Phys 66(4): 523–582
51. Decker R, Brede J, Atodiresei N, Caciuc V, Blügel S, Wiesendanger R (2013) Atomic-scale magnetism of cobalt-intercalated graphene. Phys Rev B 87(4):041403(R)
52. Hofmann T, Welker J, Giessibl FJ (2010) Preparation of light-atom tips for scanning probe microscopy by explosive delamination. J Vac Sci Technol B 28(3):C4E28
53. Kaneko R, Oguchi S (1990) Ion-implanted diamond tip for a scanning tunneling microscope. Jpn J Appl Phys 29(9):1854–1855

54. Visser EP, Gerritsen JW, van Enckevort WJP, van Kempen H (1992) Tips for scanning tunneling microscopy made of monocrystalline, semiconducting, chemical vapor deposited diamond. Appl Phys Lett 60(26):3232–3234
55. Albin S, Zheng J, Cooper JB, Fu W, Lavarias AC (1997) Microwave plasma chemical vapor deposited diamond tips for scanning tunneling microscopy. Appl Phys Lett 71(19): 2848–2850
56. Meyer T, Klemenc M, von Kanel H, Ph N (2000) Diamond tips in low temperature scanning tunnelling microscopy. Surf Sci 470(1–2):164–170
57. Grushko V, Lubben O, Chaika AN, Novikov N, Mitskevich E, Chepugov A, Lysenko O, Murphy BE, Krasnikov SA, Shvets IV (2014) Atomically resolved STM imaging with a diamond tip: simulation and experiment. Nanotechnology 25(2):025706
58. Yu ZQ, Wang CM, Du Y, Thevuthasan S, Lyubinetsky I (2008) Reproducible tip fabrication and cleaning for UHV STM. Ultramicroscopy 108(9):873–877
59. Fink H-W (1986) Mono-atomic tips for scanning tunneling microscopy. IBM J Res Dev 30(5):460–465
60. Stroscio JA, Feenstra RM, Fein PA (1987) Local density and long-range screening of adsorbed oxygen atoms on the GaAs(110) surface. Phys Rev Lett 58(16):1668–1671
61. Neddermeyer H, Drechsler M (1988) Electric field-induced changes of W(110) and W(111) tips. J Microsc 152(2):459–466
62. Wintterlin J, Wiechers J, Brune H, Gritsch T, Hofer H, Behm RJ (1989) Atomic-resolution imaging of close-packed metal surfaces by scanning tunneling microscopy. Phys Rev Lett 62(1):59–62
63. Chen CJ (1991) Microscopic view of scanning tunneling microscopy. J Vac Sci Technol A 9(1):44–50
64. Heike S, Hashizume T, Wada Y (1996) In situ control and analysis of the scanning tunneling microscope tip by formation of sharp needles on the Si sample and W tip. J Vac Sci Technol B 14(2):1522–1526
65. Castellanos-Gomez A, Rubio-Bollinger G, Garnica M, Barja S, Vazquez de Parga AL, Miranda R, Agraıt N (2012) Highly reproducible low temperature scanning tunnelling microscopy and spectroscopy with in situ prepared tips. Ultramicroscopy 122:1–5
66. Biegelsen DK, Ponce FA, Tramontana JC, Koch SM (1987) Ion milled tips for scanning tunneling microscopy. Appl Phys Lett 50(11):696–698
67. Biegelsen DK, Ponce FA, Tramontana JC (1989) Simple ion milling preparation of <111> tungsten tips. Appl Phys Lett 54(13):1223–1225
68. Morishita S, Okuyama F (1991) Sharpening of monocrystalline molybdenum tips by means of inert-gas ion sputtering. J Vac Sci Technol A 9(1):167–169
69. Eltsov KN, Shevlyuga VM, Yurov VY, Kvit AV, Kogan MS (1996) Sharp tungsten tips prepared for STM study of deep nanostructures in UHV. Phys Low-Dim Struct 9–10:7–14
70. Hansma PK, Tersoff J (1987) Scanning tunneling microscopy. J Appl Phys 61(2):R1–R23
71. Demuth JE, Koehler U, Hamers RJ (1988) The STM learning curve and where it may take us. J Microsc 152(2):299–316
72. Kuk Y, Silverman PJ (1986) Role of tip structure in scanning tunneling microscopy. Appl Phys Lett 48(23):1597–1599
73. Dai H, Hafner JH, Rinzler AG, Colbert DT, Smalley RE (1996) Nanotubes as nanoprobes in scanning probe microscopy. Nature 384(6605):147–150
74. Kelly KF, Sarkar D, Hale GD, Oldenburg SJ, Halas NJ (1996) Threefold electron scattering on graphite observed with C60-adsorbed STM tips. Science 273(5280):1371–1373
75. Repp J, Meyer G, Stojkovic SM, Gourdon A, Joachim C (2005) Molecules on insulating films: scanning tunneling microscopy imaging of individual molecular orbitals. Phys Rev Lett 94(2):026803
76. Deng ZT, Lin H, Ji W, Gao L, Lin X, Cheng ZH, He XB, Lu JL, Shi DX, Hofer WA, Gao H-J (2006) Selective analysis of molecular states by functionalized scanning tunneling microscopy tips. Phys Rev Lett 96(15):156102

77. Temirov R, Soubatch S, Neucheva O, Lassise AC, Tautz FS (2008) A novel method achieving ultra-high geometrical resolution in scanning tunnelling microscopy. New J Phys 10(5):053012
78. Weiss C, Wagner C, Kleimann C, Rohlfing M, Tautz FS, Temirov R (2010) Imaging Pauli repulsion in scanning tunneling microscopy. Phys Rev Lett 105(8):086103
79. Gross L, Moll N, Mohn F, Curioni A, Meyer G, Hanke F, Persson M (2011) High-resolution molecular orbital imaging using a *p*-wave STM tip. Phys Rev Lett 107(8):086101
80. Cheng Z, Du S, Guo W, Gao L, Deng Z, Jiang N, Guo H, Tang H, Gao H-J (2011) Direct imaging of molecular orbitals of metal phthalocyanines on metal surfaces with an O_2-functionalized tip of a scanning tunneling microscope. Nano Res 4(6):523–530
81. Martinez JI, Abad E, Gonzalez C, Flores F, Ortega J (2012) Improvement of scanning tunneling microscopy resolution with H-sensitized tips. Phys Rev Lett 108(24):246102
82. Mohn F, Gross L, Moll N, Meyer G (2012) Imaging the charge distribution within a single molecule. Nat Nanotechnol 7(4):227–231
83. Tromp RM, Van Loenen EJ, Demuth JE, Lang ND (1988) Tip electronic structure in scanning tunneling microscopy. Phys Rev B 37(15):9042–9045
84. Chiutu C, Sweetman AM, Lakin AJ, Stannard A, Jarvis S, Kantorovich L, Dunn JL, Moriarty P (2012) Precise orientation of a single C60 molecule on the tip of a scanning probe microscope. Phys Rev Lett 108(26):268302
85. Lakin AJ, Chiutu C, Sweetman AM, Moriarty P, Dunn JL (2013) Recovering molecular orientation from convoluted orbitals. Phys Rev B 88(3):035447
86. Fink H-W, Stocker W, Schmid H (1990) Coherent point source electron beams. J Vac Sci Technol B 8(8):1323–1324
87. Ottaviano L, Lozzi L, Santucci S (2003) Scanning Auger microscopy study of W tips for scanning tunneling microscopy. Rev Sci Instrum 74(7):3368
88. Kirakosian A, Bennewitz R, Crain JN, Fauster T, Lin J-L, Petrovykh DY, Himpsel FJ (2001) Atomically accurate Si grating with 5.73 nm period. Appl Phys Lett 79(11):1608–1610
89. Chaika AN, Fokin DA, Bozhko SI, Ionov AM, Debontridder F, Dubost V, Cren T, Roditchev D (2009) Regular stepped structures on clean Si(hhm)-7 × 7 surfaces. J Appl Phys 105(3):034304
90. Chaika AN, Fokin DA, Bozhko SI, Ionov AM, Debontridder F, Dubost V, Cren T, Roditchev D (2009) Atomic structure of a regular Si(223) triple step staircase. Surf Sci 603(5):752–761
91. Chaika AN, Semenov VN, Glebovskiy VG, Bozhko SI (2009) Scanning tunneling microscopy with single crystal W[001] tips: high resolution studies of Si(557)5 × 5 surface. Appl Phys Lett 95(17):173107
92. Takayanagi K, Tanishiro Y, Takahashi M, Takahashi S (1985) Structural analysis of Si(111)-(7 × 7) by UHV-transmission electron diffraction and microscopy. J Vac Sci Technol A 3(3):1502–1506
93. Wang YL, Gao H-J, Guo HM, Liu HW, Batyrev IG, McMahon WE, Zhang SB (2004) Tip size effect on the appearance of a STM image for complex surfaces: theory versus experiment for Si(111)-(7 × 7). Phys Rev B 70(7):073312
94. Hamers RJ, Tromp RM, Demuth JE (1986) Surface electronic structure of Si(111)-(7 × 7) resolved in real space. Phys Rev Lett 56(18):1972–1975
95. Tromp RM, Hamers RJ, Demuth JE (1986) Atomic and electronic contributions to Si(111)-(7 × 7) scanning tunneling-microscopy images. Phys Rev B 34(2):1388–1391
96. Hamers RJ, Tromp RM, Demuth JE (1987) Electronic and geometric structure of Si(111)-(7 × 7) and Si(001) surfaces. Surf Sci 181(1–2):346–355
97. Paz O, Brihuega I, Gomez-Rodriguez JM, Soler JM (2005) Tip and surface determination from experiments and simulations of scanning tunneling microscopy and spectroscopy. Phys Rev Lett 94(5):056103
98. Dubois M, Perdigao L, Delerue C, Allan G, Grandidier B, Deresme D, Stievenard D (2005) Scanning tunneling microscopy and spectroscopy of reconstructed Si(100) surfaces. Phys Rev B 71(16):165322

99. Hamers RJ, Tromp RM, Demuth JE (1987) Scanning tunneling microscopy of Si(001). Phys Rev B 34(8):5343–5357
100. Wolkow RA (1992) Direct observation of an increase in buckled dimmers on Si(001) at low temperatures. Phys Rev Lett 68(17):2636–2639
101. Garleff JK, Wenderoth M, Sauthoff K, Ulbrich RG, Rohlfing M (2004) 2 × 1 reconstructed Si(111) surface: STM experiments versus ab initio calculations. Phys Rev B 70(24):245424
102. Zotti LA, Hofer WA, Giessibl FJ (2006) Electron scattering in scanning probe microscopy experiments. Chem Phys Lett 420(1–3):177–182
103. Hallmark V, Chiang S, Rabalt J, Swalen J, Wilson R (1987) Observation of atomic corrugation on Au(111) by scanning tunneling microscopy. Phys Rev Lett 59(25):2879–2882
104. Wintterlin J, Brune H, Hofer H, Behm R (1988) Atomic scale characterization of oxygen adsorbates on Al(111) by scanning tunneling microscopy. Appl Phys A 47(1):99–102
105. Clarke ARH, Pethica JB, Nieminen JA, Besenbacher F, Lægsgaard E, Stensgaard I (1996) Quantitative scanning tunneling microscopy at atomic resolution: influence of forces and tip configuration. Phys Rev Lett 76(8):1276–1279
106. Bobrov K, Mayne AJ, Dujardin G (2001) Atomic-scale imaging of insulating diamond through resonant electron injection. Nature 413(6856):616–619
107. Castell MR, Dudarev SL, Briggs GAD, Sutton AP (1999) Unexpected differences in the surface electronic structure of NiO and CoO observed by STM and explained by first-principles theory. Phys Rev B 59(11):7342–7345
108. Repp J, Meyer G, Paavilainen S, Olsson FE, Persson M (2005) Scanning tunneling spectroscopy of Cl vacancies in NaCl films: strong electron-phonon coupling in double-barrier tunneling junctions. Phys Rev Lett 95(22):225503
109. Olsson FE, Paavilainen S, Persson M, Repp J, Meyer G (2007) Multiple charge states of Ag atoms on ultrathin NaCl films. Phys Rev Lett 98(17):176803
110. Olsson FE, Persson M, Repp J, Meyer G (2005) Scanning tunneling microscopy and spectroscopy of NaCl overlayers on the stepped Cu(311) surface: experimental and theoretical study. Phys Rev B 71(7):075419
111. Schoiswohl J, Agnoli S, Xu B, Surnev S, Sambi M, Ramsey MG, Granozzi G, Netzer FP (2005) Growth and thermal behaviour of NiO nanolayers on Pd(100). Surf Sci 599(1–3): 1–13
112. Caffio M, Atrei A, Cortigiani B, Rovida G (2006) STM study of the nanostructures prepared by deposition of NiO on Ag(001). J Phys Condens Matter 18:2379–2384
113. Steurer W, Allegretti F, Surnev S, Barcaro G, Sementa L, Negreiros F, Fortunelli A, Netzer FP (2011) Metamorphosis of ultrathin Ni oxide nanostructures on Ag(100). Phys Rev B 84(11):115446
114. Barth JV, Costantini G, Kern K (2005) Engineering atomic and molecular nanostructures at surfaces. Nature 437(7059):671–679
115. Gambardella P, Stepanow S, Dmitriev A, Honolka J, de Groot FMF, Lingenfelder M, Gupta SS, Sarma DD, Bencok P, Stanescu S, Clair S, Pons S, Lin N, Seitsonen AP, Brune H, Barth JV, Kern K (2009) Supramolecular control of the magnetic anisotropy in two-dimensional high-spin Fe arrays at a metal interface. Nat Mater 8(3):189–193
116. Krasnikov SA, Beggan JP, Sergeeva NN, Senge MO, Cafolla AA (2009) Ni(II) porphine nanolines grown on a Ag(111) surface at room temperature. Nanotechnology 20(13):135301
117. Moriarty PJ (2010) Fullerene adsorption on semiconductor surfaces. Surf Sci Rep 65(7):175–227
118. Krasnikov SA, Doyle CM, Sergeeva NN, Preobrajenski AB, Vinogradov NA, Sergeeva YN, Zakharov AA, Senge MO, Cafolla AA (2011) Formation of extended covalently bonded Ni porphyrin networks on the Au(111) surface. Nano Res 4(4):376–384
119. Krasnikov SA, Bozhko SI, Radican K, Lubben O, Murphy BE, Vadapoo SR, Han-Chun W, Abid M, Semenov VN, Shvets IV (2011) Self-assembly and ordering of C60 on the WO2/W(110) surface. Nano Res 4(2):194–203

120. Bozhko SI, Krasnikov SA, Lubben O, Murphy BE, Radican K, Semenov VN, Wu H-C, Bulfin B, Shvets IV (2011) Rotational transitions in a C60 monolayer on the WO2/W(110) surface. Phys Rev B 84(19):195412
121. Mugarza A, Krull C, Robles R, Stepanow S, Ceballos G, Gambardella P (2011) Spin coupling and relaxation inside molecule–metal contacts. Nat Commun 2:490. doi:10.1038/ncomms1497
122. Swart I, Sonnleitner T, Repp J (2011) Charge state control of molecules reveals modification of the tunneling barrier with intramolecular contrast. Nano Lett 11(4):1580–1584
123. Beggan JP, Krasnikov SA, Sergeeva NN, Senge MO, Cafolla AA (2012) Control of the axial coordination of a surface-confined manganese(III) porphyrin complex. Nanotechnology 23(23):235606
124. Murphy BE, Krasnikov SA, Cafolla AA, Sergeeva NN, Vinogradov NA, Beggan JP, Lübben O, Senge MO, Shvets IV (2012) Growth and ordering of Ni(II) diphenylporphyrin monolayers on Ag(111) and Ag/Si(111) studied by STM and LEED. J Phys Condens Matter 24(4):045005
125. Bazarnik M, Brede J, Decker R, Wiesedanger R (2013) Tailoring molecular self-assembly of magnetic phthalocyanine molecules on Fe- and Co-intercalated graphene. ACS Nano 7(12):11341–11349
126. Garnica M, Stradi D, Barja S, Calleja F, Díaz C, Alcamí M, Martín N, Vázquez de Parga AL, Martín F, Miranda R (2013) Long-range magnetic order in a purely organic 2D layer adsorbed on epitaxial graphene. Nat Phys 9(6):368–374
127. Swart I, Gross L, Liljeroth P (2011) Single-molecule chemistry and physics explored by low-temperature scanning probe microscopy. Chem Commun 47(32):9011–9023
128. Tersoff J, Hamann DR (1983) Theory and application for the scanning tunneling microscope. Phys Rev Lett 50(25):1998–2001
129. Tersoff J, Hamann DR (1985) Theory of the scanning tunneling microscope. Phys Rev B 31(2):805–813
130. Hofer WA, Garcia-Lekue A, Brune H (2004) The role of surface elasticity in giant corrugations observed by scanning tunneling microscopes. Chem Phys Lett 397(4–6):354–359
131. Tersoff J, Lang ND (1990) Tip-dependent corrugation of graphite in scanning tunneling microscopy. Phys Rev Lett 65(9):1132–1135
132. Chen CJ (1990) Origin of atomic resolution on metal surfaces in scanning tunneling microscopy. Phys Rev Lett 65(4):448–451
133. Chen CJ (1990) Tunneling matrix elements in three-dimensional space: the derivative rule and the sum rule. Phys Rev B 42(14):8841–8857
134. Chen CJ (1992) Effects of $m \neq 0$ tip states in scanning tunneling microscopy: the explanation of corrugation reversal. Phys Rev Lett 69(11):1656–1659
135. Sacks W (2000) Tip orbitals and the atomic corrugation of metal surfaces in scanning tunneling microscopy. Phys Rev B 61(11):7656–7668
136. Suominen I, Nieminen J, Markiewicz RS, Bansil A (2011) Effect of orbital symmetry of the tip on scanning tunneling spectra of $Bi_2Sr_2CaCu_2O_{8+\delta}$. Phys Rev B 84(1):014528
137. Polok M, Fedorov DV, Bagrets A, Zahn P, Mertig I (2011) Evaluation of conduction eigenchannels of an adatom probed by an STM tip. Phys Rev B 83(24):245426
138. Choi H, Longo RC, Huang M, Randall JN, Wallace RM, Cho K (2013) A density-functional theory study of tip electronic structures in scanning tunneling microscopy. Nanotechnology 24(10):105201
139. Wright CA, Solares SD (2013) Computational study of tip apex symmetry characterization in high-resolution atomic force microscopy. J Phys D Appl Phys 46(15):155307
140. Hembacher S, Giessibl FJ, Mannhart J (2004) Force microscopy with light-atom probes. Science 305(5682):380–383
141. Wright CA, Solares SD (2011) On mapping subångström electron clouds with force microscopy. Nano Lett 11(11):5026–5033

142. Wright CA, Solares SD (2012) Imaging of subatomic electron cloud interactions: effect of higher harmonics processing in noncontact atomic force microscopy. Appl Phys Lett 100(16):163104
143. Binnig G, Garcia N, Rohrer H, Soler JM, Flores F (1984) Electron-metal-surface interaction potential with vacuum tunneling: observation of the image force. Phys Rev B 30(8): 4816–4818
144. Zheng NJ, Tsong IST (1990) Resonant-tunneling theory of imaging close-packed metal surfaces by scanning tunneling microscopy. Phys Rev B 41(5):2671–2677
145. Hofer WA, Foster AS, Shluger AL (2003) Theories of scanning probe microscopes at the atomic scale. Rev Mod Phys 75(4):1287–1331
146. Hofer WA (2003) Challenges and errors: interpreting high resolution images in scanning tunneling microscopy. Prog Surf Sci 71(5–8):147–183
147. Jelınek P, Shvec M, Pou P, Perez R, Chab V (2008) Tip-induced reduction of the resonant tunneling current on semiconductor surfaces. Phys Rev Lett 101(17):176101
148. Bryant A, Smith DPE, Binnig G, Harrison WA, Quate CF (1986) Anomalous distance dependence in scanning tunneling microscopy. Appl Phys Lett 49(15):936–938
149. Bode M, Pascal R, Wiesendanger R (1996) Distance-dependent STM-study of the W(110)/C-R(15 × 3) surface. Z Phys B 101(1):103–107
150. Wiesendanger R, Bode M, Pascal R, Allers W, Schwarz UD (1996) Issues of atomic-resolution structure and chemical analysis by scanning probe microscopy and spectroscopy. J Vac Sci Technol A 14(3):1161–1167
151. Klijn J, Sacharow L, Meyer C, Blugel S, Morgenstern M, Wiesendanger R (2003) STM measurements on the InAs(110) surface directly compared with surface electronic structure calculations. Phys Rev B 68(20):205327
152. Calleja F, Arnau A, Hinarejos JJ, Vazquez de Parga AL, Hofer WA, Echenique PM, Miranda R (2004) Contrast reversal and shape changes of atomic adsorbates measured with scanning tunneling microscopy. Phys Rev Lett 92(20):206101
153. Blanco JM, González C, Jelínek P, Ortega J, Flores F, Pérez R, Rose M, Salmeron M, Méndez J, Wintterlin J, Ertl G (2005) Origin of contrast in STM images of oxygen on Pd(111) and its dependence on tip structure and tunneling parameters. Phys Rev B 71(11):113402
154. Woolcot T, Teobaldi G, Pang CL, Beglitis NS, Fisher AJ, Hofer WA, Thornton G (2012) Scanning tunneling microscopy contrast mechanisms for TiO_2. Phys Rev Lett 109(15):156105
155. Mönig H, Todorovic M, Baykara MZ, Schwendemann TC, Rodrigo L, Altman EI, Pérez R, Schwarz UD (2013) Understanding scanning tunneling microscopy contrast mechanisms on metal oxides: a case study. ACS Nano 7(11):10233–10244
156. Ondracek M, Pou P, Rozsıval V, Gonzalez C, Jelınek P, Perez R (2011) Forces and currents in carbon nanostructures: are we imaging atoms? Phys Rev Lett 106(17):176101
157. Ondracek M, Gonzalez C, Jelınek P (2012) Reversal of atomic contrast in scanning probe microscopy on (111) metal surfaces. J Phys Condens Matter 24(8):084003
158. Whangbo M-H, Liang W, Ren J, Magonov SN, Wawkuschewski AJ (1994) Structural and electronic properties of graphite and graphite intercalation compounds MCs (M = K, Rb, Cs) governing their scanning tunneling microscopy images. J Phys Chem 98(31):7602–7607
159. Teobaldi G, Inami E, Kanasaki J, Tanimura K, Shluger AL (2012) Role of applied bias and tip electronic structure in the scanning tunneling microscopy imaging of highly oriented pyrolytic graphite. Phys Rev B 85(8):085433
160. Chaika AN, Bozhko SI (2005) Atomic structure of the Cu(410)-O surface: STM visualization of oxygen and copper atoms. JETP Lett 82(7):416–420
161. Ternes M, Gonzalez C, Lutz CP, Hapala P, Giessibl FJ, Jelınek P, Heinrich AJ (2011) Interplay of conductance, force, and structural change in metallic point contacts. Phys Rev Lett 106(1):016802

162. Scheer E, Agrait N, Cuevas JC, Yeyati AL, Ludoph B, Martin-Rodero A, Bollinger GR, Van Ruitenbeek JM, Urbina C (1998) The signature of chemical valence in the electrical conduction through a single-atom contact. Nature 394(6689):154–157
163. Neel N, Kröger J, Limot L, Palotas K, Hofer WA, Berndt R (2007) Conductance and Kondo effect in a controlled single-atom contact. Phys Rev Lett 98(1):016801
164. Dias LG, Leitão AA, Achete CA, Blum R-P, Niehus H, Capaz RB (2007) Chemical identification in the $Cu_3Au(100)$ surface using scanning tunneling microscopy and first-principles calculations. Surf Sci 601(23):5540–5545
165. Ruan L, Besenbacher F, Stensgaard I, Laegsgaard E (1993) Atom resolved discrimination of chemically different elements on metal surfaces. Phys Rev Lett 70(26):4079–4082
166. Diebold U, Li S-C, Schmid M (2010) Oxide surface science. Annu Rev Phys Chem 61:129–148
167. Knudsen J, Merte LR, Peng G, Vang RT, Resta A, Laegsgaard E, Andersen JN, Mavrikakis M, Besenbacher F (2010) Low-temperature, CO oxidation on Ni(111) and on a Au/Ni(111) surface alloy. ACS Nano 4(8):4380–4387
168. Baykara MZ, Todorović M, Mönig H, Schwendemann TC, Ünverdi Ö, Rodrigo L, Altman EI, Pérez R, Schwarz UD (2013) Atom-specific forces and defect identification on surface-oxidized Cu(100) with combined 3D-AFM and STM measurements. Phys Rev B 87(15): 155414
169. Gauthier Y, Dolle P, Baudoing-Savois R, Hebenstreit W, Platzgummer E, Schmid M, Varga P (1998) Chemical ordering and reconstruction of $Pt_{25}Co_{75}(100)$: an LEED/STM study. Surf Sci 396(1–3):137–155
170. Hebenstreit W, Ritz G, Schmid M, Biedermann A, Varga P (1997) Segregation and reconstructions of $Pt_xNi_{1-x}(100)$. Surf Sci 388(1–3):150–161
171. Hebenstreit ELD, Hebenstreit W, Schmid P, Varga P (1999) $Pt_{25}Rh_{75}(111)$, (110), and (100) studied by scanning tunneling microscopy with chemical contrast. Surf Sci 441(2–3):441–453
172. Schmid M, Varga P (2002) Segregation and surface chemical ordering – an experimental view on the atomic scale, Chapter 4. In: Woodruff DP (ed) The chemical physics of solid surfaces, vol 10, Surface alloys and Alloy surfaces. Elsevier, Amsterdam, 2002
173. Yashina LV, Püttner R, Volykhov AA, Stojanov P, Riley J, Vassiliev SY, Chaika AN, Dedyulin SN, Tamm ME, Vyalikh DV, Belogorokhov AI (2012) Atomic geometry and electron structure of the $GaTe(10\overline{2})$ surface. Phys Rev B 85(7):075409
174. Hofer WA, Ritz G, Hebenstreit W, Schmid M, Varga P, Redinger J, Podloucky R (1998) Scanning tunneling microscopy of binary-alloy surfaces: is chemical contrast a consequence of alloying? Surf Sci 405(2–3):L514–L519
175. Hofer WA, Redinger J (2000) Scanning tunneling microscopy of binary alloys: first principles calculation of the current for PtX(100) surfaces. Surf Sci 447(1–3):51–61
176. Serrate D, Ferriani P, Yoshida Y, Hla S-W, Menzel M, von Bergmann K, Heinze S, Kubetzka A, Wiesendanger R (2010) Imaging and manipulating the spin direction of individual atoms. Nat Nanotechnol 5(5):350–353
177. Giessibl FJ, Hembacher S, Bielefeldt H, Mannhart J (2000) Subatomic features on the silicon (111)-(7 × 7) surface observed by atomic force microscopy. Science 289(5478):422–425
178. Hug HJ, Lantz MA, Abdurixit A, van Schendel PJA, Hoffmann R, Kappenberger P, Baratoff A (2001) Subatomic features in atomic force microscopy images. Science 29(5513):2509a
179. Giessibl FJ, Bielefeldt H, Hembacher S, Mannhart J (2001) Imaging of atomic orbitals with the atomic force microscope – experiments and simulations. Ann Phys 10(11–12):887–910
180. Huang M, Cuma M, Liu F (2003) Seeing the atomic orbital: first-principles study of the effect of tip termination on atomic force microscopy. Phys Rev Lett 90(25):256101
181. Chen CJ (2006) Possibility of imaging lateral profiles of individual tetrahedral hybrid orbitals in real space. Nanotechnology 17(7):S195–S200

182. Campbellova A, Ondracek M, Pou P, Perez R, Klapetek P, Jelınek P (2011) 'Sub-atomic' resolution of non-contact atomic force microscope images induced by a heterogeneous tip structure: a density functional theory study. Nanotechnology 22(29):295710
183. Aristov VY, Urbanik G, Kummer K, Vyalikh DV, Molodtsova OV, Preobrajenski AB, Zakharov AA, Hess C, Hänke T, Büchner B, Vobornik I, Fujii J, Panaccione G, Ossipyan YA, Knupfer M (2010) Graphene synthesis on cubic SiC/Si wafers: perspectives for mass production of graphene-based electronic devices. Nano Lett 10(3):992–995
184. Fasolino A, Los JH, Katsnelson MI (2007) Intrinsic ripples in graphene. Nature Mater 6(11):858–861
185. Gross L, Mohn F, Moll N, Schuler B, Criado A, Guitian E, Pena D, Gourdon A, Meyer G (2012) Bond-order discrimination by atomic force microscopy. Science 337(6100): 1326–1329
186. Horcas I, Fernandez R, Gomez-Rodriguez JM, Colchero J, Gomez-Herrero J, Baro AM (2007) WSXM: a software for scanning probe microscopy and a tool for nanotechnology. Rev Sci Instrum 78(1):013705

Numerical and Finite Element Simulations of Nanotips for FIM/FEM

16

Moh'd Rezeq, Ahmed E. Ali, and Dirar Homouz

Contents

1 Definition of the Topic 622
2 Overview 622
3 Introduction 623
4 FEM and FIM Setup 626
5 Key Research Findings 628
5.1 Spherical Model of Nanotips 628
6 Results 633
6.1 Hyperboloid Model of Nanotips 637
7 Conclusion 640
References 641

Abstract

Due to their crucial applications in nanotechnology, several methods have been developed for fabricating nanotips. Such nanotips can be fabricated and characterized in the field ion microscope (FIM), and can be tapered down to a single atom apex. As only a top view of the tip apex can be captured and analyzed in the

M. Rezeq (✉)
Department of Applied Mathematics and Sciences and Department of Electrical and Computer Engineering, Khalifa University of Science, Technology and Research (KUSTAR), Abu Dhabi, UAE
e-mail: mohd.rezeq@kustar.ac.ae

A.E. Ali
Department of Electrical and Computer Engineering, Khalifa University of Science, Technology and Research (KUSTAR), Abu Dhabi, UAE

D. Homouz
Department of Applied Mathematics and Sciences, Khalifa University of Science, Technology and Research (KUSTAR), Abu Dhabi, UAE

© Springer-Verlag Berlin Heidelberg 2015

C.S.S.R. Kumar (ed.), *Surface Science Tools for Nanomaterials Characterization*,
DOI 10.1007/978-3-662-44551-8_16

FIM the overall nanotip shape is still undefined. The FIM images or field emission microscope (FEM) images of single-atom tips (SATs) made by different methods have been found to span a wide range of applied voltages for the respective mode. Here we present theoretical and numerical methods to analyze the distribution of the electric field in the vicinity of the nanotip apex that holds the topmost single atom. We use two different geometries for the nanotip apex, spherical and ellipsoidal shapes, to analyze its electric field. We demonstrate that the electric field at the center of the nano-protrusion is still significantly dominated by the nanotip base and enhanced further at the center of the apex by the nanotip protrusion. The analyses explicitly show that nanotips with broad bases produce even less field than some regular tips, at the same applied voltage. This pronounced effect of the tip base accounts for the relatively high voltages needed for imaging some nanotips in FIM or FEM. In addition, the overall nanotip shape can be estimated based on the radius-voltage relationship. This approach helps in the selection of nanotips for particular applications in ion and electron microscopy, nano lithography, nano characterization and other aspects of nanotechnology.

Keywords

Nanotips • Nanofabrication • Field Ion Microscope • Field Emission microscope • Single atom tip • Finite element simulation

1 Definition of the Topic

Developing analytical methods and numerical models to calculate the electric field distribution around the nanotip apex at a certain applied voltage on the tip base will help to estimate the nanotip shape over a mesoscopic scale. Such information about nanotip profile will be crucial for selecting appropriate tips for particular applications in nanotechnology, like nanomaterials characterization and manipulation, multiple probe nano-contacts, low power electron and ion microscopy, and other nanotechnology applications.

2 Overview

Tapered metal needles with a few nanometer apex, commonly referred to as nanotips, are increasingly demanded for various applications in nanotechnology. For instance, nanotips with a single-atom end can be used as a source of self-collimated electron or ion beams. Nanotips are also highly needed in scanning probe microscopy for manipulation and characterization of nanomaterials and molecular scale objects. However, characterizing these nanotips in scanning electron microscopy (SEM) or transmission electron microscopy (TEM) is technically difficult, as the nanotips will be contaminated during the transfer process from the field ion microscope (where they are usually fabricated) to the TEM or SEM machines. Actually, it is feasible to

characterize them in the field ion microscope (FIM) or the field emission microscope (FEM), but only a top view of the tip apex can be captured and analyzed. The FIM images or FEM images of single-atom tips (SATs) made by different methods and reported by different researchers were found to span a wide range of applied voltages for the respective mode (FIM or FEM). Here we present numerical and analytical methods to model the distribution of the electric field in the vicinity of the nanotip apex that holds the topmost single atom. We use two different geometries, spherical and ellipsoidal, for the tip apex to analyze its electric field. We demonstrate that the electric field at the center of the nano-protrusion is still significantly dominated by the tip base even though it is slightly enhanced at the nano-protrusion center. The analyses explicitly show that nanotips with broad bases produce even less field than some regular tips, at the same applied voltage. This pronounced effect of the tip base accounts for the relatively high voltages needed at the imaging threshold field for some nanotips. In addition, the overall nanotip shape can be estimated based on the radius-voltage relationship which helps in the selection of nanotips for specific applications, like ion microscopy and ion lithography, and multiple nano-probe measurements.

3 Introduction

Nanotips with an apex radius of a few nanometers have been increasingly demanded in various fields of nanotechnology. In scanning probe microscopes the image resolution is a direct function of the nanotip end shape, while in electron microscopes the brightness of the electron beam is enhanced dramatically with the decrease of the apex area [1, 2]. Furthermore, such nanotips are also crucial in the characterization and manipulation of nanomaterials and nanostructures [3–14]. Therefore, the improvement of nanotechnology instruments raises the need for well-defined nanotips. However, the most appropriate way for fabricating and characterizing such nanotips is utilizing the capability of the FIM where metal nanotips can be cleaned and then characterized with atomic resolution, before they are set for a sharpening process. A significant progress has been achieved over the last few decades in fabricating ultrasharp tips that terminate with an apex radius in the order of 1 nm and sometimes with a single-atom apex [15–22].

Here are some methods of fabricating nanotip with a single-atom end:

1. Field surface melting and buildup method [15, 16]
2. Annealing, sputtering, and deposition method [17]
3. Pd-covered single-atom tip [18, 19]
4. The spatially controlled field-assisted etching technique [20]
5. Fabrication of super electron-ion source and nano-probe by local electron bombardment [21]

One of the most promising applications of SATs would be for the potential use as coherent and bright electron sources in the lensless electron projection and holography microscope [15, 23, 24]. These kinds of microscopes will be crucial for

characterizing molecules and fragile nanostructures as the energy of the electron beam is small (in the order of 100 eV) compared to SEM and TEM electron beams. Such SATs can also be used to manipulate and characterize molecules, nanomaterials, and nano-devices on flat metal and semiconductor surfaces; thus, the sharpness of the tip at a mesoscopic scale and its aspect ratio are quite important.

These exciting applications of FIM and FEM microscopes have reestablished them as important tools in nanotechnology applications. The theory and mechanisms of FEM and FIM are detailed in several textbooks and journal articles [22, 25, 26].

All of nanotip fabrication methods [15, 16, 19–21] have exhibited a very sharp end that terminates with a single atom, as observed in the field ion microscope (FIM). In the field emission mode, a self-collimated and coherent electron beam with an outstanding brightness can be generated from such SATs [1, 15, 19, 27]. However, observing highly confined ion or electron spots from the last single atom in FIM and FEM microscopes, respectively, has created a misconception, as these tips are often referred to as extremely sharp or atomically sharp tips. In fact, the results published in the literature revealed that although all of these SATs have similar appearance in FIM and FEM microscopes, the applied voltages needed to generate a threshold imaging field vary broadly. For instance, the field electron emission from SATs made from different initial metals tips was found at voltages to vary from 200 to 1,600 V (negative bias) [28–30]. The field ionization of these SATs was obtained at voltages spanning a wide range, from 1.6 to 7.2 kV (positive bias) [16, 27–30]. In the latter SAT (at 7.2 kV), a neon gas (which has a lower ionization barrier than He) is used for imaging, which means that the applied voltage would be even higher if He gas were used. Presuming that these SATs, reported in the literature, are extremely sharp then the applied voltages required to generate an FEM image (normally a single bright spot) should be at least one order of magnitude less than what has been used for some SATs. The same concept applies to FIM images of SATs. In contrast, some SATs were reported to field emit electrons or ions at voltages even higher than moderate tips (5–10 nm radii without the 1 nm nanotip protrusion). These observations actually raise a legitimate question about how sharp these SATs are.

Characterizing these nanotips experimentally in ultrahigh-resolution microscopes like SEM and TEM is hindered by many technical difficulties. These nanotips are fabricated in ultrahigh vacuum (UHV) FEM and FIM systems. Removing those ultraclean nanotips from a UHV system and transferring them in air to SEM or TEM systems exposes them to the risk of contamination. Tiny amounts, ~1–5 nm layer, of oxide and other contaminants will damage these tips and distort the SEM/TEM characterization process.

Here, we introduce a new method for estimating the nanotip sharpness in situ where they are fabricated. This method utilizes numerical and analytical models of the tip electric field. Since the electric field depends directly on the nanotip shape and the applied voltage, we can extract a simulated picture of the entire tip shape with reasonable accuracy.

Some numerical analysis methods have been used to estimate the overall tip shape and to analyze the tip electric field distribution and its interaction with the surrounding medium for some particular applications, as in the following examples:

Finite element method is used to simulate the near-field enhancement on an atomic force microscope (AFM) metal probe used in near-field scanning optical microscopy (NSOM) [31]. The field enhancement factor is calculated under different situations by changing the wavelength of the incident laser irradiating the tip, the tip sample distance, and the tip geometry. The effect of the sample presence on the field distribution at the tip surface is also simulated. Those observations help in understanding the effect of various parameters on the field enhancement factor, and hence a new scheme to improve near-field nanolithography is proposed [31].

The three-dimensional finite element method is used to characterize nanoscale dual carbon electrodes (DCE) which are used in scanning electrochemical microscopy [32]. The electrodes are modeled as a semielliptical shape with an arbitrary major axis. Finite element method is used to estimate the major axis for each electrode using linear sweep voltammograms (LSV) [32].

Finite element method is also used to investigate nanoscale biosensors. Those sensors are used to detect biological molecules by taking advantage of the dielectrophoretic (DEP) force acting on them. "Immersed finite element method (IFEM)" was developed in this regard to study the interaction between the fluid and deformable particles [33, 34]. This method went through several improvement stages to include other factors such as electrohydrodynamics and molecular interactions [34]. Recently, the "immersed molecular electrokinetic finite element method (IMEFEM)" was introduced in which it includes electrokinetics as well [34]. The method is used to characterize different biosensor designs such as nanotip and coil (NTC) which contains either a single nanowire (SNW) or a dendritic nanotip (DNT) [35, 36]. IMEFEM was used to simulate the electric field distribution for SNW and DNT sensors in order to determine the interaction effect between the sensor and immersed spherical Au nanoparticles with different sizes [36]. For SNW, IMEFEM was used to find the optimum nanowire size to be used in SNW sensors. The DEP forces applied on the immersed nanoparticles was found to increase when reducing the nanowire diameter, thus suggesting a higher retention efficacy. However, this effect was found to be insignificant at larger radial distance from the tip. Moreover, SNW and DNT sensors were compared in terms of concentration and retention efficacy; it was found that DNT produces lower DEP forces than SNW. However, the electric field does not decay quickly compared to SNW for 1 nm Au nanoparticles, thus indicating a higher concentration efficacy for DNT. Moreover, the SNW was found to produce higher DEP forces than the DNT, thus having a higher retention efficacy [33–36].

Finite element electrostatic method was also applied to Kelvin probe force microscopy (KPFM). The cantilever part of the probe is included in the simulation in order to get better agreement between the simulation and experimental results [37]. To numerically characterize the KPFM probe, the capacitance between the probe and the sample was determined from the simulation and then used to calculate the Kelvin voltage. Different cantilever dynamics were studied in the simulation and compared with the experimental data. Results show that considering bending dynamics in the simulated model resulted in the closest agreement between the simulation and experimental data [37].

It is worth indicating that in the above, finite element simulation examples represent the tip and its surrounding medium in the same scale. In the case of nanotips used in FEM/FIM microscopes, the distance between the nanotip and the screen is around 5–6 orders of magnitude larger than the dimensions of the nanotip. Therefore, building an exact model geometry for the simulation process is quite difficult, and the finite element simulation program will take substantially long time to perform the required computations. To overcome this simulation problem, and since we are interested in the electric field distribution in the vicinity of the tip apex, we introduce a new boundary at a reasonable distance from the tip to simulate the potential and the field within that region. This approach will help us to extract the value of the ionization field and emission field at the tip apex, as will be detailed in the upcoming sections.

In the next section we will give a brief description about FEM/FIM microscopes. We will demonstrate that although the fabrication of a SAT, as observed in FEM and FIM, gives an impression that the nanotip is extremely sharp, the overall tip shape at a microscopic scale is found to be considerably larger. Our analyses will help in using FEM/FIM microscopes to select the desired sharp tips for particular applications in STM, like defined atomic contacts with molecules or atoms on a substrate or multiple nano-probe contacts with nanoparticles [38, 39].

4 FEM and FIM Setup

The first tool used for the characterization of ultrasharp tips was the field electron microscope (FEM) (also called field emission microscope) in 1936 with a resolution of a few nanometers followed by the demonstration of atomic resolution through the invention of the field ion microscope (FIM) in 1955, both techniques were developed by Muller [25, 26]. The use of these microscopes is still limited to the characterization of sharp objects, typically less than 0.1 μm in radius, as a high electric field (in the range of 5 and 50 V/nm for FEM and FIM, respectively) is required for the imaging process.

The design of the FEM/FIM microscope is quite simple, where a sharp tip is placed in front of a phosphorus screen, usually supported by microchannel plates (MCPs) to intensify the image, all are placed in an ultrahigh vacuum chamber, as depicted in Fig. 16.1. In the FEM mode the tip is negatively biased where electrons are ejected from the tip at a high electric field, around 5 V/nm. In FIM mode an inert gas, like Helium, is introduced in the UHV chamber while the tip is exposed to a high voltage, 5–20 KV. The extremely high electric field on the apex, around 5 V/Angstrom, is sufficient to ionize the He atoms in the vicinity of the tip and then expel them toward the screen.

This process results in an atomic resolution image of the surface structure of the tip apex; see Fig. 16.2a. On the other hand, the image in FEM is simply formed from the electrons emanated from atomic planes of lower work functions, where different atomic facets have different local work functions and local fields, which results in bright and dark areas in the field emission pattern; see Fig. 16.2b. Therefore, the

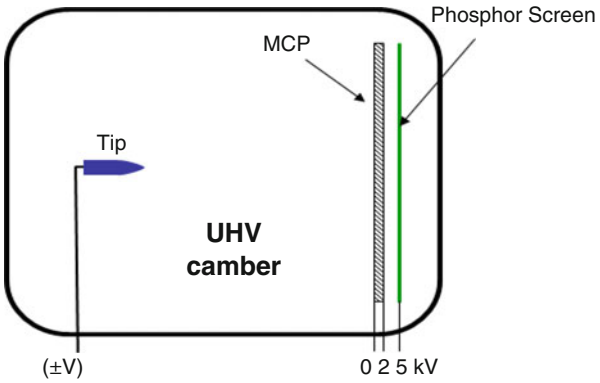


Fig. 16.1 A schematic diagram of FEM/FIM experimental setup

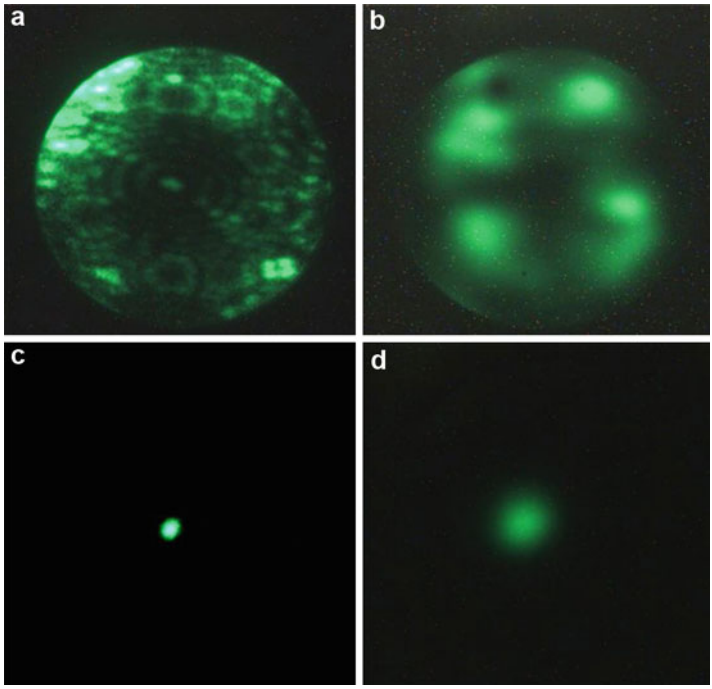


Fig. 16.2 (**a**) A FIM image of a nanotip revealing the surface structure of the tip. (**b**) A FEM image of the same tip showing the field emission pattern on the tip. (**c**) A FIM image of a SAT prepared by sharpening down the tip shown in (**a**). (**d**) A FEM of the same SAT

FEM can be used to characterize the tip shape, orientation, and crystallography. However, after sharpening the tip down to a single atom, only the last topmost atom will be observed in FIM, as shown in Fig. 16.2c, and this will emit electrons in FEM mode and produce a highly collimated and bright electron beam, as shown in Fig. 16.2d.

5 Key Research Findings

5.1 Spherical Model of Nanotips

The threshold electric field E_0 on the tip apex is usually given by [26]

$$E_0 = \frac{V}{\beta R} \tag{16.1a}$$

where V is the tip applied voltage, R is the tip radius, and β is a characteristic factor that depends on the tip-screen geometry [40] as follows:

$$\beta = \frac{1}{2}\ln\left(\frac{4s}{R}\right), \tag{16.1b}$$

where s is the distance between the tip and the screen and R is the radius of the blunt tip (or the tip base). Since β changes slightly with the tip-screen configuration, one can infer that E_0 changes strictly with the tip radius R. It has been demonstrated that SATs can generate field emission confined to the single-atom end when the underneath apex radius is in the range of 1 nm or less [41, 42].

In this section, for feasible analytical calculations, we will assume a hemispherical shape for nanotips, which are most likely elliptical. However, in the case of nanotips having pyramid-like or conical apex, the hemispherical model will represent the average size of the nanotip apex. Even though we are highlighting the features of the SATs, there is no need to show such a single atom in the model. What really matters here is the geometry of the tip shape below this atom. This can be seen in Fig. 16.3 which presents experimental data for a blunt tip (Fig. 16.3a) before the formation of a nanotip. Figure 16.3b shows the FIM image of a SAT after the tip sharpening process, and Fig. 16.3c shows the corresponding FEM image. Figure 16.3d shows the image of the apex of the same nanotip after removing the topmost atom. This image represents a nanotip structure with a radius of ~7.7 nm (Fig. 16.3e).

Therefore, our mathematical model will consider a nanotip with 1 nm radius sitting on various bases. The model is schematically depicted in Fig. 16.4. The nanotip is represented by a hemisphere of a 1 nm radius placed on the top of a larger spherical base. We will perform some analysis to calculate the electric field in the vicinity of the apex and then use a finite element method software tool (COMSOL), to numerically find the field distribution for the same nanotip shape.

5.1.1 Analytical Modeling

The solution of Laplace's equation for the geometry in Fig. 16.4 cannot be obtained directly. Our approach for solving this problem is based on extrapolating the behavior of the electric field along a curved path passing through the apex and concentric with the tip base (the dotted curve in Fig. 16.4). We can readily predict that the electric field is perpendicular to the tip surface at the center of the nanotip

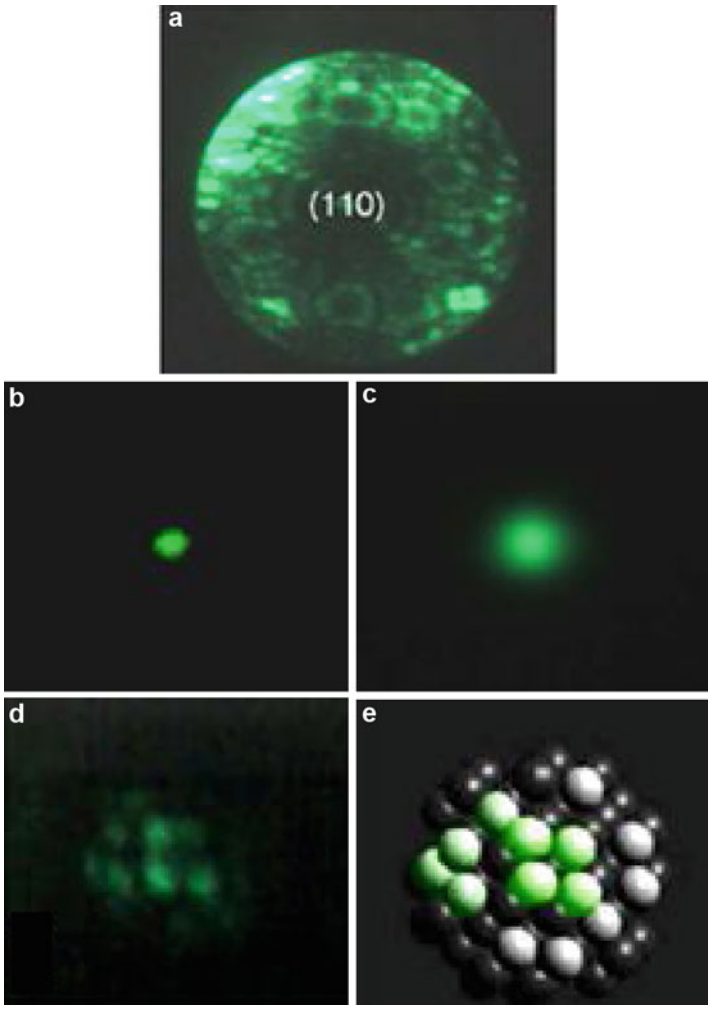


Fig. 16.3 A FIM image of a W(110) tip base, $R \sim 15$ nm, before the formation of the SAT. (**b**) A SAT formed by the nitrogen etching method. (**c**) The field electron emission is confined to the last atom (**a**, **b**, and **c** from Rezeq et al. [28]). (**d**) The nanotip apex after the removal of the topmost atom from a similar SAT. (**e**) The atomic structure of the nanotip is reproduced by a ball model with a spherical crystal of a radius = 7.7 Å (**a** and **e** from Rezeq et al. [28])

apex; hence, there is only a radial component E_r and no tangential component, i.e., $E_\theta = 0$. As we move along the dotted curve away from the apex toward the base, the tangential electric field E_θ increases and reaches its maximum value between $\theta = 0$ and $\theta = \theta_c$ (θ_c is depicted in Fig. 16.4). Then it decreases drastically (almost exponentially) until it vanishes completely, i.e., $E_\theta = 0$. Beyond this point the electric field is totally dominated by the tip base.

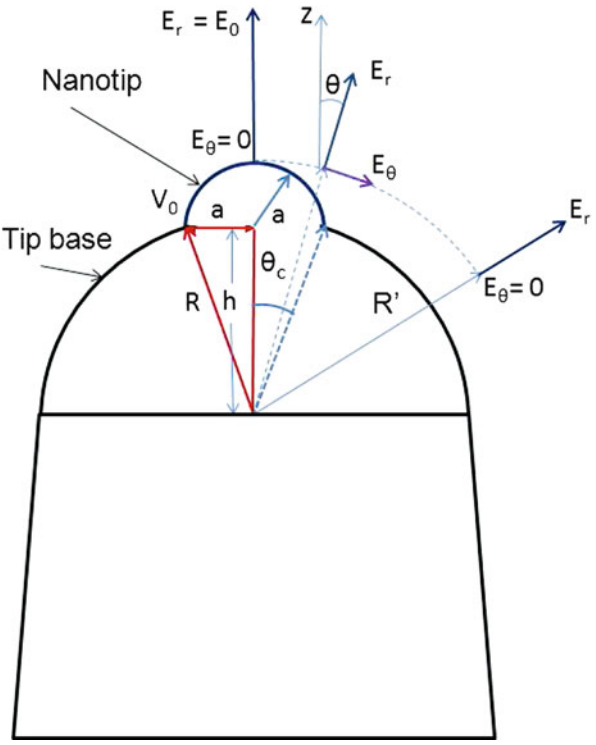


Fig. 16.4 A schematic of the spherical model of the nanotip with a radius "*a*" on a base of a radius "*R*." A circular path (*dotted curve*) with a radius *R*′ starts from the center of the nanotip apex is used as a guide for electric field analysis

This behavior can be captured mathematically by the following empirical function:

$$E_\theta = Ce^{-k(n\theta)} \sin(n\theta) \tag{16.2a}$$

where n and k are real numbers and C is a parameter to be determined from the boundary conditions. The factor n in front of θ is used to minimize the number of terms of Legendre polynomials in the solution when applying the boundary conditions as E_θ drops rapidly after passing the nanotip, particularly for nanotips with large bases, and vanishes when $(n\theta = \pi)$. For simplicity we will denote $n\theta$ by θ'. However, the solution is still possible without using n but many terms will be involved in the polynomial expansion. This implies that

$$E_\theta = \begin{cases} Ce^{-k(n\theta)} \sin(n\theta) & 0 \le \theta \le \pi/n \\ 0, & \pi/n \le \theta \le \pi \end{cases} \tag{16.2b}$$

or

$$E_{\theta'} = \begin{cases} Ce^{-k\theta'} \sin(n\theta) & 0 \le \theta \le \pi/n \\ 0, & \pi/n \le \theta \le \pi \end{cases} \tag{16.2c}$$

k is chosen such that the peak is located at $\theta_c/2$, i.e., when $\frac{d}{d\theta'}E_{\theta'} = 0$. This leads to $k = \cot\left(\frac{n\theta_c}{2}\right)$.

The analytical calculations are strictly needed for the region $0 \leq \theta \leq \frac{\pi}{n}$ or $0 \leq \theta' \leq \pi$, whereas the potential and thus the electric field in the region $\frac{\pi}{n} < \theta$ $(\pi < \theta')$ only depend on the tip base. Therefore, our analysis will be confined to the first region. Since $E_{\theta'} = \frac{1}{r}\frac{\partial}{\partial\theta'}V(r,\theta'), V(r,\theta')$ can be calculated along the dotted path in Fig. 16.4, where $r = R'$. By taking the integral of Eq. 16.2c over the region $0 \leq \theta' \leq \pi$, we found that

$$V(R',\theta') = A - Be^{-k\theta'}(k\sin\theta' + \cos\theta'), \quad 0 \leq \theta' \leq \pi \tag{16.3}$$

A and B can be found from the boundary conditions at $\theta' = 0$, where $V = V_0$ (the applied voltage of the tip), and at $\theta' = \pi$ where $V = V_0R/R'$. This leads to

$$B = V_0\left(1 - \frac{R}{R'}\right)/\left(-1 - e^{-k\pi}\right) \tag{16.4a}$$

and

$$A = V_0 + B \tag{16.4b}$$

Regarding the region below the dotted curve, around the nanotip, $r < R'$, the electric field can be calculated from Eqs. 16.2c and 16.3, by replacing R' with r and then taking the gradient of the potential, i.e., $E(r, \theta') = -\nabla V(r, \theta')$. However, this region is not of our interest like the apex field and it is beyond the scope of this chapter.

As the possible site of the topmost single atom is located at the center of the spherical nanotip ($r = R'$), we are interested in solving Laplace's equation in the spherical space where $r \geq R'$. The Laplace's equation can be written as

$$\frac{1}{r^2}\frac{\partial V}{\partial r}\left(r^2\frac{\partial V}{\partial r}\right) + \frac{1}{r^2\sin\theta'}\frac{\partial V}{\partial\theta'}\left(\sin\theta'\frac{\partial V}{\partial\theta'}\right) + \frac{1}{r^2\sin\theta'^2}\frac{\partial^2 V}{\partial Ø^2} = 0 \tag{16.5}$$

Because of the azimuthal symmetry of the system around z-axis, we can take the last term to be zero. By separation of variables, this differential equation has a common solution in terms of Legendre polynomials, as follows (see details in Ref. [43]):

$$V(r,\theta') = \sum_{l=0}^{\infty}\left(A_l r^{j1} + B_l r^{-j2}\right)P_l(\cos\theta') \tag{16.6}$$

where A_l and B_l are constants, j_1 is a positive real number and given by $j_1 = \frac{-1+\sqrt{1+4n^2l(l+1)}}{2} \geq 0$, and $-j_2$ is a negative real number and given by $-j_2 = \frac{-\left(1+\sqrt{1+4n^2l(l+1)}\right)}{2} < 0, P_l(\cos\theta')$ is the Legendre polynomial of $(cos\ \theta')$.

According to our model the electric field decreases radially as we move away from $r = R'$ and approaches zero at $r = \infty$; this means that all terms with A_l must be zero. Then Eq. 16.6 can be simplified to

$$V(r, \theta') = \sum_{l=0}^{\infty} \left(B_l r^{-j_2}\right) P_l(\cos\theta'). \tag{16.7}$$

By applying the boundary condition for $V(R', \theta')$, in Eq. 16.3, we get

$$V(R', \theta') = A - Be^{-k\theta'}(k\sin\theta' + \cos\theta') = \sum_{l=0}^{\infty} \left(B_l R'^{-j_2}\right) P_l(\cos\theta') \tag{16.8}$$

Since Legendre polynomials are orthogonal functions over $-1 \leq \cos\theta' \leq 1$, B_l can be found as follows: assuming $C_l = B_l R'^{-j_2}$, then,

$$C_l = \frac{2l+1}{2} \int_{-1}^{1} V(R', \theta') P_l(\cos\theta') d(\cos\theta'). \tag{16.9a}$$

Then,

$$B_l = C_l R'^{j_2} \tag{16.9b}$$

Here we can demonstrate the reason for choosing n greater than 1, particularly for broad tip bases. To minimize the number of terms of C_l in the expansion in Eq. 16.7 and later in Eq. 16.10b when the tip base = 5 nm, for example, we choose $n = 5$; this leads to having 11 terms with $l = 0, \ldots, 10$. For larger l values we found the subsequent terms of C_l to be very small, for instance, C_{11} is around 1–2 % of the maximum C_l value. Therefore, n is selected in a way that at $l = 10$, $V(r, \theta)$ in Eq. 16.7 reasonably satisfies the boundary conditions at the apex center ($r = R'$ and $\Theta' = 0$), thus $V(R', 0) = V_0$. In fact the summation of 11 terms in Eq. 16.7 will give a value very close to V_0. Table 16.1 presents the values of C_l calculated from Eq. 16.9a at given n and k parameters for some nanotips with different bases [43]. Since the goal is to find the electric field at the tip apex, where the single atom is experiencing the apex field, we just need to calculate the radial field along the tip axis (θ' *or* $\theta = 0$) starting from the apex. These calculations are demonstrated below:

$$E_r = E(r, 0) = -\frac{dV(r, 0)}{dr} \tag{16.10a}$$

$$E_r = E(r, 0) = \sum_{l=0}^{\infty} j_e B_l r^{-(j_2+1)} P_l(1) \tag{16.10b}$$

where $P_l(1) = 1$.

From Eq. 16.10b the electric field profile can be calculated starting from the nanotip apex (R') to any distance (r) along the tip axis.

Table 16.1 The values of C_l for the first 10 terms in Eq. 16.9a, b, for the electrostatic potential around the nanotip apex. These values are listed for different nanotips with different sizes (R), thus different n and k parameters (This table is reproduced from Ref. [43])

	$R = 5$ nm	$R = 10$ nm	$R = 15$ nm	$R = 20$ nm
	$n = 5$	$n = 8$	$n = 11$	$n = 14$
Tip base radius	$k = 1.82$	$k = 2.36$	$k = 2.61$	$k = 2.73$
C_0	0.3112	0.1358	0.0843	0.0606
C_1	0.5577	0.2679	0.1726	0.1268
C_2	0.3465	0.2068	0.1438	0.1096
C_3	0.1516	0.1139	0.0859	0.0683
C_4	0.0682	0.0589	0.0470	0.0385
C_5	0.0332	0.0314	0.0261	0.0218
C_6	0.0180	0.0178	0.0151	0.0128
C_7	0.0104	0.0107	0.0092	0.0079
C_8	0.0064	0.0067	0.0059	0.0051
C_9	0.0042	0.0044	0.0039	0.0034
C_{10}	0.0028	0.0030	0.0027	0.0023

5.1.2 Finite Element Simulation Modeling

We build a model for our nanotip system using the finite element simulation software (COMSOL). We draw the tip geometry in two dimensions and choose the axis of the tip to be along z-axis. By selecting 2D-axial symmetry mode, we only need to draw half of the tip picture as we see in Fig. 16.5. We add a boundary condition at the tip surface by setting the electrostatic potential value at V_0. Since we cannot calculate the electric field using the whole tip-screen configuration where the tip-screen distance is several orders of magnitude larger than the tip geometry, we introduce another boundary condition by drawing a circle of 100 nm radius concentric with the tip base at a potential $V = (R/100\text{ nm})V_0$ (not shown in the figure). This new boundary has been used only for the meshing purposes. Then the numerical program was used to solve for Laplace's equation between these boundaries. We were able to calculate the potential variation and, hence, the electric field, in the vicinity of the nanotip.

6 Results

Figure 16.5 demonstrates two examples of simulation models for 1 nm nanotips on tip bases of 10 and 20 nm, respectively. The color scale displays the electric field strength around the tip at an applied voltage $V_0 = 10\ V$; the maximum field is shown in red color. Here we have to indicate that this applied voltage does not represent the actual voltage needed to generate such an electric field. However, to calculate the actual voltage, we need to multiply this value by the characteristic constant β, which is given by Eq. 16.1b [40]. For instance, if the tip base radius is around 10 nm and the tip is placed 5 cm away from the screen, this leads to $\beta = 8.4$. This means

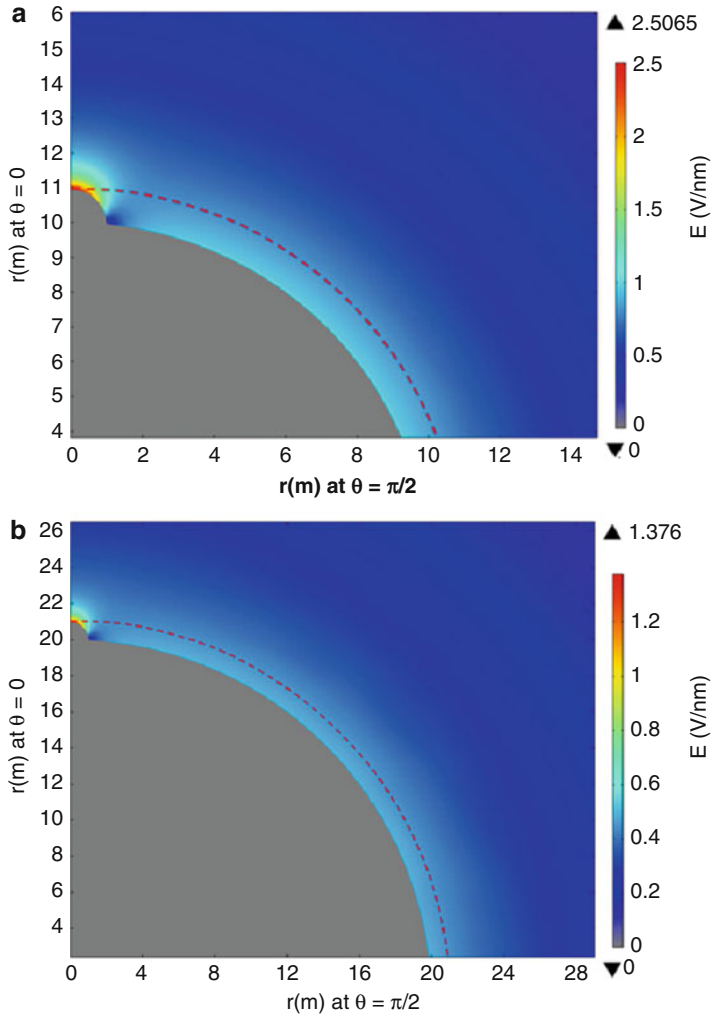


Fig. 16.5 Finite element simulation models for the apex field of nanotips with bases (**a**) $R = 10$ nm and (**b**) $R = 20$ nm at $V_0 = 10$ V

that the voltage needed to generate the electric emission field in Fig. 16.5a should be 84 V. In fact the typical emission field strength for nano-metal tips, like tungsten tips, is around $E = 5$ V/nm. Using the analytical model and the finite element simulation model discussed here, we found that the voltage needed to generate such an electric field, for a nanotip with 10 nm tip base, is 21 V, which implies that the actual voltage is $21 \times 8.4 \approx 176$ V (negative bias).

Figure 16.6a, b shows the profiles of the potential and the tangential electric field, respectively, as a function of θ along the dotted path in Fig. 16.4, and the

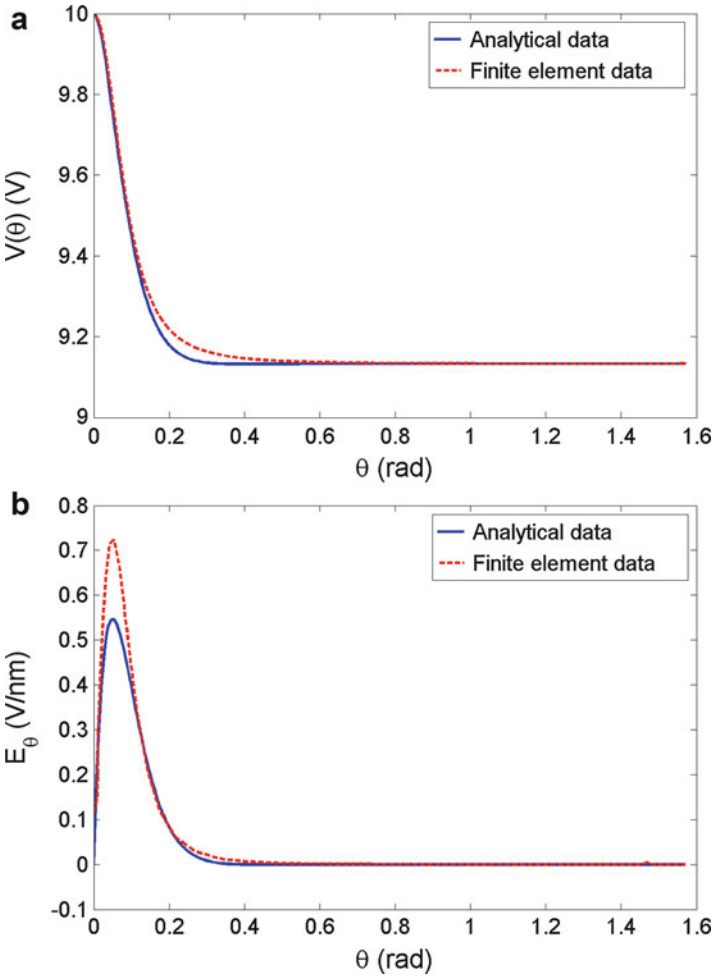


Fig. 16.6 (**a**) The potential (V vs θ) profile along the circular path at $r = R'$, calculated by the numerical and analytical approaches. (**b**) The tangential component of the electric field profile along that path, at $r = R'$, calculated by the numerical and analytical methods. $V_0 = 10$ V

corresponding red curve around the tip base in the model (Fig. 16.5a), for a nanotip with a 10 nm base radius. The voltage profiles in Fig. 16.6a satisfy the conditions that $V = V_0$ at the apex center and then decays almost exponentially and reaches a constant value along the side of the tip base, where the potential depends strictly on the base radius, i.e., $V = (R/R')\, V_0$. The results show good agreement between the two curves, from the analytical formula, Eq. 16.3, and the numerical data. Figure 16.6b also shows the variation of the tangential electric field (E_θ) with the angle θ. In the same figure we can readily observe the position of the peak to be around $\theta_c/2$, which justifies the selection of the earlier empirical function we proposed with the predefined value of k.

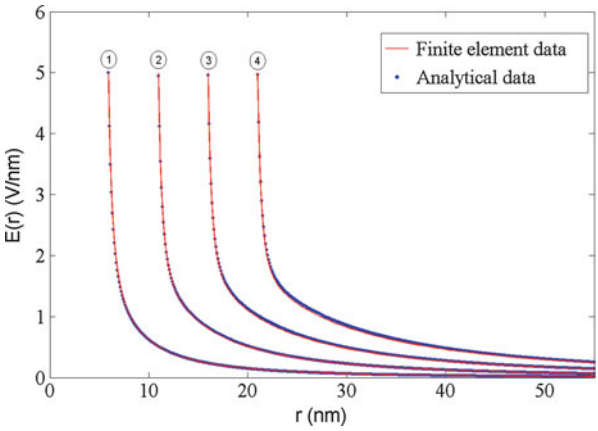


Fig. 16.7 The radial electric field along the tip axis starting from the nanotip apex, i.e., $r = R'$, (1) represents a tip base of 5 nm where the effective applied voltage is 103 V (2) for a tip base of 10 nm where the effective applied voltage is 176 V, (3) for a tip base of 15 nm where the effective applied voltage is 245 V, and (4) for a tip base of 20 nm where the effective applied voltage is 306 V

As the focus in this study is on the apex center field, which is the field that the single atom experiences at this location, we will try to get more detailed data for the field along the axis of the tip starting from the nanotip apex center at $\theta = 0$ and $r = R'$. We have calculated this field analytically using Eq. 16.10b and numerically from the finite element simulation model. Figure 16.7 depicts the electric field profiles as a function of r, for a nanotip apex with a radius = 1 nm. The electric field was calculated for various nanotip bases, R = 5,10,15 and 20 nm, and showed that threshold apex electric field (E = 5 V/nm) is reached at voltages of 103, 176, 245, and 306 V, respectively. Figure 16.7 also shows good agreement between the theoretical (dots) and numerical data (solid lines).

To thoroughly understand the effect of the tip base on the nanotip field and to link the value we used for the applied voltage with the actual tip, we have to use the characteristic factor β, as discussed earlier in this section. If we choose, for instance, tip bases of radii 5 and 20 nm as mentioned above, we found that the applied voltages needed to generate the threshold emission field are 220 and 800 V, respectively. However, after building a nanotip of a radius = 1 nm, on the same bases, the required voltages change to 103 and 306 V, respectively. This indicates that the 5 nm regular tip requires less voltage (220 V) than the nanotip (1 nm) with a base of 20 nm (at 306 V) to generate the same threshold field. Therefore, observing a single-atom tip in FIM with a well-defined FEM spot is necessarily an indication of the tip sharpness.

We have also calculated the voltage required to produce the threshold FEM emission field for a wide range of tip base radii (5–50 nm) before and after placing the nanotip (with radius = 1 nm). The results are plotted in Fig. 16.8. The dotted horizontal and vertical lines indicate the same voltage (around 420 V) needed to generate a field of 5 V/nm for a regular tip with a base of 10 nm and a nanotip with a base of 30 nm. Therefore, the tip sharpness has to be estimated with rigorous analysis considering the applied voltage on the tip, not just by observing a single-atom tip.

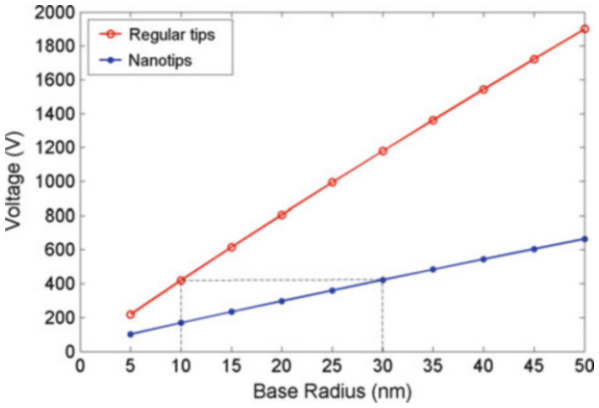


Fig. 16.8 The voltage required to produce a threshold field of 5 V/nm for regular tips (*red line* with *open circles*) and nanotips (*blue line* with *solid circles*) with different base radii

6.1 Hyperboloid Model of Nanotips

6.1.1 Finite Element Simulations with Hyperbolic Coordinates

Here we use a different method to estimate the nanotip shape over a mesoscopic range. This method requires the characterization of the tip base prior to the formation of the nanotip or after its removal. The radius of the tip base can be estimated with reasonable accuracy in the field ion microscope where an atomic resolution image of a perfectly clean apex can be obtained. By counting the number of atomic steps between the centers of two successive planes, where the step height is known for a given crystal structure, and with a simple geometrical analysis the tip radius can be readily calculated, this method is detailed elsewhere [26, 40]. The tip apex in Fig. 16.9a was prepared just before the formation of the SAT in Fig. 16.9b, the voltage of the tip base is 5.9 kV, and the radius of the tip was estimated to be 12.8 nm. The SAT image in Fig. 16.9b was obtained at 2.0 kV. The removal of such a single atom in Fig. 16.9b revealed an apex of around 0.8 nm radius, as have been observed and estimated in a previous work [28]. In this section, for modeling and estimating the overall tip shape along the shank, we are going to use the hyperboloid coordinate system [40, 44–47], as depicted in Fig. 16.10a. This model will be used to represent the geometry of the tip base and the nanotip when using the finite element method software in 2D axial symmetry mode. As we did for the spherical model in the previous section, we cannot plot the tip and screen configuration in the same scale. Instead, we will plot the boundaries that represent the tip base profile (u_0) and a profile of an equipotential surface (u) at a given distance, 200 nm, from the tip, as shown in Fig. 16.10b, which can be extracted from Eqs. 16.11 and 16.12 [45, 46]:

$$z = L \cos u \cosh v \tag{16.11}$$

$$\rho = L \sin u \sinh v \tag{16.12}$$

where L is the tip-screen distance, which can be also the same as the distance between the screen and the center of the tip base. We will plot the profiles in

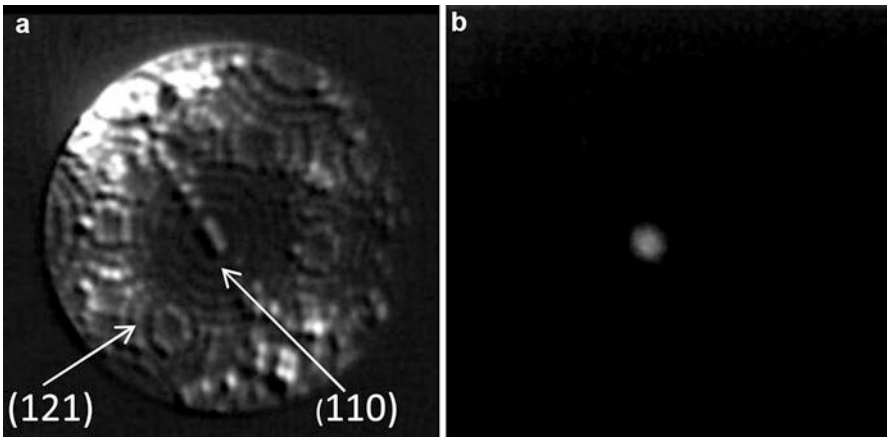


Fig. 16.9 (**a**) A FIM image (at 5.9 kV) for the initial blunt tip, $R = 12.8$ nm, before the formation of the SAT tip (at 2.4 kV), the bright spot in (**b**)

z-ρ plane within COMSOL program where we identify curve (u) for the boundary condition away from the tip. This boundary curve is chosen to be at a distance within the scale, 200 nm from the tip (i.e., $z = L$ - 200 nm). Whereas u_0 of the tip base with a radius R is plotted at $z = L$ - R, with the help of Eqs. 16.11 and 16.13, u and u_0 are plotted over $z - \rho$ plane. The value of L in Eq. 16.13 is chosen to be 5 cm.

$$v = \sinh^{-1}\left(\frac{\rho}{L \sin u_0}\right) \tag{16.13}$$

This model is built within COMSOL where the Laplace's equation is solved with the boundary conditions specified above. To find the electric field distribution in the region between the two boundaries, u_0 and u, we need to determine our boundary potential values. The tip surface is exposed to the applied voltage at FIM threshold voltage which forms the first boundary condition. The potential on the second boundary will drop according to Eq. 16.14, which is derived in other places [40, 45]:

$$V(u) = V_0\left(\frac{\ln(\tan\left(\frac{u}{2}\right))}{\ln(\tan\left(\frac{u_0}{2}\right))}\right) \tag{16.14}$$

where V_0 is the applied tip voltage.

After plotting the profiles of the tip (u_0) and (u), we can calculate the electric field distribution in the vicinity of the tip apex. Since the threshold field, i.e., the field needed to ionize helium atoms in the FIM, is known to be ~5 V/Å, we have to adjust V_0 (the tip voltage) until we reach that electric field value. We have found that V_0 for a tip with a radius $R = 12.8$ nm (as in Fig. 16.11a, b) is 5.8 kV which is fairly close to the experimental value in Fig. 16.9a (i.e., 5.9 kV). The nanotip is represented in our

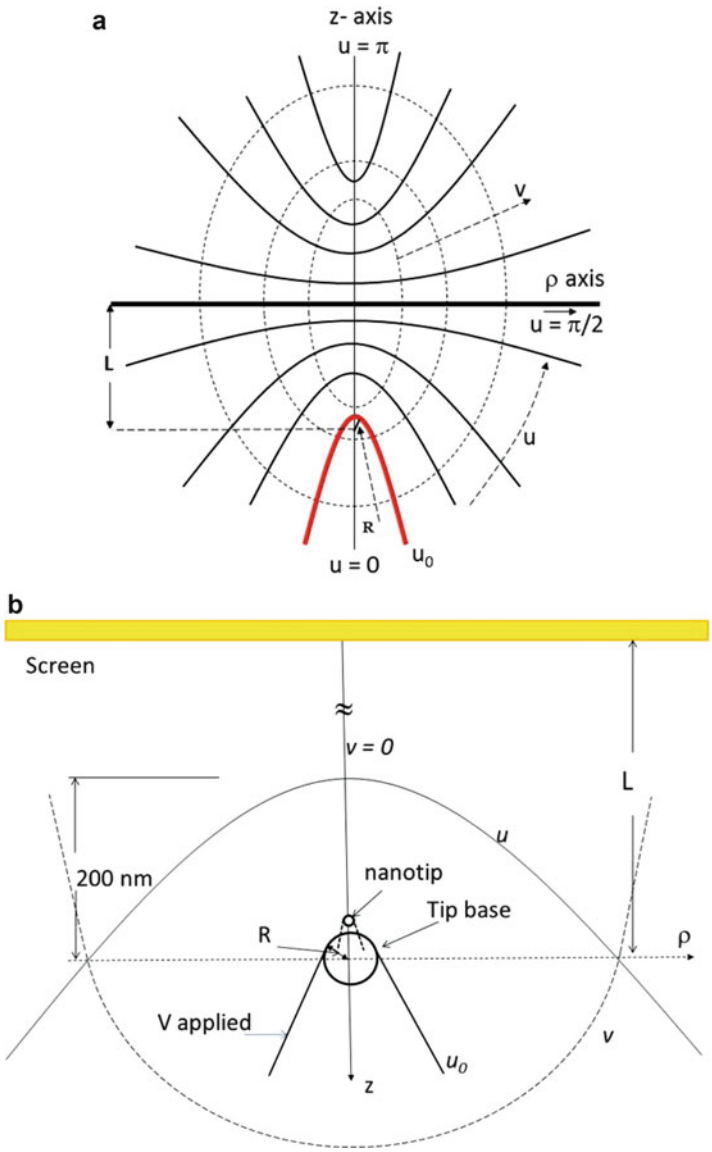


Fig. 16.10 (**a**) The hyperbolic coordinate system. (**b**) Representation of the tip-screen geometry in the hyperboloid system, showing the position of the nanotip

model by a hyperboloid shell structure with the right curvature and height that produces the required average shape of the nanotip protrusion. Here we consider the nanotip radius to be 8 Å on average. As we know from the experimental results, the FIM voltage is 2.0 kV. We have found that any little change of the position of the nanotip profile will have significant effect on the nanotip apex field at a fixed voltage; therefore,

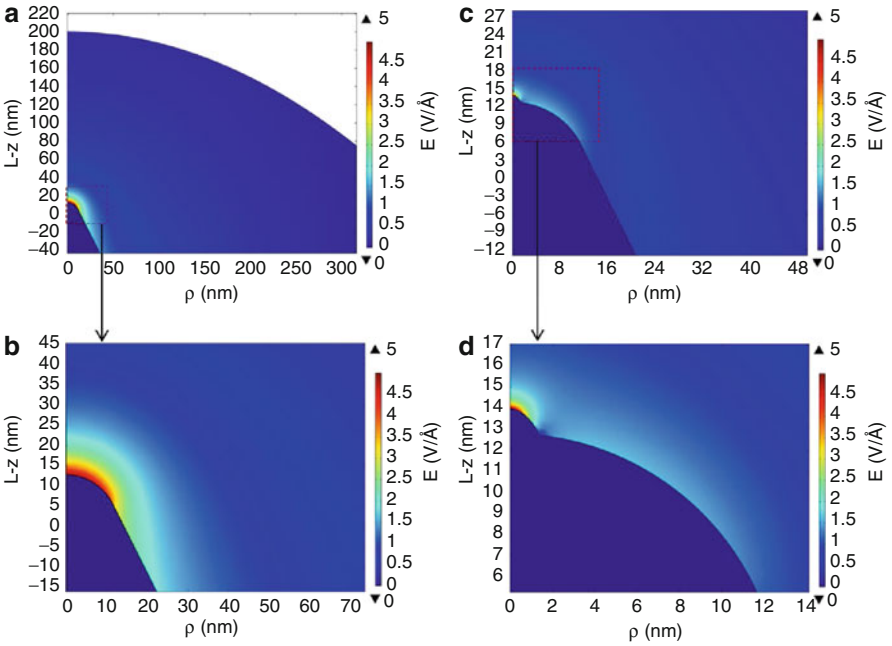


Fig. 16.11 (**a**) The geometry of the tip base plotted for the tip in Fig. 16.9a. (**b**) The enlarged image of the tip apex in (**a**) showing the field distribution. (**c**) The geometry after placing the nanotip to generate the same threshold field, $E_0 = 5$ V/Å. (**d**) The overall tip shape, E_0, is strictly localized on the nanotip apex. The threshold field was produced at 5.8 and 2.0 kV for the base tip and the nanotip, respectively

the electric field on the apex of the nanotip is very sensitive to the height of the nanotip protrusion. Thus, we maintain the tip voltage at 2.0 kV and adjust the height of the nanotip to get the same threshold field, as shown with the dashed nanotip profile in Fig. 16.10b. The resulting profile in the model represents a side view of the overall tip shape over a long range as shown in Fig. 16.11c, d. It is obvious from Fig. 16.11c, d that although the field is focused on the nanotip, the nano-protrusion is quite small compared to the tip base. It is worth indicating here that the same approach can be applied after the removal of the nanotip completely by the field evaporation process, which would reveal slightly larger base than the initial tip due to the elliptical tip shape.

7 Conclusion

We have introduced new analytical and numerical approaches for calculating the electric field generated at nanotips that end with a single atom of different base radii. The analytical data is in good agreement with the numerical results obtained by the finite element simulations.

Both spherical and elliptical models demonstrate that the observation of small and focused electron and ion beams, i.e., small bright spots in FEM and FIM,

respectively, is not a definite indication of the tip sharpness. The models demonstrate the significant effect of the tip base on the voltage required to generate the threshold field (either FIM or FEM fields). In addition, finite element software is used to estimate the overall tip shape based on the experimental values of the applied voltages used to generate the threshold FIM field for the tip base and for the SAT.

These calculations show that the sharpness of the nanotip cannot be simply determined from observing a single-atom apex in FEM or FIM microscopes, but rather from the combination of the apex FIM image and the required voltage to produce such an image. These analyses will help explain FIM or FEM measurements when utilized for determining the tip sharpness, not only at the apex but also over the entire tip shank. This approach is quite important in some nanotechnology applications, especially in multiple probe measurements. To make physical contacts with molecules, nanomaterials, or nanostructures, the closest distance between two nearby nanotips is limited by their base dimensions.

References

1. Knoblauch A, Wilbertz C, Miller T, Kalbitzer S (1996) Field electron emission properties of a supertip. J Phys D Appl Phys 29(2):470–473
2. Fransen M, Overwijk M, Kruit P (1999) Brightness measurements of a ZrO/W Schottky electron emitter in a transmission electron microscope. Appl Surf Sci 146(1):357–362
3. Hasegawa S, Shiraki I, Tanabe F, Hobara R, Kanagawa T, Tanikawa T, Matsuda I, Petersen CL, Hansen TM, Boggild P (2003) Electrical conduction through surface superstructures measured by microscopic four-point probes. Surf Rev Lett 10(06):963–980
4. Rochet F, Dufour G, Roulet H, Motta N, Sgarlata A, Piancastelli M, De Crescenzi M (1994) Copper phthalocyanine on Si(111)-7× 7 and Si(001)-2× 1: an XPS/AES and STM study. Surf Sci 319(1):10–20
5. Haiss W, Nichols RJ, van Zalinge H, Higgins SJ, Bethell D, Schiffrin DJ (2004) Measurement of single molecule conductivity using the spontaneous formation of molecular wires. Phys Chem Chem Phys 6(17):4330–4337
6. Avouris P (1995) Manipulation of matter at the atomic and molecular levels. Acc Chem Res 28(3):95–102
7. Haiss W, van Zalinge H, Höbenreich H, Bethell D, Schiffrin DJ, Higgins SJ, Nichols RJ (2004) Molecular wire formation from viologen assemblies. Langmuir 20(18):7694–7702
8. Joachim C, Gimzewski JK, Schlittler RR, Chavy C (1995) Electronic transparence of a single C_{60} molecule. Phys Rev Lett 74(11):2102–2105
9. Doumergue P, Pizzagalli L, Joachim C, Altibelli A, Baratoff A (1999) Conductance of a finite missing hydrogen atomic line on Si (001)-(2 × 1)-H. Phys Rev B 59(24):15910–15916
10. Natelson D, Yu LH, Ciszek JW, Keane ZK, Tour JM (2006) Single-molecule transistors: electron transfer in the solid state. Chem Phys 324(1):267–275
11. Gao HJ, Sohlberg K, Xue ZQ, Chen HY, Hou SM, Ma LP, Fang XW, Pang SJ, Pennycook SJ (2000) Reversible, nanometer-scale conductance transitions in an organic complex. Phys Rev Lett 84(8):1780–1783
12. Rezeq M, Joachim C, Lwin M, Navarro F (2013) Observations of individual Cu-phthalocyanine molecules deposited on nano-tips in the field emission microscope. In: Grill L, Joachim C (eds) Imaging and manipulating molecular orbitals. Springer, Berlin/Heidelberg, pp 3–13
13. Stafford CA, Cardamone DM, Mazumdar S (2007) The quantum interference effect transistor. Nanotechnology 18(42):424014

14. Meyer G, Bartels L, Rieder K-H (2001) Atom manipulation with the STM: nanostructuring, tip functionalization, and femtochemistry. Comput Mater Sci 20(3):443–450
15. Binh VT, Purcell S, Semet V, Feschet F (1998) Nanotips and nanomagnetism. Appl Surf Sci 130:803–814
16. Binh VT, Marien J (1988) Characterization of microtips for scanning tunneling microscopy. Surf Sci 202(1):L539–L549
17. Fink H-W (1986) Mono-atomic tips for scanning tunneling microscopy. IBM J Res Dev 30(5):460–465
18. Fu T-Y, Cheng L-C, Nien C-H, Tsong TT (2001) Method of creating a Pd- covered single-atom sharp W pyramidal tip: mechanism and energetics of its formation. Phys Rev B 64(11):113401–113404
19. Kuo H-S, Hwang I-S, Fu T-Y, Wu J-Y, Chang C-C, Tsong TT (2004) Preparation and characterization of single-atom tips. Nano Lett 4(12):2379–2382
20. Rezeq M, Pitters J, Wolkow R (2006) Tungsten nanotip fabrication by spatially controlled field-assisted reaction with nitrogen. J Chem Phys 124:204716
21. Rezeq M (2013) Fabrication of super ion—electron source and nanoprobe by local electron bombardment. US Patent 8,460,049
22. Tsong T (1990) Atom probe field ion microscopy. Cambridge University Press, New York
23. Fink H-W, Stocker W, Schmid H (1990) Holography with low-energy electrons. Phys Rev Lett 65(10):1204–1206
24. Schmid H, Fink H-W (1994) Mechanical and electronic manipulation of nanometer-sized wires. Nanotechnology 5(1):26–32
25. Fursey G (2005) Field emission in vacuum microelectronics. Kluwer/Plenum, New York
26. Müller E, Tsong T (1969) Field ion microscopy, principles and applications. Elsevier, New York
27. Rezeq M, Pitters J, Wolkow R (2007) A well defined electron beam source produced by the controlled field assisted etching of metal tips to 1 nm radius. J Scan Probe Microsc 2(1–2):1–4
28. Rezeq M, Joachim C, Chandrasekhar N (2009) Nanotip apex modification with atomic precision and single atom tips restoration. Microelectron Eng 86(4):996–998
29. Rokuta E, Itagaki T, Ishikawa T, Cho B-L, Kuo H-S, Tsong T, Oshima C (2006) Single-atom coherent field electron emitters for practical application to electron microscopy: buildup controllability, self-repairing function and demountable characteristic. Appl Surf Sci 252(10):3686–3691
30. Kuo H-S, Hwang I-S, Fu T-Y, Lin Y-C, Chang C-C, Tsong TT (2006) Noble metal/W (111) single-atom tips and their field electron and ion emission characteristics. Jap J Appl Phys 45(11):8972–8983
31. Cui J, Yang L, Wang Y (2013) Simulation study of near-field enhancement on a laser-irradiated AFM metal probe. Laser Phys 23:076003
32. McKelvey K, Nadappuram BP, Actis P, Takahashi Y, Korchev YE, Matsue T, Robinson C, Unwin PR (2013) Fabrication, characterization, and functionalization of dual carbon electrodes as probes for scanning electrochemical microscopy (SECM). Anal Chem 85:7519–7526
33. Zhang L, Gerstenberger A, Wang X, Liu WK (2004) Immersed finite element method. Comput Methods Appl Mech Eng 193:2051–2067
34. Liu WK, Kopacz AM, Lee T, Kim H, Decuzzi P (2013) Immersed molecular electrokinetic finite element method for nano-devices in biotechnology and gene delivery. In: Griebel M, Schweitzer MA (eds), Meshfree methods for partial differential equations VI. Springer, Verlag Berlin Heidelberg, pp 67–74
35. Kopacz AM, Liu WK (2012) Immersed molecular electrokinetic finite element method. Comput Mech 1–7
36. Kopacz AM, Yeo W, Chung J, Liu WK (2012) Nanoscale sensor analysis using the immersed molecular electrokinetic finite element method. Nanoscale 4:5189–5194
37. Brown KA, Westervelt RM, Satzinger KJ (2012) The importance of cantilever dynamics in the interpretation of kelvin probe force microscopy. J Appl Phys 112:064510

38. Piva PG, DiLabio GA, Pitters JL, Zikovsky J, Rezeq M, Dogel S, Hofer WA, Wolkow RA (2005) Field regulation of single-molecule conductivity by a charged surface atom. Nature 435(7042):658–661
39. Joachim C, Martrou D, Rezeq M, Troadec C, Deng J, Chandrasekhar N, Gauthier S (2010) Multiple atomic scale solid surface interconnects for atom circuits and molecule logic gates. J Phys Condens Matter 22(8):084025
40. Miller M, Cerezo A, Hetherington M, Smith G (1996) Atom probe field ion microscopy. Clarendon, Oxford
41. Rezeq M, Joachim C, Chandrasekhar N (2009) Confinement of the field electron emission to atomic sites on ultra sharp tips. Surf Sci 603(4):697–702
42. Rose DJ (1956) On the magnification and resolution of the field emission electron microscope. J Appl Phys 27(3):215–220
43. Rezeq M (2011) Finite element simulation and analytical analysis for nano field emission sources that terminate with a single atom: a new perspective on nanotips. Appl Surf Sci 258(5):1750–1755
44. Rezeq M (2013) Nanotips with a single atom end as ideal sources of electron and ion beams: modeling of the nanotip shape. Microelectron Eng 102:2–5
45. Yuasa K, Shimoi A, Ohba I, Oshima C (2002) Modified fowler-nordheim field emission formulae from a nonplanar emitter model. Surf Sci 520(1):18–28
46. Peridier VJ, Pan LH, Sullivan TE (1995) Methods for calculating electrostatic quantities due to a free charge in a nanoscale three-dimensional tip/base junction. J Appl Phys 78(8):4888–4894
47. Feenstra RM (2003) Electrostatic potential for a hyperbolic probe tip near a semiconductor. J Vacuum Sci Tech B: Microelectron Nanometer Struct 21(5):2080–2088

Index

A
AFC. *See* Antiferromagnetic coupling (AFC)
AFM. *See* Atomic force microscopy (AFM)
Alternating gradient magnetometer (AGM), 464, 471
Amplitude modulation (AM), 203, 278
Amplitude modulation KPFM (AM-KPFM), 118, 122–125, 127–129, 132, 133
Angle-resolved PES (ARPES), 367–399
Angle-resolved UPS (ARUPS), 416
Angle-resolved XPS (ARXPS), 412, 416
Anisotropy, 54, 177, 382, 464, 465, 467, 470, 474, 476, 479, 481–484, 506, 516, 533, 550, 553
Antiferromagnetic coupling (AFC), 474–476, 478, 479, 481–484
APFIM. *See* Atom probe field ion microscopy (AP-FIM)
Atomic force microscopy (AFM), 70, 71, 73–75, 78–81, 91, 93, 94, 96, 99–101, 103, 106, 108, 134–137, 141, 143, 153, 160–163, 182, 189–191, 200, 202–204, 206, 219–222, 229, 265, 273–304, 415, 490–517, 536, 550–555, 566, 580–581, 596, 598, 605, 606, 609
  force reconstruction, 73, 87
Atomic resolution, 563, 566, 568, 573, 575, 579, 582, 596, 608, 609
Atomic-resolution force spectroscopy, 290–303
Atomic-resolution imaging, 274–275, 277, 279, 281–290
Atomic-scale nanoindentation, 189–192
Atom probe field ion microscopy (AP-FIM), 162, 231, 257–258
Atom-tracking/feedforward methods, 280, 281, 292, 299
Auger electron spectroscopy (AES), 414, 415
Azurin, 37–39, 41–43, 45, 46, 49, 58–60

B
Band bending, 406–455
Band mapping, 382, 400
Batteries, 357–362
Binding energies (BE), 372, 375, 384, 387, 392, 395, 407–414, 418–421, 423, 424, 434, 435, 437, 441–443, 445, 446, 448–450, 453, 455
Biomolecules, 37–60
Bit error rate (BER), 470, 471
Bit-patterned media (BPM), 471, 474, 476, 483
Bloch functions, 371
Block copolymer (BCP), 108
Blue copper proteins, 41
Bohr–Sommerfeld quantization rule, 389
Boltzmann constant, 167, 179
BPM. *See* Bit-patterned media (BPM)

C
Cantilevers, 465, 466, 480, 481, 484, 491–499, 502–504, 508–513, 515
Cap electronic states, 263
Carbon contamination, 443
Carbon nanostructures, 139–144
Carbon nanotubes (CNTs), 118, 139, 147, 149, 262–263, 265, 290, 480–481
Carrier injection, 384
Catalysis, 319, 349, 350
Catalyst poison, 19
Catalytic atom probe (CAP), 246, 264
CCM. *See* Constant current mode (CCM)
Characterization, 318–362
Charge transfer, 118, 134, 144–148
Charge-up, 376
Chemical contrast, 585, 591–596
Chemical shifts, 410, 411, 414
CHM. *See* Constant-height mode (CHM)
Chronoamperometric measurements, 21

© Springer-Verlag Berlin Heidelberg 2015

C.S.S.R. Kumar (ed.), *Surface Science Tools for Nanomaterials Characterization*,
DOI 10.1007/978-3-662-44551-8

CNTs. *See* Carbon nanotubes (CNTs)
Coadsorption systems, 250, 259
Cobalt atoms, 601–603
Coherent length, 388
Comb filtering method, 73
COMSOL, 628, 633, 638
Conducting polymers, 209
Conjugated polymer blends, 204, 211
Constant current mode (CCM), 565, 574, 577, 578, 591, 603
Constant-height mode (CHM), 565, 569, 570, 577, 585
Contact mode AFM, 275–278, 495
Contact potential difference (CPD), 118–121, 123, 137–139, 142, 146, 151, 152, 374
Core-level spectroscopy, 413, 417, 437, 445, 450
Critical energy deficit, 240
Curling nucleation model, 549
Current sensing, 201–203, 206, 221–223
Curve-by-curve method, 280, 281, 294, 299

D
Debye length, 13, 75
Deconvolution, 9–14, 412, 437, 453
Dendritic nanotip (DNT), 625
Density functional theory (DFT), 26, 27, 29
Density of states (DOS), 371, 565–567, 578, 580, 584, 587, 588, 591, 592, 594, 598, 601, 606–608
Depolarization charge sheet, 409, 433, 447, 454
Depolarization field, 409, 422
Depth profile, 329, 341, 352
Derjaguin-Landau-Verway-Overbeek (DLVO) theory, 75
Derjaguin-Muller-Toporov (DMT) potential, 75
DFT. *See* Density functional theory (DFT)
Dielectrophoretic (DEP) force, 625
Diffusion coefficient, 255, 256, 261
Diffusion length, 426, 432
Diheme protein cytochrome c_4, 41, 48, 61
Dimer-adatom-stacking fault (DAS) model, 573, 574
Dip-pen nanolithography (DPN), 94, 96, 135
Dirac's delta function, 77
Domain walls, 532, 533, 538, 542, 548, 550, 552–556
DOS. *See* Density of states (DOS)
DPN. *See* Dip-pen nanolithography (DPN)
Drude model, 388
Dual carbon electrodes (DCE), 625
Dynamic atomic force microscopy (dynamic AFM), 494, 497

E
EBID. *See* Electron beam-induced deposition (EBID)
EBL. *See* Electron beam lithography (EBL)
ECDL. *See* Electrochemical double layer (ECDL)
EC-STM. *See* Electrochemical scanning tunnelling microscopy (EC-STM)
EDS. *See* Energy-dispersive X-ray spectroscopy (EDS/EDX)
Effective mass, 369, 374, 381, 382, 386, 388, 389, 391
EIS. *See* Electrochemical impedance spectroscopy (EIS)
E-K. *See* Energy-momentum (*E-K*) dispersion relation
Electrocatalysis, 14–37
Electrochemical double layer (ECDL), 3, 7, 12–14, 49, 52, 54, 61
Electrochemical etching, 230
Electrochemical impedance spectroscopy (EIS), 52, 54
Electrochemical polishing, 232
Electrochemical scanning tunnelling microscopy (EC-STM), 2–61
Electron beam-induced deposition (EBID), 93, 95, 105–107
Electron beam lithography (EBL), 93–95, 97, 99, 103, 105, 107
Electron microscopy (EM), 228, 229
Electron orbital, 562–564, 567, 568, 575, 579, 580, 583, 586, 587, 591, 592, 594–610
Electron-phonon coupling, 382
Electron transfer (ET), 4, 9–12, 37, 38, 40–50, 52–54, 56, 58–61
Electropolymerization, 211, 218–220
Electrostatic forces, 466
EM. *See* Electron microscopy (EM)
Energy-dispersive X-ray spectroscopy (EDS/EDX), 95
Energy-momentum (*E-K*) dispersion relation, 371, 385, 386
ET. *See* Electron transfer (ET)
Excitation energy-dependent PES, 381
External photoemission, 370, 372, 373, 398

F
FAD. *See* Flavin adenine dinucleotide (FAD)
FDM. *See* Field desorption microscopy (FDM)
FEBID. *See* Focused electron beam-induced deposition (FEBID)
FEBIP. *See* Focused electron beam-induced processing (FEBIP)
Felling method, 545–555
FEM. *See* Field emission microscopy (FEM)
Femtosecond pump-probe microscope (FPM), 94, 102
Fe-protoporphyrin IX (FePP), 38, 39, 42–47, 52
Fermi energy, 407, 409, 414, 418, 425, 428
Fermi energy of the tip (E_F^{tip}), 11
Fermi level, 372–375, 391, 394, 395
Fermi's golden rule, 370, 382
Ferroelectric lithography (FL), 100
Ferroelectric surfaces, 406–455
Few-layered graphene (FLG) film, 136
FFM. *See* Friction force microscopy (FFM)
FIAE. *See* Field ion appearance energy (FIAE)
FIAES. *See* Field ion appearance energy spectroscopy (FIAES)
FIB. *See* Focused ion beam (FIB)
Field-desorbed ions, 234–238
Field desorption microscopy (FDM), 227–231, 234, 236, 250–259
Field effect, 260, 265
Field electron emission microscopy (FEEM), 570
Field emission, 169, 176, 178, 183
Field emission microscopy (FEM), 229–231, 244, 245, 248, 249, 260, 262, 622–641
Field ion appearance energy (FIAE), 233, 240, 258, 260
Field ion appearance energy spectroscopy (FIAES), 228, 229, 231, 238–241, 256–262
Field ionization, 164–165
Field ion mass spectrometry (FIMS), 238, 257
Field ion microscopy (FIM), 159–193, 228, 232–234, 263, 264, 569, 570, 622–641
Field ion-scanning tunneling microscopy (FI-STM), 182
FIMS. *See* Field ion mass spectrometry (FIMS)
Finite element simulation models, 633, 634, 636
FL. *See* Ferroelectric lithography (FL)
Flavin adenine dinucleotide (FAD), 37, 41, 47, 52
Flood gun, 376
Fluctuation-induced effects, 247–250
FM. *See* Frequency modulation (FM)
FM growth. *See* Frank-van der Merwe (FM) growth
Focused electron beam-induced deposition (FEBID), 93, 105, 107, 109, 533–540, 542, 545, 548, 550, 551, 553, 555
Focused electron beam-induced processing (FEBIP), 95–96, 106–107
Focused ion beam (FIB), 479–480, 484, 534, 545
Force field protocol, 175–181, 184, 192
Fourier transform, 71, 72, 77
FPM. *See* Femtosecond pump-probe microscope (FPM)
Frank-van der Merwe (FM) growth, 16
Free ferroelectric surfaces, 406, 415, 422–424, 429–431, 443–445, 454, 455
Frequency modulation (FM), 221, 277, 278, 282, 484
Frequency modulation KPFM (FM-KPFM), 118, 124–125, 128–130, 132, 133
Friction force microscopy (FFM), 275, 297
Fuel cells, 15, 18

G
Gas injection systems (GIS), 534, 540, 551
Gas-phase electron beam-induced deposition (GEBID), 105
Gauss's law, 121
GCS model. *See* Gouy-Chapman-Stern (GCS) model
Gerischer's theory, 11, 45
Gibbs energy, 15
GIS. *See* Gas injection systems (GIS)
Glucose oxidase (GOx), 37, 39, 41, 47, 48, 50–53, 58
Gold substrates, 27–33, 42
Gouy-Chapman-Stern (GCS) model, 12, 13
Graphene, 565, 608–610

H
Haar wavelet analysis, 249
Hamaker constant, 75, 79–82, 84, 85
Hamaker-type interaction model, 280
Hard X-ray photoelectron Spectroscopy (HXPES), 321, 357–362
HER. *See* Hydrogen evolution reaction (HER)
Highest occupied molecular orbital (HOMO), 375, 380, 383–385, 394, 420

Highly oriented pyrolytic graphite (HOPG), 9, 10, 33, 39, 42, 44, 45, 50–58, 60, 182, 185, 290, 291, 293–295, 298, 300, 582–585, 604–609
Hole mode AFM, 285–288
HOMO. *See* Highest occupied molecular orbital (HOMO)
Honeycomb-chained-trimer (HCT) model, 282
HOPG. *See* Highly oriented pyrolytic graphite (HOPG)
Hopping mobility, 387, 388
Horseradish peroxidase (HPR), 4, 39, 41, 42, 54–58, 60, 61
HXPES. *See* Hard X-ray photoelectron Spectroscopy (HXPES)
Hydrogen evolution reaction (HER), 8, 15, 16, 19, 28, 29, 32, 60
Hydrogen oxidation reaction (HOR), 8, 15, 16, 28, 29, 32, 60

I
Ice lithography, 107
IET model. *See* Inequivalent trimer (IET) model
IHP. *See* Inner Helmholtz plane (IHP)
Imaging forces, 70–87
IMFP. *See* Inelastic mean free path (IMFP)
Immersed finite element method (IFEM), 625
Immersed molecular electrokinetic finite element method (IMEFEM), 625
Indentation lithography (IndL), 100–101
Independent atomic center (IAC) model, 372
Indium tin oxides (ITO), 418, 419, 423
IndL. *See* Indentation lithography (IndL)
Inelastic mean free path (IMFP), 372, 373
Inequivalent trimer (IET) model, 282
Inner Helmholtz plane (IHP), 12
Inner shell photoemission process, 411
Insulators, 575–576
Interface state (IS), 394
Intermittent contact mode AFM, 495, 503
Inter-potential, 374
Inter-track interference, 468
Inverse photoelectron spectroscopy (IPES), 398
Ionic crystal surfaces, 288–290, 292, 299
Ionization energy, 375, 379, 380, 383, 384

J
Joule-heat exchange method, 97
Jump-to-contact method, 18, 33, 35, 279

K
Kelvin probe force microscopy (KPFM), 94, 100, 118–154, 210, 625
Kelvin probe lithography (KPL), 100
Kelvin probe method, 118–127
Kerr microscopes, 464
Kinetic energy (KE), 410, 411, 413, 437
Kondorsky propagation model, 549, 550
KPFM. *See* Kelvin probe force microscopy (KPFM)

L
Landau–Ginsburg–Devonshire theory, 432
LAO. *See* Local anodic oxidation (LAO)
Laplace's equation, 628, 631, 633, 638
Larmor frequency, 509, 510
Laser-assisted electron beam-induced deposition (LAEBID), 96, 107
Layer-by-layer method, 280, 281, 294, 299, 300
LDOS. *See* Local density of states (LDOS)
Lead composite, 27–28
LEAP. *See* Local-electrode atom probe (LEAP)
LEED. *See* Low-energy electron diffraction (LEED)
Legendre polynomials, 630–632
Li FDM. *See* Lithium field desorption microscopy (Li FDM)
Linear superposition approximation (LSA), 13
Linear sweep voltammograms (LSV), 625
Liquid-phase electron beam-induced deposition (LPEBID), 93, 95, 105–106
Lithium field desorption microscopy (Li FDM), 228–231, 234, 236–238, 252, 254, 255, 259
Local anodic oxidation (LAO), 94, 100
Local contact potential difference (LCPD), 151–154
Local density of states (LDOS), 9, 10, 566, 579, 580, 588–590, 595, 602, 603
Local-electrode atom probe (LEAP), 231, 238, 258, 263
Localized thermal analysis (LTA), 97
Local-oxidation lithography, 99
Longitudinal magnetic recording media, 467–470
Lorentz transmission electron microscopy (Lorentz TEM), 464
Low-energy electron diffraction (LEED), 415, 434, 437
Low-energy electron microscopy (LEEM), 423

Low-energy ion scattering (LEIS), 415
Low temperatures (LTs), 566
LPEBID. *See* Liquid-phase electron beam-induced deposition (LPEBID)

M
Macroscopic rate law, 228, 247–248
Madelung surface potential, 152
Magnetic exchange force microscopy (MExFM), 498–500, 515–518
Magnetic exchange force spectroscopy (MExFS), 516, 517
Magnetic force microscopy (MFM), 463–484, 490–518, 533, 535–538, 550, 552–556
Magnetic moment, 499, 500, 502, 504–509
Magnetic recording, 466–474, 483
Magnetic resonance (MR), 498, 509, 512, 513
Magnetic resonance force microscopy (MRFM), 491, 498–500, 509–515, 518
Magnetic sector field atom-probe (MSAP), 238, 239
Magnetic thin films, 504, 505
Magnetic vortex, 475, 476
Magnetization, 465–468, 470, 474, 476, 478, 481–484, 490, 491, 498, 500–507, 510, 512
Magneto-optical Kerr effect (MOKE), 533, 535–537, 540–545, 548–550, 555
Magnetotactic bacteria, 479
Marcus electron transfer theory, 387
Marcus theory, 37
Maximum force-modulated current-sensing, 222–223
Maxwell-Boltzmann velocity distribution, 179
MBE. *See* Molecular beam epitaxy (MBE) method
Mean-field theory, 244, 249
Medium-energy ion scattering (MEIS), 415
Metal-ferroelectric interfaces, 406–455
Metallic nanostructures, 137–138
Metalloproteins, 12, 37, 38, 41, 42, 61
Metal-mesh lithography, 97
Metal oxide surfaces, 284–288, 591, 594–596
Metal-semiconductor interfaces, 407–455
Metal single-crystal surfaces, 15, 16
MExFM. *See* Magnetic exchange force microscopy (MExFM)
MFM. *See* Magnetic force microscopy (MFM)
Microchannel plates (MCPs), 163, 165, 176, 626
Micromanipulators, 534, 537, 545–548, 551, 555
Mirror electron microscopy (MEM), 423
Mobility, 381, 383, 384, 387, 388
MOKE. *See* Magneto-optical Kerr effect (MOKE)
Molecular beam epitaxy (MBE) method, 412, 415, 416
Moore's law, 92, 107
MPL. *See* Multiphoton lithography (MPL)
MRFM. *See* Magnetic resonance force microscopy (MRFM)
MSAP. *See* Magnetic sector field atom-probe (MSAP)
Multiphoton lithography (MPL), 95, 102–103
Multiwall carbon nanotubes (MWNTs), 262

N
Nanocrystals, 320, 353
Nanodot arrays, 473, 474
Nanoelectronics, 532, 536, 555
Nanofabrication, 622–624
Nanomaterials, 318–362
Nanomechanics, 174, 193
Nanoparticles deposition, 17–18
Nanopillar arrays, 216–218
Nanotip and coil (NTC), 625
Nanotips, 622–641
Nanotriboelectrification, 134, 135
Nanowires, 532, 533, 536–556
NC-AFM. *See* Noncontact atomic force microscopy (NC-AFM)
Near ambient pressure XPS (NAP-XPS), 349
Near-field scanning optical microscopy (NSOM), 625
Neutral mode AFM, 286–288
Nitrogen etching, 174
Noncontact atomic force microscopy (NC-AFM), 273–304
Non-contact mode, 202, 203, 495, 503, 515–517

O
OFET. *See* Organic field effect transistor (OFET)
OFSL. *See* Optical force stamping lithography (OFSL)
OLED. *See* Organic light-emitting diode (OLED)
Omniprobe®, 545
One-electron model, 372
OPD. *See* Overpotential or bulk deposition range (OPD)

Open circuit potential (OCV), 13, 59
Optical force stamping lithography (OFSL), 94, 101–102
Orbital tomography, 383
Organic electronics, 201, 218, 368, 389, 398, 399
Organic field effect transistor (OFET), 148, 381, 382, 388, 398
Organic light-emitting diode (OLED), 369, 398
Organic semiconductors, 367–399
Organic solar cells (OSCs), 147
Outer Helmholtz plane (OHP), 12
Overcompensation, 433, 447, 452, 454
Overpotential or bulk deposition range (OPD), 17, 18
Oxidation scanning probe lithography (OSPL), 94, 99

P
Palladium deposition, 18–19
Partial density of electron states (PDOS), 588, 600, 602, 604–606, 610
Particle-in-a-box, 389
Patterned media, 471–474, 483
Pauli repulsion, 391
PCET. *See* Proton-coupled electron transfer (PCET)
PCM. *See* Phase change memory (PCM)
PDOS. *See* Partial density of electron states (PDOS)
PeakForce tapping (PFT) mode, 123, 133
PEEM. *See* Photoemission electron microscope (PEEM)
Pentacene, 377, 380–383
Perpendicular magnetic anisotropy (PMA), 465, 470, 479, 481–484
Perpendicular magnetic recording media, 465, 470–472, 483
PES. *See* Photoelectron spectroscopy (PES)
PFDMS. *See* Pulsed field desorption mass spectrometry (PFDMS)
PFM. *See* Piezoresponse force microscopy (PFM)
Phase change memory (PCM), 108
Phase shifts, 389, 390, 392, 393, 396
Phenyl-capped aniline tetramer (PCAT), 420–421
Photocatalytic lithography, 95, 104
Photoelectric effect, 411
Photoelectrons, 370, 372–379, 383, 384, 387, 392
Photoelectron spectroscopy (PES), 368–376, 379–382, 384, 385, 389–391, 395–398
Photoelectron yield spectroscopy (PYS), 377–380, 383, 384, 397
Photoemission analysis, 445
Photoemission electron microscope (PEEM), 241
Phthalocyanine, 393–395
Piezoelectric bimorph, 71
Piezoresponse force microscopy (PFM), 423, 443, 446, 451
Plasma treatment, 418, 421
Platinum substrates, 18–27
PLD. *See* Pulsed laser deposition (PLD)
PMA. *See* Perpendicular magnetic anisotropy (PMA)
POD. *See* Proper orthogonal decomposition (POD)
Poisson distribution, 180
Poisson equation, 424–426, 431, 432
Polymer-pen lithography (PPL), 94, 97
Probe-hole ion analysis, 238, 256–262, 264
Probe-sample-force, 492, 494–497, 499, 502, 516
Proper orthogonal decomposition (POD), 249
Proton-coupled electron transfer (PCET), 38
Protrusion mode AFM, 285–288
P-stacking, 381
Pulsed field desorption mass spectrometry (PFDMS), 231, 246, 257
Pulsed laser deposition (PLD), 415, 417, 422, 432, 443
PYS. *See* Photoelectron yield spectroscopy (PYS)

Q
QSE. *See* Quantum size effect (QSE)
Quality factor *(Q),* 278, 279, 281
Quantization energy, 389, 396
Quantum-mechanical theory, 264
Quantum size effect (QSE), 389, 395, 396, 399
Quantum tunneling effect, 275
Quantum well resonance (QWR), 389, 391, 393
Quantum wells (QWs), 368, 389–397
QWR. *See* Quantum well resonance (QWR)

R
Radiation damage, 398
Reflection high-energy electron diffraction (RHEED), 415, 417

Relaxation time, 388
Reorganization energy, 388
Residual gas analysis, 415
Resonance frequency (f_0), 277–279
Resonant slice, 510–512, 514
Resonant tunnelling, 11, 39, 45, 46
Ring counting method, 169–173
Rock magnetism, 466, 479
Room temperature (RT), 566
Rubrene, 369, 380, 381, 383–388, 397, 398

S
SAM. *See* Self assembled monolayers (SAM)
Sample charging problem, 376, 380
SATs. *See* Single-atom tips (SATs)
Scanning atom probe (SAP), 229
Scanning conductive torsion mode microscopy, 199–223
Scanning electrochemical microscopy (SECM), 94, 99
Scanning electrochemical potential microscopy (SECPM), 2–61
Scanning electron microscopy (SEM), 534, 537, 538, 540, 544, 546, 551, 552, 570, 572, 622, 624
Scanning force microscopy (SFM), 49
Scanning ion conductance microscopy (SICM), 94, 99
Scanning Kelvin probe microscopy (SKPM), 118
Scanning near-field optical lithography (SNOL), 103–104
Scanning near-field optical microscopy (SNOM), 95, 103, 104
Scanning near-field photo-lithography (SNPL), 95
Scanning potential microscopy (SPoM), 118–119
Scanning probe acceleration microscopy (SPAM), 70–87
Scanning probe block copolymer lithography (SPBCL), 94, 96–97
Scanning probe lithography (SPL) process, 91–94, 96–104, 107–109
Scanning probe microscopy (SPM), 3, 15, 17, 33–37, 42, 60, 61, 91–109, 118, 127, 160–164, 168, 173–178, 180, 182–189, 192, 193, 220, 229, 263, 264, 274, 293, 490, 491, 495, 563, 581, 596, 609
Scanning thermal lithography (SThL), 94, 97
Scanning thermal twisted microscopy (STTM), 94, 98–99
Scanning transmission electron microscope (STEM), 93
Scanning tunneling atom probe (STAP), 183
Scanning tunneling hydrogen microscopy (STHM), 569, 570
Scanning tunneling microscopy (STM), 3–9, 13, 18, 22, 23, 25, 27, 28, 32–36, 43, 44, 228–230, 241, 265, 266, 275, 278, 282, 284, 285, 287, 288, 415, 416, 562–610
Scanning tunneling spectroscopy (STS), 182, 183, 423, 566, 568–570, 573, 575, 582
Schmickler's model, 45
Schottky barrier, 406–408, 419, 422, 424, 426–428, 431, 434–443
Schottky diodes, 407, 408, 421, 446
SECO. *See* Secondary electron cutoff (SECO)
Secondary electron, 372
Secondary electron cutoff (SECO), 375
Secondary ion mass spectroscopy (SIMS), 415
SECPM. *See* Scanning electrochemical potential microscopy (SECPM)
Self assembled monolayers (SAM), 39, 40, 43, 48, 61, 420
Self-assembly molecules
SEM. *See* Scanning electron microscope (SEM)
Semiconducting nanostructures, 139
Semiconductors, 573–575, 579, 591–592
SFD. *See* Switching field distribution (SFD)
SFM. *See* Scanning force microscopy (SFM)
Shockley surface state, 390, 391
Silicon atoms, 573, 596–599
Silver composite, 27–28
Simmons–Schottky model, 423
Single-atom tips (SATs), 174, 175, 623, 624, 626–629, 636–638, 641
Single crystal diamond tips, 606–608
Single-crystal surfaces, 33, 35–37
Single nanowire (SNW), 625
Single-wall carbon nanotubes (SWNTs), 139–141, 147–149, 263
SK mode. *See* Stranski–Krastanov (SK) mode
SLRR. *See* Surface-limited redox replacement (SLRR)
Soft materials and fragile structures, 200–202, 204, 221, 223
Spatial resolution, 562–564, 566–570, 576, 578–580, 582, 598, 606, 608, 609
Spin, 490, 498–500, 509–518
Spin mapping, 498, 515–518
Spintronics, 490, 509, 518, 532, 533, 538
SPL. *See* Scanning probe lithography (SPL) process

SPM. *See* Scanning probe microscopy (SPM)
Spring constant *(k),* 279
STM. *See* Scanning tunneling microscopy (STM)
Stranski–Krastanov (SK) mode, 17
Structure-properties relationship, 200, 201, 211–216
Sub-bands, 389, 391, 393, 396
Superparamagnetic nanoparticles, 501, 503, 506–508, 518
Supported lipid bilayer, 72, 76, 85, 86
Surface chemistry, 229, 231, 238, 240–247
Surface-limited redox replacement (SLRR), 17, 29, 30
Surface-sensitive, 372, 376
Switching field distribution (SFD), 466, 472–474
SWNTs. *See* Single-wall carbon nanotubes (SWNTs)
Synchrotron X-ray photoelectron spectroscopy (Synchrotron XPS), 318–362

T
Tapping-mode atomic force microscopy (TMAFM), 70–78, 80, 81, 83, 84, 87
TEM. *See* Transmission electron microscopy (TEM)
Tetratetracontane (TTC), 390–393, 396
Thermal averaging effect, 282
Thermal dip-pen technique (t-DPN), 96
Thermal treatment, 437–443, 445, 450, 453, 454
Thermofield annealing, 175
Thin-film field effect transistors (TFTs), 148, 149
3-D atom-probe tomography (3-D APT), 257–258
Three-dimensional devices, 533
Three-dimensional force spectroscopy, 292–300
Three-step model, 370
Tight-binding, 382
Time-of-flight spectroscopy, 231, 238
Time-resolved tip/sample force, 70–72, 75–79, 81–85
Tip-adatom system, 589
Tip characterization, 163, 182, 189
Tip-sample interaction, 562, 575, 578, 580, 581, 583, 587, 588, 592, 594, 598, 606, 608
Tip-surface distance, 566, 580, 585, 605, 610
Topography, 200, 201, 203–206, 209, 210, 212, 213, 215–217, 219, 221, 222
Torsional resonance, 201, 203, 207, 221
Transfer integral, 369, 382, 385–387
Transition dipole moment, 371, 372
Transmission electron microscopy (TEM), 571, 572, 605, 622, 624
TTC. *See* Tetratetracontane (TTC)
Tungsten tips, 569, 571, 572, 574, 581–583, 587, 591, 594, 597, 601, 604–606, 608, 609
Tunneling current, 563, 565–569, 582, 585–592, 597, 598, 600, 601, 604, 605
Two pass scanning method, 466

U
Ultrahigh vacuum (UHV), 3, 161, 168, 175, 176, 178–182, 191, 192, 566, 568–572, 604, 624, 626
Ultraviolet PES (UPS), 371, 372, 376
Ultraviolet photoelectron spectroscopy (UVS), 415
Under-compensation, 454
Underpotential deposition range (UPD), 17–19, 27
Universal curve, 373
UPS. *See* Ultraviolet PES (UPS)

V
Vacuum level, 372, 374, 375, 379, 380, 383, 384
Valence band, 367–399
van der Waals interaction, 75
Vertical excitation, 371
Vibrating sample magnetometer (VSM), 471
Virtual probe-hole technique, 250
Volmer-Weber (VW) growth, 16–17

W
Wide-area adjacent track erasure (WATER), 470–471
Work function, 373, 374, 389–391

X
XPS. *See* X-ray photoelectron spectroscopy (XPS)
X-ray diffraction (XRD), 474, 483
X-ray photoelectron diffraction, 452, 455
X-ray photoelectron spectroscopy (XPS), 372, 376, 406–455

Y
Young's modulus, 71, 75, 76, 78–86